Innovative Self-centering Connection for CCFT Composite Columns

Yu Gao

Dissertation submitted to the academic faculty of the Virginia Polytechnic Institute and State University in partial fulfillment of the requirements for the degree of

Doctor of Philosophy
in
Civil Engineering

Roberto T. Leon, Chair
Matthew R. Eatherton
Finley A. Charney
Cristopher D. Moen
Ioannis Koutromanos

December 17, 2015
Blacksburg, Virginia

Keywords: Earthquake Engineering, Seismic Design, Partially Restrained Connection, Self-centering System, Shape Memory Alloy, Circular Concrete Filled Steel Tube

Innovative Self-centering Connection for CCFT Composite Columns

Yu Gao

ABSTRACT

Concrete filled steel tubes are regarded as ideal frame members in seismic resisting systems, as they combine large axial and flexural capacity with ductility. The combination of the two materials increases the strength of the confined concrete and avoids premature local buckling of the steel tube. These benefits are more prominent for circular than for rectangular concrete filled steel tubes. However, most common connection configurations for circular concrete filled tubes are not economic in the US market due to (a) the desire of designers to use only fully restrained connections and its associated (b) high cost of fabrication and field welding. Research indicates that well designed partially restrained connections can supply equal or even better cyclic behavior. Partially restrained connections also possess potential capability to develop self-centering system, which has many merits in seismic design.

The goal of this research is to develop a new connection configuration between circular concrete filled steel columns and conventional W steel beams. The new connection configuration is intended to provide another option for rapid assembling on site with low erection costs. The proposed connection is based on an extended stiffened end plate that utilizes through rods. The rods are a combination of conventional steel and shape memory alloy that provide both energy dissipation and self-centering capacity. The new connection configuration should be workable for large beam sizes and can be easily expanded to a biaxial bending moment connection.

ACKNOWLEDGEMENTS

I had much help in completing this research study. First of all, I would like to thank my advisor, Dr. Roberto Leon, for the opportunity of this interesting and challenging project. Dr. Leon guided me on how to do research with his great patience and rich experience. I was a solver for specific problems before I worked with him, it did take me a long time to figure out how to find out problems by myself. In the end, I find that in addition to the countless thoughtful and inspiring ideas he gave me, the most important thing he taught me is how to think independently. I believe that what I learnt from him will have a far-reaching influence throughout my entire life.

I am grateful my graduate committee for their suggestions and kindness. They were always ready to help me when I got in trouble. Thanks to Dr. Matthew Eatherton for his "Shape Memory Alloy" material model in OpenSees, which was very important for me to complete this research study on schedule. Thanks to Dr. Finley Charney for his great classes to help me understand many key concepts on seismic design. Thanks to Dr. Cristopher Moen for his guidance on the 2013 international cold formed steel design competition and his help on my job applying process. And thanks to Dr. Ioannis Koutromanos for his great course to help me understand many important concepts on finite element analysis and thanks for his care about my research progress.

I would like to acknowledge all my friends and colleague for their self-giving help. Thanks to my best friend Dr. Chia-hung Fang (Kenny) for his great encouragement, precious suggestions and indispensable care on my research and daily life. Thanks to Dr. Johnn Judd for his patient explanations of many complicated concepts and many thoughtful discussions. Thanks also to Jeena Jayamon for her valuable help and suggestions. And thanks to all my other friends, especially Dr. Youyou Cao, for the great happiness they brought into my life.

I would like to give my sincere appreciation to my family for their comprehension and accompany during these bitter-sweet days. Their unwavering support and trust gave me the courage and freedom to pursue my aims and to achieve my self-actualization.

TABLE OF CONTENTS

APPENDICES

LIST OF FIGURES

LIST OF TABLES

ABBREVIATIONS

45SL	45 Degree Angle
2D	2 Dimensional
3D	3 Dimensional
AF	Axial-Flexural
AFS	Axial-Flexural-Shear
AHSL	Approximate Horizontal Straight Line
ASD	Allowable Strength Design
BBC	Biaxial Bending Connection
BIKM	Beam-IK Model
CCFT	Circular Concrete Filled Steel Tube
CDPM	Concrete Damaged Plasticity Model
CFB	Collar Flange Bottom
CFT	Concrete Filled Steel Tube
CSBF	Composite Special Braced Frame
CSMF	Composite Special Moment Frame
DOFs	Degrees of Freedom
EEC	Extended End plate Configuration
ELFM	Equivalent Lateral Force Method
FE	Finite Element

FEA	Finite Element Analysis
FR	Fully Restrained
FS	Full Strength
GFS	Gravity Frame System
GSR	Global Strength Ratio
HCC	Highly Confined Concrete
LRFD	Load and Resistance Factor Design
LFRS	Lateral Force Resistance System
M1-CIKM	Modified Column-IK-Model based on “Method 1”
M2-CIKM	Modified Column-IK-Model based on “Method 2”
MR	Moment Rotation
MRR	Moment Rotation Relationship
NPSC	New Proposed Smart Connection
NRHA	Nonlinear Response History Analyses
OCIKM	Original-Column-IK Model
PBD	Performance Based Design
PDP	Preliminary Design Procedure
PHC	Plastic Hinge of CCFT Column
PHR	Plastic Hinge of the RBS
PR	Partially Restrained
PS	Partial Strength

PT	Post-tensioned
RBS	Reduced Beam Section
RC	Reinforced Concrete
RCFT	Rectangular Concrete Filled Steel Tube
RDC	Rigid Diaphragm Constraints
RPM	Rigid Plastic Method
SBIKM	Strong-Beam-IK Model
SC	Self-centering
SCFT	Square Concrete Filled Steel Tube
SCM	Strain Compatibility Method
SFRS	Seismic Force Resistance System
SMA	Shape Memory Alloy
SP	Simple / Pinned
SSM	Simplified Spring Model
UBC	Uniaxial Bending Connection

Chapter 1

Introduction

1.1 Research Background

Since the use of *Concrete Filled Steel Tubes* (**CFTs**) was first proposed and applied in the early 1900s [1], CFTs have been used as structural components with large axial forces and moments in *gravity frame system* (**GFS**) and *seismic force resistance system* (**SFRS**). These structural members exhibit high load bearing capacity, high strength to weight ratio, large stiffness and ductility, excellent energy dissipation capacity, and good structural fire behavior [1]. Many of these characteristics make CFTs ideal for seismic design. In CFTs, the steel works primarily in tension and the concrete in compression, using their properties most favorably and resulting in very economical components. The steel tube is also used as permanent formwork for the infill concrete, reducing construction cost and accelerating the construction process.

Usually CFTs are classified into two categories: *Circular CFTs* (**CCFTs**) and *Rectangular CFTs* (**RCFTs**), which includes *Square CFTs* (**SCFTs**). Many theoretical and experimental studies show that for seismic resistance (strength, ductility, and energy dissipation), CCFTs provide better performance than RCFTs. This is due primarily to the CCFTs' better confinement effects on concrete due to their circular shape, which results in CCFTs having a higher

confinement and bond stress than RCFTs (Figure 1-1). As interaction is key to the performance of composite systems, bond is a key factor to ensure composite behavior between two materials. The AISC specification [2] allows to use $0.95f_c'$ as the concrete strength for CCFTs rather than $0.85f_c'$ for RCFTs to distinguish their confinement effects; however, it has not recognized the benefit from higher bond stress yet [3]. CCFTs have the same flexural strength in each direction due to their circular cross sections, which makes them the most ideal members for biaxial bending and thus for use in 3D moment frame structures.

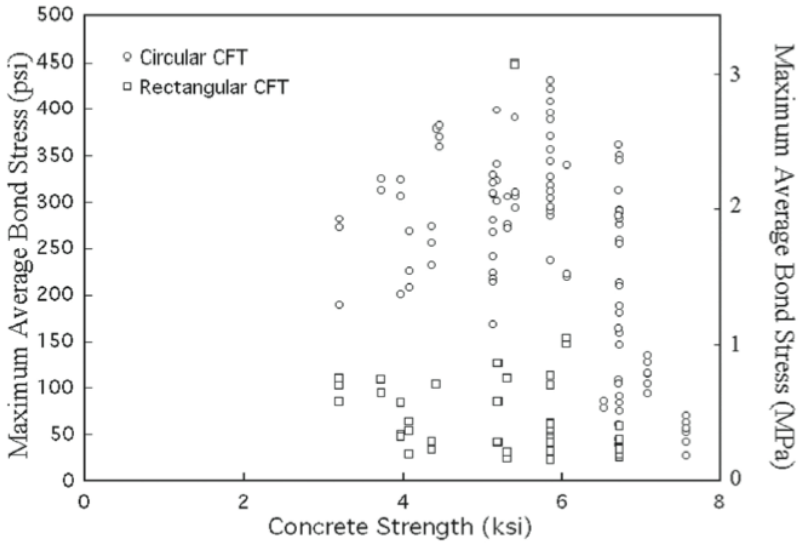

Figure 1-1: Measured average bond stress capacity as a function of concrete strength [4]

Although CCFTs possess many advantages, one main reason that designers choose RCFT columns over CCFT ones, or do not use CFTs at all, is their inherent difficulties in connecting a circular tube to other components such as W steel beams. Thus, in order to take advantage of these merits of CCFTs, it is necessary to find more reliable and economic connecting methods

between a CCFT column and other conventional shapes. In particular, better connecting methods for biaxial bending will promote a much broader application of CCFT columns.

Connections can be categorized by stiffness as *fully restrained* (**FR**), *partially restrained* (**PR**), or *simple*/*pinned* (**SP**) connections according to how much moment they can transfer at a given rotation. A large body of research [5-7] indicates that compared with their FR counterparts, well-detailed PR systems can supply similar or even superior seismic performance. This benefit is brought by the combination of three effects: (a) PR systems will decrease the structure demands as they exhibit longer natural periods; (b) PR systems distribute the strength and resistance throughout the structure as more connections are needed to provide the required stiffness; and (c) PR connections will exhibit better structural strength reserve capacity with a lower probability of brittle failure [8]. Moreover, the superior cyclic performance of PR connections also brings the potential capability for self-centering, which has become a very important research field in structural systems recently. A structure with self-centering ability will have less residual deformation after an earthquake, and damage to both structural and nonstructural components of the building may be reduced. Simultaneously, the probability of losing building functionalities will also be reduced and result in more rapid recovery. Damage limitation and speedy recovery are design objectives consistent with next generation design concepts. i.e., seismic *performance based design* (**PBD**) and *community resilience*.

However, until recently nearly all research on self-centering structures has been focused on

either concrete or steel structures. Relevant research on structural systems with composite columns and beams, especially CCFT columns, is scant in the US [9]. This knowledge gap has limited the development and application of CCFT columns, and also their benefits on both economics and seismic performance. This gap has been exacerbated by the lack of enabling code provisions for connections between CFT columns and other components.

In order to take full advantage of all merits of CCFT columns and promote their comprehensive application in the future, an innovative self-centering PR connection for uniaxial bending between a CCFT column and W steel beams will be developed, designed and analyzed in this research. The seismic performance of composite special moment frames with CCFT columns and *new proposed smart connections* (**NPSCs**) will also be evaluated.

1.2 Research Objectives

This thesis intends to develop a connection with radically different performance characteristics from those in use today in special moment resisting frames. The expected performance for this connection can be summarized as follows:

- The connection will avoid any brittle failure modes that may occur due to poor QA/QC issues by minimizing the use of any demand critical welds. An end plate connection will be used for the beams as this type of connection has been shown to be the most robust of the connections tested as part of the SAC project. The demand input into the

connection will be controlled through the use of a reduced bam section (RBS) in the beams in the region immediately adjacent to the joint.

- The connection will be designed to provide a large overstrength both for column flexural and joint shear capacity. These characteristics can be easily extended to the biaxial case, allowing for the development of true 3D frame action, in addition to making possible much longer clear spans.
- The connection will be very ductile through the use of shape memory alloy (SMA) components working in tension. The characteristics of this material provide a predictable long deformation plateau through phase transformation at a relative low percentage of its ultimate strength. This property will allow for "tuning" the amount of drift coming from the connection and the adjacent RBS beam plastic hinges to minimize any permanent deformations from earthquakes below the MCE level.
- The connection will provide recentering capacity up to the MCE level. This means that damage to deformation-controlled non-structural elements will be minimized and residual deformations will be well below the 0.5% limit proposed as the threshold for building demolition.
- The connection will provide energy dissipation through yielding of conventional steel rods in parallel with the SMA ones. The steel rods will be detailed to have an initial gap so that they do not engage until the SMA has reached its transformation plateau.
- If the MCE design ground motion is exceeded, the SMA components will revert to their original stiffness, providing limits to deformation and shifting the yielding to the

plastic hinges in the beams. In addition, they are expected to allow for interstory drifts at least twice that of a conventional moment frame. This effectively provides almost unlimited collapse protection.

- The connection will eliminate or limit any deterioration of its monotonic moment-rotation envelope to ensure maximum robustness.
- Should the design capacity for any of the key connection components be exceeded, the components should be easily replaceable.
- Finally, the connection should be economical and efficient to fabricate. This aspect, however, will not be the subject of this thesis, except to note that the connection details were developed with the advice of two fabricators familiar with seismic detailing.

The connection characteristics proposed above should approach those of the ideal connection in a moment frame. The development of this connection requires careful balancing between yielding in the joint and yielding in the RBS. The intent is that for low to moderate earthquake the connection provide full recentering and avoid significant yielding in the RBS; as the demands increase, some permanent residual deformation will be allowed mostly due to yielding in the RBS.

The objectives of this research study are as follows:

(1) Develop a new partially restrained connection configuration between CCFT columns and W steel beams that utilizes SMA for self-centering capacity.

(2) Propose a *Preliminary Design Procedure* (**PDP**) for designers for the *New Proposed Smart Connections* (**NPSC**).

(3) Propose a practical *2-Dimensional* (**2D**) *simplified spring model* (**SSM**) to simulate the cyclic behavior of the new proposed connection under uniaxial bending that minimizes the computational cost for analyses of large structures.

(4) Investigate possible failure modes of the NPSC by using *Finite Element Analysis* (**FEA**) to ensure a more reliable connection and provide a strong basis for practical design.

(5) Optimize the design parameters of the NPSCs to obtain superior seismic performance of self-centering CSMFs in order to promote the development and application of the self-centering CSMFs.

1.3 Research Methodology

Only a theoretical approach will be applied to complete the research on this NPSC as efforts to secure funding for large-scale experimental testing have not borne fruit. The bulk of the work conducted is described by the following tasks:

(1) Develop a preliminary configuration for the NPSC by discussing its feasibility with other researchers, fabricators, and detailers. A NPSC for biaxial bending is shown in Figure 1-2; and its counterpart for uniaxial bending is presented in Figure 1-4. The current proposed configuration is composed of: (1) a CCFT column with a collar, which is made of a rectangular steel tube, two inner steel diaphragms and infill expansive

grout; (2) two beams with RBS connected to the extended stiffened end plates by fillet welds; and (3) sixteen through rods connecting the end plates, including two SMA and two steel rods on each rod level (an eight rod pattern is introduced in Chapter 3 for small beams).

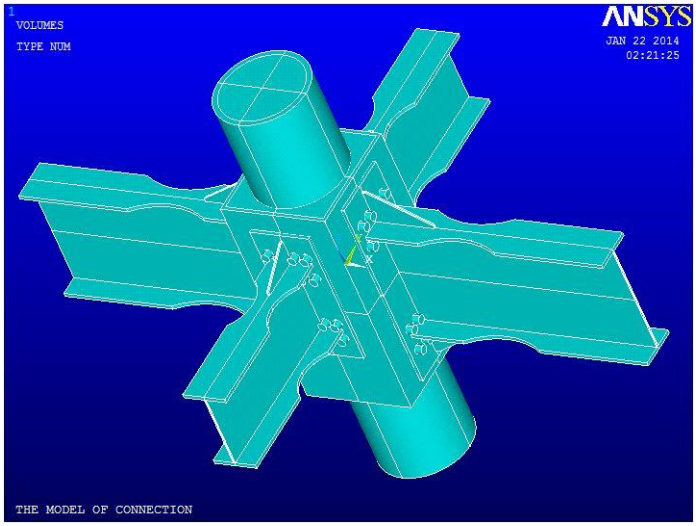

Figure 1-2: Proposed smart PR connection for biaxial bending

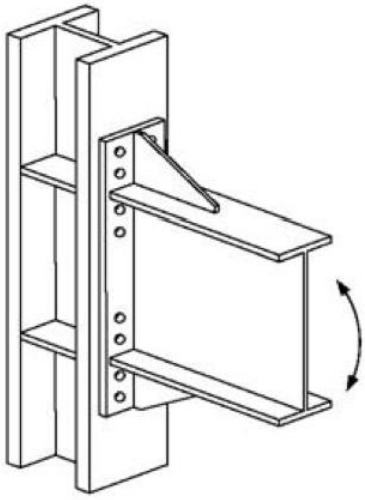

Figure 1-3: Prequalified 8-bolt extended stiffened end plate connectionb [10]

(2) Compare the NPSC with the current prequalified 8-bolt extended stiffened end plate connection in Figure 1-3 [10] to understand their similarities and differences. Based on these similarities and differences, a detailed preliminary design procedure for each component of the NPSC will be proposed.

(3) Establish a 2D-SSM to simulate the cyclic behavior of the NPSC for uniaxial bending (Figure 1-4) using Beam, Link, Hook, and Gap elements in SAP2000. As part of this task, a detailed procedure to calculate the properties of each element of the 2D-SSM

will be proposed. Due to the independency of bending in two directions with a similar behavior, the 2D-SSM is easy to expand for biaxial bending.

(4) Investigate all potential failure modes of the NPSCs under ultimate loading by using ABAQUS. The results are used to verify the effectiveness of the assumptions of the PDP and 2D-SSM.

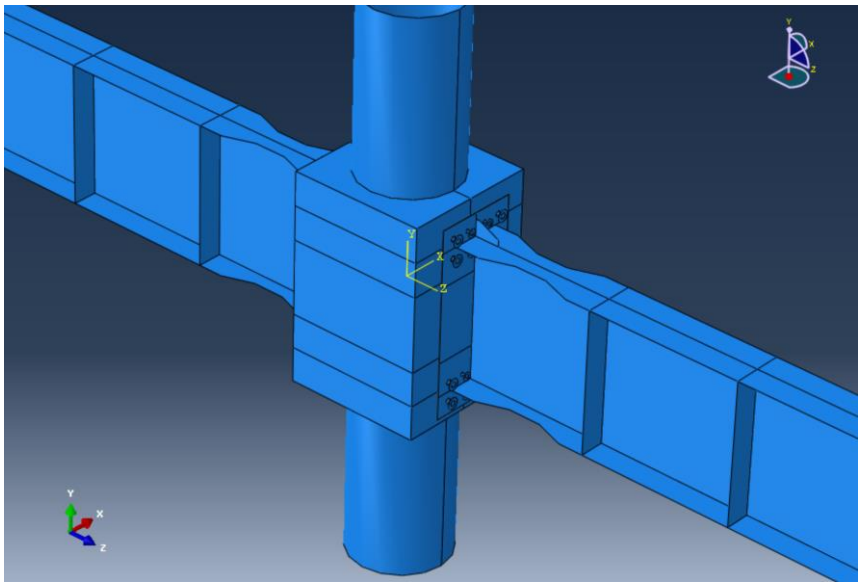

Figure 1-4: The new proposed smart connection for uniaxial bending

(5) Design two 2D composite special moment frames in SAP2000: (1) one has traditional FR moment connections; and (2) the other has the NPSCs. The columns will be CCFTs, and the beams are W steel beams with *reduced beam sections* (**RBS**).

(6) Carry out nonlinear static pushover analysis in OpenSees and conduct parametric studies to investigate the factors that influence the system's self-centering capacity.

(7) Assess whether current seismic design parameters (R, C_d, Ω_0) are applicable to the new

proposed self-centering CSMFs, through a limited study that parallels principles laid out in FEMA-P695 [11].

(8) Improve the preliminary design procedure and optimize the connection design, for best system performance under a far-field set of ground motions *nonlinear response history analyses* (**NRHA**) in OpenSees.

1.4 Original Contributions

This dissertation intends to provide the following original contributions:

(1) Augment research on *composite special moment frames* (**CSMFs**) with CCFT columns and *self-centering* (**SC**) capacity to promote a broader application of the CCFT columns and prefabricated connections in future structural seismic design in the USA.

(2) Develop and calibrate an original connection spring model in both SAP2000 and OpenSees. The model provides a simple method to simulate behavior of both (a) SMA through rods with pretensioning effect and (b) steel through rods with sliding and pretensioning effects.

(3) Promote the use of alternative materials such as shape memory alloys that possess great mechanistic advantages but which are not in use today due primarily to lack of design provisions and substantiated performance advantages.

1.5 Thesis Organization

The thesis will be composed of ten main chapters and thirteen appendices. The main chapters will include research background, literature review, design procedures, modeling, analyses and evaluation of results. Corresponding examples and detailed calculations will be presented in the appendices.

- Chapter 1 summarizes the motivation, objectives, methodology, expected original contributions, and overall organization of the proposed research.
- Chapter 2 presents an overview of the most relevant research to this thesis.
- Chapter 3 introduces the configuration of the new proposed smart connection (**NPSC**). It proposes design principles and a detailed design procedure for each component based on a simplified model. Two modified Sumner's equations for the end plate yield line mechanisms are derived in Appendix A, which are adopted by a new proposed step-by-step design procedure for an individual connection in Appendix B, and a detailed design example for an interior connection is presented in Appendix C. Several design methods for CCFT columns and a detailed example are supplied in Appendices D and E.
- Chapter 4 gives a detailed description of the 2D simplified model (2D-SSM) in SAP2000, including model components, model assemblage method, and detailed steps to calculate properties of each element. A detailed introduction for the CCFT column design method in AISC is supplied in Appendix F, which is used to decide the properties of CCFT columns. Details of a Modified-IK Model to determine the properties of RBS is presented in

Appendix G, and the analysis results of the connection 2D-SSM with beam plastic hinges are illustrated in Appendix H.

- Chapter 5 investigates potential failure modes to confirm the assumptions for the proposed design procedure and 2D-SSM by using ABAQUS. Current theoretical models for confined concrete by circular steel tubes are described in Appendix I. The concrete damaged plasticity model used in ABAQUS is discussed in Appendix J.
- Chapter 6 presents the design of two composite special moment frames based on the current seismic design provisions. Detailed design calculations are presented in Appendix K.
- Chapter 7 discusses nonlinear static pushover analyses carried out in OpenSees to examine the design results of the two CSMFs. A more advanced model for the new proposed connection considering weak panel zone effects is developed in OpenSees, and examples are supplied to verify its robustness.
- Chapter 8 examines the system's self-centering capacity based on nonlinear static pushover analysis. An effective method to allow for column separation control is discussed, and the effects of rigid diaphragm constraints on self-centering capacity are investigated.
- Chapter 9 presents nonlinear dynamic analyses to evaluate the system performance under both DBE and MCE level ground motions. The corresponding results are presented in Appendices L and M. These results are used to improve the preliminary design procedure.
- Chapter 10 summarizes this research and discusses further work needed.

Chapter 2

Literature Review

This chapter presents a brief review on relevant research for this work. Section 2.1 focuses on the benefits brought by CFTs, especially CCFTs, as applied in structural design. Section 2.2 illustrates connection categories and emphasizes the merits of PR connections. Section 2.3 reviews some common connection configurations for CCFTs. Section 2.4 introduces the development of self-centering systems in seismic design, an area of great research interest recently. Section 2.5 discusses SMA as a material which has great potential advantages to help develop new types of self-centering systems in civil engineering. Section 2.6 gives a summary for the whole chapter.

2.1 Concrete Filled Steel Tubes

Compared with conventional steel or reinforced concrete beam-columns, *concrete filled steel tubes* (**CFTs**) combine the large compressive strength of concrete and high ductility of steel members. In CFTs, the steel tube supplies both tensile capacity to the structural element and confinement for the inner concrete core; this confinement increases the concrete's compressive strength and ductility. In addition, due to the tough and ductile steel tube, the cracked concrete can carry shear and compression even after reaching its maximum capacity. On the other hand, the concrete prevents early inward local buckling of the steel tube wall under compression and

limits the damage to the steel member. The CFTs also have the required large stiffness to resist the lateral drift under seismic loadings for mid- to high-rise buildings in high seismic zones [12]. This makes them attractive members for seismic design.

Usually CFTs are classified into two categories: *Circular CFTs* (**CCFTs**) and *Rectangular CFTs* (**RCFTs**), which includes *Square CFTs* (**SCFTs**). Many research studies show that for the overall seismic resistance capacity (strength, ductility, energy dissipation, and fire behavior) CCFTs provide better performance than RCFTs based on both theoretical and experimental results because of CCFTs' better confinement effects on concrete. A complete summary of CFT research in a wiki at Northeastern University has been supplied by Hajjar et al. [13]. Among the historically important test series, that by Knowles and Park indicated that although confinement effect did occur when the slenderness of the concrete core is less than 44.3, the increase of axial strength for RCFTs with small slenderness ratio was still not obvious [14]. Tomii and Yoshimaro [15] conducted and reviewed 286 CFT tests and proved that confinement greatly increased the axial capacity of CCFTs. However, for the RCFT columns the increase in axial strength was insignificant even for elements with small column slenderness ratio and thick tube walls. Many theoretical models for predicting the axial load capacity of RCFT columns do not consider the confinement benefit as it is difficult to model and provides only marginal improvements [16]. However, for super high strength concrete, Okamoto's test results indicate that RCFTs can benefit greatly from the concrete confinement effect [17]. This is probably because the concrete was hardened by using centrifugal force.

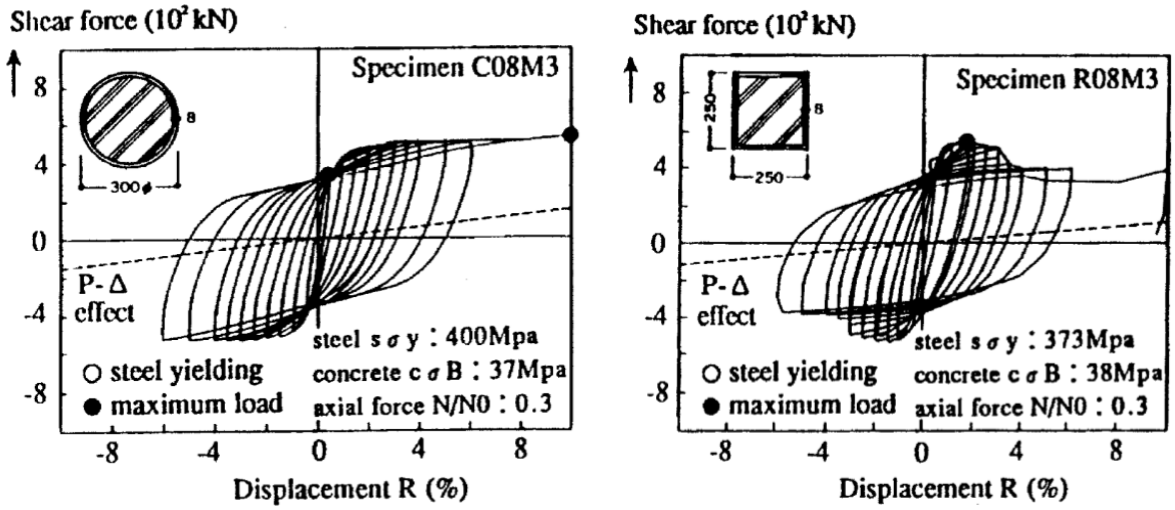

Figure 2-1: Typical hysteresis curves for circular and square CFT columns [1]

The load deformation relationships are also different between CCFTs and RCFTs. CCFTs usually show a strong and ductile strain-hardening behavior after the ultimate strength is reached. On the other hand, RCFTs show a softening post peak behavior because of the weak confinement effects (Figure 2-1) [15, 18, 19]. Furthermore, these effects result in large and stable hysteresis curves under cyclic loadings for CCFTs, while RCFTs only possess ductile behavior if the section is very compact and the axial load levels are low [20, 21]. More recently Schneider [22] showed that with aspect ratios ranging from 17 to 50, CCFTs exhibited more post-yield axial ductility than RCFTs. Local buckling of the steel tube wall occurred at an axial ductility of 10 or more for CCFTs, while corresponding values ranged from 2 to 8 for the RCFTs. Moreover, the required length/thickness ratio for CCFTs is considerably lower than for RCFTs [1, 23]. Finally, from the fire behavior standpoint, Dai and Lam [24] showed that CCFTs possess the best performance among all different cross sectional shapes.

However, no matter what cross section shapes are used, in order to fully take advantage of the CFT behavior, there are still two prerequisites that need to be met: (1) there must be effective composite interaction between the concrete fill and the steel tube wall; and, (2) there must be a reliable connection between the CFT columns and other structural components [1, 3]. The consensus amongst researchers is that CCFT columns have a much stronger bond strength than the RCFT columns [4], which is a very important factor to ensure the composite action between these two materials. The results in Figure 1-1 show that the concrete strength has no consistent effect on the stress bond. Other results show that the bond stress is clearly influenced by the steel tube dimension and slenderness, although these influences are not understood fully [4]. Okamoto posited that bond strength had little effect on the flexural capacity of RCFT columns [17], but an opposite trend was indicated by Shams and Saadeghvaziri [1] which showed that higher bond strengths will increase the bending capacity of RCFTs if inner ribs were present. However, such tubes may not be practical due to complexities in fabrication.

2.2 Partially Restrained Connections

Although many researchers point out that CCFTs have better performance than RCFTs, more reliable connecting methods still need to be developed for CCFTs. Connections are classified by three main parameters: strength, stiffness, and ductility [25]. For strength, connections can be considered as either *full strength* (**FS**) or *partial strength* (**PS**) based on whether they can

transfer the full plastic moment of the connecting beams. For stiffness, connections can be categorized as *fully restrained* (**FR**), *partially restrained* (**PR**), or *simple pinned* (**SP**) connections according to whether and how much moment they can transfer at given specific rotational angles. Finally, for ductility, connections are classified as either brittle or ductile connections depending on their ability to reach certain plastic rotational limits. Different rotational demands are required for different structural systems (ordinary, intermediate and special moment frames, etc.). For example, in the aftermath of Northridge Earthquake, the rotational limit to distinguishing between brittle and ductile connections in special moment frames was defined as 0.03 radian of plastic rotation [8]. All of these characteristics are summarized by a moment-rotation curve as shown in Figure 2-2.

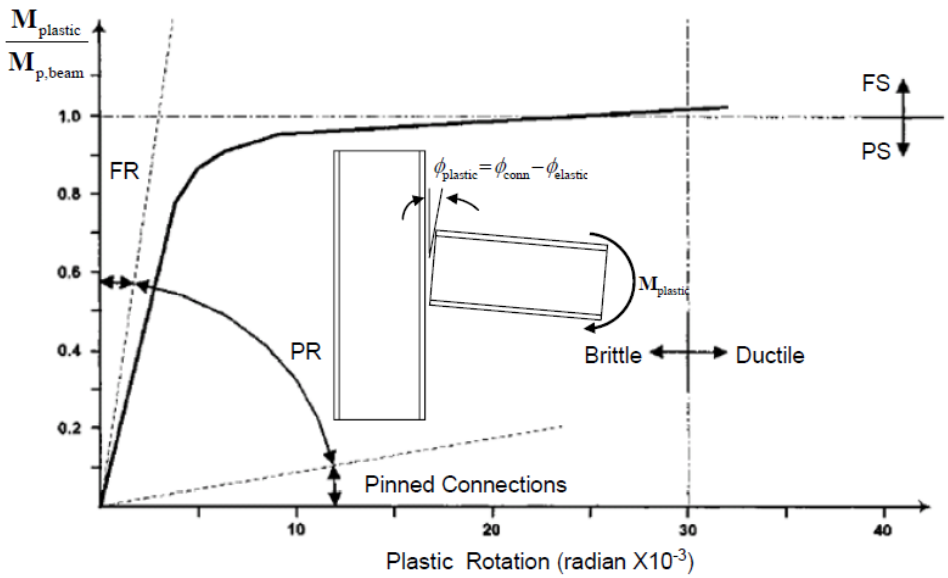

Figure 2-2: Typical moment rotation curve [8]

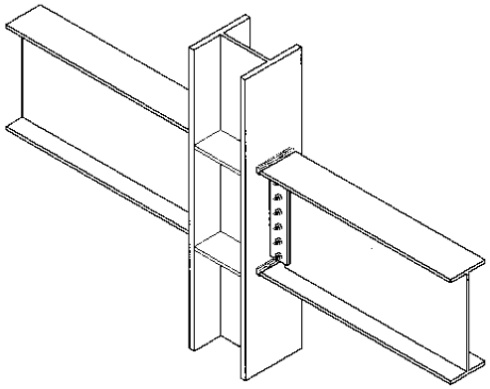

Figure 2-3: Fully restrained connection [26]

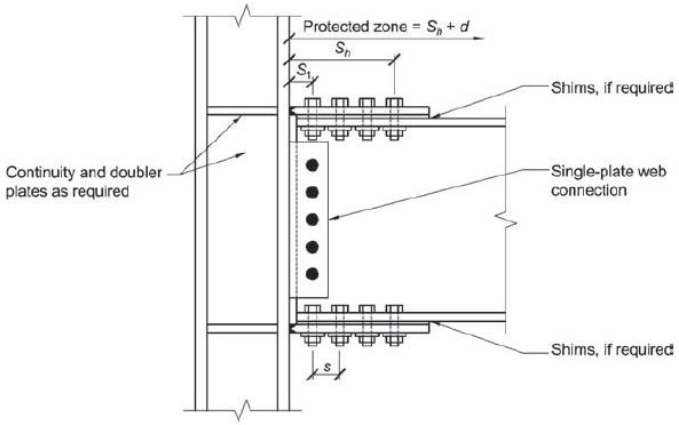

Figure 2-4: Bolted flange plate moment connection [10]

The three main parameters of the connections will depend to some degree on the fabrication methods of the connections. In steel structural design, welding and bolting are the two main methods to connect the column and steel beams. They are also the main methods in composite structural design. A typical FR connection is erected by bolting a shear tab between the beam web and the column, followed by the welding of the flanges as shown in Figure 2-3. On the other hand, a typical PR connection has the flanges bolted to either welded plates, as shown in Figure 2-4, or to bolted T-stubs or angles, as shown in Figure 2-5. A more common and easier configuration is to weld the whole cross section of the steel beam to an end-plate and then bolt the end-plate to the steel column flange as shown in Figure 2-6.

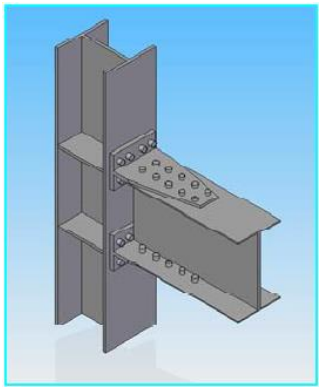

Figure 2-5: T-stub connection [8]

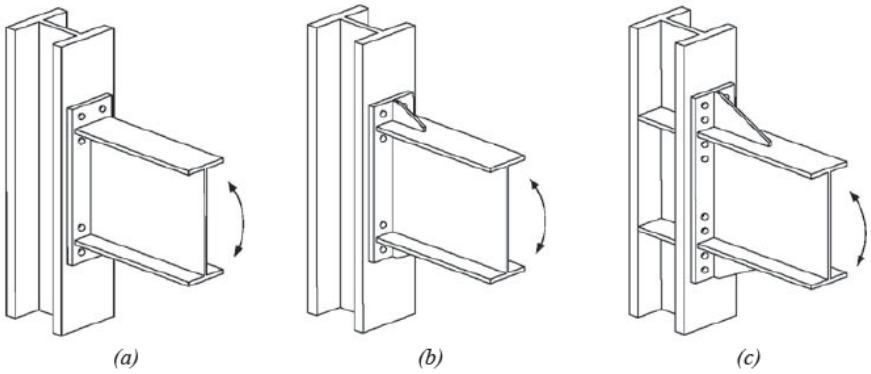

Figure 2-6: Extended end plate connection: (a) 4-bolt unstiffened (4E); (b) 4-bolt stiffened (4ES); (c) 8-bolt stiffened (8ES). [10]

Energy dissipation capacity is one of the most important factors to assess the seismic performance of a structure. For FR moment connections, the energy dissipation of the connection itself is very limited or negligible; all the energy dissipation will come from the plastic yielding of structural components such as columns and beams, which will cause severe damage to the structural system itself and large residual deformation after an earthquake. This will results in considerable costs and time for repair, and, as shown by the performance of modern structures in the 2011 Christchurch earthquake [27-29], often the damage is too large to be fixed.

The damage and downtime for these buildings will cause huge economic loss and aggravate public concerns about the safety of these structures. One feasible solution is to add additional energy dissipation devices in the buildings to protect structural components [30]. Although many of these devices have been shown to be efficient energy dissipators, most of them depend on developing large displacement or velocity, which means a large deformation demand of the

building is required. PR moment connections can supply both larger deformation capacity for these additional devices and more options for new energy dissipation methods. The two most common methods are friction mechanism (Figure 2-7) and yielding of nonstructural components combined with PR moment connections (Figure 2-8) [31, 32].

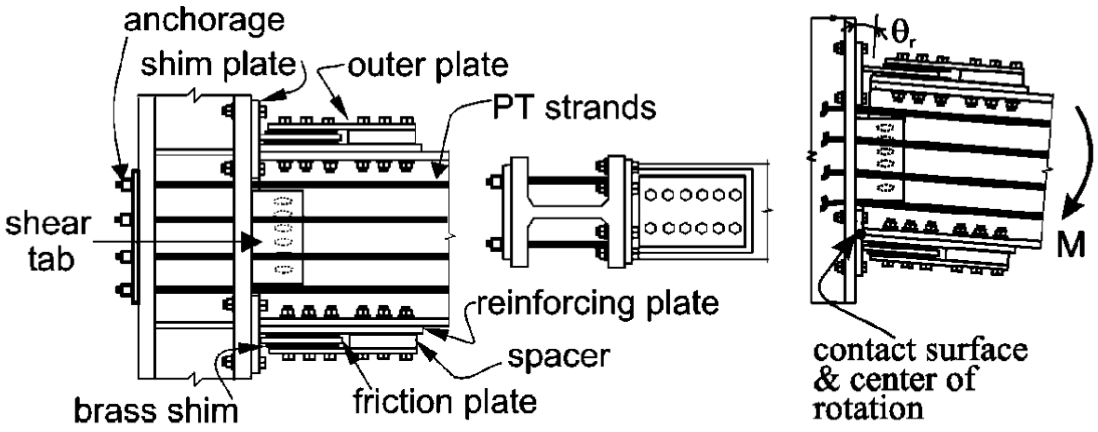

(a) Original configuration *(b) Deformed configuration*

Figure 2-7: PR connection with friction mechanism [33]

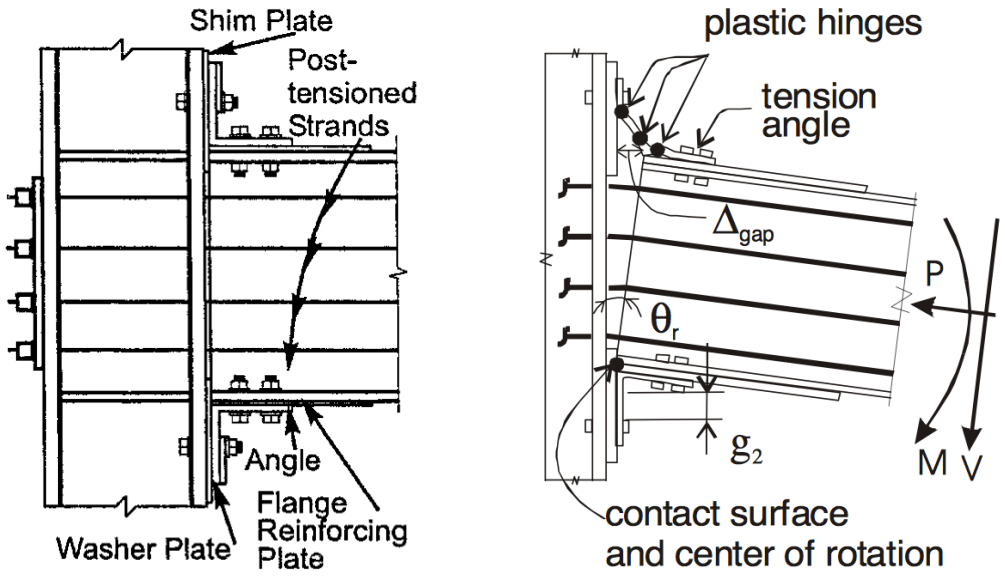

(a) Original configuration [32] *(b) Deformed configuration [31]*

Figure 2-8: PR connection with steel angles

2.3 Cyclic Deterioration Models

Although utilizing PR connections can reduce component damage, the yielding of the structural members is still unavoidable for special moment frames under seismic loading. In recent years, significant progress has been made in both collapse prediction methods and component deterioration models for structural analysis [34-38]. Experimental studies have shown that the hysteretic behavior of the structural components is influenced by numerous parameters, including geometry and material properties. Since 1960s, many different hysteresis models have been developed [39]. For example, the well-known Bouc-Wen model has been modified by some researchers to consider the deterioration effects [40-42] and the Iwan [43] and Mostaghel [44] models were modified by Sivaselvan and Reinhorn [45, 46] to consider strength and stiffness deterioration behavior and pinching effects.

More recently, an energy-based model was developed by Ibarra and Krawinkler (IK) [36], which can capture most component deterioration characteristics. This model was modified by Lignos and Krawinkler [47] to address asymmetric hysteresis behavior. The Modified-IK Model allows users to define different rate of cyclic deterioration in the two loading directions, consider residual strength and designate an ultimate deformation where the component strength drops to zero [39]. The Modified-IK Model can be applied to any force-deformation relationship. For this thesis, a Modified-IK Model based on a moment-rotation relationship will be used.

2.4 Connection Configurations for CCFTs

As introduced in Section 2.1, CCFTs possess many advantages. One main reason that designers choose RCFT columns over CCFT ones is its inherent difficulties in connecting to other components, such as W steel beams. Thus, in order to take advantage of these merits of CCFTs, it is necessary to find more reliable and economic connecting methods between the CCFT column and other conventional shapes.

Unlike the simple connection configurations shown above for W section columns with flat surfaces, the connections to CCFT columns are usually more complicated due to the curved column surface. Some design patterns based on external (Figure 2-9), internal and through diaphragms have been proposed during the past decades [48-52]. Alternatives include: (1) bolted external diaphragm (Figure 2-10); (2) external diaphragm combined with welding and bolting (Figure 2-11); (3) welded through diaphragm (Figure 2-12); (4) external diaphragm with embedded deformed bars (Figure 2-13); or (5) continuous through beam with or without continuous through web (Figure 2-14, Figure 2-15, Figure 2-19, and Figure 2-20). Another method to connect CCFT column and W steel beam is using welding anchor stiffeners at critical locations (Figure 2-16). However, most of these connection types are not common in USA practice due to fabrication costs.

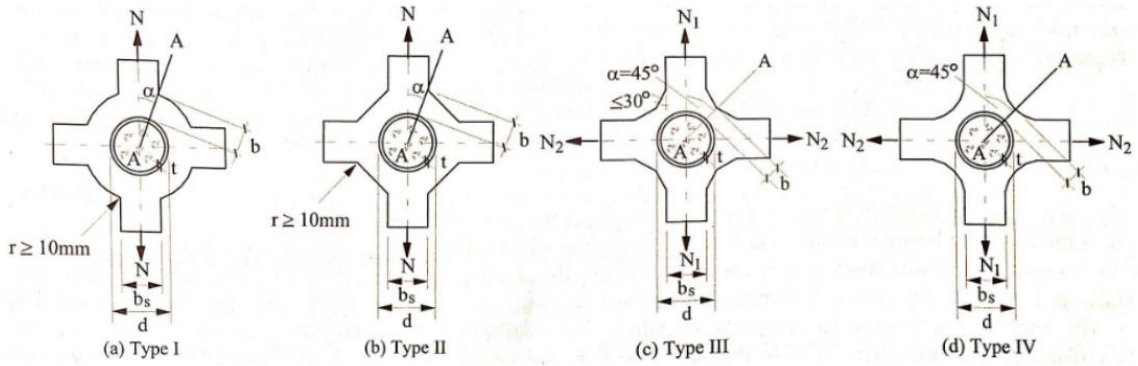

Figure 2-9: Four types of external diaphragm configurations [48]

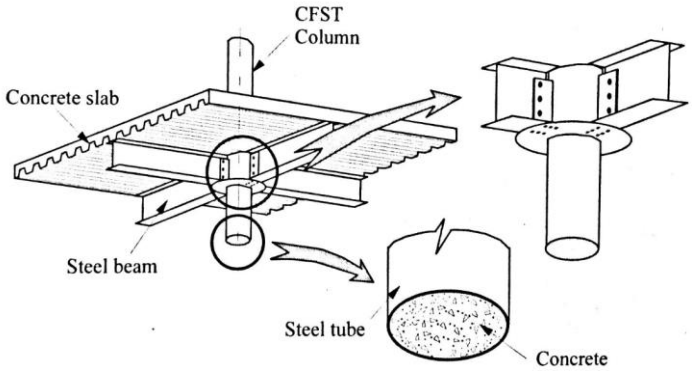

Figure 2-10: Bolted connection by external diaphragm [49]

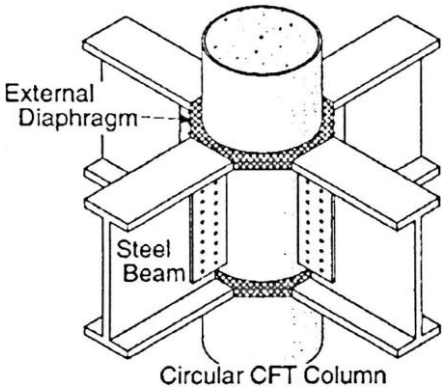

Figure 2-11: Combined bolting and welding [50]

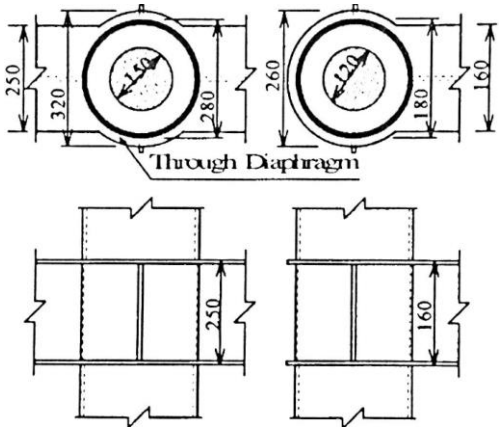

Figure 2-12: Welded connection with through diaphragm [51]

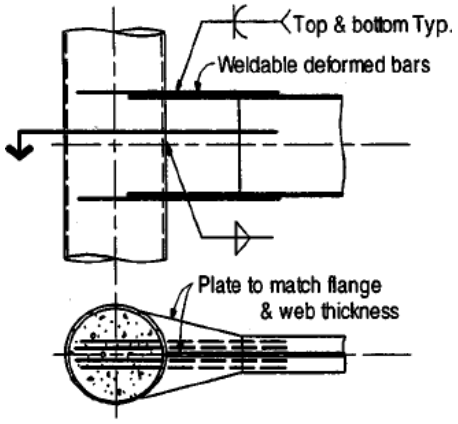

Figure 2-13: Welded with embedded deformed bar [53]

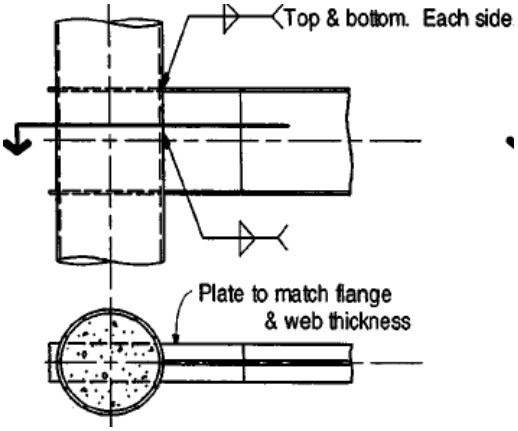

Figure 2-14: Continuous through flange connection [53]

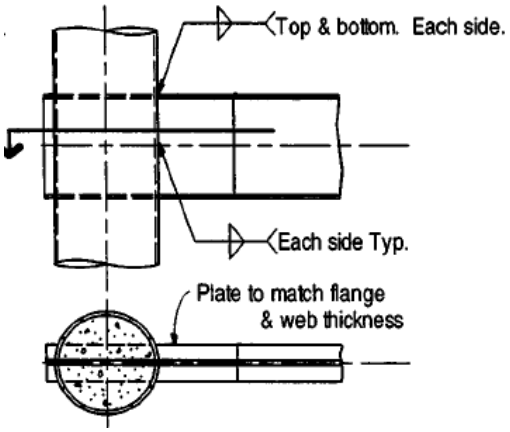

Figure 2-15: Continuous through beam section connection [53]

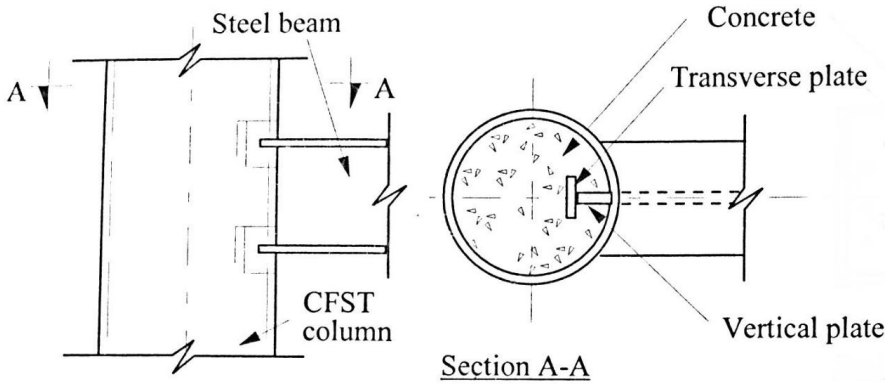

Figure 2-16: Welded connection with anchor stiffeners [54]

Some common FR moment connections for CCFT and W steel beam include configurations where the beam flanges are welded or bolted onto extended diaphragms which, in turn, are welded onto the steel tube wall directly as shown in Figure 2-17 and Figure 2-18. Other FR connections are fabricated with either the flanges or the whole beam section going through the steel tube as shown in Figure 2-19 and Figure 2-20. All of these FR connections have been shown through testing to possess very good seismic resistance capacity, but they are complicated, time consuming and expensive for fabrication. This is primarily because a large amount of field full penetration welding will be unavoidable. In addition, there are interference

limitations for biaxial bending that make the connections in Figure 2-19 and Figure 2-20 difficult if not impossible to use.

Currently, the only prequalified connection by AISC 358 for US practice is the ConXtech ConXL moment connection (Figure 2-21), which is a full-strength and fully restrained connection for W steel beam [10]. For this connection most components are shop fabricated. The only assembling operation on site consists on bolting the *collar flange top* (**CFT**) pieces and *collar flange bottom* (**CFB**) pieces (Figure 2-22) together onto the collar corner pieces (Figure 2-23); the collar comer pieces are attached to the column by fillet welding in the shop. This connection configuration supplies a method for connecting beams on to columns in orthogonal frames. However, this prequalified connection has many limitations: (1) it is only available for RCFT columns, and the CCFT benefits can not be utilized by adopting it; (2) it is only workable for beams with five types of nominal depth, and the connecting beam must have the same size; (3) it can only be used for the column with square 16 in. HSS sections or square 16 in. built-up box sections. These requirements greatly limit its application scope.

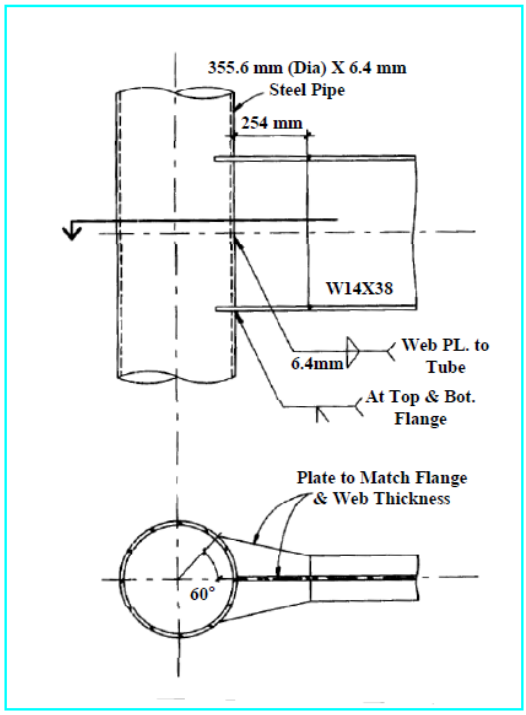

Figure 2-17: Simple welded connection [52]

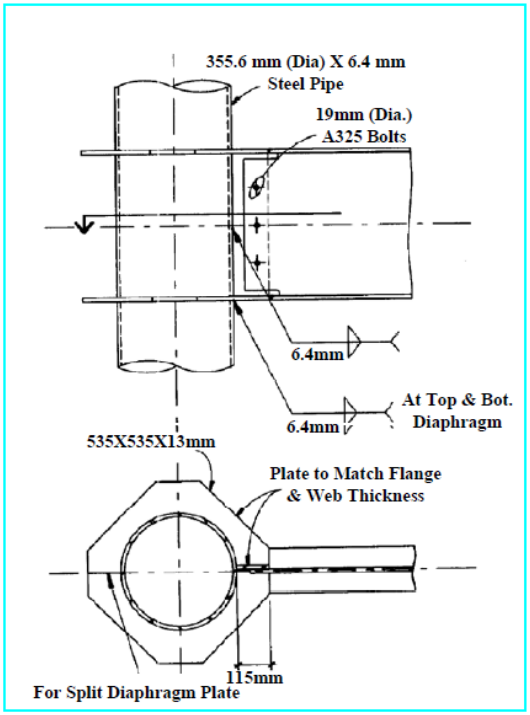

Figure 2-18: Diaphragm plate connection [52]

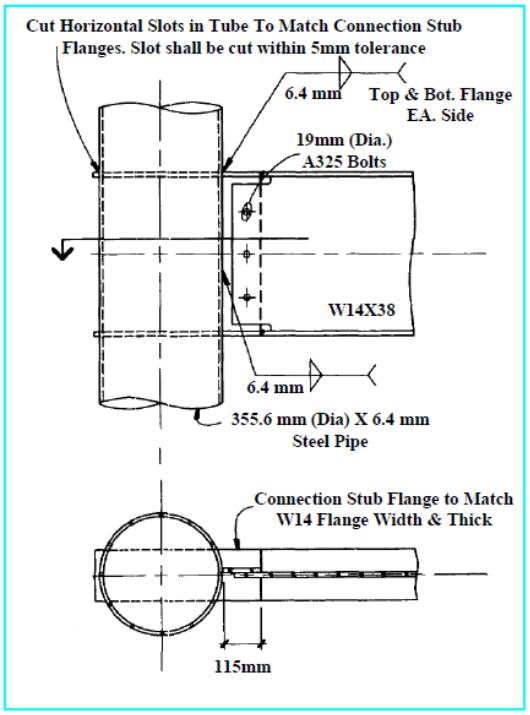

Figure 2-19: Continuous flange connection [52]

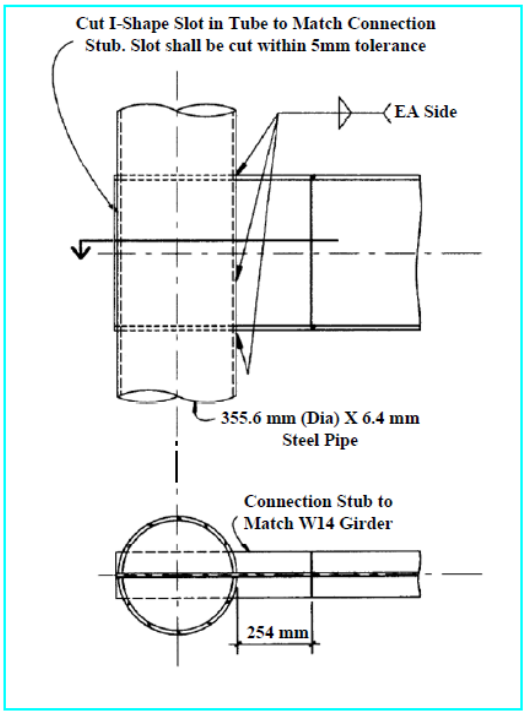

Figure 2-20: Continuous cross-section connection [52]

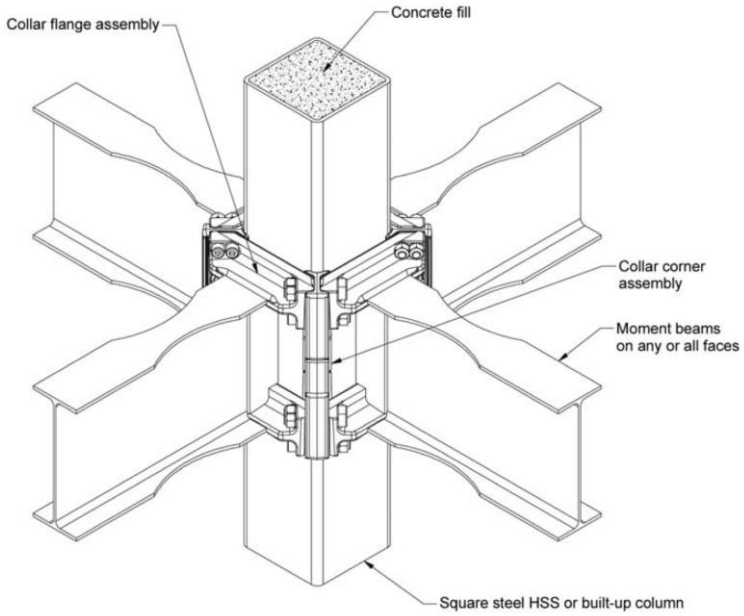

Figure 2-21: Assembled ConXL moment connection [10]

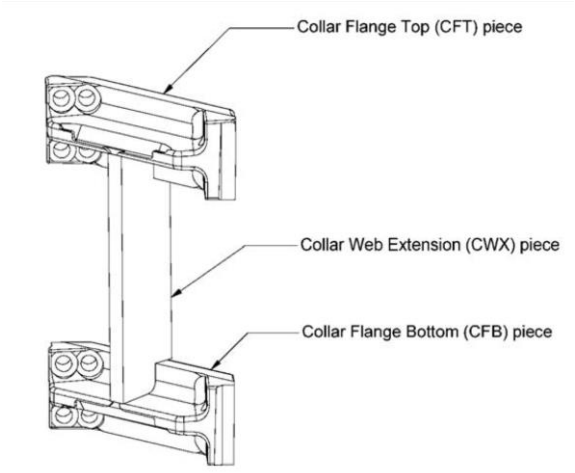

Figure 2-22: Collar flange assembly of a ConXL connection [10]

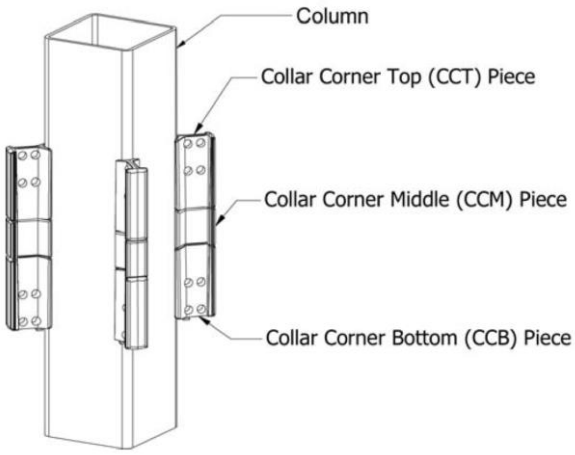

Figure 2-23: Column with attached collar corner assemblies [10]

On the other hand, PR connections have many advantages compared with their FR counterparts as illustrated in section 2.2. Although attention has already been put on development of PR connections for CCFT columns, most of these new connection configurations will sacrifice the CCFT benefit on delaying of tube wall local buckling by using blind bolts and curved end

plates, as shown in Figure 2-24 and Figure 2-25 [55-58]. In these configurations, the bolts will either try to pull out the circular tube wall and cause untimely local buckling or have poor contact properties between the nuts and end plate due to the curved surface. This poor contact between the nuts and connecting members will cause local stress and strain concentrations, difficulties in fabrication, and will also set a limitation for applying post-tension on bolts. Because not all the bolts are on the same plane, there will be large horizontal shear forces in the bolts, which will decrease their capacity greatly. The research of Hu, Rassati, and Leon [7, 8] has proposed some better configurations; however, much further research is still necessary to reach the desirable design level. As this research was being completed, Hu published a very complete state-of the-art book on this topic [9].

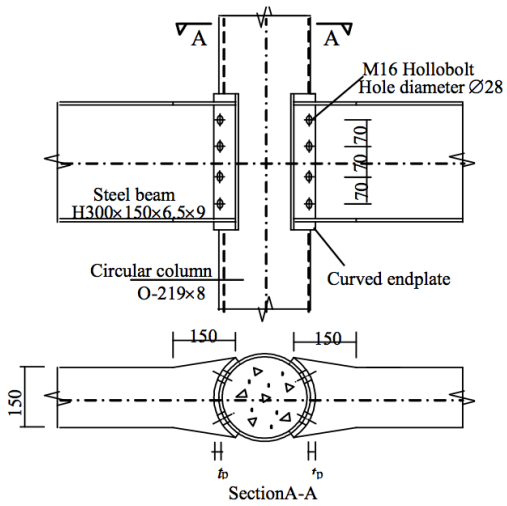

Figure 2-24: CCFT connection with blind bolts [55]

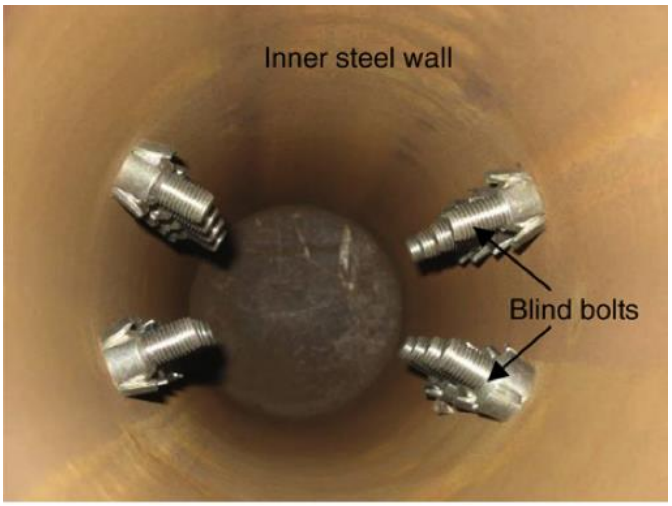

Figure 2-25: Blind bolts inside of CCFT [56]

Another FR connection configuration for the CCFT column has been proposed as shown in Figure 2-26 [59]. Compared with the configuration in Figure 2-24, this innovative CCFT

connection changes to use flat end plate and through high strength rods, instead of curved end plate and bolts, so the previous mentioned disadvantages can be eliminated. The test results show that this innovative configuration is strong enough to fully yield the connecting RBS under cyclic loading (Figure 2-27) and can generate stable hysteretic behavior for the connecting RBS. However, only the fully restrained exterior connection is investigated in the test. It is still far away from practical design for this new connection.

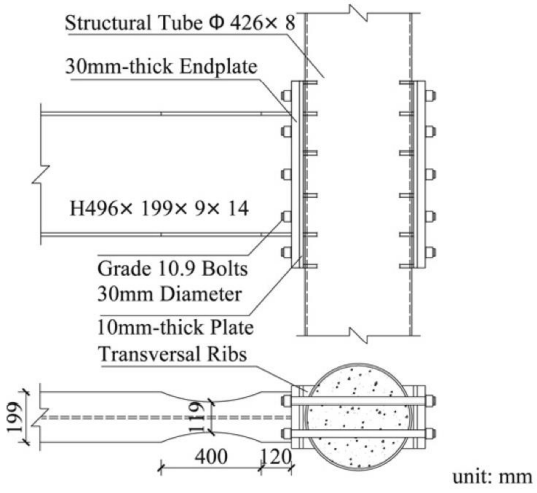

Figure 2-26: Detailed configuration of an innovative CCFT connection [59]

Figure 2-27: Fully cyclic yielding of the RBS with the innovative CCFT connection from test [59]

2.5 Self-Centering Systems

Use of PR connections also brings the potential capability for self-centering, which has become a very hot research field in structural systems recently. A structure with self-centering ability will have less residual deformation after an earthquake, and damage to both structural and

nonstructural components of the building will be mitigated. At the same time, the probability for the structures to lose functionality will be reduced and result in more rapid recovery. Damage limitation and speedy recovery are design objectives consistent with next generation design concepts. i.e., seismic *performance based design* (**PBD**).

The two most common methods to achieve self-centering capacity in structural systems are to utilize *post-tensioned* (**PT**) wires or bars [31-33] and rocking mechanism [60], or combined these two together [61, 62]. These systems usually require each PT strand to go through all bays of one moment frame along beams at each level (Figure 2-28) or go through all stories along columns (Figure 2-29) continuously. The design concept of these self-centering systems includes: (1) keep all the structural members, including all beams and columns, elastic during the earthquake; (2) all the deformation should come from elastic deformation of PT wires or bars; and (3) after unloading, the structures try to achieve their original shapes under effects of PT forces. The key point of these systems is to maintain near elastic behavior of the PT components. If these PT strands or bars go into the plastic range during an earthquake, there will be a loss of PT force due to residual deformation and the self-centering capacity will be diminished.

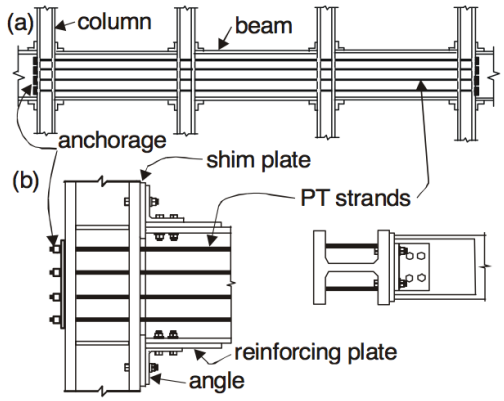

Figure 2-28: (a) Schematic elevation of one floor of a PT frame; (b) Connection details. [31]

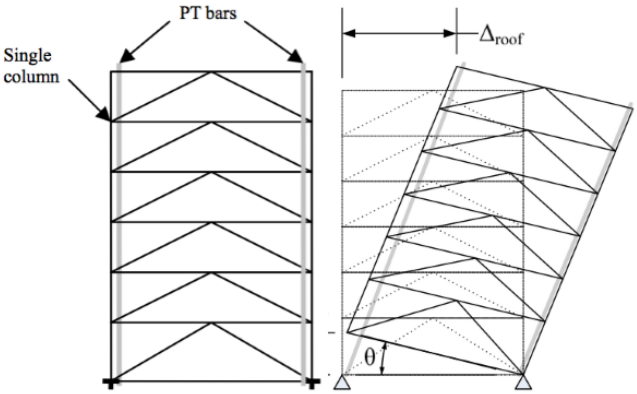

Figure 2-29: Frame with PT bars and rocking mechanism [61]

A more severe situation is that shown in Figure 2-28, where all three beams on each level are stressed by the same PT strands. Once one or more of these PT strands fail during an unexpected earthquake, the aftermath will be worst - collapse of the whole 3-span story. Although steel angles on both top and bottom of the steel beam maybe provide limited redundancy, Garlock's [31] research shows that both these two steel angles will definitely fracture under cyclic loading in design with small initial PT force. However, this small initial PT force is very important to ensure adequate deformation capacity of the connection. A large initial PT force will cause untimely beam local bucking at less than a 2% story drift ratio, which violates the design concept to keep all beams elastic and will increase residual deformation after earthquake [31]. This means the inherent redundancy of this self-centering system is relatively low for seismic design, and the application on different structural systems will also be limited. In order to reduce the probability of collapse, a very large safety factor for the design of PT strands is required. Another concern is that to keep all the structural members in elastic

during earthquake will be uneconomical due to the natural low probability of occurrence of earthquakes.

2.6 Shape Memory Alloy in Civil Engineering

Shape memory alloys (**SMA**) provide another method to offer self-centering capacity for structures. One type of the most common SMA is based on nickel-titanium alloys or Nitinol [63-66]. SMA have two different phases: martensite and austenite [67, 68]. The martensitic phase is stable at low temperatures with high strengths; the austenitic phase is stable at relative high temperatures with low strengths [64]. From a crystallographic perspective, austenite crystals have super-lattice body centered cubic structures, which are classified as β-phase alloys. On the other hand, martensite crystals have periodic stacking order structures [64]. The more-ordered atom structures of the austenite phase causes lower strengths than the martensite phase.

In a stress-free state, the two phases are reversible by changing temperatures through a solid-solid displacive-diffusionless phase transformation [64]. During the phase transformation, the fraction of each phase in SMA is a function of only temperature and not of the length of time [69]. Holding the alloy at the same temperature for a longer time will have no effects on the phase composition [64]. Figure 2-30 presents the relationship between the phase transformation and the temperatures. The martensitic phase transforms to an austenitic phase by increasing

temperature, that starts at temperature A_s and is completed at A_f. This phase transformation is reversible by decreasing temperature, that starts at temperature M_s and finished at M_f.

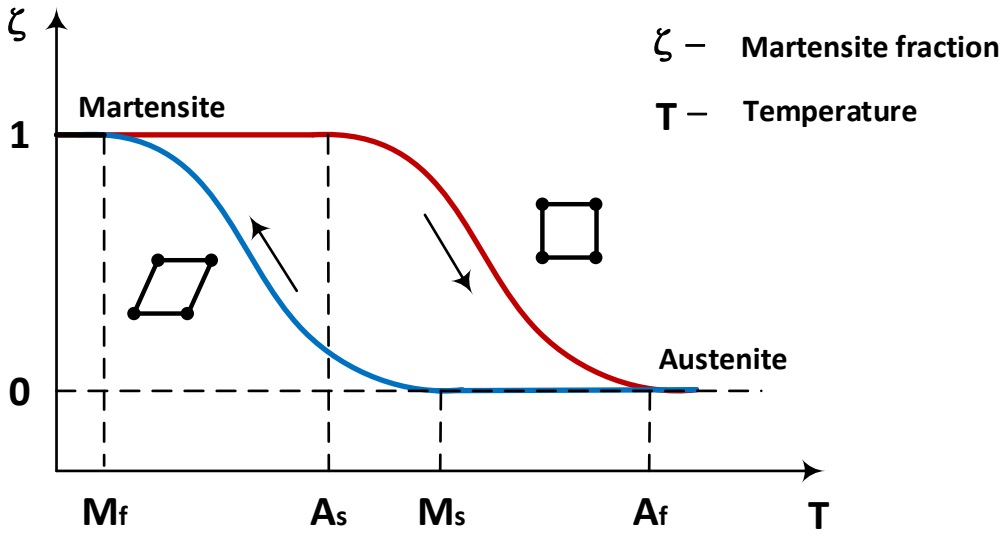

Figure 2-30: SMA phase transformation by changing temperatures

The most important characteristic of SMA is its ability to memorize its original shape. As shown in Figure 2-31, after loading and unloading along a load path A-B-C at a constant temperature, there is a considerable residual strain left in a SMA specimen. However, by increasing the temperature to *T* and cooling the specimen to the original temperature along a load path *C-D-A*, the deformed specimen can fully recover its original shape.

Another characteristic of SMA is its superelastic behavior. In a well defined austenite phase, the phase transformation can also be initiated by a specific stress at a constant temperature. As shown in Figure 2-32, when a SMA specimen is loaded along the path *A-B-C*, the austenite

phase transforms to martensite phase and presents a martensite hardening effect after completing the phase transformation. The deformed specimen can also transform from a martensite phase to an autenite phase back along the unloading path *C-D-A* to generate a closed loop. The amount of heat recovery memory strain, the specific phase transformation stress, and the size of the loop highly depend on the alloy composition, thermomechanical processing, testing direction and deformation mode [64]. For a full austenite-martensite phase transformation, the recovery memory strain can reach up to 8%.

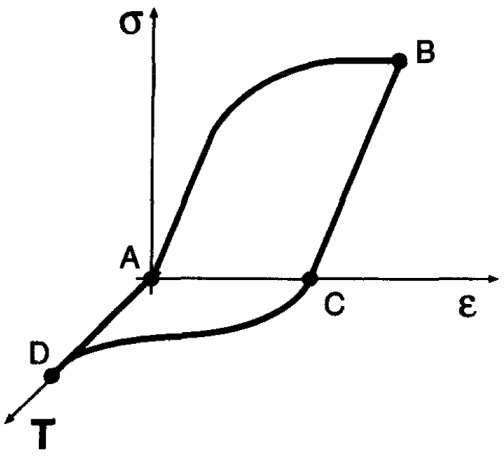

Figure 2-31: Shape memory effects [64]

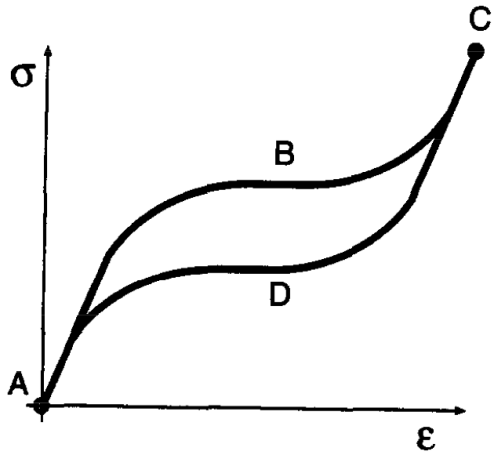

Figure 2-32: Superelasticity behavior [64]

The very good mechanical behavior of SMA makes it attractive to be applied in civil engineering, especially the superelastic behavior, reaching up to 6-8% strain with nearly no residual deformation [70, 71]. At the same time, SMA will present martensite hardening behavior at strains greater than 5%, which will ensure higher redundancy of the structure for seismic design. Its hysteresis behavior within the super-elastic range can also increase the energy dissipation. More importantly, SMA materials display very good fatigue and corrosion

resistance [70], which are very favorable properties of material for seismic design. This will ensure long term reliable functioning of the components and reduce maintenance cost. Although there are many good properties and potential applications in innovative fields, research on devices based on SMA in civil engineering are still not common due to its high price. However the development and marketing of cheaper SMA materials is changing this limitation [72]. Like all other new materials, the price will not be always a problem as long as its benefits are attractive enough. The feasibility of application of SMA in civil engineering has already been proved by many researches [70, 71, 73-75] for both wire and large diameter bars [76].

2.7 Conclusions

In this chapter, the benefits of CFTs applied in civil engineering are discussed. CCFTs have many advantages over RTFCs as structural components due to their higher confinement and better bond strength between the two materials. However, the promotion of CCFTs is impeded by the inherent difficulty of connecting with other members with conventional shapes. To develop more reliable and economical connections for CCFTs, more research and development is necessary for its comprehensive application in structural design in the future. The rest of this thesis addresses that need.

Chapter 3

Proposed Preliminary Design Procedure

In this chapter, the configuration of a *new proposed smart connection* (**NPSC**) between a CCFT column and W steel beams is introduced; and a *preliminary design procedure* (**PDP**) for the NPSC is developed. Section 3.1 gives a detailed description of the NPSC configuration for uniaxial bending. Section 3.2 introduces a design procedure for a prequalified connection for seismic design, which has numerous similarities to the NPSC. Section 3.3 illustrates the design principles for the NPSC, and provides a step-by-step design procedure. Section 3.4 supplies examples for some NPSCs to check the feasibility of the new PDP. Section 3.5 introduces some design methods in different standards for CCFTs, and provides some examples for comparisons among these standards. Section 3.6 summarizes the conclusions from this chapter.

3.1 Proposed Connection Configuration

In Chapter 1 a detailed introduction has been given about the benefits from applying *Concrete Filled Tubes* (**CFTs**), especially *Circular CFTs* (**CCFTs**), in *Composite Special Moment Frames* (**CSMFs**). However, in order to encourage the designers to choose this economic structural member, more reliable rigid or semi-rigid (FR or PR) moment connections between a CCFT column and W steel beams must be developed. These connections should meet the current design provisions, such as "Seismic Provisions for Structural Steel Buildings" [77] and

"Prequalified Connections"[10], as well as the required design loads [78].

Several FR and PR connections for CCFTs have been proposed in the past decades, as shown from Figure 2-9 to Figure 2-24. The current design patterns are primarily based on external, internal diaphragms, or their combination; a few adopt through flanges, through beam, or through bars. And as mentioned previously, a well fabricated PR connection is believed to have equivalent or even better performance than its FR counterpart. In order to promote a further development of the CCFTs, a PR connection with self-centering capacity is believed to be necessary. The new connection should also be easy and economical to be assembled on site. Also as discussed in Chapter 1, SMA is a great potential material to supply self-centering capacity for the new proposed smart connection.

The new configuration should follow some simple principles: (1) be a partially restrained connection; (2) use SMA to supply self-centering capacity; (3) be easily assembled without full penetration welds on site; and (4) be expandable for biaxial bending. One possible solution is to use a bolted extended end plate pattern (Figure 2-6); some of bolts can be made of SMA and others can be made of steel. The SMA bolts are expected to supply self-centering capacity, while the steel bolts are used to increase both ultimate strength and stiffness of the connection. Because large rotations are expected in order for the NPSC to supply self-centering capacity and meet the seismic design provisions, the bolts should have large elongation capacity. In order to make sure the strain in bolts is kept below 7% under the ultimate deformation, long

through rods are adopted instead of short bolts. The limit 7% is used because there is relative small residual deformation when the strain in SMA is less than this value. This will help ensure a better self-centering effect. In order to use a extended end plate, one should make sure a flat surface can be supplied by the column to the extended end plate for a tight contact. This tight contact along with the necessary pretension in the rods should be sufficient to develop enough friction to resist the shear force in the beam. Therefore, additional components are required to connect both the curved surface of the CCFT and the flat surface of extended end plate.

In Figure 1-4, a new proposed configuration for uniaxial bending connection is presented. This through-bolted CCFT connection possesses self-centering capability and several hierarchical ductile damage mechanisms that can be tuned to provide different performance levels. The connection is a modular one, where both the beam and column sections will be prefabricated, and the main connection will be made in the field with large rods. Figure 3-1 shows a cut-away view through the proposed connections, along with its principle components:

- A circular concrete filled tube with a moment-axial force interaction capacity well in excess of that of the girders. For low to moderate rise structures, it is possible to use current HSS sections which range up to 22 in. in diameter and 0.5 in. in thickness. Much larger tube sections, and at higher strengths, are available as API pipe sections [79]. Almost any thickness and diameter of plate is available from multiple fabricators worldwide, which can be used for making spirally welded circular tubes. The column will be filled with a suitable normal or high-strength concrete, probably on the order of

4 to 12 ksi depending on local availability.

- A reduced beam section (RBS) girder that limits the force input to the connection while maintaining most of the frame stiffness. The RBS is used because the design procedure intends to keep the maximum strain in all rods below 7% under ultimate beam strength, but to avoid large rod diameters.

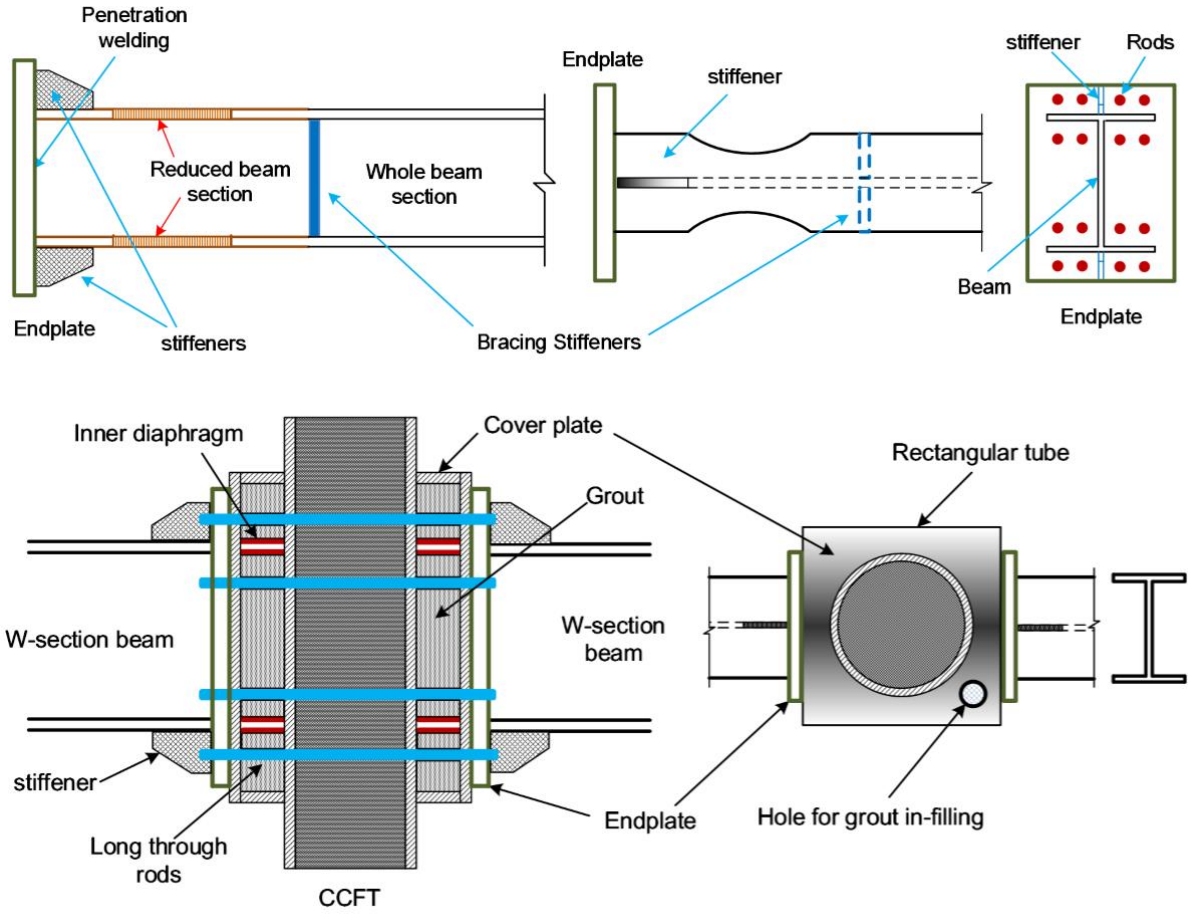

Figure 3-1: Details of proposed CCFT connection

- A stiff extended end plate connection with stiffeners to transfer all girder forces into the through rods. End plates are fabricated with fillet welds and have been shown to be a

very efficient and economical system in certain parts of the USA [80]. As shown in Figure 3-1, the end plate will carry at least 4 connectors on each bolt line, an extension from current practice that allows only 2 bolts per line [10].

- The end plates will bear on a thick steel rectangular tube, which in turn will be connected to the circular tube column by internal diaphragms and external cover plates using fillet welds (Figure 3-2). The space between the external rectangular tube and the internal circular one will be filled by a high strength expansive grout. This portion of the connection is intended to remain essentially elastic and will be shop fabricated along with the RBS girders; the only field work will be the post-tensioning of the rods.

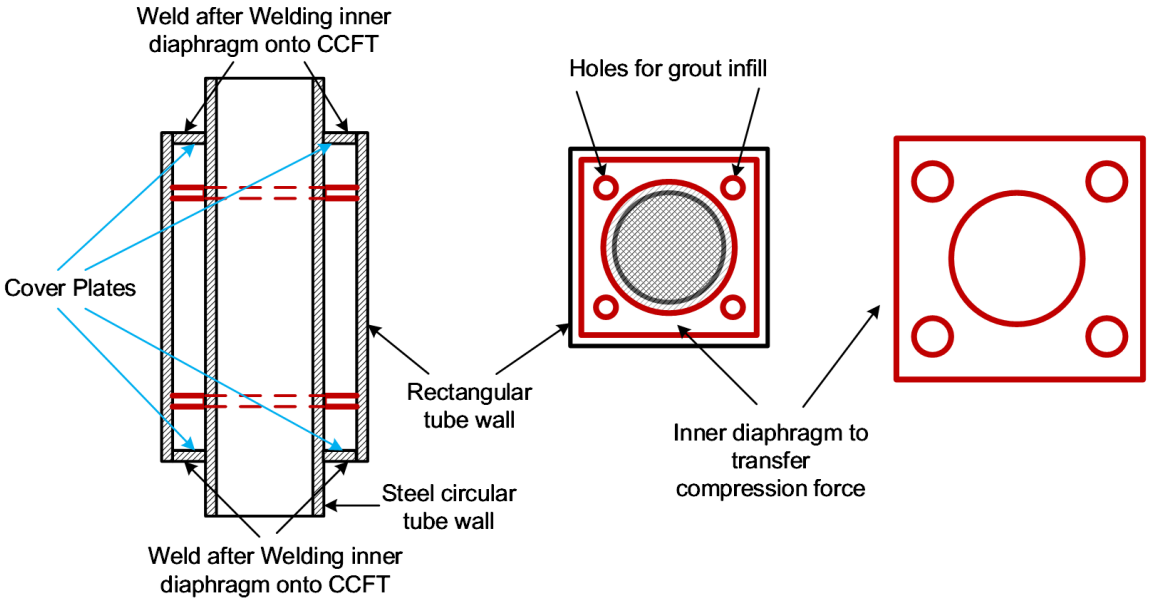

Figure 3-2: Details of the steel skeleton of the connection collar

- A series of large diameter rods composed of both SMA and conventional steel rods.

Currently, the designs are for SMA that yields around 60 ksi and Gr.50 steel. These rods will be post-tensioned to resist any moments due to wind loads and have diameters in the 1 in. to 1 ½ in. range. The steel rods will yield first at low end plate rotation, with associated permanent deformations. The SMA rods start to center the connection once the steel rods have begun to yield. Great care will be needed to consider the interaction between axial tension and shear in these elements once the total separation occurs between the end plate and the rectangular tube during the earthquakes. The steel rods will be easily replaceable if they sustain large permanent deformations, and their use is intended to provide additional strength and stiffness to the SMA rods.

While this connection may initially appear overly complex, it compensates for initial costs through its extensive prefabrication, ease of erection, self-centering capacity and robustness. As mentioned above, the connection can result in several ductile mechanisms activating at different deformations, and thus the designer is free to tune his design to obtain any desired level of performance by using different combinations of strength and stiffness in its components, such as higher strength steel rods. As an example of what a designer utilizing PBD can do with this CCFT connection can do, consider the ability of this connection to transition from a rigid connection (RBS governing), to a strong partially restrained one (steel rods yielding), to a soft PR one (SMA rods yielding) and back to a strong or rigid one as the SMA begins to strain harden (usually starts at around 5% strain). The desired force-deformation behavior for the whole connection region, including one such connection that includes some

initial prestressing and the RBSs, is shown in Figure 3-3 and is composed of three ranges: (1) when subjected to small earthquakes, all the components will be in elastic stage and there will be no permanent deformations after unloading; (2) when subjected to a moderate earthquake, limited yielding of the RBS and steel rods will be expected, but the structure will almost completely re-center; and (3) when subjected to a severe earthquake, the steel rods, SMA rods and the RBS will be allowed to yield for more energy dissipation; because of recovery force in the SMA rods and the PR connection behavior, small residual drifts are expected.

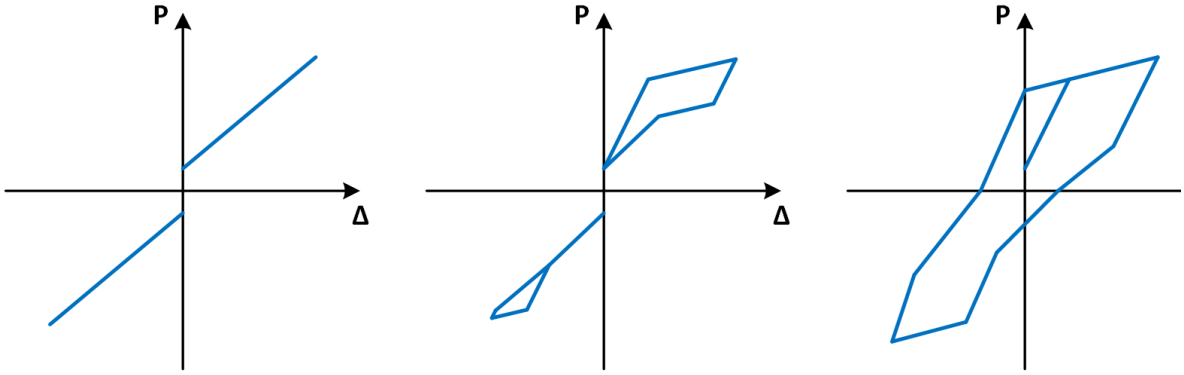

(a) Small earthquake ***(b) Moderate earthquake*** ***(c) Severe earthquake***

Figure 3-3: Desired force-deformation behaviors of the connection region

3.2 Extended End plate Design

The new proposed PR connection will adopt an *extended end plate configuration* (**EEC**). The current prequalified patterns are described in AISC358-10 [10]. They are (a) four bolt unstiffened EEC; (b) four bolt stiffened EEC; and (c) eight bolt stiffened EEC (Figure 2-6).

Compared with the NPSC in Figure 1-4, which has an eight bolt stiffened EEC and takes four bolts on each bolt line, the current prequalified patterns only take two bolts on each bolt line. Thus a design procedure for four bolts on a line is needed. Sumner [81] has generated relatively comprehensive design procedures for several different patterns, including the eight bolt, four bolts wide stiffened/unstiffened EECs. These design procedures are based on yield line analysis. Figure 3-4 presents two cases of the controlling yield line mechanisms proposed by Sumner for the eight bolt, four bolts wide stiffened extended end-plate moment connections.

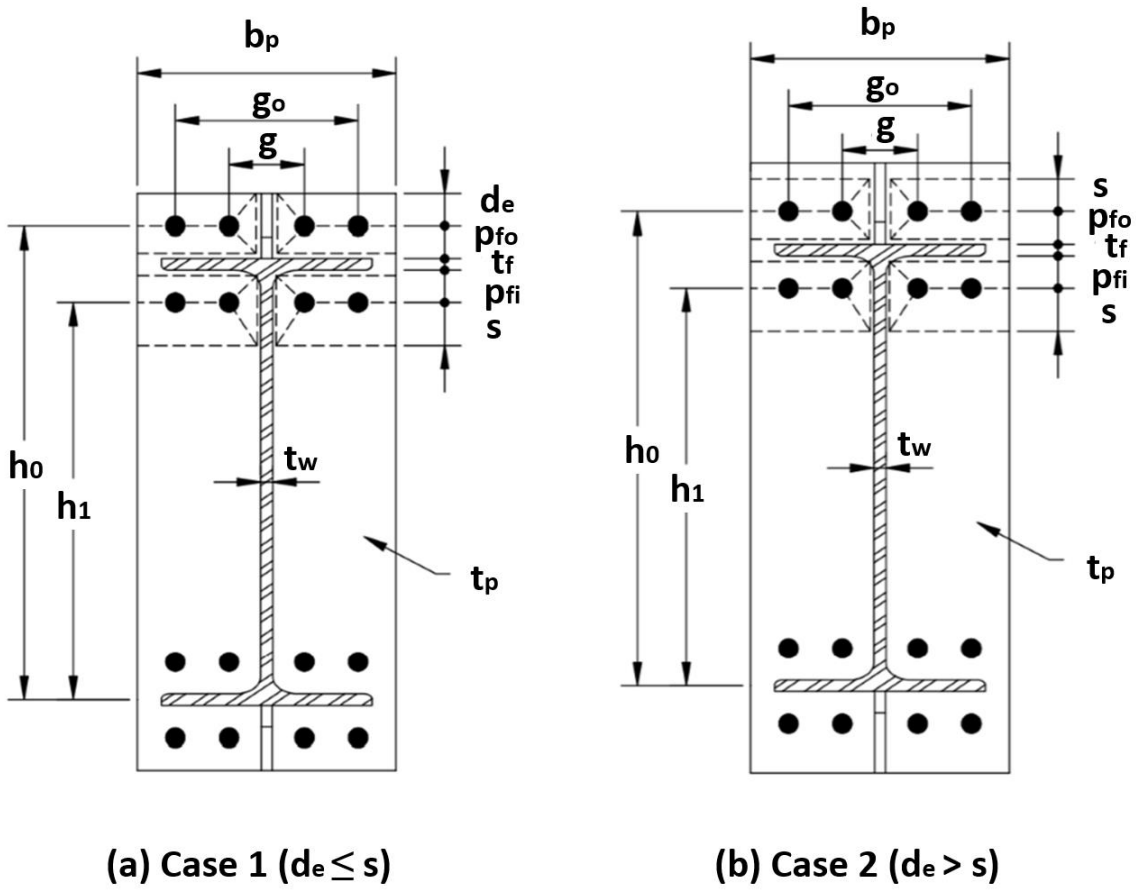

Figure 3-4: Yield line pattern for eight bolt, four bolts wide extended stiffened end-plate moment connections (modified based on Sumner's Figure [81])

A similar study is conducted by Meng [82] on the eight bolt, four bolts wide stiffened extended end-plate moment connections. The following solutions for the two mechanisms in Figure 3-4 were modified by Sumner [81] based on Meng's research [82].

Required thickness of the end plate:

$$t_{p,req} = \sqrt{\frac{M_d}{F_{yp} \cdot Y_p}} \qquad \textbf{(Eq. 3-1)}$$

Case 1 (when $d_e \leq s$):

$$Y_p = \frac{b_p}{2}\left[h_1\left(\frac{1}{p_{fi}} + \frac{1}{s}\right) + h_0\left(\frac{1}{p_{fo}} + \frac{1}{s}\right)\right] + \frac{2}{g}\left[h_1\left(p_{fi} + s\right) + h_0\left(p_{fo} + s\right)\right] \qquad \textbf{(Eq. 3-2)}$$

Case 2 (when $d_e > s$):

$$Y_p = \frac{b_p}{2}\left[h_1\left(\frac{1}{p_{fi}} + \frac{1}{s}\right) + h_0\left(\frac{1}{p_{fo}} + \frac{1}{2s}\right)\right] + \frac{2}{g}\left[h_1\left(p_{fi} + s\right) + h_0\left(d_e + p_{fo}\right)\right] \qquad \textbf{(Eq. 3-3)}$$

where,

$s = \frac{1}{2}\sqrt{b_p \cdot g}$, in.

M_d = moment demand of the end plate, k-in.

F_{yp} = nominal yield strength of the end plate, ksi.

All other dimensional parameters are presented in Figure 3-4, in.

If the inner pitch distance of the connections is larger than the distance s, $p_{fi} > s$, then use s as the value of the inner pitch distance p_{fi} in the calculation.

Sumner didn't supply a detailed derivation to obtain these solutions in his thesis. But if only the yield line mechanisms in Figure 3-4 are considered, the following two facts should be clear: (1) For case one with $d_e \leq s$, it is obvious that d_e should be the controlling parameter for the yield line mechanism and be involved in the calculation. However, (Eq. 3-2) does not include parameter d_e in its relationship. (2) On the other hand, for case two with $d_e > s$, only the value s should control the calculation but term d_e is also included in (Eq. 3-3). In order to make the solutions more self-consistent, (Eq. 3-2) and (Eq. 3-3) are modified as follows. The detailed derivations are supplied in Appendix A.

Case 1 (when $d_e \leq s$):

$$Y_p = \frac{b_p}{2}\left[h_1\left(\frac{1}{p_{fi}}+\frac{1}{s}\right)+h_0\left(\frac{1}{p_{fo}}+\frac{1}{2d_e}\right)\right]+\frac{2}{g}\left[h_1\left(p_{fi}+s\right)+h_0\left(p_{fo}+d_e\right)\right] \qquad \textbf{(Eq. 3-4)}$$

Case 2 (when $d_e > s$):

$$Y_p = \frac{b_p}{2}\left[h_1\left(\frac{1}{p_{fi}}+\frac{1}{s}\right)+h_0\left(\frac{1}{p_{fo}}+\frac{1}{2s}\right)\right]+\frac{2}{g}\left[h_1\left(p_{fi}+s\right)+h_0\left(s+p_{fo}\right)\right] \qquad \textbf{(Eq. 3-5)}$$

3.3 Preliminary Design Procedure for the Proposed Connection

In this section, a preliminary detailed design procedure for the new proposed connection is illustrated for both interior and exterior columns (Figure 3-5). The simplified computational models on which the design is based are shown in Figure 3-6. For both computational models, it is assumed that the end plates yield and rotate about one yield line at the level of beam flange in compression, while all other parts of the end plate are assumed to behave as a rigid body. The procedure assumes that the plastic moment capacity supplied by the end plate is relative low compared with that from all rods tension, and it will be ignored. Due to the existence of inner diaphragms and the infill grout enclosed by the square steel tube, the inward displacements caused by the compression force to be transferred from the end plate to the square tube wall is expected to be insignificant and is also ignored. Thus the end plate is considered to be placed on a rigid foundation.

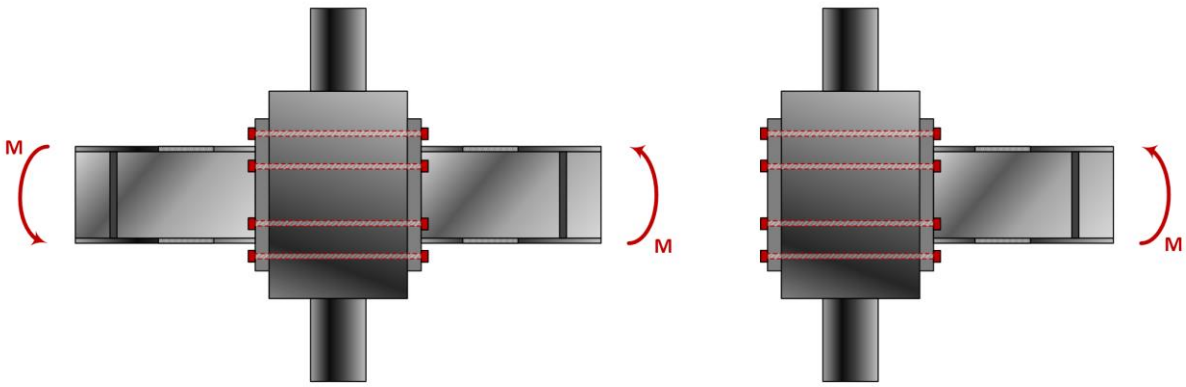

(a) Interior connection *(b) Exterior connection*

Figure 3-5: Connection configurations for uniaxial bending

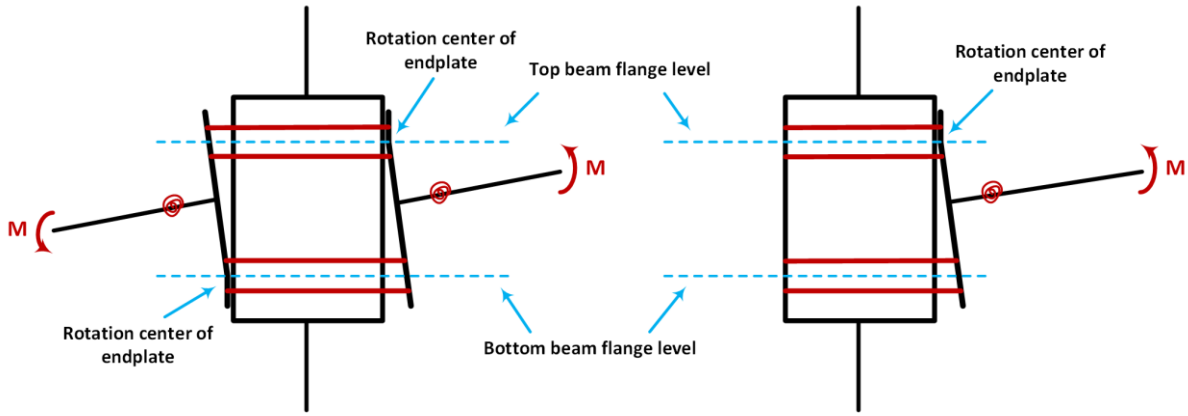

(a) Interial connection *(b) Exterior connection*

Figure 3-6: Simplified computational model for design

The new proposed connection has many possible limit states. The desirable sequence of these limit states is as follows:

- separation of end plates from columns surface,
- yielding of steel rods,
- end plate yielding,
- SMA phase change,
- SMA full martensite hardening,
- beam plastic hinges, and
- panel zone yielding.

In the preliminary design procedure, the ‘strong column-weak beam’ concept is employed. In order to reduce the connection demands so as to limit the rod diameters, the RBSs are used at both beam ends. In the future, the sizes of RBSs can be modified, even removed by using full

beam sections, in an improved design procedure to obtain different relative strength and stiffness between the connection and the beam to adjust beam plastic behavior.

The proposed preliminary design procedure includes twenty-six steps in total. A detailed description of each design step is illustrated in Appendix B. The main design concept is to determine the rod diameters to obtain specific moment capacities at specific rod elongations. In other words, this design procedure is a deformation-based design, instead of a strength-based design. The design procedure requires only four key parameters to determine the shape of the connection moment-rotation behavior. These parameters, which are at the designer's discretion, including:

1. the damage parameter, γ, in Step 5, which is used to determine the percentage of the beam full yielding reached at specific rods' elongation, see Figure 7-3;
2. the self-centering parameter, ζ, in Step 8, which is used to determine the moment capacity supplied by only SMA rods after steel rods yield, see Figure 7-3;
3. the recovery parameter, β, in Step 10, which is used to determine the pretensions in SMA rods; and,
4. the non-yielding parameter, χ, in Step 15, which is used to determine the pretensions in steel rods.

For each key parameter, a suggested range is given. Studies have proven that the design results are not very sensitive to the key parameters within the suggested ranges.

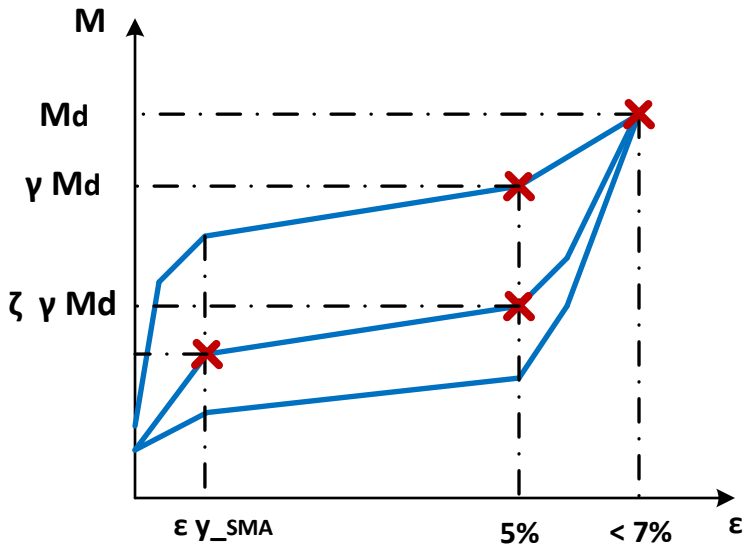

Figure 3-7: Relationships of design parameters γ and ζ

Generally speaking, the twenty-six steps can be divided into following parts:

- Step 1 to step 4 address the preliminary RBS dimensions, moment demand of the end plate, and end plate thickness.
- Step 5 to step 17 address the design of both SMA and steel rods, including rod dimensions and pretension. Both the connection rotation capacity and the maximum strain in rods are also checked. While the flexural capacity of the NPSC is supplied by both SMA and steel rods together, they are designed separately. The design of the SMA rods will be based on the required self-centering capacity at specific connection rotation. The steel rods will be designed based on the total moment demand of the connection at the same specific connection rotation. Then the maximum strain in SMA rods is checked to make sure the design limit of 7% is not exceeded under the ultimate moment

demand. Specific calculations are as follows:

- From step 5 to step 8, the designed moment capacity of the SMA rods, the length of all rods, and the designed connection rotation capacity are calculated.
- From step 9 to step 12, the dimension of the SMA rods and their pretension are determined. There are three rod patterns being considered in the design (Figure 3-8) based on the size of the connected beams. The SMA rods are designed at their maximum strain of 5%, which can be considered as a non-residual strain limit.

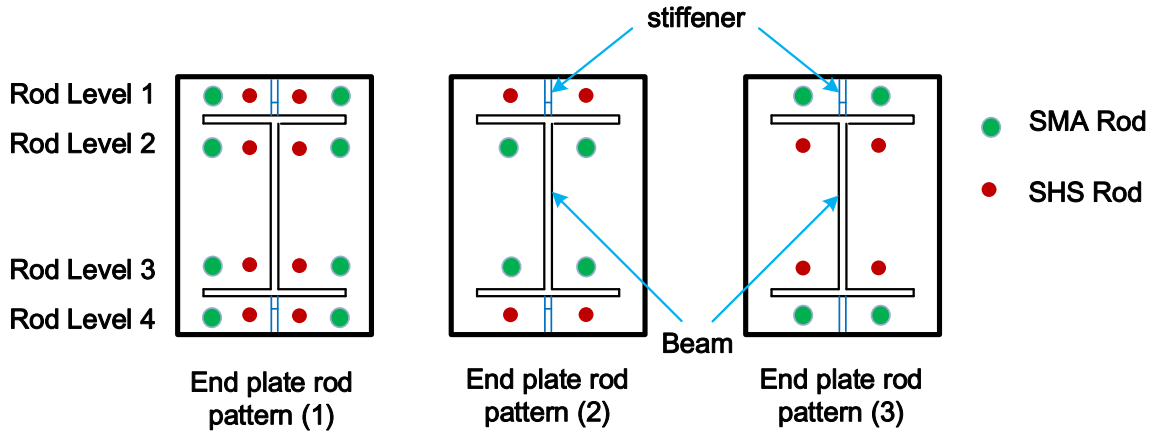

Figure 3-8: Three end plate rod patterns

- From step 13 to step 15, the dimension of the steel rods and their pretension are determined. The design moment capacity of the connection for the design of the steel rods is calculated from the difference between the total connection moment demand and the flexural capacity supplied by the SMA rods at the same specific connection rotation. The rotation is determined when the maximum strain in SMA rods is 5%.

- From step 16 to step 17, the ultimate connection flexural capacity is calculated and compared with the ultimate demand. Also the maximum strain in SMA rods is checked. The upper strain limit for SMA rods is 7%.

- From step 18 to step 22, the shear failure modes are checked for the end plate and rods, including shear yielding and rupture.
- From step 23 to step 26, all the remaining components of the NPSC are designed, including the thicknesses of the inner diaphragm, rectangular steel tube, and beam stiffeners, and the fillet welds size between the circular tube and the rectangular tube.

3.4 Design Examples for the Proposed Connection

In this section, two design examples are introduced based on the proposed design procedure in section 3.3. Example one (E.1) uses material A572 Gr. 55 for the steel rods; example two (E.2) uses material A572 Gr. 50 for the steel rods. All other materials' properties are the same for both examples. All the material information is listed in Table 3-1. The yield and ultimate strength of the SMA come from the experimental stress-strain curve. This assumption is made because SMA is not a common material used for structural components at present, and it is hard to decide its specified nominal properties. The experimental stress-strain curve for SMA is plotted in Figure 3-9, and the design stress-strain curve for the steel rods with Gr. 55 and Gr. 50 are plotted in Figure 3-10. For steel A572 Gr. 55 and Gr. 50, the strength degradation branch is not considered for design purposes.

Table 3-1: Material Properties for Each Component

Component	Material	F_y (ksi)	F_u (ksi)
Beam	A992	50	65
Circular tube	A572 Gr.50	50	65
Square tube	A500 Gr.B	46	58
End plate	A572 Gr.50	50	65
SMA rods	Nickel-Titanium Alloy based on ASTM F2063-12	66.7	74.5 at strain of 5% 116 at strain of 7%
Steel rods	A572 Gr.55 for E.1	55	70
	A572 Gr.50 for E.2	50	65
Inner diaphragm	A572 Gr.50	50	65
Beam stiffener	A992	50	65
Cover plate	A36	36	58
Welds	E70	70	-

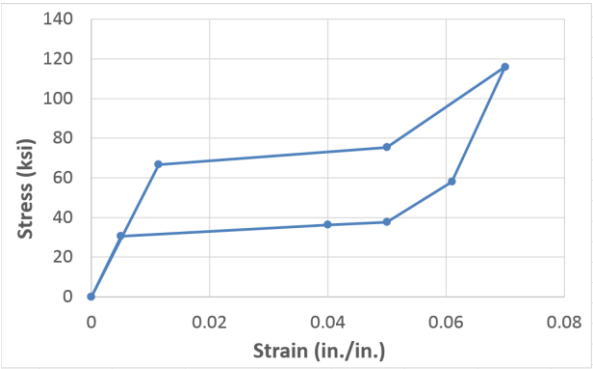

Figure 3-9: Experimental stress-strain curve of SMA

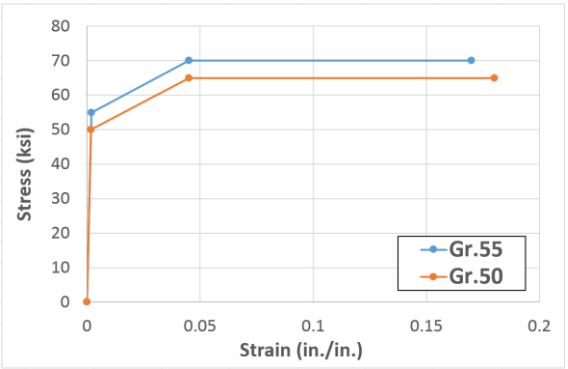

Figure 3-10: Design stress-strain curve of A572 Gr.55 and Gr.50 steel

In each example, the column and the square tube sizes are kept the same for all different beams. For the circular steel tube, the outer diameter is 24” and the wall thickness is 1.375”. For the square steel tube, the outer width is 30”, and the wall thickness is 1.0”. The frame member sizes are determined by the preliminary design in Appendix K. The size of the rectangular tube is designed based on the outer diameter of the circular tube.

The design results of E.1 and E.2 are presented in Table 3-2 and Table 3-3, respectively. The number in parenthesis next to the beam size refers to the rod pattern given in Figure 3-8. In order to make the practical design as simple as possible, the rods diameters are selected as either 1.128'' or 1.270'' for all rods. Comparing the results in the two tables, one can notice that the diameters of the SMA rods (d_{SMA}) for beams W33*130 and W30*116 increase from 1.128'' in E.1 to 1.270'' in E.2, and the corresponding diameters of the steel rods (d_{steel}) for these beams decrease from 1.270'' in E.1 to 1.128'' in E.2; for other beams, the rods diameter are the same. The following facts can be observed:

- Connections of E.2 requires larger SMA rods and smaller steel rods for the W30*130 and W30*116 case; for all other cases, the numbers are generally the same.
- If the total number of rods is constant, more and larger SMA rods will be needed in E.2 as the steel rods will provide less of the total flexural capacity.
- The corresponding maximum strains on the SMA (ε_{SMA}) and steel rods (ε_{Steel}) for both E.1 and E.2 are similar to each other, as is also the maximum stress (σ_{SMA}) of SMA rods.
- The pretension ratio, α, given as a percent of the SMA strength for E.1 is larger than E.2 for beams W33*130 and W30*116. The total designed capacity required from the SMA rods pretension is related to the beam span and load combinations as described in the design procedure in Appendix B. Because the total area of SMA rods for E.1 is less than that of E.2, a relatively higher pretension ratio is needed for the SMA rods in E.1.

Table 3-2: Design Results of E.1 (units: in., k-in.)

Beam	W33*130 (1)		W30*124 (1)		W30*116 (1)		W21*57 (2)		W21*57 (3)	
Location	Inter.	Exter.	Inter.	Exter.	Inter.	Exter.	Inter.	Exter.	Inter.	Exter.
d_{SMA}	1.128	1.128	1.27	1.27	1.128	1.128	1.128	1.128	1.128	1.128
σ_{SMA}	104	111	104	110	103	109	91	94	91	93
ε_{SMA}	0.0645	0.0674	0.0640	0.0672	0.0635	0.0666	0.0580	0.0592	0.0580	0.0591
α	40%	40%	35%	35%	45%	45%	70%	70%	65%	65%
d_{steel}	1.27	1.27	1.128	1.128	1.27	1.27	1.27	1.27	1.27	1.27
σ_{steel}	70	70	70	70	70	70	70	70	70	69
ε_{steel}	0.0608	0.0638	0.0610	0.0642	0.0593	0.0624	0.0560	0.0638	0.0468	0.0431
η	50%	50%	50%	50%	50%	50%	50%	50%	50%	50%
t_{ep}	1.125	1.125	1.25	1.25	1.125	1.125	1.125	1.125	1.25	1.25
t_{inn}	2	1.25	2.25	1.5	2.25	1.5	1.75	1.125	1.75	1.125
θ	0.0726	0.0726	0.0775	0.0775	0.0762	0.0762	0.0902	0.0902	0.0915	0.0915
ζ	0.484	0.476	0.593	0.582	0.490	0.482	0.487	0.482	0.536	0.536
Υ	0.852	0.826	0.828	0.802	0.861	0.834	0.908	0.903	0.885	0.827
β	0.891	0.891	0.901	0.901	0.910	0.910	0.852	0.852	0.871	0.871
M_{pre}	7376		6236		7054		3128		3037	
M_{preSMA}	3198		3232		3263		1717		1756	
M_d	22705		21409		20356		6939		6948	

Table 3-3: Design Results of E.2 (units: in., k-in.)

Beam	W33*130 (1)		W30*124 (1)		W30*116 (1)		W21*57 (2)		W21*57 (3)	
Location	Inter.	Exter.	Inter.	Exter.	Inter.	Exter.	Inter.	Exter.	Inter.	Exter.
d_{SMA}	1.27	1.27	1.27	1.27	1.27	1.27	1.128	1.128	1.128	1.128
σ_{SMA}	102	108	108	115	100	107	98	102	97	98
ε_{SMA}	0.0632	0.0662	0.0660	0.0693	0.0625	0.0656	0.0614	0.0631	0.0606	0.0614
α	30%	30%	35%	35%	35%	35%	70%	70%	65%	65%
d_{steel}	1.128	1.128	1.128	1.128	1.128	1.128	1.27	1.27	1.27	1.27
σ_{steel}	65	65	65	65	65	65	65	65	65	65
ε_{steel}	0.0607	0.0636	0.0629	0.0662	0.0594	0.0625	0.0597	0.0685	0.0492	0.0449
η	50%	50%	50%	50%	50%	50%	50%	50%	50%	50%
t_{ep}	1.125	1.125	1.25	1.25	1.125	1.125	1.25	1.25	1.125	1.125
t_{inn}	2	1.25	2.25	1.5	2.25	1.5	1.75	1.125	1.75	1.125
θ	0.0736	0.0736	0.0775	0.0775	0.0774	0.0774	0.0906	0.0906	0.0910	0.0910

ζ	0.614	0.602	0.593	0.582	0.621	0.609	0.486	0.481	0.536	0.536
Υ	0.832	0.807	0.802	0.777	0.841	0.815	0.867	0.863	0.851	0.797
β	0.847	0.847	0.901	0.901	0.897	0.897	0.852	0.852	0.871	0.871
M_{pre}	6037		5963		5936		3000		2921	
M_{preSMA}	3040		3232		3218		1717		1756	
M_d	22705		21409		20356		6948		6939	

- The pretension ratio, η, of steel rods is fixed at 50% of yield strength for both examples.
- The thicknesses of the end plates (t_{ep}) and inner diaphragms (t_{inn}) are almost the same for the two examples based on the proposed design procedure.
- For the four design parameters:
    - θ, the rotation capacity of the connection (including the RBS portion which is assumed to contribute 3%) when the maximum strain in SMA rods reaches 5%, is similar for both examples.
    - ζ, the percentage of the total moment capacity provided by the SMA rods when the maximum strain in SMA rods reaches 5%, increases by about 27% from E.1 to E.2 for beams W33*130 and W30*116, and remains the same for the other two beams.
    - Υ, the damage parameter of the RBS when the maximum strain of SMA reaches 5%, has slightly larger values for E.1 than for E.2. This means when the maximum strain of SMA reaches 5%, there will be more plastic behavior generates at the RBS in E.1 design case.
    - β, a recovery parameter which is calculated based on the self-centering capacity from the pretension of SMA rods, has larger values for E.1.

- E.1 has larger moment capacity from rod pretension, M_{pre}, than E.2 based on the design procedures. The difference between two examples is about 20% for beams W33*130 and W30*116, but only about 4% for beams W30*124 and W21*57.
- The ultimate design capacity of the connection, M_d, is the same for both examples as it is calculated based on the connecting beam size and the distance between the center of the RBS to the surface of the rectangular tube.

In summary, if a lower steel grade is used for steel rods (Example 2 vs. Example 1):

(1) The required total area of SMA rods increases, and the required total area of steel rods decreases.

(2) If the pretension ratio in the steel rods is fixed as designed, then the required pretension ratio in the SMA rods decreases.

(3) The maximum stress and strain on all rods under the ultimate design moment is about the same.

(4) The required thicknesses of the end plates and inner diaphragms are similar.

(5) The connection behavior, including rotation capacity, RBS plastic damage, and relative recovery capacity under SMA pretension do not vary much.

(6) A large increase in the parameter ζ means the SMA rods will supply more moment capacity under the target design moment M_{tar}.

(7) The absolute moment capacities from rods pretension decreases.

Although the design results show some differences by using higher steel grade for steel rods, there are no obvious advantages to utilizing a higher steel grade. Because A572 Gr.50 is easier and cheaper than its higher grade counterpart, it will be selected as the material for the steel rods in all the future designs. An optimized connection behavior will be obtained by modifying other parameters of the connection, such as the pretension ratios of both SMA and steel rods, and the four design parameters (θ, ζ, Υ, β).

As one can see, there are three rods patterns of the connection (Figure 3-8) utilized in the above two examples. Generally speaking, pattern (1) is applicable for the beams with large depth, and patterns (2) and (3) are workable for the beams with small depth. Table 3-2 and Table 3-3 present the design results for the W21*57 beam with both pattern (2) and pattern (3). Both of these two patterns for the W21*57 beam generate the same rods diameters, 1.128'' for SMA rods and 1.27'' for steel rods. For both examples, rod pattern (3) indicates: (A) a lower required pretension ratio for SMA rods; (B) a lower maximum strains in all rods under the ultimate design moment M_d, especially for the steel rods; (C) a larger rotation capacity of the connection (parameter θ); (D) a larger moment capacity from SMA rods under M_{tar} (parameter ζ); (E) a larger relative recovery capacity (parameter β); and (F) a smaller plastic damage at RBS (parameter Υ). All these results indicate a better connection performance is given by pattern (3) than by pattern (2).

The two examples also reveal a 'defect' of the current design procedure, i.e., that the calculated

thickness for the inner diaphragm is relative large, sometimes greater than 2”. This is because the design is based on the assumption that all the compressive force from the end plate is resisted only by the inner diaphragm, and the bearing capacity from the infill grout is neglected. There are two ways to alleviate this issue: (1) modify the design equations based on the FE analysis results in Chapter 5 to consider the infill grout bearing capacity; (2) widen the end portion of the beam flanges to distribute the concentrated load to a larger bearing area on the square tube face. The first method is relative simple, although it will require more FE models to verify the effectiveness of the modified design equations. The second method involves more complicated issues, because a large number of different samples are needed to be analyzed from both FE analysis and experimental tests aspects to make sure this new beam configuration (both RBS and widen flanges at the end of beam) works reliably.

Another very important concern that requires careful investigation to improve the current design procedure is the design of the shear capacity of the composite panel zone. Although the FE results in Chapter 5 indicate that the strength of the composite panel zone is strong enough to resist the ultimate reverse loadings, a simple and clear failure model is still needed.

Two other assumptions should be mentioned about the proposed design procedure. One is that the shear capacity of the SMA is assumed as $0.6F_y$, where F_y is the yielding strength of the SMA. This is a same assumption as for the steel material. The other one is that in the design procedure, the tension and shear interaction effect for both SMA and steel rods are neglected.

This is because the vertical shear from the beam is supposed to be resisted by the friction between the end plate and the square steel tube face. These two assumptions will be kept constant during this research and will not be discussed further.

3.5 Design of the CCFT Columns

As an important structural component, columns are usually used to bear load combinations with axial, flexural and shear forces. To calculate the design capacity of columns, the ***A***xial-***F***lexural-***S***hear (AFS) interaction should be considered, especially for concrete members. For steel members, studies indicate that the interaction between shear and other two loading cases (axial and flexural loading) is not significant unless all three components are large. In our case, shear forces in the columns are relatively small and assuming that all shear forces are taken by the steel tube, so it is reasonable to calculate the CCFT column capacities for ***A***xial-***F***lexural (AF) interaction only.

In order to simplify the calculation models for a design, the following assumptions are made in CCFT design:

- The tensile strength of concrete is ignored.
- The effects of slippage between the infill concrete and the circular steel tube on CCFTs capacity are ignored. Experimental data shows that if bending is present, the full plastic moment capacity of the section will be reached regardless of the slip at the interface.

- Only AF interaction is assumed to be considered for the CCFT column. All shear applied on the CCFT column is assumed to be resisted by the steel tube only.

There are many methods that have been proposed in several different design specifications to calculate the ultimate axial and flexural capacity, and their interaction of the CCFT columns. The US, European, Australian, Canadian and Chinese provisions for the CCFT design are described briefly in Appendix D, and a corresponding design examples are presented in Appendix E.

3.6 Summary and Conclusions

In this chapter, the configuration of the new proposed smart connection is introduced in detail (Figure 3-1 and Figure 3-2), which consists of: (1) a CCFT column with a collar, which is made of a rectangular steel tube, two inner steel diaphragms and infill expansive grout; (2) two beams with RBS connecting to the extended stiffened end plates by fillet welding; and (3) sixteen or eight through rods connecting the end plates with beams and the CCFT column with a collar together, including two SMA and two steel rods on each rod level or every two rod levels depending on connecting beam sizes.

A step-by-step preliminary design procedure is proposed for the new connection (see Appendix B). All components are to be fabricated in the shop under ideal QA/QC. The only remaining

step needed on site is to bolt the end plates onto columns by using through rods and pretensioning the rods. The preliminary design procedure is described in Section 3.3, and a complete design example is provided in Appendix C. The preliminary design procedure is mainly based on three assumptions: (1) the CCFT columns have adequate shear strength in panel zone to avoid shear yielding; (2) the inward displacement of the rectangular tube wall is insignificant; and (3) end plate remains rigid under rotation except at yield line locations.

Several conclusions were obtained as follows:

- The new proposed smart connection configuration supplies another method to connection CCFT columns and W beams. It has several merits: (1) no need for penetration welds and inspection on site; (2) simple assemblage and good quality control in the shop; (3) rapid erection on site; and (4) self-centering capacity.
- The proposed preliminary design procedure is feasible for NPSCs for both interior and exterior columns. There are no size limitations on beams and columns.
- For small beam size, rod pattern (3) is better than (2) based on the example results.

Different design methods for CCFT columns were introduced in Appendix D and a detailed example is supplied in Appendix E. The results indicated that different capacities can be obtained based on the chosen design method. The AISC is the most conservative method and was used in this research study.

Chapter 4

Simplified Spring Model

This chapter is divided into five sections. In Section 4.1, a *2D simplified spring model* (2D-SSM) and its improved counterpart in SAP2000 for uniaxial bending for the proposed connection are described. In Section 4.2, calculation procedures for each component of the 2D-SSM are presented. A number of different connections taken from a composite special moment frame designed in Appendix K are modeled using the procedure in Section 4.2. A detailed calculation for one typical connection model is shown in Appendix C, and the results of the others are also provided in this section. In Section 4.3, the cyclic behavior of the 2D-SSM and its improved counterpart for the same typical connection calculated in Appendix C are analyzed in SAP2000. This section contains an extremely detailed discussion of the connection behavior and its associated model. In Section 4.4, the behavior of the new proposed 2D-SSM in SAP2000 is summarized, and the comparisons between the 2D-SSM and its improved counterpart are discussed.

4.1 2D Simplified Spring Model in SAP2000

In this section, a *2D simplified spring model* (2D-SSM) for uniaxial bending is developed in SAP2000. This model aims to capture the main characteristics of the new proposed connection behavior, including self-centering capacity, pretension effects, stiffness softening caused by

yielding and sliding of the steel rods, rotation of end plates, and plastic hinges due to RBS and column yielding, among others.

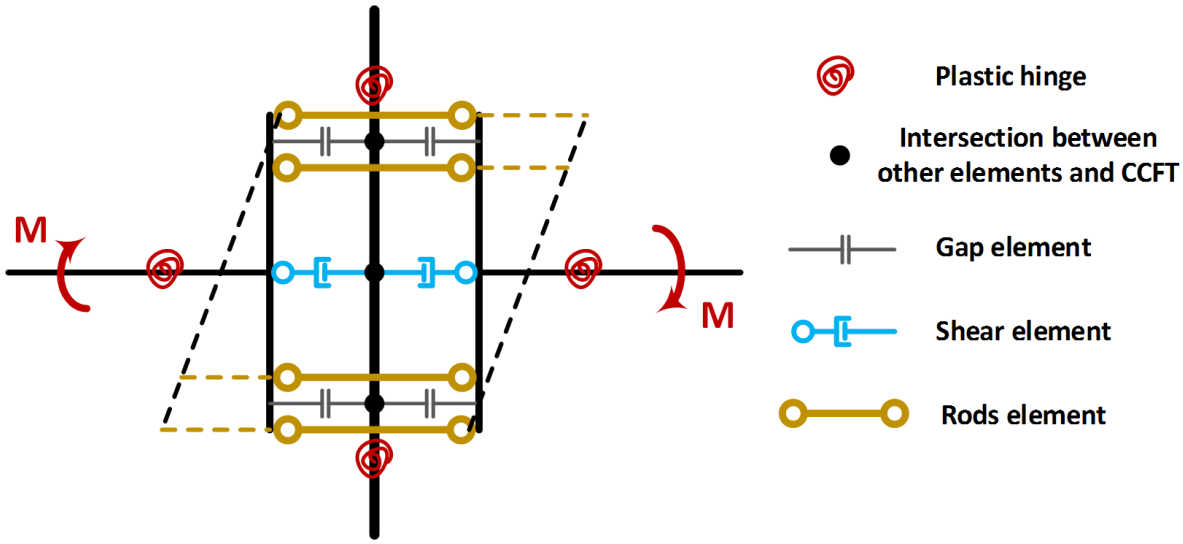

Figure 4-1: 2D-SSM for uniaxial bending connection

In Figure 4-1, a 2D-SSM for an interior connection with all components is illustrated. The vertical dark bold line in the middle stands for the CCFT column, the other two shorter vertical dark bold lines on both sides of the CCFT column represent the two end plates and the two horizontal dark bold lines are used to simulate two beams on either side of the CCFT column. The four plastic hinge elements in red placed on both beams and the CCFT columns represent the plastic hinges in both the RBS and CCFTs, respectively. The four gap elements in gray are used to model the bearing behavior of both the inner diaphragms and infill grout. The two shear elements in blue are adopted to transfer the vertical shear forces from the beams to the CCFT column. The four rod elements in brown are adopted to simulate all rod behavior on four levels and help resist the moment at the ends of beams by supplying tension forces. A detailed

description for each element is as follows:

- For the CCFT column, a beam element is used. Three *degrees of freedom* (**DOFs**) in plane are kept at each node. The three out of plane DOFs are removed as typical for a 2D model; these DOFs are also eliminated from all other elements unless otherwise noted. Elastic cross section properties for the CCFT column are assigned to this beam element. All plastic behavior will be considered only by the two plastic hinges on the top and bottom CCFT columns near the joint.
- For the two end plates, either two rigid link elements or two elastic beam elements with very large elastic stiffness for all axial, flexural and transverse DOFs are used. The end plate in the model can therefore be considered as rigid if the end plate is very thick or flexible if it is not. The initial modeling decision to use a rigid element was motivated primarily by perceived numerical problems. This constraint was later removed when it became clear that end plate deformations needed to be considered for proper computation of the moments at beam ends.
- For the two beams on both sides of the CCFT column, two linear beam elements are used. The elastic cross section properties of the W sections are assigned to these beam elements. All plastic behavior of the RBSs will be considered within the two plastic hinges on the beams.
- The four plastic hinge elements are classified into two groups. One is the *plastic hinge* of the CCFT *column* (**PHC**), which is located at both ends of each CCFT column. The other is the *plastic hinge of the RBS* (**PHR**), which is located at the center of the RBS

cross section on the beams. For the PHRs, only a non-linear moment-rotation curve for the RBS is defined based on the procedure described in section 4.2.1. For the PHCs, the P-M interaction effect for the CCFT column is considered based on the procedure described in section 4.2.2.

- Four gap elements with very large elastic stiffness are used to model the bearing behavior of the inner diaphragms and the infill grout. The gap elements have only axial stiffness in compression. A very large elastic stiffness is assigned to them, so the contribution to the overall deformation of the 2D-SSM of the inner diaphragms and the infill grout under compression is very small.
- Two so-called 'shear elements' are defined by using two linear beam elements. This type element is designed to transfer only the vertical shear forces from the beams to the CCFT column, and doesn't supply any axial and flexural capacities. To accomplish this, the axial and flexural DOFs at the end connecting to the end plate are released. For the proposed connection, the vertical shear forces from the beams are assumed to be resisted by the friction between the end plates and the square steel tube faces, and there are very small relative vertical movements between them. To achieve this aim, a very large elastic transverse stiffness will be assigned to these shear elements. Therefore, the relative vertical movements between the end plates and the CCFT column will be insignificant as intended in design.
- There are four so-called 'Rod elements' used in the 2D-SSM. In reality, each of the 'Rod elements' is composed of three sub-elements: (1) one 'MultiLinear elastic link

element' and one 'MultiLinear plastic link element with Kinematic hysteresis law'; (2) one 'Hook element' and one 'MultiLinear plastic link element with Takeda hysteresis law'; and (3) the combination of the above two types. For all the hook and plastic link elements, only the axial DOF is defined; all others are released. The choice of the 'Rod element' depends on the different rods patterns for the connection configuration shown in Figure 3-8 and the rod locations (on the exterior or interior rod level). Generally speaking, each 'Rod element' should be able to simulate the combined behavior expected of all rods on each level (SMA only, steel only or combination): (1) only the SMA rod behavior with flag-shape pseudoelastic self-centering and pretensioning effect; or (2) only the steel rod behavior with stiffness softening due to yielding and sliding effects and pretensioning effect; or (3) the combination of the above two to simulate both SMA and steel rods on that rod level. These three types of behavior correspond to the three types of the 'Rod element' described above, respectively. In other words, the behavior of SMA rods can be simulated by the combination of one 'MultiLinear elastic link element' and one 'MultiLinear plastic link element with Kinematic hysteresis law'; and the behavior of steel rods can be simulated by the combination of one 'Hook element' and one 'MultiLinear plastic link element with Takeda hysteresis law'. The detailed components of different rods patterns are presented in Figure 4-2, and the calculation procedures for each element are introduced in Sections 4.2.3 and 4.2.4 for SMA rods and steel rods, respectively. The rod patterns are shown in Figure 3-8.

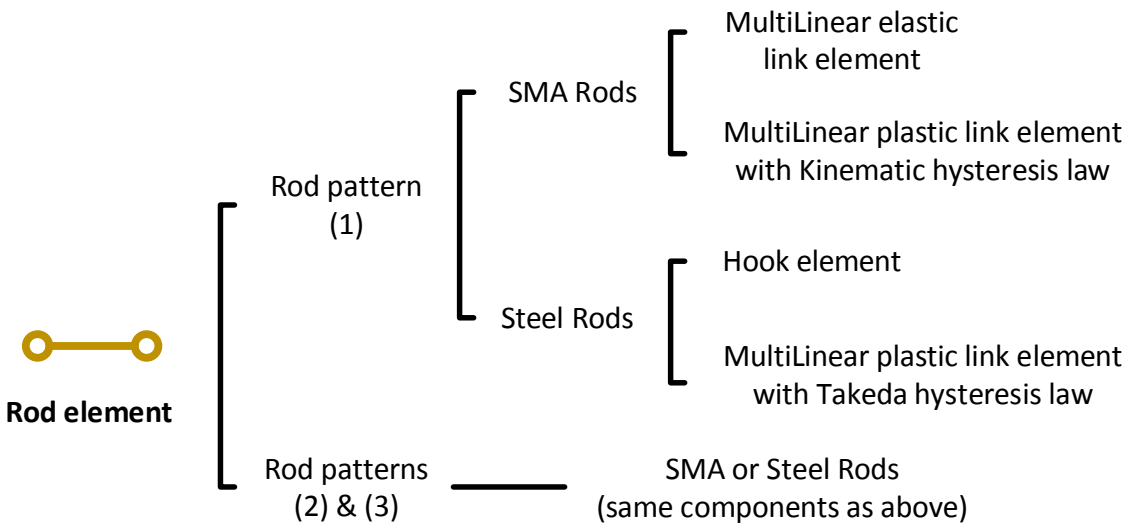

Figure 4-2: Components of each rod element

All elements of the proposed 2D-SSM must be assembled properly to achieve their designed function. The assembly procedure is divided into the following steps:

(1) The beam element for the CCFT column is continuously connected to the CCFTs elements above and below the story being modeled.

(2) The beam element for the CCFT column are connected to either the rigid link or elastic beam element used for each end plate by two gap elements and one 'Shear element' horizontally on either side of the column. The two gap elements are at the level of beam flanges, and the 'Shear element' is at the center of the connection. The released end of the beam element for the 'Shear element' is on the side of the end plate.

(3) Four 'Rod elements' connect the two rigid links or beam elements for the end plates on each rod level directly; there are no intersections (indicated by the large black dots on the CCFT column for the gap and shear elements) between the 'Rod elements' and the

beam element for the CCFT column.

(4) The two beam elements for the steel beams on both sides of the CCFT column are connected rigidly to the corresponding end plate at its middle point.

(5) The two plastic hinges of the CCFT column and the two plastic hinges of the RBSs are defined at their proper locations as described above.

After the assemblage, the finalized configuration of the 2D-SSM is shown in Figure 4-1 and Figure 4-3. The dashed lines represent the main deformation of the proposed model under clockwise moments at the end of beams, including rotation of the end plates and elongation of the rods. In reality, it is not necessary that the two end plates deform in parallel as explained in step 9 of the preliminary design procedure in Appendix B.

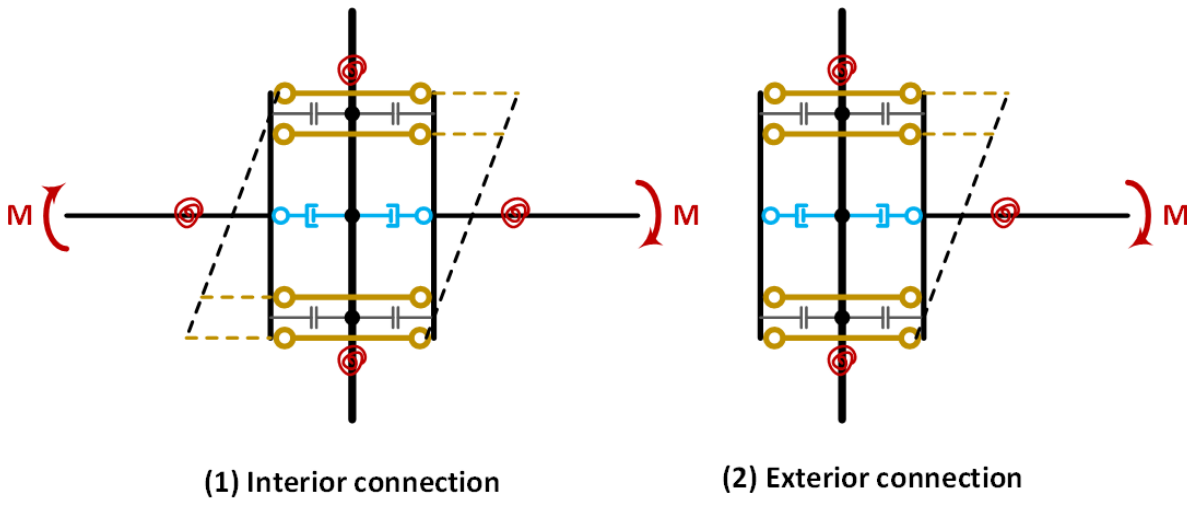

Figure 4-3: Deformation of the interior and exterior connection under the clockwise moment

There are two models presented in Figure 4-3: one is for an interior connection and the other is for an exterior connection. One can notice that under a clockwise moment, the end plate rotates about the point where the gap element and the end plate intersect one another. All rods on a given level of the interior connection will elongate by the same amount; however, the rods on the top three levels of the exterior connection will elongate by different amounts, and the rods on the bottom level will shrink. The proposed 2D-SSM will present a slightly different behavior for the interior as compared to the exterior connection because:

- For the interior connection, one knows that all rods will be in tension (or slack) to resist the moments from the two beams. If one takes the right end plate and beam in Figure 4-3(1) for an example, the rods in tension on the upper three levels supply the moment resistance capacity about the rotation center. However, the rods' tension on the bottom level contributes to the rotation deformation of the right end plate. In reality, this tension in the rods on the bottom level should be transferred into the CCFT column directly through the inner diaphragm and the infill grout, and have no effect on the rotation of the right end plate. So this behavior is expected to make the connection softer in both strength and stiffness. Under the given moments, a larger rotation of the end plates will be generated than one would expect in reality. Thus more strength in the rods should be supplied to resist the additional moment caused by the tension in the rods on the bottom level. However, this additional moment is very small compared with the moment from the beam due to the small distance between the exterior rod level and the adjacent gap element level where the rotation center is located. Thus this softening behavior has

insignificant effect on the overall connection behavior.

- In addition, the yielding of the end plate is ignored in the 2D-SSM, because the plastic behavior of the end plate is not considered in the design procedure. Based on the deformation shown in Figure 4-1, the whole end plate will remain rigid and will not contribute to the strength and stiffness of the connection if its plastic behavior is not considered. Compared with the real case where the end plate would generate a yield line at the level of the rotation center and supply some bending resistance, this assumption will also cause the connection to show a decrease in both strength and stiffness with a slightly lower energy dissipation capacity. This softness effect is related to the plastic strength and stiffness of the end plate cross section. The thicker the end plate is, the more softening effect will be introduced. Generally speaking, the ratio of the width to the thickness of the end plate is very large, and the plastic strength and stiffness of the end plate cross section is relative small. Thus this assumption is also believed to have minor effect on the real connection behavior.
- For the exterior connection, one can notice that only the rods on the upper three levels supply tension to resist the moment at the end of the beam. Although the rod elements on the bottom will theoretically decrease in length, there will be no compressive force generated on this level due to the fact that the rods are assumed to carry no compressive forces; all those forces are transferred by bearing through the gap elements. As defined in Section 4.2.3 and 4.2.4, the compressive strength of the rods element is set to be zero. This assumption is reasonable because the rods in the real connection cannot supply

any compressive resistance. Compared with the real exterior connection behavior, the 2D-SSM in Figure 4-3(2) still causes a small decrease of both connection strength and stiffness. This softening effect only comes from the assumption on the end plates, which is the same as that discussed above for the interior connection.

In order to address these two defects mentioned above in the proposed 2D-SSM, four additional gap elements and four additional plastic hinges can be added as shown in Figure 4-4. The additional four gap elements are placed on the two exterior rod levels, with the same properties as the others in the model. The connecting method is also the same as other gap elements between the CCFT column and the two end plates. These four additional gap elements on the exterior rod levels are used to transfer the tension in the rods on that level to the CCFT column directly. The additional moment on the end plate caused by the tension in the rods on the exterior levels will be eliminated. Also, four additional plastic hinges are added at the four intersections between the four gap elements on the two beam flange levels and the two end plates. These four intersections are considered as the rotation centers of the two end plates under the beam end moments. Both the original 2D-SSM and the modified one will be modeled in SAP2000, and their accuracy are compared to assess which model is more effective and should be adopted in the future analysis.

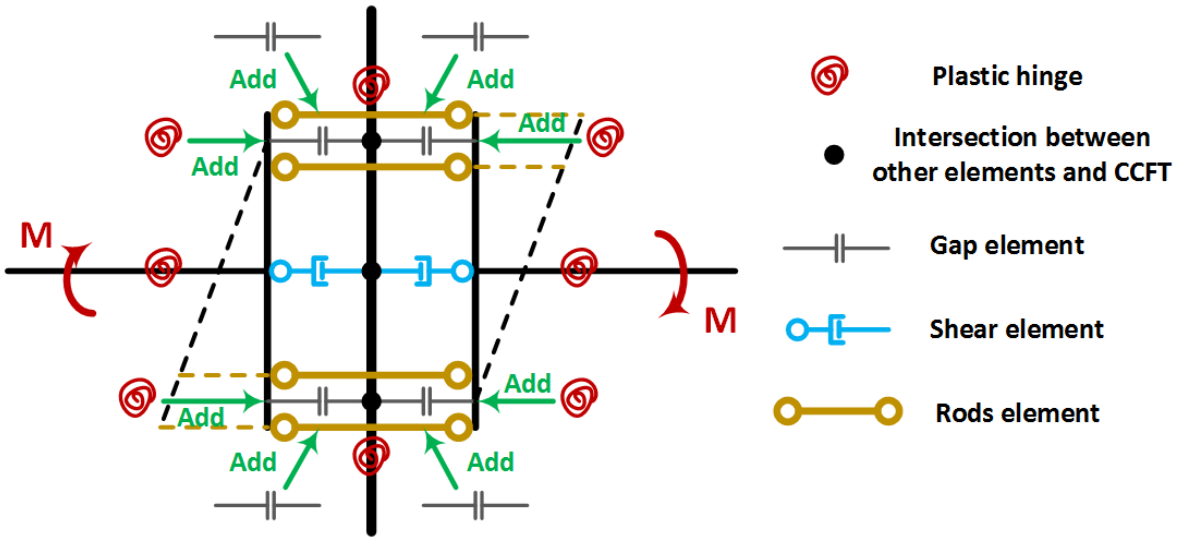

Figure 4-4: Improved 2D-SSM for uniaxial bending

4.2 Calculation of Each Element Properties

In this section, the properties of each element of the 2D-SSM are determined based on the design assumptions in Chapter 3 and the element properties defined in section 4.1:

- The rigid link or beam elements for the end plates, the gap elements, and the shear elements will be assigned very large values for stiffness. They are assumed to be rigid and undeformed compared with other elements. These elements will have no strength limits during the whole loading history.
- The CCFT column and the two steel beams are assumed to be elastic members. Their plastic behaviors will be considered only by the adjacent plastic hinges. Thus their properties are determined based on the section configurations and the elastic material properties.

- The properties of the plastic hinges are calculated assuming full yielding of the whole cross section. The detailed calculations are described in Section 4.2.1 for the RBSs on the beams, and in Section 4.2.2 for the CCFT column.
- All possible components of each 'Rod element' are listed below. The detailed calculations of the properties for each component are described in Section 4.2.3 for the SMA rods, and in Section 4.2.4 for the steel rods:
    - MultiLinear Elastic Link Element for SMA rods,
    - MultiLinear Plastic Link Element for SMA rods,
    - Hook Element for steel rods, and
    - MultiLinear Plastic Link Element for steel rods.

4.2.1 Determination of Properties for the Plastic Hinges Representing the RBS

Steel beams with RBS sections are usually used in *special moment frames* (**SMFs**) in steel buildings to protect the connections and limit the column sizes. For many configurations of steel moment connections with the whole cross section beams, the plastic hinges occur just at or very close to the ends of the beams depending on if there are stiffeners or not. The large plastic strain demand in this region can cause brittle fractures in the beam flange welds and reduce the structural ductility. For a SMF, larger beam sizes are usually needed to meet the stiffness requirements. However, in order to meet the 'strong column - weak beam' concept, even larger column sizes have to be adopted. Large size members cause economic inefficiency and decrease the usable space. The application of beams with RBSs can both reduce the demand

in the beam flange welds and decrease the column size for a couple of reasons. First, because of the smaller moment capacities, most of the plastic yielding in a beam of a SMF will occur at the RBSs. This will move the plastic hinge away from the beam ends and decrease the plastic strain demands on the beam flange welds. Research by both Engelhardt, et al. [83] and Deierlein, et al. [84] indicate that not all the plastic strain demand on the beam flange welds is eliminated by using an RBSs, but a significant reduction in this demand is observed. Second, Grubbs [85], Iwankiw, et al. [86], Almudhafar and Chambers [87] studied the reduction on the overall frames stiffness brought by the RBSs. Their results indicate that 40% reduction in the beam strength by using RBSs only causes 4% to 5% decrease in the overall frame stiffness. The large reduction in beams' strength with an only slight penalty on the frame stiffness will decrease the strength demand on the connecting columns greatly, and reduce the column size effectively.

During a devastating earthquake, most beams will undergo significant deformation reversals in both bending directions several times. Research shows that traditional structural components, such as steel beams and columns, will undergo deterioration in both strength and stiffness under large cyclic loading [88]. In order to have reliable evaluation of the post yielding behavior of the SMFs, one challenge is to develop reliable models that include these deterioration characteristics for each component. There are many such models have been established [36, 39-47]. In this section, only the Modified-IK Model in Appendix G is used to determine the moment rotation relationship for the RBSs as a method to model their cyclic deterioration

behavior.

To determine the controlled strength capacity on the monotonic backbone curves in the Modified-IK Model, the effective yield strength M_y is used to account for the cyclic strain hardening effect. Typically the value of M_y is larger by a small amount than the predicted bending strength $M_{y,p}$, which is defined as the plastic section modulus (Z_x) times the measured material yield strength (F_y) from coupon tests. Lignos and Krawinkler [39] suggest that M_y is about 1.06 (but 1.1 is used in this thesis) times $M_{y,p}$. Also a factor R_y of 1.1 is suggested by AISC 341-10 [77] to multiply to the nominal yield strength to estimate the material yield strength from coupon tests for hot rolled structural sections. Generally speaking, the effective yield strength M_y can be calculated as $1.21F_{y,n}Z_x$, where $F_{y,n}$ is the nominal yield strength of the material.

Another very important parameter for the Modified-IK Model is the yielding deformation, θ_y, at the effective moment strength, M_y. This deformation is the reference for other parameters. M_y is larger than F_yS_x, where F_y is the measured material yield strength and S_x is the elastic section modulus. This means that before θ_y is reached, parts of the section has already gone into the plastic range and the stiffness has begun to soften. This softening behavior before θ_y is reasonable as it considers the yield plateau of typical mild structural steels. However, from the Modified-IK Model in Appendix Figure G-1 one can see that a uniform stiffness is used until θ_y is reached. In order to simulate the elastic stiffness of the plastic hinge before

yielding more accurately, an elastic behavior of the RBSs is assumed before M_y is reached. Although some plastic behavior is ignored at the yield rotation θ_y, this assumption is reasonable because this slight changing of the stiffness of the plastic hinges for the RBSs will not influence the overall stiffness of a SMF very much as discussed above [85-87].

Figure 4-5 shows a sketch of a beam with a double curvature deformation due to the lateral load on the SMF, with the yield rotation θ_y noted in the plot. This beam has two RBSs at both ends, and the moments at the middle of both RBSs is M_y. θ_y should be calculated by integrating the rotation from point A to B (Figure 4-5), where point A is the start point of the plastic hinge, and point B is the ending point of the plastic hinge.

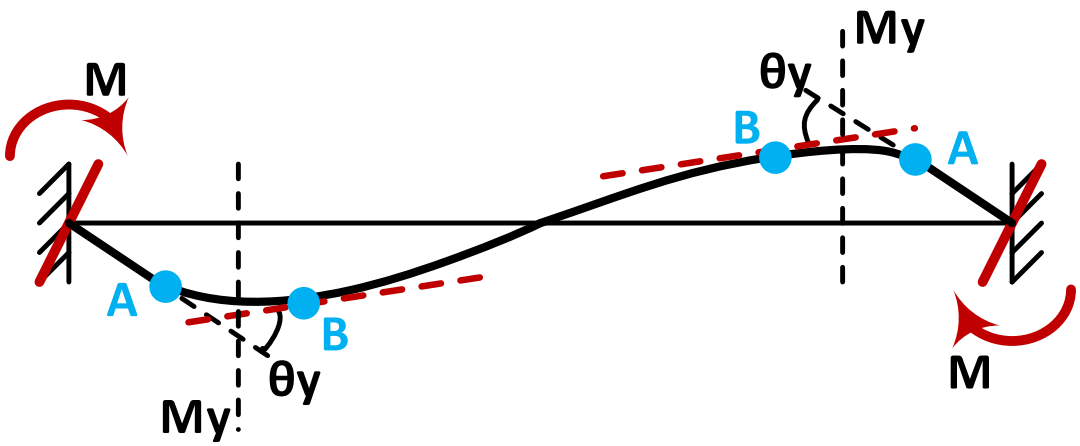

Figure 4-5: Sketch of θ_y for the beam with RBSs

For a beam with a RBSs, the moment of inertia is not constant along the beam length. Thus, it is reasonable to assume that the RBSs contributes most of the yield deformation. Because the moment along the RBS changes linearly and the section properties of the RBS about the middle

section is symmetric, the mean value of the two moments at the beginning and end of the RBS is the same as the moment at the middle section. Thus the θ_y calculated by using a moment diagram with a linear gradient along the RBSs should be the same as the value calculated based on a uniform moment gradient with a value of M_y, the effective yield moment of the middle section of the RBS.

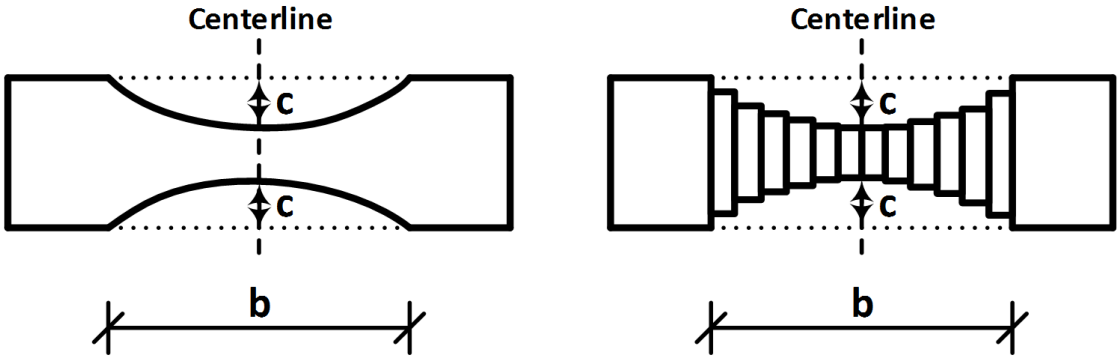

(a) The radius cut RBS *(b) The idealized discrete RBS*

Figure 4-6: The RBS section

The radius of the RBS shown in Figure 4-6(a) can be idealized as a series of rectangular sections as shown in Figure 4-6(b). The flange width of this set of W-sections increases gradually from the minimum flange width of the RBS to the full-size W-section. Assuming the total number of the discrete sections is 2N, assign a sequence number i for each discrete section, starting with i equal to 1 for the section with minimum flange width. The yield rotation θ_y of the RBS under uniform moment M_y can be estimated by the following equations:

$$\theta_y = 2 \cdot \sum_{i=1}^{N} \theta_i \qquad \textbf{(Eq. 4-1)}$$

where,

$$\theta_i = \Delta L \cdot \dot{\theta}_i$$

$$\Delta L = \frac{b}{2 \cdot N}$$

$$\dot{\theta}_i = \frac{M_y}{E_s \cdot I_i}$$

$$I_i = I_x - \Delta I \cdot (N + 1 - i)$$

$$\Delta I = 2 \cdot \left[\frac{1}{12} \cdot \Delta b \cdot t_f^3 + \Delta b \cdot t_f \cdot \left(\frac{d - t_f}{2} \right)^2 \right]$$

$$\Delta b = \frac{2 \cdot c}{N}$$

b, c = parameters of RBS, in.

M_y = expected yield strength at the RBS, k-in.

N = the number of discrete sections on half RBS section

E_s = elastic Young's modulus, ksi.

I_s = moment inertia of the whole W, $in.^4$

t_f = beam flange thickness, in.

d = beam depth, in.

For the 2D composite special moment frame that is designed in Appendix K, there are four sizes of steel beams used, as shown in Table 4-1. In order to define the cyclic behavior of each plastic hinge, the Modified-IK Model introduced above is utilized. Instead of using test data, the required parameters for the Modified-IK Model will adopt the values suggested by Lignos and Krawinkler [39], including $M_c/M_y = 1.09$, $\kappa = 0.4$, and $M_y = 1.21F_{y,n}Z_x$; and the ultimate rotations are assumed to be either $\theta_u = 0.18\ or\ 0.21$. The other three deterioration parameters ($\theta_p, \theta_{pc}, and\ \Lambda$) will be determined by using the three regression equations (AEq. G-5), (AEq. G-7), and (AEq. G-9) in Appendix G. In Table 4-2, L is the distance from the center of the RBS to the midpoint of the beam; L_b is defined as the distance from the beam end to the surface of the beam bracing stiffener (Figure 4-7); B is the width of the rectangular tube; and t_{ep} is the thickness of the end plate. The results are presented in Table 4-1, Table 4-2, Table 4-3 and Figure 4-8.

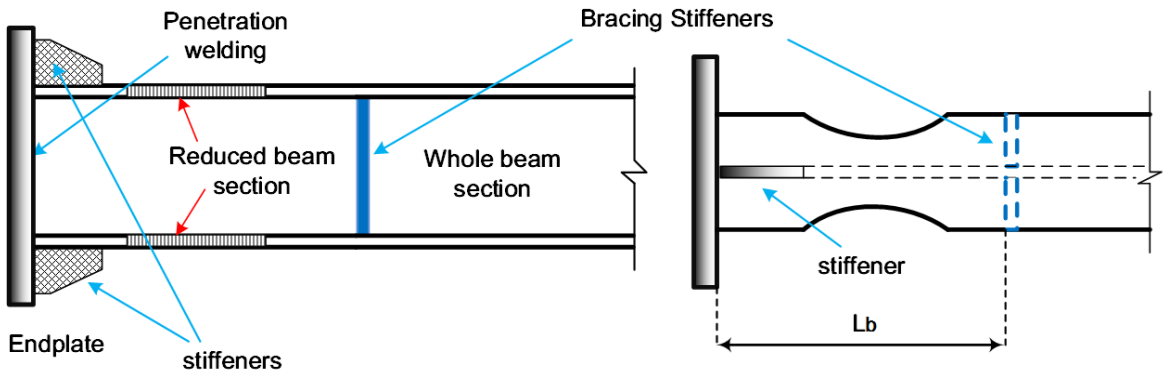

Figure 4-7: The unbraced length of the RBS

Table 4-1: Yielding Deformation θ_y for RBS in the 2D-SMF (units: in., rad., $in.^4$)

Level	Section	a	b	c	N	ΔL	Δb	ΔI	$d/2$	θ_y
1 & 2	W33*130	5.75	22	2.875	10	1.1	0.575	255.64	16.55	0.00273
3	W30*124	5.25	20	2.1	10	1	0.42	167.38	15.1	0.00279
4	W30*116	5.25	20	2	10	1	0.40	144.49	15.0	0.00284
Roof	W21*57	3.5	14	1.2	10	0.7	0.24	32.63	10.55	0.00289

Table 4-2: Deformation Properties of the Plastic Hinges for the RBSs in the 2D-SMF (units: in., rad.)

Level	Section	Span	B	t_{ep}	L_b	L	θ_p	θ_{pc}	θ_u	Λ
1 & 2	W33*130	384	30	1.5	33.5	158.75	0.023	0.178	0.18	1.108
3	W30*124	384	30	1.5	30.5	160.25	0.027	0.22	0.18	1.414
4	W30*116	384	30	1.5	30.5	160.25	0.026	0.20	0.18	1.28
Roof	W21*57	384	30	1.5	21	165	0.036	0.239	0.21	1.474

Table 4-3: Strength Properties of the Plastic Hinges for the RBSs in the 2D-SMF (units: ksi, $in.^3$, k-in.)

Level	Section	F_y	Z_x	$M_{y,p}$	M_y	M_c	M_r	M_u
1 & 2	W33*130	55	308.5	16968	18665	20345	7466	7466
3	W30*124	55	293.7	16154	17769	19369	7108	7108
4	W30*116	55	278.9	15340	16874	18393	6750	6750
Roof	W21*57	55	97.1	5341	5875	6404	2350	2350

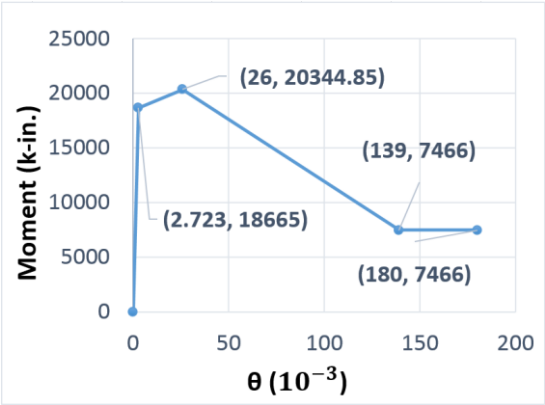

*(a) bam W33*130*

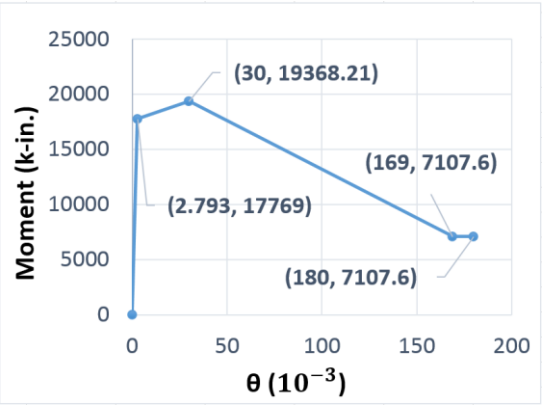

*(b) beam W30*124*

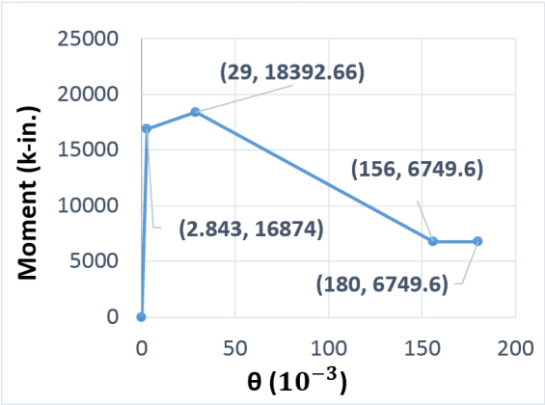

*(c) beam W30*116*

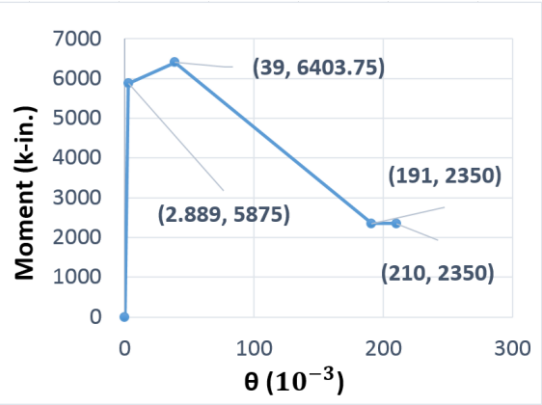

*(d) beam W21*57*

Figure 4-8: The backbone curves based on modifined-IK model for RBSs in Table 4-1

4.2.2 Determination of Properties for the Plastic Hinge for CCFT Column

Although the 'strong column - weak beam' concept is always required for SMF design, many analyses show that plastic hinges will be generated at some column ends in the SMFs during a severe earthquake, especially at the foundation. The behavior of column plastic hinges (PHCs) has a great effect on the seismic performance, primarily in terms of drift ratios (at roof and story level), maximum acceleration, energy dissipation, and collapse behavior.

As mentioned in Chapter 3, there are several design specifications that can be used to determine the CCFT column capacities. In order to be compatible with the design of other members in this thesis, only the AISC method is adopted, as discussed in detail in Appendix F.

As opposed to beams, columns bear not only moments and shear, but also considerable axial forces. As discussed in Section 3.5, only *Axial-Flexural* (**AF**) interaction is considered herein for CCFT columns. According to the discussion in Appendix F, a whole interaction diagram in Figure 4-9 for axial force (compressive and tensile) and moment can be determined for an arbitrary CCFT column. To make the analyses results match the real structural behavior as much as possible, the expected true material properties can be used, including the strain hardening effects. The anchor points for the curve representing the true beam-column capacity are defined by i_{tr} ($i = A, B, C, D, E, F, and\ G$), where the subscript tr indicates the use of "true" material properties (see Table 4-6). One can use $1.1R_yF_y$ to take place of steel nominal yield strength F_y to obtain the true steel strength. R_y is the ratio of the expected yield stress to the specified minimum yield stress. The factor 1.1 is used to consider the strain hardening effect, which is the same as that used for RBS in section 4.2.1. The compressive strength f_c' is still used for concrete. In order to consider column length effects which are indicated by λ, the curve defined by points $i_{tr\lambda}$ in Figure 4-9 should be used, instead of the curves defined by either point i or i_d, which are determined based on norminal material strengths and considering length effects and resistance factors, respectively.

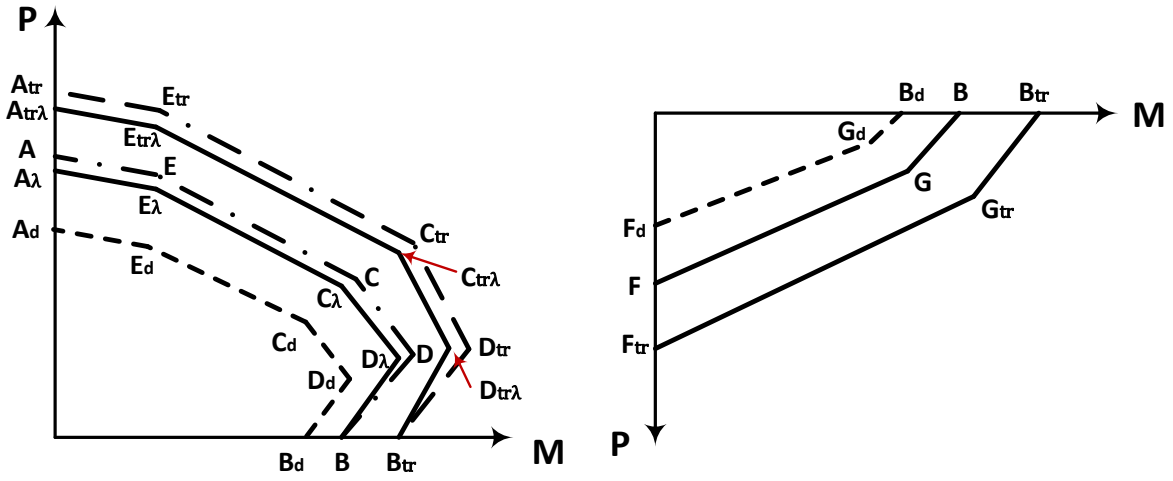

(a) Compression *(b) Tension*

Figure 4-9: Definition of column P-M interaction curves based on different material strength levels and column length effects

As designed for the composite SMF in Appendix K, the CCFT24*1.375 cross section is adopted for all composite columns, whose detailed information is shown in Table 4-4. As the diameter of the steel tube is larger than those of the conventional HSS sections, a spirally welded circular tube will be used, utilizing ASTM A572 Gr.50 steel plate. The associated parameters of the strength deduction of the CCFT column due to length effects are presented in Table 4-5, with considering nominal and true strength for the steel tube. The values of the anchor points i, i_λ, i_d, i_{tr}, and $i_{tr\lambda}$ $(i = A, B, C, D, E, F, and\ G)$ of the AF interaction curves in Figure 4-9 are listed in Table 4-6 and these curves are plotted in Figure 4-10. LRFD method is used to determine the design curve.

*Table 4-4: Properties of CCFT 24*1.375*

CCFT	D (in.)	t (in.)	A_s (in^2)	A_c (in^2)	L (ft.)	F_y (ksi)	R_y	f'_c (ksi)
24*1.375	24	1.375	97.7	354.7	14	50	1.1	4.67

Table 4-5: Deduction Parameters for CCFT Column Associated with Length Effect

F_y (ksi)	C_3	I_s (in^4)	I_c (in^4)	EI_{eff} $(k\text{-}in^2)$	P_e (kips)	P_0 (kips)	λ	P_λ (kips)
50	0.9	6277	10010	$2.172 * 10^8$	75940	6460	0.29	6234
$1.1R_yF_y$ (ksi)	C_3	I_s (in^4)	I_c (in^4)	EI_{eff} $(k\text{-}in^2)$	P_e (kips)	P_0 (kips)	λ	P_λ (kips)
60.5	0.9	6277	10010	$2.172 * 10^8$	75940	7486	0.31	7184

Table 4-6: Values of the Anchor Points for different column P-M interaction curves

i	A	B	C	D	E	F	G
P (kips)	6460	0	1573	786.7	3082	-4887	-977.3
M (k-in.)	0	37880	37880	38780	28390	0	34090
i_λ	A_λ	B_λ	C_λ	D_λ	E_λ	F_λ	G_λ
P (kips)	6234	0	1518	759.1	2974	-4887	-977.3
M (k-in.)	0	37880	37880	38780	28390	0	34090
i_d	A_d	B_d	C_d	D_d	E_d	F_d	G_d
P (kips)	4675	0	1139	569.4	2230	-3665	-733
M (k-in.)	0	34090	34090	34910	25560	0	30680
i_{tr}	A_{tr}	B_{tr}	C_{tr}	D_{tr}	E_{tr}	F_{tr}	G_{tr}
P (kips)	7486	0	1573	786.7	3329	-5913	-1183
M (k-in.)	0	45400	45400	46180	34470	0	40860
$i_{tr\lambda}$	$A_{tr\lambda}$	$B_{tr\lambda}$	$C_{tr\lambda}$	$D_{tr\lambda}$	$E_{tr\lambda}$	$F_{tr\lambda}$	$G_{tr\lambda}$
P (kips)	7184	0	1510	754.9	3195	-5913	-1183
M (k-in.)	0	45400	45400	46180	34470	0	40860

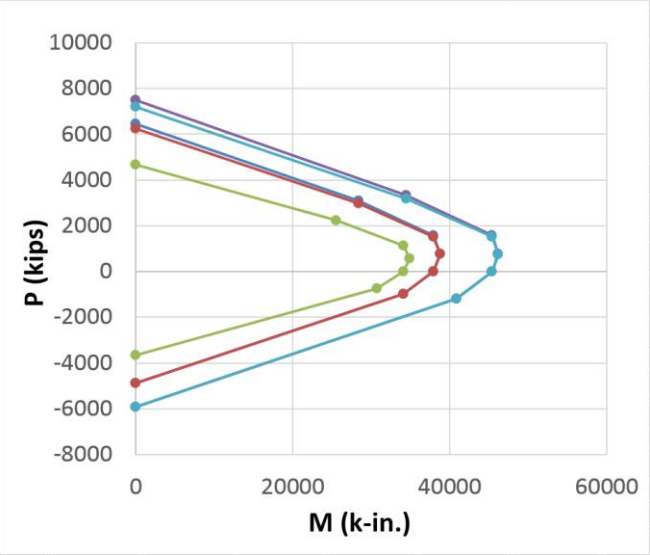

Figure 4-10: P-M interaction curves for CCFT 24*1.375

The five curves in Figure 4-10 from outside toward inside are as follows:

- Ultimate envelope from true steel strength without length effect (i_{tr})
- Ultimate envelope from true steel strength with length effect ($i_{tr\lambda}$)
- Ultimate envelope from minimum specific strength without length effect (i)
- Ultimate envelope from minimum specific strength with length effect (i_{λ})
- Design envelope with length effect and design factors (i_d)

The column interaction curves can be used in SAP2000 to define column plastic hinges for the system preliminary design. However, these plastic hinges are unable to consider strength and stiffness degradations under cyclic loadings. Although the cyclic behavior of the CCFTs has been investigated, a general set of equations to estimate their stiffness, moment rotation behavior and their cyclic degradation behavior have not been commonly accepted. Usually these behaviors are simulated based on the tests, but this approximation depends strongly on the properties of the individual specimens. The development of these general equations is not the main purpose of this research, so only the behavior of the specific specimen used for this research are simulated. Because there are no available test results, an FE analysis with fiber sections can be used to catch both cyclic deterioration and AF interaction characteristics. Some material constitutive models have been proposed for the steel tubes of the CFTs and their infill

concrete [89-92].

However, the computational cost of the FE analyses with fiber sections may be very high. In order to minimize this cost, the *moment rotation relationships* (**MRR**) of the CCFT column plastic hinges will first be developed by using a fiber model with the existing material constitutive models in OpenSees, and then this MRR is used to define a simpler and more efficient model for the CCFT column plastic hinges for the system analyses.

For the steel tube, A572 Gr. 50 steel is used. The engineering stress-strain curve from test is presented in Figure 4-11. The curve with 'initial condition' is used to generate a corresponding simplified stress-strain curve, which is shown in Figure 4-12. The 'Pinching4 Material' model in OpenSees is adopted to simulate steel tube, which has enough defined points to catch the main characteristic of the steel monotonic stress-strain curve, and can consider both stiffness (unloading and reloading stiffness) and strength cyclic degradation behavior. For the infill concrete core, the 'Concrete02 Material' model is used. The unconfined stress-strain curve is shown in Figure 4-13, and the detailed values are listed in Table 4-7. In OpenSees, each fiber section of the infill concrete core should be defined by confined concrete. The properties of the corresponding confined concrete are determined by using Popovics' [89] and Mander's [90] models for the compressive strength, Saenz's model [91] for the crushing strength, and Tsai's model [92] for the whole tension branch, respectively.

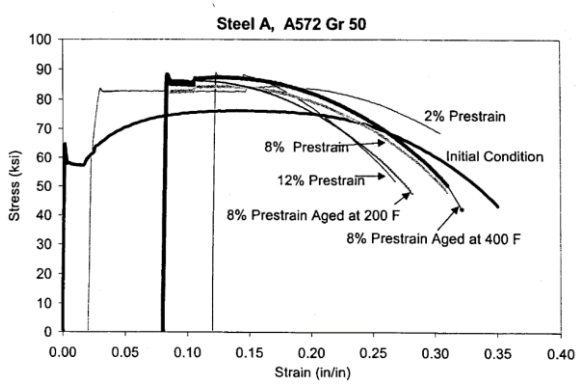

Figure 4-11: Stress-strain curve of A572 Gr.50 steel with various prestrains [93]

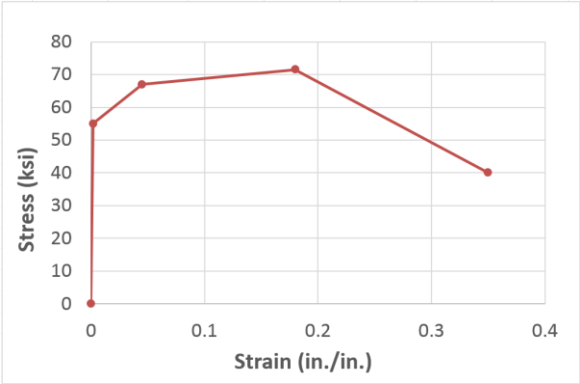

Figure 4-12: Simplified experimental stress-strain curve of A572 Gr.50 steel

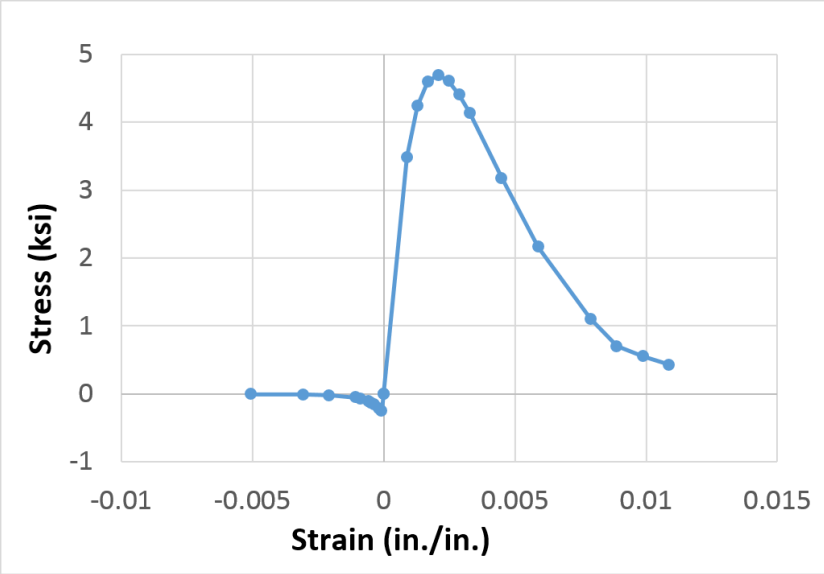

Figure 4-13: Concrete stress-strain curve

Table 4-7: Tensile and Compressive Stress-Strain Data for Figure 4-13

Compression		Tension	
f'_c (ksi)	ε_c (in./in.)	f_t (ksi)	ε_t (in./in.)
0	0	0	0
3.483	0.00089308	***0.2581***	***6.61795E-05***
4.235	0.00129308	0.2113	0.000166179
4.598	0.00169308	0.1614	0.000366179
4.692	***0.00209308***	0.1392	0.000466179
4.606	0.00249308	0.116	0.000566179

4.405	0.00289308	0.0777	0.000866179
4.134	0.00329308	0.0521	0.001066179
3.177	0.00449308	0.0233	0.002066179
2.16	0.00589308	0.0106	0.003066179
1.1	0.00789308	0.0058	0.005066179
0.7	0.00889308		
0.55	0.00989308		
0.428	0.01089308		

Both monotonic and cyclic *moment rotation* (**MR**) relationships are presented in Figure 4-14. Compared with the monotonic behavior, the cyclic behavior shows obvious degradation effects on both strength, stiffness, and ductility. As defined in the steel stress-strain curve, fracture occurs when the ultimate strain reaches 0.35.

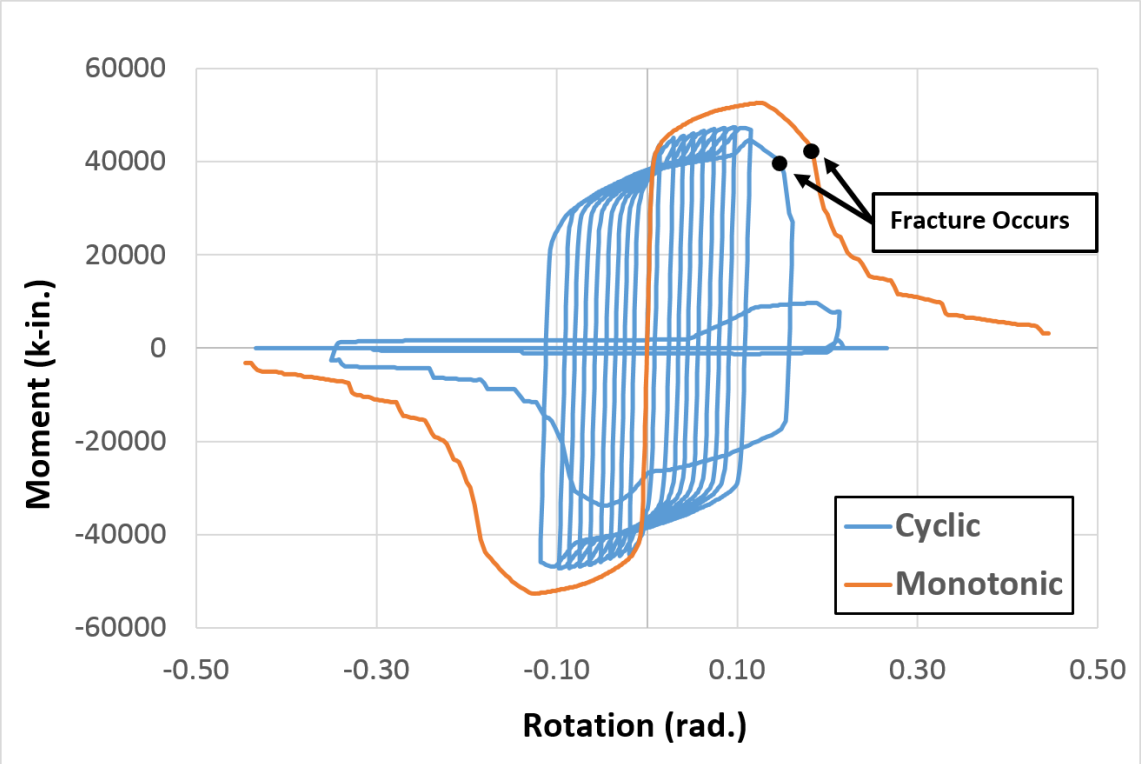

Figure 4-14: MR curve of CCFT24*1.375 for both monotonic and cyclic loadings

Previous experiments indicates that the cyclic behavior of the CFTs can be classified into four categories based on their aspect ratio λ_s, which is defined as (Eq. 4-2) with units of inch and ksi. The four classes are defined as: (1) $\lambda_s \leq 60$; (2) $60 < \lambda_s \leq 124$; (3) $124 < \lambda_s \leq 188$; and (4) $\lambda_s > 188$ [94]. Elchalakani and Zhao give an example of the MR curves for each of the above four classes by using FE analyses as shown in Figure 4-15 [95]. For the CCFT section used for this research ($D = 24\ in$, $t = 1.375\ in$, and $\sigma_y = 55\ ksi$), the aspect ratio λ_s is calculated as 26.5, so the CCFT section in this thesis should be classified into 'Class 1'. It is clear to see that the cyclic behavior in Figure 4-14 is similar to that in Figure 4-15 (a); the differences between two curves come from the materials' stress-strain relationships.

$$\lambda_s = \frac{D}{t}\frac{\sigma_y}{36.26} \qquad \textit{(Eq. 4-2)}$$

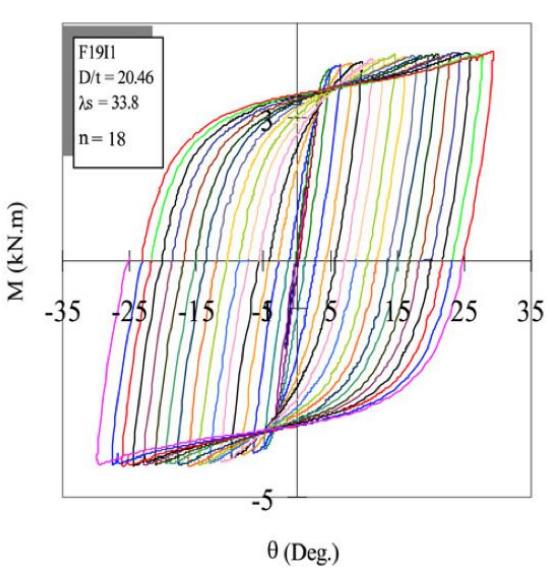

(a) Class 1 with $\lambda_s \leq 60$

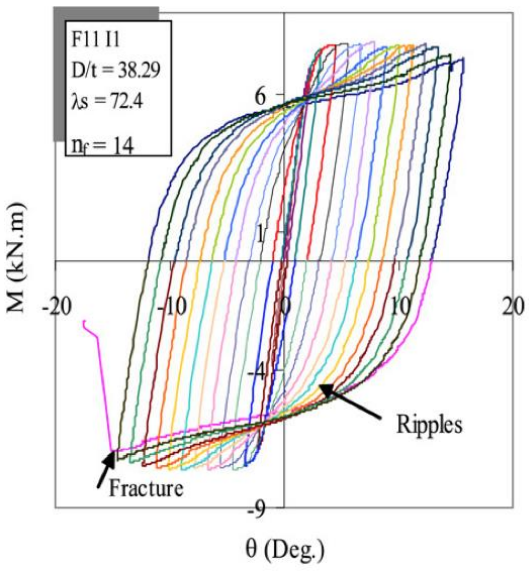

(b) Class 2 with $60 < \lambda_s \leq 124$

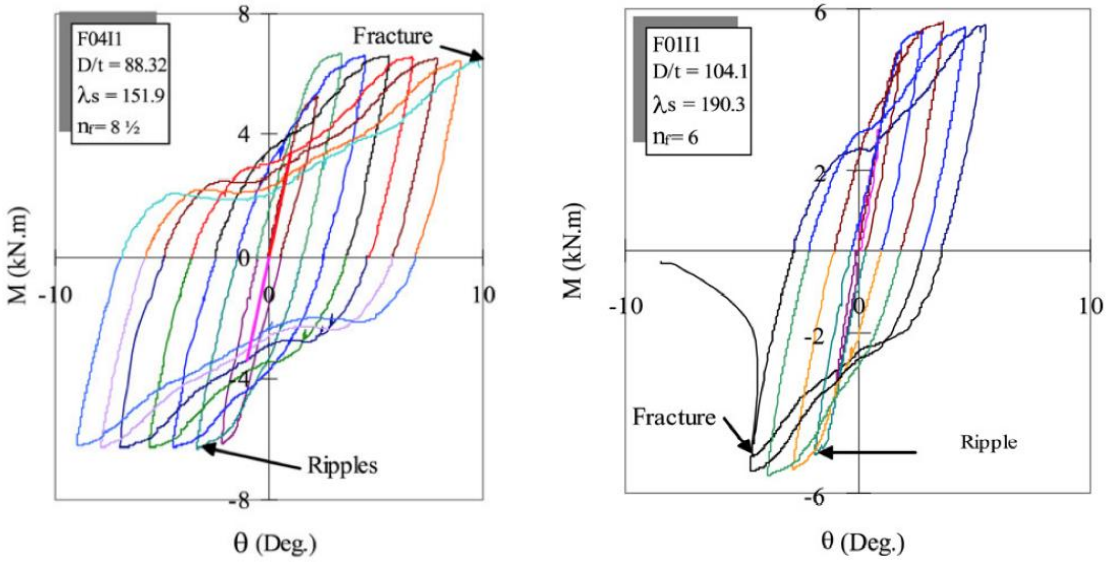

(c) Class 3 with $\mathbf{124 < \lambda_s \leq 188}$ *(d) Class 4 with* $\boldsymbol{\lambda_s > 188}$

Figure 4-15: Hysteresis curves for four classes of CFTs [95]

In addition to the interaction curve determined by AISC method, the simplified backbone curve in Figure 4-16 of the hysteresis curve can also be used for the preliminary design in SAP2000 based on the equivalent lateral load approach. The fiber sections can be used for more accurate dynamic analyses in OpenSees. The anchor points of the simplified backbone curve are defined as: $A\ (\theta_y, M_y)$, $B\ (15\theta_y, 1.21M_y)$, $C\ (33\theta_y, 0.36M_y)$, $D\ (60\theta_y, 0.36M_y)$, and $E\ (60\theta_y, 0)$. For the section CCFT24*1.375, the yield flexural capacity M_y is 37880 k-in and its rotational stiffness is 7874370 k-in/rad based on the results in Figure 4-14, so its corresponding yield rotation θ_y is calculated as 4.811×10^{-3} rad.

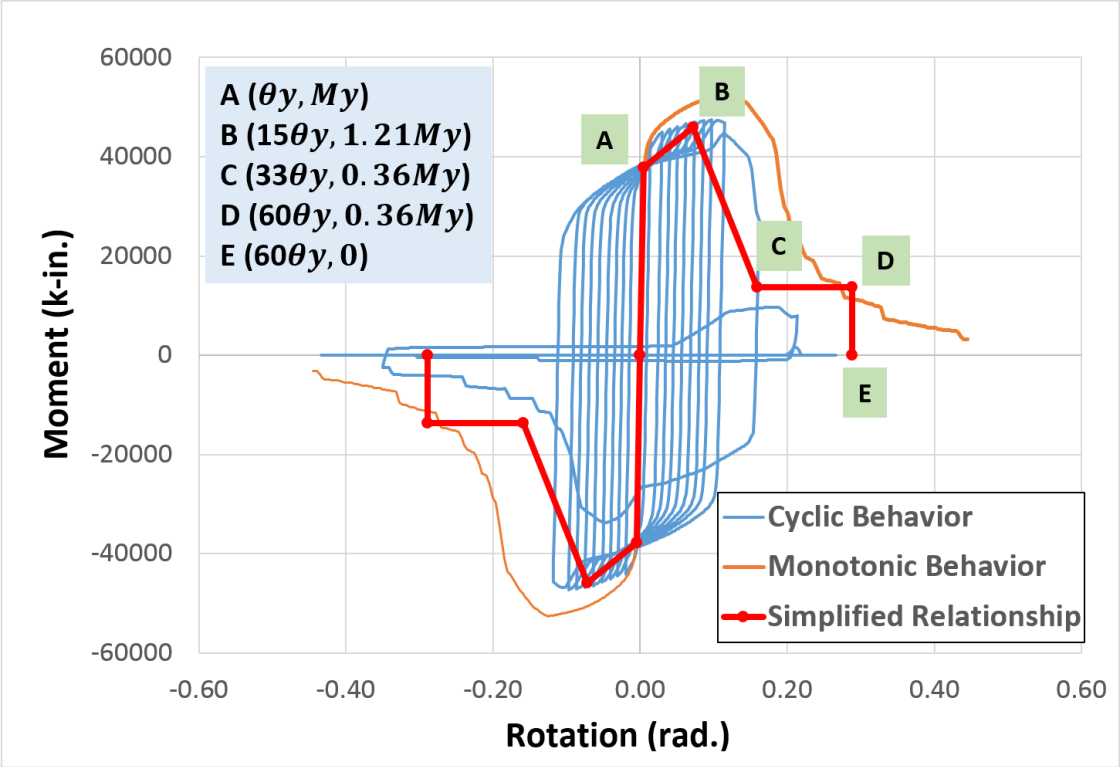

Figure 4-16: Simplified backbone curve for the hysteresis curve of CCFT24*1.375

4.2.3 Determination of Links Properties for SMA Rods

A typical stress-strain curve for a Ni-Ti SMA wire, the type of SMA to be used in this research, at slightly lower than room temperature (61°F/16°C), is shown in Figure 4-17. An approximate stress-strain curve used for design up to a strain of 7% is shown on the same plot with bold red solid lines. Generally speaking, SMA has a slightly higher yield strength than Gr.50 steel, but a larger yield strain (≈1.14%) as the modulus of elasticity of the SMA (≈5,000-14,000 ksi) [70, 96] is smaller than that of steel and shows a much larger variation with temperature. The plateau in the SMA stress-strain curve is a reversible phenomenon, as it does not represent the conventional yielding observed in mild steel but a reversible phases transformation between the austenitic and martensitic phase of the material.

When the cyclic strain is less than 5%, a full recovery of strain can be expected in a SMA. When the cyclic strain is between 5% and 7%, the residual strain is less than 0.5% and is accompanied by little strength degradation. With strain less than 5%, the SMA behavior can be simulated properly by the bold red lines in Figure 4-17. For a maximum design strain from 5% to 7%, the model will overestimate its capacity a little by ignoring the residual strain and the accompanied strength degradation. After adding an initial pretension of αF_y (where α is the pretension ratio of SMA rods defined in Section 3.3), the modified stress-strain curve is shown by the bold red solid lines in Figure 4-18. This curve is the one to be used as the SMA material properties for the FE analysis of the 2D-SSM in SAP2000.

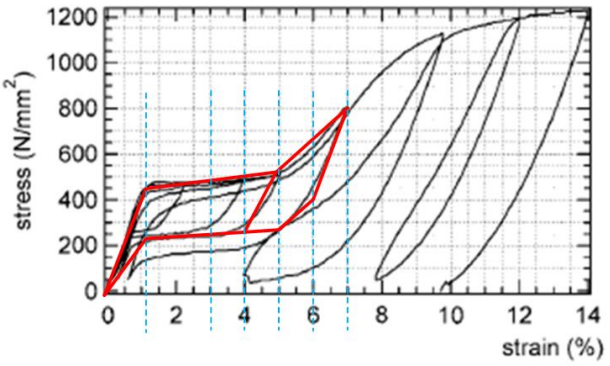

Figure 4-17: Stress-strain relationship of SMA [97]

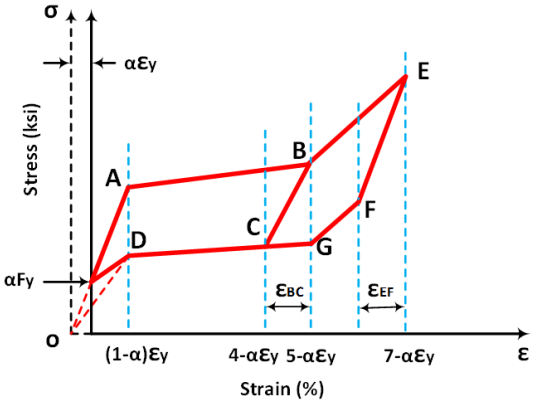

Figure 4-18: Modified stress-strain curve for a SMA with an initial prestress of αFy

A 'MultiLinear Elastic Link Element' and a 'MultiLinear Plastic Link Element with Kinematic Hysteresis Law' are combined together to simulate the SMA behavior with pretension of αF_y represented by the red solid lines in Figure 4-18. These two link elements are connected in

parallel as illustrated in Figure 4-19. The compressive strength of the 'MultiLinear Plastic Link Element' is defined to be zero, so the compressive capacity from this element will be zero as expected.

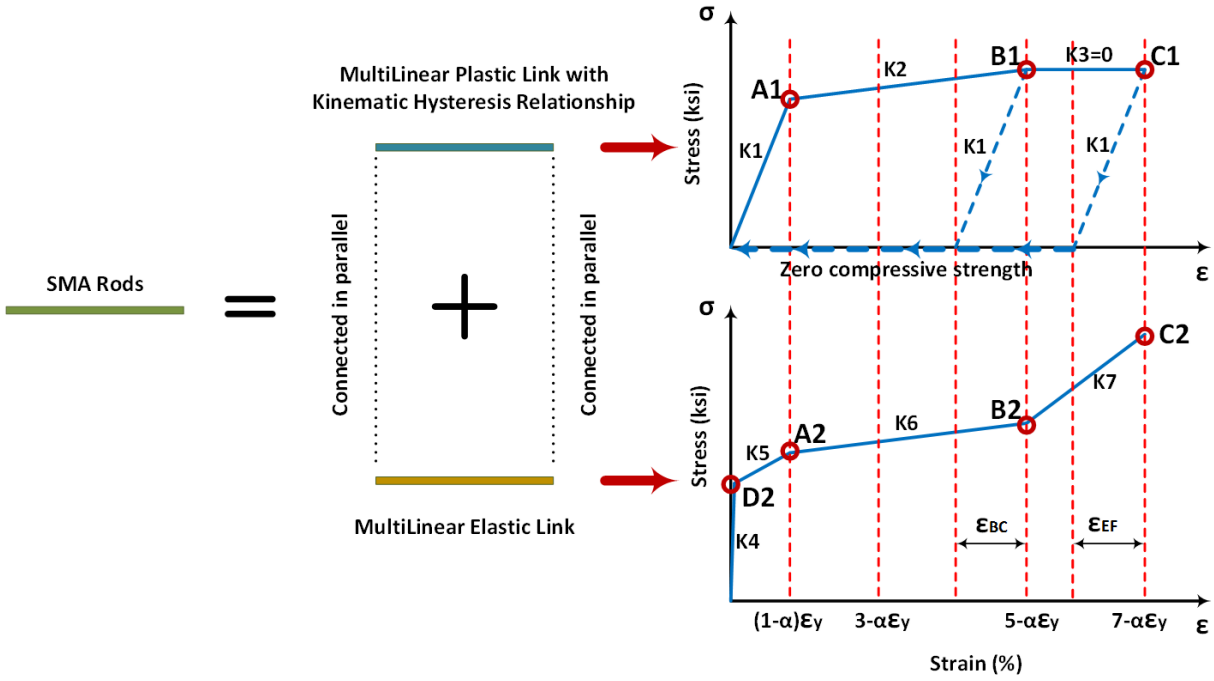

Figure 4-19: Components of SMA rods

The stiffness of each segment of the two stress-strain relationships in Figure 4-19 ($K_1, K_2, K_3, K_4, K_5, K_6, K_7$) has to satisfy the following relationships:

Relationship 1:

$$K_3 = 0 \qquad \textit{(Eq. 4-3)}$$

Relationship 2:

$$K_4 = \frac{\alpha \cdot f_{ySMA}}{\varepsilon_{D_2}} \qquad \textit{(Eq. 4-4)}$$

Relationship 3:

$$f_{ySMA} - (1-\alpha) \cdot \varepsilon_{y\_SMA} \cdot K_1 = \sigma_D \qquad \textit{(Eq. 4-5)}$$

Relationship 4:

$$(1-\alpha) \cdot \varepsilon_{y\_SMA} \cdot K_1 + \left[(1-\alpha) \cdot \varepsilon_{y\_SMA} - \varepsilon_{D_2} \right] \cdot K_5 = (1-\alpha) \cdot f_{ySMA} \qquad \textit{(Eq. 4-6)}$$

or simplified: $(1-\alpha) \cdot \varepsilon_{y\_SMA} \cdot (K_1 + K_5) = (1-\alpha) \cdot f_{ySMA}$ ***(Eq. 4-7)***

Relationship 5:

$$K_6 = K_{DG} \qquad \textit{(Eq. 4-8)}$$

Relationship 6:

$$K_2 + K_6 = K_{AB} \qquad \textit{(Eq. 4-9)}$$

Relationship 7:

$$K_7 = K_{BE} \qquad \textit{(Eq. 4-10)}$$

where,

ε_{D_2} = assume a very small value, such as 10^{-5} (the actual value should be zero), in./in.

K_{AB} = slope of line AB in Figure 4-18, ksi.

K_{DG} = slope of line DG in Figure 4-18, ksi.

K_{BE} = slope of line BE in Figure 4-18, ksi.

σ_D = strength of SMA at point D in Figure 4-18, ksi.

f_{ySMA} = yield strength of SMA, strength at point A in Figure 4-18, ksi.

Note that if the prestress factor of the SMA rods α is greater than the value determined in (Eq. 4-11, K_5 will have a negative value.

$$\alpha = \frac{\sigma_D}{f_{ySMA}} \qquad \textit{(Eq. 4-11)}$$

Based on the seven relationships above to simulate SMA behavior in SAP2000, the loading path can be controlled to be the same as the defined ideal curve. The unloading strength on the lower backbone curve of the SMA stress-strain relationship can be simulated very well. However, there is no relationship defining the unloading stiffness, which will be determined by the combination of K_1 of MultiLinear plastic link and the stiffnesses of MultiLinear elastic link. Because the prestress factor α has obvious effect on K_1 based on (Eq. 4-5), it also influences the unloading stiffness greatly. If the pretension in SMA rods is greater, the unloading stiffness is greater, too.

4.2.4 Determination of the Links Properties for Steel Rods

A typical stress-strain curve of A572 Gr.50 for steel rods is presented in Figure 4-11, while its corresponding simplified curve can be represented as shown in Figure 4-20. For this particular steel rod, although a strength of 50 ksi is reached at yield strain of only about 0.17%, the maximum strain capacity can reach up to 18%. This is large enough to ensure ductile behavior for the new proposed connection configuration. Its simplified design stress-strain relationship

with a pretension of ηF_y (where η is the pretension ratio of steel rods defined in Section 3.3) is shown in Figure 4-21.

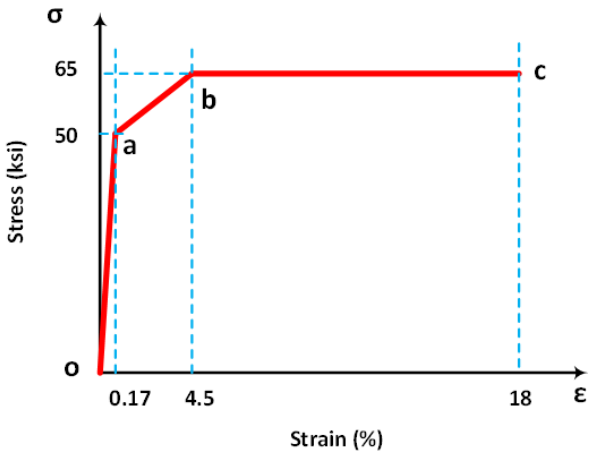

Figure 4-20: A typical design stress-strain curve of A572 Gr.50 for steel rods

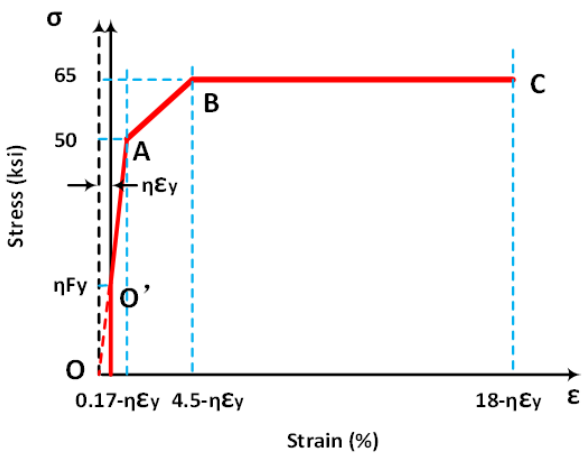

Figure 4-21: A typical design stress-strain curve of A572 Gr.50 with prestressed strength ηF_y

A 'Hook Element' and a 'MultiLinear Plastic Link Element with Takeda Hysteresis Law' are combined together to simulate the stress-strain relationship of the steel rods with a pretension effect, as represented by the red solid lines in Figure 4-21. These two link elements are connected in series and their stress-strain relationships are illustrated in Figure 4-22. The two components have the same length, $L/2$ (Figure 4-23). A hook element has zero compressive strength and can store the compressive deformation; it is used here to simulate the sliding effect of the steel rods after yielding has resulted in rod lengthning. If the tensile deformation is assumed to be generated only by the plastic link element, a relative large stiffness is assigned to the hook element.

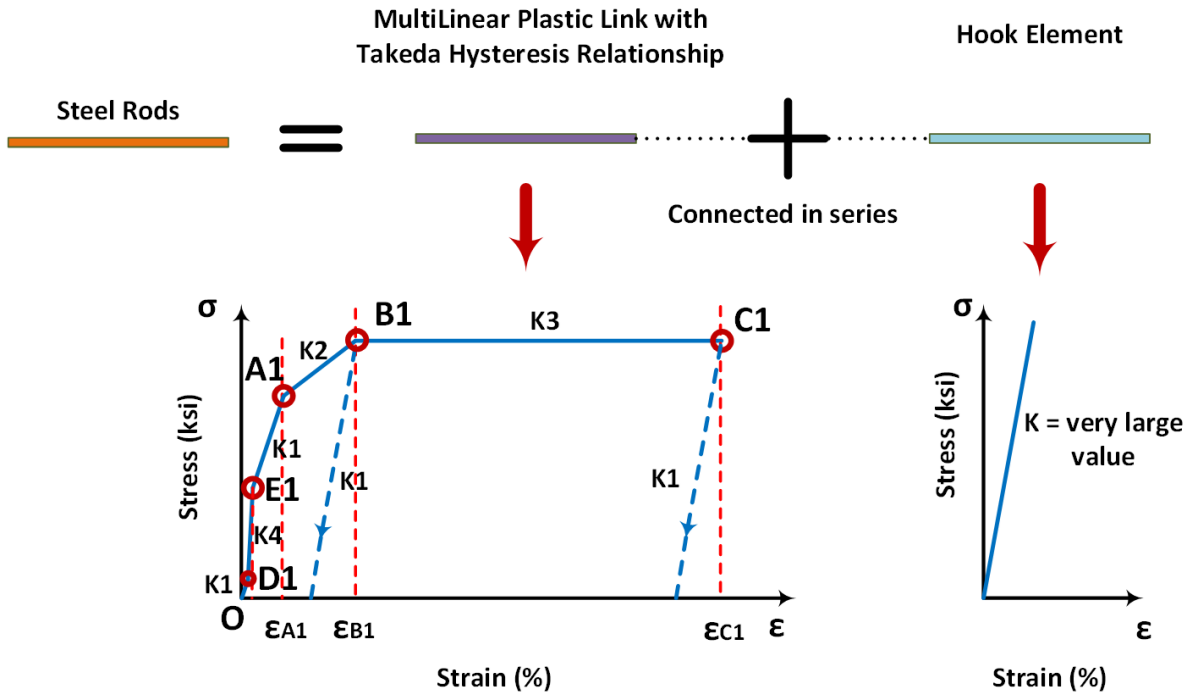

Figure 4-22: Components of steel rods

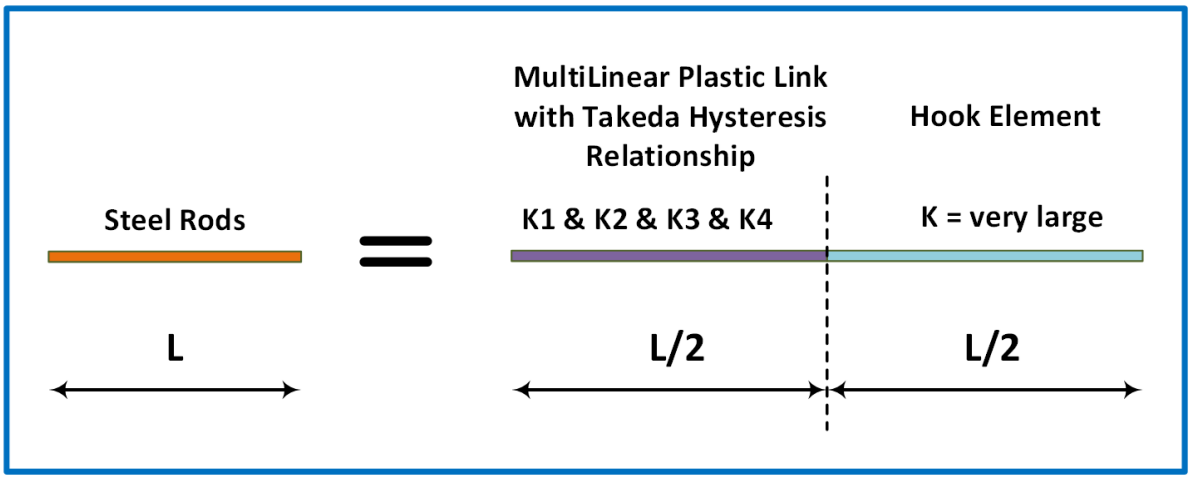

Figure 4-23: Geometric relationship between two elements of steel rods

The stress-strain curve of the 'MultiLinear Plastic Link Element' is defined by five key points, A1, B1, C1, D1 and E1 (Figure 4-22). Their strain and the corresponding stress are $(\varepsilon_{A1}, \sigma_{A1})$, $(\varepsilon_{B1}, \sigma_{B1})$, $(\varepsilon_{C1}, \sigma_{C1})$, $(\varepsilon_{D1}, \sigma_{D1})$ and $(\varepsilon_{E1}, \sigma_{E1})$, and the four slopes of the five segments of

the curve are defined as K_1, K_2, K_3, and K_4. In order to make sure that the global behavior of the steel rods can be simulated correctly by the combination of the two elements, the following relationships must be satisfied:

Relationship 1:

$$\begin{cases} \frac{L}{2}\cdot\varepsilon_{A1} = L\cdot(\varepsilon_A - \eta\cdot\varepsilon_{ySHS}) \\ \frac{L}{2}\cdot\varepsilon_{B1} = L\cdot(\varepsilon_B - \eta\cdot\varepsilon_{ySHS}) \\ \frac{L}{2}\cdot\varepsilon_{C1} = L\cdot(\varepsilon_C - \eta\cdot\varepsilon_{ySHS}) \end{cases} \quad \text{or} \quad \begin{cases} \varepsilon_{A1} = 2\cdot(\varepsilon_A - \eta\cdot\varepsilon_{ySHS}) \\ \varepsilon_{B1} = 2\cdot(\varepsilon_B - \eta\cdot\varepsilon_{ySHS}) \\ \varepsilon_{C1} = 2\cdot(\varepsilon_C - \eta\cdot\varepsilon_{ySHS}) \end{cases} \qquad \textit{(Eq. 4-12)}$$

Relationship 2:

$$\begin{cases} \sigma_{A1} = \sigma_A \\ \sigma_{B1} = \sigma_B \\ \sigma_{C1} = \sigma_C \end{cases} \qquad \textit{(Eq. 4-13)}$$

Relationship 3:

$$\varepsilon_{D1} = \frac{\varepsilon_{A1}}{50} \qquad \textit{(Eq. 4-14)}$$

Relationship 4:

$$\sigma_{D1} = K_1\cdot\varepsilon_{D1} = \frac{K_{OA}}{2}\cdot\varepsilon_{D1} \qquad \textit{(Eq. 4-15)}$$

Relationship 5:

$$\varepsilon_{E1} = 1.1\cdot\varepsilon_{D1} \qquad \textit{(Eq. 4-16)}$$

Relationship 6:

$$\sigma_{E1} = \eta\cdot\sigma_{A1} \qquad \textit{(Eq. 4-17)}$$

where,

K_{OA} = slope of line OA in Figure 4-21, ksi.

L = length of the designed steel rods, in.

η = prestressed ratio for steel rods, ratio of prestressed strength to the yielding strength of steel rods

$\sigma_A, \sigma_B, \sigma_C$ = strength at points A, B, C in Figure 4-21, ksi.

$\varepsilon_A, \varepsilon_B, \varepsilon_C$ = strain at points A, B, C in Figure 4-21, in./in.

The theoretical slope of segment A_1E_1 in Figure 4-22 should be $K_1 = K_{OA}/2$, but the calculated slope of that segment based on the above relationships is $1.022 * K_1$. The difference between the theoretical and the calculated value is insignificant (2.2%), so the simulated curve can be considered to be valid.

4.3 Behavior of the Proposed 2D-SSM in SAP2000

In this section, detailed examples will be introduced for both SMA rods and steel rods based on the above relationships. After verifying the effectiveness of the two rod models, two whole simplified connection models are established and analyzed. One model is the original simplified model (Figure 4-1), and the other one is the improved one (Figure 4-4). Their analysis results will be compared, and the most effective one will be adopted in the future work.

The software used in this section is SAP2000.

4.3.1 Example for the SMA Rods Model

A SMA rod in one connection of the CSMF designed in Appendix K is chosen. This connection is an interior connection with two W33*130 steel beams. The rod has a length of 32.25'' and a diameter of 1.27''. The pretension in rod is 30% of its yielding strength.

The ideal SMA stress-strain relationship is defined based on Figure 4-17, which is presented in Figure 4-24 by the red solid line. By applying the proposed model, a simulated curve is obtained as the green dashed line shown in Figure 4-24. Comparing the original defined relationship and the simulated curve, one can notice that the two curves are perfectly identical in most regions except for a small portion on the unloading path when the strain is relative small. This small difference will slightly reduce the self-centering force and slightly increase the energy dissipation ability. The yellow dotted line in Figure 4-24 represents the cyclic behavior of the proposed model under the strain loading history defined in Figure 4-25. This cyclic behavior is very well simulated and shows that the proposed SMA model in SAP2000 is valid to simulate the 'Flag-Shape' stress-strain relationship of the SMA with pretension under both monotonic and cyclic loadings. For 30% pretension, the unloading stiffness of the cyclic behavior is similar to the elastic Young's modulus of the SMA.

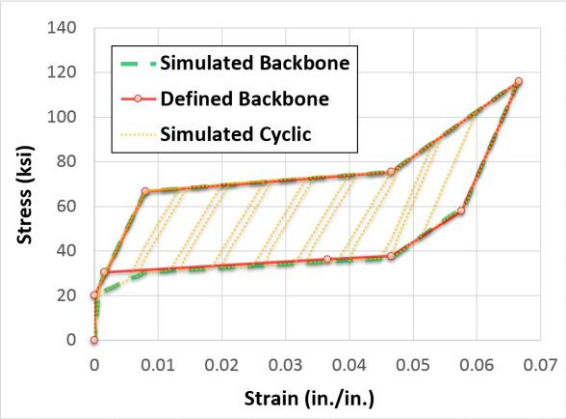

Figure 4-24: The simulated SMA stress-strain curves by the proposed model

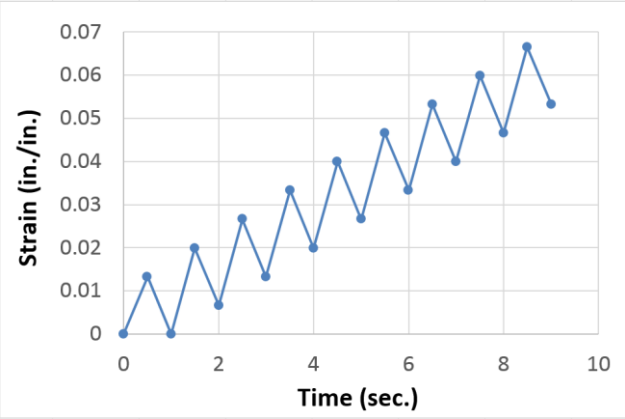

Figure 4-25: The cyclic strain loading history for the SMA rod

4.3.2 Example for the Steel Rods Model

A steel rod on the same connection as the SMA rod in the previous example is chosen as the prototype in this section. The length of the rod is also 32.25”. Its diameter is 1.128”, and the prestress ratio is 50%. The stress-strain curve is defined based on the simplified experimental curve for A572 Gr.50 in Figure 4-12 with the maximum strain of 18%. It is important to note that although the experimental value of $55\ ksi$ is used as the practical yielding strength in Figure 4-12, the pretension force on the rods is arbitrarily based on the nominal yielding strength $F_y = 50\ ksi$ for Gr.50 steel. For a prestressed ratio 50%, the actual prestress on the rods is only $25\ ksi$, instead of $27.5\ ksi$. This is not a concern for the SMA rods, because there is only one experimental yielding strength defined in this research, and there is no nominal yielding strength for design.

In Figure 4-26, the red solid line represents the defined stress-strain relationship with pretension, and the green dashed line stands for the simulated stress-strain relationship based

on the proposed model. The yellow dotted line in Figure 4-26 is obtained by applying the cyclic strain loading history defined in Figure 4-27. For the first two loading cycles from 0 to 2s, the paths of the cyclic behavior are $O-A-B-C-D-O$ and $O-D-C-E-F-O$ as shown in Figure 4-26(b). For the first loading cycle, the unloading path follows $C-D-O$, and the stress stays at zero after it reaches point D. This characteristic indicates that the simplified steel rod model does not provide any compressive capacity. For the second loading cycle, the reloading path does follow path $O-D-C$ instead of $O-A-B-C$. The stress in the steel rod doesn't recover until passing point D. Point D represents the residual strain of the steel rod due to the previous loading cycle. This means that when the elongation of the steel rod is less than the residual deformation, the steel rod has no effects on the global behavior of the whole connection. This characteristic is exactly the same as the sliding effects of the steel rods in a practical connection shown in Figure 3-5. Also, one can notice that the stress at point A is equal to the prestress of $25\ ksi$ as defined, and the unloading stiffness is equal to the elastic stiffness.

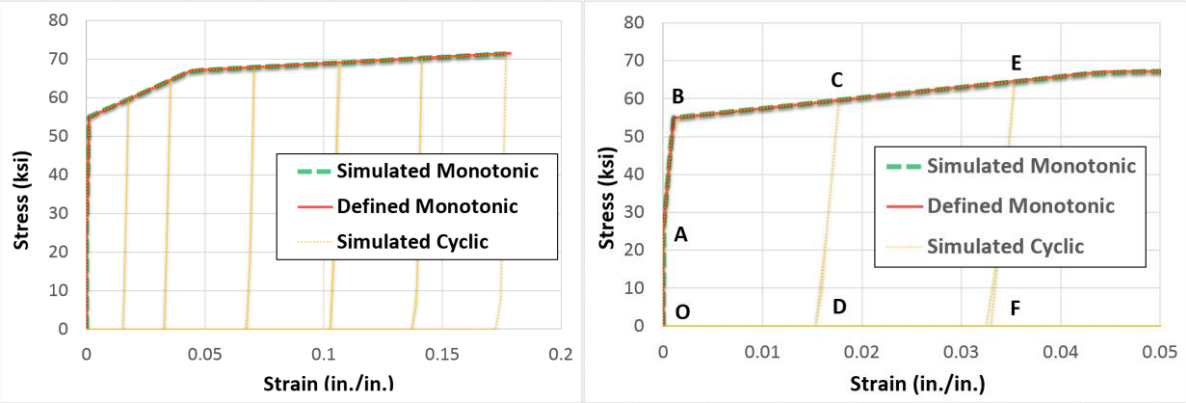

(a) Curve with whole strain range *(b) Curve with small strain range*

Figure 4-26: The simulated steel rod stress-strain curve by proposed relationships

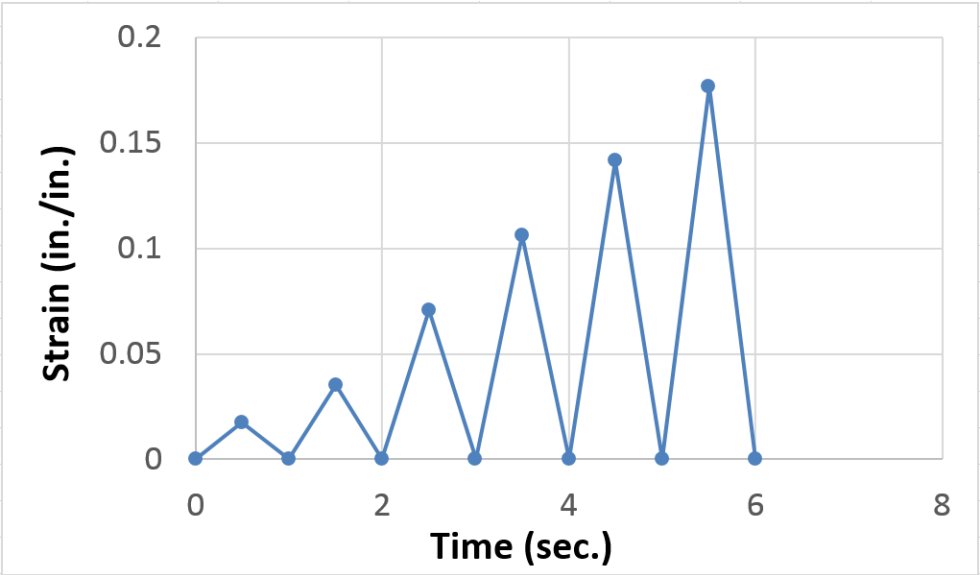

Figure 4-27: The cyclic strain loading history for the steel rod

4.3.3 Example for the Simplified Connection Model

An interior connection of the CSMF designed in Appendix K is used as the example in this section. The dimension of the CCFT column is 24*1.375, and its connecting steel beam is a W33*130 with RBSs. The behaviors of single SMA and steel rods of this connection are introduced in section 4.3.1 and 4.3.2, respectively. The main aims of this section include the following aspects:

- Investigate the connection behavior itself without the plasticity effects of the frame members.
- Investigate how much improvement the improved 2D-SSM in Figure 4-4 can brought.
- Investigate the overall behavior of the plastic region, including the connection itself and the plastic hinges of beams, and the effects on the overall behavior from different

strength and stiffness ratios of the beam plastic hinge to the connection.

In order to achieve the expected results, the simple analysis model presented in Figure 4-28 is adopted. There are two loading histories used in this section, which are shown in Figure 4-29.

- Loading history 1 has a symmetric loading pattern. All peak values increase continuously with the increment of one inch in either direction. The greater magnitudes always initially occur in the positive direction.
- Loading history 2 has an asymmetric loading pattern. All peak values increase continuously with the increment of two inches in either direction, except of the last increment in the negative direction. The greater magnitudes initially occur in the two directions alternatively.

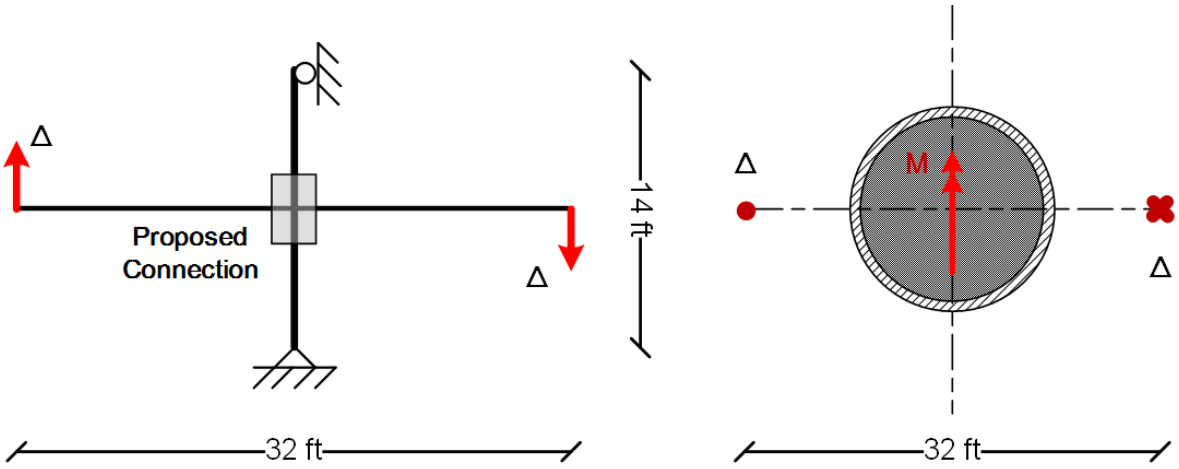

Figure 4-28: The model in SAP2000 for the cyclic behavior of the proposed connection

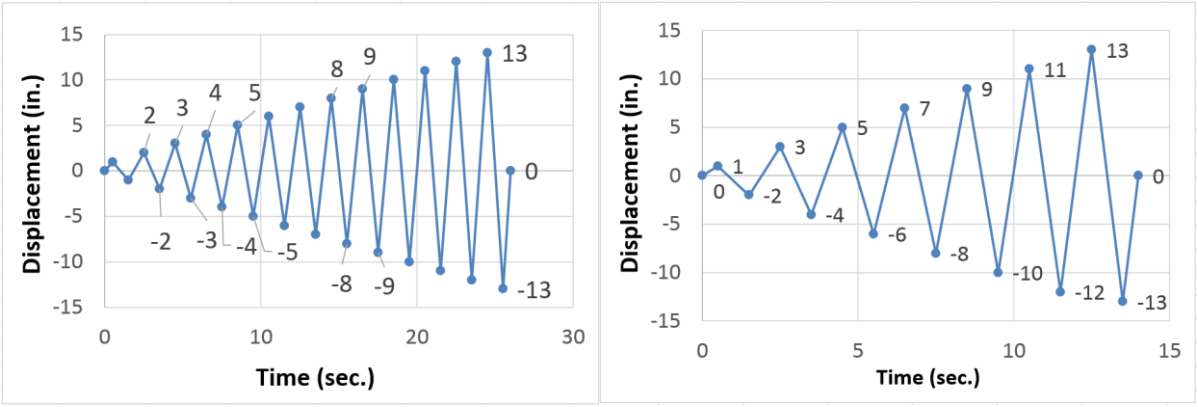

(a) Loading history 1 *(b) Loading history 2*

Figure 4-29: Two displacement loading histories

4.3.3.1 Cyclic Behavior of the Connection

In this subsection the connection behavior is described in detail. After applying the two displacement loading histories on the analysis model in Figure 4-28, the corresponding cyclic *moment rotation* (**MR**) relationships were obtained as presented in Figure 4-30 and Figure 4-31. These behaviors are similar to the expected behavior shown in Appendix Figure B-2. There are six key points in red circles on the two MR curves. These points will be used as the reference points for comparisons. The rotations of these points are fixed for one specific connection because they are determined based on the preliminary design procedure in Appendix B. The six points of one specific connection used for this example are defined as follows:

- Point A stands for the flexural capacity of the connection at rotation of 0.055 (rad.), which is the connection rotation when the maximum moments of the connecting beams are reached as determined from the proposed design procedure.
- Point B stands for the flexural capacity of the connection at a rotation of 0.044 (rad.),

which is the connection rotation when the maximum strain of some SMA rods reaches 5%.

- Point C stands for the flexural capacity of the connection provided by only the SMA rods at a rotation of 0.044 (rad.).
- Point D stands for the flexural capacity of the connection provided by the pretension of only the SMA rods. The corresponding rotation of the connection is nearly zero.
- Point E stands for the flexural capacity of the connection provided by the pretension of both SMA and steel rods. The corresponding rotation is also nearly zero.
- Point F stands for the flexural capacity of the connection provided by only the SMA rods at rotation of 0.0075 (rad.), which is the connection rotation when the SMA rods start to yield.

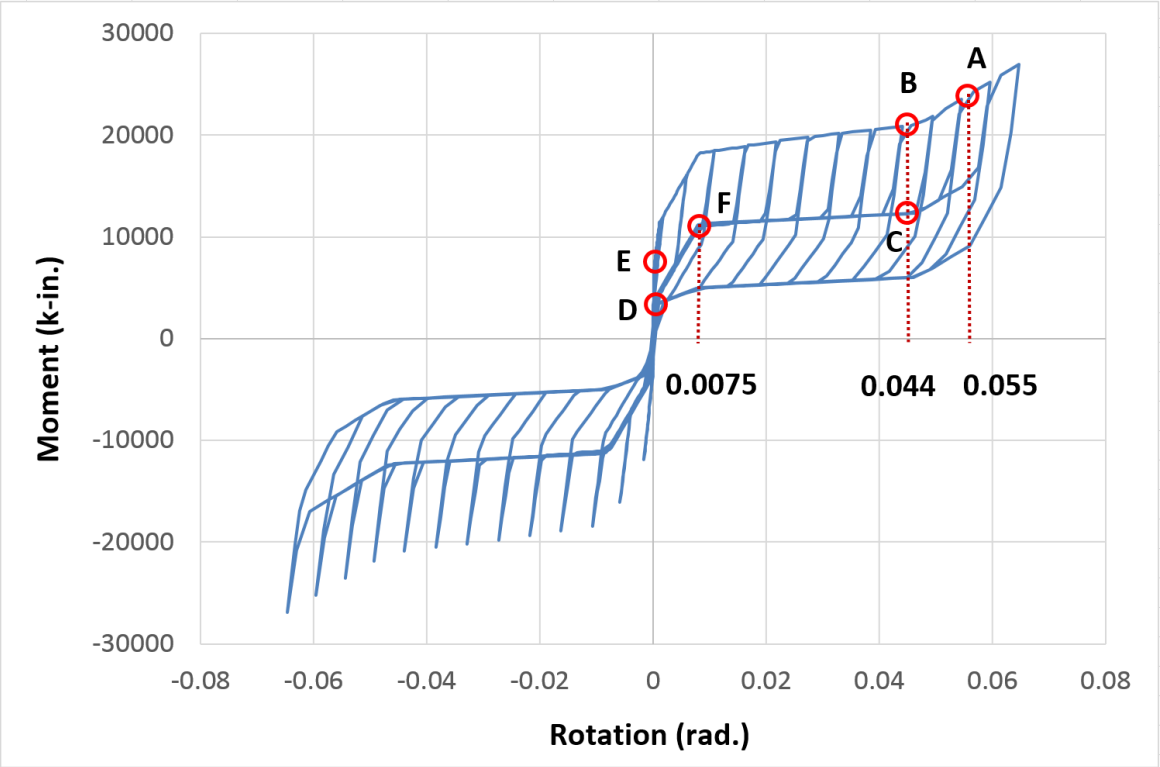

Figure 4-30: Moment rotation relationship of connection itself under loading history 1

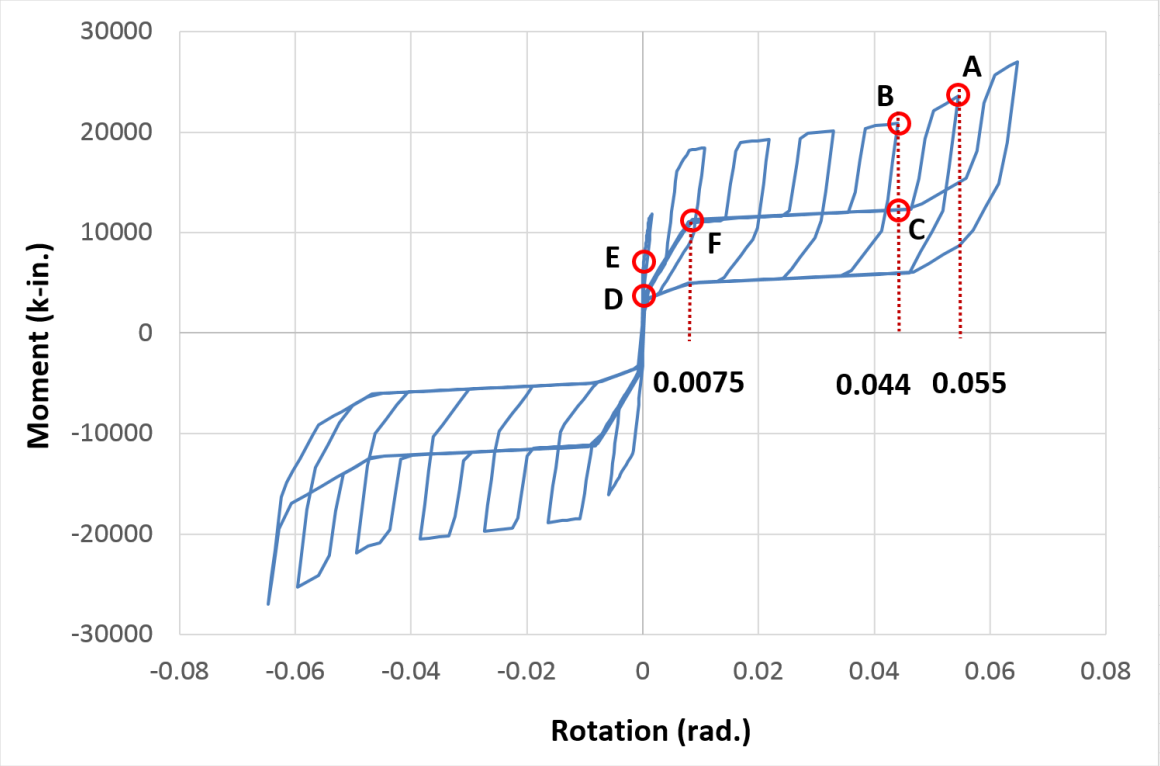

Figure 4-31: Moment rotation relationship of connection itself under loading history 2

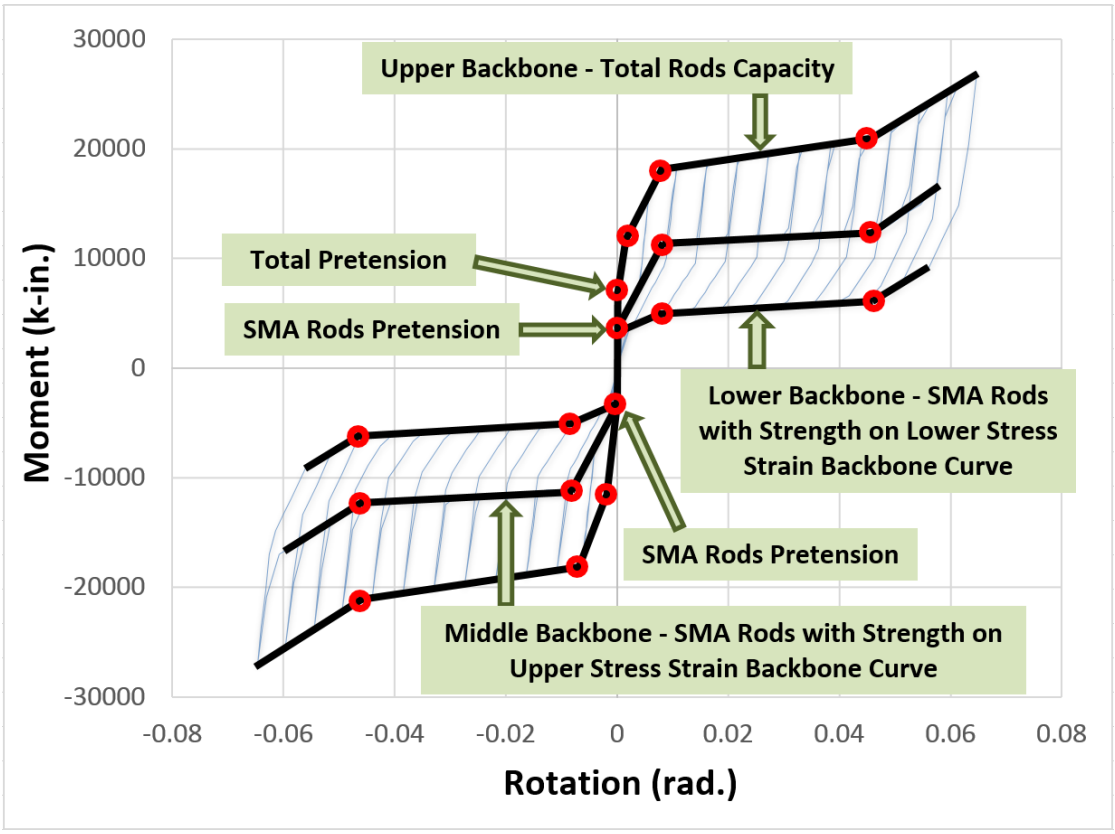

Figure 4-32: Three backbone curves of the connection MR behavior

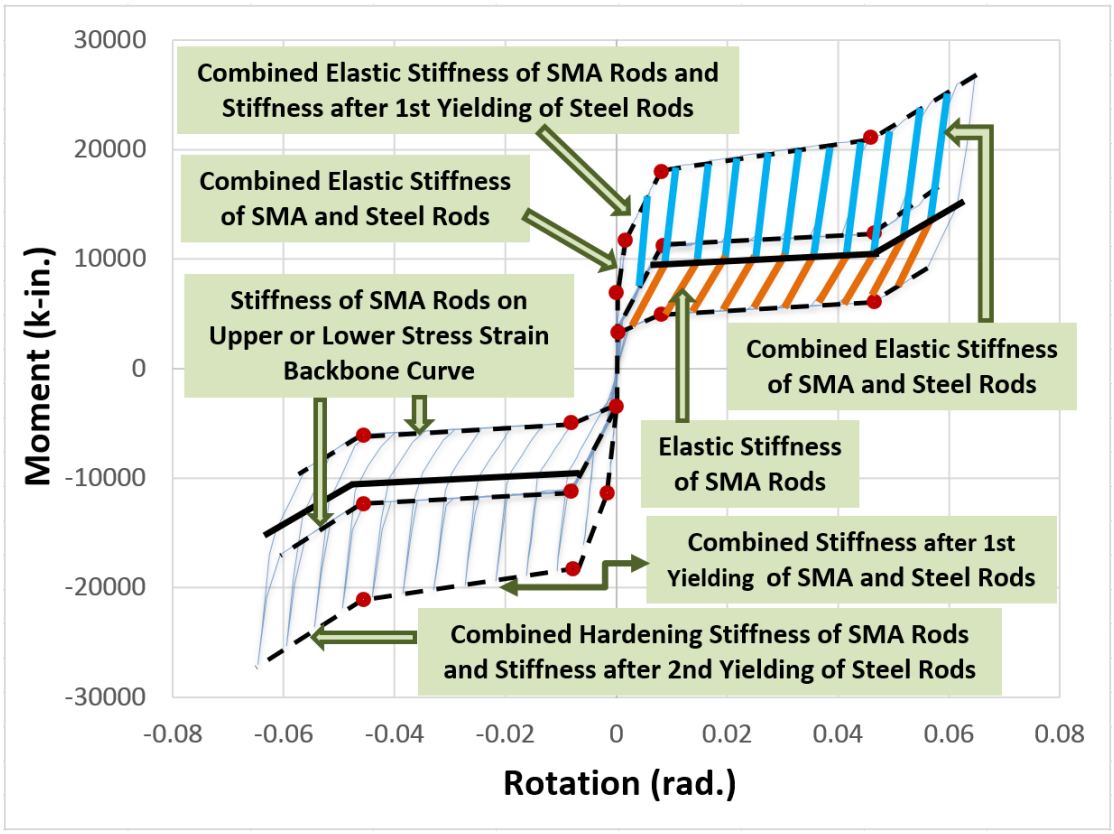

Figure 4-33: Stiffness of each segment of the connection MR curve

The overall behavior of the connection MR curves is explained in Figure 4-32 and Figure 4-33. At first, one can easily tell three backbone curves in both positive and negative rotation directions (Figure 4-32). Within the positive rotation range, the moment capacity on the top backbone curve is provided by all rods in their reloading process after the steel rods fully recover from the previous residual deformation. For the middle backbone curve, the moment is provided by only the SMA rods in their reloading path with the steel rods fully released due to previous yielding. For the bottom backbone curve, the moment is provided by only the SMA rods with their strength on the lower backbone of the SMA stress-strain curve in the unloading process. The difference of the moment capacity at a specific connection rotation between the middle and the upper backbone curves of the MR response is the moment capacity provided by only the steel rods with compatible deformations. Also the difference of the moment capacity at a specific connection rotation between the lower two backbone curves is caused by the different strength of the SMA rods with compatible deformations on either upper or lower backbone curve of the 'Flag-Shape' stress-strain curve in Figure 4-24. The upper backbone curve of the connection MR curve and the y-axis intersect together at point E in Figure 4-30; the lower two backbone curves of the MR curve and the y-axis intersect at point D. As defined previously, point D stands for the moment capacity provided by the pretension of only the SMA rods, and point E represents the moment capacity provided by the pretension of all rods.

The cyclic behaviors shown in Figure 4-30 and Figure 4-31 have not been described in any

literature that the author is familiar with, so a detailed presentation will be given to help get a better understanding of the overall behavior. From Figure 4-34 to Figure 4-41, the MR behavior of the connection under the first eight load steps of loading history 1 is presented step-by-step. The relative small plot on the right bottom corner of each figure shows the corresponding load step. In these plots of the connection MR behavior, the solid red line stands for the current behavior under the present load step, and the blue solid line represents all the previous behavior. The detailed explanation for each load step is presented as follows:

(1) For displacement loading Δ at two beam ends in Figure 4-28 from 0 to 1″, the maximum connection rotation is θ_1 and the response path is $o-a-b-c$ (Figure 4-34). At point a, the moment capacity provided by the total pretension forces in both SMA and steel rods is reached; at point b, steel rods start to yield and the connection stiffness begins to reduce. The slope of path ab is equal to the combined elastic stiffness of both SMA and steel rods.

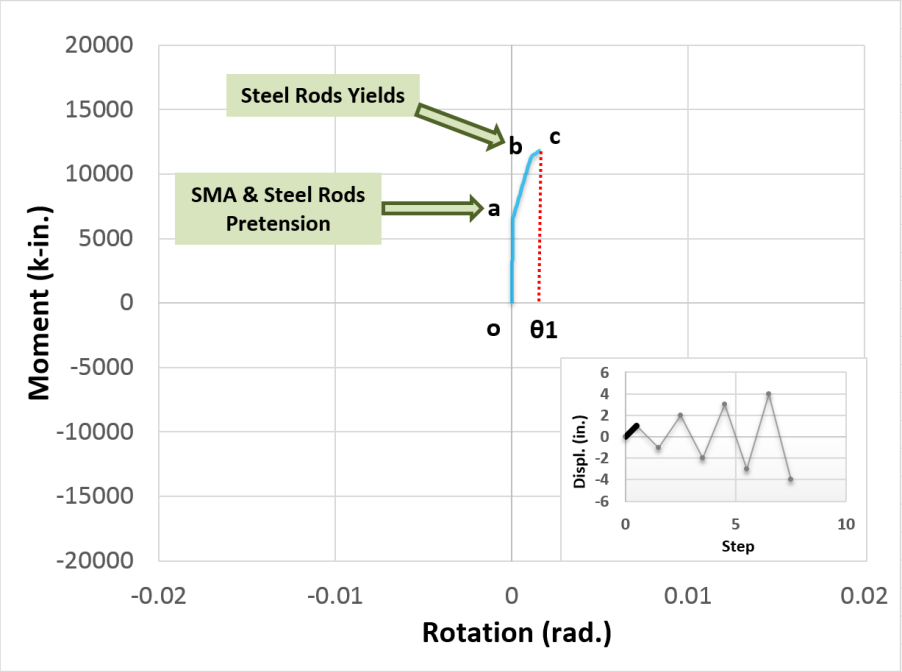

Figure 4-34: MR behavior of connection under load step 1 of loading history 1

(2) For Δ from $1''$ to $-1''$, the maximum rotation in the negative direction reaches $-\theta_1$ due to the symmetric loading, and the response path is $c-d-o-d'-c'$ (Figure 4-35). Path cd and $d'c'$ represent the unloading and reloading of the connection including the steel rods, respectively. Due to the characteristic of the model, all the pretension in the steel rods will be lost during the first unloading process. The same moment capacity at point d and d' is provided only by the pretension of all SMA rods. For this particular loading step, the unloading and reloading stiffnesses are considered to be approximately accurate because the paths cd and $d'c'$ are not exactly parallel to the path ab, which is an accurate combined elastic stiffness of all rods. This theoretical defect will only slightly influence the stiffness of the connection between point a and c, which is a very small range of deformation, and this defect

can be eliminated in a real loading case as will be described later in this chapter. Between points d and d', the strength of the steel rods does not recover from the previous yielding.

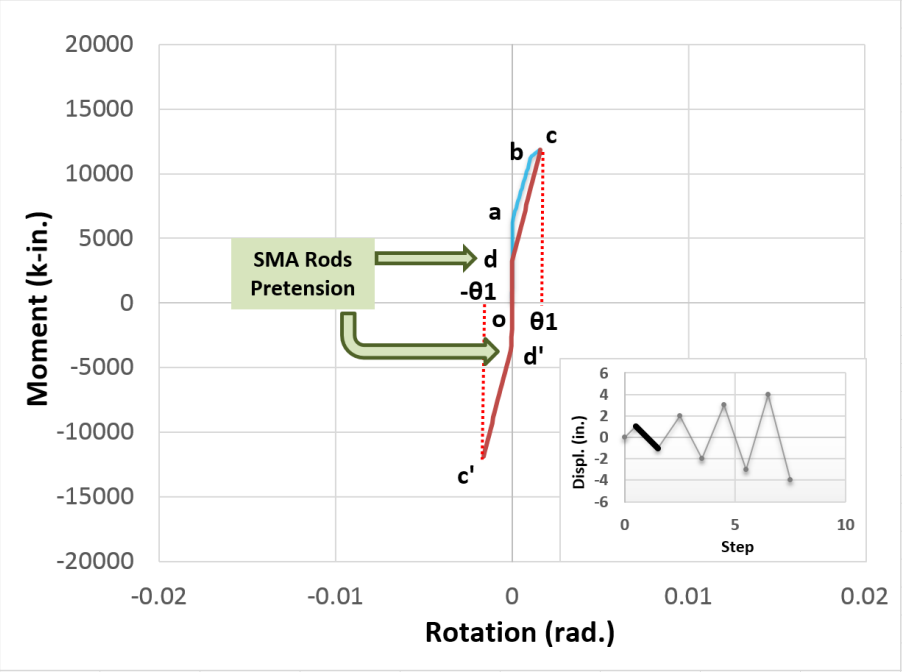

Figure 4-35: MR behavior of connection under load step 2 of loading history 1

(3) For Δ from $-1''$ to $2''$, the maximum rotation in the positive direction reaches θ_2, and the response path is $c' - d' - o - d - c - e$ (Figure 4-36). The connection is unloaded following path $c'd'$ with a combined elastic stiffness; the loading direction changes from point d' to d; then both SMA and steel rods are reloaded from d to c linearly until point c; finally, the MR response of the connection follows the path ce until the maximum deflection θ_2 is reached with a new combined stiffness, which is composed by the elastic stiffness of the SMA rods and the first yielding stiffness of the

steel rods (the stiffness which is calculated based on the slope of AB in Figure 4-21).

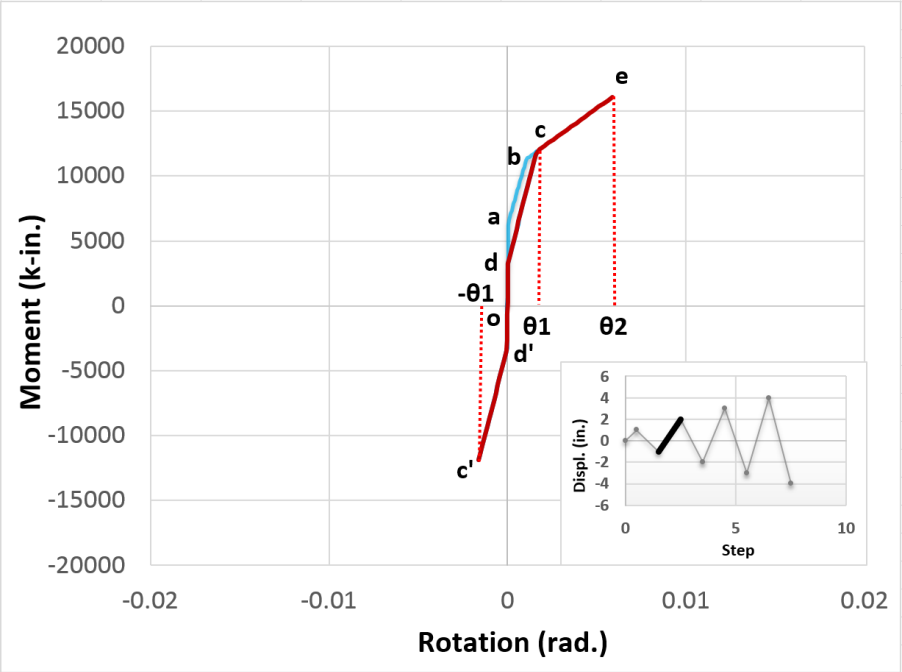

Figure 4-36: MR behavior of connection under load step 3 of loading history 1

(4) For Δ from $2''$ to $-2''$, the maximum rotation in the negative direction reaches $-\theta_2$, and the response path is $e-f-d-o-d'-f'-e'$ (Figure 4-37). Path ef and $f'e'$ stand for unloading and reloading of the connection including all rods with a combined elastic stiffness, respectively. At point f, the steel rods are unloaded fully, and they will not be reloaded until point f'. In the state that the steel rods are fully released from point f to f', only the elastic behavior of the SMA rods with pretension determines the connection MR curve.

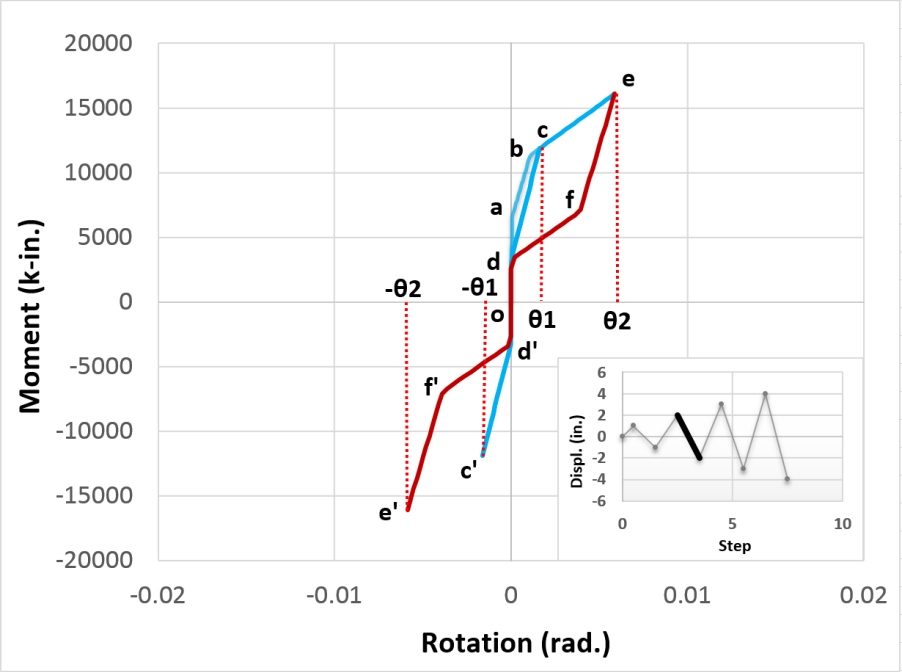

Figure 4-37: MR behavior of connection under load step 4 of loading history 1

(5) For Δ from $-2''$ to $3''$, the maximum rotation in the positive direction reaches θ_3, and the response path is $e' - f' - d' - o - d - f - e - g - h$ (Figure 4-38). Paths $e'f'$ and fe stand for unloading and reloading of the connection including all rods, respectively. The path $f'f$ is the MR behavior controlled by the elastic SMA rods only with pretension effect. After the strength of the steel rods is fully recovered at point e, the connection keeps rotating until θ_3 is reached at point h. The path eg has the same combined stiffness of path ce. At point g, the second stiffness softening of the connection occurs due to the SMA rods starting to yield. On the path gh, both SMA and steel rods are in their own plastic state due to yielding.

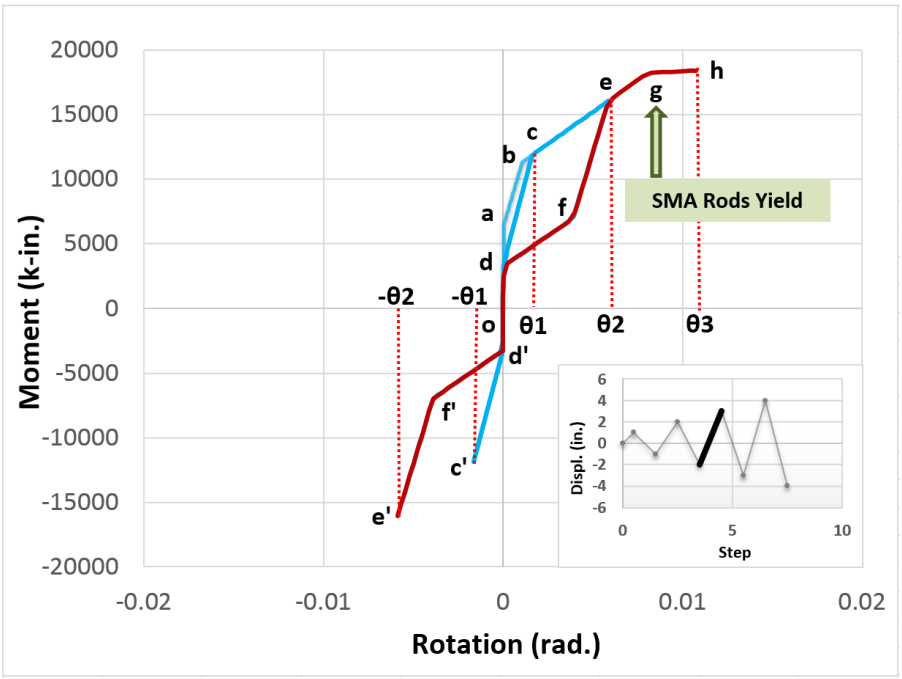

Figure 4-38: MR behavior of connection under load step 5 of loading history 1

(6) For Δ from 3" to -3", the maximum rotation in the negative direction reaches $-\theta_3$, and the response path is $h-i-j-d-o-d'-k'-m'-h'$ (Figure 4-39). Paths hi and $m'h'$ stand for unloading and reloading of the connection including all rods, respectively. After the steel rods are fully released at point i, the SMA rods continue to unload linearly with their elastic stiffness along path ij. The stress of the SMA rods will decrease from the upper backbone to the lower backbone of its 'Flag-Shape' stress-strain curve in Figure 4-24 because of their previous yielding at point g. After point j, the unloading path of the connection changes to follow path jd, which is determined only by the lower backbone of SMA stress-strain curve. After unloading fully, the connection is reloaded in the opposite direction. The strength of steel rods doesn't recover until point m' is reached. Path $d'm'$ is determined only by the upper bond of

SMA stress-strain curve. Before point m' is reached, the SMA rods start to yield in the opposite direction at point k'.

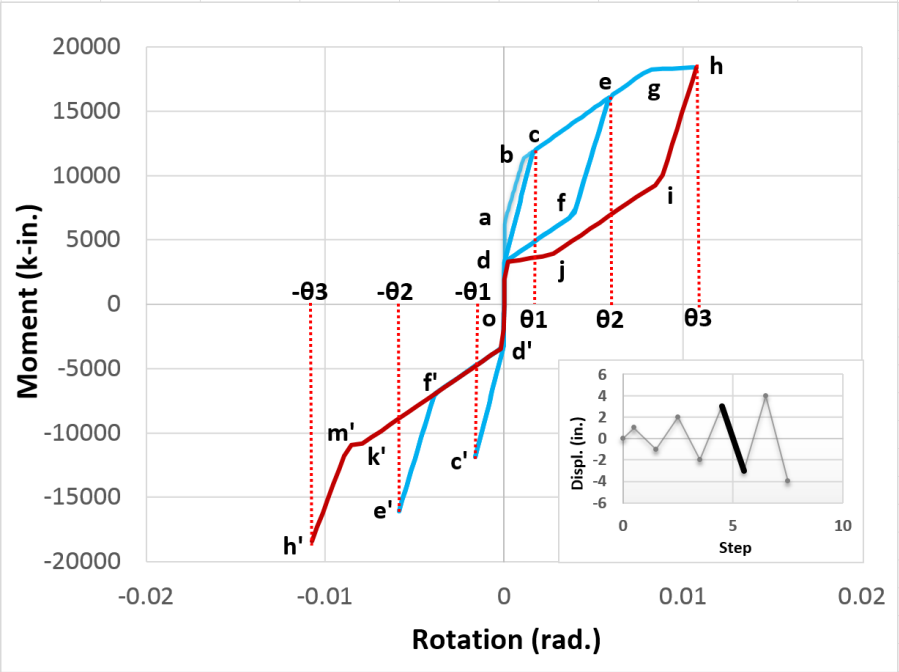

Figure 4-39: MR behavior of connection under load step 6 of loading history 1

(7) For Δ from $-3''$ to $4''$, the maximum rotation in the positive direction reaches θ_4, and the response path is $h' - i' - j' - d' - o - d - k - m - h - n$ (Figure 4-40). Paths $h'i'$ and mh stand for unloading and reloading of the connection including all rods, respectively. The steel rods are fully unloaded at point i' and reloaded beginning at point m. The SMA rods finish unloading with the elastic stiffness at point j', then the lower backbone curve of the SMA stress-strain relationship begins to control the MR response of the connection until point d'. In the reloading branch, path dm is controlled by the upper backbone curve of the SMA stress-strain relationship, and the

SMA rods yield at point k in the positive direction. The connection has the same rotation at points g and k. After fully recovering the steel rod strength at positive rotation θ_3, the rotation keeps increasing to θ_4 at point n with the combined stiffness after the second softening.

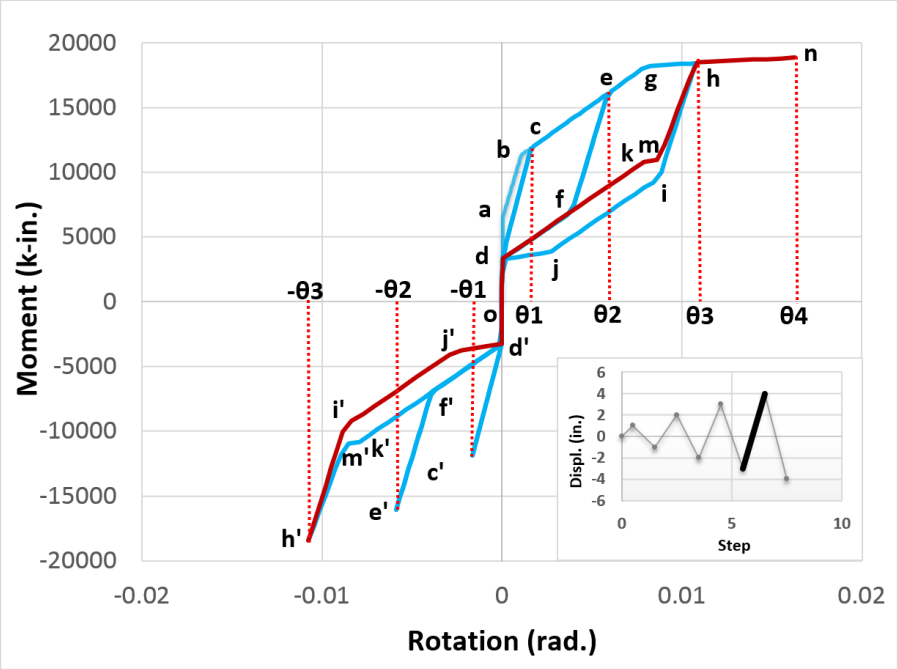

Figure 4-40: MR behavior of connection under load step 7 of loading history 1

(8) For Δ from $4''$ to $-4''$, the maximum rotation in the negative direction reaches $-\theta_4$, and the response path is $n-p-q-d-o-d'-k'-r'-n'$ (Figure 4-41). The response in this step is similar to step 6. Paths np and $r'n'$ represent unloading and reloading of the connection including all rods, respectively. After the steel rods are fully released at point p, the SMA rods continue unloading with their elastic stiffness to point q. The following path qd is determined only by the lower backbond of the SMA

stress-strain relationship. Before starting to recover the steel rods at point r', the MR response following the path $o - d' - k' - r'$ is determined only by the upper backbone of the SMA stress-strain relationship. The SMA rods yield at point k' in the opposite direction.

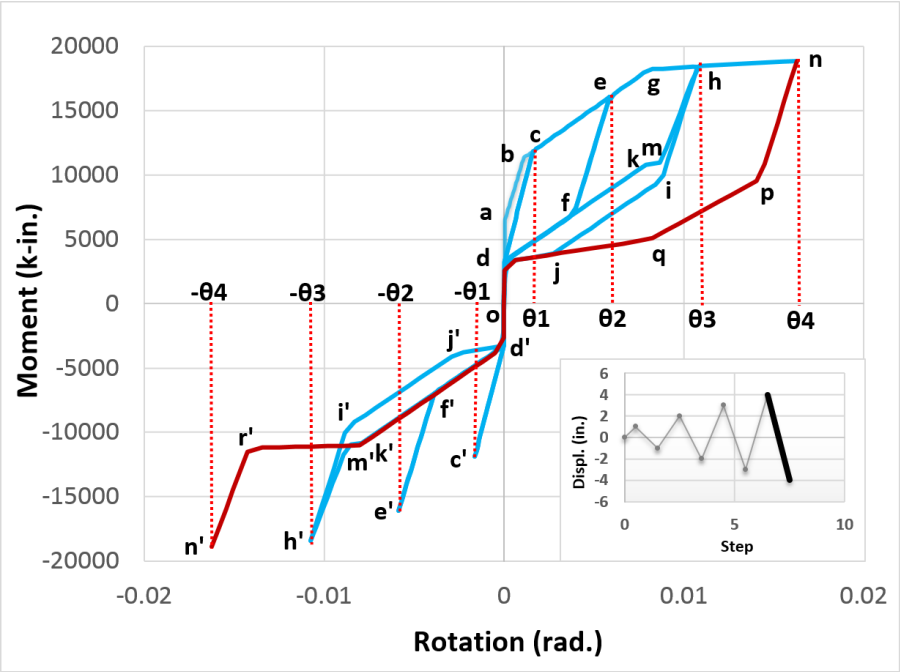

Figure 4-41: MR behavior of connection under load step 8 of loading history 1

One should be aware that the stiffness of the unloading path is a little higher than that of the reloading path after first yielding of the SMA rods, such as shown by paths hi and mh in Figure 4-41. The unloading stiffness is the combined elastic stiffness of both SMA and steel rods; however, the reloading stiffness combines the stiffness of the SMA rods after their first yielding, which is very small, and the elastic stiffness of the steel rods. Because both of the elastic stiffness and the stiffness after their first yielding of the SMA rods are considerablely

less than the elastic stiffness of the steel rods, the two combined stiffnesses are dominated by the steel rods' stiffness, and the difference in slopes between them is not very obvious. This combined reloading stiffness of the connection will slightly change again if the strain of the SMA is greater than 5%, which is caused by the obvious strain hardening effect as shown in Figure 4-24.

Based on the stiffness, the unloading paths between the middle and lower backbone curves of the connection MR response can be separated into two parts: (1) the upper part with combined elastic stiffness of both SMA and steel rods; and (2) the lower part with the elastic stiffness of only the SMA rods. Take the unloading path $h-i-j$ in step 6 as an example. This unloading path intersects the middle backbone curve of the connection MR response at point T in Figure 4-42. The curve in Figure 4-42 is modified by adding the dashed blue line on the response curve for step 8 in Figure 4-41. The dashed blue line stands for the "missing" part of the middle backbone curve of the whole MR response at step 8, which is supposed to be generated in the following loading steps after step 8. The intersection region indicated by a red circle in Figure 4-42 is also highlighted on the full connection MR response curve by a red circle in Figure 4-43. The unloading path Tj in Figure 4-42 can be separated into paths Ti and ij with different unloading stiffnesses. Assume the connection begins to unload at rotation θ_3, where the corresponding stress and strain in the SMA and steel rods are $(\varepsilon_1, \sigma_1)$ at point a in Figure 4-44 and $(\varepsilon_4, \sigma_5)$ at point d in Figure 4-45, respectively. When the steel rods of the connection are just fully released at point i, the connection rotation is reduced to θ in Figure

4-42. The corresponding stress and strain in the SMA and steel rods are $(\varepsilon_2, \sigma_3)$ at point b in Figure 4-44 and $(\varepsilon_5, 0)$ at point e in Figure 4-45, respectively. The strain reduction of both the SMA and steel rods is the same, $(\varepsilon_1 - \varepsilon_2) = (\varepsilon_4 - \varepsilon_5)$. Because the unloading stiffness of the steel rods is much greater than that of the SMA rods, the SMA rods only have a relative small strength reduction of $(\sigma_1 - \sigma_3)$ while the steel rods are fully released. After fully unloading the steel rods, the SMA rods continue to be unloaded until point j in Figure 4-42 with their elastic stiffness, and the state of the steel rods will keep constant caused by the sliding effects. The corresponding stress-strain state of the SMA rods at point j in Figure 4-42 is $(\varepsilon_3, \sigma_4)$ at point c in Figure 4-44.

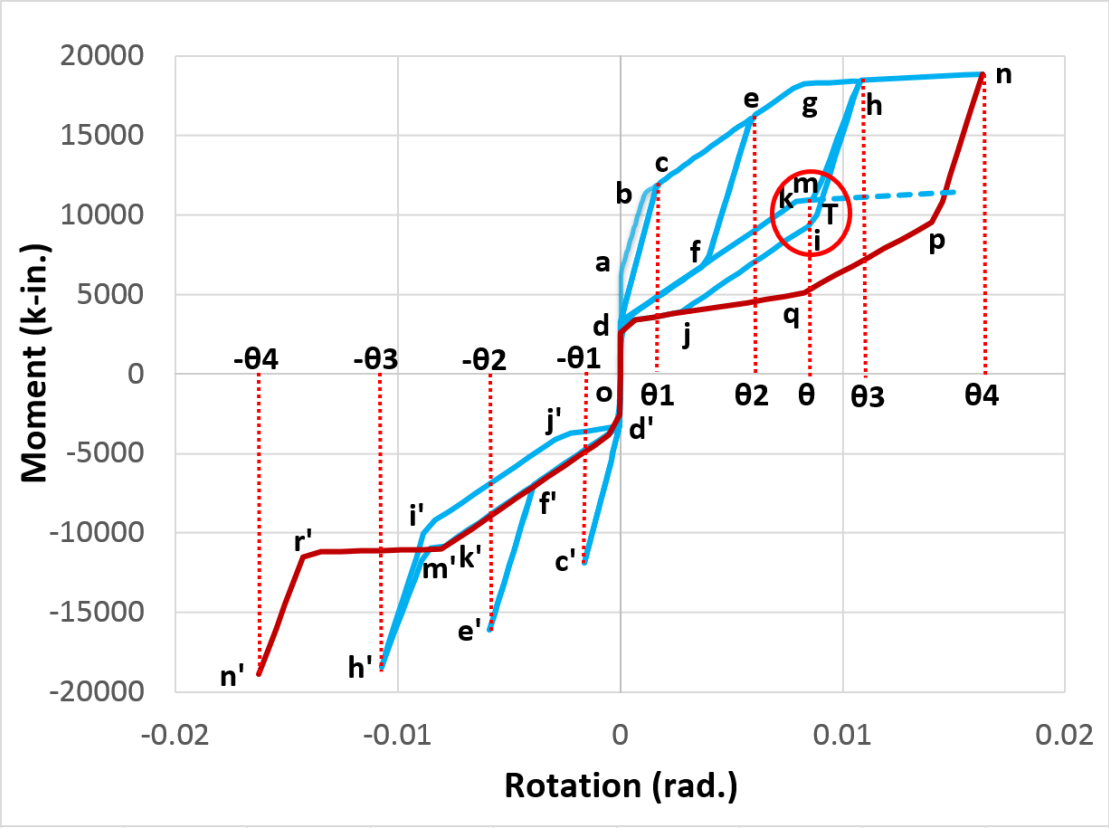

Figure 4-42: Modified MR curve for step 8 in Figure 4-41

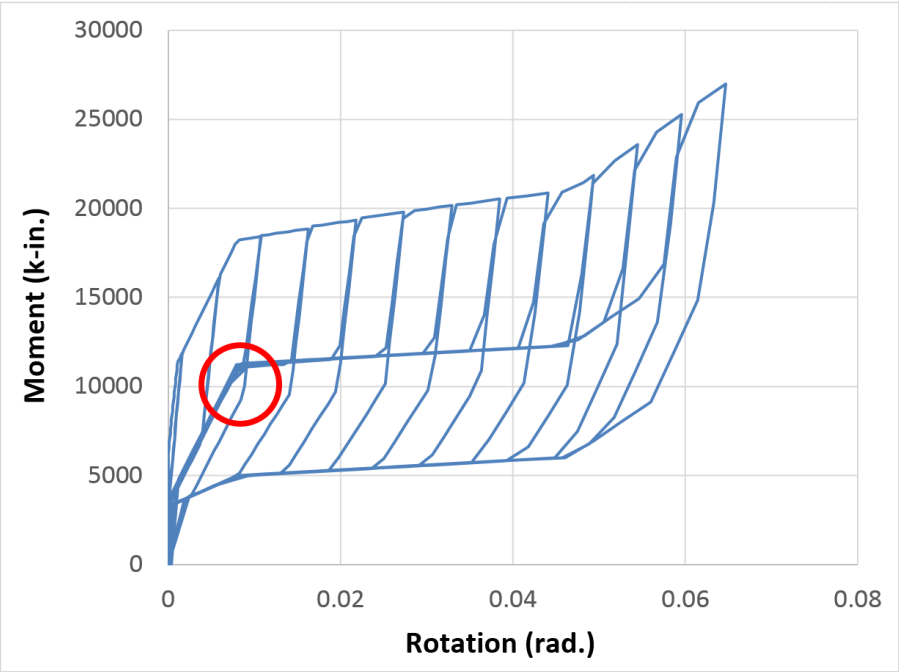

Figure 4-43: MR curve in positive rotation range under loading case 1

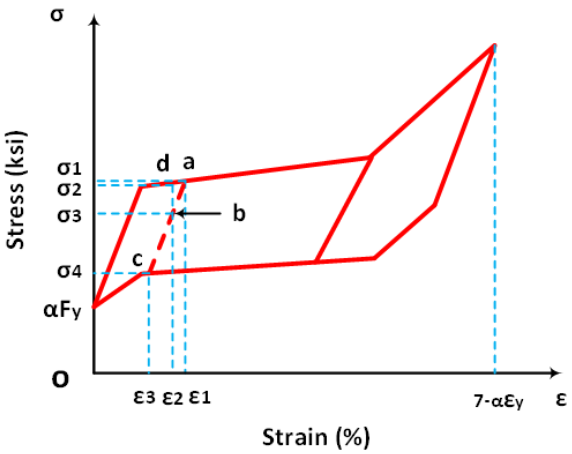

Figure 4-44: stress-strain state of SMA rods for unloading path Tj

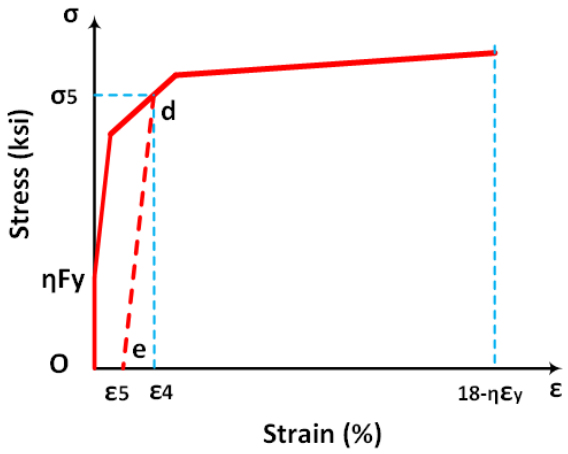

Figure 4-45: stress-strain state of steel rods for unloading path Tj

As discussed above, compared with the state that the steel rods just start to be reloaded, which is represented by the middle backbone curves in Figure 4-32, the connection moment capacity is less when the steel rods are just fully unloaded, which can be represented by the dark bold

backbone curves in Figure 4-33, although the connection deformation is the same under both states. This fourth backbone curve in Figure 4-33 is an imaginary backbone curve and is composed of a series of inflection points of the unloading paths between the middle and the lower backbone curves of the connection MR response, i.e., point i on path Tj in Figure 4-42. In reality, the connection MR behavior does not actually follow this imaginary backbone curve.

For example, in Figure 4-40 the connection is unloaded from the negative direction at rotation $-\theta_3$ and is reloaded again in the positive direction, its reloading path follows $o-d-k-m-h$. At point m, the steel rods just start to be reloaded again. It's easy to prove that the connection has the same rotation θ at point m as point i where the steel rods are just fully released as shown in Figure 4-42. The difference of the connection moment capacity between points m and i is caused by the different strength states of the SMA rods at these two points. Due to the fact that the reloading path of the SMA rods follows the upper backbone of the 'Flag-Shape' stress-strain curve in Figure 4-44, which is different from their unloading path, although the strain of the SMA rods is the same, their stresses are still different. If points d and b in Figure 4-44 represent the stress-strain state of points m and i in Figure 4-40, respectively, it is clear to see that they have the same strain ε_2, but different stresses σ_2 and σ_3. This is the reason why the connection has higher moment capacity during reloading process compared with the unloading process at the same connection deformation.

Unlike the MR curve of the connection in the positive rotation range, there are only two obvious

backbone curves in the range with negative rotation (Figure 4-30). The backbone curves in the negative and positive rotation ranges are anti-symmetric about the origin. The upper one with negative rotation has the same meaning as the lowest one with positive rotation. The two middle ones have the same meaning. The lowest backbone curve in the negative rotation range can only be imagined by connecting all the peak points together. This imagined backbone curve has the same meaning as the upper one with positive rotation. The lack of a solid line for the third backbone curve is caused by the sliding effect of the steel rods. This effect means that the reloading of the steel rods doesn't start until their elongation exceeds the previous residual deformation. The only deformation of all rods in the simplified model of the connection is elongation. The rods cannot take any compressive loading. The maximum plastic deformation after yielding due to tension in the previous loading history will be kept as the current residual deformation. For loading history 1, a symmetric load pattern is used with monotonic increasing magnitudes in either direction. The same loading peak occurs once in each direction alternatively, but all of their first appearances are in the same direction, in the positive rotation range. In the positive direction, the moment capacity can keep increasing after full recovering of the steel rods at the same connection rotation where the previous unloading in the positive direction occurs. However, in the opposite direction, unloading begins once the peak moment is reached or the full recovering of the steel rods just finishes. That's why in Figure 4-30 there are many pin-shape MR curves are generated in the negative rotation direction.

In loading history 2 successively higher displacements occur in each peak. For example, if the

sequence of the loading magnitudes is $(\Delta, 2\Delta, 3\Delta, 4\Delta)$, loading history 2 allows the adjacent two peak loadings, such as Δ and -2Δ, to occur in the two opposite directions (Figure 4-29). When the connection is unloaded from the positive direction at loading Δ and then reloaded in the opposite direction, the connection will reach its previous peak moment at $-\Delta$ and keep increasing until loading -2Δ is reached in the opposite direction. And the next larger loading magnitude, 3Δ, occurs in the positive direction (Figure 4-29). Loading case 2 keeps increasing the connection moment in both directions, alternatively. For loading case 1, if the loading $-\Delta$ for reloading is reached from loading Δ where unloading occurs, the loading is not allowed to increase further beyond $-\Delta$. If one wants to reload the connection to -2Δ, the loading magnitude must be at least 2Δ or larger for unloading. This is the reason why loading case 1 generates a sequence of 'pins' in the negative rotation range; while loading case 2 generates 'teeth' in both directions. This 'teeth-shape' behavior is shown in Figure 4-31. One can notice that during the whole loading history, if the portion of the upper backbone curve of the connection MR response between two adjacent peaks in the positive rotation range occurs, the corresponding portion of the lowest backbone curve of the MR response will be missing in the negative rotation range. It's not hard to prove that any loading history can be composed of finite numbers of loadings with loading pattern of loading case 1 or loading case 2, so the connection MR response will be mixed with 'pins' and 'teeth'. This complimentary characteristic of the behavior of the new proposed connection can be defined as '***Pins-Teeth Cyclic Behavior***'.

In order to check the accuracy of the proposed simplified connection model, the results of the

six key points in Figure 4-46 from the design procedure and SAP2000 are compared in Table 4-8. The design results are determined by following the proposed design procedure in Chapter 3. The nominal un-factored strength are used as the design results, which are identical to the material properties defined in SAP2000. The stress-strain curve used in the design procedure for the steel rods doesn't consider the strain hardening effect when the strain is beyond 4.5%. However, the connection behavior in Figure 4-30 is obtained based on the stress-strain curve defined in Figure 4-12 for the steel rods with strain hardening effect when the strain is beyond 4.5%. The connection behavior which is obtained based on the steel rods without strain hardening effect (Figure 4-47) is represented by the blue solid line in Figure 4-46. The curve obtained with steel rods strain hardening effect is represented in the same plot by the red dashed line. The two curves are identical. This is because the maximum strain of the steel rods is only about 0.061, and the strengths have no obvious difference at this strain whether the strain hardening is considered or not. This connection behavior without considering the strain hardening effect of the steel rods is only used for the comparison with the design results to check the accuracy of the simplified model. The models for all other analysis, if unless otherwise specified, are using the stress-strain curve in Figure 4-12 for the steel rods.

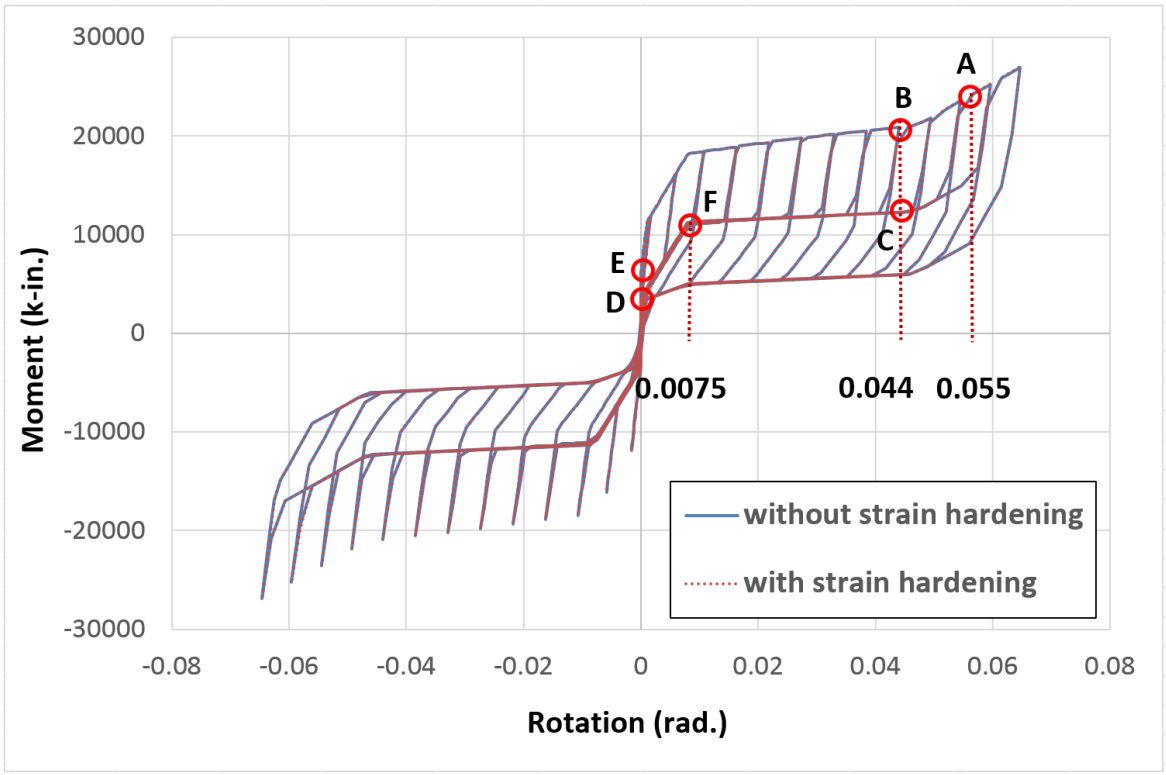

Figure 4-46: MR curves under loading case 1 with and w/o strain hardening for the steel rods

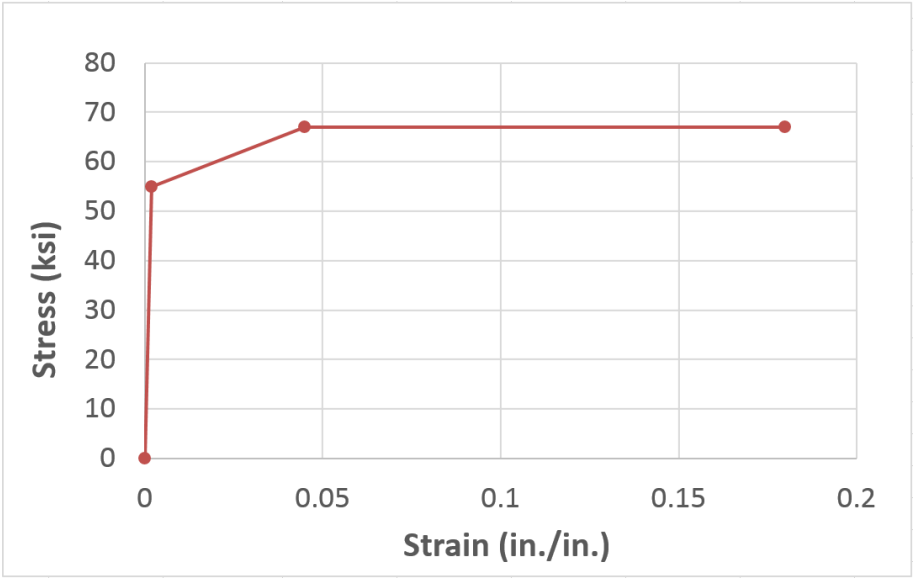

Figure 4-47: stress-strain curve for the steel rods without strain hardening effect

*Table 4-8: Design vs. SAP2000 Moment Capacities of the Interior Connection with W33*130 Beam*

Moment Capacity Item	Point	Corresponding Rotation (rad.)	Moment (k-in)		
			Design w/o Φ	SAP2000	Difference (%)
Ultimate capacity	A	0.0553	25228	23805	-5.6%
Capacity when max strain in SMA rods is equal to 5%	B	0.0436	21442	20840	-2.8%
Capacity from SMA rods when max strain in SMA rods is equal to 5%	C	0.0436	12528	12231	-2.4%
Capacity from the SMA rods pretension	D	0	3378	3258	-3.5%
Capacity from the all rods pretension	E	0	6708	6586	-1.8%
Capacity supplied by the SMA rods yield strength	F	0.0075	11019	10821	-1.8%

The comparison in Table 4-8 indicates that the design and the SAP2000 results in Figure 4-46 have very good correspondence, except that point A has a relative large difference. This indicates that if the connection deformation is not very large, the proposed simplified model is accurate enough to catch the main designed characteristics of the real connection behavior. As previously discussed in section 4.1, the simplified connection model would tend to present a slight softening for both strength and stiffness. This softening effect is introduced by the additional moment which is caused by the tension in the rods on the exterior level. This tension is supposed to transfer into the CCFT column directly in reality. As the connection rotation

increases, the additional moment increases because of the larger tension force in the rods. It also causes the introduced softening effect to be more obvious. This tendency can be easily observed from the comparisons in Figure 4-48, Figure 4-49 and Figure 4-50. In Figure 4-48, three design backbone curves of the connection MR response are plotted only in positive rotation range; and their counterparts based on the SAP2000 results are presented on the same plot for an overall comparison. The absolute and relative errors of the three backbone curves are plotted in Figure 4-49 and Figure 4-50, respectively.

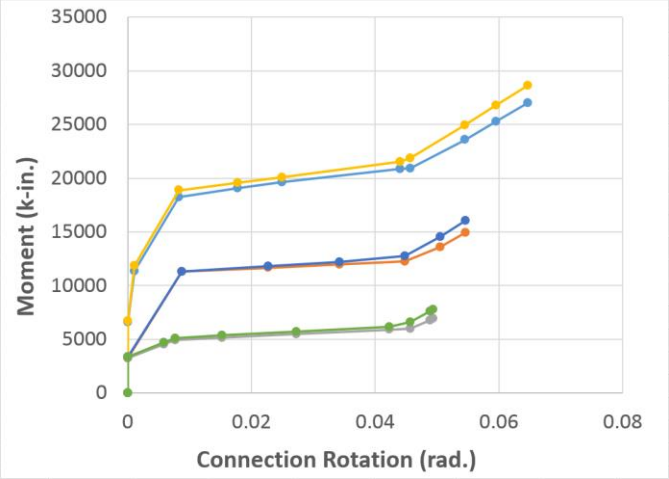

The six curves from top to bottom are:

1. Design upper backbone curve
2. SAP2000 upper backbone curve
3. Design middle backbone curve
4. SAP2000 middle backbone curve
5. Design lower backbone curve
6. SAP2000 lower backbone curve

Figure 4-48: The overall comparisons of the design vs. SAP2000 results of three backbone curves of the MR relationship

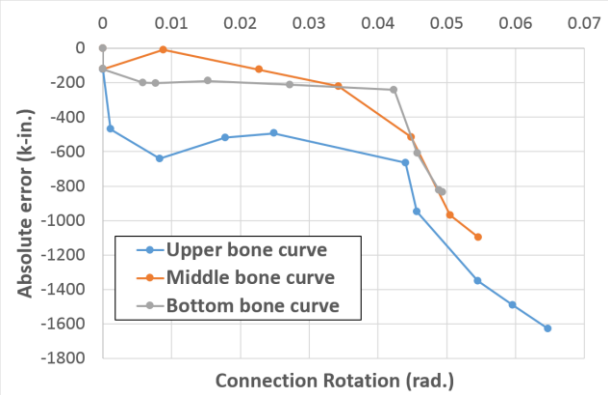

Figure 4-49: Absolute errors of the three backbone curves of the connection MR curve

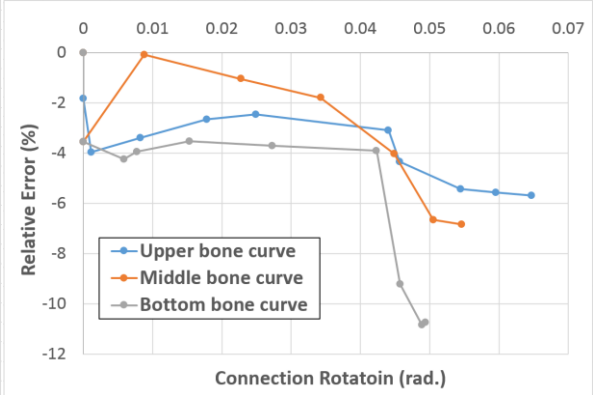

Figure 4-50: Relative errors of the three backbone curves of the connection MR curve

The absolute and relative errors are measuring the results difference between the SAP2000 and the design procedure. The negative values of the errors indicate that SAP2000 gives less moment capacity than the design procedure at a specific connection rotation. This is the so called softening effect. These comparisons also indicate that when the connection rotation is greater than about 4.3%, the errors increase rapidly, especially for the lower backbone curve. From the MR curve, the unloading stiffness between the upper and middle backbone curve is estimated as $4.608 \times 10^6\ (k \cdot in/rad)$. The stiffness between the middle and the lower backbone curve is approximately $7.656 \times 10^5\ (k \cdot in/rad)$. Under the ultimate moment from the connecting beam, the maximum connection rotation on the upper backbone curve is about 0.0553. The maximum rotations on the middle and lower backbone curves can be calculated based on the unloading stiffness as 0.052 and 0.046, respectively. At these three connection rotations, the corresponding maximum relative errors of the three backbone curves are about -5.6%, -6.6%, and -9.2%. This means during the analysis, the maximum error that can be

introduced into the analysis is less than 10%.

4.3.3.2 Cyclic Behavior of the Improved Connection

In order to reduce the errors caused by the additional moment, the improved model introduced in section 4.1 will be analyzed in this section, and its results are compared with the design results. As described previously, the improved model will add an additional four gap elements and four end plate plastic hinges (Figure 4-4). There are two types of end plate plastic hinges analyzed:

(1) Pin connections are assigned to the end plate hinges, because the moment capacity of the end plate is actually not considered in the design procedure. However, these pins are only allowed to rotate in one direction to ensure the expected end plate behavior shown in Figure 4-4 can be obtained. The results of this model are compared with the results based on the design procedure to prove the higher accuracy of the improved model over the original model.

(2) The real moment rotation relationship of the end plate is assigned as the properties of the end plate plastic hinges for cases of stiff plates. The stiffener between the end plate and the beam changes the end plate cross-section from a rectangular to a 'T-shape'. This stiffening effect increases both the strength and the stiffness of the end plate plastic hinges. The connection behavior with or without considering the end plate moment capacity are compared and discussed below based on this model.

The strain hardening effect of the steel rods in these two models are not considered. The result for the model with pin connections for the end plate hinges is plotted in Figure 4-51. The blue curve represents the improved behavior. It is obvious that the improved curve has higher strength compared with the original behavior, especially in the larger connection rotation range. This means the softening effect is somewhat compensated for in the improved model.

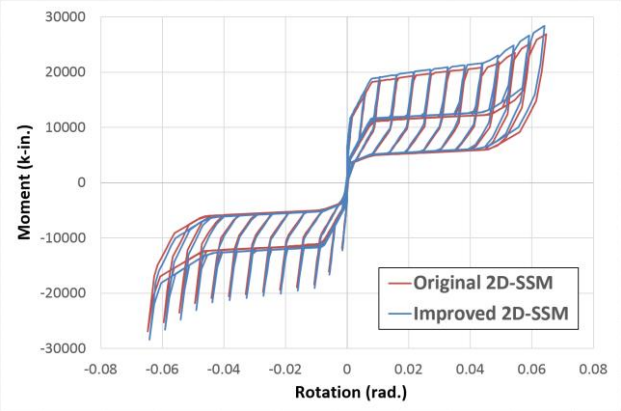

Figure 4-51: Connection MR curves of improved model vs. original model

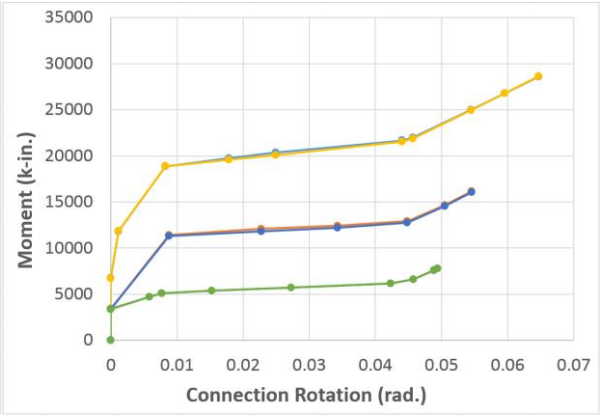

Figure 4-52: The overall comparisons of the design vs. improved SAP2000 results of three backbone curves of the MR relationship

The three backbone curves of this model and their counterparts based on the design procedure are compared in Figure 4-52. The six curves from top to bottom are as follows:

(1) Improved SAP2000 upper backbone curve;

(2) Design upper backbone curve;

(3) Improved SAP2000 middle backbone curve;

(4) Design middle backbone curve;

(5) Improved SAP2000 lower backbone curve;

(6) Design lower backbone curve.

Figure 4-52 indicates that the difference between the improved SAP2000 and the design procedure on the three backbone curves are very slight. It also indicates nearly identical performance between the improved model and the design procedure. The absolute and relative errors of the improved SAP2000 model are plotted in Figure 4-53 and Figure 4-54, compared with the design procedure. These two plots are showing that the improved model gives a little higher strengths than the design procedure. This means that the softening effect caused by the additional moment in the original model is almost totally removed. The relative errors of all three backbone curves are limited to less than $\pm 2.5\%$ in the whole connection rotation range, and even less with large connection rotation for both upper and middle backbone curves. The effectiveness of the improved model is thus proved.

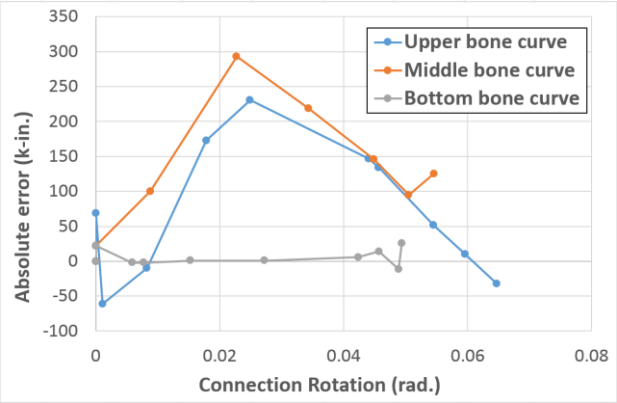

Figure 4-53: Absolute errors of the three backbone curves for the improved model

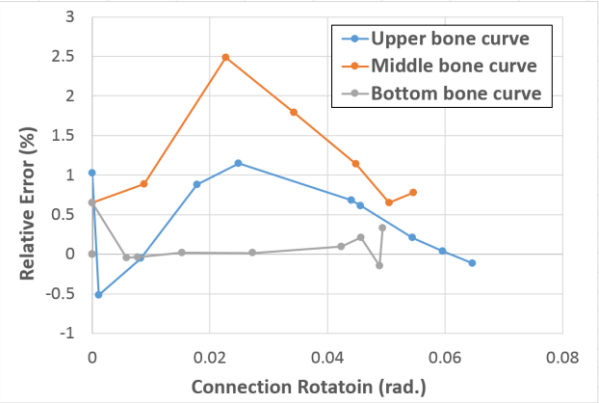

Figure 4-54: Relative errors of the three backbone curves for the improved model

In reality, the moment capacity of the end plate will supply some bending capacity and increase

the connection strength. In order to investigate the influence of the end plate strength on the connection strength, the 2nd type of end plate plastic hinge is applied. As mentioned above, the bending strength and stiffness of the end plate are enhanced by the stiffening effect from the stiffeners between beam and end plate. The elastic perfectly plastic moment rotation relationship in Figure 4-55 is used as the property of the end plate plastic hinges. This relationship is obtained from the ABAQUS analysis in Chapter 5 under four assumptions: (1) yielding occurs when the stiffener fully yields in compression; (2) only 60% of the end plate thickness contributes to the yielding moment capacity because the average stress of the end plate at this step is about 60% of the end plate yielding strength; (3) the net area of the end plate is used; (4) the rotation centerline is on the beam flange level. The dimensions of the end plate are identical to the ones in Chapter 5. The thickness of the end plate is 2'' in Chapter 5, although the design procedure gives only 1.125'' in Chapter 3. The effective width of the end plate is 16.7'', and the effective thickness is 1.2''. The design procedure determines the thickness of the end plate based on the shear demand. The moment capacity is not considered; it is assumed to be adequate enough with the stiffening effect from the stiffeners. In this section, the thicker end plate is used to obtain a connection behavior without weak end plate effect. The effect from an inadequate end plate on the connection behavior will be discussed in the next section.

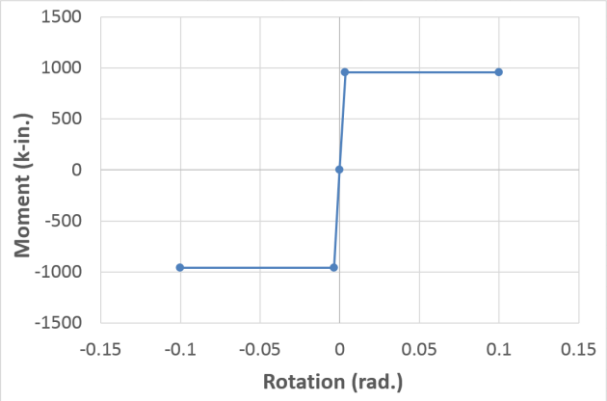

Figure 4-55: Moment rotation curve of the end plate plastic hinges

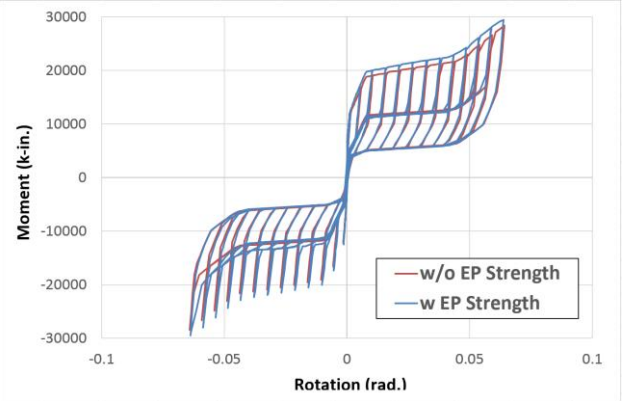

Figure 4-56: Connection MR of the improved model with vs. without end plate strength

In Figure 4-56, the blue solid line represents the connection MR curve for the end plate plastic hinges with moment rotation relationship in Figure 4-55; the red solid line stands for the MR curve for pin connection as the end plate hinges. There are two most obvious differences after the bending capacity of the end plate is considered:

(1) The upper backbone curve in the positive direction has higher strength than its counterpart with zero end plate bending capacity, and this is also the case for the peaks in the negative direction.

(2) The two MR curves have identical middle and lower backbone curves in the positive rotation direction, and lower backbone curve in the negative rotation direction. The MR curve with considering end plate strength has two middle backbone curves in the negative rotation direction.

As expected, the bending capacity of the end plate will increase both the strength and the stiffness of the connection. Based on the comparison in Figure 4-56, this enhancement effect

clearly influences both the negative upper and middle backbone curves, but only the positive upper backbone curve. The upper backbone curves stands for the ultimate capacity of the connection at specific rotation with all rods fully recover from the previous unloading process. It's not hard to understand the strength increase for both two upper backbone curves. The middle backbone curves represent the connection capacity before the steel rods begin to recover. After a careful investigation, one can actually find that the two negative middle backbone curves are composed by a sequence of lines whose previous portion are the same as the unenhanced middle backbone curve, and whose following portion increases gradually to the higher strength middle backbone curve. These lines are generated by the corresponding sequence of loading cycles. As the loading magnitude becomes greater, the previous portion of the middle backbone curve also becomes longer. Because there is some overlap between the middle curves from the previous and the following loading steps, it seems like there are two different middle backbone curves in the negative direction.

In fact, the same phenomenon exists for the positive middle backbone curve, but it is too insignificant to be noticed. The reason is that in the positive rotation, the bending of the end plate starts just a little bit earlier than the recovery of the steel rods; however, in the negative rotation, the steel rods will not recover steadily until considerable amount of the end plate rotation has already been generated. The rotational stiffness of the end plate hinges is 2.765×10^5 $(k \cdot in/rad)$, which is far less than the total reloading stiffness of all rods of 4.608×10^6 $(k \cdot in/rad)$. Once the steel rods begin to recover, the effect of the end plate hinge stiffness

can be ignored. After a small rotation of the end plate, the strength of the steel rods increases rapidly and the connection moment capacity reaches its previous peak value. Although the bending of the end plate continues, it is hard to separate the positive middle backbone curve with the effect of all rods stiffness. But this is not the case in the opposite direction. Before the steel starts to work, there is quite large deformation of the end plate. Due to fact that the SMA rods stiffness is about 7.656×10^5 $(k \cdot in/rad)$, which is only about 2.7 times greater than the end plate stiffness, there will be a considerable influence of the end plate stiffness. That's why the increasing strength is more obvious for the negative middle backbone curve.

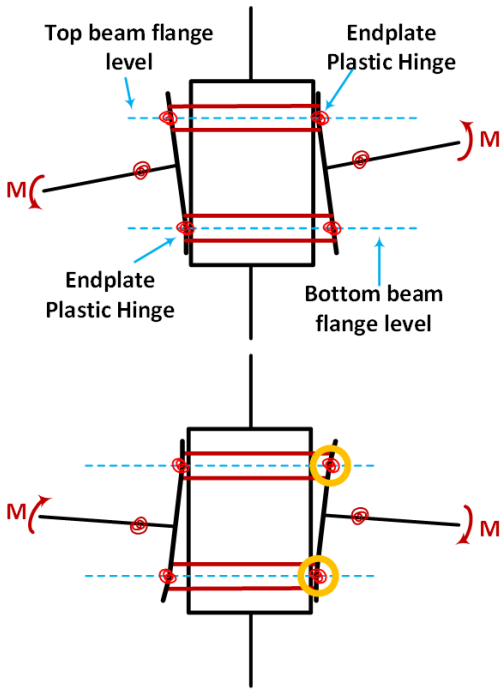

Figure 4-57: Connection mechanism with end plate plastic hinges

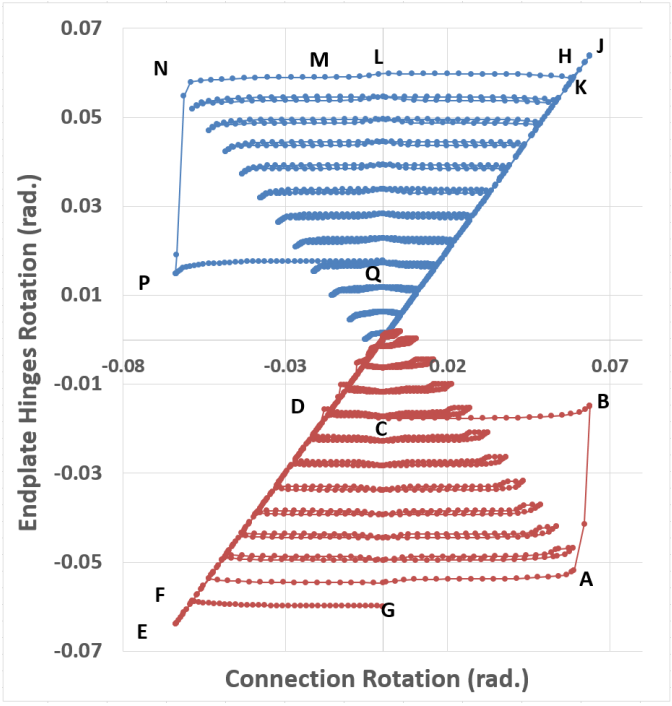

Figure 4-58: End plate hinges rotation vs. connection rotation

Before probing into the further reasons for the MR curve in Figure 4-56, the behavior of the

end plate plastic hinges is investigated first. The symmetric loading case 1 is applied in the analysis, and the connection rotates in the positive direction first. After adding plastic hinges on the end plate, the connection deformation mechanism is presented in Figure 4-57. The top deformation is under counterclockwise moments, and the bottom one is under clockwise end moments. Under loading case 1, the two mechanisms occur alternatively, and the rotational behavior of the two end plate hinges which are highlighted by two yellow circles are plotted in Figure 4-58. The top curve in blue comes from the top end plate hinge, and the bottom curve in red is from the bottom end plate hinge. The x-axis stands for the connection rotation, and the y-axis represents the end plate hinge rotation. There are several key characteristics of the curves in Figure 4-58 that require an explanation:

(1) Each curve (in blue or red) is composed of several *Approximately Horizontal Straight Lines* (**AHSLs**) and a *Straight Line* with about *45 degree* angle (**45SL**). These AHSLs are approximately symmetric about the y-axis. The lengths of these lines increase gradually as their distances from the x-axis increase. One end of each AHSL, on the same side, is connected by the 45SL.

(2) On each AHSL, the end plate hinge rotation keeps the same value throughout most of the connection rotation. Because the hinge rotation won't change, the loading must be stable and the hinge must be elastic. As discussed previously, the pretension of the SMA rods remains constant during the whole loading history, so the SMA rods will not fully released. This means that when the connection rotates under loading case 1, most of time the end plate hinges are in the elastic state and the steel rods are in the loosened

state. The unchanged loading on the end plate for each AHSL is believed to come from two sources: (1) pretension of the SMA rods; and (2) and the small elongation of the SMA rods caused by the residual deformation of the end plate hinges.

(3) Most of AHSLs are composed by two lines which are almost identical to each other. This means that when the connection rotates between the two ends of each AHSL back and forth, the residual deformation of the end plate hinges doesn't change. When the curve path follows the 45SL from one AHSL to another, the end plate hinges yield further and their residual deformations also increase.

(4) The positive connection rotation is caused by the counterclockwise moments. From Figure 4-57, one can tell that for the two end plate hinges under investigation, the bending of the top one in the positive connection rotation and the bending of the bottom one in the negative connection rotation are caused by the compression on the tube wall; the bending of the top one in the negative connection rotation and the bending of the bottom one in the positive connection rotation are caused by the tension of the rods on the exterior rod level. Only under the compression on the tube wall, the end plate hinges can yield more and the curve path follows the 45SL.

(5) On the other hand, for each AHSL, its tip away from the end connected by the 45SL presents a slight decreasing of the end plate rotation. This decreasing is caused by the tension of the exterior rods. As discussed previously, the residual deformation of the end plate hinge is caused by the pushing from the tube wall. However, under the opposite connection rotation, pushing of the tube wall changes to pulling of the rods.

This will reduce the residual deformation a little bit. However, the tension force is not enough to yield the end plate hinge, so this elastic reduction will disappear as the connection changes rotation direction again. This ensures that the residual deformation on each AHSL stays almost constant as the connection rotates back and forth.

(6) The points on the 45SL have the same end plate hinge rotation as the connection rotates. This means that the change of the end plate hinge rotation is almost equal to the change of the connection rotation. In other words, after the end plate hinges yield under the compression on the tube wall, the plastic rotation of the end plate hinges will constitute nearly all the connection rotation.

(7) There are two obvious drops of the end plate hinges rotation for both types of hinges. However, the drop for each end plate hinge occurs in a different loading cycle. The first drop occurs on the bottom end plate hinge at point A. It is caused by the fact that the tension force on the bottom exterior rods is large enough to yield the end plate hinge. This generates a very large plastic rotation towards the tube wall, which is opposite to the existing residual rotation. The residual deformation is reduced to point B. At the same time, the top end plate hinge is bending further under the tube wall pressing form point H to J and generates a larger residual deformation. At this stage, the connection reaches its maximum displacement in this loading cycle, and then it begins to unload. When the connection is fully released to zero rotation, the curve of the bottom hinge goes form point B to C. There is a little increase of the hinge rotation at the tip of point B. This is the elastic recovery caused by the decreasing of the tension force in

the exterior rods. As discussed previously, the tension force tries to reduce the residual rotation of the end plate hinge. After the elastic deformation recovers, the residual deformation stays the same as the connection rotation goes to zero at point C. On the other hand, the curve of the top hinge goes from point J to K to L. At the beginning, the rotation of the top hinge is reduced from point J to K linearly. Because the pushing of the tube wall is the reason for the rotation for the top hinge, when the top end of the end plate moves away from the tube wall, the hinge is unloaded linearly until all the elastic deformation is removed. One can question that given that both the top and bottom end plate hinges are unloaded from the same plastic moment capacity, why is the elastic deformation change for the top hinge obviously greater than that of the bottom hinge? The reason is that the top hinge is fully unloaded from its plastic moment once the end plate separates from the tube wall and even when reloaded in the opposite direction a little. However, the bottom hinge is not fully unloaded and there is still some tension force left in the exterior rods. When the connection is reloaded in the opposite direction again to its ultimate deformation, the curve of the bottom hinge goes from point C to D to E. Because the previous yielding under the tension force from the exterior rods, the bottom hinge yields and generates quite a large plastic deformation from point D to E. At the same time, the curve of the top hinge goes from point L to M to N to P. When the bottom hinge yields rapidly after point D, the top hinge is still in the elastic range from point M until point N. This indicates that the inner force of the end plate hinge introduced by the exterior rods in tension increases much less

than that caused by the tube wall pressing. At point N, the top hinge starts to yield under the rods tension and the residual rotation drops to point P. At this stage, the ultimate deformation in this loading cycle is reached. The last loading cycle of loading history 1 is to reload the whole connection. The bottom hinge is linearly unloaded from point E to F, then keeps the residual rotation to point G. The top hinge is unloaded from point P to Q accompanied with a little bit elastic recovery of the hinge rotation at the tip of point P. In the end, the residual deformation of the bottom hinge is about -0.06 radian at point G; and it is about 0.0178 for the top hinge at point Q.

(8) For both two drops from point A to B and N to P there is a slight increase of the connection rotation after the drop occurs. This slight increase is necessary to ensure the elongation of the rods on the exterior rod level stays the same and is not reduced due to the decreasing of the end plate hinge rotation. The same elongation causes the same tension force to make sure the moment at the end plate hinge is equal to its plastic yielding capacity.

To understand the reason why end plate bending begins in the negative direction, a sequence of the connection deformations are plotted in Figure 4-59. The counterclockwise rotation is defined as the positive rotation. The MR behavior in Figure 4-56 indicates that the connection starts to rotate in positive direction under loading case 1. According to the characteristics of loading case 1, 'Step N+1' has the same maximum loading magnitude as the previous 'Step N', which is greater than 'Step N-2' and 'Step N-1'; and it will increase in 'Step N+2' again. After

unloading from ‘Step N’, the steel rods will have an amount of residual deformation, and this residual deformation will be kept after ‘Step N+1’. So for both ‘Step N+1’ and ‘Step N+2’, the same amount of separation of the end plate is needed to offset the residual deformation before the steel rods start to be reloaded.

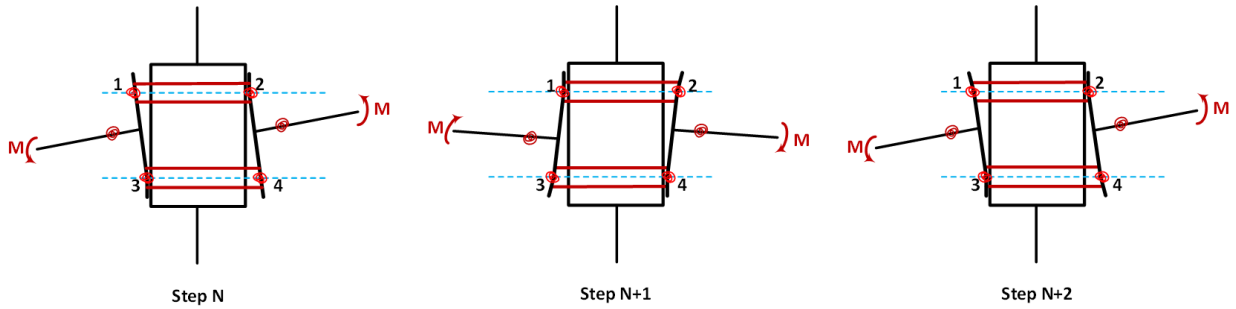

Figure 4-59: A sequence of the connection deformations under loading case 1

Because the yielding of the end plate hinge by tension in the exterior rods occurs at very large connection rotation (about 0.06 radian), it is assumed that the yielding of the end plate hinge due to tension in rods will not occur before ‘Step N+3’. This ensures that only the bearing from tube wall can yield the end plate hinges, and the elastic deformation caused by the rod tension can be fully removed after unloading. In the initial ‘Step N’, all four end plate hinges have been subjected to the same loading history, so they have the same residual deformation which is caused only by the bearing of the tube wall. After ‘Step N’, the steel rods yield more and generate larger residual deformation to cause the end plate hinges at locations 2 and 3 also to generate more plastic rotation, while yielding at hinges at locations 1 and 4 will not occur until ‘Step N+1’ finishes. The residual deformation caused by the bearing of the tube wall is away

from the tube wall; this means that the larger residual rotations of the end plate hinges are, the larger separation between the two ends of the rods on the exterior rod level is. As discussed above, the same amount of the end plate separation is needed for both 'Step N+1' and 'Step N+2' to make sure that the two ends of the steel rods can be in contact with their corresponding end plate before the steel rods can be reloaded again. For the steel rods on the top (or bottom) exterior level in 'Step N+1' before the steel rods are reloaded, the residual deformation of end plate hinge at location 1 (or 4) is less than that at location 2 (or 3), but in 'Step N+2' they are the same. Therefore before the connection is reloaded from its fully released state, the separation of the end plates in 'Step N+2' is greater than it in 'Step N+1'. This means that 'Step N+1' needs more end plate rotation before the steel rods are reloaded. The end plate rotations should be the same in both 'Step N+1' and 'Step N+2' just before the steel rods are reloaded. Then the only way to generate larger end plate rotation in 'Step N+1' is to allow the end plate hinges to yield and rotate earlier than that in 'Step N+2'. 'Step N+1' and 'Step N+2' are one common loading step for the negative and positive connection rotation, respectively. Generally speaking, the end plate hinges start to yield earlier in the negative rotation direction than in the positive rotation direction, and the steel rods begins to recover at the same end plate or connection rotation in both directions.

4.3.3.3 Cyclic Behavior of the Connection Including Beam Plastic Hinges

A parametric study on beam strengths has been done to investigate the interaction effects between the proposed connection and the connecting beams in Appendix H. The results

indicate that the proposed 2D-SSM in SAP2000 is robust without a dependence on beam strengths.

4.3.3.4 Relative Stiffness between the Proposed Connection and the Connecting Beams

AISC Design Guide 16 employs a moment-rotation diagram to distinguish connections into three types based on their stiffness as shown in Figure 4-60: (1) FR connection; (2) PR connection; and (3) simple shear connection [98]. The "Beam Line Equation", which is represented by the dashed line, is defined as $M = M_F - 2EI\theta/L$, where M is the beam line end-moment (*kips-in.*); M_F is the fixed end-moment (*kips-in.*); E is the Yong's modulus of steel (*ksi*); I is the moment inertia ($in.^4$); θ is the beam line end-rotation (*rad.*); and θ_s is the simple span beam end-rotation (*rad.*). In this research study, M_F is defined as the moment when the SMA rods start to change phase at point g in Figure 4-38. For the connection in Section 4.3.3.1, $M_F = 18282.6$ *kips-in.*, which is less than the yielding capacity of the RBS ($S_x F_y = 19499.6$ *kips-in.*). Two paths in Figure 4-38 and one path in Figure 4-41 are used to describe how does the type of the new proposed connection changes among three categories (FR, PR, and Simple) defined by AISC as shown in Figure 4-61. Path 1 is $o - a - b - g$, which represents the initial monotonic behavior; path 2 is $o - d - f - e - g$, which represents the reloading path with yielding of steel rods; and path 3 is $o - d - q - p - n$, which represents the unloading path after all rods yielding. From the results in Figure 4-61, it is clear to see that most of the connection behavior is located in the range of the partially restrained connections.

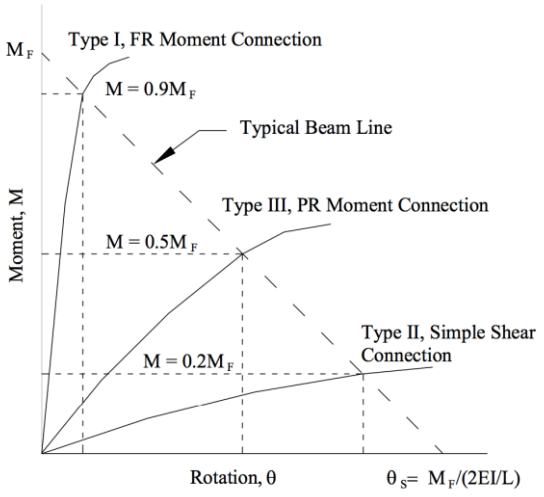

Figure 4-60: Moment-rotation curves to define three connection types [98]

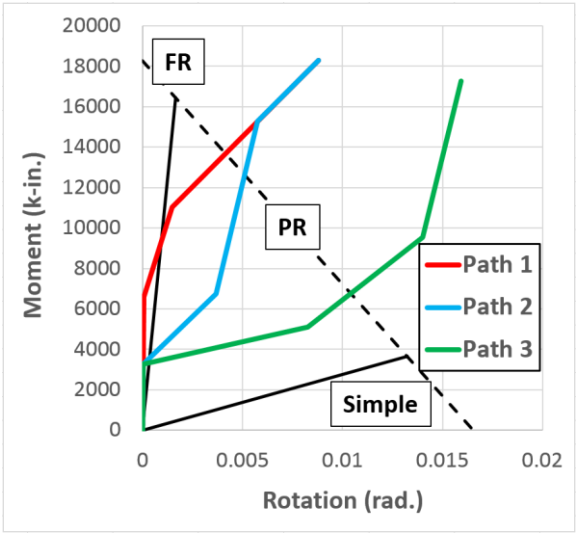

Figure 4-61: Behavior of the new proposed connection compared with Figure 4-60

4.4 Summary and Conclusions

In order to reduce the computational cost of analyzing structures with the new proposed self-centering connection configuration, a 2D Simplified Spring Model (2D-SSM) for uniaxial bending was developed in SAP2000. The 2D-SSM is established based on the same assumptions as for the preliminary design procedure in Chapter 3. The characteristics of the 2D-SSM in SAP2000 are summerized as follows:

- No end plate yielding is considered in the original 2D-SSM (see Figure 4-1).
- A SMA through rod model was developed to simulate the flag-shape self-centering behavior with pretension effects. However, this model is not able to account for either residual strains or strength or stiffness degradation under cyclic loading (see Section

4.2.3).

- The SAM model is composed of one ‘MultiLinear Elastic Link Element’ and one ‘MultiLinear Plastic Link Element with Kinematic Hysteresis Law’. A set of relationships were provided for calculating the required link parameters (Section 4.2.3).
- A steel through rod model was developed to simulate its pretensioning and sliding effects. The model is composed of one ‘MultiLinear Elastic Link Element’ and one ‘MultiLinear Plastic Link Element with Takeda Hysteresis Law’. A set of relationships were provided for calculating the required link parameters (Section 4.2.4).
- The model is believed to be sufficiently accurate for design checks if the ultimate strain in the SMA rods is limited to less than 7%.
- An improved model was developed to considering yielding effects of end plates.

Detailed examples are given in Section 4.3.3. The results are compared with those from the proposed preliminary design procedure in Chapter 3. Several conclusions can be obtained as follows:

- The proposed simple models in SAP2000 for SMA and steel through rods are capable of simulating their self-centering, pretension, and sliding effects.
- The proposed 2D simplified spring model (2D-SSM) for NPSCs is effective in capturing the main characteristics of the NPSCs.
- Compared with the original 2D-SSM in SAP2000, the improved model can eliminate the unexpected softening effects.

- The difference in key results between the preliminary design procedure and the 2D-SSM in SAP2000 is less than $\pm 2.5\%$. This proves the effectiveness of the proposed 2D-SSM.

Chapter 5

Finite Element Analysis

In this chapter, a detailed *finite element* (**FE**) model of a uniaxial bending connection in ABAQUS is described. In Section 5.1, the current basic concrete models that consider confinement effects are introduced, and an example is provided for comparison among these methods. In Section 5.2, a concrete model in ABAQUS named '*concrete damaged plasticity* (**CDP**)' model, which can simulate the cracks in the concrete core and infill grout after damage, is discussed. In Section 5.3, the components of the uniaxial bending connection and their corresponding materials are introduced. The boundary conditions and assumptions of the model are also described. In Section 5.4, the FE results are presented and discussed. Section 5.5 summarizes the whole chapter and discusses future work.

5.1 Confined Concrete Models

Concrete has large compressive strength and a relative lower price than steel, and is usually used as an ideal material in structural design to carry large compressive axial loads. However, as a typical brittle material, it has very low tensile strength, so components made of plain concrete are not recommended in structural design, especially for seismic design. The traditional solution to improve the ductility of concrete components is to add steel reinforcement. In the tensile region, reinforcements can supply tension capacity after cracking

occurs in the concrete. On the other hand, the combination of stirrups and longitudinal reinforcement can supply some confinement to the concrete core. Based on the results from both theoretical analysis and experimental tests, larger confinement usually bring larger improvement of concrete strength and ductility. As discussed in previous chapters, a circular steel tube can supply the maximum confinement on concrete, and result in a significant increase of both its strength and ductility.

In order to utilize this great benefit from confinement on concrete, effective analysis models are very important. There are several such models to consider the confinement effect on the concrete core by circular steel tubes as discussed in detail in Appendix I.

5.2 Concrete Damaged Plasticity Model in ABAQUS

There are three models in ABAQUS to simulate brittle behavior of concrete with cracking: the concrete smeared cracking model, the brittle cracking model, and the *concrete damaged plasticity* (**CDP**) model. The first model is only available for the ABAQUS Standard solver, the second model is only available for the ABAQUS Explicit solver, and the third one is available for both solvers. In this research, the CDP model is utilized. This model combines the concept of isotropic damaged elasticity and the concept of isotropic tensile and compressive plasticity to represent the inelastic behavior of concrete. It can simulate cracking caused by both tensile cracking and compressive crushing under monotonic or cyclic loading with low

confining pressures (less than four or five times the ultimate compressive stress in uniaxial compression loading). When the confining pressure is sufficiently large, crack propagation can be prevented. This model can be used for all types of structures, such as beams, trusses, shells, and solids.

5.3 ABAQUS Model of the Proposed Connection

ABAQUS is a powerful finite element software for engineering simulation, and is utilized broadly in both industry and research fields. It has a very rich element library to support simulations of various practical problems, from simple linear issues to very complicated nonlinear ones, such as complex contacts, large geometric nonlinearities, coupling analysis between heat and electronic fields, and brittle materials failing thru fracture. At the same time, ABAQUS supplies a large number of materials options for these elements, which makes it possible to simulate nearly all kinds of material behavior. What's more, it allows users to generate their own subroutines for new material properties, which extends its capability of solving problems greatly. In this section, a detailed Finite Element Model in ABAQUS v6.12-1 for the new proposed composite connection for uniaxial bending is introduced, including the geometry of each component of the model, materials properties, and boundary conditions. More details on the concrete damaged plasticity model are given in Appendix J.

5.3.1: Model Components and Geometry Dimensions

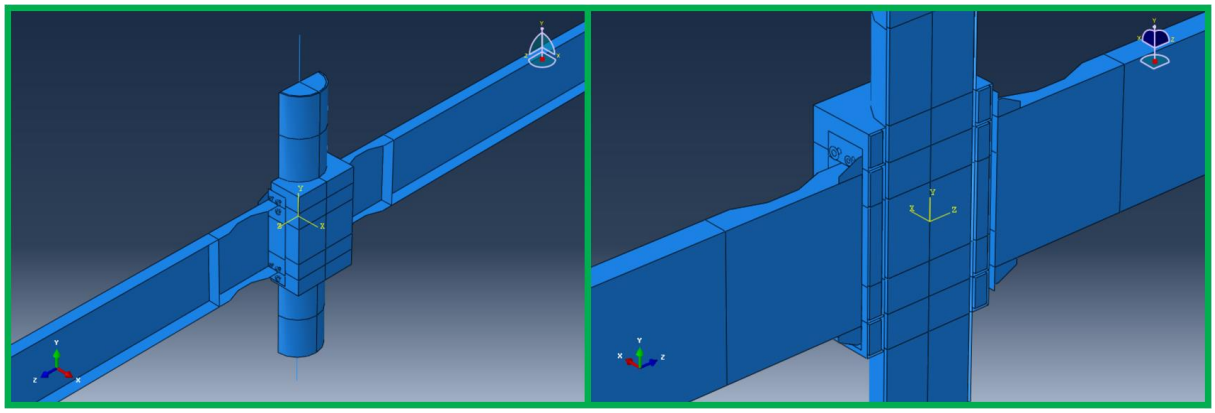

Figure 5-1: The model of a half connection configuration for uniaxial bending

In Figure 5-1, an FE model for a half of an uniaxial connection configuration is presented from both front and rear views. This model is composed of thirteen components:

(1) One concrete core surrounded by the circular steel tube;

(2) One circular steel tube;

(3) One grout block bounded by both circular and square steel tubes;

(4) Two inner diaphragms piercing the grout block at the levels of beam flanges, and splitting the grout block into three parts;

(5) Two cover plates holding and covering grout on its bottom and top surfaces;

(6) One square steel tube;

(7) Two beam-element based columns on both ends of solid CCFT column;

(8) Two end plates;

(9) Eight rods in total, including four steel rods and four SMA rods;

(10) Eight nuts in total, including 4 nuts for the steel rods and 4 nuts for the SMA rods;

(11) Four stiffeners between beam flanges and end plates;

(12) Two bracing stiffeners for beam flanges and webs; and

(13) Two W steel beams with RBS.

The model shown in Figure 5-1 simulates a relative large size connection with W33*130 beams. The size of each component is calculated based on the design procedure proposed in Chapter 3, with some slight modifications. A detailed design example is presented in Appendix C. The specific size information of each part of the connection model above is listed in Table 5-1.

Table 5-1: Sizes of the Components of Uniaxial Bending Connection

Component	Size Description	Component	Size Description
Circular steel tube	Outer diameter is 24 in., wall thickness is 1.5 in. and height is 10.5 ft.	Inner diaphragm in grout	In plane dimensions are fit to sizes of circular and square steel tubes, and thickness is 1.0 in.
Beam-element based column	Length is 1.75 ft. with equivalent circular steel cross section with diameter of 16.9 in.	Cover plate	In plane dimensions are fit to sizes of circular and square steel tubes, and thickness is 1.0 in.
Square steel tube	Sides' width is 32 in., wall thickness is 1.0 in. and height is 42.6 in.	Concrete core	Fit to size of circular steel tube
End plate	In plane dimension is 36.6 in. by 19 in. and the thickness is 2.0 in.	Grout block	Fit to sizes of circular and square steel tubes
W steel beam with RBS	Cross section is W33*130, and beam length is 175 in. The parameters a, b and c of RBS are 0.5, 0.65 and 0.25, respectively	Rods	Length is 36 in., diameter for steel rods and holes is 13/16 in., and for SMA rods and holes is 19/16 in.
Stiffener	Length is 5.75 in., height	Nuts	Inner and outer

between beam flange and end plate	is 3.32 in., landing is 1.0 in., and the thickness is 0.29 in. (same as beam web thickness)		diameter for steel rods are 14/16 in. and 31.5/16 in.; and for SMA rods are 20/16 in. and 42/16 in.
Bracing stiffener	In plane dimensions are fit to beam cross section, and the thickness is 2.0 in.	NA	NA

5.3.2: Material Models and Properties

Simplified true stress-strain relationships are used in the FE analyses. There are six different materials are in the model:

(1) "Concrete Damaged Plasticity" material model is used for both the concrete core and the infill grout. The compressive and tensile strengths are 4.692 ksi and 0.258 ksi, respectively. The Young's modulus is taken as 3900 ksi and the Poisson ratio as 0.2. The concrete stress-strain curve is plotted in Figure 4-13.

(2) "Plastic" material model and the experimental stress-strain curve are used for the SMA rods. Only the upper backbone curve is used in the analysis, which is defined by three strengths as 66.7 ksi, 74.5 ksi, and 116.0 ksi at the corresponding strains of 0.0114, 0.05 and 0.07. The Young's modulus is taken as 5850.9 ksi and the Poisson ratio as 0.3. The stress-strain curve is plotted in Figure 5-4, which is simplified from Figure 4-17.

(3) "Plastic" material model and A572 Grade 50 steel are used for the steel rods, circular steel tubes, inner diaphragms, and the beam-element based columns. The yield and ultimate strengths are taken as 50 ksi and 65 ksi with R_y equal to 1.1 at the

corresponding strains of 0.002 and 0.1, respectively. The Young's modulus is taken as 29000 ksi and the Poisson ratio as 0.3. The true stress-strain relationship is presented in Figure 4-12.

(4) "Plastic" material model and A992 Grade 50 steel is used for components including the W steel beams, the stiffeners, and the end plates. The same properties as of A572 Grade 50 steel are assumed.

(5) "Plastic" material model and A36 steel is used for the cover plates. The yield strength and ultimate strengths are taken as 36 ksi and 58 ksi with R_y equal to 1.3 at the corresponding strains of 0.002 and 0.1, respectively. The Young's modulus is taken as 29000 ksi and the Poisson ratio as 0.3. The stress-strain curve is shown in Figure 5-2.

(6) "Plastic" material model and A500 Grade B steel is used for the rectangular steel tube. The yield strength and ultimate strengths are taken as 46 ksi and 58 ksi with R_y equal to 1.4 at the corresponding strains of 0.0022 and 0.1, respectively. The Young's modulus is taken as 29000 ksi and the Poisson ratio as 0.3. The true stress-strain curve is shown in Figure 5-3.

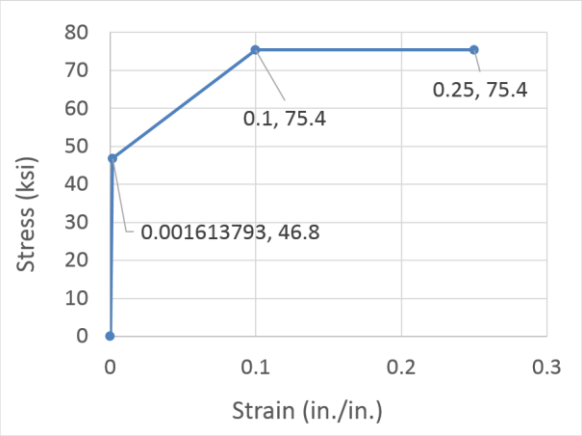

Figure 5-2: True stress-strain curve of A36 steel

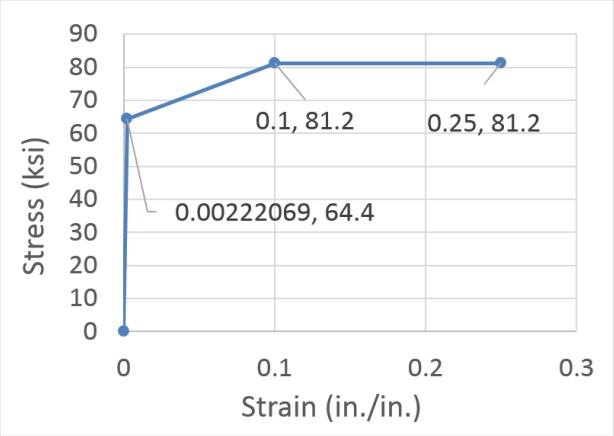

Figure 5-3: True stress-strain curve of A500 Grade B steel

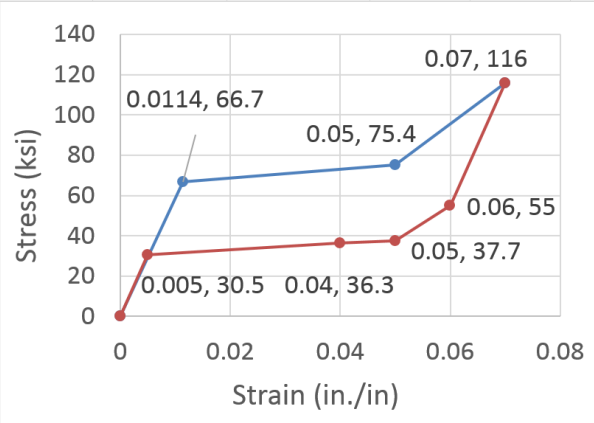

(a) Full evelope

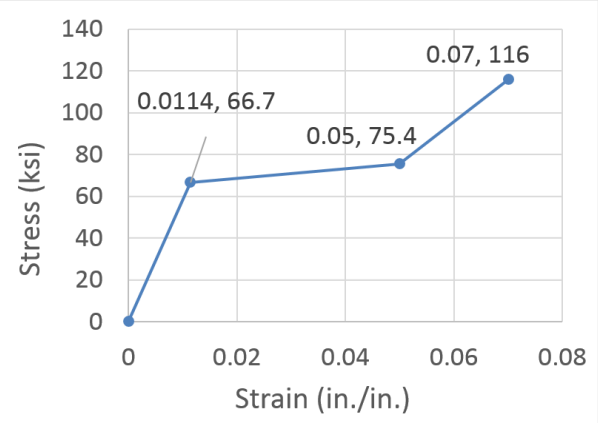

(b) Upper backbone curve

Figure 5-4: Experimental stress-strain curve of SMA

As metioned above, only the upper backbone curve is used in the analysis as shown in Figure 5-4(b). Because the "Plastic" material model is used, there will be large residual deformation generated in the SMA rods when the maximum strain reaches 5%, which is not true in reality. However, the aim of the FE analysis is to investigate the connection's failure modes under the ultimate beam strength. The SMA rods carry tension forces. For a static analysis under force control, the amount of residual strain in the SMA rods has insignificant influence on the states

of the model at a series of peak loadings in a loading history if the following loading magnitudes are not less than the previous maximum one. The loading case used in this chapter will be introduced later, which meets the requirement to use only upper backbone curve for the SMA rods in the analysis.

5.3.3: Model Element Types

The FE model is meshed into 190904 elements in total, involving four types of elements: (1) C3D8R, an 8-node linear brick solid element with reduced integration and hourglass control; (2) C3D4, a 4-node linear tetrahedron solid element; (3) S4R, a 4-node doubly curved thin or thick shell element with reduced integration, hourglass control, and finite membrane strains; and, (4) B31, a 2-node linear beam element in space. For the concrete core, both C3D8R and C3D4 elements are used. For the grout block, only C3D4 elements are used for meshing. Except for the eight rods and two beam-element based columns, all other remaining components are meshed using S4R shell elements.

All rods in the FE model are simulated using beam elements instead of 3D solid elements, and there are no interactions between the rods' longitudinal surfaces and the rods' through holes. The rods' ends and the corresponding nuts are fixed together (Figure 5-5), which will allow them to have the same deformation. The tension forces in the rods are transferred from the nuts to the end plates by defining normal interactions between the nuts and the end plates. The rods in the proposed connection are mainly subjected to tension forces and only small shear forces.

Most of the shear from the beams is assumed to be resisted by the friction between the end plates and the square steel tube walls. Therefore, the shear forces around the rods holes are relatively small and their influence on the connection behavior can be ignored. If this is the case, using beam element to simulate all rods and ignoring the rod-hole interactions is reasonable.

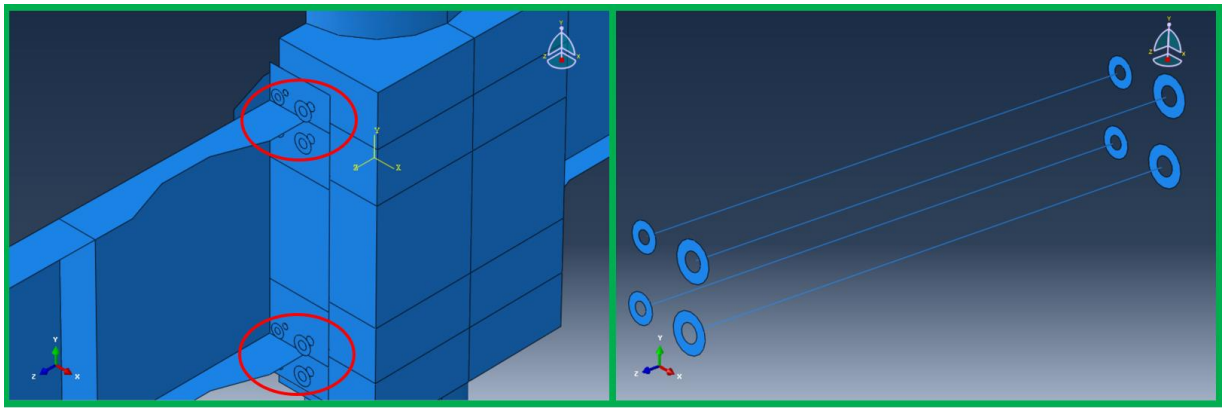

Figure 5-5: Beam-element based rods

5.3.4: Model Boundary Conditions

In order to avoid solution singularities and to ensure convergence, limits on the model's degrees of freedoms should be defined very carefully. The whole model can be divided into six groups:

(1) Concrete core group;

(2) Grout block group;

(3) Steel beam group;

(4) Beam-element based columns group;

(5) Tube skeleton group; and,

(6) Rods and nuts group.

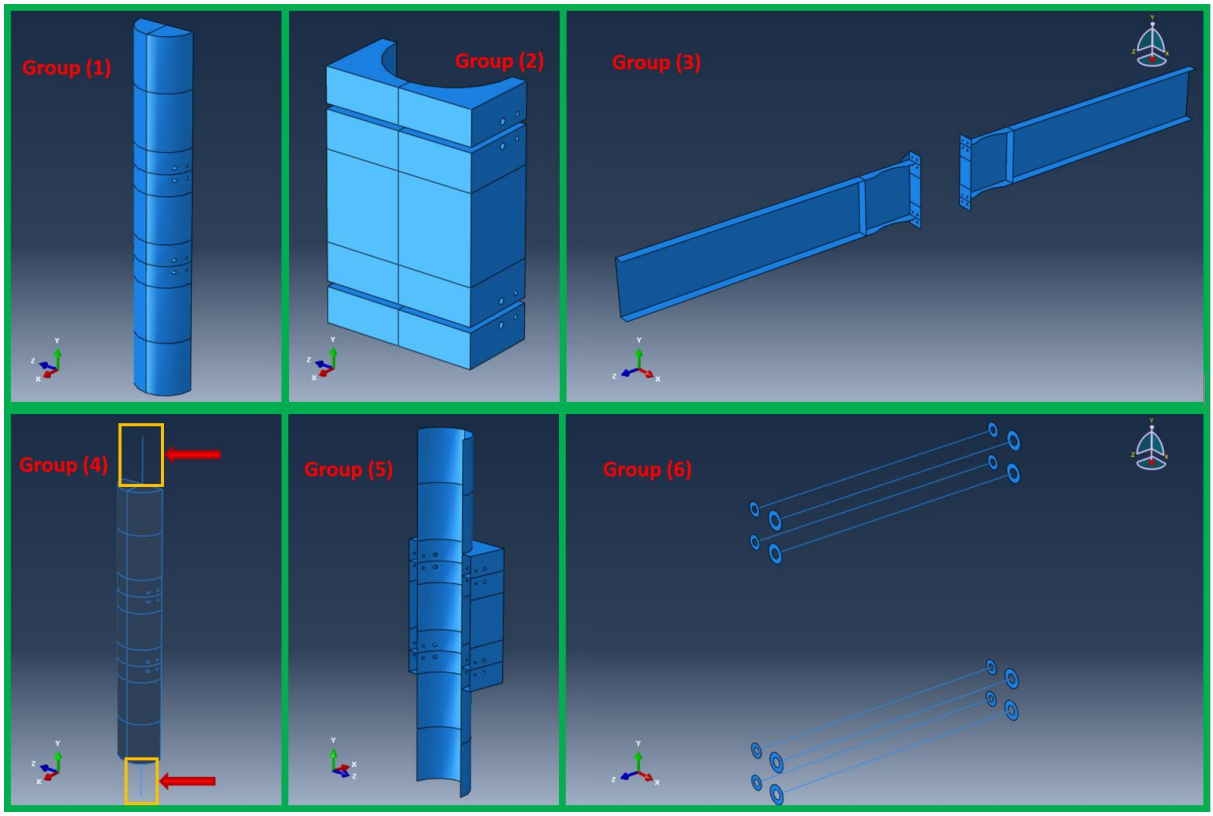

Figure 5-6: The six groups of the components of the FE model in ABAQUS

The six groups are shown in Figure 5-6. There is only one component in group (1) and group (2), respectively, the concrete core and the grout block. All eight rods and their corresponding nuts are considered as parts of group (6), and each nut and its corresponding rod end are melded into one unit by defining the interactions between them. Group (4) includes only two beam-element based columns. All the parts in groups (3) and (5) are connected into a single unit at their intersections, respectively, to simulate actual welds at these intersections. Group (3) includes two W steel beams with RBS, two end plates, two bracing stiffeners, and four stiffeners between beam flanges and end plates. Group (5) includes one circular steel tube, one

square steel tube, two inner diaphragms, and two cover plates.

The whole FE model is assembled together from these six groups. First, the outer curved surface of concrete core in group (1) and inner curved surface of circular steel tube in group (5) are tied together. Second, the grout block in group (2) is inserted into the cavity of the tube skeleton in group (5). The contact surfaces between the grout block and the circular steel tube or square steel tube are tied together, and the remaining contact surfaces between the grout block and the inner diaphragms or cover plates will interact to each other through normal contact interaction. Third, all six DOFs of the two ends of the beam-element based columns and all six DOFs of all nodes on the two corresponding CCFT column cross sections are tied together to make the CCFT column continuous. Fourth, normal contact interactions are defined between end plates in group (3) and square tube walls in group (5), and between nuts in group (6) and end plates in group (3).

In addition to the boundary conditions between each component of the FE model, the exterior boundary conditions between the FE model and the 'ground' are also very important. First, symmetric boundary conditions are defined at the symmetric surface of the FE model. This will allow the rotation of the beam to occur in the YZ plane and avoid twisting of the connection about its longitudinal axis. Secondly, a pinned support is defined at the bottom of the column, while a roller support is defined at the top end of the column (Figure 5-7). This is used to simulate two points of inflection of the columns in the adjacent stories, and to allow for the

vertical deformation in the columns during lateral loading. Thirdly, the vertical rigid body motions of the two end plates are eliminated by adding a limit on the vertical displacement onto the top or bottom edges of the end plates, depending on which edge the beam is to rotate under the prescribed loading case. Finally, the transverse displacement of all the ends of the rods should be limited and the longitudinal DOFs are released to simulate free elongation of the rods without any rigid body motions.

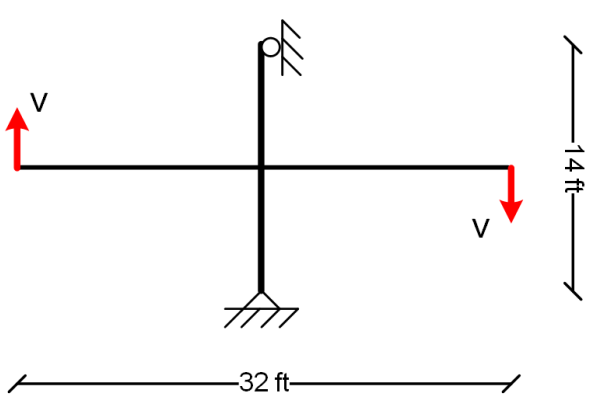

Figure 5-7: Simple structure for loading

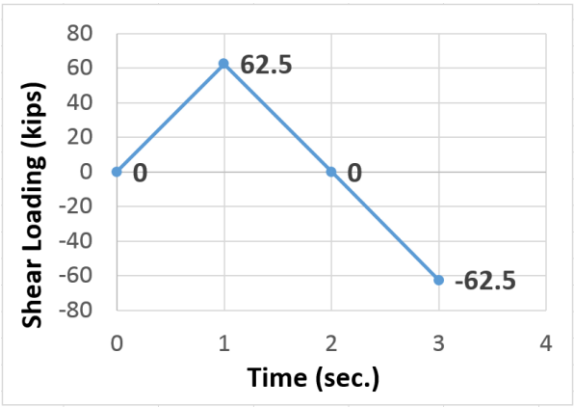

Figure 5-8: Loading history

5.3.5: Loading History

The analyses' aims are twofold. First, to detect possible failure modes of the proposed connection, especially cracking in the grout block and the concrete core, under cyclic ultimate loadings. Second, to find out whether or not the residual capacity of the proposed connection is sufficient to carry the same ultimate loading in the opposite direction after cracking has occurred in the grout block and the concrete core. A cyclic loading history with three half cycles is applied (Figure 5-8). The amplitude of the shear imposed corresponds to the ultimate shear

resistance when the RBS reaches its maximum moment capacity, including strain hardening and the material maximum strength.

5.4 Finite Element Analysis Results

Figure 5-9 shows Von-Mises stress state of the connection when it is subjected to the positive ultimate loading (time 1 in Figure 5-8) and the following reverse ultimate loading (time 3 in Figure 5-8). The results prove that this connection configuration is strong and ductile enough to ensure that the connecting RBSs reach their ultimate flexural strength in both directions under cyclic loading. Due to strain hardening effects in the steel, the plastic hinge depth in RBS section under reverse ultimate loading is less than the depth of the plastic hinge in the same RBS section under the positive ultimate loading.

In order to ensure the strength of the connection is sufficient it to transfer large compression forces from beam flange to the CCFT column, the bearing strength of the grout between circular and square steel tubes needs to be carefully checked. Figure 5-10 shows Von-Mises stress state of infill grout under the reverse ultimate loading. Stress distribution in grout presents obvious local effects at the two corners where the compression forces are introduced. Due to confining, effects, the average stress in compressive region reaches up to 8.0 ksi.

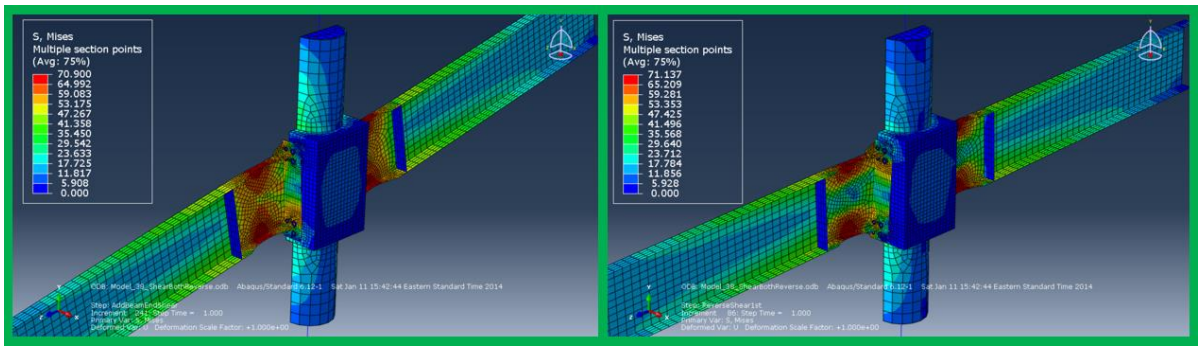

(a) Positive ultimate loading *(b) Following reverse ultimate loading*

Figure 5-9: Von-Mises stress under positive and following reverse ultimate loading

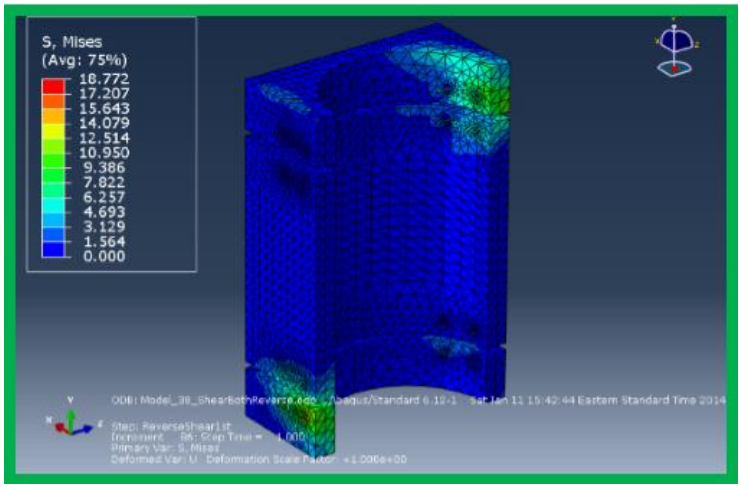

Figure 5-10: Von-Mises stress state of grout under reverse ultimate loading

The whole compressive crushing damage state is shown in the first plot in Figure 5-11. The other two plots in Figure 5-11 focus on two corners on one side of the grout. Due to the symmetry, the other two corners are not presented here. Because the CDP model for concrete in ABAQUS will accumulate all previous damage for the following analysis, the compressive damage state at the end of reverse ultimate loading includes the damage produced in the previous positive ultimate loading step.

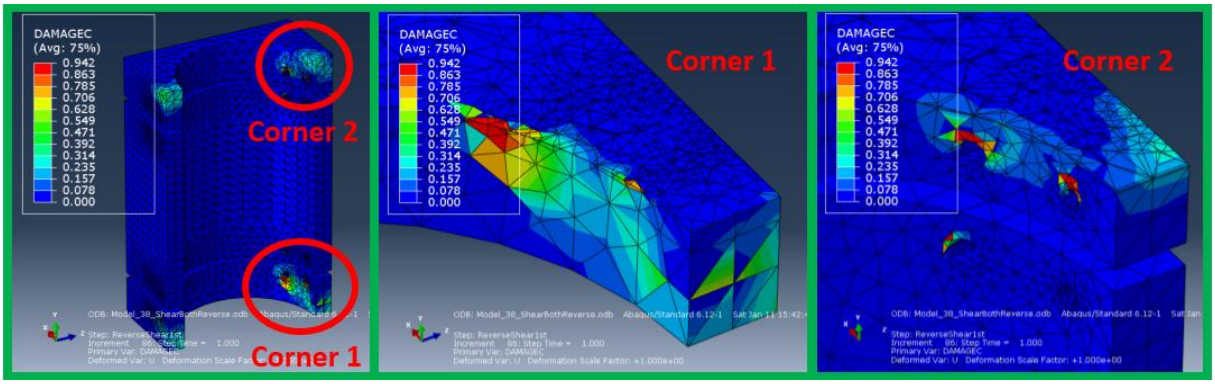

Figure 5-11: Compressive damage state of grout under reverse ultimate loading

The analysis results in Figure 5-11 shows that crushing damage due to large compression transferred in is very limited in both spatial distribution and damage severity. All damage is located in the regions where the forces transfer in directly. The overwhelming majority of damage variables are less than 60%; this means most of so-called damaged parts still keep at least 40% of their original undamaged capacity. The most damaged parts are the contact surface, which is a very thin layer, between the grout and the circular steel tube.

In addition to compressive damage, there are also numerous tensile cracks distributed in the grout. There are six plots in Figure 5-12 showing the tensile damage state under the positive ultimate loading. From the first plot we can see that there is a very severe separation between grout and CCFT column at the location of "Corner 1" because nearly all elements on this contact surface have a very high value of the tensile damage variable. The second and third plot on the first row present two cut views of "Corner 1" by a horizontal and a vertical plane, respectively. From these two plots, one can clearly observe that: (1) there is a crack generated along the rod hole's longitudinal direction and going through the whole depth of the rod hole

(actually there is another crack going through the whole depth of the other rod hole on the same level, which is not presented in these two plots); (2) there will be a cracking plane starting close to the outer surface and tending to propagate on each rod holes' level between two rod holes. From the first plot on the second row, we can see that around "Corner 1" there is also a severe separation between the grout and the outer square steel tube. However, around "Corner 2" where the compression is transferred directly into the grout, there is nearly no tensile cracking except at the bottom edge (see the last plot in Figure 5-12). Although the stress around "Corner 2" is very high, confinement from both circular and square tubes puts the grout around this corner in a tri-axial compressive state and effectively protects this region from tensile cracks. Generally speaking, instead of the corner where the compressive force transferring directly into, the corner of the grout on the opposite side of the CCFT column will have much more tensile damage with separation between grout and both circular and square steel tubes, and through cracks between rod holes on the same level.

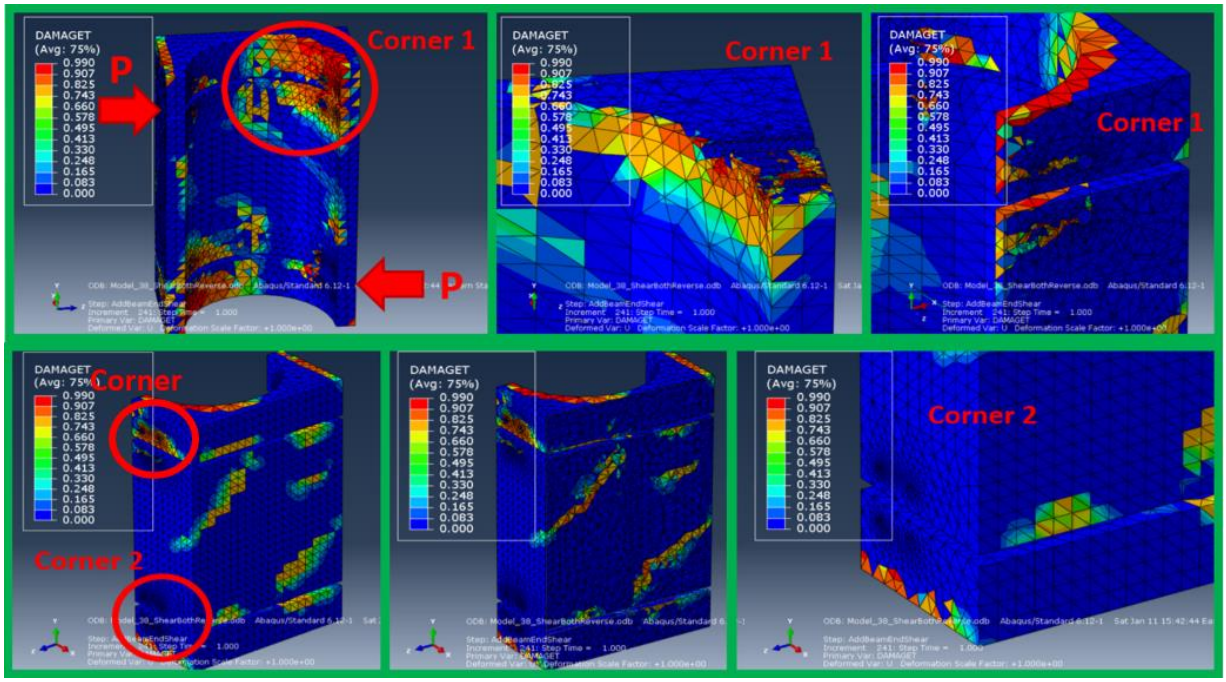

Figure 5-12: Tensile damage state of grout under positive ultimate loading

In addition, the second plot on the second row in Figure 5-12 presents two inclined cracks at about 45 degree from the horizontal plane. These two cracks are parallel to an imagined line connecting the two beam flanges in compression, and on the face of the grout which is orthogonal to the faces bearing great compressive forces. These two cracks are believed to be generated by shear yielding in the connection panel zone. A simplified shear yielding mechanism for the panel zone is proposed and presented in Figure 5-13. This model is composed of three parts: (1) two inner diaphragms; (2) two stiff grout blocks at left top and right bottom corners; (3) deformed grout block in the middle. When two large compressive loads are applied on the inner diaphragms, the same as in Figure 5-13, there is a small amount relative displacement generated between the two inner diaphragms. Because the square tube walls at the corners are much stiffer and can supply higher confinements on the grout blocks at

the corners, grout blocks at corners are stiffer and stronger than the one in the middle. Under the relative displacement loading, the grout blocks at the corners tend to have a rigid body motion, and the deformed grout block in the middle will try to deform to the shape shown by the red dashed line. However, because of the brittle characteristics of grout, tensile cracks will be expected between the red dashed lines and grout blocks at corners, and they will tend to propagate into the adjacent grout facets, as shown in the second plot in Figure 5-13. Additional cracks around the vertical red dashed lines may also be generated, as represented by the green lines in the simplified model. From this FE analysis results, we can see that there is only one small horizontal crack generated in the deformed grout block, which may be caused by the additional cracks and slippage between the grout and the inner diaphragms, which are very obvious in Figure 5-12 and Figure 5-13.

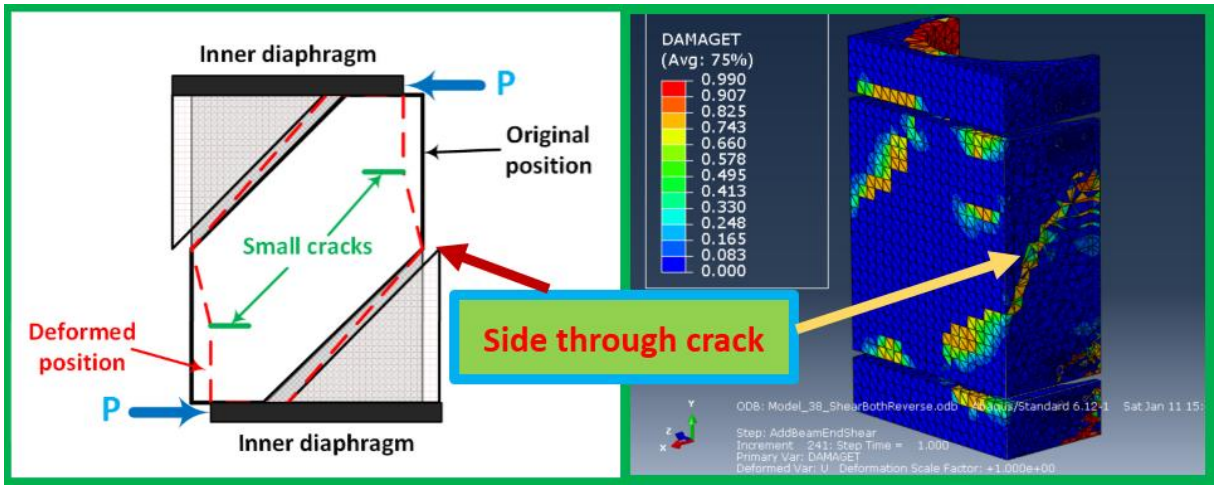

Figure 5-13: Shear yielding model for grout block in panel zone

Although a lot of tensile cracks have already been generated under the first positive ultimate

loading, the FE results prove that the strength of the grout with these cracks is still adequate to bear the following reverse ultimate loading. The RBS sections also reach their ultimate capacity as shown in Figure 5-9(b).

The tensile damage at the end of the reverse ultimate loading is shown in Figure 5-14, which also includes cracks from the previous load steps. The results from the first plot in Figure 5-14 show that at the end of the reverse ultimate loading, there is a nearly total separation between the inner surface of grout and the outer surface of CCFT column, most of elements on this surface show severe tensile damage. At the same time, as mentioned previously, the separation also occurs between the grout and the square tube wall on the opposite side of CCFT. And this time the separation between grout and square tube is much more severe. As one can expect, under the reverse ultimate loading, there are another two inclined cracks generating on the grout face which is not loaded directly (see second plot in Figure 5-14). These two inclined cracks are also caused by shear yielding of panel zone. These inclined cracks propagate into the side facet on which the compressive forces are directly loaded, and generate cracks going through the whole depth of the grout, which are shown in the third plot of Figure 5-14.

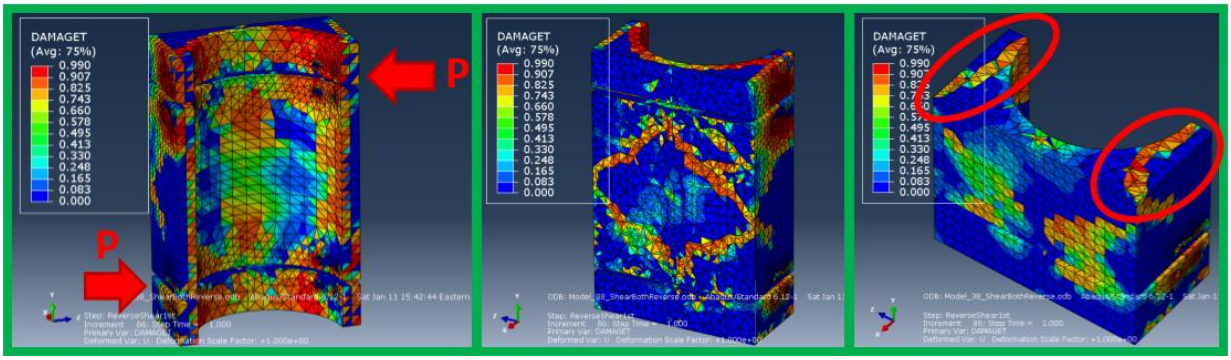

Figure 5-14: Tensile damage state of grout under following reverse ultimate loading

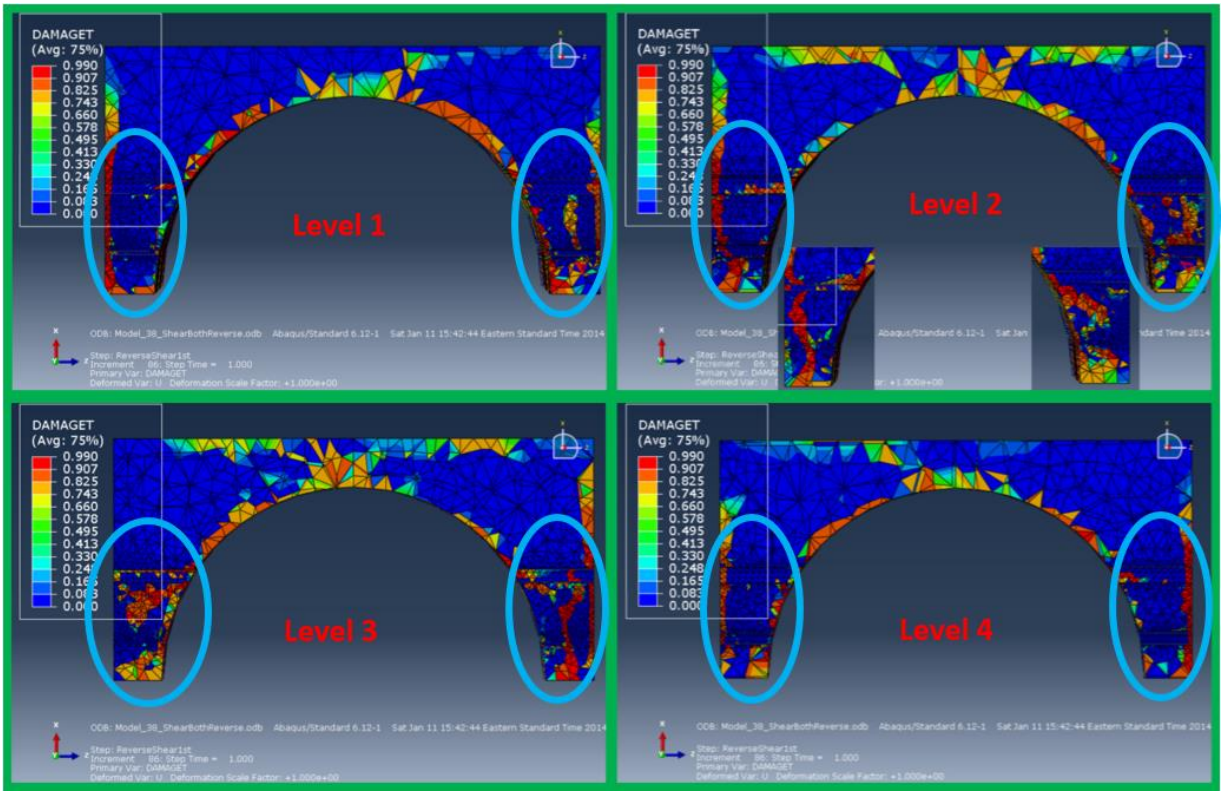

Figure 5-15: Tensile cracks around rods' hole region on each rods' level from top to bottom

In Figure 5-15, there are four horizontal cuts at the four different rod levels. The cutting sequence is from the top level to the bottom level. Cutting views labeled by 'Level 1' and 'Level 4' represent the two exterior rod levels; and the other two represent the two interior rod

levels. In the second plot, there are two additional smaller plots which are obtained from another two slightly different cutting planes. Based on the observation of these plots, we can easily find that there are more tensile cracks running through the whole depth of grout around the rods hole region on the interior rod levels. On the other hand, the tensile damage is concentrated only on the surface between the grout and two tubes on the exterior rod levels. The Von-Mises stress state shown by Figure 5-10 indicates that the stress around the exterior rods' hole region is much higher than for any other location, including the interior rods' hole. The high stress around exterior rods holes are believed to be caused by the higher confinement effects from tubes and inner diaphragms in this region, and this high confinement effects are enough to control the cracking propagation.

The overall mechanical behavior of CCFT column is also clear. The two plots in Figure 5-16 present Von-Mises stress and corresponding cracking states under ultimate positive ultimate loading and the following reverse ultimate loading, respectively. There are two main reasons to cause cracking in the concrete core of the CCFT column: flexural bending along column and shear yielding in the panel zone. First, flexural cracks due to CCFT bending starts when loadings on both sides reaches about 17.55% of ultimate capacity, and the shear cracking starts in panel zone when loading reaches 50% of the ultimate capacity.

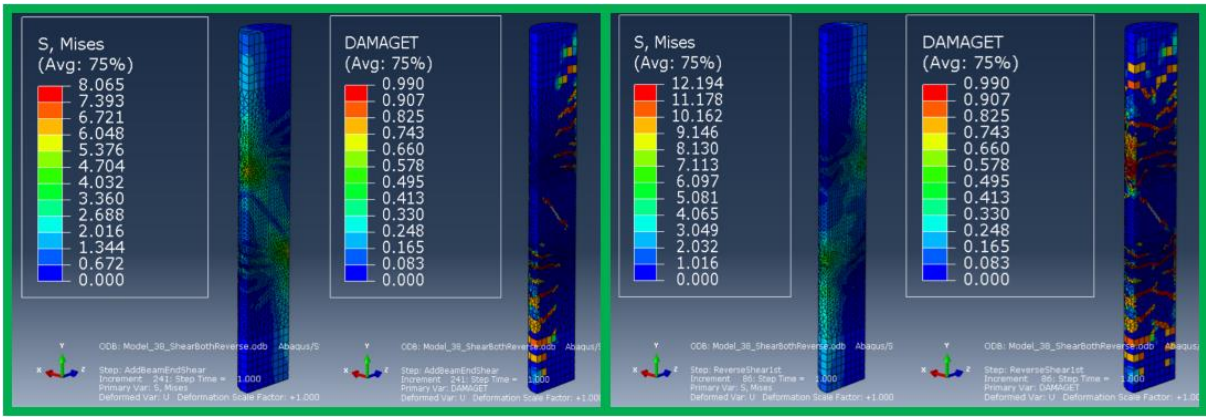

(a) Positive ultimate loading ***(b) Following reverse ultimate loading***

Figure 5-16: Von-Mises stress & Cracking under ultimate positive and following reverse loading

When the connection is under positive ultimate loading, the flexural cracks are only generated in the tensile region of CCFT column; when the loading direction reverses, cracks on the whole cross sections are generated. However, this is not the case for the shear cracks. There is only one shear crack in panel zone under the positive ultimate loading; after that, although loading direction is reversed, there are no more shear cracks generated in the panel zone. This means the direction of shear crack depends on the direction of loading, which reaches the minimum value to cause the shear crack at the first peak.

From the stress state under the positive ultimate loading case in Figure 5-16(a), two compressive concrete struts between the two regions in high compression can be observed easily. The long and narrow region with low stress separating the two struts represents the shear crack. When the loading reverses, the existing shear crack in the panel zone closes under compressive stress, and only one concrete compressive strut is generated passing through the

existing shear crack. The CDP model used assumes that the compressive damage will have full reduction effects on tensile strength, but compressive strength can totally recover from tensile damage. This is why the concrete strut can pass through the existing crack and transfer the compression.

Figure 5-17 shows the compressive damage state at the end of the reverse ultimate loading. These plots indicate that there is nearly no crushing damage in the concrete core of the CCFT column except in a very limited region around one rod hole. This means that when compressive strength is needed, the concrete core can totally recover and behave like an undamaged component, although there are lots of tensile cracks due to flexural bending of the CCFT column.

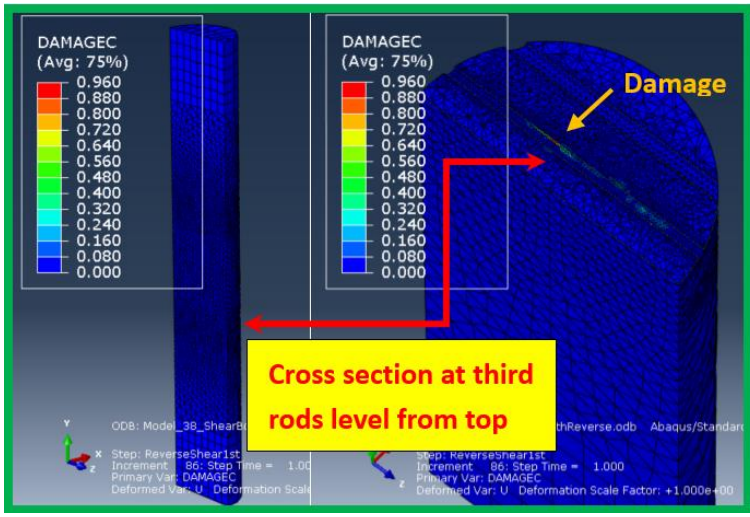

Figure 5-17: Compressive damage state at the end of reverse ultimate loading

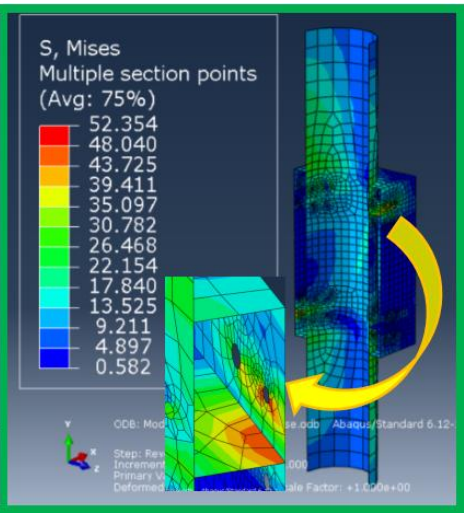

Figure 5-18: Von-Mises stress of steel skeleton

The confinement from the steel skeleton, which is composed of the circular steel tube, the

square steel tube, inner diaphragms, and cover plates (see Figure 5-18), is the key factor to ensure that the concrete core and grout can supply adequate strength. Their behavior during the whole cyclic loading history is very important. From the analysis results, the maximum stress occurs around the rods holes on the square tube wall and the inner diaphragm close to the application point of the compression, but this stress is less than the yield strength of 55 ksi. On the other hand, the whole steel skeleton will stay in the elastic state during the whole loading history.

Based on the discussion above, the proposed connection configuration is robust enough to supply the required capacity. Although numerous tensile cracks are generated during the loading history, these cracks can close again under reversed loading and supply the same compressive strength as the undamaged material. Due to the existence of confinement from the steel skeleton, the surrounded concrete and grout can avoid brittle failure, and maintain their high compressive strength. And as a partially restrained connection, the deformation is also a concern factor for the designer. In this analysis example, the maximum separation distance between the end plate and the square tube wall is 2.4'' (see Figure 5-19), and corresponding rotation capacity supplied by the end plate is about 7%. This means the proposed connection has very large rotation capacity.

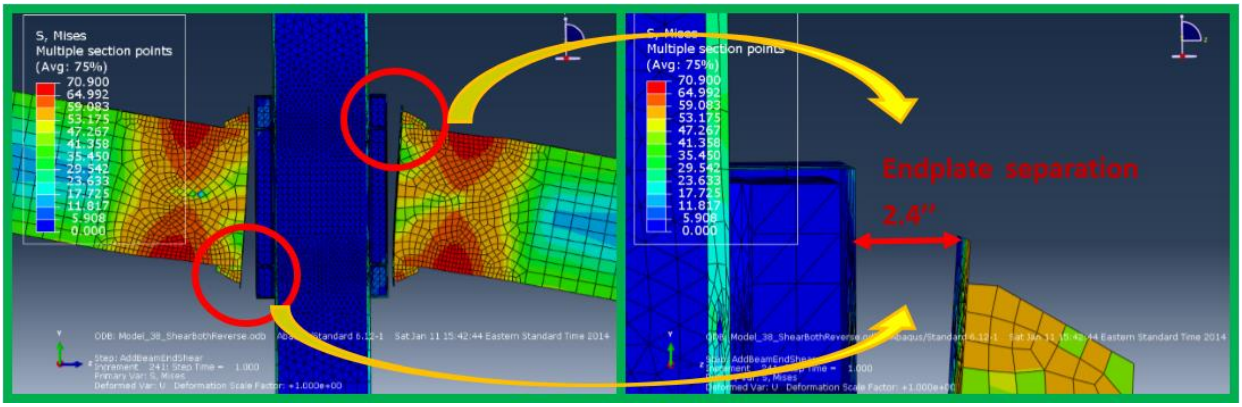

Figure 5-19: Sketch of end plate rotation under positive ultimate loading

5.5 Summary and Conclusions

In this chapter, FE analyses were performed to investigate potential failure modes for the proposed connection. The results were used to verify the effectiveness of the assumptions for both preliminary design procedure and 2D-SSM. These assumptions include: (1) strong panel zone without shear yielding; (2) adequate bearing capacity of expansive grout between circular and rectangular steel tubes; (3) large stiffness of the column collar to avoid end plate inward displacement under beam ultimate strength; and (4) rigid body rotation of each end plate about one yielding line around beam flange in compression.

The FE model was designed based on the proposed preliminary design procedure (see Table 5-1). Among the features of this model are:

- A Concrete Damaged Plasticity (CDP) model was used for both the concrete core in the CCFT column and the expansive grout between the two tubes (see Section 5.2 and

Appendix J).

- Beam elements, instead of solid elements, were used to simulate through rods to reduce the computational cost (see Figure 5-5).
- Only the upper backbone cure of SMA stress-strain relationship was defined (see Figure 5-4). This is reasonable if only the ultimate states were investigated with no need to consider residual deformation in the SMA rods.

By checking the damage states of the concrete core and the infill grout, the deformations of the end plates and the rectangular tube wall, the results prove the validity of the assumptions mentioned above. Several conclusions are obtained as follows:

- Panel zone of the NPSC is strong enough to transfer ultimate strength from beams to column (see Figure 5-9).
- Only minor and moderate damage in concrete core and expansive grout were generated under ultimate beam strength:
    - For the concrete core, there were shear cracks in the PZ and several flexural cracks along the column (see Figure 5-16).
    - For the infill grout, there are four obvious inclined cracks at 45 degree angle showing on the two faces without connecting beams due to shear in PZ, and several cracks generated around the rods holes (see Section 5.4, Figure 5-14 and Figure 5-15).
    - The adhesion between the infill grout and the outer circular tube wall is totally

lost (see Figure 5-14).

- Confinement effects from the steel tubes will increase concrete ultimate strength greatly (see Figure 5-10).
- The inward deformation of the rectangular tube wall is very small (see Figure 5-19).

Chapter 6

Design of the Composite Special Moment Frames

In this chapter, the structural design for a library located in a high seismic zone but without near-fault effects is described. The library has five stories above grade and a one story basement. Composite special moment frames (CSMFs) and special concentrically braced frames (SCBFs) are combined as the main lateral force resistance systems in the two orthogonal directions, and a separate gravity system is used to provide the vertical load-carrying capacity (Figure 6-1). CCFT columns and W steel beams with RBSs are used in the CSMFs, while only W steel members are used for both beams and columns in the SCBFs and the gravity system. The elevations of the two lateral resistance systems employed, which are highlighted by two dashed red blocks in Figure 6-1, are shown in Figure 6-2. In this research, only 2D structural analyses on the CSMFs will be carried out as described in the following chapters, so detailed designs of the SCBFs and gravity system will not be included.

There are two CSMFs that will be designed in this Chapter. The first is a "conventional" composite special moment frame (CSMF) with fully restrained beam column moment connections; the second adopts the new proposed self-centering partially restrained moment joints to connect beams and columns. The "conventional" CSMF should not be constructed as a realistic design alternative to the CSMF. Rather this frame is used as a "target" frame. In this context, "target" means a frame which will have the best possible behavior and which the self-

centering CSMF should mimic. Because the two CSMF models used for the comparisons only consider failure due to accumulation of plastic strain and do not consider any failure modes associated with weld defects, local buckling, and similar, they are considered to provide "ideal" or "target" behavior. The intent here is to compare only connection behavior while keeping the rest of the structures similar. Section 6.1 provides general information and the layout of the building. Section 6.2 presents the design results of the two CSMFs and gives a brief comparison of the two systems. Section 6.3 makes a summary of the whole chapter. The structural designs in this chapter are only based on strength; serviceability will be not considered in design. SAP2000 is used for the preliminary design. The detailed design calculations are presented in Appendix K.

6.1 General Information of the Composite Structures

A public library with five stories above the grade and one story basement is to be constructed in a high seismic zone. The soil has been classified as Site Class D. The plan dimensions of the building are approximately 120 ft. in the N-S direction, and 160 ft. in the E-W direction. The structural system is intended to work within a grid spacing of 32 ft. by 24 ft. Story height is 14 ft. According to ASCE 7, a risk category II should be used for design of a library.

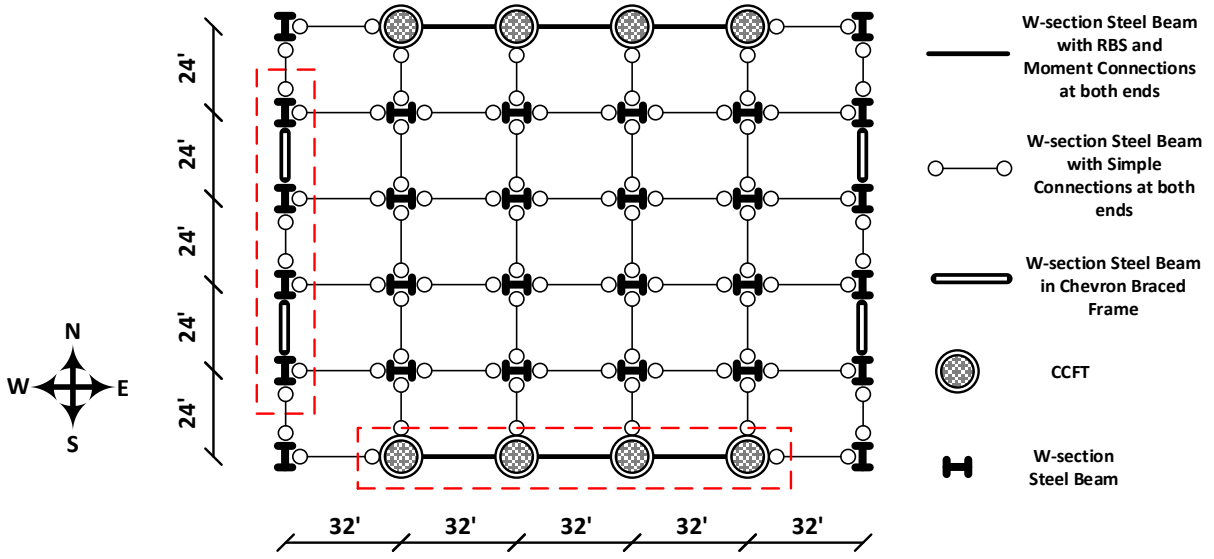

Figure 6-1: The plan layout of the library

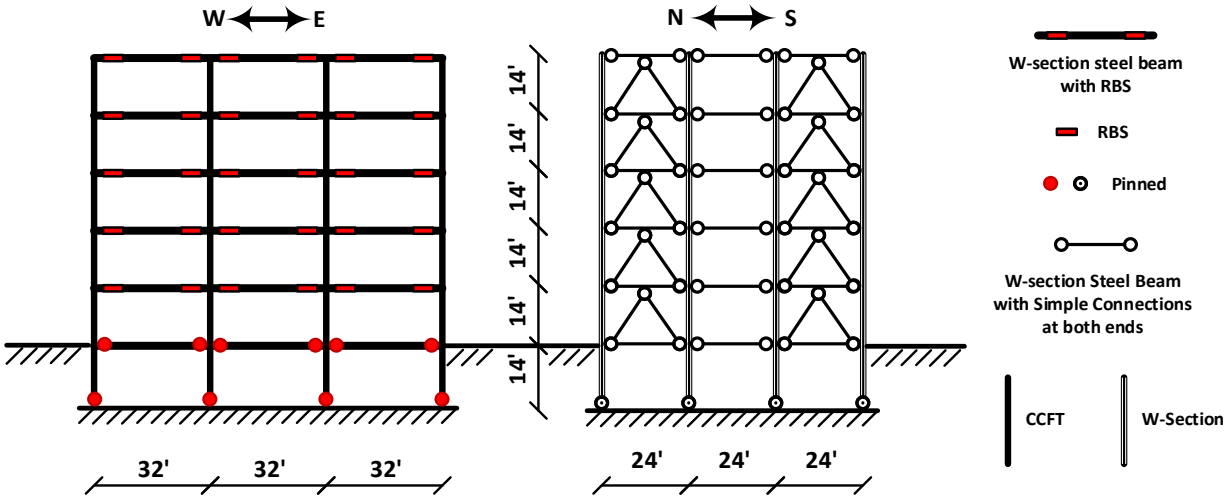

Figure 6-2: Elevations of CSMFs in W-E and CSBFs in N-S

As the plan layout shows, two 3-bay composite special moment frames are employed to resist lateral forces in the W-E direction. For each CSMF, the span is 32 ft. with three intermediate beams at 8 ft.; the story height is 14 ft. According to the architecture requirements, about 40 percent of floor area is designed for book storage, 40 percent for reading rooms, 18 percent for

offices and 2 percent for openings for elevators and stairs on each main level. Most of offices are located along the building perimeter.

The library will use a composite slab as its floor. Because book storage will contribute considerably to the building seismic weight, in order to reduce its equivalent lateral load demand, lightweight concrete is employed. According to VULCRAFT Manual 2010 [99], a 3VLI19 steel deck with a lightweight concrete with total thickness of 5.5 inches is able to supply sufficient strength and stiffness capacity at a beam spacing of 8 ft. The uniform dead load for the slab is 41.5 psf. The self-weight of structural members, such as beams and columns, is estimated at 12 psf. A total value of 20 psf is assumed for superimposed dead load, including 15 psf for ceiling and mechanical pipelines, 2.5 psf for floor finishes, and 2.5 psf for others. The building façade is designed to use normal weight precast concrete panel, whose self-weight is about 40 psf. The openings on the façade occupy about 35% of the whole area and are filled of windows with self-weight of 12 psf. The total height of façade is above 4 ft. of the roof level for a parapet. In addition, anchor system for book shelves is necessary for libraries. A steel rack system, which is anchored onto the slab, is installed where book are stored. Its weight is approximated at 20 psf. Total dead loads for mass calculation are about 92.6 psf and 83.2 psf on gross area of the main floors and the roof, respectively.

Live loads are different for design based on the room or area functions. According to ASCE7-10 [78], the value of 150 psf is used for stack rooms, 60 psf for reading rooms, and 50 psf for

offices. On the roof level, the live load is assumed to be 20 psf. Live load from partition allowance in offices area is assumed to be 15 psf for vertical loading, but only two thirds are used to calculate seismic force. Total live load for mass calculation is about 25.8 psf based on gross area on the main floors. The detailed calculation is supplied in Appendix K.

6.2 Design Results and Comparisons

In Appendix K, detailed design calculations for the CSMFs in the W-E direction are provided based on the building dimensions and loadings introduced in Section 6.1. There are two CSMFs being designed in total. One is a "conventional" CSMF with traditional FR moment connections, and the other is a self-centering CSMF with new proposed PR moment connections. In this section, design results of the two CSMFs are presented and compared.

The equivalent lateral force (ELF) method, which includes both strength and a drift check, is employed as the preliminary design method. According to ASCE7-10, the "conventional" moment frame is classified as a 'Steel and Concrete Composite Special Moment Frames'. The corresponding seismic coefficients of this category are used in design, including the response modification coefficient, $R = 8$, the overstrength factor, $\Omega_0 = 3$, and the deflection amplification factor, $C_d = 5.5$. Although the self-centering system with PR connections can be regarded as a new proposed structural system, the same values as the "conventional" CSMF are used as the trial values of the seismic coefficients ($R = 8$, $\Omega_0 = 3$, and $C_d = 5.5$) for its

design. The validation of these trial values will be checked by using the Dynamic Incremental Analysis (IDA) method in Chapter 8. If they do not pass the criteria indicated in FEMA-P695 [11], new values will be proposed and checked.

In order to calculate the base shears for use in the ELF design of the two systems for strength design, the fundamental period, T should be determined by equation (Eq. 6-1). The fundamental period only depends on the building dimensions and the structural system type, so (Eq. 6-1) will give the same T for the two CSMFs. This will generate the same ELFs for the strength design.

$$T = C_u \cdot T_a = C_u \cdot C_t \cdot h_n^x \geq 0.25 \qquad \textbf{(Eq. 6-1)}$$

ASCE7 allows to use the actual period of the system first mode, T_0, instead of fundamental period, T, to calculate a new set of ELFs for the drift check. Usually the period obtained from a modal analysis is greater than the period from (Eq. 6-1) ($T_0 > T$). This will generate a lower lateral force demand on the system for checking drift. Member sizes for the moment frames, generally speaking, are controlled by stiffness rather than strength. . A better estimate of T_0 can be obtained from a more detailed FE model. In this research, SAP2000 is used to calculate T_0 for both CSMFs. The model of the self-centering system can be obtained by changing the FR moment connections of traditional CSMF into PR moment connections. This change will cause some reduction of system stiffness and yield a slightly larger T_0.

6.2.1: Calculate ELFs for Strength Design

In order to use ELF method to design the lateral force resisting system, the fundamental period, T, should be calculated first by using (Eq. 6-1). The corresponding parameters of structure type of 'Steel moment-resisting frames' in Table 12.8-2 in ASCE7-10 are employed. These indicate that $C_t = 0.028$ and $x = 0.8$ resulting in a T_0 of 1.173 seconds. No composite effects from either the composite deck or columns are considered in these coefficients. Only bare steel beams are used in the analysis. If parameters for the structure type given as 'All other structural systems' are used ($C_t = 0.02$ and $x = 0.75$), it will yield a fundamental period T_0 of 0.678 seconds. This will result in a 'too stiff' structure for a five-story special moment frame with bare steel beams. Therefore the parameters for the structure type 'Steel moment-resisting frames' will be used, generating a reasonable value of 1.173 seconds for T_0.

6.2.2: CSMF Models in SAP2000

In this subsection, a detailed description of the two CSMF models is provided. The trial member sizes for the two CSMFs are determined based on the same simplified design model. Simplified indicates that some design details are not modelled in the initial design phase, including the panel zone sizes and locations of either beam or column plastic hinges. Also, the slight stiffness reduction of the self-centering system from the PR connections is ignored in the simplified design. In addition, although the RBSs are used on both CSMFs, the stiffness reduction from RBSs is not considered in the analysis. As discussed in Chapter 4, the effects

from stiffness reduction of RBSs on special moment frames are not of significance. Once the trial member sizes pass all the strength and deflection criteria, more accurate finite element models will be established and checked for the two frames. The preliminary design will be completed based on the new more accurate models and the deflection criteria in ASCE7-10.

The simplified model used to determine the trial member sizes for both two CSMFs is shown in Figure 6-3. The following assumptions are made:

- The shear capacity of panel zone of the CCFT column is strong enough to avoid panel zone yielding.
- An equivalent round steel section is calculated to replace CCFT composite section.
- The panel zone size is not considered to reduce the clear length of beams and columns.
- Zero length plastic hinges for both beams and columns are defined at the member ends.
- A beam section without RBS is used.
- Rigid elements are used for all members of the leaning column system.
- No rigid diaphragm constraints are used, it will be explained later.

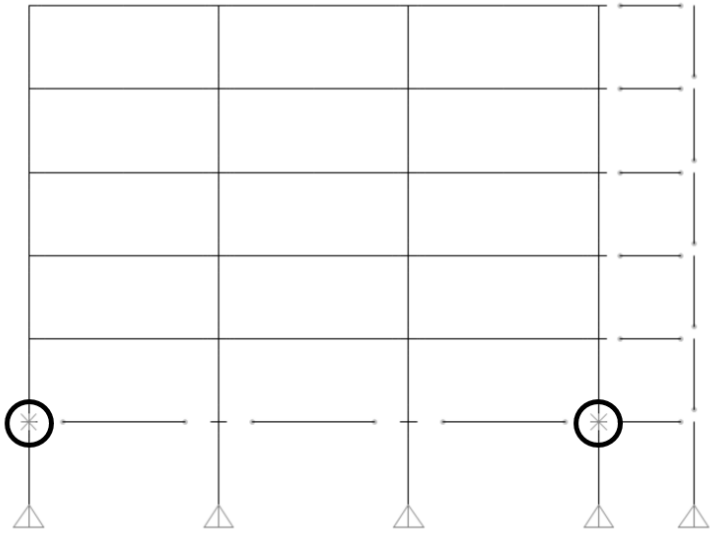

Figure 6-3: The schetch of the computational model in SAP2000

As described previously, there is a one story basement in the building. The lateral resistance from the soil will be considered by adding two horizontal supports on the exterior columns at the ground level, as indicated in Figure 6-3 by two black circles. Due to the existence of the horizontal supports, most of base shear will not be transferred into the four columns at the ground level. Thus it is reasonable to use pinned connections for the beam ends at the ground level, and pinned connections for the columns at their base.

Load combinations from (Eq. 6-2) to (Eq. 6-6) are considered in the preliminary design [78]. The contribution of second order effects from the gravity system is considered by applying equivalent vertical forces on the attaching leaning column system.

(1) $1.4D$ ***(Eq. 6-2)***

(2) $1.2D+1.6L+0.5L_r$ ***(Eq. 6-3)***

(3) $1.2D+1.6L_r+L$ ***(Eq. 6-4)***

(4) $(1.2+0.2S_{DS})D+(\rho \; or \; \Omega_0)Q_E+L$ ***(Eq. 6-5)***

(5) $(0.9-0.2S_{DS})D+(\rho \; or \; \Omega_0)Q_E$ ***(Eq. 6-6)***

In order to minimize the lateral stiffness contribution from the leaning column system, zero lateral stiffness for all modes is obtained by releasing moment at one end of leaning columns on each story. These moment releases are presented by the small gaps on the leaning columns in Figure 6-3. The link elements between leaning columns and the CSMF are supposed to transfer only axial force, so rigid truss elements are assigned to them. The gravity loading on the moment frame is assigned based on the distributed area, and the rest of the half building is assigned to the leaning columns.

Based on the simplified model and load combinations mentioned above, trial member sizes obtained are obtained and listed in Table 6-1. The corresponding first mode period is 1.672 seconds. The column size label CCFT 24*1.375 means that the columns section is a CCFT section, the outer diameter is 24 inch and the steel tube wall thickness is 1.375 inch.

Table 6-1: Preliminary Structural Member Sizes of the Traditional CSMF

Story	Member Name		Beam RBS Parameters (in.)		
	Column	Beam	a	b	c
Basement	CCFT 24*1.375	W30*116	Na	Na	Na
1	CCFT 24*1.375	W33*130	5.75	22	2.875
2	CCFT 24*1.375	W33*130	5.75	22	2.875
3	CCFT 24*1.375	W30*124	5.25	20	2.1
4	CCFT 24*1.375	W30*116	5.25	20	2
5	CCFT 24*1.375	W21*57	3.5	14	1.2

Once the trial member sizes are obtained, more accurate models were developed to establish a more complete CSMF. As compared to the simplified models, these include:

- Concentrated plastic hinges for both beams and columns with zero hinge length.
- Beam plastic hinges located at the centerline of the RBSs.
- Column plastic hinges located at the mid height of the total hinge length.
- A uniform reduced section with minimum area of the corresponding RBS is used for a length of one half of total RBS length, and the other half length of RBS is assigned for a whole beam section. The centerline of the reduced section is identical to the original centerline of the RBS (Figure 6-4).

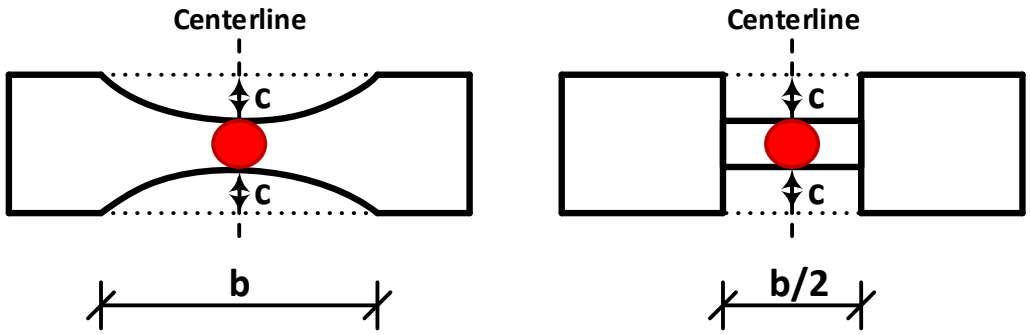

(a) Radius Cut RBS *(b) Simplified RBS*

Figure 6-4: The simplified model for a RBS with plastic hinge location

- Rigid bars are used in panel zone to connect the center of panel zone to the adjacent beams and columns.
- For the self-centering system with PR connections, special construction methods are needed to allow the adjacent columns separation caused by the separation of the end plate of the PR connection from the column surface during its rotation under large beam end moments (Figure 6-5). For this case, rigid diaphragm constraints on each story should not be used in then analysis. The use of rigid diaphragm constraints will reduce the self-centering capacity and influence the axial forces in beams, as will be discussed in the following chapters. The differences from the modal analyses between models with and without rigid diaphragm constraints will be discussed later in this chapter.

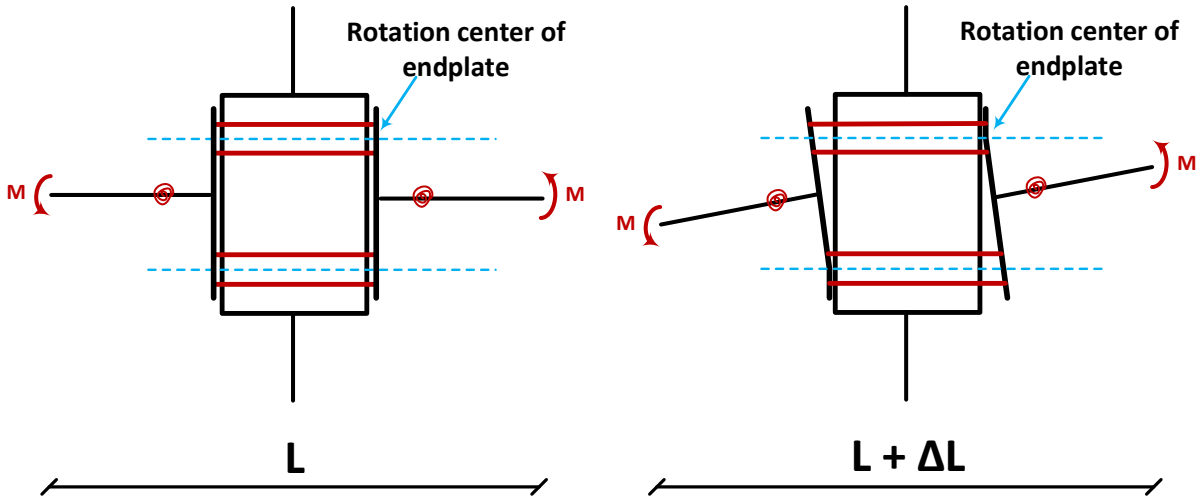

(a) Undeformed *(b) Deformed*

Figure 6-5: Schetch of PR connection expansion under beam ends moments

- In order to compare with the self-centering CSMF with PR connections, rigid diaphragm constraints will not be set for the "conventional" CSMF either.
- A distributed leaning column system is employed to be compatible with the assumption of removing rigid diaphragm constraints for both CSMFs (Figure 6-6). This allows second order effects from the gravity system to be introduced into the lateral resistance system uniformly, and not concentrated on one particular column due to rigid diaphragm constraints. The distributed leaning column system is composed of the same number of column lines as the CSMF. Equal displacement constraint in horizontal direction between each connection and its corresponding location on the leaning columns is used to connect the CSMF and its leaning columns as a single system.

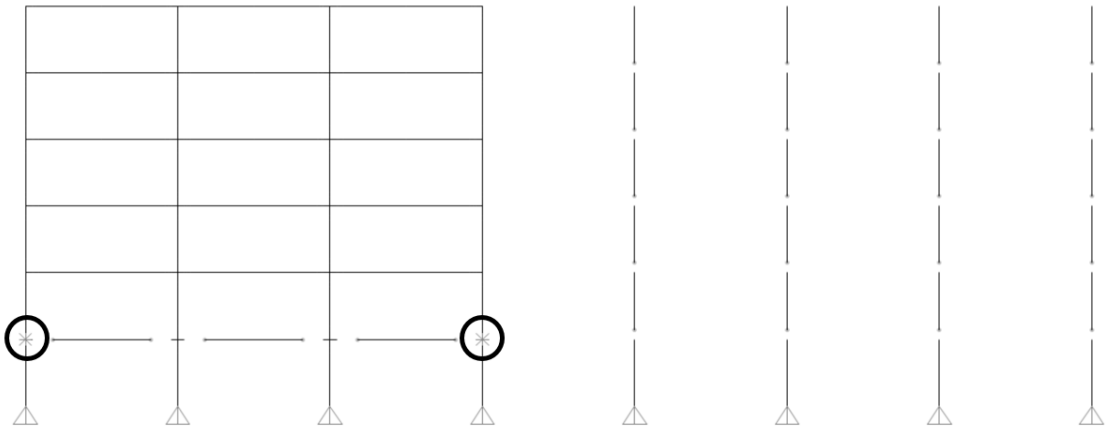

Figure 6-6: The schetch of the computational model of the traditional CSMF in SAP2000 with FR connections

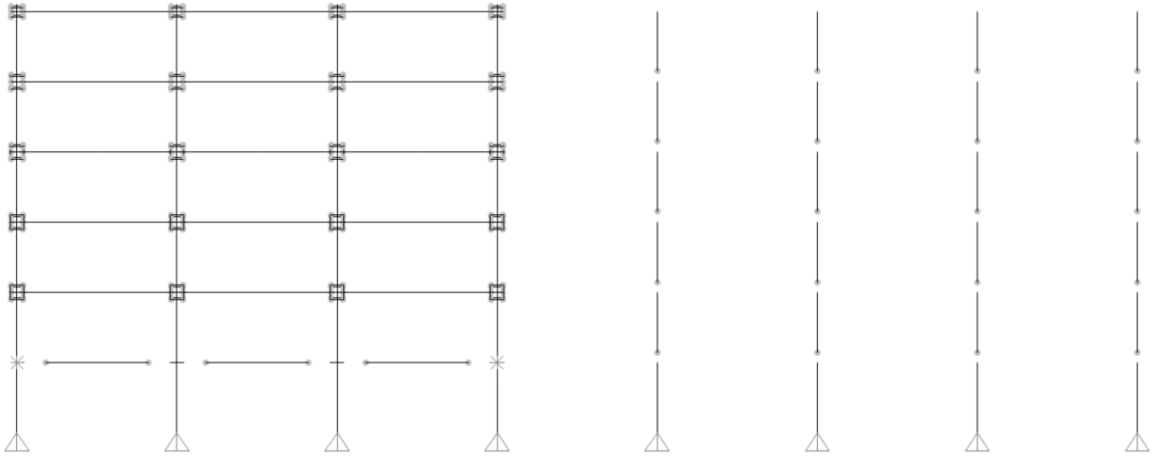

Figure 6-7: The schetch of the computational model of the self-centering CSMF in SAP2000 with PR connections

The only difference between the traditional CSMF and the self-centering CSMF is the connection type. If the 2D simplified spring model of the PR connection described in Chapter 4 is applied to replace each FR connection, then the self-centering CSMF is obtained as shown in Figure 6-7. The two model sketches above do not show the beam column plastic hinges, a detailed sketch of their locations is supplied in Figure 6-8. The blue dashed lines in the left plot present the locations of the plastic hinges. The shadow regions on the CCFT column indicate

the yielding plastic zone, with their height is determined as per Section 6.2.3. In the right plot, the four red springs stand for plastic hinges; the dashed rectangular panel stands for the region of the connection panel zone; and the bold black cross stands for rigid elements which connect beams and columns at the locations of the plastic hinges. Although the real sections should be used for the parts out of panel zone region, because the four segments between the plastic hinges and the panel zone region are very short compared with the structural dimension, it is believed that this simplification will have insignificant effect on structural behavior.

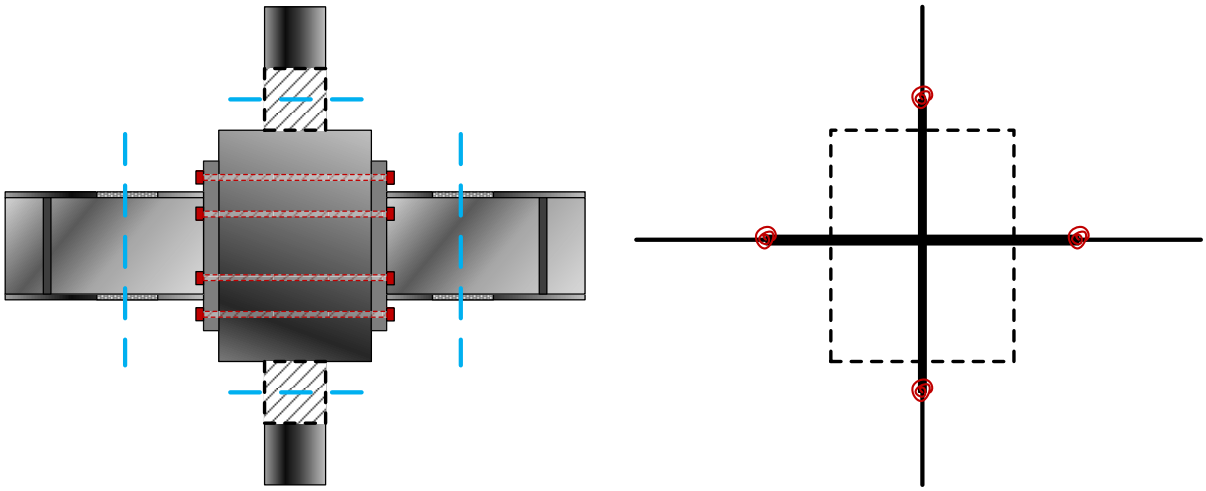

Figure 6-8: The schetch of the connection panel zone and the beam column plastic hinge locations

As mentioned above, the panel zone size should be assessed and more carefully modeled if necessary. From Table 6-1, one can see that these member sizes are identical to the member sizes of the design example of the new proposed connections in Chapter 3. Therefore the heights and widths of the panel zones of the PR connections can be determined based on the

design results in Table 3-3. The height of panel zone is assumed to be equal to the depth of corresponding beam plus 13.5 inches, and the width is calculated as the sum of the widths of the outer rectangular steel tube and the double thickness of the corresponding end plate of the PR connection. According to the results in Table 3-3, the thickness of end plates is similar within a range from 1.125 to 1.25 inch. For convenience, the value of 1.125 is used as the end plat thickness to calculate the panel zone width for all locations. In order to minimize differences between the "conventional" and self-centering CSMFs, the panel zone dimensions are assumed to be the same for both systems.

6.2.3: Plastic Hinge Length of CCFT Section

In this section, a simple cantilever column is analyzed under a given displacement as presented in Figure 6-9. The bottom end is fixed on the ground and the top end is free. The cross section of the column is a CCFT. The outer diameter is 24 in. and the steel tube wall thickness is 1.375 in. The total length of the column is 7 ft., which is half of the story height. The same materials properties are used as those in Chapter 4.

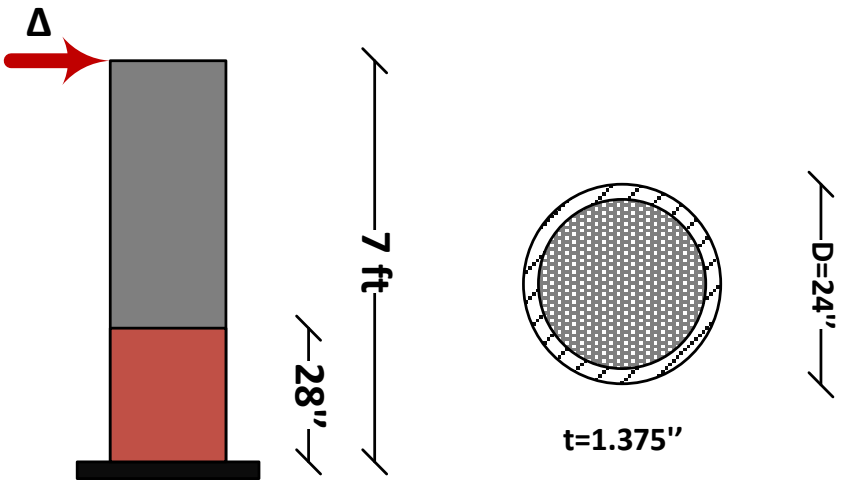

Figure 6-9: Cantilever column structure

There are four loading cases analyzed with the corresponding drift ratio of the cantilever column equal to 1%, 1.5%, 2%, and 6%, respectively. The structure is modeled in OpenSees and fibers are used along the whole column length. There are ten integration points in total including two at both ends. These integration points divide the whole column length into nine segments with an equal length of 9.33 in. There are four plots generated for each loading case. The horizontal coordinate of each plot stands for the curvature under the specific loading case and the vertical coordinate represents the given number for an integration point. The sequence of the ten integration points starts from 0 at the bottom end to 9 at the top end. These results of curvature at each integration point are shown in Figure 6-10.

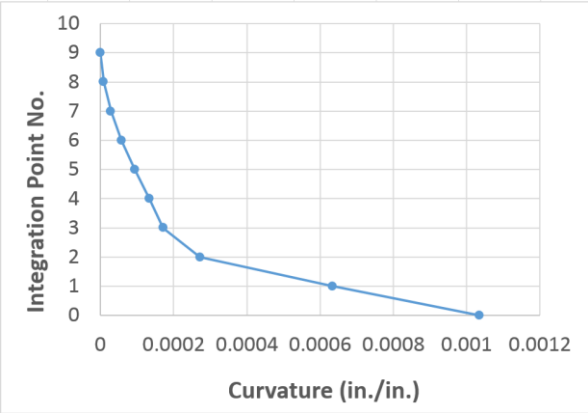

(a) Drift ratio of 1%

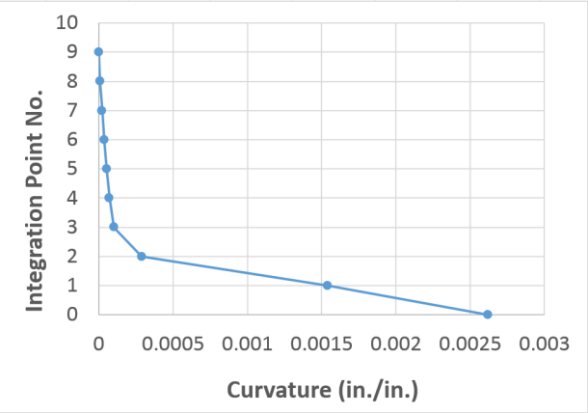

(b) Drift ratio of 1.5%

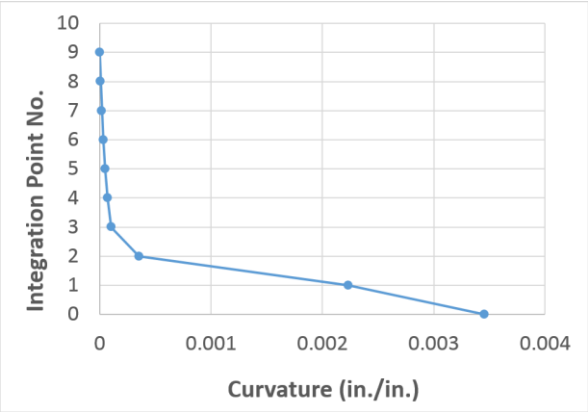

(c) Drift ratio of 2%

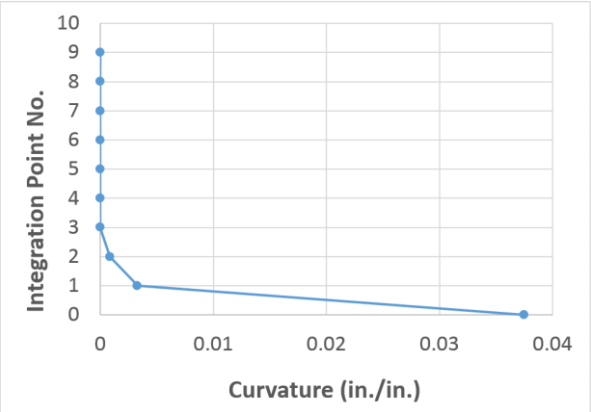

(d) Drift ratio of 6%

Figure 6-10: Curvatures at each integration point along the column

From the results in Figure 6-10, one can see that the curvature at the bottom end has the maximum value and decreases towards the top end. As the loading increases, curvature at the bottom end increases rapidly. When the drift reaches 6%, the first three integration points give considerably higher curvatures than the rest of the column. For the other two loading cases, the first three segments contribute more than 97% of the total deformation. The total length of the first three segments is 28 inch as defined previously. According to the results in Figure 6-10, it is reasonable to make the assumption that the plastic region of the column with a section of CCFT 24*1.375 occurs within a length of 28 inch from the fixed end. In this research, a plastic

hinge length of 24 inch is assumed to be used in the analysis, which is equal to the outer diameter of the CCFT cross section.

6.2.4: Preliminary Design Results

Table 6-2 shows both the fundamental periods from (Eq. 6-1) and the first mode periods of the two more refined CSMFs models. As discussed previously, the first mode period from the modal analysis is less than the equation calculated fundamental period. However, there is an obvious conflict in that, although they are similar, the period of the self-centering system with PR connections is slightly less than that of "conventional" system with FR connections. This conflict is believed to be caused by the complexity of the 2D-SSM of the new proposed connection which results in some additional stiffness. The initial connection stiffness is increased by applying pre-tensions in all rods so that the end plates do not separate under gravity loads.

Table 6-2: Fundamental Periods and First Mode Periods of Eigenvalue Analysis of both Two CSMFs

System Type	Fundamental Period T (s)	1st Mode Period T_0 (s)
CSMF with FR Connections	1.173	1.386
CSMF with PR Connections	1.173	1.328

The remaining six periods of the first seven mode shapes are listed in Table 6-3. All of first seven periods are similar to each other, and the corresponding mode shapes are presented

through Figure 6-11 to Figure 6-24. One can see that they are similar to each other, and the leaning column systems are compatible with the main frames. This indicates that the 2D-SSM does not appear to introduce any spurious modes in the frequency range of interest.

Table 6-3: Periods of modes 2 to 7 of both two CSMFs (Unit: seconds)

System Type	2^{nd}	3^{rd}	4^{th}	5^{th}	6^{th}	7^{th}
CSMF with FR Connections	0.469	0.244	0.150	0.142	0.126	0.116
CSMF with PR Connections	0.450	0.233	0.150	0.136	0.126	0.114

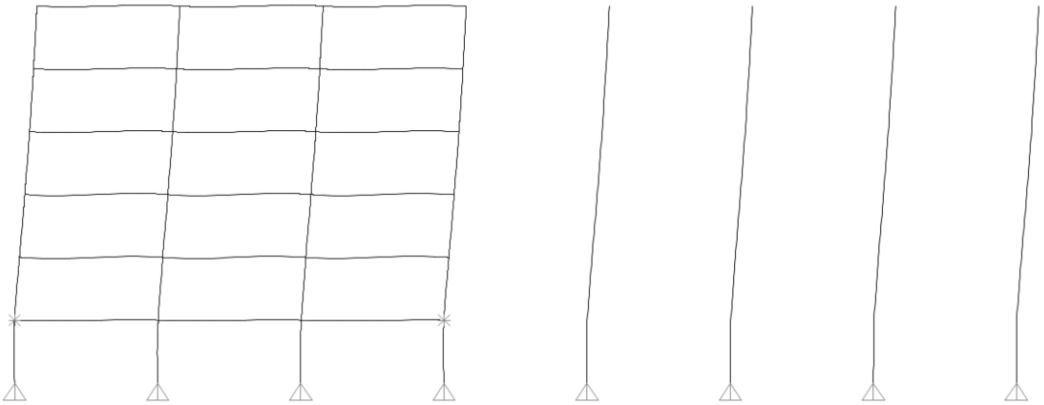

Figure 6-11: The first mode shape of the convertional CSMF

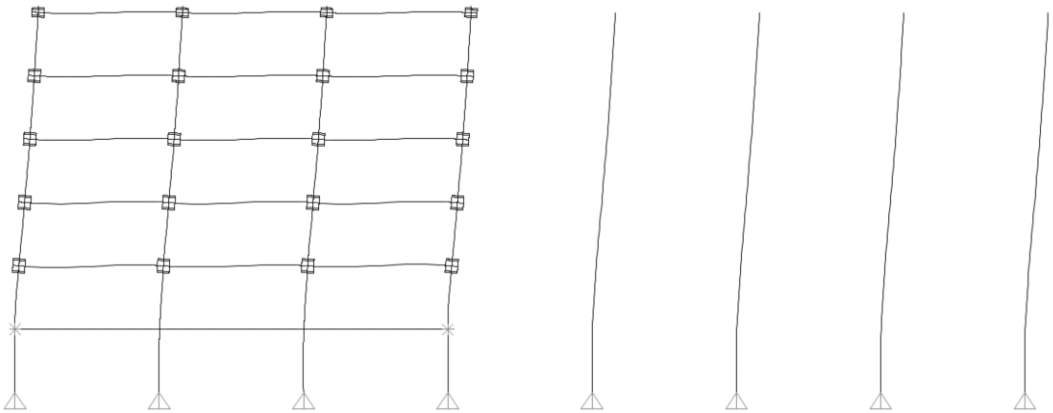

Figure 6-12: The first mode shape of the self-centering CSMF

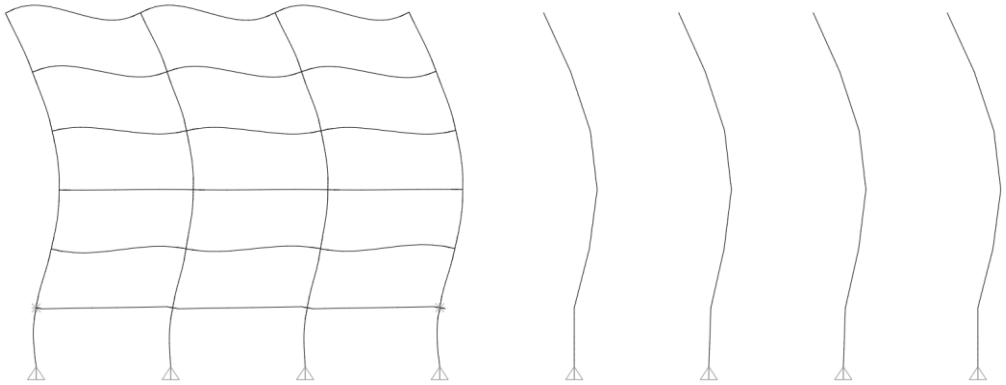

Figure 6-13: The second mode shape of the convertional CSMF

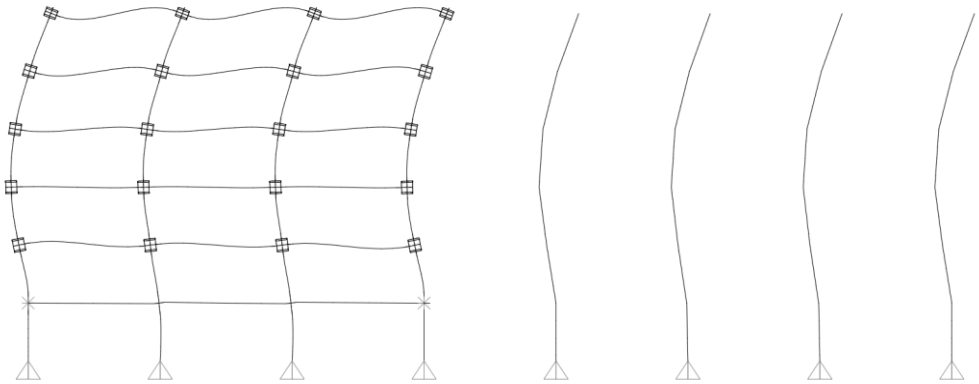

Figure 6-14: The second mode shape of the self-centering CSMF

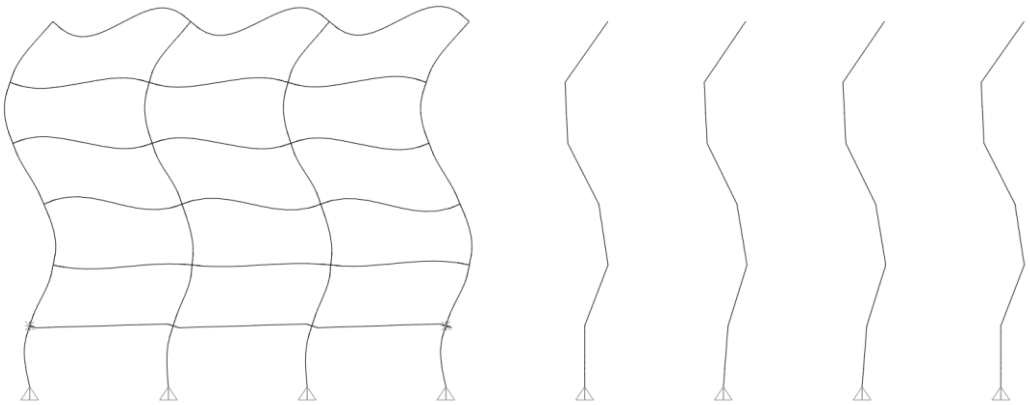

Figure 6-15: The third mode shape of the convertional CSMF

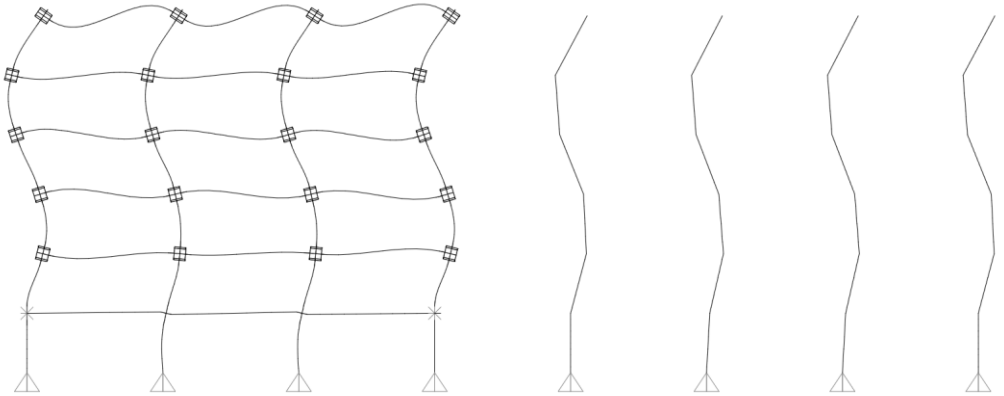

Figure 6-16: The third mode shape of the self-centering CSMF

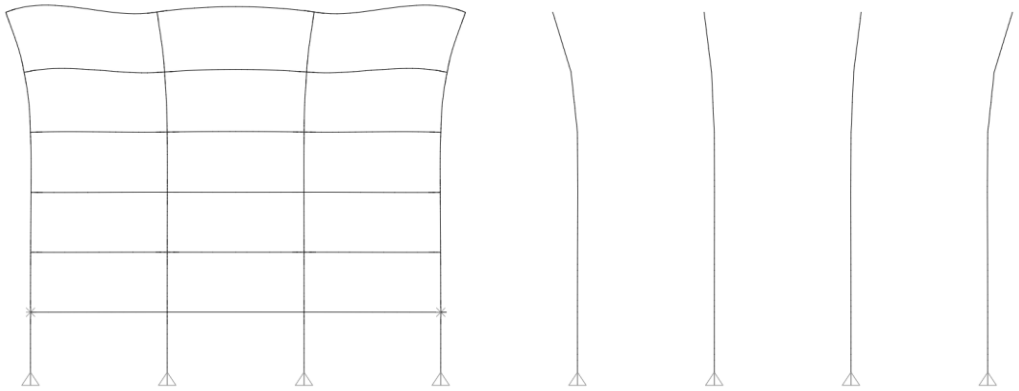

Figure 6-17: The fourth mode shape of the convertional CSMF

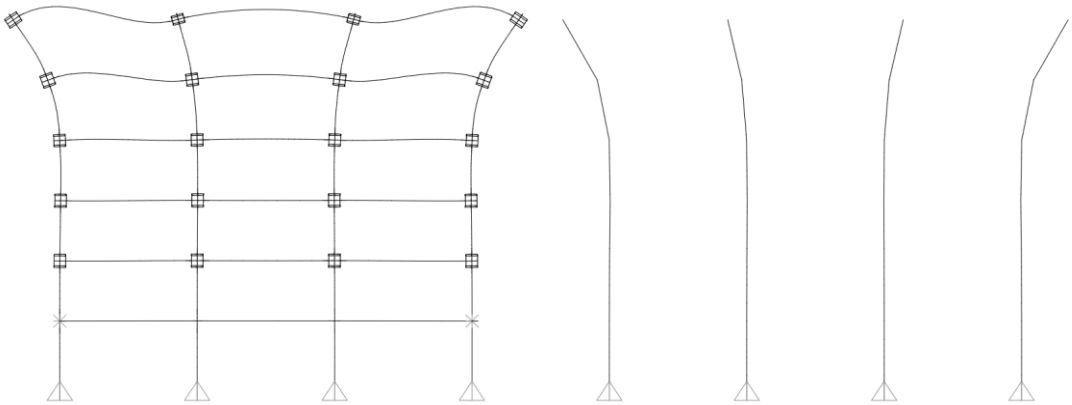

Figure 6-18: The fourth mode shape of the self-centering CSMF

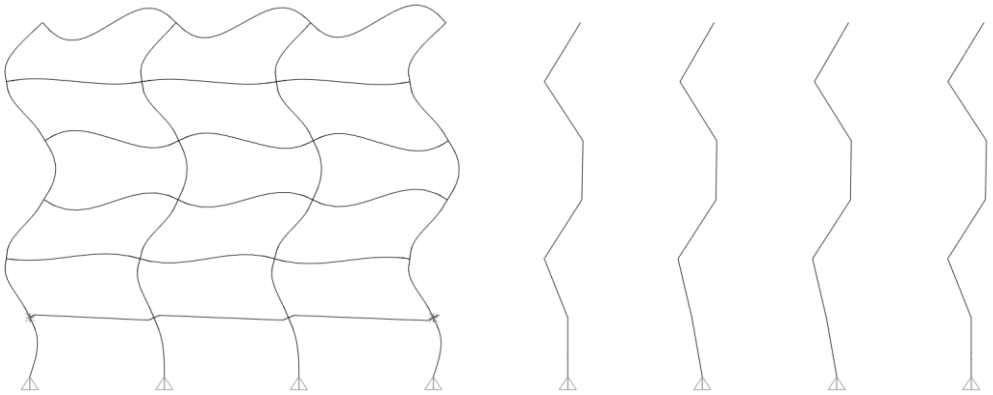

Figure 6-19: The fifth mode shape of the convertional CSMF

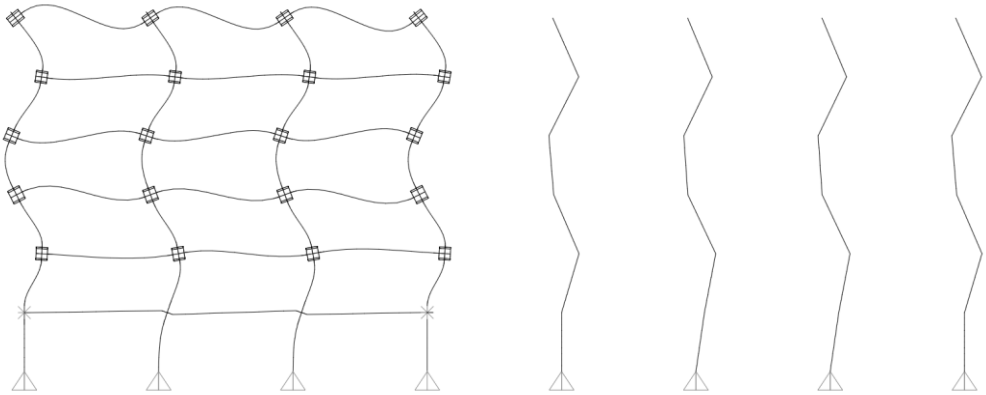

Figure 6-20: The fifth mode shape of the self-centering CSMF

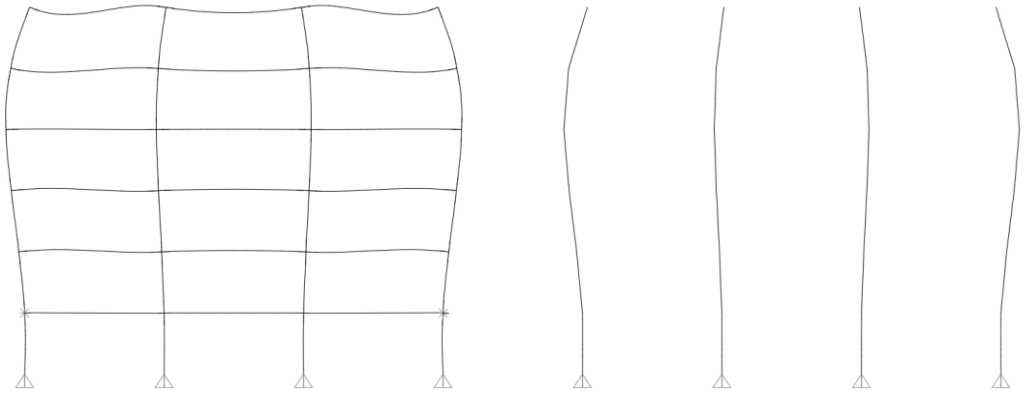

Figure 6-21: The sixth mode shape of the convertional CSMF

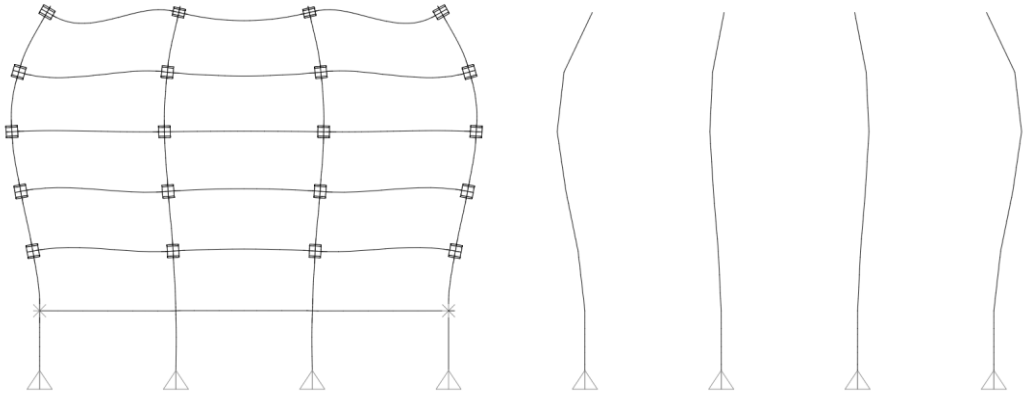

Figure 6-22: The sixth mode shape of the self-centering CSMF

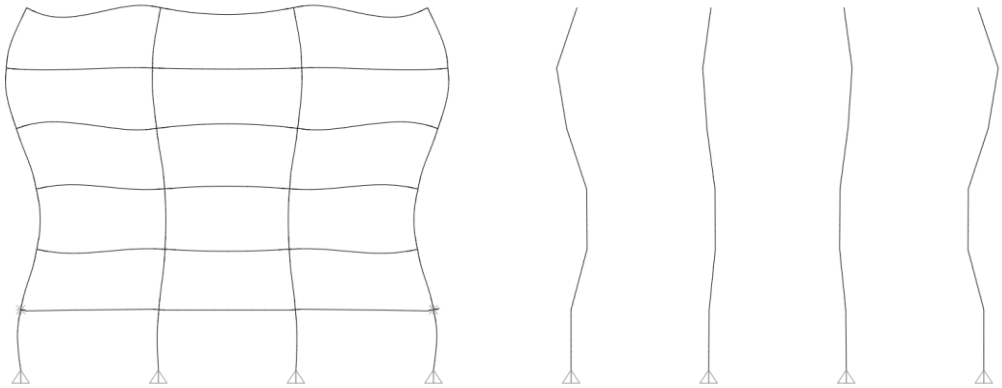

Figure 6-23: The seventh mode shape of the convertional CSMF

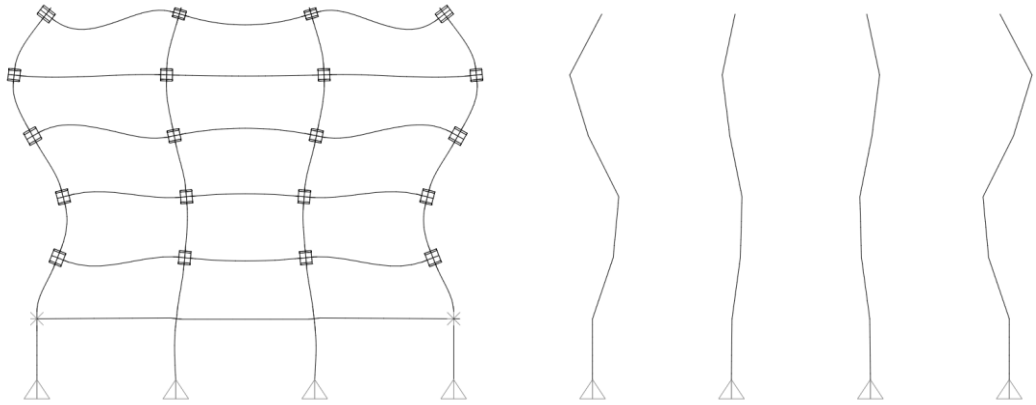

Figure 6-24: The seventh mode shape of the self-centering CSMF

As mentioned above, two new sets of ELFs will be calculated based on the periods in Table 6-2 for the two CSMFs, respectively. They are used for deflection check only. In Appendix K, only the check for the "conventional" CSMF is presented in detail. In order to see how ELF method works for the new proposed self-centering system, the deflection check results under load combination (4) mentioned above are shown and compared in Table 6-4, as stiffness demands for both two CSMFs control the design results. From the plan layout in Figure 6-1, it is obvious that all columns of the two CSMFs are interior columns and the tributary area of each column is nearly the same. Thus it is reasonable to assume that the vertical loads from the gravity system on each story should be evenly divided by four and assigned to each leaning column. Because of the lack of rigid diaphragm constraints, the horizontal displacement on each level column is different. Results in Table 6-4 are the maximum value of the four displacements on each story. According to Table 12.12-1 in ASCE 7-10, the design story drift ratio limit is 2% for a library in risk category II. The values in brackets in Table 6-4 indicate the ratios of maximum story drifts to the design limit.

Table 6-4: Design Inter Story Drifts based on ELF from 1st Mode Period of Eigenvalue Analysis in Table 6-2

Story	"conventional" CSMF		Self-centering CSMF	
	ELF (kips)	Inter Story Drift (in.)	ELF (kips)	Inter Story Drift (in.)
1	13.114	2.259 (0.672)	14.193	2.446 (0.728)
2	35.656	2.483 (0.739)	37.82	3.225 (0.959)
3	64.007	2.34 (0.697)	67.099	2.975 (0.886)
4	96.943	2.031 (0.605)	100.781	2.448 (0.728)
5	93.987	1.886 (0.561)	97.078	2.108 (0.627)

Note: Numbers in brackets indicate that how much ratios of the drift limit are reached.
The inter story drifts are the elastic analysis values amplified by $C_d = 5.5$.

The design interstory drift limit is 3.36 in. From the results shown in Table 6-4, one can see that both two CSMFs pass the deflection check by using the trial member sizes based on the analysis of simplified model. The design interstory drifts of the self-centering system is about 10% greater on the first story and the roof story, and about 20 - 30% greater in the middle stories than those of the "conventional" system. This buttresses the belief that a two-step applications of the ELF method can be used for preliminary design: (1) determine the trial member sizes based on a model without PR connections; (2) once the trial member sizes are obtained, change the FR connections into the PR connections by using the proposed 2D-SSM in Chapter 4, and then check the new model.

Although ELFs for the self-centering system is about 4% greater than those for "conventional" system, the deflections increase much more, i.e., not linearly. This indicates that the stiffness of the self-centering system is smaller than "conventional" system once significant loads are applied. The greater deflections are primarily caused by the expansions of PR connections.

In order to investigate how much benefit can be obtained by using the first mode period, instead of fundamental period, to calculate ELFs for deflection check, the interstory drifts under the ELFs based on the fundamental period are presented in Table 6-5. Comparing the results in Table 6-4 and Table 6-5, one can see that the interstory drift can be reduced by about 12 - 15% for both two systems by using the first mode period.

Table 6-5: Design Inter Story Drift based on ELF from Fundamental Periods in Table 6-2

Story	ELF (kips)	Design Inter Story Drift (in.)		
		Simplified Model	"conventional" CSMF	Self-centering CSMF
1	17.688	4.143 (1.233)	2.659 (0.791)	2.808 (0.835)
2	44.672	4.329 (1.288)	2.913 (0.867)	3.688 (1.098)
3	76.806	4.012 (1.194)	2.722 (0.81)	3.378 (1.005)
4	112.821	3.397 (1.011)	2.345 (0.698)	2.759 (0.821)
5	106.814	2.758 (0.821)	2.152 (0.641)	2.357 (0.701)

Note: Numbers in brackets indicate that how much ratios of the drift limit are reached.
The inter story drifts are the elastic analysis values amplified by $C_d = 5.5$.

From the results in Table 6-5, one can conclude that the simplified model is less accurate. This difference is probably due to the fact that both panel zone size and the location of member plastic hinges is neglected in the simplified model.

6.2.5: Effects of Lateral Stiffness of Leaning Columns and Rigid Diaphragm Constraints

In reality, the gravity system will contribute some level of lateral stiffness to the system. In this research, the gravity columns are designed to support stack rooms with a live load of 150 psf. Live load reduction is not applicable. Under load combination (2) in (Eq. 6-3), the columns are designed for compressive loading of 623.8 kips on top three levels and 1432.9 kips on bottom three levels (including one basement). The unbraced length is 14 ft, according to AISC360, section W14*68 is used for top columns and W14*132 is used for bottom columns.

In this research, a zero lateral stiffness can be used conservertively for the leaning column system by releasing one end moment of leaning columns on each story. In order to investigate how much effect leaning columns with continuous flexural stiffness can bring, another CSMF model in SAP2000 is analyzed in this section. The new model is the same as the accurate model for the “conventional” CSMF introduced above except that columns with continuous flexural stiffness are employed in the leaning column system. The flexural stiffness is determined based on the gravity system. As shown in Table 6-6, it is clear that the periods of the system with continuous leaning columns are slightly less than those of its counterpart. It means that the

introduced stiffness from continuous leaning column system is not large.

Table 6-6: First Seven Periods of Systems with/without Flexural Continuous Leaning Columns without Rigid Diaphragm Constraints (unit: seconds)

Mode	Leaning Columns with Moment Release	Leaning Columns with Flexural Stiffness	Difference
1	1.3856	1.3639	1.6%
2	0.4688	0.4575	2.4%
3	0.2435	0.2331	4.3%
4	0.1504	0.1502	0.1%
5	0.1416	0.1350	4.7%
6	0.1257	0.1255	0.2%
7	0.1157	0.1145	1.0%

6.3 Summary and Conclusions

In this section, the lateral resisting system of a library located in San Francisco is designed. Detailed building information is supplied in Section 6.1. A simplified computational finite element model was established in SAP2000, and the equivalent lateral force method (ELF) in ASCE7-10 was employed to do preliminary design for both "conventional" and self-centering CSMFs.

Some conclusions based on the preliminary design results can be obtained as follows:

- System elastic stiffness will not be reduced significantly by applying the NPSCs.
- The ELF method can also be used to do preliminary design for the self-centering system

with PR connections by two steps:

  - At first, the model without PR connections can be used to determine the trial member sizes.
  - Secondly, the FR connections are replaced by the PR self-centering connections and the strength and drift checks are executed to confirm the design.

- The same member sizes can be used for both "conventional" and self-centering CSMFs based on ELF method. This indicates that applying PR connections does not reduce the system stiffness a lot.
- A distributed leaning column system should be used for system with PR connections to consider 2nd order effects from gravity system (see Figure 6-6 and Figure 6-7).

Chapter 7

Advanced 2D-SSM and CSMFs in OpenSees

In this chapter, the results of nonlinear static pushover analyses will be discussed for two structural systems: a "conventional" CSMF with FR connections and a self-centering CSMF with PR connections. OpenSees will be used for the pushover analyses. In order to establish the model for the self-centering CSMF, an advanced simplified spring model (2D-SSM) will be developed in OpenSees based on its prototype in SAP2000. In Section 7.1, a detailed introduction of the advanced 2D-SSM in OpenSees will be provided. In Section 7.2, its validation will be discussed by comparing the OpenSees results with the SAP2000 results under the same cyclic loadings. In Section 7.3, two CSMFs and their corresponding models in OpenSees are described in detail. Both fiber sections and zero length elements with concentrated plasticity are employed to simulate the beam and column plastic hinges, and their behavior is discussed and compared. Finally, in Section 7.4, conclusions obtained in this chapter will be summarized and their limitations discussed. Figure 7-1 and Figure 7-2 provide a visual organization chart of this Chapter and should be used as a guide.

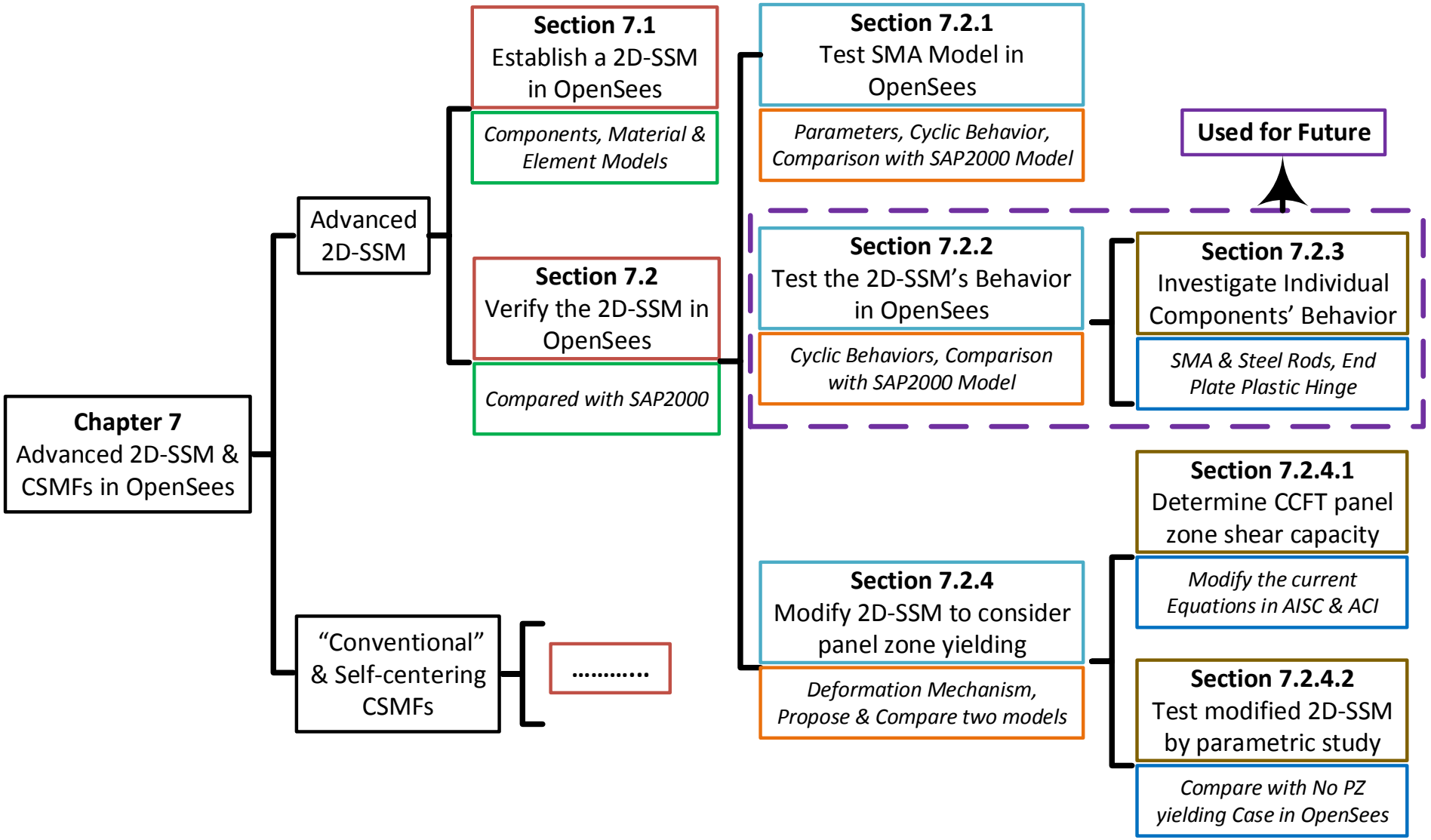

Figure 7-1: Organization of Chapter 7

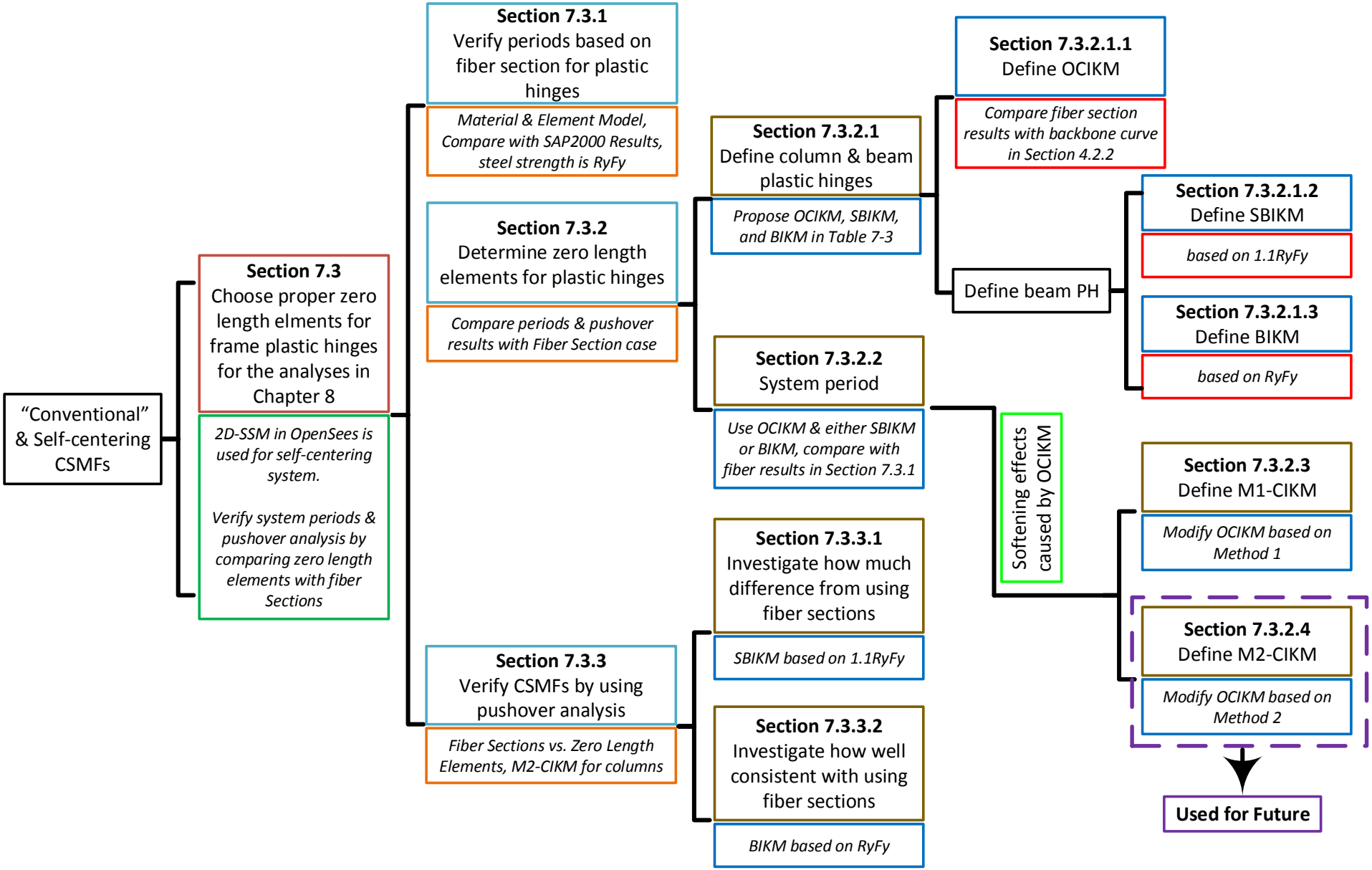

Figure 7-2: Organization of Chapter 7 (con.)

7.1 Advanced 2D-SSM in OpenSees

An efficient 2D simplified spring model (2D-SSM) for the new proposed smart connection was proposed in Chapter 4 and implemented in SAP2000. In this section, a more advanced 2D-SSM is built up in OpenSees based on the model in Figure 4-4. In this section, a detailed description of components of the 2D-SSM in OpenSees is shown in Figure 7-3.

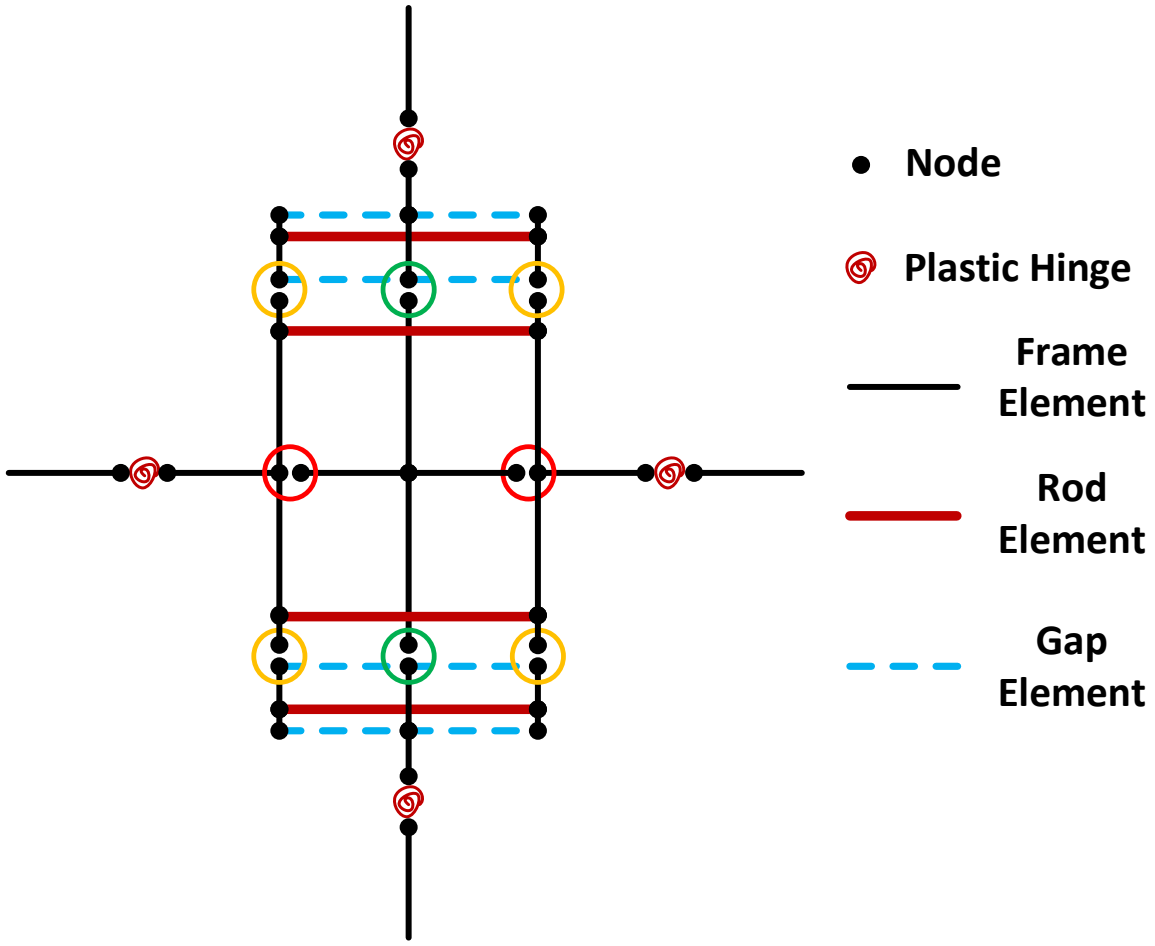

Figure 7-3: The detailed model for the 2D-SSM in OpenSees

The components of the model can be described as follows:

- Black bars compose the main structure of the connection and are defined by frame elements in OpenSees:
    - The vertical black bars in the middle stand for the CCFT column;
    - The vertical black bars on both sides of CCFT column stand for the rigid end plates;
    - The two horizontal black bars farther from the middle stand for the beams on either side of the connection;
    - The remaining four horizontal black bars are rigid elements as explained in the previous chapters (See Section 6.2.2 and Figure 6-8).
- Black dots represent nodes.
- The small gap between the two black dots within a color circle indicates that there is either a plastic hinge defined by a zero-length length element or a DOF release. The two dots in one color circle should have identical coordinates, and the gap is imaginary:
    - The green circles correspond to shear plastic hinges of the panel zone:
    - The orange circles represent flexural plastic hinges in the end plates:
    - The red circles are used to define a moment release between the two nodes by assigning a very small value to their rotational stiffness.
- The blue dashed lines represent the rigid gap elements that transfer the compression from end plates to the column directly.
- The red lines represent all rods on the same level. These are truss elements connecting the two end plates directly and do not connect to any of the column elements.

- Four springs represent the plastic hinges on both beams and columns. They are defined by either zero-length elements at the center of the plastic yielding zones of the corresponding members, or fiber sections with real lengths of the plastic yielding zones.

Comparing the two models in Figure 7-3 and Figure 4-4, one can find two modifications:

- For the 2D-SSM in OpenSees, there are two additional rotational plastic hinges on the CCFT column panel zone introduced to simulate the panel zone shear yielding mechanism. They are indicated by two green circles in Figure 7-3. More detailed description of these hinges will be given in Section 7.2.4.
- As described in Chapter 4, there are four additional rigid gap elements being added to transfer compression from the end plate to the column directly in the improved 2D-SSM in SAP2000. They are located on the same levels of the exterior rods in the 2D-SSM in SAP2000. However, in the 2D-SSM in OpenSees they are moved to the positons where the top and bottom cover plates of the rectangular steel tube are located (Figure 3-1). This modification is believed to have an insignificant effect on connection behavior when the distance between exterior rod level and the top or bottom surfaces of the cover plates is not large. However, this modification provides a choice to analysts to locate these compressive elements freely when the distance is large (Figure 7-3).

In addition to the above two configuration modifications, there is another important change in 2D-SSM in OpenSees. It is that a more advanced SMA material model in OpenSees will be

employed. Because there is no SMA material in SAP2000, several elements with existing material modes were combined to approximately simulate SMA behavior as described in Chapter 4. The method used in SAP2000 is not convenient to add pretension on the SMA rods and also it cannot simulate residual strain in the SMA rods. By using an advanced SMA material model in OpenSees, the above two limitations are removed and a more accurate behavior is obtained. In addition, this is accomplished with fewer elements. Another advantage of 2D-SSM in OpenSees is that it is much easier to define pre-tension in steel rods with sliding effect. In Table 7-1, a summary of element types and material models of 2D-SSM in OpenSees is presented.

Table 7-1: Summary of Element Types and Material Properties of 2D-SSM in OpenSees

Model Component Name	Element Type	Material Model
Column	ElasticBeamColumn	-
Beam	ElasticBeamColumn	-
Rigid End Plate	ElasticBeamColumn	-
Plastic Hinge of End Plate	Zero-Length	ElasticPP
Plastic Hinge of Beam/Column	Zero-Length	Modified-IK Model
SMA Rod	Truss	Superelastic Material
Steel Rod	Truss	Steel02
Shear Element	ElasticBeamColumn	-
Gap Element	Truss	Elastic

Note: (1) The component named 'Shear Element' is the same as defined in Figure 4-1.
(2) For components with ElasticBeamColumn element, the material and section properties are defined directly in the element command.
(3) 'Rigid End Plate' and 'Shear Element' are defined as rigid materials.
(4) For rods, 'Series' material is used to combine the original rods material with zero compression stiffness material to simulate sliding effect of rods.
(5) For 'Gap Element', zero tension and rigid compression stiffnesses are used.

7.2 Analysis Results of 2D-SSM in OpenSees

Although there are two shear plastic hinges introduced into the 2D-SSM in OpenSees, the assumption of no shear yielding has been used in this research. This assumption is made in all chapters so that results from different chapters can be compared. However, the new proposed 2D-SSM in OpenSees can also be used for a connection with a relatively weak panel zone, for example if the column section is changed from CCFT to conventional W section. Connection behavior with a reduced panel zone shear capacity will be investigated later in this Chapter.

7.2.1 SMA Model in OpenSees

For the 2D-SSM in OpenSees, an advanced SMA material model is used to define the SMA rods. This model was proposed by Taftali in 2005 [100], and then was modified by Eatherton in 2011 [101]. The modification adds the ability to handle residual strains under cyclic loading to Taftali's model. The modified model is defined by fourteen property variables as shown in Table 7-2, where the plus and minus signs indicate that the same variables are used for both positive and negative regimes. These variables are also presented in Figure 7-4.

Table 7-2: Variables Defined in OpenSees for the Modified SMA Model

Variable	Name	Values Used in This Thesis
E_{SMA}	Elastic Stiffness	5851 ksi
F_s^{AS} (+ & -)	Loading Plateau Stress	$\pm$66.7 ksi
F_F^{SA} (+ & -)	Unloading Plateau Stress	$\pm$43.5 ksi

R_s (+ & -)	Loading Plateau Stiffness	0.03454
d_F^{AS} (+ & -)	Transformation Strain	0.05
R_m (+ & -)	Martensite Stiffness Ratio	0.35464
F_e^{SA} (+ & -)	Unloading Return Stress	22.0 ksi
$RStFact$	Residual Strain Factor	0.000497

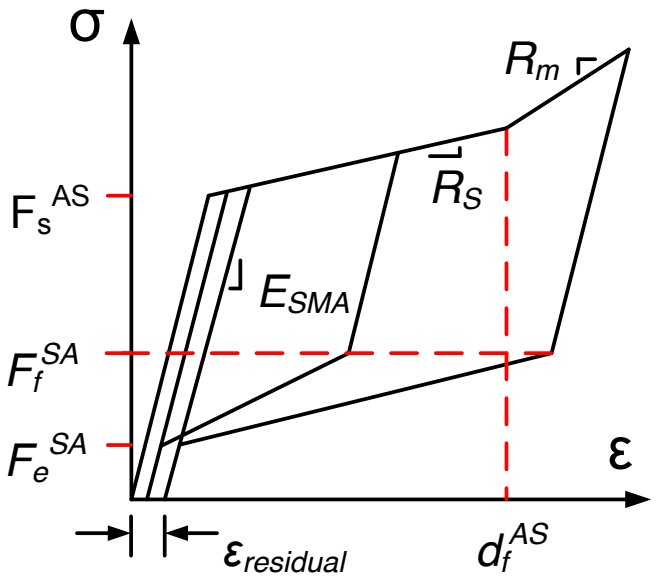

Figure 7-4: Modified SMA Model in OpenSees [101]

The same ideal SMA backbone stress-strain curve is used for both the OpenSees and SAP2000 models. As mentioned in Chapter 4, this ideal curve is defined based on the test data shown in Figure 4-17. The corresponding values of variables to simulate the ideal curve in OpenSees are calculated and listed in the third column of Table 7-2. The cyclic stress-strain curve simulated in OpenSees is presented in Figure 7-5 under the strain loading history shown in Figure 7-6. In Figure 7-7, the portion of the simulated curves in the positive regime is compared. From the comparison, one can see that two curves are identical for the upper backbone curves. However, there are several differences for the subsequent portion of the unloading paths:

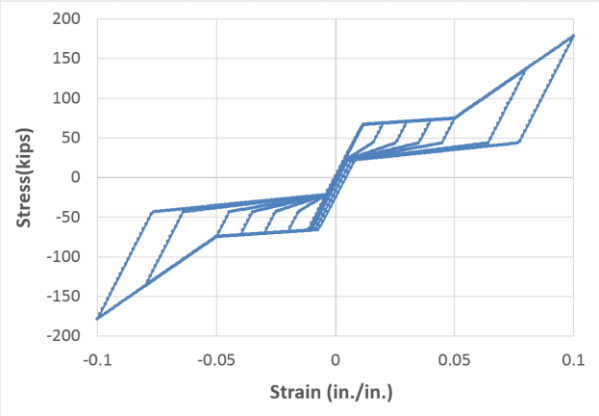

Figure 7-5:Cyclic SMA stress-strain curve in OpenSees

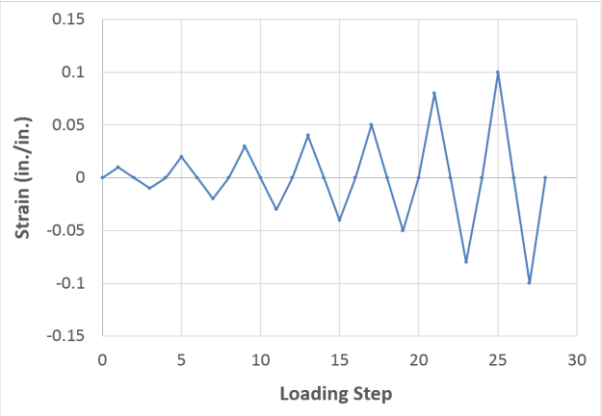

Figure 7-6: Strain loading history of SMA in OpenSees

- The most important difference is that the OpenSees model can simulate cyclic residual strain, which is ignored by the SAP2000 model.
- Another obvious difference is that two models have different initial unloading stiffnesses. For the OpenSees model, the initial unloading stiffness is the same as its elastic Young's modulus. However, for the SAP2000 model, the initial unloading stiffness is much smaller. For the example above, the significant difference is that there is no pretension added to the SMA rods as explained in Section 4.2.3.
- There is only one lower backbone curve in the SAP2000 model, and all unloading paths will eventually merge into it. However, each unloading path in the OpenSees model is unique as each unloading path has its own lower backbone curve. If the strain is less than 5%, the lower backbone curve of the SAP2000 model can be roughly considered as an average of all lower backbone curves of the OpenSees model.
- When the strain is greater than 5%, the lower backbone curve of the SAP2000 model

is greater than that of the OpenSees model. As described in Figure 7-4, all unloading paths of the OpenSees model will not change unloading stiffness until the same strength F_F^{SA} is reached. However, due to the strain limit of SMA 7% assumed in the proposed preliminary design procedure, this difference is believed to have insignificant effects on connection overall behavior.

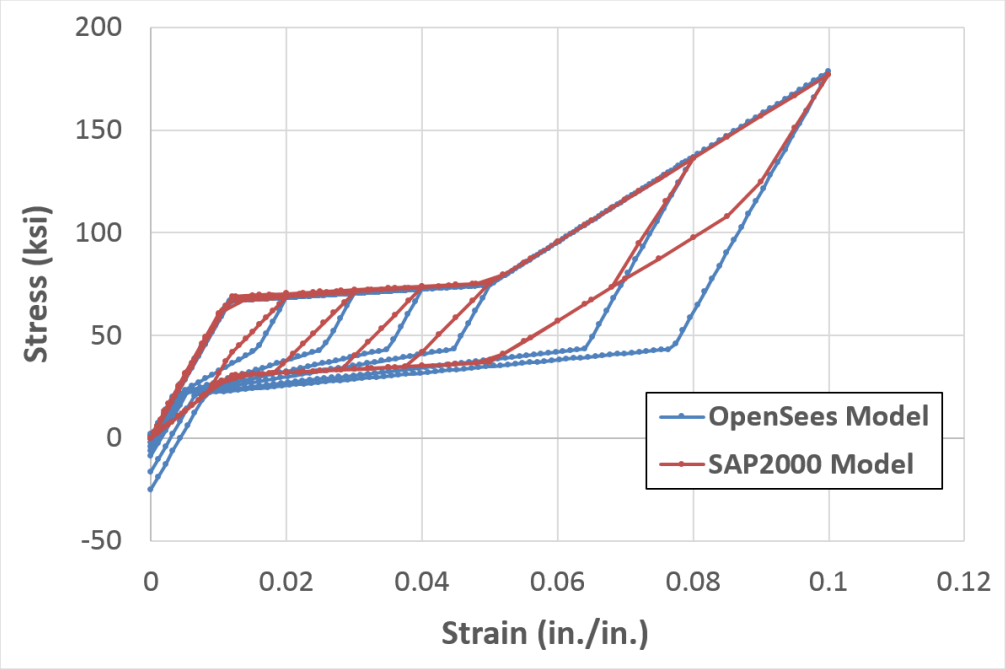

Figure 7-7: Comparison of SMA stress-strain curve without pretension between the OpenSees and SAP2000 models

As mentioned in Chapter 4, the pretension will influence the unloading stiffness of the SMA model in SAP2000. For a pretension of 30% of yield strength, Figure 7-8 shows the comparison between OpenSees and SAP2000. The figure indicates that the two models generate fairly similar unloading stiffness.

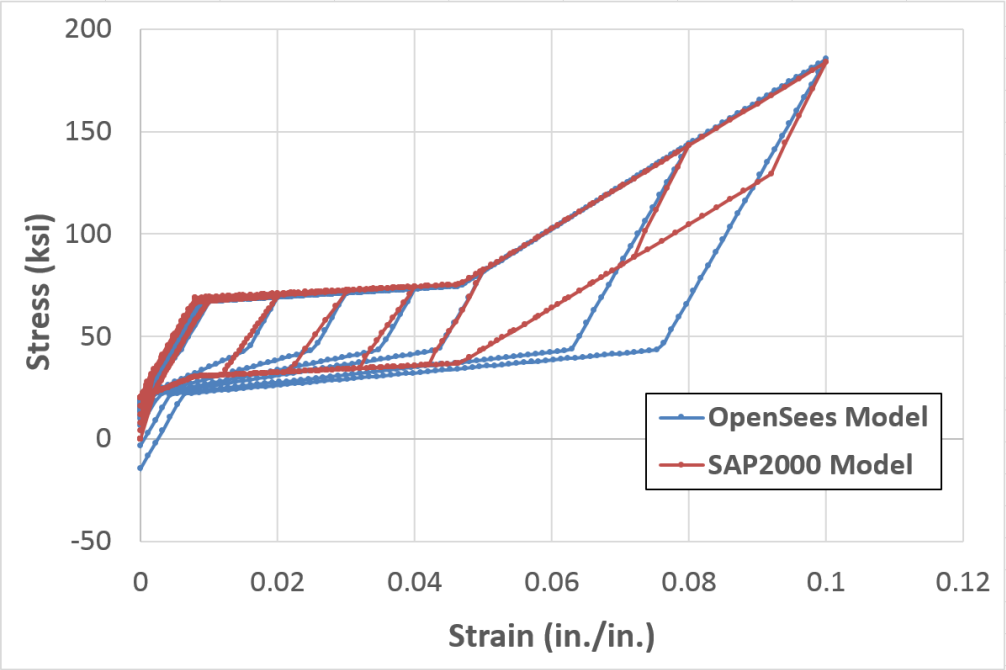

Figure 7-8: Comparison of SMA stress-strain curve with 30% yield strength pretension between the OpenSees and SAP2000 models

7.2.2 Analysis Results of Single Connection

In this section, a similar analysis to that done with the SAP2000 model in Chapter 4 will be repeated using the advanced SMA material model and the 2D-SSM in OpenSees. The results will be used to evaluate the effectiveness of the 2D-SSM in OpenSees. In this section, only connection behavior itself is investigated.

The same simple structure as shown in Figure 4-28 is employed for the individual connection analysis under the two loading histories in Figure 4-29. The dimension of the CCFT column is 24*1.375, and its connecting steel beam is a W33*130 with RBSs. Similar elements and

material properties as for the SAP2000 model in Chapter 4 are used. The analysis results for the moment rotation (MR) relationships of the connection are presented in Figure 7-9 for the two loading cases. The comparisons are illustrated in Figure 7-10 and Figure 7-11. Similar to the results in Figure 4-56, these results come from the improved model with end plate plastic hinges.

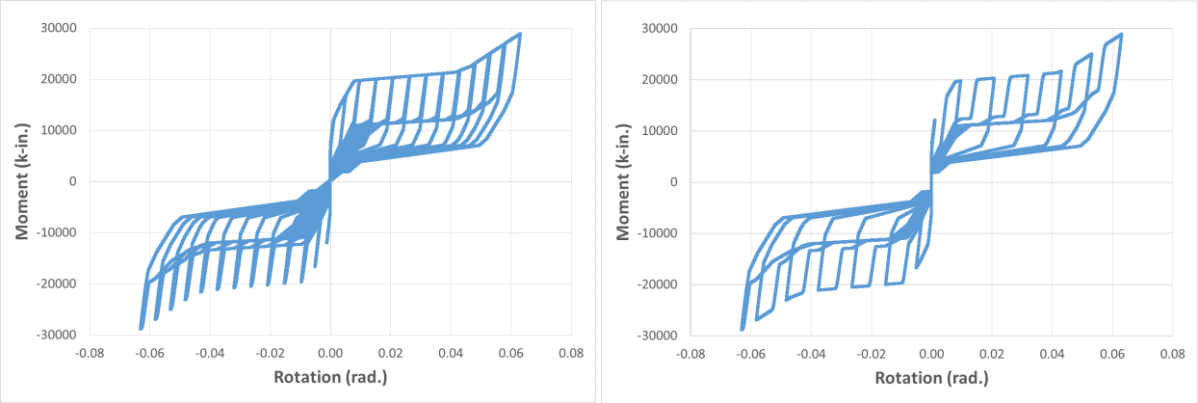

(a) under loading case 1 *(b) under loading case 2*

Figure 7-9: Moment rotation relationship of the connection in OpenSees

From the comparisons in Figure 7-10 and Figure 7-11, one can see that the MR relationships obtained from the OpenSees model is similar to those from the SAP2000 model under both two loading cases. The results of SAP2000 have already been explained in detail in Chapter 4. The OpenSees model can simulate the cyclic behavior of the new proposed smart connection as well as the SAP2000 model. However, there are still some minor discrepancies between the two models. Although they are believed to have little influence, it is not redundant to point them out as follows:

- First, there is a “thick” region at the beginning of the reloading paths in both positive

and negative directions, where the SAP2000 model generates a clear and concise region while the OpenSees model results in numerous different curves. The reason of this difference is that the SMA model in OpenSees considers residual strain under cyclic loading while the SAP2000 model does not. Compared with loading history 1, loading history 2 causes smaller differences in this region. This is because loading history 2 has less loading cycles and generates less residual deformations in SMA rods.

- Second, under both two loading histories, the lower backbone curves of the MR relationship is different. For the SAP2000 model, the lower backbone curve seems to be composed of one line while for the OpenSees model all unloading paths are unique. This is because the SMA material model in OpenSees is defined to have a non-uniform stress-strain lower backbone curve as discussed above (Figure 7-7).
- Third, the last cycles of the two MR relationships in the negative regime under loading history 2 does not match perfectly (Figure 7-11). For the SAP2000 model, the earlier reloading of end plates causes premature separation of the middle backbone curve in the moment-rotation relationship. This causes the inconsistencies between the loading and unloading paths between the middle and upper backbone curves. It is believed that numerical issues cause larger differences for the last cycle and the OpenSees result is believed to be more accurate. Relevant information, such as the separation of middle backbone curve of the MR relationship is caused by the reloading of end plate, is provided in the discussion on Figure 4-56 in Chapter 4.

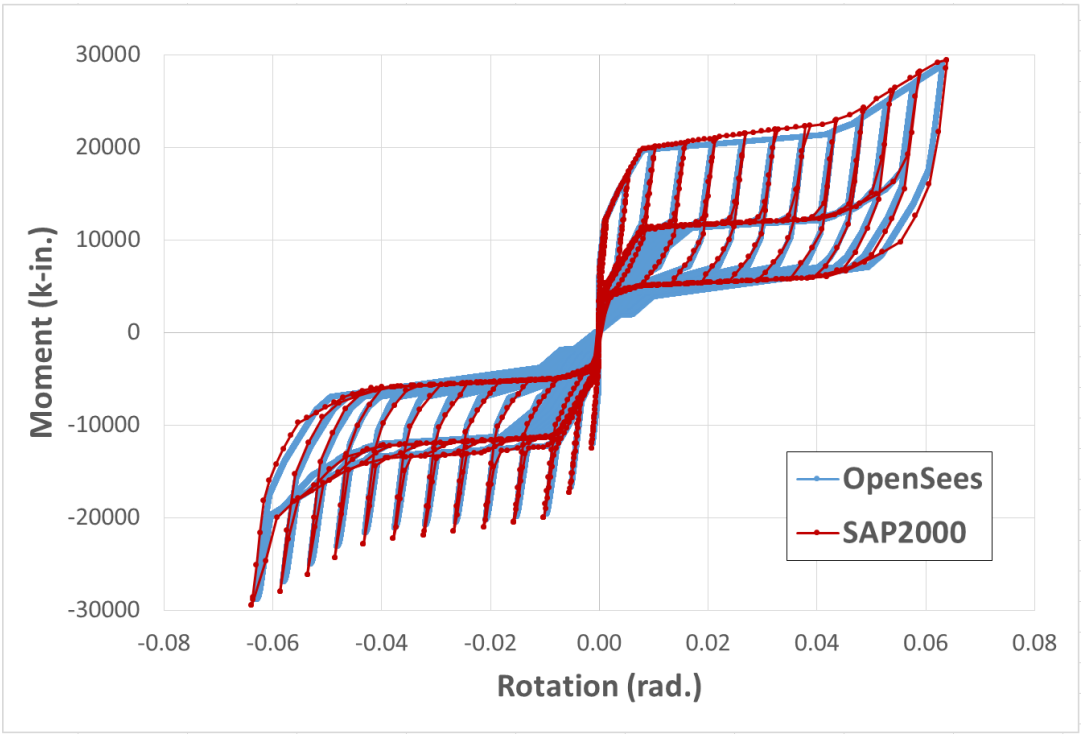

Figure 7-10: Comparison of M-R Relationship of Connection Itself between OpenSees and SAP2000 under Loading History 1

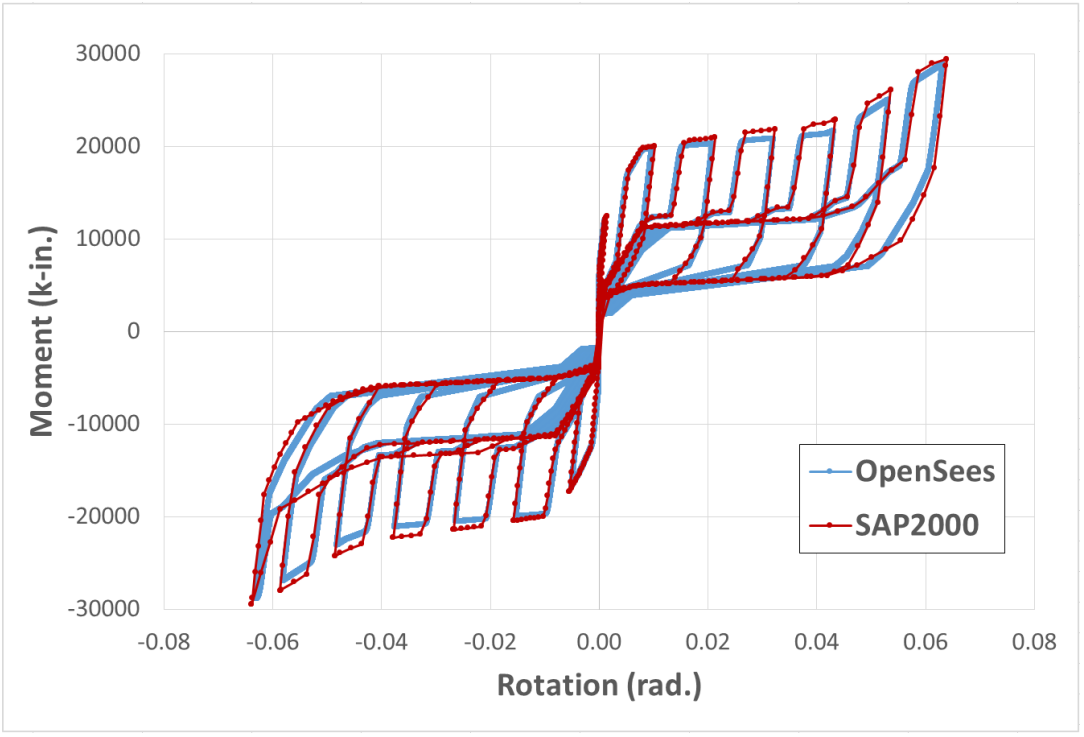

Figure 7-11: Comparison of M-R Relationship of Connection Itself between OpenSees and SAP2000 under Loading History 2

7.2.3 Cyclic Behavior of Important Components

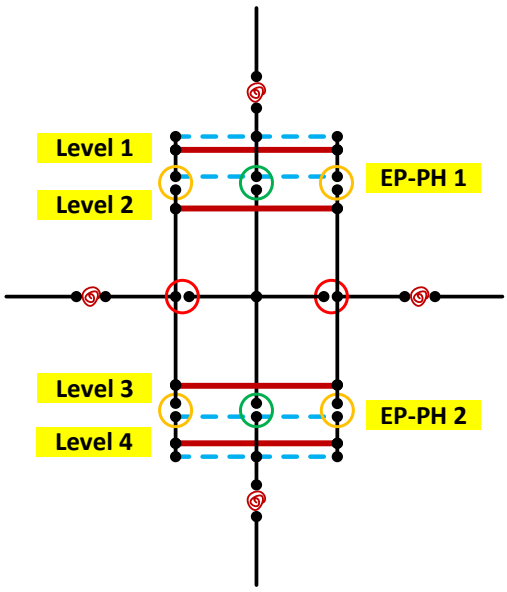

Figure 7-12: Illustration of rod levels and end plate positions

In order to investigate the behavior of the individual connection more comprehensively, the cyclic behavior of important components of the connection is presented in this subsection. This includes the SMA rods, steel rods, and plastic hinges in the end plates. As shown in Figure 7-12, the SMA and steel rods are located on four rod levels; in addition, the location of the two plastic hinges (PH) on the right end plate are also highlighted. Only the results from loading history 1 will discussed. As mentioned before, the study focuses on the connection so the beam and column plastic hinges are not included in the analysis and these elements are elastic.

7.2.3.1 Cyclic Behavior of the SMA Rods

One assumption made here is that on each rod level, all SMA rods share the axial force equally during the entire loading history. In Figure 7-13 the cyclic behavior of all SMA rods on different

levels is presented. The vertical axis is the average stress in each SMA rod, and the horizontal axis represents the distance of two holes on two end plates connected by the corresponding rod. If the two holes close to or separate from each other while the stress in the SMA rod between the two holes remains zero, this is an indication that the rods are sliding. The positive and negative signs in Figure 7-13 only indicate the two opposite directions of rod elongation. From Figure 4-29, one can see that loading history 1 is composed of thirteen full loading cycles, or twenty-six half loading cycles. Based on the connection deformation mechanism in Figure 4-4 and the initial loading direction information in Figure 4-28, the convention is that distances are plotted in the positive regime when the rods are displaced to the right.

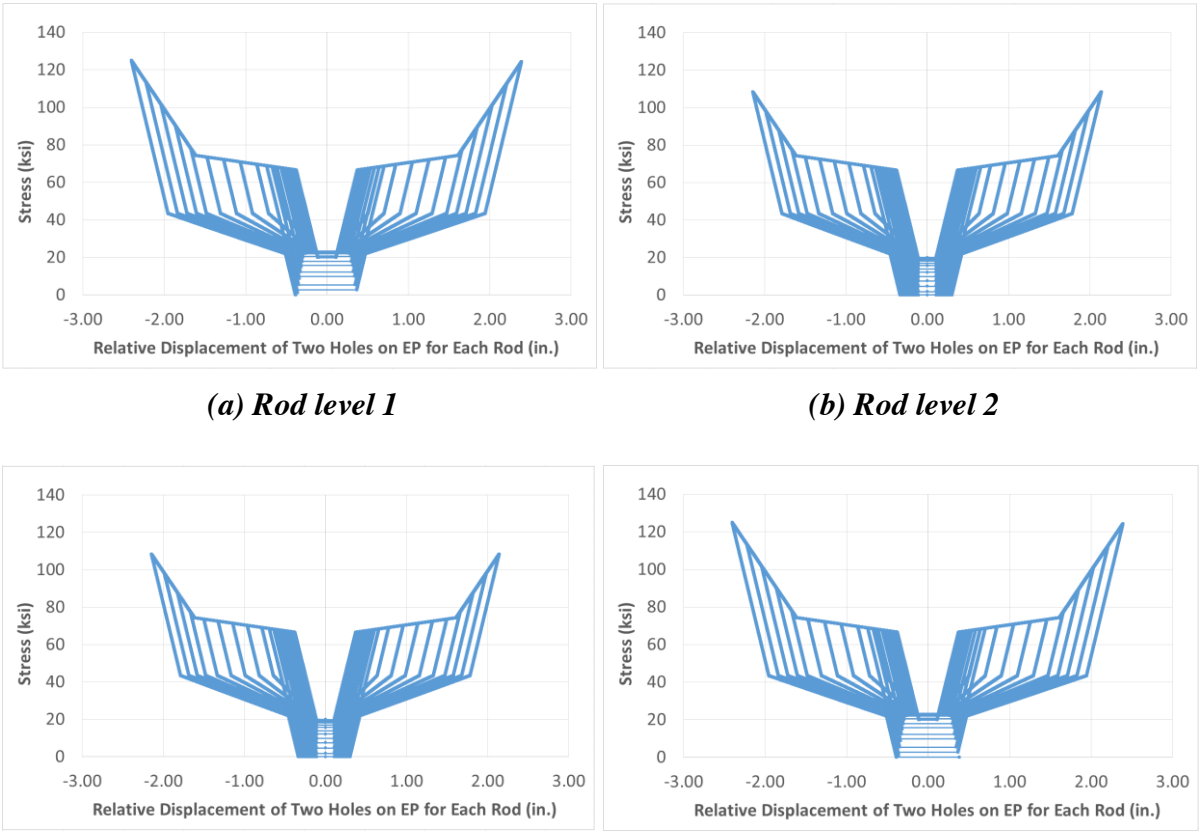

(a) Rod level 1

(b) Rod level 2

(c) Rod level 3

(d) Rod level 4

Figure 7-13: Cyclic behavior of SMA rods on each rod level

Results in Figure 7-13 indicate that the cyclic behavior is nearly the same in the two directions. As the loading magnitude increases, residual strains also increase and pretensions decrease. The rod sliding effect is indicated by the horizontal lines between the two curves in the positive and negative regimes. Only half the length of each horizontal line represents the actual sliding distance because during each loading cycle, the end plate closes and re-opens. While closing and with rods fully released, the rods do not move until the end plate fully closes. Latter, they start to slide together with the end plate as the end plate re-opens, until the rods are stretched in the opposite direction. In each 'close and re-open' cycle, the end plate moves twice the distance that the rods slide.

From the connection deformation mechanism in Figure 4-4, it is clear that both the SMA and steel rods on the exterior rod levels have greater deformation; this is also obvious in Figure 7-13.

7.2.3.2 Cyclic Behavior of Steel Rods

The cyclic behavior of the steel rods is presented in Figure 7-14. Similar results as for the SMA rods were expected when comparing the two exterior and interior rod levels. However, each group (exterior or interior rods) has a different initial stretching direction. For example, the rods on level 2 are stretching to the right under the first loading step, while the rods on level 3 start to be stretched to the left. This is much easier to tell for steel rods than SMA rods because

the self-centering characteristic of SMA rods masks the rods initial stretching direction. The steel rods will generate much greater residual strains than the SMA rods for the same rod level.

Due to the symmetric characteristic of the connection configuration and the loading cases all rods are stretched in tension under the first quarter cycle and then are fully released under the second quarter cycle. They are then reloaded in tension in the third quarter cycle the same maximum peak value as the first quarter cycle. Because of the residual strain generated in the first half loading cycle, the steel rods start to be reloaded elastically once this previous residual deformation is offset during the second half loading cycle. Once the same maximum stress is reached under the same peak loading of the first half loading cycle, the rods will be unloaded again without generating any more plastic deformation. That's why under the second half loading cycle, there are many 'pins' generated in the steel stress-strain curves. These 'pins' indicate where the steel rods start to be reloaded. Because the steel rods always yield more during all first half cycles, there are no 'pins' generated in the other direction. The side without 'pins' is the direction where the steel rods are stretched initially.

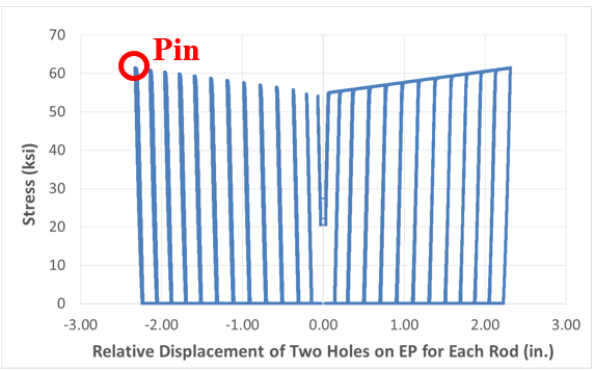

(a) Rod level 1

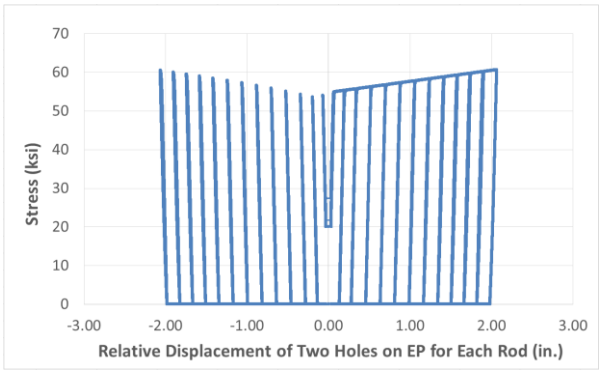

(b) Rod level 2

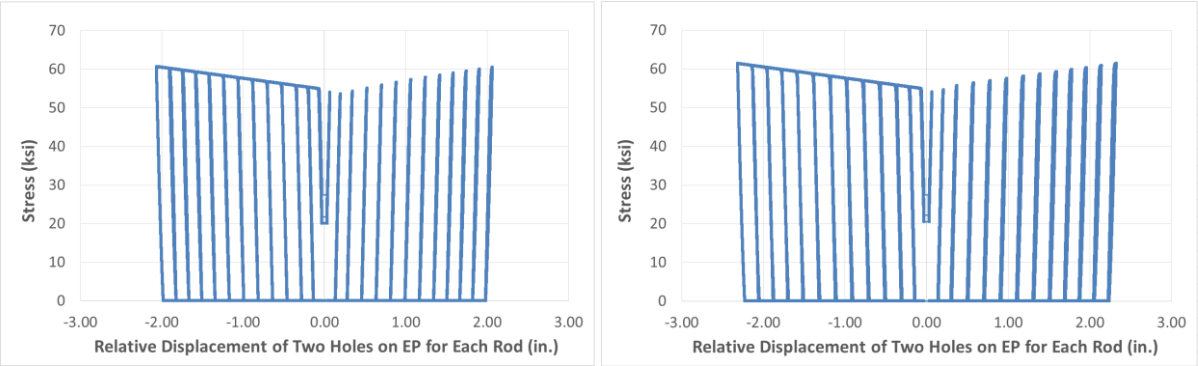

(c) Rod level 3 ***(d) Rod level 4***

Figure 7-14: Cyclic behavior of steel rods on each rod level

7.2.3.3 Cyclic Behavior of the End Plate Plastic Hinge

The end plate plastic hinges are defined in the OpenSees 2D-SSM by employing an elastic perfectly plastic material model. Figure 7-15 shows the cyclic moment-rotation relationships for the two plastic hinges on the right end plate. These curves resemble a 'comb'. The 'comb ridge' indicates that the plastic hinges have fully yield, and the 'comb teeth' are generated by elastic unloading and reloading of the plastic hinges. From these results, one can see that each end plate plastic hinge only yields in one direction. The plastic hinge closer to the rotation center of the end plate bears a much greater bending moment than the other. This larger bending moment is caused by the large compression force between the end plate and the column surface. The bending moment on the other plastic hinge results from the total tension force of all rods on the nearest exterior level.

After a load reversal, this end plate plastic hinge only bears the moment from the rods tension on the exterior rod level and will not yield. Results in Figure 7-13 show that the maximum

strain on the SMA rods under loading history 1 is about 7% with the rod length of 32.25’’, which is the design limit for the new proposed smart connection. For a well-designed self-centering connection, if its SMA rods do not exceed their strain limit of 7%, the end plate will not yield.

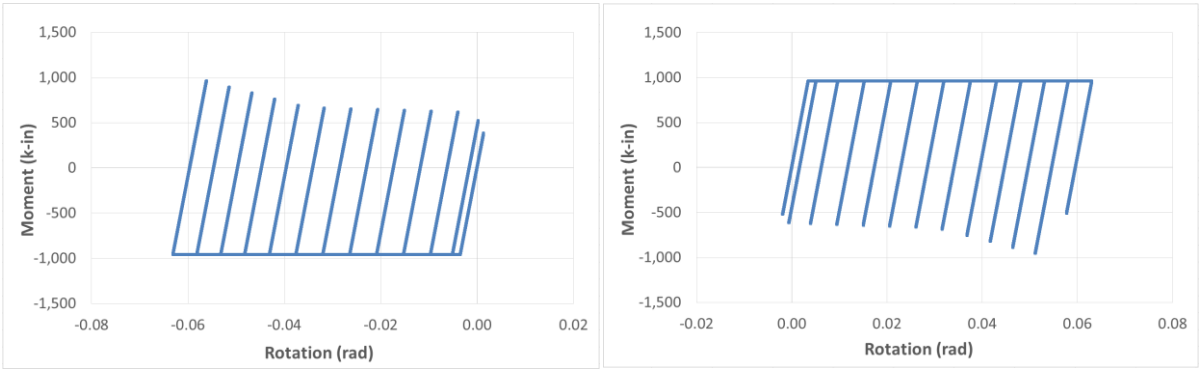

(a) Top ***(b) Bottom***

Figure 7-15: Cyclic behavior of plastis hinges on the right end pate

7.2.4 Connection Behavior with Weak Panel Zone

There are two additional rotational plastic hinges in the panel zone in the new proposed 2D-SSM in OpenSees. These hinges provide the ability to consider the effect of panel zone shear strength and deformation on the connection behavior. There are many different models that have been proposed to simulate the panel zone shear deformation mechanism [102]. In this section, another new method is proposed for the 2D-SSM in OpenSees as shown in Figure 7-16 (a). The connection panel zone is supposed to rotate relative to both the top and bottom columns about the two rotational plastic hinges shown as green circles. Once the connection panel zone is loaded, relative shear deformation between top and bottom columns will be generated.

However, the moment in one rotational plastic hinge is always greater than the other. Thus only one rotational plastic hinge is generated. A sketch of deformation for this case is presented in Figure 7-17, and an example based on this mechanism is also provided in Figure 7-18. One can see that the expected mechanism in Figure 7-16 (a) to simulate shear deformation in panel zone cannot be obtained by only adding two additional rotation plastic hinges.

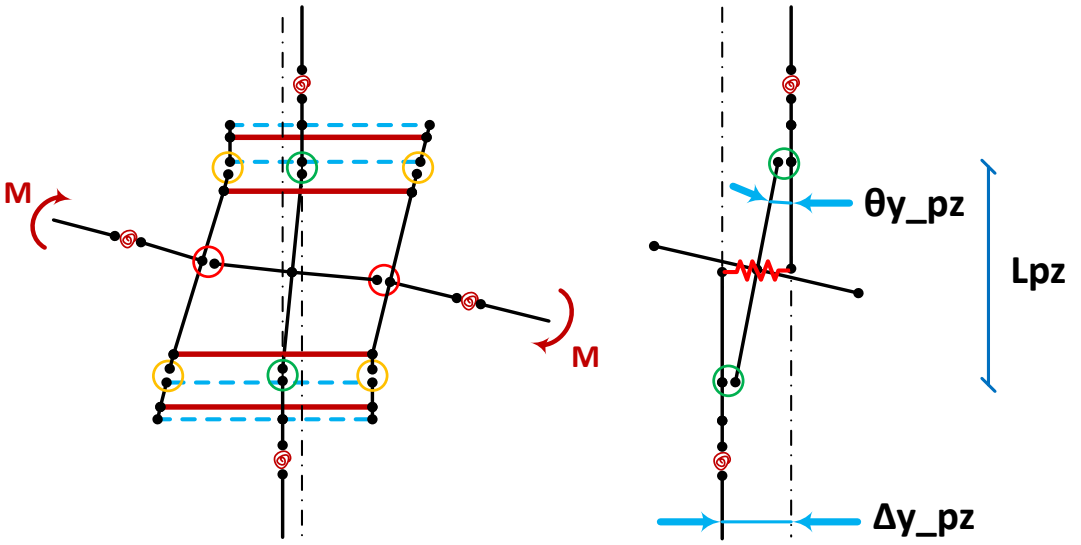

(a) with two rotational plastic hinges *(b) add one more shear plastic hinge*

Figure 7-16: Connection deformation mechanisms for different panel zone plastic hinges simulation methods

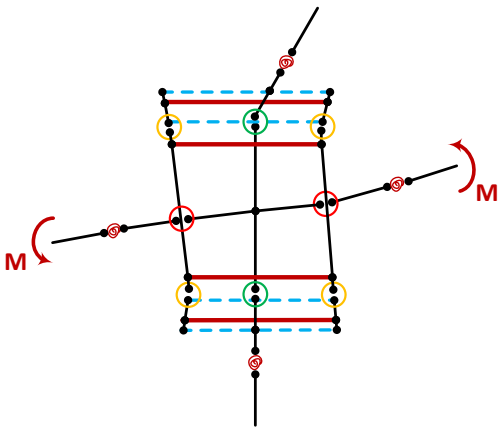

Figure 7-17: Mechanism of shear deformation with only one rotational PH yielding

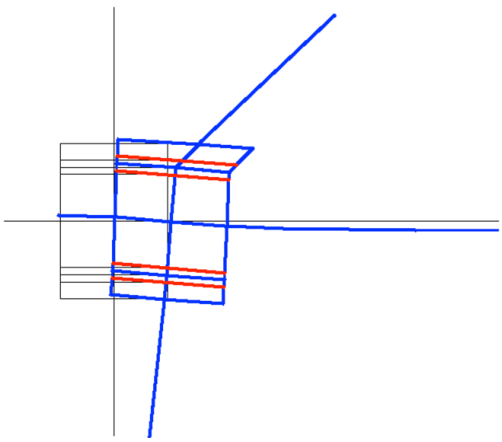

Figure 7-18: An example for the mechanism in Figure 7-17

In order to achieve the right deforming mechanism in Figure 7-16 (a), one more transverse shear plastic hinge is added in the panel zone. The deforming mechanism of the column in panel zone of the improved model is shown in Figure 7-16 (b). This is achieved by elongating the top and bottom column to the connection center, connecting the two column segments with a zero-length element, and changing the two rotational plastic hinges in the green circles into pin connections. This ensures that the two hinges rotate simultaneously and that the transfer in the panel zone is controlled by the shear plastic hinge at the connection center. From the deformation mechanism in Figure 7-16 (b), one can see that the deformation at the connection center will be changed by shear forces. This is reasonable because in reality the shear deformation in panel zone should not cause the end plate to separate from the column. The separation between end plates and column is only brought forth by the beam end moments.

The shear plastic hinge is defined based on the shear force and deformation relationship of the column. Shear yield strength V_{y_pz} is determined by modifying the existing equations in AISC360-10 [103]. The corresponding shear yield deformation is based on the properties of a proposed hypothetical flexural plastic hinge in the CCFT column. The moment rotation relationship of the hypothetical plastic hinge is presented in Figure 7-19, which is a reduced curve from the simplified backbone curve for the CCFT section given in Figure 4-46. The two curves have the same elastic stiffness. If the two yielding points of the two curves are (θ_y, M_y) and $(\theta_{y\_pz}, M_{y\_pz})$, respectively, then the relationship of (Eq. 7-1) will hold.

$$M_y / \theta_y = M_{y\_pz} / \theta_{y\_pz} \qquad \textit{(Eq. 7-1)}$$

The yield rotation of the hypothetical plastic hinge is defined as θ_{y_pz}, and the yield deformation of the shear plastic hinge is defined as Δ_{y_pz}. There are two hypothetical plastic hinges located in the green circles in Figure 7-16, and their distance is defined as L_{pz}. Based on the simple relationship in Figure 7-16 (b), it is easy to approximately calculate the yield deformation of the shear plastic hinges by (Eq. 7-2). Once the shear strength V_{y_pz} and its corresponding deformation Δ_{y_pz} are determined, a biaxial linear plastic model as shown in Figure 7-20 will be employed to define the shear plastic hinge. A strain hardening ratio of 0.1 is used after yielding point $(\Delta_{y\_pz}, V_{y\_pz})$ is reached.

$$\Delta_{y\_pz} = \theta_{y\_pz} \cdot L_{pz} \qquad \textit{(Eq. 7-2)}$$

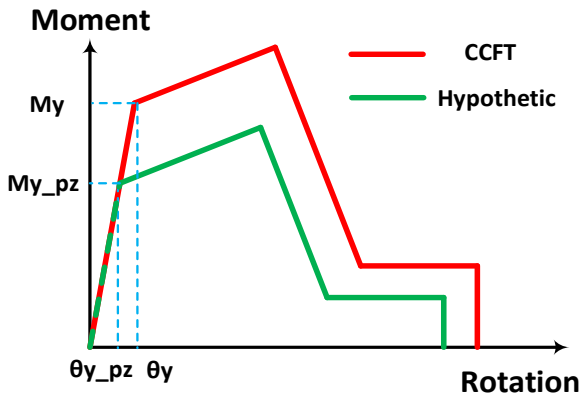

Figure 7-19: Moment rotation relationship of the hypothetical plastic hinge

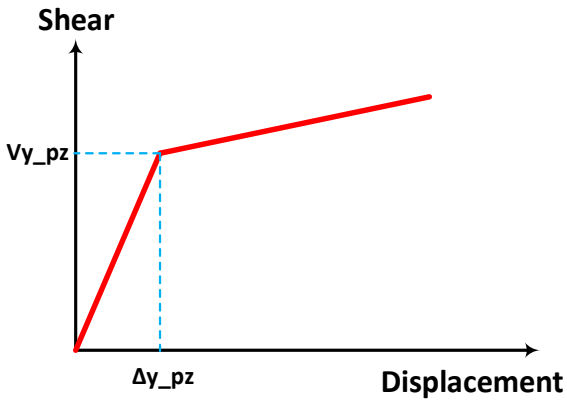

Figure 7-20: Shear deformation relationship of shear plastic hinge

7.2.4.1 Determine Shear Plastic Hinge

The rods in the new proposed connection will reduce the transverse section area of both the circular steel tube wall and the infill concrete in the panel zone. Although this reduction will decrease the axial, flexural and shear capacity of the panel zone, an exact formulation of the reduction mechanisms is not available in the open literature and is beyond the scope of this thesis. It will be assumed that the rectangular steel tube and the infill high strength grout between the two steel tubes can supply enough additional capacities to offset these reductions.

According to AISC360-10 [103], the shear strength of a composite section can be calculated by calculating the shear capacity of either the steel and an equivalent concrete cross section separately. The nominal shear strength of a circular steel tube and circular infill concrete section can be calculated by using (Eq. 7-3) and (Eq. 7-4), respectively. (Eq. 7-4) is modified form of Equation (11-4) in ACI 318-11 [104]. The benefit from axial force is not considered and the circular gross area is used instead of effective area according to commentary ACI318 - R11.2.3.

$$V_{ns} = F_{cr} \cdot (A_{gs} - A_{hs}) / 2 \qquad \textit{(Eq. 7-3)}$$

$$V_{nc} = 2\sqrt{f_c'}\left(A_{gc} - A_{hc}\right) \qquad \textit{(Eq. 7-4)}$$

where,

$$F_{cr} = \max\left(\frac{1.60E}{\sqrt{\frac{L_v}{D}}\left(\frac{D}{t}\right)^{5/4}}, \frac{0.78E}{\left(\frac{D}{t}\right)^{3/2}}\right), \text{ but should not exceed } 0.6F_y, \text{ ksi.}$$

$$L_v = (d - t_f)/2$$

$A_{gs} =$ gross cross-sectional area of circular steel tube, $in.^2$

$A_{hs} =$ reduced area of circular steel tube due to through holes, $in.^2$

$A_{gc} =$ gross cross-sectional area of circular concrete core, $in.^2$

$A_{hc} =$ reduced area of circular concrete core due to through holes, $in.^2$

$E =$ elastic stiffness of steel, ksi

$F_y =$ yield strength of circular steel tube, $in.^2$

$D =$ outside diameter of circular steel tube, in.

$t =$ wall thickness of circular steel tube, in.

$f_c' =$ specified compressive strength of concrete, psi

$d =$ depth of connecting W steel beam, in.

$t_f =$ flange thickness of connecting W steel beam, in.

If the same material and section properties of both steel and concrete as in Chapter 3 and 4 are used, the nominal shear strength of circular steel tube and infill concrete core are 1395 kips and 34.6 kips, respectively. Then the total nominal shear strength of the CCFT 24*1.375 with

through holes is $V_{y\_pz} = 1429.6$ kips. If a resistance factor, $\emptyset_v$, is equal to 0.75, the design shear capacity is equal to $\emptyset_v V_{y\_pz} = 1072.2$ kips. In the finite element analysis, the nominal value is used to define the panel zone shear plastic hinge described above.

The shear yield deformation Δ_{y_pz} is calculated by (Eq. 7-2), where θ_{y_pz} is yield rotation of the proposed hypothetical plastic hinge, as determined by (Eq. 7-1). The yield moment of the hypothetical plastic hinge M_{y_pz} are defined by (Eq. 7-5). This relationship is deduced from the 'ideal mechanism' (two plastic hinges in green circles can yield simultaneously) in Figure 7-16 (a).

$$M_{y\_pz} = \frac{V_{y\_pz} \cdot L_{pz}}{2} \qquad \textbf{(Eq. 7-5)}$$

In the 2D-SSM, the distance between the two panel zone plastic hinges L_{pz} is defined as the distance between the centerlines of beam flanges, as described in Chapter 4. For the example in this section, the beam size is W33*130, the beam depth is 33.1'' and the flange thickness is 0.855'', so the corresponding L_{pz} is 32.245''. It is not hard to determine the value of M_{y_pz} equal to 23049 k-in based on shear strength calculated above. Furthermore, as calculated in Chapter 4, the nominal yield moment strength of the CCFT 24*1.375 is 37880 k-in. and the corresponding yield rotation is 4.811×10^{-3} rad. Based on (Eq. 7-1) and (Eq. 7-2), one can calculate θ_{y_pz} and Δ_{y_pz} to be 2.927×10^{-3} rad and 0.0944 inch, respectively.

7.2.4.2 Connection Behavior with Shear Plastic Hinges

The original (Eq. 7-3) in AISC360-10 is used to calculate shear strength of round HSS cross section, according to the limit states of shear yielding and shear buckling. Although usually the panel zone of the CCFT column is believed to be strong enough to resist shear yielding, it is still worthwhile to investigate the connection behavior with possible shear yielding and buckling effects in panel zone.

After introducing shear plastic hinge into the 2D-SSM in OpenSees, the cyclic behavior of the same connection in Section 7.2.2 under the two loading histories in Figure 4-29 are shown in Figure 7-21 and Figure 7-22, respectively. The comparisons indicate that there is very small influence on the connection cyclic behavior whether shear yielding and buckling effects are involved or not in the analysis. The total connection deformation is composed of end plate rotation and panel zone rotation, and only the relationship of end plate rotation versus beam end moment is plotted in Figure 7-21 and Figure 7-22. The difference in behavior in the two figures is caused by only shear deformation.

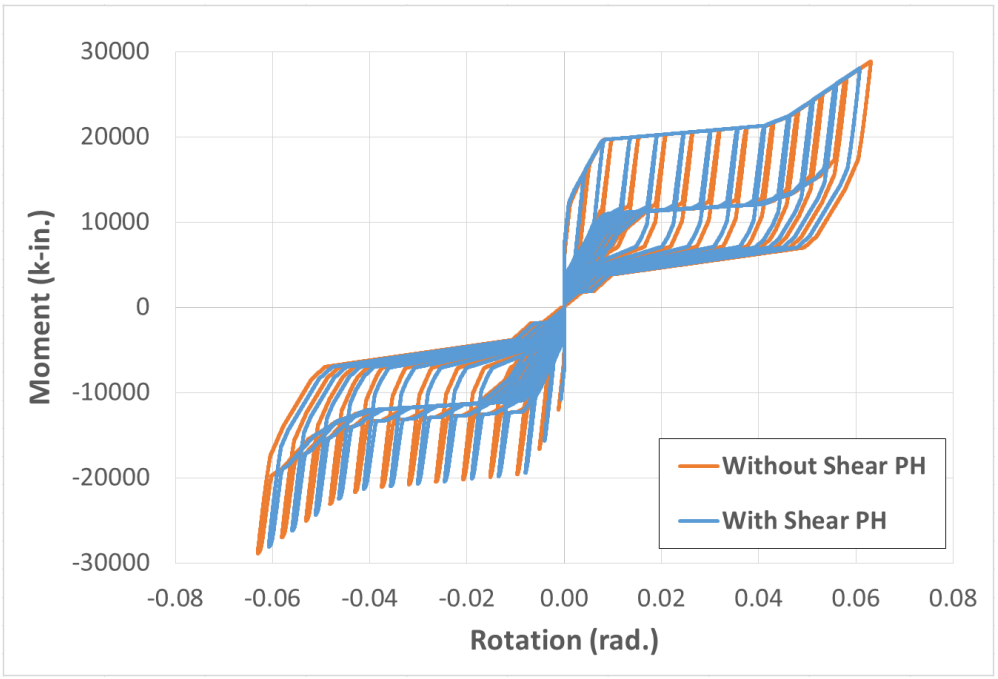

Figure 7-21: Comparison of beam end moment vs. end plate rotation under loading history 1 between OpenSees with and without plastic hinge in panel zone

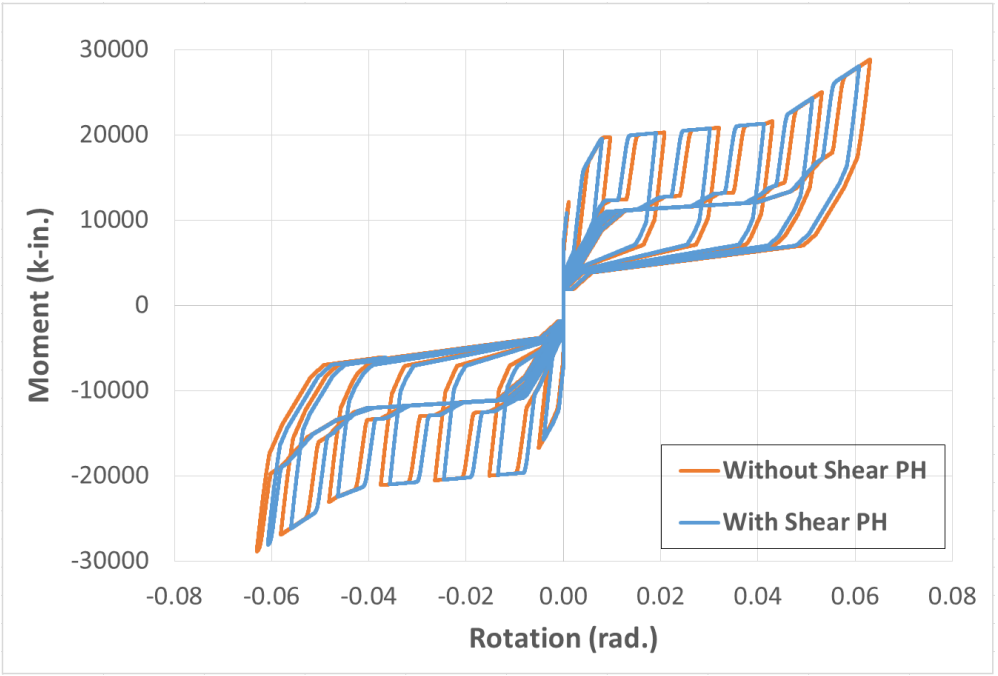

Figure 7-22: Comparison of beam end moment vs. end plate rotation under loading history 2 between OpenSees with and without plastic hinge in panel zone

In order to investigate the shear strength based on the modified AISC360-10 equations, the

same connection discussed in this section with shear plastic hinge is analyzed under monotonic loading. Three different strength levels are employed for the shear plastic hinge: (1) Full shear strength; (2) 90% of full shear strength; and (3) 80% of full shear strength. These analysis results are plotted in Figure 7-23. It is clear to see that once the shear yielding begins, the connection cannot absorb additional flexural forces from the beams determined from (AEq. B-4). From these results one can see that when the shear strength is about 80% of the full strength calculated based on the modified AISC360-10 equations, the ultimate moment capacity of the connection is roughly equal to the required design beam end moment. So the shear overstrength in panel zone can be considered as the reciprocal of 0.8, which is equal to 1.25. Since the same reduction factor is applied on both shear strength and its corresponding deformation, the elastic stiffness of the three curves in Figure 7-23 stays the same. When the RBS reaches its ultimate strength, the contribution of panel zone shear deformation to the total connection rotation is only about 0.0023 rad. Thus it is reasonable to ignore shear deformation in the panel zone for the future analysis if shear yielding is prevented by careful design.

The connection cyclic behavior with reduced shear strengths under loading history 1 are presented in Figure 7-24. If the reduced shear plastic hinge has 80% of designed strength, the ultimate capacity of the connection can still reach the required strength as expected. However, if only 50% of designed strength is used, panel zone is too weak to fully yield the connection.

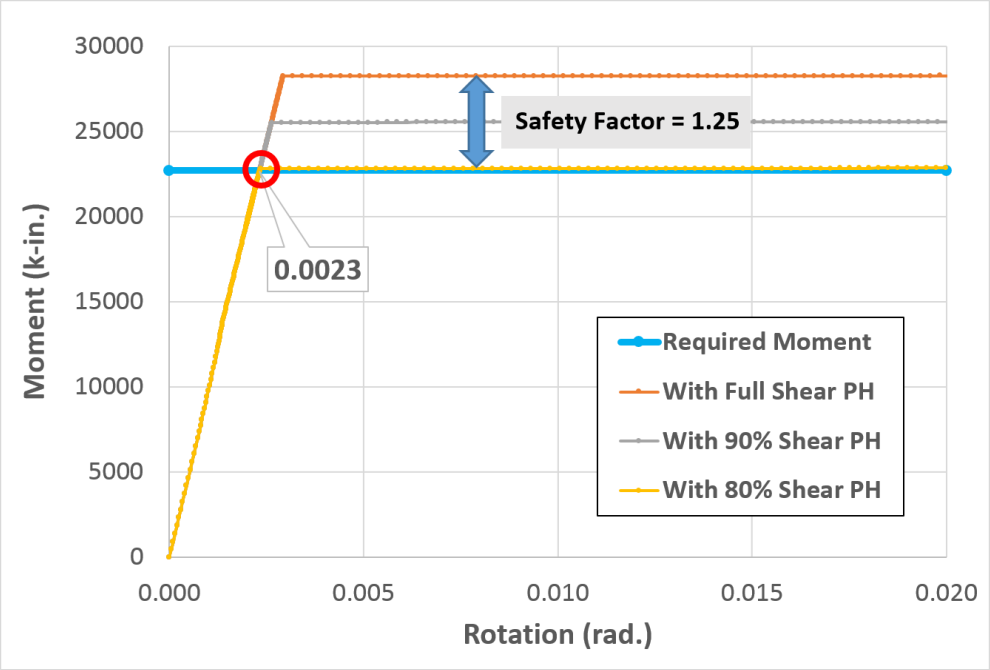

Figure 7-23: Beam bnd moment vs. panel zone rotation of connection with different panel zone shear strength level under monotonic loading

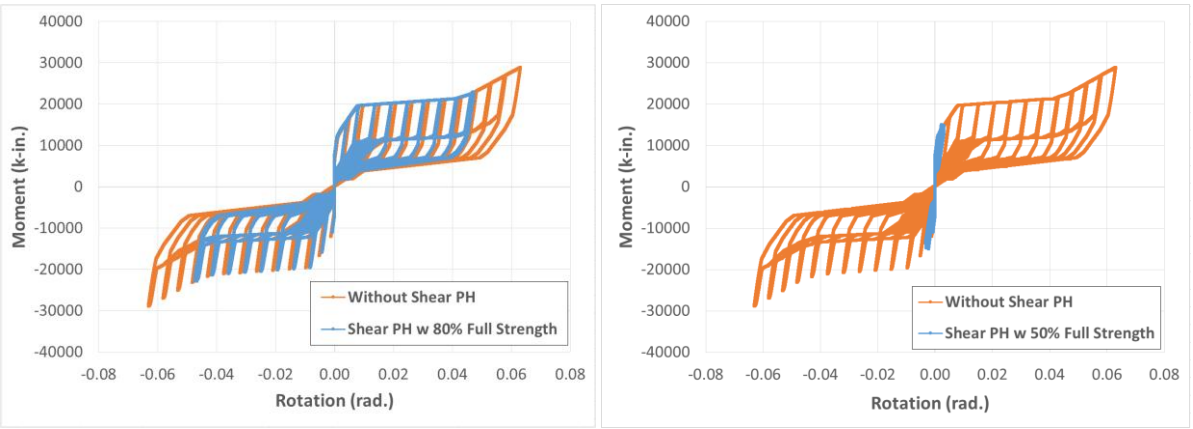

(a) 80% of full strength *(b) 50% of full strength*

Figure 7-24: Comparison of beam end moment vs. end plate rotation under loading history 1 with full and reduced shear strength plastic hinge

7.3 FE Model of CSMFs in OpenSees

The cyclic behavior of an individual PR self-centering connection in OpenSees has already been simulated successfully (see Section 7.2). In this section, the 2D-SSM will be employed to construct a similar CSMF with self-centering connections in OpenSees. This CSMF model will be used to investigate the system performance under nonlinear static pushover analysis. A "conventional" CSMF with FR moment connections, described in Section 6.2, will be used for comparisons.

In this section, several different models will be introduced to simulate the plastic hinges of the beams and columns. These models are described in advance in Table 7-3.

Table 7-3: The Descriptions of the Models for the Simulation of Beams and Columns PHs

Model Name	Descriptions

Fiber Model	• Used for both beam and column plastic hinges.
	  o Column tube wall: 160 integration points
	  o Column core: 480 integration points
	  o Steel flange: 80 integration points
	  o Steel web: 64 integration points
	  o Material models are in Table 7-4.
	• The steel yield strength is $R_y F_y$.
	• Concrete is defined with confinement effects.

Original-Column-IK Model (OCIKM)	• Defined based on the Modified-IK Model in OpenSees. • Used for column plastic hinges only. • Use the same simplified backbone curve in Figure 4-16. • "Method 1" and "Method 2" are used to modify the parameters of the CIKM based on the column plastic hinge locations.
Modified Column-IK	• Used for column plastic hinges only.

Model based on Method 1 (M1-CIKM)	• Modify the OCIKM based on Method 1.
Modified Column-IK Model based on Method 2 (M2-CIKM)	• Used for column plastic hinges only. • Modify the OCIKM based on Method 2.
Strong-Beam-IK Model (SBIKM)	• Defined based on the Modified-IK Model in OpenSees. • Used for beam plastic hinges only. • The steel yield strength is $1.1R_yF_y$. • Use the same simplified backbone curves in Figure 4-8.
Beam-IK Model (BIKM)	• Defined based on the Modified-IK Model in OpenSees. • Used for beam plastic hinges only. • The steel yield strength is R_yF_y, the same as Fiber Model. • Reduced the strengths by 1.1 for the simplified backbone curves in Figure 4-8.

7.3.1 Fiber Sections for Plastic Hinges in OpenSees

Similar assumptions as for the CSMF models in SAP2000 used for preliminary design (Section 6.2.2) are made for the system models in OpenSees, with the following additional modifications:

- Fiber sections, instead of zero-length springs, are used to define the plastic hinges in the columns and beams. This change is done by removing the zero-length springs at the center of plastic yield zones on frame members, and then assigning the corresponding fiber sections to the entire plastic yield zones. The material models and element types for both column and steel fiber sections are listed in Table 7-4.
- The equal horizontal displacement constraints between the centers of the panel zones of the moment frame and their corresponding points on the equivalent leaning columns are replaced by rigid truss elements.

Table 7-4: Material Models and Element Types of Fiber Sections for Frame PHs

Component Name	Material Model	Element Type
Concrete Core of CCFT	Concrete02	forceBeamColumn
Steel Tube of CCFT	Steel02, Fatigue	forceBeamColumn
Steel Beam	Steel02, Fatigue	forceBeamColumn

The material properties of the steel are defined as the Steel02 material model based on the stress-strain curve in Figure 4-12. The ultimate strain of steel at rupture is defined in the Fatigue material model and is set to be 0.15 for dynamic analysis. In order to consider fatigue effects in monotonic pushover analysis, a reduced ultimate strain of 0.1 is used. Confined concrete properties are employed to define the Concrete02 material model for the concrete core of the CCFT column. These confined concrete properties are calculated based on the unconfined concrete stress-strain curve in Figure 4-13; the corresponding theoretical models are described in Appendix I. The detailed procedure of applying these theoretical models to simulate the confined concrete in OpenSees has already been introduced in Section 4.2.2.

The SAP2000 models with zero-length plastic hinges should be equivalent to the OpenSees Models with fiber-section plastic hinges. The periods for the first five modes in OpenSees are presented in Table 7-5 and compared with those from SAP2000. The difference is less than 5% for both the “conventional” and self-centering systems. This shows that the OpenSees system models match well the SAP2000 model. Another point needs to be noticed is that the periods of self-centering system with PR connections are longer than those of “conventional” system

with FR connections for the OpenSees models. This was not the case in the SAP2000 results. As explained in Chapter 6, there is an inherent inaccuracy in SAP2000 because of the complex material models are used to simulate pretension and rods sliding effects.

The first two mode shapes in OpenSees are presented in Figure 7-25 and Figure 7-26 for both "conventional" and self-centering systems, respectively. Each CSMF is composed of one main frame and one leaning column system connected by a set of rigid truss members as described above.

Table 7-5: Comparison of CSMFs Periods between SAP2000 and OpenSees Models (unit: seconds)

Mode Shape	"conventional" CSMFs		Self-Centering CSMFs	
	SAP2000	OpenSees	SAP2000	OpenSees
1st	1.386	1.362	1.328	1.386
2nd	0.469	0.462	0.450	0.468
3rd	0.244	0.242	0.233	0.244
4th	0.150	0.149	0.150	0.151
5th	0.142	0.141	0.136	0.141

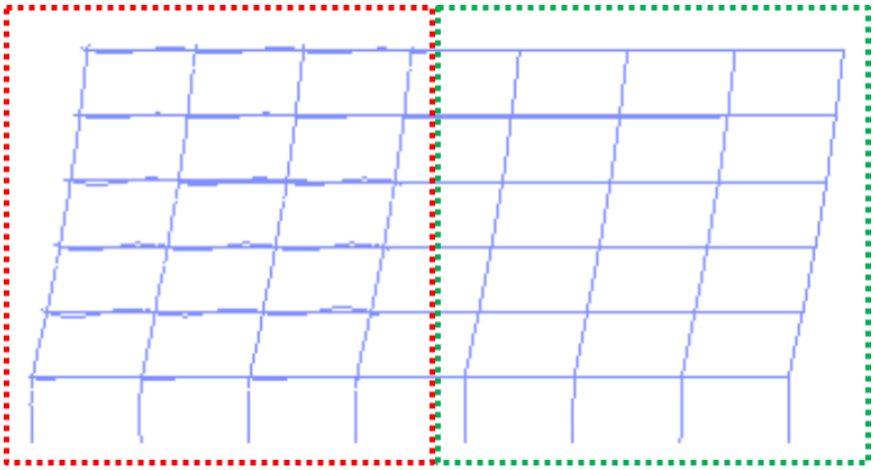

Main Frame *Leaning Column System*

Figure 7-25: 1st mode shape of th convensional CSMF in OpenSees

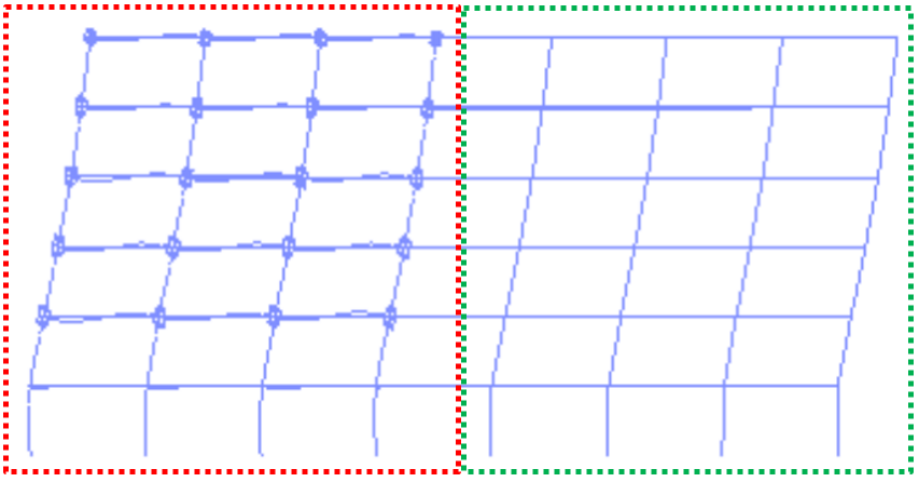

Main Frame *Leaning Column System*

Figure 7-26: 1st mode shape of the self-centering CSMF in OpenSees

7.3.2 Zero-Length Elements for Plastic Hinges in OpenSees

An alternative method to build a computational model of the CSMF in OpenSees is to use zero-length elements to replace the fiber sections used to simulate frame member plastic hinges. The same assumptions as those made for SAP2000 modes, except that the full size beam sections

are used in the RBS regions. The moment rotation relationships of the RBS regions are defined by the Strong-Beam-IK Model (SBIKM) in Table 7-3. The steel strength is defined as $1.1R_yF_y$ based on the experiments. The stiffness reduction of the RBS has already been included to a certain degree, so it is reasonable to use the full beam section with plastic hinges defined by the SBIKM.

7.3.2.1 Comparison between Fiber Sections and Zero Length Elements for Plastic Hinges

7.3.2.1.1 Original-Column-IK Model for Column Plastic Hinges

The Original-Column-IK Model (OCIKM) in Table 7-3 with zero length is used to simulate CCFT column plastic hinges, which is based on the same simplified moment rotation relationship described in Section 4.2.2. In Section 4.2.2, the Pinching4 material model is employed to simulate circular steel tube and the Concrete02 model is used for concrete core in OpenSees.

However, the Pinching4 material model is more complicated than the Steel02 and Fatigue material models. In order to reduce the computational cost, a combination of the Steel02 and Fatigue material models is adopted to define the fiber sections for the circular steel tubes. In order to check whether the previously proposed simplified moment rotation relationship for a CCFT column based on the Pinching4 model is still applicable for the CCFT column simulated by Steel02 and Fatigue models or not, the same cantilever structure in Section 4.2.2 based on

Steel02 and Fatigue models is analyzed under both monotonic and cyclic loadings in OpenSees.

The corresponding moment rotation relationships for both monotonic and cyclic loadings are compared in Figure 7-27. Comparing these two curves with the results in Figure 4-14 for the same structure and loading cases, one can easily find that the column ductility based on Steel02 and Fatigue material models for circular steel tube is less than that based on Pinching4 material model. In addition, unlike the case with the Pinching4 material model, the maximum strength of column is reached in the monotonic curve of the CCFT column based on Steel02 and Fatigue material models. These comparisons indicate that reliable results can only be obtained if the material properties are well defined.

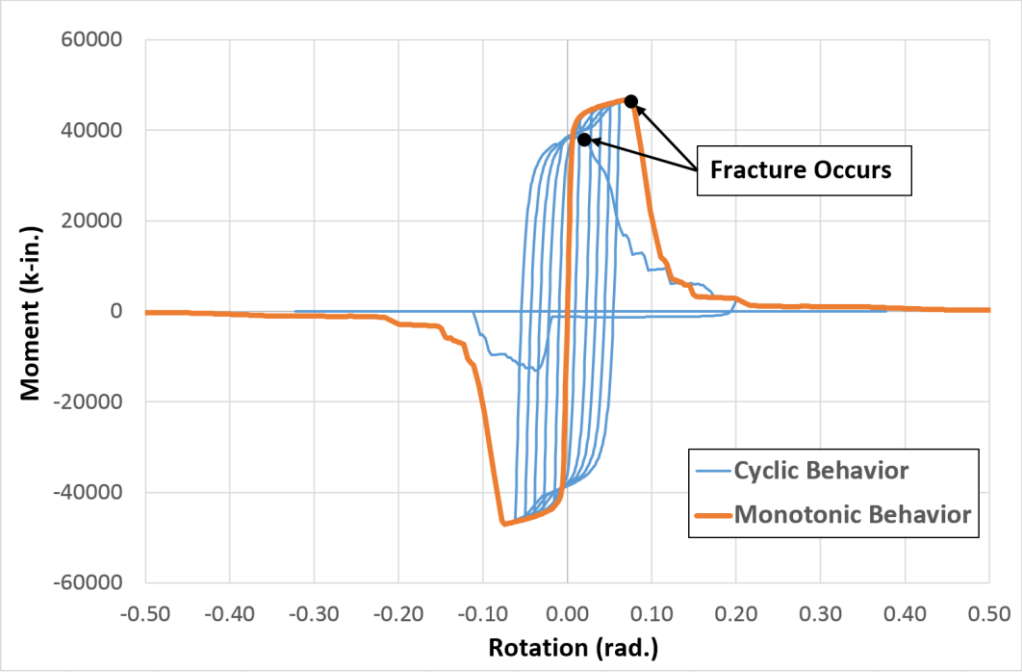

Figure 7-27: Moment rotation curve of the CCFT 24*1.375 column based on Steel02 and Fatigue models in OpenSees

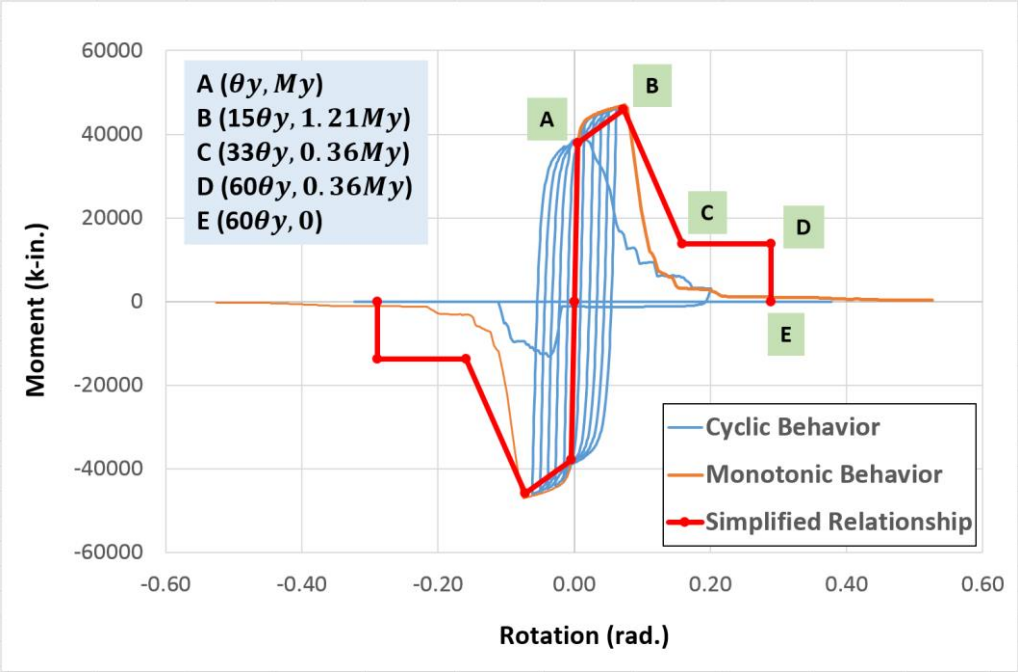

Figure 7-28: Comparison between the backbone curve of Pinching4 model and the behavior of Steel02 and Fatigue models

The simplified backbone curve in Figure 4-16 is determined based on the Pinching4 material model in OpenSees. This curve is also plotted in Figure 7-28 with the other behavior based on the Steel02 and Fatigue material models for comparison. One can see that the simplified backbone curve in Figure 7-28 matches well up to the ultimate moment capacity and rotation. However, for the post peak behavior, the simplified backbone curve supplies a slightly more gently decreasing branch, and starts to keep the strength constant once the defined remaining strength is reached until a sudden drop to zero occurs. Although they do not match each other perfectly, it is still reasonable to use the same simplified backbone curve based on Pinching4 model to approximately simulate the column plastic hinge monotonic behavior based on the Steel02 and Fatigue models.

7.3.2.1.2 Strong-Beam-IK Model for Beam Plastic Hinges

The Strong-Beam-IK Model (SBIKM) in Table 7-3 with zero length is used to simulate RBS plastic hinges, which is based on the same simplified moment rotation relationships described in Section 4.2.1 (Figure 4-8), which are determined by using a set of equations based on experimental data. In Figure 7-29, these SBIKMs are compared with both the monotonic and cyclic behavior of fiber sections of the corresponding RBS simulated in OpenSees. From these comparisons, one can find that:

- The SBIKMs have similar elastic stiffness to the corresponding fiber models.
- The SBIKMs have a much better ductility than fiber models.
- The SBIKMs can match the key deformations at yield and ultimate of the fiber models.
- Both yielding and ultimate strengths of the SBIKMs are greater than those of fiber sections. This difference of strength is presented more clearly by comparing the monotonic moment rotation curve of fiber section and that of the SBIKMs Figure 7-30. The reason for this difference is that the yielding and ultimate strengths of the SBIKMs are calculated by using $1.1R_yF_y$ as its steel yielding strength, while for the fiber model in OpenSees, the steel yielding strength is defined as R_yF_y. The additional factor 1.1 (or 1.06) is suggested by Lignos and Krawinkler to better match experimental results [39].

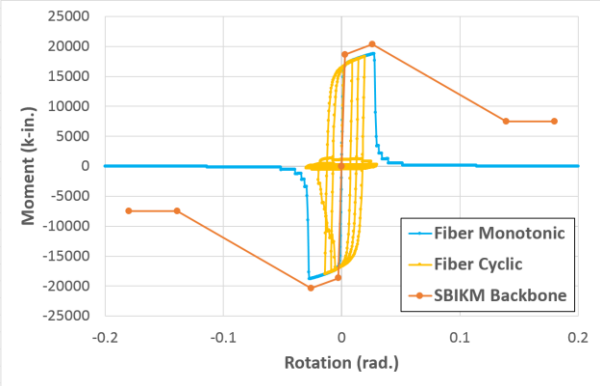

*(a) W33*130*

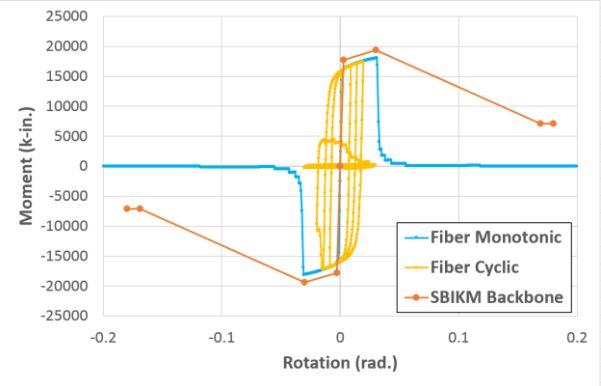

*(b) W30*124*

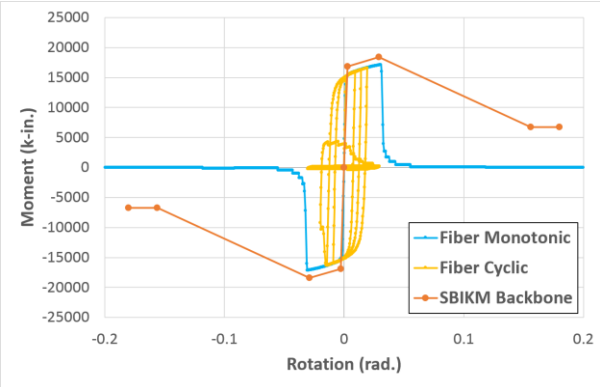

*(c) W30*116*

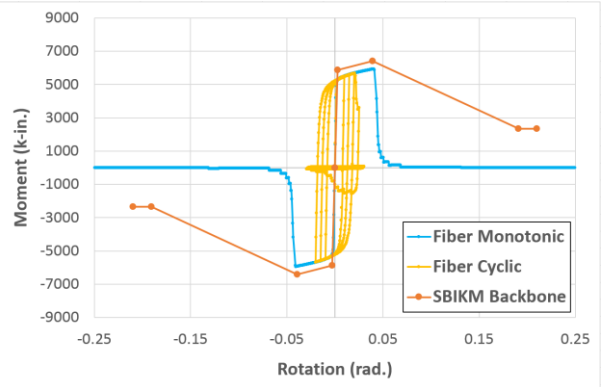

*(d) W21*57*

Figure 7-29: Comparison of the moment rotation relationships of the RBSs between Fiber Section and SBIKM

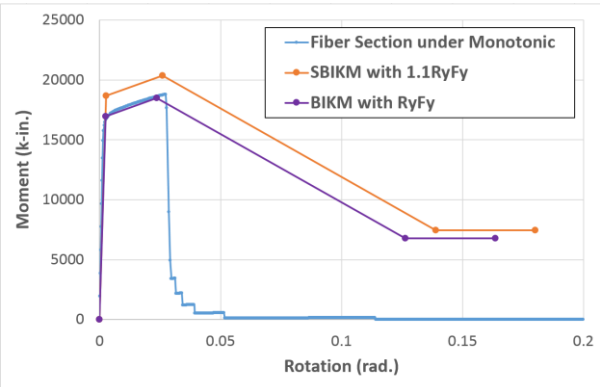

*(a) W33*130*

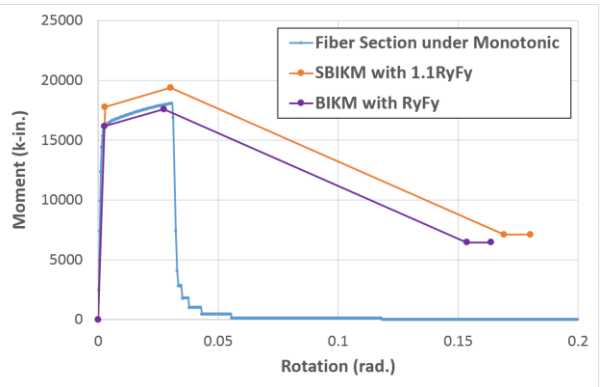

*(b) W30*124*

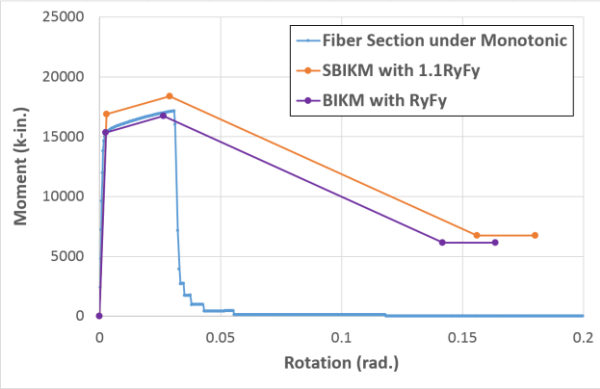

*(c) W30*116*

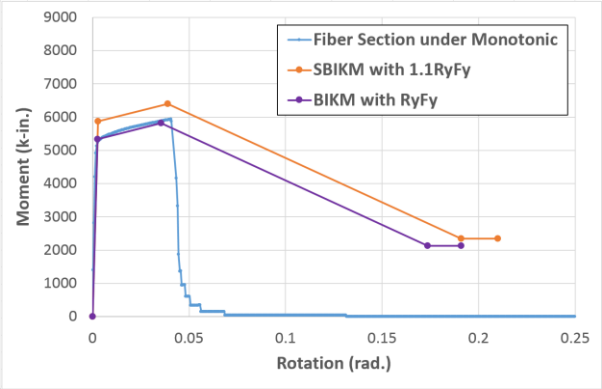

*(d) W21*57*

Figure 7-30: Comparison of the moment rotation relationship of the RBSs among Fiber Section, SBIKM and BIKM

7.3.2.1.3 Beam-IK Model for Beam Plastic Hinges

A Beam-IK Model (BIKM) in Table 7-3 is defined for each RBS to fit the corresponding fiber analysis results as shown in Figure 7-30. In order to keep the same stiffness of each segment of the SBIKM, a reduction factor of 1.1 is applied on both moment capacity and rotation for all anchor points. From the comparison between the BIKM and the fiber model, one can find that the yield and ultimate strengths of the two models are similar, although the ultimate rotation of the BIKM is slightly less than that of the fiber model. The post peak behavior needs not to be the same because their plastic hinges are simulated with different post peak decreasing stiffness and ductility.

7.3.2.2 System Periods with Zero Length Elements vs. Fiber Sections for Plastic Hinges

In Table 7-6, the first five periods of the CSMFs with zero length element for both beam and column plastic hinges are presented, and they are compared with the periods of the CSMFs

with fiber sections. One can see that the CSMFs with zero length elements are softer when compared with their counterparts based on fiber sections. One important reason for the significant decrease of system stiffness is the assumption that the location of column plastic hinges is at the middle of their plastic regions.

Table 7-6: Comparison of CSMFs Periods between Zero Length Elements and Fiber Sections for Plastic Hinges in OpenSees (unit: seconds)

Mode Shape	"Conventional" CSMFs		Self-Centering CSMFs	
	Fiber PHs	Zero Length PHs	Fiber PHs	Zero Length PHs
1st	1.362	1.521	1.386	1.466
2nd	0.462	0.513	0.468	0.499
3rd	0.242	0.269	0.244	0.263
4th	0.149	0.157	0.151	0.155
5th	0.141	0.148	0.141	0.147

The correct column deformation mechanism is presented in Figure 7-31. The total rotation at the column top end θ is divided into two parts: (1) rigid body rotation of the elastic part θ_{ph}, which is caused by the plastic deformation of column plastic region; and (2) the elastic deformation of the elastic part θ_e. The elastic deformation θ_e depends on the square of elastic column length.

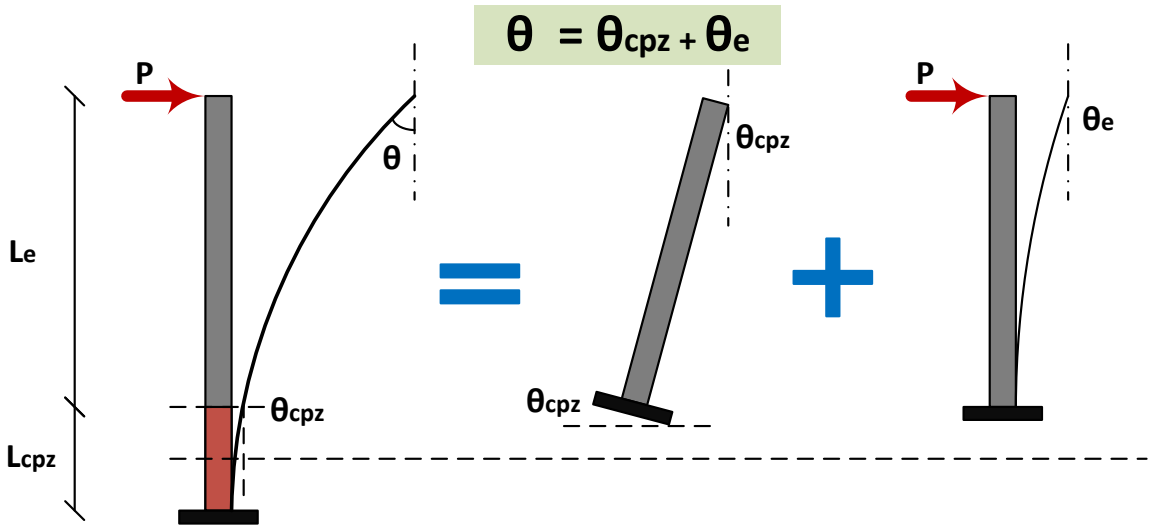

Figure 7-31: Column deformation mechanism

The location of column plastic hinge will influence the length of the column elastic part. Based on the mechanism in Figure 7-31, one can see that the column plastic hinge should be placed at the top end of the plastic region. Because the OCIKM has already been defined to include all plastic deformation of the entire plastic zone, the location of the plastic hinge will have no effect on the plastic deformation θ_{ph}. However, if the OCIKMs are located at the middle of the column plastic region, additional rotation will be introduced into the column elastic rotation θ_e because a longer elastic column length is used. In order to avoid this additional stiffness reduction, there are two methods (Method 1 and Method 2) are proposed by modifying the column plastic hinges location.

7.3.2.3 Method 1

The first method is to adopt the following two modifications:

- Move the OCIKM plastic hinge from the middle height of the plastic zone to its one end which is far away from the closest panel zone (Figure 7-32).
- Use a rigid element to connect the OCIKM and the panel zone.

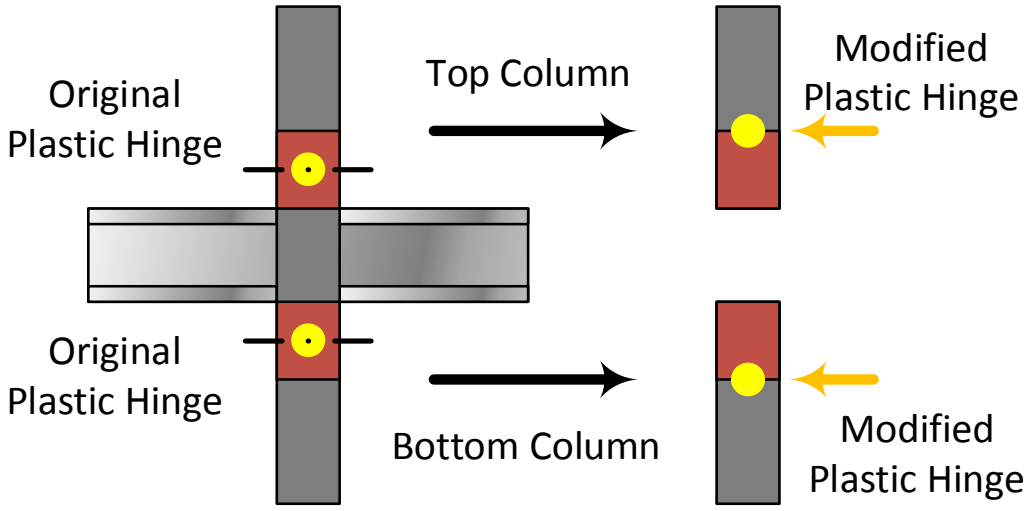

Figure 7-32: Location of column plastic hinge for "Method 1"

By applying the above two modifications, one can ensure the correct column elastic deformation. The results of the modified model are presented in Table 7-7. One can see that periods difference are largely reduced with differences being less than 5% for both "conventional" and self-centering systems, except for the first period of "conventional" CSMF which shows a 5.4% difference. According to the modified results, one can see that Method 1 is effective to obtain more accurate periods. However, it actually introduces additional lateral resisting capacity into the system.

Table 7-7: Comparison of CSMFs Periods between Zero Length Elements and Fiber Sections for Plastic Hinges in OpenSees based on Method 1 for M1-CIKMs (unit: seconds)

Mode Shape	"conventional" CSMFs		Self-Centering CSMFs	
	Fiber PHs	Zero Length PHs	Fiber PHs	Zero Length PHs
1st	1 .362	1.436	1.386	1.384
2nd	0.462	0.482	0.468	0.468
3rd	0.242	0.244	0.244	0.238
4th	0.149	0.147	0.151	0.147
5th	0.141	0.135	0.141	0.133

7.3.2.3.1 Static Pushover Analysis

There are two models that can be used to simulate beam plastic hinges: the SBIKM and the BIKM. The SBIKM has greater moment capacity, while the BIKM is more consistent with the fiber sections if strength considerations prevail.

Because the SBIKMs for RBSs are used in the design, they are also employed to execute pushover analyses in this section.

In Figure 7-33, the results of static pushover analysis for both "conventional" and self-centering CSMFs are presented. The load combination, $1.05D + 0.25L$, in Chapter 6 of FEMA-P695 is employed [11], where D is dead load and L is live load. From the comparison, four important characteristics about the system stiffness, ductility and overstrength are:

- Compared with the "conventional" CSMF, the self-centering CSMF has greater ductility. This additional deformation capacity is believed to come from self-centering connection deformation. The two systems have a similar post peak decreasing stiffness

when the story drift ratio is greater than 6%. The self-centering system possesses greater lateral resisting capacity under the same post peak roof drifts and thus has better ability to prevent collapse.

- Both systems have a similar initial stiffness. Although the modal analysis results indicate that the "conventional" CSMF has a slightly smaller initial stiffness, the pushover analyses proves that the self-centering CSMF is softer and presents plastic behavior much earlier than the "conventional" frame.
- The "conventional" CSMF has a higher ultimate lateral resistance than the self-centering system. This is because the self-centering system produces larger lateral deformations, which aggravates the second order effects and reduces its ultimate strength.

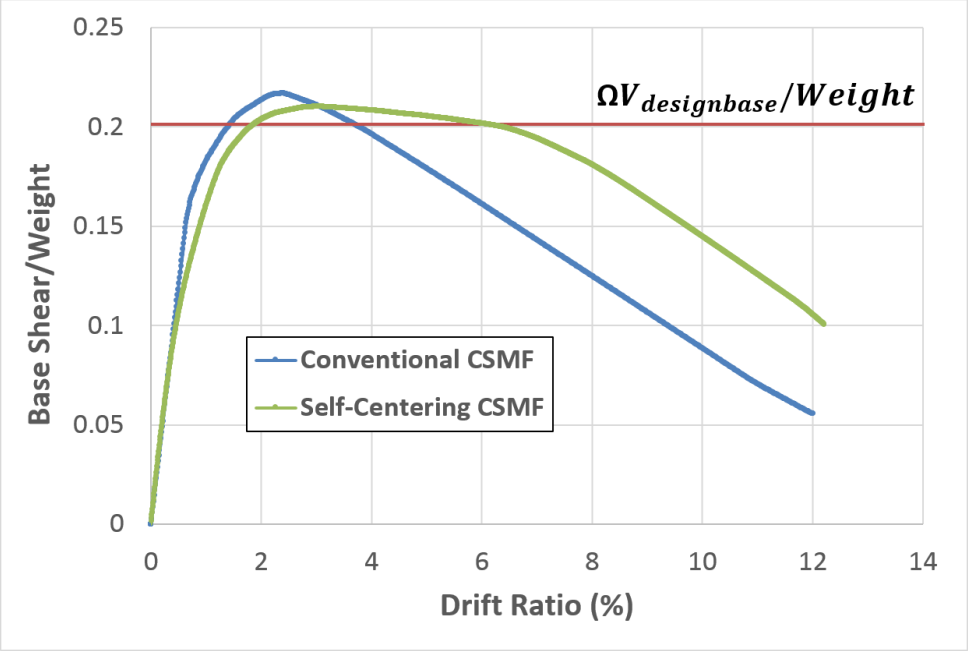

Figure 7-33: Pushover curves of the CSMFs with SBIKMs for RBSs

- Both systems possess an overstrength factor slightly greater than the assumed value of 3. This additional lateral strength capacity is believed to be brought mainly by the location of column plastic hinges. However, the columns start to yield at the end attaching to the panel zone, where the moment is largest (see the left plot in Figure 7-34). If the location of column plastic hinges are modified by 'Method 1' (see the right plot in Figure 7-34), the distance between the two plastic hinges of a column on each story are shortened by twice length of one entire column plastic zone. A greater shear is needed to get the column yield. If there is only one plastic hinge on each column (such as the columns on the first story of a moment frame), the required shear force is still increased.

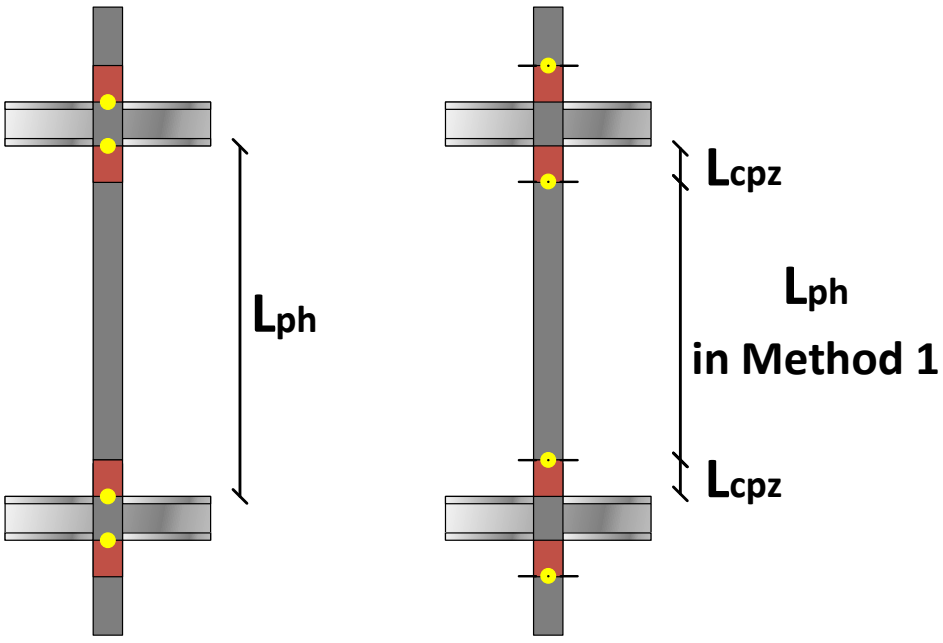

Figure 7-34: Distance between two column plastic hinges on each story for two different hinge locations

According to the description above, there is a conflict in balancing strength and stiffness when column plastic hinges are simulated by concentrated rotational elements, such as zero-length elements defined by the OCIKMs. Placing the column plastic hinges at the ends of column plastic zones away from their corresponding closest panel zones will fit the system stiffness behavior, but will bring additional shear strength into the system. Moving the hinges to the other end will fit the system's shear capacity, but will soften the system's stiffness. One way of trying to balance this conflict is to modify the properties of the OCIKM determined above based on the hinge locations.

7.3.2.3.2 Corrected Lateral Capacity for Method 1

For method 1, the plastic hinges are placed the end of the hinge zone farthest away from the panel zone (Figure 7-32). A reduction factor (RF) is applied on column flexural strengths (yielding, ultimate, and rupture strength) to offset the additional shear capacity (Figure 7-35). In order to keep the initial stiffness unchanged, the introduced RF should also be applied to the yielding deformation. The problem with this correction is that it reduces the yielding rotation and ductility of the column plastic hinges. In order to avoid influencing the total ductility of the plastic hinges much, this RF will not be applied on other plastic deformations. The RF can be determined by (Eq. 7-6).

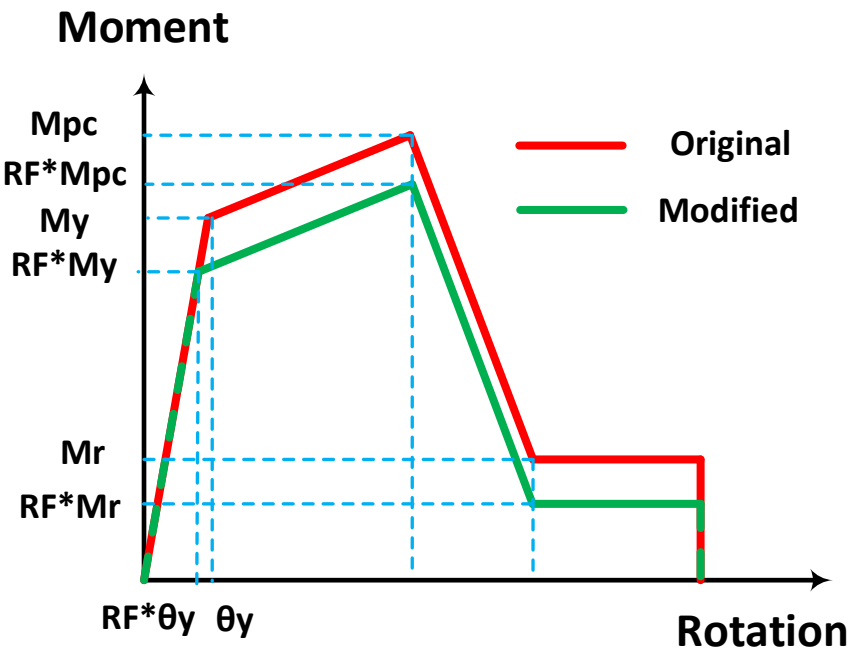

Figure 7-35: M1-CIKM for the column plastic hinge based on "Method 1"

$$RF = \left(L_{ph} + 2L_{cpz}\right) / L_{ph} \qquad \textit{(Eq. 7-6)}$$

where,

L_{ph} = the distance between two column plastic hinges (right plot in Figure 7-34), in.

L_{cpz} = the length of the column plastic zone (right plot in Figure 7-34), in.

For the CCFT 24*1.375 columns in this thesis, different RFs should be used for each story level due to fact that the height of the panel zone L_{cpz} is not the same on each story level. These story factors (SFs) are listed in Table 7-8.

Table 7-8: Reduction Factors of M1-CIKM for Each Story Level to Correct System Strength for Method 1 (unit: inch)

Story	Column Length w/o Panel Zone	L_{cpz}	L_{hp}	SF
Basement	146.25	24	98.25	1.49
Story 1	122.95	24	74.95	1.64
Story 2	121.4	24	73.40	1.65
Story 3	122.85	24	74.85	1.64
Story 4	124.4	24	76.40	1.63
Story 5	128.95	24	80.95	1.59

The pushover analysis results of both "conventional" and self-centering CSMFs with the new M1-CIKMs based on (Eq. 7-6) are shown in Figure 7-36. They are also compared with the original pushover curves based on the assumption that column plastic hinges are at the middle of the column plastic regions. From these comparisons, one can see three obvious changes.

- The ultimate base shear of both two systems is reduced by a similar magnitude. The ultimate base shear of the "conventional" CSMF matches the design target much better, while the base shear capacity of the self-centering CSMF is slightly less than the design target.
- The elastic stiffnesses of both systems remains the same, as expected.
- Both systems reach their ultimate base shears earlier. This is caused by the reduction of the yielding deformation of the column plastic hinges. Consequently, the system ductilities are also reduced.

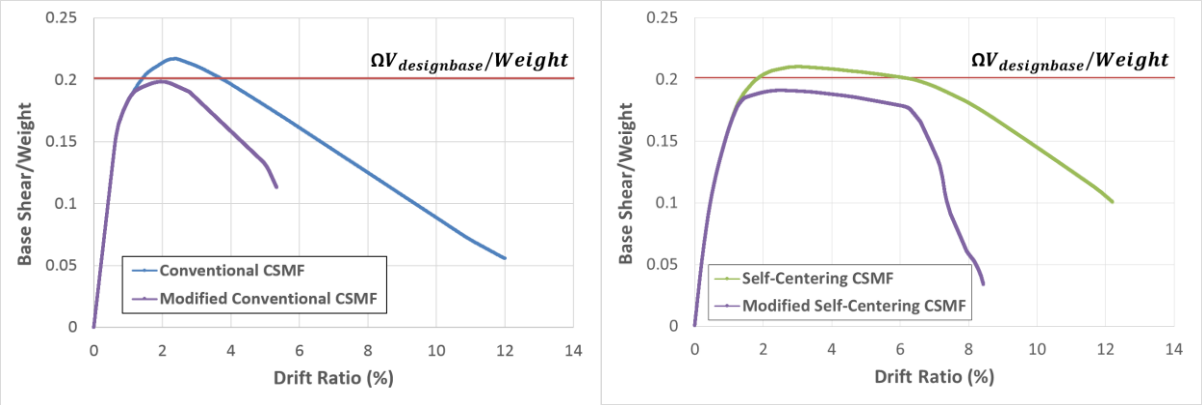

(a) "conventional" *(b) self-centering*

Figure 7-36: Pushover analyses of the CSMFs with M1-CIKMs for column PHs based on "Method 1"

7.3.2.4 Method 2

The second method to correct system stiffness is to move the concentrated column plastic hinges from the middle height of the plastic zone to its end closest to the panel zone (Figure 7-37).

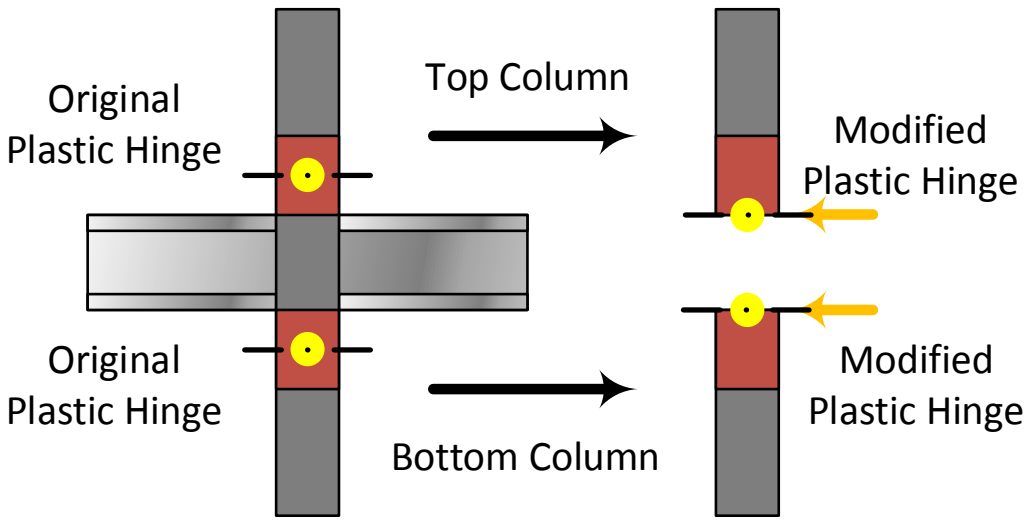

Figure 7-37: Location of the column plastic hinge for "Method 2"

Compared with Method 1, there is no need to modify the flexural strength of the column for Method 2. However, the system stiffness is reduced even more, due to the greater elastic rotation θ_e coming from a longer elastic column length (Figure 7-31). Therefore the properties of the OCIKM should still be modified for deformation to remove this softening effect.

The modification principle is explained in Figure 7-38. As explained above, the system stiffness can be properly simulated when the column plastic hinges are placed at the locations in Model 1. Assume the story drift Δ is obtained when the shear in the column is V. The relationship between Δ and yielding rotation of OCIKM θ_{yo} is expressed in the plot. When one moves the hinges to the positions in Model 2, the yielding rotation of the OCIKM is modified into θ_{ym} to obtain the same story drift Δ under the same column shear V. For both Model 1 and 2, the column plastic zones are simulated by rigid elements (black bold lines in the plots). If one removes the rigid elements in the column plastic zones, Model 2 is reduced to Model 3 (Figure 7-36), and the yielding rotation of the OCIKM is modified into θ_y. There is an additional deformation $\Delta_{elastic}$ introduced into the relationship caused by the elastic behavior of the column plastic zones.

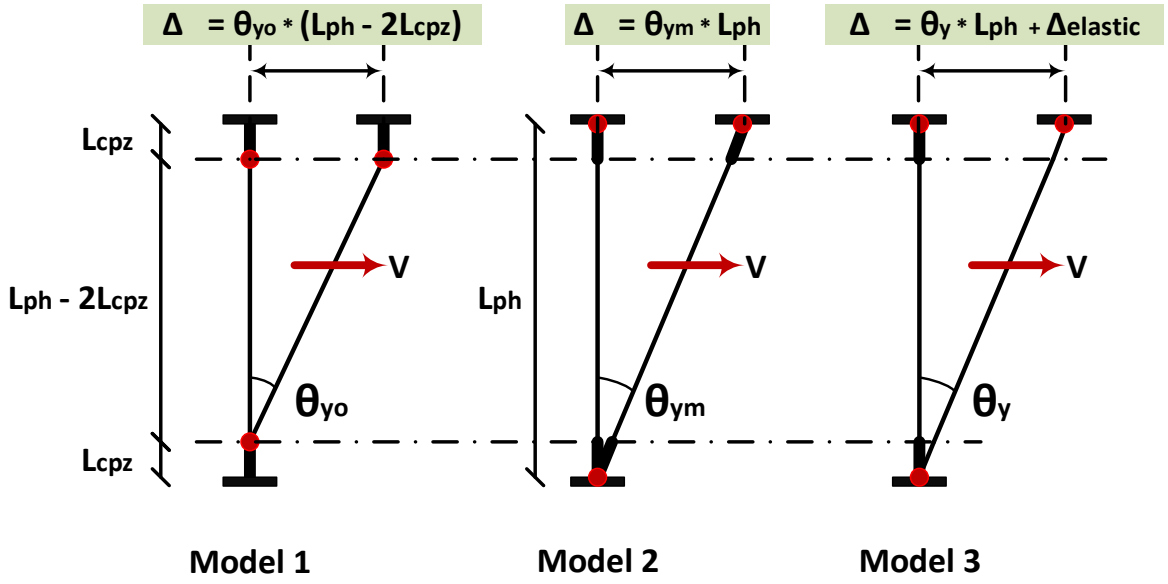

Figure 7-38: Deformation modification principle of "Method 2"

If Model 3 is adopted, the modified yielding rotation of each plastic hinge can be calculated by relationship in (Eq. 7-7) or (Eq. 7-8). The sum of the second and third terms on the right of (Eq. 7-7) is $\Delta_{elastic}$. The introduced additional rotation θ_{add} is defined by (Eq. 7-9). By applying this modification, the initial stiffnesses of the M2-CIKMs will be increased.

$$\theta_{yo} \cdot \left(L_{ph} - 2L_{cpz}\right) = \theta_{y} \cdot L_{ph} + \theta_{elastic} \cdot \left(L_{ph} - L_{cpz}\right) + 2\Delta_{cpz} \qquad \textit{(Eq. 7-7)}$$

$$\theta_{y} = \theta_{yo} \cdot \left(1 - \frac{2L_{cpz}}{L_{ph}}\right) - \theta_{elastic} \cdot \left(1 - \frac{L_{cpz}}{L_{ph}}\right) - \frac{2\Delta_{cpz}}{L_{ph}} \qquad \textit{(Eq. 7-8)}$$

$$\theta_{add} = \theta_{yo} - \theta_{y} \qquad \textit{(Eq. 7-9)}$$

$$\theta_{elastic} = \frac{V \cdot L_{cpz}^{2}}{2EI} \qquad \textit{(Eq. 7-10)}$$

$$\Delta_{cpz} = \frac{V \cdot L_{cpz}^{3}}{3EI} \qquad \textit{(Eq. 7-11)}$$

$$V = \frac{2M_c}{L_{ph}} \qquad \textbf{(Eq. 7-12)}$$

where,

θ_y = modified yielding rotation of the M2-CIKM, rad.

θ_{yo} = original yielding rotation of the M2-CIKM, rad.

L_{ph} = distance between two plastic hinges of column on each story level, in.

L_{cpz} = length of column plastic zone, in.

E = elastic Young's modulus of column, ksi.

I = moment inertia of column section, $in.^4$

M_c = yielding moment strength of column, k-in.

The important results of this method for the CCFT 24*1.375 column are presented in Table 7-9. The M2-CIKM is compared with the OCIKM in Figure 7-39. For each anchor point, the strength capacity is kept the same, while the corresponding deformation is reduced by a same amount of θ_{add}. After the M2-CIKM is applied in the system analysis, the periods of both "conventional" and self-centering CSMFs are presented in Table 7-10. Compared with the results from the systems with fiber sections, one can see that Method 2 cannot generate accurate periods when compared to Method 1. The differences for the first three modes are greater than 5% for both two systems.

Table 7-9: Modifications of the M2-CIKM Properties for Column PHs based on Method 2 (units: inch, kips, rad.)

Story	L_{ph}	L_{cpz}	θ_{yo}	V	Δ_{cpz}	$\theta_{elastic}$	θ_{y}	θ_{add}
Base	146.25	24	0.004811	518	0.010967	0.000685	0.002509	0.002302
Story 1	122.95	24	0.004811	616	0.013042	0.000815	0.002065	0.002746
Story 2	121.4	24	0.004811	624	0.013211	0.000826	0.002028	0.002783
Story 3	122.85	24	0.004811	617	0.013063	0.000816	0.002062	0.002749
Story 4	124.4	24	0.004811	609	0.012894	0.000806	0.002097	0.002714
Story 5	128.95	24	0.004811	588	0.012449	0.000778	0.002194	0.002617

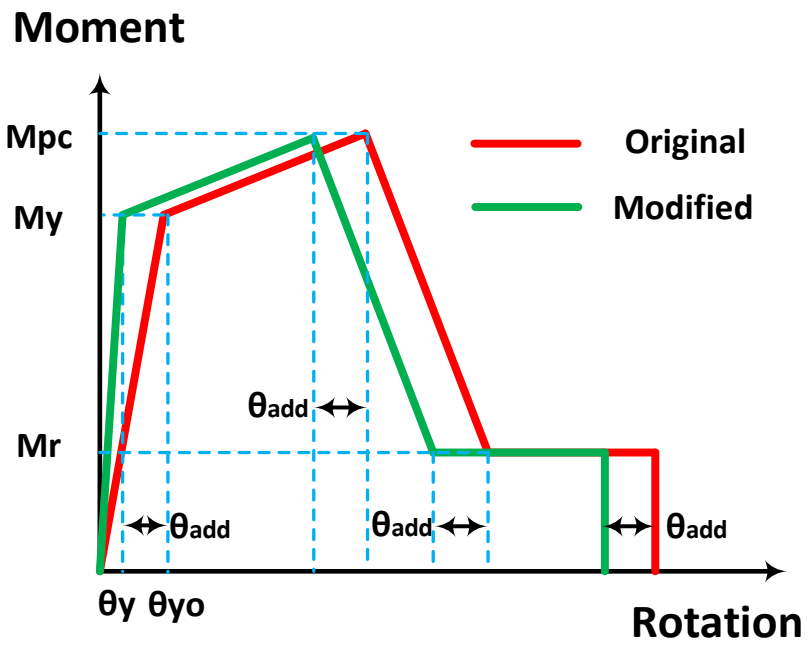

Figure 7-39: M2-CIKM for the column plastic hinge based on "Method 2"

Table 7-10: Comparison of CSMFs Periods between Zero Length Elements and Fiber Sections for Plastic Hinges in OpenSees based on Method 2 for M2-CIKMs (unit: seconds)

Mode Shape	"conventional" CSMFs		Self-Centering CSMFs	
	Fiber PHs	Zero Length PHs	Fiber PHs	Zero Length PHs
1st	1 .362	1.540	1.386	1.482
2nd	0.462	0.518	0.468	0.503

3rd	0.242	0.272	0.244	0.265
4th	0.149	0.160	0.151	0.157
5th	0.141	0.148	0.141	0.147

The pushover analyses results for both CSMFs with the M2-CIKMs for column plastic hinges are presented in Figure 7-40. The figure compares the results from the models with column plastic hinges at the panel zone end and at the middle of the column plastic regions. By relocating the column plastic hinges and using the M2-CIKMs based on Method 2, the ultimate base shear of both two CSMFs will be reduced by about 4.8%. Compared with Method 1, the reduction in strength and ductility are smaller, especially for ductility capacity.

Although the system periods from eigenvalue analyses indicate two relatively soft systems by using Method 2, the pushover results do not present obvious discrepancies. From the comparisons in Figure 7-40, one can see that for both the "conventional" and the self-centering CSMFs, the modified models have nearly the same elastic stiffness as the original systems. If the pushover analysis results are used for the evaluation of the system performance, Method 2 is better than Method 1 to solve the inherent imbalance of the system between strength and stiffness. Method 2 changes the strength capacity without appreciably affecting system ductility.

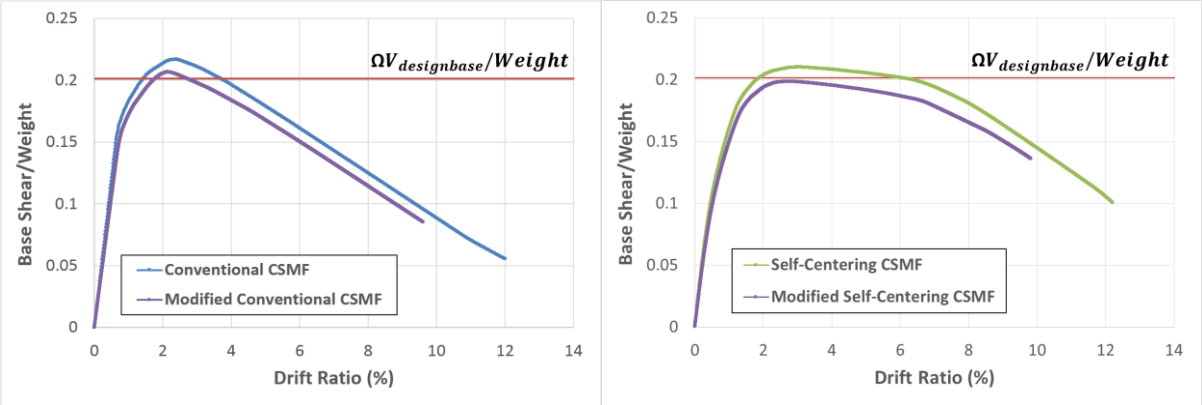

(a) "conventional" ***(b) self-centering***

Figure 7-40: Pushover Analyses of the CSMFs with M2-CIKMs based on "Method 2"

7.3.3 Pushover Analysis based on Fiber Sections vs. Zero Length Elements

As compared above, the system with concentrated column plastic hinges attaching to the closest panel zone (Method 2) is a better way to balance both system stiffness and strength. In the following analyses, Method 2 will be adopted to establish both "conventional" and self-centering CSMFs with concentrated column plastic hinges in OpenSees.

7.3.3.1 SBIKMs for Beam Plastic Hinges

In order to investigate how much difference between the system with SBIKMs, which are based on $1.1R_yF_y$ and the system with fiber sections, which is based on R_yF_y, their pushover analysis results are compared in Figure 7-41 for both "conventional" and self-centering CSMFs. From these results, one can obtain the following conclusions:

- The ultimate base shears of the systems with SBIKMs are greater, as expected. For the "conventional" CSMF, the difference of the ultimate base shear is about 8.4% while for

the self-centering system, this difference is about 5.3%.

- Besides strength, the system ductility at the peak is also different. The "conventional" CSMF with fiber sections has a greater capacity to maintain the ultimate strength with very limited reduction. However, for the "conventional" CSMF with zero length elements, an obvious strength reduction occurs immediately once the ultimate base shear is reached.
- The post peak behavior of the systems are also different (including the decreasing stiffness and total ductility), because the SBIKMs and the fiber sections have different post peak behavior as discussed in Section 7.3.2.1. The SBIKM possesses larger post peak strength and ductility, which is also reflected on the global system behaviors.
- Although both of the CSMFs with fiber sections have slightly greater stiffnesses than their counterparts with SBIKMs, the difference between them is not significant.

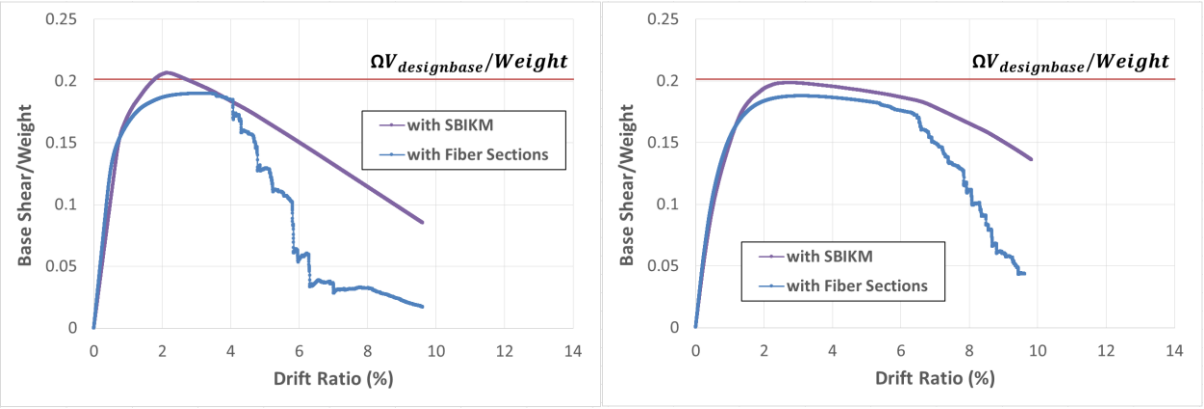

(a) "conventional" ***(b) self-centering***

Figure 7-41: Comparison of pushover analyses results of between the CSMFs with SBIKMs and Fiber Sections for beam PHs

7.3.3.2 BIKMs for Beam Plastic Hinges

If the BIKMs are used to replace the SBIKMs as beam plastic hinges, the elastic behavior and ultimate base shears are similar for both CSMFs (Figure 7-42). This indicates that using BIKMs to simulate plastic hinges of beam RBSs can provide similar behavior to those based on fiber sections at a much reduced computational cost.

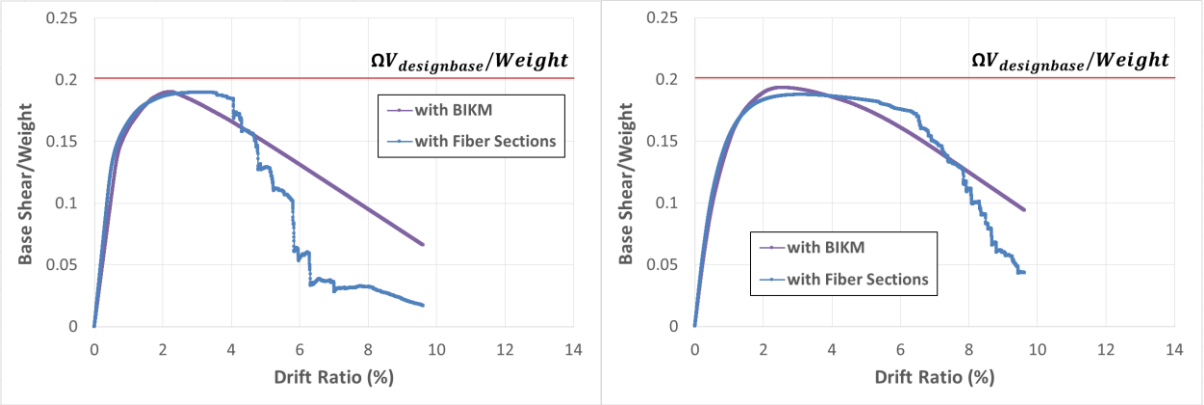

(a) "conventional" ***(b) self-centering***

Figure 7-42: Comparison of pushover analyses results of between the CSMFs with BIKMs and Fiber Sections for beam PHs

7.4 Summary and Conclusions

In this Chapter, nonlinear static pushover analyses were executed in OpenSees to check the preliminary design results of the two CSMFs from Chapter 6. A 2D simplified spring model (SSM) for the NPSCs were implemented in OpenSees based on the improved 2D-SSM in SAP2000 (Figure 4-4). In order to reduce computational cost, concentrated springs with zero

length elements in OpenSees were used to simulate both beam and column plastic hinges. Their properties should be well defined based on the results of fiber sections.

The main conclusions are:

- The cyclic behavior of 2D-SSM in OpenSees matches well that of the 2D-SSM in SAP2000 (see Section 7.2.2).
- The modified 2D-SSM in OpenSees is robust enough to simulate the connection cyclic behavior including panel zone shear yielding (see Section 7.2.4).
- The unloading stiffness of the proposed SMA model in SAP2000 depends on the pretension forces in the SMA rods (Section 7.2.2).
- The locations of concentrated plastic hinges of columns can generate significant changes on system strength and stiffness. Two methods are supplied to modify the properties of the OCIKM for column plastic hinges based on their locations (see Section 7.3.2.3 and Section 7.3.2.4).
- A new set of equations to calculate shear capacity of CCFT sections with through holes are also proposed as (Eq. 7-3) and (Eq. 7-4) in Section 7.2.4, as a modification to the existing equations in AISC360 [2] and ACI318 [104].

Chapter 8

Self-centering Performance Evaluation

In this Chapter, the system's self-centering performance will be evaluated based on the nonlinear static pushover analysis results. The pushover analysis results for both "conventional" and self-centering CSMFs are carried out based on using the zero length elements. Method 2 in Section7.3.2.4 is employed to determine the location and parameters of the column plastic hinges. In Section 8.1, the deformation mechanism of the self-centering system is explained in detail. In Section 8.2, parametric studies on the system's self-centering capacity are executed for potentially important parameters. In Section 8.3, the effects of column separation caused by the expansion behavior of the new proposed PR smart connections are discussed, and suggestions are given for separation control in design. In Section 8.4, the effects of rigid diaphragm constraints will be investigated, and a method is proposed to remove the rigid diaphragm constraints from construction perspective. In Section 8.5, conclusions in this Chapter will be summarized and the suggestions for the new proposed connection design will be discussed. Figure 8-1 and Figure 8-2 provide a visual organization chart of this Chapter and should be used as a guide.

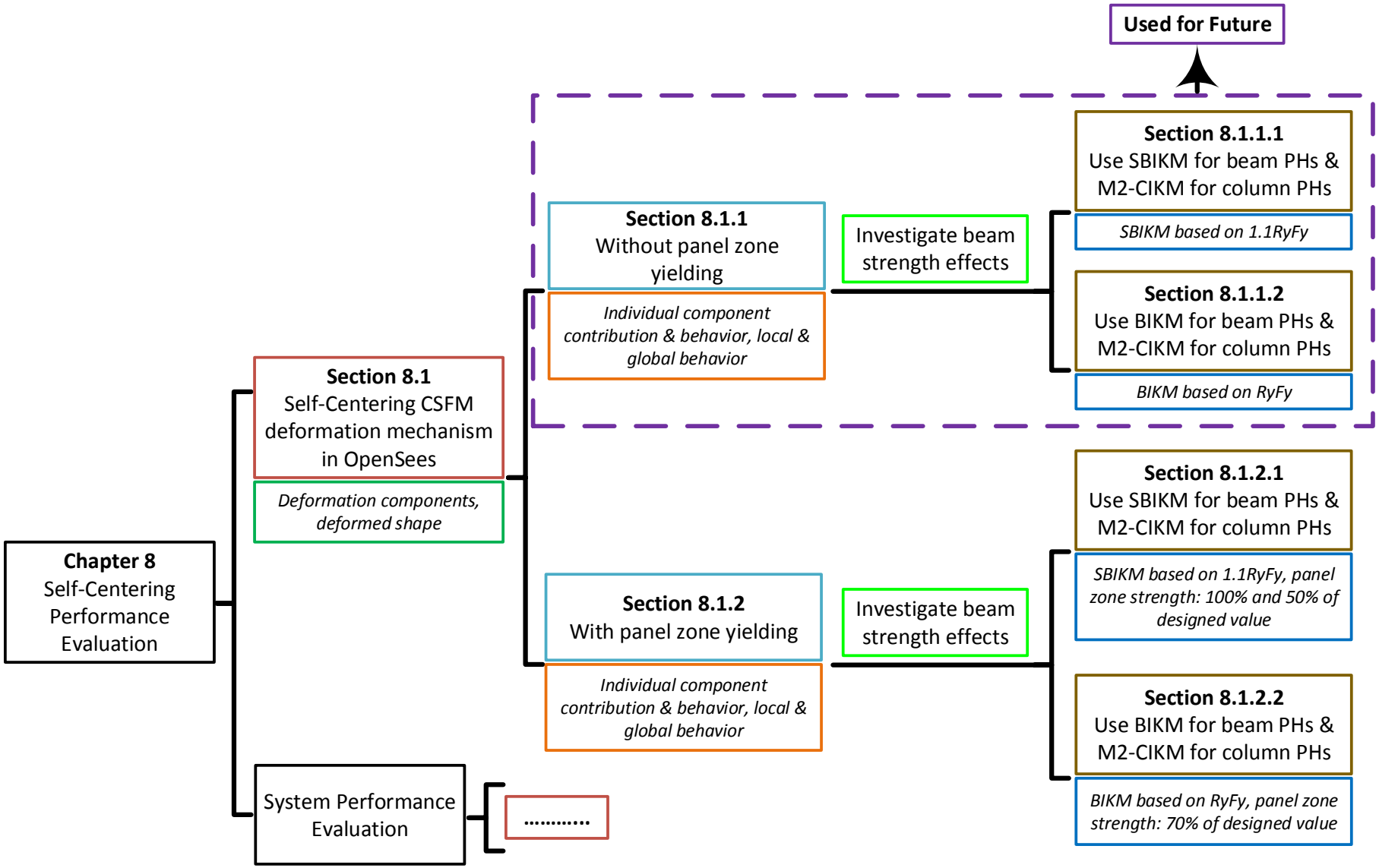

Figure 8-1: Organization of Chapter 8

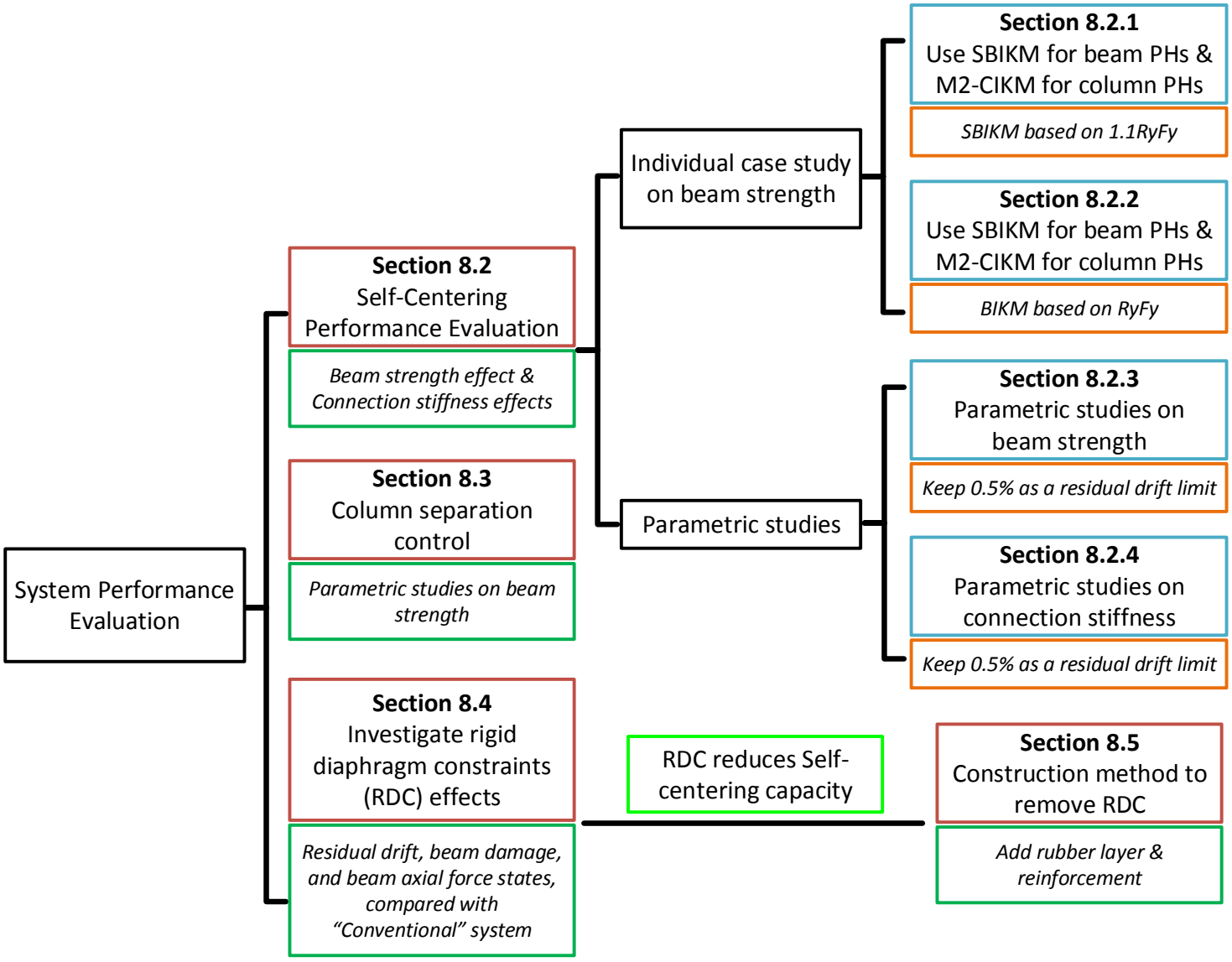

Figure 8-2: Organization of Chapter 8 (cont.)

8.1 Deformation Mechanism of the Self-centering System

The new proposed self-centering PR connection exhibits complex behavior. In this section, the deformation mechanism of the self-centering CSMF is explained by investigating the behavior of a portion of the system surrounded by the red lines in Figure 8-3. The deformation of this portion is presented in Figure 8-4. The undeformed shape is shown in gray color; the deformed shape is represented in blue color, and the rods are highlighted in red color. The deformation shown is from a pushover analysis with a target roof drift ratio of 3.6%. The amplification factor (AF) for the deformations is 10. The deformed shape of the left connection is also presented in Figure 8-5 and Figure 8-6. From Figure 8-5, it is clear to see that the two end plates will separate from the column; these separations are too small to be detected in a structure with a real deformed shape (Figure 8-6).

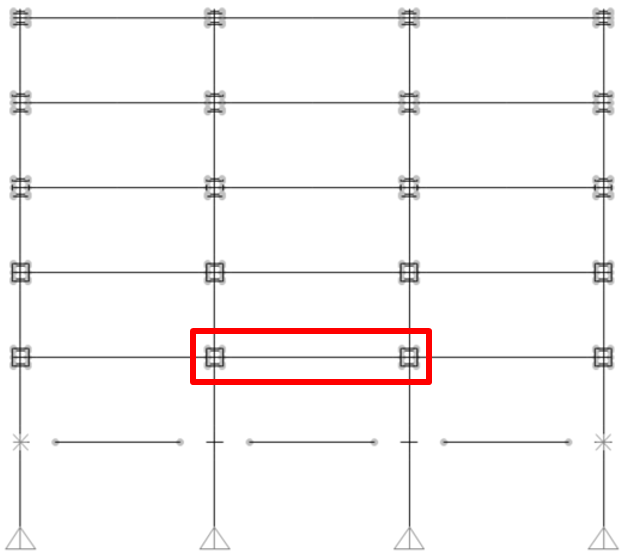

Figure 8-3: The investigated portion of the self-centering system

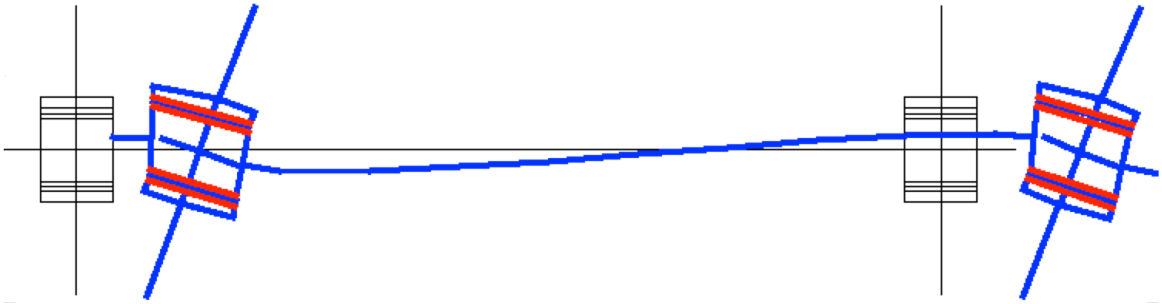

Figure 8-4: Deformation of the investigated portion in Figure 8-3

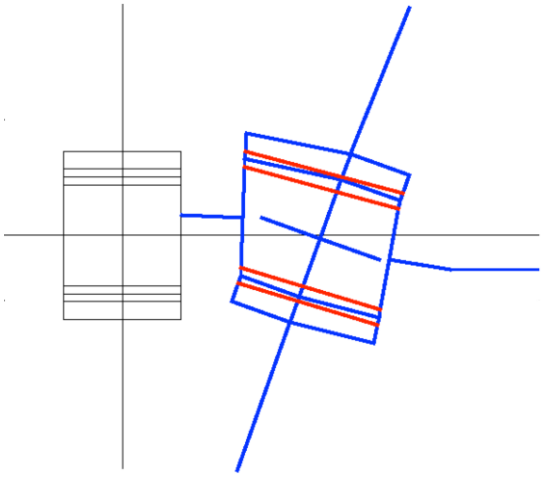

Figure 8-5: Deformed shape of the left connection in Figure 8-4 with an amplification factor of 10

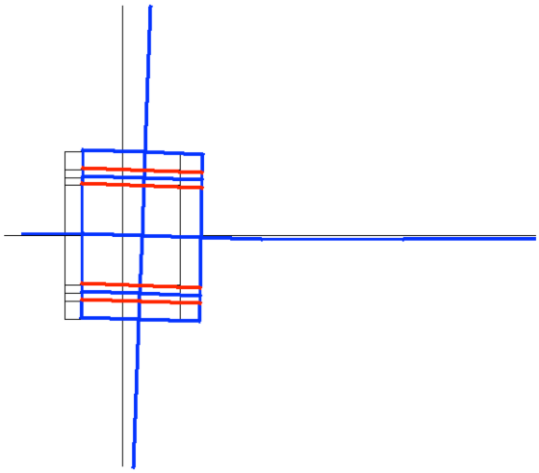

Figure 8-6: Deformed shape of the left connection in Figure 8-4 with an amplification factor of 1

From the deformed shape in Figure 8-4, a clear deformation mechanism is generated in Figure 8-7, including the panel zone shear deformation. The meaning of each character from A to N is listed as follows:

- **A & G**: node at the connection center
- **B & H**: node on the middle of end plate
- **C & J**: node of beam plastic hinge, which is connected to the connection
- **D & K**: node of beam plastic hinge, which is connected to the beam

- **E & L**: node at the top of the connection
- **F & N**: node at the bottom of the connection

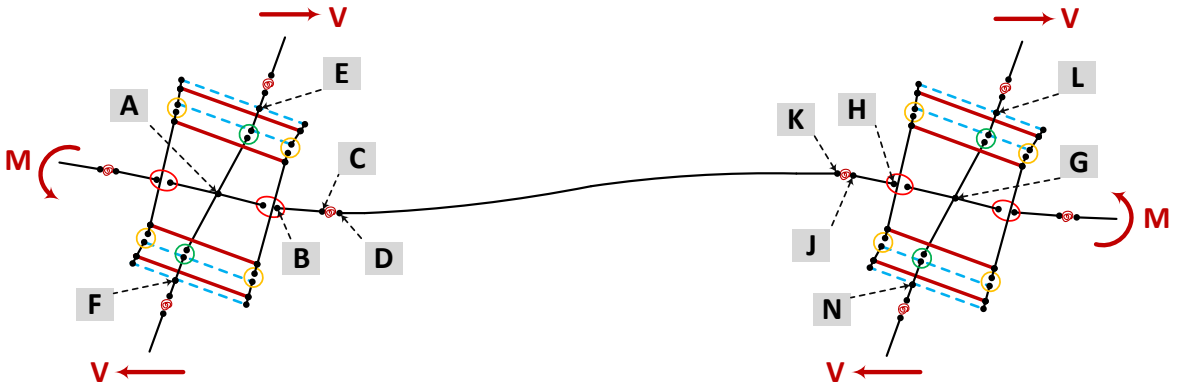

Figure 8-7: Simplified deformation mechanism of the self-centering system

According to the deformation mechanism for panel zone shear yielding in Figure 7-16, the relative rotation between both nodes E and F and nodes L and N should be insignificant. The total relative rotation between two adjacent columns can be considered as the relative rotation between nodes E and L, or between nodes F and N. They are defined as θ_{EL} and θ_{FN}. Similarly, the other relevant rotations are defined as follows:

- θ_{EA} and θ_{LG}: shear rotation of left and right panel zone
- θ_{AB} and θ_{GH}: end plate rotation relative to corresponding connection
- θ_{CD} and θ_{JK}: left and right beam plastic hinge rotation
- θ_{BC} and θ_{HJ}: rotations between segments BC and HJ
- θ_{DK}: adjusting rotation, defined as the relative angle between the two tangents at nodes D and K. The main purpose for θ_{DK} is to make the definition of the relationships

from (Eq. 8-1) and (Eq. 8-3) shown below easier.

- θ_{AG} : total relative rotation between two adjacent connections except of shear deformation, which is equal to the sum of rotations between two adjacent end plates.

It is easy to obtain a relationship among these rotations as (Eq. 8-1). Because segments BC and HJ are defined by rigid elements and have short lengths, rotations θ_{BC} and θ_{HJ} are very small, and can be ignored. The relationship in (Eq. 8-1) can be simplified into (Eq. 8-2). If shear plastic hinges in panel zone are not included in analysis, the relationship can be simplified further more as (Eq. 8-3).

$$\theta_{EL} = \theta_{EA} + \theta_{AB} + \theta_{BC} + \theta_{CD} + \theta_{DK} + \theta_{JK} + \theta_{HJ} + \theta_{GH} + \theta_{LG} \quad \textbf{(Eq. 8-1)}$$

$$\theta_{EL} = \theta_{EA} + \theta_{AB} + \theta_{CD} + \theta_{DK} + \theta_{JK} + \theta_{GH} + \theta_{LG} \quad \textbf{(Eq. 8-2)}$$

$$\theta_{EL} = \theta_{AB} + \theta_{CD} + \theta_{DK} + \theta_{JK} + \theta_{GH} \quad \textbf{(Eq. 8-3)}$$

8.1.1 Deformations without Panel Zone Plastic Hinges

At first, the shear plastic hinges in the panel zone are not included in the analysis based on the assumption that the panel zone of the CCFT column is strong enough to avoid shear yielding. It is believed that the relative strength of connection to beam plastic hinges will have great

effects on each component deformation.

8.1.1.1 SBIKMs for Beam Plastic Hinges

If the SBIKMs in Table 7-3 are used to define the beam plastic hinges, the relationship between the rotation of each component and the structure roof drift ratio is presented in Figure 8-8. The results are obtained from nonlinear static pushover analysis with a target roof drift ratio of 3.6%. Each term in Figure 8-8 is defined as follows:

- LeftPZ: left panel zone
- RightPZ: right panel zone
- AdjustingRot.: adjusting rotation θ_{DK} as defined in Section 8.1
- LeftEP: left end plate
- RightEP: right end plate
- LeftBeamPH: left beam plastic hinge
- RightBeamPH: right beam plastic hinge
- SumEPs: θ_{AG} as defined in Section 8.1
- Total: θ_{EL} as defined in Section 8.1

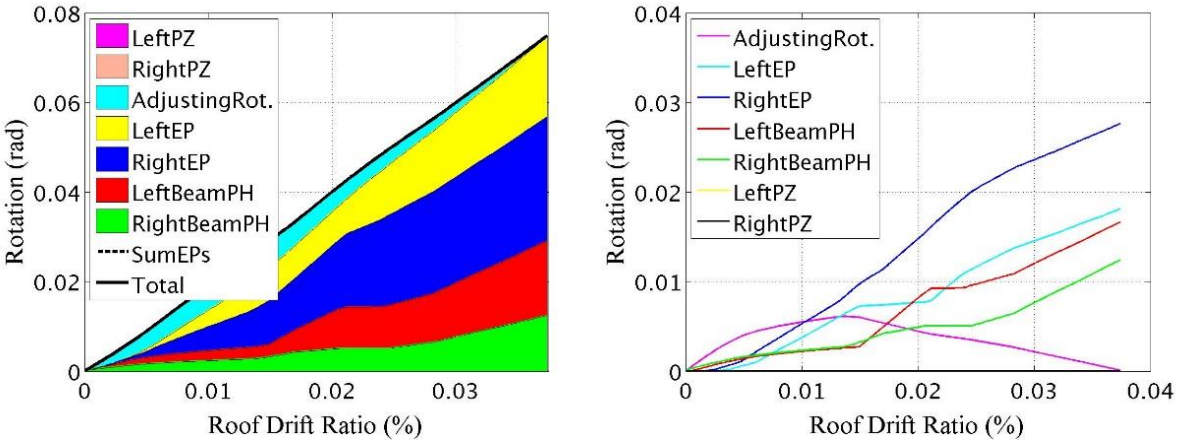

(a) Accumulative ***(b) Individual***

Figure 8-8: Rotation variation of each component of the investigated portion in Figure 8-3

From the results in Figure 8-8, the following observations can be obtained:

- Because the deformation caused by panel zone is zero, the total rotation θ_{EL} is equal to the sum of each component of rotation between the two end plates θ_{AG}.
- The two end plates rotations (θ_{AB} and θ_{GH}) and the two beam plastic hinges rotations (θ_{CD} and θ_{JK}) are not symmetrical. On the left side, the end plate rotation is much smaller than on the right. Meanwhile, the left beam plastic hinge has an obviously greater rotation compared with its counterpart on the right.
- The adjusting rotation θ_{DK} starts to increase at beginning of the load history and then decreases after the roof drift ratio reaches 1.5%. At this rotation the left beam plastic hinge begins to increase its contribution to overall deformation.

Although the curves in Figure 8-8 (b) show that the rotations of the two beam plastic hinges are not the same, they begin to yield at a similar roof drift ratio of about 1.3% (Figure 8-9). The

small difference is caused by the different initial moments from gravity loadings. However, after fully yielding, the left beam plastic hinge presents a more rapid increase of plastic deformation, although actually the left hinge yields later than the right one. The horizontal forces are applied on the system from the left to the right and the original loading direction has a great influence on the individual components' contribution. A system with PR connections presents a loading-orientation feature that causes unsymmetrical behavior in a symmetric structure.

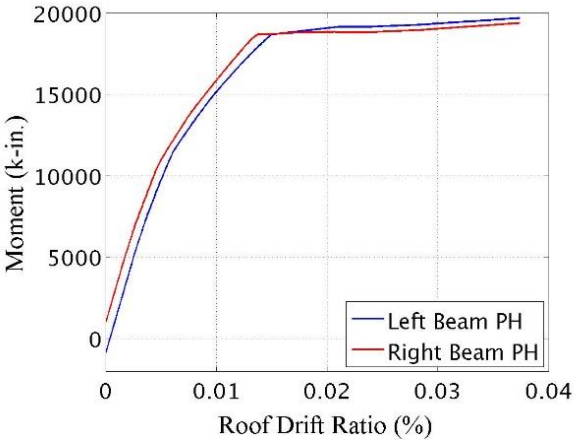

Figure 8-9: Moment vs. roof drift ratio of two beam PHs of the investigated portion in Figure 8-3

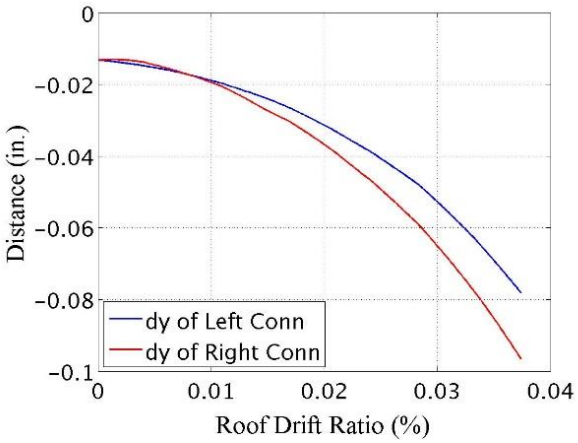

Figure 8-10: Vertical displacement vs. roof drift ratio of two connections of the investigated portion in Figure 8-3

The system loading-orientation dependence can also be observed to influence the vertical displacements of the two adjacent connections as shown in Figure 8-10. The new proposed smart PR connection will expand under beam end moments. This expansion will cause different horizontal displacements of adjacent column lines, with the horizontal displacement increasing along the loading direction. Because the loading direction is towards the right in Figure 8-4,

the right column should have greater horizontal displacement than the left one. The greater horizontal displacement also causes a greater vertical displacement at the connection center on the right column. This phenomenon also indicates that for a system with PR connections, the different horizontal displacement will bring slightly different second order effects for different columns.

Column separation is mainly caused by the separation of end plates from the connections. Due to the existing of pretension in both SMA and steel rods, end plate separation from the connection does not occur at the very beginning of loading. When beam end moments are small, the relative rotation between end plates and connection should be insignificant, the end plate will move together with the corresponding connection. For the investigated portion in Figure 8-3, the relative rotation between end plate and the connection begins when the roof drift ratio is about 0.3% as shown in Figure 8-11 by the bifurcation between the green curve and all other curves. The green curve represents the relative rotation between two connections except for the relative rotations between the end plates and the corresponding connections. As mentioned before, there is no panel zone shear deformation, so the rotation between two connections (curve 'Conn-Conn') is the same as the total rotation θ_{EL}. If the relationship in (Eq. 8-3) is applied, one can obtain that the sum of rotations of individual component between two end plates (curve 'SumEPs') is equal to the total rotation θ_{EL}. Except for the green curve, all other three curves overlap each other. The difference between the green curve and all other curves is the relative rotation between end plates and the corresponding connections. In Figure 8-12, the

separation between two adjacent column (node E and L) is also presented. Compared with Figure 8-11, it is very clear in this figure that the column separation occurs exactly when the end plate separation starts.

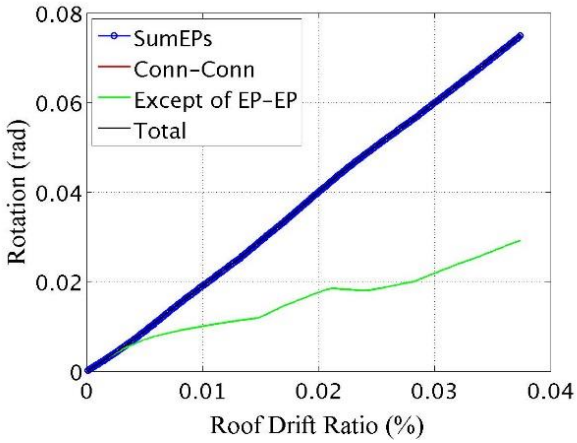

Figure 8-11: Total vs. end plate rotation of the investigated portion in Figure 8-3

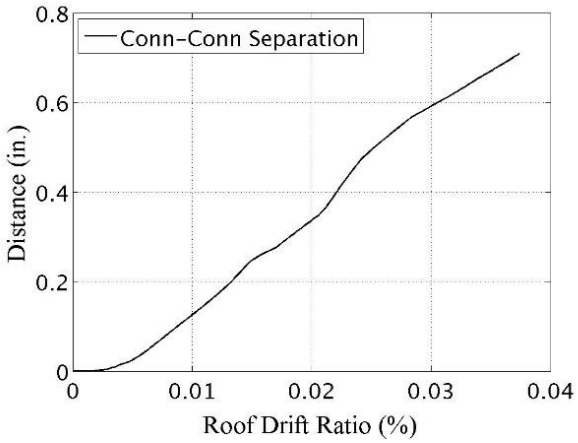

Figure 8-12: Separation of two columns of the investigated portion in Figure 8-3

In order to obtain a better understanding of the deformation mechanism in Figure 8-3, both horizontal and vertical displacements of the key nodes of the deformed shape under the roof drift ratio of 3.6% are listed in Table 8-1 and presented in Figure 8-13. The colors used in Figure 8-13 are defined as follows:

- Green: location at the rod level where the maximum rod elongation occurs
- Yellow: location at either the top or the bottom of the connection
- Pink: location at beam plastic hinge

From these results, there are several observations can be made:

- The separation of the connections at the top (nodes E and L) is 7.10 - 6.31 = 0.79 in., and slightly larger than the value of 5.24 – 4.61 = 0.63 in. at the bottom (node F and N). This is caused by the slightly different rotation between the two columns.
- The beam contraction between two plastic hinges Δ_b is only |5.73 – 5.75| = 0.02 in. For the 32 ft. beams used here, this means the axial force in the beam is small.
- The separation of the two connections Δ_{cc} can be estimated as 6.17 – 5.46 = 0.71 in., which is equal to the average of the two separations at the connections' top and bottom.
- The separation between the end plate at mid height and the connection can be estimated as a half of the maximum rod elongation. Therefore the total separation of the end plates between two columns Δ_{EP} is about (1.220 + 1.055)/2 = 1.14 in.
- The difference between Δ_{EP} and Δ_{cc} is (1.14 – 0.71) = 0.43 in., which is much greater than Δ_b of 0.02 in. In another words, the beam contraction is much smaller than the actual contraction of the spacing between two end plates. It is believed that the relative vertical displacement between two beam plastic hinges supplies the additional spacing for beam by causing beam rotation.
- The relative vertical displacement between two beam plastic hinges is (0.952 + 0.725) = 1. 68 in.

Table 8-1: Displacements of Key Nodes of the Deformed Shape in Figure 8-4 (unit: inch)

Location	Left Connection & Beam PH		Right Connection & Beam PH	
	Horizontal	Vertical	Horizontal	Vertical
Connection Top	6.31	-0.078	7.10	-0.097
Connection Bottom	4.61	-0.078	5.24	-0.096
Connection Center	5.46	-0.078	6.17	-0.097
Beam PH	5.75	-0.952	5.73	0.725
Max. Rod Elongation	***1.220***		***1.055***	

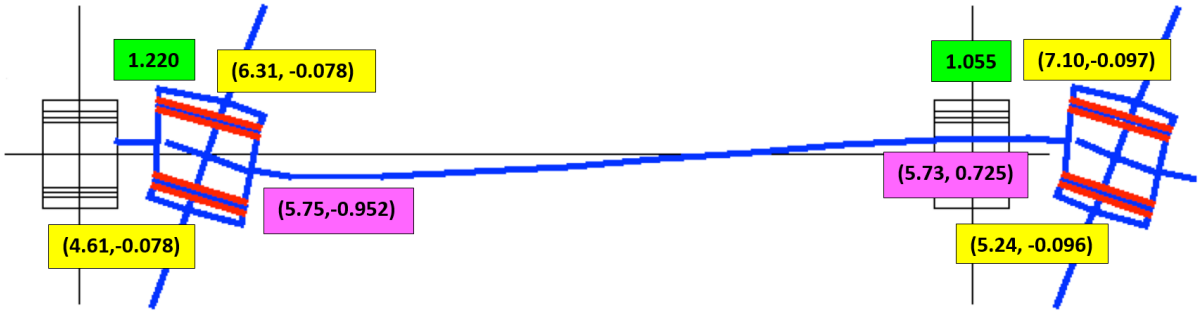

Figure 8-13: Displacements of the key nodes of the deformed shape in Figure 8-4

8.1.1.2 BIKMs for Beam Plastic Hinges

Beam strength has great influence on relative magnitudes of the components of deformation. When strong beams are used, most of the deformation will come from components within the connections; when relative weak beams are employed, most deformation will be generated by the beam deformation components. Less connection deformation also results in smaller connection expansion and column separation. In this section, BIKMs with lower strengths are used to replace the SBIKMs in the beam plastic hinges.

Both the cumulative and individual rotation of each component is plotted in Figure 8-14 for the case of a beam strength with 10% reduction from SBIKMs to BIKMs. Compared with the same results from the system with SBIKMs, the most obvious change is that the rotation of both two beam plastic hinges contribute much more, while the end plate rotations are significantly reduced. Another change is that when roof drift ratio is greater than 3%, the adjusting rotation becomes negative. Because the adjusting rotation is a calculated number, instead of a physical angle, it can be negative. This change also causes that the total rotation θ_{EL} be less than the accumulative rotation after 3% roof drift ratio. The reason of this phenomenon is that rotations in beam plastic hinges become very large.

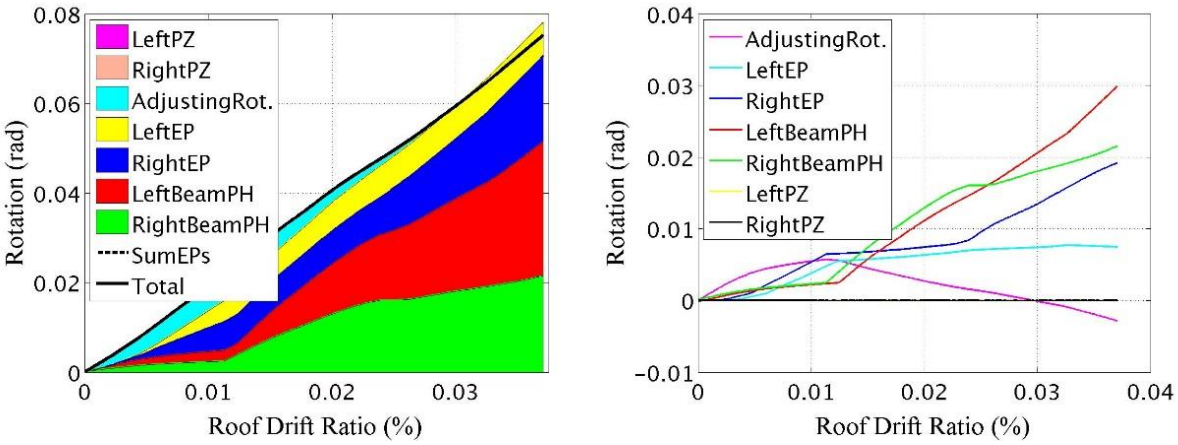

(a) Accumulative ***(b) Individual***

Figure 8-14: Rotation variation of each component with BIKMs

From Figure 8-15 one can see that the maximum rod elongation and the end plate separation from the connection are reduced by about 27% from the SBIKMs case in the previous section. The separation between the centers of the two connections is also reduced by about 38%. Thus

relative weak beam plastic hinges will help reduce the column separation. However, the reduction of column separation is much greater than the reduction of end plate separation (38% vs. 27%), while the beam contraction in axial direction remains the same at 0.02 in. This indicates that there should be a greater beam rotation coming from the vertical displacement between two beam ends to supply the additional spacing. In this case, the relative vertical displacement between the two beam plastic hinges is increased by 20%.

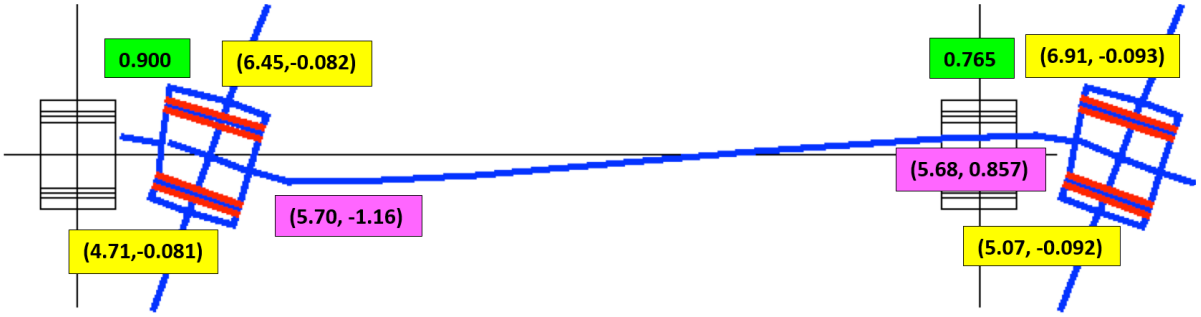

Figure 8-15: Displacements of the key nodes of the system with BIKMs

8.1.2 Deformations with Panel Zone Plastic Hinges

As shown in the simple deformation mechanism in Figure 8-7, shear yielding in the panel zone will also contribute to the total deformation. In the following subsection, we will look at the influence of the relative strength between beams and connections.

8.1.2.1 SBIKMs for Beam Plastic Hinges

When the shear strength of panel zone is determined based on (Eq. 7-3) and (Eq. 7-4), the connection cyclic behavior is nearly the same as the one without considering panel zone shear

yielding (Figure 7-21 and Figure 7-22). Their deformation components are shown in Figure 8-16. Due to the existing of shear plastic hinges, the total rotation θ_{EL} is no longer equal to the relative rotation between the two connections θ_{AG} (or curve 'SumEPs'). Compared with other components, the contribution from panel zone shear deformation is very small.

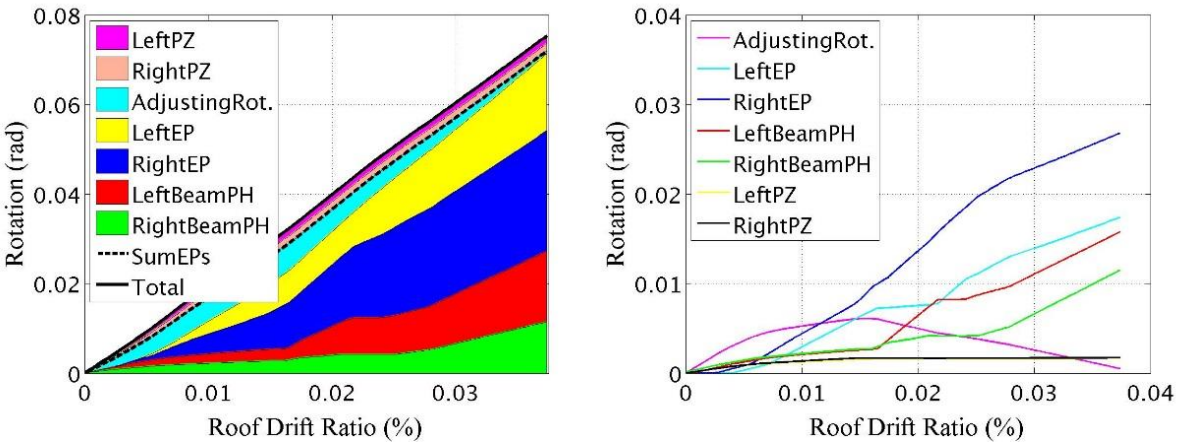

(a) Accumulative ***(b) Individual***

Figure 8-16: Rotation variation of each component with SBIKMs for beams and shear PH in panel zone

As explained in Chapter 7, the overstrength of the panel zone shear capacity is about 1.25. This means that if the panel zone shear capacity is not reduced to less than 80% of the designed value, shear yielding will not occur or have little overall influence under the ultimate beam end moments. In order to check the robustness of the proposed 2D-SSM model for shear yielding simulation, relative weak shear plastic hinges with only 50% of the designed strength are used in the following analyses. At a roof drift ratio of 3.6%, the deformed shape from the pushover analysis is shown in Figure 8-17, obvious shear deformation in the column panel zone is shown. The rotation of each component is plotted in Figure 8-18. Compared with other components,

deformation from panel zone shear yielding is much greater than others, and contributes more than 75% of total deformation. This indicates that the proposed 2D-SSM can simulate connection shear yielding very well although it does not have a cumulative shear rotation limit.

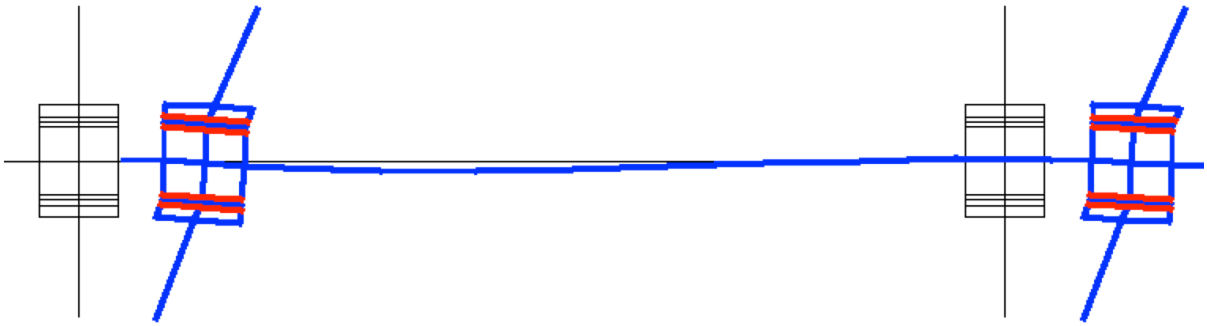

Figure 8-17: Deformation of the investigated portion in Figure 8-3 with 50% reduction of shear plastic hinges

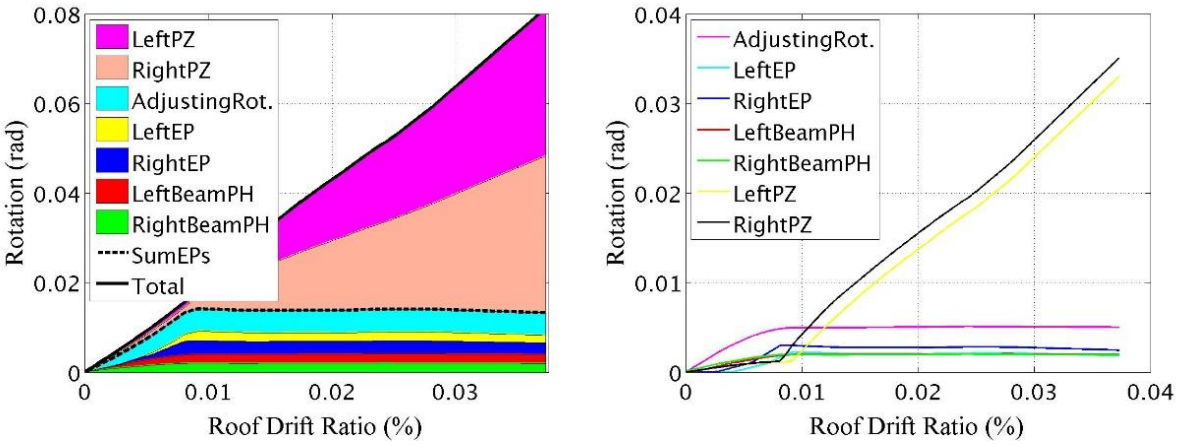

(a) Accumulative ***(b) Individual***

Figure 8-18: Rotation variation of each component with SBIKMs for beams and 50% reduction of shear PH in panel zone

8.1.2.2 BIKMs for Beam Plastic Hinges

The required panel zone shear strength is determined by the ultimate strength of the connecting

beams. For strong beams with SBIKMs, the required shear strength should be greater than 80% of the designed value as noted in the previous subsection. However, if BIKM, whose strengths are only 91% of the SBIKMs, are used for beams the required shear strength can also be reduced. For example, with the BIKMs for beams, a shear strength of panel zone of only 70% of the required design value can still sustain the ultimate beam ends moments. The results of components rotations are presented in Figure 8-19 for the 70% panel zone strength with BIKMs for the beam plastic hinges. As the beam strengths are reduced, there is much more deformation coming from the beam plastic hinges. This figure also shows that the proposed 2D-SSM can track for different strength combinations of panel zone and beam.

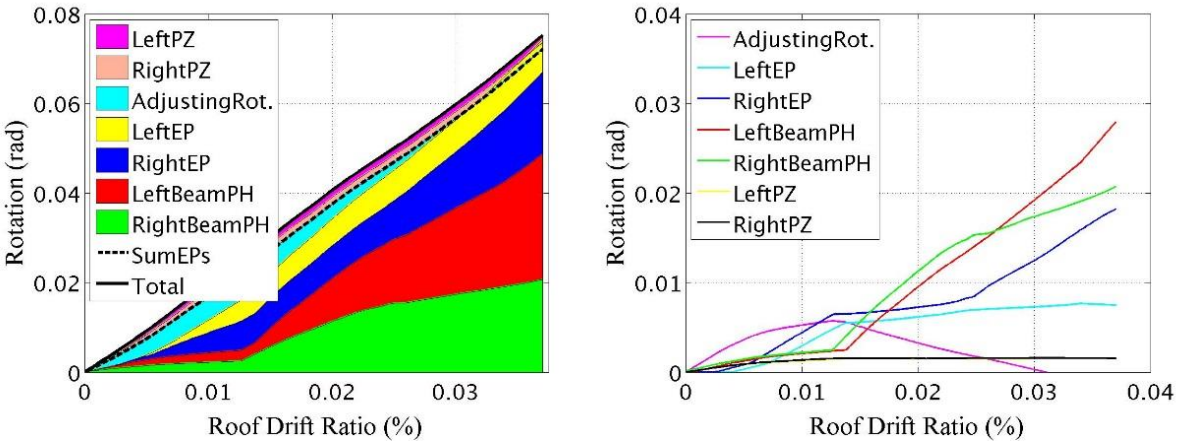

(a) Accumulative ***(b) Individual***

Figure 8-19: Rotation variation of each component with BIKMs for beams and 70% reduction of shear PH in panel zone

8.2 Self-centering Capacity

When a special moment frame undergoes large horizontal loadings, its structural components will go into plastic state and the frame will have residual deformation left after the loads are removed. If the residual deformation exceeds a relatively small value, typically taken as 0.5%, it is likely that the structure cannot be brought back into service at a reasonable economic cost.

In this thesis, in order to reduce residual deformations, a new smart PR connection with self-centering capacity is proposed. In this section, the self-centering capability of the CSMF designed in Chapter 6 will be investigated, and its behavior will be used to evaluate and improve the proposed preliminary design procedure for an individual connection.

In order to reduce the computational cost, only systems with zero length elements will be analyzed in this Chapter. The locations of column plastic hinges and their parameters for the M2-CIKM are determined based on method 2 in Section 7.3.2.4. For the beam plastic hinges, both SBIKMs and BIKMs are used. SBIKMs are determined based on a steel strength of $1.1R_yF_y$; while the BIKMs are based on R_yF_y.

8.2.1 BIKMs for Beam Plastic Hinges

Initially, BIKMs for beams are used for analyses. The CSMFs will be pushed to three target displacements (2.4%, 3.12%, and 3.6%) and then released. These results are presented in Figure

8-20 for both self-centering and "conventional" CSMFs. The corresponding residual deformations under different peak roof ratios are compared in Table 8-2. From these results, one can see that the residual roof displacements of the self-centering system are about 50% less than those of "conventional" system depending on the maximum target roof drift ratio. As the maximum target roof drift ratio increases, the self-centering effect decreases. This is because under larger deformations, the frame members will yield more, and these permanent plastic deformations in the frame members cannot be eliminated by the new proposed smart connections. Although the self-centering effect supplied by the new proposed smart connections is very obvious, it is still may not be enough to satisfy the proposed 0.5% residual drift criterion. Under a peak target roof drift ratio of only 2.4%, the level at which the ultimate base shear of the self-centering CSMF is just reached, the residual roof drift ratio still exceeds the limit of 0.5%.

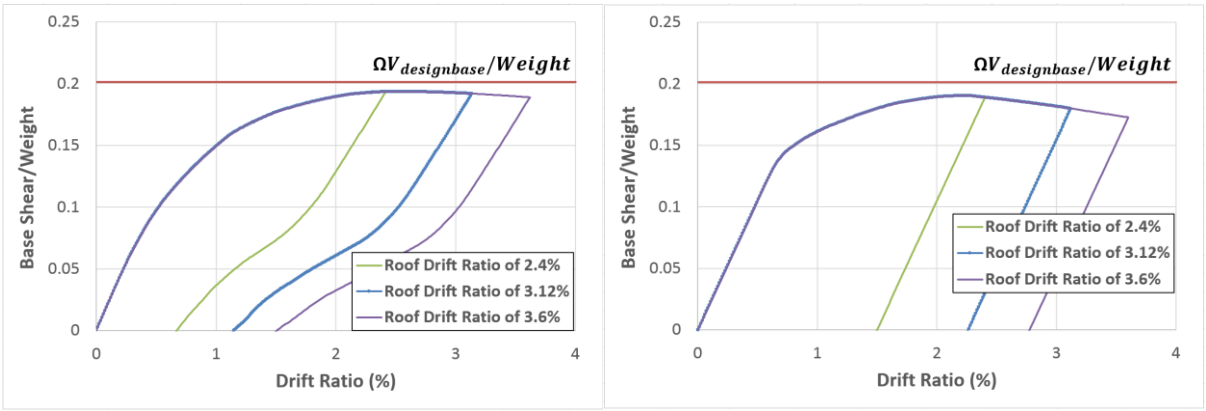

(a) Self-centering *(b) "conventional"*

Figure 8-20: Self-centering effect for the CSMFs with BIKMs for beam PHs

Table 8-2: Comparisons of Residual Roof Drift Ratio between Self-centering and "conventional" Systems with BIKMs for Beam PHs

Roof Drift Ratio	Self-Centering	"conventional"	Difference
2.4%	0.67%	1.48%	-54.7%
3.12%	1.15%	2.25%	-48.9%
3.6%	1.50%	2.77%	-45.8%

8.2.2 SBIKMs for Beam Plastic Hinges

In this section, the SBIKMs will be used for beam plastic hinges to investigate the self-centering performance if the strength ratio between connections and beams are determined based on the preliminary design procedure in Chapter 3. New pushover analyses for both self-centering and "conventional" systems are executed. The corresponding results are presented in Figure 8-21 and Table 8-3. According to the comparison between Table 8-2 and Table 8-3, one can see that with stronger beams, the greater the self-centering capacity. The system reverts to close to its initial condition (less than 0.5% residual deformation) if the roof drift ratio is less than 3.2%. This indicates that the structures connections designed based on the principles outlined in Chapter 3 can deliver excellent self-centering performance.

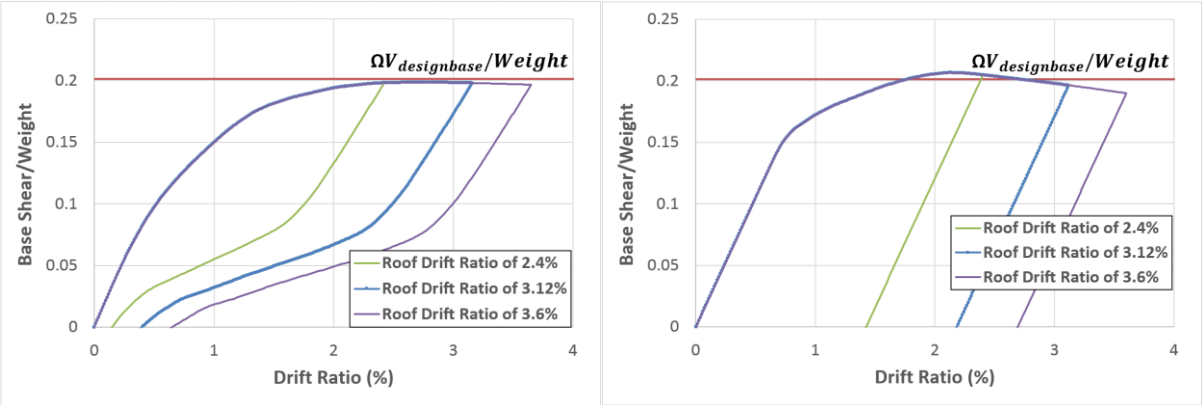

(a) Self-centering *(b) "conventional"*

Figure 8-21: Self-centering effect for the CSMFs with SBIKMs for beam PHs

Table 8-3: Comparisons of Residual Roof Drift Ratio between Self-centering and "conventional" Systems with SBIKMs for Beam PHs

Roof Drift Ratio	Self-Centering	"conventional"	Difference
2.4%	0.14%	1.42%	-90.1%
3.12%	0.39%	2.18%	-82.1%
3.6%	0.65%	2.70%	-75.9%

8.2.3 Global Strength Ratio

From the above discussion, it is clear that the strength ratio between the smart connection and its connecting beams is a very important factor for the the system's self-centering capacity. In order to investigate the sensitivity of the self-centering capacity to the strength ratio between connection and its connecting beams, different beam strengths are employed in the following studies. However, the original strength ratios between beams and their corresponding connections are not the same on all story levels. Thus, it is hard to define one baseline point for the strength ratio of all story levels. In order to simplify the discussion, no matter what the

strength ratio is for each individual story level, a global strength ratio of 1.0 is defined as a baseline for a particular CSMF. This is obtained when the new proposed smart connections are designed based on the proposed preliminary design procedure in Chapter 3. For a different global strength ratio, the strengths of connections are fixed, and all the strengths of connecting beams are increased or reduced proportionally by the same amplification factor. For example, if a global strength ratio of 1.2 is used, this means that all beam strengths are increased by 20%. A sensitivity curve for the self-centering capacity to the global strength ratio is shown in Figure 8-22. The blue line corresponds to a 0.5% residual drift.

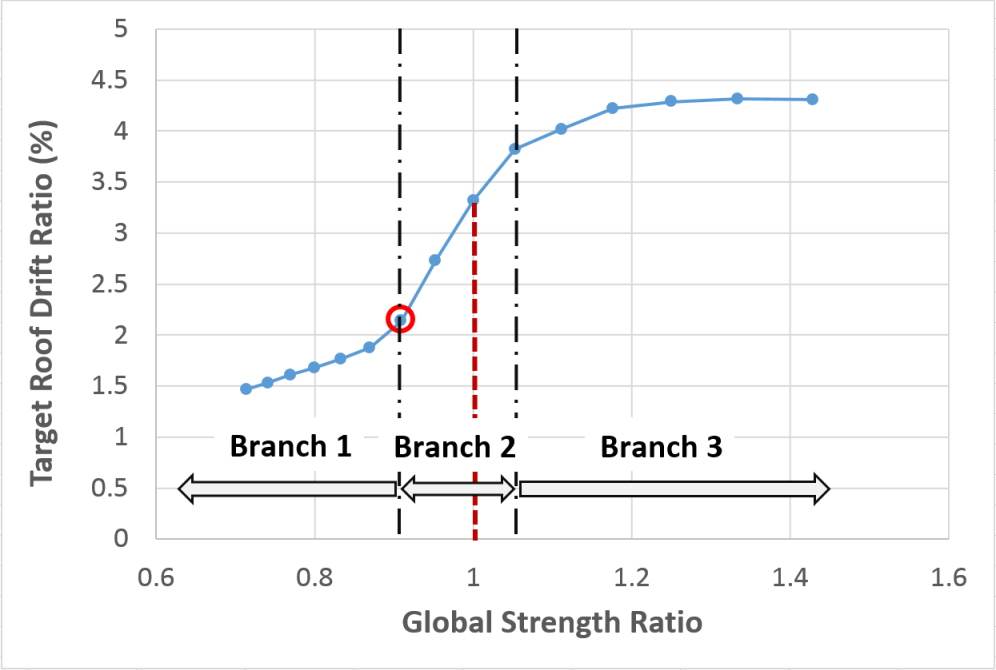

Figure 8-22: Global strength ratios vs. target roof drift ratios for 0.5% residual roof drift ratio

In this sensitivity curve, one can see three regions: (1) branch 1 with a gently increasing slope; (2) branch 2 with a steep increasing slope indicating great sensitivity in residual drift to the

ratio of beam to connection strength; and (3) branch 3 with an another shallow slope and an upper cap. The benchmark global strength ratio of 1.0 is located around two thirds along branch 2. This means that the system's self-centering capacity based on the proposed design method is very sensitive to the strength ratio between beams and corresponding smart connections. The starting point of branch 2 is highlighted by a red circle with a global strength ratio of 0.91, this is equivalent to reducing the beam strengths by 1.1. Thus a global strength ratio of the system with beams simulated by BIKMs or fiber sections can be taken as 0.91.

In branch 1, the self-centering capacity decreases almost linearly as the beam strengths are reduced. Compared with connection strength, beam strengths in branch 1 are much weaker. Much more system deformation comes from beam plastic deformation as the ratio decreases; this type of deformation cannot be fully recovered after unloading.

If the global strength ratio is greater than about 1.05, the sensitivity curve will be located along branch 3. In branch 3, the initial increasing rate of the system's self-centering capacity slows down rapidly when compared with that in branch 2. Once the capping self-centering capacity is reached when the global strength ratio is 1.15, further increases of beam strength have no obvious effects on self-centering capacity. This is because the beams are far stronger than the connections and most of the system deformation comes from the through rods. The beams will remain almost elastic, and they will not contribute any plastic deformation to the system. For the target roof drift ratio greater than 4.3%, considerable residual strain will generated in the

SMA through rods, and they will take over to control the self-centering capacity.

Thus the global strength ratio should be limited in branch 2 region or in the very beginning of branch 3 for practical design, not much greater than 1.0. The further investigation of system cyclic behavior will be discussed in Chapter 9.

8.2.4 Global Stiffness Ratio

In addition to the global strength ratio, the initial connection stiffness (ICS) may be another potential factor to influence the system's self-centering behavior. The initial stiffness is mainly dependent on the pretension force in the rods. A similar concept to the one used for considering relative beam strength effects is employed to consider stiffness effects on self-centering capacity. The benchmark for a global stiffness ratio of 1.0 is defined as the results from the preliminary design procedure in Chapter 3. As the global stiffness ratio changes, pretension in both all SMA and steel rods are increased or reduced by the same amplification factor. For example, for a global stiffness ratio of 1.2, all rods pretensions are increased by 20%. The same self-centering CSMF designed in Chapter 6 is used for the analysis.

The sensitivity curve based on different global stiffness ratios is presented in Figure 8-23. The range of rods pretension in Figure 8-23 are listed in Table 8-4 for all different story levels. The parametric study covers quite a large range of pretensions for both SMA and steel rods. From the sensitivity curve, one can see that as the global stiffness ratio decreases, the target roof drift

ratio increases slightly. This is because a relative small pretension in rods means a longer elastic range before going into tensile yielding. This, in turn, will bring less residual strains to the rods for the same roof drift ratio. However, this difference is insignificant from the practical standpoint. However, adequate rods pretension is still necessary to ensure a reasonable system initial stiffness, and to make sure there are no separations between end plates and connections under service gravity loads.

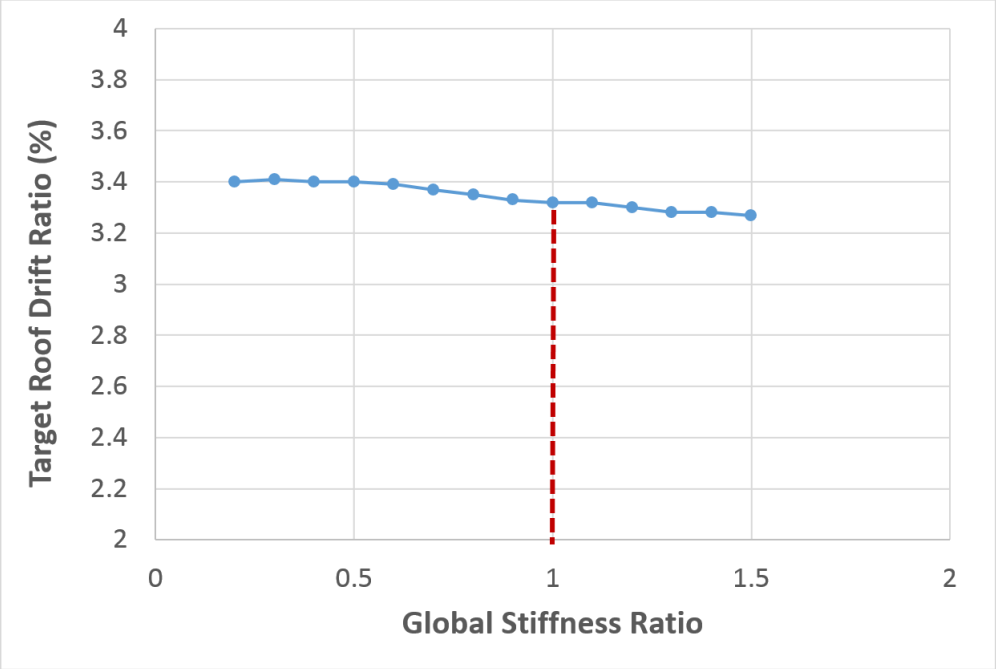

Figure 8-23: Global stiffness ratios vs. target roof drift ratios for 0.5% residual roof drift ratio

Table 8-4: Pretension Ranges of Rods based on Global Stiffness Ratio in Figure 8-23

Story Level	Global Stiffness Ratio of 0.2		Global Stiffness Ratio of 1.5	
	SMA	Steel	SMA	Steel
1	6%	10%	45%	75%
2	6%	10%	45%	75%

3	7%	10%	52.5%	75%
4	7%	10%	52.5%	75%
5	13%	10%	97.5%	75%

8.3 End Plate and Column Separation Control

Although the self-centering capacity is the main criteria to evaluate the system performance, the separation between end plates and columns is also very important. Too much separation will lead to excessive slab cracking and damage to nonstructural components. This type of damage can also have great impact on the continuity of use after an earthquake. Results from Section 8.1.1 indicate that the strength ratio between connections and beams has great influence on column separation. As this ratio increases, the column separation will decrease. In this section, two beam strength levels are used to illustrate this tendency: (1) high beam strength simulated by SBIKMs; and (2) relative low beam strength simulated by BIKMs. The connection strengths are kept the same for both two cases.

The maximum rod elongation in each connection can be used to estimate the maximum opening between the end plate and the corresponding column surface. The maximum rod elongation for all connections of the Self-Centering CSMF is presented in Table 8-5 for high beam strengths and Table 8-6 for relative low beam strengths. Based on these results, one can say that the maximum rod elongations can be significantly reduced if relative weak beams are used. The percentages of this reduction for each connection are listed in Table 8-7.

Table 8-5: Maximum Rod Elongation of Self-centering CSMF with SBIKMs for Beams (unit: inch)

Story Level	Column 1	Column 2	Column 3	Column 4
1	1.0297	1.2197	1.0549	1.1165
2	1.2219	1.3686	1.3651	***1.5005***
3	1.1993	1.2188	1.1751	1.1332
4	0.7808	0.8863	0.8390	0.8092
5	0.3044	0.3208	0.3726	0.6473

Table 8-6: Maximum Rod Elongation of Self-centering CSMF with BIKMs for Beams (unit: inch)

Story Level	Column 1	Column 2	Column 3	Column 4
1	0.7263	0.9001	0.7653	0.5145
2	0.8037	0.9520	0.9436	***1.0483***
3	0.7285	0.8673	0.8721	0.9787
4	0.4249	0.5379	0.5912	0.6916
5	0.2881	0.2850	0.3063	0.3545

Table 8-7: Percentage of Reduction of Maximum Rod Elongation by Applying Relative Weak Beams

Story Level	Column 1	Column 2	Column 3	Column 4
1	29%	26%	27%	54%
2	34%	30%	31%	30%
3	39%	29%	26%	14%
4	46%	39%	30%	15%
5	5%	11%	18%	45%

As explained by the deformation mechanism in Section 8.1, column separation is different from end plate opening. Because the diaphragm is placed on the top of the beam, an assessment of column separations based on separation at the top node of the connection will best reflect the impact of this parameter. The column separations based on the top node of the connection are presented in Table 8-8 for high beam strengths and Table 8-9 for relative low beam strengths. Comparing the results between these two tables, one can see that the column separation can be greatly reduced using lower beam strengths. The percentages of reduction of column separations are shown in Table 8-10.

Table 8-8: Column Separations of Self-centering CSMF with SBIKMs for Beams (unit: inch)

Story Level	Connection Top			Connection Bottom		
	Span 1	Span 2	Span 3	Span 1	Span 2	Span 3
1	0.9681	0.7866	0.8466	0.9255	0.6312	0.5354
2	1.0857	1.0627	1.1608	1.1289	1.0304	1.1168
3	0.9637	0.927	0.889	1.0578	0.9953	0.9472
4	0.5565	0.5351	0.5755	0.7407	0.6542	0.6118
5	0.05592	0.0452	0.2442	0.1156	0.1547	0.2987

Table 8-9: Column Separations of Self-Centering CSMF with BIKMs for Beams (unit: inch)

Story Level	Connection Top			Connection Bottom		
	Span 1	Span 2	Span 3	Span 1	Span 2	Span 3
1	0.6587	0.4631	0.3864	0.6642	0.3653	0.3696
2	0.6930	0.6343	0.7302	0.7425	0.6139	0.6474
3	0.5712	0.5518	0.6278	0.6639	0.5957	0.6471
4	0.2619	0.3003	0.3735	0.3962	0.3745	0.4031

5	0.0444	0.0206	0.0807	0.0433	0.0751	0.1293

Table 8-10: Percentage of Reduction of Column Separations by Applying Relative Weak Beams

Story Level	Connection Top			Connection Bottom		
	Span 1	Span 2	Span 3	Span 1	Span 2	Span 3
1	32%	41%	54%	28%	42%	31%
2	36%	40%	37%	34%	40%	42%
3	41%	40%	29%	37%	40%	32%
4	53%	44%	35%	47%	43%	34%
5	21%	54%	67%	63%	51%	57%

In order to determine the range of strength ratio between connection and beams in which the column separations can be reduced most effectively, different Global Strength Ratios (GSRs), as defined in Section 8.2.3, are employed to investigate column separations. In Figure 8-24, relationships between the maximum column separation of the whole self-centering CSMF and the roof drift ratio are plotted for different GSRs. It is very clear to see that when the GSR changes between 0.8 and 1.0, a slight change of GSR will cause a measurable increase of column separation once the roof drift ratio is greater than 1.2%. So the most effective range of GSR to control column separation is from 0.8 to 1.0.

For a GSR equal to 1.0, the beam strengths are the same as for the SBIKMs; for a GSR equal to 0.9, the beam strengths are nearly the same as BIKMs. This indicates that if the connections are designed based on the preliminary design procedure given in Chapter 3, the system will be in the most inefficient range for column separation. However, the relationship in Figure 8-22

also shows that the system with a GSR equal to1.0 is also in a sensitive range of system's self-centering capacity. A slight reduction of GSR will also cause an obvious reduction of self-centering capacity. Thus great care has to be exercised to obtain an optimal balance between the self-centering capacity and column separation.

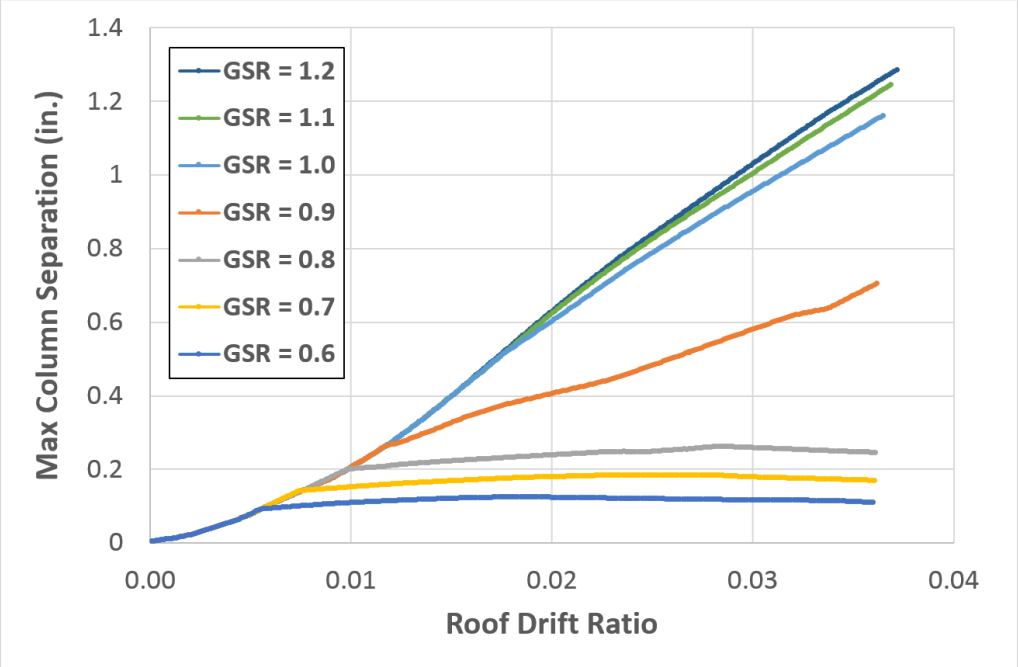

Figure 8-24: Maximum column separation vs. roof drift ratio with different global strength ratios

8.4 Rigid Diaphragm Constraints

The deformation mechanism of the new proposed connection requires the elongation of rods and separation of end plates from columns. If rigid diaphragm constraints are used in the analysis, the connection deformation will be restricted. In order to investigate the influence of

the assumption of rigid diaphragms, static pushover analyses of both self-centering and "conventional" CSMFs with rigid diaphragm constraints are executed for the same loading cases as in Figure 8-21. For the two systems, SBIKMs are used for the beams plastic hinges. The results are presented in Figure 8-25 and Table 8-11. From these results, one can see that with rigid diaphragm constraints, the behavior of the self-centering and "conventional" systems are not very different. Compared with Figure 8-21, the ultimate base shear of the self-centering system is increased about 5.5%; however, its self-centering capacity almost disappears. On the other hand, the effects from adding rigid diaphragm constraints on the "conventional" system's behavior are insignificant.

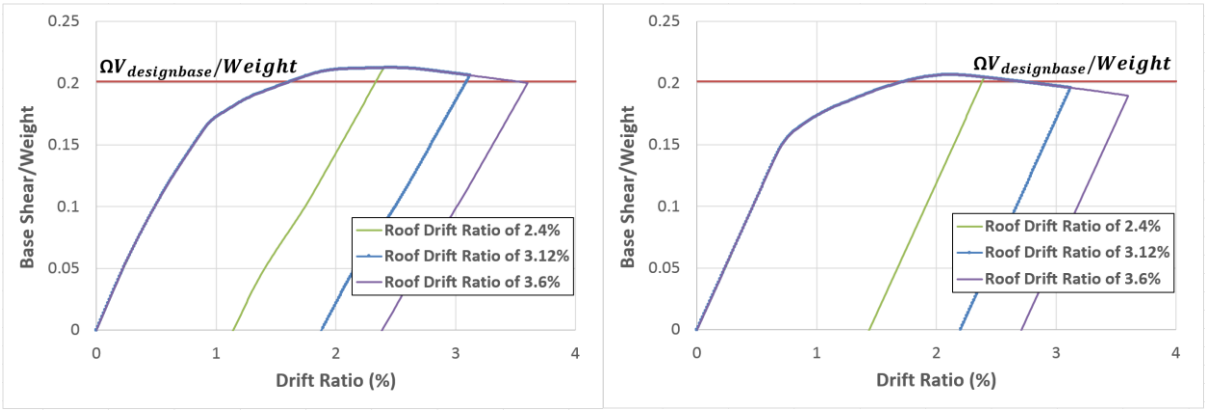

(a) Self-centering ***(b) "conventional"***

Figure 8-25: Pushover analyses of two systems with rigid diphragm constraints

Table 8-11: Influence of Rigid Diaphragm Constriants (RDC) on Residual Roof Drift Ratio

Roof Drift Ratio	Self-Centering			"conventional"		
	RDC	w/o RDC	Different	RDC	w/o RDC	Different
2.4%	1.15%	0.14%	721%	1.43%	1.42%	0.7%
3.12%	1.87%	0.39%	379%	2.19%	2.18%	0.46%

3.6%	2.38%	0.65%	266%	2.71%	2.70%	0.37%

It is believed that the use of rigid diaphragm constraints will cause greater plastic deformation of the beam plastic hinges in the self-centering system. The peak beam plastic rotations for the self-centering system are given in Table 8-12, and the ratios between the self-centering systems with and without rigid diaphragm constraints are given in Table 8-13 at the target roof drift ratio of 3.6%. From the results in Table 8-13, one can see that for the self-centering system most of these ratios are greater than 1.0, indicating much greater plastic behavior for the rigid diaphragm constraint case, as expected. Similar ratios between the self-centering and "conventional" systems without rigid diaphragm constraints are given in Table 8-14. From Table 8-14, one can see that compared with the "conventional" system, self-centering system undergoes much smaller beam plastic rotations, except for the roof level. The ratios of beam plastic hinges rotations for the "conventional" system with and without rigid diaphragm constraints are given in Table 8-15. All these ratios are nearly equal to 1.0, which indicates that adding rigid diaphragm constraints on the "conventional" system will have insignificant effect on the beam plastic hinge behavior.

Table 8-12: Peak Rotations of Beam PHs for Self-centering System without RDC (unit: rad.)

Story Level	Span 1		Span 2		Span 3	
	Left	Right	Left	Right	Left	Right
1	0.005956	0.003273	0.016613	0.012404	0.022758	0.017952
2	0.008086	0.004887	0.010894	0.005954	0.009678	0.002748
3	0.002704	0.002646	0.002705	0.002612	0.002677	0.002549

4	0.008791	0.004086	0.006934	0.002802	0.003263	0.002718
5	0.018559	0.022779	0.012946	0.016919	0.007005	0.002857

Table 8-13: Ratios of Maximum Beam Plastic Hinge Rotation for Self-centering System with RDC to those based on without RDC

Story Level	Span 1		Span 2		Span 3	
	Left	Right	Left	Right	Left	Right
1	7.0	12.7	2.4	3.3	1.8	2.4
2	5.3	8.9	3.9	7.3	4.3	15.8
3	10.9	11.4	10.6	11.5	10.8	12.1
4	2.2	4.9	2.6	7.1	5.6	7.5
5	0.56	0.81	0.79	1.1	1.4	6.5

Table 8-14: Ratios of Maximum Beam Plastic Hinge Rotation of Self-centering to "conventional" System without RDC

Story Level	Span 1		Span 2		Span 3	
	Left	Right	Left	Right	Left	Right
1	0.12	0.067	0.35	0.25	0.48	0.35
2	0.18	0.10	0.24	0.12	0.21	0.057
3	0.085	0.080	0.088	0.078	0.087	0.074
4	0.45	0.20	0.38	0.13	0.18	0.12
5	2.1	1.3	1.58	0.97	0.87	0.16

Table 8-15: Ratios of Maximum Beam Plastic Hinge Rotation for "conventional" System with RDC to those based on without RDC

Story Level	Span 1		Span 2		Span 3	
	Left	Right	Left	Right	Left	Right
1	0.995	1.010	1.012	1.012	1.012	0.999
2	1.006	1.002	1.003	1.002	1.003	1.005
3	1.006	1.005	1.006	1.004	1.006	1.004

4	1.002	1.008	1.011	1.010	1.012	1.005
5	1.007	1.005	1.026	1.013	1.023	1.010

Another consequence from the assumption of rigid diaphragm constraints is that the distribution of the axial force state (compression or tension) in beams will change. The beam axial forces of the self-centering systems with or without rigid diaphragm constraints are presented for both self-centering and "conventional" systems in Table 8-16 and Table 8-17. The axial forces in these two tables are determined when the corresponding system reaches its ultimate base shear.

From these results, one can see that the existence of rigid diaphragm constraints indeed has an obvious influence on the beam axial force states for the self-centering system. The changes are outlined in Figure 8-26 which assumes a 'strut and tie' model for the overall force distribution. There is an obvious concentration of the beams in compression on the lower story levels for the self-centering system without rigid diaphragm constraints. Beyond that, the rigid diaphragm constraints do not influence the axial force magnitude very much. From the results in Table 8-17, it is clear that the beam axial force states in the "conventional" frame will not be influenced by rigid diaphragm constraints. It is not an exaggeration to say that rigid diaphragm constraints will make a self-centering system into a "conventional" system.

Table 8-16: Beam Axial Force of Self-centering System with or without Rigid Diaphragm Constraints (RDCs) (unit: kips)

Story Level	Without RDC			With RDC		
	Span 1	Span 2	Span 3	Span 1	Span 2	Span 3
5	-42.5	3.8	43.9	-52.6	-6.5	39.3
4	-16.8	5.2	23.7	-17.4	5.8	29.4
3	21.0	28.9	32.4	7.4	0.95	-5.6
2	-25.7	-25.7	-9.6	-21.6	7.2	35.9
1	2.0	-61.0	-100.3	64.3	-4.1	-72.5
Base	554.0	11.2	-560.3	572.8	1.5	-569.8

Table 8-17: Beam Axial Force of "conventional" System with or without Rigid Diaphragm Constraints (RDCs) (unit: kips)

Story Level	w/o RDC			RDC		
	Span 1	Span 2	Span 3	Span 1	Span 2	Span 3
5	-51.1	-7.6	34.5	-53.0	-9.6	33.4
4	-19.9	4.6	31.6	-16.7	9.0	35.3
3	7.8	3.7	-1.9	7.1	0.6	-6.2
2	-28.8	3.2	35.4	-23.3	4.4	32.0
1	80.6	3.1	-75.1	67.6	1.3	-64.8
Base	531.9	1.0	-529.4	537.6	1.2	-535.1

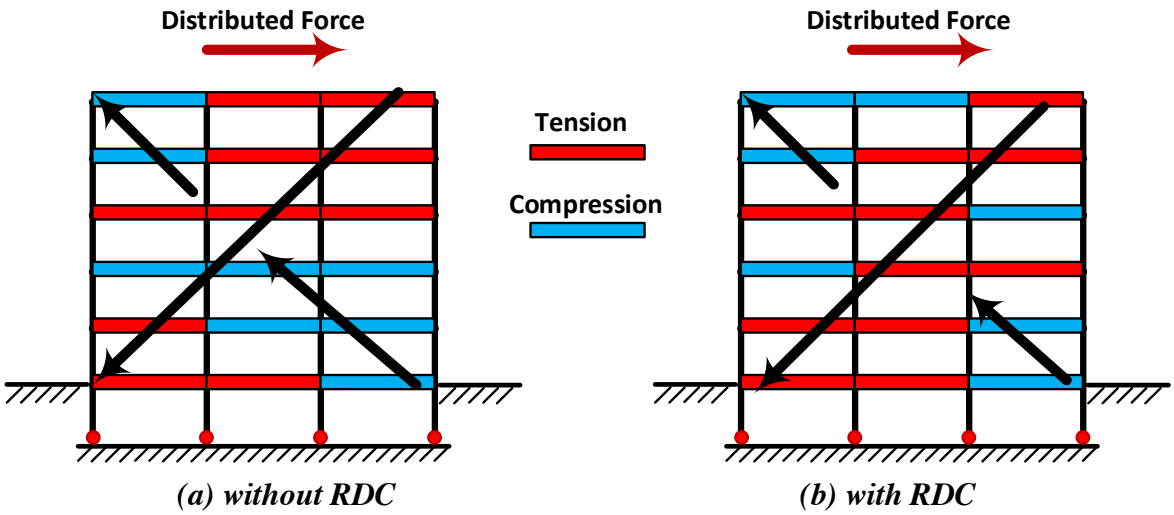

Figure 8-26: Beam axial force states in the self-centering system with vs. without rigid diaphragm constraints

8.5 Construction Method to Remove Rigid Diaphragm Constraints

According to the previous discussion, the rigid diaphragm constraints should be removed to preserve the system's self-centering capacity. These constraints come mainly from the in plane strength and stiffness of the floor slab. In actual construction, special techniques will need to be applied on the composite concrete slabs to ensure that the new proposed smart connections can deform freely. For the self-centering system under pushover analysis with roof drift ratio of 3.6%, the maximum opening between end plate and connection can be estimated as the maximum rod elongation, which is given in Table 8-5 for each connection. From these results, one can see that the maximum opening of the end plate is about 1.5'' from a W33*130 beam with RBS. For this beam, the flexural capacity is reduced by 33.9% compared with the original whole section.

For the beam size in the above example, the concrete slab should have the ability to supply enough spacing for connection expansion, of 1.5” to 2”. A simple construction method is proposed to release the in-plane constraints from the slab on the end plate rotation. As shown in Figure 8-27, a layer of rubber with low stiffness is added between each end plate and the concrete slab. This rubber layer should supply adequate spacing for the local connection. When the separation of end plate is large, cracking will grow into the slab. In order to further reduce the slab constraints on connection deformation and to control the propagation of cracking in the slab, additional reinforcement should be employed near the tips of the rubber layers to enhance the slab stiffness and strength. The detail of this and similar ideas depend on the lab test results.

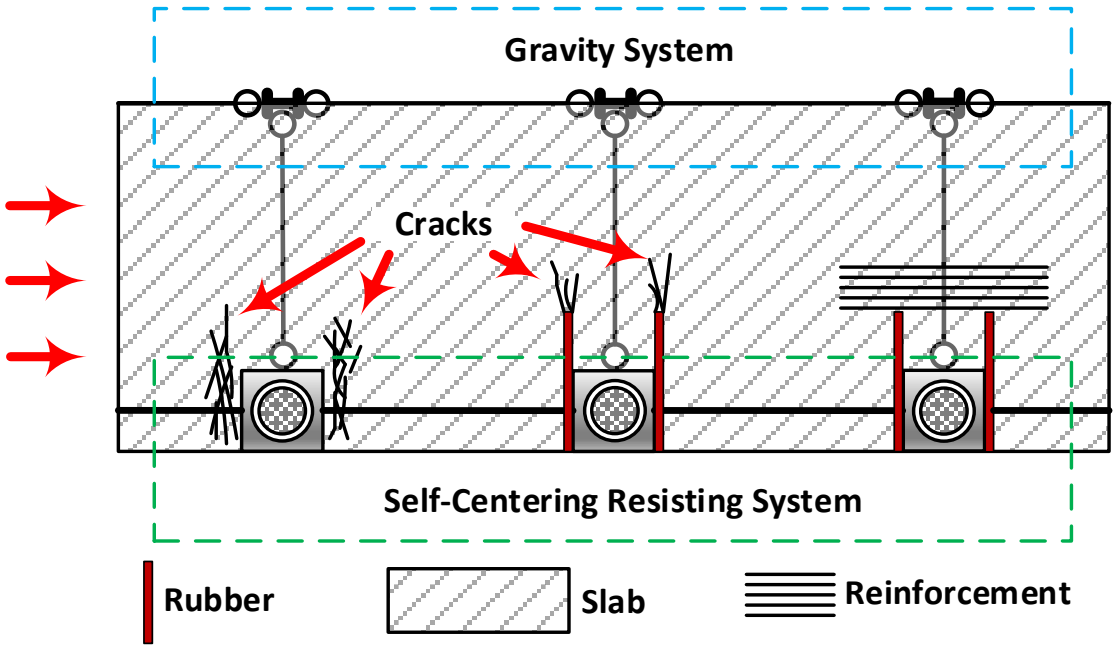

Figure 8-27: Plan sketch of the construction method to remove rigid diaphragm constraints

8.6 Summary and Conclusions

In this chapter, nonlinear static pushover analyses were executed to investigate system's self-centering capacity of the new proposed systems. In order to have a better understanding of the NPSC, their deformation mechanism was illustrated in detail. The system's self-centering capacity was investigated by checking the effects from: (1) strengths of beams; (2) stiffness of connections from rods pretensioning; and (3) rigid diaphragm constraints. Global Strength Ratio (GSR) and global stiffness ratio are defined for parametric study.

The results of nonlinear static pushover analyses indicated that:

- The improved 2D-SSM is robust and capable of including panel zone yielding (see Section 8.1.2).
- The new proposed preliminary design procedure in Chapter 3 is able to deliver a system with great self-centering capacity (see Section 8.2.2 and Figure 8-21).
- Higher beam strength will generate greater self-centering capacity but there is an upper limit to this effect. Parametric studies can be used to develop sensitivity curves between beam strength and system's self-centering capacity to optimize design (see Figure 8-22).
- The sensitivity curves show three distinct range of behavior, with the most sensitivity occurring with a global strength ratio from 0.9 to 1.05 (see Figure 8-22).
- Connection stiffness from rods pretensioning has insignificant impacts on system's self-centering capacity (see Figure 8-23).

- Parametric study indicated that the most effective range of beam strength to reduce column separations is GSR from 0.8 to 1.0 (see Figure 8-24).
- When a GSR is greater than 1.0, the increase rate of the column separations is small (see Figure 8-24).
- System's self-centering capacity will be eliminated by adding rigid diaphragm constraints (RDC) because RDC will cause more plastic yielding in beams (see Section 8.4 and Figure 8-25).

Chapter 9

Nonlinear Dynamic Analysis

In this Chapter, nonlinear dynamic analyses of both "conventional" CSMF with FR connections and self-centering PR connections are described. The corresponding results will be employed to evaluate the seismic performance of the new proposed self-centering system. The analyses will utilize the OpenSees with the advanced 2D-SSM proposed in Chapter 7.

The Chapter is organized as follows: The "conventional" and self-centering CSMFs are described in Section 9.1. Their collapse assessment following the nonlinear Incremental Dynamic Analysis (IDA) methodology in FEMA-P695 FEMA-P695 [11] is given in Section 9.2. Global system seismic performance and individual component seismic responses are evaluated in Section 9.3. The spectral shape effects of ground motions on self-centering system are discussed in Section 9.4. The effects of Global Strength Ratio (GSR) between the new smart connections and their connecting beams on structural dynamic performance are investigated in Section 9.5. The effects of varying damping ratios and panel zone strengths on system performance are investigated in Section 9.6 and Section 9.7, respectively. The impacts of the scaling method for the ground motions on system performance evaluation is investigated in Section 9.8. Finally, summary and conclusions are given in Section 9.9. Figure 9-1 and Figure 9-2 provide a visual organization chart of this Chapter and should be used as a guide.

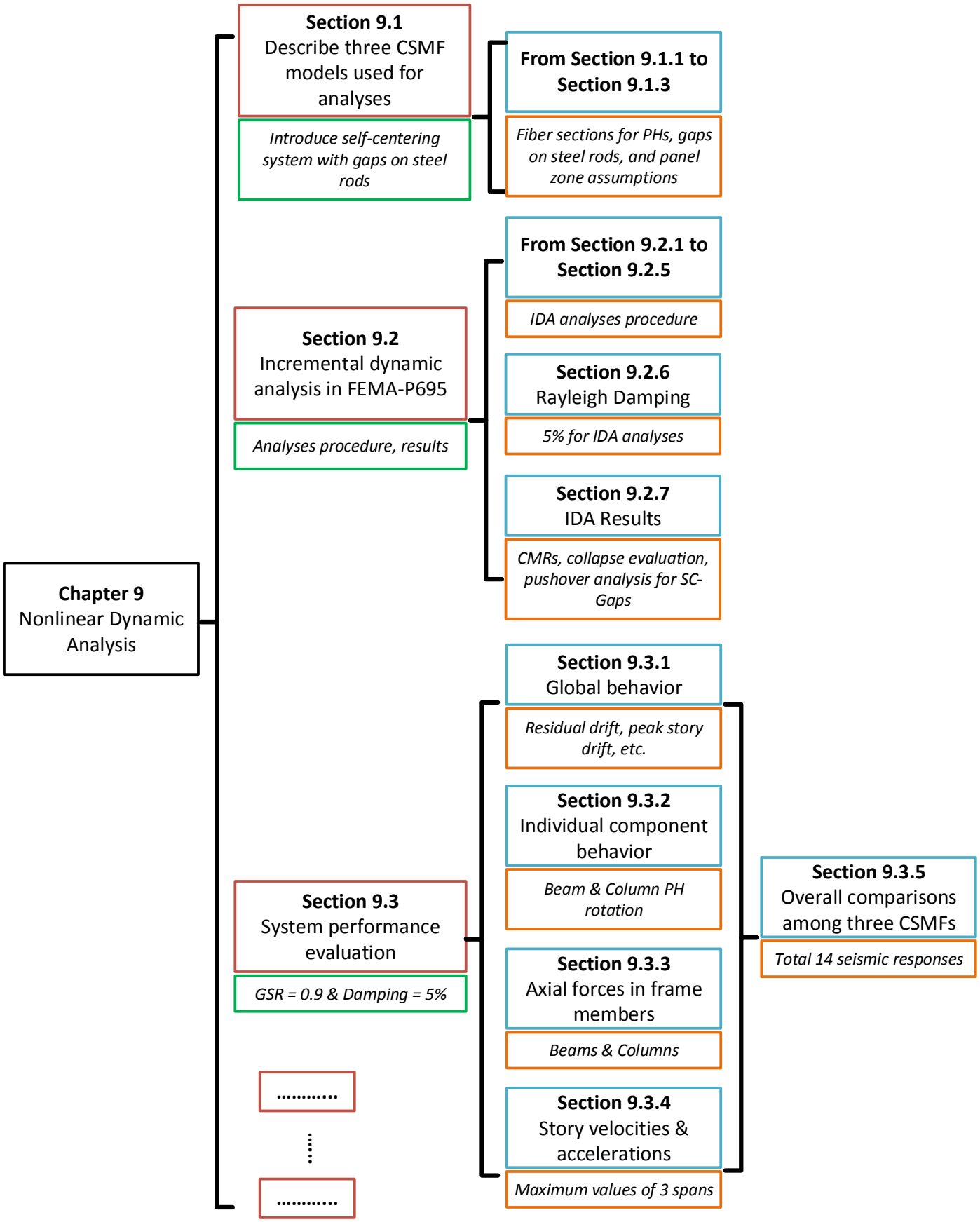

Figure 9-1: Organization of Chapter 9

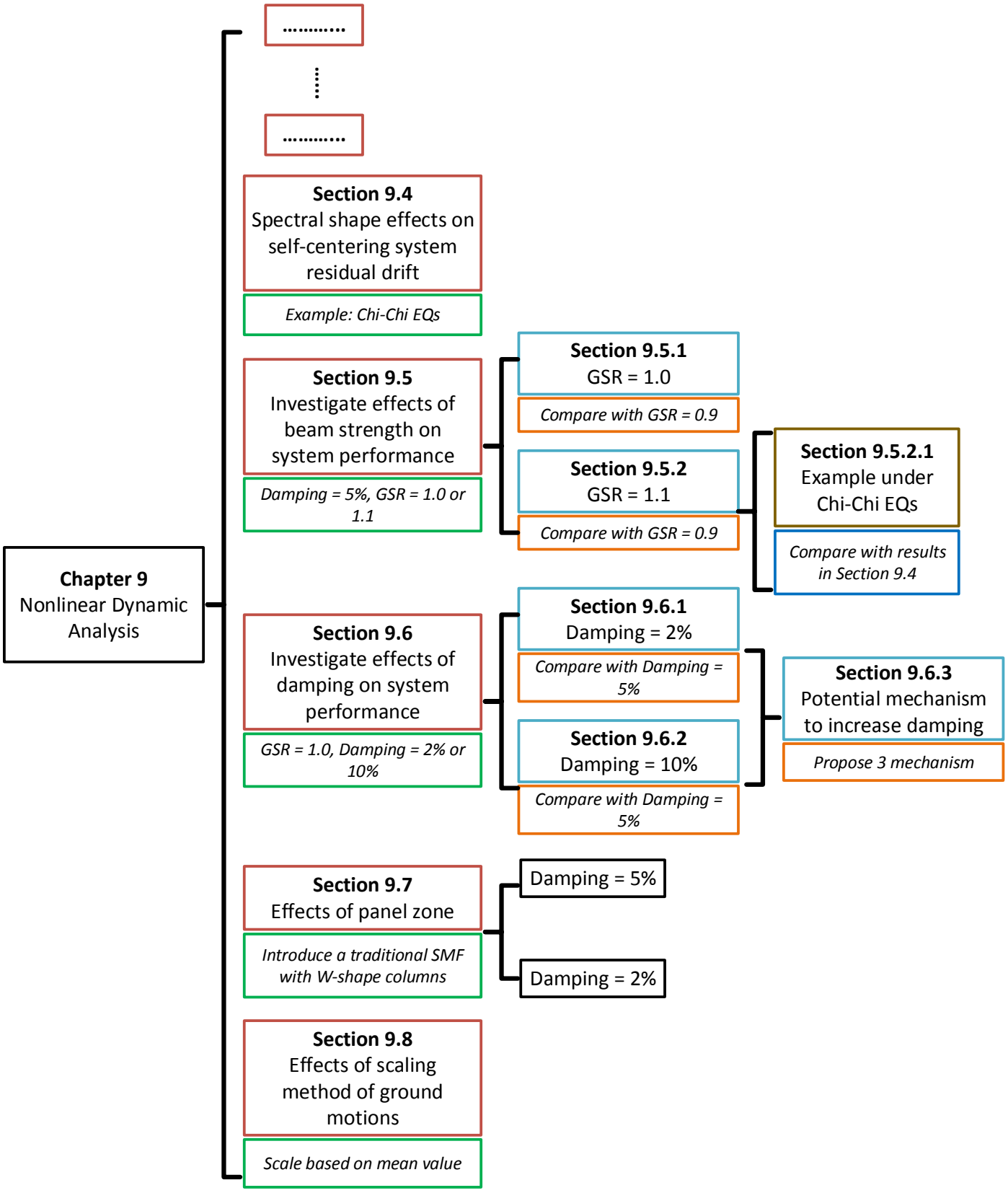

Figure 9-2: Organization of Chapter 9 (con.)

9.1 Structures for Dynamic Analysis

9.1.1 Fiber-Sections for Plastic Hinges

In Chapter 8 a global strength ratio (GSR) is used to describe the strength ratio between all beams and connections. If the required self-centering capacity in Figure 8-22 is defined as a residual roof drift ratio less than 0.5% after the nominal design drift of 2% in ASCE-7 is reached, then the corresponding GSR should be slightly less than 0.9. In this Chapter, a GSR of 0.9 is chosen as the balance point between self-centering capacity and column separation.

Both BIKMs and fiber sections can be used, as described in previous chapters. In this Chapter, only CSMF with fiber sections will be employed for dynamic analysis because:

- For dynamic analyses, initial system period is important. As mentioned in Section 7.3.1, the CSMF with fiber sections gives more reasonable periods.
- The concentrated spring models cannot simulate axial-flexural interaction effects for member plastic hinges. However, this is not a problem for fiber sections.

9.1.2 Gaps on Steel Rods

For the self-centering system utilized herein, an ideal design concept is to design the connection to (1) be relative weak to supply full self-centering capacity for moderate earthquakes, and (b) be strong enough to both control the column peak separation and limit residual drift for large earthquakes. A good way to implement this ideal design concept is to introduce a small initial

gap in each steel rod. When earthquakes are moderate, only the SMA rods are activated to supply flexural capacity for connections. As the earthquake magnitude increases, the steel rods will be activated after the gaps are offset by the end plate rotation. This will introduce a variable GSR into the system. Before steel rods start to work, the GSR will be much greater and the connections will supply most of deformation; after the steel rods engage, the GSR will be reduced and more beam plastic rotation will occur.

By introducing small gaps into steel rods, the system initial stiffness will be supplied only by the pretension in the SMA rods. However, this possible stiffness reduction will probably not reduce the system's self-centering capacity, because the global stiffness ratio has an insignificant effects on this characteristic based on the results in Figure 8-23. So theoretically speaking, using gaps on the steel rods will result in behavior close to the ideal design concept.

In this chapter, three CSMFs with fiber sections and GSRs of 0.9, will be analyzed: (1) a "conventional" CSMF; (2) a self-centering CSMF; and (3) a self-centering CSMF with gaps for steel rods. A gap of 0.5 in. for each steel rod is assumed based on a few trail-and-error studies. Comparisons among dynamic results of three systems will be used to improve the preliminary design procedure.

9.1.3 Effects of Panel Zone and Welds Failure

For the traditional steel special moment frames with W steel beams and columns, the sources

of system residual deformation come from the plastic behavior of the main structural components, including yielding of beams, columns, and connections. A major component of connection deformation is caused by the distortion of connection panel zone. For flexural steel moment frames, the contribution of panel zone on structural deformation can be considerable [102, 105]. In the 1994 Northridge earthquake in California, panel zone distortions were commonly observed in steel moment frames [106]. This triggered the interest of researchers in developing a new generation of models and design criteria for connection panel zones. Aside from panel zone distortion, connection brittle failures triggered by cracking beginning at welds was another alarming feature in the poor performance of steel moment frames in the Northridge and Kobe earthquakes. [106, 107]. These failures led to significant changes in design and QA/QC procedures for welds, considerably increasing the cost of SMRFs.

The new proposed self-centering system is expected to reduce the residual deformation of traditional steel special moment frames after earthquakes and eliminate some of the problems of observed in SMRFs in the Northridge and Kobe events. First, by using CCFTs as columns, it is believed that the panel zone deformation will be very limited because of the combined shear strength and stiffness provided by a relatively thick steel pipe and a well-confined concrete core. Thus panel zone deformation will not be considered in analysis of the three CSMFs in this Chapter. Second, the proposed joints use bolts and rods with high deformation capacity instead of field welds to make most critical connections, reducing the possibility of weld failures and the QA/QC costs. End plates have been shown to be the most robust type of

moment connection, with predictable and reproducible strengths and deformation capacities [81, 82]. In the new proposed self-centering connection, the welds between beams and end plates will be finished in the shop under ideal quality control conditions. This procedure will considerable reduce the risk of brittle weld failures. For the "conventional" CSMF with FR connections analyzed in this Chapter, full penetration welding on site will be needed. However, the same assumption that there will be no occurrence of weld brittle failure is made for all three CSMFs. It is reasonable for the two self-centering CSMFs, but will overestimate the performance of the "conventional" CSMF. The performance of the "conventional" CSMF obtained based on the dynamic analysis in this Chapter is the best behavior one can expect for a CSMF with CCFT columns. This best behavior is what one would expect from ideal but not real SMRFs, and should be seen only as a way of benchmarking the CMRFs performance as discussed in the beginning of Chapter 6.

9.2 Incremental Dynamic Analysis

This section presents a brief and necessarily incomplete review of the procedures in FEMA P-695 [9] and is meant for readers not familiar with that document. Readers familiar with the P-695 approaches and terminology can skip to Section 9.2.6.

Incremental Dynamic Analysis (IDA) method is usually used to assess the collapse demand and capacity of the new proposed structural systems. It is an important method to predict the

adequate collapse performance of new structures in Performance-Based Earthquake Engineering, especially to estimate the mean annual frequency (the probability in one year) of exceeding a particular limit state [11], such as interstory drift ratio, peak story acceleration, peak story velocity, and residual deformation, etc. Usually different structural limit states will be employed for different evaluation purposes. Interstory drift ratio can be used to evaluate the system sidesway collapse; peak story acceleration and velocity can be used to evaluate non-structural components damage. Residual deformation can be used to evaluate the reparability and economic loss of damaged structures. The detailed procedure of incremental dynamic analysis is described in FEMA P-695 [9], and can be summarized as follows:

(1) Design the structure under investigation according to the current design provisions or the new proposed design procedures.

(2) Establish an appropriate analytical model for the structure being investigated. Properly define each component and analysis parameters based on test data and reasonable assumptions, including material properties, loadings, boundary conditions, and damping, etc.

(3) Select a set of ground motions for nonlinear dynamic analysis.

(4) Incrementally scales the magnitude of each ground motion record uniformly but keep its frequency content invariable until system collapse occurs, and execute nonlinear dynamic analysis for each scaled record.

(5) Define a ground motion intensity measure (e.g., 5% damped spectral acceleration with first mode period of system under investigated) and a damage measure (e.g., the

maximum interstory drift ratio) to postprocessor the dynamic results and generate one IDA curve for each individual ground motion.

(6) Repeat step (4) and (5) to generate an IDA curve for each record.

(7) Define limit state and evaluate each IDA curve to calculate collapse margin ratio (CMR) for the structure under the selected set of records.

For the intended use of the FEMA P-695 methodology, which is to assess the system performance factors, this process will be repeated for a large set of archetype designs that bound the common practice design space.

The initial scaling factor should be small enough (maybe less than 1.0) to ensure that the elastic behavior of structures is reflected in the analysis. The increment used should be small enough to make sure all important changes of structural states can be captured accurately, including the start of system nonlinear behavior and the state of incipient collapse. The mathematical model should be able to capture all significant structural nonlinear behavior related to collapse. Some failure modes can be simulated by the computational model directly. However, other potential non-simulated failure modes may not be explicitly captured by the analytical model, and should be evaluated by using alternative limit state checks.

9.2.1 FEMA-P695 Far-Field Record Set

Records in the Far-Field record set (records at sites at least 10 km from fault rupture) are

considered as robust samples of strong motions with large magnitude for far field studies. The Far-Field record set is more applicable for the western United States, whose tectonic setting and fault mechanism is more likely to generate shallow crustal earthquakes, which is consistent with the dominant sources of the Far-Field record set.

In this study, the ground motion records of in the Far-Field record set were chosen to evaluate collapse performance by using IDA. The building under investigation is located in the western United States with more than 10 km distance away from the nearest active fault, and its elastic period is less than 4 seconds. Therefore, it is reasonable to use the Far-Field record set to evaluate the collapse performance. In Table 9-1, some basic information of the Far-Field record set are listed, and more detailed information is found in Appendix A of FEMA-P695 [11].

Table 9-1: Summary of Information of Far-Field Record Set in FEMA-P695 [11]

ID No.	Earthquake Name	Magnitude	Site Class	Epicentral Dis. (km)	PGAmax (g)	PGVmax (cm/s.)
1	Northridge	6.7	D	13.3	0.52	63
2	Northridge	6.7	D	26.5	0.48	45
3	Duzce, Turkey	7.1	D	41.3	0.82	62
4	Hector Mine	7.1	C	26.5	0.34	42
5	Imperial Valley	6.5	D	33.7	0.35	33
6	Imperial Valley	6.5	D	29.4	0.38	42
7	Kobe, Japan	6.9	C	8.7	0.51	37
8	Kobe, Japan	6.9	D	46	0.24	38
9	Kocaeli, Turkey	7.5	D	98.2	0.36	59
10	Kocaeli, Turkey	7.5	C	53.7	0.22	40
11	Landers	7.3	D	86	0.24	52
12	Landers	7.3	D	82.1	0.42	42
13	Loma Prieta	6.9	D	9.8	0.53	35
14	Loma Prieta	6.9	D	31.4	0.56	45

15	Manjil, Iran	7.4	C	40.4	0.51	54
16	Superstition Hills	6.5	D	35.8	0.36	46
17	Superstition Hills	6.5	D	11.2	0.45	36
18	Cape Mendocino	7.0	D	22.7	0.55	44
19	Chi-Chi, Taiwan	7.6	D	32	0.44	115
20	Chi-Chi, Taiwan	7.6	C	77.5	0.51	39
21	San Fernando	6.6	D	39.5	0.21	19
22	Friuli, Italy	6.5	C	20.2	0.35	31

9.2.2 Collapse Margin Ratio (CMR)

One of the most important results obtained by IDA is the collapse margin ratio (CMR), which is used to assess the system collapse capacity. The CMR can be calculated by (Eq. 9-1).

$$CMR = S_{CT} / S_{MT} \qquad \textbf{(Eq. 9-1)}$$

where,

$\hat{S}_{CT}$ = the median collapse level acceleration, g.

S_{MT} = maximum considered earthquake (MCE) ground motion demand, g.

Research indicates that the value of CMR can be influenced greatly by the spectral shape of the ground motion. Under very rare record, the collapse demand on ductile structures can be significant overestimated. In order to avoid the overestimation of structural nonlinear response from spectral content of ground motions, a spectral shape factor (SSF) is introduced into the methodology to adjust the CMR as given in (Eq. 9-2). The value of SSF depends on

fundamental period, Period-Based Ductility (μ_T), and seismic design category. SSF can be determined from Tables 7-1a and 7-1b in FEMA-P695.

$$ACMR = SSF \cdot CMR \qquad \textbf{(Eq. 9-2)}$$

Research also shows that the CMR is dependent on the system stiffness, seismic design category and overstrength of the system, and that it can be governed by the strongest ground motion which is applicable for the particular system type. This is because that as the seismic design load decreases, the contribution from gravity system effects increases, but the capacity of lateral resisting system does not decrease proportionally. Most of these complicating factors are not addressed in this thesis, as the focus will be on an individual structure type.

Besides the aspects mentioned above, the secondary systems (gravity system or non-structural components) and structural irregularity can also improve or reduce the collapse performance. In this study, these effects are not included in the analysis because only a 2D computation model is employed in the analysis to simulate the nonlinear behavior of the structure.

9.2.3 Spectral Shape Effects

The prediction of structure collapse capacity can be affected by the spectral shape of the ground motions selected. The spectral shape of very rare earthquakes in California, such as those on the MCE level, can be very different from the building design spectrum in ASCE/SEI-7 [78]

or a uniform hazard spectrum [108, 109]. In order to consider this discrepancy between the ground motion used for dynamic analysis and the median spectra predicted by some attenuation function, a logarithmic standard deviation 'Epsilon ε' is introduced if the spectra intensity S_a follows a lognormal distribution. ε is a function of the ground motion of interest, the building period of observation, and the attenuation relationship for response spectra prediction. A positive ε indicates that the hazard level of interest is greater than its expected level, and a negative ε stands for a smaller hazard level than the predicted level for a particular site.

Usually the collapse capacity is defined as $S_a(T_1)$, which is the intensity, S_a, at the calculated fundamental period of the structure, T_1. However, the spectral shape of the ground motion at periods other than T_1 can also affect the structural behavior greatly if either the inelastic behavior causes period elongation or if higher mode effects contribute significantly to the performance of the building. This means that the ground motions with similar $S_a(T_1)$ and $\varepsilon(T_1)$ can result in very different collapse capacities for a building on a particular site [108-112]. In order to account for the effects of spectral shape, the most direct method is to select a unique set of ground motions with appropriate $\varepsilon(T_1)$ for each building and T_1. However, this makes the ground motion selection very inefficient and complicated.

A simple way is proposed by Haselton and Deierlein to account for the spectral shape by introducing a correction to the median collapse capacity estimates based on a general set of ground motions which is independent of the ε values [37]. Haselton and Deierlein proposed

a linear relationship between the collapse capacity S_{CT1} and $\varepsilon(T_1)$ by doing a regression analysis for 65 modern reinforced special moment frames under 80 ground motions for each frame. This linear relationship is given by (Eq. 9-3). The parameter β_0 indicates the average collapse capacity when $\varepsilon(T_1)$ is equal to 0; the parameter β_1 indicates the sensitivity of the collapse capacity changes for different $\varepsilon(T_1)$.

$$LN[S_{CT1}] = \beta_0 + \beta_1 \cdot \varepsilon(T_1) \qquad \textbf{(Eq. 9-3)}$$

Haselton and Deierlein suggested that the value of 0.29 should be used for parameter β_1 for the modern reinforced special moment frame buildings. Further study shows that there is a strong impact of the building inelastic ductility on β_1. For buildings with large inelastic deformation, a considerable elongation of building period at collapse can be expected. Thus the spectral shape of the ground motion in the range of period greater than T_1 will have a large impact on the system collapse performance, and a larger β_1 is obtained. In contrast, a smaller β_1 is expected for buildings with lower ductility capacity, which indicates that spectral shape ε has less effect on the collapse capacity.

Another simplified method is proposed in FEMA-P695 to correct the collapse capacity distribution to account for spectral shape ε effects. By employing this method, there is no need to calculate $\varepsilon(T_1)$ and perform the regression analysis for a set of ground motions. In order to make the adjusting process, a parameter $\bar{\varepsilon}_0$ named target ε is defined, which is a

function of both site and hazard level of interest. The target ε values for each seismic design category (SDC) are determined based on the database from the United States Geological Survey (USGS), such as 1.0 for SDC B and C; 1.5 for SDC D; and 1.2 for SDC E at 1.0 second.

Similar to the method proposed by Haselton and Deierlein, the parameter β_1 is also used to quantify the sensitivity of spectral shape impact on collapse capacity. Due to the effect of building period extension caused by system nonlinear performance, the larger ductile deformation capacity the building has, the greater β_1 should be. Thus β_1 is a parameter depending on building ductility and can be defined as a function of Period-Based ductility μ_T as shown in (Eq. 9-4). The coefficients in (Eq. 9-4) come from a large amount of regression analyses for β_1 based on a large database of structural models with different ductility capacity.

$$\beta_1 = \begin{cases} (0.14)(\mu_T - 1)^{0.42} & for\ \mu_T \le 8.0 \\ 0.32 & for\ \mu_T > 8.0 \end{cases} \qquad \textbf{(Eq. 9-4)}$$

The spectral shape factor (SSF) can be defined as given by (Eq. 9-5), which is then used in (Eq. 9-2) to adjust the building collapse capacity accounting for the spectral shape effects.

$$SSF = \exp\left[\beta_1 \cdot \left(\bar{\varepsilon}_0(T) - \bar{\varepsilon}(T)_{,records}\right)\right] \qquad \textbf{(Eq. 9-5)}$$

For a non-site-specific collapse performance assessment, the values of target spectral shape $\bar{\varepsilon}_0$ (1.0 for SDC B and C; 1.5 for SDC D; and 1.2 for SDC E) are used; for a site-specific collapse performance assessment, $\bar{\varepsilon}_0(T)$ should be determined directly based on a hazard analysis of the site. For the Far-Field record set of ground motions, $\bar{\varepsilon}(T)_{,records}$ can be determined by (Eq. 9-6) with a range from 0.0 to 0.6. For the Near-Field record set, it can be calculated by (Eq. 9-7) with a range from 0.0 to 0.2. In order to be consistent with the design methodology, the fundamental period T calculated by (Eq. 6-1) is used instead of the computed period of system first mode.

$$\bar{\varepsilon}(T)_{,records} = (0.6)(1.5 - T) \qquad \textbf{(Eq. 9-6)}$$

$$\bar{\varepsilon}(T)_{,records} = (0.2)(T - 1.5) \qquad \textbf{(Eq. 9-7)}$$

9.2.4 Period-Based Ductility μ_T

Period-Based ductility μ_T is defined as a ratio of structure ultimate deformation to its effective yield deformation. An idealized nonlinear static pushover curve is presented in Figure 9-3. As shown in Figure 9-3, the ultimate deformation capacity δ_u is defined as the displacement where the associated system lateral resistance decreases to 80% of the ultimate base shear capacity. The effective yield deformation $\delta_{y,eff}$ is also illustrated on the nonlinear static pushover curve, but it is actually determined based on structural period by (Eq. 9-8). So Period-Based ductility can be computed as $\mu_T = \delta_u/\delta_{y,eff}$.

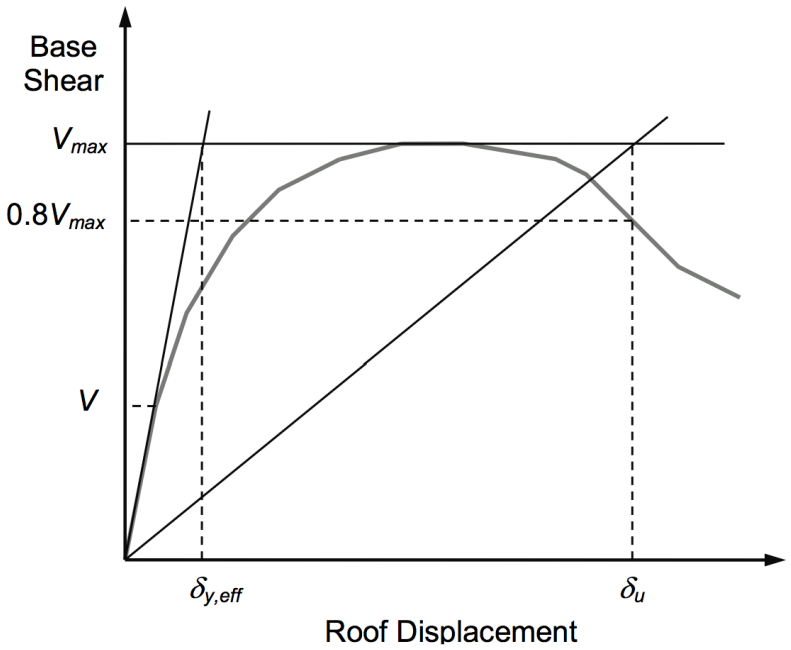

Figure 9-3: Idealized nonlinear static pushover curve [11]

$$\delta_{y,eff} = C_0 \cdot \frac{V_{\max}}{W} \cdot \left[\frac{g}{4\pi^2}\right] \cdot \left[\max\left(T, T_1\right)\right]^2 \qquad \textbf{(Eq. 9-8)}$$

$$C_0 = \phi_{1,r} \cdot \frac{\sum_1^N m_x \phi_{1,x}}{\sum_1^N m_x \phi_{1,x}^2} \qquad \textbf{(Eq. 9-9)}$$

where,

C_0 = parameter relates SDOF displacement to the roof displacement.

V_{max} = ultimate base shear of the structure, kips.

W = total effective weight of the structure, kips.

g = the gravity constant, $386\ in./sec^2$.

T = fundamental period calculated by (Eq. 6-1), second.

T_1 = calculate period of first mode of system, second.

m_x = Mass at story level x, $lb - sec^2/ft$.

$\phi_{1,x}$ = the ordinate of the fundamental mode at level x.

$\phi_{1,r}$ = the ordinate of the fundamental mode at roof.

N = the number of story levels.

9.2.5 Acceptable ACMR

The adjusted collapse margin ratio (ACMR) is employed to evaluate the trial value of the response modification coefficient, R. The minimum value of the acceptable ACMR is determined by: (1) considering the total system uncertainties, including 'Record-to-Record Uncertainty (RTR)', 'Design Requirements Uncertainty (DR)', 'Test Data Uncertainty (TD)', and 'Modeling Uncertainty (MDL)'. In addition a desirable collapse probability, such as 10% collapse probability for each performance group, and 20% collapse probability for each index archetype within a performance group must be selected [11].

Each source of system uncertainty is assumed to have a lognormal distribution, and to be independent of each other. For the Far-Field set of ground motions, a fixed uncertainty is employed for the 'Record-to-Record Uncertainty' when the period based ductility is greater

than 3. For other three uncertainties, four quality ratings (Superior, Good, Fair, and Poor) are defined with specific values. According to the quality rating for each uncertainty, the total uncertainty of the system can be determined (from Table 7-2a to Table 7-2d in FEMA-P695), and an acceptable ACMR with specific collapse probability can be obtained (Table 7-3 in FEMA-P695). For the three CMSFs in this Chapter, their quality ratings, total uncertainties, and corresponding acceptable ACMRs are presented in Table 9-2. For individual index archetype, 20% collapse probability is used to determine the acceptable ACMRs.

Table 9-2: Quality Ratings, Total Uncertainties, and Acceptable ACMRs of Three CSMFs

System Type	DR	TD	MDL	Total Uncertainty	ACMR(20%)
"conventional"	Good	Good	Good	0.525	1.56
Self-Centering	Fair	Poor	Good	0.750	1.88
SC with Gaps	Fair	Poor	Good	0.750	1.88

9.2.6 Damping

Buildings dissipate energy during their vibration via various mechanisms[113]. It is hard to measure how much energy is dissipated by any specific mechanism, so the total energy dissipation capacity is usually described in terms of damping. Some of energy is dissipated by the hysteretic behavior of structural components, friction between structural and non-structural components, opening and closing of microcracks in concrete, and soil-structure interaction, and so on [113]. Additionally, there are many types of energy dissipation devices have been

developed to increase the system damping. These types include, but not limited to, viscoelastic dampers, fluid dampers, friction dampers, and metallic yielding plate dampers [114]. All of these types are regarded as passive devices because there is no interaction between the devices and the structures, which are in contrast to active, and semi-active dampers.

Damping in actual structures is usually considered as a highly idealized structural behavior. Rayleigh damping, as a viscous model for damping, is used in this research. Rayleigh damping is a mathematically convenient model; it assembles a damping matrix as a linear combination of the existing stiffness and mass matrices [113]. However, many researchers indicate that viscous damping tends to overestimate structural damping [115-118]. One reason is that as the hysteretic degradation of structural components increases, the contribution of these components to energy dissipation will be reduced. However, this reduction effect cannot be easily incorporated into the nonlinear dynamic analysis. Another reason is that structural stiffness is reduced due to component's nonlinearity, and the system velocity will increase; if the initial stiffness matrix is used to assemble damping matrix, the influence damping force in the motion equation will be magnified [115]. Several methods have been proposed to remedy the structural damping effects for buildings with nonlinearity [115].

Typically, a 2% to 5% total constant critical damping is assumed for buildings in seismic design. Rayleigh damping is a frequency dependent damping, and it requires two natural frequencies to determine its corresponding parameters. In this research, a relative high damping ratio of 5%

is used to define Rayleigh damping at both the first and third natural frequencies, and the initial damping is used to reduce the computational cost. Because Rayleigh damping is assumed to represent actual damping when system is in elastic state, once system starts to have inelastic responses, an overestimation of damping will occur in the analysis. The Rayleigh damping ratios for the first seven modes are presented in Table 9-3 based on the periods in Table 6-2 and Table 6-3.

Table 9-3: Rayleigh Damping Ratios of the First Seven Modes for both two Systems

System	1st	2nd	3rd	4th	5th	6th	7th
Convent.	0.050	0.036	0.050	0.074	0.077	0.086	0.093
SC	0.050	0.036	0.050	0.071	0.077	0.083	0.091

9.2.7 IDA Results

The FEMA-P695 Far-Field record set is chosen for the IDA analyses for all three CSMFs described in Section 9.1. Because a few unscaled ground motions are strong enough to collapse the designed buildings, they are usually scaled to match the MCE spectral acceleration S_{MT} at only the fundamental period T as determined from (Eq. 6-1). For all three CSMFs discussed in this Chapter, (Eq. 6-1) will give the same fundamental period as 1.173 sec. The scaling method in FEMA-P695 is followed, which will ensure that the median spectrum of the scaled 44 ground motions has the same acceleration demand as the standard spectrum in ASCE7-10 at the fundamental period. The scaled acceleration response spectra of FEMA-P695 Far-Field

set of 44 ground motions and their median spectrum are plotted in Figure 9-4.

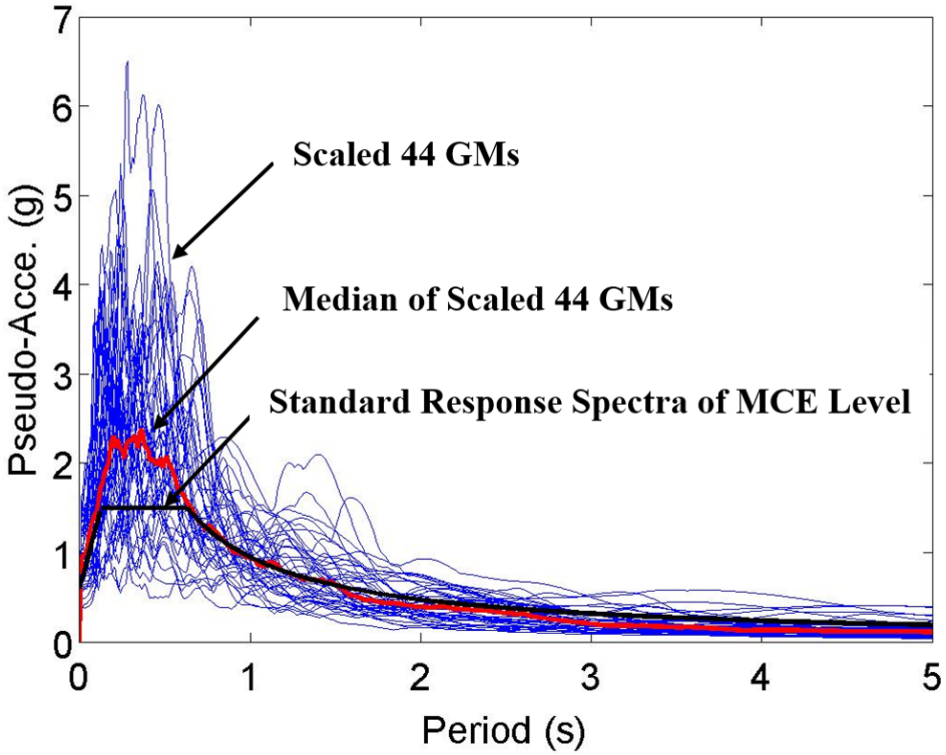

Figure 9-4: Scaled pseudo acceleration spectra of the FEMA-P695 Far-Field set of 44 ground motions on MCE level with damping = 5%

Because FEMA-P695 defines the MCE and DBE level ground motions by a range of spectral accelerations for different SDCs, the MCE ground motion intensity S_{MT} will change in a specific range for each SDC. In this Chapter, in order to determine the CMR, the maximum intensity in the corresponding SDC range will be assumed, e.g. $1.5\,g$ and $0.9\,g$ for short period and 1-second spectral acceleration for SDC D, respectively. The IDA curve for each CSMF based on the scaled ground motions are presented in Figure 9-5, Figure 9-6 and Figure 9-7, respectively. A non-simulated failure criteria of the structure is applied, instead of using

simulated structural collapse directly. If the maximum inter-story drift ratio of any column is greater than 10%, the structure is assumed to have failed.

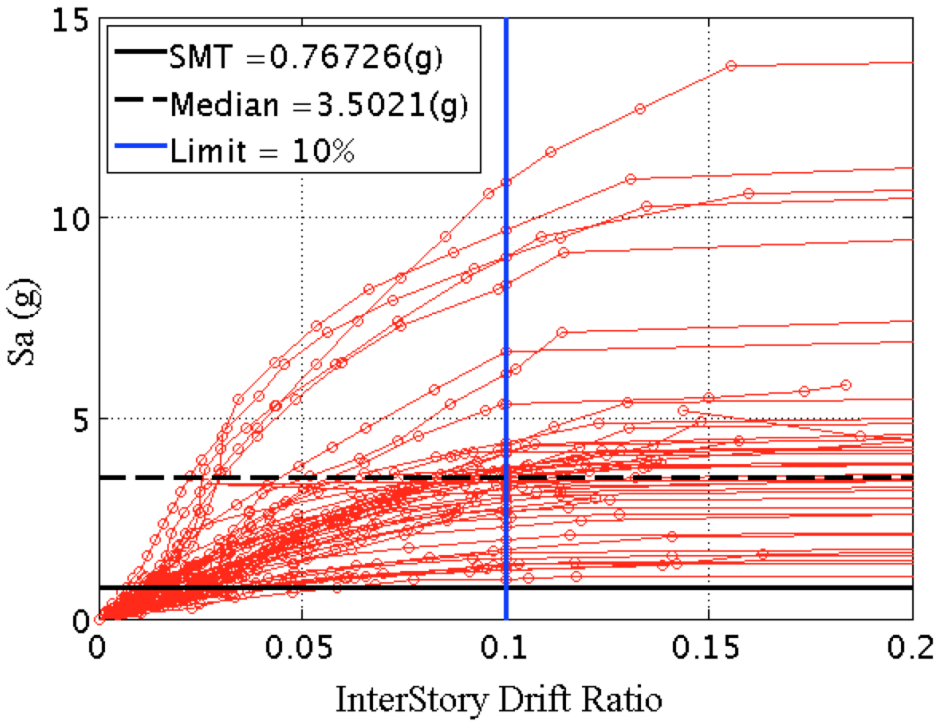

Figure 9-5: IDA curve for the "conventional" CSMF with a maximum inter-story drift ratio of 10%

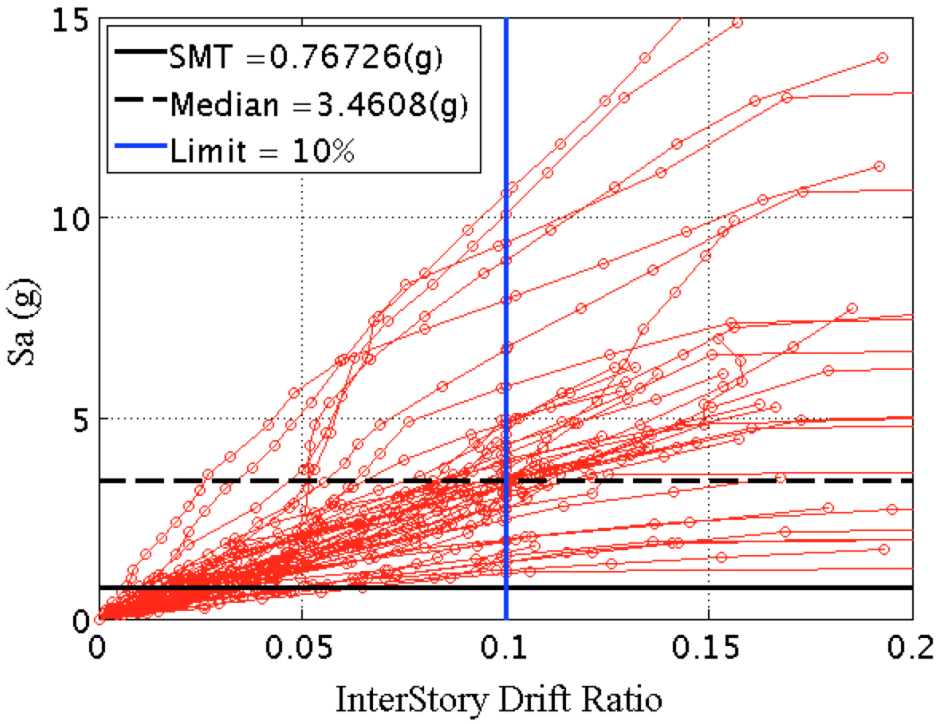

Figure 9-6: IDA curve for the self-centering CSMF with a maximum inter-story drift ratio of 10%

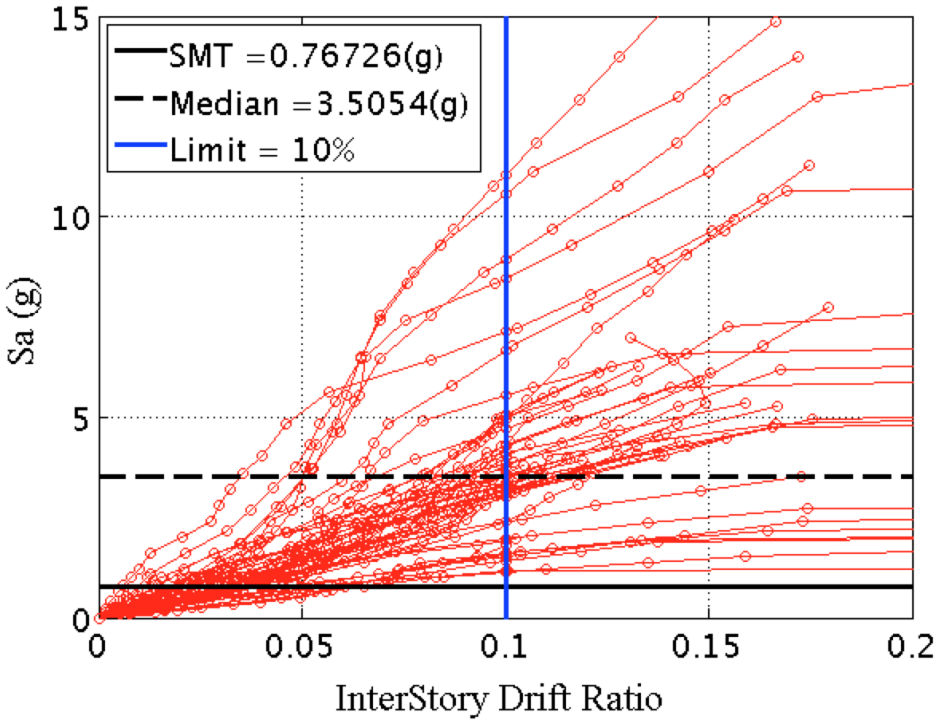

Figure 9-7: IDA curve for the self-centering CSMF with a 0.5" gap on each steel rod with a maximum inter-story drift ratio of 10%

The median collapse intensities of all three CSMFs are similar to one another, with a value of around $3.5\ g$. Both the CMR and ACMR for each system are presented in Table 9-4. The corresponding parameters for the SSF calculation are listed in Table 9-5. The structural ultimate displacements δ_u for the "conventional" and self-centering CSMFs are determined from pushover analyses results using fiber sections as shown in Figure 7-42. The ultimate displacement δ_u of the self-centering CMSF with gaps is determined based on the pushover analysis curve in Figure 9-8.

Table 9-4: CMR and ACMR for Both "conventional" and Self-Centering CSMFs

System Type	CMR	SSF	ACMR	Accept ACMR	Pass or Fail
"conventional"	4.564	1.574	7.184	1.56	Pass
Self-Centering	4.511	1.581	7.132	1.88	Pass
SC with Gap	4.569	1.581	7.224	1.88	Pass

Table 9-5: Parameters for SSF Calculation for Three CSMFs

System Type	C_0	$\delta_{y,eff}$	δ_u	μ_T	β_1	$T\ (s)$	$\bar{\varepsilon}(T)_{,records}$	$\bar{\varepsilon}_0$
"conventional"	1.3465	4.65"	39.5"	8.49	0.32	1.362	0.0828	1.5
Self-Centering	1.3586	4.80"	58.8"	12.25	0.32	1.386	0.0684	1.5
SC with Gaps	1.3583	4.65"	77.3"	16.62	0.32	1.386	0.0684	1.5

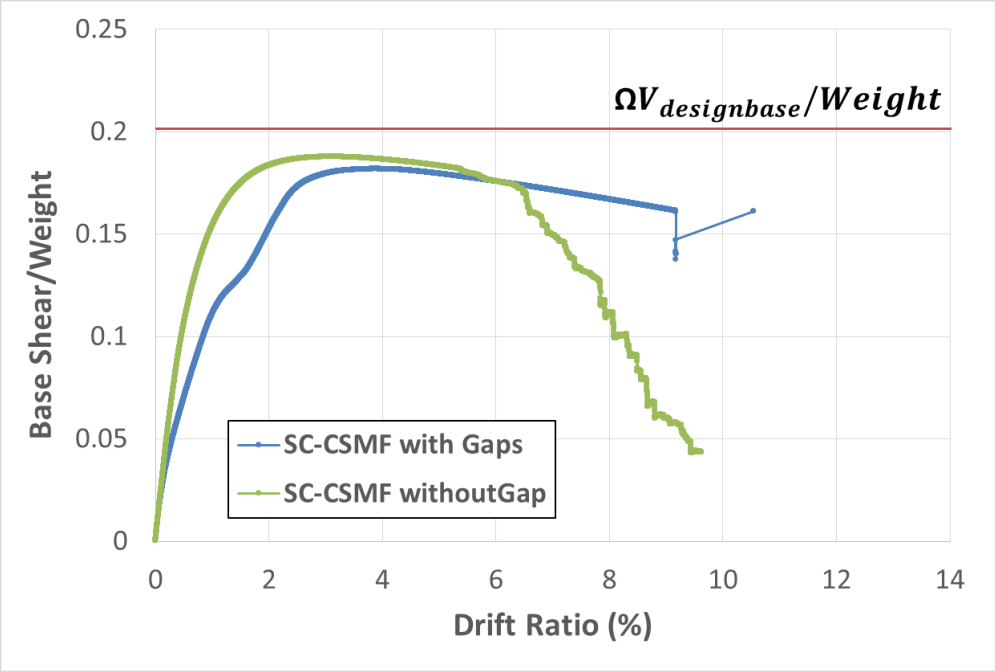

Figure 9-8: Pushover curves of the self-centering systems with vs. without gaps

From Figure 9-8, one can see that the self-centering CSMF with gaps has greater ductility than its counterpart without gaps. Although gaps for the steel rods reduce the connection pretension capacity, this has little influence on the system's initial stiffness. This is also reflected by the calculated fundamental periods from eigenvalue analyses for both two self-centering CSMFs (Table 9-5), which are essentially equal. The ultimate lateral resisting capacity is slightly reduced by the use of gaps because greater deformations increase the second order effects.

Another characteristic of the self-centering CSMF with gaps is a stiffness reduction and hardening fluctuation in a range of roof drift ratio between 1.0% and 1.7% (Figure 9-8). The reduction is believed to be caused by the yielding of SMA rods, and the hardening is believed to be brought by the engaging of the steel rods. There are 144 SMA and 144 steel rods in the

self-centering CSMF with gaps, respectively. The axial force vs. roof drift ratio relationships of all SMA or steel rods are plotted in Figure 9-9 for the pushover case in Figure 9-6. Because at the very beginning only the SMA rods supply connection strength and stiffness, most of SMA rods start to work at the same time once the loading is applied. It is clear that most of SMA rods yields around a roof drift ratio of 1%, as expected. There are two different SMA rods sizes and pretensions used in the system, so two different yielding strengths and pretensions are present in the plot. Interestingly, there are some SMA rods will keep their original pretensions during the whole loading history. When the ultimate deformation of about 9% roof drift ratio is reached, some beams fracture and the corresponding rods are unloaded to fully released state. On the other hand, steel rods start to be loaded around a roof drift ratio of 1.7% successively. Although the system reaches its ultimate capacity around a roof drift ratio of 3%, because of redistribution of internal forces, some steel rods begin to work only after a roof drift ratio of 3% is reached. Also, due to beam fracture, some steel rods are fully released at the ultimate deformation, which is indicated by the sudden drops of the axial forces at the ultimate drift ratio. Some steel rods will also keep their original unloaded state during the entire loading history.

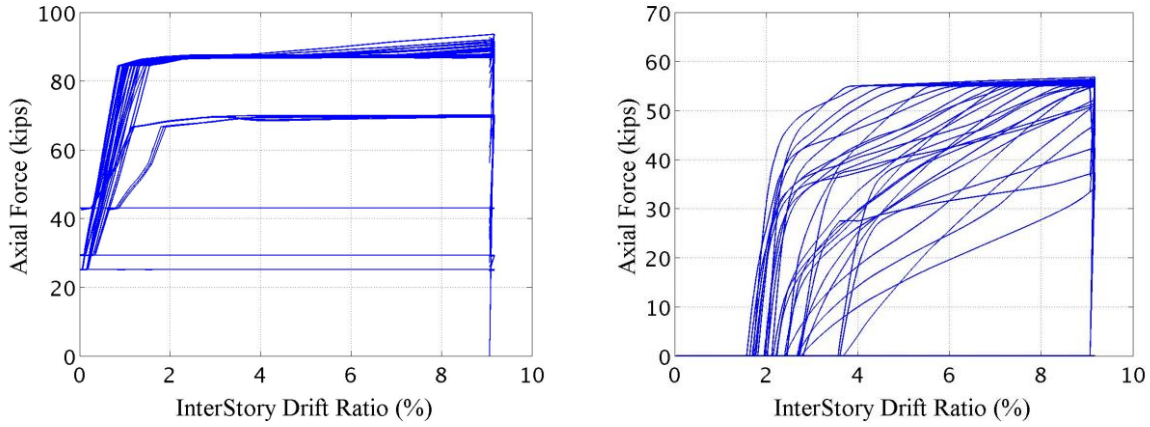

(a) All SMA Rods *(b) All Steel Rods*

Figure 9-9: Aixal force vs. roof drift ratio relationships of all SMA or steel rods in the self-centering CMSF with gaps

Results in Table 9-4 indicate that the minimum values of acceptable ACMRs for all three CSMFs are easily reached. This means that it is reasonable to apply the response modification coefficient, $R = 8$, in ASCE7-10 for both "conventional" and self-centering CSMFs. There is no obvious difference on both CMR and ACMR between the self-centering system with and without gaps on steel rods. The spectral shape factor (SSF) obtained from Table 7-1b in FEMA-P695 are very consistent with the calculated values in Table 9-4.

From the three IDA curves, one can find that the post-failure capacity of the "conventional" CSMF is poor. Once the maximum inter-story drift ratio of 10% is reached, the "conventional" CSMF has already reached its ultimate capacity. The median intensity based on non-simulated and simulated structural collapse are similar to each other. However, this is not the case for the other two self-centering CSMFs. After the non-simulated failure is reached, the two self-centering systems still have considerable lateral load resisting capacity. The median intensity

of simulated structural collapse is much higher than its non-simulated counterpart. This indicates that although non-structural components may be severely damaged, the self-centering system is likely to prevent overall collapse of the structural system.

9.3 Dynamic Performance of Self-centering Systems

In this section, dynamic response of all three CSMFs are evaluated under the 44 scaled ground motions in Figure 9-4, scaled to the median intensity at the system fundamental period, is presented.

9.3.1 Global Behavior Response

Residual drift on each story is investigated under 44 scaled ground motions for both the DBE and the MCE levels. Because there is no rigid diaphragm constraint for all three CSMFs, the residual deformations of beams and columns in each story are slightly different from each other. Here the maximum value of each specific response on each story is employed for discussion. From Figure 9-10, one can see that under DBE level ground motions, the medians of maximum residual story drifts of all three CSMFs are less than the defined limit of 0.5% story drift ratio. Although the difference is not large, the trend shows that the two self-centering systems have less residual deformation than their "conventional" counterpart, and that the self-centering system with gaps has the best performance. Similar conclusions can also be observed from the

results under MCE level ground motions shown in Figure 9-11. However, the advantages of self-centering systems at the MCE level are not as evident. It should be remembered here that the "conventional" frame being used is providing the best possible behavior and is being used as the target for the self-centering ones. Thus the "conventional" frame should not be construed as one that is just code-compliant. An additional important caveat is the "conventional" frame was designed using the same column sections as the self-centering one in order to only capture differences due to connection performance; in reality one would be using a large W sections instead of a CCFT.

Although the median of maximum residual story drifts of self-centering systems are less than "conventional" system, the performance of self-centering systems under individual ground motions do not present any advantages. It is recognized that the use of the 44 ground motions should be made in the context of many archetype structures to generate robust results. As only one structure is being assessed, the use of the median value may not be necessarily correct. From Figure 9-10 and Figure 9-11, the largest residual story drifts are generated by the self-centering system under both the DBE and MCE level ground motions. If the variability of ground motions is considered by adding one standard deviation to the median, the responses among three CSMFs are similar to each other. One can see that the variability effects for the self-centering systems are slightly greater than the "conventional" system. Under the MCE level ground motions, the residual drift limit will be exceeded if one time of standard deviation is added.

The maximum inter-story residual drifts are presented in Figure 9-12 and Figure 9-13. The performance of the self-centering systems still does not show the overwhelming advantages expected. This indicates that if (1) the brittle failure of welds and (2) the probable substantial contribution of panel zone shear are neglected for the "conventional" system, SMRFs will show similar residual deformation as the self-centering system.

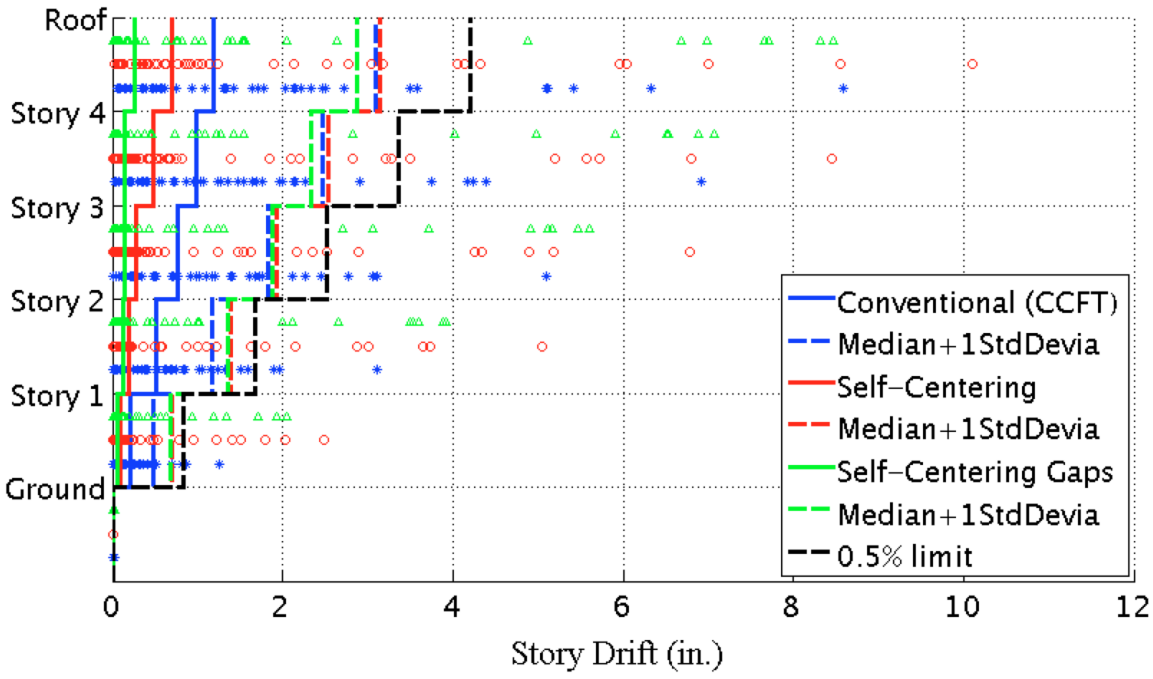

Figure 9-10: Median of the maximum story residual drift under 44 DBE level ground motions with a GSR = 0.9 & damping = 5%

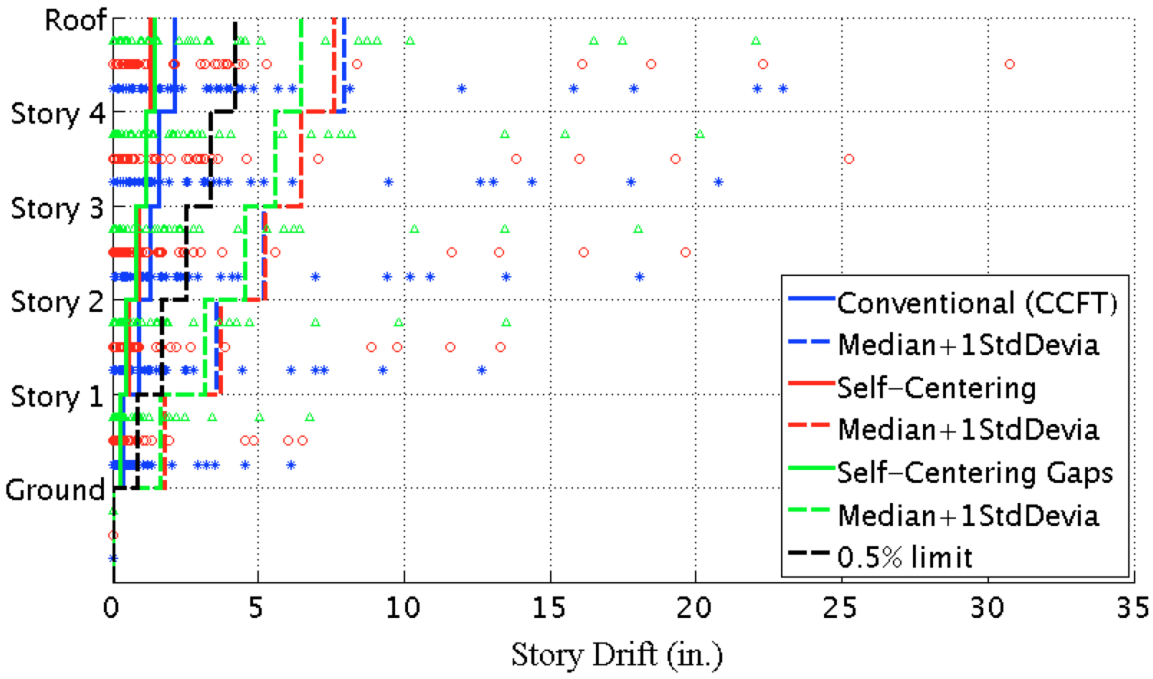

Figure 9-11: Median of the maximum story residual drift under 44 MCE level ground motions with a GSR = 0.9 & damping = 5%

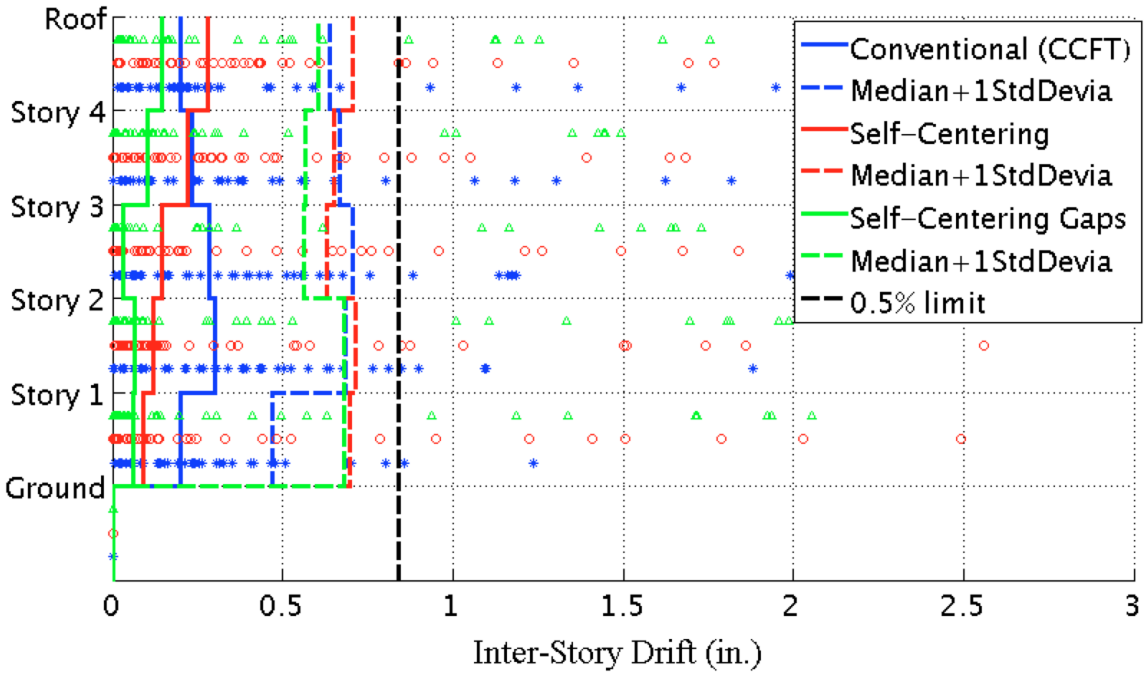

Figure 9-12: Median of the maximum inter-story residual drift under 44 DBE level ground motions with a GSR = 0.9 & damping = 5%

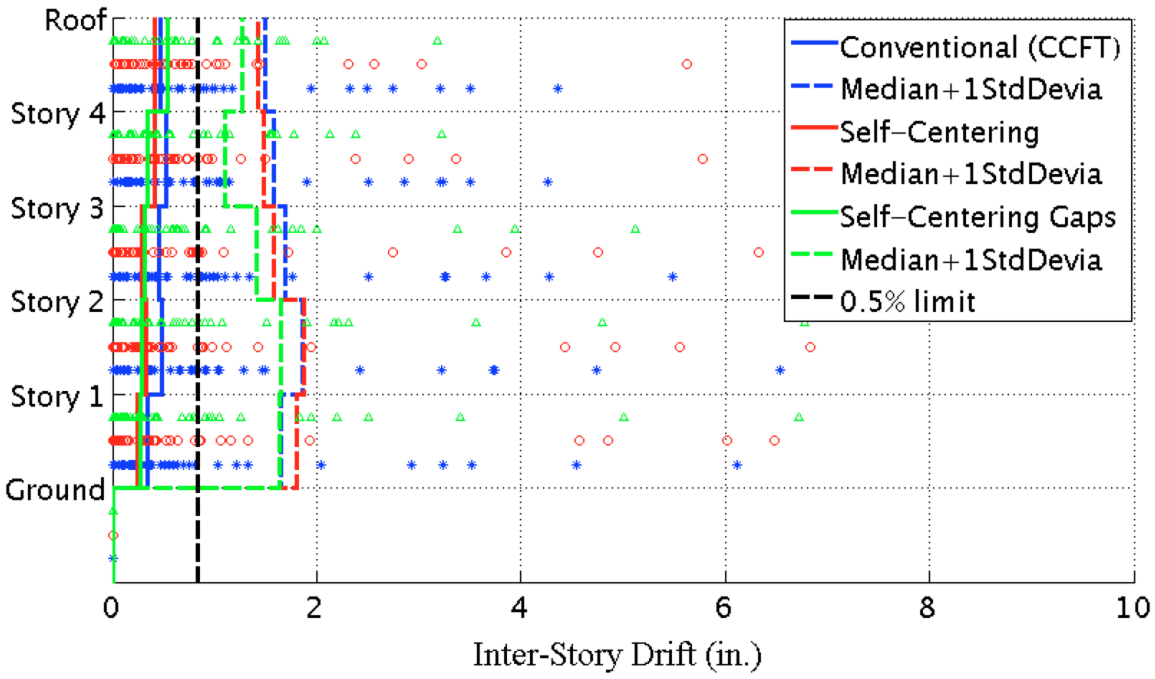

Figure 9-13: Median of the maximum inter-story residual drift under 44 MCE level ground motions with a GSR = 0.9 & damping = 5%

Since partially restrained connections are used, greater peak inter-story drifts would be expected in the self-centering systems. From the results in Figure 9-14 and Figure 9-15, it is clear to see that the peak inter-story drifts of "conventional" CSMF are less than those of self-centering CSMFs, especially for the upper three levels. For the self-centering CSMF with gaps, greater peak deformations are reached due to its more flexible connections when compared to the system without gaps. The self-centering CSMF without gaps is more likely to generate a uniform inter-story drift distribution among different stories.

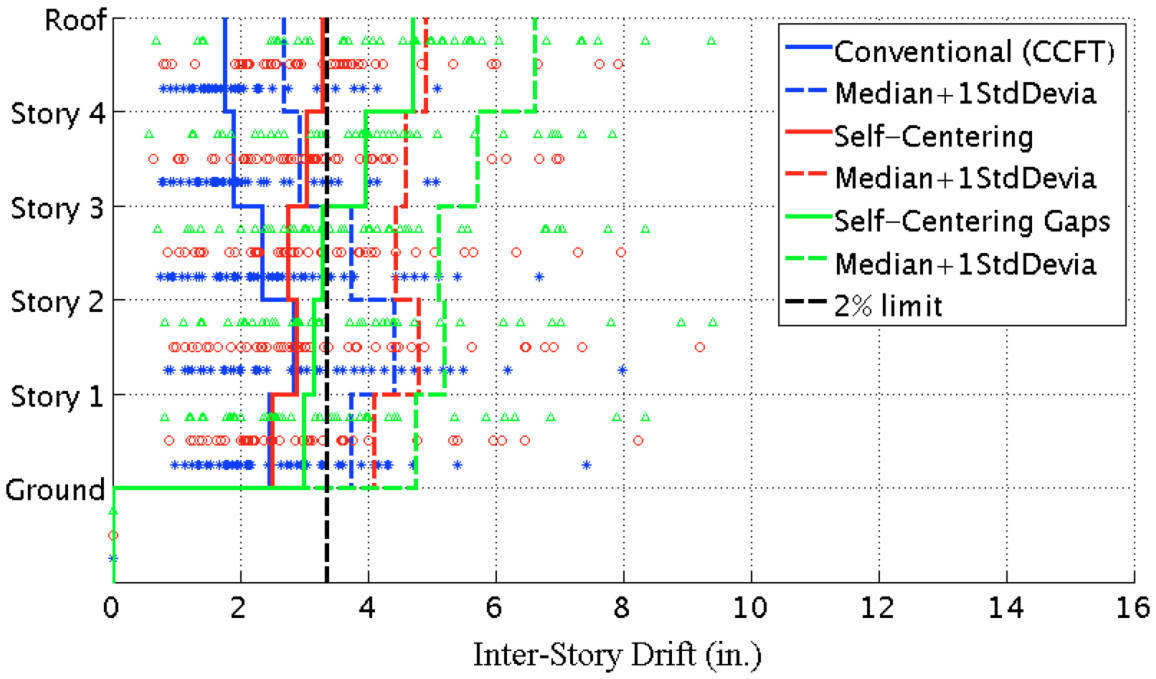

Figure 9-14: Median of the peak inter-story drift under 44 DBE level ground motions with a GSR = 0.9 & damping = 5%

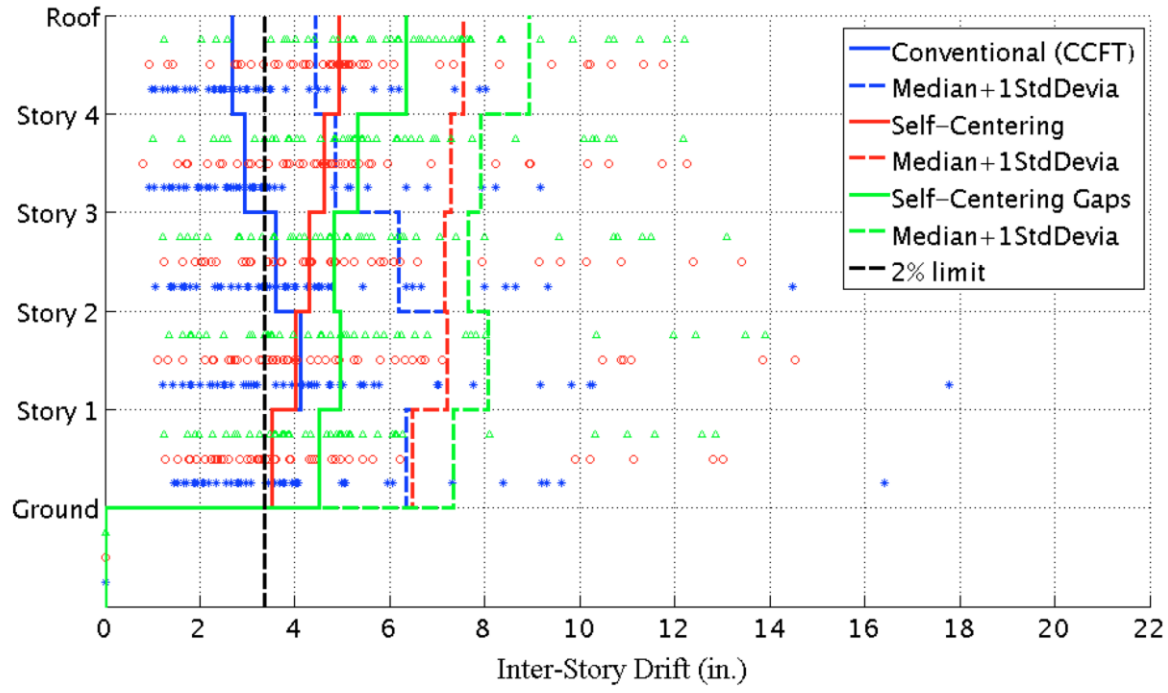

Figure 9-15: Median of the peak inter-story drift under 44 MCE level ground motions with a GSR = 0.9 & damping = 5%

Another parameter that needs to be checked carefully is the peak separation between columns of self-centering systems. The median and standard deviation of peak column separations of the two self-centering CSMFs are presented in Figure 9-16 and Figure 9-17 for both DBE and MCE level ground motions, respectively. Results indicate that gaps on the steel rods will significantly increase the column separation. Moreover, the column separation at different story levels is not as uniform as for the system without gaps. As the intensity of ground motions increases, the peak column separation will also increase on all story levels. The results indicate that a 1-inch gap in the slab may be sufficient to allow the self-centering systems to work as envisioned.

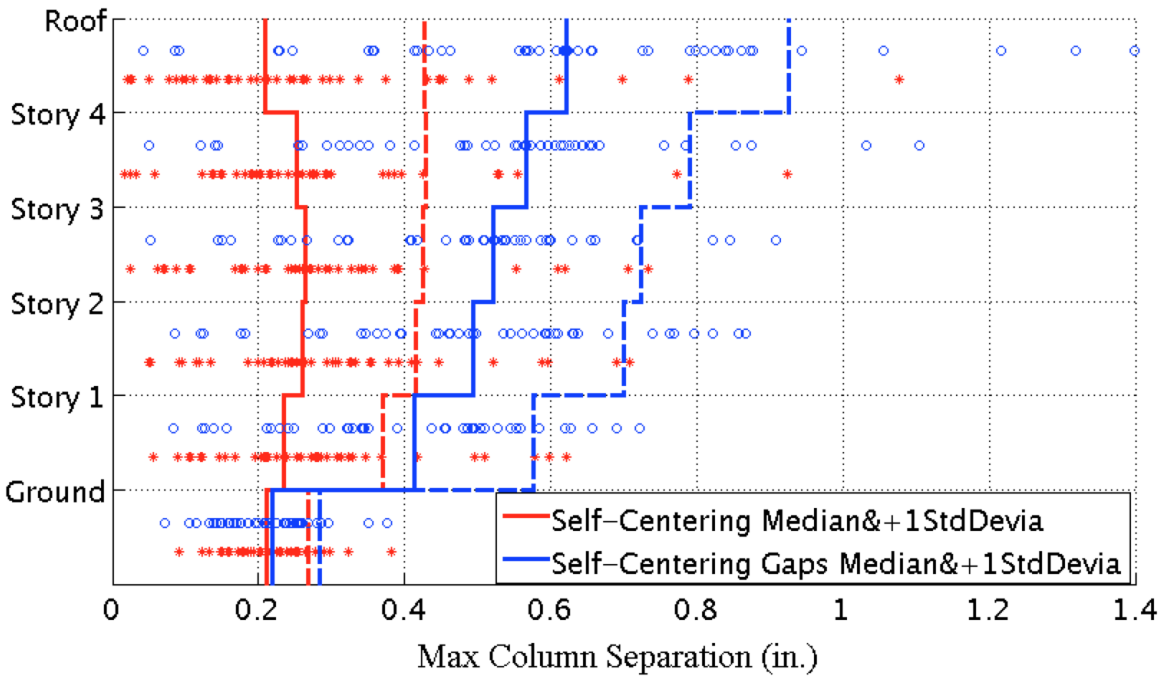

Figure 9-16: Median of the maximum column separation under 44 DBE level ground motions with a GSR = 0.9 & damping = 5%

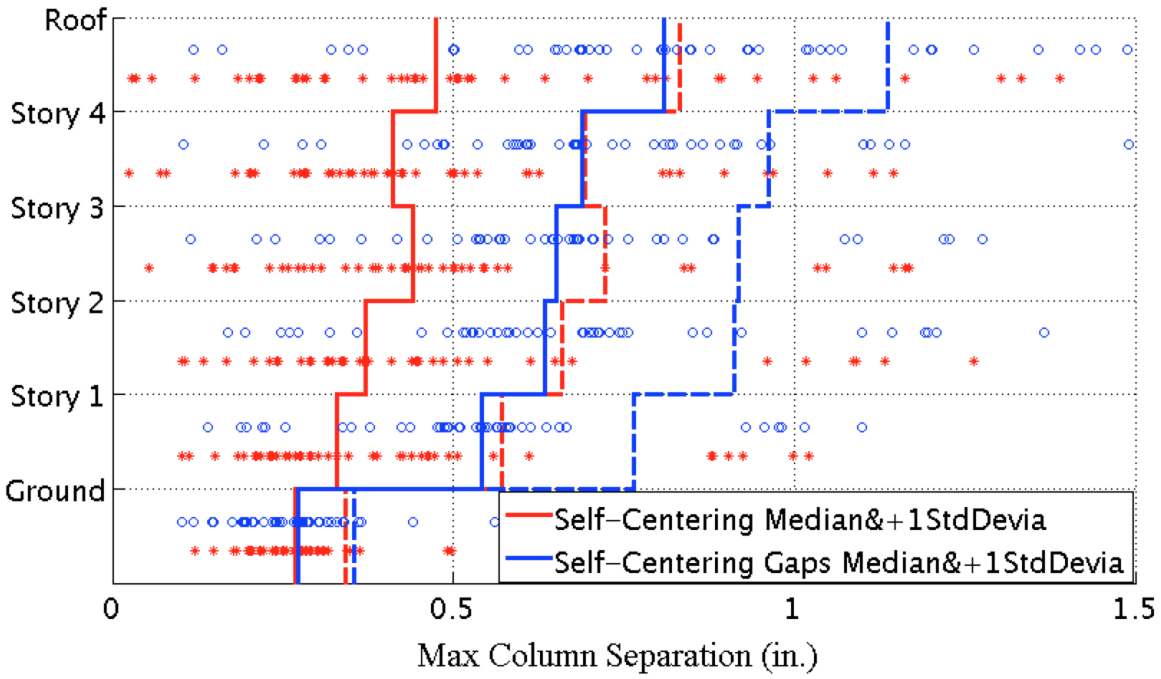

Figure 9-17: Median of the maximum column separation under 44 MCE level ground motions with a GSR = 0.9 & damping = 5%

9.3.2 Response of Individual Components

Because of the use of PR connections, greater deformation should be expected from connections as opposed to plastic deformations of the beams and columns as in the "conventional" frame. Figure 9-18 and Figure 9-19 show the peak rotation range (the difference between maximum rotations in positive and negative directions) of beam plastic hinges on each story. Figure 9-20 and Figure 9-21 show the maximum rotation of beam plastic hinges on each story level. The peak rotations of the beams in the self-centering CSMFs are obviously less than those in the "conventional" CSMF on the lower story levels. For the self-centering CSMF with gaps, the maximum rotation in beams on all story levels is reduced. However, for the self-centering CSMF without gaps, this benefit is seen only for the beams on the lower levels; the

beams on upper levels will see greater demands than their “conventional” counterpart.

Previous experiments indicate that the rotation capacity of connections with RBSs exceeds 0.04 radian [119]. Although results in Figure 9-21 show that the peak beam rotations can be as large as 0.12 radian in one isolated case, most of the values are well within the 0.04 radian limit. If the moment-rotation relationships of the two beam plastic hinges which are located in the 1st span and on the 3rd story are investigated (Figure 9-22 (a) and (b)) under the isolated load case (0.12 radian case) identified above, it is clear that the beams in the “conventional” CSMF have fractured. The beams do not fracture immediately at the peak rotation; they fracture in the following cycles under a relative low deformation due to accumulated plastic damage. However, they can also fracture at the peak rotation, such as for the beams on the first story under the same ground motion presented in Figure 9-22 (c) and (d).

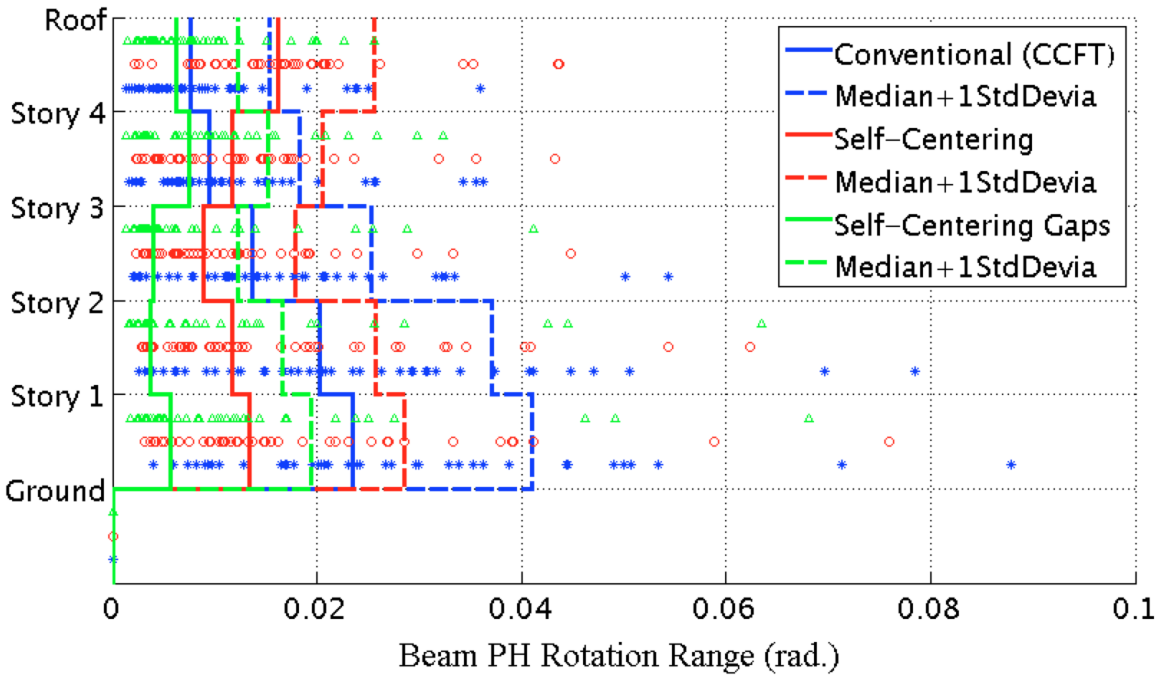

Figure 9-18: Median of the beam PH rotation range under 44 DBE level ground motions with a GSR = 0.9 & damping = 5%

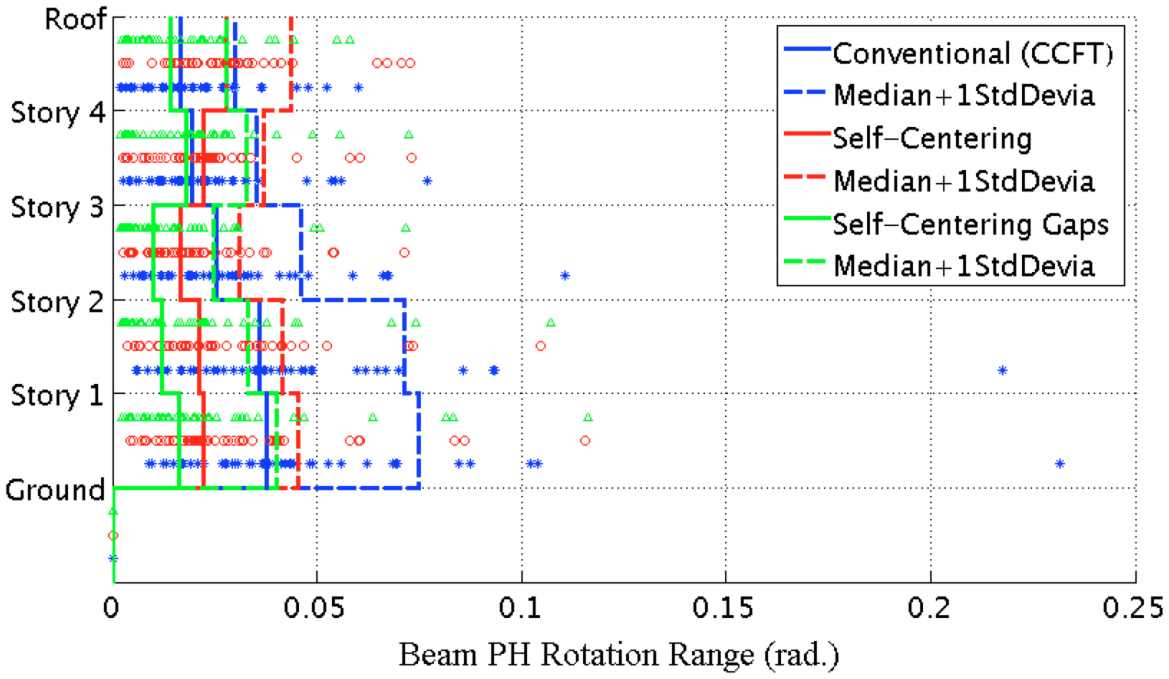

Figure 9-19: Median of the beam PH rotation range under 44 MCE level ground motions with a GSR = 0.9 & damping = 5%

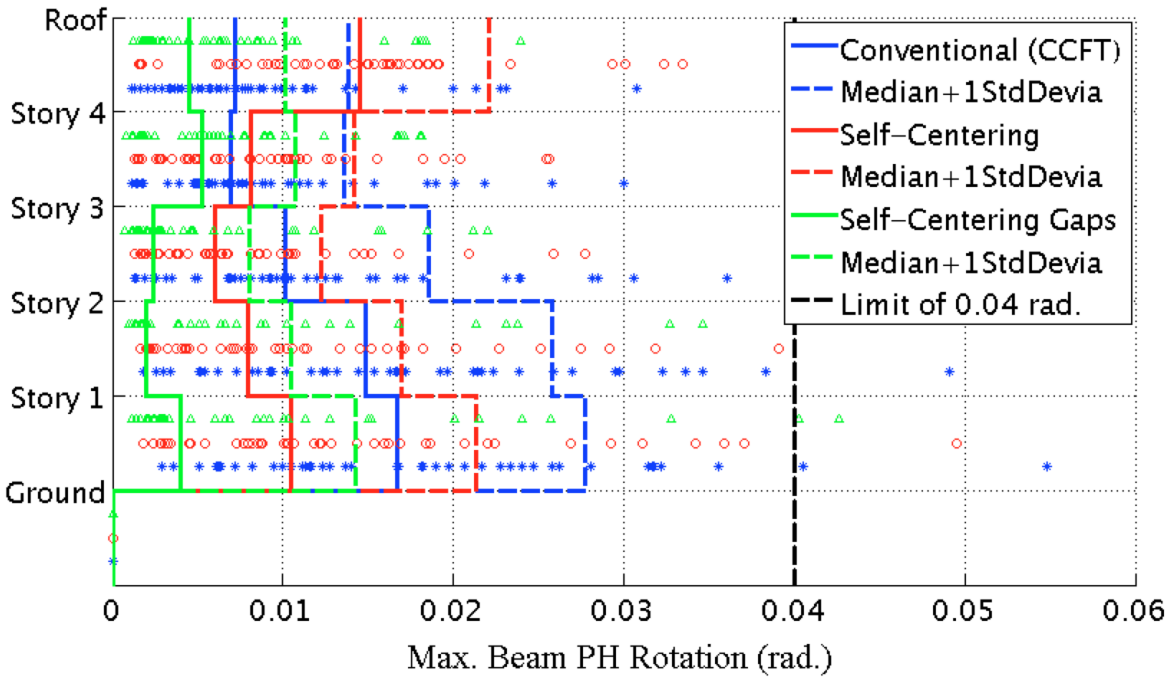

Figure 9-20: Median of the maximum beam PH rotation under 44 DBE level ground motions with a GSR = 0.9 & damping = 5%

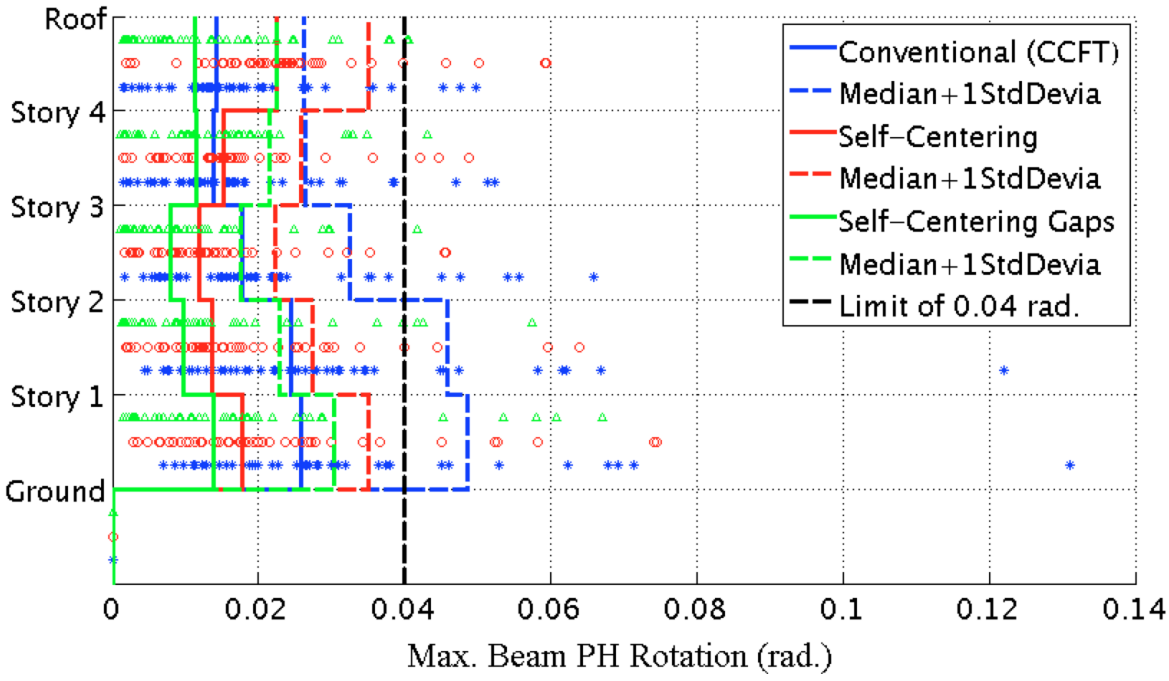

Figure 9-21: Median of the maximum beam PH rotation under 44 MCE level ground motions with a GSR = 0.9 & damping = 5%

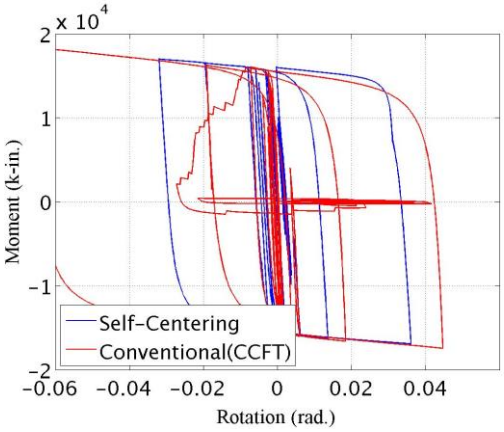

(a) Left in Span 1 on 3rd Story

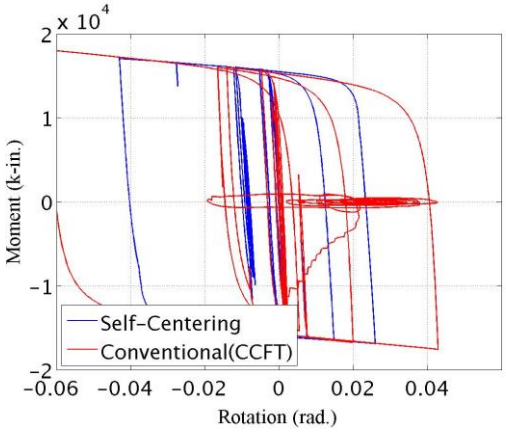

(b) Right in Span 1 on 3rd Story

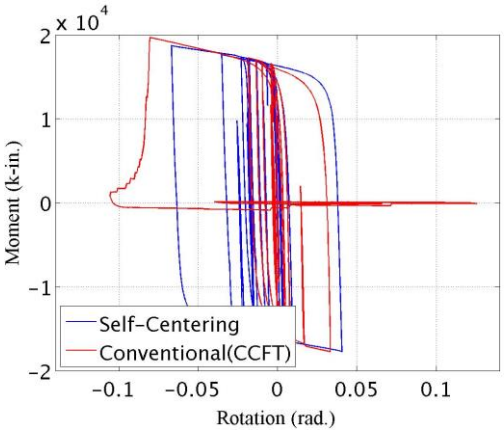

(c) Left in Span 1 on 1st Story

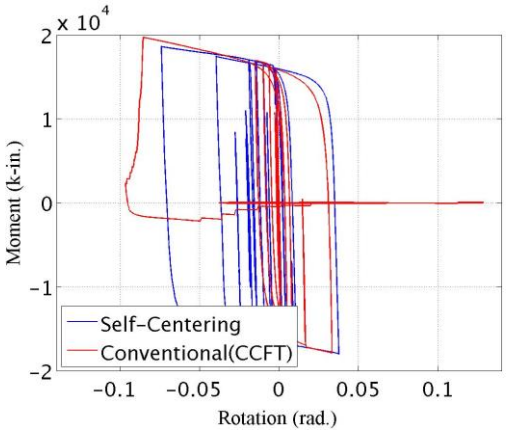

(d) Right in Span 1 on 3rd Story

Figure 9-22: Moment rotation relationship of beams in the 1st span on the 1st and 3rd stories under the ground motion which causes the largest peak rotation of 0.12 rad. in beams on the 1st story

Another phenomenon observed from the results of beam plastic hinge rotations (from Figure 9-18 to Figure 9-21) is that the maximum beam rotations are not symmetrical and there will be considerable residual deformation left in these beams. In Figure 9-23 and Figure 9-24, results of residual deformation of beam plastic hinges are presented. From these results, one can see that the residual deformation of beam plastic hinges of the self-centering CSMFs are not better than those of "conventional" CSMF as expected, in fact even worse on the first and roof levels.

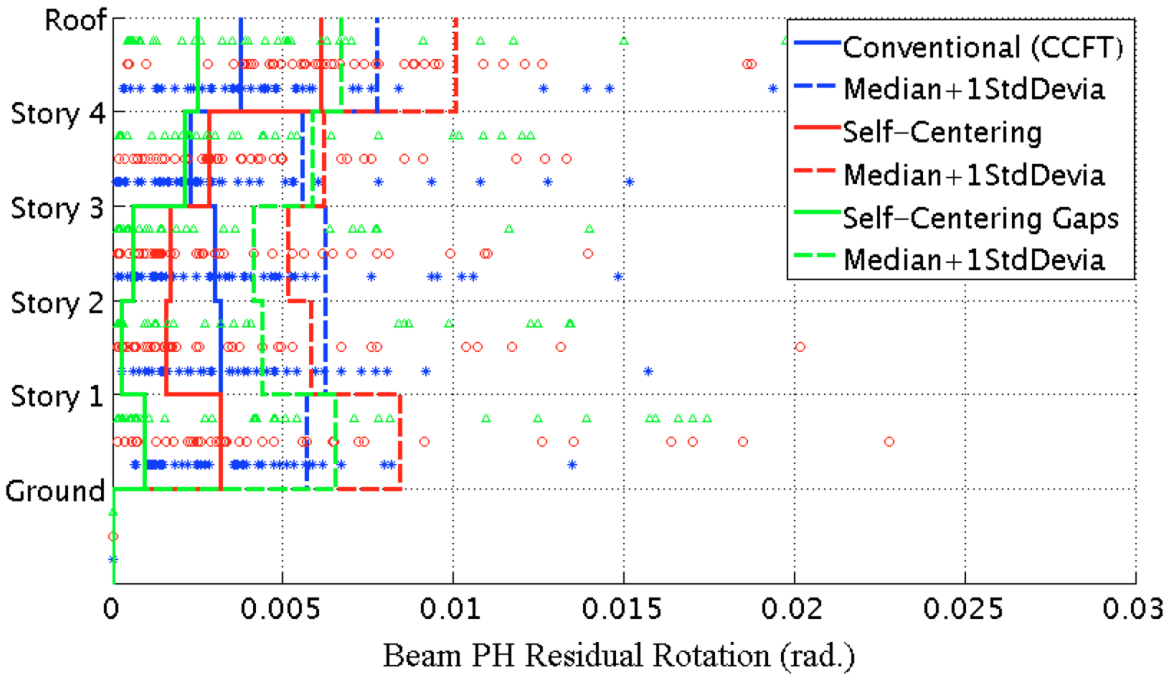

Figure 9-23: Median of the maximum residual rotation of beam plastic hinges under 44 DBE level ground motions with a GSR = 0.9 & damping = 5%

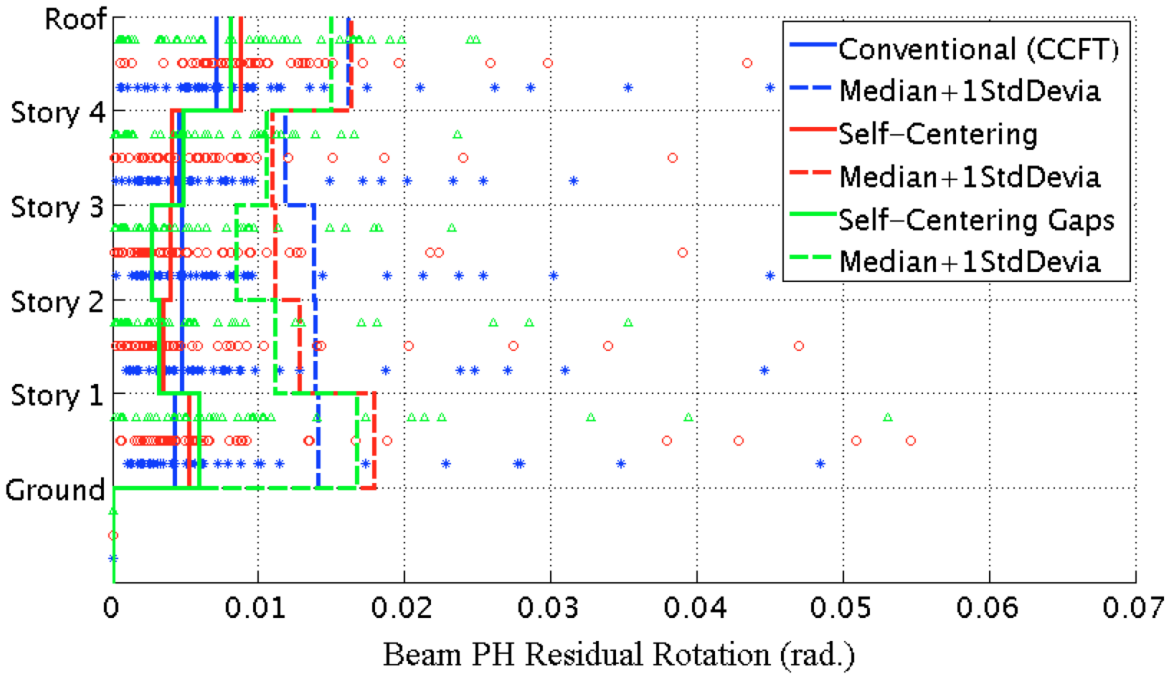

Figure 9-24: Median of the maximum residual rotation of beam plastic hinges under 44 MCE level ground motions with a GSR = 0.9 & damping = 5%

The reason of large residual deformation of beam plastic hinges in self-centering CMSFs originate from two situations: (1) when beams are yielded by some relative big pulses, and considerable residual rotations are generated, and/or (2) residual deformations can not be recovered by the following small cyclic plastic behavior. However, for the "conventional" CSMF, the idealized non-degrading plastic behavior is more likely to reduce the beam residual deformation. On the other hand, the damage in the beams of the "conventional" CSMF would be expected to be greater than for those in the self-centering CSMFs, resulting in local buckling or micro cracks in the flanges. In Figure 9-25, the cyclic behavior of six beam plastic hinges are presented; the hinges are located at both ends of three beams on the first story level. The ground motion is the component in North direction of the 20th record in Table 9-1. It is scaled to generate the largest residual rotation of beam plastic hinges in the self-centering system on the first story (0.0227 radian in Figure 9-23). From these results, one can see that the maximum rotation of both "conventional" and self-centering CSMFs are similar, but beams in "conventional" CSMF go through much larger plastic cycles. This indicates that the self-centering system does protect beams from severe damage although it doesn't reduce residual deformation as effectively as expected.

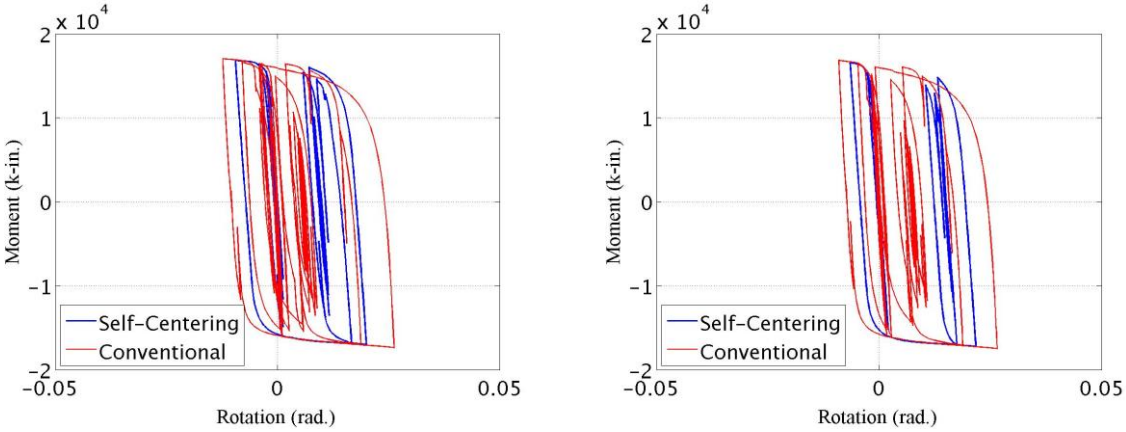

(a) Left in Span 1

(b) Right in Span 1

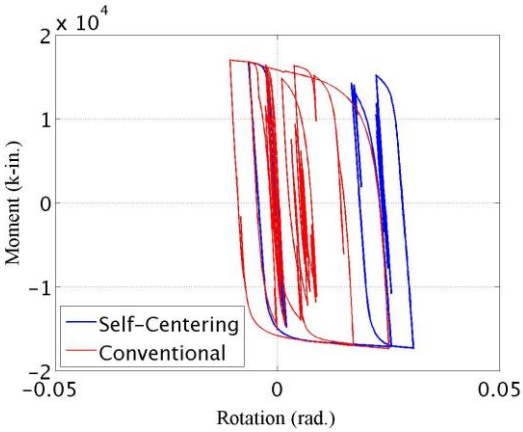

(c) Left in Span 2

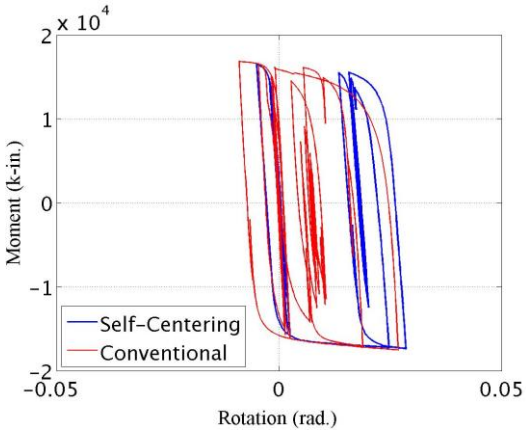

(d) Right in Span 2

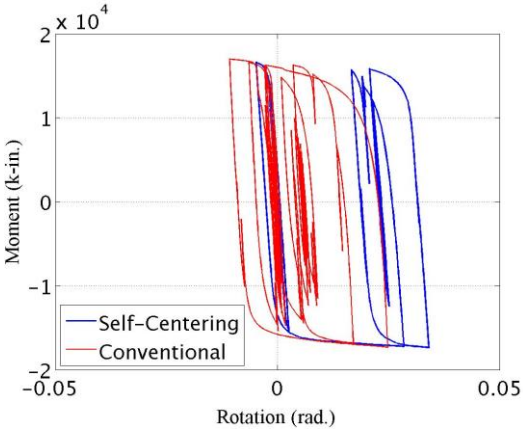

(e) Left in Span 3

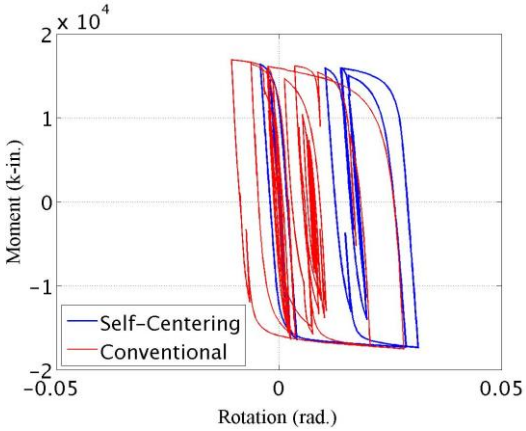

(f) Right in Span 3

Figure 9-25: Cyclic behavior of beam plastic hinges on the 1st story under the ground motion causing the largest residual deformation in the self-centering system

Plastic deformation of columns is another important source of system residual deformation.

For self-centering system, due to relatively low stiffness of the PR connections, greater lateral drifts will be observed than in "conventional" CSMF with FR connections. Therefore, greater plastic deformation of columns will be expected in the self-centering systems. Column plastic hinge rotation ranges (the difference of maximum rotations between positive and negative directions) on each story level are presented in Figure 9-26 and Figure 9-27. Maximum rotations of column plastic hinges are presented in Figure 9-28 and Figure 9-29. The self-centering CSMF will generate greater column plastic hinge rotations than the "conventional" CSMF.

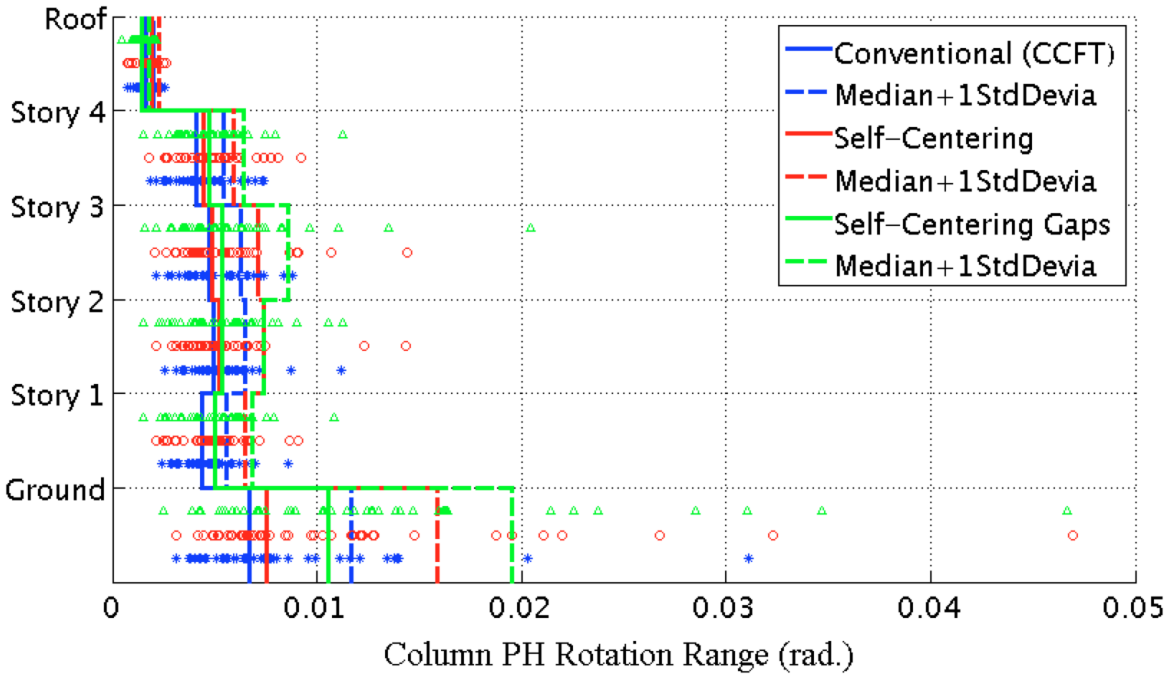

Figure 9-26: Median of the column PH rotation range under 44 DBE level ground motions with a GSR = 0.9 & damping = 5%

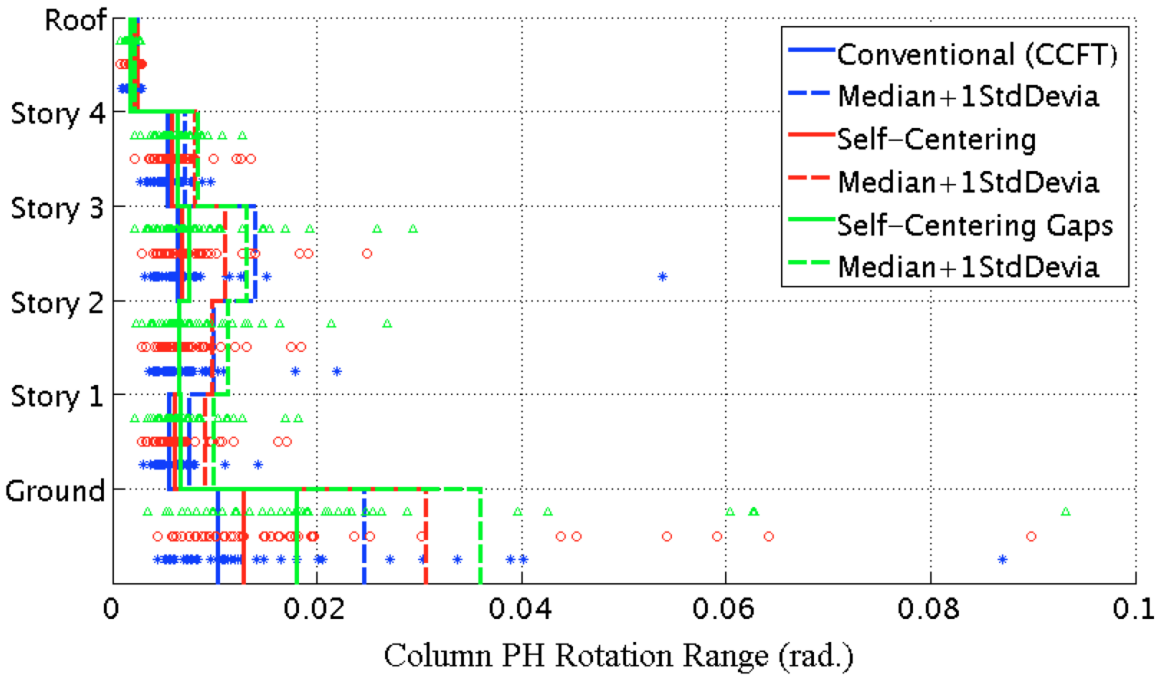

Figure 9-27: Median of the column PH rotation range under 44 MCE level ground motions with a GSR = 0.9 & damping = 5%

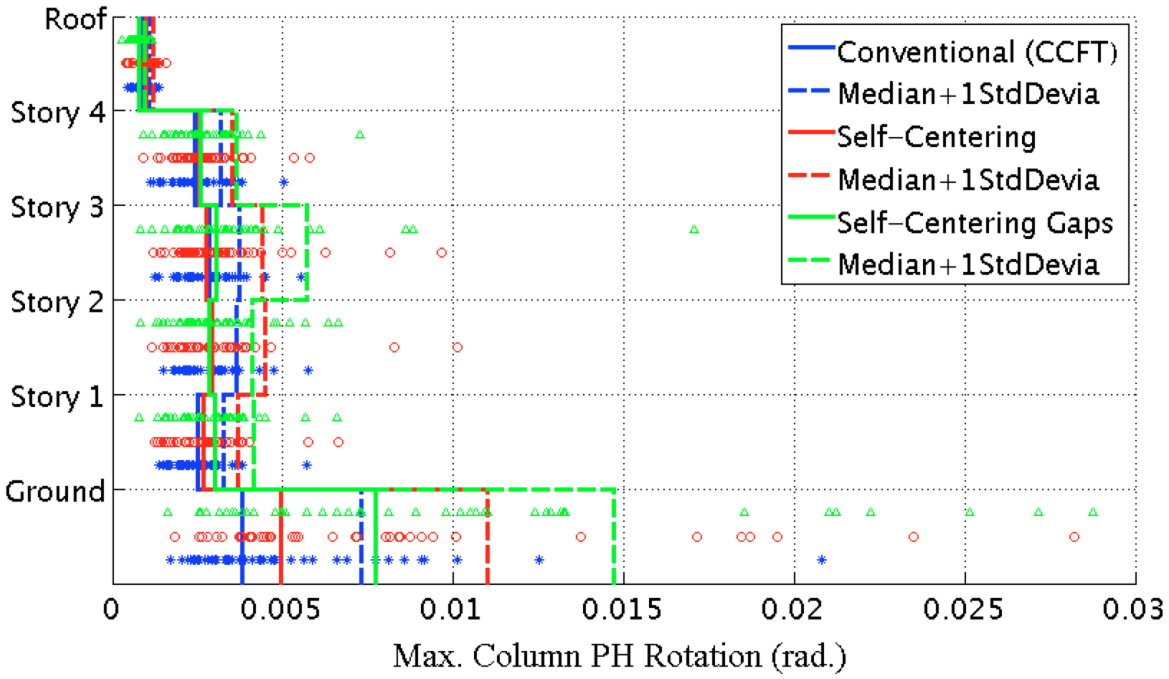

Figure 9-28: Median of the maximum column PH rotation under 44 DBE level ground motions with a GSR = 0.9 & damping = 5%

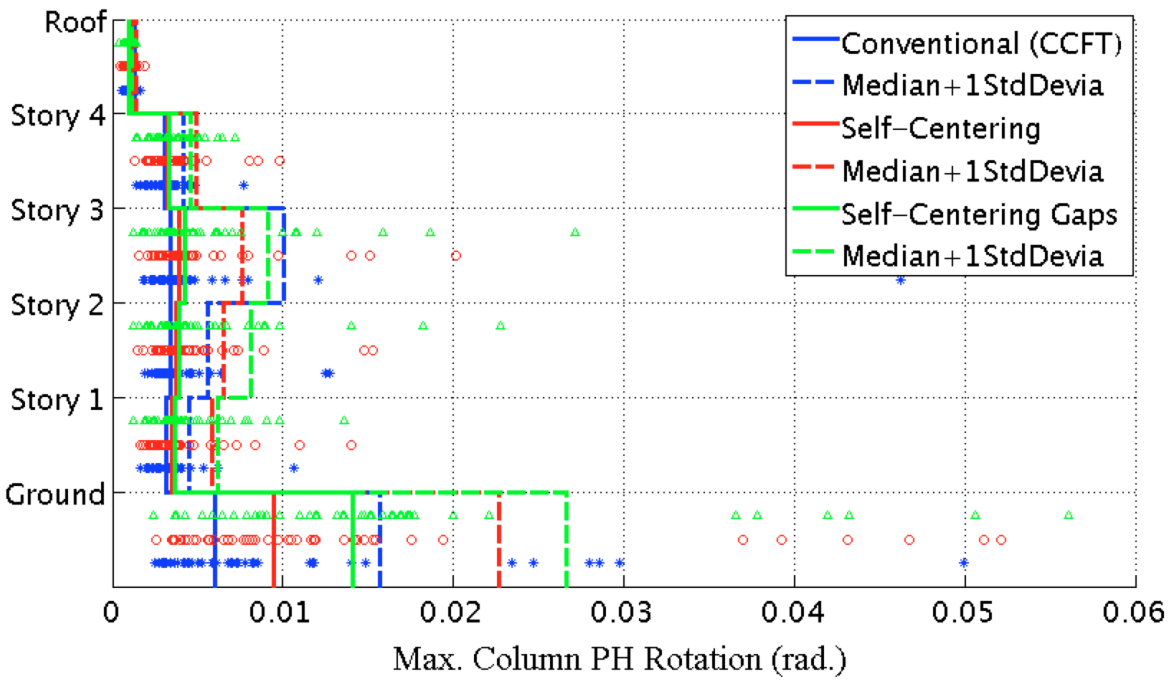

Figure 9-29: Median of the maximum column PH rotation under 44 MCE level ground motions with a GSR = 0.9 & damping = 5%

The residual deformation of the columns under both DBE and MCE level ground motions are shown in Figure 9-30 and Figure 9-31. The same tendency as for column plastic hinge deformations can be observed, with the maximum residual deformations concentrating at the base level. Due to greater yielding of columns in the self-centering systems, there will be larger residual deformation for those structures.

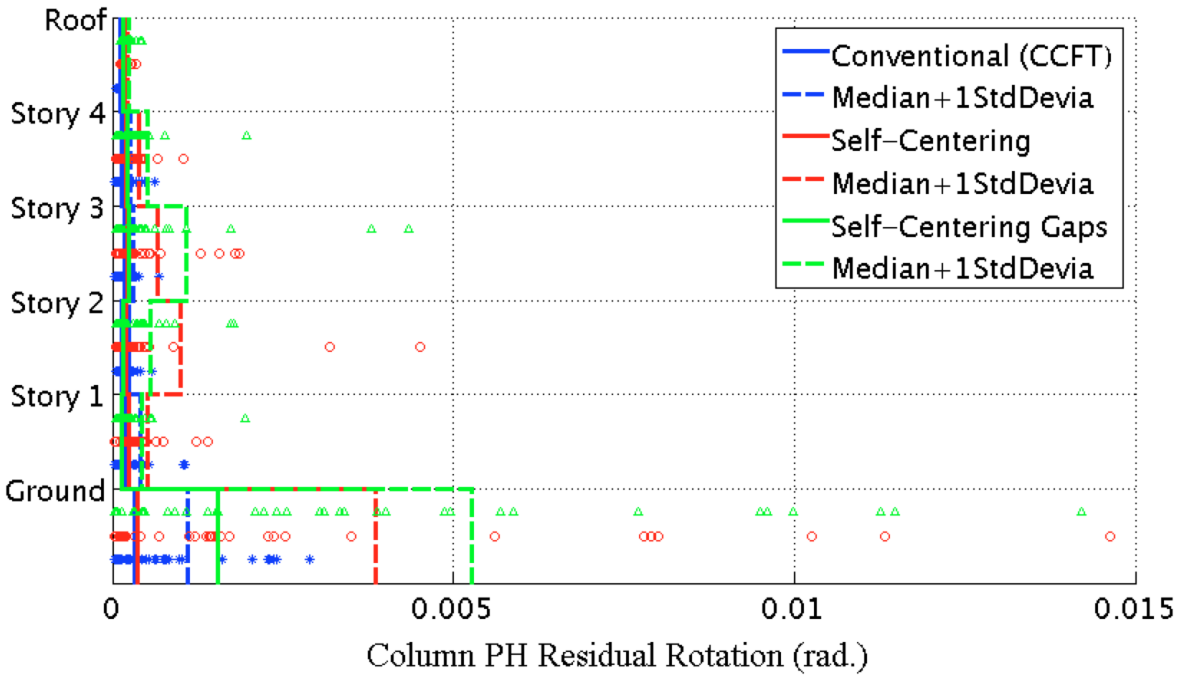

Figure 9-30: Median of the maximum residual rotation of column plastic hinges under 44 DBE level ground motions with a GSR = 0.9 & damping = 5%

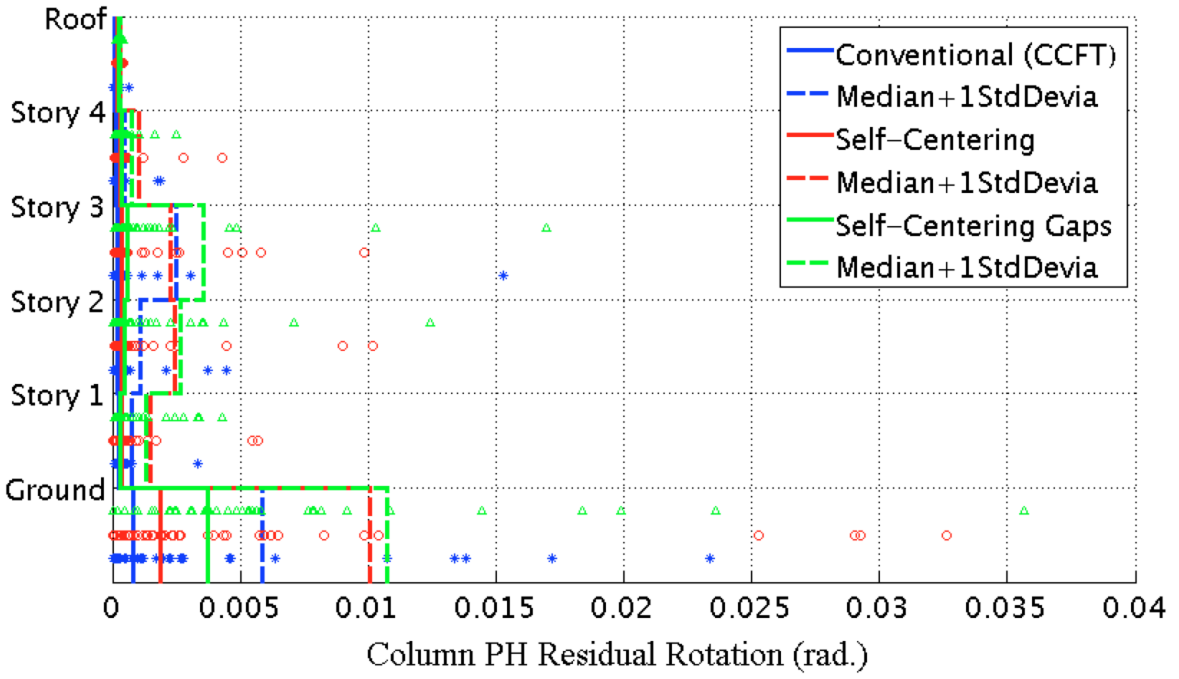

Figure 9-31: Median of the maximum residual rotation of column plastic hinges under 44 MCE level ground motions with a GSR = 0.9 & damping = 5%

The total number of times that the yield strength is reached by all column plastic hinges on each story under both DBE and MCE level ground motions are presented in Table 9-6, Table 9-7 and Table 9-8. For each story, there are eight column plastic hinges (two hinges in each of four columns). The tables correspond to the three chosen strength levels shown in Figure 9-32: (1) Level 1 is defined as the strength of Point A on the simplified column moment rotation curve (Figure 7-28); (2) Level 2 is defined as 1.05 times of Level 1 strength; and (3) Level 3 is defined as 1.1 times of Level 1 strength. The green curve in Figure 9-32 is the monotonic moment rotation relationship coming from fiber section analyses. Compared with the monotonic curve, one can see that when Level 1 is reached, the columns are in the very beginning state of their plastic stage, and that even for Level 3 the column plastic damage is still very limited.

Compared with the "conventional" CSMF, the self-centering CSMFs will have more column plastic hinges reaching the first two level strengths, especially in the middle stories. However, for a higher level strength, results in Table 9-8 shows that there is no big difference between the "conventional" and self-centering CSMFs. There are even more column hinges reaching Level 3 in the "conventional" CSMF in the middle stories. As mentioned above, plastic demand even under Level 3 is moderate, and column damage for all three CSMFs is limited.

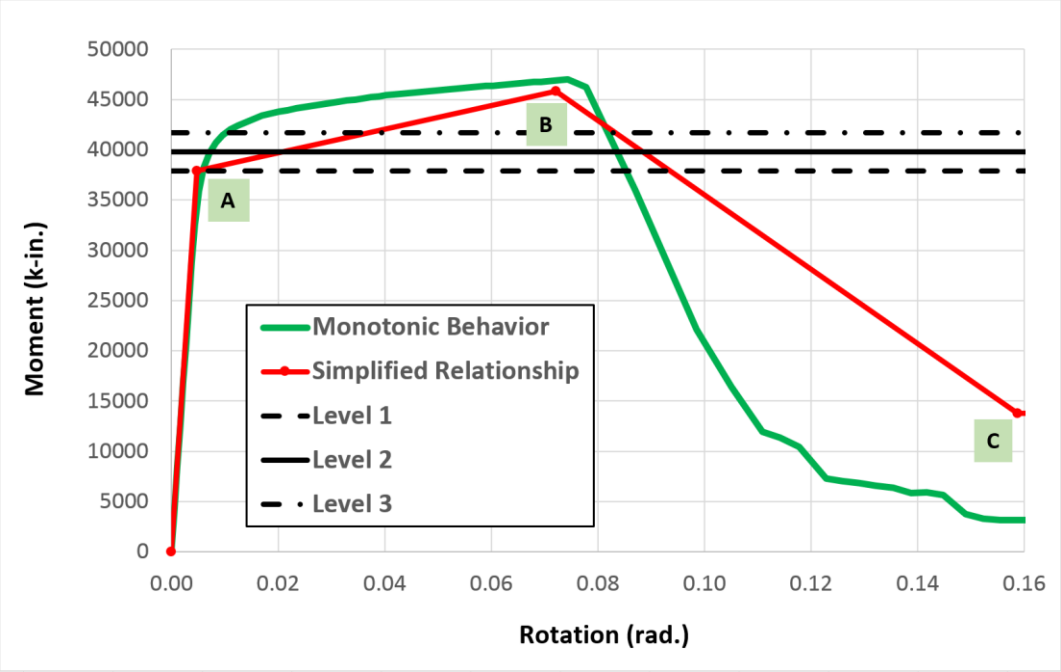

Figure 9-32: Three strength levels for the column yielding investigation

Table 9-6: Number of Column Plastic Hinges Reaching Strength of Level 1 under 44 Ground Motions on Each Story Level

Story	DBE			MCE		
	Convent.	Self-Cent.	SC-Gaps	Convent.	Self-Cent.	SC-Gaps
Ground	70	97	129	147	185	239
Level 1	0	1	1	8	15	18
Level 2	0	6	2	13	17	29
Level 3	2	7	14	16	29	45
Level 4	0	0	3	2	4	2
Roof	0	0	0	0	0	0
Total	72	111	149	186	250	333

Table 9-7: Number of Column Plastic Hinges Reaching Strength of Level 2 under 44 Ground Motions on Each Story Level

Story	DBE			MCE		
	Convent.	Self-Cent.	SC-Gaps	Convent.	Self-Cent.	SC-Gaps
Ground	29	59	79	88	121	171
Level 1	0	0	0	4	4	3
Level 2	0	1	0	5	8	11
Level 3	0	0	1	9	14	18
Level 4	0	0	0	0	0	0
Roof	0	0	0	0	0	0
Total	29	60	80	106	147	203

Table 9-8: Number of Column Plastic Hinges Reaching Strength of Level 3 under 44 Ground Motions on Each Story Level

Story	DBE			MCE		
	Convent.	Self-Cent.	SC-Gaps	Convent.	Self-Cent.	SC-Gaps
Ground	8	25	31	46	61	76
Level 1	0	0	0	0	0	0
Level 2	0	0	0	0	0	1
Level 3	0	0	0	4	0	0
Level 4	0	0	0	0	0	0
Roof	0	0	0	0	0	0
Total	8	25	31	50	61	77

9.3.3 Axial Force in Beams and Columns

For traditional moment frames with rigid diaphragm constraints, axial forces in beams are not significant, but they can be high in the beams of the new proposed self-centering CSMFs because of column separations.

In Figure 9-35 and Figure 9-36, results of peak tension and compression forces in the beams are plotted, indicating that there is no big difference in peak magnitudes of tension and compression in all story levels. Therefore, both tension and compression should be considered in the design checks.

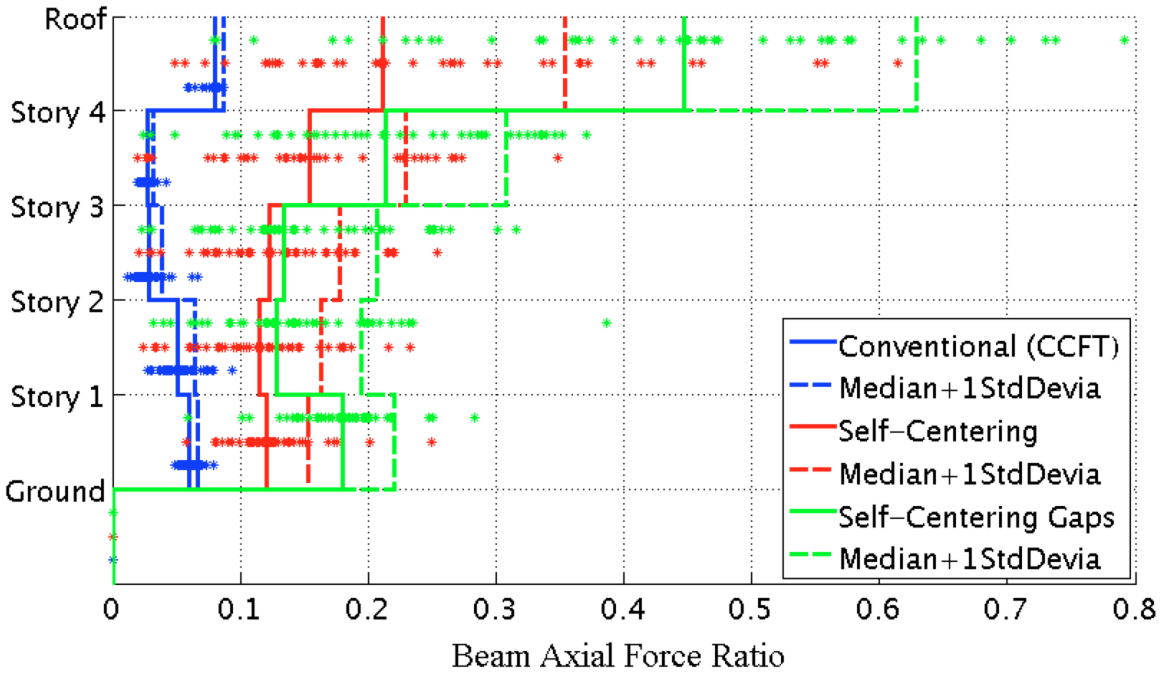

Figure 9-33: Median of the peak axial force in beams under 44 DBE level ground motions with a GSR = 0.9 & damping = 5%

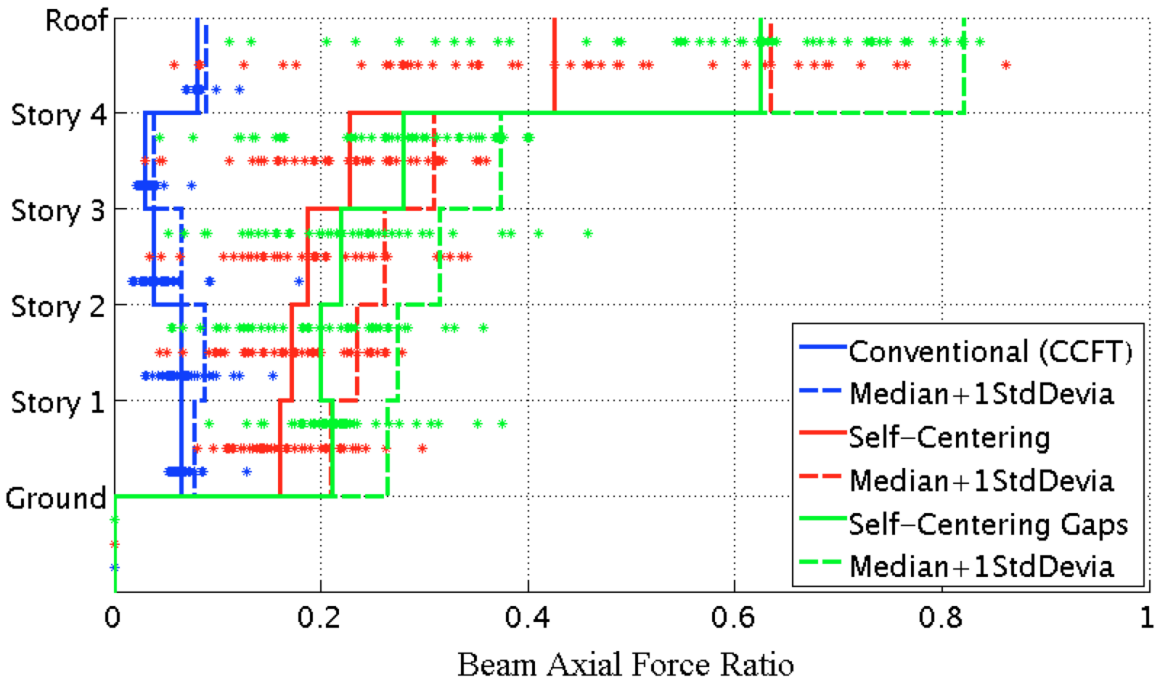

Figure 9-34: Median of the peak axial force in beams under 44 MCE level ground motions with a GSR = 0.9 & damping = 5%

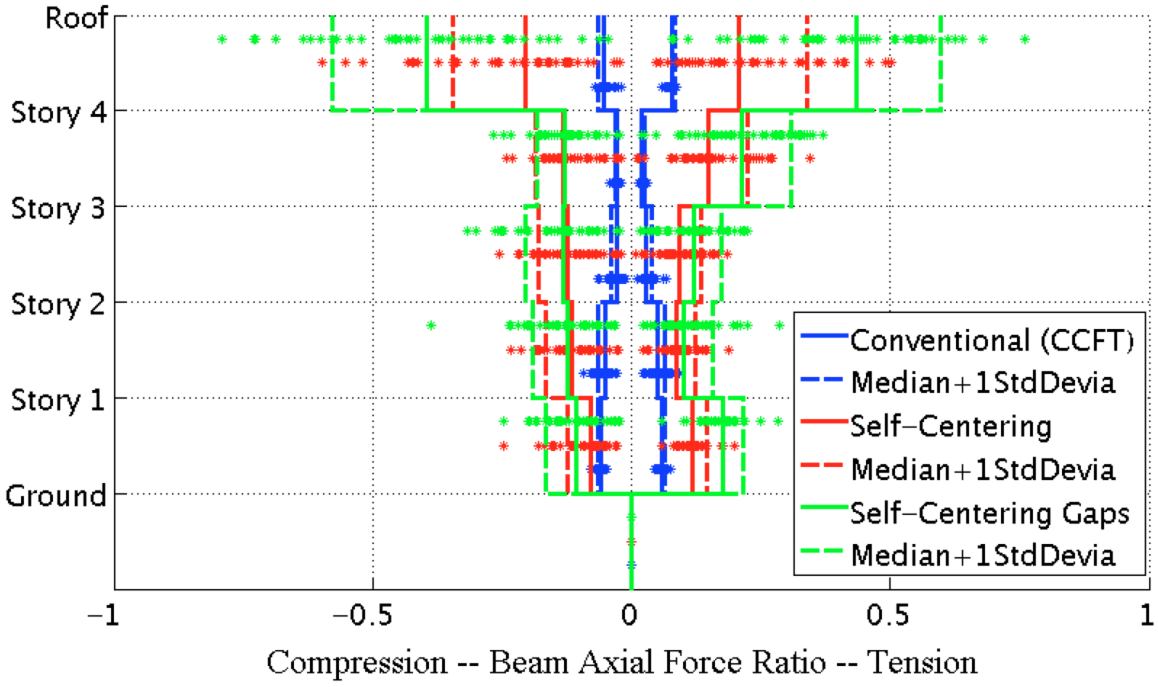

Figure 9-35: Median of the peak tension vs.compression in beams under 44 DBE level ground motions with a GSR = 0.9 & damping = 5%

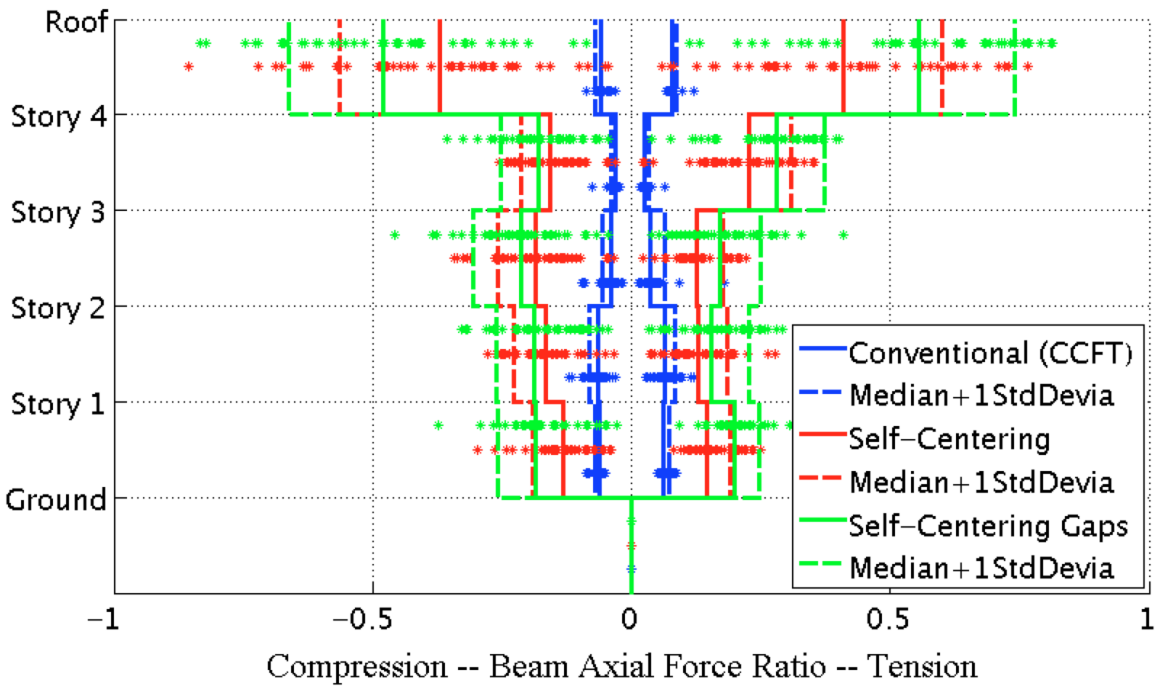

Figure 9-36: Median of the peak tension vs.compression in beams under 44 MCE level ground motions with a GSR = 0.9 & damping = 5%

The axial force levels in columns are also investigated to whether further refinement in the modeling of column plastic hinges is necessary. Axial forces in columns are presented in Figure 9-37 and Figure 9-38. Unlike the increases in axial forces for beams, the self-centering systems generate similar axial forces in columns to the "conventional" system. Results show that for most of cases, the axial forces in columns will be less than 12% of specified yielding capacity of the column cross section, indicating that the axial-flexural interaction effects in columns are not significant. Thus, it is reasonable to use concentrated nonlinear springs to simulate column plastic hinges without considering axial-flexural interactions, instead of using fiber sections.

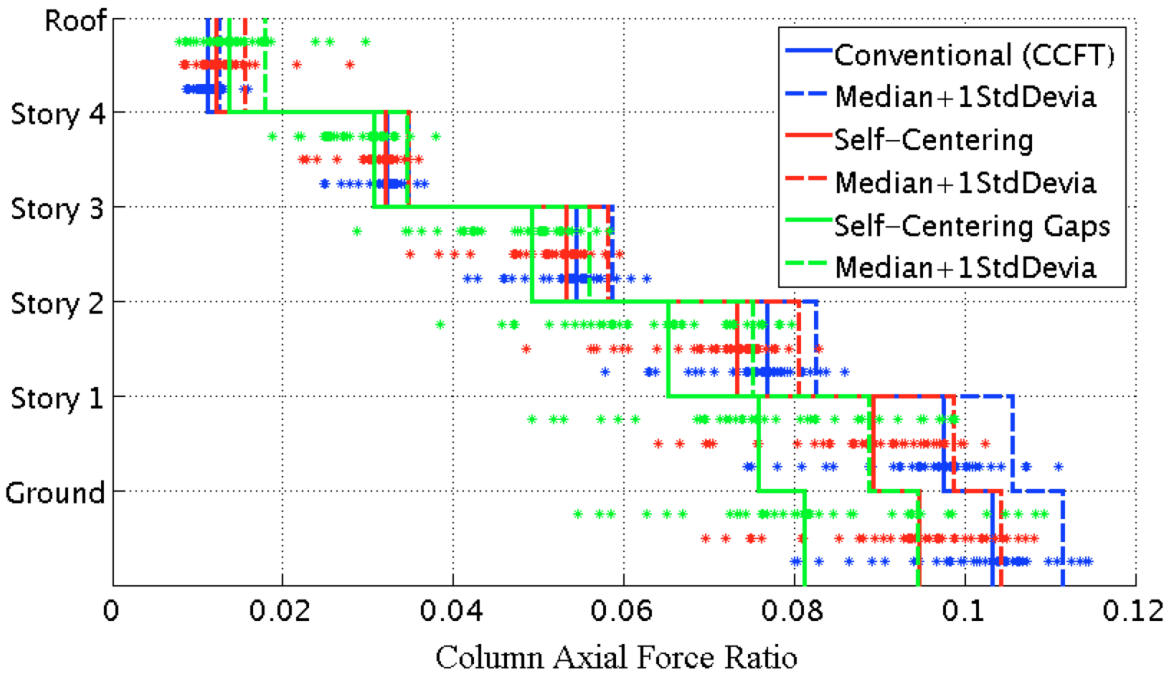

Figure 9-37: Median of the peak axial force in columns under 44 DBE level ground motions with a GSR = 0.9 & damping = 5%

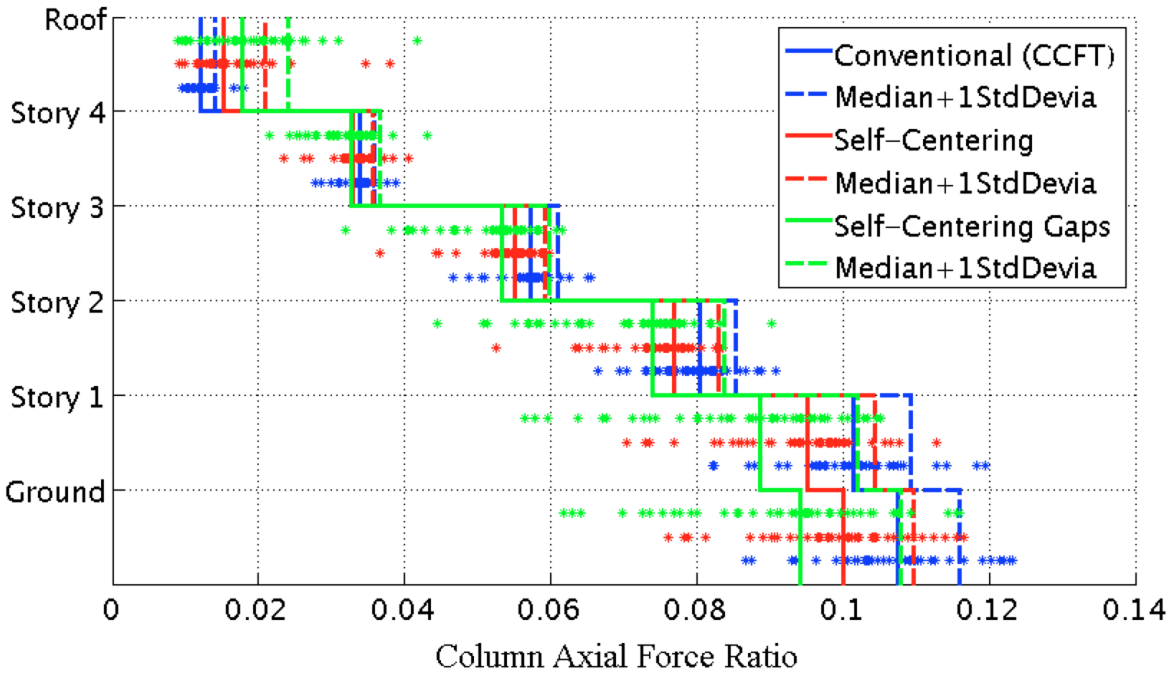

Figure 9-38: Median of the peak axial force in columns under 44 MCE level ground motions with a GSR = 0.9 & damping = 5%

9.3.4 Story Velocity and Acceleration

Damage of non-structural components is a great contributor to direct economic losses and business interruption for many facilities after an earthquake. Besides peak inter-story drifts, peak story velocity and acceleration will have an impact on non-structural component damage [120, 121]. The peak story velocities and accelerations of three CSMFs are presented in Figure 9-39 to Figure 9-42. Results indicate that the self-centering system show larger values for both floor velocity and acceleration. As the floor height increases, the corresponding story velocity also increases; however, floor acceleration has less dependence on floor height.

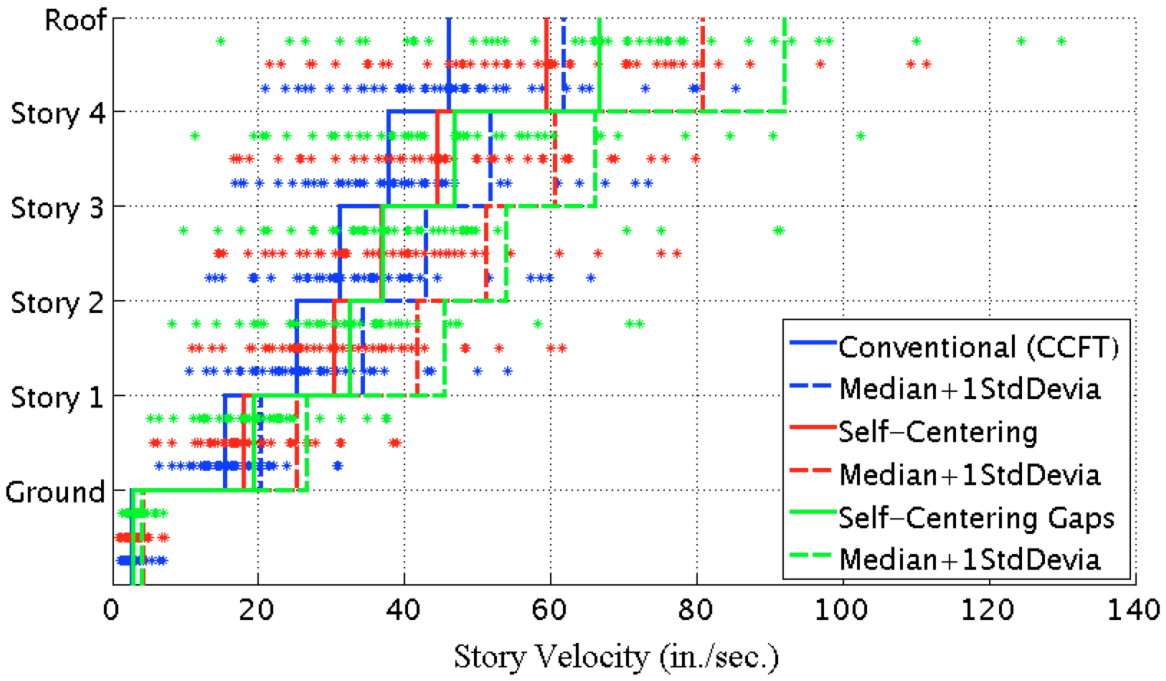

Figure 9-39: Median of the peak story velocity under 44 DBE level ground motions with a GSR = 0.9 & damping = 5%

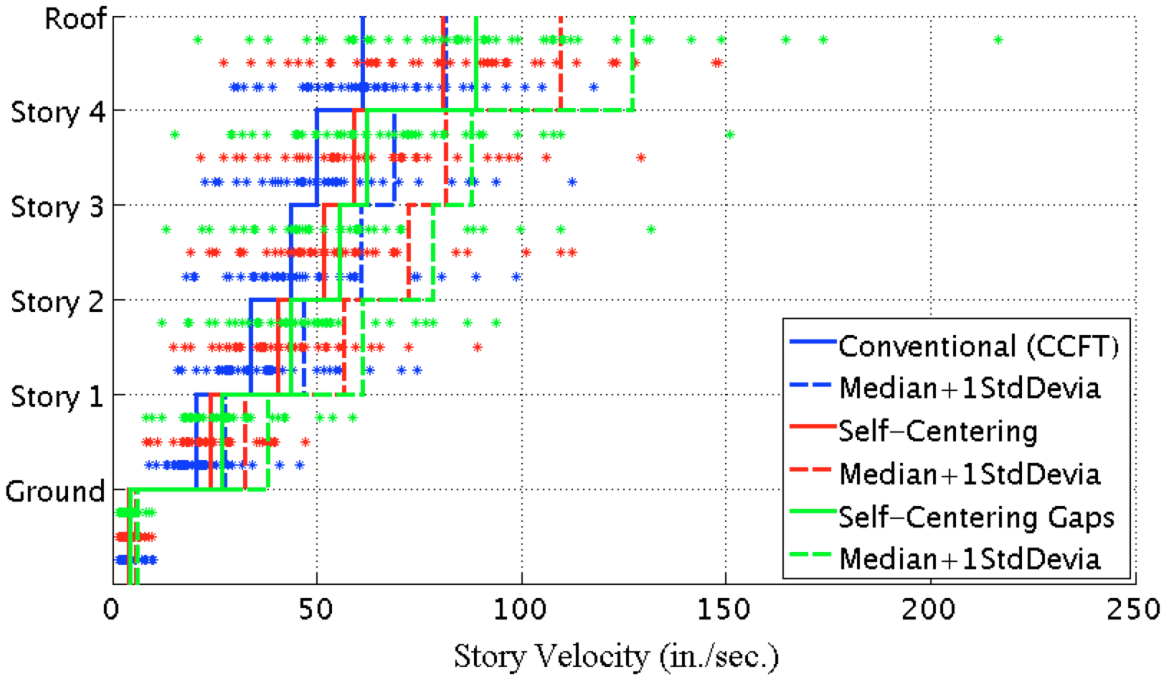

Figure 9-40: Median of the peak story velocity under 44 MCE level ground motions with a GSR = 0.9 & damping = 5%

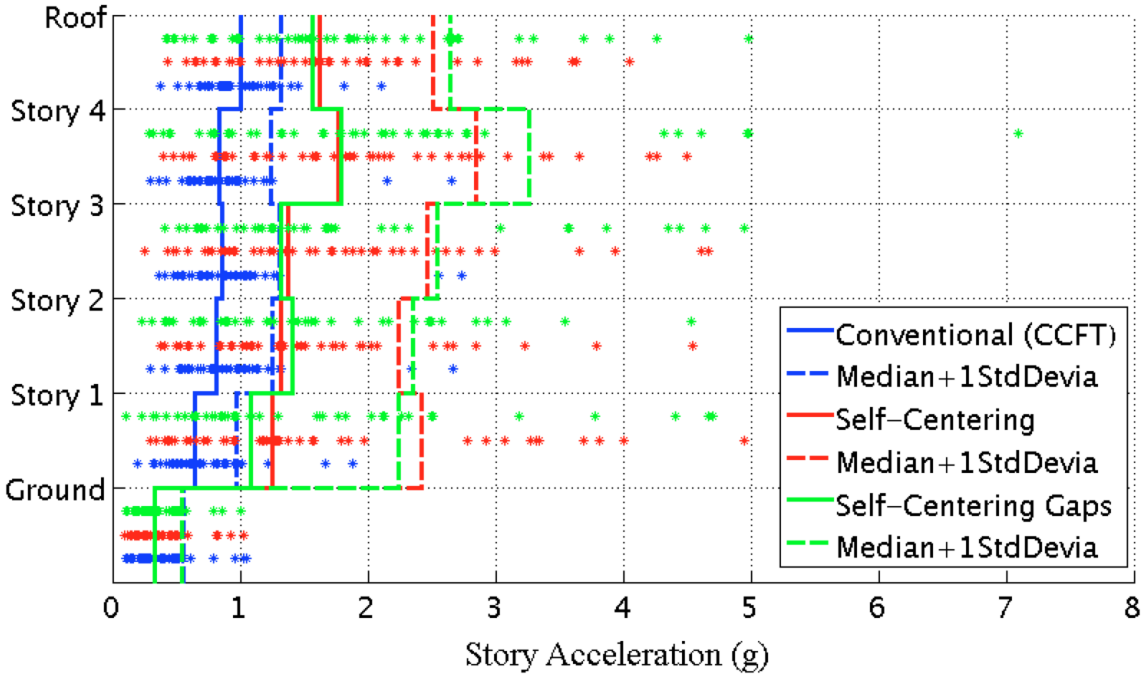

Figure 9-41: Median of the peak story acceleration under 44 DBE level ground motions with a GSR = 0.9 & damping = 5%

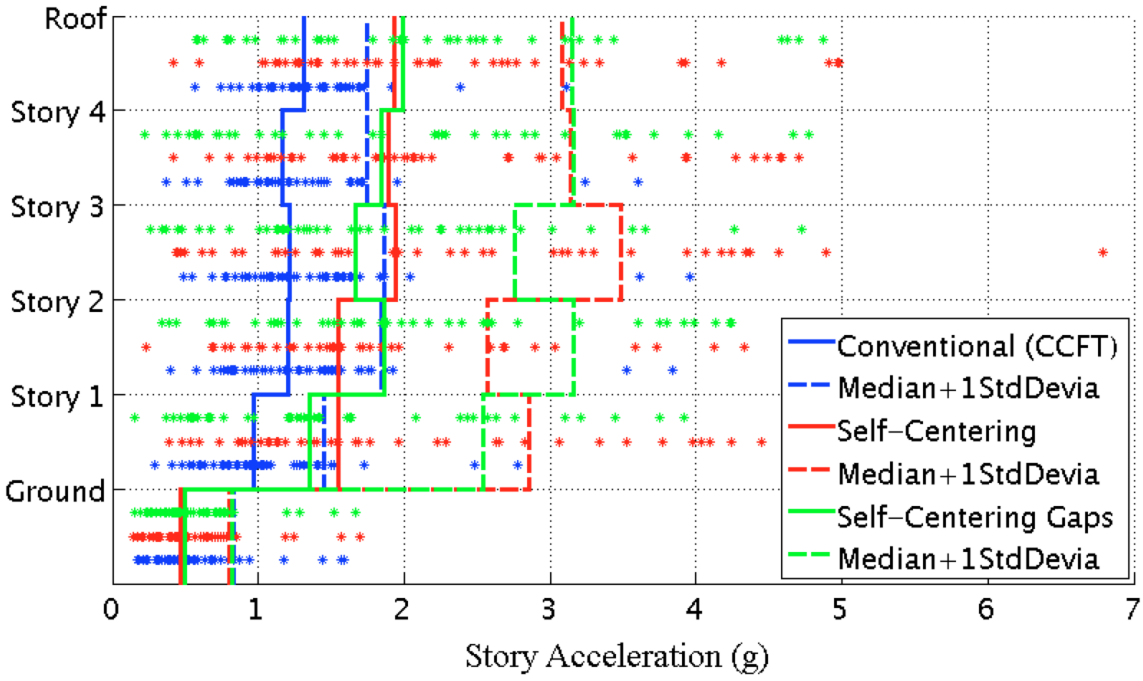

Figure 9-42: Median of the peak story acceleration under 44 MCE level ground motions with a GSR = 0.9 & damping = 5%

From the greater standard deviations in Figure 9-41 and Figure 9-42, one can see that peak floor acceleration of the self-centering CSMFs is more sensitive to spectral shapes of different ground motions than the "conventional" CSMF. This may require the use of additional damping devices. Potential methods for mitigation on floor acceleration response should be proposed in future research.

9.3.5 Overall Comparisons

Overall comparisons of all seismic responses of three CSMFs are presented in Table 9-9. From these comparison, one can see that by applying the new proposed self-centering connections, the seismic performance is not as good as the best one expected for a "conventional" CSMF

with CCFT columns. However, the caveat that the "conventional" CSMF represents "ideal" behavior should be kept in mind.

Table 9-9: Comparisons of Seismic Responses among Three CSMFs with a GSR = 0.9 & Damping = 5%

Seismic Response	Convent. vs. SC & SC-Gaps		SC vs. SC-Gaps	
	Best	Advantage	Better	Advantage
Story Residual Drift	SC-Gaps	Small	SC-Gaps	Small
Inter-Story Residual Drift	SC-Gaps	Small	SC-Gaps	Small
Peak Inter-Story Drift	Convent.	Large	SC	Obvious
Column Separation	Convent.	Obvious	SC	Large
Beam PH Rot. Range	SC-Gaps	Large	SC-Gaps	Obvious
Peak Beam PH Rotation	SC-Gaps	Large	SC-Gaps	Obvious
Beam PH Residual Rot.	SC-Gaps	Small	SC-Gaps	Small
Column PH Rot. Range	Convent.	Obvious	SC	Small
Peak Column PH Rotation	Convent.	Obvious	SC	Small
Column PH Residual Rot.	Convent.	Obvious	SC	Small
Peak Beam Axial Force	Convent.	Large	SC	Obvious
Peak Column Axial Force	SC-Gaps	Obvious	SC-Gaps	Small
Peak Story Velocity	Convent.	Obvious	SC	Small
Peak Story Acceleration	Convent.	Large	SC	Small

Note: Small < Obvious < Large

9.4 Spectral Shape Effects on System Residual Drift

Duration, frequency content and peak acceleration of a ground motion have an impact on system dynamic response. In order to find out how spectral shapes influence the residual drifts

of self-centering systems, the response spectra of two components of one record at the same recording station are compared.

The two chosen ground motions are the two orthogonal components of the Chi-Chi, Taiwan earthquake (ID No. 19 in Table 9-1). The original ground motions are recorded at Station CHY101, and they are scaled to MCE level as two individual records in Figure 9-4. These records were selected as they maximize the system residual displacements of the self-centering CSMFs.

The maximum residual story drifts of the three CSMFs under these two scaled ground motions are presented in Table 9-10. The self-centering systems show obvious differences under these two ground motions. They have greater residual drifts under the component in the East direction, and much less in the North direction. Also, the self-centering system with gaps has substantially less residual drifts than its counterpart without gaps. However, for the "conventional" CSMF, the residual drifts are greater under the ground motion component in the North direction but the differences are much less than for the self-centering systems. This may indicate that the self-centering system is much more sensitive to the different characteristics of the two chosen ground motions than the "conventional" system. Obviously the sample size used here is insufficient to make this a general conclusion, but is consistent with spot checking of a few other ground motions.

Table 9-10: Maximum Residual Story Drift under Two Scaled Components of Chi-Chi Earthquake on MCE Level with a GSR = 0.9 & Damping = 5% (unit: inch)

Level	"conventional"		Self-Centering		SC with Gaps	
	CHY101-East	CHY101-North	CHY101-East	CHY101-North	CHY101-East	CHY101-North
Basement	0.0136	0.0195	0.0215	0.0083	0.0152	0.0129
Story 1	3.5264	6.1164	6.4891	1.3291	3.4096	0.0827
Story 2	7.2502	12.658	13.311	2.6775	6.9641	0.0513
Story 3	10.890	18.071	19.642	3.7684	10.347	0.0886
Story 4	14.370	20.769	25.225	4.6089	13.433	0.2349
Roof	17.857	23.005	30.725	5.2894	16.516	0.6456

The two scaled ground motions are plotted in Figure 9-43. Their acceleration, velocity and displacement response spectra are shown in Figure 9-44, Figure 9-45, and Figure 9-46, respectively. From these plots, one can see that around the first period of all three CSMFs, which are between 1.3 and 1.4 seconds, all three spectra indicate that the component of ground motion in the North direction will yield greater peak responses. For example, all three CSMFs will have greater peak inter-story as indicated in Table 9-11. However, it is hard to predict residual drifts based on the three response spectra. Therefore, the dynamic behavior of self-centering systems can be very different from those of "conventional" system, and should be investigated very carefully.

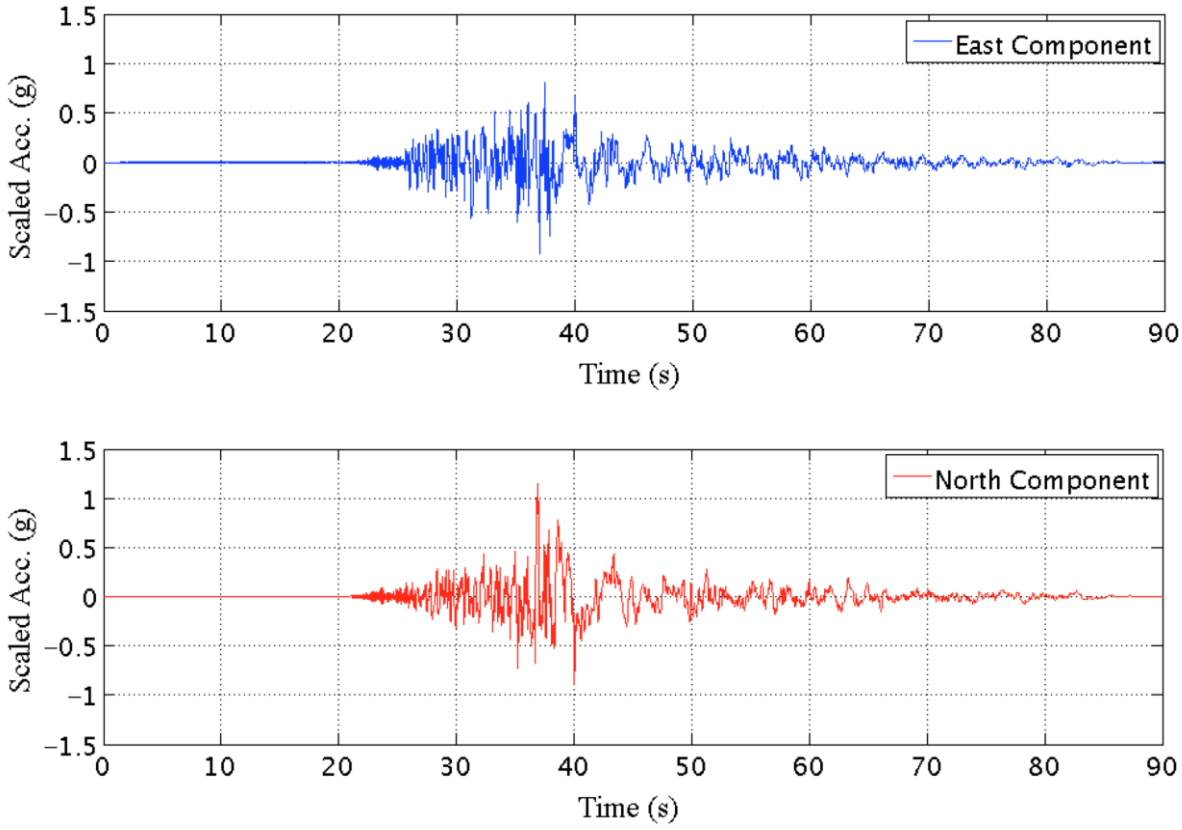

Figure 9-43: Scaled records of two orthogonal components of Chi-Chi earthquake

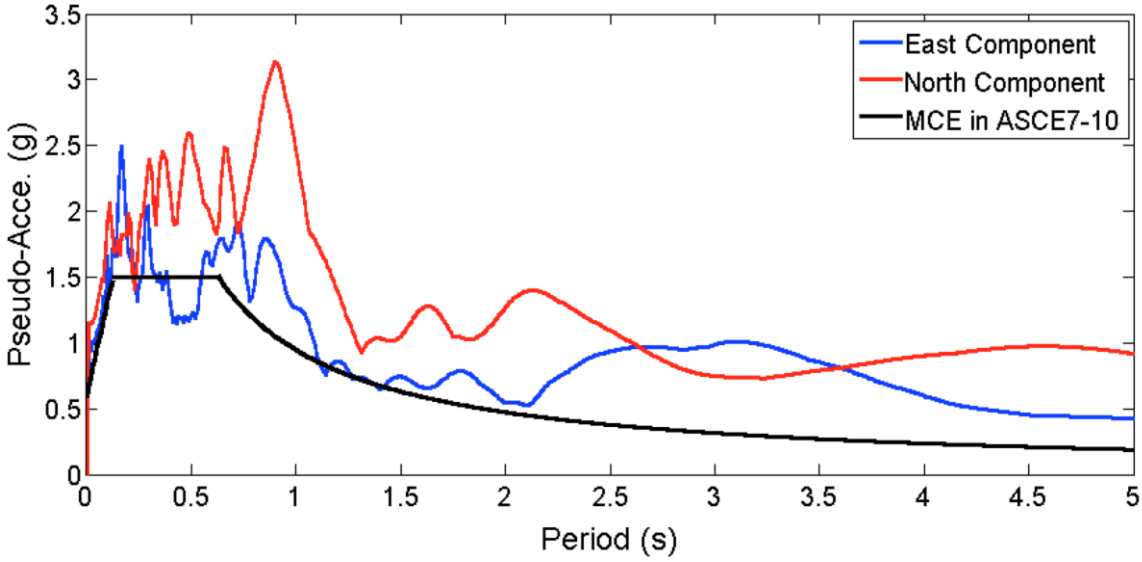

Figure 9-44: Pseudo acceleration response spectra of two scaled components of Chi-Chi earthquake

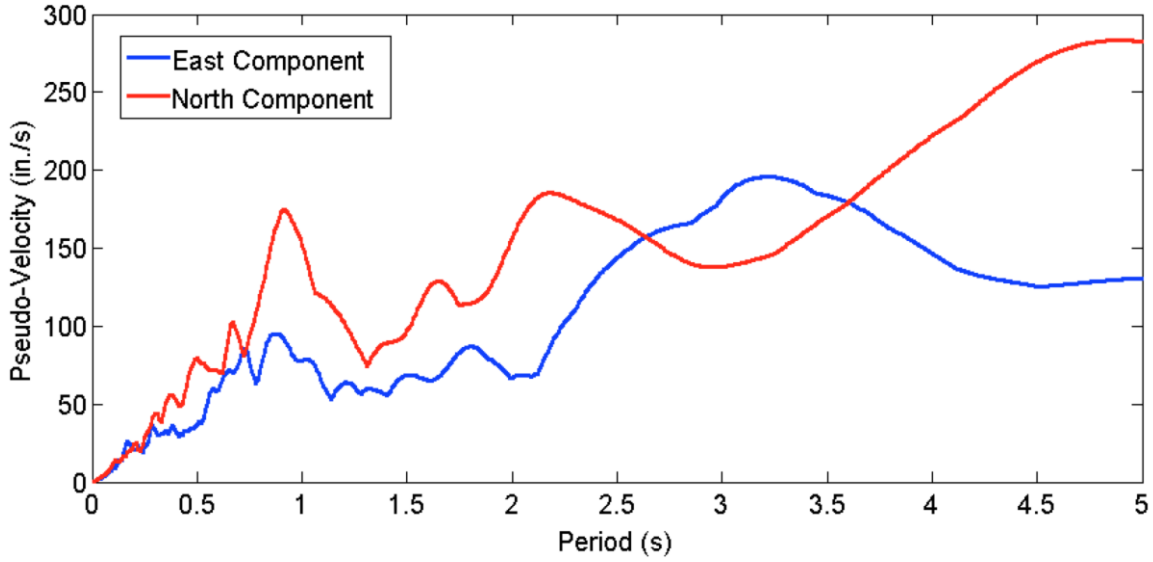

Figure 9-45: Pseudo velocity response spectra of two scaled components of Chi-Chi earthquake

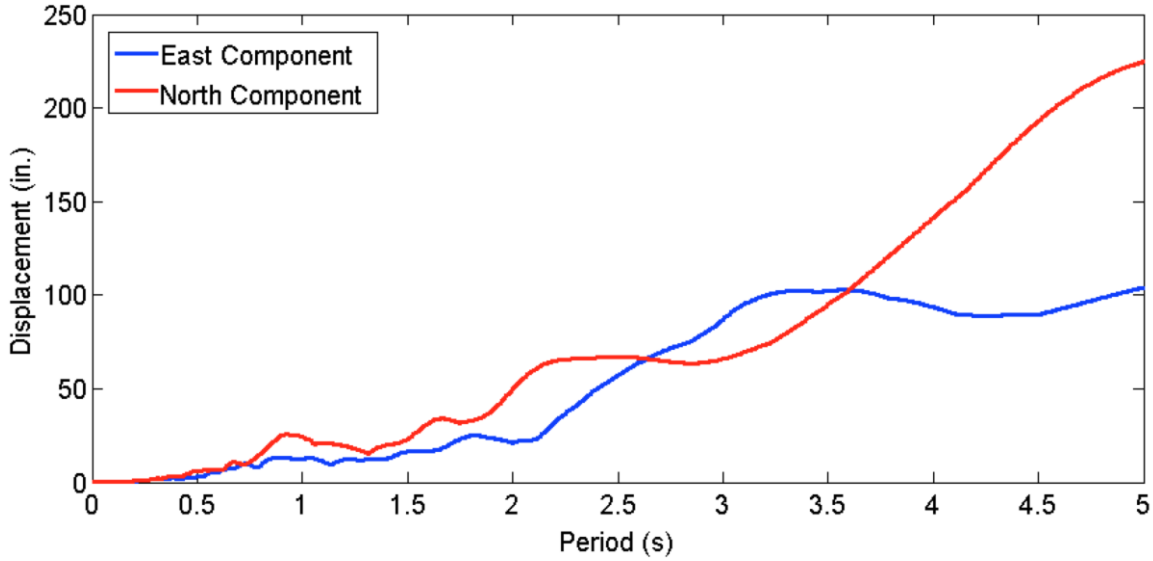

Figure 9-46: Displacement response spectra of two scaled components of Chi-Chi earthquake

Table 9-11: Maximum Peak Inter-story Drifts under Two Scaled Components of Chi-Chi Earthquake (unit: inch)

Level	"conventional"		Self-Centering		SC with Gaps	
	CHY101-East	CHY101-North	CHY101-East	CHY101-North	CHY101-East	CHY101-North
Basement	0	0	0	0	0	0
Story 1	9.19145	16.4038	12.7945	13.0151	10.9948	12.8444
Story 2	9.82918	17.7709	13.8446	14.5336	11.9639	13.9093
Story 3	8.4465	14.4788	12.3914	13.402	10.8007	13.0942
Story 4	6.8009	9.1596	11.7242	12.2471	10.0972	12.189
Roof	6.0324	7.8957	11.347	11.7681	9.8509	11.8309

9.5 Effects of Global Strength Ratio

As explained in Section 9.1, the reason for using beams with a Global Strength Ratio (GSR) of 0.9 is to reduce column separation. As presented in Figure 8-22, a lower GSR will also reduce self-centering capacity. In this section, two additional larger GSRs are used to investigate how sensitive the seismic responses of self-centering systems can be to different GSRs. In order to exclude the stiffness influence, the beams sizes are kept the same; higher material strengths are used for steel beams to increase GSRs. The detailed results are presented in Section L.1 and L.2 in Appendix L, and the discussions is given in the following subsections.

9.5.1 Systems with a GSR = 1.0 & Damping = 5%

The comparisons of seismic response among the three CSMFs with a GSR equal to 1.0 are presented in Table 9-12. From these comparisons, one can obtain the following two conclusions:

(1) Compared with the "conventional" CSMF, the advantages of self-centering systems are not obvious. The self-centering system with gaps reduces the residual deformation and peak rotations of beam plastic hinges, while the "conventional" system tends to reduce peak system deformation, rotations of column at base and axial forces in beams.

(2) Adding gaps to self-centering system does not bring great benefits on system seismic responses. It only brings slight advantages on reducing system residual drifts and damage of beams at the cost of greater system peak deformation and axial forces in beams.

Table 9-12: Comparisons of Seismic Responses among Three CSMFs with a GSR = 1.0 & Damping = 5%

Seismic Response	Convent. vs. SC & SC-Gaps		SC vs. SC-Gaps	
	Best	Advantage	Better	Advantage
Story Residual Drift	SC-Gaps	Obvious	SC-Gaps	Small
Inter-Story Residual Drift	SC-Gaps	Obvious	SC-Gaps	Small
Peak Inter-Story Drift	Convent.	Large	SC	Obvious
Column Separation	Convent.	Large	SC	Large
Beam PH Rot. Range	SC-Gaps	Large	SC-Gaps	Obvious
Peak Beam PH Rotation	SC-Gaps	Large	SC-Gaps	Small
Beam PH Residual Rot.	SC-Gaps	Obvious	SC-Gaps	Obvious
Column PH Rot. Range	Convent.	Obvious	SC	Small
Peak Column PH Rotation	Convent.	Obvious	SC	Small
Column PH Residual Rot.	Convent.	Obvious	SC	Small
Peak Beam Axial Force	Convent.	Large	SC	Obvious
Peak Column Axial Force	SC-Gaps	Obvious	SC-Gaps	Small
Peak Story Velocity	Convent.	Obvious	SC	Small
Peak Story Acceleration	Convent.	Obvious	SC	Small

Note: Small < Obvious < Large

The overall effects on each seismic response discussed above from increasing the GSR for all three CSMFs are summarized in Table 9-13 in lieu of showing many plots. From these comparisons, it is clear to see that using a higher GSR will bring a greater impact on self-centering systems than for the "conventional" system.

Table 9-13: Effects of Increasing GSR from 0.9 to 1.0 on Seismic Responses of All Three CMSFs with Damping = 5%

Seismic Response	Effects of GSR = 1.0 vs. GSR = 0.9
Story Residual Drift	• Reduces the response of self-centering systems. • Has less effects on the "conventional" system. • As ground motion intensity increases, effects on "conventional" system also increases.
Inter-Story Residual Drift	Same as above.
Peak Inter-Story Drift	Insignificant effects.
Column Separation	• Effects on self-centering system is greater. • Gaps can reduce the increase in response due to a higher GSR.
Beam Plastic Hinge Rot. Range	• Reduces the response of self-centering systems effectively. • Reductions on response of self-centering system with gaps is more obvious. • Has insignificant effects on "conventional" system.
Peak Beam Plastic Hinge Rotation	• Slightly reduces the response of self-centering systems. • Has little effect on "conventional" system.
Beam Plastic Hinge Residual Rot.	Same as above.
Column Plastic Hinge Rot. Range	• Increases the response of the self-centering systems a little bit. • Has little effects on "conventional" system.
Peak Column Plastic Hinge Rotation	Same as above.
Column Plastic Hinge Residual Rot.	Insignificant effects.

Peak Beam Axial Force	• Reduces the response of the self-centering system with gaps slightly. • Increases the response of the self-centering system slightly. • Has insignificant effects on "conventional" system.
Peak Column Axial Force	Increases the response slightly.
Peak Story Velocity	Insignificant effects.
Peak Story Acceleration	• Increases slightly the response of SC-Gaps on roof level. • Has insignificant effects on the other two.

9.5.2 Systems with a GSR = 1.1 & Damping = 5%

According to the relationship between GSR and self-centering capacity in Figure 8-22, increasing the GSR to more than 1.1 will not bring great benefits on self-centering capacity. A self-centering system with a GSR of 1.1 is close to the ultimate system's self-centering capacity. Based on comparisons among three CSMFs, one can see that self-centering system with gaps has obvious advantages than the other two systems; especially, it has overwhelming advantages on reducing system residual deformations (Figure 9-47), damage of beams (Figure 9-48), and axial forces in beams (Figure 9-49). Although the peak axial forces in columns are increased, for most cases, they are still less than 13% of the column specified axial yielding capacity. The overall comparison among three systems is presented in Table 9-14.

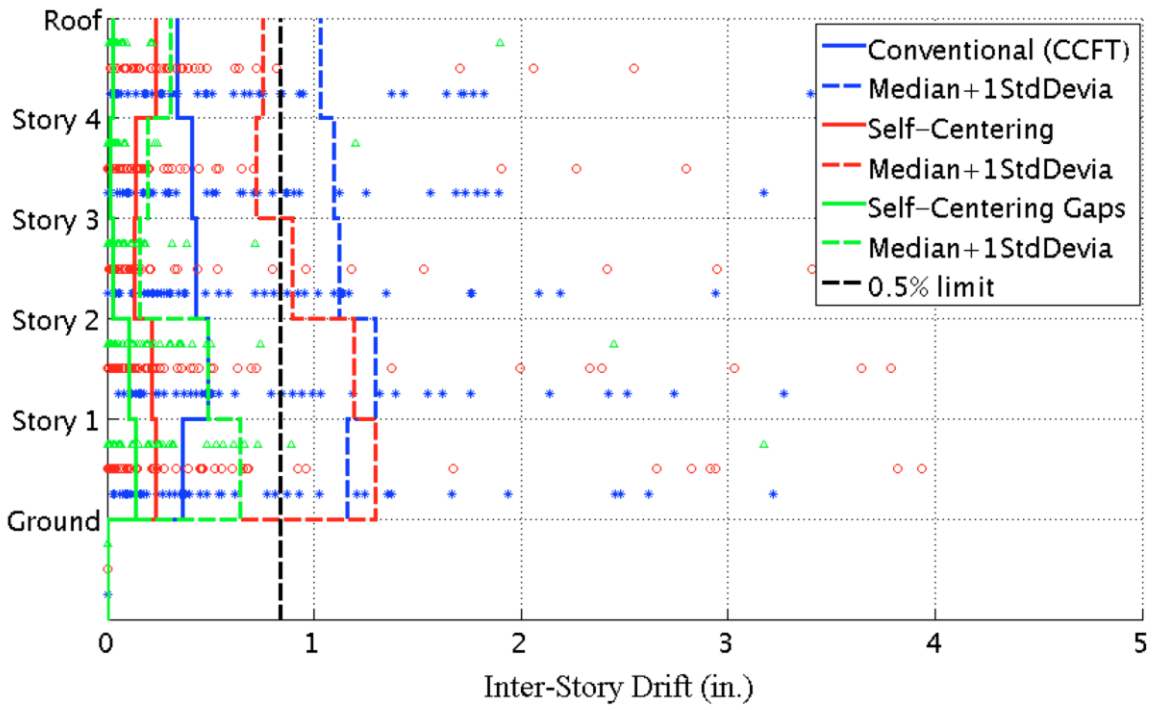

Figure 9-47:Median of the maximum inter-story residual drift under 44 MCE level ground motions with a GSR = 1.1 & damping = 5%

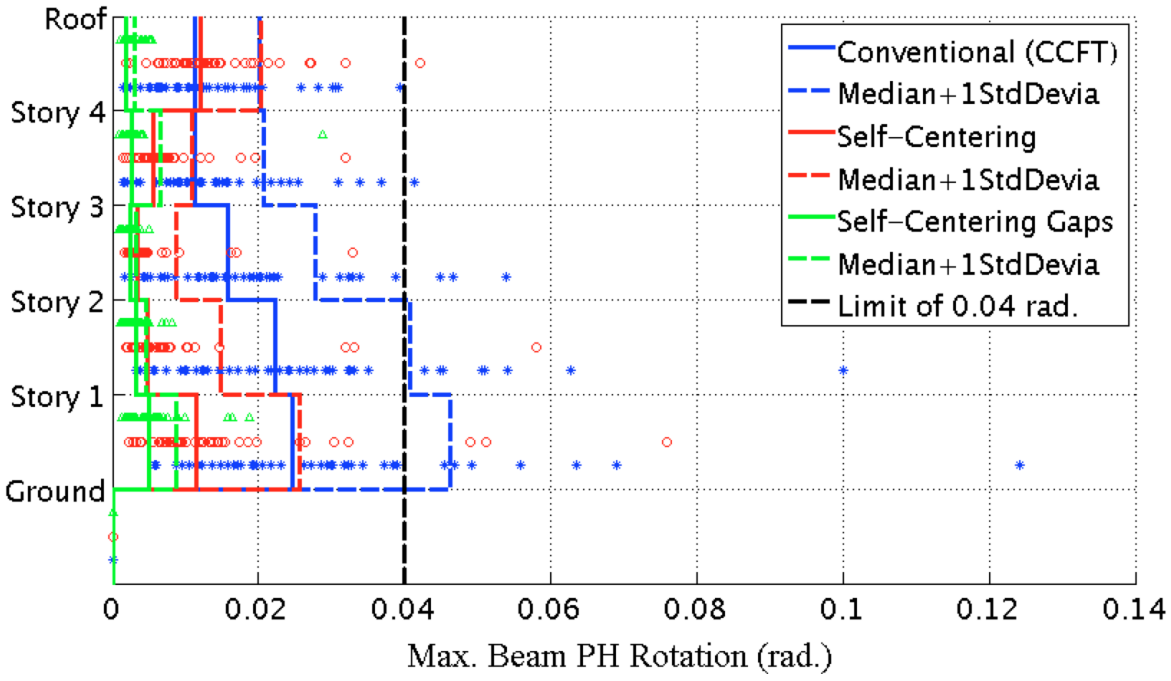

Figure 9-48: Median of the maximum beam PH rotation under 44 MCE level ground motions with a GSR = 1.1 & damping = 5%

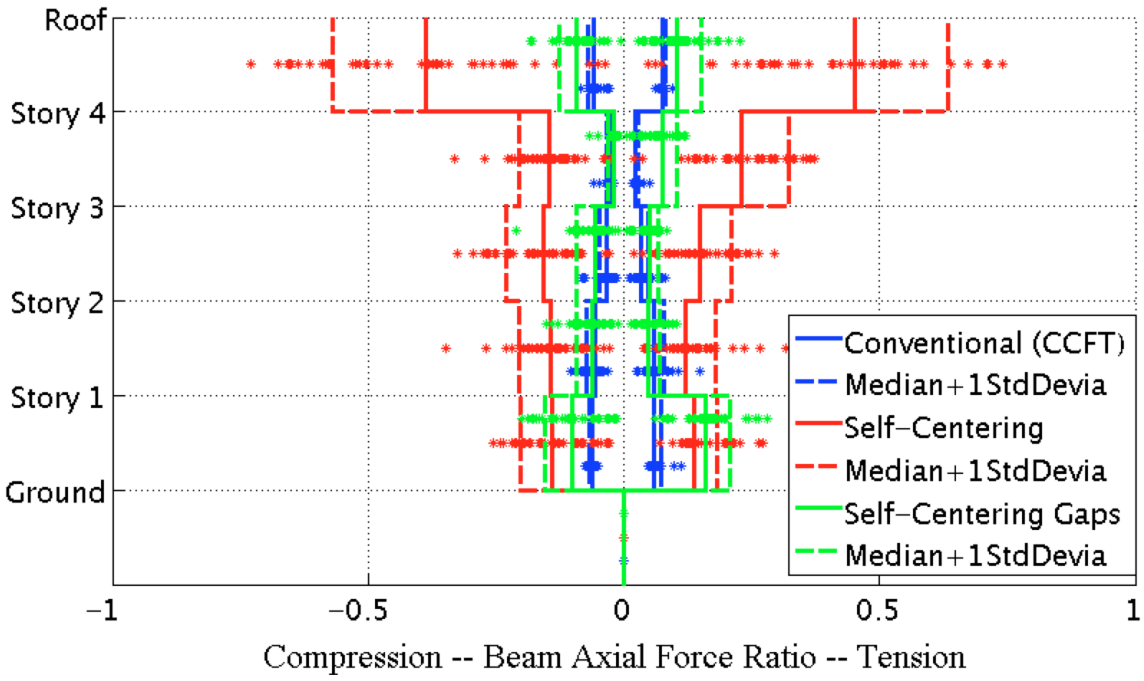

Figure 9-49: Median of the peak tension vs.compression in beams under 44 MCE level ground motions with a GSR = 1.1 & damping = 5%

Table 9-14: Comparisons of Seismic Responses among Three CSMFs with a GSR = 1.1 & Damping = 5%

Seismic Response	Convent. vs. SC & SC-Gaps		SC vs. SC-Gaps	
	Best	Advantage	Better	Advantage
Story Residual Drift	SC-Gaps	Large	SC-Gaps	Large
Inter-Story Residual Drift	SC-Gaps	Large	SC-Gaps	Large
Peak Inter-Story Drift	Convent.	Obvious	SC-Gaps	Obvious
Column Separation	Convent.	Large	SC-Gaps	Obvious
Beam PH Rot. Range	SC-Gaps	Large	SC-Gaps	Large
Peak Beam PH Rotation	SC-Gaps	Large	SC-Gaps	Large
Beam PH Residual Rot.	SC-Gaps	Large	SC-Gaps	Large
Column PH Rot. Range	Convent.	Small	SC-Gaps	Small
Peak Column PH Rotation	Convent.	Small	SC-Gaps	Small
Column PH Residual Rot.	Convent.	Small	SC-Gaps	Small
Peak Beam Axial Force	Convent.	Obvious	SC-Gaps	Large

Peak Column Axial Force	SC	Small	SC	Obvious
Peak Story Velocity	Convent.	Obvious	SC-Gaps	Obvious
Peak Story Acceleration	Convent.	Obvious	SC-Gaps	Obvious

Note: Small < Obvious < Large

Increasing GSR from 0.9 to 1.1 will bring different effects on seismic responses among the three CSMFs. For most cases, increasing beam strengths will cause more significant changes for the self-centering system with gaps, and less impact on self-centering system without gaps. Increasing beam strength has only a slight or insignificant effects on the "conventional" system. These comparisons are presented in Table 9-15 for different seismic responses. For some cases, increasing GSR will cause an opposite change between self-centering systems with and without gaps, such as peak inter-story drift, column separations, peak and residual rotations of columns, and axial forces in beams. Unlike what was expected, a higher GSR will actually reduce the column separations of the self-centering system with gaps on the upper stories. Increasing beam strengths in the self-centering system without gaps does not result in the axial forces in the beams to be reduced as effectively as expected. This phenomenon is consistent with the results for column separations. Higher beam strengths will cause greater column separations in self-centering system without gaps. This indicates that axial forces in beams are controlled by displacements or column separations. This consistency can also be observed in the SC-Gaps system.

Table 9-15: Effects of Increasing GSR from 0.9 to 1.1 on Seismic Responses of All Three CMSFs with Damping = 5%

Seismic Response	Effects of GSR = 1.1 vs. GSR = 0.9
Story Residual Drift	• Greatly reduces the response of the self-centering system with gaps. • Reduces the response of the self-centering system. • Reduces the response of the "conventional" system slightly.
Inter-Story Residual Drift	Same as above.
Peak Inter-Story Drift	• Reduces the response of the self-centering system with gaps. • Increases the response of the self-centering system slightly. • Reduces slightly the response of the "conventional" system.
Column Separation	• Increases the response of the self-centering system. • Reduces the response of the self-centering system with gaps, especially for upper stories.
Beam Plastic Hinge Rot. Range	• Reduces the response of self-centering systems effectively. • Reduces effects on self-centering system with gaps more. • Has insignificant effects on "conventional" system.
Peak Beam Plastic Hinge Rotation	• Reduces the response of the self-centering system with gaps greatly. • Reduces the response of the self-centering system. • Reduces the response of the "conventional" system slightly.
Beam Plastic Hinge Residual Rot.	Same as above.
Column Plastic Hinge Rot. Range	• Reduces the response of the self-centering system with gaps. • Increases the response of the self-centering system. • Has little effects on the "conventional" system.
Peak Column Plastic Hinge Rotation	Same as above.
Column Plastic Hinge Residual Rot.	• Reduces the response of the self-centering system with gaps. • Increases the response of the self-centering system

	slightly. • Has little effects on the “conventional” system.
Peak Beam Axial Force	• Reduces the response of the self-centering system with gaps greatly. • Increases the response of the self-centering system. • Has insignificant effects on the “conventional” system.
Peak Column Axial Force	• Increases the response of the self-centering system with gaps. • Increases the response of other two systems slightly.
Peak Story Velocity	• Reduces slightly the response of the self-centering system with gaps. • Increases slightly the response of the self-centering system. • Has insignificant effects on the “conventional” system.
Peak Story Acceleration	• Reduces the response of the self-centering system with gaps. • Increases slightly the response of the self-centering system on lower stories. • Has insignificant effects on the “conventional” system.

9.5.2.1 Example of Systems with a GSR = 1.1

Previous section results show that the self-centering system with gaps can provide superior performance if the system GSR is increased to 1.1. Results of same response (maximum residual story drift) under the same ground motions (two components of Chi-Chi earthquake on MCE level) as in Table 9-10 are presented in Table 9-16 for systems with a GSR equal to 1.1. Comparing the results in the two tables, one can see that increasing beam strength can reduce system residual deformation effectively. The results in Table 9-16 prove that adding gaps on steel rods and using stronger beams is the most effective way to increase self-centering capacity. Important component behavior for the “conventional” CSMF and the self-centering

CSMF with gaps under the 'CHY101-East' ground motion are compared in detail in Appendix M.

Table 9-16: Maximum Residual Story Drift under Two Scaled Components of Chi-Chi Earthquake on MCE Level with a GSR = 1.1 & Damping = 5% (unit: inch)

Level	"conventional"		Self-Centering		SC with Gaps	
	CHY101-East	CHY101-North	CHY101-East	CHY101-North	CHY101-East	CHY101-North
Basement	0.0030	0.0121	0.0126	0.0175	0.0122	0.0144
Story 1	2.4833	2.6238	3.9355	3.8176	0.8873	0.2193
Story 2	4.8876	5.1270	7.5263	7.5423	1.4737	0.2434
Story 3	6.9587	5.7717	10.476	10.946	1.8439	0.3646
Story 4	8.5042	4.1015	12.685	13.703	2.0544	0.4480
Roof	9.8727	2.3660	14.702	16.248	2.2303	0.5192

9.6 Effects of Damping

Damping ratio is also believed to have a considerable impact on system seismic performance. In this section, the sensitivity of seismic responses of self-centering systems to damping ratios will be investigated based on two different damping levels. Beam strengths with a GSR of 1.0 are used; the aim is to find out whether aside from using higher beam strengths, better seismic performance as a GSR of 1.1 can also be obtained by using higher damping ratio. The use of a significantly larger damping ratio is meant to mimic the larger damping expected from the many frictional surfaces present in the self-centering connections. The corresponding results are presented in Section L.3 and L.4 in Appendix L.

9.6.1 Systems with a GSR = 1.0 & Damping = 10%

The inherent limitations of using viscous damping are understood, so the comparison here are meaningful in the conventional design sense only, i.e., if Rayleigh damping is assumed to be the correct approach.

Table 9-17: Comparisons of Seismic Responses among Three CSMFs with a GSR = 1.0 & Damping = 10%

Seismic Response	Convent. vs. SC & SC-Gaps		SC vs. SC-Gaps	
	Best	Advantage	Better	Advantage
Story Residual Drift	SC-Gaps	Obvious	SC-Gaps	Small
Inter-Story Residual Drift	SC-Gaps	Obvious	SC-Gaps	Small
Peak Inter-Story Drift	Convent.	Large	SC	Obvious
Column Separation	Convent.	Obvious	SC	Obvious
Beam PH Rot. Range	SC-Gaps	Large	SC-Gaps	Obvious
Peak Beam PH Rotation	SC-Gaps	Large	SC-Gaps	Small
Beam PH Residual Rot.	SC-Gaps	Obvious	SC-Gaps	Small
Column PH Rot. Range	Convent.	Small	SC	Small
Peak Column PH Rotation	Convent.	Small	SC	Small
Column PH Residual Rot.	Convent.	Small	SC	Small
Peak Beam Axial Force	Convent.	Large	SC	Obvious
Peak Column Axial Force	SC-Gaps	Obvious	SC-Gaps	Small
Peak Story Velocity	Convent.	Obvious	SC	Small
Peak Story Acceleration	Convent.	Obvious	SC	Small

Note: Small < Obvious < Large

It is clear that using higher damping ratio is more effective for self-centering systems. Detailed

effects on each seismic response for three systems are presented in Table 9-18.

Table 9-18: Effects of Increasing Damping from 5% to 10% on Seismic Responses of All Three CMSFs with a GSR = 1.0

Seismic Response	Effects of Damping = 10% vs. Damping = 5%
Story Residual Drift	• Reduces the response of all three systems. • Slightly greater effects on the two self-centering systems.
Inter-Story Residual Drift	Same as above.
Peak Inter-Story Drift	• Reduces the response of all three systems. • Slightly greater effects on the self-centering system with gaps.
Column Separation	• Reduces the response of the two self-centering systems.
Beam Plastic Hinge Rot. Range	• Reduces the response of all three systems.
Peak Beam Plastic Hinge Rotation	Same as above.
Beam Plastic Hinge Residual Rot.	Same as above.
Column Plastic Hinge Rot. Range	• Reduces the response of all three systems. • Effects on the two self-centering systems are greater.
Peak Column Plastic Hinge Rotation	Same as above.
Column Plastic Hinge Residual Rot.	• Reduces the response of all three systems slightly.
Peak Beam Axial Force	• Reduces the response of the two self-centering systems. • Less effects on the “conventional” system.
Peak Column Axial Force	• Reduces the response of the two self-centering systems slightly. • Increase the response of the “conventional” system slightly.
Peak Story Velocity	• Reduces the response of all three systems slightly.
Peak Story Acceleration	• Reduces the response of the two self-centering systems on most stories. • Has insignificant effects on the “conventional” system.

9.6.2 Systems with a GSR = 1.0 & Damping = 2%

If a lower damping ratio is used in the dynamic analysis, most seismic responses will increase as expected. The advantages of each seismic performance parameter among the three systems with a damping ratio of 2% are presented in Table 9-19.

Table 9-19: Comparisons of Seismic Responses among Three CSMFs with a GSR = 1.0 & Damping = 2%

Seismic Response	Convent. vs. SC & SC-Gaps		SC vs. SC-Gaps	
	Best	Advantage	Better	Advantage
Story Residual Drift	SC-Gaps	Small	SC-Gaps	Small
Inter-Story Residual Drift	SC-Gaps	Small	SC-Gaps	Small
Peak Inter-Story Drift	Convent.	Large	SC	Obvious
Column Separation	Convent.	Large	SC	Obvious
Beam PH Rot. Range	SC-Gaps	Large	SC-Gaps	Small
Peak Beam PH Rotation	SC-Gaps	Large	SC-Gaps	Small
Beam PH Residual Rot.	SC-Gaps	Small	SC-Gaps	Small
Column PH Rot. Range	Convent.	Obvious	SC	Small
Peak Column PH Rotation	Convent.	Obvious	SC	Small
Column PH Residual Rot.	Convent.	Small	SC	Small
Peak Beam Axial Force	Convent.	Large	SC	Obvious
Peak Column Axial Force	SC-Gaps	Small	SC-Gaps	Small
Peak Story Velocity	Convent.	Obvious	SC	Small
Peak Story Acceleration	Convent.	Obvious	SC	Small

Note: Small < Obvious < Large

Under the DBE level ground motions, the increase of seismic responses of all three systems

are similar, or slightly greater for the self-centering systems; under the MCE level ground motions, greater effects are obtained for the "conventional" system on some responses, particularly the occurrence of system collapse. This is because the self-centering systems have greater capacity to prevent system collapse as indicated by the IDA results in Section 9.2.7. Detailed effects on each seismic response for three systems are presented in Table 9-20.

Table 9-20: Effects of Reducing Damping from 5% to 2% on Seismic Responses of All Three CMSFs with a GSR = 1.0

Seismic Response	Effects of Damping = 2% vs. Damping = 5%
Story Residual Drift	• Increases the response of all three systems greatly. • Greater effects on the two self-centering systems on DBE level ground motions. • Greater effects on the "conventional" system under MCE level ground motions.
Inter-Story Residual Drift	Same as above.
Peak Inter-Story Drift	• Increases the response of all three systems.
Column Separation	• Increases the response of the two self-centering systems.
Beam Plastic Hinge Rot. Range	• Increases the response of all three systems.
Peak Beam Plastic Hinge Rotation	Same as above.
Beam Plastic Hinge Residual Rot.	• Increases the response of all three systems greatly. • Greater effects on the "conventional" system under MCE level ground motions.
Column Plastic Hinge Rot. Range	• Increases the response of all three systems.
Peak Column Plastic Hinge Rotation	Same as above.
Column Plastic Hinge Residual Rot.	Same as above.
Peak Beam Axial Force	• Increases the response of the two self-centering systems. • Less effects on the "conventional" systems.

Peak Column Axial Force	Insignificant effects.
Peak Story Velocity	• Increases the response of the two self-centering systems. • Less effects on the "conventional" systems.
Peak Story Acceleration	• Increases the response of the two self-centering systems. • Greater effects on the self-centering system. • Less effects on the "conventional" system.

9.6.3 Potential Methods to Increase Damping

In order to ensure the seismic performance of self-centering systems, additional non-structural components can be applied in the system to increase damping by taking advantages of greater deformation capacity of connections or column separations. Three mechanisms are proposed in Figure 9-50 to utilize the column separation for energy dissipation. The first one is adding viscous dampers, which are fixed between two adjacent columns and can be placed on either top or bottom of the beams, or both. The viscous dampers can also be replaced by either (a) yielding vertical metal plates under relative motions between top and bottom plates or (b) friction supplied by sliding between two metal components. However, the axial yielding capacity of these adding dampers should be designed carefully to avoid from hurting system's self-centering capacity.

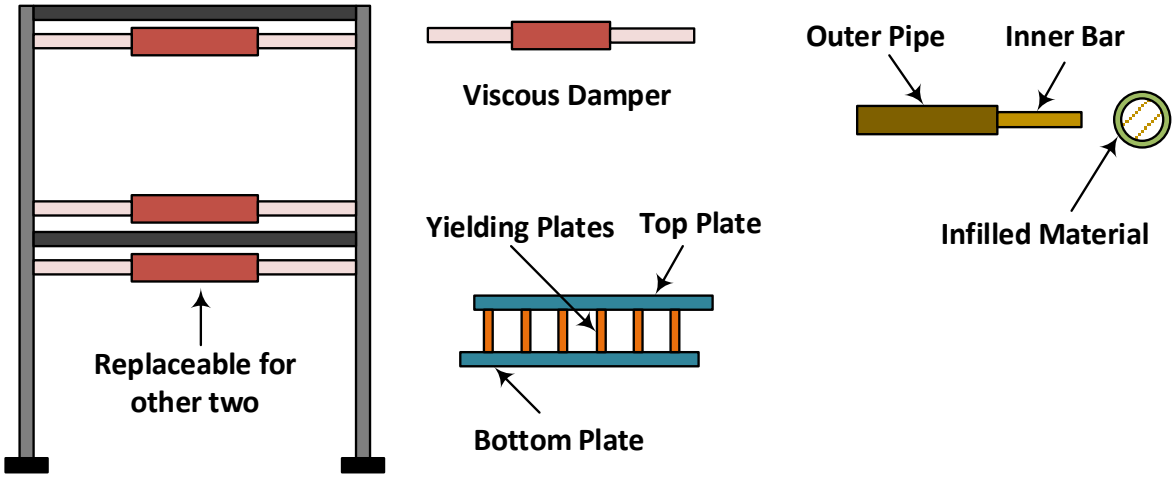

Figure 9-50: Three mechanisms to increase system damping by utilizing column separations in the self-centering systems

9.7 Panel Zone Effects on Traditional Steel Special Moment Frame

All systems analyzed above are composed of circular concrete filled steel (CCFT) columns. For traditional steel special moment frames (SMFs) with W section columns, many researchers indicate that panel zone deformation will considerable increase drift [102, 105]. Therefore, it is also worthy to investigate the panel zone effects on other seismic responses. In this section, a new steel SMF with W section columns will be designed and analyzed under the same ground motions scaled in Figure 9-4, and the seismic responses are compared with the composite special moment frame (CSMF) with CCFT columns.

The layout of the CSMFs has three 32.ft. spans as presented in Figure 6-2. However, there is no W section that can be used to meet the stiffness requirement for this frame configuration.

The original three span layout was therefore changed to a four span layout with the beam sizes adjusted accordingly. Both beams, columns and panel zones are designed based on the current design provisions [77, 103]. Detailed design results for the new steel SMF are presented in Table 9-21 and Table 9-22.

Table 9-21: Beam Sections, Capacities and RBS Parameters of Steel SMF vs. CSMF

Story	4 Span SMF with W Section Columns (Span = 24 ft.)			3 Span SMF with CCFT Columns (Span = 32 ft.)		
	Section	RBS – a, b, c (in.)	Reduced Zx ($in.^3$)	Section	RBS – a, b, c (in.)	Reduced Zx ($in.^3$)
Basement	W27*94	NA	NA	W30*116	NA	NA
Story 1	W30*116	5.25, 20, 2.5	254.1	W33*130	5.75, 22, 2.875	308.5
Story 2	W30*116	5.25, 20, 2.5	254.1	W33*130	5.75, 22, 2.875	308.5
Story 3	W30*99	5.25, 20, 2.5	214.7	W30*124	5.25, 20, 2.1	293.7
Story 4	W27*94	5, 20, 1.8	207.8	W30*116	5.25, 20, 2.0	278.9
Story 5	W21*44	3.5, 15, 1.2	73.53	W21*57	3.5, 14, 1.2	97.1

Table 9-22: Column Section and Doubler Plates of Steel SMF

Story	Column Section	Column Web Thickness (in.)	Doubler Plate Thickness (in.)
Basement	W24*162	0.705	NA
Story 1	W24*162	0.705	0.75
Story 2	W24*162	0.705	0.75
Story 3	W24*162	0.705	0.54
Story 4	W24*162	0.705	0.65
Story 5	W24*162	0.705	NA

For the steel SMF, both flexible and rigid panel zone will be considered in the analysis for

investigation of panel zone effects. Two models will be employed to simulate panel zone behavior: (1) 'Krawinkler Model'; and (2) 'Scissors Model'. Research has proven that proper use of these two models will generate the same results [95]. In this section, the 'Scissors Model' is employed. The calculated periods for the 1st mode from eigenvalue analyses of the steel SMF with flexible and rigid panel zones are presented in Table 9-23. The pushover analysis results are shown in Figure 9-51. All of these results are compared with the "conventional" CSMF with rigid panel zone and a GSR of 0.9 in the same Table and Figure.

Table 9-23: 1st Mode Period of Steel SMF with Flexible and Rigid Panel Zone vs. "conventional" CSMF with Rigid Panel Zone (unit: second)

Model	SSMF - Flexible PZ	SSMF - Rigid PZ	Convent. CSMF - Rigid PZ
T_1	1.356	1.176	1.362

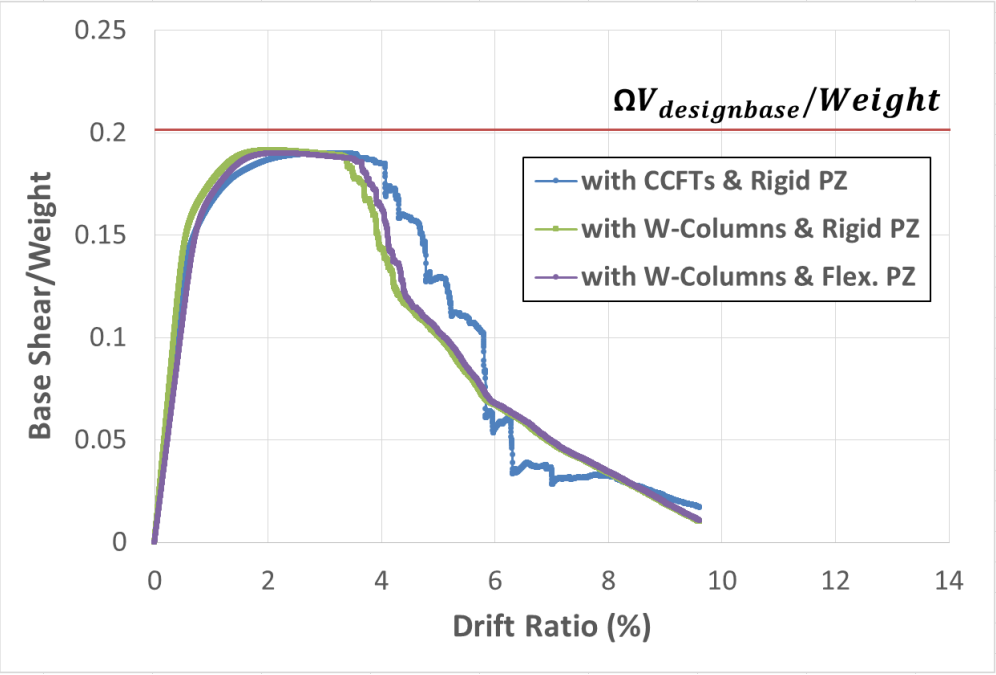

Figure 9-51: Poushover curves of the steel SMFs with flexible and rigid panel zone vs. the "conventional" CSMF with rigid panel zone

From the above results, one can see that panel zone deformation has obvious effects on system initial stiffness, but has little effects on the ultimate lateral resisting strength of the system based on pushover analysis. The new designed steel SMF with flexible panel zone has similar behaviors to the "conventional" CSMF, and they have a slightly less elastic stiffness than the steel SMF with rigid panel zone.

Seismic responses of the new designed steel moment frame with a damping ratio of both 5% and 2% were also analyzed and the corresponding results were compared with the "conventional" CSMF. The required strengths of panel zones were calculated based on the maximum beam capacities using a factor of $1.1R_y$. This results in panel zones strong enough compared with beam capacities such that there should be very limited plastic deformation generated in the panel zones. The 'Elastic Perfectly Plastic Model' is used to simulate panel zone behavior in OpenSees. No degradation effects are considered; such degradation can be caused by the fracture of welds between doubler plates and column flanges due to large deformations at the intersection of the panel zone and the beam flange welds. These strong and ideal panel zones models used in this section are named 'Ideally Well-Defined PZ Model'. The maximum rotation of the 'Scissors Model' for the panel zone is presented in Figure 9-52 and Figure 9-53 for damping ratios of 5% and 2%. Unexpectedly, peak rotations of panel zones with 5% damping have greater values than those with 2% damping.

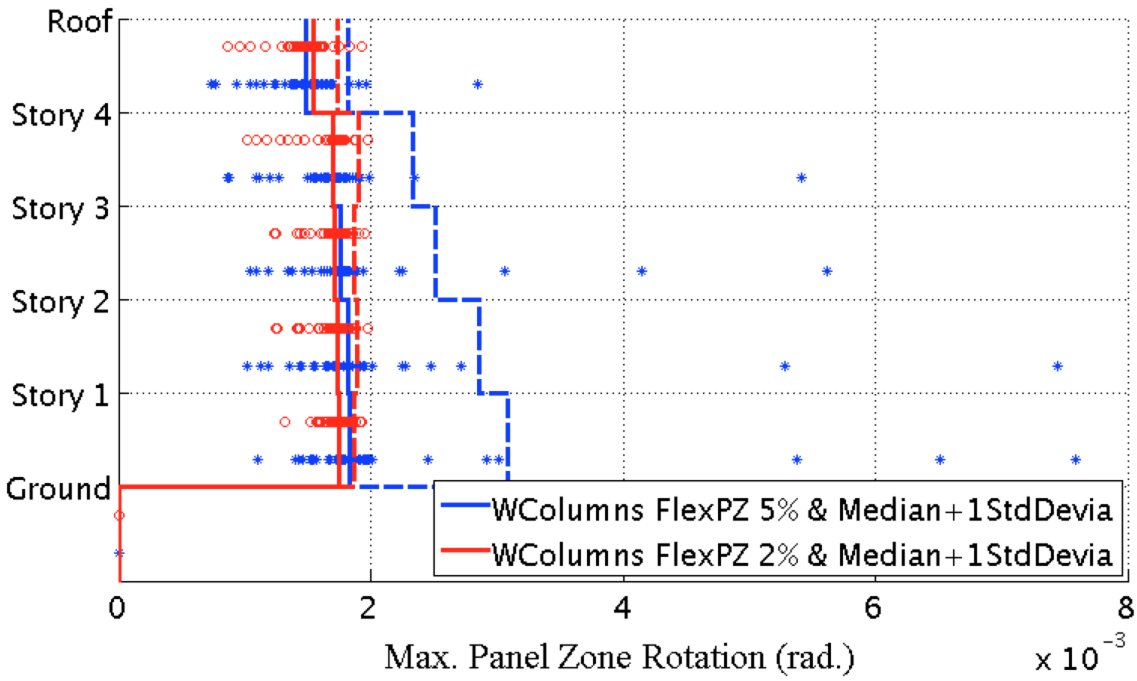

Figure 9-52: Median of the maximum PZ PH rotation under 44 DBE level ground motions with damping = 5% vs. 2% for the steel SMF with flexibule PZ

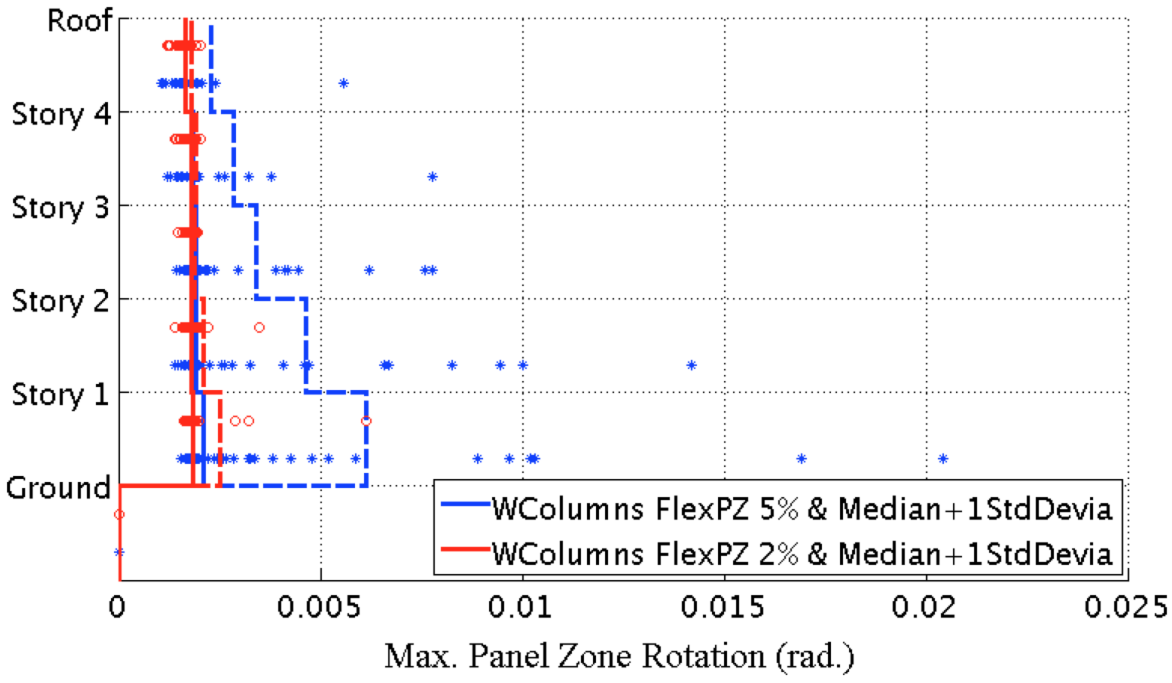

Figure 9-53: Median of the maximum PZ PH rotation under 44 MCE level ground motions with damping = 5% vs. 2% for the steel SMF with flexibule PZ

The peak interstory drifts of steel SMFs are presented in Figure 9-54, Figure 9-55, Figure 9-56 and Figure 9-57 under both DBE and MCE level ground motions. One can see that flexible panel zone does increase system deformation as expected. However, there is no clear tendency indicating that flexible panel zone will increase system residual deformation. Inter-story residual drifts are present in Figure 9-58, Figure 9-59, Figure 9-60 and Figure 9-61. One can see that if variability is considered by adding one standard deviation to the median, the steel SMF with rigid panel zones can have even greater inter-story residual deformation than the one with flexible panel zones. The plots in Figure 9-57 and Figure 9-61 are modified by filtering the ground motions which cause too much variability. Both original and modified plots of all responses are presented in Section L.5 and L.6 in Appendix L. Comparing with system with rigid panel zones, strong flexible panel zones will also cause greater story velocities; however, for other responses, strong flexible panel zones do not bring obvious differences from rigid panel zones (can be slightly better or worse).

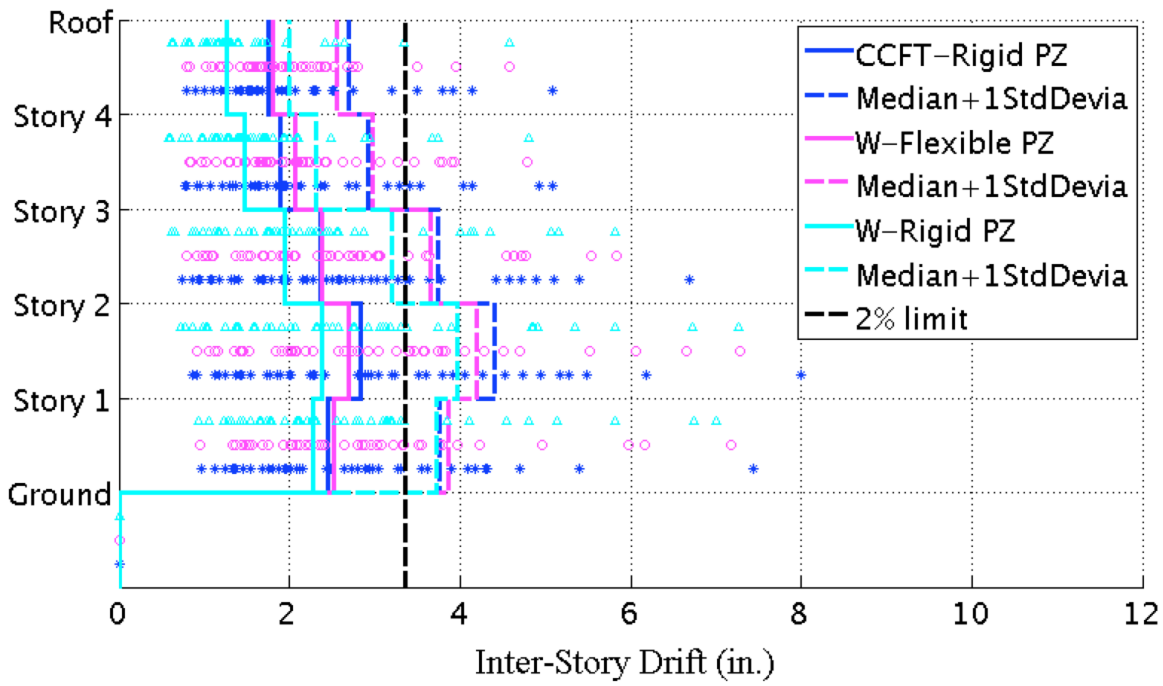

Figure 9-54: Median of the peak inter-story drift under 44 DBE level ground motions with damping = 5% for the steel SMFs and the CSMF with a GSR = 0.9

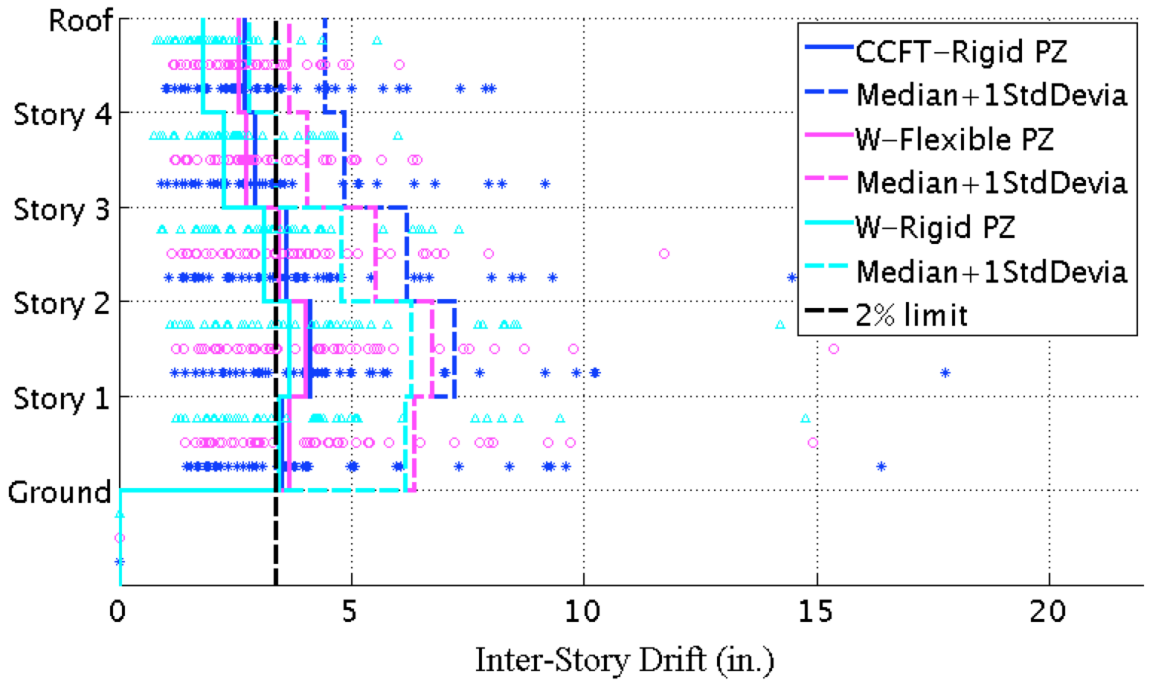

Figure 9-55: Median of the peak inter-story drift under 44 MCE level ground motions with damping = 5% for the steel SMFs and the CSMF with a GSR = 0.9

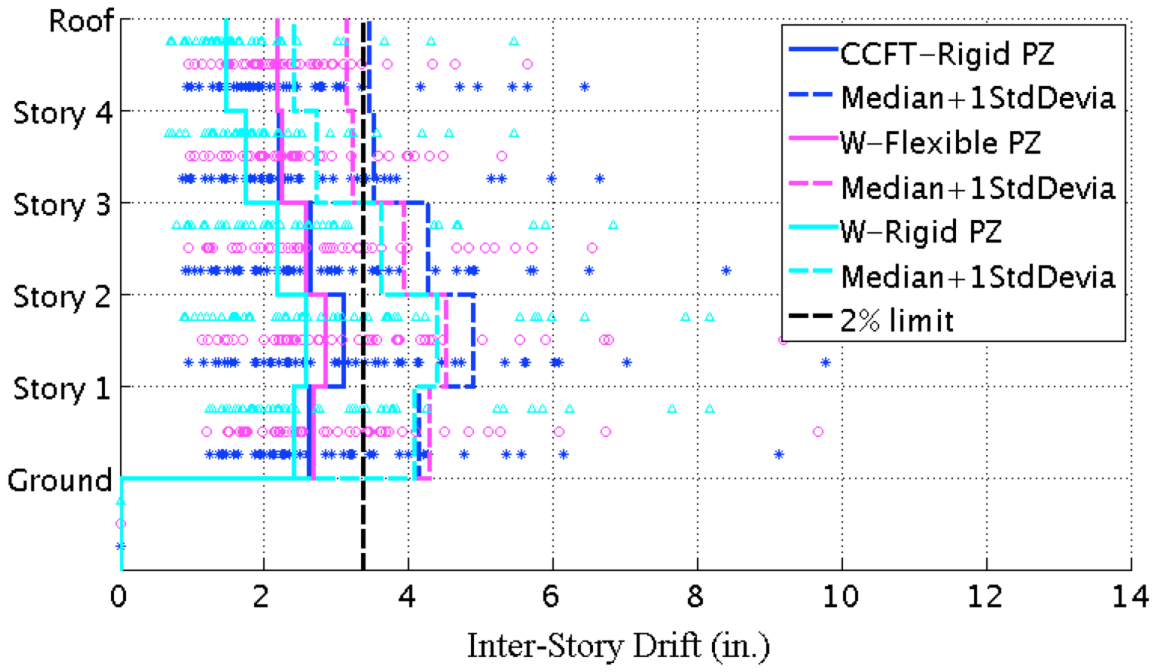

Figure 9-56: Median of the peak inter-story drift under 44 DBE level ground motions with damping = 2% for the steel SMFs and the CSMF with a GSR = 0.9

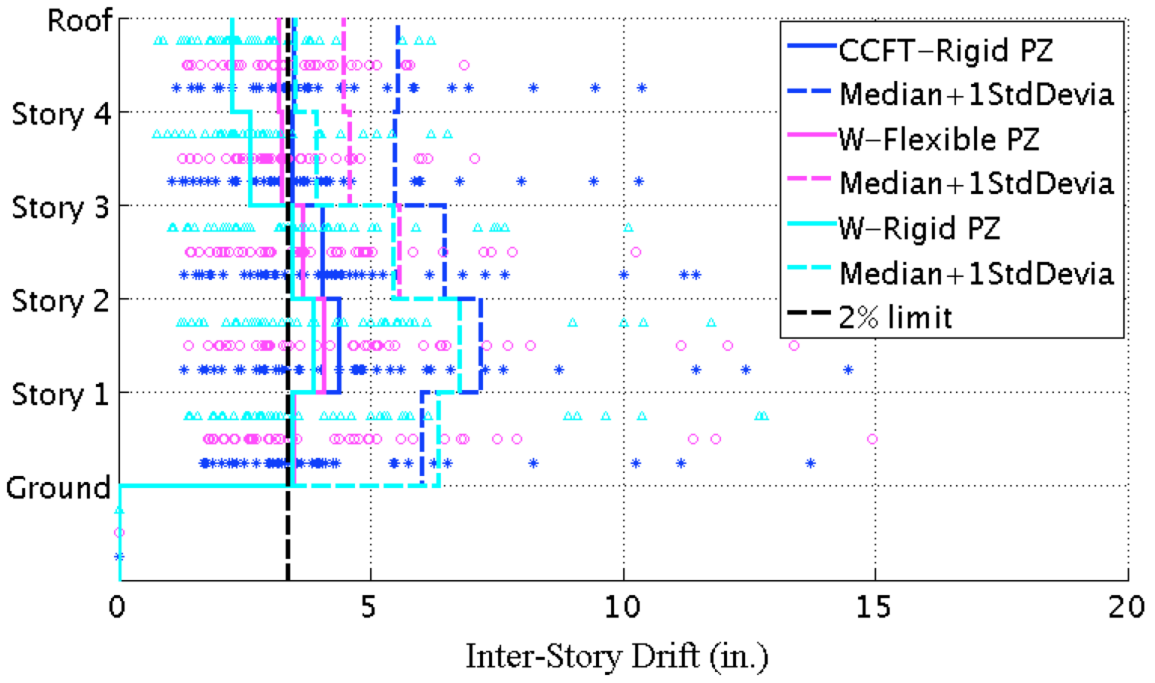

Figure 9-57: Median of the peak inter-story drift under the 'Filtered 44' MCE level ground motions with damping = 2% for the steel SMFs and the CSMF with a GSR = 0.9

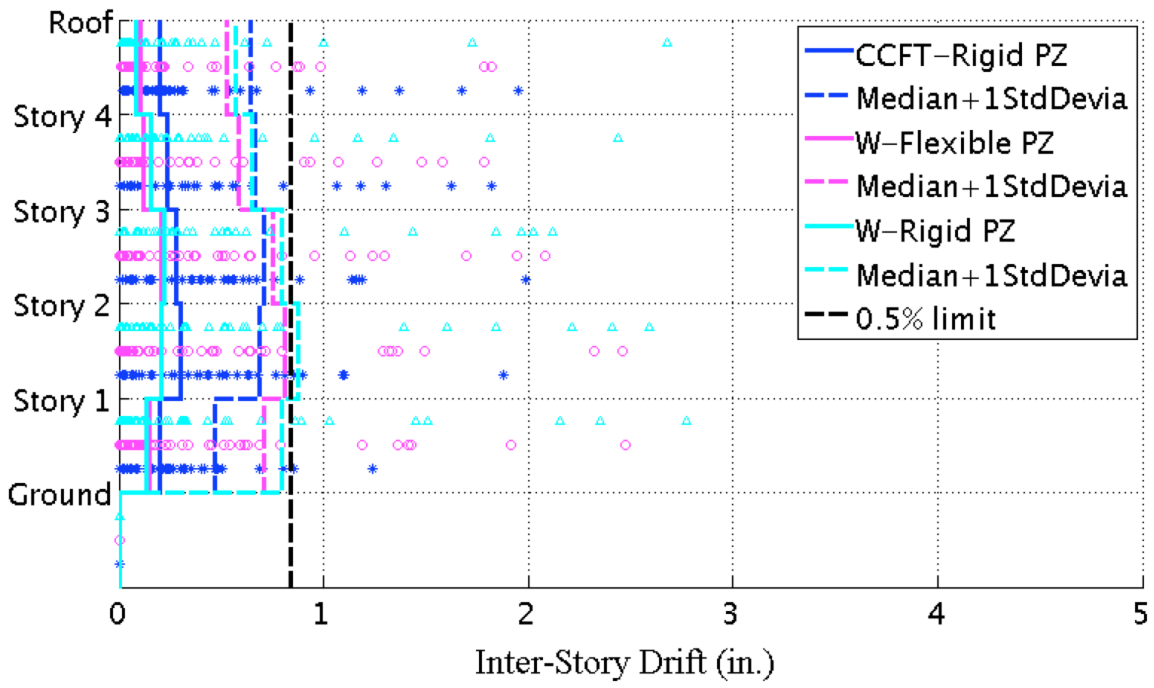

Figure 9-58: Median of the maximum inter-story residual drift under 44 DBE level ground motions with damping = 5% for the steel SMFs and the CSMF with a GSR = 0.9

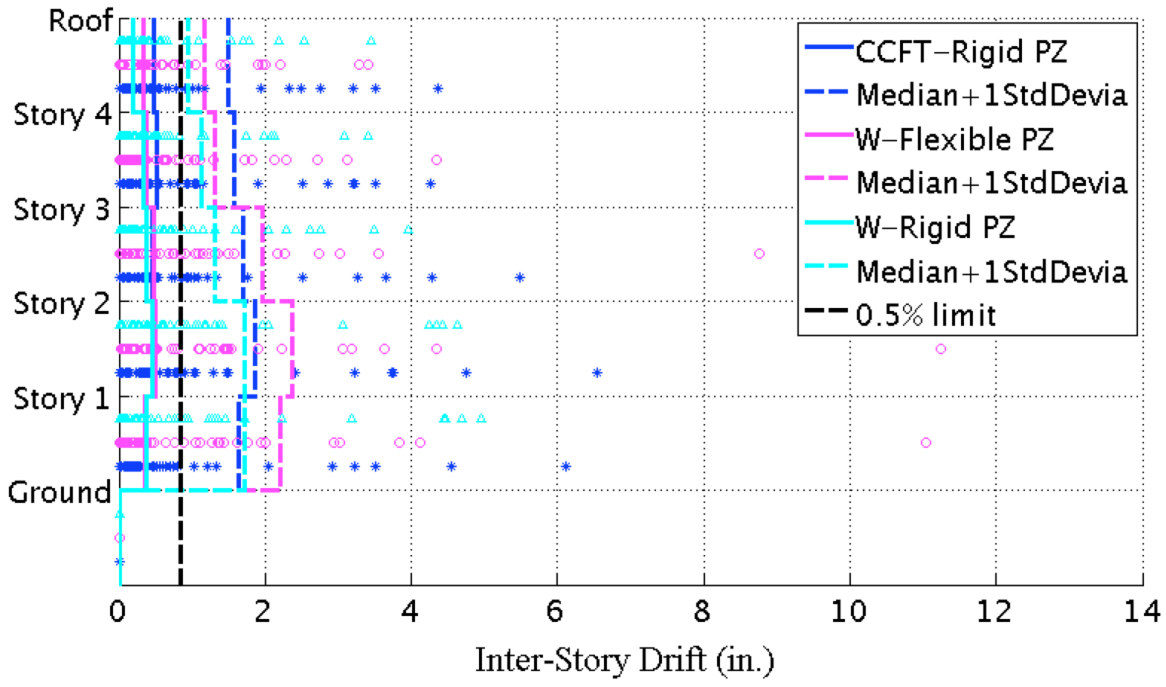

Figure 9-59: Median of the maximum inter-story residual drift under 44 MCE level ground motions with damping = 5% for the steel SMFs and the CSMF with a GSR = 0.9

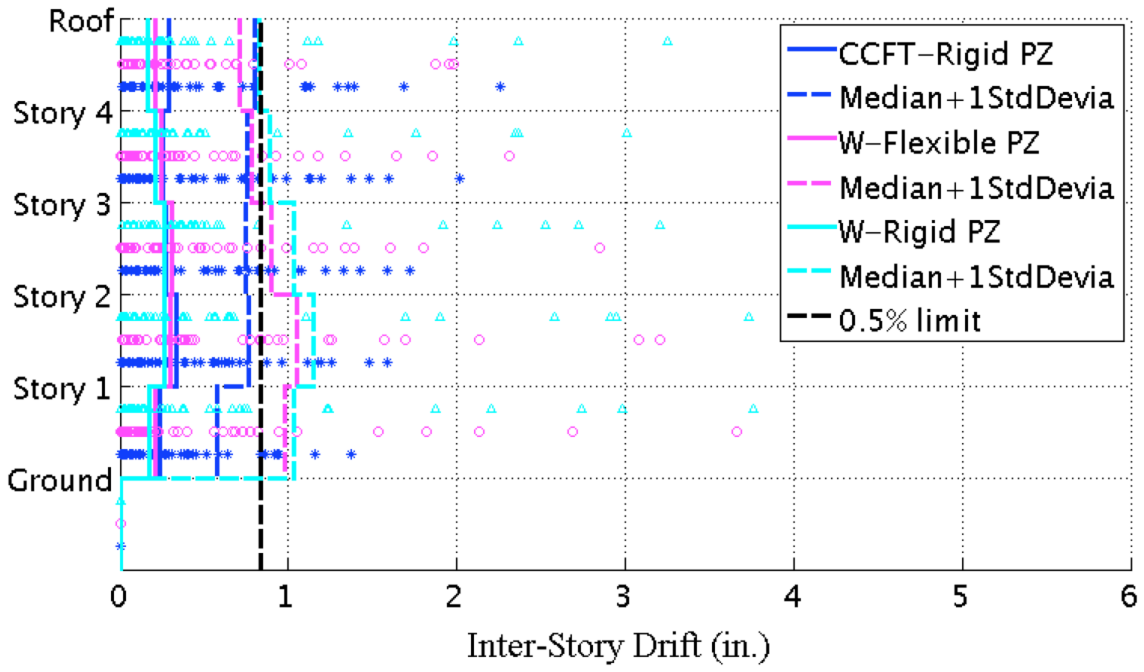

Figure 9-60: Median of the maximum inter-story residual drift under 44 DBE level ground motions with damping = 2% for the steel SMFs and the CSMF with a GSR = 0.9

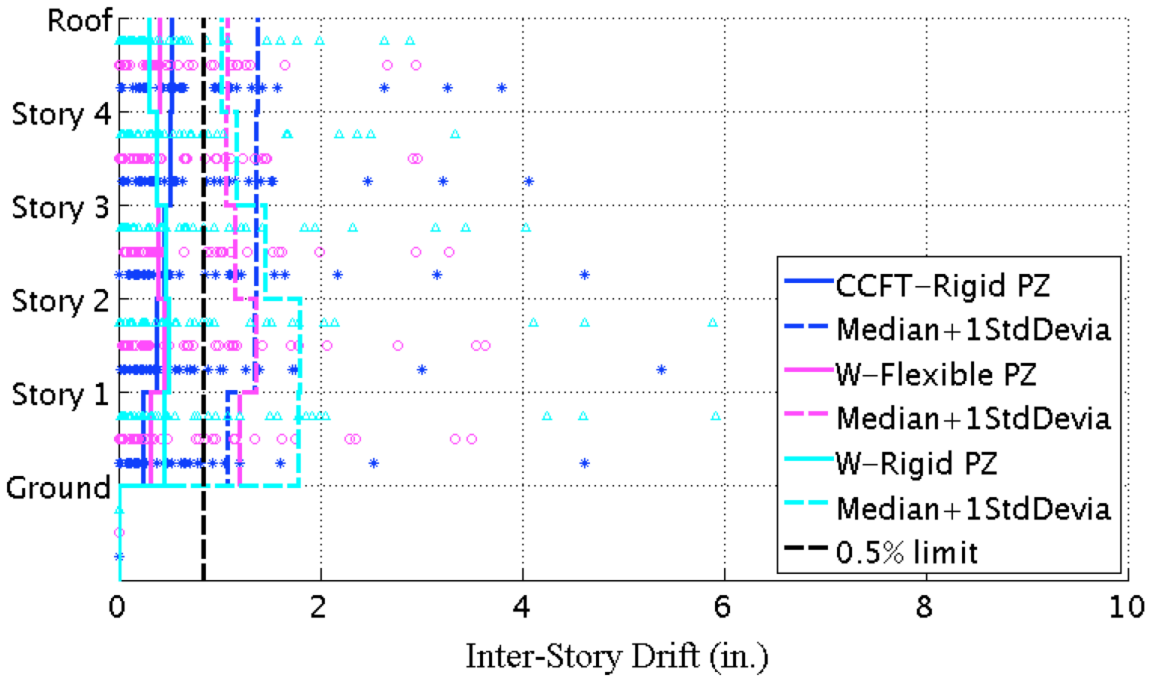

Figure 9-61: Median of the maximum inter-story residual drift under 44 MCE level ground motions with damping = 2% for the steel SMFs and the CSMF with a GSR = 0.9

The “conventional” CSMF with CCFT columns were compared with steel SMFs for all seismic responses. Generally speaking, except for the fact that axial force ratios in columns are significantly lower in the CSMF system, there are no obvious differences on other responses. This indicates that by using CCFT columns, CSMF with greater span lengths can obtain similar performance to steel SMFs with smaller span lengths if the degradation effects of panel zones in the steel SMFs are not considered.

9.8 Scale All Ground Motions to MCE Level

In FEMA-P695, ground motions is scaled to DBE or MCE levels based on their median intensity at the fundamental period, and the median of the seismic responses is used to evaluate the system performance. There are other scaling methods, and the corresponding responses would likely be also different. In this section, an alternative methodology that scales all 44 ground motions to match the standard response spectrum in ASCE7-10 at the first mode period of each system will be examined. In Figure 9-62 and Figure 9-63, the scaled acceleration spectra on MCE level for both the “conventional” and the self-centering CSMFs are presented.

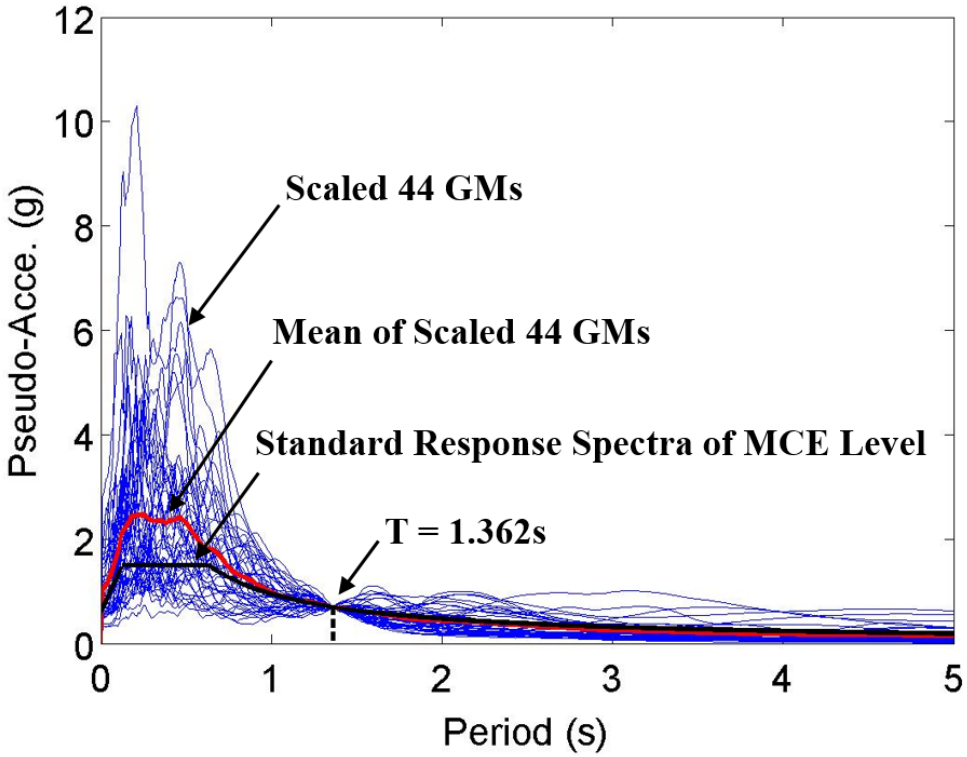

Figure 9-62: New scaled pseudo acceleration spectra of FEMA-P695 Far-Field set of 44 ground motions for the "conventional" CSMF on MCE level with damping = 5%

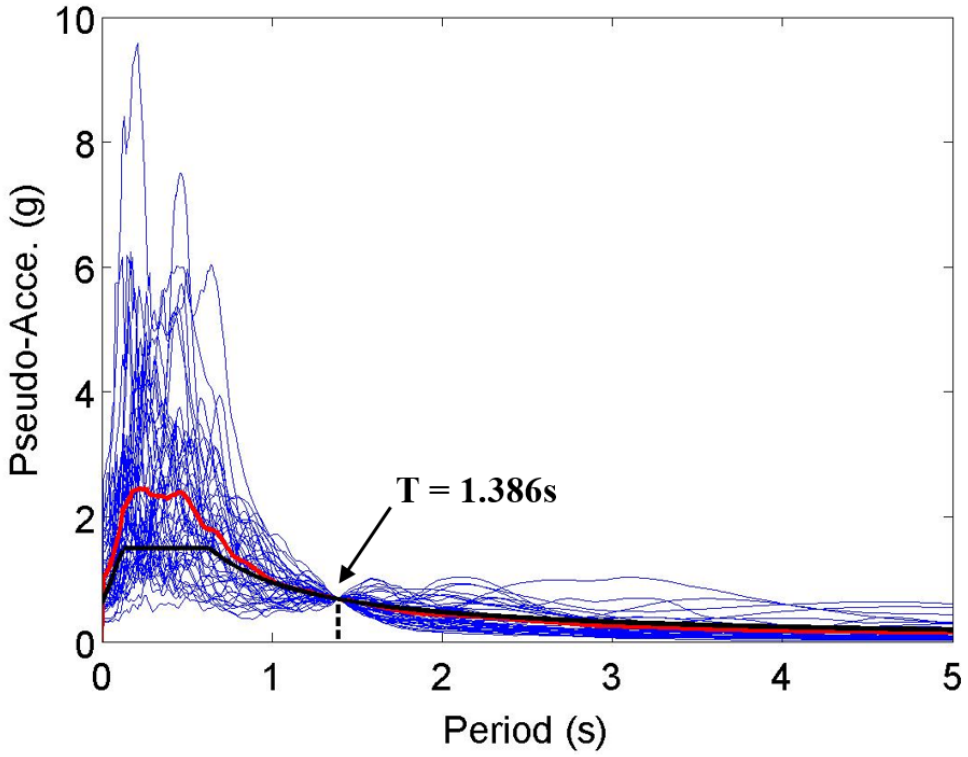

Figure 9-63: New scaled pseudo acceleration spectra of FEMA-P695 Far-Field set of 44 ground motions for the self-centering CSMFs on MCE level with damping = 5%

Comparing the two acceleration spectra in Figure 9-62 and Figure 9-63 with the one in Figure 9-4, one can see that the new spectra have greater peak intensities for some individual ground motions. As all ground motions are scaled to MCE level, it is reasonable to use a mean value, instead of median, of each response to evaluate the system performance. For some individual ground motions, which will cause obviously large difference from others, responses from them will not be considered for all three CSMFs. For example, the two ground motions which cause the very large story residual drifts for "conventional" CSMF in Figure 9-64 will be removed and only the remaining 42 ground motions are used to evaluate this specific system performance. The new results under the filtered ground motions are presented in Figure 9-65.

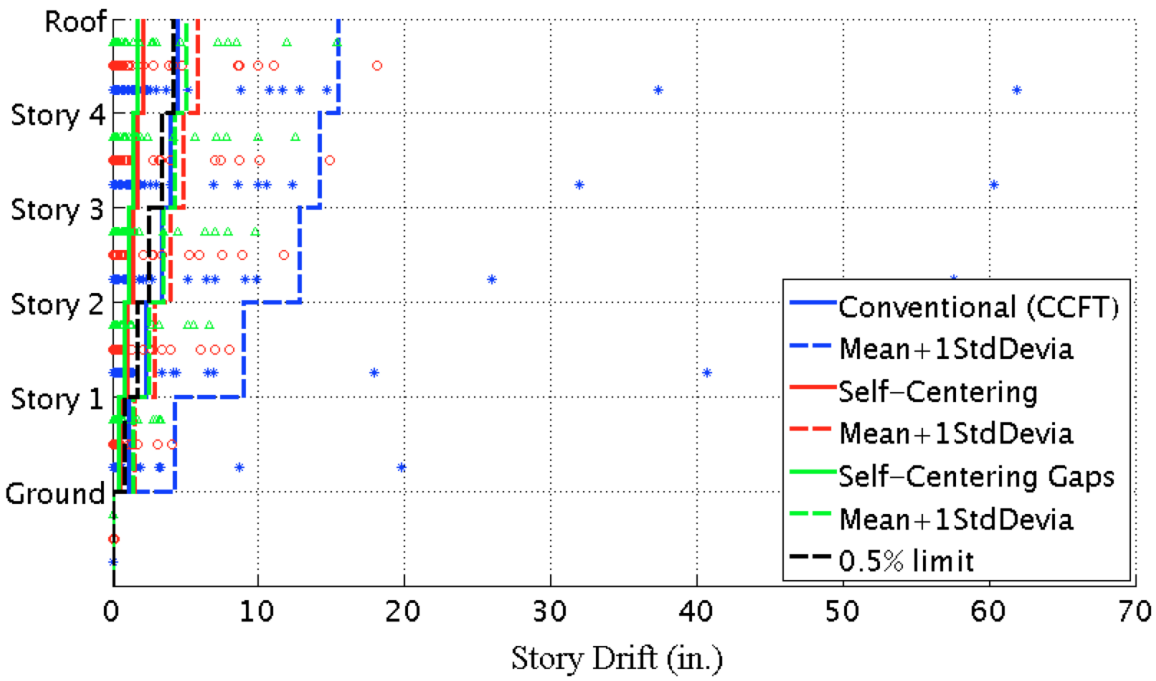

Figure 9-64: Mean of the maximum story residual drift under 44 DBE level ground motions with a GSR = 1.0 & damping = 5%

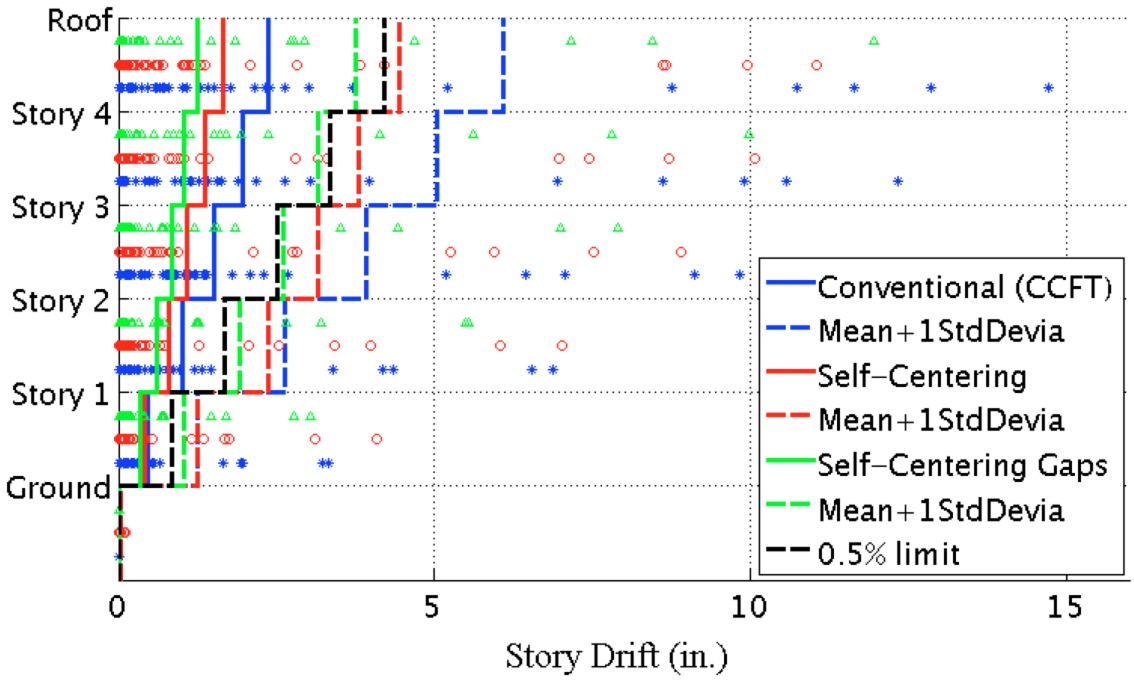

Figure 9-65: Mean of the maximum story residual drift under the 'Filtered 44' DBE level ground motions with a GSR = 1.0 & damping = 5%

There are more results presented in Section L.7 in Appendix L for other seismic responses. Comparing the results from two different sets of scaled ground motions based on different scaling methods, the two following conclusions are reached:

- The values of median or median plus 1 standard deviation are usually less than the values of mean or mean plus 1 standard deviation for most responses. For axial forces in beams and columns, the two methods will generate similar results.
- Results from both two sets of scaled ground motions indicate similar relative advantages for each system on different seismic responses.

9.9 Summary and Conclusions

In this Chapter, nonlinear dynamic analyses are executed for both "conventional" CSMF and self-centering CSMFs with CCFT columns. In order to obtain an optimized balance between greater self-centering capacity and column separation control, a new mechanism is proposed by adding small gaps on the steel rods.

Several important assumptions for all three CSMFs were made as follows:

- In order to reduce column separations to protect non-structural components from severe damage, an initial global strength ratio (GSR) of all three CSMFs is set to be 0.9.
- In order to ensure free deformation of the new proposed smart connections, no rigid diaphragm constraints are applied in the analysis.
- Fiber sections are employed to simulate plastic hinges to consider axial-flexural interaction effects for both beams and columns.
- The 2D-SSM in OpenSees without considering panel zone yielding mechanism is used to reduce computational cost because the CCFT columns was assumed to have adequate panel zone strength.
- No strength and stiffness cyclic degradation was considered in analyses, which can be caused by the weld fractures between beams and connections. This assumption is reasonable for self-centering systems, but it is believed to overestimate the capacity of "conventional" CSMF with FR connections.

- A non-simulated criteria of peak inter-story drift ratio of 10% was set to indicate collapse for dynamic incremental analyses.

The results from nonlinear dynamic analyses indicated that:

- Collapse margin ratios for the three CSMFs are similar, but the self-centering systems have much more remaining collapse prevention capacity.
- Seismic design parameters ($R = 8.0,\ C_d = 5.5$, and $\Omega = 3.0$) for special steel moment frames are reasonable for the self-centering systems.
- For systems with a GSR equal to 0.9:
    - The self-centering systems provide similar performance to the benchmark performance indicated by the "conventional" CSMF.
    - Considerable axial forces (especially on upper stories), and greater peak inter-story drifts, story velocity and acceleration are introduced into beams in the self-centering systems.
    - Plastic behavior of columns in all three CSMFs is limited.
    - Less plastic yielding of beams is observed in the self-centering systems. Residual deformation is not a good indicator of beam plastic damage.
    - Axial-flexural interaction should be considered for beams in the analysis of self-centering systems.
    - Axial forces in columns are less than 12% for most cases, and axial-flexural interaction can be ignored.

- Systems with a GSR equal to 1.0 do not show a meaningful improvement in system performance for the self-centering CSMFs.
- Systems with a GSR equal to 1.1 brings overwhelming advantages to self-centering CSMF with gaps over the other two systems. Axial forces in beams are reduced greatly, and the peak column separation is reasonable.
- Greater damping is helpful to obtain better performance for all three CSMFs, and response is more sensitive in the self-centering systems.
- A well-designed CSMF will have performance similar or better to a steel SMF with strong panel zones with lower cost.
- CSMFs allow for a much longer spans and consequently larger usable space.
- Different scaling methods for the ground motions do not result in appreciable differences in performance.

Chapter 10

Conclusions and Future Work

In this Chapter, a summary and conclusions of this research study are described in Section 10.1; recommendations are given in Section 10.2; original contributions are explained in Section 10.3; and finally, future work is discussed in Section 10.4.

10.1 Summary and Conclusions

In this research, an innovative self-centering PR connection configuration was developed to connect CCFT columns and conventional W steel beams. Some of the connecting elements used were shape memory alloy bars to generate self-centering capacity and others were steel rods with initial gaps to provide energy dissipation and additional stiffness. The connection is intended (1) to provide a reliable method to prevent structural collapse under severe earthquakes, and (2) to promote the application of CCFTs in seismic design for mid-rise buildings in US.

10.1.1 New Proposed Self-centering Connection Configuration

The proposed connection consists of (Figure 10-1):

1. a CCFT column with a rectangular steel tube collar that includes two inner steel

diaphragms and is filled with an expansive grout;

2. two beams with RBS connecting to extended stiffened end plates; and,
3. eight to sixteen through rods connecting the end plates with beams and the CCFT column with a collar together. The rods are grouped at several levels, with either two SMA and two steel rods on level for the case of sixteen rods, or two SMA or steel rods on each level for the case of eight rods.

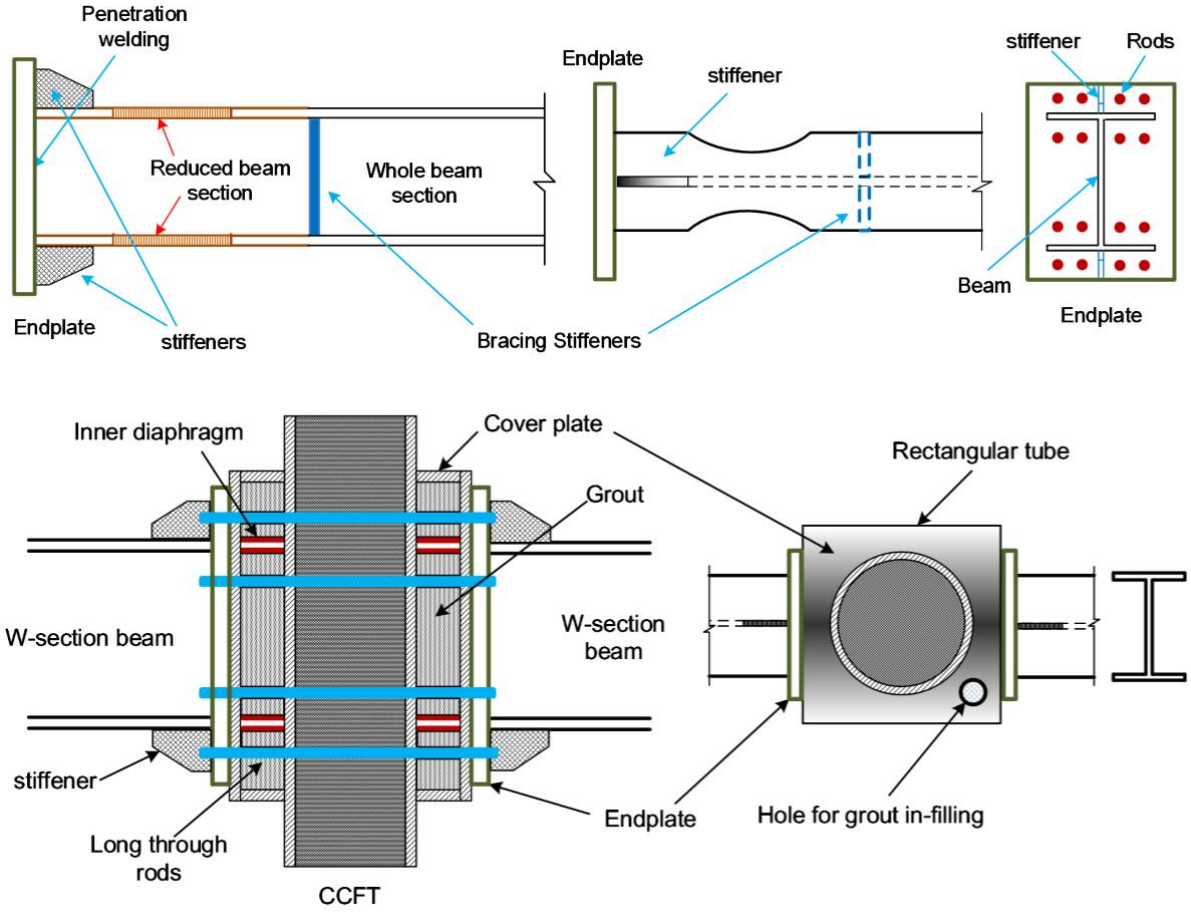

Figure 10-1: Details of the new proposed CCFT connection

All components are to be fabricated in the shop under ideal QA/QC conditions. The only

assembling needed on site is to (a) bolt the end plates onto the CCFT columns by using through rods and (b) pretension the rods. The design procedure for this connection is described in Section 3.3 and Appendix B, and a complete design example is provided in Appendix C.

The new proposed smart connection has several merits: (1) no need for full penetration welds and related QA/QC issues; (2) shop fabricated in its entirety; (3) rapid erection on site; and (4) self-centering capacity.

10.1.2 2D Simplified Spring Model for New Smart Connection

In order to reduce the computational cost of analyzing structures with the new proposed self-centering connection configuration, a 2D Simplified Spring Model (2D-SSM) for uniaxial bending was developed in both SAP2000 and OpenSees. The main characteristics of the 2D-SSMs are summarized as follows:

(1) 2D-SSM in SAP2000:

- The 2D-SSM in SAP2000 was developed for a connection with strong panel zone and rigid end plates; neither shear yielding in panel zone nor end plate yielding is considered in the original 2D-SSM (see Figure 4-1).
- A SMA through rod model was developed to simulate the flag-shape self-centering behavior with pretension effects based on the available elements. However, the model is not able to account for either residual strain or strength or stiffness degradation under cyclic loading (see Section 4.2.3).

- The SMA model is composed of one 'MultiLinear Elastic Link Element' and one 'MultiLinear Plastic Link Element with Kinematic Hysteresis Law'. A set of relationships were provided for calculating the required link parameters (Section 4.2.3).
- A steel through rod model was developed to simulate its pretensioning and sliding effects. The model is composed of one 'MultiLinear Elastic Link Element' and one 'MultiLinear Plastic Link Element with Takeda Hysteresis Law'. A set of relationships were provided for calculating the required link parameters (Section 4.2.4).
- The model is believed to be sufficiently accurate for design checks if the ultimate strain in the SMA rods is limited to less than 7%.
- An improved model was developed to considering yielding effects of end plates.

(2) 2D-SSM in OpenSees:

- The 2D-SSM in OpenSees was developed based on the improved model in SAP2000.
- A more advanced SMA material model (Section 7.2.1) was implemented, which can consider the residual strains under cyclic loadings.
- This model was further improved by adding a shear yielding mechanism in the panel zone.
- A set of relationships are proposed to calculate shear capacity of CCFT sections with through holes by modifying the current equations in AISC-14th and ACI318-11[2] [104].

Comparisons of the moment-rotation relationships (Section 7.2.2) indicated that the 2D-SSM

in SAP 2000matches well with the OpenSees model. The only difference between two models is that the OpenSees model is able to consider residual deformation in SMA rods.

10.1.3 Finite Element Analysis of New Smart Connection

Important assumptions were made in the preliminary design procedure and the 2D simplified spring models, including: (1) strong panel zone behavior without shear yielding; (2) adequate bearing capacity of expansive grout between the circular and rectangular steel tubes; (3) large stiffness of the column collar to avoid end plate inward displacement under beam ultimate strength; and (4) rigid body rotation of each end plate about one yield line at the beam flange in compression.

The effectiveness of these assumptions was investigated through detailed ABAQUS finite element analyses in which all relevant failure modes were checked. Among the features of this model are:

- A Concrete Damaged Plasticity (CDP) model was used for both the concrete core in the CCFT column and the expansive grout between the two tubes. The model includes the confinement effect on the concrete and grout from the steel tubes.
- Beam elements, instead of solid elements, were used to simulate through rods to reduce the computational cost.
- Only the upper backbone cure of SMA stress-strain relationship was defined. This is reasonable if only the ultimate states were investigated with no need to consider residual

deformation in the SMA rods.

By checking the damage of the concrete core, infill grout, end plates and the rectangular tube walls, the results prove the reasonableness of the assumptions for the preliminary design procedure and the 2D simplified spring model.

10.1.4 Nonlinear Static Pushover Analysis

To evaluate the system's self-centering capacity, nonlinear static pushover analyses (NSPOA) were carried out for two composite special moment frames (CSMFs) with five stories above grade and one basement: one has traditional fully restrained connections, and the other has partially restrained NPSCs. In order to establish robust computational models, parametric studies were run to justify the:

- Use of RBSs to reduce the connection demands.
- Use of zero length elements in OpenSees for both beam and column plastic hinges to reduce computational costs.
- Selection of "Method 2" to modify the properties of the modified Ibarra-Krawinkler model (OCIKMs) for the nonlinear analyses.
- Assumptions about the expected deformation mechanisms under cyclic loads, which were then illustrated in considerable detail.
- Robustness of the panel zone model.
- Sensitivity of the self-centering capacity to: (1) beams to connection strength; (2)

stiffness of connections from rods pretensioning; and (3) rigid diaphragm constraints.

The results of nonlinear static pushover analyses indicated that:

- Higher beam strength will generate greater self-centering capacity for a considerable range of the global strength ratio (GSR). The most sensitive range of beam strength is GSR from 0.9 to 1.05.
- Connection stiffness from rods pretensioning has insignificant impact on system's self-centering capacity.
- The most effective range of beam strength to reduce column separations is GSR from 0.8 to 1.0.
- System's self-centering capacity will be eliminated by adding rigid diaphragm constraints.

10.1.5 Nonlinear Dynamic Analysis

Nonlinear response history analyses are executed to evaluate thee CSMFs subjected to 44 DBE and MCE level ground motions. The systems analyzed included: (1) a "conventional" CSMF with FR connections; (2) a self-centering CSMF; and (3) a self-centering CSMF with Gaps (SC-Gaps) on the steel through rods. Gaps on steel rods are introduced into the self-centering system to simultaneously achieve two design goals: (1) a relatively strong beam-weak connection for greater self-centering capacity under moderate earthquakes; and (2) a relatively weak beam-strong connection for column separation control under large earthquakes. Several

important assumptions for all three CSMFs included:

- Use of fiber sections in OpenSees to simulate axial-flexural interactions for both beam and column plastic hinges. No cyclic strength and stiffness degradations were considered; this was believed to overestimate the "conventional" frame capacity.
- Use of a GSR of 0.9 to balance the system's self-centering capacity and column separation.
- Use of Dynamic Incremental Analyses (IDA) with a non-simulated criteria of peak inter-story drift ratio of 10% to indicate collapse.

The results of IDA and nonlinear dynamic analyses indicated that:

- Collapse margin ratios of three CSMFs are similar, but the self-centering systems have more remaining collapse prevention capacity.
- Seismic design parameters ($R = 8.0,\ C_d = 5.5$, and $\Omega = 3.0$) for special steel moment frames are reasonable for the self-centering systems.
- For systems with a GSR equal to 0.9:
    - Self-centering systems can deliver similar performance to the benchmark "conventional" CSMF.
    - Considerable axial forces, and greater peak inter-story drifts, story velocity and acceleration are introduced into beams in self-centering systems.
- A GSR equal to 1.0 cannot improve system performance of self-centering CSMFs; increasing beam strength for self-centering system without gaps is not an effective way

to obtain better seismic performance.

- A GSR equal to 1.1 brings overwhelming advantages to the self-centering CSMF with gaps over the other two systems.
- Greater damping is helpful to obtain better performance for all three CSMFs, and system response is more sensitive for the self-centering systems.

10.2 Recommendations

The recommendations on analysis and design of the new self-centering system from this research can be summarized as follows:

- Rod pattern 1 (Figure 3-8) is good for large beams; rod patterns 2 and 3 are good for smaller beams. Rods pattern 3 has slightly advantages over rod pattern 2.
- A distributed leaning column system should be used for self-centering system without rigid diaphragm constraints.
- Using a GSR equal to 1.1 with gaps on the steel rods is the most effective method to obtain superior seismic performance for the self-centering systems.
- Considerable axial forces will be introduced into the self-centering systems; fiber sections must be used to consider axial-flexural interaction in the plastic hinges.
- An effective way to reduce story velocity and acceleration in self-centering system should be investigated.
- Although pretensioning in rods has insignificant effects on system's self-centering

capacity, enough connection stiffness is needed to avoid end plate separation from columns under gravity loads.

10.3 Original Contributions

This research study is believed to have several original contributions as follows:

- Developed a new partially restrained connection configuration between CCFT columns and W steel beams that: (1) provides self-centering capacity by utilizing the 'Flag-shape' stress-strain characteristics of the SMA less than the 7% strain limit used in the design; and (2) prevents system collapse by utilizing the large residual strength and deformation capacity of the SMA beyond the 7% strain.
- Developed a connections that is almost entirely shop fabricated, which reduces erection cost and QA/QC field requirements when compared to conventional FR connections.
- Developed a connection that adapts to the different requirements of moderate and large earthquakes by shifting from a weak connection-strong beam to a strong connection-weak beam behavior as the drifts increase.
- Added significant new insights on behavior of composite special moment frames with self-centering capacity. Filling this research gap will be helpful in promoting the application of CCFT columns and SMA in seismic design in US. It supplies more ideas to other researchers insofar as (1) what are the most potential important factors for system's self-centering performance; (2) what are the potential failure modes of

structural and non-structural components of systems with PR connections; and (3) how to alleviate their damage.

- Provided a good example of the advantages of special moment frames with PR connections in high seismic zones, contributing to the development of mature design concepts for performance based design engineering.

10.4 Future Work

This research study is mainly based on theoretical modeling and analyses. Some fundamental assumptions were verified by using finite element analysis in ABAQUS. However, there are very few experimental results to support these conclusions. In order to promote more comprehensive design concepts and procedures, further research is needed, including:

10.4.1 Experiments

(1) Test axial, flexural and shear capacities of CCFT columns with through holes;

(2) Test individual self-centering connections to find out its governing limit states in order to improve the current design procedure and computational spring models;

(3) Test a composite special moment frame with new proposed self-centering connections to investigate static and dynamic performances of both structural and non-structural components.

(4) Conduct tests to ascertain if the large velocities and accelerations found in the analytical studies actually occur in real structures.

10.4.2 Theoretical Analysis

(1) Expand the 2D models to 3D models, and execute 3D model analyses to investigate gravity system effects on the system's self-centering capacity;

(2) Investigate effects from composite behaviors of concrete slabs;

(3) Generate different configurations of composite special moment frames, and evaluate their performance;

(4) Execute parametric study on the gap size of a self-centering system with gaps on steel rods to optimize the design procedure;

(5) Investigate effective methods to reduce the peak story velocity and acceleration in self-centering systems;

(6) Investigate the effectiveness of the proposed preliminary design procedure for an interior connection with different size beams;

(7) Investigate cyclic performance of the new smart connection by using FE analysis.

Reference

1. Shams, M. and M.A. Saadeghvaziri, *State of the art of concrete-filled steel tubular columns*. ACI Structural Journal, 1997. **94**(5): p. 558-571.
2. Manual, S.C., *American Institute of Steel Construction*. Inc., Fourteenth Edition, First Print, 2010.
3. Roeder, C.W., D.E. Lehman, and R. Thody, *Composite action in CFT components and connections*. ENGINEERING JOURNAL-AMERICAN INSTITUTE OF STEEL CONSTRUCTION INC, 2009. **46**(4): p. 229-242.
4. Roeder, C.W., B. Cameron, and C.B. Brown, *Composite action in concrete filled tubes*. Journal of Structural Engineering, 1999. **125**(5): p. 477-484.
5. Chen, W.-F., R.F. Lorenz, and B. Kato, *Semi-rigid connections in steel frames*. 1993: McGraw-Hill.
6. Chen, W.F., N. Kishi, and M. Komuro, *Semi-rigid Connections Handbook*. 1st ed. Civil and Environmental Engineering. 2011, Fort Lauderdale, FL: J. Ross.
7. Rassati, G.A., R.T. Leon, and S. Noe, *Component modeling of partially restrained composite joints under cyclic and dynamic loading*. Journal of Structural Engineering, 2004. **130**(2): p. 343-351.
8. Hu, J.W., *Seismic performance evaluations and analyses for composite moment frames with smart SMA PR-CFT connections*, in *Civil and Enviornmental Department*. 2008, Georgia Institute of Technology.
9. Hu, J.W., *Smart Connection Systems: Design and Seismic Analysis*. 2016: CRC Press. 404.
10. ANSI/AISC358-10, *Prequalified Connections for Special and Intermediate Steel Moment Frames for Seismic Applications*, AISC, Editor. 2010, AMERICAN INSTITUTE OF STEEL CONSTRUCTION.
11. FEMA-P695, *Quantification of Building Seismic Performance Factors*. FEMA Publication, Federal Emergency Management Association, Washington D.C., March., 2009.
12. Y., X. and M. S., *Composite and hybrid structures*. Proceedings of 6th ASCCS international conference, 2000. **1 and 2**.
13. Hajjar, J.F. *Jerome F. Hajjar Research Wiki*. Available from: http://www.northeastern.edu/compositesystems/wiki/Main_Page.
14. Knowles, R.B. and R. Park, *Strength of concrete filled steel tubular columns*. Journal of Structural Division, ASCE, 1969. **95**(12): p. 2565-2587.
15. Tomii, M., K. Yoshimura, and Y. Morishita, *Experimental studies on concrete-filled steel tubular stub columns under concentric loading*. Stability of Structures Under Static and Dynamic Loads, 1977: p. 718-741.
16. Tomii, M. and K. Sakino, *Experimental studies on the ultimate moment of concrete filled square steel tubular beam-columns*. Transactions of the Architectural Institute of

Japan, 1979. **275**: p. 55-65.
17. Okamato, T. and T. Maeno, *Experimental study on rectangular steel tube columns infilled with ultra high strength concrete hardened by centrifugal force*. Proc., Annual Meeting of AIJ, 1988: p. 1359-.
18. Susantha, K., H. Ge, and T. Usami, *Uniaxial stress–strain relationship of concrete confined by various shaped steel tubes*. Engineering Structures, 2001. **23**(10): p. 1331-1347.
19. Sugano, S., T. Nagashima, and T. Kei, *Seismic behavior of concrete-filled tubular steel columns*. Tenth Structures Congress, ASCE, 1992: p. 914-917.
20. Morino, S., et al., *Behavior of concrete-filled steel tubular three-dimensional subassemblages*. Proceeding of the Engineering Foundation Conference on Composite Construction in Steel and Concrete II. Potosi, USA: ASCE, 1993. **7262741**.
21. Nagashima, T., et al., *An Experimental Study on Behavior of Concrete-Filled Steel Tubular Columns under Cyclic Loading Axial Load*. Abstract, Annual Meeting of AIJ, 1989: p. 1601-1602.
22. Schneider, S.P., *Axially loaded concrete-filled steel tubes*. Journal of structural Engineering, 1998. **124**(10): p. 1125-1138.
23. ACI-318, *Building Code Requirements of Reinforced Concrete (ACI 318-89)*. American Concrete Institute, Farmington Hills, MI, 1989: p. 130-131.
24. Dai, X.H. and D. Lam, *Shape effect on the behaviour of axially loaded concrete filled steel tubular stub columns at elevated temperature*. Journal of Constructional Steel Research, 2012. **73**: p. 117-127.
25. SAC-95-09, *Background Reports: Metallurgy, Fracture Mechanics, Welding, Moment Connections and Frame Systems Behavior.* SAC Joint Venture, 1997.
26. GSA, *Alternate Path Analysis & Design Guidelines For Progressive Collapse Resistance*. General Services Administration, 2013.
27. Kam, W.Y., S. Pampanin, and K. Elwood, *Seismic performance of reinforced concrete buildings in the 22 February Christchurch (Lyttleton) earthquake*. 2011.
28. Cole, G.L., R.P. Dhakal, and F.M. Turner, *Building pounding damage observed in the 2011 Christchurch earthquake*. Earthquake Engineering & Structural Dynamics, 2012. **41**(5): p. 893-913.
29. Clifton, C., et al., *Steel Structures Damage from the Christchurch earthquake series of 2010 and 2011*. Bulletin of the New Zealand Society for Earthquake Engineering, 2011. **44**(4): p. 297-318.
30. Symans, M., et al., *Energy dissipation systems for seismic applications: current practice and recent developments*. Journal of Structural Engineering, 2008. **134**(1): p. 3-21.
31. Garlock, M., J.M. Ricles, and R. Sause, *Experimental studies on full-scale post-tensioned steel moment connections*. 13th World Conference on Earthquake Engineering, 2004.
32. Ricles, J.M., et al., *Posttensioned seismic-resistant connections for steel frames*. Journal of Structural Engineering, 2001. **127**(2): p. 113-121.

33. Rojas, P., J. Ricles, and R. Sause, *Seismic performance of post-tensioned steel moment resisting frames with friction devices*. Journal of structural engineering, 2005. **131**(4): p. 529-540.
34. Ibarra, L., R. Medina, and H. Krawinkler. *Collapse assessment of deteriorating SDOF systems*. in *Proceedings of the 12th European Conference on Earthquake Engineering*. 2002.
35. Vamvatsikos, D. and C.A. Cornell, *Incremental dynamic analysis*. Earthquake Engineering & Structural Dynamics, 2002. **31**(3): p. 491-514.
36. Ibarra, L.F. and H. Krawinkler, *Global collapse of frame structures under seismic excitations*. 2005: Pacific Earthquake Engineering Research Center.
37. Haselton, C.B., *Assessing seismic collapse safety of modern reinforced concrete moment frame buildings*. 2006, Stanford University.
38. Zareian, F. and H. Krawinkler, *Simplified performance-based earthquake engineering*. 2009, Rep. No. TB 169, The John A. Blume Earthquake Engineering Research Center, Stanford Univ., Stanford, CA.
39. Lignos, D.G. and H. Krawinkler, *Deterioration modeling of steel components in support of collapse prediction of steel moment frames under earthquake loading*. Journal of Structural Engineering, 2010. **137**(11): p. 1291-1302.
40. Baber, T.T. and M.N. Noori, *Random vibration of degrading, pinching systems*. Journal of Engineering Mechanics, 1985. **111**(8): p. 1010-1026.
41. Casciati, F., *Stochastic dynamics of hysteretic media*. Structural Safety, 1989. **6**(2): p. 259-269.
42. Reinhorn, A.M., et al., *Modeling of masonry infill panels for structural analysis*. 1995.
43. Iwan, W.D., *A distributed-element model for hysteresis and its steady-state dynamic response*. Journal of Applied Mechanics, 1966. **33**(4): p. 893-900.
44. Mostaghel, N., *Analytical description of pinching, degrading hysteretic systems*. Journal of Engineering Mechanics, 1999. **125**(2): p. 216-224.
45. Sivaselvan, M.V. and A.M. Reinhorn, *Hysteretic models for deteriorating inelastic structures*. Journal of Engineering Mechanics, 2000. **126**(6): p. 633-640.
46. Sivaselvan, M.V. and A.M. Reinhorn, *Lagrangian approach to structural collapse simulation*. Journal of Engineering mechanics, 2006. **132**(8): p. 795-805.
47. Lignos, D.G. and H. Krawinkler, *Sidesway collapse of deteriorating structural systems under seismic excitations*. Rep. No. TB 172, The John A. Blume Earthquake Engineering Center, Stanford Univ., Stanford, CA, 2009.
48. AIJ, *Recommendations for design and construction of concrete filled steel tubular structures*. 1997: Architectural Institute of Japan, Tokyo.
49. de Winkel, G.D., *The static strength of I-beam to circular hollow section column connections*. 1998: PhD thesis, Delft University Press, Delft, The Netherlands.
50. Fukumoto, T. and K. Morita, *Elastoplastic behavior of panel zone in steel beam-to-concrete filled steel tube column moment connections*. Journal of structural engineering, 2005. **131**(12): p. 1841-1853.
51. Nishiyama, I., et al., *Inelastic force-deformation response of joint shear panels in beam-*

column moment connections to concrete-filled tubes. Journal of Structural Engineering, 2004. **130**(2): p. 244-252.
52. Alostaz, Y.M. and S.P. Schneider, *Analytical behavior of connections to concrete-filled steel tubes*. Journal of Constructional Steel Research, 1996. **40**(2): p. 95-127.
53. Azizinamini, A. and S.P. Schneider, *Moment connections to circular concrete-filled steel tube columns*. Journal of Structural Engineering, 2004. **130**(2): p. 213-222.
54. DBJ-13-51, *Technical specification for concrete-filled steel tubular structures*. 2003, The Construction Department of Fujian Province, Fu Zhou.
55. Wang, J.F. and L.H. Han, *Seismic Behaviour of Semi-Rigid Joints to Concrete Filled Steel Tubular Columns*. Key Engineering Materials, 2009. **400**: p. 693-699.
56. Wang, J.-F., L.-H. Han, and B. Uy, *Behaviour of flush end plate joints to concrete-filled steel tubular columns*. Journal of Constructional Steel Research, 2009. **65**(4): p. 925-939.
57. Yao, H., H. Goldsworthy, and E. Gad, *Experimental and numerical investigation of the tensile behavior of blind-bolted T-stub connections to concrete-filled circular columns*. Journal of structural engineering, 2008. **134**(2): p. 198-208.
58. Sheet, I.S., U. Gunasekaran, and G.A. MacRae, *Experimental investigation of CFT column to steel beam connections under cyclic loading*. Journal of Constructional Steel Research, 2013. **86**: p. 167-182.
59. Li, X., Y. Xiao, and Y. Wu, *Seismic behavior of exterior connections with steel beams bolted to CFT columns*. Journal of Constructional Steel Research, 2009. **65**(7): p. 1438-1446.
60. Eatherton, M., et al. *Steel-framed rocking structural systems for moderate seismic zones*. in *ASCE/SEI Structures Congress, Austin, TX*. 2009.
61. Roke, D., et al., *Design concepts for damage-free seismicresistant self-centering steel concentrically-braced frames*. Proceedings of 14th WCEE (DVD, paper S16-01-006), Beijing, 2008.
62. Chi, H. and J. Liu, *Seismic behavior of post-tensioned column base for steel self-centering moment resisting frame*. Journal of Constructional Steel Research, 2012. **78**: p. 117-130.
63. Jackson, C., H. Wagner, and R. Wasilewski, *55-Nitinol-The Alloy with a Memory: It's Physical Metallurgy Properties, and Applications*. *NASA SP-5110*. NASA Special Publication, 1972. **5110**.
64. Auricchio, F., R.L. Taylor, and J. Lubliner, *Shape-memory alloys: macromodelling and numerical simulations of the superelastic behavior.* Computer methods in applied mechanics and engineering, 1997. **146**(3): p. 281-312.
65. Cederstrom, J. and J. Van Humbeeck, *Relationship between shape-memory material properties and applications*. Journal de physique iv, 1995. **5**(C2): p. 335-341.
66. Wilkes, K.E. and P.K. Liaw, *The fatigue behavior of shape-memory alloys*. JOM, 2000. **52**(10): p. 45-51.
67. Sun, L. and W. Huang, *Nature of the multistage transformation in shape memory alloys upon heating*. Metal Science and Heat Treatment, 2009. **51**(11): p. 573-578.

68. Mihálcz, I., *Fundamental characteristics and design method for nickel-titanium shape memory alloy*. Mechanical Engineering, 2001. **45**(1): p. 75-86.
69. Duerig, T. and A. Pelton, *Ti-Ni shape memory alloys*. Materials properties handbook: titanium alloys, 1994: p. 1035-1048.
70. Wilson, J.C. and M.J. Wesolowsky, *Shape memory alloys for seismic response modification: a state-of-the-art review*. Earthquake Spectra, 2005. **21**(2): p. 569-601.
71. Song, G., N. Ma, and H.-N. Li, *Applications of shape memory alloys in civil structures*. Engineering Structures, 2006. **28**(9): p. 1266-1274.
72. Saiidi, M.S., M.O. Brien, and M. Sadrossadat-Zadeh, *Cyclic response of concrete bridge columns using superelastic nitinol and bendable concrete*. ACI Structural Journal, 2009. **106**(1).
73. Andrawes, B. and R. DesRoches, *Effect of hysteretic properties of superelastic shape memory alloys on the seismic performance of structures*. Structural Control and Health Monitoring, 2007. **14**(2): p. 301-320.
74. DesRoches, R. and M. Delemont, *Seismic retrofit of simply supported bridges using shape memory alloys*. Engineering Structures, 2002. **24**(3): p. 325-332.
75. Roh, H. and A.M. Reinhorn, *Hysteretic behavior of precast segmental bridge piers with superelastic shape memory alloy bars*. Engineering Structures, 2010. **32**(10): p. 3394-3403.
76. DesRoches, R., J. McCormick, and M. Delemont, *Cyclic properties of superelastic shape memory alloy wires and bars*. Journal of Structural Engineering, 2004. **130**(1): p. 38-46.
77. ANSI/AISC341-10, *Seismic Provisions for Structural Steel Buildings*, AISC, Editor. 2010, AMERICAN INSTITUTE OF STEEL CONSTRUCTION.
78. ASCE/SEI7-10, *Minimum Design Loads for Buildings and Other Structures*, ASCE, Editor. 2010, American Society of Civil Engineers.
79. API, *API Spec 2B-1: Specification for Fabrication of Structural Steel Pipe (R2012), 6th Ed*. 2012, American Petroleum Institute, Washington, D.C.
80. Leon, R.T., *Seismic Performance of Bolted and Riveted Connections, Background Reports: Metallurgy, Fracture Mechanics, Welding, Moment Connections, and Frame System Behavior*. FEMA Publication, Federal Emergency Management Association, Washington D.C., March., 1997. **No.288**.
81. Sumner III, E.A., *Unified design of extended end-plate moment connections subject to cyclic loading*, in *Civil and Environmental Engineering*. 2003, Virginia Polytechnic Institute and State University.
82. Meng, R.L., *Design of moment end-plate connections for seismic loading*, in *Civil and Environmental Engineering*. 1996, Virginia Polytechnic Institute and State University, Blacksburg, Virginia.
83. Engelhardt, M.D., et al., *Behavior and design of radius-cut, reduced beam section connections*. A draft report of SAC task, 2000. **7**.
84. Deierlein, G.G. and W.M. Chi, *SAC TASK 5.3.3 - Integrative Analytical Investigations on the Fracture Behavior of Welded Moment Resisting Connections*. Final Report, John

A. Blume Earthquake Engineering Center, Dept. of Civil and Environmental Engineering, Stanford University, Palo Alto, California., 1999.
85. Grubbs, K.V., *The effect of the dogbone connection on the elastic stiffness of steel moment frames*. 1997, University of Texas at Austin.
86. Iwankiw, N.R. and C.J. Carter, *The dogbone: a new idea to chew on*. Modern Steel Construction, 1996. **36**(4): p. 18-23.
87. Almudhafar, S. and J.J. Chambers, *Stiffness Implications of Beams with Reduced Flanges*. Proceedings of US-Japan Workshop on Seismic Fracture Issues in Steel Structures, San Francisco, California., 2000.
88. FEMA-355D, *State of the Art Report on Connection Performance*. Federal Emergency Management Agency, 2000.
89. Popovics, S., *A numerical approach to the complete stress-strain curve of concrete*. Cement and concrete research, 1973. **3**(5): p. 583-599.
90. Mander, J.B., M.J. Priestley, and R. Park, *Theoretical stress-strain model for confined concrete*. Journal of structural engineering, 1988. **114**(8): p. 1804-1826.
91. Saenz, L.P., *Discussion of equation for the stress-strain curve of concrete by Desayi and Krishnan*. ACI journal, 1964. **61**(9): p. 1229-1235.
92. Tsai, W.T., *Uniaxial compressional stress-strain relation of concrete*. Journal of Structural Engineering, 1988. **114**(9): p. 2133-2136.
93. Kaufmann, E., B. Metrovich, and A. Pense, *Characterization of cyclic inelastic strain behavior on properties of A572 Gr. 50 and A913 Gr. 50 rolled sections*. 2001.
94. Elchalakani, M., X.-L. Zhao, and R. Grzebieta, *Concrete-filled steel circular tubes subjected to constant amplitude cyclic pure bending*. Engineering structures, 2004. **26**(14): p. 2125-2135.
95. Elchalakani, M. and X.-L. Zhao, *Concrete-filled cold-formed circular steel tubes subjected to variable amplitude cyclic pure bending*. Engineering Structures, 2008. **30**(2): p. 287-299.
96. Tatsuoka, T., Y. Takagi, and T. Sawa. *Sealing performance of pipe flange connections with shape memory alloy gaskets under internal pressure*. in *ASME/JSME 2004 Pressure Vessels and Piping Conference*. 2004. American Society of Mechanical Engineers.
97. Fukuta, T., et al. *Experimental study on stress-strain property of shape memory alloy and its application to self-restoration of structural members*. in *Proc., 13th World Conf. of Earthquake Engineering*. 2004.
98. Construction, A.I.o.S., *AISC Steel Design Guide Series 16*, in *Flush and Extended Multiple-Row Moment End-Plate Connections*. 2002.
99. Institute, S.D., *VULCRAFT - Composite deck with composite stud tables*. 2010.
100. Berk, T., *Probabilistic Seismic Demand Assessment of Steel Frames with Shape Memory Alloy Connections*, in *Civil and Environmental Engineering*. 2007, Georgian Institute of Technology.
101. Eatherton, M.R., L.A. Fahnestock, and D.J. Miller, *Computational study of self‐centering buckling‐restrained braced frame seismic performance*. Earthquake

Engineering & Structural Dynamics, 2014. **43**(13): p. 1897-1914.
102. Charney, F.A. and W.M. Downs. *Modeling procedures for panel zone deformations in moment resisting frames*. in *Proceedings*. 2004.
103. ANSI/AISC360-10, *Specification for Structural Steel Buildings*, AISC, Editor. 2010, AMERICAN INSTITUTE OF STEEL CONSTRUCTION.
104. ACI-318, *Building Code Requirements of Reinforced Concrete (ACI 318-11)*. American Concrete Institute, Farmington Hills, MI, 2011.
105. Gupta, A. and H. Krawinkler, *Seismic demands for the performance evaluation of steel moment resisting frame structures*. 1999, Stanford University.
106. Tremblay, R., et al., *Performance of steel structures during the 1994 Northridge earthquake*. Canadian Journal of Civil Engineering, 1995. **22**(2): p. 338-360.
107. Kanvinde, A.M., *Micromechanical simulation of earthquake-induced fracture in steel structures*. 2004.
108. Baker, J.W., *Vector-Valued Ground Motion Intensity Measures for Probabilistic Seismic Demand Analysis*, in *Department of Civil and Environmental Engineering*. 2005, Stanford University, Stanford, California.
109. Baker, J.W. and C. Allin Cornell, *Spectral shape, epsilon and record selection*. Earthquake Engineering & Structural Dynamics, 2006. **35**(9): p. 1077-1095.
110. Haselton, C. and J. Baker. *Ground motion intensity measures for collapse capacity prediction: Choice of optimal spectral period and effect of spectral shape*. in *8th National Conference on Earthquake Engineering*. 2006.
111. Goulet, C., et al. *Evaluation of the seismic performance of a code-conforming reinforced-concrete frame building-Part I: Ground motion selection and structural collapse simulation*. in *8th National Conference on Earthquake Engineering (100th Anniversary Earthquake Conference)*. 2006.
112. Zareian, F. and H. Krawinkler, *Simplified performance-based earthquake engineering*. 2006, Stanford University.
113. Chopra, A.K., *Dynamics of Structures - Theory and Applications to Earthquake Engineering*. Fourth ed. 2012: PEARSON.
114. Charney, F.A. *Analysis of Building and Cable Structures with Geometric Nonlinearities*. 2002.
115. Alipour, A. and F. Zareian. *Study Rayleigh damping in structures; unceratinties and treatments*. in *Proceedings of 14th World Conference on Earthquake Engineering, Beijing, China*. 2008.
116. Bernal, D., *Viscous damping in inelastic structural response*. Journal of structural engineering, 1994. **120**(4): p. 1240-1254.
117. Charney, F.A. *Consequences of using Rayleigh damping in inelastic response history analysis*. in *Proc., 17th Analysis and Computation Speciality Conference*. 2006.
118. Hall, J.F., *Problems encountered from the use (or misuse) of Rayleigh damping*. Earthquake engineering & structural dynamics, 2006. **35**(5): p. 525-545.
119. Engelhardt, M.D., et al., *Behavior and design of radius cut reduced beam section connections*. A draft report of SAC task, 2000. **7**.

120. Miranda, E. and S. Taghavi, *Approximate floor acceleration demands in multistory buildings. I: Formulation*. Journal of structural engineering, 2005. **131**(2): p. 203-211.
121. FEMA-P58, *Seismic performance assessment of buildings, volume 1 - Methodology (FEMA P-58-1)*. 2012a.
122. Zhao, X.-L., L.-H. Han, and H. Lu, *Concrete-filled tubular members and connections*. 2010: Spon Press.
123. Elchalakani, M., X.-L. Zhao, and R. Grzebieta, *Concrete-filled circular steel tubes subjected to pure bending*. Journal of Constructional Steel Research, 2001. **57**(11): p. 1141-1168.
124. Bergmann, R., C. Matsui, and C. Meinsma, *Design guide for concrete filled hollow section columns under static and seismic loading*. 1995: Verlag TÜV Rheinland.
125. BSI, *Steel, concrete and composite bridges, BS5400, Part 5: Code of Practice for Design of Composite Bridges*, B.S. Institution, Editor. 2005: London.
126. Bruneau, M. and J. Marson, *Seismic design of concrete-filled circular steel bridge piers*. Journal of bridge engineering, 2004. **9**(1): p. 24-34.
127. GB50010, *Code for Design of Concrete Structures, GB50010-2002* 2002, Beijing: China Architecture & Building Press.
128. Roik, K. and R. Bergmann, *Composite columns*. Constructional steel design. Dowling, P. Harding, J. and Bjorhovde, R.(eds.). Elsevier Sc. Publ. ISBN, 1992. **1**: p. 85166-895.
129. Leon, R.T., D.K. Kim, and J.F. Hajjar, *Limit state response of composite columns and beam-columns part 1: Formulation of design provisions for the 2005 AISC specification*. ENGINEERING JOURNAL-AMERICAN INSTITUTE OF STEEL CONSTRUCTION, 2007. **44**(4): p. 341.
130. Leon, R.T. and J.F. Hajjar, *Limit State Response of Composite Columns and Beam-Columns. Part II: Application of Design Provisions for 2005 AISC Specification*. Engineering journal, 2008. **45**(1): p. 21.
131. Roark, R.J. and W.C. Young, *Formulas for Stress and Strain*. 5th ed. 1975: McGraw-Hill, New York.
132. Rahnama, M. and H. Krawinkler, *Effect of soft soils and hysteresis models on seismic design spectra*. Rep. No. TB 108, The John A. Blume Earthquake Engineering Center, Stanford Univ., Stanford, CA, 1993.
133. Lignos, D.G. and H. Krawinkler. *A database in support of modeling of component deterioration for collapse prediction of steel frame structures*. in *ASCE Structures Congress*. 2007.
134. Ricles, J.M., et al., *Development of seismic guidelines for deep-column steel moment connections*. 2004, Rep. No. 04-13, Advanced Technology for Large Structural Systems, Lehigh Univ., Bethlehem, PA.
135. Mander, J.B., M.J.N. Priestley, and R. Park, *Seismic Design of Bridge Piers*. Research Report No. 84-2, Univ. of Canterbury, New Zealand., 1984.
136. Richart, F.E., A. Brandtzæg, and R.L. Brown, *Failure of plain and spirally reinforced concrete in compression*. 1929.
137. Sheikh, S.A. and S.M. Uzumeri, *Strength and ductility of tied concrete columns*. Journal

of the structural division, 1980. **106**(ASCE 15388 Proceeding).
138. Hu, H.-T., et al., *Nonlinear analysis of axially loaded concrete-filled tube columns with confinement effect*. Journal of Structural Engineering, 2003. **129**(10): p. 1322-1329.
139. Hu, H.-T. and W.C. Schnobrich, *Constitutive modeling of concrete by using nonassociated plasticity*. Journal of Materials in Civil Engineering, 1989. **1**(4): p. 199-216.
140. Giakoumelis, G. and D. Lam, *Axial capacity of circular concrete-filled tube columns*. Journal of Constructional Steel Research, 2004. **60**(7): p. 1049-1068.
141. Tomii, M. *Ductile and strong columns composed of steel tube, infilled concrete and longitudinal steel bars*. in *Special Volume, Proc., 3rd Int. Conf. on Steel-Concrete Composite Structures*. 1991.
142. Mursi, M. and B. Uy, *Strength of concrete filled steel box columns incorporating interaction buckling*. Journal of Structural Engineering, 2003. **129**(5): p. 626-639.
143. Ellobody, E., B. Young, and D. Lam, *Behaviour of normal and high strength concrete-filled compact steel tube circular stub columns*. Journal of Constructional Steel Research, 2006. **62**(7): p. 706-715.
144. Kent, D.C. and R. Park, *Flexural members with confined concrete*. Journal of the Structural Division, 1971. **97**(7): p. 1969-1990.
145. Hoshikuma, J., et al., *Stress-strain model for confined reinforced concrete in bridge piers*. Journal of Structural Engineering, 1997. **123**(5): p. 624-633.
146. Akiyama, M., M. Suzuki, and D.M. Frangopol, *Stress-averaged strain model for confined high-strength concrete*. ACI Structural Journal, 2010. **107**(02).
147. Denavit, M., *Characterization of behavior of steel-concrete composite members and frames with applications for design*. 2013, University of Illinois at Urbana-Champaign.
148. Tort, C. and J.F. Hajjar, *Reliability-Based Performance-Based Design of Rectangular Concrete-Filled Steel Tube (RCFT) Members and Frames*. Structural Engineering Report No. ST-07-1, Department of Civil Engineering, University of Minnesota, Minneapolis, Minnesota., 2007.
149. Denavit, M.D. and J.F. Hajjar, *Nonlinear seismic analysis of circular concrete-filled steel tube members and frames*. Journal of Structural Engineering, 2011. **138**(9): p. 1089-1098.
150. ABAQUS-Manual, *ABAQUS User Analysis Manual, V6.12*.
151. Lee, J. and G.L. Fenves, *Plastic-damage model for cyclic loading of concrete structures*. Journal of engineering mechanics, 1998. **124**(8): p. 892-900.
152. Lubliner, J., et al., *A plastic-damage model for concrete*. International Journal of solids and structures, 1989. **25**(3): p. 299-326.
153. Bazant, Z.P. and J. Planas, *Fracture and size effect in concrete and other quasibrittle materials*. Vol. 16. 1997: CRC press.

Appendix A

Detailed Derivations of the Modified Sumner's Equations

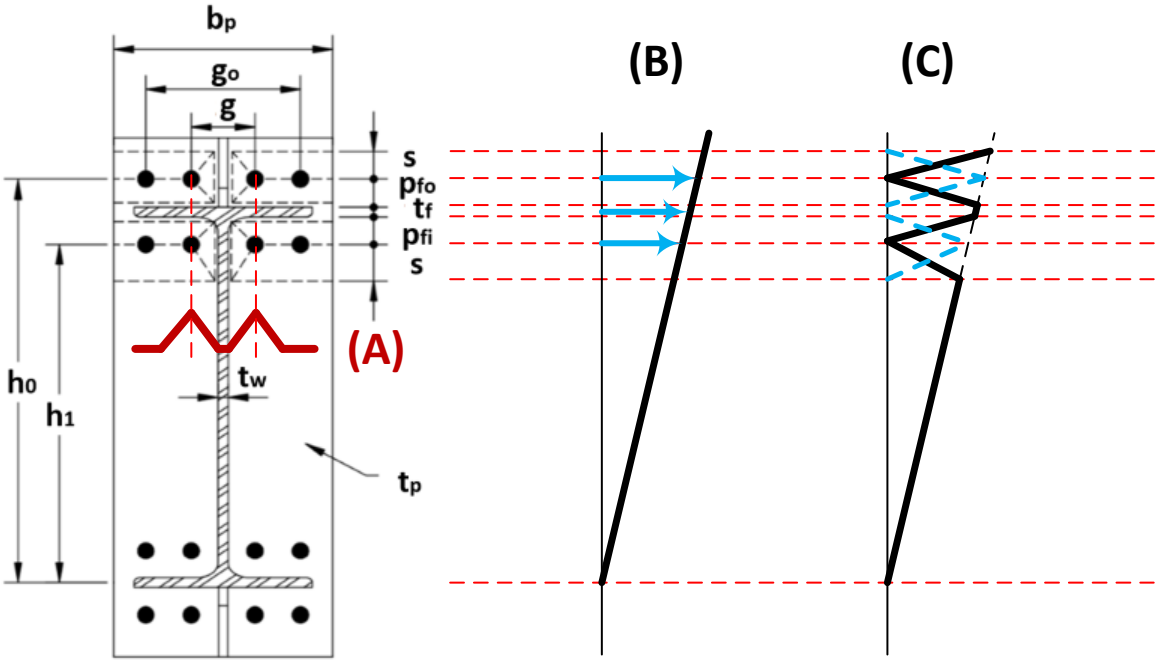

Appendix Figure A-1: Yield Line Mechnism of End Plate for Case $d_e > s$

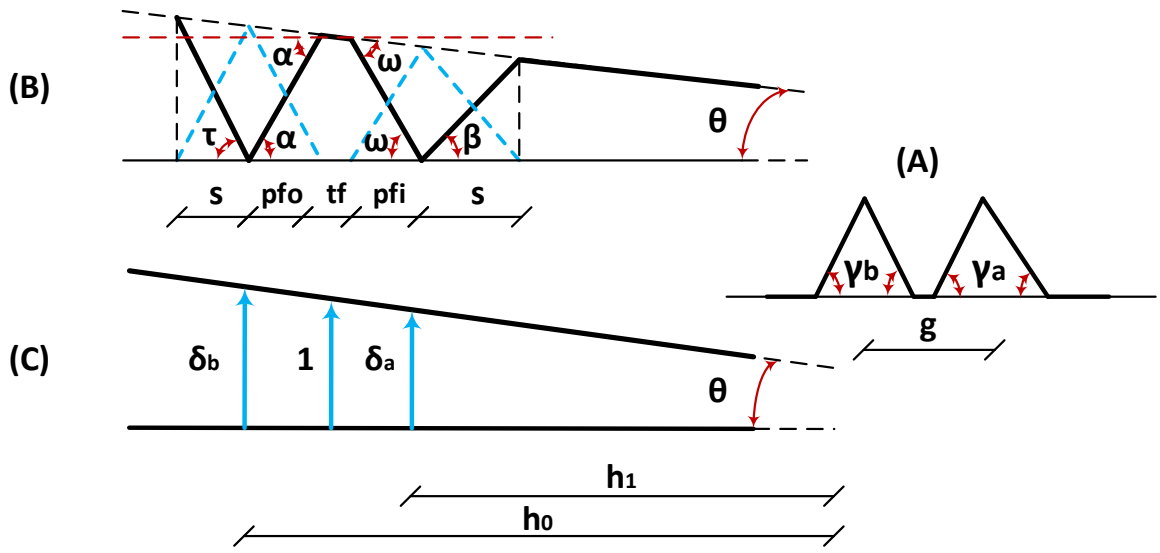

Appendix Figure A-2: Amplified Plote of Appendix Figure A-1

A.1 Case 1 (when $d_e > s$):

$$W_I = m_p \cdot b_p \cdot \left[(\alpha + \tau) + (\alpha + \omega) + (\omega + \beta) + (\beta + \theta) \right] + 2m_p \cdot \left(s + p_{fi} \right)(\gamma_a + \gamma_a)$$

$$+ 2m_p \cdot \left(s + p_{fo} \right)(\gamma_b + \gamma_b)$$

$$= 2m_p \cdot b_p \cdot \left(\alpha + \omega + \beta + \frac{1}{2} \cdot \tau + \frac{1}{2} \cdot \theta \right) + 4m_p \left[\left(s + p_{fi} \right) \cdot \gamma_a + \left(s + p_{fo} \right) \cdot \gamma_b \right]$$

$$= 2m_p \cdot b_p \cdot \left[\left(\frac{\delta_b}{p_{fo}} - \theta \right) + \left(\frac{\delta_a}{p_{fi}} + \theta \right) + \left(\frac{\delta_a}{s} - \theta \right) + \frac{1}{2}\left(\frac{\delta_b}{s} + \theta \right) + \frac{1}{2} \cdot \theta \right]$$

$$+ 4m_p \left[\left(s + p_{fi} \right) \cdot \gamma_a + \left(s + p_{fo} \right) \cdot \gamma_b \right]$$

$$= 2m_p \cdot b_p \cdot \left(\frac{\delta_b}{p_{fo}} + \frac{\delta_a}{p_{fi}} + \frac{\delta_a}{s} + \frac{\delta_b}{2 \cdot s} \right) + 4m_p \left[\left(s + p_{fi} \right) \cdot \frac{2\delta_a}{g} + \left(s + p_{fo} \right) \cdot \frac{2\delta_b}{g} \right]$$

$$= 2m_p \cdot b_p \cdot \theta \cdot \left(\frac{h_0}{p_{fo}} + \frac{h_1}{p_{fi}} + \frac{h_1}{s} + \frac{h_0}{2 \cdot s} \right) + \frac{8m_p}{g} \cdot \theta \cdot \left[\left(s + p_{fi} \right) \cdot h_1 + \left(s + p_{fo} \right) \cdot h_0 \right]$$

$$= \frac{t^2 \cdot F_y \cdot b_p}{2} \cdot \theta \cdot \left(\frac{h_0}{p_{fo}} + \frac{h_1}{p_{fi}} + \frac{2 \cdot h_1 + h_0}{2 \cdot s} \right) + \frac{2 \cdot t^2 \cdot F_y}{g} \cdot \theta \cdot \left[\left(s + p_{fi} \right) \cdot h_1 + \left(s + p_{fo} \right) \cdot h_0 \right]$$

$$= t^2 \cdot F_y \cdot \theta \cdot \left\{ \frac{b_p}{2} \left(\frac{h_0}{p_{fo}} + \frac{h_1}{p_{fi}} + \frac{2 \cdot h_1 + h_0}{2 \cdot s} \right) + \frac{2}{g} \left[\left(s + p_{fi} \right) \cdot h_1 + \left(s + p_{fo} \right) \cdot h_0 \right] \right\}$$

$$= t^2 \cdot F_y \cdot \theta \cdot \left\{ \frac{b_p}{2} \left[h_1 \left(\frac{1}{p_{fi}} + \frac{1}{s} \right) + h_0 \left(\frac{1}{p_{fo}} + \frac{1}{2 \cdot s} \right) \right] + \frac{2}{g} \left[h_1 \left(p_{fi} + s \right) + h_0 \left(p_{fo} + s \right) \right] \right\}$$

$$= t^2 \cdot F_y \cdot \theta \cdot Y_p$$

$$Y_p = \frac{b_p}{2} \left[h_1 \left(\frac{1}{p_{fi}} + \frac{1}{s} \right) + h_0 \left(\frac{1}{p_{fo}} + \frac{1}{2 \cdot s} \right) \right] + \frac{2}{g} \left[h_1 \left(p_{fi} + s \right) + h_0 \left(p_{fo} + s \right) \right]$$

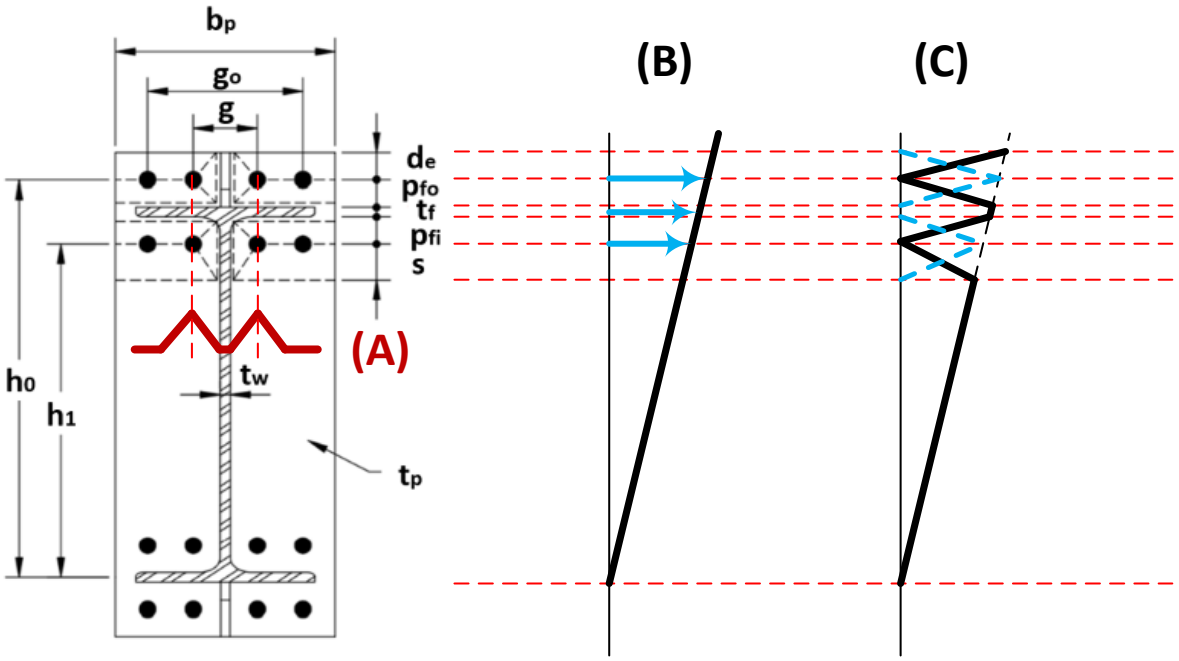

Appendix Figure A-3: Yield Line Mechnism of End Plate for Case $d_e \leq s$

A.2 Case 1 (when $d_e \le s$):

$$W_I = m_p \cdot b_p \cdot \left[(\alpha + \tau) + (\alpha + \omega) + (\omega + \beta) + (\beta + \theta) \right] + 2m_p \cdot \left(s + p_{fi} \right)(\gamma_a + \gamma_a)$$

$$+ 2m_p \cdot \left(d_e + p_{fo} \right)(\gamma_b + \gamma_b)$$

$$= 2m_p \cdot b_p \cdot \left(\alpha + \omega + \beta + \frac{1}{2} \cdot \tau + \frac{1}{2} \cdot \theta \right) + 4m_p \left[\left(s + p_{fi} \right) \cdot \gamma_a + \left(s + p_{fo} \right) \cdot \gamma_b \right]$$

$$= 2m_p \cdot b_p \cdot \left[\left(\frac{\delta_b}{p_{fo}} - \theta \right) + \left(\frac{\delta_a}{p_{fi}} + \theta \right) + \left(\frac{\delta_a}{s} - \theta \right) + \frac{1}{2} \left(\frac{\delta_b}{d_e} + \theta \right) + \frac{1}{2} \cdot \theta \right]$$

$$+ 4m_p \left[\left(s + p_{fi} \right) \cdot \gamma_a + \left(s + p_{fo} \right) \cdot \gamma_b \right]$$

$$= 2m_p \cdot b_p \cdot \left(\frac{\delta_b}{p_{fo}} + \frac{\delta_a}{p_{fi}} + \frac{\delta_a}{s} + \frac{\delta_b}{2 \cdot d_e} \right) + 4m_p \left[\left(s + p_{fi} \right) \cdot \frac{2\delta_a}{g} + \left(d_e + p_{fo} \right) \cdot \frac{2\delta_b}{g} \right]$$

$$= 2m_p \cdot b_p \cdot \theta \cdot \left(\frac{h_0}{p_{fo}} + \frac{h_1}{p_{fi}} + \frac{h_1}{s} + \frac{h_0}{2 \cdot d_e} \right) + \frac{8m_p}{g} \cdot \theta \cdot \left[\left(s + p_{fi} \right) \cdot h_1 + \left(d_e + p_{fo} \right) \cdot h_0 \right]$$

$$= \frac{t^2 \cdot F_y \cdot b_p}{2} \cdot \theta \cdot \left(\frac{h_0}{p_{fo}} + \frac{h_1}{p_{fi}} + \frac{h_1}{s} + \frac{h_0}{2 \cdot d_e} \right) + \frac{2 \cdot t^2 \cdot F_y}{g} \cdot \theta \cdot \left[\left(s + p_{fi} \right) \cdot h_1 + \left(d_e + p_{fo} \right) \cdot h_0 \right]$$

$$= t^2 \cdot F_y \cdot \theta \cdot \left\{ \frac{b_p}{2} \left(\frac{h_0}{p_{fo}} + \frac{h_1}{p_{fi}} + \frac{h_1}{s} + \frac{h_0}{2 \cdot d_e} \right) + \frac{2}{g} \left[\left(s + p_{fi} \right) \cdot h_1 + \left(d_e + p_{fo} \right) \cdot h_0 \right] \right\}$$

$$= t^2 \cdot F_y \cdot \theta \cdot \left\{ \frac{b_p}{2} \left[h_1 \left(\frac{1}{p_{fi}} + \frac{1}{s} \right) + h_0 \left(\frac{1}{p_{fo}} + \frac{1}{2d_e} \right) \right] + \frac{2}{g} \left[h_1 \left(p_{fi} + s \right) + h_0 \left(p_{fo} + d_e \right) \right] \right\}$$

$$= t^2 \cdot F_y \cdot \theta \cdot Y_p$$

$$Y_p = \frac{b_p}{2} \left[h_1 \left(\frac{1}{p_{fi}} + \frac{1}{s} \right) + h_0 \left(\frac{1}{p_{fo}} + \frac{1}{2d_e} \right) \right] + \frac{2}{g} \left[h_1 \left(p_{fi} + s \right) + h_0 \left(p_{fo} + d_e \right) \right]$$

Appendix B

Preliminary Design Procedure of the New Smart Connection

The new proposed preliminary design procedure of the new smart connection includes twenty-six steps in total, including RBS design, end plate design, rods design, welding design, and the remaining components deign.

Step 1: Determine RBS section dimensions:

The requirements from AISC358 [10] are used to determine the RBS dimensions. The corresponding parameters a, b, and c are defined in Appendix Figure B-1and are subjected to limits:

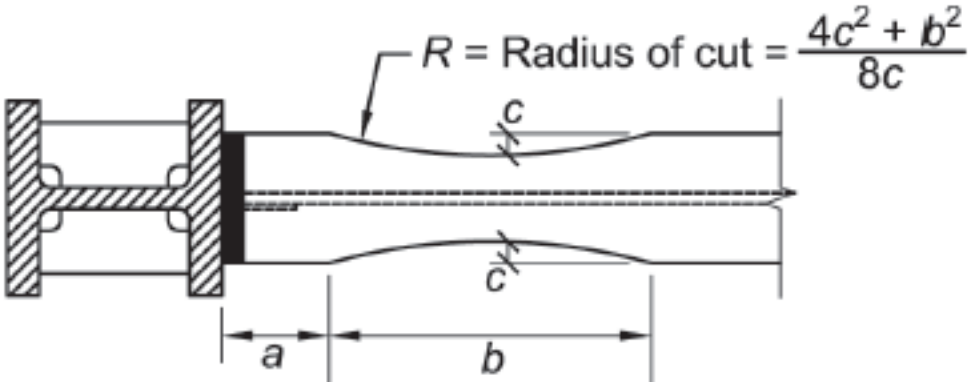

Appendix Figure B-1: Dimensions of the RBS section [10]

$$0.5 \cdot b_{bf} \le a \le 0.75 \cdot b_{bf} \qquad \textbf{(AEq. B-1)}$$

$$0.65 \cdot d \le b \le 0.85 \cdot d \qquad \textit{(AEq. B-2)}$$

$$0.1 \cdot b_{bf} \le c \le 0.25 \cdot b_{bf} \qquad \textit{(AEq. B-3)}$$

where,

b_{bf} = width of beam flange, in.

a = horizontal distance from face of column flange to the start of an RBS cut, in.

b = length of an RBS cut, in.

c = depth of cut at center of the reduced beam section, in.

d = depth of beam, in.

Step 2: Compute ultimate moment demand at the plane between the end plate and the square steel tube resisted by all rods:

The connection ultimate capacity is designed based on the flexural demand at the plane between the end plate and the column face. The provisions in AISC314-10 [77] are used to calculate this demand.

$$M_d = M_{pr} + V_a \cdot d_a \qquad \textit{(AEq. B-4)}$$

where,

M_{pr} = the probable maximum moment at the center of the RBS section, k-in.

$$M_{pr} = C_{pr} R_y F_{yb} Z_{RBS}$$

$$Z_{RBS} = Z_x - 2c \cdot t_{bf} \cdot (d - t_{bf})$$

F_{yb} = nominal yield strength of beam, ksi

Z_{RBS} = plastic section modulus at center of the reduced beam section, in^3.

Z_x = plastic section modulus about the x-axis, for whole beam cross section, in^3.

t_{bf} = thickness of beam flange, in.

V_a = probable maximum shear force at the center of the RBS section, kips. V_a should include the shear force caused by the fully yield of the two RBS sections at the ends of the beam introduced by lateral loads, and the portion introduced by the vertical dead load and live load.

$$V_a = \frac{2M_{pr}}{L_h} + \omega_u \frac{L_s}{2}$$

$$d_a = a + \frac{b}{2} + t_p$$

$$L_h = L_s - B_{SST} - 2 \cdot \left(t_p + a\right) - b$$

ω_u = distributed line loads on beam computed based on the load combination from ASCE7-10 [78], $(1.2 + 0.2S_{DS}) + L\ (or\ L_r) + 0.2$S, k/in.

L_h = distance between plastic hinge locations, in.

d_a = distance from the center of RBS section to the square tube surface, in.

t_p = thickness of end plate, in.

B_{SST} = width of square steel tube, in. Suggested value is greater than the outer diamemter of CCFT column plus 4 inches.

L_s = span between centerlines of two adjacent CCFT columns, in.

Step 3: Check the flexural strength of the beam at the face of the square steel tube:

Use RBS is to add a fuse to limit the loading transferred into the connection, and remove the plastic hinge region away from the column surface. It should make sure the RBS yield earlier than the whole beam section at the column surface.

$$M_d \le \phi_d \cdot M_p \qquad \textbf{(AEq. B-5)}$$

$$M_p = R_y \cdot F_{yb} \cdot Z_x \qquad \textbf{(AEq. B-6)}$$

where,

ϕ_d = 1.0 for ductile limit states

M_p = the probable maximum moment of the whole beam cross section, k-in.

Step 4: Calculate required end plate thickness:

The yield line analysis is applied to calculate the required thickness of the end plate. The yield line mechanism in Figure 3-4 (b) is expected and (Eq. 3-5) is used for this case with $d_e > s$. (Eq. 3-1) is modified to be (AEq. B-7) based on AISC358-10 [10].

$$t_{p,req'd} \geq \sqrt{\frac{1.11 \cdot M_d}{\phi_d \cdot F_{yp} \cdot Y_p}} \qquad \textit{(AEq. B-7)}$$

where,

Y_p = is calculated using (Eq. 3-5) with $s = \frac{1}{2} \cdot \sqrt{b_p \cdot g} < d_e$.

M_d = moment demand of the end plate, k-in.

F_{yp} = nominal yield strength of the end plate, ksi.

b_p = width of the end plate, in.

$h_0 = d - \frac{1}{2} \cdot t_{bf} + p_{fo}$

$h_1 = d - \frac{3}{2} \cdot t_{bf} - p_{fi}$

All other dimensional parameters are presented in Figure 3-4, in.

Step 5: Compute target design moment demand at the surface of square tube resisted by all rods when maximum strain in SMA rods reaches 5%:

A moment demand named 'Target Design Moment' is defined at the surface of the column, under which the probable maximum plastic moment at the center of RBS is reached its specific defined percentage and the maximum strain in SMA just reaches 5%. This specific defined percentage is represented by another parameter, γ, which is also named damage parameter, because the development of plastic moment is larger, the damage of the RBS is more severe.

$$M_{tar} = \gamma M_{pr} + V_a^{'} \cdot d_a \qquad \textbf{(AEq. B-8)}$$

$$V_a^{'} = \frac{2\gamma M_{pr}}{L_h} + \omega_u \frac{L_s}{2} \qquad \textbf{(AEq. B-9)}$$

where,

$\gamma =$ target design damage parameter, as the ratio of the target design moment at the center of RBS, γM_{pr}, to the probable maximum moment at RBS section, M_{pr}, when the maximum strain in SMA rods reaches 5%. γ ranges from 0.7 to 0.9. This parameter controls how much damage is expected on RBS section when 5% strain in SMA rods is reached.

$V_a' =$ shear force at the surface of square tube at the target design moment, kips

Step 6: Calculate the required rods length:

The rods length should be long enough so that the designed connection rotation capacity can be obtained when the maximum strain in SMA reaches 5%.

$$L_{req'd} = B_{SST} + 2t_p \geq \frac{h_0 \cdot \left(\theta_{tar} - \theta_{RBS}\right)}{5\% - \alpha \cdot \varepsilon_{y\_SMA}} \qquad \textbf{(AEq. B-10)}$$

$$B_{SST} = D + 2\left(d_{\min} + t_{squ}\right) \qquad \textbf{(AEq. B-11)}$$

where,

α = prestressed parameter for SMA rods, ratio of prestressed strength in SMA rods to yield strength of SMA. The value assumed in this step should be greater than the value calculated in Stpe 11.

θ_{tar} = target design rotation of connection including RBS section when maximum strain in SMA rods reaches 5%, at least 0.04 for ductile connection for special moment frames, rad.

θ_{RBS} = rotation supplied by RBS region under target design moment, γM_{pr}, when the maximum strain in SMA reaches 5%, rad. Suggested range is from 0.00 to 0.03 rad.

ε_{y_SMA} = yield strain of SMA rods, in./in.

D = outer diameter of circular steel tube, in.

d_{min} = minimum distance between circular and square steel tube, in.

t_{squ} = thickness of square steel tube, in.

Step 7: Calculate connection design rotation, including RBS section, at γM_{pr}

Calculate the actual connection rotation capacity at SMA strain of 5% with the actual rods length.

$$\theta_d = \theta_{rod} + \theta_{RBS} \qquad \textbf{(AEq. B-12)}$$

$$\theta_{rod} = \frac{L \cdot \left(5\% - \alpha \cdot \varepsilon_{y\_SMA}\right)}{h_0} \qquad \textbf{(AEq. B-13)}$$

where,

θ_{rod} = rotation supplied by rods' elongation, rad.

L = actual rods length, in.

Step 8: Calculate target design moment demand at the surface of square steel tube resisted by all SMA rods when some SMA rods start to yield headmost:

SMA rods are designed actually based on their yield strength instead of strength at strain of 5%. The actual moment capacity at yield strength level or M_{y_SMA} is defined as the moment supplied by all SMA rods when the maximum strength in some of SMA rods reaches their yield strength. This design principle is compatible with the current design concept. So a new design moment demand for SMA rods at yield strength level, M_{TARSMA}, needs to be determined. Another parameter, ζ, is introduced to the design procedure. It stands for the percentage of the portion, ζM_{tar}, supplied by only SMA rods of the total target moment demand, M_{tar}, at maximum strain of 5% in SMA. Connection capacity from only SMA rods stands for the self-centering capacity with steel rods sliding after their yielding, so parameter, ζ, can also be called self-centering parameter. The relationship among the ultimate design demand, M_d, total target demand at maximum SMA strain of 5%, M_{tar}, and target demand of SMA rods at maximum SMA strain of 5%, ζM_{tar}, is presented in Appendix Figure B-2. And the actual moment capacity of SMA rods at their yield strength level, M_{y_SMA}, is also presented in the same plot.

The actual moment capacity of SMA rods at yield strength level, M_{y_SMA}, can be determined based on the target demand of SMA rods at maximum strain of 5% in SMA, ζM_{tar}. Only SMA rods are discussed here.

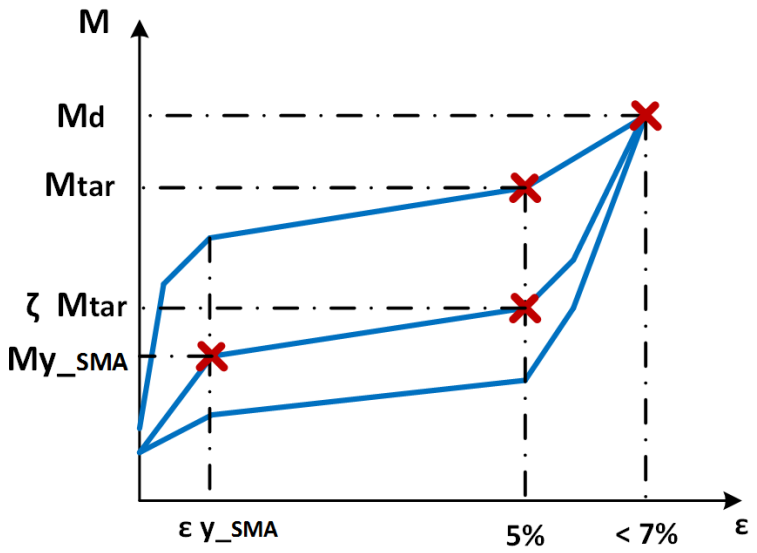

Appendix Figure B-2: Relationships of all target moments and ultimate moment

- For a connection with rods pattern (1) (Figure 3-8), SMA rods are located on all four rods lines. As presented in Figure 3-6, the end plate will rotate about its yield line at the level of beam flange in compression. The four rod levels can be classified into two groups: (1) group one with relative large distances from the end plate rotation center; and (2) group two with relative small distances from the end plate rotation center. Because the rods on group two levels contribute small moment capacity to the connection compared with the rods on group one levels due to small

moment arms, only rods on group one levels are considered. One can notice that the rods elongations on the two rod levels in group one are not equal to each other. Generally speaking, the elongation on exterior rod level is larger than the one on interior rod level. This means that when the SMA rods on exterior rod level start to yield under moment M_{y_SMA}, the SMA rods on interior rod level are still in elastic; and when the strain in SMA rods on exterior rod level reaches 5% under moment ζM_{tar}, the strain in SMA rods on interior rod level is less than 5% with less corresponding strength. So the ratio of M_{y_SMA} to ζM_{tar} is not equal to the ratio of SMA yielding strength to the strength at strain of 5%. However, due to the distance between two rod levels in group one is relative small compared with their distance to the rotation center (this is true because rods pattern (1) is used for large beams), the elongations on these two rod levels are similar to each other. This means that the stress-strain states in all rods on group one rod levels are almost identical. Then the ratio of moment and the ratio of strength for SMA rods can be considered to be the same.

- For a connection with rods pattern (2) and (3) (Figure 3-8) (they are used for relative small beams), if only the rods on group one rod levels with large distance to the end plate rotation center are considered, all SMA rods should have the same elongation due to they are all on the same rod level. Then the same as mentioned previously, the ratio of moment and the ratio of strength for SMA rods are identical.

In a word, the ratio of moment and the ratio of strength for SMA rods can be considered as approximately identical for all three rods patterns. Then the relationship in (AEq. B-14 can be obtained.

$$\frac{M_{y\_SMA}}{\zeta \cdot M_{tar}} \approx \frac{f_{ySMA}}{f_{uSMA}} \quad \text{or} \quad M_{y\_SMA} \approx \left(\frac{f_{ySMA}}{f_{uSMA}}\right) \cdot \left(\zeta \cdot M_{tar}\right) \qquad \textbf{(AEq. B-14)}$$

If the design moment demand for SMA rods at yield strength level, M_{TARSMA}, is defined as (AEq. B-15, it is easy to get that the design moment demand is approximately equal to the real moment capacity of the SMA rods at the yield level, $M_{TARSMA} \approx M_{y\_SMA}$. It is reasonable to use M_{TARSMA} for design.

$$M_{TARSMA} = \left(\frac{f_{ySMA}}{f_{uSMA}}\right) \cdot \left(\zeta \cdot M_{tar}\right) \qquad \textbf{(AEq. B-15)}$$

where,

ζ = self-centering parameter, ratio of the design target moment demand of all SMA rods, ζM_{tar}, to the total design target moment demand for all rods, M_{tar}, when the maximum strain in SMA rods reaches 5%. Suggested range is from 0.4 to 0.6.

f_{ySMA} = yield strength of SMA, ksi.

f_{uSMA} = strength of SMA at 5% strain, ksi.

Step 9: Calculate diameter of SMA rods:

The SMA rods are designed to resist the design target moment demand at their yield level, M_{TARSMA}. Except that three rods patterns are considered in the design procedure, the connection location is also important.

- The interior connection is designed based on the assumption that the two connecting beams have the same size and reach their plastic flexural capacities simultaneously; if the two connecting beams are not the same, the larger size is assumed for both. This assumption is made based on two facts that (1) the two connecting beams on the same interior connection usually have similar, if not the same, size; and (2) during the seismic loadings, the plastic damages of the two beam ends connecting to the same interior connection are also similar to each other. This assumption makes sure that the rods on two exterior and two interior rod levels have the same elongation, respectively, under the design moment demands. This is because the two end plates on the same interior connection will generate the same rotation (Figure 3-6 (a)) under the same plastic flexural capacity. If the two beams are different in reality, the end plate connecting to the smaller one will generate a smaller rotation than the other one when both two beams reach their plastic flexural capacities; and there is no the same rods elongation on any two rod levels. The rods on each rods line are located on group one rod levels for one end plate and at the same time on group two rod levels for the other end plate. It is obvious that the rotation of each end plate only has great influence on the elongation of the rods on

the group one rod levels of the corresponding end plate. For example, in Figure 3-6 (a), the left end plate rotation influences the rods on top two rods lines much; but the right end plate rotation only has great effect on the rods on bottom two rod levels. If the left beam is assumed to have a smaller size, it is easy to know that under the specific loading step in Figure 3-6 (a) the rods on top two rod levels has less elongation than the rods on the bottom two rod levels. As mentioned previously, the stress-strain states in the rods on the group one rod levels have little effect on the total resisting capacity for the loading from the corresponding beam due to relative small moment arms. To design rods on bottom two rod levels based on the loading from the right larger beam, it has insignificant effect on the design results by elongating the rods on top two rod levels a little bit to make that rods on two exterior rod levels and two interior rod levels have the same elongation, respectively. This modification causes the same connection behavior if the same beam size is assumed for the two beams connecting to the same interior connection. The more similar the two beam sizes are, the less modification of elongation is needed. Due to the loading can reverse, all rods size should be symmetric about the centerline of the connection. No matter the two connecting beams on the same interior connection are the same or not, it is reasonable to assume they are the same as the larger one for design.

- For the exterior connection, the rods elongations are all different on each rod level (Figure 3-6 (b)).

The elongation will influence the stress-strain states of the rods, and it will determine the design results directly. For the interior connection, the design procedure is based on the assumption that the rods on two exterior and two interior rod levels are the same, respectively; for the exterior connection, the design procedure is based on the fact that the elongation on each rod levels are different from each other. All the SMA rods are designed to have the same diameter. The design procedure is presented as follows:

$$d_{SMA,req'd} \geq \sqrt{\frac{2 \cdot M_{TARSMA}}{\pi \cdot \phi_t \cdot f_{ySMA}} \cdot \frac{1}{h_{e\_SMA}}} \qquad \textit{(AEq. B-16)}$$

For rods pattern (1) in Figure 3-8:

<u>For interior connection:</u>

$$h_{e\_SMA} = \left[\frac{d - t_{bf}}{h_0}(1-\alpha) + \alpha \right](h_1 + h_2) + h_0 \qquad \textit{(AEq. B-17)}$$

<u>For exterior connection:</u>

$$h_{e\_SMA} = \left[\frac{h_1}{h_0}(1-\alpha) + \alpha \right] h_1 + \left[\frac{h_2}{h_0}(1-\alpha) + \alpha \right] h_2 + h_0 \qquad \textit{(AEq. B-18)}$$

For rods pattern (2) in Figure 3-8:

<u>For interior connection:</u>

$$h_{e\_SMA} = \left(h_1 + h_2\right) \qquad \textit{(AEq. B-19)}$$

For exterior connection:

$$h_{e\_SMA} = \left[\frac{h_2}{h_1}\left(1-\alpha\right)+\alpha\right]h_2 + h_1 \qquad \textit{(AEq. B-20)}$$

For rods pattern (3) in Figure 3-8:

$$h_{e\_SMA} = h_0 \qquad \textit{(AEq. B-21)}$$

where,

h_{e_SMA} = effective moment arm for SMA rods, in.

ϕ_t = 0.9 (LRFD)

$h_2 = \frac{1}{2}\cdot t_{bf} + pfi$

Step 10: Compute recovery capacity supplied by prestressed strength in SMA rods:

In order to increase the stiffness of the proposed PR connection, pretension forces are applied in both SMA and steel rods. If steel rods fully yield to some degree during a large seismic loading, the pretension forces in steel rods will be lost totally. After the lateral seismic loading is removed, only the pretension forces in SMA rods are remained to resist the beam ends moments caused by the service gravity loads. If this resistance is large

enough and the beam damage is not severe, the connection can recover to its original position with the end plates contacting to the column tightly. This resistance is defined as a connection recovery capacity, and can be calculated as a proper portion of the beam end moments caused by the gravity loads, M_{END}. The gravity load combination $(1.2 + 0.2S_{DS})D + L$, instead of the service gravity load combination $D + L$, is used to calculate the beam end moments to increase the safety margin. A recovery parameter, β, is introduced into design procedure to define the recovery capacity as βM_{END}.

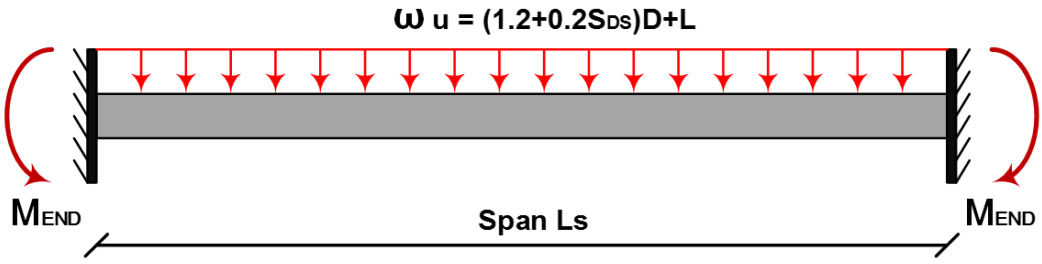

Appendix Figure B-3: Simple model to calculate beam end moments under gravity loads

$$M_{RECO} = \beta \cdot M_{END} = \beta \cdot \frac{\omega_u \cdot L_s^2}{12} \qquad \textbf{(AEq. B-22)}$$

where,

M_{END} = beam end moment calculated based on the structure in Appendix Figure B-3, k-in.

β = recovery parameter, ratio of moment capacity supplied by prestressed

strength in SMA rods to the end moment, M_{END}. Suggested range is from 0.8 to 1.0.

Step 11: Calculate required prestressed parameter α for SMA rods:

The connection recovery capacity is supplied by the pretension forces in all SMA rods. The same design principle in Step 9 is applied.

$$\alpha_{req'd} \geq \frac{2 \cdot M_{RECO}}{\phi_t \cdot \pi \cdot d_{SMA}^2 \cdot f_{ySMA} \cdot h_{e\_RECO}} \qquad \textbf{(AEq. B-23)}$$

For rods pattern (1) in Figure 3-8:

$$h_{e\_RECO} = h_0 + h_1 + h_2 \qquad \textbf{(AEq. B-24)}$$

For rods pattern (2) in Figure 3-8:

$$h_{e\_RECO} = h_1 + h_2 \qquad \textbf{(AEq. B-25)}$$

For rods pattern (3) in Figure 3-8:

$$h_{e\_RECO} = h_0 \qquad \textbf{(AEq. B-26)}$$

where,

h_{e_RECO} = effective recovery moment arm, in.

Step 12: Calculate moment demand at the surface of square steel tube resisted by all SMA rods when the maximum strain in some SMA rods reaches 5%:

According to the designed diameter of the SMA rods for the previous steps, the actual moment capacity supplied by all SMA rods when some of them reach strain of 5% headmost.

$$M_{SMA} = \frac{1}{2} \cdot \phi_t \cdot \pi \cdot d_{SMA}^2 \cdot FH_{SMA} \qquad \textbf{(AEq. B-27)}$$

For rods pattern (1) in Figure 3-8:

<u>For interior connection:</u>

$$FH_{SMA} = f_{uSMA} \cdot h_0 + f_{SMA}^{'} \cdot \left(h_1 + h_2\right) \qquad \textbf{(AEq. B-28)}$$

$$f_{SMA}^{'} = \frac{\varepsilon_{SMA}^{'} - \varepsilon_{y\_SMA}}{5\% - \varepsilon_{y\_SMA}} \cdot \left(f_{uSMA} - f_{ySMA}\right) + f_{ySMA} \qquad \textbf{(AEq. B-29)}$$

$$\varepsilon_{SMA}^{'} = \frac{d - t_{bf}}{h_0} \cdot \left(5\% - \alpha \cdot \varepsilon_{y\_SMA}\right) + \alpha \cdot \varepsilon_{y\_SMA} \qquad \textbf{(AEq. B-30)}$$

<u>For exterior connection:</u>

$$FH_{SMA} = f_{uSMA} \cdot h_0 + f_{SMA}^{'} \cdot h_1 + f_{SMA}^{''} \cdot h_2 \qquad \textbf{(AEq. B-31)}$$

$$f_{SMA}^{'} = \frac{\varepsilon_{SMA}^{'} - \varepsilon_{y\_SMA}}{5\% - \varepsilon_{y\_SMA}} \cdot \left(f_{uSMA} - f_{ySMA}\right) + f_{ySMA} \qquad \textbf{(AEq. B-32)}$$

$$\varepsilon_{SMA}^{'}=\frac{h_1}{h_0}\cdot\left(5\%-\alpha\cdot\varepsilon_{y\_SMA}\right)+\alpha\cdot\varepsilon_{y\_SMA} \qquad \textit{(AEq. B-33)}$$

$$f_{SMA}^{''}=\min\left(\begin{array}{c}\frac{\varepsilon_{SMA}^{''}-\varepsilon_{y\_SMA}}{5\%-\varepsilon_{y\_SMA}}\cdot\left(f_{uSMA}-f_{ySMA}\right)+f_{ySMA}\\ \frac{\varepsilon_{SMA}^{''}}{\varepsilon_{y\_SMA}}\cdot f_{ySMA}\end{array}\right) \qquad \textit{(AEq. B-34)}$$

$$\varepsilon_{SMA}^{''}=\frac{h_2}{h_0}\cdot\left(5\%-\alpha\cdot\varepsilon_{y\_SMA}\right)+\alpha\cdot\varepsilon_{y\_SMA} \qquad \textit{(AEq. B-35)}$$

For rods pattern (2) in Figure 3-8:

<u>For interior connection:</u>

$$FH_{SMA}=f_{uSMA}\cdot\left(h_1+h_2\right) \qquad \textit{(AEq. B-36)}$$

<u>For exterior connection:</u>

$$FH_{SMA}=f_{uSMA}\cdot h_1+f_{SMA}^{'}\cdot h_2 \qquad \textit{(AEq. B-37)}$$

$$f_{SMA}^{'}=\min\left(\begin{array}{c}\frac{\varepsilon_{SMA}^{'}-\varepsilon_{y\_SMA}}{5\%-\varepsilon_{y\_SMA}}\cdot\left(f_{uSMA}-f_{ySMA}\right)+f_{ySMA}\\ \frac{\varepsilon_{SMA}^{'}}{\varepsilon_{y\_SMA}}\cdot f_{ySMA}\end{array}\right) \qquad \textit{(AEq. B-38)}$$

$$\varepsilon_{SMA}^{'}=\frac{h_2}{h_1}\cdot\left(5\%-\alpha\cdot\varepsilon_{y\_SMA}\right)+\alpha\cdot\varepsilon_{y\_SMA} \qquad \textit{(AEq. B-39)}$$

For rods pattern (3) in Figure 3-8:

$$FH_{SMA}=f_{uSMA}\cdot h_0 \qquad \textit{(AEq. B-40)}$$

Step 13: Calculate target design moment demand at the surface of square steel tube resisted by all steel rods when the maximum strain in SMA rods reaches 5%:

Calculate the portion of the total design moment demand, M_{tar}, resisted by only steel rods.

$$M_{TARsteel} = M_{tar} - M_{SMA} \qquad \textbf{(AEq. B-41)}$$

Step 14: Calculate diameter of steel rods:

Steel rods are not designed at their yield level. They are designed based on some specific portion of the ultimate moment demand. The same principle as SMA rods is used to design the steel rods.

$$d_{steel,req'd} \geq \sqrt{\frac{2 \cdot M_{TARsteel}}{\pi \cdot \phi_t} \cdot \frac{1}{FH_{steel}}} \qquad \textbf{(AEq. B-42)}$$

For rods pattern (1) in Figure 3-8:

<u>For interior connection:</u>

$$FH_{steel} = f'_{steel} \cdot h_0 + f''_{steel} \cdot (h_1 + h_2) \qquad \textbf{(AEq. B-43)}$$

$$f'_{steel} = \min \begin{pmatrix} \lambda \cdot (\varepsilon'_{steel} - \varepsilon_{y\_S}) + f_{y\_S} \\ f_{u\_S} \end{pmatrix} \qquad \textbf{(AEq. B-44)}$$

$$\varepsilon'_{steel} = (5\% - \alpha \cdot \varepsilon_{y\_SMA}) + \eta \cdot \varepsilon_{y\_S} \qquad \textbf{(AEq. B-45)}$$

$$f''_{steel} = \min\begin{pmatrix} \lambda \cdot \left(\varepsilon''_{steel} - \varepsilon_{y\_S}\right) + f_{y\_S} \\ f_{u\_S} \end{pmatrix} \quad \textit{(AEq. B-46)}$$

$$\varepsilon''_{steel} = \frac{d - t_{bf}}{h_0} \cdot \left(5\% - \alpha \cdot \varepsilon_{y\_SMA}\right) + \eta \cdot \varepsilon_{y\_S} \quad \textit{(AEq. B-47)}$$

For exterior connection:

$$FH_{steel} = f'_{steel} \cdot h_0 + f''_{steel} \cdot h_1 \quad \textit{(AEq. B-48)}$$

$$f'_{steel} = \lambda \cdot \left(\varepsilon'_{steel} - \varepsilon_{y\_S}\right) + f_{y\_S} \quad \textit{(AEq. B-49)}$$

$$\varepsilon'_{steel} = \left(5\% - \alpha \cdot \varepsilon_{y\_SMA}\right) + \eta \cdot \varepsilon_{y\_S} \quad \textit{(AEq. B-50)}$$

$$f''_{steel} = \lambda \cdot \left(\varepsilon''_{steel} - \varepsilon_{y\_S}\right) + f_{y\_S} \quad \textit{(AEq. B-51)}$$

$$\varepsilon''_{steel} = \frac{h_1}{h_0} \cdot \left(5\% - \alpha \cdot \varepsilon_{y\_SMA}\right) + \eta \cdot \varepsilon_{y\_S} \quad \textit{(AEq. B-52)}$$

Note that: On exterior connections, the capacity from steel rods on the interior rod level with a small moment arm should be ignored. This is because once the steel rods on this level fully yield under the reverse moment and large enough residual strain is present, it is unlikely that these rods can be activated in the current moment direction.

For rods pattern (2) in Figure 3-8:

$$FH_{steel} = f'_{steel} \cdot h_0 \quad \textit{(AEq. B-53)}$$

$$f'_{steel} = \lambda \cdot \left(\varepsilon'_{steel} - \varepsilon_{y\_S}\right) + f_{y\_S} \quad \textit{(AEq. B-54)}$$

For interior connection:

$$\varepsilon'_{steel} = \frac{h_0}{d - t_{bf}} \cdot \left(5\% - \alpha \cdot \varepsilon_{y\_SMA}\right) + \eta \cdot \varepsilon_{y\_S} \qquad \textit{(AEq. B-55)}$$

For exterior connection:

$$\varepsilon'_{steel} = \frac{h_0}{h_1} \cdot \left(5\% - \alpha \cdot \varepsilon_{y\_SMA}\right) + \eta \cdot \varepsilon_{y\_S} \qquad \textit{(AEq. B-56)}$$

For rods pattern (3) in Figure 3-8:

For interior connection:

$$FH_{steel} = f'_{steel} \cdot \left(h_1 + h_2\right) \qquad \textit{(AEq. B-57)}$$

$$f'_{steel} = \lambda \cdot \left(\varepsilon'_{steel} - \varepsilon_{y\_S}\right) + f_{y\_S} \qquad \textit{(AEq. B-58)}$$

$$\varepsilon'_{steel} = \frac{d - t_{bf}}{h_0} \cdot \left(5\% - \alpha \cdot \varepsilon_{y\_SMA}\right) + \eta \cdot \varepsilon_{y\_S} \qquad \textit{(AEq. B-59)}$$

For exterior connection:

$$FH_{steel} = f'_{steel} \cdot h_1 \qquad \textit{(AEq. B-60)}$$

$$f'_{steel} = \lambda \cdot \left(\varepsilon'_{steel} - \varepsilon_{y\_S}\right) + f_{y\_S} \qquad \textit{(AEq. B-61)}$$

$$\varepsilon'_{steel} = \frac{h_1}{h_0} \cdot \left(5\% - \alpha \cdot \varepsilon_{y\_SMA}\right) + \eta \cdot \varepsilon_{y\_S} \qquad \textit{(AEq. B-62)}$$

Note that: On exterior connections, the capacity from steel rods on the interior rod level with a small moment arm should be ignored. This is because once the steel rods on this level fully yield under the reverse moment and large enough residual strain is present, it is unlikely that these rods can be activated in the current moment direction.

where,

λ = strain hardening parameter of steel rods, ksi.

ε_{y_S} = yield strain of steel rods, in./in.

f_{y_S} = yield strength of steel rods, ksi.

f_{u_S} = ultimate strength of steel rods, ksi.

η = prestressed parameter for steel rods, ratio of prestressed strength in steel rods to yield strength of steel, ranges from 0.3 to 1.0.

Step 15: Calculate required prestressed parameter η for steel rods:

As discussed previously, the pretension effects of steel rods will be lost totally under large beam end moments due to their yielding. The design concept is to define a flexural capacity, M_{MR}, supplied by the pretension forces in all rods, which can resist some specific beam ends moment so that the end plate will not separate from the column and the pretension forces in steel rods can be fully remained. This flexural capacity, M_{MR}, can be calculated based on either recovery flexural capacity, M_{RECO}, defined previously and a new defined parameter, χ, or structural analysis results based on only service gravity and wind loads

combination. The rods design method is still the same as the one used for SMA rods.

$$\eta_{req'd} \geq \frac{2 \cdot M_{PREsteel}}{\phi_t \cdot \pi \cdot d_{steel}^2 \cdot f_{y\_S} \cdot h_{e\_steel}} \quad \textbf{(AEq. B-63)}$$

$$M_{PREsteel} = M_{MR} - M_{PRESMA} \quad \textbf{(AEq. B-64)}$$

$$M_{PRESMA} = \frac{1}{2} \cdot \phi_t \cdot \pi \cdot d_{SMA}^2 \cdot \alpha \cdot f_{ySMA} \cdot h_{e\_SMA} \quad \textbf{(AEq. B-65)}$$

$$M_{MR} = \chi \cdot M_{RECO} \text{ or analysis results} \quad \textbf{(AEq. B-66)}$$

For rods pattern (1) in Figure 3-8:

$$h_{e\_steel} = h_{e\_SMA} = h_0 + h_1 + h_2 \quad \textbf{(AEq. B-67)}$$

For rods pattern (2) in Figure 3-8:

$$h_{e\_steel} = h_0 \quad \textbf{(AEq. B-68)}$$

$$h_{e\_SMA} = h_1 + h_2 \quad \textbf{(AEq. B-69)}$$

For rods pattern (3) in Figure 3-8:

$$h_{e\_steel} = h_1 + h_2 \quad \textbf{(AEq. B-70)}$$

$$h_{e\_SMA} = h_0 \quad \textbf{(AEq. B-71)}$$

where,

h_{e_steel} = effective moment arm for steel rods, in.

h_{e_SMA} = effective moment arm for SMA rods, in.

M_{MR} = moment capacity supplied by all rods' pretension forces, k-in. It can be determined by two methods: (1) Introduce another parameter, χ, and define M_{MR} as χM_{RECO}. (2) Define M_{MR} as the maximum beam ends moment under service gravity and wind loads from the elastic analysis of the system with FR connections by using analysis software, such as SAP2000.

χ = non-yielding parameter, which is used to define the moment capacity to resist the yielding of steel rods under specific load combination by all rods pretension forces. Its reciprocal approximately represents the ratio of the moment capacity supplied by only SMA rods pretension forces to that from all rods pretension forces. Suggested range is from 1.0 to 1.5.

$M_{PREsteel}$ = moment capacity supplied by pretension forces in steel rods, k-in.

M_{PRESMA} = moment capacity supplied by pretension forces in SMA rods, k-in.

Step 16: Check maximum allowable moment capacity when the maximum strain in SMA rods reaches 7%:

The upper strain limit for SMA is 7% in the proposed design procedure. Under this limit, there will be insignificant residual strain generated in SMA rods. The real connection capacity with all designed rods is calculated when the upper limit of SMA rods is reached, which should be greater than the ultimate design moment demand of the connection, M_d.

$$M_{MC} = M_{MCSMA} + M_{MCsteel} \geq M_d \qquad \textit{(AEq. B-72)}$$

$$M_{MCSMA} = \frac{1}{2} \cdot \phi_t \cdot \pi \cdot d_{SMA}^2 \cdot FH_{mSMA} \qquad \textit{(AEq. B-73)}$$

$$M_{MCsteel} = \frac{1}{2} \cdot \phi_t \cdot \pi \cdot d_{steel}^2 \cdot FH_{msteel} \qquad \textit{(AEq. B-74)}$$

For rods pattern (1) in Figure 3-8:

For interior connection:

SMA rods:

$$FH_{mSMA} = f_{mSMA} \cdot h_0 + f_{SMA}^{'} \cdot \left(h_1 + h_2\right) \qquad \textit{(AEq. B-75)}$$

$$f_{SMA}^{'} = \max \begin{pmatrix} \frac{\varepsilon_{SMA}^{'} - \varepsilon_{y\_SMA}}{5\% - \varepsilon_{y\_SMA}} \cdot \left(f_{uSMA} - f_{ySMA}\right) + f_{ySMA} \\ \frac{\varepsilon_{SMA}^{'} - 5\%}{7\% - 5\%} \cdot \left(f_{mSMA} - f_{uSMA}\right) + f_{uSMA} \end{pmatrix} \qquad \textit{(AEq. B-76)}$$

$$\varepsilon_{SMA}^{'} = \frac{d - t_{bf}}{h_0} \cdot \left(7\% - \alpha \cdot \varepsilon_{y\_SMA}\right) + \alpha \cdot \varepsilon_{y\_SMA} \qquad \textit{(AEq. B-77)}$$

Steel rods:

$$FH_{msteel} = f_{steel}^{'} \cdot h_0 + f_{steel}^{"} \cdot \left(h_1 + h_2\right) \qquad \textit{(AEq. B-78)}$$

$$f_{steel}^{'} = \min \begin{pmatrix} \lambda \cdot \left(\varepsilon_{steel}^{'} - \varepsilon_{y\_S}\right) + f_{y\_S} \\ f_{u\_S} \end{pmatrix} \qquad \textit{(AEq. B-79)}$$

$$\varepsilon_{steel}^{'} = \left(7\% - \alpha \cdot \varepsilon_{y\_SMA}\right) + \eta \cdot \varepsilon_{y\_S} \qquad \textit{(AEq. B-80)}$$

$$f_{steel}^{"} = \min\begin{pmatrix} \lambda \cdot \left(\varepsilon_{steel}^{"} - \varepsilon_{y\_S}\right) + f_{y\_S} \\ f_{u\_S} \end{pmatrix} \quad \textbf{(AEq. B-81)}$$

$$\varepsilon_{steel}^{"} = \frac{d - t_{bf}}{h_0} \cdot \left(7\% - \alpha \cdot \varepsilon_{y\_SMA}\right) + \eta \cdot \varepsilon_{y\_S} \quad \textbf{(AEq. B-82)}$$

For exterior connection:

SMA rods:

$$FH_{mSMA} = f_{mSMA} \cdot h_0 + f_{SMA}^{'} \cdot h_1 + f_{SMA}^{"} \cdot h_2 \quad \textbf{(AEq. B-83)}$$

$$f_{SMA}^{'} = \max\begin{pmatrix} \frac{\varepsilon_{SMA}^{'} - \varepsilon_{y\_SMA}}{5\% - \varepsilon_{y\_SMA}} \cdot \left(f_{uSMA} - f_{ySMA}\right) + f_{ySMA} \\ \frac{\varepsilon_{SMA}^{'} - 5\%}{7\% - 5\%} \cdot \left(f_{mSMA} - f_{uSMA}\right) + f_{uSMA} \end{pmatrix} \quad \textbf{(AEq. B-84)}$$

$$\varepsilon_{SMA}^{'} = \frac{h_1}{h_0} \cdot \left(7\% - \alpha \cdot \varepsilon_{y\_SMA}\right) + \alpha \cdot \varepsilon_{y\_SMA} \quad \textbf{(AEq. B-85)}$$

$$f_{SMA}^{"} = \min\begin{pmatrix} \frac{\varepsilon_{SMA}^{"} - \varepsilon_{y\_SMA}}{5\% - \varepsilon_{y\_SMA}} \cdot \left(f_{uSMA} - f_{ySMA}\right) + f_{ySMA} \\ \frac{\varepsilon_{SMA}^{"}}{\varepsilon_{y\_SMA}} \cdot f_{ySMA} \end{pmatrix} \quad \textbf{(AEq. B-86)}$$

$$\varepsilon_{SMA}^{"} = \frac{h_2}{h_0} \cdot \left(7\% - \alpha \cdot \varepsilon_{y\_SMA}\right) + \alpha \cdot \varepsilon_{y\_SMA} \quad \textbf{(AEq. B-87)}$$

Steel rods:

$$FH_{msteel} = f_{steel}^{'} \cdot h_0 + f_{steel}^{"} \cdot h_1 + f_{steel}^{'''} \cdot h_2 \quad \textbf{(AEq. B-88)}$$

$$f_{steel}^{'} = \lambda \cdot \left(\varepsilon_{steel}^{'} - \varepsilon_{y\_S}\right) + f_{y\_S} \quad \textbf{(AEq. B-89)}$$

$$\varepsilon_{steel}^{'} = \left(7\% - \alpha \cdot \varepsilon_{y\_SMA}\right) + \eta \cdot \varepsilon_{y\_S} \quad \textbf{(AEq. B-90)}$$

$$f''_{steel} = \lambda \cdot \left(\varepsilon''_{steel} - \varepsilon_{y\_S} \right) + f_{y\_S} \qquad \textit{(AEq. B-91)}$$

$$\varepsilon''_{steel} = \frac{h_1}{h_0} \cdot \left(7\% - \alpha \cdot \varepsilon_{y\_SMA} \right) + \eta \cdot \varepsilon_{y\_S} \qquad \textit{(AEq. B-92)}$$

$$f'''_{steel} = \min \begin{pmatrix} \lambda \cdot \left(\varepsilon'''_{steel} - \varepsilon_{y\_S} \right) + f_{y\_S} \\ \dfrac{\varepsilon'''_{steel}}{\varepsilon_{y\_S}} \cdot f_{y\_S} \end{pmatrix} \qquad \textit{(AEq. B-93)}$$

$$\varepsilon'''_{steel} = \frac{h_2}{h_0} \cdot \left(7\% - \alpha \cdot \varepsilon_{y\_SMA} \right) + \eta \cdot \varepsilon_{y\_S} \qquad \textit{(AEq. B-94)}$$

For rods pattern (2) in Figure 3-8:

<u>For interior connection:</u>

<u>SMA rods:</u>

$$FH_{mSMA} = f_{mSMA} \cdot \left(h_1 + h_2 \right) \qquad \textit{(AEq. B-95)}$$

<u>Steel rods:</u>

$$FH_{msteel} = f'_{steel} \cdot h_0 \qquad \textit{(AEq. B-96)}$$

$$f'_{steel} = \lambda \cdot \left(\varepsilon'_{steel} - \varepsilon_{y\_S} \right) + f_{y\_S} \qquad \textit{(AEq. B-97)}$$

$$\varepsilon'_{steel} = \frac{h_0}{d - t_{bf}} \cdot \left(7\% - \alpha \cdot \varepsilon_{y\_SMA} \right) + \eta \cdot \varepsilon_{y\_S} \qquad \textit{(AEq. B-98)}$$

<u>For exterior connection:</u>

<u>SMA rods:</u>

$$FH_{mSMA} = f_{mSMA} \cdot h_1 + f'_{SMA} \cdot h_2 \qquad \textbf{(AEq. B-99)}$$

$$f'_{SMA} = \min \begin{pmatrix} \dfrac{\varepsilon'_{SMA} - \varepsilon_{y\_SMA}}{5\% - \varepsilon_{y\_SMA}} \cdot \left(f_{uSMA} - f_{ySMA} \right) + f_{ySMA} \\ \dfrac{\varepsilon'_{SMA}}{\varepsilon_{y\_SMA}} \cdot f_{ySMA} \end{pmatrix} \qquad \textbf{(AEq. B-100)}$$

$$\varepsilon'_{SMA} = \frac{h_2}{h_1} \cdot \left(7\% - \alpha \cdot \varepsilon_{y\_SMA} \right) + \alpha \cdot \varepsilon_{y\_SMA} \qquad \textbf{(AEq. B-101)}$$

Steel rods:

$$FH_{msteel} = f'_{steel} \cdot h_0 \qquad \textbf{(AEq. B-102)}$$

$$f'_{steel} = \lambda \cdot \left(\varepsilon'_{steel} - \varepsilon_{y\_S} \right) + f_{y\_S} \qquad \textbf{(AEq. B-103)}$$

$$\varepsilon'_{steel} = \frac{h_0}{h_1} \cdot \left(7\% - \alpha \cdot \varepsilon_{y\_SMA} \right) + \eta \cdot \varepsilon_{y\_S} \qquad \textbf{(AEq. B-104)}$$

For rods pattern (3) in Figure 3-8:

SMA rods:

$$FH_{mSMA} = f_{mSMA} \cdot h_0 \qquad \textbf{(AEq. B-105)}$$

Steel rods:

For interior connection:

$$FH_{msteel} = f'_{steel} \cdot \left(h_1 + h_2 \right) \qquad \textbf{(AEq. B-106)}$$

$$f'_{steel} = \lambda \cdot \left(\varepsilon'_{steel} - \varepsilon_{y\_S} \right) + f_{y\_S} \qquad \textbf{(AEq. B-107)}$$

$$\varepsilon'_{steel} = \frac{d - t_{bf}}{h_0} \cdot \left(7\% - \alpha \cdot \varepsilon_{y\_SMA} \right) + \eta \cdot \varepsilon_{y\_S} \qquad \textbf{(AEq. B-108)}$$

For exterior connection:

$$FH_{msteel} = f'_{steel} \cdot h_1 + f''_{steel} \cdot h_2 \qquad \textbf{(AEq. B-109)}$$

$$f'_{steel} = \lambda \cdot \left(\varepsilon'_{steel} - \varepsilon_{y\_S} \right) + f_{y\_S} \qquad \textbf{(AEq. B-110)}$$

$$\varepsilon'_{steel} = \frac{h_1}{h_0} \cdot \left(7\% - \alpha \cdot \varepsilon_{y\_SMA} \right) + \eta \cdot \varepsilon_{y\_S} \qquad \textbf{(AEq. B-111)}$$

$$f''_{steel} = \min \begin{pmatrix} \lambda \cdot \left(\varepsilon''_{steel} - \varepsilon_{y\_S} \right) + f_{y\_S} \\ \dfrac{\varepsilon''_{steel}}{\varepsilon_{y\_S}} \cdot f_{y\_S} \end{pmatrix} \qquad \textbf{(AEq. B-112)}$$

$$\varepsilon''_{steel} = \frac{h_2}{h_0} \cdot \left(7\% - \alpha \cdot \varepsilon_{y\_SMA} \right) + \eta \cdot \varepsilon_{y\_S} \qquad \textbf{(AEq. B-113)}$$

where,

M_{MCSMA} = maximum moment capacity supplied by all SMA rods when the maximum strain in SMA rods reaches 7%, k-in.

$M_{MCsteel}$ = maximum moment capacity supplied by all steel rods when the maximum strain in SMA rods reaches 7%, k-in.

f_{mSMA} = strength of SMA at strain of 7%, ksi.

Step 17: Calculate maximum strain in SMA rods under M_d:

To calculate the real maximum strain in SMA rods under the ultimate moment demand, M_d. The result of this step will be used in the next step to calculate the shear forces on different levels of the end plate. Define ε_{maxSMA} as the maximum strain in the SMA rods under moment M_d and f_{maxSMA} as the corresponding strength, which are used to recalculate the moment capacity supplied by all rods, M_{MC}. Using the same procedures in *Step 16* except of replacing 7% and f_{mSMA} by ε_{maxSMA} and f_{maxSMA}, respectively. Modify ε_{maxSMA} between 5% and 7% with initial value of around 6% until that M_{MC} is equal to M_d.

$$f_{\max SMA} = \frac{\varepsilon_{\max SMA} - 5\%}{7\% - 5\%} \cdot \left(f_{mSMA} - f_{uSMA} \right) + f_{uSMA} \qquad \textbf{(AEq. B-114)}$$

Step 18: Calculate shear forces on three levels of end plate under, M_d:

Three shear forces are calculated on different levels of the end plate under M_d. The three location is defined in Appendix Figure B-4. Assume that the beam end moment is resisted by only beam flanges and the web contribution will not be considered.

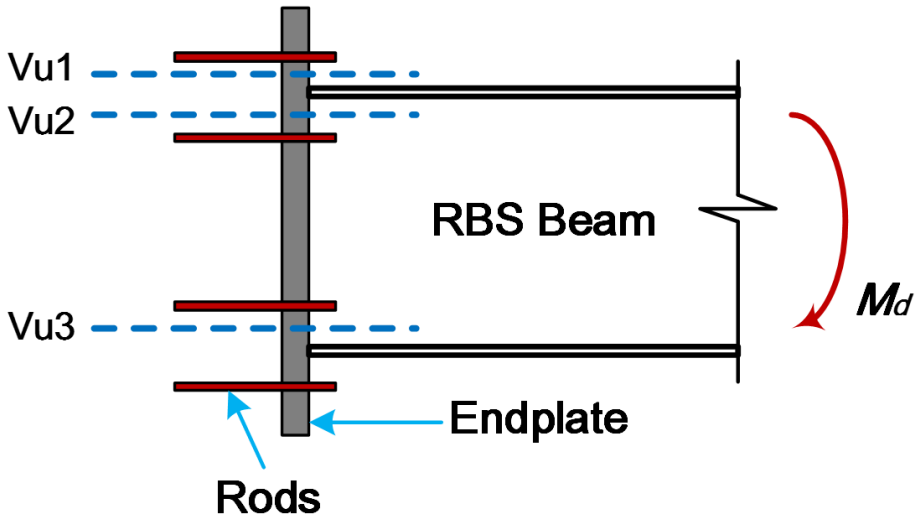

Appendix Figure B-4: Three levels of shear forces on end plate

For rods pattern (1) in Figure 3-8:

$$V_{u1} = \frac{1}{2} \cdot \pi \cdot \left(d_{SMA}^2 \cdot f_{\max SMA} + d_{steel}^2 \cdot f_{steel}^{'} \right) \quad \textit{(AEq. B-115)}$$

$$V_{u2} = \frac{M_d}{d - t_{bf}} - V_{u1} \quad \textit{(AEq. B-116)}$$

For interior connection:

$$V_{u3} = \left| V_{u2} - \pi \cdot \left(d_{SMA}^2 \cdot f_{SMA}^{'} + d_{steel}^2 \cdot f_{steel}^{''} \right) \right| \quad \textit{(AEq. B-117)}$$

$$f_{SMA}^{'} = \max \left(\begin{array}{l} \frac{\varepsilon_{SMA}^{'} - \varepsilon_{y\_SMA}}{5\% - \varepsilon_{y\_SMA}} \cdot \left(f_{uSMA} - f_{ySMA} \right) + f_{ySMA} \\ \frac{\varepsilon_{SMA}^{'} - 5\%}{7\% - 5\%} \cdot \left(f_{mSMA} - f_{uSMA} \right) + f_{uSMA} \end{array} \right) \quad \textit{(AEq. B-118)}$$

$$\varepsilon_{SMA}^{'} = \frac{d - t_{bf}}{h_0} \cdot \left(\varepsilon_{\max SMA} - \alpha \cdot \varepsilon_{y\_SMA} \right) + \alpha \cdot \varepsilon_{y\_SMA} \quad \textit{(AEq. B-119)}$$

$$f_{steel}^{'} = \lambda \cdot \left(\varepsilon_{steel}^{'} - \varepsilon_{y\_S} \right) + f_{y\_S} \quad \textit{(AEq. B-120)}$$

$$\varepsilon_{steel}^{'} = \left(\varepsilon_{\max SMA} - \alpha \cdot \varepsilon_{y\_SMA}\right) + \eta \cdot \varepsilon_{y\_S} \quad \textit{(AEq. B-121)}$$

$$f_{steel}^{''} = \lambda \cdot \left(\varepsilon_{steel}^{''} - \varepsilon_{y\_S}\right) + f_{y\_S} \quad \textit{(AEq. B-122)}$$

$$\varepsilon_{steel}^{''} = \frac{d - t_{bf}}{h_0} \cdot \left(\varepsilon_{\max SMA} - \alpha \cdot \varepsilon_{y\_SMA}\right) + \eta \cdot \varepsilon_{y\_S} \quad \textit{(AEq. B-123)}$$

For exterior connection:

$$f_{steel}^{'} = \lambda \cdot \left(\varepsilon_{steel}^{'} - \varepsilon_{y\_S}\right) + f_{y\_S} \quad \textit{(AEq. B-124)}$$

$$\varepsilon_{steel}^{'} = \left(\varepsilon_{\max SMA} - \alpha \cdot \varepsilon_{y\_SMA}\right) + \eta \cdot \varepsilon_{y\_S} \quad \textit{(AEq. B-125)}$$

V_{u3} does not control for exterior connection, and is simply assumed to be zero.

For rods pattern (2) in Figure 3-8:

$$V_{u1} = \frac{1}{2} \cdot \pi \cdot d_{steel}^2 \cdot f_{steel}^{'} \quad \textit{(AEq. B-126)}$$

$$V_{u2} = \frac{M_d}{d - t_{bf}} - V_{u1} \quad \textit{(AEq. B-127)}$$

For interior connection:

$$V_{u3} = \left| V_{u2} - \pi \cdot d_{SMA}^2 \cdot f_{\max SMA} \right| \quad \textit{(AEq. B-128)}$$

$$f_{steel}^{'} = \lambda \cdot \left(\varepsilon_{steel}^{'} - \varepsilon_{y\_S}\right) + f_{y\_S} \quad \textit{(AEq. B-129)}$$

$$\varepsilon_{steel}^{'} = \frac{h_0}{d - t_{bf}} \cdot \left(\varepsilon_{\max SMA} - \alpha \cdot \varepsilon_{y\_SMA}\right) + \eta \cdot \varepsilon_{y\_S} \quad \textit{(AEq. B-130)}$$

For exterior connection:

$$f'_{steel} = \lambda \cdot \left(\varepsilon'_{steel} - \varepsilon_{y\_S} \right) + f_{y\_S} \qquad \textit{(AEq. B-131)}$$

$$\varepsilon'_{steel} = \frac{h_0}{h_1} \cdot \left(\varepsilon_{\max SMA} - \alpha \cdot \varepsilon_{y\_SMA} \right) + \eta \cdot \varepsilon_{y\_S} \qquad \textit{(AEq. B-132)}$$

V_{u3} does not control for exterior connection, and is simply assumed to be zero.

For rods pattern (3) in Figure 3-8:

$$V_{u1} = \frac{1}{2} \cdot \pi \cdot d_{SMA}^2 \cdot f_{\max SMA} \qquad \textit{(AEq. B-133)}$$

$$V_{u2} = \frac{M_d}{d - t_{bf}} - V_{u1} \qquad \textit{(AEq. B-134)}$$

For interior connection:

$$V_{u3} = \left| V_{u2} - \pi \cdot d_{steel}^2 \cdot f'_{steel} \right| \qquad \textit{(AEq. B-135)}$$

$$f'_{steel} = \lambda \cdot \left(\varepsilon'_{steel} - \varepsilon_{y\_S} \right) + f_{y\_S} \qquad \textit{(AEq. B-136)}$$

$$\varepsilon'_{steel} = \frac{d - t_{bf}}{h_0} \cdot \left(\varepsilon_{\max SMA} - \alpha \cdot \varepsilon_{y\_SMA} \right) + \eta \cdot \varepsilon_{y\_S} \qquad \textit{(AEq. B-137)}$$

For exterior connection:

V_{u3} does not control for exterior connection, and is simply assumed to be zero.

Step 19: Check shear yielding capacity of end plate:

To check shear yielding for the end plate under the three shear forces, an effective width of the end plate for calculation should be defined properly. The effective width, b_{pe}, for three rods patterns are defined based on the dimensions in Appendix Figure B-5.

$$\phi V_n = \phi_d \cdot 0.6 \cdot F_{yp} \cdot b_{pe} \cdot t_p \geq \max\left(V_{u1}, V_{u2}, V_{u3}\right) \qquad \textit{(AEq. B-138)}$$

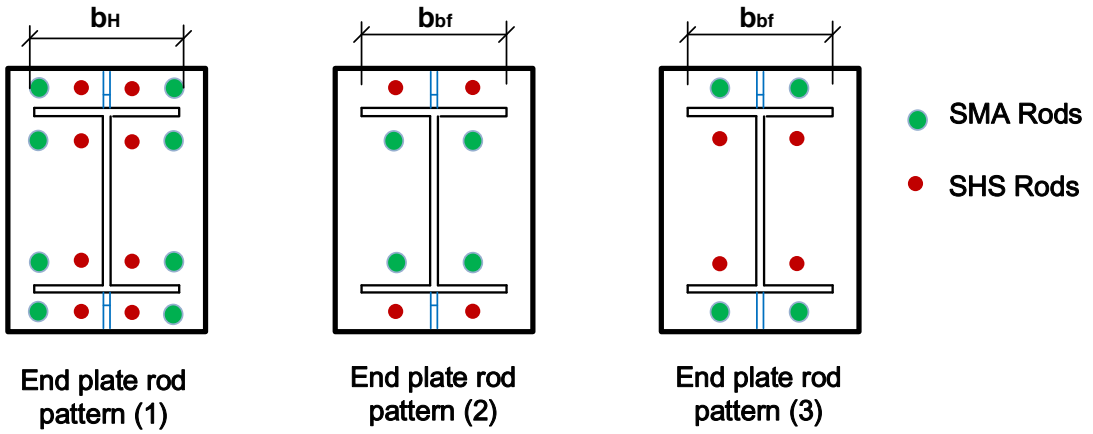

Appendix Figure B-5: Effective width of end plate for three rods patterns

where,

b_{pe} = effective width of end plate, in. For rods pattern (1), $b_{pe} = b_H + 1$; for rods pattern (2) and (3), $b_{pe} = b_{bf} + 1$.

b_H = distance from the left most hole edge to the right most hole edge on each rods line, in.

Step 20: Check shear rupture capacity of end plate:

The same effective end plate width is used as the previous step with net area instead of gross area.

$$\frac{\phi V_n}{A_n} = \phi_n \cdot 0.6 \cdot F_{up} \geq \max\left(\frac{V_{u1}}{A_{n1}}, \frac{V_{u2}}{A_{n2}}, \frac{V_{u3}}{A_{n3}}\right) \quad \textbf{(AEq. B-139)}$$

For rods pattern (1) in Figure 3-8:

$$A_{n1} = A_{n2} = A_{n3} = \left[b_{pe} - 2 \cdot \left(d_{hSMA} + d_{hsteel}\right)\right] \cdot t_p \quad \textbf{(AEq. B-140)}$$

For rods pattern (2) in Figure 3-8:

$$A_{n1} = \left(b_{pe} - 2 \cdot d_{hsteel}\right) \cdot t_p \quad \textbf{(AEq. B-141)}$$

$$A_{n2} = A_{n3} = \left(b_{pe} - 2 \cdot d_{hSMA}\right) \cdot t_p \quad \textbf{(AEq. B-142)}$$

For rods pattern (3) in Figure 3-8:

$$A_{n1} = \left(b_{pe} - 2 \cdot d_{hSMA}\right) \cdot t_p \quad \textbf{(AEq. B-143)}$$

$$A_{n2} = A_{n3} = \left(b_{pe} - 2 \cdot d_{hsteel}\right) \cdot t_p \quad \textbf{(AEq. B-144)}$$

where,

A_n = effective net area of end plate on the level with rods' holes, $in.^2$

ϕ_n = 0.9 for nonductile limit states.

F_{up} = ultimate strength of end plate, ksi.

d_{hSMA} = diameter of SMA rod's hole, in. $d_{hSMA} = d_{SMA} + 1/8$

d_{hsteel} = diameter of steel rod's hole, in. $d_{hsteel} = d_{steel} + 1/8$

Step 21: Check rods' rupture capacity:

Assume the rods have ability to resist total vertical beam shear, V_a, from shear rupture failure.

$$\phi V = \frac{1}{4} \cdot \phi_n \cdot \pi \cdot n \cdot \left(f_{vSMA} \cdot d_{SMA}^2 + f_{v\_S} \cdot d_{steel}^2 \right) \geq V_a \qquad \textbf{(AEq. B-145)}$$

where,

n = number of SMA or steel rods. For rods' pattern (1), $n = 8$; for rod patterns (2) and (3), $n = 4$.

f_{vSMA} = nominal shear strength of SMA rods, ksi.

f_{v_S} = nominal shear strength of steel rods, ksi.

Step 22: Check rods' hole bearing capacity of end plate:

Assume the vertical shear force is resisted by all rods uniformly. The design procedure in steel construction manual is applied in this step [2].

$$\phi_v \cdot F_{up} \cdot t_p \cdot \min\left(1.2 \cdot l_{hc}, 2.4 \cdot d_b\right) \geq \frac{V_a}{n_t} \qquad \textbf{(AEq. B-146)}$$

where,

n_t = total number of all rods. For rods' pattern (1), $n_t = 16$; for rods' pattern (2) and (3), $n_t = 8$.

ϕ_v = 0.75 for LRFD

l_{hc} = vertical clear distance between the edge of the hole and the edge of the adjacent hole, or the edge of the material, in.

for rods' pattern (1) in Figure 3-8:

for SMA rods: $l_{hc} = \min\left(p_{fo} + p_{fi} + t_{bf} - d_{SMA}, d_{meSMA}\right)$

for steel rods: $l_{hc} = \min\left(p_{fo} + p_{fi} + t_{bf} - d_{steel}, d_{mesteel}\right)$

for rods' pattern (2) in Figure 3-8:

for SMA rods: $l_{hc} = p_{fo} + p_{fi} + t_{bf} - \frac{1}{2} \cdot \left(d_{SMA} + d_{steel}\right)$

for steel rods: $l_{hc} = d_{mesteel}$

for rods' pattern (3) in Figure 3-8:

for SMA rods: $l_{hc} = d_{meSMA}$

for steel rods: $l_{hc} = p_{fo} + p_{fi} + t_{bf} - \frac{1}{2} \cdot \left(d_{SMA} + d_{steel}\right)$

d_{meSMA} = clear distance between the edge of SMA rods hole and edge of material, in.

$d_{mesteel}$ = clear distance between the edge of steel rods hole and edge of material, in.

d_b = rods' diameter, in. For SMA rods, $d_b = d_{SMA}$; for steel rods, $d_b = d_{steel}$.

Step 23: Calculate the thickness of inner diaphragm:

Assume all the compression force on the rectangular tube from the end plate will be resisted by only the inner diaphragm. The bearing capacity of the infill grout is not considered in this preliminary design procedure.

$$t_{diap,req'd} \geq \frac{P_u}{\phi_d \cdot F_{ydiap} \cdot b_{bf}} \qquad \textbf{(AEq. B-147)}$$

For interior connection:

$$P_u = \frac{M_d}{d - t_{bf}} + V_{u3} \qquad \textbf{(AEq. B-148)}$$

For exterior connection:

$$P_u = \frac{M_d}{d - t_{bf}} \qquad \textbf{(AEq. B-149)}$$

where,

P_u = compressive force transferred onto rectangular tube, kips

F_{ydiap} = yielding strength of inner diaphragm, ksi.

Step 24: Calculate the wall thickness of square steel tube:

Assume the vertical shear force is resisted by all rods uniformly. The design procedure in steel construction manual is applied in this step [2].

$$t_{SST,req'd} \geq \frac{V_a}{n_t \cdot \phi_v \cdot F_{uSST} \cdot \min\left(1.2 \cdot l_{hc}, 2.4 \cdot d_b\right)} \qquad \textbf{(AEq. B-150)}$$

where,

F_{uSST} = ultimate strength of square steel tube, ksi.

Step 25: Calculate the thickness of beam stiffeners:

The same design procedure in AISC358 is adopted in this step [10].

Strength requirement:

$$t_{st,req'd} \geq t_{bw} \cdot \frac{F_{yb}}{F_{yst}} \qquad \textbf{(AEq. B-151)}$$

Geometry requirement:

$$t_{st,req'd} \geq \frac{h_{st}}{0.56 \cdot \sqrt{\frac{E_s}{F_{yst}}}} \qquad \textbf{(AEq. B-152)}$$

where,

t_{bw} = thickness of beam web, in.

h_{st} = height of beam stiffener, in.

E_s = elastic modulus of steel, ksi.

F_{yst} = yielding strength of beam stiffener, ksi.

Step 26: Calculate fillet welds between square steel tube and circular steel tube:

The size of the fillet welds between the cover plate of the rectangular tube and the circular tube is calculated based on the total vertical shear force transferred from beams. Each circular fillet weld line is divided into four parts equally as shown in Appendix Figure B-6. The blue line represents the circular weld line which is divided by two red lines equally into four parts. Assume only one fourth portion of the whole weld will contribute to the total shear capacity to resist the vertical shear from the corresponding beam. There are two weld lines on both top and bottom cover plates being considered.

$$\phi V_n = l_w \cdot \min\left(\phi_v \cdot V_{uni}, 0.6 \cdot f_{ycp} \cdot t_{cp}, \phi_v \cdot 0.6 \cdot f_{ucp} \cdot t_{cp}\right) \geq V_{u\max} \qquad \textbf{(AEq. B-153)}$$

$$V_{uni} = \frac{0.6 \cdot 1.5}{\sqrt{2}} \cdot h_{toe} \cdot F_{filler} \qquad \textbf{(AEq. B-154)}$$

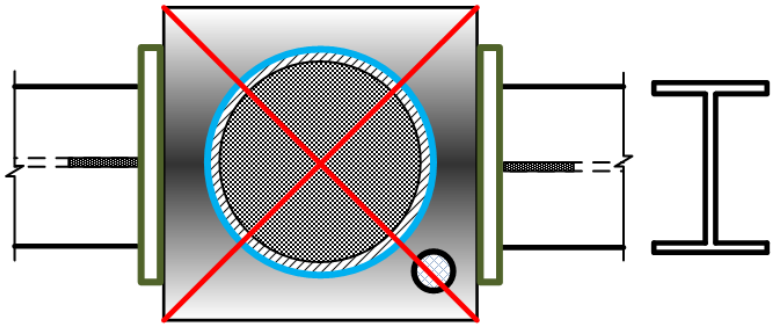

Appendix Figure B-6: Division of a circular fillet weld line

where,

l_w = half of the perimeter of the intersection between two tubes for uniaxial bending connection; and one fourth for biaxial bending connection in.

V_{uni} = nominal shear capacity of unit length fillet welds, kips

f_{ycp} = yielding strength of cover plate, ksi.

f_{ucp} = ultimate strength of cover plate, ksi.

t_{cp} = thickness of cover plate, in.

V_{umax} = maximum value of all factored shear loadings from all beams on the same connection, kips

h_{toe} = height of fillet weld toe, in.

F_{filler} = nominal strength of filler metal, ksi.

Appendix C

Design Example of One Typical Interior Proposed Smart Connection

Inputs:

Beam W33*130

d = 33.1	A = 38.3	tw = 0.58	bf = 11.5
tf = 0.855	Zx = 467	ry = 2.39	

RBS parameters

a = 5.75	b = 22	c = 2.875	θRBS = 0.03

Beam steel

Fy = 50	Fu = 65	E = 29000

Seismic design parameters

Cpr = 1.15	< 1.2 OK	Ry = 1.1	ϕd = 1
ϕt = 0.9	ϕn = 0.9	ϕv = 0.75	

Structural information

Span = 384

Circular steel tube

D = 24	t = 1.375	Fy = 50	Fu = 65

Square steel tube

B = 30	MinSpacing = 2		Fy = 46
t = 1	> 0.094829	OK	Fu = 58

Endplate

t = 1.125	> 1.118363	OK	
pfi = 1.75	pfo = 1.75	bp = 16	g = 6
h0 = 34.4225	h1 = 30.0675	h2 = 2.1775	de = 6
s = 4.898979	< 6	Min distance between exterior row and edge	
Fy = 50	Fup = 65		

Load Cases

ωd = 0.11	ωl = 0.1	ωu = 0.292	Roof ?
	ωlr = 0.02		

Design parameters

ϒ = 0.8	α = 0.3	> 0.300949	ζ = 0.45
θtar = 0.04	β = 0.85	η = 0.5	> 0.256059
λ = 346.6135			

SMA rods

L = 32.25	d = 1.27	> 1.096957	OK

Fy =	66.7	**εy =**	0.0114	**F5% =**	74.5	**F7% =**	116

Steel rods

L =	32.25	**d =**	1.128	**>**	**1.076677**	**OK**	
Fy =	50	**εy =**	0.001724	**Fu =**	65	**εu =**	0.045
ε_max =	0.18						

MMR

MMR =	4574.822

Temperary using 1.5 times M_reco

εmax_SMA

εmax_SMA =	0.063232	**<**	**0.07**				
	Make	**MMC - Md =**	**0**		**=**	**0**	**OK**

Rods Patton One

n =	4	Rod's number on each level
nt =	16	Rod's total number

Inner diaphragms

t =	2	**>**	**1.955338**	**OK**	**Fy =**	50	
be =	11.5				**Fu =**	65	

Beam stiffeners

t =	0.58	**>=**	**0.58**	**OK**	**Fy =**	50	
hst =	5	**Es =**	29000	**Landing =**	1		

Weld material

htoe =	0.1875	**make**	**236.0473**	**not less than**	**178.6788**
FEXX =	70	E70			

Cover plate

Fy =	36	**Fu =**	58	**t =**	0.5

Check List

Rods pattern one & Interior		**Main Story**			
a =	5.75	**From**	**5.75**	**to**	**8.625**
b =	22	**From**	**21.515**	**to**	**28.135**
c =	2.875	**From**	**1.15**	**to**	**2.875**
Md =	22704.96	**<**	**25685**	**OK**	
t req'd =	0.989362	**<**	**1.125**	**OK**	
Lreq'd =	7.389974	**<**	**32.25**	**OK**	
d_SMAreq'd =	1.096957	**<**	**1.27**	**OK**	
α_req'd =	0.300949	**<**	**0.3**	**OK**	
d_Steelreq'd =	1.076677	**<**	**1.128**	**OK**	
η_req'd =	0.256059	**<**	**0.5**	**OK**	
MMC =	24773.38	**>**	**22704.96**	**OK**	

fmax_SMA =	101.9567	<	116	OK
Mmc - Md =	0	=	0	OK
ΦVn =	540	>	420.1805	OK
t_req'd =	0.875376	<	1.125	OK
ΦVn / An =	35.1	>	34.89292	OK
t_req'd =	1.118363	<	1.125	OK
ΦVn =	290.2861	>	178.6788	OK
ΦVn =	167.1638	>	11.16742	OK
ΦVn =	148.473	>	11.16742	OK
tdiap_req'd =	1.955338	<	2	OK
t_SSTreq'd =	0.094829	<	1	OK
t_STreq'd =	0.58	<=	0.58	OK
ΦVn =	236.0473	>	178.6788	OK

Detailed Design Procedure:

Step 1: Determine RBS Parameters

a =	5.75	From	5.75	to	8.625	(AEq. B-1)
b =	22	From	21.515	to	28.135	(AEq. B-2)
c =	2.875	From	1.15	to	2.875	(AEq. B-3)

Step 2: Calcualte ultimate moment demand at the face of square steel tube

Z_RBS =	308.4755	Mpr =	19511.07656	
Lh =	318.25	da =	17.875	
Va =	178.6788	Md =	22704.95972	(AEq. B-4)

Step 3: Check the flexural strength of the beam at the face of the square steel tube

Md =	22704.96	<	25685	OK
Mp =	25685	(AEq. B-6)		

Step 4: Calculate required endplate thickness

Yp =	514.9482				
t req'd =	0.989362	<	1.125	OK	(AEq. B-7)

Step 5: Compute target design at surface of square tube when max strain in SMA is 5%

Va' =	154.1558	(AEq. B-9)	Mtar =	18364.39658	(AEq. B-8)

Step 6: Calculate required rods' length

Lreq'd =	7.389974	<	32.25	OK	(AEq. B-10)

Step 7: Calculate design rotation under target moment

θrod =	0.04364	(AEq. B-13)	θd =	0.073640206	(AEq. B-12)

Step 8: Calculate target capacity supplied by SMA rods at yield strength

MtarSMA = 7398.757 **(AEq. B-15)**

Step 9: Calculate diameter of SMA rods

Rods pattern one & Interior

he_SMA = 65.23967 **(AEq. B-17)**

d_SMAreq'd = 1.096957 < 1.27 OK **(AEq. B-16)**

Step 10: Compute recovery capacity supplied by pre-stressed strength in SMA rods

M_reco = 3049.882 **(AEq. B-22)** M_end = 3588.096

Step 11: Calculate required pre-stressed parameter for SMA rods

Rods pattern one

he_reco = 66.6675 **(AEq. B-24)**

α_req'd = 0.300949 < 0.3 OK **(AEq. B-23)**

Step 12: Calculate capacity at square tube surface supplied by SMA rods with max strain of 5%

Rods pattern one & Interior

ε'_SMA = 0.047053 **(AEq. B-30)** f'_SMA = 73.90458 **(AEq. B-29)**

FH_SMA = 4947.529 **(AEq. B-28)** M_SMA = 11275.56 **(AEq. B-27)**

Step 13: Calculate target design moment capacity at surface of square tube supplied by Steel rods with max strain of 5% in SMA rods

MtarSteel = 7088.84 **(AEq. B-41)**

Step 14: Calculate diameter of Steel rods

Rods pattern one & Interior

ε''_Steel = 0.044496 **(AEq. B-47)**

f''_Steel = min (64.82514 65) = 64.82514 **(AEq. B-46)**

ε'_Steel = 0.047442 **(AEq. B-45)**

f'_Steel = min (65.84645 65) = 65 **(AEq. B-44)**

FH_Steel = 4327.749 **(AEq. B-43)**

d_Steelreq'd = 1.076677 < 1.128 OK **(AEq. B-42)**

Step 15: Calculate required pre-stressed parameter for Steel rods

Rods pattern one

he_SMA = 66.6675 **(AEq. B-67)** he_Steel = 66.6675 **(AEq. B-67)**

MpreSMA = 3040.261 MpreSteel = 1534.561 **(AEq. B-64)**

η_req'd = 0.256059 < 0.5 OK **(AEq. B-63)**

Step 16: Check max allowable moment capacity when max strain in SMA reaches 7%

Rods pattern one & Interior

ε'_SMA = 0.065788 **(AEq. B-77)**

f'_SMA = max (77.69038 107.2606799) = 107.2607 **(AEq. B-76)**

FH_mSMA = 7451.631 M_mcSMA = 16982.47 **(AEq. B-73)**

ε''_Steel = 0.06323 **(AEq. B-82)**

f''_Steel = min (71.31889 65) = 65 **(AEq. B-81)**

ε'_Steel = 0.067442 **(AEq. B-80)**

f'_Steel = min (72.77873 65) = 65 **(AEq. B-79)**

FH_mSteel = 4333.388 M_mcSteel = 7790.905 **(AEq. B-74)**

Mmc = 24773.38 > 22704.95972 OK **(AEq. B-72)**

Step 17: Calculate max strain in SMA rods under Md

Rods pattern one & Interior

εmax_SMA =	0.063232		**fmax_SMA =**	101.9567	<	116	OK
ε'_SMA =	0.059449	**(AEq. B-77)**					
f'_SMA =	max (	76.40929	94.10571864)	=	94.10572	**(AEq. B-76)**	
FH_mSMA =	6544.043		**M_mcSMA =**	14914.06	**(AEq. B-73)**		
ε''_Steel =	0.056891	**(AEq. B-82)**					
f''_Steel =	min (	69.12145	65)	=	65	**(AEq. B-81)**	
ε'_Steel =	0.060674	**(AEq. B-80)**					
f'_Steel =	min (	70.43289	65)	=	65	**(AEq. B-79)**	
FH_mSteel =	4333.388		**M_mcSteel =**	7790.905	**(AEq. B-74)**		
Mmc =	22704.96	**(AEq. B-72)**					
Mmc - Md =	0	=	0	OK			

Step 18: Calculate shear forces on three levels of endplate under Md

Rods pattern one & Interior

Vu1 =	388.0269	**(AEq. B-115)**
Vu2 =	316.112	**(AEq. B-116)**
Vu3 =	420.1805	**(AEq. B-117)**

Step 19: Check shear yielding of endplate

bpe = 16

ΦVn =	540	>	420.1805	OK	**(AEq. B-138)**
t_req'd =	0.875376	<	1.125	OK	

Step 20: Check shear rupture of endplate

Rods pattern one

d_hSMA =	1.395	**d_hSteel =**	1.253

An1 = An2 = An3 = 12.042 **(AEq. B-140)**

ΦVn / An = 35.1 **>** **34.89291938** **OK** **(AEq. B-139)**

t_req'd = max (1.032782 0.841371482 1.118363) = 1.118363

< **1.125** **OK**

Step 21: Check rods rupture

fv_SMA = 40.02 **fv_Steel =** 30

ΦVn = 290.2861 **>** **178.6788** **OK** **(AEq. B-145)**

Step 22: Check rods' hole bearing capacity of endplate

Rods pattern one

SMA: **l_hc =** min (2.96 5.3025) = 2.96

ΦVn = 167.1638 **>** **11.16742363** **OK** **(AEq. B-146)**

Steel: **l_hc =** min (3.102 5.3735) = 3.102

ΦVn = 148.473 **>** **11.16742363** **OK** **(AEq. B-146)**

Step 23: Calculate the thickness of inner diaphragms

Interior

Pu = 1124.319 **(AEq. B-148)**

tdiap_req'd = 1.955338 **<** **2** **OK** **(AEq. B-147)**

Step 24: Calculate the wall thickness of square steel tube

Rods pattern one

t_SSTreq'd = max (0.084227 0.094829485) = 0.094829

(AEq. B-150)

< **1** **OK**

Step 25: Calculate the thickness of beam stiffeners

t_STreq'd = max (0.58 0.370739) = 0.58 **(AEq. B-151 & 152)**

< **0.58** **OK**

Step 26: Calculate fillet welds between square steel tube and circular steel tube

FTy = 18 **FTu =** 29

Vuni = 8.352699 **Vumax = Va =** 178.6787781

lw = 37.68

ΦVn = 37.68 min (6.264524 10.8 13.05)

= 236.0473 **>** **178.6788** **OK** **(AEq. B-153)**

Additional check 1: Calcualte capacity from Steel rods when max strain in SMA reaches 5%

Rods pattern one & Interior

ε''_Steel = 0.044496

f''_Steel = min (64.82514 65) = 64.82514

ε'_Steel = 0.047442

f'_Steel = min (65.84645 65) = 65

FH_mSteel = 4327.749 **M_mcSteel =** 7780.767

Additional check 2: Calculate actural moment capacity at max strain 5% of SMA rods

M5% = 19056.32

ϒ = 0.831882

Additional check 3: Calculate moment capacity from rods pretension

Rods pattern one

MpreSMA = 3040.261 **MpreSteel =** 2996.502

Mpre = 6036.763

Results:

Beam W33*130

Material:	A992		
	Fy = 50	**Fu =** 65	

RBS parameters

a = 5.75	**b =** 22	**c =** 2.875

Circular steel tube

Material:	A572 Gr.50		
	Fy = 50	**Fu =** 65	
Size:			
	D = 24	**t =** 1.375	

Square steel tube

Material:	A500 Gr.B		
	Fy = 46	**Fu =** 58	
Size:			
	B = 30	**t =** 1	

Endplate

Material:	A572 Gr.50		
	Fy = 50	**Fu =** 65	
Size:			
	t = 1.125	**b =** 16	**g =** 6
	pfi = 1.75	**pfo =** 1.75	**de =** 6

SMA rods

Material:	Ni-Ti ASTM-F2063		
	Fy = 66.7	**F5% =** 74.5	**F7% =** 116
	εy = 0.0114		
Size:			
	L = 32.25	**d =** 1.27	

Steel rods

Material:	A572 Gr.50		
	Fy = 50	**Fu =** 65	
	εy = 0.001724	**εu =** 0.045	**ε_max =** 0.18
Size:			
	L = 32.25	**d =** 1.128	

Inner diaphragms

Material:	A572 Gr.50

	Fy = 50	**Fu =** 65	
Size:			
	t = 2	**b =** 28	

Beam stiffeners

Material:	A992		
	Fy = 50		
Size:			
	t = 0.58	**hst =** 5	**Landing =** 1

Cover plate

Material:	A36		
	Fy = 36	**Fu =** 58	
Size:			
	t = 0.5	**b =** 28	

Weld material

Material:	E70
	FEXX = 70
Size:	
	htoe = 0.1875

Design Behaviors:

SMA rods

	Design	Allowable
σmax =	101.9567	116
εmax =	0.063232	0.07

Steel rods

	Design	Allowable
σmax =	65	65
εmax =	0.060674	0.18

Design parameters

	Initial	Final	
θ =	0.04	0.07364	Connection rotation @ max 5% strain of SMA
α =	0.3	0.3	SMA pretension ratio
β =	0.85	0.847319	Recover parameter
ϒ =	0.8	0.831882	RBS damage parameter @ max 5% strain of SMA
η =	0.5	0.5	Steel rods pretension ratio
ζ =	0.45	0.61399	Ratio of capacity from SMA to Mtar at max 5% of SMA

Pretension capacity

MMR =	4574.822		
Mpre =	6036.763	**ratio =**	1.319562
M_end =	3588.096		
Mpre_SMA =	3040.261	**ratio (β) =**	0.847319

M-R curve key pionts

Rotation from Rods		Moment w/o Φ		
θ1 =	0.056037	**M1 =**	25227.73	Ultimate moment capacity
θ2 =	0.04364	**M2 =**	21173.69	Mtar

θ3 =	0.04364	**M3 =**	12528.4	ζ Mtar
θ4 =	0	**M4 =**	3378.068	Capacity from SMA pretension
θ5 =	0	**M5 =**	6707.514	Capacity from ALL pretension
θ6 =	0.007476	**M6 =**	11019.06	Capacity from SMA yielding strength

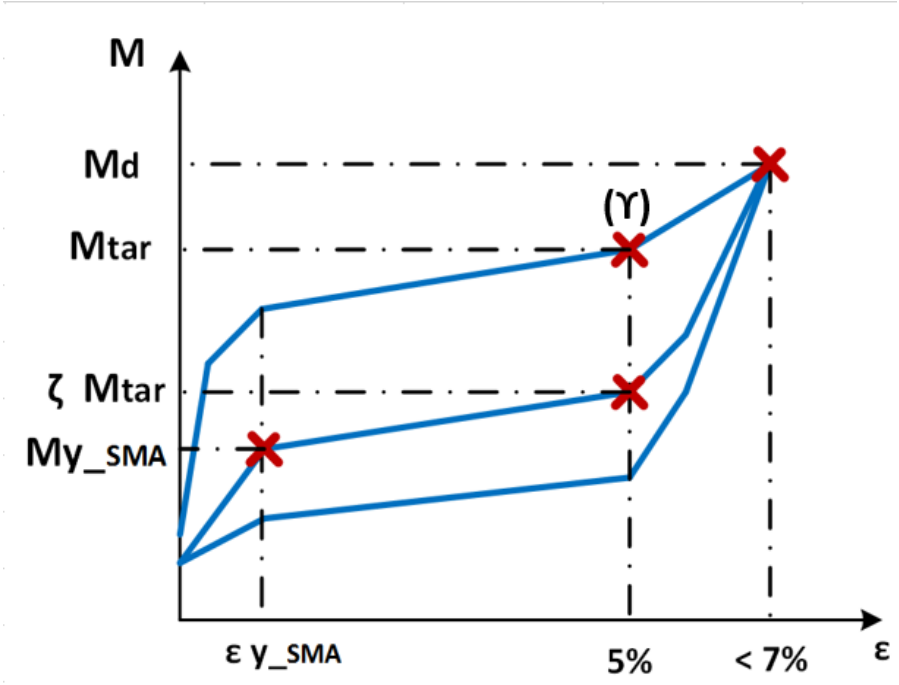

Calculate theoretical moment capacity at key points

Ultimate moment capcity

From step 17: **Rods pattern one & Interior**

εmax_SMA = 0.063232 **σmax_SMA =** 101.9567

Mu_SMA = 16571.17

Mu_Steel = 8656.561

Mu = 25227.73

Moment capcity @ 5% SMA strain

From step 12 & 14: **Rods pattern one & Interior**

εmax_SMA = 0.05

M_SMA_5% = 12528.4

M_Steel_5% = 8645.297 **FH_Steel =** 4327.749

M_5% = 21173.69

Moment capcity due to pretension

Mpre_SMA = 3378.068

Mpre_Steel = 3329.446

Mpre = 6707.514

Moment capacity from SMA yielding strength

εmax_SMA = 0.0114 **σmax_SMA =** 66.7

ε'_SMA = 0.010895 **f'_SMA =** 63.74648

FH_SMA = 4351.486

M_SMA = 11019.06

Appendix D

Design Methods of CCFT Columns in Different Codes

In this Section, the current design methods of CCFT columns in the main design codes are introduced as follows, and an detailed example is provided for comparison among these methods.

D.1 AISC – US Specification for Structural Steel Buildings

In the US, both ACI 318 and AISC provisions can address the composite columns design. ACI 318 provisions would like to consider such composite columns basically as various types of regular reinforced concrete columns. Different from ACI 318, the AISC provisions treat the columns with composite cross sections as equivalent steel columns by utilizing a modified cross-sectional properties. Due to CCFT columns are usually used in steel structures, the method in steel construction manual [2] will be introduced in this section.

Axial capacity:

Nominal section axial capacity:

$$P_0 = A_s \cdot F_y + 0.95 \cdot A_c \cdot f_c^{'} \qquad \textit{(AEq. D-1)}$$

Nominal member axial capacity:

when $\lambda \leq 1.5$,

$$P_n = 0.658^{\lambda^2} \cdot P_0 = 0.658^{\left(\frac{P_0}{P_e}\right)} \cdot P_0 \qquad \textit{(AEq. D-2)}$$

when $\lambda > 1.5$,

$$P_n = \left(\frac{0.877}{\lambda^2}\right) \cdot P_0 = 0.877 \cdot P_e \qquad \textit{(AEq. D-3)}$$

Design member axial capacity:

$$P_c = 0.75 \cdot P_n \text{ (LRFD)} \qquad \text{or} \qquad P_c = P_n / 2.0 \text{ (ASD)} \qquad \textit{(AEq. D-4)}$$

where,

$$\lambda = \sqrt{P_0 / P_e}$$

$$P_e = \frac{\pi^2 \cdot EI_{eff}}{\left(K \cdot L\right)^2}$$

$$EI_{eff} = E_s \cdot I_s + C_3 \cdot E_c \cdot I_c$$

$$C_3 = 0.6 + 2 \cdot \left(\frac{A_s}{A_c + A_s}\right) \leq 0.9$$

F_y = normal yield strength of steel, ksi.

f_c' = characteristic compressive cylinder strength of concrete at 28 days, ksi.

A_s = area of steel tube cross section, $in.^2$

A_c = area of infill concrete of CCFTs, $in.^2$

K = effective column length factor (Appendix Table D-4)

L = column length, in.

E_s = elastic Young's modulus of steel tube, ksi.

E_c = elastic Young's modulus of infill concrete, ksi.

I_s = moment of inertia of steel tube, $in.^4$

I_c = moment of inertia of infill concrete, $in.^4$

Flexural capacity:

Nominal moment capacity:

$$M_n = Z_s F_y + \frac{Z_c(0.95 f_c^{'})}{2} \qquad \textit{(AEq. D-5)}$$

Design moment capacity:

$$M_c = 0.9 \cdot M_n \ \text{(LRFD)} \quad \text{or} \quad M_c = M_n / 1.67 \ \text{(ASD)} \qquad \textit{(AEq. D-6)}$$

where,

$$Z_c = \frac{h^3 \sin^3(\theta/2)}{6}$$

$$Z_s = \frac{d^3 - h^3}{12} \sin^3(\theta/2) \left[\frac{\theta}{\theta - \sin\theta} + \frac{(2\pi - \theta)}{(2\pi - \theta) - \sin(2\pi - \theta)} \right]$$

$$\text{or } Z_s \approx \frac{d^3 - h^3}{6} \sin^{4/3}(\theta/2)$$

$$\theta = \frac{0.0260K_c - 2K_s}{0.0848K_c} + \frac{\sqrt{(0.0260K_c + 2K_s)^2 + 0.857K_cK_s}}{0.0848K_c}$$

$$K_c = f_c^{'} h^2$$

$$K_s = F_y r_m t$$

$$h = d - 2t$$

$$r_m = \frac{(d-t)}{2}$$

d = diameter of the circular steel tube, in.

t = wall thickness of the circular steel tube, in.

The above design formulae are based on the assumption that the local buckling will not occur. The suggested limit ratio of overall diameter to thickness (d/t) is: $d/t \leq 0.15E_s/F_y$ (unit of F_y is ksi.) [122].

AF interaction:

For $\frac{P_r}{P_c} \geq 0.2$, $\frac{P_r}{P_c} + \frac{8}{9} \cdot \left(\frac{M_{rx}}{M_c} + \frac{M_{ry}}{M_c} \right) \leq 1.0$ ***(AEq. D-7)***

For $\frac{P_r}{P_c} < 0.2$, $\frac{P_r}{2 \cdot P_c} + \left(\frac{M_{rx}}{M_c} + \frac{M_{ry}}{M_c} \right) \leq 1.0$ ***(AEq. D-8)***

where,

P_r = required compressive strength, kips

P_c = available compressive strength, kips

M_r = required flexural strength, k-in.

M_c = available flexural strength, k-in.

x = subscript relating symbol to x- x axis bending

y = subscript relating symbol to y- y axis bending

D.2 AS5100 – Australian bridge design standard

AS5100 considers the increase in the infill concrete from steel tube confinement directly if both the slenderness λ_r and the eccentricity e of the column are within the limit of 0.5 and $d/10$, respectively. A factor greater than 1.0 will be multiplied on the capacity of the infill concrete. A slenderness reduction factor will be applied to calculate the member capacity based on the section capacity. For the ultimate flexural strength of CCFTs, AS5100 doesn't give any design formulae. It suggests that any simple plastic theory can be applicable. The formulae proposed by Elchalakani [123] for the CCFT flexural capacity will be introduced and all their notations are shown in Appendix Figure D-1.

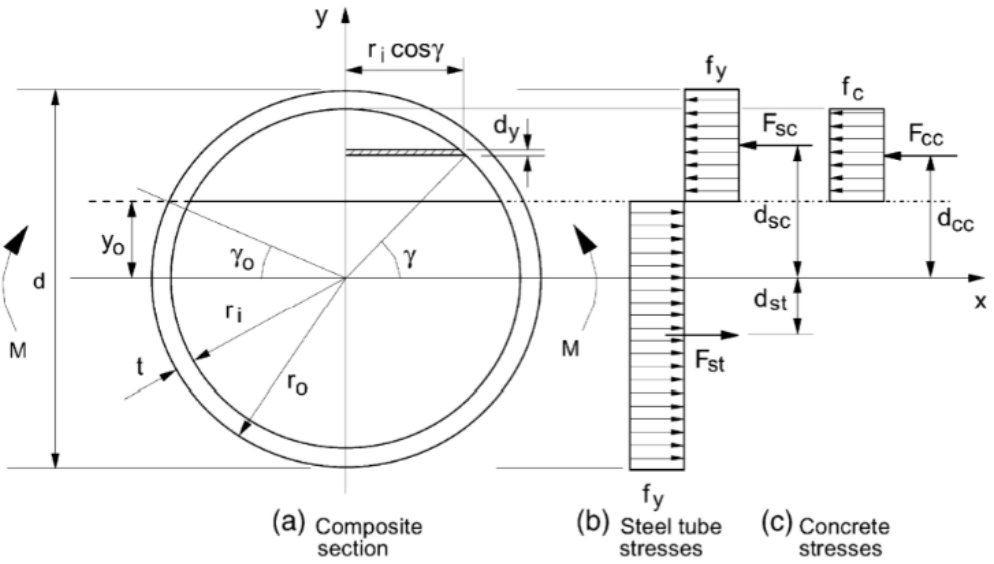

Appendix Figure D-1: Neutral axis and stress distribution for CCFT [123]

Axial capacity:

Nominal section axial capacity:

$$P_{sn} = A_s \cdot \eta_2 \cdot F_y + A_c \cdot f_c^{'} \cdot \left(1 + \eta_1 \cdot \frac{t}{d} \cdot \frac{F_y}{f_c^{'}}\right) \qquad \textit{(AEq. D-9)}$$

Nominal member axial capacity:

$$P_n = \alpha_c \cdot P_{sn} \qquad \textit{(AEq. D-10)}$$

Design section axial capacity:

$$P_{sc} = A_s \cdot \eta_2 \cdot \left(\phi_s \cdot F_y\right) + A_c \cdot \left(\phi_c \cdot f_c^{'}\right) \cdot \left(1 + \eta_1 \cdot \frac{t}{d} \cdot \frac{F_y}{f_c^{'}}\right) \qquad \textit{(AEq. D-11)}$$

Design member axial capacity:

$$P_c = \alpha_c \cdot P_{sc} \qquad \textit{(AEq. D-12)}$$

where,

if $0 \le \frac{e}{d} \le 0.1$ & $\lambda_r \le 0.5$

$$\eta_1 = \left(4.9 - 18.5 \cdot \lambda_r + 17 \cdot \lambda_r^2\right) \cdot \left(1 - \frac{10 \cdot e}{d}\right) \ge 0$$

$$\eta_2 = \left[0.25 \cdot \left(3 + 2 \cdot \lambda_r\right)\right] + \left\{1 - \left[0.25 \cdot \left(3 + 2 \cdot \lambda_r\right)\right]\right\} \cdot \frac{10 \cdot \mathrm{e}}{d} \le 1.0$$

otherwise

$$\eta_1 = 0 \text{, and } \eta_2 = 1.0$$

$$\lambda_r = \sqrt{P_s / P_{cr}}$$

$$P_s = A_s \cdot F_y + A_c \cdot f_c^{'}$$

$$P_{cr} = \frac{\pi^2 \cdot EI_{eff}}{\left(K \cdot L\right)^2}$$

$$EI_{eff} = \phi_s \cdot E_s \cdot I_s + \phi_c \cdot E_c \cdot I_c$$

$$\alpha_c = \xi \cdot \left[1 - \sqrt{1 - \left(\frac{90}{\xi \cdot \lambda}\right)^2}\right]$$

$$\xi = \frac{\left(\frac{\lambda}{90}\right)^2 + 1 + \eta}{2 \cdot \left(\frac{\lambda}{90}\right)^2}$$

$$\lambda = \lambda_n + \alpha_a \cdot \alpha_b$$

$$\eta = 0.00326 \cdot \left(\lambda - 13.5\right) \ge 0$$

$\lambda_n = 90 \cdot \lambda_r$

$$\alpha_a = \frac{2100 \cdot (\lambda_n - 13.5)}{\lambda_n^2 - 15.3 \cdot \lambda_n + 2050}$$

α_b = -1.0 for hot-formed CHS with form factor of 1.0, or cold-formed (stress relieved) CHS with form factor of 1.0;

= -0.5 for hot-formed or cold-formed CHS with form factor less than 1.0, or cold-formed (non-stress relieved) CHS with form factor of 1.0.

$\phi_s = 0.9$

$\phi_c = 0.6$

e = eccentricity of the column, in.

d = outer diameter of the steel tube, in.

t = wall thickness of the steel tube, in.

F_y = normal yield strength, ksi.

f_c' = characteristic compressive cylinder strength of concrete at 28-days, ksi.

A_s = area of steel tube cross section, $in.^2$

A_c = area of infill concrete of CCFTs, $in.^2$

K = effective column length factor (Appendix Table D-4)

L = column length, in.

E_s = elastic Young's modulus of steel tube, ksi.

E_c = elastic Young's modulus of infill concrete, ksi

I_s = moment of inertia of steel tube, $in.^4$

I_c = moment of inertia of infill concrete, $in.^4$

Flexural capacity:

Nominal moment capacity:

$$M_n = 4 \cdot F_y \cdot t \cdot r_m{}^2 \cdot \cos(\gamma_0) + \frac{2}{3} \cdot f_c^{'} \cdot r_i^3 \cdot \cos^3(\gamma_0) \qquad \textit{(AEq. D-13)}$$

Design moment capacity:

$$M_c = 0.9 \cdot M_n \qquad \textit{(AEq. D-14)}$$

where,

$$r_m = \frac{d-t}{2}$$

$$r_i = \frac{d-2 \cdot t}{2}$$

$$\gamma_0 = \frac{\frac{\pi}{4}\left(\frac{f_c^{'} \cdot r_i^2}{F_y \cdot r_m \cdot t}\right)}{2 + \frac{1}{2}\left(\frac{f_c^{'} \cdot r_i^2}{F_y \cdot r_m \cdot t}\right)}$$

The above design formulae are based on the assumption that the local buckling will not occur. The suggested limit ratio of overall diameter to thickness (d/t) by Bergmann [124] is: $d/t \leq 3067/F_y$ (unit of F_y is ksi).

AF interaction:

The design rules for combined compression and bending in AS5100 is very similar to the ones given in Eurocode 4 (2004). It will not be given here but the following brief introduction, please refer to section 3.5.4 for details.

The material properties should be $\phi_s F_y$ for steel and $\phi_c f_c'$ for concrete, instead of F_y/γ_s and f_c'/γ_c used in Eurocode 4. The anchor points $A, B, C, and\ D$ of the column interaction curve for CCFTs in Appendix Figure D-6 are defined by Eurocode 4 as follows:

- Point A (0, P_{sc})
- Point B (M_c, 0)
- Point C (M_c, $\phi_c f_c' A_c$)
- Point D (M_{max}, $0.5\phi_c f_c' A_c$)

Assume the neural axis at Point D is coincide with centroid of the CCFT section. So the angle γ_0 at point D is equal to 0, and the M_{max} can be taken as:

$$M_{\max} = 0.9 \cdot \left(4 \cdot F_y \cdot t \cdot r_m^{\,2} + \frac{2}{3} \cdot f_c^{'} \cdot r_i^3 \right) \qquad \textbf{(AEq. D-15)}$$

D.3 BS5400 – British bridge code

BS5400 modifies the materials strengths to consider both the confinement effect on the concrete compressive strength and the reduction on the steel tube strength from local buckling. Then the modified strengths are used to calculate the design axial section capacity. The slenderness effect is involved in the axial member capacity. For the ultimate design flexural capacity, the concrete contribution is introduced by a parameter m, which is determined by the aspect ratio D_e/t of the steel tube and the ratio ρ of the average compressive stress in the concrete at failure to the design yield stress of the steel tube. And the modified materials properties will be adopted for the nominal strength. Their relationship is shown in Appendix Figure D-3.

.

Axial capacity:

Nominal section axial capacity:

$$P_{sn} = F_y \cdot A_s + f_{cu} \cdot A_c \qquad \textit{(AEq. D-16)}$$

Nominal member axial capacity:

$$P_n = 0.85 \cdot K_1 \cdot P_{sn} \qquad \textit{(AEq. D-17)}$$

Design section axial capacity:

$$P_{sc} = 0.95 \cdot f_y^{'} \cdot A_s + 0.45 \cdot f_{cc} \cdot A_c \qquad \textit{(AEq. D-18)}$$

Design member axial capacity:

$$P_c = 0.85 \cdot K_1 \cdot P_{sc} \qquad \textit{(AEq. D-19)}$$

The following two requirements must by satisfied in the design:

Wall thickness requirement:

$$t \geq D_e \cdot \sqrt{\frac{F_y}{8 \cdot E_s}} \qquad \textit{(AEq. D-20)}$$

Concrete contribution requirement:

$$0.1 < \alpha_c = \frac{0.45 \cdot f_{cc} \cdot A_c}{P_{sc}} < 0.8 \qquad \textit{(AEq. D-21)}$$

where,

$$f_{cc} = f_{cu} + C_1 \cdot \frac{t}{D_e} \cdot F_y$$

$$f_y' = C_2 \cdot F_y$$

$$K_1 = 0.5 \cdot \left[\left(1 + \frac{1+\eta}{\lambda^2} \right) - \sqrt{\left(1 + \frac{1+\eta}{\lambda^2} \right)^2 - \frac{4}{\lambda^2}} \right]$$

$$\eta = \begin{cases} 0 & \text{if } \lambda \leq 0.2 \\ 75.5 \cdot \alpha \cdot (\lambda - 0.2) & \text{if } \lambda > 0.2 \end{cases}$$

$$L = L_e / I_e$$

$$I_e = \pi \cdot \sqrt{\frac{0.95 \cdot E_s \cdot I_s + 0.45 \cdot E_c \cdot I_c}{P_{sc}}}$$

$$E_c = 450 \cdot f_{cu}$$

C_1 , C_2 = material modification factors, which are determined in Appendix Table D-1 or in Appendix Figure D-2.

L_e = $0.7L$ for fixed – fixed end condition; $0.85L$ for fixed – pinned end condition; L for pinned – pinned end condition; $1.5L$ for fixed – slide end condition; $2L$ for fixed – free or pinned – slide end condition.

α = 0.0025 for curve A; 0.0045 for curve B; 0.0062 for curve C; and 0.0083 for curve D. Selection of curves is determined in Appendix Table D-2.

F_y = normal yield strength, ksi.

f_{cu} = characteristic compressive cube strength of concrete at 28 days, ksi.

A_s = area of steel tube cross section, $in.^2$

A_c = area of infill concrete of CCFTs, $in.^2$

L = column length, in.

E_s = elastic Young's modulus of steel tube, ksi.

E_c = elastic Young's modulus of infill concrete, ksi.

I_s = moment of inertia of steel tube, $in.^4$

I_c = moment of inertia of infill concrete, $in.^4$

D_e = outer diameter of the steel tube, in.

t = wall thickness of the steel tube, in.

r = radius of gyration of the section, in.

y = distance from the centroid to the extreme fiber of the section, $D_e/2$ for CCFTs, in.

Appendix Table D-1: Values of Constants C_1 and C_2 [125]

L_e/D_e	C_1	C_2
0	9.47	0.76
5	6.40	0.80
10	3.81	0.85
15	1.80	0.90
20	0.48	0.95
25	0	1.0

Appendix Table D-2: Selection of Column Curves in BS5400 Specification for CCFTs [125]

r/y	**Members fabricated by welding**	**All other members (including stress relieved welded members)**
$r/y \geq 0.7$	Curve B	Curve A
$r/y = 0.6$	Curve C	Curve B
$r/y = 0.5$	Curve C	Curve B
$r/y \leq 0.45$	Curve C	Curve C
Hot-finished hollow sections	Curve A	

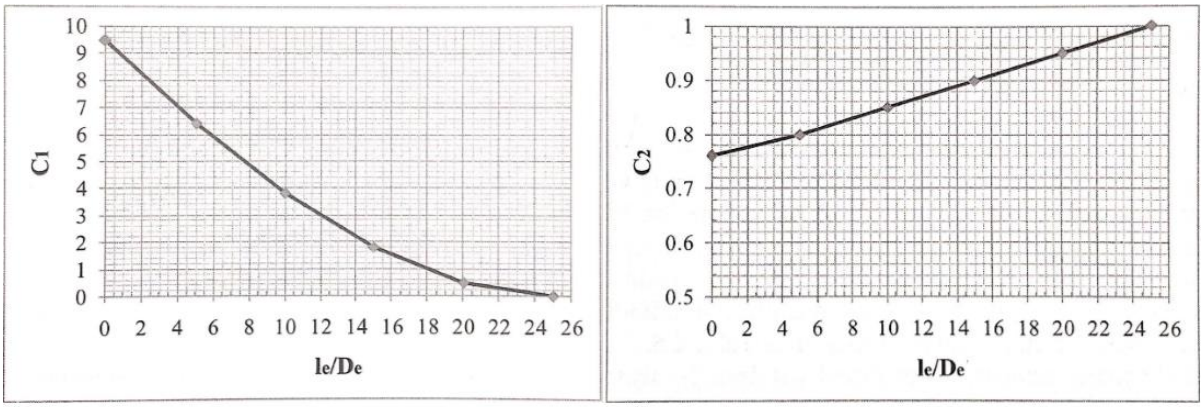

Appendix Figure D-2: Values of the constants C_1 and C_2 [125]

Flexural capacity:

Nominal moment capacity:

$$M_n = S \cdot F_y \cdot \left[1 + 0.01 \cdot m(\rho_n)\right] \qquad \textit{(AEq. D-22)}$$

Design moment capacity:

$$M_c = 0.95 \cdot S \cdot F_y \cdot \left[1 + 0.01 \cdot m(\rho)\right] \qquad \textit{(AEq. D-23)}$$

where,

$$S = t^3 \cdot \left(\frac{D_e}{t} - 1\right)^2$$

$$\rho_n = \frac{f_{cu}}{F_y}$$

$$\rho = \frac{0.4 \cdot f_{cu}}{0.95 \cdot F_y}$$

To calculate the nominal moment capacity M_n, use F_y to replace $0.95F_y$ and f_{cu} to replace $0.4f_{cu}$, and use ρ_n to replace ρ in Appendix Figure D-3. The suggested wall thickness of steel tube is the same as the one for axial capacity.

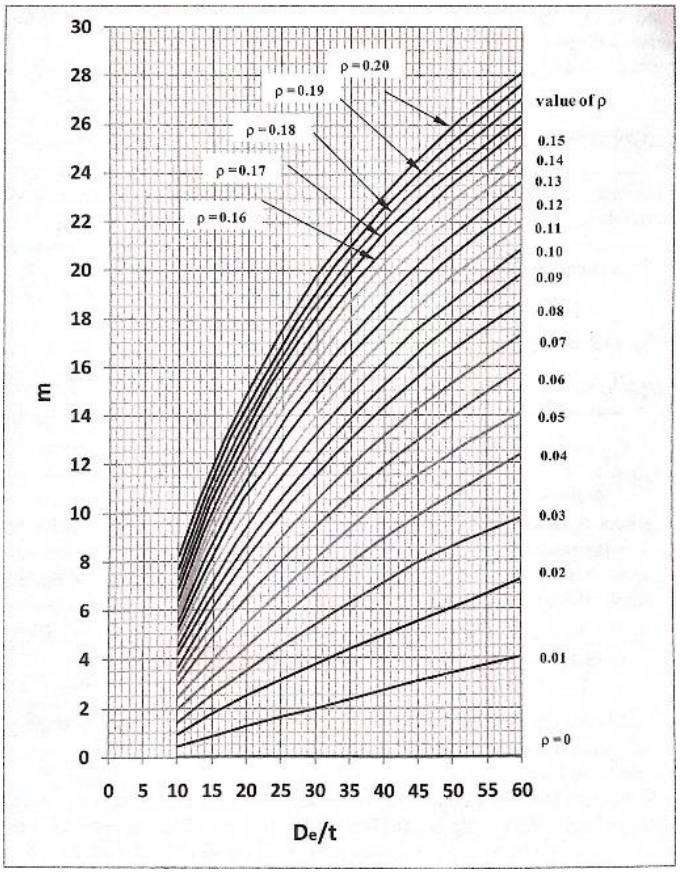

Appendix Figure D-3: The chart to determine parameter m [125]

AF interaction:

$$M_{rx} = \max\left[P_r \cdot (0.03 \cdot D_e), M_x\right] \le M_c \qquad \textit{(AEq. D-24)}$$

$$M_{ry} = \max\left[P_r \cdot (0.03 \cdot D_e), M_y\right] \le M_c \qquad \textit{(AEq. D-25)}$$

$$P_r \le \frac{1}{\frac{1}{P_x}+\frac{1}{P_y}-\frac{1}{P_{ax}}} \qquad \textbf{(AEq. D-26)}$$

where,

$$P_x = P_{sc}\cdot\left[K_1-\left(K_1-K_{2x}-4\cdot K_{3x}\right)\cdot\frac{M_{rx}}{M_c}-4\cdot K_{3x}\cdot\left(\frac{M_{rx}}{M_c}\right)^2\right]$$

$$P_y = P_{sc}\cdot\left[K_1-\left(K_1-K_{2y}-4\cdot K_{3y}\right)\cdot\frac{M_{ry}}{M_c}-4\cdot K_{3y}\cdot\left(\frac{M_{ry}}{M_c}\right)^2\right]$$

$$P_{ax} = K_1\cdot P_{sc}$$

$$K_{2x} = \left(0.9\cdot\alpha_c^2+0.2\right)\cdot\left[\frac{115-30\cdot\left(2\cdot\beta_x-1\right)\cdot\left(1.8-\alpha_c\right)-100\cdot\lambda}{50\cdot\left(2.1-\beta_x\right)}\right]$$

$$K_{2y} = \left(0.9\cdot\alpha_c^2+0.2\right)\cdot\left[\frac{115-30\cdot\left(2\cdot\beta_y-1\right)\cdot\left(1.8-\alpha_c\right)-100\cdot\lambda}{50\cdot\left(2.1-\beta_y\right)}\right]$$

$$K_{3x} = K_{30}+\frac{\left[\left(0.5\cdot\beta_x+0.4\right)\cdot\left(\alpha_c^2-0.5\right)+0.15\right]\cdot\lambda}{1+\lambda^3}$$

$$K_{3y} = K_{30}+\frac{\left[\left(0.5\cdot\beta_y+0.4\right)\cdot\left(\alpha_c^2-0.5\right)+0.15\right]\cdot\lambda}{1+\lambda^3}$$

$$K_{30} = 0.04-\frac{\alpha_c}{15}\ge 0$$

β_i = the ratio of the smaller to the larger of the two end moments about the i axis ($i = x, y$). It is positive for single curvature bending; if there are transverse loads, 1.0 can be used as a conservative estimation.

M_i = maximum moment at two ends about i axis ($i = x, y$), k-in.

P_r = required compressive strength, kips

P_{sc} = available section compressive strength, kips

M_r = required flexural strength, k-in.

M_c = available flexural strength, k-in.

x = subscript relating symbol to x- x axis bending

y = subscript relating symbol to y- y axis bending

λ = slenderness of CCFT column

α_c = concrete contribution factor

D_e = outer diameter of the steel tube, in.

$m(\rho)$ = function m of ρ

$m(\rho_n)$ = function m of ρ_n

For uniaxial bending, if the out of plane displacements at both ends are limited, P_y and P_{ax} can be taken as 0, and the corresponding limits on them can be removed.

D.4 Eurocode 4 – European code

Eurocode 4 considers the length effect on the column axial capacity by adopting a reduction factor χ based on the column slenderness. The reduction factor χ is determined by one of the two curves in Appendix Figure D-4 depending on the ratio of reinforcing. To calculate the CFT column slenderness, an effective stiffness will be introduced. Eurocode 4 also doesn't

supply specific design formulae for the flexural strength of CFTs, and prefers to use the rigid-plastic theory. So the design formulae introduced above for both AISC and AS5100 are applicable. Eurocode 4 uses the characteristic cylinder strength of concrete at 28 days f_c' and nominal yield strength of steel F_y to calculate the nominal capacities. While the same formulae but the design material strengths of f_c'/γ_c and F_y/γ_s are used to calculate the design capacities, where $\gamma_c = 1.5$ and $\gamma_s = 1.0$.

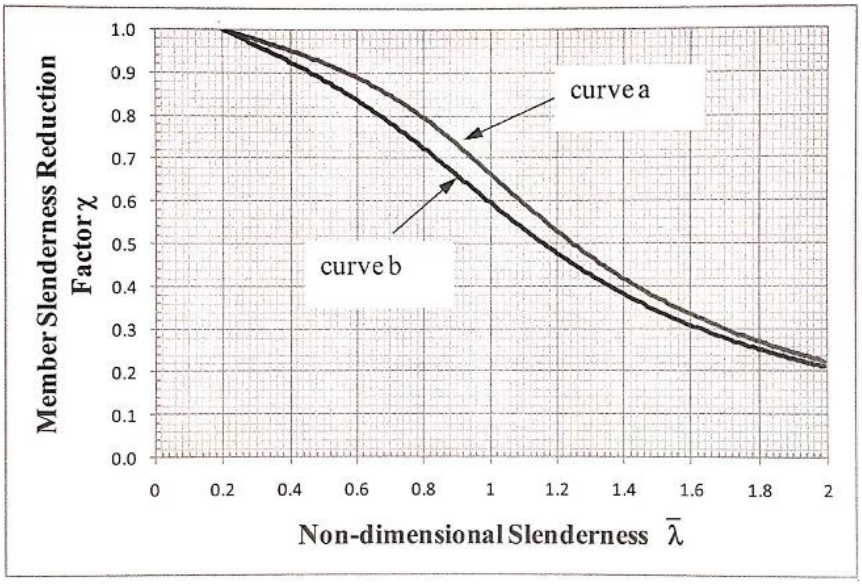

Appendix Figure D-4: Column slenderness reduction factor for Eurocode 4 [125]

Axial capacity:

The same calculation procedures for P_{sn} and P_{sc} are used as AS5100 except that different material strengths are used (f_c' and f_c'/γ_c for concrete; F_y and F_y/γ_s for steel), and a different effective stiffness is defined for the composite section by (AEq. D-27. And the design capacities P_n and P_c are calculated as: $P_n = \chi P_{sn}$ and $P_c = \chi P_{sc}$, where the

slenderness reduction factor χ is determined in Appendix Figure D-4. Curve a is used for the CFST members with the ratio of reinforcing A_{sr}/A_c less than 3%, whereas curve b is used for the ratio A_{sr}/A_c between 3% and 6%, where A_{sr} is the area of reinforcing, and A_c is the area of concrete.

$$EI_{eff} = E_s \cdot I_s + 0.6 \cdot E_c \cdot I_c \qquad \textbf{(AEq. D-27)}$$

The same limit ratio of overall diameter to thickness (d/t) is suggested as in AS5100: $d/t \leq 3067/F_y$ (unit of F_y is ksi).

Flexural capacity:

The design method in either AISC or AS5100 can be used. In this section, another method proposed by Bruneau and Marson is introduced, which is mainly based on the equilibrium diagram shown in Appendix Figure D-5 [126].

Nominal moment capacity:

$$M_n = C_r \cdot e + C_r' \cdot e' \qquad \textbf{(AEq. D-28)}$$

Design moment capacity:

$$M_c = \frac{1}{\gamma_s} \cdot C_r \cdot e + \frac{1}{\gamma_c} \cdot C_r' \cdot e' \qquad \textbf{(AEq. D-29)}$$

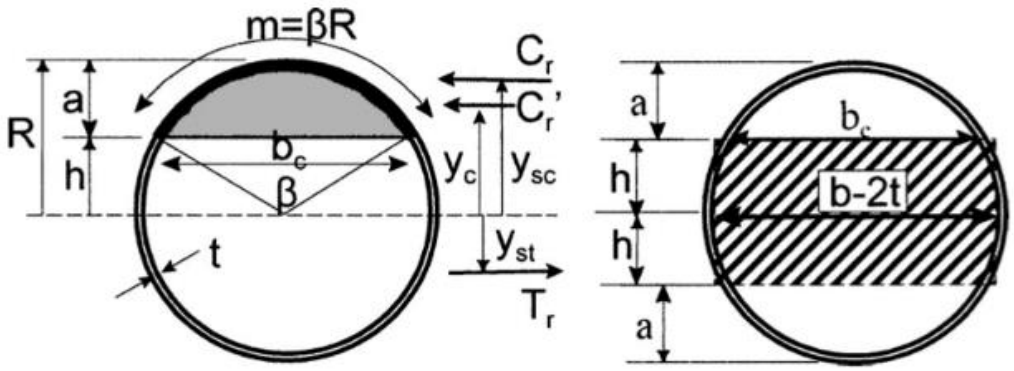

Appendix Figure D-5: Free-body diagrams used to develop flexural strength equations for CCFTs [126]

where,

$$C_r = F_y \cdot m \cdot t$$

$$C_r' = \left[\frac{\beta \cdot d^2}{8} - \frac{b_c}{2} \cdot \left(\frac{d}{2} - a\right)\right] \cdot f_c'$$

$$e = y_{st} + y_{sc} = b_c \cdot \left[\frac{1}{(2 \cdot \pi - \beta)} + \frac{1}{\beta}\right]$$

$$e' = y_{st} + y_c = b_c \cdot \left[\frac{1}{(2 \cdot \pi - \beta)} + \frac{b_c^2}{1.5 \cdot \beta \cdot d^2 - 6 \cdot b_c \cdot (0.5 \cdot d - a)}\right]$$

$$m = \frac{\beta \cdot d}{2}$$

$$a = \frac{b_c}{2} \cdot \tan\left(\frac{\beta}{4}\right)$$

$$b_c = d \cdot \sin\left(\frac{\beta}{2}\right)$$

β = the solution of the following closed-form equation:

$$\beta = \frac{A_s \cdot F_y + 0.25 \cdot d^2 \cdot f_c^{'} \cdot \left[\sin\left(\beta/2\right) - \sin^2\left(\beta/2\right) \cdot \tan\left(\beta/4\right) \right]}{\left(0.125 \cdot d^2 \cdot f_c^{'} + d \cdot t \cdot F_y\right)}$$

Alternatively, using an approximate geometry method, in which the contribution of the concrete with a rectangular section of height $2h$ is subtracted from the plastic moment of the entire section (Appendix Figure D-5). Then a conservative moment capacity is given as:

Nominal moment capacity:

$$M_n = \left(Z - 2 \cdot t \cdot h^2\right) \cdot F_y + \left[\frac{2}{5} \cdot \left(0.5 \cdot d - t\right)^3 - \left(0.5 \cdot d - t\right) \cdot h^2 \right] \cdot f_c^{'} \qquad \textbf{(AEq. D-30)}$$

Design moment capacity:

$$M_c = \left(Z - 2 \cdot t \cdot h^2\right) \cdot \frac{F_y}{\gamma_s} + \left[\frac{2}{5} \cdot \left(0.5 \cdot d - t\right)^3 - \left(0.5 \cdot d - t\right) \cdot h^2 \right] \cdot \frac{f_c^{'}}{\gamma_c} \qquad \textbf{(AEq. D-31)}$$

where,

$$Z = \frac{d^3}{6} - \frac{\left(d - 2 \cdot t\right)^3}{6}$$

$$h = \frac{A_c \cdot f_c^{'}}{2 \cdot d \cdot f_c^{'} + 4 \cdot t \cdot \left(2 \cdot F_y - f_c^{'}\right)}$$

$$A_c = \frac{\pi}{4} \cdot \left(d - 2 \cdot t\right)^2$$

F_y = normal yield strength, ksi.

f_c' = characteristic compressive cylinder strength of concrete at 28 days, ksi.

E_s = elastic Young's modulus of steel tube, ksi.

E_c = elastic Young's modulus of infill concrete, ksi.

I_s = moment of inertia of steel tube, $in.^4$

I_c = moment of inertia of infill concrete, $in.^4$

d = outer diameter of circular steel tube, in.

t = wall thickness of the steel tube, in.

AF interaction:

The anchor points $A, B, C, and\ D$ of the column interaction curve for CCFTs in Appendix Figure D-6 are defined by Eurocode 4 as follows:

- Point A (0, P_{sc})
- Point B (M_c, 0)
- Point C (M_c, $f_c' A_c/\gamma_c$)
- Point D (M_{max}, $0.5 f_c' A_c/\gamma_c$)

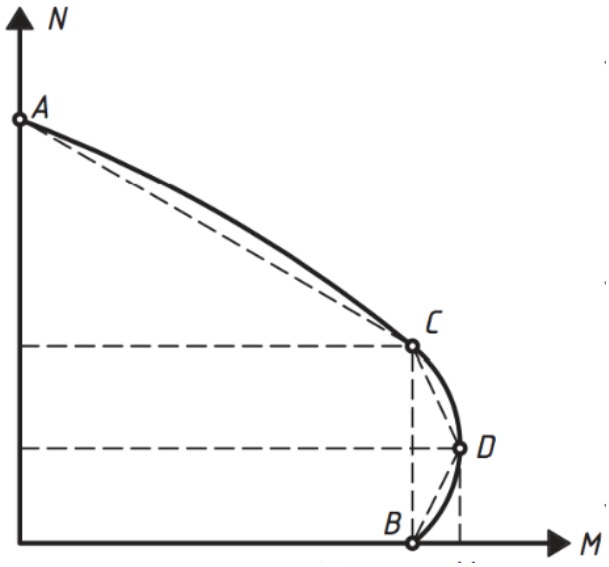

Appendix Figure D-6: Column interaction curve in Eurocode 4 for CCFT

Assume the neural axis at Point D is coincide with centroid of the CCFT section. So the angle β at point D is equal to π, and the M_{max} can be taken as:

$$M_{\max} = \frac{F_y}{\gamma_s} \cdot d^2 \cdot t + \frac{5}{24} \cdot \frac{f_c^{'}}{\gamma_c} \cdot d^3 \qquad \textbf{(AEq. D-32)}$$

Then the interaction curve can be written as follows:

For $P_r \geq \frac{A_c \cdot f_c^{'}}{\gamma_r}$,

$$M_{pl,N} = \frac{P_{sc} - P_r}{P_r - A_c \cdot f_c^{'} / \gamma_c} \cdot M_c \qquad \textbf{(AEq. D-33)}$$

For $\frac{A_c \cdot f_c^{'}}{2 \cdot \gamma_r} \leq P_r \leq \frac{A_c \cdot f_c^{'}}{\gamma_r}$,

$$M_{pl,N} = M_c + \frac{A_c \cdot f_c^{'} / \gamma_c - P_r}{0.5 \cdot A_c \cdot f_c^{'} / \gamma_c} \cdot \left(M_{\max} - M_c\right) \qquad \textbf{(AEq. D-34)}$$

For $P_r \le \dfrac{A_c \cdot f_c^{'}}{2 \cdot \gamma_r}$,

$$M_{pl,N} = M_c + \frac{P_r}{0.5 \cdot A_c \cdot f_c^{'} / \gamma_c} \cdot \left(M_{\max} - M_c \right) \qquad \textbf{(AEq. D-35)}$$

It requires that:

$$\begin{cases} \max\left(M_{2nd,x}, M_{2nd,y} \right) \le \alpha_m \cdot M_{pl,N} \\ \dfrac{M_{2nd,x} + M_{2nd,y}}{M_{pl,N}} \le 1.0 \end{cases} \qquad \textbf{(AEq. D-36)}$$

where,

$$M_{2nd,i} = K_{1,i} \cdot M_{r,i} + K_2 \cdot P_r \cdot e_0$$

$$K_{1,i} = \frac{\mu_i}{1 - P_r / N_{cr}} \ge 1.0$$

$$K_2 = \frac{1}{1 - P_r / N_{cr}}$$

$$N_{cr} = \frac{\pi^2 \cdot 0.9 \cdot \left(E_s \cdot I_s + 0.5 \cdot E_c \cdot I_c \right)}{L^2}$$

$$e_0 = \begin{cases} L/300 & for \ \ A_{sr} / A_c \le 3\% \\ L/200 & for \ \ 3\% \le A_{sr} / A_c \le 6\% \end{cases}$$

$$\mu_i = \begin{cases} 0.66 + 0.44 \cdot \dfrac{M_{2,i}}{M_{1,i}} \ge 0.44 & \textit{for members subject to end moments only} \\ 1.0 & \textit{for members with transverse loads} \end{cases}$$

$M_{2nd,i}$ = maximum moment at two ends about i axis ($i = x, y$) including 2nd order

effect, k-in.

$M_{r,i}$ = maximum moment at two ends about i axis ($i = x, y$), k-in.

M_c = available flexural strength, k-in.

$M_{1,i}$, $M_{2,i}$ = end moments with $|M_{1,i}| \geq |M_{2,i}|$ ($i = x, y$), k-in.

P_r = required compressive strength, kips

P_{sc} = available section compressive strength, kips

L = column length, in.

A_{sr} = area of reinforcement, $in.^2$

A_c = area of infill concrete, $in.^2$

α_m = 0.9 for steel with yield strength F_y between 36 to 50 ksi.

= 0.8 for steel with yield strength F_y between 60 to 67 ksi.

x = subscript relating symbol to x- x axis bending

y = subscript relating symbol to y- y axis bending

D.5 DBJ13-51 – Chinese code

In the Chinese Code DBJ13-51, the CFST section axial capacity is calculated by introducing an equivalent section area A_{sc} and an equivalent section strength f_{sc}. A stability factor φ is used to consider the slenderness effect of the column. The stability factor φ can be determined by the curves in Appendix Figure D-7 which are classified based on steel ratio α_s and material strengths F_y and f_{ck}. The ultimate moment capacity defined in DBJ13-51 is based on the

section curvature. Han *et al*. believes that when the extreme fiber strain of the CFST section reaches 0.01, the corresponding moment can be regarded as the ultimate moment capacity [122, 127]. To calculate design capacities for both compression and bending, the modified material strengths F_y/γ_s and f_{ck}/γ_c are used, where $\gamma_s = 1.12$ and $\gamma_c = 1.4$.

Axial capacity:

Nominal section axial capacity:

$$P_{sn} = f_{sc} \cdot A_{sc} \qquad \textit{(AEq. D-37)}$$

Nominal member axial capacity:

$$P_n = \varphi \cdot P_{sn} \qquad \textit{(AEq. D-38)}$$

Design section axial capacity:

$$P_{sc} = function\left(\frac{F_y}{\gamma_s}, \frac{f_{ck}}{\gamma_c}\right) \qquad \textit{(AEq. D-39)}$$

Design member axial capacity:

$$P_c = \varphi \cdot P_{sc} \qquad \textit{(AEq. D-40)}$$

where,

$$f_{sc} = \left(1.14 + 1.02 \cdot \xi\right) \cdot f_{ck}$$

$$\xi = \frac{A_s \cdot F_y}{A_c \cdot f_{ck}}$$

$$\xi_0 = \frac{A_s \cdot \left(F_y / \gamma_s\right)}{A_c \cdot \left(f_{ck} / \gamma_c\right)}$$

ξ = nominal constraining factor

ξ_0 = design constraining factor, which is used to replace ξ to get design values

$A_{sc} = A_s + A_c$

φ = stability factor, which is determined by Appendix Figure D-7. The corresponding factor α_s and slenderness λ are calculated as follows:

$$\alpha_s = A_s / A_c \qquad \& \qquad \lambda = 4 \cdot L / d$$

F_y = normal yield strength, ksi

f_{ck} = characteristic strength of concrete given in GB50010 2002, ksi.

A_s = area of circular steel tube, $in.^2$

A_c = area of infill concrete, $in.^2$

d = outer diameter of circular steel tube, in.

L = the length of column, in.

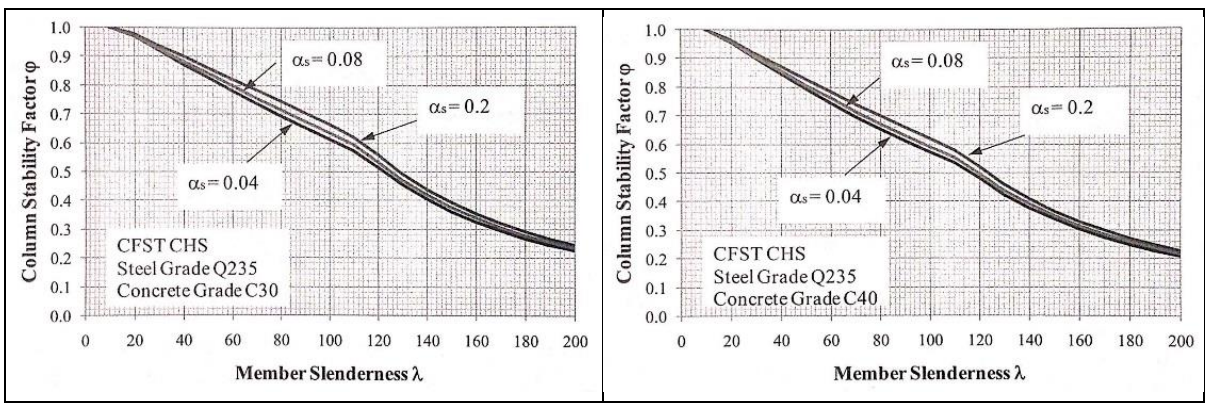

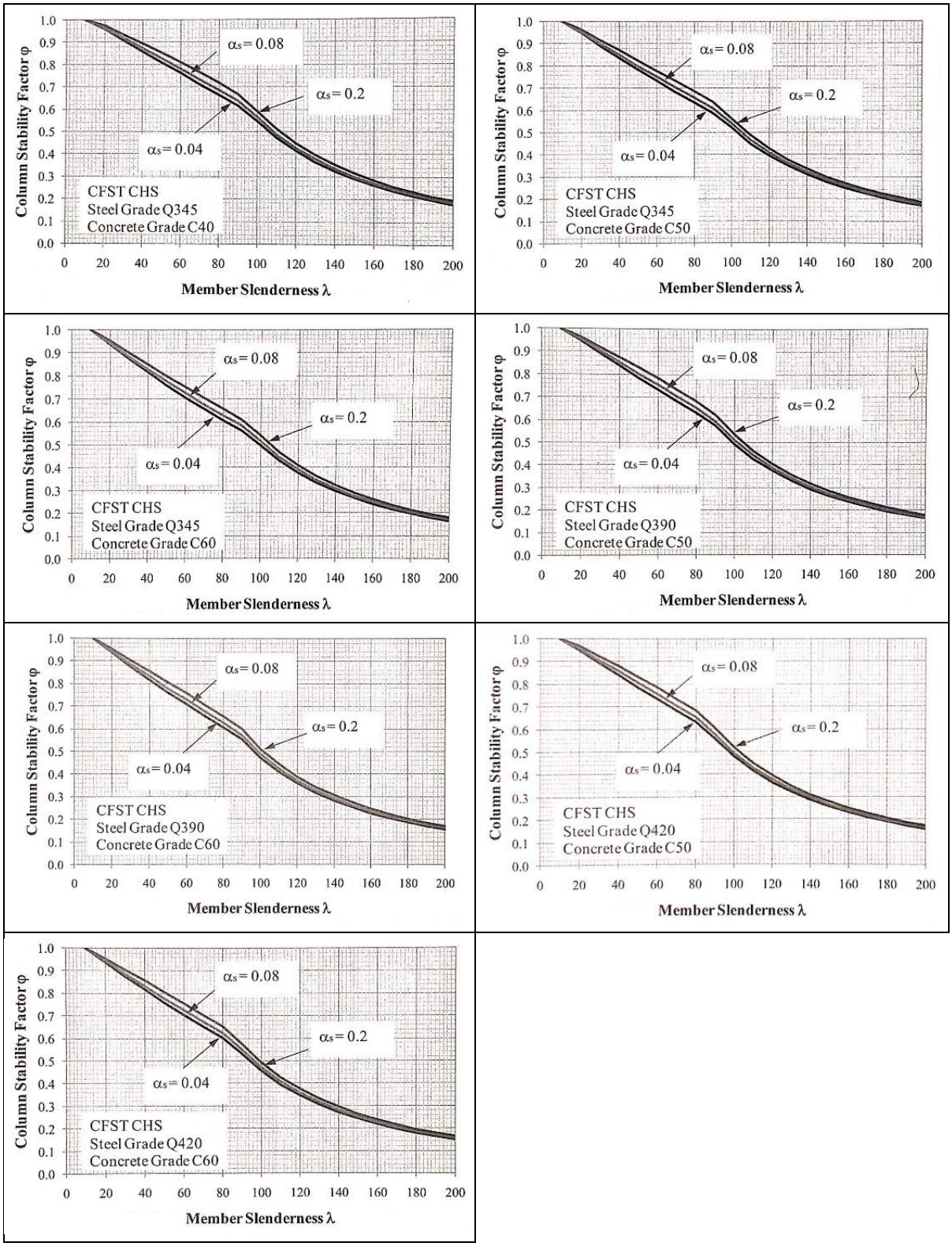

Appendix Figure D-7: Stability factors φ in DBJ13-51

Flexural capacity:

Nominal moment capacity:

$$M_n = \gamma_m \cdot W_{sc} \cdot f_{sc} \qquad \textit{(AEq. D-41)}$$

Design moment capacity:

$$M_c = function\left(\frac{F_y}{\gamma_s}, \frac{f_{ck}}{\gamma_c}\right) \qquad \textit{(AEq. D-42)}$$

where,

$$\gamma_m = 1.1 + 0.48 \cdot \ln(\xi + 0.1)$$

$$W_{sc} = \frac{\pi \cdot d^3}{32}$$

The above design formulae are based on the assumption that the local buckling will not occur. The suggested limit ratio of overall diameter to thickness (d/t) by DBJ13-51 is: $d/t \leq 5112/F_y$ (unit of F_y is ksi).

AF interaction:

Appendix Figure D-8 and Appendix Figure D-9 represent the interaction diagrams in DBJ13-51 for both section capacity and member capacity, respectively. Different from the linear interaction diagrams in AISC and Eurocode, a nonlinear relationship between anchor point B and C is adopted. The detailed design procedures are introduced as follows.

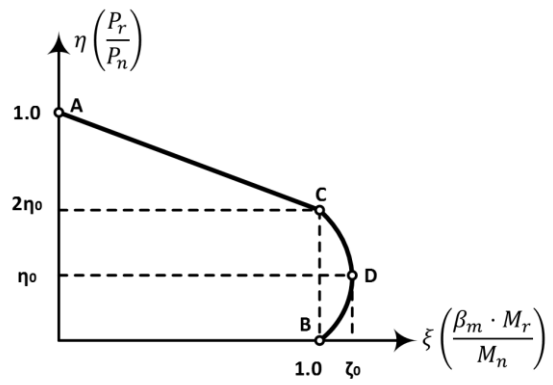

Appendix Figure D-8: Interaction diagram for section capacity in DBJ13-51

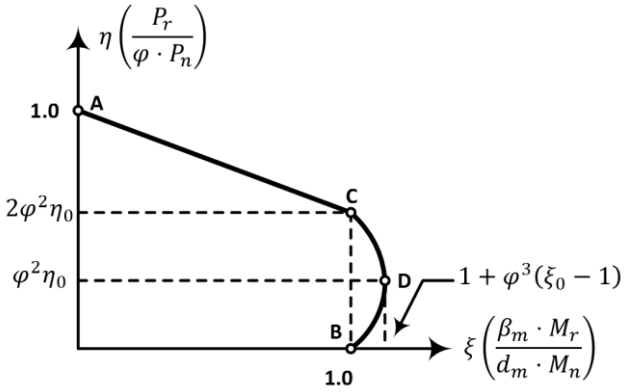

Appendix Figure D-9: Interaction diagram for member capacity in DBJ13-51

For the interaction diagram for member capacity, the anchor points are defined as follows:

- Point A (0, 1.0)
- Point B (1.0, 0)
- Point C (1.0, $2\varphi^2\eta_0$)
- Point D ($1+\varphi^3(\zeta-1)$, $\varphi^2\eta_0$)

Then the interaction curve can be written as follows:

For $\frac{P_r}{P_c} \geq 2\cdot\varphi^2\cdot\eta_0$, $\frac{P_r}{P_c}+\frac{a\cdot\beta_m\cdot M_r}{d_m\cdot M_c}\leq 1.0$ ***(AEq. D-43)***

For $\frac{P_r}{P_c} < 2\cdot\varphi^2\cdot\eta_0$, $-b\cdot\left(\frac{P_r}{P_c}\right)^2 - c\cdot\frac{P_r}{P_c}+\frac{\beta_m\cdot M_r}{d_m\cdot M_c}\leq 1.0$ ***(AEq. D-44)***

where,

$$a = 1 - 2 \cdot \varphi^2 \cdot \eta_0$$

$$b = \frac{1 - \zeta}{\varphi \cdot \eta_0^2}$$

$$c = \frac{2 \cdot \varphi \cdot (\zeta - 1)}{\eta_0}$$

$$\zeta = 1 + 0.18 \cdot \xi^{-1.15}$$

$$\eta_0 = \begin{cases} 0.5 - 0.2445 \cdot \xi & \text{for } \xi \le 0.4 \\ 0.1 + 0.14 \cdot \xi^{-0.84} & \text{for } \xi > 0.4 \end{cases}$$

$$\beta_m = \begin{cases} 0.65 + 0.35 \cdot \dfrac{M_2}{M_1} & \textit{for members subject to end moments only} \\ 1.0 & \textit{for members with transverse loads} \end{cases}$$

$$d_m = 1 - 0.4 \cdot \frac{P_r}{P_E}$$

$$P_E = \frac{\pi^2 \cdot E_{sc} \cdot A_{sc}}{\lambda^2}$$

$$E_{sc} = f_{scp} / \varepsilon_{scp}$$

$$f_{scp} = \begin{cases} \left[0.192 \cdot \left(\dfrac{F_y}{34.1} \right) + 0.488 \right] \cdot f_{scy} & \textit{for unit of ksi} \\ \left[0.192 \cdot \left(\dfrac{F_y}{235} \right) + 0.488 \right] \cdot f_{scy} & \textit{for unit of MPa} \end{cases}$$

$$f_{scy} = \left(1.14 + 1.02 \cdot \xi\right) \cdot \frac{f_{ck}}{\gamma_c}$$

$$\varepsilon_{scp} = \begin{cases} 2.2425 \cdot 10^{-5} \cdot F_y & for\ unit\ of\ ksi \\ 3.25 \cdot 10^{-6} \cdot F_y & for\ unit\ of\ MPa \end{cases}$$

P_r = required compressive strength, kips

P_c = available member compressive strength, kips

M_r = required flexural strength, k-in.

M_c = available flexural strength, k-in.

P_E = elastic buckling load, kips

M_1, M_2 = end moments with $|M_1| > |M_2|$. The ratio of M_1/M_2 is positive for single curvature bending, k-in.

ξ = constraining factor defined in the previous section for axial capacity

β_m = equivalent moment factor specified in GB50017(2003)

d_m = second-order effect factor

In order to get an interaction diagram for section capacity, factor φ and d_m should be set to zero. For a uniaxial bending with axial loading case, if the out of plan buckling is not prevented by enough bracing, the following requirement should be met:

$$\frac{P_r}{P_c} + \frac{\beta_m \cdot M_r}{1.4 \cdot M_c} \le 1.0 \qquad \textbf{\textit{(AEq. D-45)}}$$

For biaxial bending plus axial loading case, only the interaction between two moments is considered. The axial loading is not involved directly in the interaction relationship, its effect is considered by increasing the bending contribution using the following equation:

$$\left(\frac{M_{rx}}{M_c}\right)^{1.8}+\left(\frac{M_{ry}}{M_c}\right)^{1.8}\le 1.0 \qquad \textbf{(AEq. D-46)}$$

The effectiveness of this equation is not very clear. It seems that this interaction relationship will be conservative for larger moments with small compressive force; and un-conservative for small moments with large compressive force. It should be used carefully.

D.6 Example for comparison among different codes

In this section, an example for a CCFT column under axial force and uniaxial bending is to be introduced to supply a comparison among different codes for calculating the CCFT column capacities. As discussed above, different codes use different concrete properties to determine the CCFT column capacities. These properties are tested based on the shapes and sizes of specimen, or test methods. Appendix Table D-3 summarizes some standard strengths of concrete. Appendix Table D-4 compares the different effective column length factors adopted by different codes. From Appendix Table D-4, one can notice that the values used in AISC are most close to the theoretical values, and the values used by other standards are more

conservative. Appendix Table D-5 summarizes the design concepts and the corresponding design factors adopted by different codes. Most codes consider material design factor for each material to calculate the design capacities. On the other hand, AISC and AS5100 obtain the design capacity by using one capacity factor to deduct the nominal capacity.

Appendix Table D-3: Material Properties of Concrete in Different Codes [122]

Standard	Characteristic compressive cylinder strength at 28 days f'_c (ksi)	Standard compressive strength f_{ck} (ksi)	Design compressive strength f_c (ksi)	Standard tensile strength f_{tk} (ksi)	Tensile strength f_t (ksi)
AISC	3.05	NA	NA	NA	NA
	4.06				
	5.08				
	5.80				
	7.25				
AS5100	3.63	NA	NA	0.29	NA
	4.64			0.33	
	5.80			0.36	
	7.25			0.41	
	9.43			0.46	
BS5400	NA	2.90	1.93	NA	0.16
		3.63	2.42		0.17
		4.35	2.90		0.19
		5.80	3.87		0.22
		7.25	4.83		0.25
		8.70	5.80		0.28
DBJ13-51	NA	2.90	2.07	0.29	0.20
		3.92	2.77	0.35	0.25
		4.64	3.35	0.38	0.28
		5.66	3.99	0.42	0.29
		6.53	4.61	0.44	0.30
		7.25	5.21	0.45	0.32
Eurocode 4	2.90	NA	1.93	0.22	0.15
	3.63		2.42	0.26	0.17
	4.35		2.90	0.29	0.19

	5.80		3.87	0.36	0.25
	7.25		4.83	0.42	0.28
	8.70		5.80	0.45	0.30

Appendix Table D-4: Effective Column Length Factor K Values in Different Codes

End Condition	Theoretical	AISC	AS5100	BS5400	Eurocode 4
Fixed-Fixed	0.5	0.65	0.7	0.7	0.7
Fixed-Pinned	0.7	0.8	0.85	0.85	0.85
Pinned-Pinned	1.0	1.0	1.0	1.0	1.0
Fixed-Slide	1.0	1.2	1.2	1.5	1.2
Fixed-Free	2.0	2.1	2.2	2.0	2.2
Pinned-Slide	2.0	2.0	2.2	2.0	2.2

Appendix Table D-5: Summary of Design Factors for Load, Material Strength and Capacity in Different Codes [122]

Standard	Criterion	Load factors		Material factors		Capacity factors
		Live	Dead	γ_c	γ_s	
AISC	$S \leq \phi R_n$	1.6	1.2	NA	NA	• 0.9 on capacity in bending; • 0.75 on capacity in compression; • 0.95 on concrete capacity in compression.
AS5100	$S \leq \phi R_n$	1.5	1.2	NA	NA	• 0.9 on capacity in bending; • 0.9 on steel capacity in compression; • 0.6 on concrete capacity in compression.
BS5400	$S \leq R_n/\gamma$	1.5	1.2	1.5	1.05	NA
Eurocode 4	$S \leq R_d$	1.4	1.2	1.4	1.12	NA
DBJ13-51	$\gamma_0 S \leq R_u$	1.5	1.1	1.5	1.0	NA
where, S is the design effect; R_n is the nominal resistance; R_d is the design resistance; R_u is the ultimate resistance; ϕ and γ are the design factors; and γ_0 is the building important factor.						

In the following example, concrete with the same strength grade C40 will be applied for all specifications, which presents that the characteristic compressive cube strength at 28 days is 40MPa or 5.8ksi. Generally speaking, a 5% to 25% reduction of the characteristic compressive cube strength at 28 days is expected for the characteristic compressive cylinder strength at 28 days. A factor of 1.25 is used to convert the compressive cube strength to the cylinder strength, i.e. $f_{cu} = 1.25f_c'$. For AISC, AS5100, and Eurocode 4, $f_c' = 4.64ksi$ is used; for BS5400, $f_{cu} = 5.8ksi$ is used; and for DBJ13-51, $f_{ck} = 3.89ksi$ is used, which is given by GB50010 (2010) associated to grade C40 concrete.

Material information:

- Concrete: C40 concrete - $f_c' = 4.64ksi$, $f_{cu} = 5.8ksi$, and $f_{ck} = 3.89ksi$.
- Steel: A572 Gr.50 - $F_y = 50ksi$

Dimension information:

- Column length: $L = 14ft$
- Outer diameter of circular steel tube: $D = 24in$
- Wall thickness of circular steel tube: $t = 1.375in$

Assumptions:

- Two ends condition is assumed to be Pinned-Pinned;

- A double curvature is assumed for column with two equal end moments;
- Out of plane unbraced length is also column length L, which is the same as the in plane unbraced length;
- Eccentricity is assumed to be zero: $e = 0$.

Results:

The section capacities and member capacities are listed in Appendix Table D-6 for different codes. And the axial-flexural interaction diagrams on design level given by all specifications are shown in Appendix Figure D-10. The detailed calculation is presented in Appendix E.

Appendix Table D-6: Section and Member Capacities Given by Different Codes

CCFT 24*1.375	AISC	AS5100	BS5400	Eurocode 4	DBJ13-51
P_{sn} $(kips)$	6450	6847	6944	6928	8364
P_n $(kips)$	6225	6801	5777	6796	7862
P_{sc} $(kips)$	-	5439	7155	6086	7110
P_c $(kips)$	4668	5403	5953	5970	6683
M_n *(k-in.)*	37870	37730	38450	40860	43170
M_c *(k-in.)*	34080	33960	35020	37910	38920
where, P_{sn} is the nominal section axial capacity; P_n is the nominal member axial capacity; P_{sc} is the design section axial capacity; P_c is the design member axial capacity; M_n is the nominal flexural capacity; and M_c is the design flexural capacity.					

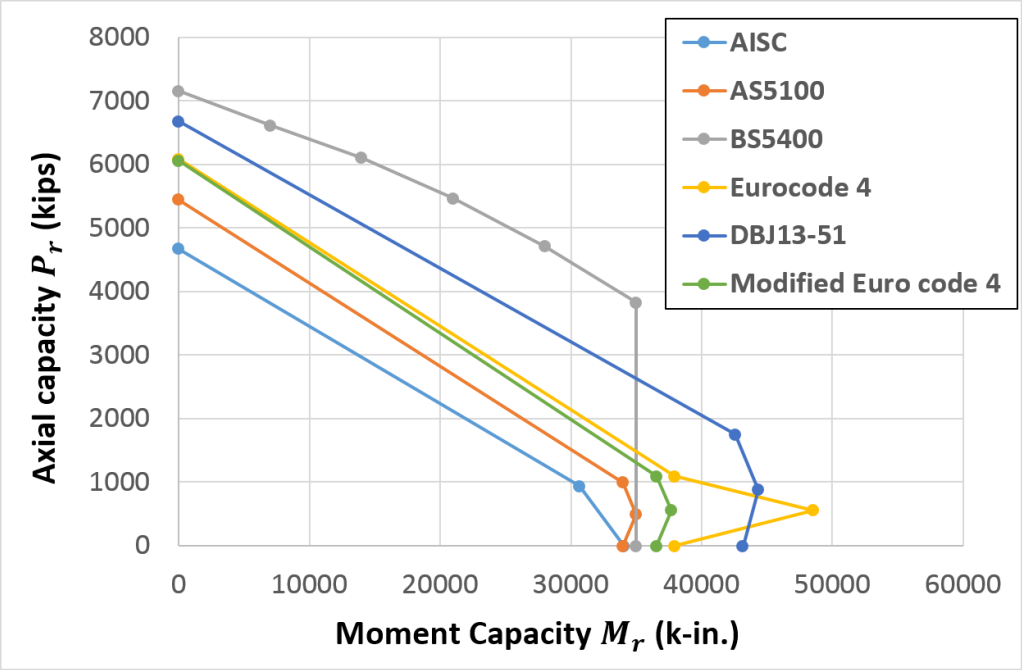

Appendix Figure D-10: Design AF interaction diagrams given by all codes

From Appendix Table D-6, there are some conclusions can be obtained. The following conclusions are based on the above example with a large steel wall thickness. Some of these conclusions may not stand for a thinner wall thickness.

1. First, the divergence of the moment capacity given by all codes is less than that of the axial capacity.
2. Secondly, AISC gives the most conservative design capacities, and DBJ13-51 gives the maximum design capacities.
3. Thirdly, for moment capacities, one part of difference comes from the application of different methods to calculate the plastic section capacity. The similar results indicate that each of these methods is effective to calculate the CCFT column flexural capacities.
4. Fourthly, except of DBJ13-51, all other standards give similar nominal section axial

capacities, however, quite different design member axial capacities. This indicates that different reduction degrees are considered by different codes due to slenderness effect and 2nd order effect.

5. Fifthly, when to calculate axial capacity, AISC doesn't consider the benefit of the increase of concrete compressive strength from steel tube confinement effect, so it gives a minimum value; however, other codes include this confinement effect in their calculation.
6. Sixthly, the design procedure in BS5400 gives a larger design section axial capacity than the nominal section capacity. This occurs when the ratio of circular steel tube wall thickness to outer diameter is large to cause that the modified concrete strength $0.45 * f_{cc}$ which is modified to consider the increase of strength due to circular steel tube confinement is much larger than the unconfined concrete strength f_{cu}. However, although the calculated design section capacity can be regarded to be valid if the confinement effect is considered, the effective range of this method in BS5400 to be applied should be checked carefully.
7. Seventhly, another notice about results from BS5400 is that for axial capacities it uses a relative large reduction from section capacity to the member capacity and a relative small reduction from nominal capacities to design capacities, which is the opposite situation for other standards.

Appendix Figure D-10 represents Axial-Flexural diagrams using the methods in all codes

mentioned above. In these curves, only the curve from AISC and DBJ13-51 has already consider the column slenderness effects for the axial capacity. All other curves are generated based on the design section axial capacity. And when these curves are used for design, additional modification on the required design loads should be executed to consider the reduction from column slenderness and 2nd order effects. From these curves design procedures introduced previously, one can find that although the method given by AISC is the most simplified, it supplies the minimum design capacities among all standards. Due to the thick steel wall thickness, too much increase of concrete strength is considered by BS5400 method. This causes that BS5400 supplies a highest axial capacity, but its effectiveness should be checked carefully. The curve for DBJ13-51 in Appendix Figure D-10 doesn't consider its nonlinear sections for simplification. It can be considered when the design equations are used. When the Bruneau and Marson model is adopted to calculate the plastic section capacity by Eurocode 4, an unreasonable region where the moment capacity is larger than M_c will occur (represented by the yellow lines). This is because the simplification in the Bruneau and Marson model overestimates the maximum moment capacity. It indicates that the Bruneau and Marson model is not workable for the AF interaction model in Eurocode 4 (but it can be workable for other AF interaction models, i.e. the model in AISC), although it is valid for deign under uniaxial bending (The values in Appendix Table D-6 for Eurocode 4 is calculated using the Bruneau and Marson model, and it seems to be reasonable to estimate the flexural capacity.) A modified AF interaction curve for Eurocode 4 is generated by utilizing the method introduced for AS5100. The values for this modified curve is not supplied in Appendix Table D-6. The

detailed information can be found in Appendix E.

Appendix E

Design Example of a CCFT Column under Uniaxial Bending by Using Different Design Codes

Method 1: AISC

Materials: concrete compressive strength: $fc' := 4.64 \ \ ksi$

steel yield strength: $Fy := 50 \ \ ksi$

steel elastic modulus: $Es := 29000 \ \ ksi$

Dimensions: circular steel tube outer diameter: $d := 24 \ \ in$

circular steel tube wall thickness: $t := 1.375 \ \ in$

column length: $L := 14 \cdot 12 = 168 \ \ in$

Assumptions: effective column length factor: $K := 1.0$

Calculate relevant properties:

cross area of steel tube: $As := \frac{\pi}{4} \cdot \left[d^2 - (d - 2 \cdot t)^2 \right] = 97.733 \ \ in^2$

cross area of concrete: $Ac := \frac{\pi}{4} \cdot (d - 2 \cdot t)^2 = 354.656 \ \ in^2$

concrete elastic modulus: $Ec := 57 \cdot \sqrt{fc' \cdot 1000} = 3.883 \times 10^3 \ \ ksi$

moment inertia of steel tube: $Is := \frac{\pi}{64} \cdot \left[d^4 - (d - 2 \cdot t)^4 \right] = 6.277 \times 10^3 \ \ in^4$

moment inertia of concrete: $Ic := \frac{\pi}{64} \cdot (d - 2 \cdot t)^4 = 1.001 \times 10^4 \ \ in^4$

Calculate axial capacity:

concrete contribution factor: $C3 := \min\left[0.6 + 2 \cdot \left(\frac{As}{Ac + As} \right), 0.9 \right] = 0.9$

CCFT column effective stiffness: $EIeff := Es \cdot Is + C3 \cdot Ec \cdot Ic = 2.17 \times 10^{8} \quad k \cdot in^{2}$

column elastic buckling capacity: $Pe := \frac{\pi^{2} \cdot EIeff}{(K \cdot L)^{2}} = 7.588 \times 10^{4} \quad kips$

nominal section axial capacity: $P0 := As \cdot Fy + 0.95 \cdot Ac \cdot fc' = 6.45 \times 10^{3} \quad kips$

column slenderness: $\lambda := \sqrt{\frac{P0}{Pe}} = 0.292 \quad \blacksquare < 1.5$

nominal member axial capacity: $Pn := 0.658^{\lambda^{2}} \cdot P0 = 6.225 \times 10^{3}$ kips

design member axial capacity: $Pc := 0.75 \cdot Pn = 4.668 \times 10^{3}$ kips

Calculate flexural capacity:

relevant parameters:

$rm := \frac{d - t}{2} = 11.313 \quad in \qquad h := d - 2 \cdot t = 21.25 \quad in$

$Kc := fc' \cdot h^{2} = 2.095 \times 10^{3} \quad kips \qquad Ks := Fy \cdot rm \cdot t = 777.734 \quad kips$

$\theta := \frac{0.026 \cdot Kc - 2 \cdot Ks}{0.0848 \cdot Kc} + \frac{\sqrt{(0.026 \cdot Kc + 2 \cdot Ks)^{2} + 0.857 \cdot Kc \cdot Ks}}{0.0848 \cdot Kc} = 2.792$

$Zs := \frac{d^{3} - h^{3}}{12} \cdot \left(\sin\left(\frac{\theta}{2}\right)\right)^{3} \cdot \left(\frac{\theta}{\theta - \sin(\theta)} + \frac{2 \cdot \pi - \theta}{2 \cdot \pi - \theta - \sin(2 \cdot \pi - \theta)}\right) = 689.998 \quad in^{3}$

$Zc := \frac{h^{3} \cdot \left(\sin\left(\frac{\theta}{2}\right)\right)^{3}}{6} = 1.527 \times 10^{3} \quad in^{3}$

nominal moment capacity: $Mn := Zs \cdot Fy + \frac{Zc \cdot (0.95 \cdot fc')}{2} = 3.787 \times 10^{4} \quad k \cdot in$

design moment capacity: $Mc := 0.9 \cdot Mn = 3.408 \times 10^{4} \quad k \cdot in$

Check steel tube wall thickness reqirement:

$\frac{d}{t} = 17.455$ ▮ < ▮ $0.15 \cdot \frac{Es}{Fy} = 87$ OK

Calculate anchor points for AF interaction diagram:

point 1 is at: (0, Pc) = (0, 4668)

point 2 is at: (Mc, 0) = (34080, 0)

point 3 is at: (0.9*Mc, 0.2*Pc) = (30672, 933.6)

Method 2: AS5100

Materials: concrete compressive strength: $fc' := 4.64 \ ksi$

steel yield strength: $Fy := 50 \ ksi$

steel elastic modulus: $Es := 29000 \ ksi$

Dimensions: circular steel tube outer diameter: $d := 24 \ in$

circular steel tube wall thickness: $t := 1.375 \ in$

column length: $L := 14 \cdot 12 = 168 \ in$

Assumptions: effective column length factor: $K := 1.0$

axial force eccentricity: $e := 0$

Calculate relevant properties:

cross area of steel tube: $As := \frac{\pi}{4} \cdot \left[d^2 - (d - 2 \cdot t)^2 \right] = 97.733 \ in^2$

cross area of concrete: $Ac := \frac{\pi}{4} \cdot (d - 2 \cdot t)^2 = 354.656 \ in^2$

concrete elastic modulus: $Ec := 57 \cdot \sqrt{fc' \cdot 1000} = 3.883 \times 10^3 \ ksi$

moment inertia of steel tube: $Is := \frac{\pi}{64} \cdot \left[d^4 - (d - 2 \cdot t)^4 \right] = 6.277 \times 10^3 \ in^4$

moment inertia of concrete: $Ic := \frac{\pi}{64} \cdot (d - 2 \cdot t)^4 = 1.001 \times 10^4 \ in^4$

Calculate axial capacity:

form factor is assumed to be 1.0, then $\alpha b := -1.0$

$\phi s := 0.9 \qquad \phi c := 0.6$

column effective stiffness: $EIeff := \phi s \cdot Es \cdot Is + \phi c \cdot Ec \cdot Ic = 1.871 \times 10^{8} \quad k \cdot in^2$

column elastic buckling capacity: $Pcr := \frac{\pi^2 \cdot EIeff}{(K \cdot L)^2} = 6.544 \times 10^{4} \quad kips$

$Ps := As \cdot Fy + Ac \cdot fc' = 6.532 \times 10^{3} \quad kips$

column slenderness: $\lambda r := \sqrt{\frac{Ps}{Pcr}} = 0.316 \quad < 0.5$

relevant parameters:

$$\eta 1 := \max\left[\left(4.9 - 18.5 \cdot \lambda r + 17 \cdot \lambda r^2\right) \cdot \left(1 - \frac{10 \cdot e}{d}\right), 0\right] = 0.752$$

$$\eta 2 := \min\left[0.25 \cdot (3 + 2 \cdot \lambda r) + \left[1 - \left[0.25 \cdot (3 + 2 \cdot \lambda r)\right]\right] \cdot \frac{10 \cdot e}{d}, 1.0\right] = 0.908$$

$$\lambda n := 90 \cdot \lambda r = 28.435$$

$$\alpha a := \frac{2100 \cdot (\lambda n - 13.5)}{\lambda n^2 - 15.3 \cdot \lambda n + 2050} = 12.941$$

$$\lambda := \lambda n + \alpha a \cdot \alpha b = 15.494$$

$$\eta := \max\left[0.00326 \cdot (\lambda - 13.5), 0\right] = 6.499 \times 10^{-3}$$

$$\xi := \frac{\left(\frac{\lambda}{90}\right)^2 + 1 + \eta}{2 \cdot \left(\frac{\lambda}{90}\right)^2} = 17.481$$

$$\alpha c := \xi \cdot \left[1 - \sqrt{1 - \left(\frac{90}{\xi \cdot \lambda}\right)^2}\right] = 0.993$$

nominal section axial capacity: $Psn := As\cdot\eta2\cdot Fy + Ac\cdot fc'\cdot\left(1+\eta1\cdot\frac{t}{d}\cdot\frac{Fy}{fc'}\right)$

$Psn = 6.847\times10^{3}$ kips

nominal member axial capacity: $Pn := \alpha c\cdot Psn = 6.801\times10^{3}$ kips

design section axial capacity: $Psc := As\cdot\eta2\cdot(\phi s\cdot Fy) + Ac\cdot(\phi c\cdot fc')\cdot\left(1+\eta1\cdot\frac{t}{d}\cdot\frac{Fy}{fc'}\right)$

$Psc = 5.439\times10^{3}$ kips

design member axial capacity: $Pc := \alpha c\cdot Psc = 5.403\times10^{3}$ kips

Calculate flexural capacity:

relevant parameters:

$rm := \frac{d-t}{2} = 11.313$ in $\qquad ri := \frac{d-2\cdot t}{2} = 10.625$ in

$$\gamma0 := \frac{\frac{\pi}{4}\cdot\frac{fc'\cdot ri^{2}}{Fy\cdot rm\cdot t}}{2+\frac{1}{2}\cdot\frac{fc'\cdot ri^{2}}{Fy\cdot rm\cdot t}} = 0.226$$

nominal moment capacity: $Mn := 4\cdot Fy\cdot t\cdot rm^{2}\cdot\cos(\gamma0) + \frac{2}{3}\cdot fc'\cdot ri^{3}\cdot(\cos(\gamma0))^{3}$

$Mn = 3.773\times10^{4}$ k·in

design moment capacity: $Mc := 0.9\cdot Mn = 3.396\times10^{4}$ k·in

Check steel tube wall thickness reqirement:

$\frac{d}{t} = 17.455$ ▮ < ▮ $\frac{3067}{Fy} = 61.34$ OK

Calculate anchor points for AF interaction diagram:

axial capacity at point C: $\phi c \cdot fc' \cdot Ac = 987.363 \quad kips$

axial capacity at point D: $0.5 \cdot (\phi c \cdot fc' \cdot Ac) = 493.682 \quad kips$

maximum moment capacity: $Mmax := 0.9 \cdot \left(4 \cdot Fy \cdot t \cdot rm^2 + \frac{2}{3} \cdot fc' \cdot ri^3\right) = 3.501 \times 10^4 \quad k \cdot in$

point A is at: (0, Psc) = (0, 5439)

point B is at: (Mc, 0) = (33960, 0)

point C is at: (Mc, ϕc*fc`*Ac) = (33960, 987.4)

point D is at: (Mmax, 0.5*ϕc*fc`*Ac) = (35010, 493.7)

Method 3: BS5400

Materials: concrete compressive strength: $fcu := 5.8 \quad ksi$

steel yield strength: $Fy := 50 \quad ksi$

steel elastic modulus: $Es := 29000 \quad ksi$

Dimensions: circular steel tube outer diameter: $De := 24 \quad in$

circular steel tube wall thickness: $t := 1.375 \quad in$

column length: $L := 14 \cdot 12 = 168 \quad in$

Assumptions: effective column length factor: $K := 1.0$

Calculate relevant properties:

cross area of steel tube: $As := \frac{\pi}{4} \cdot \left[De^2 - (De - 2 \cdot t)^2\right] = 97.733 \quad in^2$

cross area of concrete: $Ac := \frac{\pi}{4} \cdot (De - 2 \cdot t)^2 = 354.656 \quad in^2$

concrete elastic modulus: $Ec := 450 \cdot fcu = 2.61 \times 10^3 \quad ksi$

moment inertia of steel tube: $Is := \frac{\pi}{64} \cdot \left[De^4 - (De - 2 \cdot t)^4\right] = 6.277 \times 10^3 \quad in^4$

moment inertia of concrete: $Ic := \frac{\pi}{64}\cdot(De - 2\cdot t)^4 = 1.001\times 10^4 \quad in^4$

Calculate axial capacity:

column effective length: $Le := K\cdot L = 168 \quad in$

$\frac{Le}{De} = 7$ From figure 3.2, one can obtain: $C1 := 5.3$ $C2 := 0.82$

modified concrete strength: $fcc := fcu + C1\cdot\frac{t}{De}\cdot Fy = 20.982 \quad ksi$

modified steel strength: $fy' := C2\cdot Fy = 41 \quad ksi$

design section axial capacity: $Psc := 0.95\cdot fy'\cdot As + 0.45\cdot fcc\cdot Ac = 7.155\times 10^3 \quad kips$

nominal section axial capacity: $Psn := Fy\cdot As + fcu\cdot Ac = 6.944\times 10^3 \quad kips$

concrete contribution factor: $\alpha c := \frac{0.45\cdot fcc\cdot Ac}{Psc} = 0.468$ between 0.1 and 0.8, OK

Note that: the design procedure in BS5400 gives a larger design section axial capacity than the nominal section capacity. This occurs when the ratio of circular steel tube wall thickness to outer diameter is large to cause that the modified concrete strength 0.45*fcc which is modified to consider the increase of strength due to circular steel tube confinement is much larger than the unconfined concrete strength fcu. However, although the calculated design section capacity could be regarded to be valid if the confinement effect is considered, the effective range of this method in BS5400 to be applied should be carefully checked.

relevant parameters:

$r := \sqrt{\frac{Is}{As}} = 8.014 \quad in$ $\frac{2\cdot r}{De} = 0.668$

From Table 3-2, curve B is selected, then, $\alpha := 0.0045$

$Ie := \pi\sqrt{\frac{0.95\cdot Es\cdot Is + 0.45\cdot Es\cdot Ic}{Psc}} = 647.06 \quad in$

$\lambda := \frac{Le}{Ie} = 0.26$

$\eta := 75.5 \cdot \alpha \cdot (\lambda - 0.2) = 0.02$

slenderness reduction factor: $K1 := 0.5 \cdot \left[\left(1 + \frac{1+\eta}{\lambda^2} \right) - \sqrt{\left(1 + \frac{1+\eta}{\lambda^2} \right)^2 - \frac{4}{\lambda^2}} \right] = 0.979$

nominal member axial capacity: $Pn := 0.85 \cdot K1 \cdot Psn = 5.777 \times 10^3$ kips

design member axial capacity: $Pc := 0.85 \cdot K1 \cdot Psc = 5.953 \times 10^3$ kips

Check steel tube wall thickness requirement:

$t = 1.375$ in ▮ > ▮ $De \cdot \sqrt{\frac{Fy}{8 \cdot Es}} = 0.352$ in OK

Calculate flexural capacity:

relevant parameters:

$S := t^3 \cdot \left(\frac{De}{t} - 1 \right)^2 = 703.85$ in^3

for nominal moment capacity:

$\rho n := \frac{fcu}{Fy} = 0.116$ and $\frac{De}{t} = 17.455$

From figure 3.3, one can obtain: $mn := 9.25$

for design moment capacity:

$\rho := \frac{0.4 \cdot fcu}{0.9 \cdot Fy} = 0.052$ and $\frac{De}{t} = 17.455$

From figure 3.3, one can obtain: $mc := 4.75$

nominal moment capacity: $Mn := S \cdot Fy \cdot (1 + 0.01 \cdot mn) = 3.845 \times 10^4$ k·in

design moment capacity: $Mc := 0.95 \cdot S \cdot Fy \cdot (1 + 0.01 \cdot mc) = 3.502 \times 10^4$ k·in

Calculate anchor points for AF interaction diagram:

define 7 anchor points: point 1: (0, Psc) point 2: (0.2*Mc, P2)

point 3: (0.4*Mc, P3) point 4: (0.6*Mc, P4)

point 5: (0.8*Mc, P5) point 6: (Mc, P6)

point 7: (Mc, 0)

Assume double curvature in plane and equal moments at two ends, then, $\beta x := -1.0$

For uniaxial bending, out of plane moment Mry is assumed to be zero for simplification, and ignore the minimum required moment 0.03*Pr*De. Then Py becomes a constant defined as K1*Psc, and the axial capacity under arbitrary in plane moment is simplified to be Px.

relevant parameters:

$$K30 := \max\left[\left(0.04 - \frac{\alpha c}{15}\right), 0\right] = 8.8 \times 10^{-3}$$

$$K3x := K30 + \frac{\left[(0.5 \cdot \beta x + 0.4) \cdot \left(\alpha c^2 - 0.5\right) + 0.15\right] \cdot \lambda}{1 + \lambda^3} = 0.054$$

$$K2x := \left(0.9 \cdot \alpha c^2 + 0.2\right) \cdot \frac{115 - 30 \cdot (2 \cdot \beta x - 1) \cdot (1.8 - \alpha c) - 100 \cdot \lambda}{50 \cdot (2.1 - \beta x)} = 0.535$$

Calculate P2:

$$Mrx2 := 0.2 \cdot Mc = 7.004 \times 10^3 \quad k \cdot in$$

$$P2 := Psc \cdot \left[K1 - (K1 - K2x - 4 \cdot K3x) \cdot \frac{Mrx2}{Mc} - 4 \cdot K3x \cdot \left(\frac{Mrx2}{Mc}\right)^2\right] = 6.617 \times 10^3 \quad kips$$

Calculate P3:

$$Mrx3 := 0.4 \cdot Mc = 1.401 \times 10^4 \quad k \cdot in$$

$$P3 := Psc \cdot \left[K1 - (K1 - K2x - 4 \cdot K3x) \cdot \frac{Mrx3}{Mc} - 4 \cdot K3x \cdot \left(\frac{Mrx3}{Mc}\right)^2\right] = 6.107 \times 10^3 \quad kips$$

Calculate P4:

$$Mrx4 := 0.6 \cdot Mc = 2.101 \times 10^{4} \quad k \cdot in$$

$$P4 := Psc \cdot \left[K1 - (K1 - K2x - 4 \cdot K3x) \cdot \frac{Mrx4}{Mc} - 4 \cdot K3x \cdot \left(\frac{Mrx4}{Mc} \right)^{2} \right] = 5.472 \times 10^{3} \quad kips$$

Calculate P5:

$$Mrx5 := 0.8 \cdot Mc = 2.802 \times 10^{4} \quad k \cdot in$$

$$P5 := Psc \cdot \left[K1 - (K1 - K2x - 4 \cdot K3x) \cdot \frac{Mrx5}{Mc} - 4 \cdot K3x \cdot \left(\frac{Mrx5}{Mc} \right)^{2} \right] = 4.713 \times 10^{3} \quad kips$$

Calculate P6:

$$Mrx6 := 1 \cdot Mc = 3.502 \times 10^{4} \quad k \cdot in$$

$$P6 := Psc \cdot \left[K1 - (K1 - K2x - 4 \cdot K3x) \cdot \frac{Mrx6}{Mc} - 4 \cdot K3x \cdot \left(\frac{Mrx6}{Mc} \right)^{2} \right] = 3.83 \times 10^{3} \quad kips$$

The location of the 7 anchor points:

point 1: (0, 7155)

point 2: (7004, 6617)

point 3: (14010, 6107)

point 4: (21010, 5472)

point 5: (28020, 4713)

point 6: (35020, 3830)

point 7: (35020, 0)

Method 4: Eurocode 4

Materials: concrete compressive strength: $fc' := 4.64 \quad ksi$

steel yield strength: $Fy := 50 \quad ksi$

steel elastic modulus: $Es := 29000 \quad ksi$

Dimensions: circular steel tube outer diameter: $d := 24 \quad in$

circular steel tube wall thickness: $t := 1.375 \quad in$

column length: $L := 14 \cdot 12 = 168 \quad in$

Assumptions: effective column length factor: $K := 1.0$

axial force eccentricity: $e := 0$

Calculate relevant properties:

cross area of steel tube: $As := \frac{\pi}{4} \cdot \left[d^2 - (d - 2 \cdot t)^2 \right] = 97.733 \quad in^2$

cross area of concrete: $Ac := \frac{\pi}{4} \cdot (d - 2 \cdot t)^2 = 354.656 \quad in^2$

concrete elastic modulus: $Ec := 57 \cdot \sqrt{fc' \cdot 1000} = 3.883 \times 10^3 \quad ksi$

moment inertia of steel tube: $Is := \frac{\pi}{64} \cdot \left[d^4 - (d - 2 \cdot t)^4 \right] = 6.277 \times 10^3 \quad in^4$

moment inertia of concrete: $Ic := \frac{\pi}{64} \cdot (d - 2 \cdot t)^4 = 1.001 \times 10^4 \quad in^4$

Calculate axial capacity:

material design factors: $\gamma s := 1.0 \qquad \gamma c := 1.5$

column effective stiffness: $EIeff := Es \cdot Is + 0.6 \cdot Ec \cdot Ic = 2.053 \times 10^8 \quad k \cdot in^2$

column elastic buckling capacity: $Pcr := \frac{\pi^2 \cdot EIeff}{(K \cdot L)^2} = 7.181 \times 10^4 \quad kips$

$Ps := As \cdot Fy + Ac \cdot fc' = 6.532 \times 10^3 \quad kips$

column slenderness: $\lambda r := \sqrt{\frac{Ps}{Pcr}} = 0.302 \quad \blacksquare < 0.5$

relevant parameters:

$$\eta 1 := \max\left[\left(4.9 - 18.5 \cdot \lambda r + 17 \cdot \lambda r^2\right) \cdot \left(1 - \frac{10 \cdot e}{d}\right), 0 \right] = 0.867$$

$$\eta 2 := \min\left[0.25\cdot(3+2\cdot\lambda r)+\left[1-\left[0.25\cdot(3+2\cdot\lambda r)\right]\right]\cdot\frac{10\cdot e}{d},1.0\right] = 0.901$$

According to column slenderness λr and curve a in Figure 3.4, the reduction factor is obtained as:

$$\chi := 0.981$$

nominal section axial capacity: $Psn := As\cdot\eta 2\cdot Fy + Ac\cdot fc'\cdot\left(1+\eta 1\cdot\frac{t}{d}\cdot\frac{Fy}{fc'}\right)$

$$Psn = 6.928\times 10^{3} \quad \text{kips}$$

nominal member axial capacity: $Pn := \chi\cdot Psn = 6.796\times 10^{3}$ kips

design section axial capacity: $Psc := As\cdot\eta 2\cdot\left(\frac{Fy}{\gamma s}\right)+Ac\cdot\left(\frac{fc'}{\gamma c}\right)\cdot\left(1+\eta 1\cdot\frac{t}{d}\cdot\frac{Fy}{fc'}\right)$

$$Psc = 6.086\times 10^{3} \quad \text{kips}$$

design member axial capacity: $Pc := \chi\cdot Psc = 5.97\times 10^{3}$ kips

Check steel tube wall thickness reqirement:

$\frac{d}{t} = 17.455$ ▮ < ▮ $\frac{3067}{Fy} = 61.34$ OK

Calculate flexural capacity:

calculate parameter β:

$$\beta = \blacksquare\ \frac{As\cdot Fy + 0.25\cdot d^{2}\cdot fc'\cdot\left[\sin\left(\frac{\beta}{2}\right)-\left(\sin\left(\frac{\beta}{2}\right)\right)^{2}\cdot\tan\left(\frac{\beta}{4}\right)\right]}{0.125\cdot d^{2}\cdot fc' + d\cdot t\cdot Fy} \qquad \beta := 2.56$$

relevant parameters:

$$bc := d\cdot\sin\left(\frac{\beta}{2}\right) = 22.992 \quad \text{in}$$

$$a := \frac{bc}{2}\cdot\tan\left(\frac{\beta}{4}\right) = 8.559 \quad \text{in}$$

$$m := \frac{\beta\cdot d}{2} = 30.72 \quad \text{in}$$

$$e := bc\cdot\left[\frac{1}{(2\cdot\pi-\beta)}+\frac{1}{\beta}\right] = 15.157 \quad \text{in}$$

$$e' := bc\cdot\left[\frac{1}{(2\cdot\pi-\beta)}+\frac{bc^2}{1.5\cdot\beta\cdot d^2-6\cdot bc\cdot(0.5\cdot d-a)}\right] = 13.172 \quad \text{in}$$

$$Cr := Fy\cdot m\cdot t = 2.112\times 10^3 \quad \text{kips}$$

$$Cr' := \left[\frac{\beta\cdot d^2}{8}-\frac{bc}{2}\cdot\left(\frac{d}{2}-a\right)\right]\cdot fc' = 671.716 \quad \text{kips}$$

nominal moment capacity: $Mn := Cr\cdot e + Cr'\cdot e' = 4.086\times 10^4$ k·in

design moment capacity: $Mc := \frac{1}{\gamma s}\cdot Cr\cdot e + \frac{1}{\gamma c}\cdot Cr'\cdot e' = 3.791\times 10^4$ k·in

Calculate anchor points for AF interaction diagram:

axial capacity at point C: $\frac{fc'}{\gamma c}\cdot Ac = 1.097\times 10^3$ kips

axial capacity at point D: $0.5\cdot\left(\frac{fc'}{\gamma c}\cdot Ac\right) = 548.535$ kips

maximum moment capacity: $Mmax := \frac{Fy}{\gamma s}\cdot d^2\cdot t + \frac{5}{24}\cdot\frac{fc'}{\gamma c}\cdot d^3 = 4.851\times 10^4$ k·in

point A is at: (0, Psc) = (0, 6086)

point B is at: (Mc, 0) = (37910, 0)

point C is at: (Mc, fc`*Ac/γc) = (37910, 1097)

point D is at: (Mmax, 0.5*fc`*Ac/γc) = (48510, 548.5)

Due to the maximum moment using the method given by Bruneau and Marson is too large, the method adopted by AS5100 is used to recalculate the moment capacity and the AF interaction points.

Re-calculate flexural capacity using the method adopted in AS5100:

relevant parameters:

$$rm := \frac{d - t}{2} = 11.313 \quad in \qquad ri := \frac{d - 2\cdot t}{2} = 10.625 \quad in$$

$$\gamma 0 := \frac{\frac{\pi}{4}\cdot\frac{fc'\cdot ri^2}{Fy\cdot rm\cdot t}}{2 + \frac{1}{2}\cdot\frac{fc'\cdot ri^2}{Fy\cdot rm\cdot t}} = 0.226$$

nominal moment capacity: $Mn := 4\cdot Fy\cdot t\cdot rm^2\cdot\cos(\gamma 0) + \frac{2}{3}\cdot fc'\cdot ri^3\cdot(\cos(\gamma 0))^3$

$$Mn = 3.773\times 10^4 \quad k\cdot in$$

design moment capacity: $Mc := 4\cdot\frac{Fy}{\gamma s}\cdot t\cdot rm^2\cdot\cos(\gamma 0) + \frac{2}{3}\cdot\frac{fc'}{\gamma c}\cdot ri^3\cdot(\cos(\gamma 0))^3$

$$Mc = 3.658\times 10^4 \quad k\cdot in$$

Re-calculate anchor points for AF interaction diagram:

axial capacity at point C: $\frac{fc'}{\gamma c}\cdot Ac = 1.097\times 10^3$ kips

axial capacity at point D: $0.5\cdot\left(\frac{fc'}{\gamma c}\cdot Ac\right) = 548.535$ kips

maximum moment capacity: $Mmax := \left(4\cdot\frac{Fy}{\gamma s}\cdot t\cdot rm^2 + \frac{2}{3}\cdot\frac{fc'}{\gamma c}\cdot ri^3\right) = 3.767\times 10^4$ k·in

point A is at: (0, Psc) = (0, 6086)

point B is at: (Mc, 0) = (36580, 0)

point C is at: (Mc, ϕc*fc`*Ac) = (36580, 1097)

point D is at: (Mmax, 0.5*ϕc*fc`*Ac) = (37670, 548.5)

Method 5: DBJ13-51

Materials: concrete compressive strength: $fck := 3.89 \quad ksi$

steel yield strength: $Fy := 50 \quad ksi$

steel elastic modulus: $Es := 29000 \quad ksi$

Dimensions: circular steel tube outer diameter: $d := 24 \quad in$

circular steel tube wall thickness: $t := 1.375 \quad in$

column length: $L := 14 \cdot 12 = 168 \quad in$

Assumptions: effective column length factor: $K := 1.0$

Calculate relevant properties:

cross area of steel tube: $As := \frac{\pi}{4} \cdot \left[d^2 - (d - 2 \cdot t)^2 \right] = 97.733 \quad in^2$

cross area of concrete: $Ac := \frac{\pi}{4} \cdot (d - 2 \cdot t)^2 = 354.656 \quad in^2$

moment inertia of steel tube: $Is := \frac{\pi}{64} \cdot \left[d^4 - (d - 2 \cdot t)^4 \right] = 6.277 \times 10^3 \quad in^4$

moment inertia of concrete: $Ic := \frac{\pi}{64} \cdot (d - 2 \cdot t)^4 = 1.001 \times 10^4 \quad in^4$

Calculate axial capacity:

material design factors: $\gamma s := 1.12 \qquad \gamma c := 1.4$

nominal constraining factor: $\xi := \frac{As \cdot Fy}{Ac \cdot fck} = 3.542$

design constraining factor: $\xi 0 := \frac{As \cdot Fy \cdot \gamma c}{Ac \cdot fck \cdot \gamma s} = 4.428$

equivalent section strength:

nominal strength: $fscn := (1.14 + 1.02 \cdot \xi) \cdot fck = 18.489 \quad ksi$

design strength: $fscc := (1.14 + 1.02 \cdot \xi 0) \cdot \frac{fck}{\gamma c} = 15.716 \quad ksi$

equivalent section area: $Asc := As + Ac = 452.389 \quad in^2$

steel ratio: $\alpha s := \frac{As}{Ac} = 0.276$

column slenderness: $\lambda := \frac{4 \cdot (K \cdot L)}{d} = 28$

From figure 3.7, one can obtain the stability factor as: $\psi := 0.94$

nominal section axial capacity: $Psn := fscn \cdot Asc = 8.364 \times 10^3 \quad kips$

nominal member axial capacity: $Pn := \psi \cdot Psn = 7.862 \times 10^3 \quad kips$

design section axial capacity: $Psc := fscc \cdot Asc = 7.11 \times 10^3 \quad kips$

design member axial capacity: $Pc := \psi \cdot Psc = 6.683 \times 10^3 \quad kips$

Calculate flexural capacity:

relevant parameter: $Wsc := \frac{\pi \cdot d^3}{32} = 1.357 \times 10^3 \quad in^3$

nominal moment capacity:

$\gamma mn := 1.1 + 0.48 \cdot \ln(\xi + 0.1) = 1.72$

$Mn := \gamma mn \cdot Wsc \cdot fscn = 4.317 \times 10^4 \quad k \cdot in$

design moment capacity:

$\gamma mc := 1.1 + 0.48 \cdot \ln(\xi 0 + 0.1) = 1.825$

$Mc := \gamma mc \cdot Wsc \cdot fscc = 3.892 \times 10^4 \quad k \cdot in$

Check steel tube wall thickness regirement:

$\frac{d}{t} = 17.455 \quad \blacksquare < \blacksquare \quad \frac{5112}{Fy} = 102.24 \quad$ OK

Calculate anchor points for AF interaction diagram:

the AF interaction diagram is defined using normalized ratios. In order to compared with other diagrams in other codes, it will be converted into non-normalized curve.

point A: $(0, Pc)$

point B: $\left(\frac{dm \cdot Mn}{\beta m}, 0\right)$

point C: $\left(\frac{dm \cdot Mn}{\beta m}, 2 \cdot \psi^2 \cdot \eta 0 \cdot Pc\right)$

point D: $\left(\left[1 + \psi^3 \cdot (\zeta - 1)\right] \cdot \frac{dm \cdot Mn}{\beta m}, \psi^2 \cdot \eta 0 \cdot Pc\right)$

For member with transverse load $\beta m := 1.0$

relevant parameters:

due to $\xi = 3.542$ > 0.4 then $\eta 0 := 0.1 + 0.14 \cdot \xi^{-0.84} = 0.148$

$\zeta := 1 + 0.18 \cdot \xi^{-1.15} = 1.042$

$\underset{\sim}{c} := \frac{2 \cdot \psi \cdot (\zeta - 1)}{\eta 0} = 0.533$

$b := \frac{1 - \zeta}{\psi \cdot \eta 0^2} = -2.031$

$\underset{\sim}{a} := 1 - 2 \cdot \psi^2 \cdot \eta 0 = 0.738$

$\varepsilon scp := 2.2425 \cdot 10^{-5} \cdot Fy = 1.121 \times 10^{-3}$

$fscy := (1.14 + 1.02 \cdot \xi) \cdot \frac{fck}{\gamma c} = 13.206$ ksi

$fscp := \left(0.192 \cdot \frac{Fy}{34.1} + 0.488\right) \cdot fscy = 10.163$ ksi

$$Esc := \frac{fscp}{\varepsilon scp} = 9.064 \times 10^{3} \quad ksi$$

$$PE := \frac{\pi^{2} \cdot Esc \cdot Asc}{\lambda^{2}} = 5.162 \times 10^{4} \quad kips$$

calculate moment capacity at point B:

$$dm := 1 \qquad \frac{dm \cdot Mn}{\beta m} = 4.317 \times 10^{4} \quad k \cdot in$$

calculate axial and moment capacity at point C:

axial capacity: $2 \cdot \psi^{2} \cdot \eta 0 \cdot Pc = 1.753 \times 10^{3}$ kips

moment capacity:

$$dm := 1 - 0.4 \cdot \frac{\left(2 \cdot \psi^{2} \cdot \eta 0 \cdot Pc\right)}{PE} = 0.986$$

$$\frac{dm \cdot Mn}{\beta m} = 4.258 \times 10^{4} \quad k \cdot in$$

calcualte axial and moment capacity at point D:

axial capacity: $\psi^{2} \cdot \eta 0 \cdot Pc = 876.273$ kips

moment capacity:

$$dm := 1 - 0.4 \cdot \frac{\left(\psi^{2} \cdot \eta 0 \cdot Pc\right)}{PE} = 0.993$$

$$\left[1 + \psi^{3} \cdot (\zeta - 1)\right] \cdot \frac{dm \cdot Mn}{\beta m} = 4.437 \times 10^{4} \quad k \cdot in$$

anchor points:

point A: (0, 6683) point B: (43170, 0)

point C: (42580, 1753) point D: (44370, 876.3)

Appendix F

AISC Design Method for CCFT Columns based on Plastic Strength Approach

The plastic strength approach proposed in Eurocode 4 is adopted to assess the cross sectional strength [128]. Both a statistical approach which matches the exsisting test data and the AISC method will be introduced herein.

F.1 A Statistical Approach:

According to the existing test data, the statistical approach is utilized to propose the following equations to calculate the CCFT column axial capacity [129]:

- When the column length effect is not considered, the nominal strength can be calculated by the equation:

$$P_0 = A_s \cdot F_y + 0.95 \cdot A_c \cdot f_c^{'} \qquad \textbf{(AEq. F-1)}$$

- When the column length effect is considered, the nominal strength can be calculated by the equation:

when $\lambda \le 0.5$, $P_n = P_0$ **(AEq. F-2)**

when $0.5 < \lambda \le 1.5$, $P_n = P_0 \cdot \left(\lambda^{-0.4} - 0.32\right)$ **(AEq. F-3)**

The column slenderness λ is defined by the nominal strength without length effect P_0 and the Euler elastic buckling strength P_e as:

$$\lambda = \sqrt{P_0 / P_e} \qquad \textbf{(AEq. F-4)}$$

$$P_e = \frac{\pi^2 \cdot EI_{eff}}{\left(K \cdot L\right)^2} \qquad \textbf{(AEq. F-5)}$$

$$EI_{eff} = E_s \cdot I_s + 0.2 \cdot E_c \cdot I_c \qquad \textbf{(AEq. F-6)}$$

where,

F_y = yield strength of the steel section, ksi.

A_s = the area of the steel section, $in.^2$

A_c = the area of the infill concrete, $in.^2$

f_c' = compressive strength of the infill concrete, ksi.

E_s = elastic Young's modulus of steel section, ksi.

E_c = elastic Young's modulus of infill concrete, ksi.

I_s = moment of inertia of the steel section, $in.^4$

I_c = moment of inertia of the infill concrete, $in.^4$

EI_{eff} = the equivalent stiffness of the CCFT column, $k\text{-}in.^2$

K = column effective length factor

L = column length, in.

Due to lack of test data for $\lambda > 1.5$, an upper limit 1.5 is added. The columns with $\lambda > 1.5$ are permitted only if they can be justified by analysis or testing. As one can notice that the proposed column curves above are different from the typical ones in the present AISC specifications. Although they can give an excellent correlation to the test data, they are purely empirical in nature and can not tend towards the nominal compressive strength for steel columns as the amount of infill concrete decreases.

F.2 AISC Method:

In order to keep the continuity with the existing steel design provisions, the typical AISC column curves have to be used. In this case, the definition of the equivalent stiffness EI_{eff} of the columns should be modified to make a better match to the experimental results. A more accurate equation is proposed as follows:

$$EI_{eff} = \left(0.313 + 0.00334 \cdot \frac{L}{D} - 0.203 \cdot \frac{e}{D}\right) \cdot E_c \cdot \left(I_g - I_s\right) + 0.729 \cdot E_s \cdot I_s \qquad \textbf{(AEq. F-7)}$$

where D is the diameter of the steel tube; e is the eccentricity of the axial load; and I_g is the moment of inertia of the entire cross section. However, this equation is too complicated to be used for design as the value of EI_{eff} varies with different eccentricities e. In order to overcome this defect, further simplification is made to obtain a new equation which is adopted by AISC (2010) shown as follows:

$$EI_{eff} = E_s \cdot I_s + C_3 \cdot E_c \cdot I_c \qquad \textbf{(AEq. F-8)}$$

$$C_3 = 0.6 + 2 \cdot \left(\frac{A_s}{A_c + A_s} \right) \leq 0.9 \qquad \textbf{(AEq. F-9)}$$

Although the simplified equations have a very different format from the complicated one, studies indicate that there are no large inconsistencies between them. By using the simplified equation for the column effective stiffness, the typical column curves can be used to calculate the compressive strength of the CCFT column with slenderness λ. The calculation procedure is presented as follows:

$$\text{when } \lambda \leq 1.5, \quad P_n = 0.658^{\lambda^2} \cdot P_0 = 0.658^{\left(\frac{P_0}{P_e}\right)} \cdot P_0 \qquad \textbf{(AEq. F-10)}$$

$$\text{when } \lambda > 1.5, \quad P_n = \left(\frac{0.877}{\lambda^2} \right) \cdot P_0 = 0.877 \cdot P_e \qquad \textbf{(AEq. F-11)}$$

The design capacity can be calculated as $\phi_c P_n$ based on the *Load and Resistance Factor*

Design (**LRFD**) method, where $\phi_c = 0.75$; and if the *Allowable Strength Design* (**ASD**) is used, the design capacity will be P_n/Ω_c, where $\Omega_c = 2.0$.

Except in gravity systems, columns usually are subject to considerable moments as well, such as in SMFs. The columns behave like beams to some degree, and they will be called beam-columns. For such columns, the AF interaction has great effect on the column capacity. To calculate the AF interaction diagram, Chapter I of the AISC (2010) provisions provides two options: (1) a general approach labeled the *strain compatibility method* (**SCM**); (2) a simplified approach labeled the *rigid plastic method* (**RPM**) or the plastic stress distribution method [2]. For the strain compatibility method, the entire cross section will be divided into a large number of areas (fibers). The material in each area will follow the assumed 'exact' nonlinear stress-strain relationship (the solid curves for concrete and steel tube in Appendix Figure F-1 and Appendix Figure F-2, respectively). The cross section is assumed to remain plane during deformation. With a specific location of the neutral axis, when the assumed ultimate strain on the extreme layer is reached, the strain and stress on each small area can be calculated according to the geometry and stress-strain curves. Then the ultimate axial and flexural capacity can be calculated by integrating stress on the entire cross section. Although this approach is relatively more accurate, it is time-consuming and not always necessary for preliminary design.

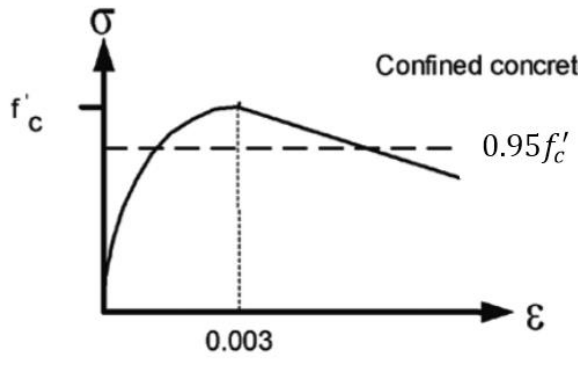

Appendix Figure F-1: stress-strain curve for concrete [130]

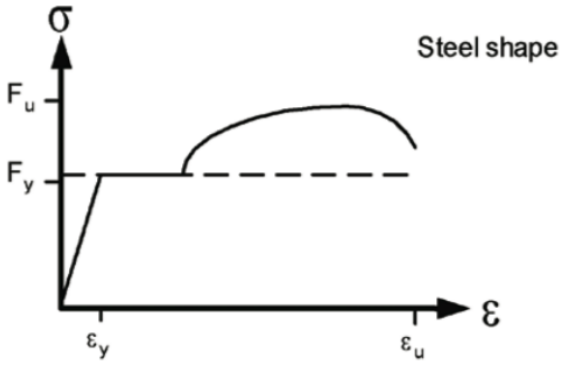

Appendix Figure F-2: stress-strain curve for steel tube [130]

For the rigid plastic method or the plastic stress distribution method, the bilinear rigid plastic stress-strain curves for the materials are utilized for simplification (the dashed lines for concrete and steel tube in Appendix Figure F-1 and Appendix Figure F-2, respectively); in other words, the plastic stress is assumed throughout the entire cross section. By making this assumption, there is no need to divide the entire cross section into small areas to determine the section plastic capacity. The same material on one side of the neutral axis will have uniform stress distribution with the assumed peak value. For the confined concrete by circular steel tube, a peak value of $0.95f_c'$ is assumed as its compressive strength; and for the steel tube, yield strength f_y is used without considering strain hardening effect. This method is intended to provide a design-oriented approach which can catch the essential characteristics of the strain compatibility one without its complexities [130]. Appendix Figure F-3 shows two typical AF interaction diagrams from the two methods. The solid line represents the curve from SCM; and the dashed line represents the curve from RPM. From these two curves, one can see that RPM is a more conservative method. However, RPM can only be used at the anchor points on the

simplified multi-linear curves (points A, B, C, D, and E), and SCM is the only currently applicable approach for a continuous AF interaction diagram.

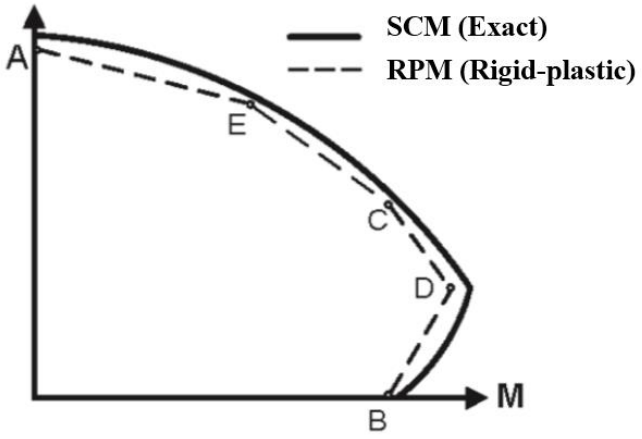

Appendix Figure F-3: AF interaction diagrams for both SCM and RPM [130]

Although the SCM is more accurate and can supply a continuous AF interaction diagram, it is not efficient enough comparing with the RPM. If the maximum compressive strain in concrete is assumed to be 0.003, and the corresponding maximum strain in steel ε_s is assumed to be not large enough to go into strain hardening state (in other words, a perfect elastic plastic stress-strain curve is assumed for steel), an AF interaction diagram given by SCM can be obtained and shown in Appendix Figure F-4 by a heavy black solid curve. On the same plot, a simplified AF interaction diagram from RPM is also shown by a multi-linear dashed curve. Based on these assumptions mentioned above for both materials, the difference between two curves is not very large. It should be acceptable to use the simplified curve to take place of the continuous one for analysis and design.

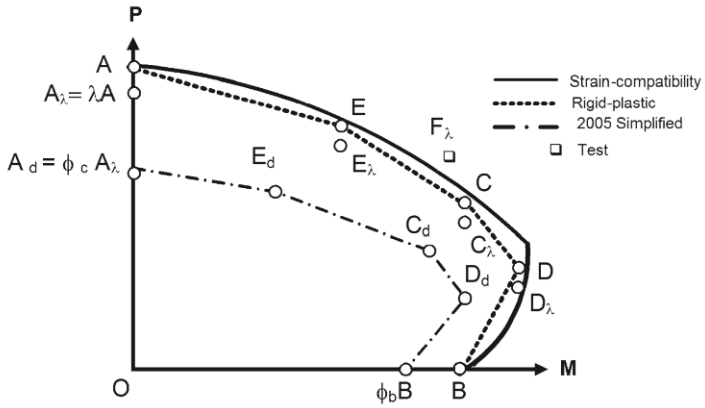

Appendix Figure F-4: AF interaction diagrams for CCFT columns [129]

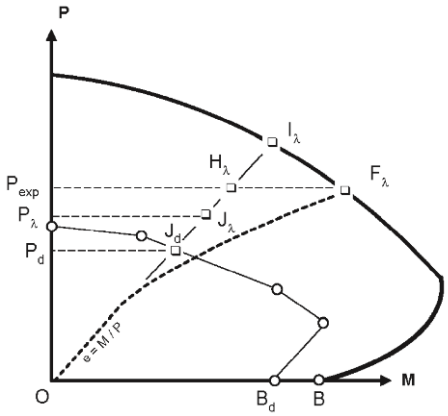

Appendix Figure F-5: Definition of ultimate strength from experimental tests [129]

The simplified AF interaction diagram is defined by five anchor points A, B, C, D, and E on the dashed line curve (Appendix Figure F-4). Point A represents the plastic axial compressive strength of the column without moment. Point B represents the plastic flexural strength of the column without axial force. The moment resistance of the column at point C is the same as that at point B, but the resistance of the axial compressive strength is taken as that of the infill concrete only. At point D, which is also called the balanced point, the maximum flexural capacity is reached due to the position of the neutral axis being right at the centroid of the cross section. Because the neutral axis at point C has the roughly same distance h_n away from the centroid of the cross section as that at point B, but on the opposite side (see plots in Appendix Table F-1), the axial resistance capacity at point D is taken as half of that at point C. Point E is taken as an arbitrary point between A and C. The detailed equations for the calculation of the plastic capacities at these five anchor points of the simplified AF interaction diagram are shown

in Appendix Table F-1.

Appendix Table F-1: Plastic capacities of CCFT at the five anchor points [130]

Section	Stress Distribution	Point	Defining Equations
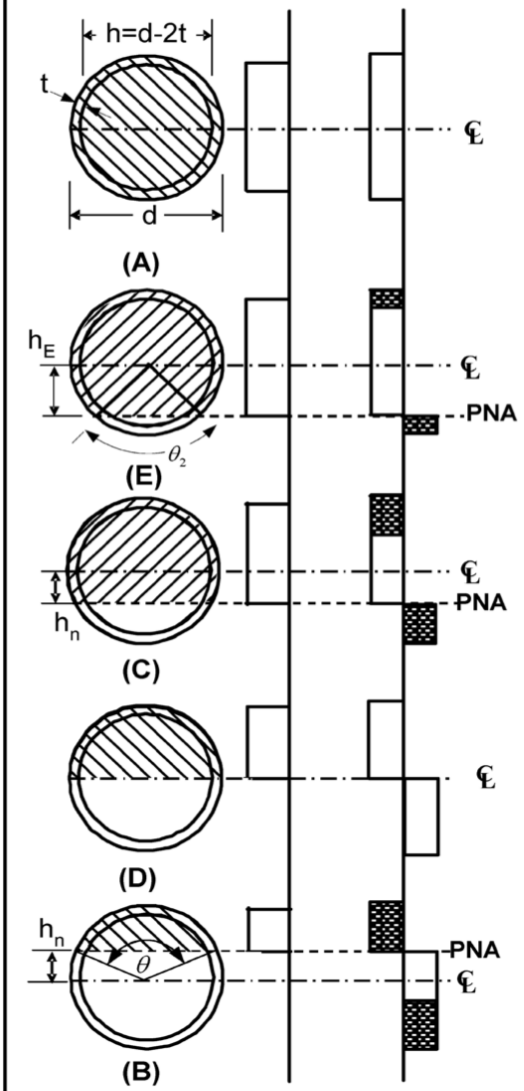		A	$P_A = A_s F_y + 0.95 f_c' A_c$ * $M_A = 0$ $A_s = 2\pi r_m t$ $r_m = \frac{d - t}{2}$ $A_c = \frac{\pi h^2}{4}$ * 0.95 instead of 0.85 can be used for the coefficient on the concrete compressive stress for all cases
		E	$h_E = \frac{h_n}{2} + \frac{h}{4}$ (h_n from Point B) $\theta_2 = \pi - 2\arcsin\left(2h_E/h\right)$ $Z_{sE} = \frac{d^3 - h^3}{6}\sin^3\left(\theta_2/2\right)X$ $X = \left[\frac{\theta_2}{\theta_2 - \sin\theta_2} + \frac{(2\pi - \theta_2)}{(2\pi - \theta_2) - \sin(2\pi - \theta_2)}\right]$ $Z_{sE} \approx \frac{d^3 - h^3}{6}\sin^{(4/3)}\left(\theta_2/2\right)$ $Z_{cE} = \frac{h^3}{6}\sin^3\left(\theta_2/2\right)$ $M_E = Z_{sE}F_y + \frac{1}{2}Z_{cE}(0.95 f_c')$ $P_E = (0.95 f_c' A_c + F_y A_s) -$ $\frac{1}{2}\left[F_y(d^2 - h^2) + \frac{1}{2}(0.95 f_c')\ h^2\right][\theta_2 - \sin\theta_2]$
		C	$P_C = 0.95 f_c'\ A_c$ $M_C = M_B$
		D	$P_D = \frac{0.95 f_c' A_c}{2}$ $M_D = Z_s F_y + \frac{1}{2} Z_c (0.95 f_c')$ Z_s = plastic section modulus of steel shape = $\frac{d^3}{6} - Z_c$ $Z_c = \frac{h^3}{6}$
		B	$P_B = 0$ $M_B = Z_{sB}F_y + \frac{Z_{cB}(0.95 f_c')}{2}$ $Z_{cB} = \frac{h^3 \sin^3(\theta/2)}{6}$ $Z_{sB} = \frac{d^3 - h^3}{12}\sin^3(\theta/2)\left[\frac{\theta}{\theta - \sin\theta} + \frac{(2\pi - \theta)}{(2\pi - \theta) - \sin(2\pi - \theta)}\right]$ $Z_{sB} \approx \frac{d^3 - h^3}{6}\sin^{(4/3)}(\theta/2)$ $\theta = \frac{0.0260K_c - 2K_s}{0.0848K_c} + \frac{\sqrt{(0.0260K_c + 2K_s)^2 + 0.857K_c K_s}}{0.0848K_c}$ $K_c = f_c' h^2$ $K_s = F_y\ r_m\ t$ $h_n = \frac{h}{2}\sin\left(\frac{\pi - \theta}{2}\right)$ (to be used in computing values for Point E)

This design method applies rigid-plastic material curves for both steel tube and infill concrete.

High strains are assumed for both materials such that degree of interaction between the steel and concrete needs not to be checked. The local buckling requirement for steel tube is also assumed to be satisfied automatically by imposing D/t or h/t ratios. Due to the high confinement effect from the circular steel tube, the compressive strength of the infill concrete through the equivalent block can be taken as $0.95f_c'$.

As most tests do not report a true failure moment or its deflection, it is unfeasible to calibrate the second order effects directly to test data. For this case, the relationship between the moment and axial force will be regarded as linear as presented schematically by line O - J_d - J_λ - H_λ - I_λ in Appendix Figure F-5. There is one test result F_λ is shown in Appendix Figure F-5, which is located on the true interaction diagram for this specific cross section representing by the heavy black solid line. This true interaction diagram also includes the over-strength effect based on the true material stress-strain curve, and should bound the one in Appendix Figure F-4 represented by a similar solid curve, just as the point F_λ from test is located outside of this interaction curve. The dashed curve in Appendix Figure F-5 stands for the true column curve including the second order effect, which interacts with the true interaction diagram at F_λ. Because failure moments are not available in the existing databases, the calculated moment from equation $M_u = eP_{exp}$ is used, where e is the eccentricity and P_{exp} is the ultimate axial capacity from test. This point with true axial capacity and pseudo moment is represented by H_λ. Because the calculated flexural capacity under the true axial force is less than the true moment resistance, there should be additional cross section capacity remaining. If the second

order effect is not considered, the column should fail at point I_λ under the proportional load combination, where both axial and flexural capacities are greater than those at point H_λ; if the second order effect is not considered, the column should fail at point F_λ, whose axial resistance is the same as that at point H_λ but with greater moment resistance. This means that the test results in the database are used in a conservative way. Because of test constraints, most of the experiments were conducted with a relative large axial force and small eccentricity [129]. This will moderate the second order effect, and the differences among the three points F_λ, I_λ, and H_λ will not be as obvious as those shown schematically in the plot. In other words, these test data are utilized properly to represent the true capacities of columns approximately under the AF interaction. According to the comparison results between the experimental compressive capacities and the predicted ones of these beam-columns, it is confident to prove the effectiveness of the two predicted methods for the CCFT column with infill concrete compressive strength up to 10 ksi [129].

The points in Appendix Figure F-4 and Appendix Figure F-5 with subscript λ and d indicate that the capacities at these points include the length effect for slenderness λ or the reduction from the design factors ϕ_c and ϕ_b (or Ω_c and Ω_b), respectively. From Appendix Figure F-4, one can notice that the length has effect only on the compressive capacity, which is reduced from point i to point i_λ $(i = A, B, C, D, and\ E)$. Then the design factors ϕ_c and ϕ_b for LRFD method are multiplied with compressive and flexural capacity at point i_λ, respectively, and yield a design capacity envelop defined by point i_d. In other words, $P_d = \phi_c P_\lambda$ and

$M_d = \phi_b M_\lambda$, where P_λ and M_λ are capacities at point i_λ, and P_d and M_d are capacities at point i_d (if ASD method is used, $P_d = P_\lambda/\Omega_c$ and $M_d = M_\lambda/\Omega_b$). For LRFD, $\phi_c = 0.75$ and $\phi_b = 0.9$; for ASD, $\Omega_c = 2.0$ and $\Omega_b = 1.67$. In order to have a sufficient design of the CCFT columns, the local buckling of the steel tubes can also be checked. The Roark and Young equation for the elastic critical stress for local buckling of a circular section can be employed [131]. However, this equation doesn't consider the bracing effect from the infill concrete. If this composite effect is considered, the ratio of D/t can be increased by about 36% (compare $D/t \leq 0.15E/F_y$ for the composite case with $D/t \leq 0.11E/F_y$ for the noncomposite case [129]). The Roark and Young equation is as follows:

$$F_{cr} = \frac{E}{\sqrt{3}\cdot\sqrt{1-\upsilon^2}}\cdot\frac{2\cdot t}{D} \qquad \textbf{(AEq. F-12)}$$

The design capacity envelope introduced above using the RPM is simply defined by five anchor points i_d ($i = A, B, C, D, and\ E$) and provides reasonable results, but it is still not convenient enough for the stability design of the beam-columns for hand calculations. To solve this issue, three methods with further simplification are suggested in the AISC commentary [2]: (1) the first method will utilize the existing interaction equations in Chapter H of the AISC (2010) specifications; (2) the second method will redefine the interaction diagram using only three points A_d, B_d, and D_d and ignore the other two; and (3) the third method will redefine the curve using another three points A_d, B_d, and C_d. The detailed checking procedures are presented as follows for these three methods:

- Method 1 – AISC equations in Chapter H

For $\frac{P_r}{P_c} \geq 0.2$, $\quad \frac{P_r}{P_c} + \frac{8}{9} \cdot \left(\frac{M_{rx}}{M_c} + \frac{M_{ry}}{M_c} \right) \leq 1.0$ ***(AEq. F-13)***

For $\frac{P_r}{P_c} < 0.2$, $\quad \frac{P_r}{2 \cdot P_c} + \left(\frac{M_{rx}}{M_c} + \frac{M_{ry}}{M_c} \right) \leq 1.0$ ***(AEq. F-14)***

where,

P_r = required compressive strength, kips

P_c = available compressive strength, kips

M_r = required flexural strength, k-in.

M_c = available flexural strength, k-in.

x = subscript relating symbol to x-x axis bending

y = subscript relating symbol to y-y axis bending

- Method 2 – Interaction diagram defined by points A_d, B_d, and D_d

(a) For $P_r < P_{cb}$,

and if $\frac{M_{rx}}{M_c} \leq 1.0$ and $\frac{M_{ry}}{M_c} \leq 1.0$ then,

$$\frac{M_{rx}+M_{ry}}{M_c} \le 1.0 \qquad \textit{(AEq. F-15)}$$

otherwise if $\frac{M_{rx}}{M_c} > 1.0$ and $\frac{M_{ry}}{M_c} \le 1.0$ then,

$$\frac{P_r}{P_{cb}} + \left(\frac{M_{cb}-M_{rx}}{M_{cb}-M_c} + \frac{M_{ry}}{M_c} \right) \le 1.0 \qquad \textit{(AEq. F-16)}$$

otherwise if $\frac{M_{rx}}{M_c} \le 1.0$ and $\frac{M_{ry}}{M_c} > 1.0$ then,

$$\frac{P_r}{P_{cb}} + \left(\frac{M_{rx}}{M_c} + \frac{M_{cb}-M_{ry}}{M_{cb}-M_c} \right) \le 1.0 \qquad \textit{(AEq. F-17)}$$

otherwise if $\frac{M_{rx}}{M_c} > 1.0$ and $\frac{M_{ry}}{M_c} > 1.0$ then,

$$\frac{P_r}{P_{cb}} + \frac{2 \cdot M_{cb} - \left(M_{rx}+M_{ry} \right)}{M_{cb}-M_c} \le 1.0 \qquad \textit{(AEq. F-18)}$$

(b) For $P_r \ge P_{cb}$,

$$\frac{P_r - P_{cb}}{P_c - P_{cb}} + \frac{M_{rx}+M_{ry}}{M_{cb}} \le 1.0 \qquad \textit{(AEq. F-19)}$$

where,

P_{cb} = available axial compressive strength at balanced point D_d, kips

M_{cb} = available flexural strength at balanced point D_d, k-in.

- Method 3 – Interaction diagram defined by points A_d, B_d, and C_d

(a) For $P_r \leq P_{Cb}$, $$\frac{M_{rx} + M_{ry}}{M_c} \leq 1.0 \qquad \textit{(AEq. F-20)}$$

(b) For $P_r > P_{Cb}$, $$\frac{P_r - P_{Cd}}{P_c - P_{Cd}} + \frac{M_{rx} + M_{ry}}{M_{Cd}} \leq 1.0 \qquad \textit{(AEq. F-21)}$$

where,

P_{Cd} = available axial compressive strength at balanced point C_d, kips

M_{Cd} = available flexural strength at balanced point C_d, k-in.

The resulting three methods are plotted schematically in Appendix Figure F-6. From this figure one can find that to use method one only two anchor points need to be calculated, as compared with three for the other two methods. Comparing the remaining two methods, the first method gives a much more conservative design. Comparing the second and third methods, the second method allows more flexural capacity to be used, while the third method permits a higher axial compressive strength to be utilized. Because two different reductions are applied on the axial and flexural capacities when stability and design factors are considered, it is possible to cause an unsafe region located outside of the ultimate strength envelop (the red region in Appendix Figure F-7). Although the possibility of the occurrence of the unsafe region is relative low, it is observed that most part of this small breach, if not all of, can be covered by the continuous

interaction diagram based on SCM even though it does occur (Appendix Figure F-7). This issue can only happen when the second methodis used but has very limited influence.

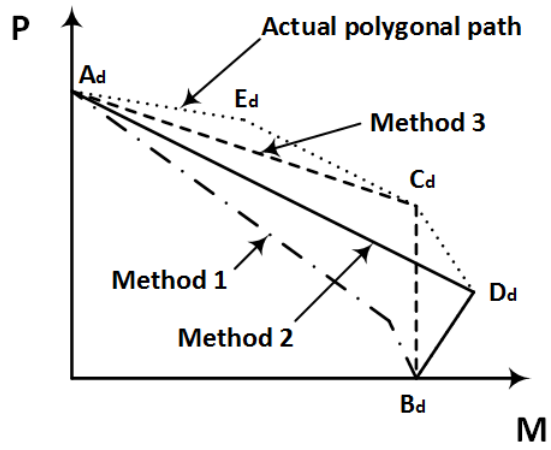

Appendix Figure F-6: Interaction curves for design based on three methods

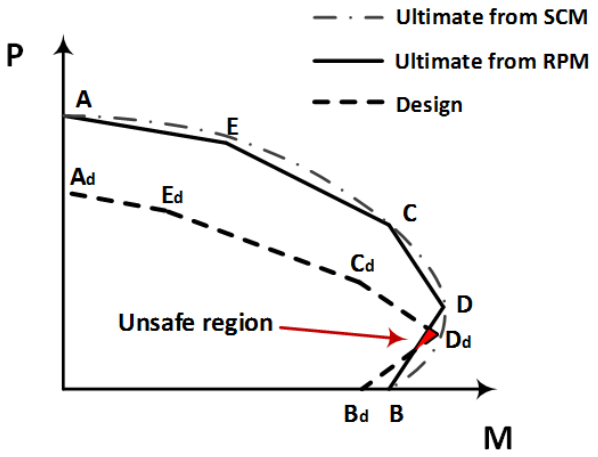

Appendix Figure F-7: Possible breach of ultimate strength envelop by design envelop

Except of the axial compressive capacity, the axial tensile capacity of the CCFT columns is also important. Concrete is a typical brittle material. Its tensile strength is very low, only about one tenth of its compressive strength. It is reasonable to ignore this insignificant contribution from the concrete tensile strength to the axial tensile capacity of the CCFT columns. The axial tensile capacity of the CCFT columns can be taken as the capacity of only the steel tube portion. The nominal and design axial tensile capacity can be calculated by the following equations:

$$P_n = F_y \cdot A_s \qquad \textbf{(AEq. F-22)}$$

$$P_t = \phi_t \cdot P_n \ \text{(LRFD)} \quad \text{or} \quad P_t = P_n / \Omega_t \ \text{(ASD)} \qquad \textbf{(AEq. F-23)}$$

where,

P_n = nominal axial tensile strength, kips

P_t = available axial tensile strength, kips

ϕ_t = 0.9, design factor for LRFD

Ω_t = 1.67, design factor for ASD

Although an interaction diagram for tensile force and moment is not given by Leon and Hajjar as its compressive counterpart [130], one can still imagine its approximate contour according to three key points: (1) The interaction curve should be symmetric about P-axis. Its derivative at point F (which is setting on the P-axis representing the nominal axial tensile capacity of the column) has to be equal to zero. (2) The interaction curve should be continuous and derivable at point B (the same point B as defined in an interaction diagram for compressive force and moment). (3) The change of the interaction curve should be monotonous and gradual. If these three requirements are met, the contour of this interaction curve has to be similar to the dashed-dotted curve shown in Appendix Figure F-8.

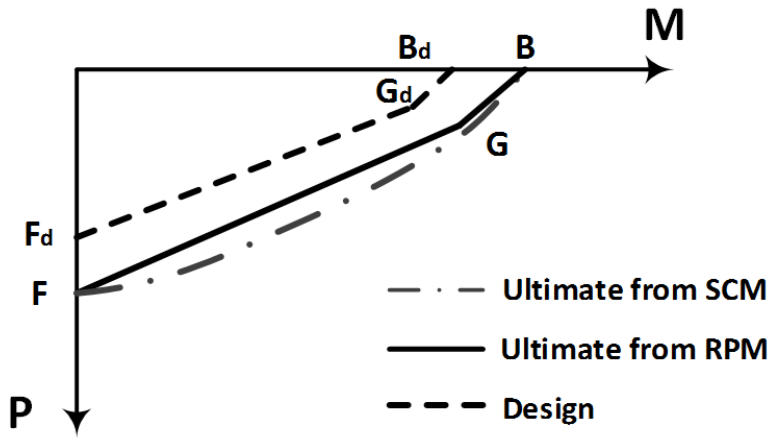

Appendix Figure F-8: Interaction diagram for tensile force and moment

One can assume that the dashed-dotted curve in Appendix Figure F-8 is obtained from the SCM, while its corresponding simplified interaction curve from the RPM is represented by the heavy black solid line on the same plot. As stability is not an issue for tension loads, the design curve presented by the dashed line in Appendix Figure F-8 can be reduced directly from the simplified ultimate curve represented by the heavy black solid line by using the resistance factors (ϕ_t, ϕ_b or Ω_t, Ω_b). Four additional anchor points i and i_d ($i = F, G$) are introduced to define the simplified curve from RPM and the design curve. Leon and Hajjar suggest that the same AISC equations in the method 1 introduced above can also be used for tension plus flexure [130]:

AISC method:

(a) For $\frac{P_r}{P_t} \geq 0.2$, $\quad \frac{P_r}{P_t} + \frac{8}{9} \cdot \left(\frac{M_{rx}}{M_c} + \frac{M_{ry}}{M_c} \right) \leq 1.0$ ***(AEq. F-24)***

(b) For $\frac{P_r}{P_t} < 0.2$, $\frac{P_r}{2 \cdot P_t} + \left(\frac{M_{rx}}{M_c} + \frac{M_{ry}}{M_c} \right) \leq 1.0$ ***(AEq. F-25)***

From each of the above two equations, one can easily get that the axial tensile resistance and the flexural resistance at point G_d are $0.2P_t$ and $0.9M_c$, respectively. Then the two corresponding values at point G can be calculated to be $0.2P_t/\phi_t = 0.2P_n$ and $0.9M_c/\phi_b = 0.9M_n$ for LRFD (or $0.2\Omega_t P_t = 0.2P_n$ and $0.9\Omega_b M_c = 0.9M_n$ for ASD), respectively. It is also known that the ordinate value of F is P_n and the abscissa value of B is M_n. All anchor points can be located and the corresponding interaction diagram for axial force plus flexural can be obtained.

Appendix G

The Modified-IK Model for RBS

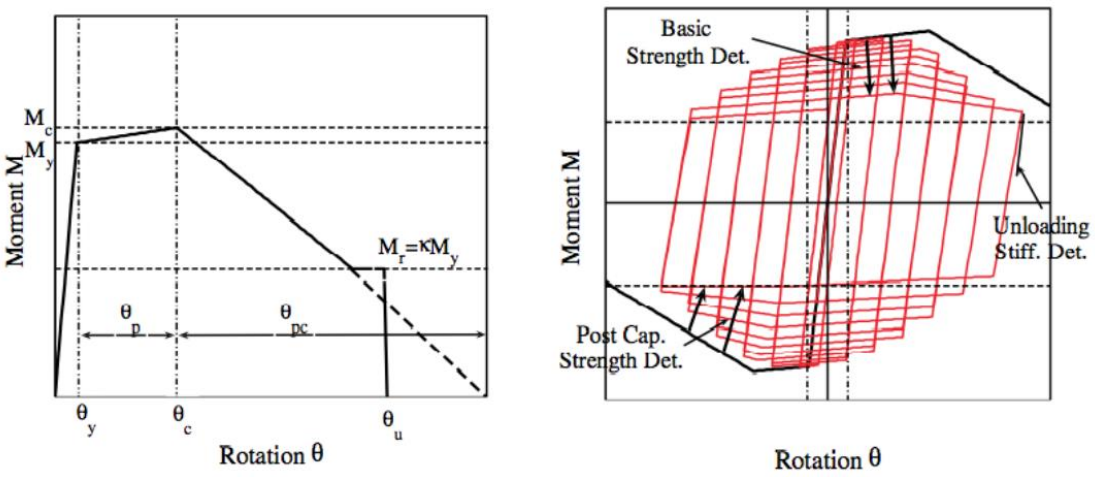

(a) Monotonic curve

(b) Basic modes of cyclic deterioration and associated definitions

Appendix Figure G-1: Modified-IK Deterioration Model [39]

In the Modified-IK Model, a monotonic strength backbone curve is established by three strength parameters and four deformation parameters as shown in Appendix Figure G-1(a):

(1) Effective yield moment, M_y;

(2) Capping moment strength, M_c (or postyield strength ratio, M_c/M_y);

(3) Residual moment, $M_r = \kappa M_y$ (κ = residual strength ratio);

(4) Yield rotation, θ_y;

(5) Pre-capping plastic rotation for monotonic loading, which is the difference between the yield rotation and the rotation at the capping moment, θ_p;

(6) Post-capping plastic rotation, which is the difference between the rotation at the capping

moment strength and the rotation at complete loss of strength, θ_{pc}; and,

(7) Ultimate rotation capacity, θ_u.

The hysteretic relationship is defined between the two monotonic strength backbone curves in both directions by a set of rules that define the cyclic strength and stiffness deterioration relationships (Appendix Figure G-1(b)). The rates of cyclic deterioration are based on the hysteretic energy dissipated when the component is under cyclic loading, as proposed by Rahnama and Krawinkler [132]. A reference hysteretic energy, E_t, is defined as (AEq. G-1), which is assumed to be an inherent property of each component, and not depend on the loading history. $\Lambda = \lambda\theta_p$, is named as the reference cumulative rotation capacity.

$$E_t = \lambda \cdot \theta_p \cdot M_y \quad \text{or} \quad E_t = \Lambda \cdot M_y \qquad \textbf{(AEq. G-1)}$$

The same concept is used to define the cyclic deterioration behavior for both strength and stiffness based on the hysteretic energy dissipation. An energy-based deterioration parameter, β_i, for each load cycle, i, is defined as:

$$\beta_i = \left(\frac{E_i}{E_t - \sum_{j=1}^{i-1} E_j} \right)^c \qquad \textbf{(AEq. G-2)}$$

where, E_i is the hysteretic energy dissipated in execution i; $\sum E_j$ is the total hysteretic

energy dissipated in the past executions; c is an empirical parameter, which is usually taken as 1.0. Then the moment and stiffness capacities in each step are defined as:

$$M_i = (1-\beta_i)\cdot M_{i-1} \qquad \textbf{(AEq. G-3)}$$

$$K_i = (1-\beta_i)\cdot K_{i-1} \qquad \textbf{(AEq. G-4)}$$

The above equation for the moment strength deterioration will transfer the two strength caps (basic strength cap and post capping strength cap, which are the two lines intersect at the capping point) toward the x-axis, see Appendix Figure G-1(b). M_i is any reference point on each cap line, such as the intersection of the cap line with the y-axis for convenience.

When different deterioration rates have to be defined for positive and negative loading directions, such as for the composite beam section with steel beam and concrete slab, there are two different methods are used for strength and stiffness, respectively:

(1) For strength deterioration, a parameter D ranging from 0 to 1.0 is introduced to replace β_i by $D\beta_i$ for the loading in positive or negative direction. Then two different energy-based deterioration parameters are defined for strength deterioration in two loading directions.

(2) For stiffness deterioration, two different values of Λ are used to calculate the energy-based deterioration parameter β_i, and then two slops are obtained for unloading – reloading stiffness in positive and negative loading directions. More detailed

discussions are made by Lignos and Krawinkler [47].

As described previously, the RBSs usually have lower strength capacity and can be used to protect other components in the SMFs. However, this also means that plastic damage will be concentrated in the RBSs. Thus the deteriorating hysteretic behavior of the RBS must be checked carefully by both experiments and effective and reliable analytical models. A recent database developed by Lignos and Krawinkler, includes comprehensive test data for more than 300 experiments on W steel beams [47, 133]. Amongst these specimens, about 80 of them have RBSs with beam depths ranging from 18'' to 36''. Studies have proven that by choosing controlled deterioration parameters ($\theta_p, \theta_{pc}, and\ \Lambda$) properly, the test data in the database can be matched satisfactory by the Modified-IK Model [47]. In order to determine the appropriate deterioration parameters for the Modified-IK Model, the following regression equations have been proposed for the RBSs based on the database:

(1) The regression equation for θ_p based on 72 test specimens:

$$\theta_p = 0.19 \cdot \left(\frac{h}{t_w}\right)^{-0.314} \cdot \left(\frac{b_f}{2 \cdot t_f}\right)^{-0.10} \cdot \left(\frac{L_b}{r_y}\right)^{-0.185} \cdot \left(\frac{L}{d}\right)^{0.113} \cdot \left(\frac{d}{21.0}\right)^{-0.76} \cdot \left(\frac{F_y}{51.5}\right)^{-0.07} \quad \textbf{(AEq. G-5)}$$

$R^2 = 0.56$, and $\sigma_{\ln} = 0.24$ **(AEq. G-6)**

(2) The regression equation for θ_{pc} based on 61 test specimens:

$$\theta_{pc} = 9.52 \cdot \left(\frac{h}{t_w}\right)^{-0.513} \cdot \left(\frac{b_f}{2 \cdot t_f}\right)^{-0.863} \cdot \left(\frac{L_b}{r_y}\right)^{-0.108} \cdot \left(\frac{F_y}{51.5}\right)^{-0.36} \quad \textbf{(AEq. G-7)}$$

$R^2 = 0.48$, and $\sigma_{\ln} = 0.26$ **(AEq. G-8)**

(3) The regression equation for Λ based on 55 test specimens:

$$\Lambda = \frac{E_t}{M_y} = 585 \cdot \left(\frac{h}{t_w}\right)^{-1.14} \cdot \left(\frac{b_f}{2 \cdot t_f}\right)^{-0.632} \cdot \left(\frac{L_b}{r_y}\right)^{-0.205} \cdot \left(\frac{F_y}{51.5}\right)^{-0.391} \quad \textbf{(AEq. G-9)}$$

$R^2 = 0.486$, and $\sigma_{\ln} = 0.35$ **(AEq. G-10)**

where,

R^2 = the coefficient of determination

σ_{ln} = standard deviation

h/t_w = depth to thickness ratio of the beam web

$b_f/2t_f$ = width to thickness ratio of the beam flange

L_b = unbraced length, in.

L = beam shear span (distance from plastic hinge to the inflection point), in.

r_y = the radius of gyration about the y-axis of the beam, in.

d = depth of the beam, in.

F_y = expected yield strength of the beam flange, ksi.

In addition to the estimation of the deformation parameters supplied by these three regression equations, the quantitative information about the ultimate deformation θ_u, the effective yield

moment M_y, the post-yield strength ratio M_c/M_y, and the residual strength ratio κ are also given based on the calibrations to the database. The analyses on the post-yield strength ratio M_c/M_y indicate that this ratio has a mean value of 1.09 and a standard deviation of 0.03 for the RBSs. In addition, a value of 0.4 is suggested for the residual strength ratio κ based on a relative small set of points [39]. The ultimate deformation of the RBSs is strongly dependent on the loading case. Under a cyclic loading, studies by Engelhardt et al. and Ricles et al. suggest that a value between 0.06 and 0.07 is reasonable [83, 134]. However, for a monotonic loading or a near-fault loading protocol, three times this value is applicable.

Appendix H

Cyclic Behavior of the Connection Including Beam Plastic Hinges

The results presented in this section were obtained based on the model which adopts a 'MultiLinear Plastic Link with Kinematic Hysteresis Law' to define the steel rods in the 2D-SSM in SAP2000. However, when compared with the model with 'MultiLinear Plastic Link with Takeda Hysteresis Law' for steel rods, the Kinematic model cannot simulate correct elastic stiffness for steel rods, results in much longer computation times, and has more difficulties to converge. It is hard to obtain a perfect 'Pines' under loading case 1 using this model. In this section, the original simplified model in Figure 4-1 is used.

The proposed simplified model for the connection is assumed to be controlled by the rods strength and ductility. From the stress-strain curve, one can notice that the larger deformation the SMA rods have, the higher strength they can provide. This means that there is no strength limits of the connection as long as the ductility demand doesn't exceed its capacity. According to the stress-strain relationships in Figure 4-17 and Figure 4-20, both SMA and steel rods have very large deformation capacity, which can supply enough ductility capacity for the connection under the ultimate design loading case to make sure the required story drift ratio by AISC 341 is reached [77].

When the analysis model in Figure 4-28 is used, the maximum moment that can be transferred

into the connection is limited by the beam flexural capacity. As previously mentioned, both beam and column are considered as elastic members in the previous analysis in Section 4.3.3.1 and 4.3.3.2. The ultimate loading which can be added on the connection will be determined by the connection capacity and not be limited by the plastic capacity of the connecting members. The cyclic behaviors in Figure 4-30 and Figure 4-31 are only focus on the connection. In order to investigate the overall performance of the frame, the interaction of the plastic behaviors between the connection and its connecting beams are analyzed in this section. The plastic properties of beams are determined in Section 4.2.1.

In order to ensure that the proposed simplified connection model is robust for different beam strengths, several combinations of the connection with full strength and the beam plastic hinge with different reduced strengths are analyzed. These MR relationships of the beam plastic hinges with different reduced strengths are shown in Appendix Figure H-1 and the changes in strength are defined at the same rotational magnitudes. For each rotational magnitude, the corresponding moment capacity for each curve is determined by different strength ratios, they are 1.0 for full strength, and 0.2, 0.4, 0.6, 0.8, 0.85, and 0.9 for reduced strength. An elastic perfectly plastic curve is also defined to investigate the strain hardening effect of beam plastic hinges on the overall interaction behavior between the connection and beam plastic hinges. The connection with full capacity is designed based on the full beam strength following the proposed design procedure in Chapter 3. The corresponding MR responses of the connection and the deformation components of the analysis model in Figure 4-28 are presented in

Appendix Figure H-2. For comparison, the corresponding behaviors of the model with elastic beam members are presented in Appendix Figure H-2 (q) and (r), too.

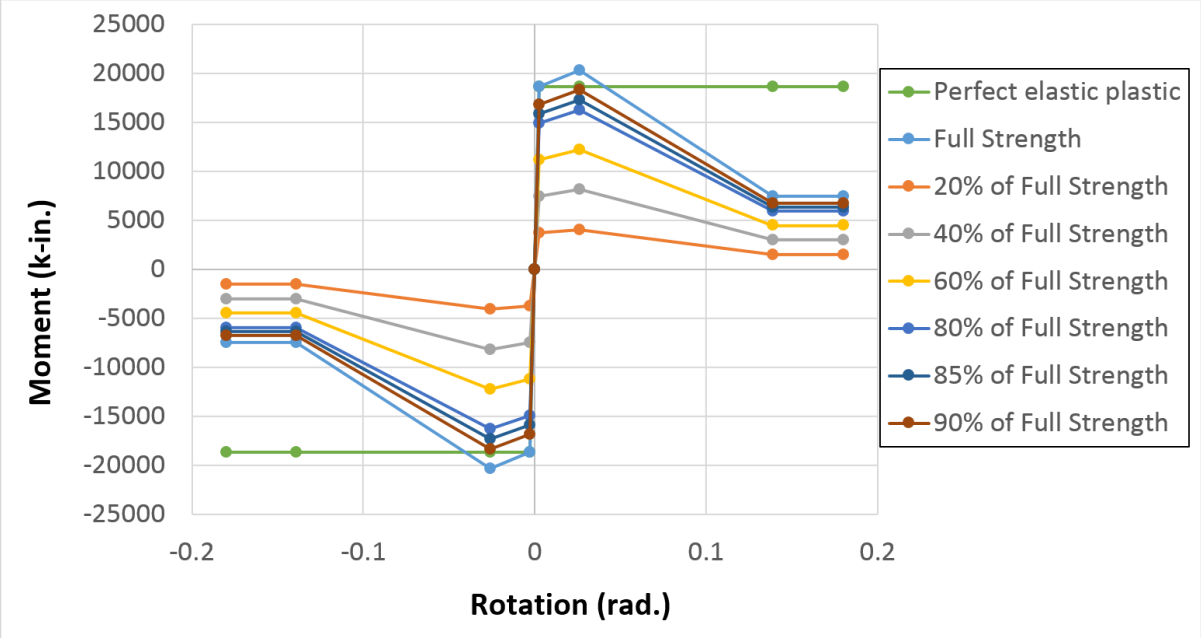

Appendix Figure H-1: Moment rotation relationships of beam plastic hinges with different strength ratios

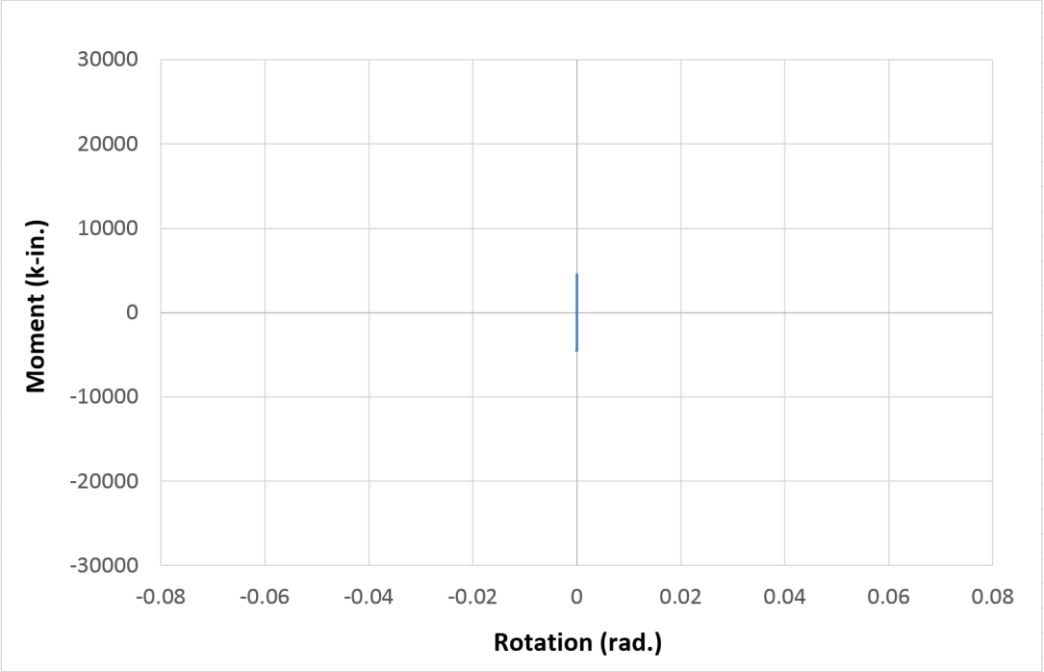

(a) connection M-R curve with beam PH strength reduction ratio of 0.2

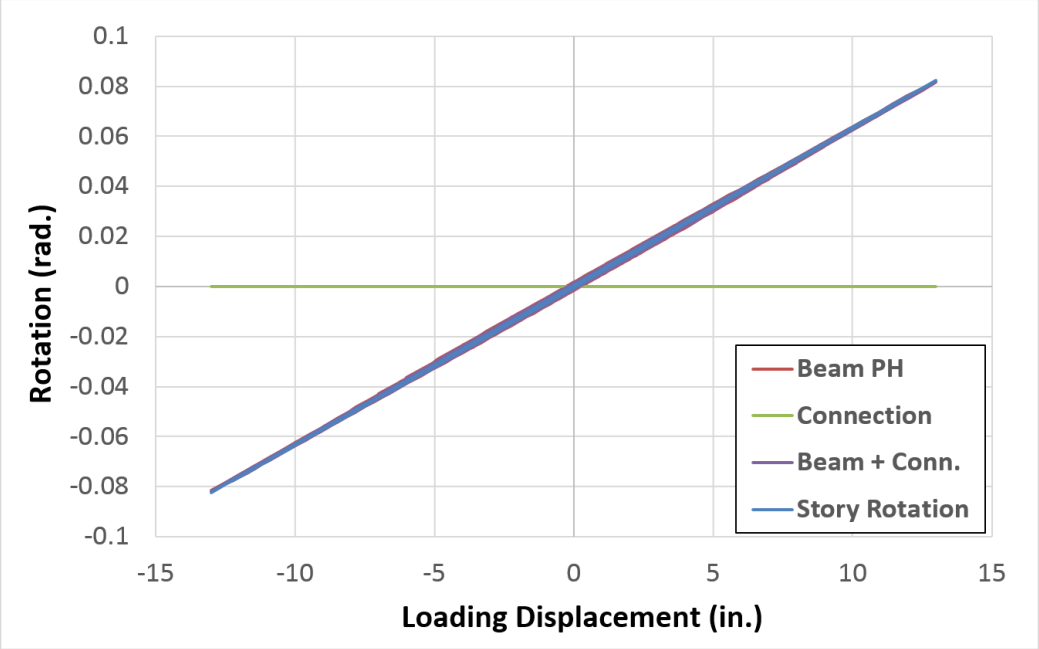

(b) FE model deformation components with beam PH strength reduction ratio of 0.2

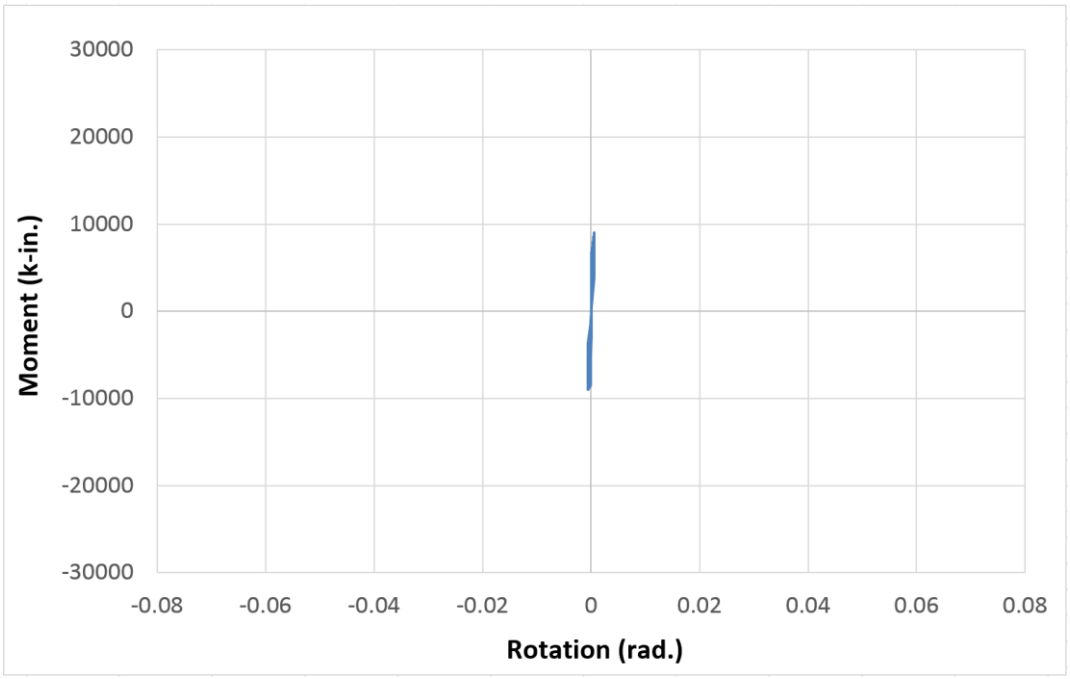

(c) connection M-R curve with beam PH strength reduction ratio of 0.4

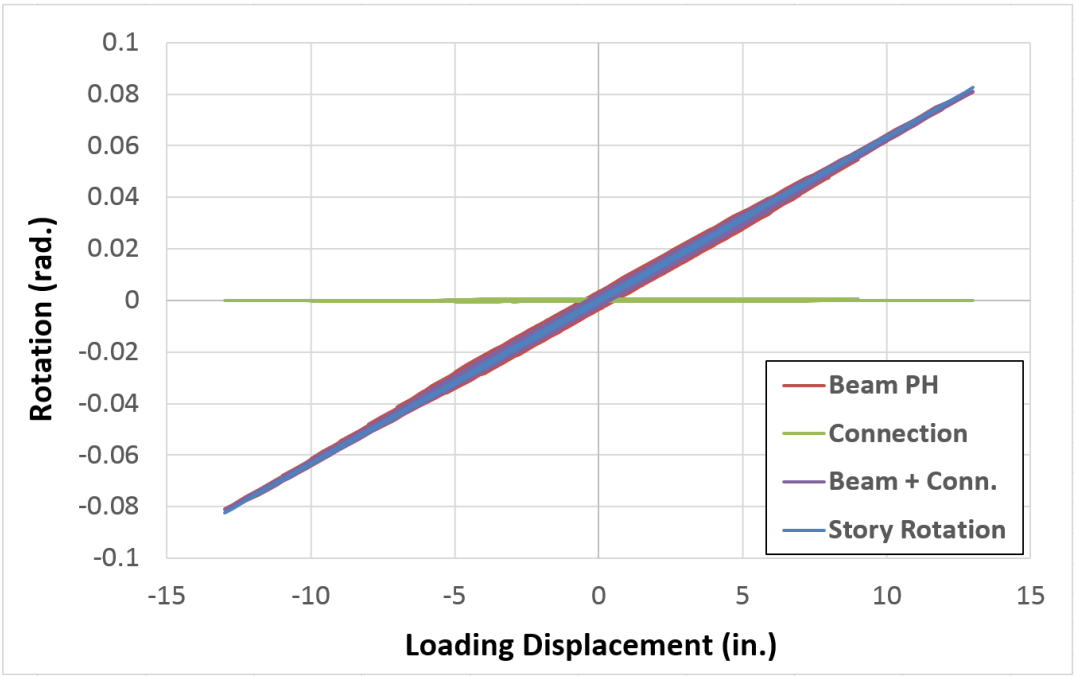

(d) FE model deformation components with beam PH strength reduction ratio of 0.4

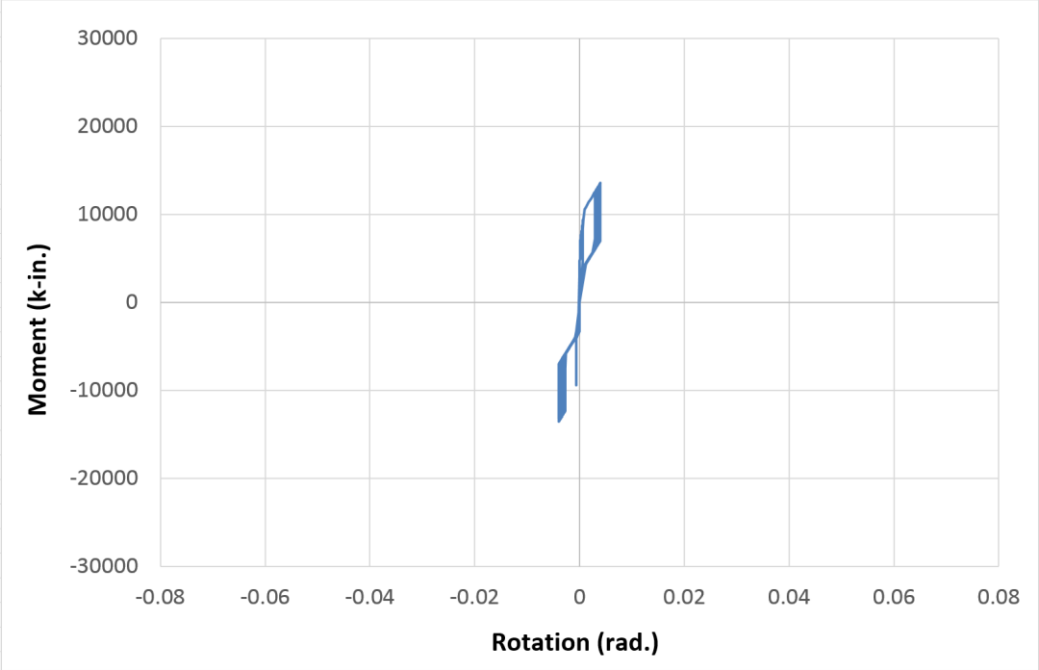

(e) connection M-R curve with beam PH strength reduction ratio of 0.6

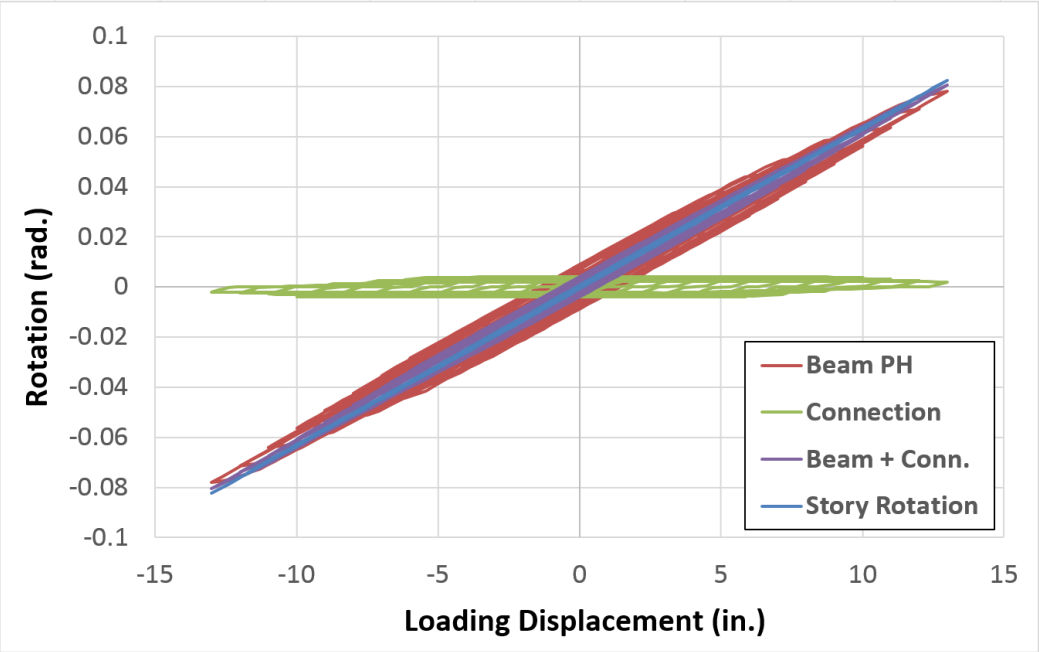

(f) FE model deformation components with beam PH strength reduction ratio of 0.6

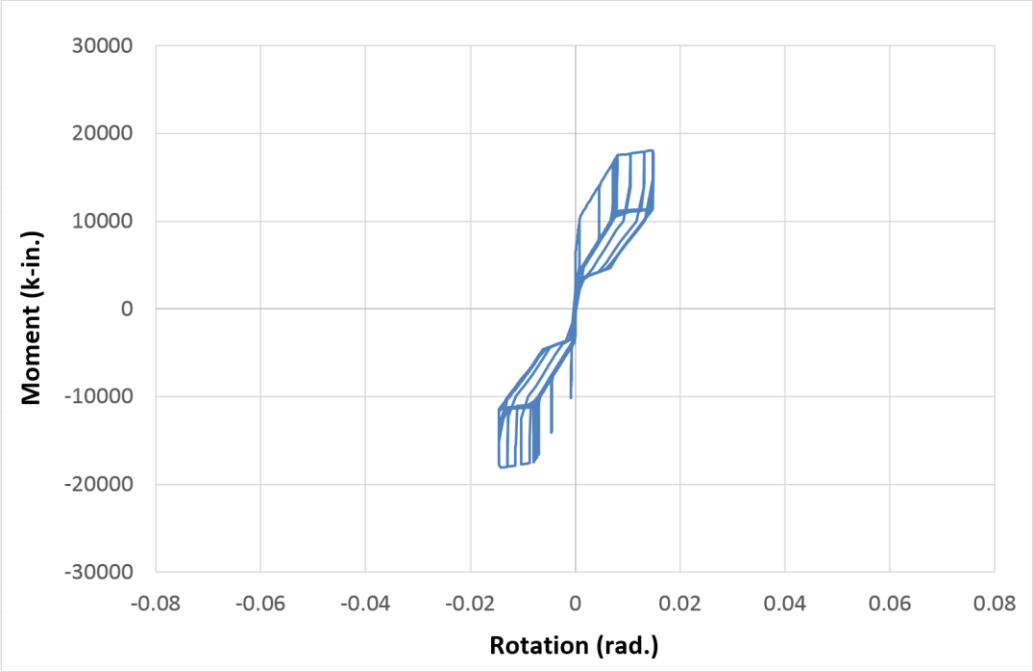

(g) connection M-R curve with beam PH strength reduction ratio of 0.8

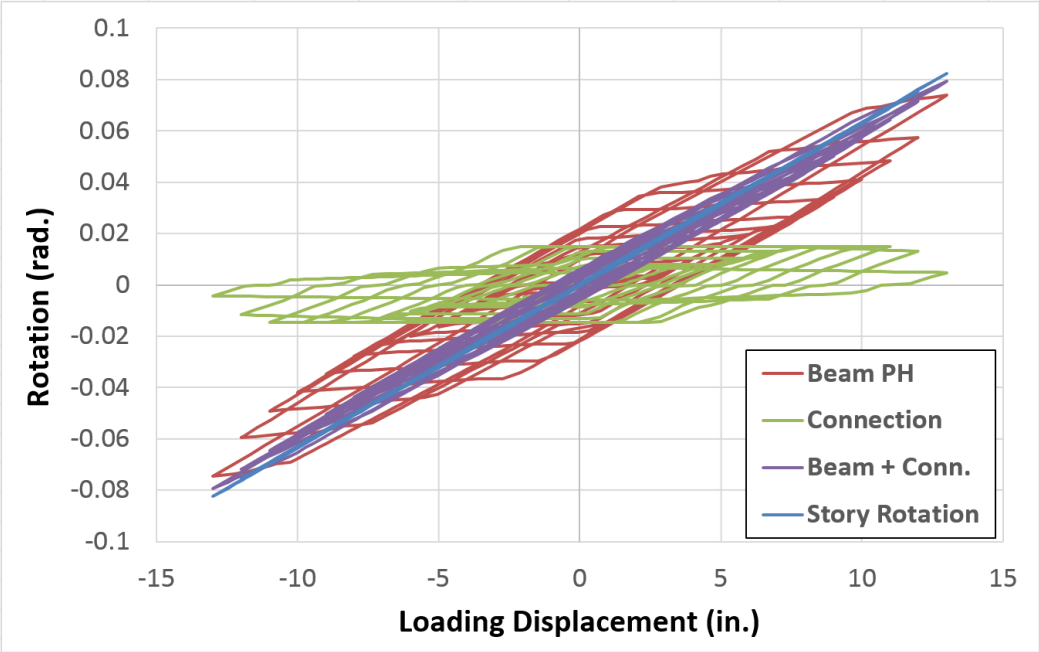

(h) FE model deformation components with beam PH strength reduction ratio of 0.8

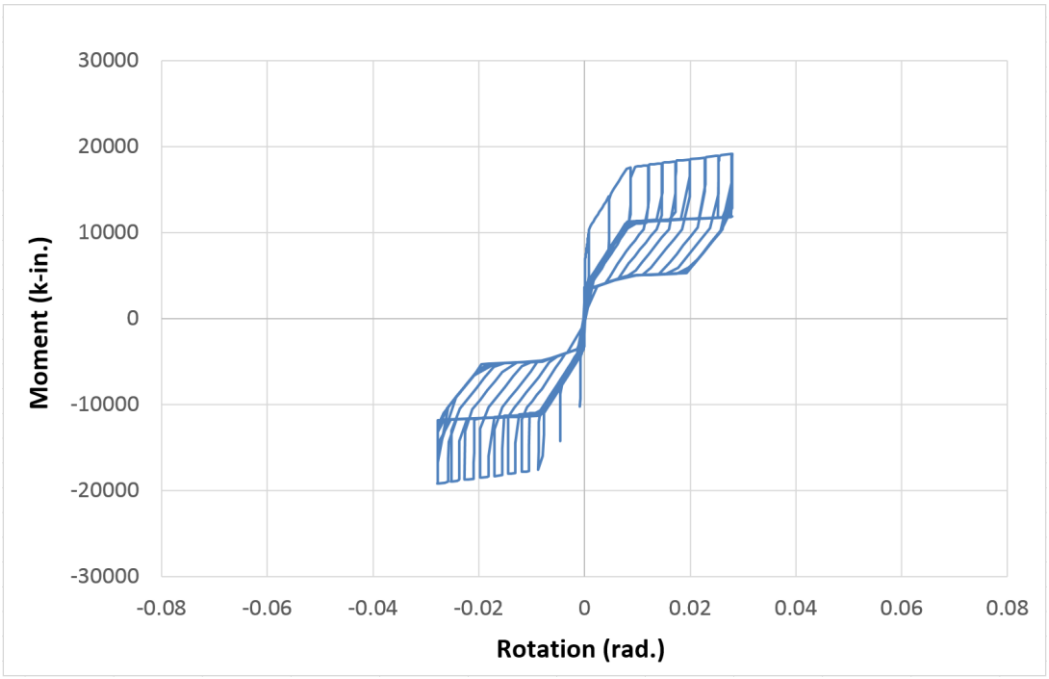

(i) connection M-R curve with beam PH strength reduction ratio of 0.85

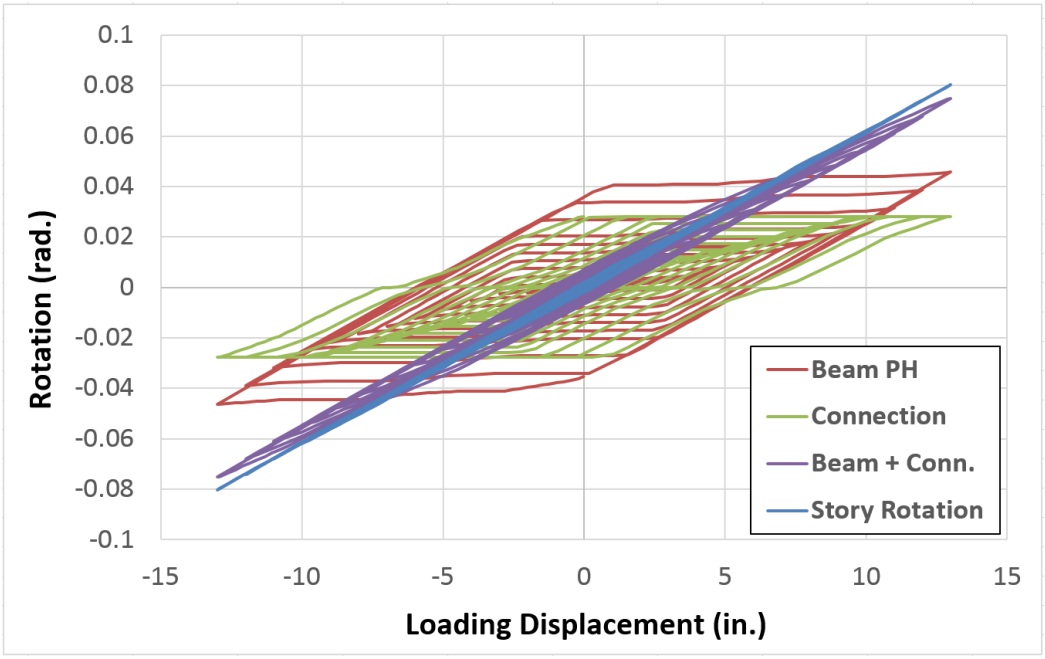

(j) FE model deformation components with beam PH strength reduction ratio of 0.85

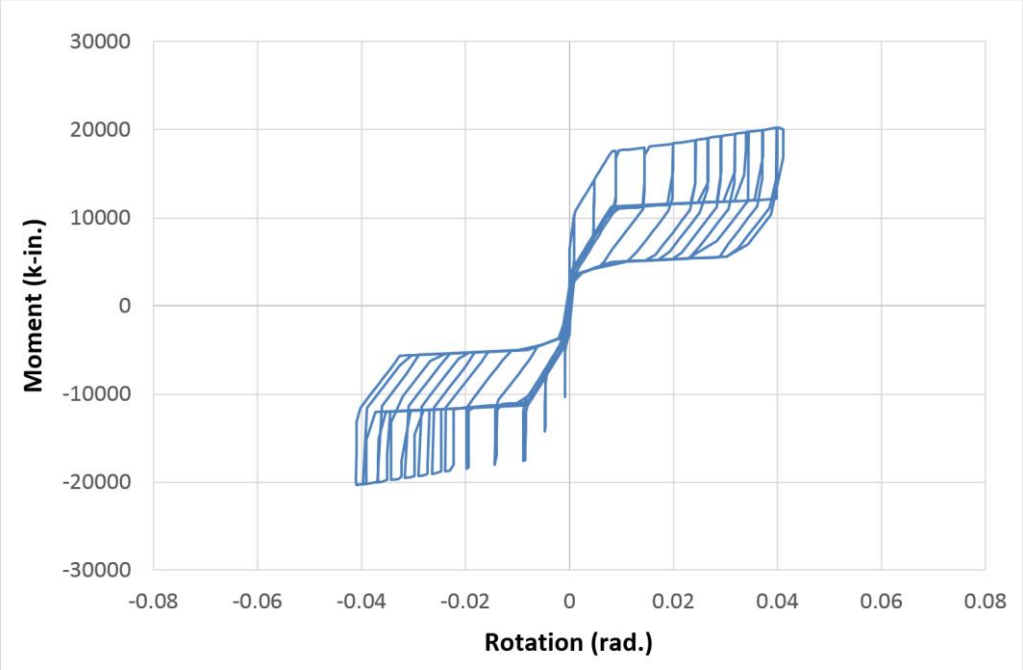

(k) connection M-R curve with beam PH strength reduction ratio of 0.9

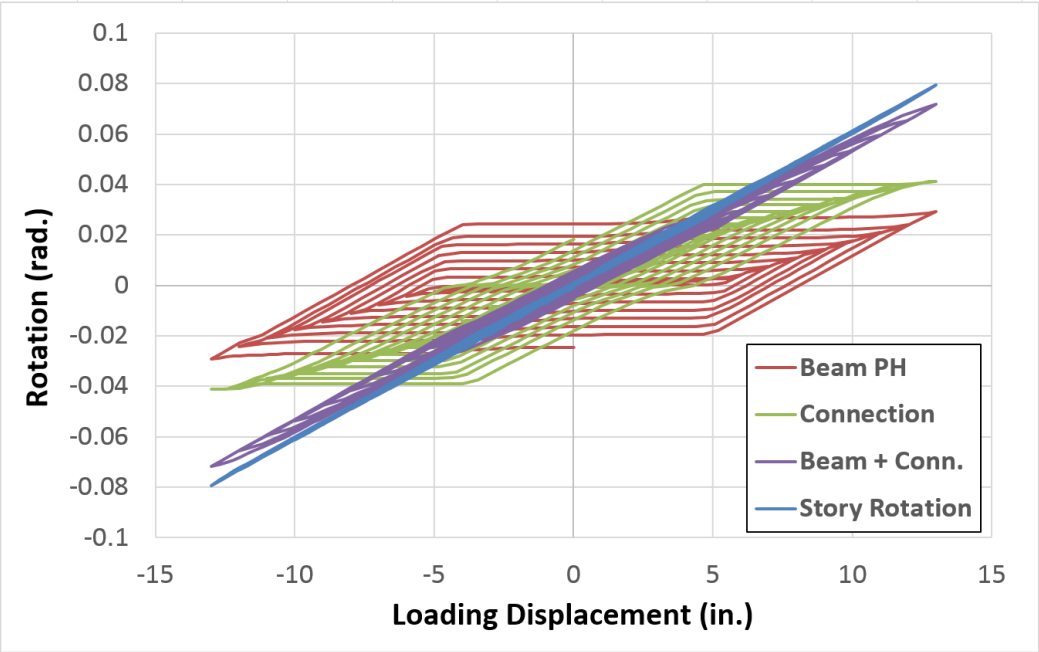

(l) FE model deformation components with beam PH strength reduction ratio of 0.9

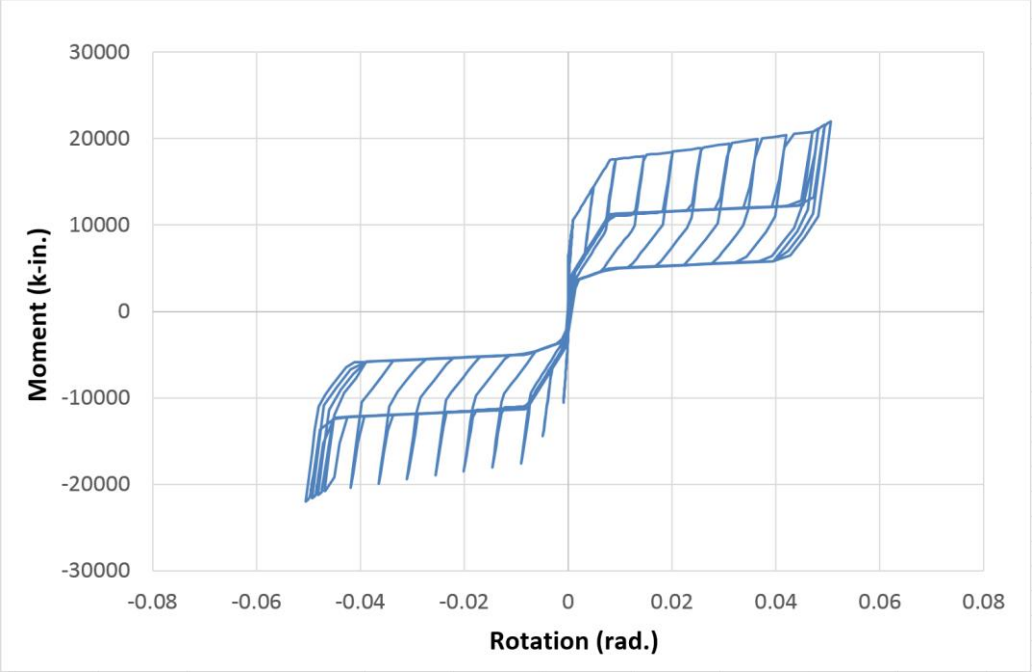

(m) connection M-R curve with beam PH with full strength

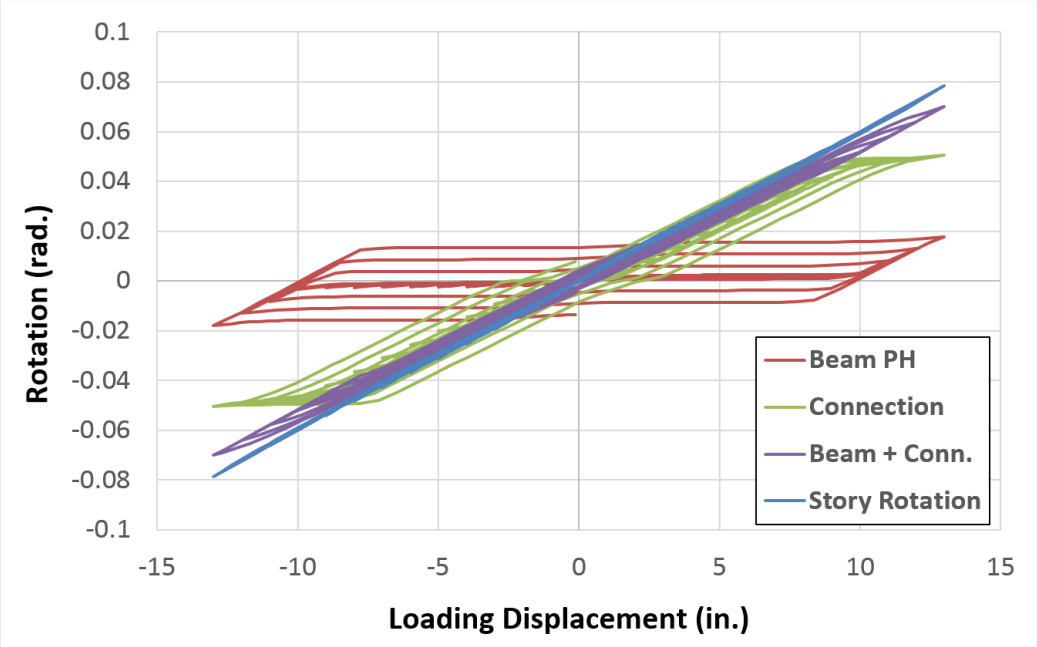

(n) FE model deformation components with beam PH with full strength

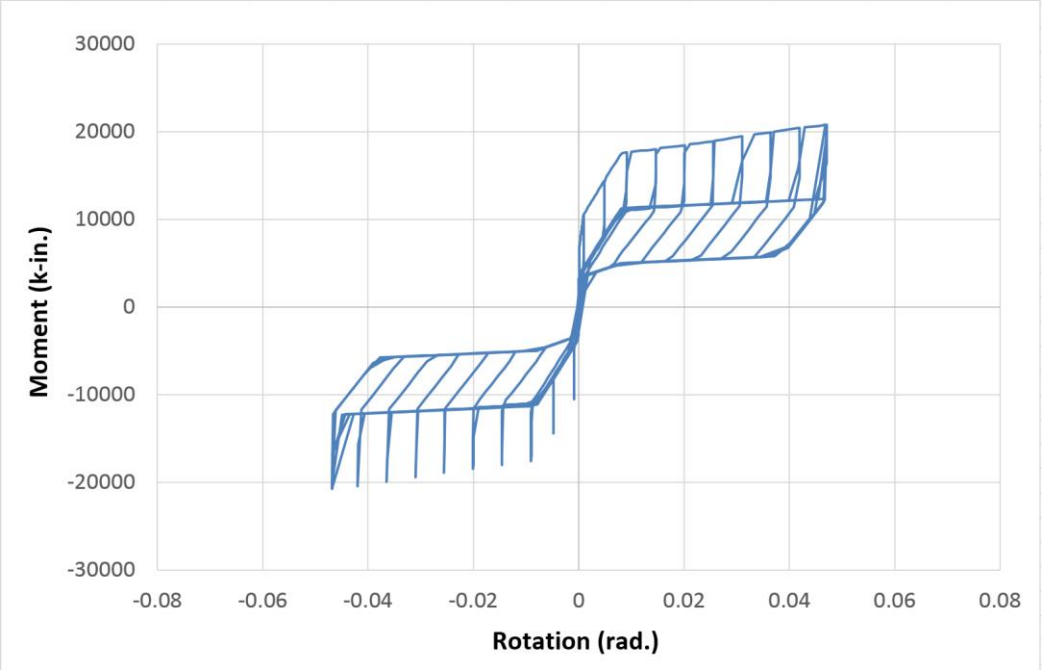

(o) connection M-R curve with elastic perfectly plastic beam hinge

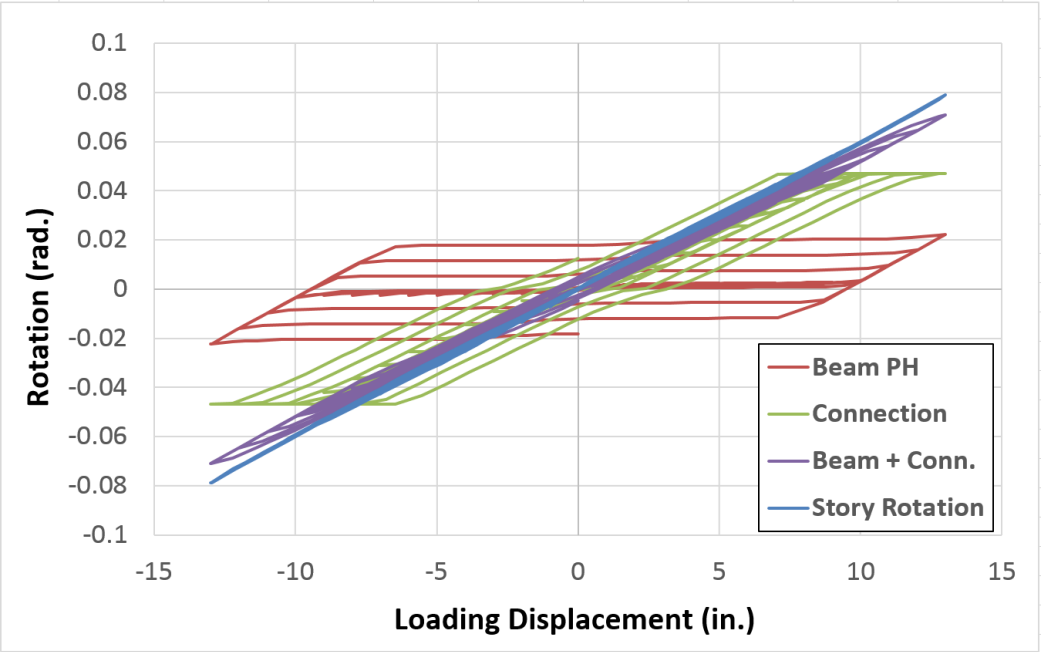

(p) FE model deformation components with elastic perfectly plastic beam hinge

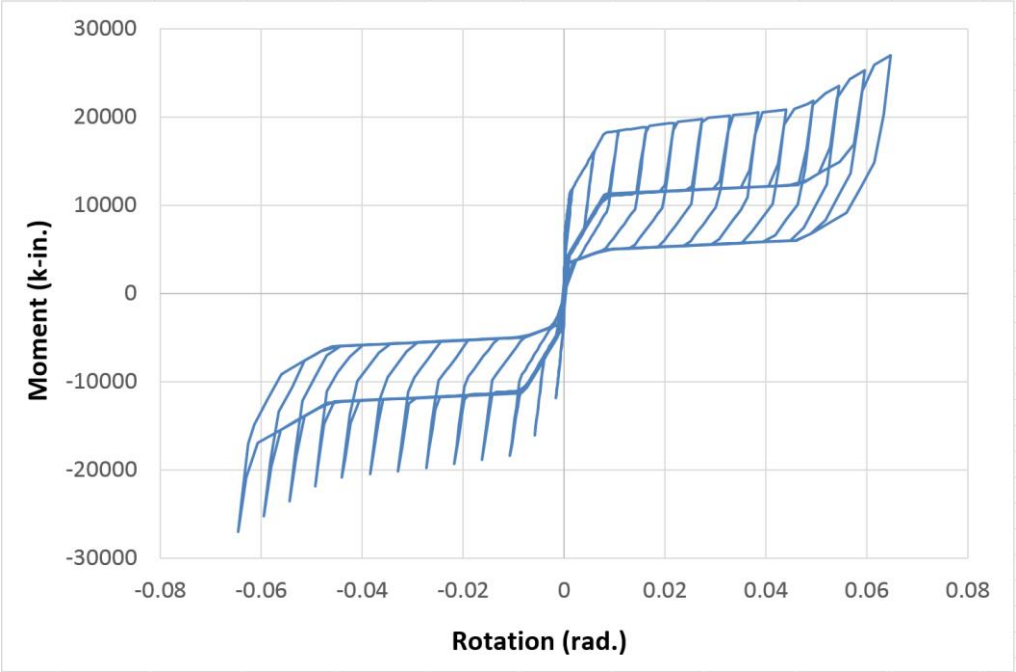

(q) connection M-R curve with elastic beam

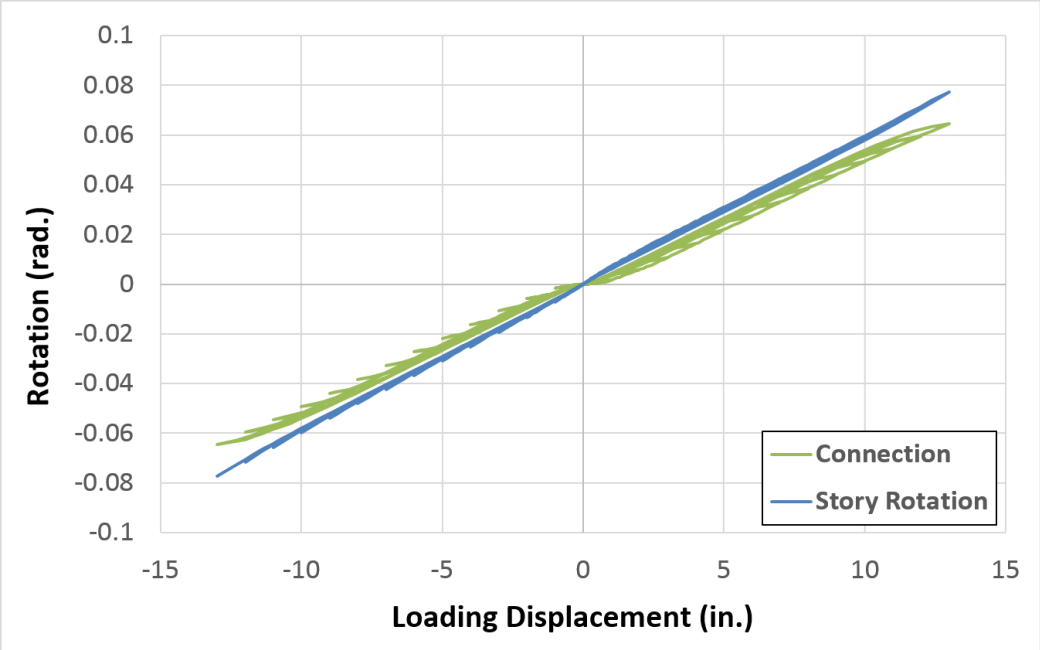

(r) FE model deformation components with elastic beam

Appendix Figure H-2: M-R relationships of the connection and the deformation components of the FE model with different strength reduction of beam plastic hinges

From the above analysis results, one can observe that when the strength of beam is too weak, such as the strength reduced ratio of the beam plastic hinge is less than or equal to 0.6, the maximum moment transferred into the connection is relative small. These corresponding MR relationships of the connection are not fully developed; this means that the connection behavior is limited in a small rotation rang (Appendix Figure H-2 (a), (c), and (e)). Most deformation of the analysis model comes from the beam plastic hinge; the contribution from the connection deformation is negligible (Appendix Figure H-2 (b), (d), and (f)). As the beam hinge becomes stronger, the interaction between the connection and the beam hinge increases, and the connection contributes more and more to the total deformation. When the strength reduced ratio increases to about 0.85, their interaction effect reaches its maximum. The connection and the beam plastic hinges generate nearly half of the total model deformation, respectively. As the beam strength continues to increase, the MR relationship of the connection is more close to be fully developed, and the deformation from connection will become dominant. Even though beam hinge increases to its full strength, it still contributes about 25% ultimate deformation (Appendix Figure H-2 (n)). Compared with the fully restrained moment connection, nearly all deformation comes from beam plastic behavior, partially restrained moment connection reduces the beam plastic damage greatly. Appendix Figure H-2 (q) shows the full MR relationship of the connection when the connecting members are elastic. When full strength beam hinges are defined with strain hardening effect, the strength increasing rate of the connection will become slow after the beam reaches its yield strength. This can be told from Appendix Figure H-2 (m), in which the MR curves of the last several cycles begin to be

close to each other. It causes slow increase of deformation. It is easy to understand that after beam yielding, more deformation of the structure will come from beam plastic behavior. If an elastic perfectly plastic beam hinge is used, after beam yielding, the maximum moment in the connection will keep the same value. This phenomenon can be clearly indicated from Appendix Figure H-2 (o), where the MR curves of the last several cycles are coincident to each other. The results presented in Appendix Figure H-2 can perfectly prove that the proposed simplified connection model is workable with the connecting beams with different strengths.

Appendix I

Models for Confined Concrete by Circular Steel Tube

In this Section, several theoretical models for confined concrete by circular steel tube is introduced as follows, including 'Mander Model', 'Saenz Model', 'Modified Saenz Model', and 'Popovics and Tsai Model'. An example in ABAQUS is also supplied in the end of this Section to compare with all other theoretical models.

I.1 The Mander Model

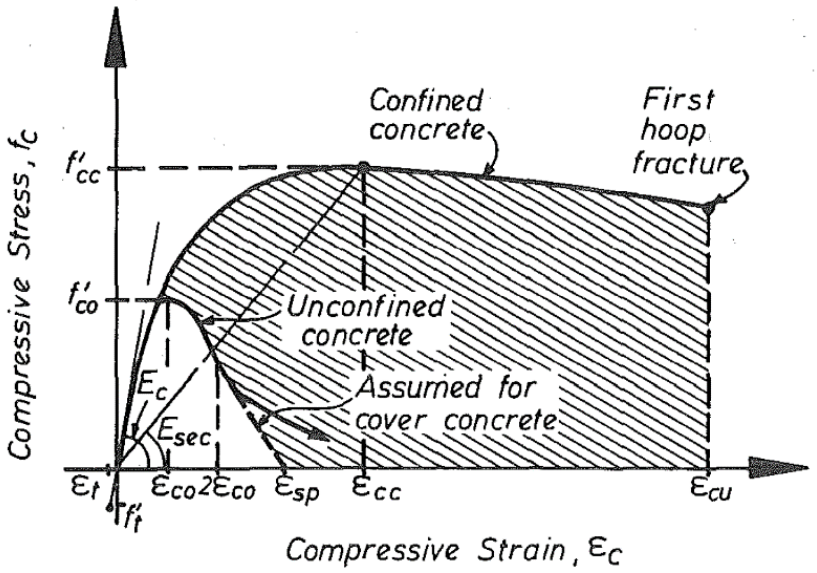

Appendix Figure I-1: stress-strain model proposed for monotonic loading of confined and unconfined concrete [90]

A unified equivalent unconfined concrete model was proposed by Mander in 1984 for considering the confinement effects on concrete strength and ductility from transverse

reinforcements with any general shape: spiral, or circular or rectangular hoops [135]. The model's stress-strain curve, which is based on an equation suggested by Popovics [89], is illustrated in Appendix Figure I-1. For a quasi-static strain rate and monotonic loading, the concrete compressive strength is given by:

$$f_c = \frac{f_{cc}^{'} \cdot x \cdot r}{r - 1 + x^r} \qquad \textbf{(AEq. I-1)}$$

$$x = \frac{\varepsilon_c}{\varepsilon_{cc}} \qquad \textbf{(AEq. I-2)}$$

$$r = \frac{E_c}{E_c - E_{\sec}} \qquad \textbf{(AEq. I-3)}$$

where,

f'_{cc} = compressive strength of confined concrete with equal effective lateral confining stresses f_l' from spiral or circular hoops, ksi.

$$f_{cc}^{'} = f_{co}^{'} \cdot \left(-1.254 + 2.254 \cdot \sqrt{1 + \frac{7.94 \cdot f_l^{'}}{f_{co}^{'}}} - 2 \cdot \frac{f_l^{'}}{f_{co}^{'}} \right)$$

= compressive strength of confined concrete with two lateral confining stresses, f'_{l1} and f'_{l2} from rectangular hoops, which can be calculated from chart in Appendix Figure I-2.

ε_{cc} = compressive strain of confined concrete, which is defined as suggested by Richart et al. [136]:

$$\varepsilon_{cc} = \varepsilon_{co} \cdot \left[1 + 5 \cdot \left(\frac{f_{cc}^{'}}{f_{co}^{'}} - 1 \right) \right]$$

f_{co}' = compressive strength of unconfined concrete, ksi.

ε_{co} = compressive strain of unconfined concrete, in./in.

E_c = elastic modulus of concrete, ksi.

$$E_c = 57 \cdot \sqrt{1000 \cdot f_{co}^{'}}$$

E_{sec} = secant modulus of confined concrete, ksi.

$$E_{\text{sec}} = \frac{f_{cc}^{'}}{\varepsilon_{cc}}$$

For the concrete cover which is outside of transverse reinforcements, a straight line stress-strain relationship is assumed after $2\varepsilon_{co}$ as shown in Appendix Figure I-1.

A similar method to the one used by Sheikh and Uzumeri [137] is adopted by Mander [90] for calculating the effective lateral confining stress. Due to the existence of the spacing between two adjacent levels of transverse reinforcements on the concrete cross section, the confinements on the section is not uniform along the longitudinal direction. However, a uniformly distributed lateral confining pressure f_l is assumed for convenience. Then the effective lateral confinement is proposed by Mander as follows:

$$f_l^{'} = f_l \cdot k_e \qquad \textbf{(AEq. I-4)}$$

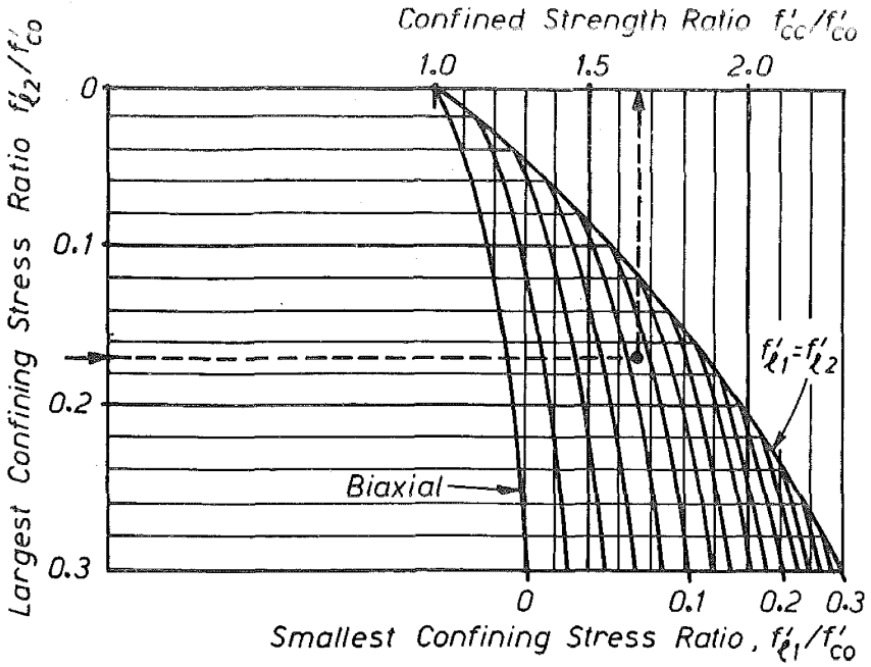

Appendix Figure I-2: Confined strength determination from lateral confining stresses for rectangular sections [90]

Case 1: For circular section confined by spiral or circular hoops shown in Appendix Figure I-3:

$$f_l = \frac{1}{2} \cdot \rho_s \cdot f_{yh} \qquad \textit{(AEq. I-5)}$$

$$\rho_s = \frac{4 \cdot A_{sp}}{d_s \cdot s} \qquad \textit{(AEq. I-6)}$$

For circular hoops: $$k_e = \frac{\left(1 - \frac{s'}{2 \cdot d_s}\right)^2}{1 - \rho_{cc}} \qquad \textit{(AEq. I-7)}$$

For circular spirals: $$k_e = \frac{1 - \frac{s'}{2 \cdot d_s}}{1 - \rho_{cc}} \qquad \textit{(AEq. I-8)}$$

where,

k_e = confinement effective coefficient

ρ_s = ratio of the volume of transverse confining steel to the volume of confined concrete core

f_l = lateral pressure from the transverse reinforcement, ksi.

f_l' = effective lateral confinement, ksi.

f_{yh} = yield strength of the transverse reinforcement, ksi.

s' = clear vertical spacing between spiral or hoop bars, in.

d_s = diameter of spiral between bar centers, in.

s = center to center spacing or pitch of spiral or circular hoop, in.

A_{sp} = area of transvers reinforcement bar, $in.^2$

ρ_{cc} = ratio of area of longitudinal reinforcement to area of core of section

$$\rho_{cc} = \frac{4 \cdot A_s}{\pi \cdot d_s^2}$$

A_s = total area of longitudinal reinforcements, $in.^2$

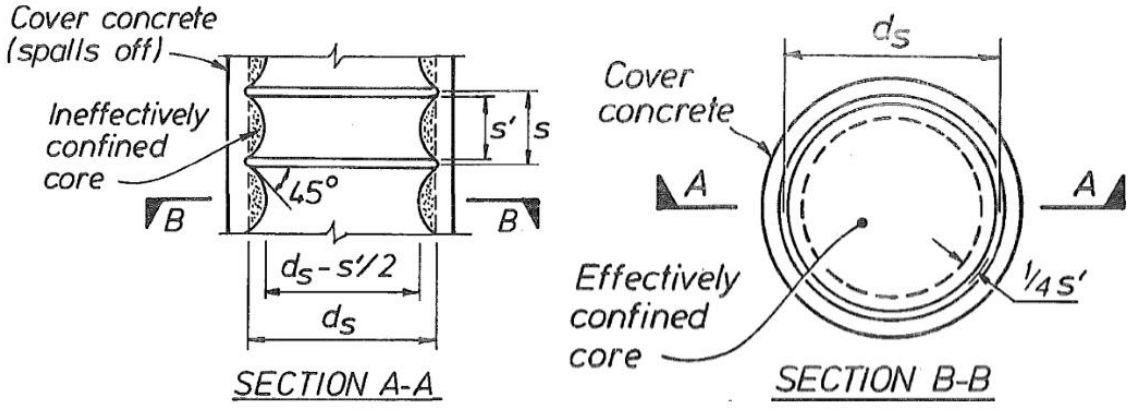

Appendix Figure I-3: Effectively confined core for circular hoop reinforcement [90]

Case 2: Rectangular section confined by rectangular hoops with or without cross ties shown in Appendix Figure I-4:

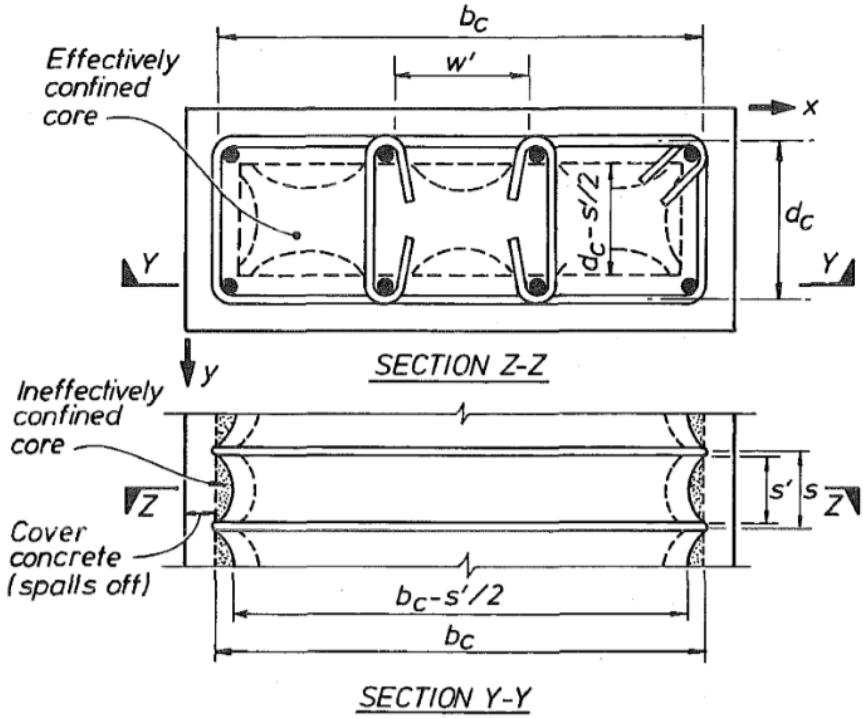

Appendix Figure I-4: Effectively confined core for rectangular hoop reinforcement [90]

Effective lateral confinement:

X-direction: $f_{lx}^{'} = k_e \cdot f_{lx}$ ***(AEq. I-9)***

Y-direction: $f_{ly}^{'} = k_e \cdot f_{ly}$ ***(AEq. I-10)***

Lateral pressure from the transverse reinforcement:

X-direction: $f_{lx} = \frac{A_{sx}}{s \cdot d_c} \cdot f_{yh}$ ***(AEq. I-11)***

Y-direction: $f_{ly} = \frac{A_{sy}}{s \cdot b_c} \cdot f_{yh}$ ***(AEq. I-12)***

Confinement effective coefficient:

$$k_e = \frac{\left(1 - \sum_{i=1}^{n} \frac{\left(w_i^{'}\right)^2}{6 \cdot b_c \cdot d_c}\right) \cdot \left(1 - \frac{s^{'}}{2 \cdot b_c}\right) \cdot \left(1 - \frac{s^{'}}{2 \cdot d_c}\right)}{1 - \rho_{cc}} \quad \textit{(AEq. I-13)}$$

where,

f_{lx} = lateral pressure from the transverse reinforcement in x direction, ksi.

f_{ly} = lateral pressure from the transverse reinforcement in y direction, ksi.

f'_{lx} = effective lateral confinement in x direction, ksi.

f'_{ly} = effective lateral confinement in y direction, ksi.

I.2 Modifications for confinement in Mander's model for CFTs

The model proposed by Mander [135] was originally applicable for concrete sections with

transverse reinforcements or ties. When the sections are changed to concrete filled steel tubes, the confining stresses will be supplied by the steel tubes. If the confinement effects from steel tubes are calculated, then the same concepts can be applied to calculate the strength and ductility of the confined concrete for the CFT case. In the following section, a simple mechanism is proposed to calculate the lateral pressure from steel tubes.

Case 1: Circular section confined by circular steel tubes in Appendix Figure I-5:

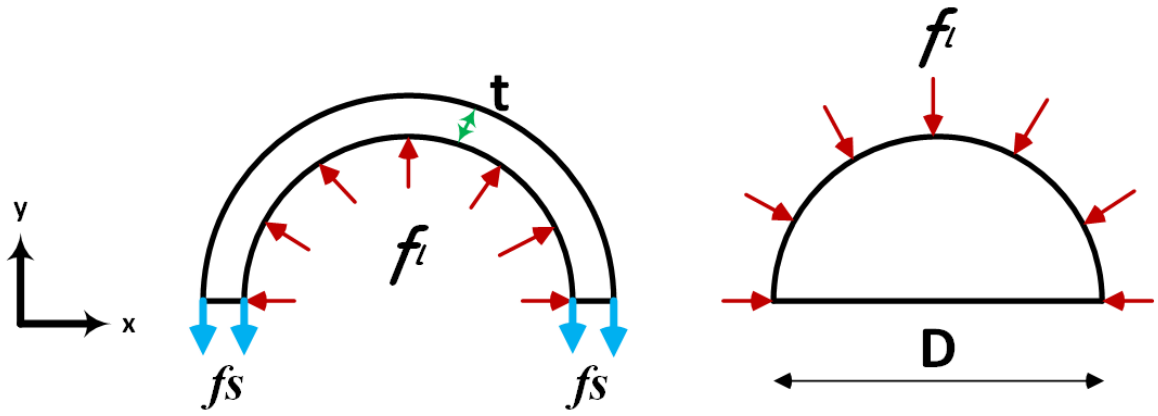

Appendix Figure I-5: Effectively confined concrete core for CCFT

Force balance in y direction:

$$\sum F_y = 0 \qquad \textit{(AEq. I-14)}$$

For unit height column:

$$f_l \cdot D \cdot 1 = 2 \cdot f_s \cdot t \cdot 1 \qquad \textit{(AEq. I-15)}$$

Lateral pressure from circular tube:

$$f_l = \frac{2 \cdot f_s \cdot t}{D} \qquad \textit{(AEq. I-16)}$$

Case 2: Rectangular section confined by rectangular steel tubes in Appendix Figure I-6:

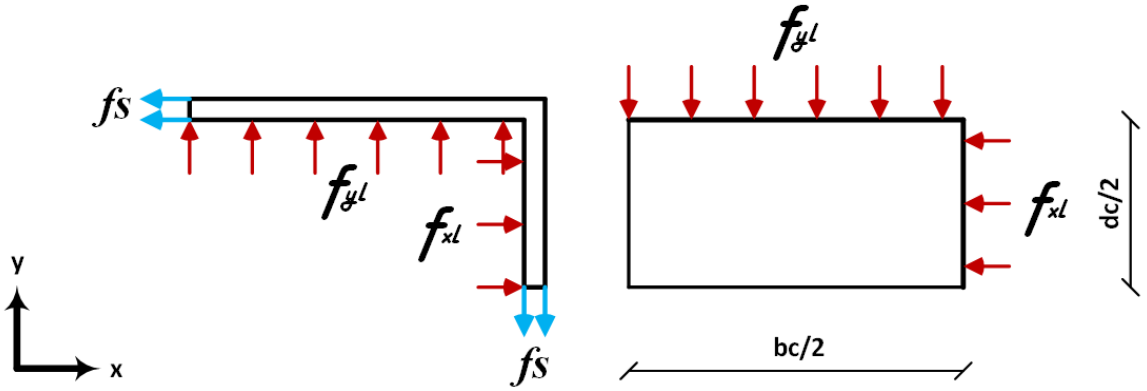

Appendix Figure I-6: Effectively confined concrete core for RCFT

Force balance in x direction:

$$\sum F_x = 0 \qquad \textit{(AEq. I-17)}$$

For unit height column:

$$f_{xl} \cdot \frac{d_c}{2} \cdot 1 = f_s \cdot t \cdot 1 \qquad \textit{(AEq. I-18)}$$

Lateral pressure in x direction:

$$f_{xl} = \frac{2 \cdot f_s \cdot t}{d_c} \qquad \textit{(AEq. I-19)}$$

Force balance in y direction:

$$\sum F_y = 0 \qquad \textbf{(AEq. I-20)}$$

For unit height column:

$$f_{yl} \cdot \frac{b_c}{2} \cdot 1 = f_s \cdot t \cdot 1 \qquad \textbf{(AEq. I-21)}$$

Lateral pressure in x direction:

$$f_{yl} = \frac{2 \cdot f_s \cdot t}{b_c} \qquad \textbf{(AEq. I-22)}$$

where,

f_s = the tensile stress in the tube orthogonal to the longitudinal direction, ksi.

k_e = 1.0, confinement effective coefficient

I.3 The Saenz Model for CFTs

In addition to Mander's model for concrete confined by transverse reinforcement, other early investigators thought that the compressive strength and strain of confined concrete and their unconfined counterparts had the following relationships [90]:

$$f_{cc}^{'} = f_c^{'} + k_1 \cdot f_l \qquad \textbf{(AEq. I-23)}$$

$$\varepsilon_{cc}^{'} = \varepsilon_{c}^{'} \cdot \left(1 + k_2 \cdot \frac{f_l}{f_c^{'}}\right) \qquad \textit{(AEq. I-24)}$$

Richart conducted lots of tests and suggested that the values of k_1 and k_2 are 4.1 and 20.5, respectively [136]. The lateral pressure f_l from circular steel tube is based on the ratio of D/t and the yield strength of tube. Hu et al. [138] proposed an empirical equation to calculate this lateral pressure, which is applicable for a wide D/t ratio range, from 21.7 to 150. After determining f'_{cc} and ε'_{cc}, a stress-strain relationship curve can be drawn based on the equation proposed by Saenz in Appendix Figure I-7 [91].

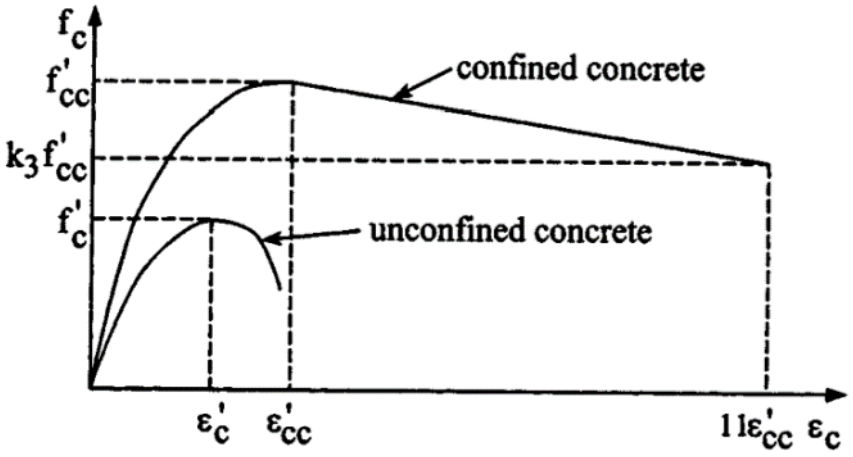

Appendix Figure I-7: Equivalent uniaxial stress-strain curve for concrete [91]

The curve in Appendix Figure I-7 for confined concrete is divided into two parts, the first part is using Saenz's model for strain ranging from 0 to ε'_{cc}, and the other part is a straight line passing through two points, (ε'_{cc}, f'_{cc}) and ($11\varepsilon'_{cc}$, $k_3 f'_{cc}$), and the strain ranging from ε'_{cc} to $11\varepsilon'_{cc}$. The parameter k_3 is determined by the empirical equation proposed by Hu et al. [138].

The proposed constitutive model has been verified using ABAQUS by comparing the FE results with experimental tests' results.

Saenz's Model:

$$f_c = \frac{E_c \cdot \varepsilon_c}{1+\left(R+R_E-2\right)\cdot\left(\frac{\varepsilon_c}{\varepsilon_{cc}^{'}}\right)-\left(2\cdot R-1\right)\cdot\left(\frac{\varepsilon_c}{\varepsilon_{cc}^{'}}\right)^2+R\cdot\left(\frac{\varepsilon_c}{\varepsilon_{cc}^{'}}\right)^3} \qquad \textit{(AEq. I-25)}$$

$$R = \frac{R_E\cdot\left(R_\sigma-1\right)}{\left(R_\varepsilon-1\right)^2}-\frac{1}{R_\varepsilon} \qquad \textit{(AEq. I-26)}$$

$$R_E = \frac{E_c\cdot\varepsilon_{cc}^{'}}{f_{cc}^{'}} \qquad \textit{(AEq. I-27)}$$

$$E_c = 57\cdot\sqrt{1000\cdot f_c^{'}} \qquad \textit{(AEq. I-28)}$$

$$R_\sigma = 4,\ \ R_\varepsilon = 4 \qquad \textit{(AEq. I-29)}$$

where,

R_σ, R_ε = are suggested by Hu and Schnobrich [139]

f_c' = compressive strength of unconfined concrete, ksi.

Hu's empirical equations for lateral pressure:

For circular steel tube:

$$\text{for } 21.7 \le \frac{D}{t} \le 47, \quad f_l = f_y \cdot \left[0.043646 - 0.000832 \cdot \left(\frac{D}{t} \right) \right] \qquad \textit{(AEq. I-30)}$$

$$\text{for } 47 \le \frac{D}{t} \le 150, \quad f_l = f_y \cdot \left[0.006241 - 0.000357 \cdot \left(\frac{D}{t} \right) \right] \qquad \textit{(AEq. I-31)}$$

For square steel tube:

$$\text{for } 17 \le \frac{B}{t} \le 29.2, \quad f_l = f_y \cdot \left[0.055048 - 0.001885 \cdot \left(\frac{B}{t} \right) \right] \qquad \textit{(AEq. I-32)}$$

$$\text{for } 29.2 \le \frac{B}{t} \le 150, \quad f_l = 0 \qquad \textit{(AEq. I-33)}$$

Hu's empirical equations for k_3:

For circular steel tube:

$$\text{for } 21.7 \le \frac{D}{t} \le 40, \quad k_3 = 1 \qquad \textit{(AEq. I-34)}$$

$$\text{for } 40 \le \frac{D}{t} \le 150, \quad k_3 = 0.0000339 \cdot \left(\frac{D}{t} \right)^2 - 0.010085 \cdot \left(\frac{D}{t} \right) + 1.3491 \qquad \textit{(AEq. I-35)}$$

For square steel tube:

$$\text{for } 17 \le \frac{D}{t} \le 70, \quad k_3 = 0.000178 \cdot \left(\frac{B}{t} \right)^2 - 0.02492 \cdot \left(\frac{B}{t} \right) + 1.2722 \qquad \textit{(AEq. I-36)}$$

$$\text{for } 70 \le \frac{D}{t} \le 150, \quad k_3 = 0.4 \qquad \textit{(AEq. I-37)}$$

I.4 Modified Saenz's Model for CCFT

Although the parametric studies for the variables involved in Saenz's model have been conducted by Hu et al. [138] using ABAQUS, including specimens' sizes and concrete and steel materials, the range of compressive strength of concrete is only from 3.45 ksi to 4.57 ksi. And experimental investigations were conducted by Giakoumelis and Lam and verified the effectiveness of Hu's equation for the concrete with compressive strength up to 4.35 ksi [140]. When the compressive strength of concrete is greater than 4.35 ksi, the decreasing branch with strain larger than ε'_{cc} will underestimate the concrete post peak capacity. In order to make the model applicable for higher strength concrete, another reduction factor r is introduced to the model based on the tests results from Giakoumelis and Lam. The value r is suggested by Tomii [141], and Mursi and Uy [142] to be 1.0 when the cube strength is equal or less than 4.35 ksi, and to be 0.5 when the cube strength is equal or greater than 14.5 ksi, and linear interpolation can be applied to calculate the value of r for the cube strength between 4.35 ksi and 14.5 ksi.

The modified model is divided into three parts, and is presented in Appendix Figure I-8. The first part is assumed to be elastic range from 0 to the proportional limit of $0.5f'_{cc}$ for the strength. The second part will adopt Saenz's Model as mentioned above with strength range from $0.5f'_{cc}$ to f'_{cc}. The third part is also assumed to be a straight line passing through two points, (ε'_{cc}, f'_{cc}) and ($11\varepsilon'_{cc}$, r$k_3 f'_{cc}$), with the maximum strain of $11\varepsilon'_{cc}$.

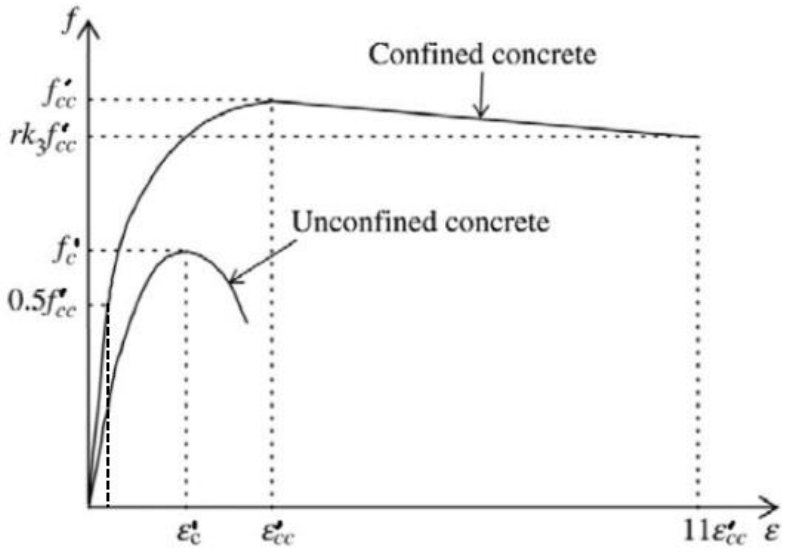

Appendix Figure I-8: Equivalent uniaxial stress–strain curves for confined and unconfined concrete [143]

I.5 Popovics's and Tsai's Models for the Backbone Curve of Concrete under Cyclic Loading

There are numerous models to simulate the backbone curves of concrete under cyclic loading, such as Kent and Park [144], Popovics [89], Tsai [92], Sheikh and Uzumeri [137], Hoshikuma et al. [145], and Akiyama et al. [146]. In the following section, Tsai's model is discussed.

In 1973 Popovics [89] proposed a model for monotonic stress-strain curve of concrete, which is defined by three parameters: the initial modulus of elasticity, the peak stress, and the strain at the peak stress. All the relationships are defined using normalized values of strain, stress, and tangent for both compression and tension.

Popovics's Model:

$$y = \frac{r \cdot x}{r - 1 + x^r} \qquad \textit{(AEq. I-38)}$$

$$r = \frac{n}{n - 1} \qquad \textit{(AEq. I-39)}$$

For compression:

$$x = \frac{\varepsilon_c}{\varepsilon_{cc}^{'}} \quad ; \quad y = \frac{f_c}{f_{cc}^{'}} \quad ; \quad n = \frac{E_c \cdot \varepsilon_{cc}^{'}}{f_{cc}^{'}} \qquad \textit{(AEq. I-40)}$$

For tension:

$$x = \frac{\varepsilon_c - \varepsilon_{to}}{\varepsilon_t^{'}} \quad ; \quad y = \frac{f_c}{f_t^{'}} \quad ; \quad n = \frac{E_c \cdot \varepsilon_t^{'}}{f_t^{'}} \qquad \textit{(AEq. I-41)}$$

where,

x = normalized strain, in./in.

ε_c = strain, in./in.

ε_{to} = tensile strain offset, in./in.

ε_{cc}' = strain at peak stress in compression, in./in.

ε_t' = strain at peak stress in tension, in./in.

y = normalized stress, ksi.

f_c = stress, ksi.

f'_{cc} = peak stress in compression, ksi.

f'_t = peak stress in tension, ksi.

n = normalized modulus

E_c = initial modulus of elasticity, ksi.

In 1988 Tsai proposed another model which is based on four parameters and also defined using the same normalized values as Popovics's model. The first three parameters are also the same as Popovics's model, and the fourth parameter is added to control the post-peak behavior, termed r (r_n in compression and r_p in tension). Tsai's model is more accurate for concrete with high confinement or high strength, and it can be simplified to Popovics's model for the case of $r = n/(n-1)$.

Tsai's Model:

$$y = \frac{n \cdot x}{D(x)} \qquad \textit{(AEq. I-42)}$$

$$D(x) = \begin{cases} 1 + \left(n - \dfrac{r}{r-1}\right) \cdot x + \dfrac{x^r}{r-1} & \text{for } r \neq 1 \\ 1 + \left(n - 1 + \ln x\right) \cdot x & \text{for } r = 1 \end{cases} \qquad \textit{(AEq. I-43)}$$

$$r_n = \begin{cases} \dfrac{f_c'[ksi]}{0.75} - 1.9 & \text{for } x \leq 1 \\ 0.4 + 0.016 \cdot \dfrac{D}{t} \cdot \dfrac{f_c'}{F_y} & \text{for CCFT with } x > 1 \\ 1.7 \cdot \dfrac{H}{t} \cdot \sqrt{\dfrac{F_y}{E_s}} \cdot \dfrac{f_c'}{F_y} & \text{for RCFT with } x > 1 \end{cases} \qquad \textit{(AEq. I-44)}$$

$$f_t^{'}[ksi] = 0.19 \cdot \sqrt{f_c^{'}[ksi]} \qquad \textbf{(AEq. I-45)}$$

$$\varepsilon_t = 1.23 \cdot \frac{f_t^{'}}{E_c} \qquad \textbf{(AEq. I-46)}$$

$$E_c[psi] = 33 \cdot w_c[lbs/ft^3]^{1.5} \cdot \sqrt{f_c^{'}[psi]} \qquad \textbf{(AEq. I-47)}$$

where,

E_c = elastic modulus of concrete, [104]

r_n = suggested by Denavit [147]

r_p = 4.0, recommended by Tort and Hajjar [148]

D = outer diameter of circular steel tube, in.

t = thickness of tube wall, in.

H = width of rectangular steel tube, in.

F_y = yield strength of steel tube, ksi.

E_s = elastic modulus of steel, ksi.

In order to calculate the compressive strength and strain of concrete under confinement, the lateral pressure must be calculated first. For CCFT, the lateral confinement is suggested by Denavit and Hajjar [149] by assuming a hoop stress equal to $\alpha_\theta F_y$. Then Mander's [90] equations will be utilized to calculate the compressive strength and the corresponding strain.

$$f_{cc}^{'} = f_c^{'} \cdot \left(-1.254 + 2.254 \cdot \sqrt{1 + \frac{7.94 \cdot f_l^{'}}{f_c^{'}}} - 2 \cdot \frac{f_l^{'}}{f_c^{'}} \right) \quad \textbf{(AEq. I-48)}$$

$$\varepsilon_{cc}^{'} = \varepsilon_c^{'} \cdot \left[1 + 5 \cdot \left(\frac{f_{cc}^{'}}{f_c^{'}} - 1 \right) \right] \quad \textbf{(AEq. I-49)}$$

$$f_l^{'} = \frac{2 \cdot \alpha_\theta \cdot F_y}{D/t - 2} \quad \textbf{(AEq. I-50)}$$

$$\alpha_\theta = 0.138 - 0.00174 \cdot \frac{D}{t} \geq 0 \quad \textbf{(AEq. I-51)}$$

I.6 Comparison among different models for CCFT

In this section, four theoretical models discussed above are compared for compressive behavior of the concrete confined by a circular steel tube: Saenz's model and its modified version, Popovics's model, and Tsai's model. Mander's model is originally proposed for concrete confined by reinforcement and the stress-strain relationship uses Popovics's model. Mander's model is not discussed in this section, but the equations proposed by Mander to calculate compressive strength and strain for confined concrete are adopted by Popovics's and Tsai's models. Furthermore, FE analysis with CDP model for concrete in ABAQUS are also conducted, and the results are compared with other theoretical models to confirm that CDP model is effective in simulating the confinement behavior of concrete. The behavior of CDP model will be illustrated in section 5.2.

There are two CCFT specimens used as indicated in Appendix Figure I-9. They have the same material properties and same height. The only different property is the CCFTs' outer diameter,

one is 21 inch and the other is 10 inch. The thickness of both steel tubes is 1.0 inch, and the height is 15 inches. The nominal yield strength of the steel tubes is 55 ksi, Young's modulus is 29000 ksi, and Poisson ratio is 0.3. The stress-strain curve for steel is shown in Figure 4-12. Infill concrete with nominal weight is used, and its unconfined compressive strength is taken as 4.7 ksi, its Young's modulus as 3900 ksi, and its Poisson ratio as 0.2. The detailed stress-strain relationship is presented in Figure 4-13, and the corresponding data is shown in Table 4-7.

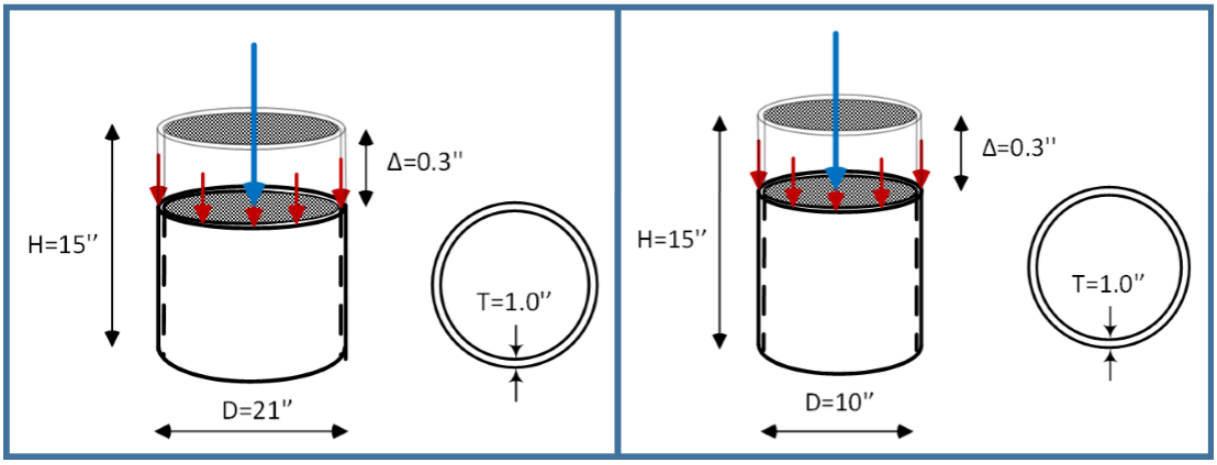

Appendix Figure I-9: Two CCFTs with both large and small diameter under compression

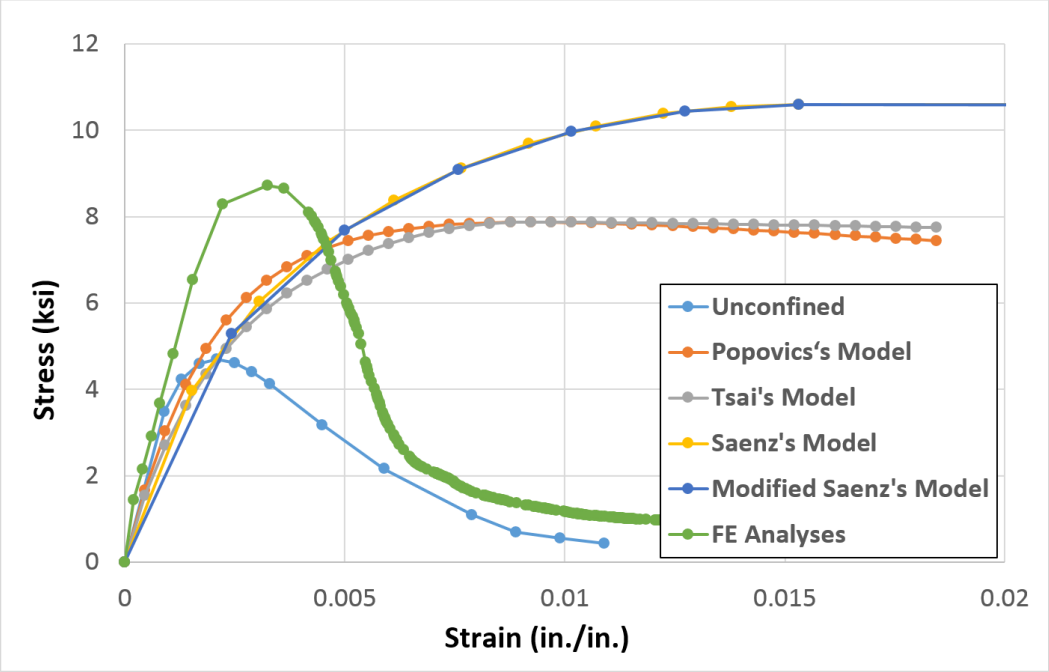

Appendix Figure I-10: Comparison of stree strain relationship for confined concrete by the circular tube with either D = 10" or D = 21" among different prediction models

Appendix Figure I-10 shows the comparison of the results of all different methods for the two CCFTs specimens. From these results, one can easily observe that: (1) All models can consider the confinement effect from circular steel tube, and the concrete strength and ductility capacity are increased greatly; (2) When strain is less than 0.5%, all four theoretical models simulate similar behaviors; when strain is greater than 0.5%, Tsai's model and Popovics's model have no obvious increase of strength, but Saenz's model and its modified one will give continuous increase of strength; (3) compared with theoretical models, the FE model with CDP presents much less ductility capacity, but indeed gives great increase of peak strength, which is greater than Tsai's and Popovics's model, but less than Saenz's and its modified one. The Von-Mises stress states are shown in Appendix Figure I-11 for both circular steel tubes in two specimens

in Appendix Figure I-9.

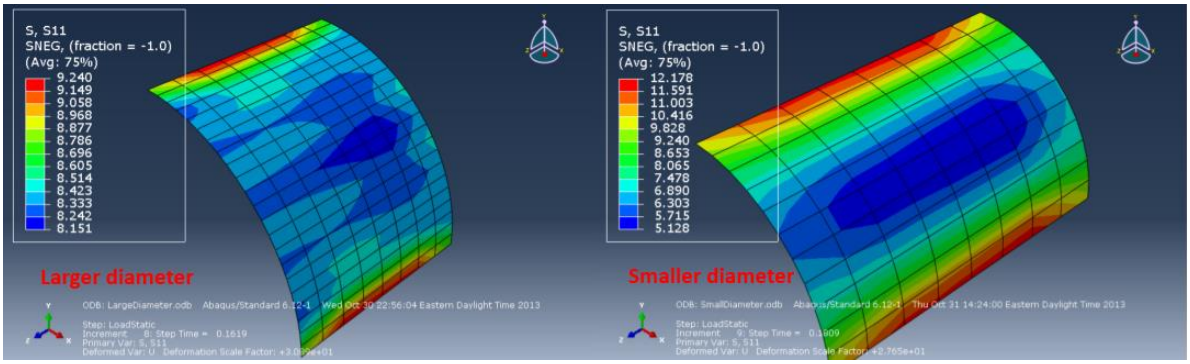

(a) Large diameter D = 21” ***(b) Small diameter D = 10”***

Appendix Figure I-11: Stress states of the steel tube when the ultimate compressive strength of the infill concrete is reached

Appendix J

Concrete Damaged Plasticity Model in ABAQUS

The *concrete damaged plasticity* (**CDP**) model is one of the three models in ABAQUS to simulate brittle behavior with cracking of the concrete, and is the only one workable for both standard and explicit solvers.

J.1 Model mechanism

Under cyclic loading, in the *concrete damaged plasticity* (**CDP**) model the sensitivity to the rate of straining can be defined, and the stiffness of recovery under loading reversals can be controlled by defining damage variables and equivalent plastic strains. The evolution of the yield (or failure) surface is controlled by two hardening variables, $\tilde{\varepsilon}_t^{pl}$ and $\tilde{\varepsilon}_c^{pl}$, linked to failure mechanisms under tension and compression loading, respectively. One can refer to $\tilde{\varepsilon}_t^{pl}$ and $\tilde{\varepsilon}_c^{pl}$ as tensile and compressive equivalent plastic strains, respectively.

Damaged plasticity is assumed for both tensile and compressive response of concrete by the model as shown in Appendix Figure J-1. For uniaxial tensile behavior, a linear response is assumed with elastic modulus of E_o until the maximum tensile strength σ_{to} is reached. After post-peak, nonlinear degradation of the tensile strength will occur due to the generation of cracking in the concrete. Under uniaxial compression, the stress-strain curve will follow an elastic relationship with slope E_o at beginning until the compressive failure strength σ_{co} is

reached. When stress exceeds σ_{co}, micro-cracks start to generate and the concrete begins to go into its inelastic stage. However, in this stage, the current cracks will not propagate if the stress is kept the same, so this is still a stable stage and the strength of concrete can continue to increase until the ultimate compressive strength σ_{cu} is reached. After passing the ultimate compressive strength σ_{cu}, concrete will go into the unstable stage and the cracking begins to extend automatically even though the loading does not increase, and the compressive strength starts to decrease gradually.

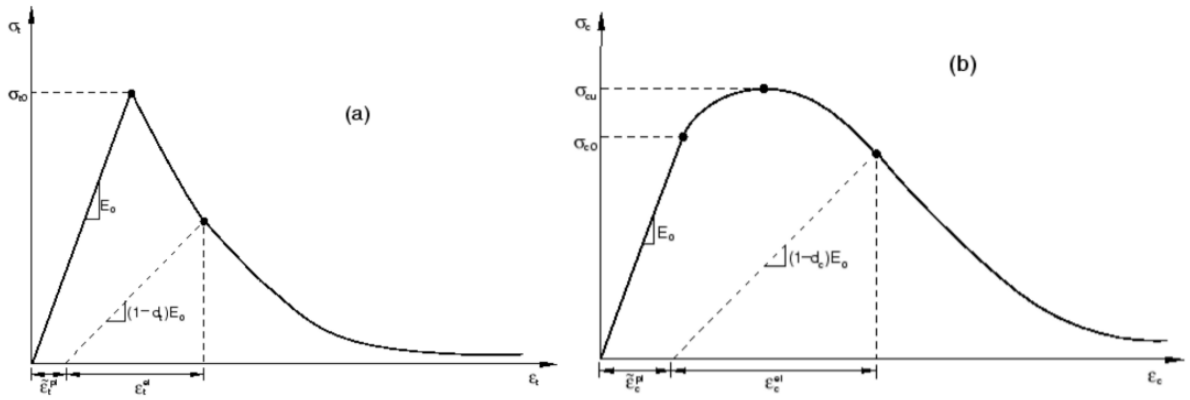

Appendix Figure J-1: Uniaxial tensile and compressive stress-strain behavior [150]

As shown in Appendix Figure J-1, when the concrete specimens are unloaded at any points on the strain softening branches (or strength degradation branches) of the stress-strain curves, the unloaded stiffness will be lower than E_o. The unloading path does not follow the elastic relationship any more, indicating the onset of "damage". There are two variables, d_t and d_c, are introduced to represent this degradation of elastic stiffness, which are assumed to be functions of the equivalent plastic strains ($\tilde{\varepsilon}_t^{pl}$ and $\tilde{\varepsilon}_c^{pl}$), temperature (θ), and field variables

(f_i) [150]:

$$d_t = d_t\left(\varepsilon_t^{pl}, \theta, f_i\right); \qquad 0 \le d_t \le 1 \qquad \textbf{(AEq. J-1)}$$

$$d_c = d_c\left(\varepsilon_c^{pl}, \theta, f_i\right); \qquad 0 \le d_c \le 1 \qquad \textbf{(AEq. J-2)}$$

The value of damage variables varies from 0, representing undamaged material, to 1, representing total loss of strength.

After defining the two monotonic stress-strain curves by using user-provided inelastic strains ($\tilde{\varepsilon}_t^{ck}$ and $\tilde{\varepsilon}_c^{in}$) and corresponding stresses (σ_t and σ_c), ABAQUS will convert these two curves into stresses (σ_t and σ_c) versus equivalent plastic strain ($\tilde{\varepsilon}_t^{pl}$ and $\tilde{\varepsilon}_c^{pl}$) curves automatically. The relationships between inelastic strains and the equivalent plastic strains are represented by the following two equations, and all corresponding terms are also presented in Appendix Figure J-2.

$$\varepsilon_t^{pl} = \varepsilon_t^{ck} - \frac{d_t}{(1-d_t)} \cdot \frac{\sigma_t}{E_0} \qquad \textbf{(AEq. J-3)}$$

$$\varepsilon_c^{pl} = \varepsilon_c^{in} - \frac{d_c}{(1-d_c)} \cdot \frac{\sigma_c}{E_0} \qquad \textbf{(AEq. J-4)}$$

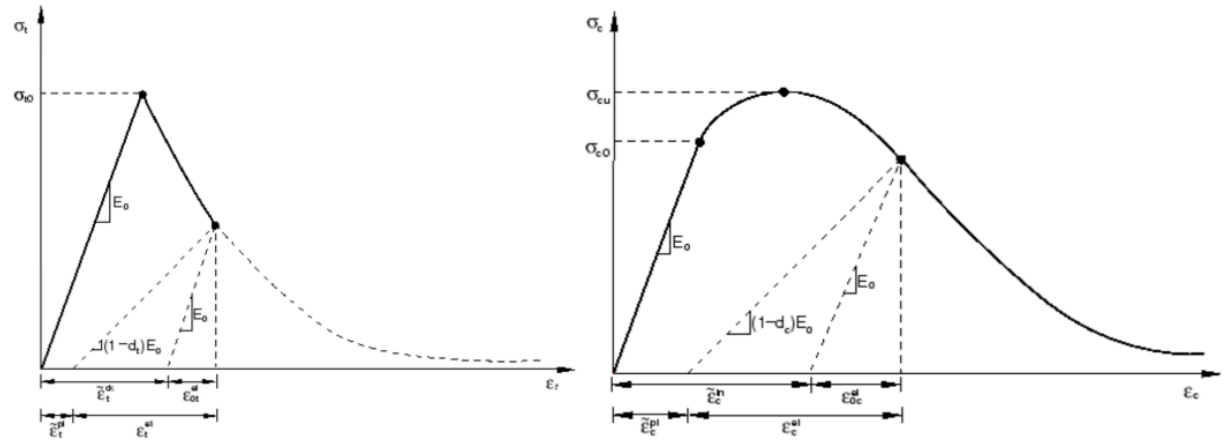

Appendix Figure J-2: Illustration of definition of equivalent plastic strain [150]

The tensile and compressive strength can be redefined by using the damage variables and equivalent plastic strains. Then two "effective" tensile and compressive cohesion stresses ($\bar{\sigma}_t$ and $\bar{\sigma}_c$) are defined to decide the size of the yield (or failure) surface.

$$\sigma_t = (1-d_t)\cdot E_0 \cdot \left(\varepsilon_t - \varepsilon_t^{pl}\right) \quad \& \quad \sigma_c = (1-d_c)\cdot E_0 \cdot \left(\varepsilon_c - \varepsilon_c^{pl}\right) \qquad \textbf{(AEq. J-5)}$$

$$\bar{\sigma}_t = \frac{\sigma_t}{(1-d_t)} = E_0 \cdot \left(\varepsilon_t - \varepsilon_t^{pl}\right) \quad \& \quad \bar{\sigma}_c = \frac{\sigma_c}{(1-d_c)} = E_0 \cdot \left(\varepsilon_c - \varepsilon_c^{pl}\right) \qquad \textbf{(AEq. J-6)}$$

The CDP model allows users to control the stiffness during the cyclic loading directly. Under uniaxial cyclic loading conditions, the degradation mechanism is designed to simulate opening and closing of the previously formed micro-cracks, as well as their interactions. The existing tests' results have shown that the elastic stiffness can be partially recovered as the load changes sign during a uniaxial cyclic test. Generally speaking, when the load changes from tension to compression, the existing tensile cracks can close due to compression and the elastic stiffness

can be recovered; on the other hand, when the load changes from the compression to tension, this recovery effect will be much weaker. This effect is well known as “unilateral effect”, which is a very important aspect for concrete behavior under cyclic loading.

The CDP model assumes one additional variable, d, to consider the total degradation effects on elastic stiffness due to previously formed cracks. This stiffness degradation variable, d, is a function of stress states for both tensile ($\sigma_{11} > 0$) and compressive ($\sigma_{11} < 0$) sides of cycle, and the two uniaxial damage variables, d_t and d_c. There are two variables, s_t and s_c, are introduced, which are the functions of stress state.

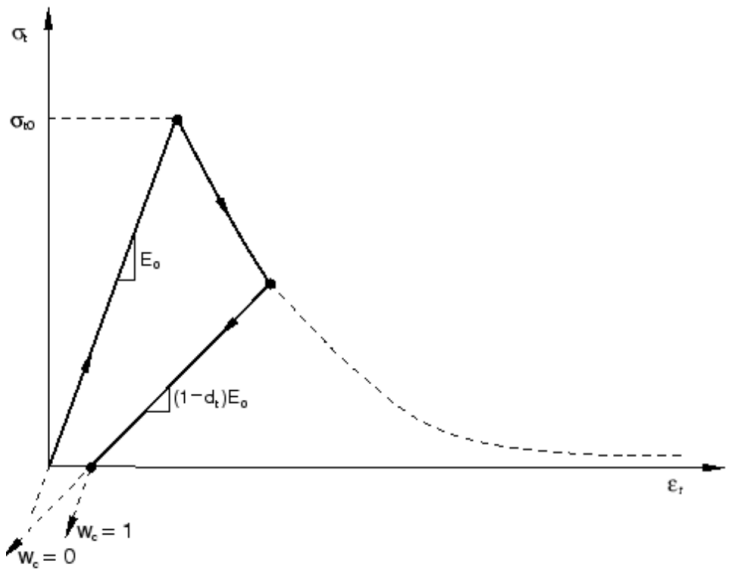

Appendix Figure J-3: Illustration of weight factor w_c [150]

There are another two weight factors, w_t and w_c, involved in the functions of s_t and s_c, whose values are taken from 0, full non-recovery, to 1, full recovery. From Appendix Figure

J-3, when the value of w_c is taken as 0, it represents that the stiffness degradation due to previous tension has the same degree of damage on the compressive elastic stiffness; when w_c is taken as 1, this means that the previous damage due to tension has no effects on the elastic stiffness of compression, and the same stiffness as the one of the last compressive load step of the last load cycle is applied. For example, in Appendix Figure J-3, the tensile load step shown in the plot is the first half cycle, and as there is no previous compressive load step, w_c is taken as 0, the weakened stiffness in tension is transferred to compression; and if w_c is taken as 1, the original undamaged stiffness E_0 is adopted. The relationships of the stiffness degradation and its involved parameters mentioned above are presented as follows:

$$E = (1-d)\cdot E_0 \qquad \textbf{(AEq. J-7)}$$

$$(1-d) = (1-s_t \cdot d_c)\cdot(1-s_c \cdot d_t) \qquad \textbf{(AEq. J-8)}$$

where,

$$s_t = 1 - w_t \cdot r^*(\sigma_{11}); \qquad 0 \le w_t \le 1,$$

$$s_c = 1 - w_c \cdot \left(1 - r^*(\sigma_{11})\right); \qquad 0 \le w_c \le 1.$$

$$r^*(\sigma_{11}) = H(\sigma_{11}) = \begin{cases} 1 & \text{if } \sigma_{11} > 0 \\ 0 & \text{if } \sigma_{11} < 0 \end{cases}$$

The default value of w_t and w_c by ABAQUS are taken as 0 and 1, respectively. In other

words, the default settings in ABAQUS consider the damage in previous tension will not influence the following compressive behavior, however, the stiffness degradation will be fully considered in the following tension load step. At the same time, ABAQUS allows users to control this "unilateral effect" directly by defining w_t and w_c by themselves.

A full loading cycle including both tensile and compressive sides is shown in Appendix Figure J-4. Before the first tensile loading step, the concrete is undamaged material, and both d_t and d_c are equal to zero. As the total tensile strain increases to the point where the corresponding defined tensile damage value is d_t, the tensile stiffness is reduced to $(1-d_t)E_0$ and the unloading path will follow the reduced stiffness. With $d_c = 0$ the relationship of $(1-d) = (1-s_t d_c)(1-s_c d_t)$ is simplified to $(1-d) = (1-s_c d_t)$. For tension ($\sigma_{11} > 0$), we can get $s_c = 1$ based on the above equations, and $d = d_t$ can be obtained. Then the loading changes sign from tension to compression ($\sigma_{11} < 0$), it yields $s_t = 1$ and $s_c = 1 - w_c$. If we use the default value of 1 for w_c, one will get $s_c = 0$ and $d = d_c$ from the above relationships. So when the compression starts to unload at the point where the corresponding users defined damage variable is d_c, the unloading path will follow the line with slope of $(1-d_c)E_0$.

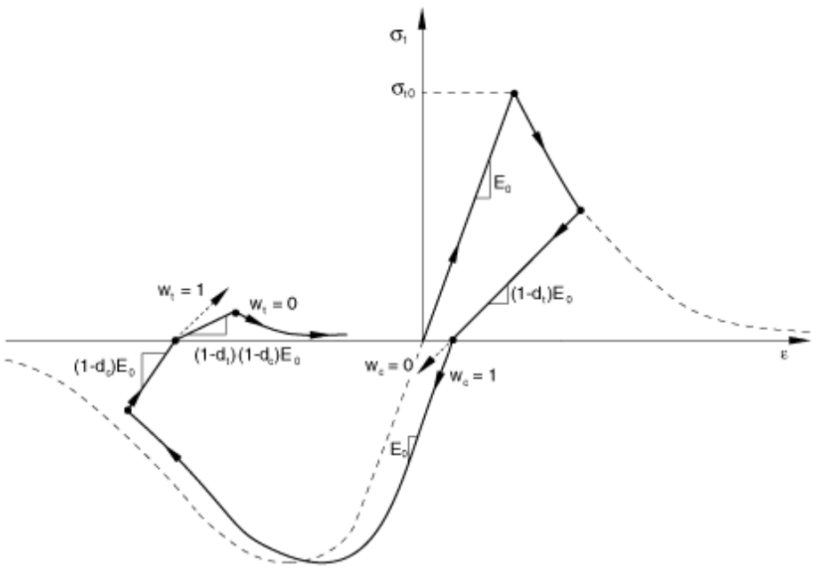

Appendix Figure J-4: stress-strain relationship under a full loading cycle based on default stiffness recovery factors [150]

After one full loading cycle, the loading sign changes again from compression ($\sigma_{11} < 0$) to tension ($\sigma_{11} > 0$), and $s_t = 1 - w_t$ and $s_c = 1$ are obtained. Because the default value of w_t is 0, then the total damage variable d should meet the relationship of $(1 - d) = (1 - d_c)(1 - d_t)$, and the tensile stiffness becomes $(1 - d_c)(1 - d_t)E_0$ for reloading. There is another point on the decreasing branch of the monotonic stress-strain curve of tension with strength σ_t' and damage variable d_t'. After the stress in the material increases linearly with stiffness of $(1 - d_c)(1 - d_t)E_0$ until it reaches σ_t', the tensile behavior will begin to follow the monotonic tensile stress-strain curve. At this point, the new damage variable d_t' should satisfy the relationship of $(1 - d_t') = (1 - d_c)(1 - d_t)$, and d_t' can be calculated. Finally the corresponding tensile strength σ_t' can be determined, and this particular point is found out. The whole loading path is presented by the solid line in Appendix Figure J-4.

In addition to simulating the uniaxial tensile and compressive stress states, the CDP model is also expected to simulate multi-axial behavior. In order to define the concrete properties, users only need to input monotonic tensile and compressive stress-strain behaviors, and do not need to consider whether the stress state is multi-axial or not. The stress-strain relationships are governed by scalar damaged plasticity showing as:

$$\sigma = \left(1-d\right)\cdot D_0^{el} : \left(\varepsilon - \varepsilon^{pl}\right) = D^{el} : \left(\varepsilon - \varepsilon^{pl}\right) \qquad \textbf{(AEq. J-9)}$$

where D_0^{el} is the initial undamaged stiffness matrix; the degradation of stiffness is isotropic and characterized by a single damage variable d, analogous to uniaxial behavior, one can define the degraded stiffness as $D^{el} = (1-d)D_0^{el}$, and the effective stress $\bar{\sigma} = D_0^{el}(\varepsilon - \varepsilon^{pl})$. To determine the damage variable d, the previous unit step function $r^*(\sigma_{11})$ is replaced by a factor $r(\hat{\sigma})$, which is defined as:

$$r\left(\sigma\right) = \frac{\sum_{i=1}^{3}\left\langle \sigma_i \right\rangle}{\sum_{i=1}^{3}\left|\sigma_i\right|}; \qquad 0 \le r\left(\sigma\right) \le 1 \qquad \textbf{(AEq. J-10)}$$

where, $\hat{\sigma}_i$ $(i = 1, 2, 3)$ are principle stresses, and $\langle x \rangle = (|x| + x)/2$.

The modified yield function of Lubliner et al. [151] by Lee and Fenves [152] are applied by the CDP model in ABAQUS. The corresponding relationships and parameters are defined as

follows, and the yield surface for both plan stress and multi-axial stress states are presented in Appendix Figure J-5 and Appendix Figure J-6, respectively.

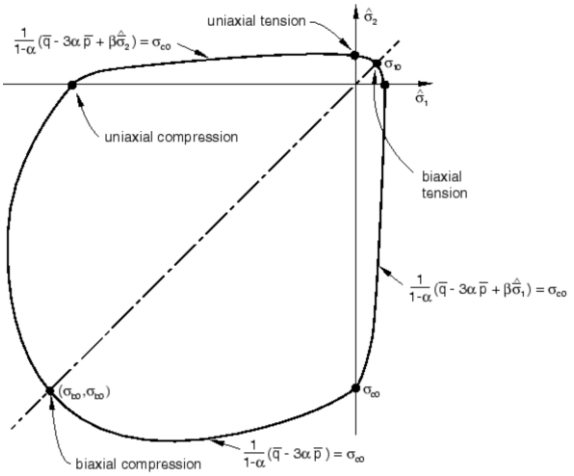

Appendix Figure J-5: Yield surface in plan stress [150]

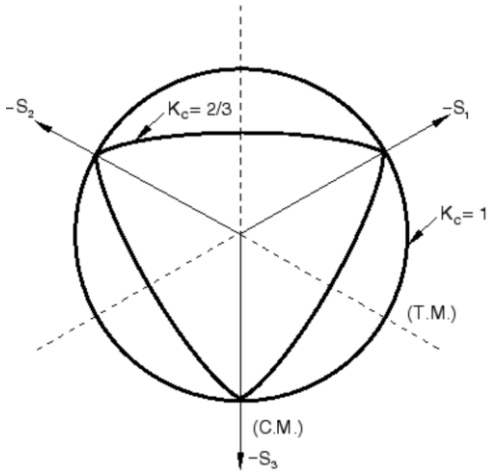

Appendix Figure J-6: Yield surfaces in the deviatoric plane [150]

Yield function:

$$F=\frac{1}{1-\alpha}\cdot\left(\bar{q}-3\cdot\alpha\cdot\bar{p}+\beta(\varepsilon^{pl})\cdot\left\langle\bar{\sigma}_{\max}\right\rangle-\gamma\cdot\left\langle-\bar{\sigma}_{\max}\right\rangle\right)-\bar{\sigma}_c(\varepsilon_c^{pl})=0 \qquad \textit{(AEq. J-11)}$$

where,

$$\alpha=\frac{\left(\sigma_{b0}/\sigma_{c0}\right)-1}{2\cdot\left(\sigma_{b0}-\sigma_{c0}\right)-1};\quad 0\le\alpha\le 0.5,$$

$$\beta=\frac{\bar{\sigma}_c\left(\varepsilon_c^{pl}\right)}{\bar{\sigma}_t\left(\varepsilon_t^{pl}\right)}\cdot(1-\alpha)-(1+\alpha);$$

$$\gamma = \frac{3 \cdot (1 - K_c)}{2 \cdot K_c - 1}.$$

$\bar{\sigma}_{\max}$ = the maximum principle effective stress, ksi.

σ_{b0}/σ_{c0} = ratio of initial equibiaxial compressive yield stress to initial uniaxial compressive yield stress

K_c = ratio of the second stress invariant on the tensile meridian to that on the compressive meridian

$\bar{\sigma}_c\left(\varepsilon_c^{pl}\right)$ = the effective compressive cohesion stresses, ksi.

$\bar{\sigma}_t\left(\varepsilon_t^{pl}\right)$ = the effective tensile cohesion stresses, ksi.

J.2 Failure modes investigation for CDP model in ABAQUS

There are two tests used for the discussions in this section. "Test One" is only a concrete cylinder being loaded without steel tube confining; "Test Two" is loading a concrete cylinder with circular steel tube confining, as shown in Appendix Figure J-7. For the models in ABAQUS, only two one-fourth CCFT columns are modeled and symmetric boundary conditions are employed. Boundary conditions are shown in Appendix Figure J-8: for the two flat vertical surfaces, symmetric BCs are applied, and for the bottom surface, the vertical degree of freedom is fixed.

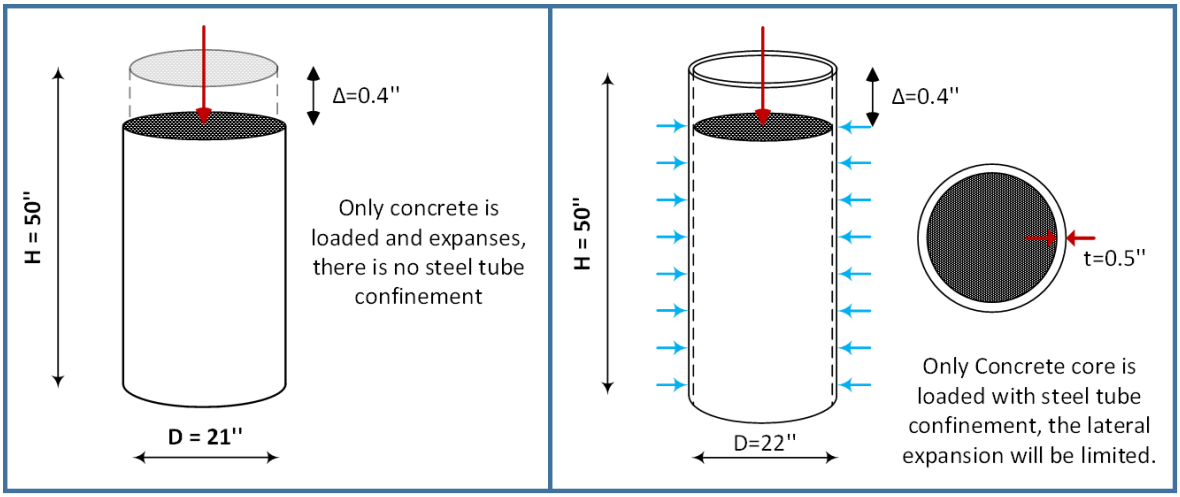

(a) "Test One" without tube *(b) "Test Two" with tube*

Appendix Figure J-7: Two concrete cylinders with and without steel tube

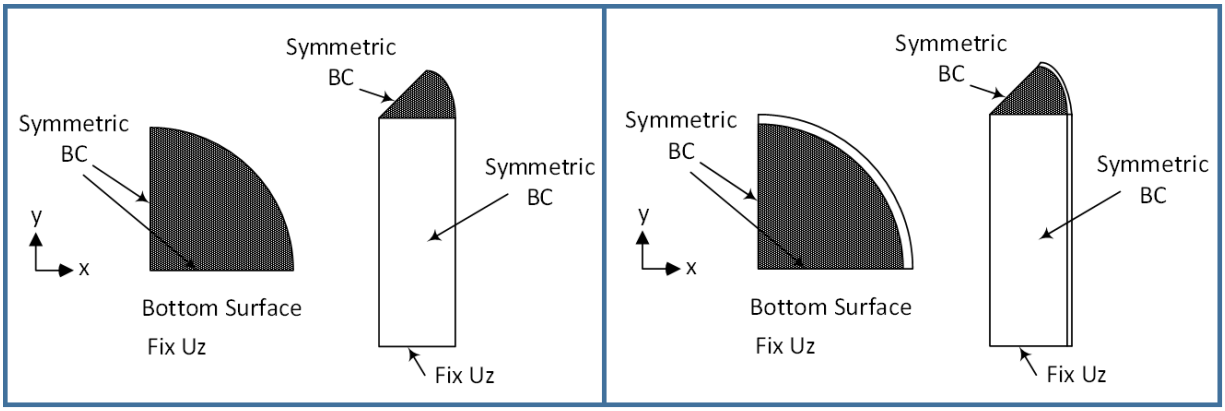

(a) "Test One" without tube *(b) "Test Two" with tube*

Appendix Figure J-8: Two models in ABAQUS with and without steel tube

The concrete properties are the same for the two specimens as defined in section 5.1.6. However, in order to investigate the failure modes and behavior after damage, both tensile and compressive damage variables are needed. They are defined in Appendix Figure J-9 and corresponding data is presented in Appendix Table J-1. For the steel tube, same material properties as in Section 5.1.6 are used.

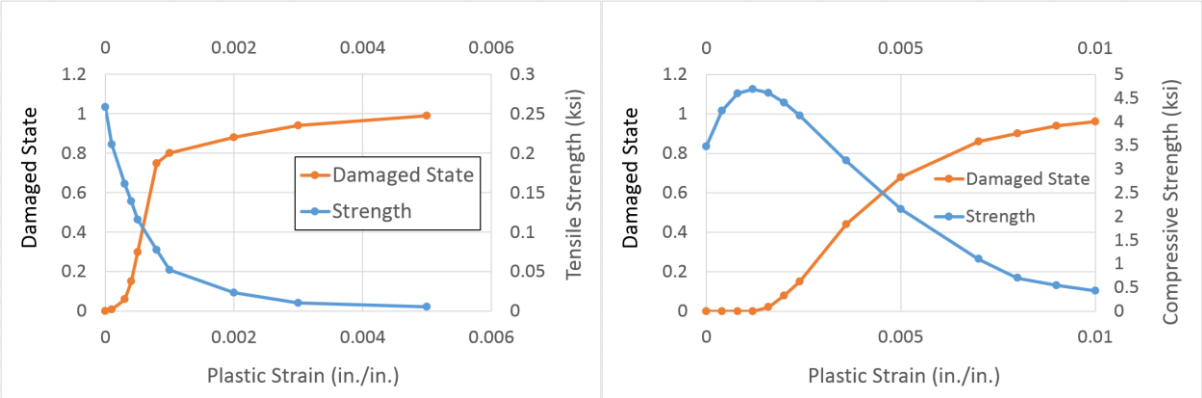

(a) Tensile *(b) Compressive*

Appendix Figure J-9: Tensile and compressive damage states for the concrete in Figure 4-13 with concrete damaged plasticity model in ABAQUS

Appendix Table J-1: Defined concrete damage variables

Compression		Tension	
ε_{in} (in./in.)	d_c	ε_{cr} (in./in.)	d_t
0	0	0	0
0.0004	0	0.0001	0.01
0.0008	0	0.0003	0.06
0.0012	0	0.0004	0.15
0.0016	0.02	0.0005	0.3
0.002	0.08	0.0008	0.75
0.0024	0.15	0.001	0.8
0.0036	0.44	0.002	0.88
0.005	0.68	0.003	0.94
0.007	0.86	0.005	0.99
0.008	0.9		
0.009	0.94		
0.01	0.96		

The purpose of "Test One" is to verify the compressive behavior with degradation of elastic stiffness due to compressive crushing. A loading history for "Test One", including unloading

and reloading, is presented in Appendix Figure J-10. From the analysis results in Appendix Figure J-11, one can see that: (1) as compression increases, the analysis results are compatible with the defined monotonic compressive stress-strain curve; (2) when unloading occurs on the strain softening branch, the unloading path will follow a linear path, and also for the reloading path; (3) both the unloading and reloading stiffness is less than the original undamaged stiffness due to damage; (4) the reloading path will follow the same path as unloading until the point on the monotonic compressive stress-strain curve where unloading previously started is reached; the reloading behavior will change to be nonlinear and continue the original defined monotonic compressive stress-strain curve.

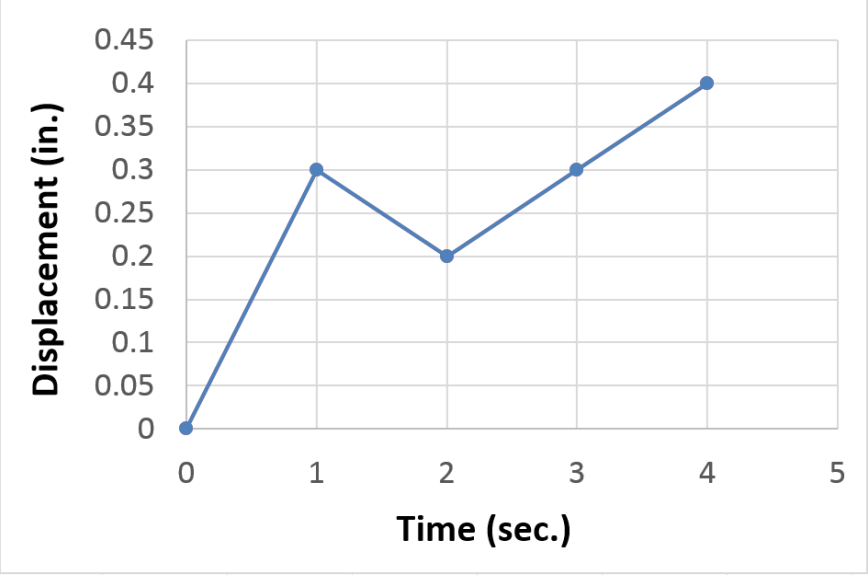

Appendix Figure J-10: Loading history for "Test One"

In addition to the research on compressive stress-strain behavior, the volumetric change of the specimen was also investigated. From the curve from ABAQUS in Appendix Figure J-12, one

can see that as compression increases, the volume of specimen shrinks linearly until concrete goes into nonlinear behavior stage, and then the volume begins to increase. Relevant research has explained that this volumetric increase is because of the generation of micro cracks in concrete.

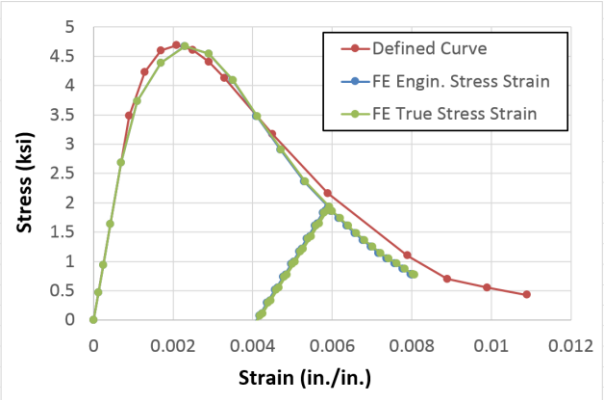

Appendix Figure J-11: Compressive stress-strain Curve

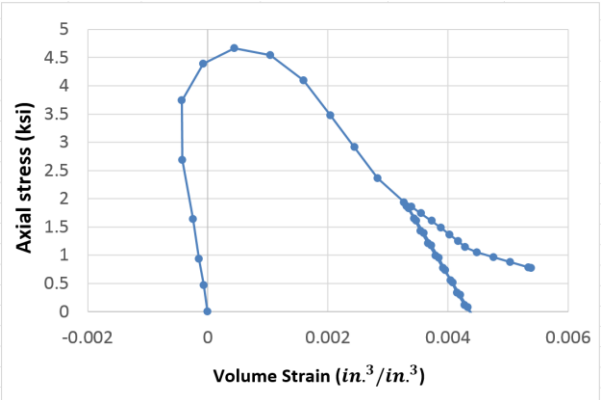

Appendix Figure J-12: Volumetric Strain and Axial Stress Curve

The second test is designed to confirm that the CDP model for concrete in ABAQUS can replicate the failure modes which have been observed in experiments for CCFT columns. When concrete cylinders are under uniaxial compression, there are three failure modes depending on different boundary conditions. When both ends are fixed, the middle part of the concrete cylinder tends to bulge out due to low confinement in this region and leave two concrete cones head to head, If there is only one end fixed and the other end is free to slip, it tends to fail in shear and this case causes one shear yielding plane at around 45 degrees. The third case is to let both ends of the concrete cylinder free to slip in the horizontal planes, and the specimen fails due to vertical through tensile crack along the longitudinal axis. All three failure modes

are shown in Appendix Figure J-13.

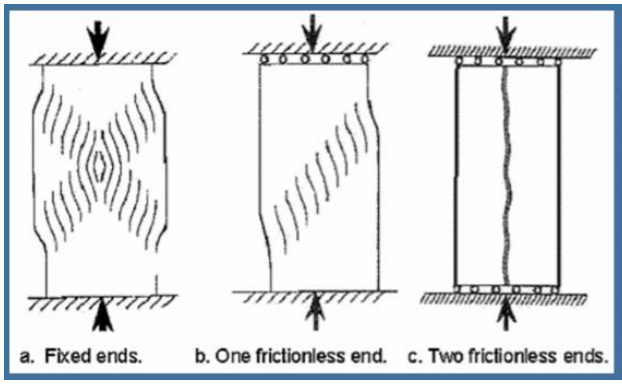

Appendix Figure J-13: Compressive Failure Mode of Concrete Cylinder without Confinement [153]

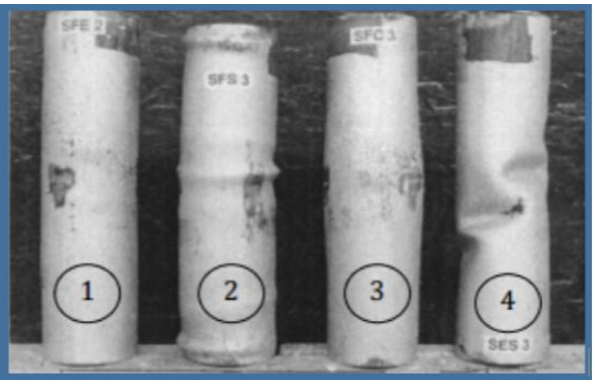

Appendix Figure J-14: Compressive Failure Modes of CCFTs: (1) whole section (2) only tube (3) only concrete (4) tube without concrete

However, when the concrete cylinder under compression is confined by the surrounding circular steel tube, the two common failure modes of the concrete core are the first and second modes in Appendix Figure J-13 as described above. The third failure mode is usually not common due to the large lateral confinement provided by the CCFT. The first failure mode is observed from test in Appendix Figure J-14 for specimen 3 for which only the concrete core is loaded. One can observe that at the middle of this specimen there is an obvious bulge, and steel tube yielding can also be observed. In Appendix Figure J-15, the shear yielding mode is observed in a test for a CCFT column. This failure mode occurs when the ultimate compressive strength of confined concrete is reached, and steel tube starts to yield. From the results of FE analysis, both compressive and shear yielding modes can also be caught by the CDP model in ABAQUS, which are shown in Appendix Figure J-16 and Appendix Figure J-17.

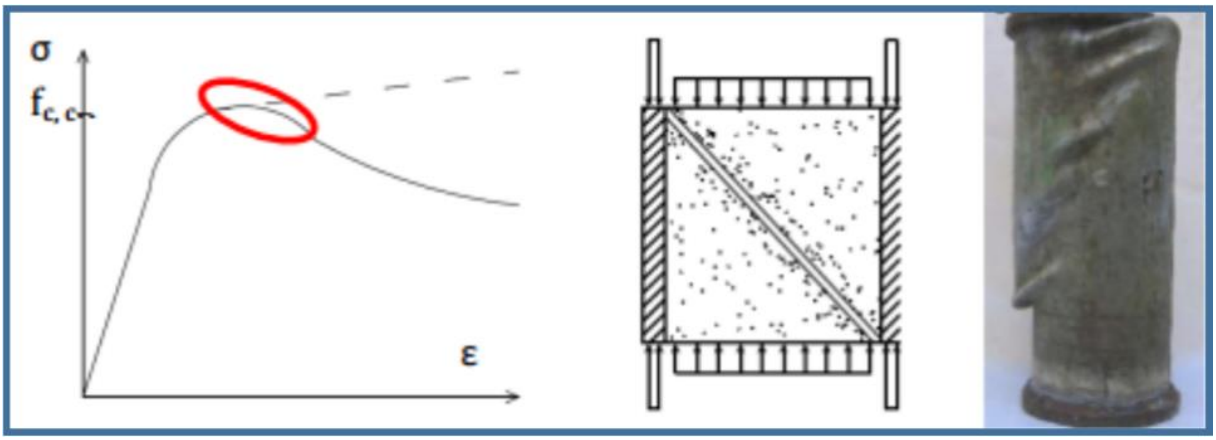

Appendix Figure J-15: Shear Yielding Mode of CCFT in the Test

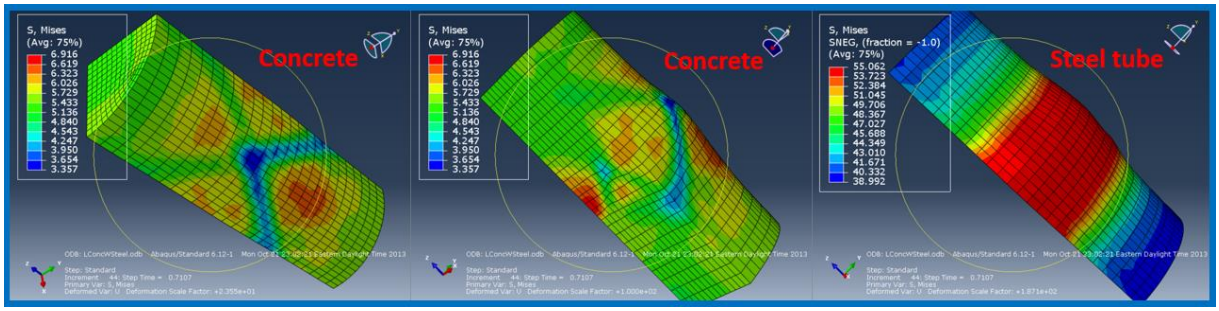

Appendix Figure J-16: Compressive Failure of Concrete Filled Core of CCFT Column

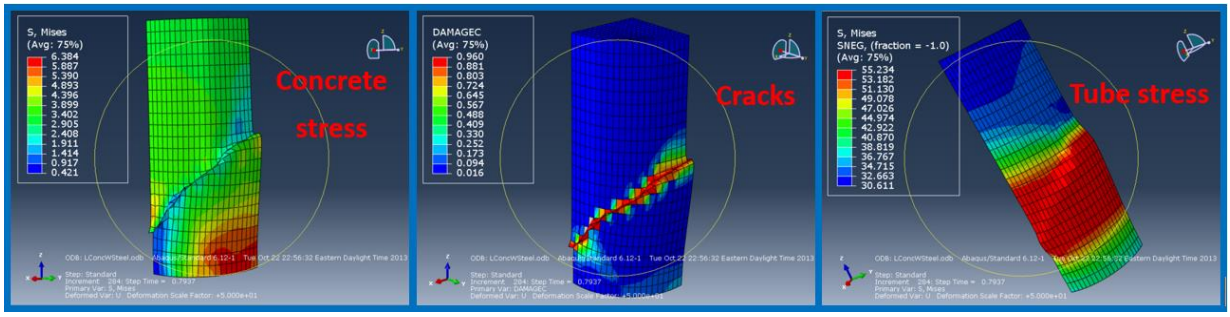

Appendix Figure J-17: Shear Failure of Concrete Filled Core of CCFT Column

Based on the discussion above in this section, one can see that CDP mode for concrete in ABAQUS is effective enough in simulating concrete behaviors for both monotonic and cyclic

loading. This model can simulate stiffness reduction of the concrete after cracks are generated, and is able to simulate both compressive and shear failure modes for concrete confined by a circular steel tube.

Appendix K

Detailed Design Procedure for the Composite Special Moment Frame in W-E direction

K.1 General information

A library with five stories above grade and one story basement is to be constructed. The library locates in San Francisco Bay area. The soil is classified as Site Class D. Based on ASCE 7-10, the library should be assigned into Risk Category II, whose important factor is 1.0;

Two three-bays composite special moment frames with CCFT columns are used as the lateral resisting system in the W-E direction. For each frame, the span is 32 ft. with 3 intermediate floor beams at 8 ft.; the story height is 14 ft. The plan and elevation of each frame are shown in Figure 6.1 and 6.2 in Chapter 6.

K.1.1 Design loads information

The library is designed to have about 40% area for book storage, 40% area for reading rooms, and 18% for offices on each floor, and 2% for openings for elevators and stairs.

The dead load is composed of the following:

1. Composite slab with 3VLI19 steel deck and lightweight concrete, the total thickness is 5.5 inches, the uniform load is 41.5 psf (Ref. VULCRAFT Manual 2010);
2. Self-weight of the structural elements, including beams and columns, the uniform load is assumed to be 12 psf;
3. Superimposed dead load except of slab is assumed to be 20 psf, including 15 psf for ceiling and mechanical pipelines, 2.5 psf for floor finishes, and 2.5 for others;
4. Normal weight precast concrete panels cover about 65% area of the facade, whose self-weight is 40 psf; and windows cover 35% area of the facade with self-weight of 12 psf; the total height of the facade is 4 ft higher than the frame for a parapet;
5. The area for book storage is covered by a steel rack system, which is anchored to the slab and weighs approximately 20 psf.

The live load is composed of the following:

1. The live load of the stack rooms is 150 psf;
2. The live load of the reading rooms is 60 psf;
3. The live load of the office is 50 psf;
4. The roof live load is 20 psf;
5. Partition allowance in the office area is 15 psf, and 10 psf is used for seismic weight.

K.2 Calculate the effective seismic weight

The effective seismic weight includes all dead load, a minimum of 25% of the floor live load in th stack rooms, and a 10 psf partition allowance in the office area. In this design, 40% of stack roo live load is accounted for the seismic weight.

For the main stories:

Total area: $At := (32 \cdot 5) \cdot (24 \cdot 5) = 1.92 \times 10^4$ ft^2

Stack rooms: $Asr := At \cdot 0.4 = 7.68 \times 10^3$ ft^2

Reading rooms: $Arr := At \cdot 0.4 = 7.68 \times 10^3$ ft^2

Office area: $Aof := At \cdot 0.18 = 3.456 \times 10^3$ ft^2

Facade area: $Afa := (32 \cdot 5 + 24 \cdot 5) \cdot 2 \cdot 14 = 7.84 \times 10^3$ ft^2

Slab: $Wslab := At \cdot 0.98 \cdot \frac{41.5}{1000} = 780.864$ kips

Structural element: $Wstruc := At \cdot \frac{12}{1000} = 230.4$ kips

Superimposed: $Wsuper := At \cdot 0.98 \cdot \frac{20}{1000} = 376.32$ kips

Precast panel: $Wpanel := Afa \cdot 0.65 \cdot \frac{40}{1000} = 203.84$ kips

Windows: $Wwin := Afa \cdot 0.35 \cdot \frac{12}{1000} = 32.928$ kips

Rack system: $Wrack := Asr \cdot \frac{20}{1000} = 153.6$ kips

Stack live load: $Wstack := Asr \cdot \frac{0.40 \cdot 150}{1000} = 460.8$ kips *(40% live load is used)*

Partition: $Wpar := Aof \cdot \frac{10}{1000} = 34.56$ kips

Total weight:

$$Wtm := Wslab + Wstruc + Wsuper + Wpanel + Wwin + Wrack + Wstack + Wpar$$

$$Wtm = 2.273 \times 10^3 \quad kips$$

For the roof story:

Total area: $Atr := At = 1.92 \times 10^4 \quad ft^2$

Facade area: $Afar := (32 \cdot 5 + 24 \cdot 5) \cdot 2 \cdot (7 + 4) = 6.16 \times 10^3 \quad ft^2$

Slab: $Wslabr := Atr \cdot \frac{41.5}{1000} = 796.8 \quad kips$

Structural element: $Wstrucr := Atr \cdot \frac{12}{1000} = 230.4 \quad kips$

Superimposed: $Wsuperr := At \cdot \frac{20}{1000} = 384 \quad kips$

Precast panel: $Wpanelr := Afar \cdot 0.65 \cdot \frac{40}{1000} = 160.16 \quad kips$

Windows: $Wwinr := Afar \cdot 0.35 \cdot \frac{12}{1000} = 25.872 \quad kips$

Total weight:

$$Wtr := Wslabr + Wstrucr + Wsuperr + Wpanelr + Wwinr$$

$$Wtr = 1.597 \times 10^3 \quad kips$$

K.3 Calculate the loads for frame design

The architecture design meets the requirements that the gravity loads of the stack rooms are transferred directly to the gravity system. The dead load of rack system will not be included.

K.3.1 Dead load for design

For the main stories:

Dead Load on slab: $DLslab := 41.5 + 12 + 20 = 73.5 \quad psf$

Dead Load on wall: $DLwall := 40 \cdot 0.65 + 12 \cdot 0.35 = 30.2 \quad psf$

Dead Load on beam: $DLbl := \frac{DLslab \cdot 12 + DLwall \cdot 14}{12000} = 0.109$ kips/in

For the roof story:

Dead Load on slab: $DLslabr := 41.5 + 12 + 20 = 73.5$ psf

Dead Load on wall: $DLwallr := 40 \cdot 0.65 + 12 \cdot 0.35 = 30.2$ psf

Dead Load on beam: $DLblr := \frac{DLslabr \cdot 12 + DLwallr \cdot (7 + 4)}{12000} = 0.101$ kips/in

K.3.2 Live load for strength design

The architecture design meets the requirements that the gravity loads of the stack rooms are transferred directly to the gravity system. The strength of the lateral resisting systems will be designed based on the office live loads, the reading room live load or the roof live load, whichever is greater for each story.

For the main stories:

Live Load on slab: $LLslab := 50 + 15 = 65$ psf

The design live load for office is greater than that for reading rooms.

For the roof story:

Live Load on slab: $LLslabr := 20$ psf

K.3.3 Live load reduction for strength design

For strength design of each special moment frame in W-E direction, live load reduciton is applied for both beams and columns.

For beams on main stories:

$KLLb := 2$ $ATb := \frac{1}{2} \cdot (32 \cdot 24 - 24 \cdot 12) = 240$ ft^2

$KLLb \cdot ATb = 480$ ft^2 ▮ > ▮ 400 ft^2

$$LLb := 65\cdot\left(0.25 + \frac{15}{\sqrt{KLLb\cdot ATb}}\right) = 60.752 \quad psf \quad \blacksquare > \blacksquare \quad 0.5\cdot 65 = 32.5 \quad psf$$

Line load: $LLbl := \frac{LLb\cdot 12}{12000} = 0.061$ kips/in

For beams on roof story:

$$ATbr := \frac{1}{2}\cdot(32\cdot 24 - 24\cdot 12) = 240 \quad ft^2 \quad \blacksquare > \blacksquare \quad 200 \quad ft^2$$

$$R1 := 1.2 - 0.001\cdot ATbr = 0.96 \qquad R2 := 1.0$$

$$LLbr := 20\cdot R1\cdot R2 = 19.2 \ psf \quad \blacksquare > \blacksquare \quad 12 \quad psf$$

Line load: $LLblr := \frac{LLbr\cdot 12}{12000} = 0.019$ kips/in

For columns:

$$ATc := \frac{1}{2}\cdot 32\cdot 24 = 384 \quad ft^2 \quad \blacksquare > \blacksquare \quad 200 \quad ft^2$$

Roof story: $R1 := 1.2 - 0.001\cdot ATc = 0.816 \qquad R2 = 1$

$$LLc5 := 20\cdot R1\cdot R2 = 16.32 \ psf \quad \blacksquare > \blacksquare \quad 12 \quad psf$$

Main stories: $KLLc := 4 \qquad KLLc\cdot ATc = 1.536\times 10^3 \quad ft^2 \quad \blacksquare > \blacksquare \quad 400 \quad ft^2$

4th story: $LLc4 := 65\cdot\left(0.25 + \frac{15}{\sqrt{KLLc\cdot ATc}}\right) = 41.128 \quad psf \quad \blacksquare > \blacksquare \quad 0.5\cdot 65 = 32.5 psf$

3rd story: $LLc3 := 65\cdot\left(0.25 + \frac{15}{\sqrt{KLLc\cdot 2ATc}}\right) = 33.841 \quad psf \quad \blacksquare > \blacksquare \quad 0.4\cdot 65 = 26 \quad psf$

2nd story: $LLc2 := 65\cdot\left(0.25 + \frac{15}{\sqrt{KLLc\cdot 3ATc}}\right) = 30.613 \quad psf \quad \blacksquare > \blacksquare \quad 0.4\cdot 65 = 26 \quad psf$

1st story: $LLc1 := 65 \cdot \left(0.25 + \frac{15}{\sqrt{KLLc \cdot 4ATc}}\right) = 28.689 \text{ psf} \quad \blacksquare > \blacksquare \quad 0.4 \cdot 65 = 26 \text{ psf}$

K.3.3.1 Upward loads on columns due to live load reduction

Due to live load on floors and live load on roof are classified into two load cases, they are calcula
seperately.

K.3.3.1.1 Upward loads due to roof live load

Column axial force due to live load from beams:

Roof story: $Pcl := LLblr \cdot 32 \cdot 12 = 7.373 \text{ kips}$

Column axial force due to live load reduction for columns:

Roof story: $Pccl := LLc5 \cdot \frac{32 \cdot 12}{1000} = 6.267 \text{ kips}$

Upward loads on columns:

Roof stroy: $Pcup := Pcl - Pccl = 1.106 \text{ kips}$

K.3.3.1.2 Upward loads due to floor live load

Column axial force due to live load from beams:

4th story: $Pcl4 := LLbl \cdot 32 \cdot 12 = 23.329 \text{ kips}$

3rd story: $Pcl3 := Pcl4 + LLbl \cdot 32 \cdot 12 = 46.658 \text{ kips}$

2nd story: $Pcl2 := Pcl3 + LLbl \cdot 32 \cdot 12 = 69.987 \text{ kips}$

1st story: $Pcl1 := Pcl2 + LLbl \cdot 32 \cdot 12 = 93.316 \text{ kips}$

Column axial force due to live load reduction for columns:

4th story: $Pccl4 := LLc4 \cdot \frac{32 \cdot 12}{1000} = 15.793 \text{ kips}$

3rd story: $Pccl3 := LLc3 \cdot \frac{32 \cdot 12 \cdot 2}{1000} = 25.99 \text{ kips}$

2nd story: $Pccl2 := LLc2 \cdot \frac{32 \cdot 12 \cdot 3}{1000} = 35.266$ kips

1st story: $Pccl1 := LLc1 \cdot \frac{32 \cdot 12 \cdot 4}{1000} = 44.066$ kips

Upward loads on columns:

4th story: $Pcup4 := Pcl4 - Pccl4 = 7.536$ kips

3rd story: $Pcup3 := Pcl3 - Pccl3 = 20.668$ kips

2nd story: $Pcup2 := Pcl2 - Pccl2 = 34.721$ kips

1st story: $Pcup1 := Pcl1 - Pccl1 = 49.25$ kips

K.3.3.2 Additional gravity loads on exterior frame columns

Additionally, for the exterior columns of the special moment frame, the missing portion of loads for half span of gravity system should be considered.

Dead Load on main stories: $Pdcex := DLbl \cdot 16 \cdot 12 = 20.877$ kips

Dead Load on roof story: $Pdcexr := DLblr \cdot 16 \cdot 12 = 19.427$ kips

Live Load on main stories: $Plcex := LLbl \cdot 16 \cdot 12 = 11.664$ kips

Live Load on roof story: $Plcexr := LLblr \cdot 16 \cdot 12 = 3.686$ kips

K.3.4 Calculate loads on gravity system for P-Delta effects

The total loads on the areas which are not tributary to the special moment frames should be accounted for the P-Delta effects.

K.3.4.1 Dead load for P-Delta effects

Dead load on main stories:

$Pdt := Wslab + Wstruc + Wsuper + Wpanel + Wwin + Wrack = 1.778 \times 10^3$ kips

Assume the tributary areas to frames are all for offices, don't include rack system.

on slab: $Atrib := 2\cdot(32\cdot 4\cdot 12) = 3.072\times 10^{3}\ ft^{2}$

$$Wtrib := Atrib\cdot\frac{41.5 + 12 + 20}{1000} = 225.792 \quad kips$$

on wall: $Atribw := 2\cdot(32\cdot 4\cdot 14) = 3.584\times 10^{3}\ ft^{2}$

$$Wtribw := Atribw\cdot\frac{40\cdot 0.65 + 12\cdot 0.35}{1000} = 108.237 \quad kips$$

the remainder: $Pdr := Pdt - (Wtrib + Wtribw) = 1.444\times 10^{3} \quad kips$

Dead load on roof story:

$Pdtr := Wslabr + Wstrucr + Wsuperr + Wpanelr + Wwinr = 1.597\times 10^{3} \quad kips$

on slab: $Atribr := 2\cdot(32\cdot 4\cdot 12) = 3.072\times 10^{3}\ ft^{2}$

$$Wtribr := Atribr\cdot\frac{41.5 + 12 + 20}{1000} = 225.792 \quad kips$$

on wall: $Atribwr := 2\cdot(32\cdot 4\cdot 14) = 3.584\times 10^{3}\ ft^{2}$

$$Wtribwr := Atribwr\cdot\frac{40\cdot 0.65 + 12\cdot 0.35}{1000} = 108.237 \quad kips$$

the remainder: $Pdrr := Pdtr - (Wtribr + Wtribwr) = 1.263\times 10^{3} \quad kips$

K.3.4.2 Live load for P-Delta effects

To calculate the live load to account for the P-Delta effects, the live load reduction for the columns on each story can be applied. However, according to ASCE 7-10, the live load in stack rooms could not be reduced.

Live load on roof story:

remaining area: $Are := At - Atrib = 1.613\times 10^{4}\ ft^{2}$ ▮ > ▮ $600\ ft^{2}$

5th story: $R1 := 0.6$ $R2 = 1$

$$LLgc5 := 20 \cdot R1 \cdot R2 = 12\,psf \quad \blacksquare > \blacksquare \quad 12 \quad psf$$

Live load on main stories: $KLLc = 4$

As assumed above, all areas which are tributary to the frame belong to offices, these area on each story is about:

$$Atrib = 3.072 \times 10^3 \quad ft^2$$

the remaining area for office: $Aoffr := At \cdot 0.18 - Atrib = 384 \quad ft^2$

office live load reduction for columns:

4th story: $LLgco4 := 65 \cdot \left(0.25 + \frac{15}{\sqrt{KLLc \cdot Aoffr}}\right) = 41.128 \quad psf \quad \blacksquare > \blacksquare \quad 0.5 \cdot 65 = 32.5 \quad psf$

3rd story: $LLgco3 := 65 \cdot \left(0.25 + \frac{15}{\sqrt{KLLc \cdot 2 \cdot Aoffr}}\right) = 33.841 \quad psf \quad \blacksquare > \blacksquare \quad 0.4 \cdot 65 = 26 \quad psf$

2nd story: $LLgco2 := 65 \cdot \left(0.25 + \frac{15}{\sqrt{KLLc \cdot 3 \cdot Aoffr}}\right) = 30.613 \quad psf \quad \blacksquare > \blacksquare \quad 0.4 \cdot 65 = 26 \quad psf$

1st story: $LLgco1 := 65 \cdot \left(0.25 + \frac{15}{\sqrt{KLLc \cdot 4 \cdot Aoffr}}\right) = 28.689 \quad psf \quad \blacksquare > \blacksquare \quad 0.4 \cdot 65 = 26 \quad psf$

reading room live load reduction for columns:

reading room area: $Arr = 7.68 \times 10^3 \quad ft^2$

4th story: $LLgcr4 := 50 \cdot \left(0.25 + \frac{15}{\sqrt{KLLc \cdot Arr}}\right) = 16.779 \quad psf \quad use \quad 0.5 \cdot 50 = 25 \quad psf$

3rd story: $LLgcr3 := 50 \cdot \left(0.25 + \frac{15}{\sqrt{KLLc \cdot 2 \cdot Arr}}\right) = 15.526 \quad psf \quad use \quad 0.4 \cdot 50 = 20 \quad psf$

2nd story: $LLgcr2 := 50 \cdot \left(0.25 + \frac{15}{\sqrt{KLLc \cdot 3 \cdot Arr}}\right) = 14.971 \quad psf \quad use \quad 0.4 \cdot 50 = 20 \quad psf$

1st story: $LLgcr1 := 50 \cdot \left(0.25 + \frac{15}{\sqrt{KLLc \cdot 4 \cdot Arr}}\right) = 14.64 \quad psf \quad use \quad 0.4 \cdot 50 = 20 \quad psf$

For roof live load:

Roof story: $Pglive := \frac{LLgc5 \cdot Are}{1000} = 193.536$ kips

For floor live load:

Live load on each story:

4th story: $Plive4 := \frac{LLgco4 \cdot Aoffr + 25 \cdot Arr + 150 \cdot Asr}{1000} = 1.36 \times 10^3$ kips

3rd story: $Plive3 := \frac{LLgco3 \cdot 2 \cdot Aoffr + 20 \cdot 2 \cdot Arr + 150 \cdot 2 \cdot Asr}{1000} = 2.637 \times 10^3$ kips

2nd story: $Plive2 := \frac{LLgco2 \cdot 3 \cdot Aoffr + 20 \cdot 3 \cdot Arr + 150 \cdot 3 \cdot Asr}{1000} = 3.952 \times 10^3$ kips

1st story: $Plive1 := \frac{LLgco1 \cdot 4 \cdot Aoffr + 20 \cdot 4 \cdot Arr + 150 \cdot 4 \cdot Asr}{1000} = 5.266 \times 10^3$ kips

Live load on each story of gravity system:

4th story: $Pglive4 := Plive4 = 1.36 \times 10^3$ kips

3rd story: $Pglive3 := Plive3 - Plive4 = 1.277 \times 10^3$ kips

2nd story: $Pglive2 := Plive2 - Plive3 = 1.315 \times 10^3$ kips

1st story: $Pglive1 := Plive1 - Plive2 = 1.314 \times 10^3$ kips

K.4 Summary for half of building

Due to a symmetric layout, for one composite special moment frame in W-E direction, only half of the total effective seismic weight and half loads on gravity system are considered in the calculation.

K.4.1 Effective seismic weight

main stories: $Wtmh := \frac{1}{2} \cdot Wtm = 1.137 \times 10^3$ kips

roof story: $Wtrh := \frac{1}{2} \cdot Wtr = 798.616$ kips

Total half building above grade: $Wth := Wtmh \cdot 4 + Wtrh = 5.345 \times 10^{3}$ kips

K.4.2 Loads on special moment frame

Loads on moment frame include dead load and live load for both main stories and roof story. They can also divided into uniform load on beams and concentrated load on beam column panel zones.

K.4.2.1 Loads on beams

main stories of frame:

Dead load on beam: $DLbl = 0.109$ kips/in

Live load on beam: $LLbl = 0.061$ kips/in

roof stories of frame:

Dead load on beam: $DLblr = 0.101$ kips/in

Live load on beam: $LLblr = 0.019$ kips/in

K.4.2.2 Loads on columns

Upward live loads for interior columns:

Roof live load:

Roof story: $Pcup = 1.106$ kips

Floor live load:

4th story: $Pcup4 = 7.536$ kips

3rd story: $Pcup3 = 20.668$ kips

2nd story: $Pcup2 = 34.721$ kips

1st story: $Pcup1 = 49.25$ kips

Additional loads on exterior columns:

Dead Load on main stories: Pdcex = 20.877 kips

Dead Load on roof story: Pdcexr = 19.427 kips

Live Load:

Roof live load:

Roof story: $Pexc := Pcup - Plcexr = -2.58$ kips

Floor live load:

4th story: $Pexc4 := Pcup4 - Plcex = -4.129$ kips

3rd story: $Pexc3 := Pcup3 - Plcex = 9.003$ kips

2nd story: $Pexc2 := Pcup2 - Plcex = 23.056$ kips

1st story: $Pexc1 := Pcup1 - Plcex = 37.585$ kips

K.4.2.3 Loads on gravity system

Dead load on main stories: $Pdrh := \frac{1}{2} \cdot Pdr = 721.962$ kips

Dead load on roof story: $Pdrrh := \frac{1}{2} \cdot Pdrr = 631.602$ kips

Live load:

Roof live load:

Roof story: $Pgliveh := \frac{1}{2} \cdot Pglive = 96.768$ kips

Floor live load:

4th story: $Pgliveh4 := \frac{1}{2} \cdot Pglive4 = 679.897$ kips

3rd story: $Pgliveh3 := \frac{1}{2} \cdot Pglive3 = 638.698$ kips

2nd story: $Pgliveh2 := \frac{1}{2}\cdot Pglive2 = 657.438$ kips

1st story: $Pgliveh1 := \frac{1}{2}\cdot Pglive1 = 657.2$ kips

K.5 Determine seismic design category

From USGS uniform hazard (UH) 5% damped response spectrum for 2% in 50 year probability of occurrence.

$S\_SUH := 2.044\ g$

$S\_1UH := 0.876\ g$

From USGS 2009 NEHRP Design Maps Tool

$C\_RS := 1.045$ $C\_R1 := 0.988$

$S\_SD := 1.5\ g$ $S\_1D := 0.63\ g$

Calculate Ss and S1:

$Ss := \min(S\_SUH\cdot C\_RS, S\_SD) = 1.5\ g$

$S1 := \min(S\_1UH\cdot C\_R1, S\_1D) = 0.63\ g$

From ASCE 7-10 Table 11.4-1 and 11.4-2:

$Fa := 1.0$ $Fv := 1.5$

Calculated risk-targeted maximum considered earthquake acceleration:

$S\_MS := Fa\cdot Ss = 1.5\ g$ $S\_M1 := Fv\cdot S1 = 0.945\ g$

Calculate design earthquake acceleration:

$S\_DS := \frac{2}{3}\cdot S\_MS = 1\ g$ ▮ $> 0.5\ g$ Seismic Design Category D

$S\_D1 := \frac{2}{3}\cdot S\_M1 = 0.63\ g$ ▮ $> 0.2\ g$ Seismic Design Category D

So the building is assigned into Seismic Design Category "D".

K.6 Determine seismic design coefficients

Structural system is Composite Special Moment Frame, based on ASCE 7-10 Table 12.2-1:

$R := 8 \qquad \Omega 0 := 3 \qquad Cd := 5.5$

And there is no limitation on height for buildings in seismic design category D using this type of structural system.

Redundancy factor is determined based on seismic design category D:

$\rho := 1.3$

According to ASCE 7-10 section 12.3.4.1, when calculate drift and P-delta effects, redundanc factor can be assigned to be 1.0.

K.7: Determine equivalent lateral force at each story level for strength design

For strength design, Tmax will be used as the approximate fundimental period.

K.7.1: Calculate time period

$S\_D1 = 0.63\,g \qquad Cu := 1.4 \qquad Ct := 0.028 \qquad hn := 14 \cdot 5 = 70\ ft \qquad x := 0.8$

$Ta := Ct \cdot hn^{x} = 0.838 \qquad Tmax := Cu \cdot Ta = 1.173\ s$

$T := Tmax = 1.173\,s$

K.7.2: Calculate base shear

$R = 8 \qquad Ie := 1.0$

$TL := 12\ s \qquad S\_DS = 1\,g \qquad S\_D1 = 0.63\ g$

$$Cs := \frac{S\_DS}{\left(\frac{R}{Ie}\right)} = 0.125$$

$$Csmax := \frac{S\_D1}{T \cdot \left(\frac{R}{Ie}\right)} = 0.067$$ when $T = 1.173\,s$ $< TL$ upper limit

$Cs := \min(Cs, Csmax) = 0.067$

first lower limit $Csmin1 := 0.044 \cdot S\_DS \cdot Ie = 0.044$

second lower limit when $S1 = 0.63 \ g$ ▮ $> 0.6 \ g$

$$Csmin2 := \frac{0.5 \cdot S1}{\left(\frac{R}{Ie}\right)} = 0.039$$

$Cs := \max(Cs, Csmin1, Csmin2) = 0.067$

effective weight of half bulding $Wth = 5.345 \times 10^3$ kips

design base shear $Vb := Cs \cdot Wth = 358.801$ kips

K.7.3: Calculate equivalent lateral force (ELF) on each level

$$k := 1 + \frac{2 - 1}{2.5 - 0.5} \cdot (T - 0.5) = 1.337$$

$h5 := 14 \cdot 12 \cdot 5 = 840$ $h4 := 14 \cdot 12 \cdot 4 = 672$ $h3 := 14 \cdot 12 \cdot 3 = 504$

$h2 := 14 \cdot 12 \cdot 2 = 336$ $h1 := 14 \cdot 12 \cdot 1 = 168$

$w1 := Wtmh = 1.137 \times 10^3$ kips $w2 := Wtmh = 1.137 \times 10^3$ kips

$w3 := Wtmh = 1.137 \times 10^3$ kips $w4 := Wtmh = 1.137 \times 10^3$ kips

$w5 := Wtrh = 798.616$ kips

$H := w1 \cdot h1^k + w2 \cdot h2^k + w3 \cdot h3^k + w4 \cdot h4^k + w5 \cdot h5^k = 2.173 \times 10^7$

$$Cv1 := \frac{w1 \cdot h1^k}{H} = 0.049$$ ELF applied on story 1: $Fx1 := Vb \cdot Cv1 = 17.688$ kips

$$Cv2 := \frac{w2 \cdot h2^k}{H} = 0.125$$ ELF applied on story 2: $Fx2 := Vb \cdot Cv2 = 44.672$ kips

$Cv3 := \frac{w3 \cdot h3^{k}}{H} = 0.214$ ELF applied on story 3: $Fx3 := Vb \cdot Cv3 = 76.806$ kips

$Cv4 := \frac{w4 \, h4^{k}}{H} = 0.314$ ELF applied on story 4: $Fx4 := Vb \cdot Cv4 = 112.821$ kips

$Cv5 := \frac{w5 \cdot h5^{k}}{H} = 0.298$ ELF applied on story 5: $Fx5 := Vb \cdot Cv5 = 106.814$ kips

Note: Equivalent lateral forces on stories through 1 to 4 are greater than 35% of the total design base shear. The lateral resisting systems on these stories meet the requirements in ASCE 7-10 12.3.4.2(b), the redundency factor is permitted to be reduced from 1.3 to 1.0.

$\rho := 1.0$

K.8: Frame design in SAP2000

Load combinations in ASCE 7-10:

1) 1.4*D

2)1.2*D* + 1.6*L* + 0.5(*Lr* or *S* or *R*)

3) 1.2*D* + 1.6(*Lr* or *S* or *R*) + (*L* or 0.5*W*)

5) (1.2+0.2S_DS)*D+ρQ_E+L+0.2*S

7) (0.9-0.2S_DS)*D+ρQ_E+1.6H

Overstrength factor will be used in load combinations to check the axial load capacity of exterior columns of the frame:

5) (1.2+0.2S_DS)*D+Ω0*Q_E+L+0.2S $\Omega 0 = 3$

7) (0.9-0.2S_DS)*D+Ω0*Q_E+1.6H $\Omega 0 = 3$

Design results of member sections are presented in Chapter 6, these sections meet both the strength and deflection requirements in ASCE 7-10.

Structural fundimental period: $T0 := 1.386 \ s$

K.9: Drift check based on equivalent lateral force method

For drift check, T from eigenvalue analysis with no limit is used, and the redundancy factor is

assigned to be 1.0.

K.9.1: Load combinations

P-Delta effects are included in the analysis automatically, using the unfactored gravity load, and the load combination is D+Q_E+L+Lr.

K.9.2: Calculate base shear

$T0 = 1.386 \quad s$ $\qquad Cs := \dfrac{S\_DS}{\left(\dfrac{R}{Ie}\right)} = 0.125$

$Csmax := \dfrac{S\_D1}{T0 \cdot \left(\dfrac{R}{Ie}\right)} = 0.057$ when $T0 = 1.386 \quad s$ ▮ $< TL$ $\qquad$ uper limit

$Cs := \min(Cs, Csmax) = 0.057$

first lower limit $\qquad Csmin1 := 0.044 \cdot S\_DS \cdot Ie = 0.044$

second lower limit $\qquad$ when $S1 = 0.63 \quad g$ ▮ $> 0.6 \quad g$

$$Csmin2 := \frac{0.5 \cdot S1}{\left(\dfrac{R}{Ie}\right)} = 0.039$$

$Cs := \max(Cs, Csmin1, Csmin2) = 0.057$

effective weight of half bulding $\qquad Wth = 5.345 \times 10^3 \quad kips$

design base shear $\qquad Vb := Cs \cdot Wth = 303.707 \quad kips$

K.9.3: Calculate equivalent lateral force (ELF) on each level

$k := 1 + \dfrac{2 - 1}{2.5 - 0.5} \cdot (T0 - 0.5) = 1.443$

$H := w1 \cdot h1^k + w2 \cdot h2^k + w3 \cdot h3^k + w4 \cdot h4^k + w5 \cdot h5^k = 4.28 \times 10^7$

$Cv1 := \frac{w1 \cdot h1^{k}}{H} = 0.043$ ELF applied on story 1: $Fx1 := Vb \cdot Cv1 = 13.114$ kips

$Cv2 := \frac{w2 \cdot h2^{k}}{H} = 0.117$ ELF applied on story 2: $Fx2 := Vb \cdot Cv2 = 35.656$ kips

$Cv3 := \frac{w3 \cdot h3^{k}}{H} = 0.211$ ELF applied on story 3: $Fx3 := Vb \cdot Cv3 = 64.007$ kips

$Cv4 := \frac{w4 \, h4^{k}}{H} = 0.319$ ELF applied on story 4: $Fx4 := Vb \cdot Cv4 = 96.943$ kips

$Cv5 := \frac{w5 \cdot h5^{k}}{H} = 0.309$ ELF applied on story 5: $Fx5 := Vb \cdot Cv5 = 93.987$ kips

K.9.4: Determine drift limit on each level based on elastic analysis

because the height of all stories is the same, so story drift limit on each level is the same:

$hsx := 14 \cdot 12 = 168$ in $\Delta := \frac{0.020 \cdot hsx}{\rho} = 3.36$ in

K.9.5: Check the deflection of the special moment frame

Story deflection from analysis:

$\delta e1 := 0.4107$ in $\delta e2 := 0.8622$ in $\delta e3 := 1.2877$ in

$\delta e4 := 1.657$ in $\delta e5 := 2.0$ in

Design story drift:

$\Delta 1 := \frac{\delta e1 \cdot Cd}{Ie} = 2.259$ in ▮ < ▮ $\Delta = 3.36$ in $\frac{\Delta 1}{\Delta} = 0.672$ OK

$\Delta 2 := \frac{(\delta e2 - \delta e1) \cdot Cd}{Ie} = 2.483$ in ▮ < ▮ $\Delta = 3.36$ in $\frac{\Delta 2}{\Delta} = 0.739$ OK

$$\Delta 3 := \frac{(\delta e3 - \delta e2)\cdot Cd}{Ie} = 2.34 \quad in \qquad \blacksquare < \blacksquare \quad \Delta = 3.36 \quad in \qquad \frac{\Delta 3}{\Delta} = 0.697 \quad OK$$

$$\Delta 4 := \frac{(\delta e4 - \delta e3)\cdot Cd}{Ie} = 2.031 \quad in \qquad \blacksquare < \blacksquare \quad \Delta = 3.36 \quad in \qquad \frac{\Delta 4}{\Delta} = 0.605 \quad OK$$

$$\Delta 5 := \frac{(\delta e5 - \delta e4)\cdot Cd}{Ie} = 1.886 \quad in \qquad \blacksquare < \blacksquare \quad \Delta = 3.36 \quad in \qquad \frac{\Delta 5}{\Delta} = 0.561 \quad OK$$

K.10: Check stability

Calculate seismic shear on each story

$V5 := Fx5 = 93.987$ kips $\qquad V4 := V5 + Fx4 = 190.93$ kips

$V3 := V4 + Fx3 = 254.937$ kips $\qquad V2 := V3 + Fx2 = 290.593$ kips

$V1 := V2 + Fx1 = 303.707$ kips

Calculate grevity load on each story

$P5 := 888.52$ kips $\qquad P4 := 2488.14$ kips

$P3 := 3993.90$ kips $\qquad P2 := 5460.79$ kips

$P1 := 6869.32$ kips

Calculate stability coefficients

$$\theta 1 := \frac{P1\cdot\Delta 1\cdot Ie}{V1\cdot hsx\cdot Cd} = 0.055 \qquad \theta 2 := \frac{P2\cdot\Delta 2\cdot Ie}{V2\cdot hsx\cdot Cd} = 0.051$$

$$\theta 3 := \frac{P3\cdot\Delta 3\cdot Ie}{V3\cdot hsx\cdot Cd} = 0.04 \qquad \theta 4 := \frac{P4\cdot\Delta 4\cdot Ie}{V4\cdot hsx\cdot Cd} = 0.029$$

$$\theta 5 := \frac{P5\cdot\Delta 5\cdot Ie}{V5\cdot hsx\cdot Cd} = 0.019$$

Because the analysis has already include the P-Delta effects, ASCE 7-10 allows to divide the above values by (1+θ). The new stability coefficients are the following:

$$\theta 1new := \frac{\theta 1}{1+\theta 1} = 0.052 \qquad \theta 2new := \frac{\theta 2}{1+\theta 2} = 0.048$$

$$\theta 3new := \frac{\theta 3}{1+\theta 3} = 0.038 \qquad \theta 4new := \frac{\theta 4}{1+\theta 4} = 0.028$$

$$\theta 5new := \frac{\theta 5}{1+\theta 5} = 0.019$$

$\theta := \max(\theta 1new, \theta 2new, \theta 3new, \theta 4new, \theta 5new) = 0.052$ ▮ < 0.1 OK

Note: The member forces and story drifts are permitted to not consider the P-Delta effects

Check upper limite of stability coefficient

the critical level is the first story, whose stability coefficient has the maximum value of 0.052

conservatively take: $\beta := 1.0$

$\theta 1new = 0.052$ ▮ < ▮ $\theta max := \frac{0.5}{\beta \cdot Cd} = 0.091$ OK

Appendix L

Dynamic Analysis Results

L.1 Systems with a GSR = 1.0 & Damping = 5%

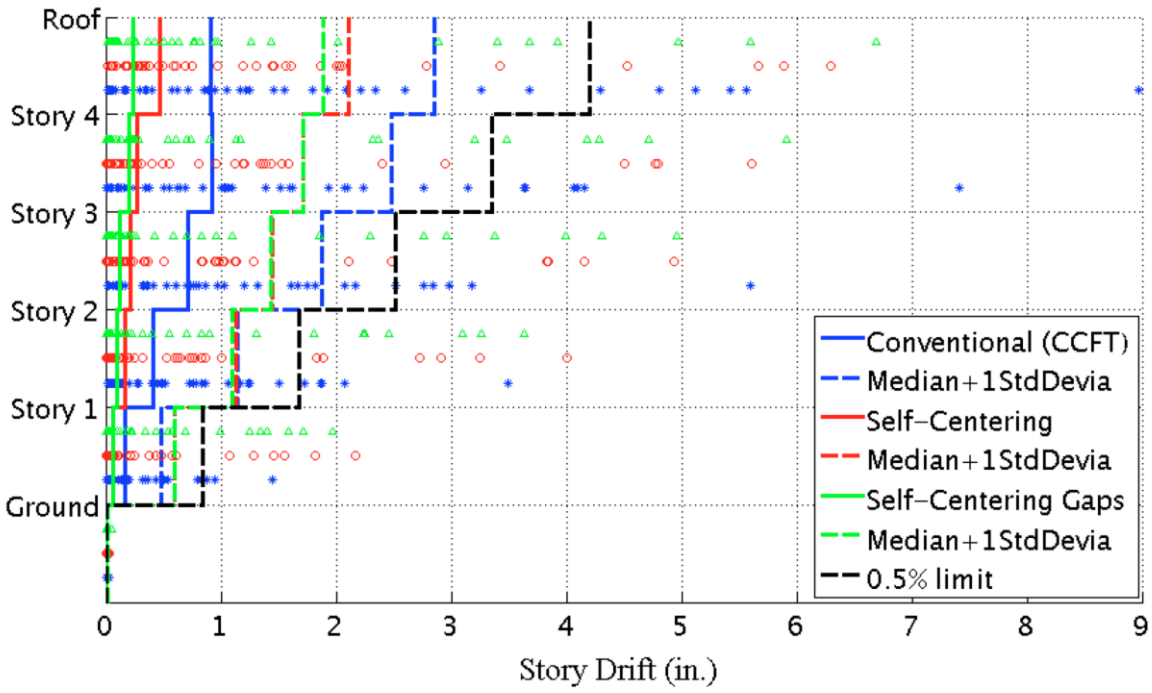

Appendix Figure L-1: Median of the maximum story residual drift under 44 DBE level ground motions with a GSR = 1.0 & damping = 5%

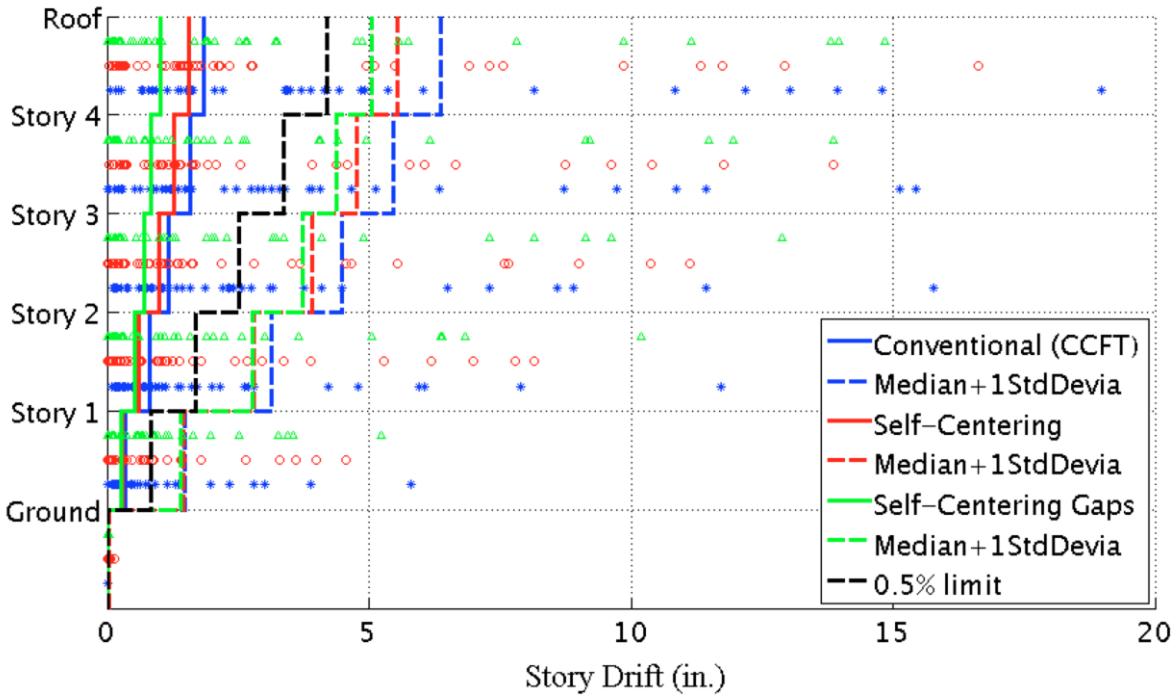

Appendix Figure L-2: Median of the maximum story residual drift under 44 MCE level ground motions with a GSR = 1.0 & damping = 5%

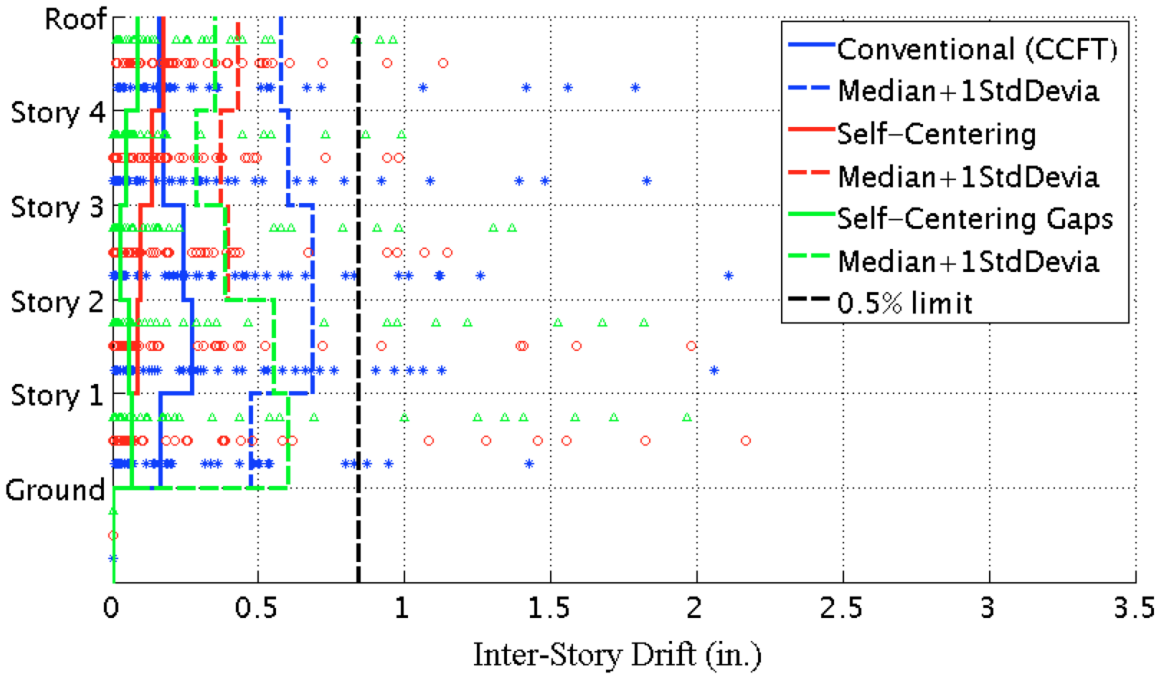

Appendix Figure L-3: Median of the maximum inter-story residual drift under 44 DBE level ground motions with a GSR = 1.0 & damping = 5%

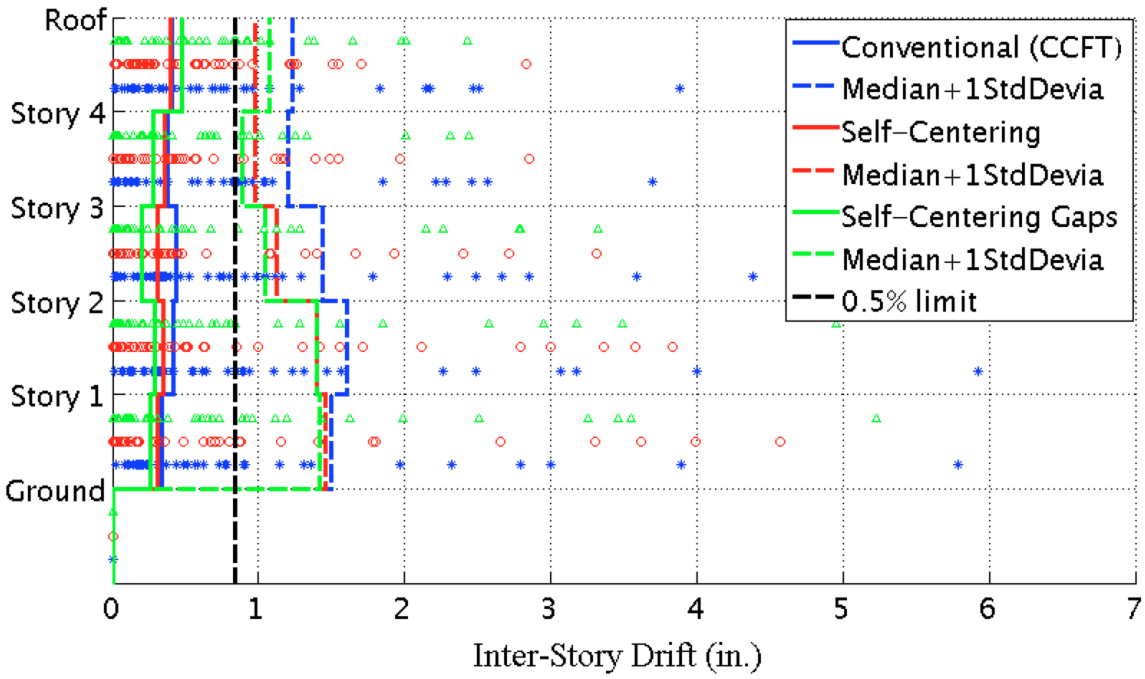

Appendix Figure L-4: Median of the maximum inter-story residual drift under 44 MCE level ground motions with a GSR = 1.0 & damping = 5%

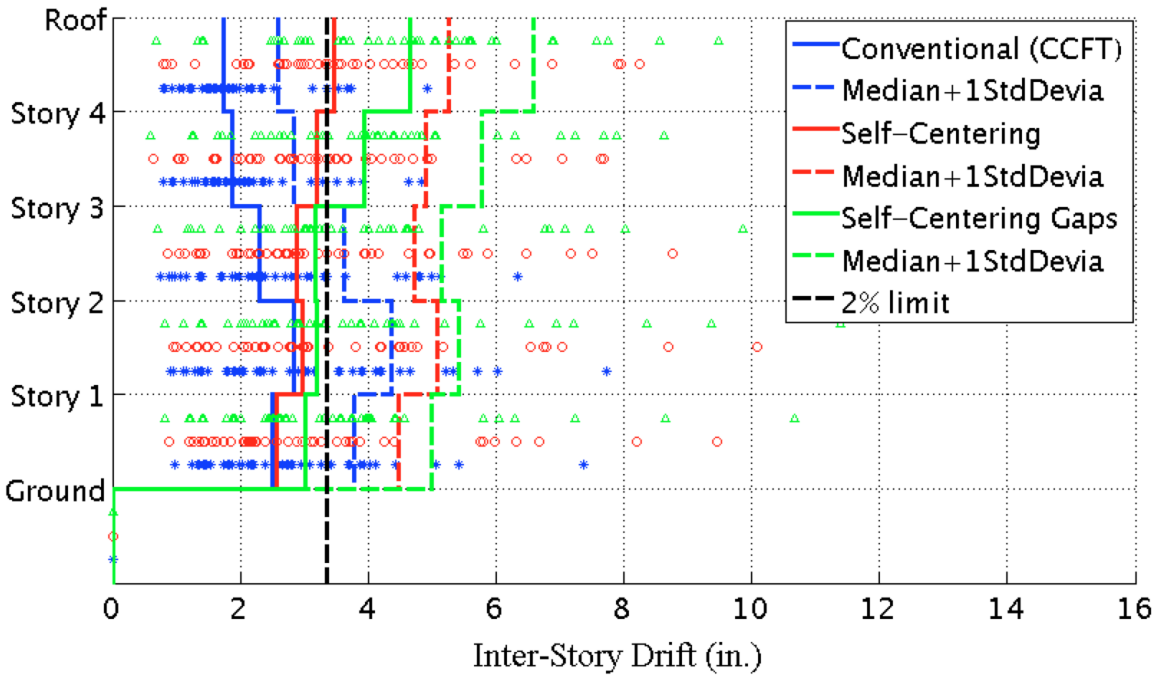

Appendix Figure L-5: Median of the peak inter-story drift under 44 DBE level ground motions with a GSR = 1.0 & damping = 5%

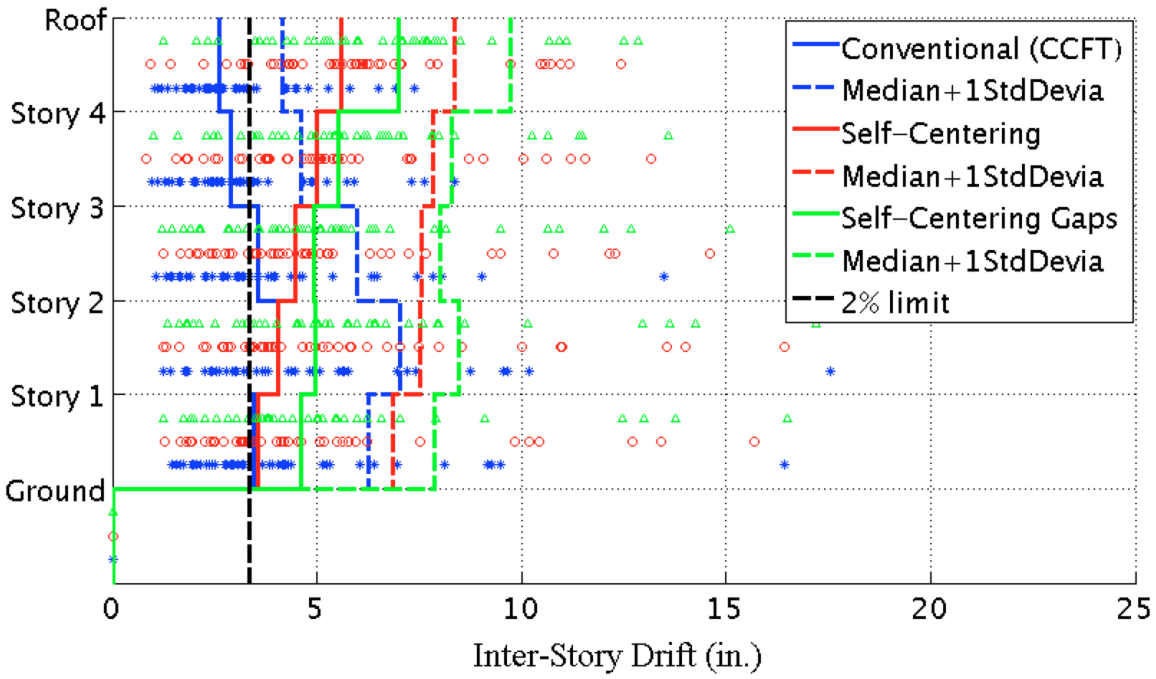

Appendix Figure L-6: Median of the peak inter-story drift under 44 MCE level ground motions with a GSR = 1.0 & damping = 5%

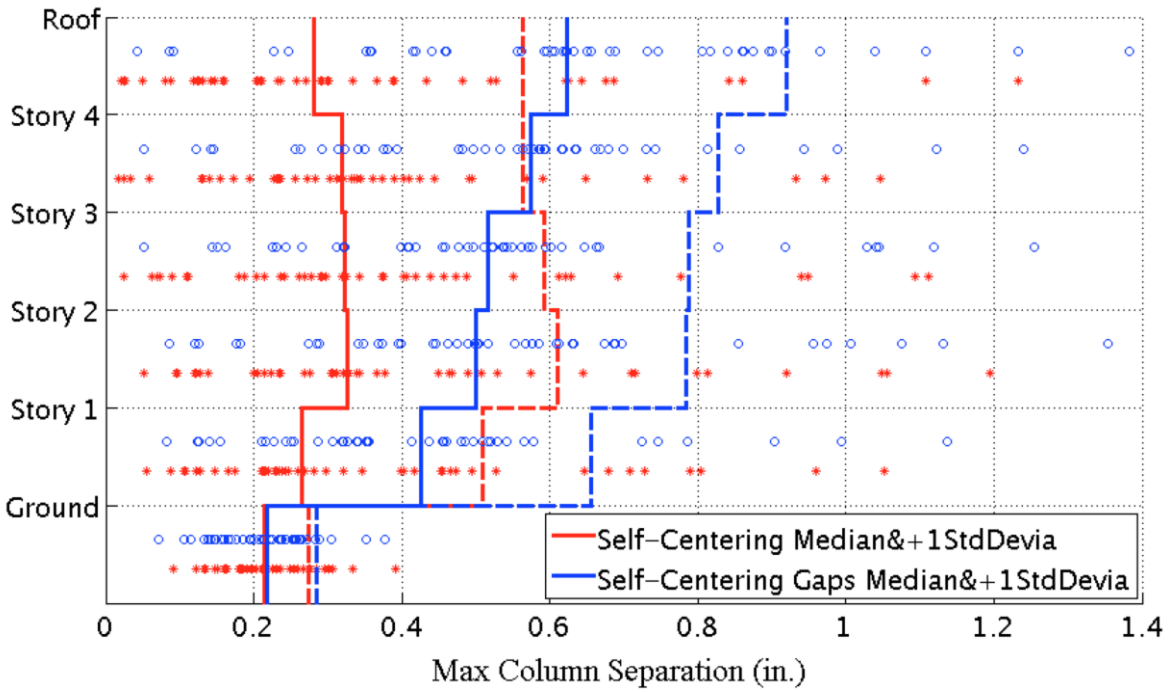

Appendix Figure L-7: Median of the maximum column separation under 44 DBE level ground motions with a GSR = 1.0 & damping = 5%

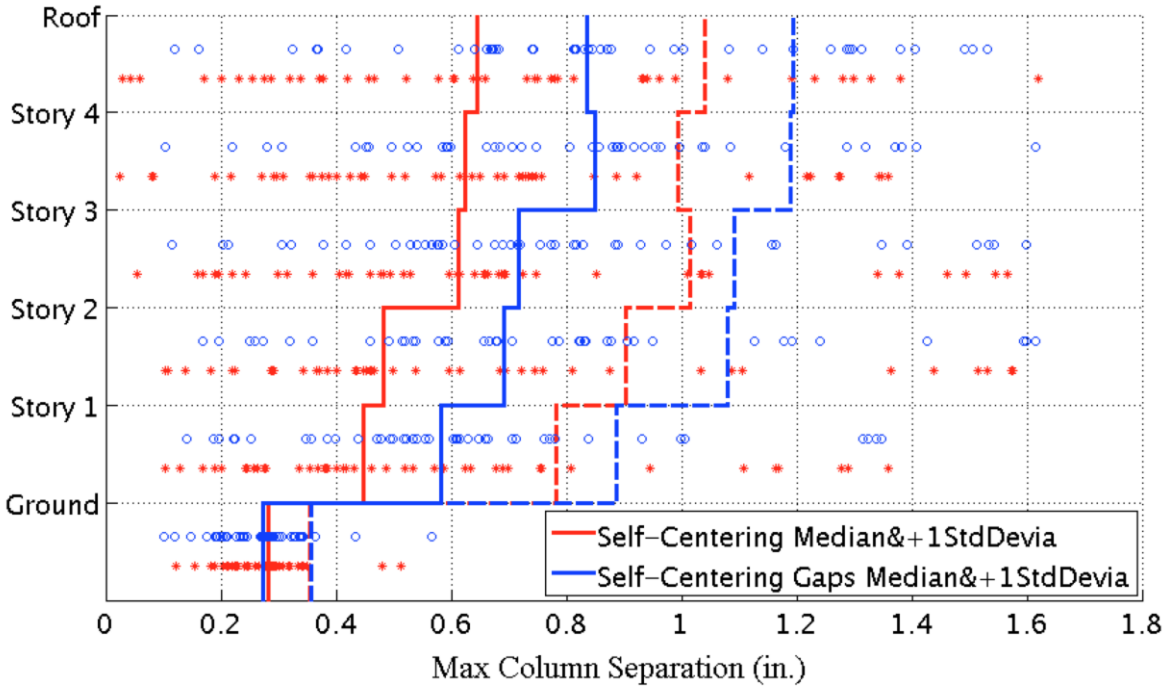

Appendix Figure L-8: Median of the maximum column separation under 44 MCE level ground motions with a GSR = 1.0 & damping = 5%

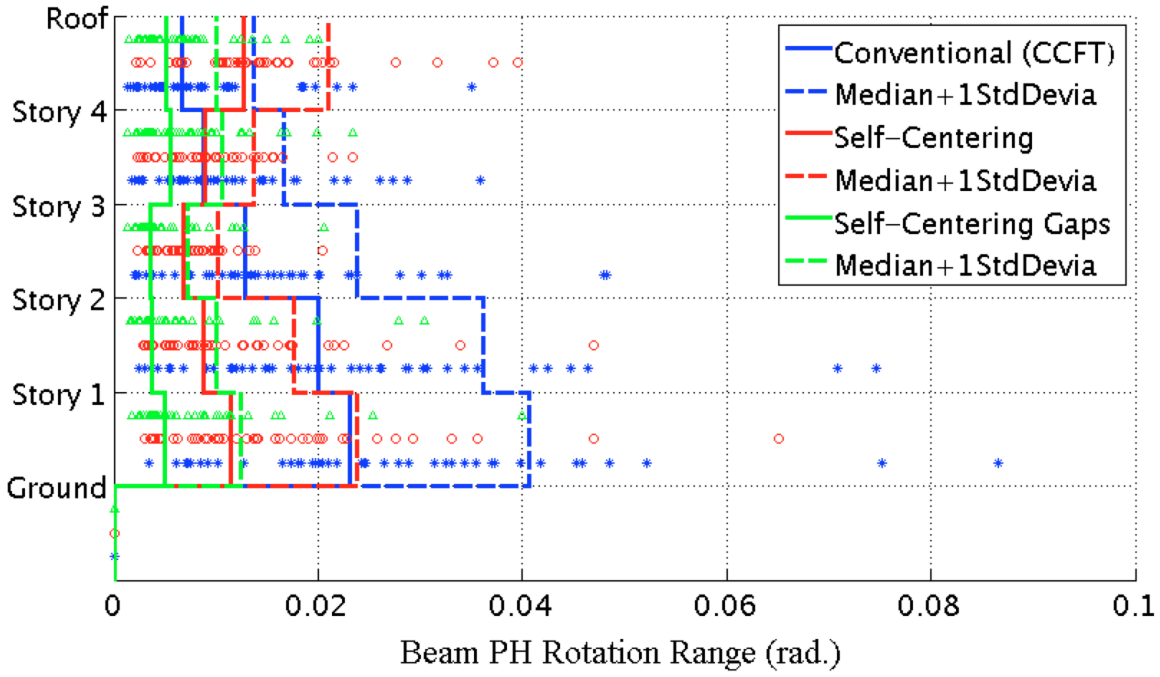

Appendix Figure L-9: Median of the beam PH rotation range under 44 DBE level ground motions with a GSR = 1.0 & damping = 5%

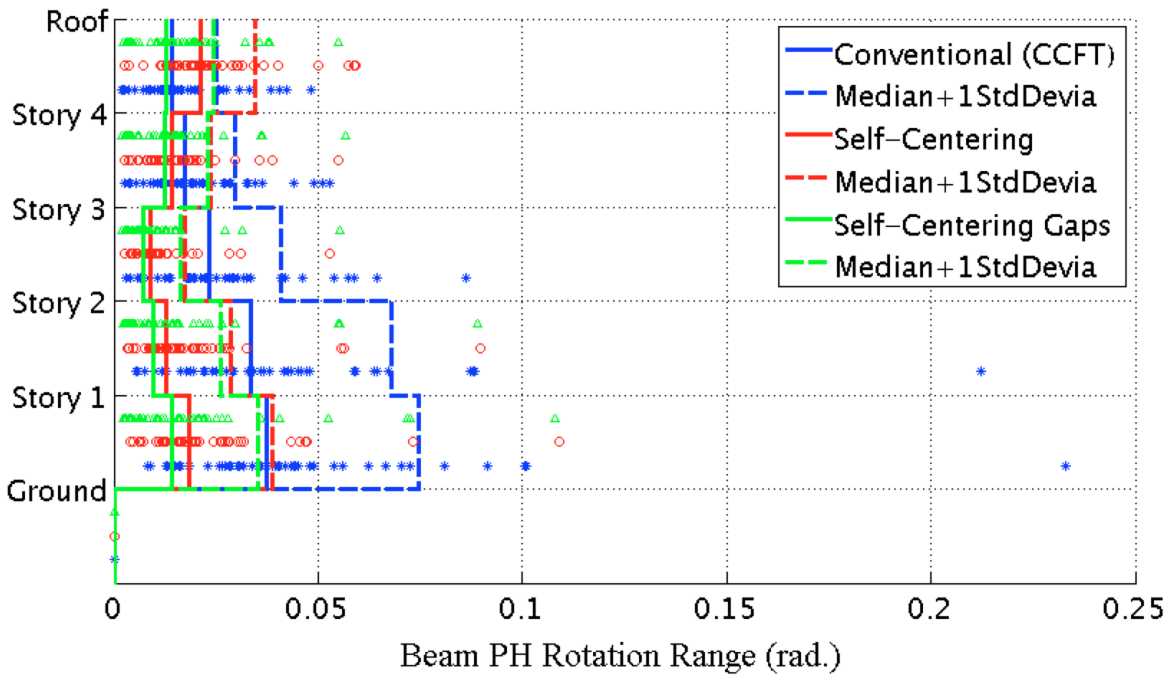

Appendix Figure L-10: Median of the beam PH rotation range under 44 MCE level ground motions with a GSR = 1.0 & damping = 5%

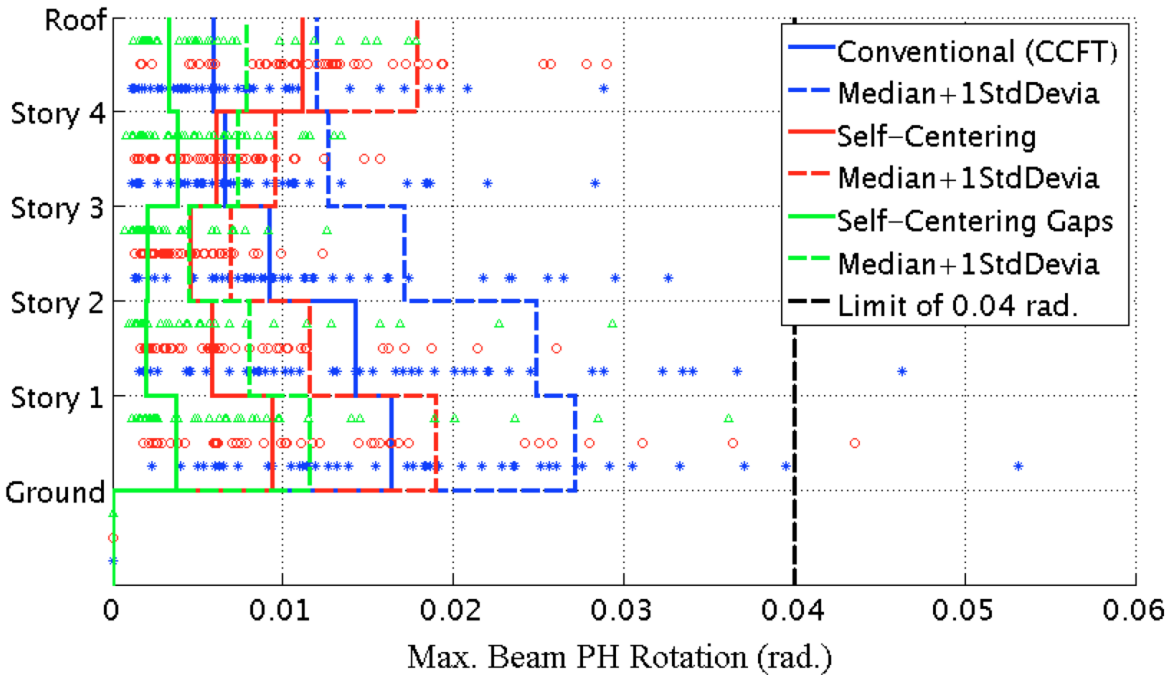

Appendix Figure L-11: Median of the maximum beam PH rotation under 44 DBE level ground motions with a GSR = 1.0 & damping = 5%

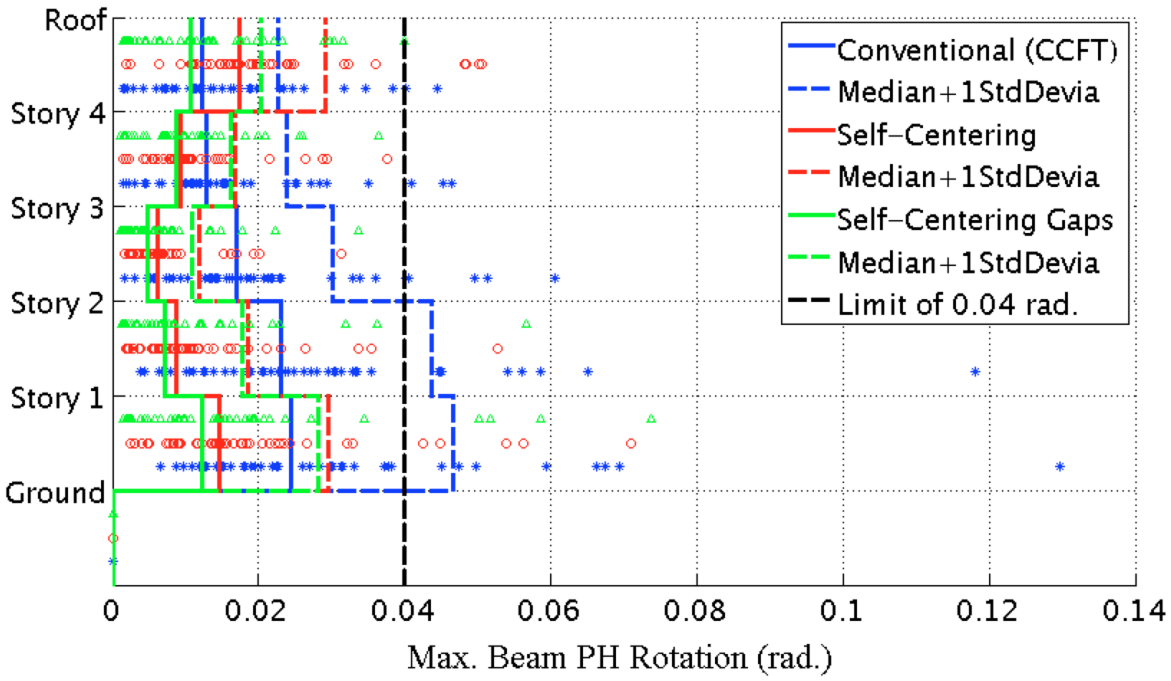

Appendix Figure L-12: Median of the maximum beam PH rotation under 44 MCE level ground motions with a GSR = 1.0 & damping = 5%

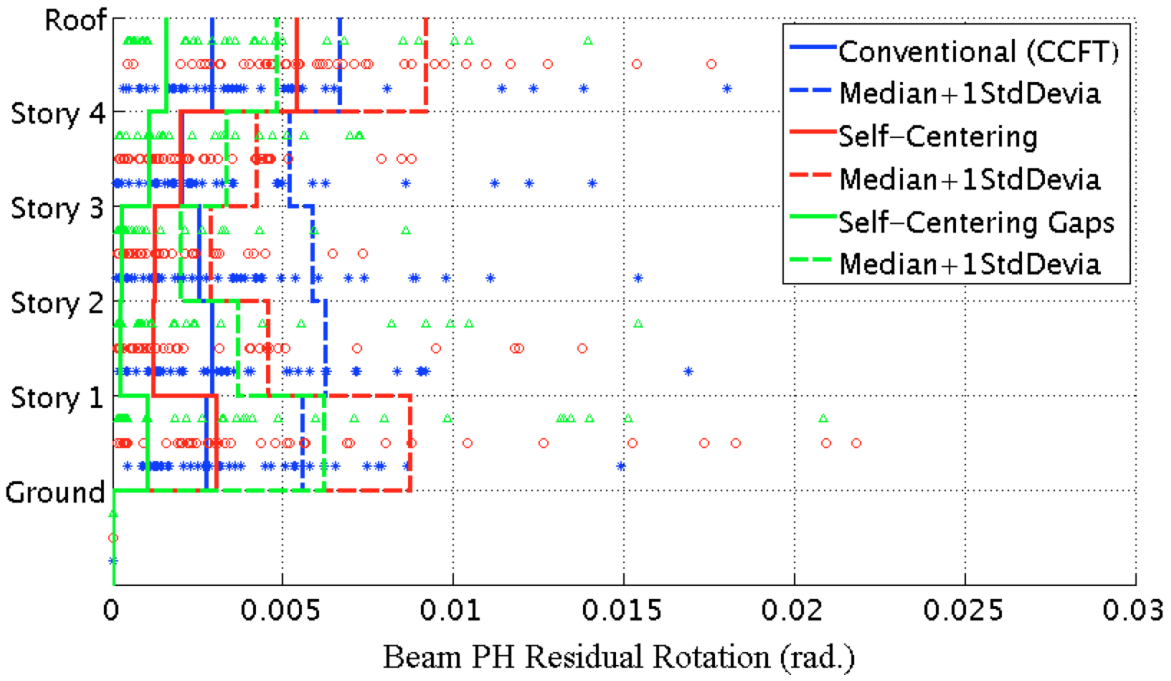

Appendix Figure L-13: Median of the maximum residual rotation of beam plastic hinges under 44 DBE level ground motions with a GSR = 1.0 & damping = 5%

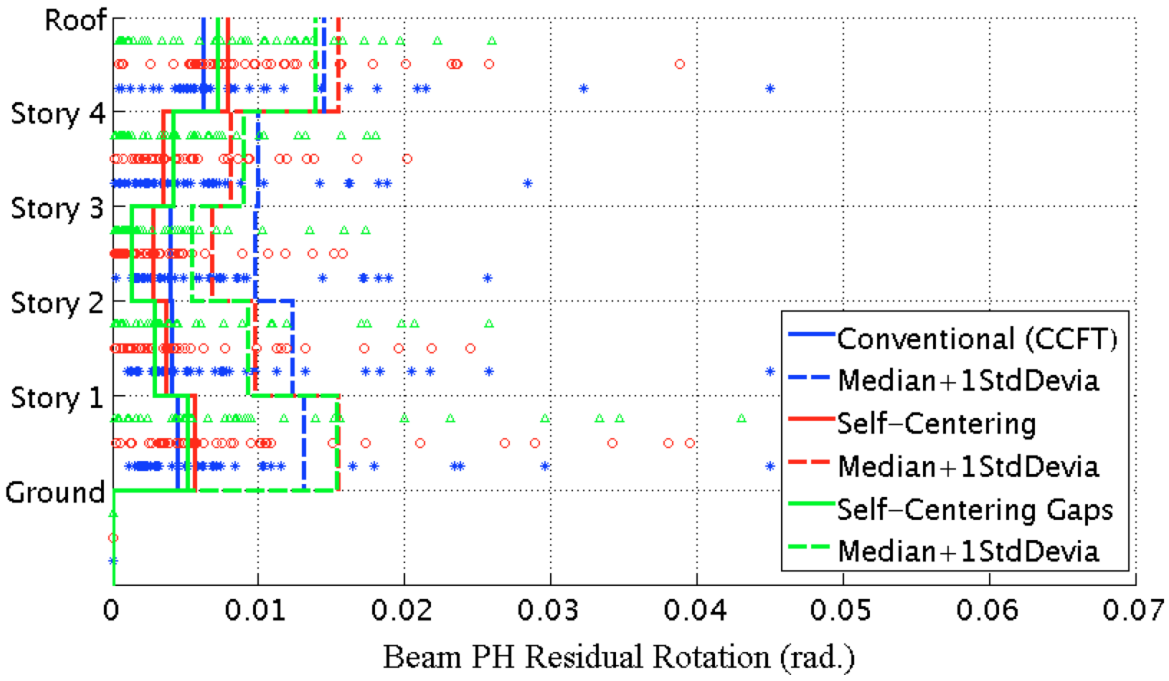

Appendix Figure L-14: Median of the maximum residual rotation of beam plastic hinges under 44 MCE level ground motions with a GSR = 1.0 & damping = 5%

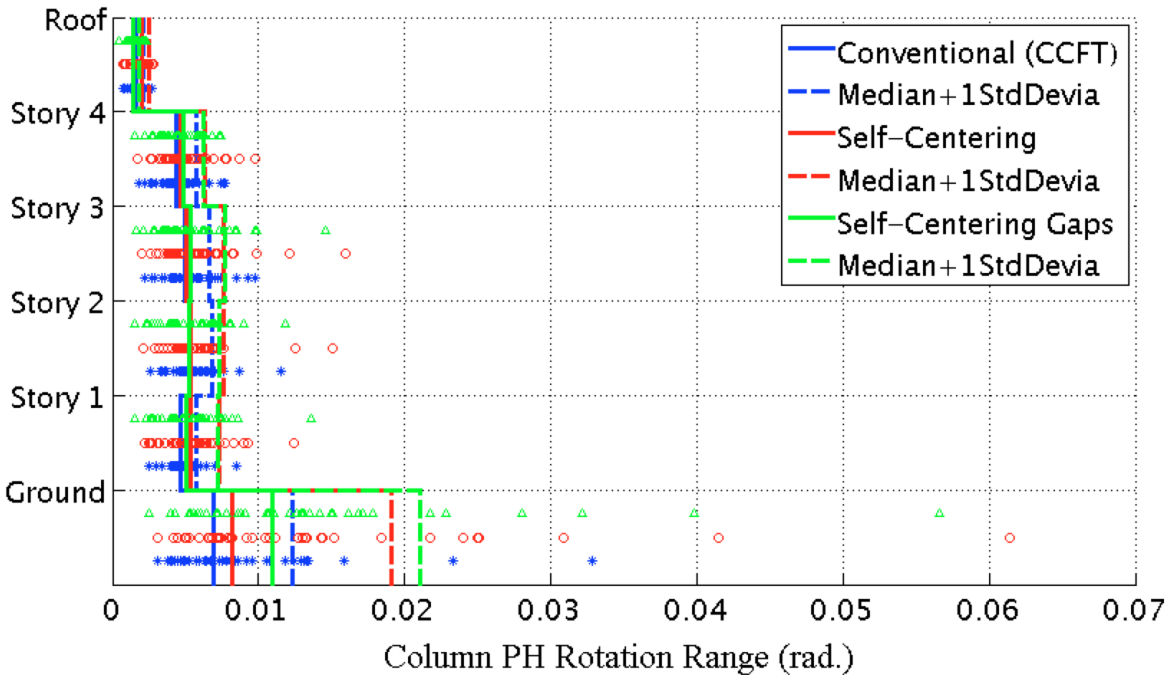

Appendix Figure L-15: Median of the column PH rotation range under 44 DBE level ground motions with a GSR = 1.0 & damping = 5%

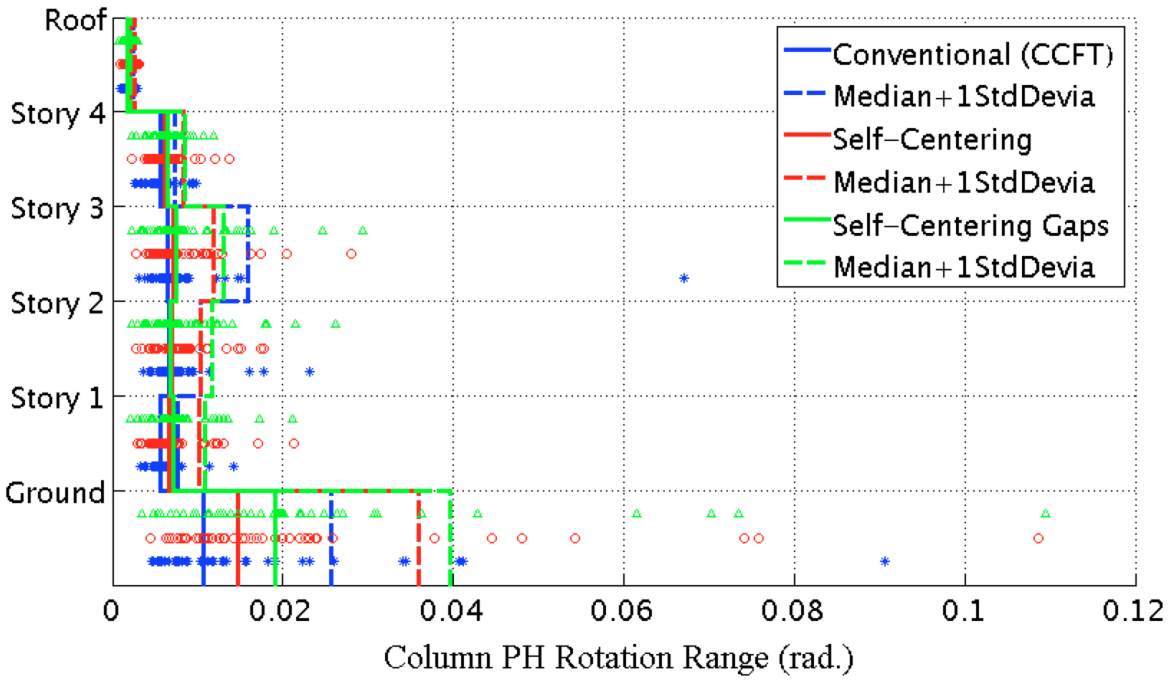

Appendix Figure L-16: Median of the column PH rotation range under 44 MCE level ground motions with a GSR = 1.0 & damping = 5%

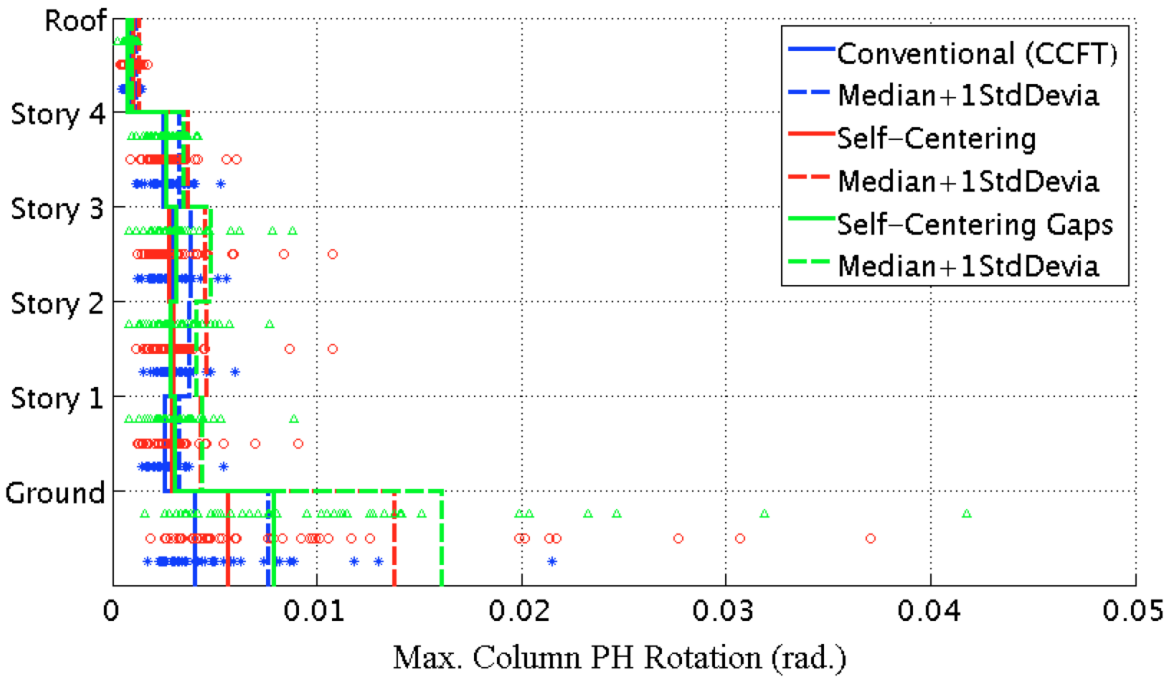

Appendix Figure L-17: Median of the maximum column PH rotation under 44 DBE level ground motions with a GSR = 1.0 & damping = 5%

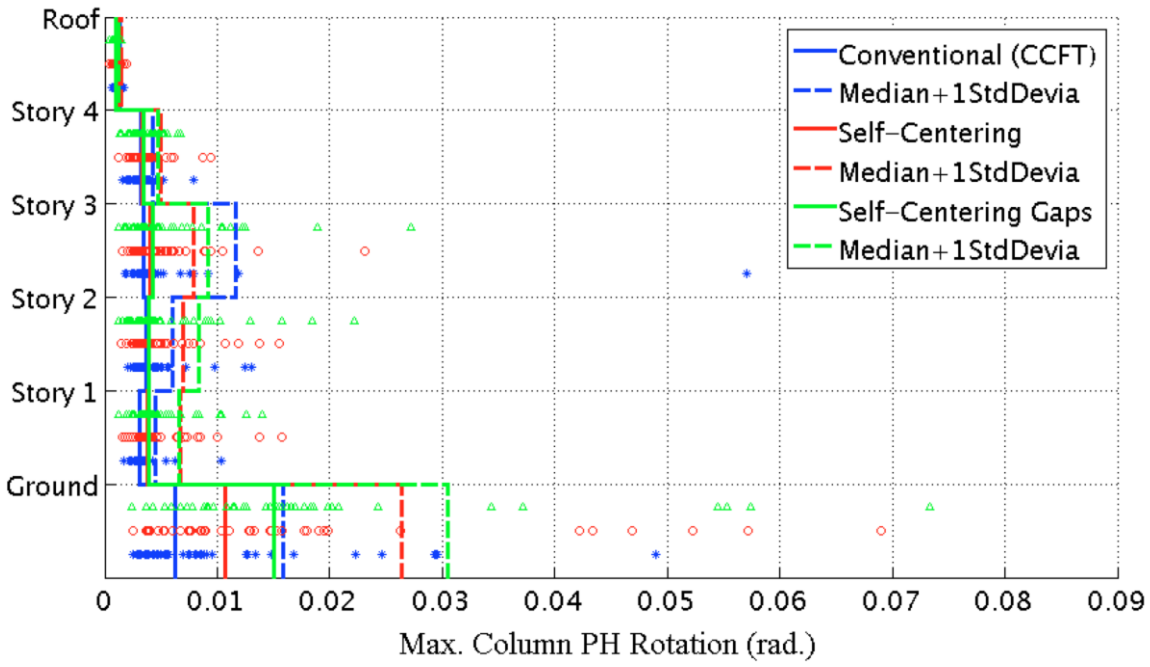

Appendix Figure L-18: Median of the maximum column PH rotation under 44 MCE level ground motions with a GSR = 1.0 & damping = 5%

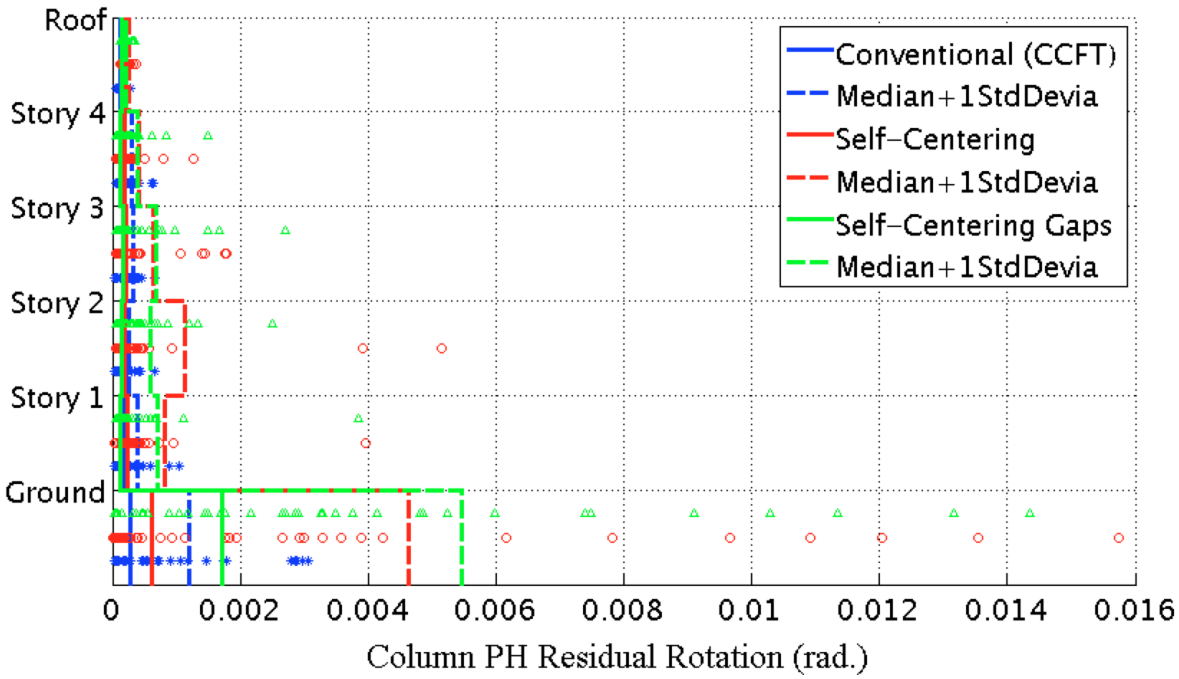

Appendix Figure L-19: Median of the maximum residual rotation of column plastic hinges under 44 DBE level ground motions with a GSR = 1.0 & damping = 5%

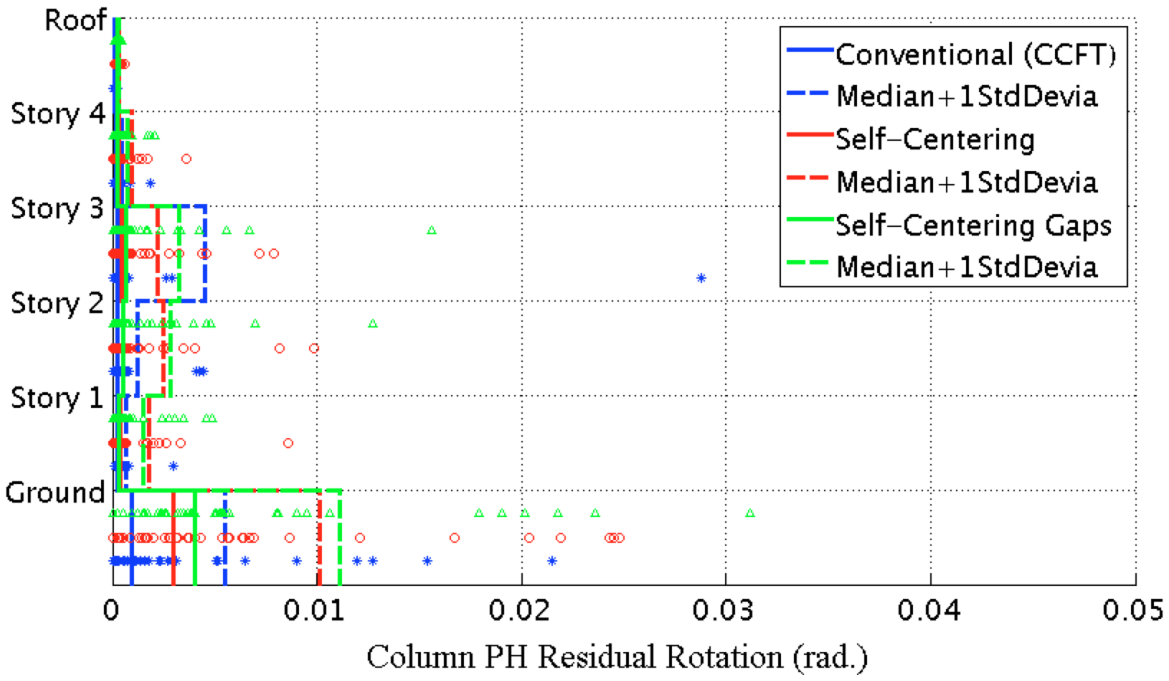

Appendix Figure L-20: Median of the maximum residual rotation of column plastic hinges under 44 MCE level ground motions with a GSR = 1.0 & damping = 5%

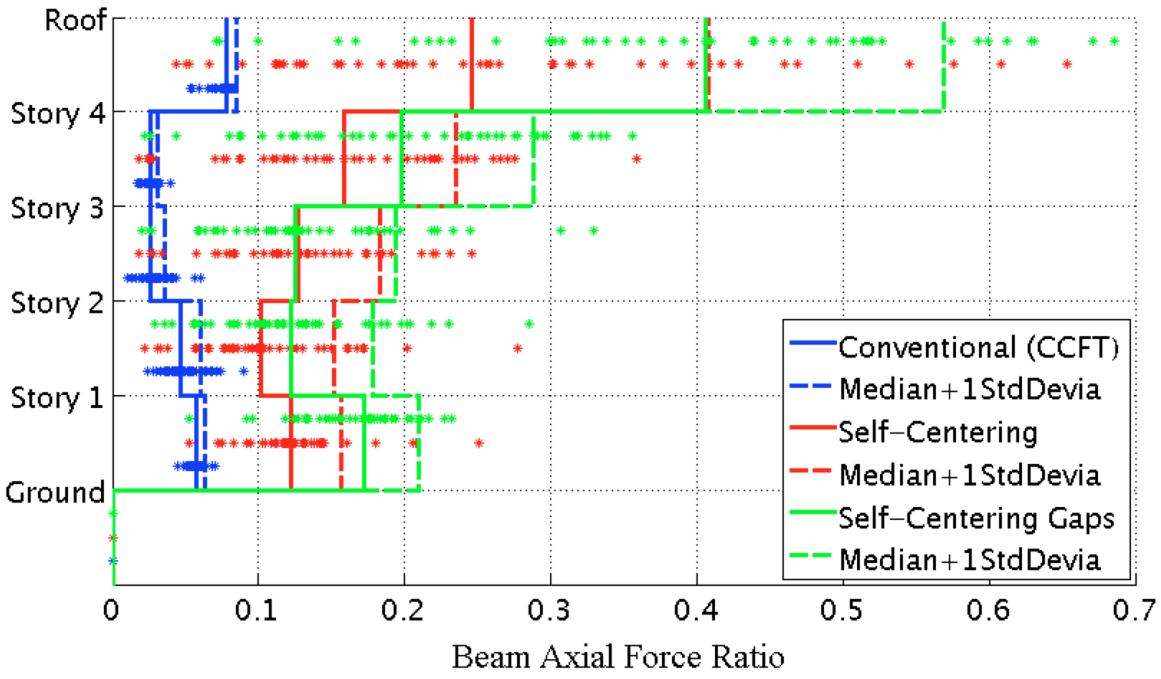

Appendix Figure L-21: Median of the peak axial force in beams under 44 DBE level ground motions with a GSR = 1.0 & damping = 5%

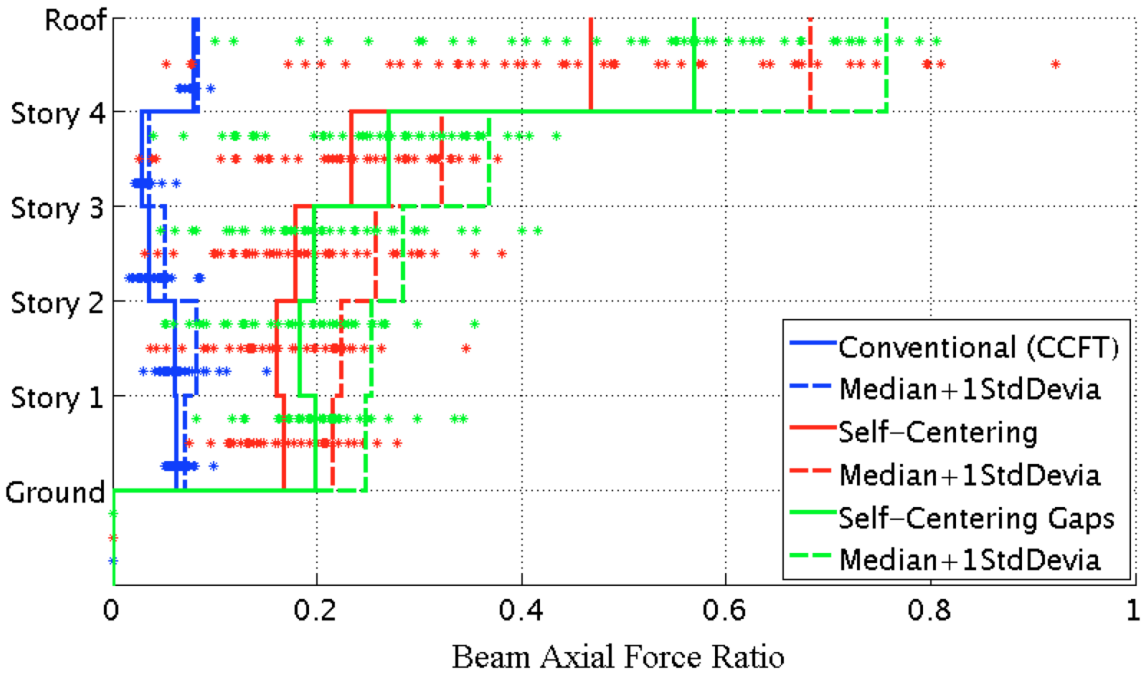

Appendix Figure L-22: Median of the peak axial force in beams under 44 MCE level ground motions with a GSR = 1.0 & damping = 5%

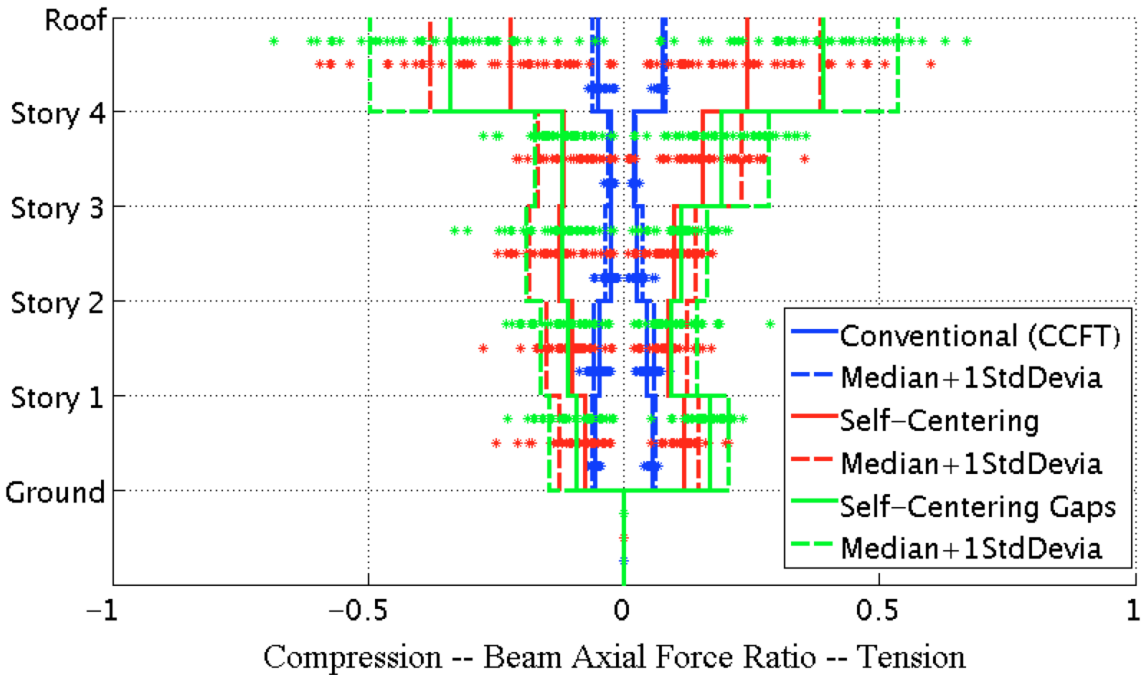

Appendix Figure L-23: Median of the peak tension vs.compression in beams under 44 DBE level ground motions with a GSR = 1.0 & damping = 5%

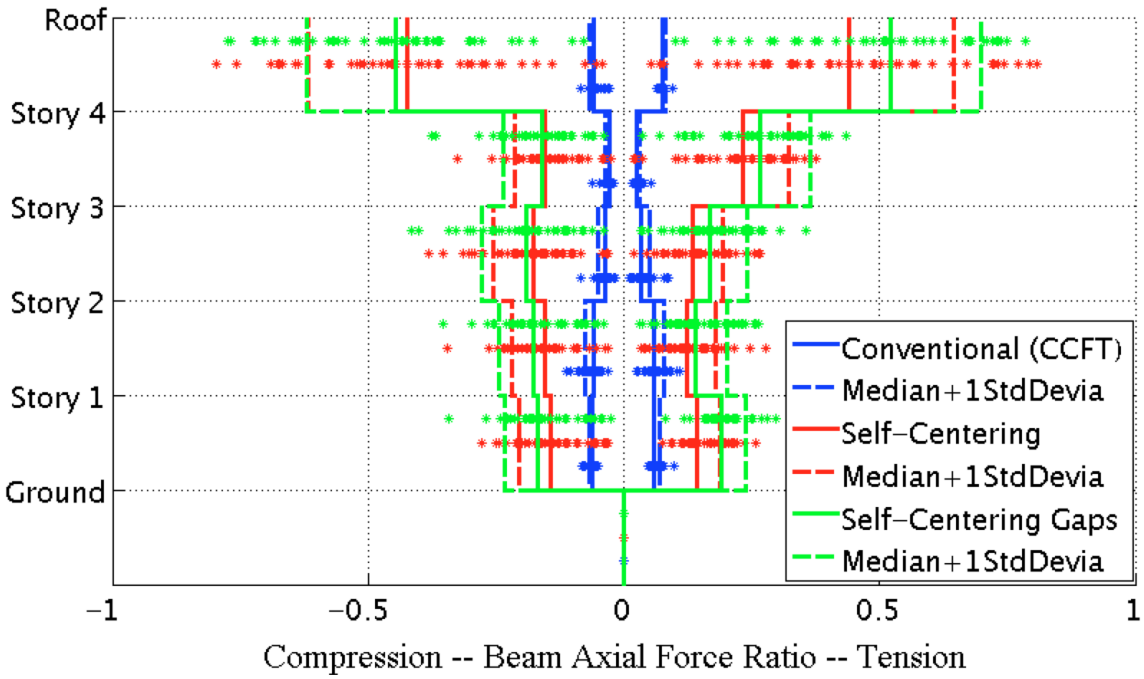

Appendix Figure L-24: Median of the peak tension vs.compression in beams under 44 MCE level ground motions with a GSR = 1.0 & damping = 5%

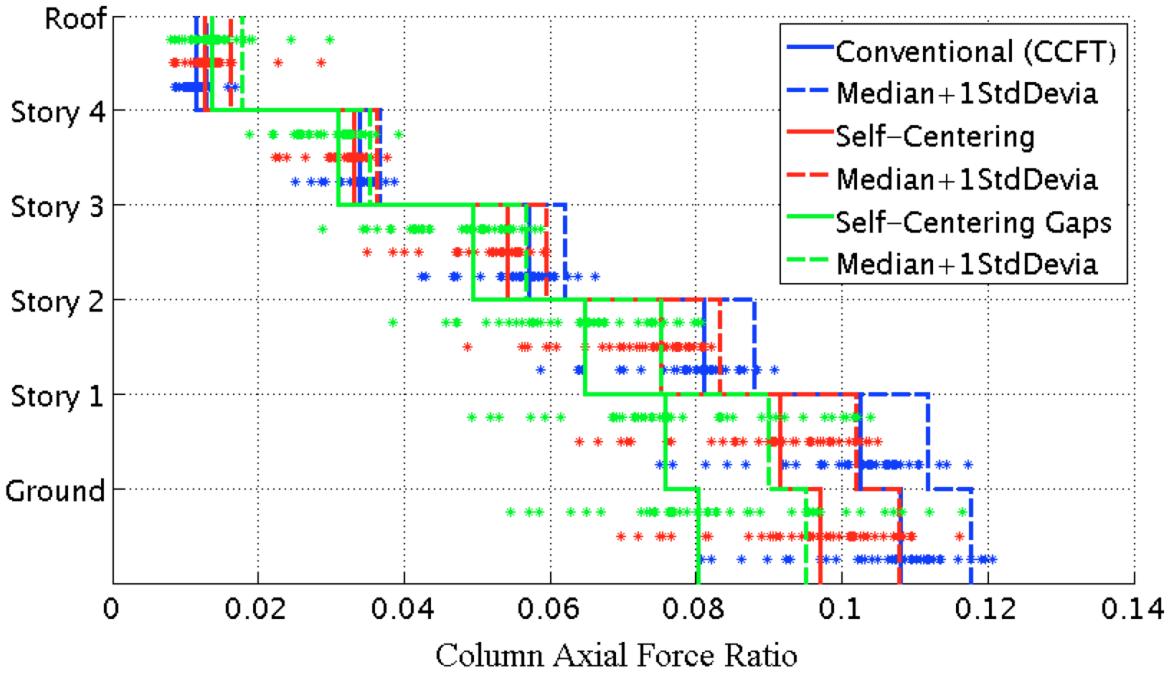

Appendix Figure L-25: Median of the peak axial force in columns under 44 DBE level ground motions with a GSR = 1.0 & damping = 5%

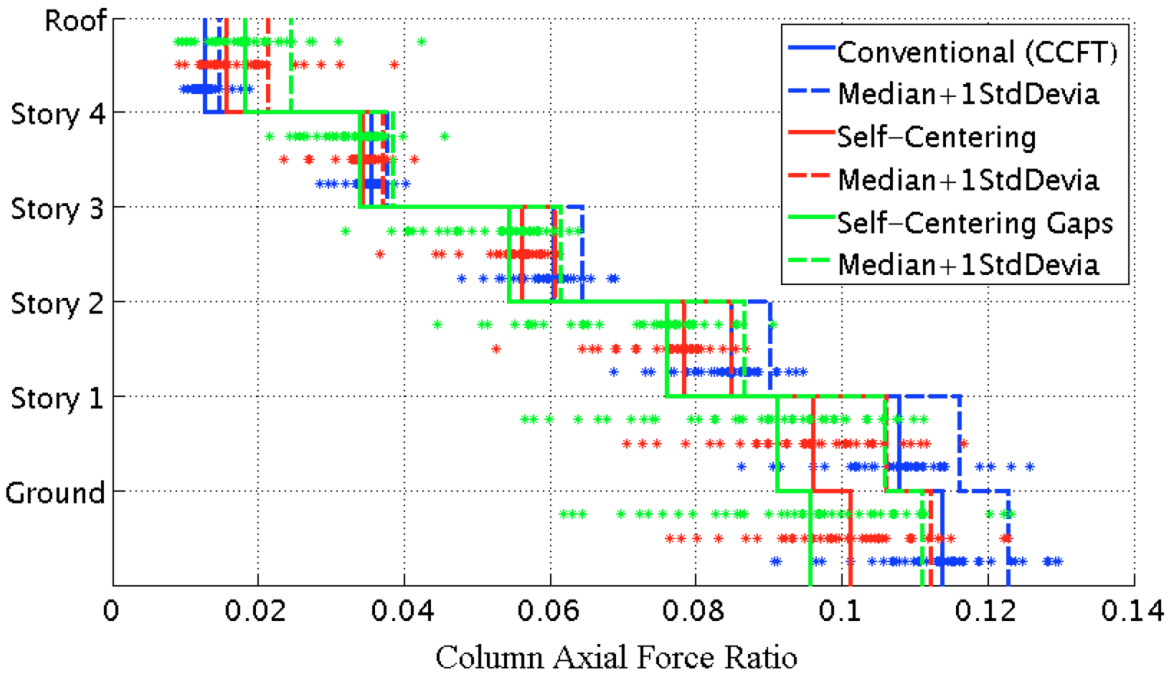

Appendix Figure L-26: Median of the peak axial force in columns under 44 MCE level ground motions with a GSR = 1.0 & damping = 5%

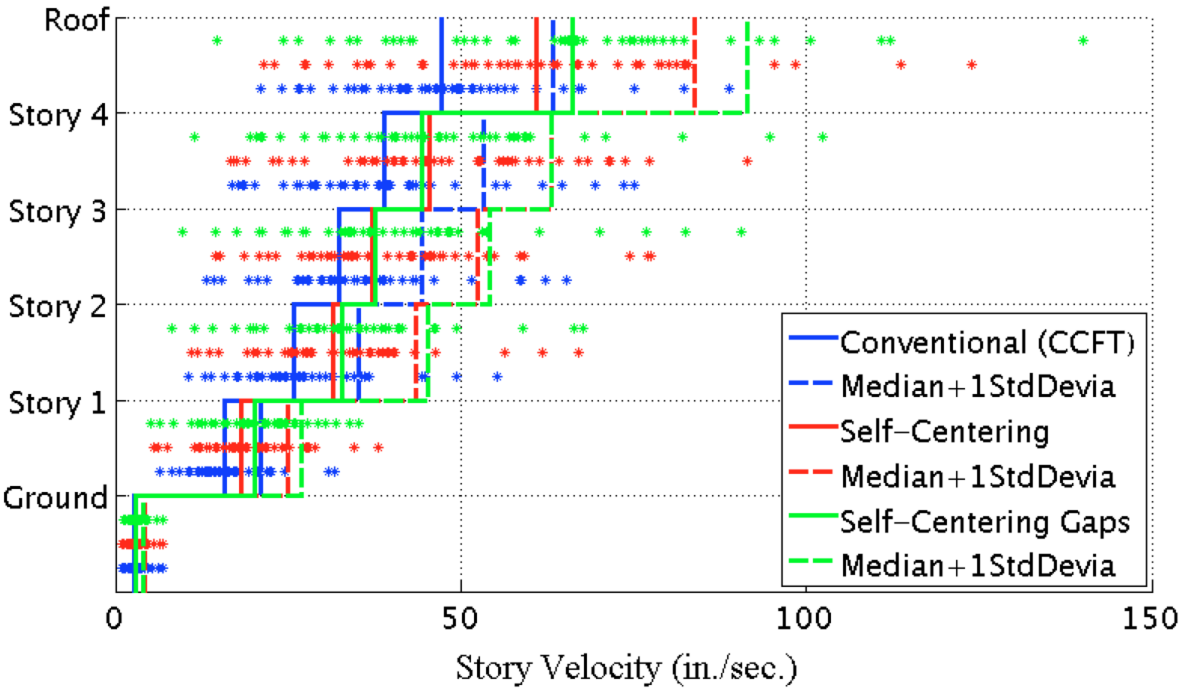

Appendix Figure L-27: Median of the peak story velocity under 44 DBE level ground motions with a GSR = 1.0 & damping = 5%

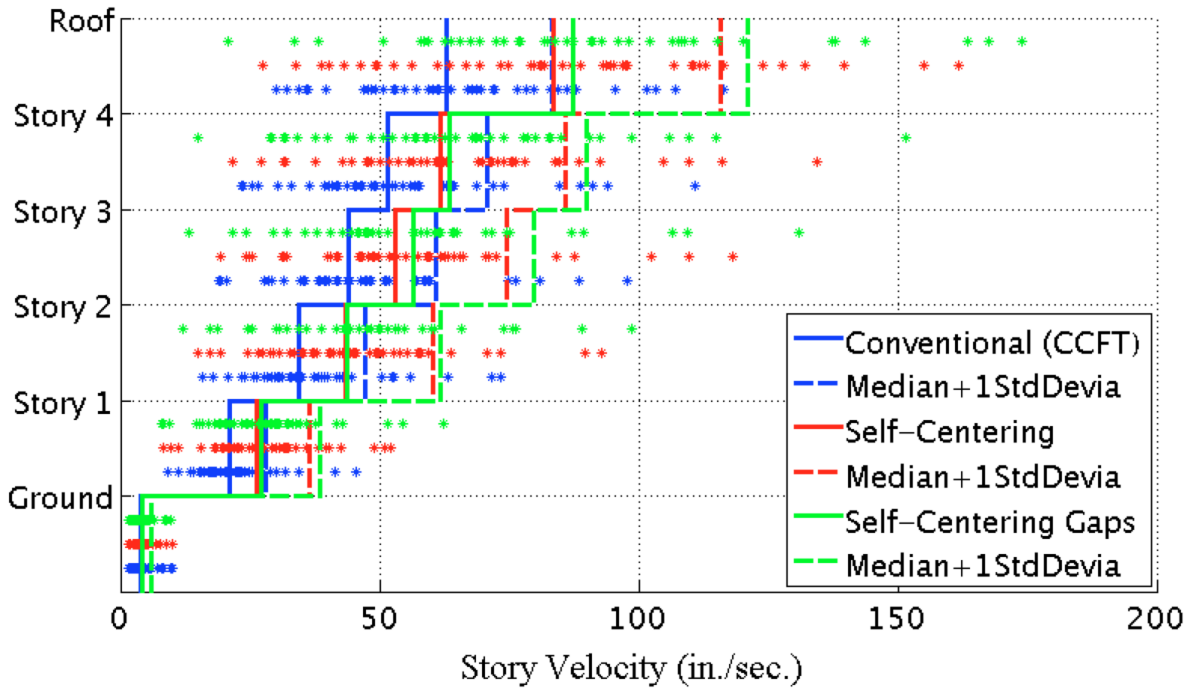

Appendix Figure L-28: Median of the peak story velocity under 44 MCE level ground motions with a GSR = 1.0 & damping = 5%

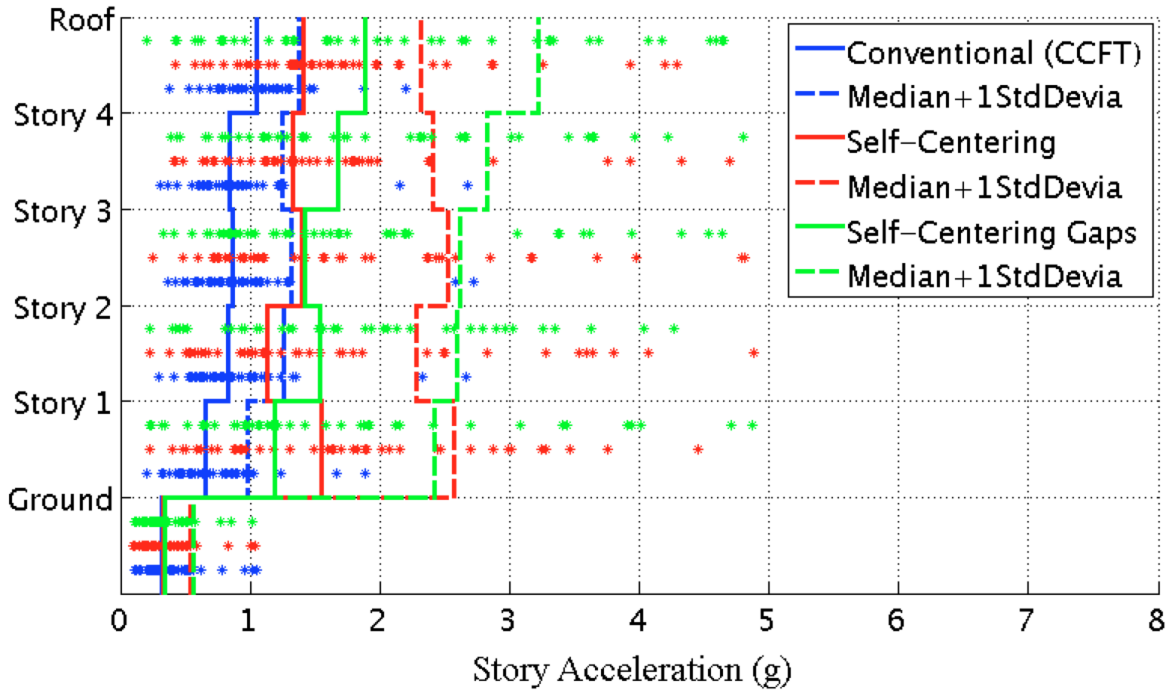

Appendix Figure L-29: Median of the peak story acceleration under 44 DBE level ground motions with a GSR = 1.0 & damping = 5%

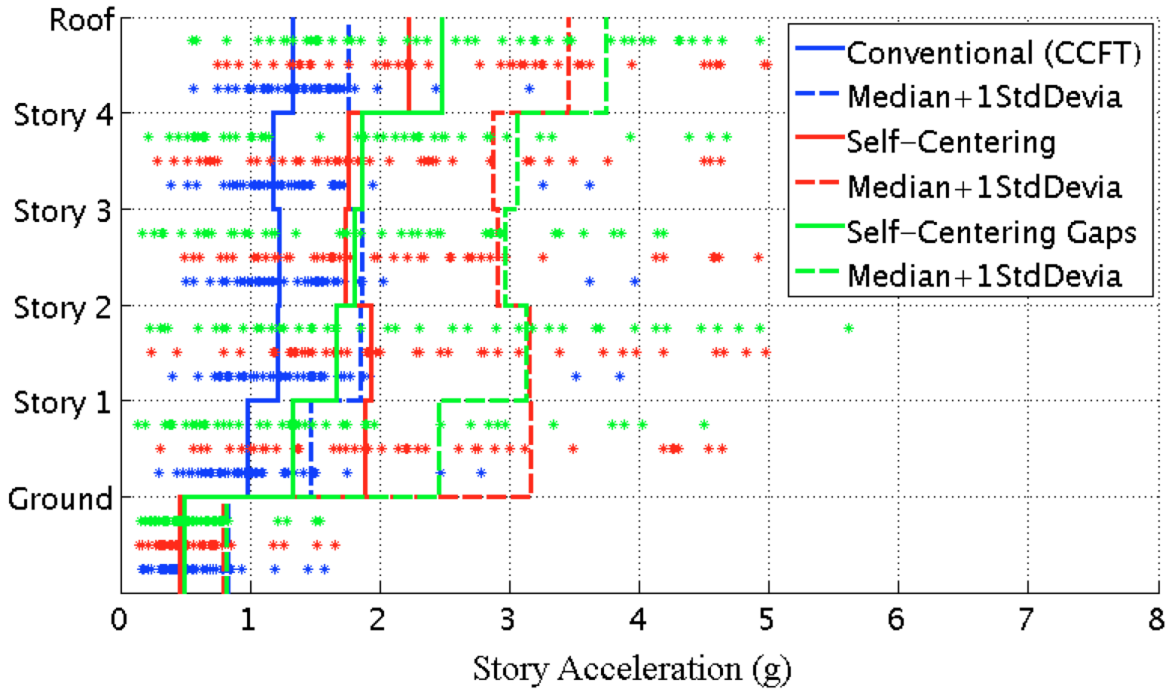

Appendix Figure L-30: Median of the peak story acceleration under 44 MCE level ground motions with a GSR = 1.0 & damping = 5%

L.2 Systems with a GSR = 1.1 & Damping = 5%

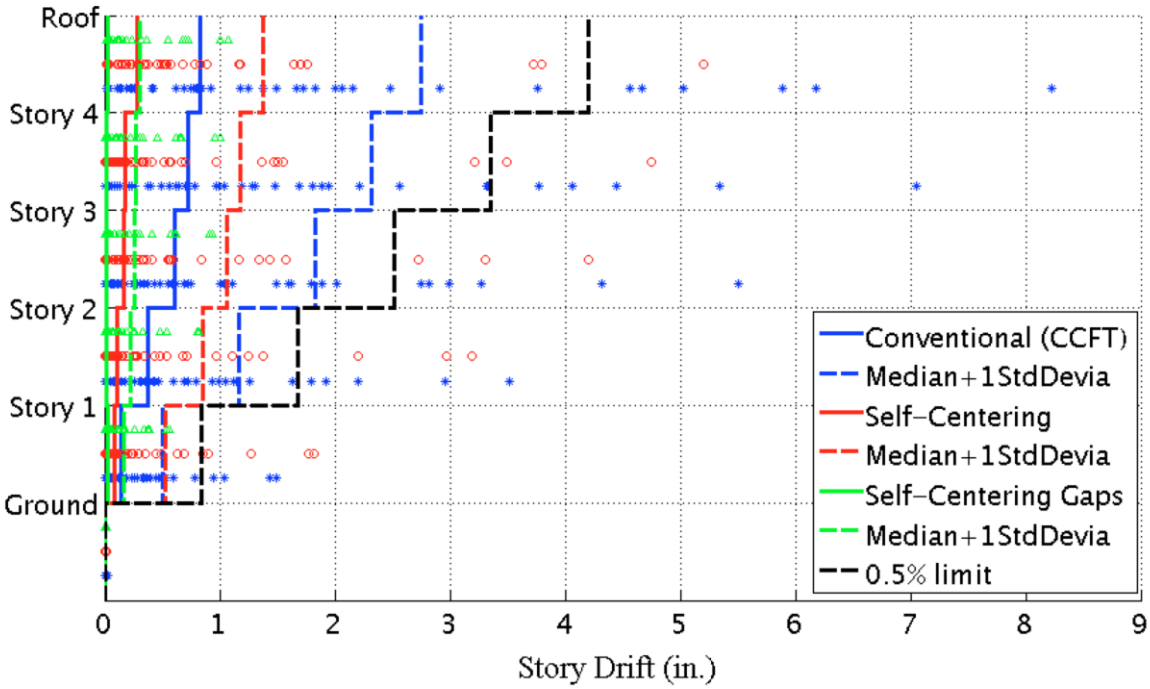

Appendix Figure L-31: Median of the maximum story residual drift under 44 DBE level ground motions with a GSR = 1.1 & damping = 5%

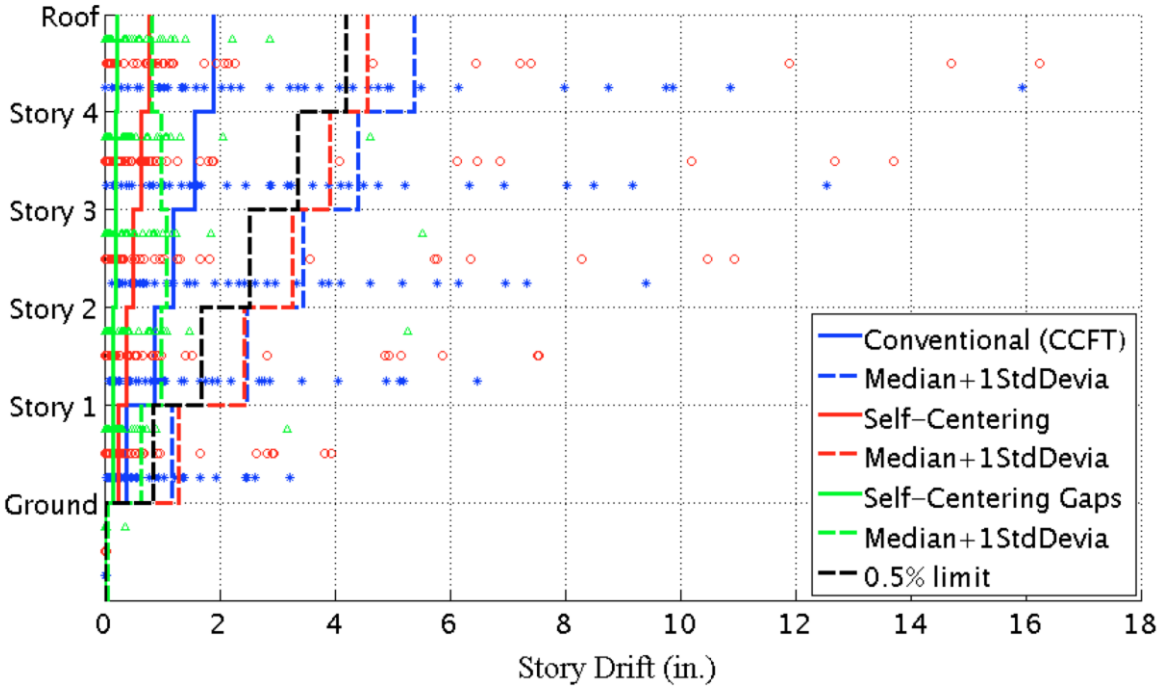

Appendix Figure L-32: Median of the maximum story residual drift under 44 MCE level ground motions with a GSR = 1.1 & damping = 5%

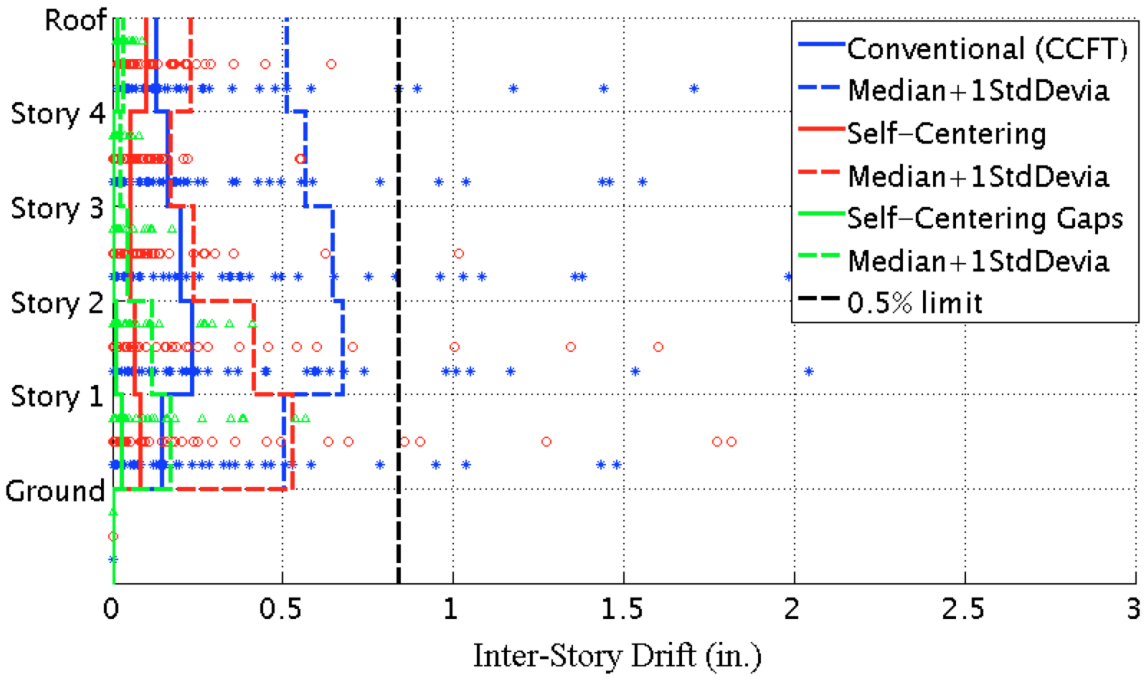

Appendix Figure L-33: Median of the maximum inter-story residual drift under 44 DBE level ground motions with a GSR = 1.1 & damping = 5%

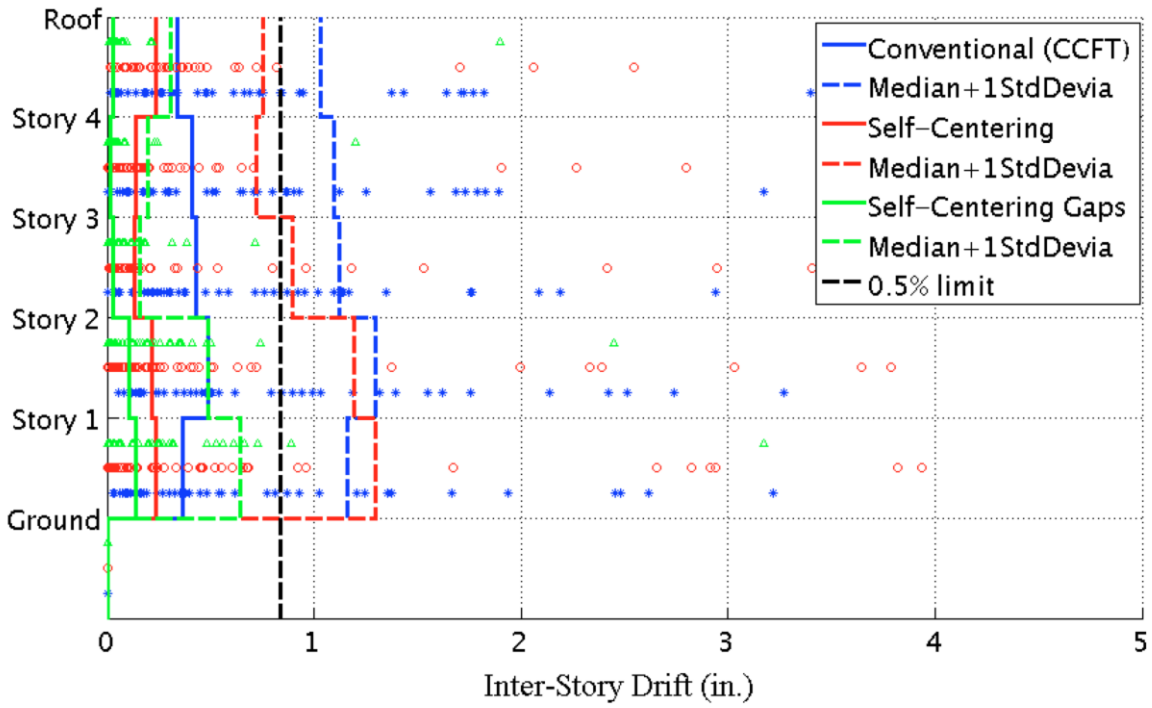

Appendix Figure L-34: Median of the maximum inter-story residual drift under 44 MCE level ground motions with a GSR = 1.1 & damping = 5%

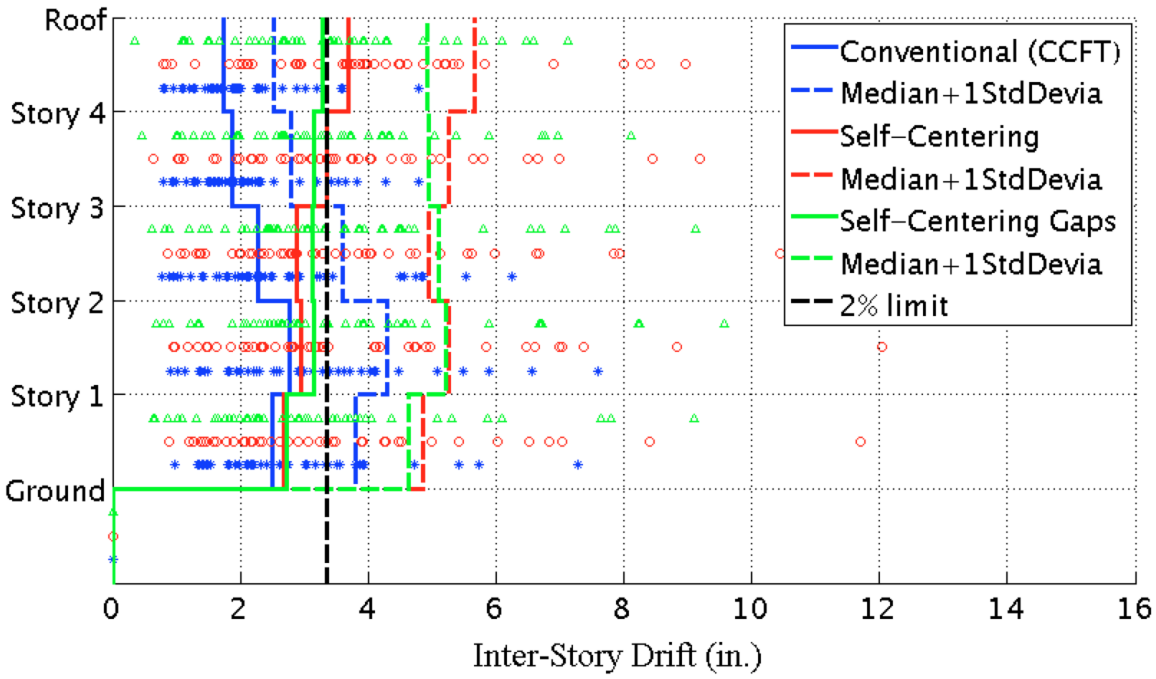

Appendix Figure L-35: Median of the peak inter-story drift under 44 DBE level ground motions with a GSR = 1.1 & damping = 5%

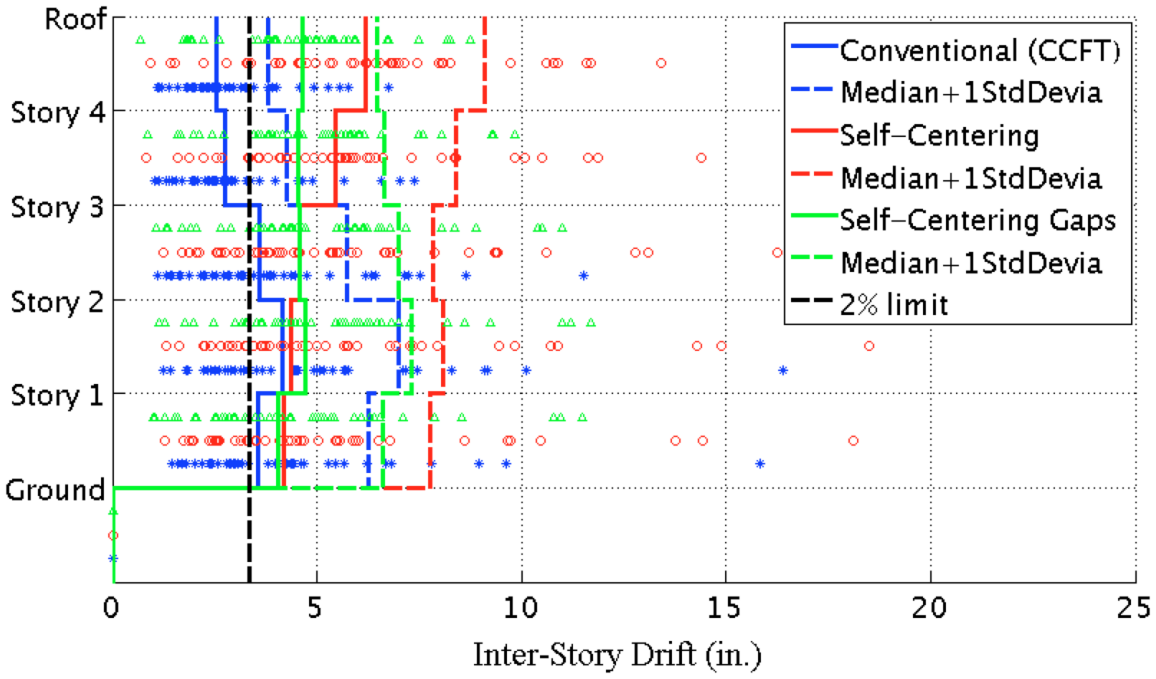

Appendix Figure L-36: Median of the peak inter-story drift under 44 MCE level ground motions with a GSR = 1.1 & damping = 5%

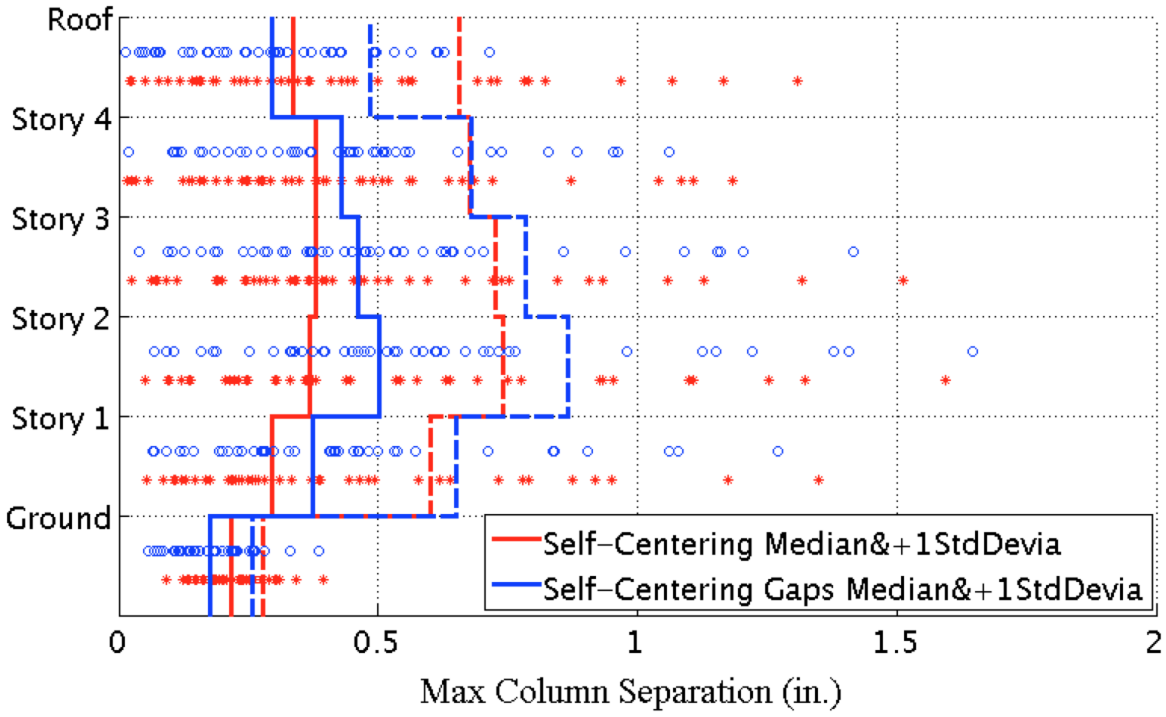

Appendix Figure L-37: Median of the maximum column separation under 44 DBE level ground motions with a GSR = 1.1 & damping = 5%

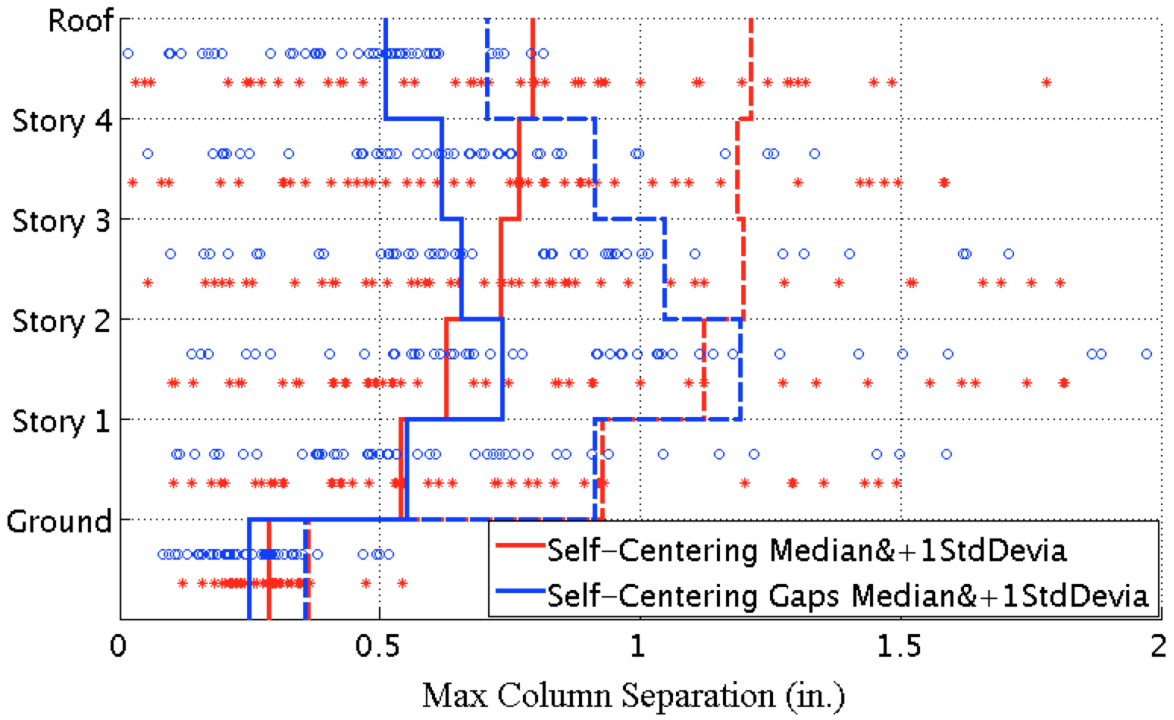

Appendix Figure L-38: Median of the maximum column separation under 44 MCE level ground motions with a GSR = 1.1 & damping = 5%

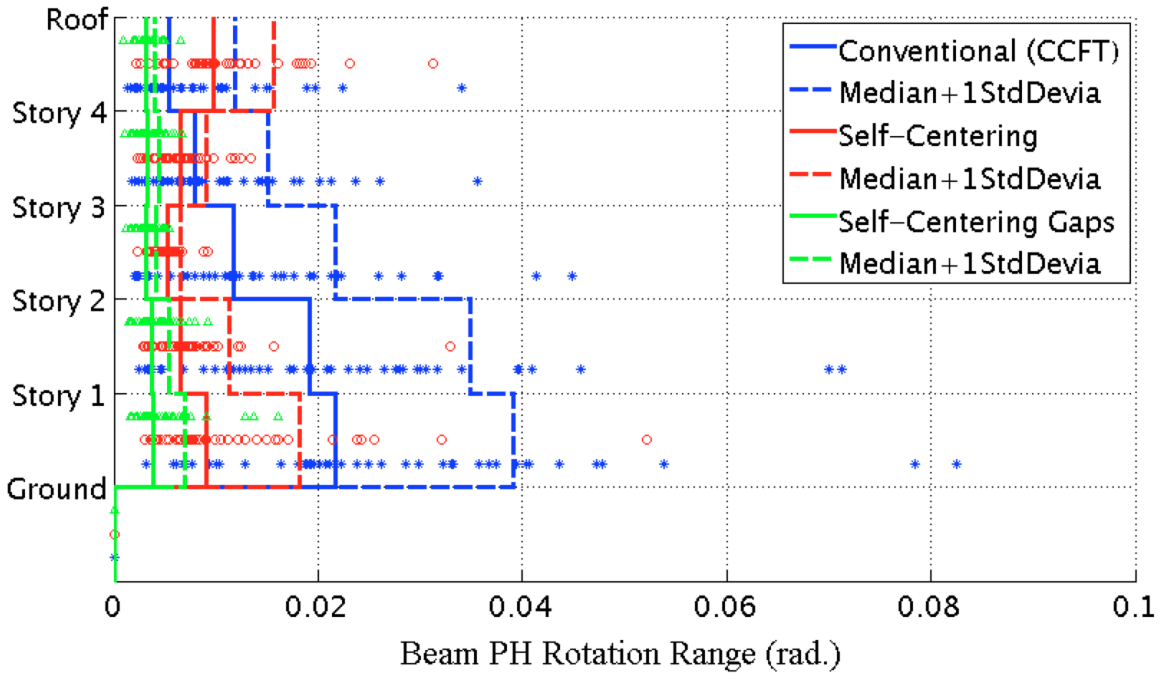

Appendix Figure L-39: Median of the beam PH rotation range under 44 DBE level ground motions with a GSR = 1.1 & damping = 5%

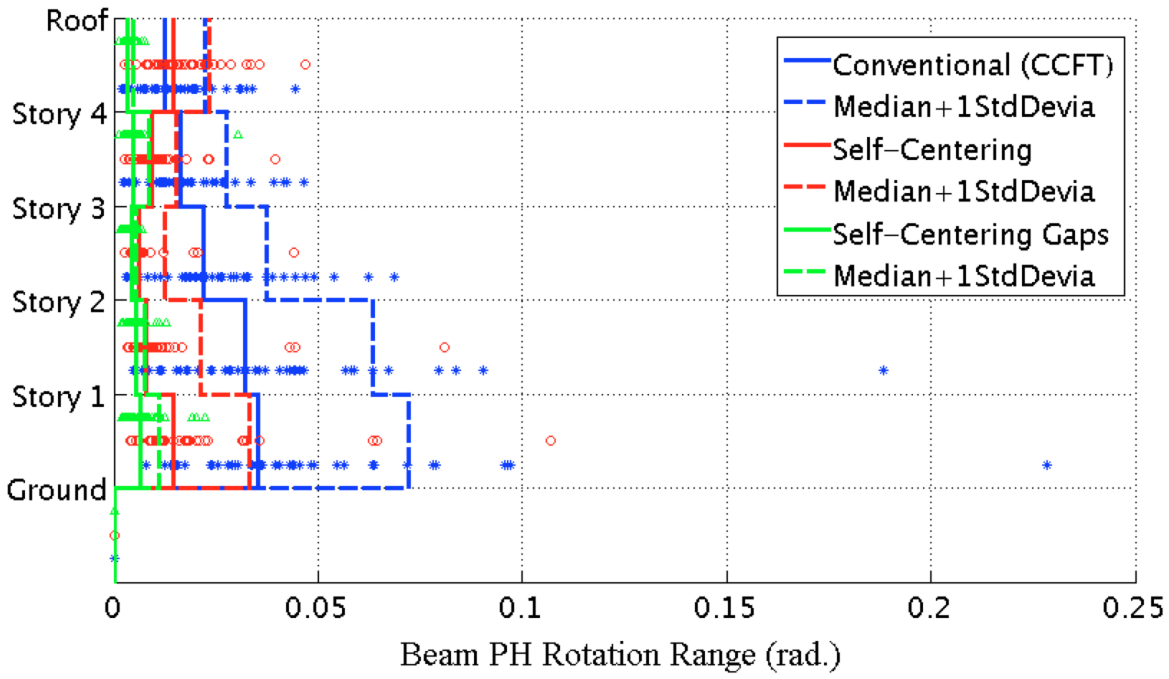

Appendix Figure L-40: Median of the beam PH rotation range under 44 MCE level ground motions with a GSR = 1.1 & damping = 5%

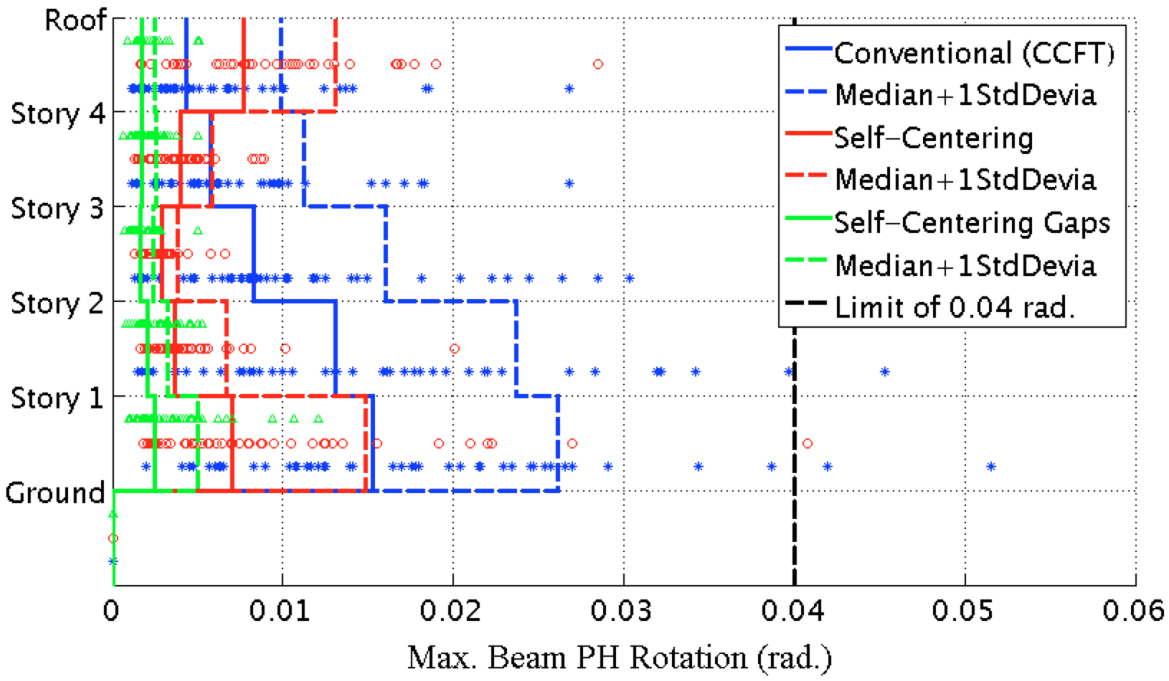

Appendix Figure L-41: Median of the maximum beam PH rotation under 44 DBE level ground motions with a GSR = 1.1 & damping = 5%

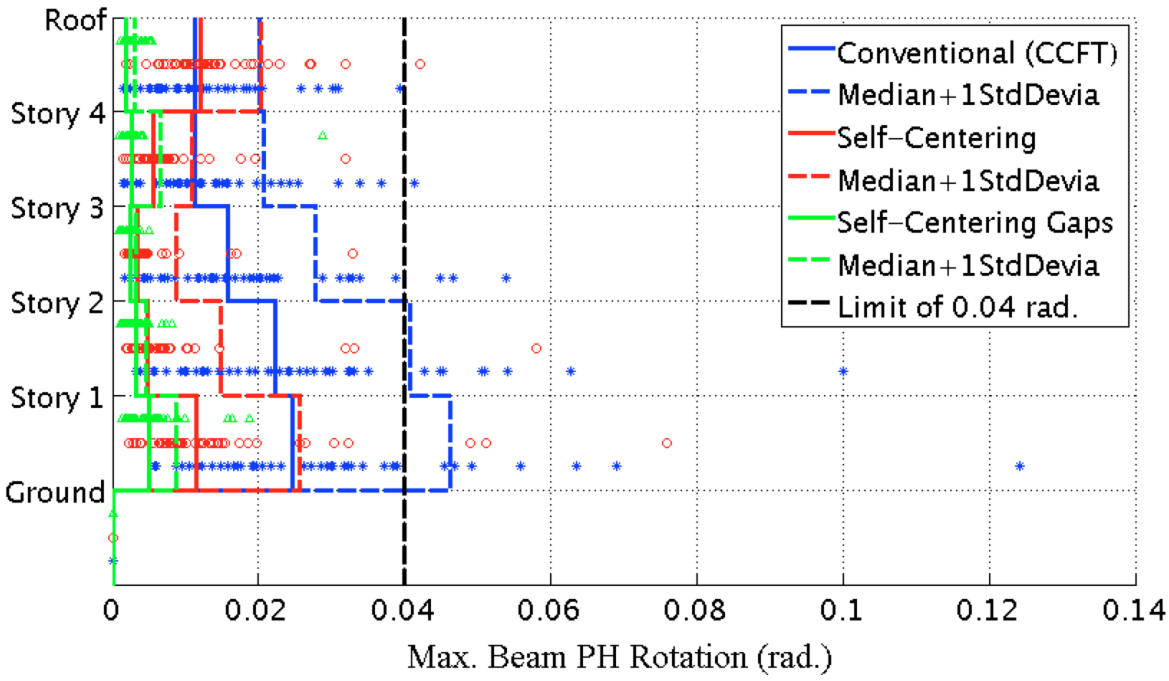

Appendix Figure L-42: Median of the maximum beam PH rotation under 44 MCE level ground motions with a GSR = 1.1 & damping = 5%

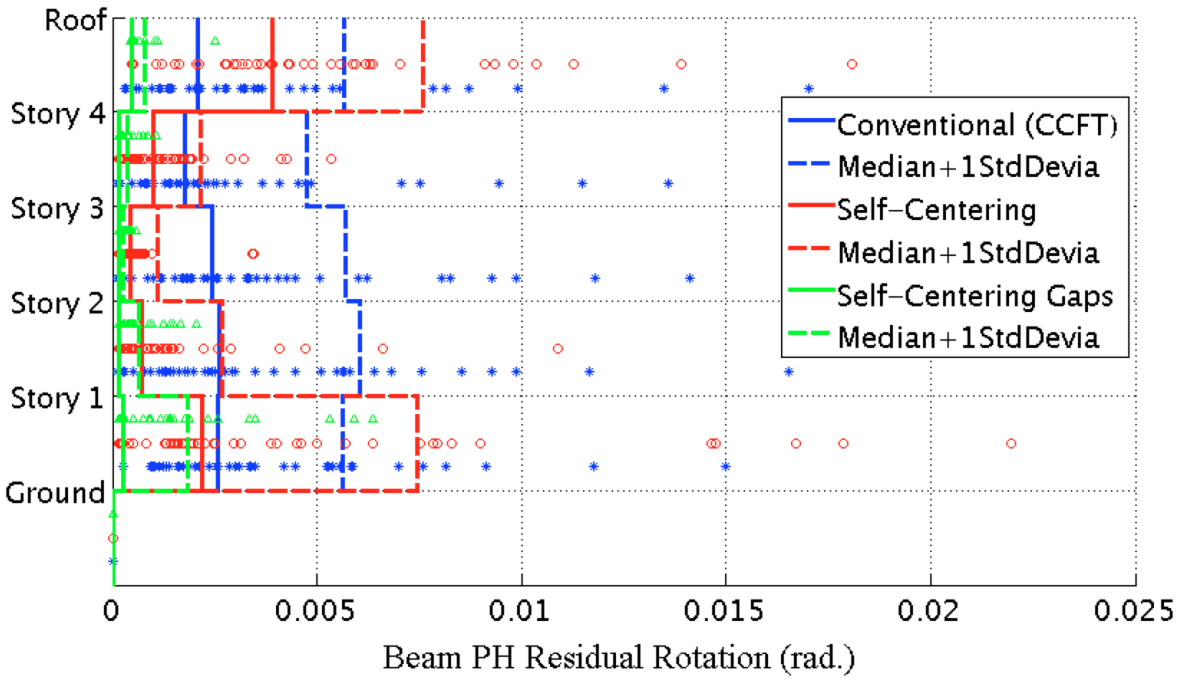

Appendix Figure L-43: Median of the maximum residual rotation of beam plastic hinges under 44 DBE level ground motions with a GSR = 1.1 & damping = 5%

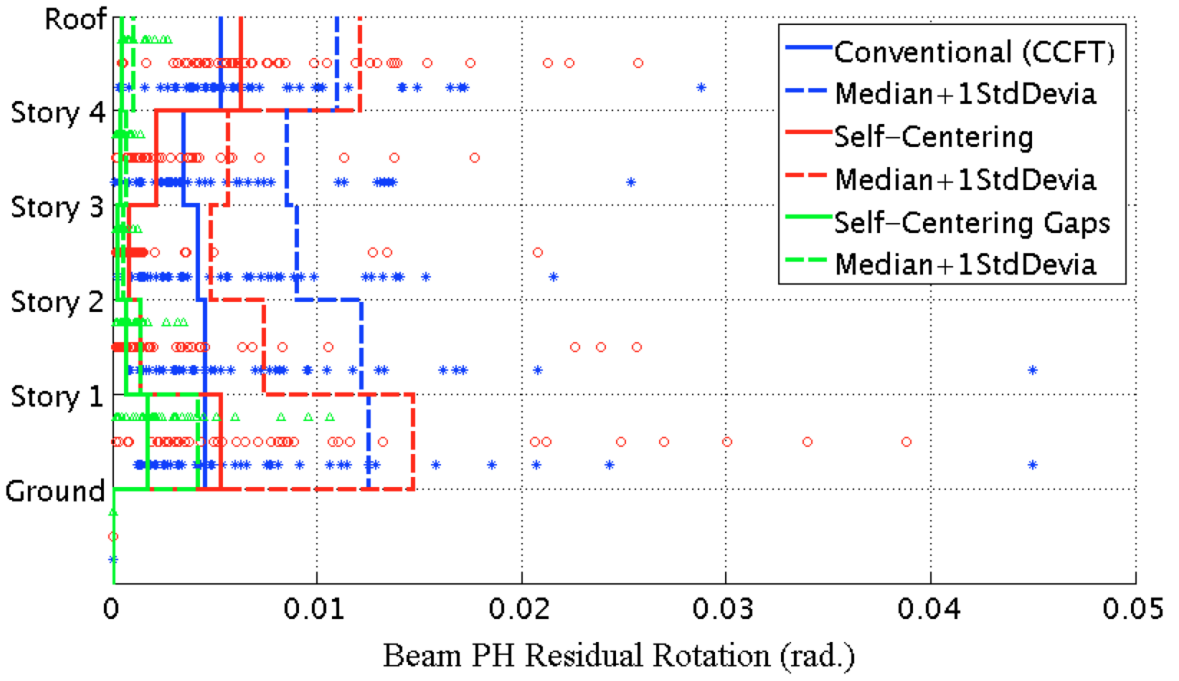

Appendix Figure L-44: Median of the maximum residual rotation of beam plastic hinges under 44 MCE level ground motions with a GSR = 1.1 & damping = 5%

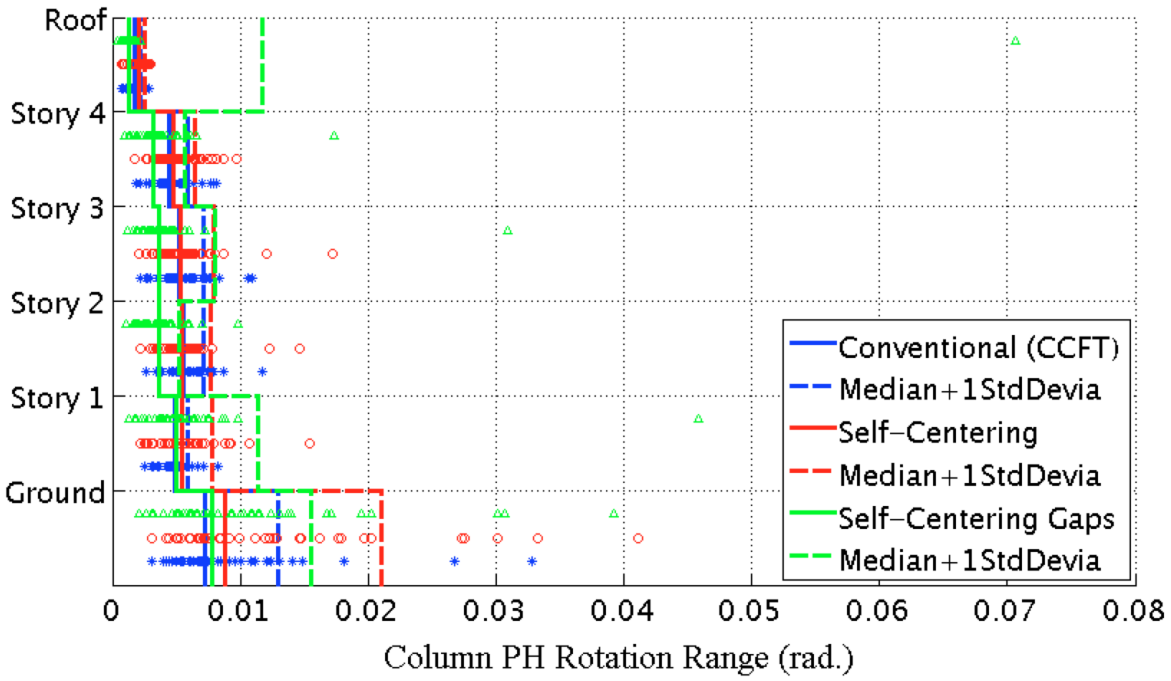

Appendix Figure L-45: Median of the column PH rotation range under 44 DBE level ground motions with a GSR = 1.1 & damping = 5%

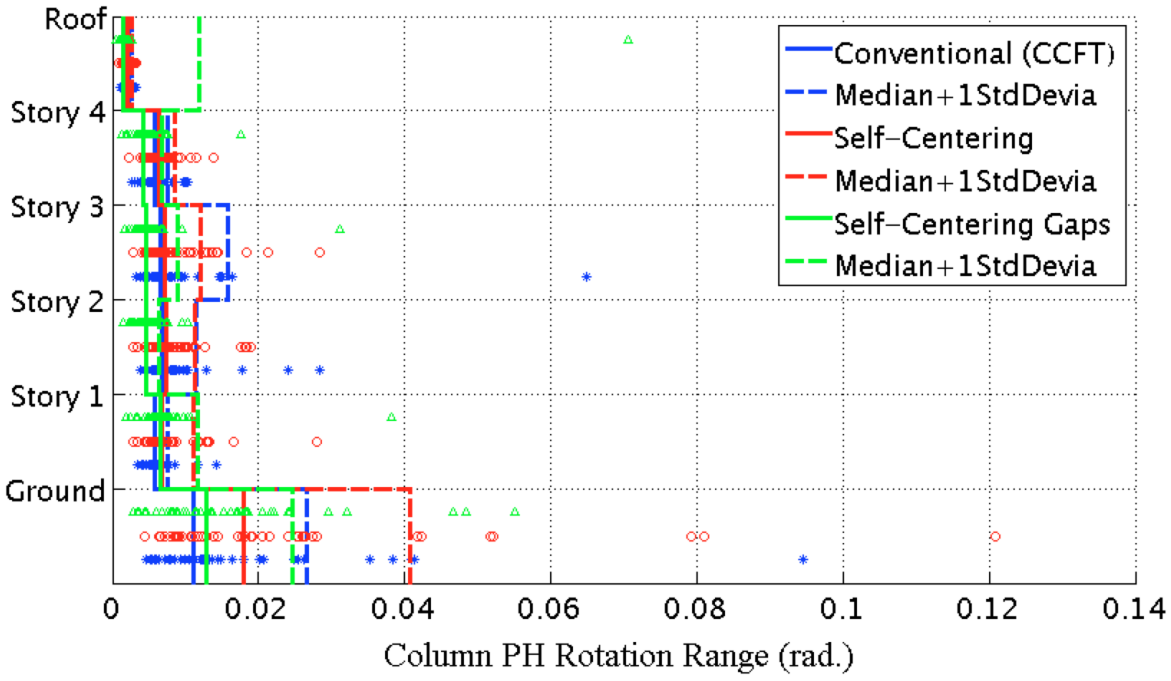

Appendix Figure L-46: Median of the column PH rotation range under 44 MCE level ground motions with a GSR = 1.1 & damping = 5%

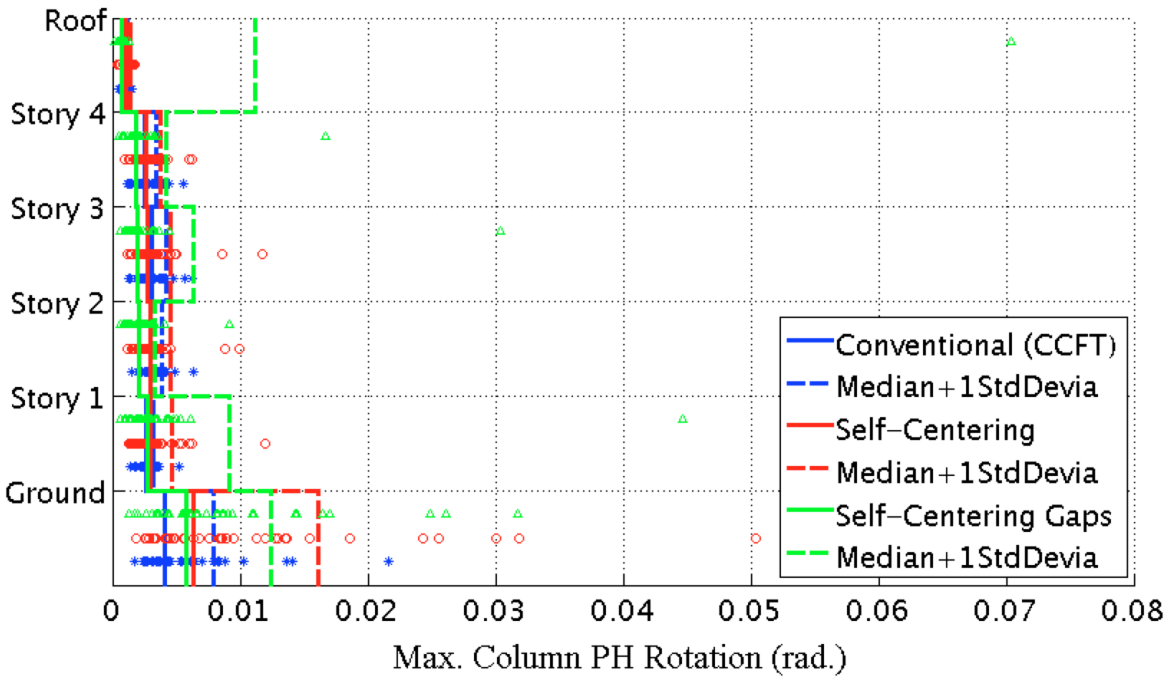

Appendix Figure L-47: Median of the maximum column PH rotation under 44 DBE level ground motions with a GSR = 1.1 & damping = 5%

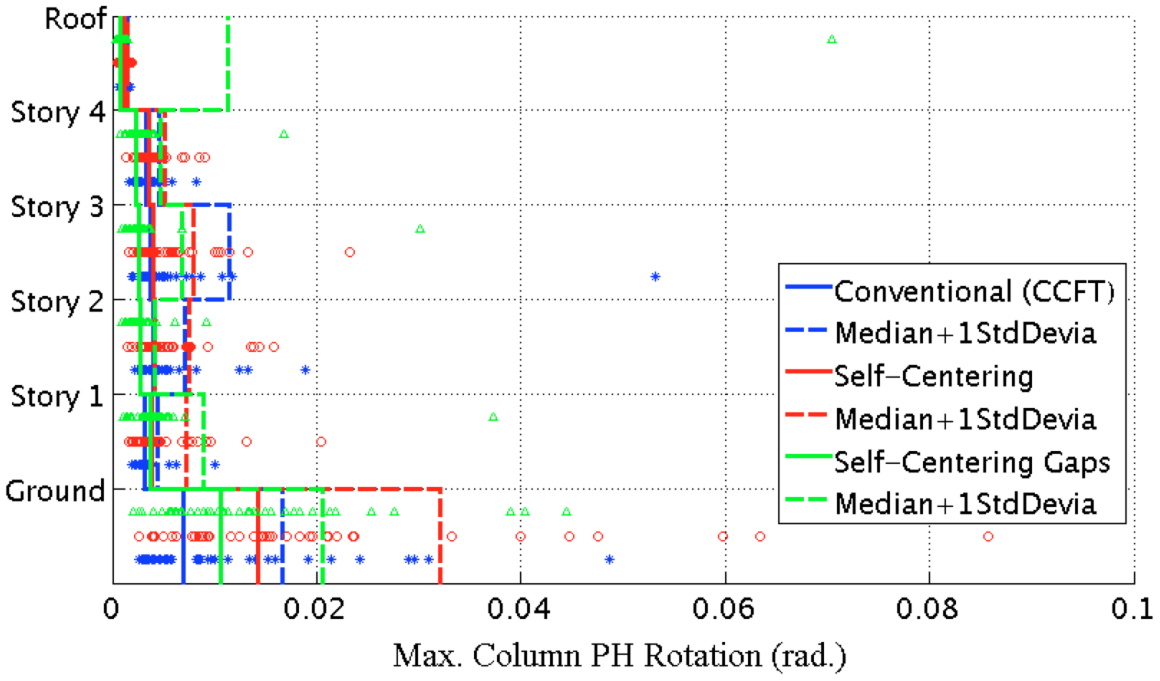

Appendix Figure L-48: Median of the maximum column PH rotation under 44 MCE level ground motions with a GSR = 1.1 & damping = 5%

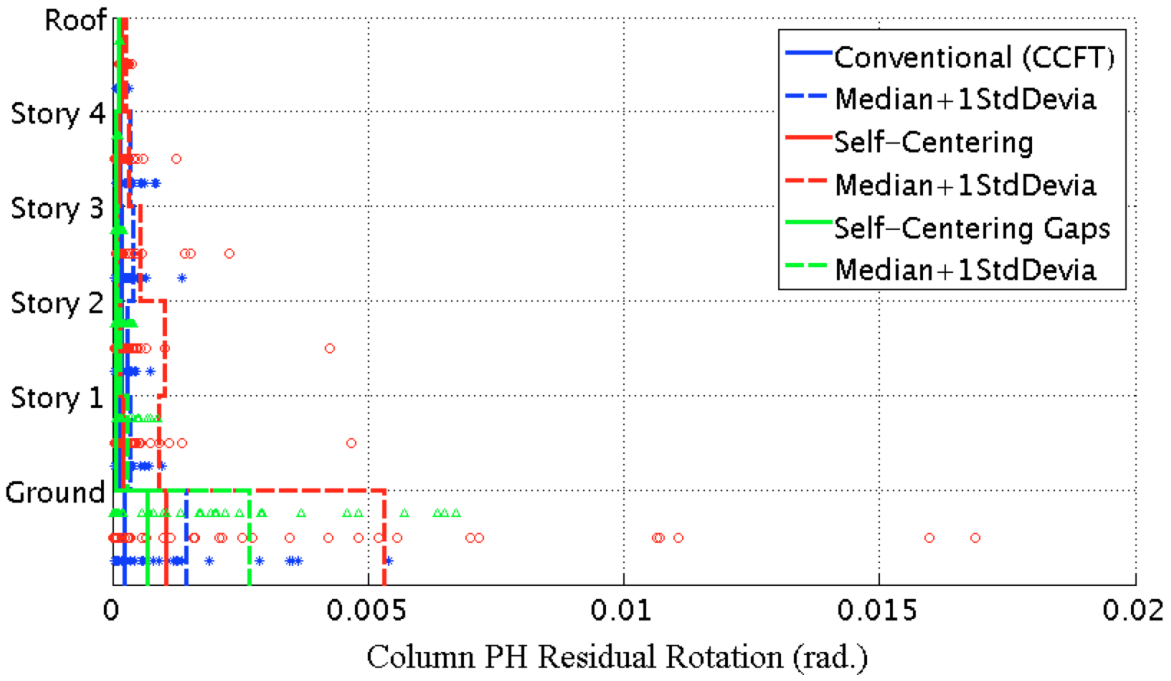

Appendix Figure L-49: Median of the maximum residual rotation of column plastic hinges under 44 DBE level ground motions with a GSR = 1.1 & damping = 5%

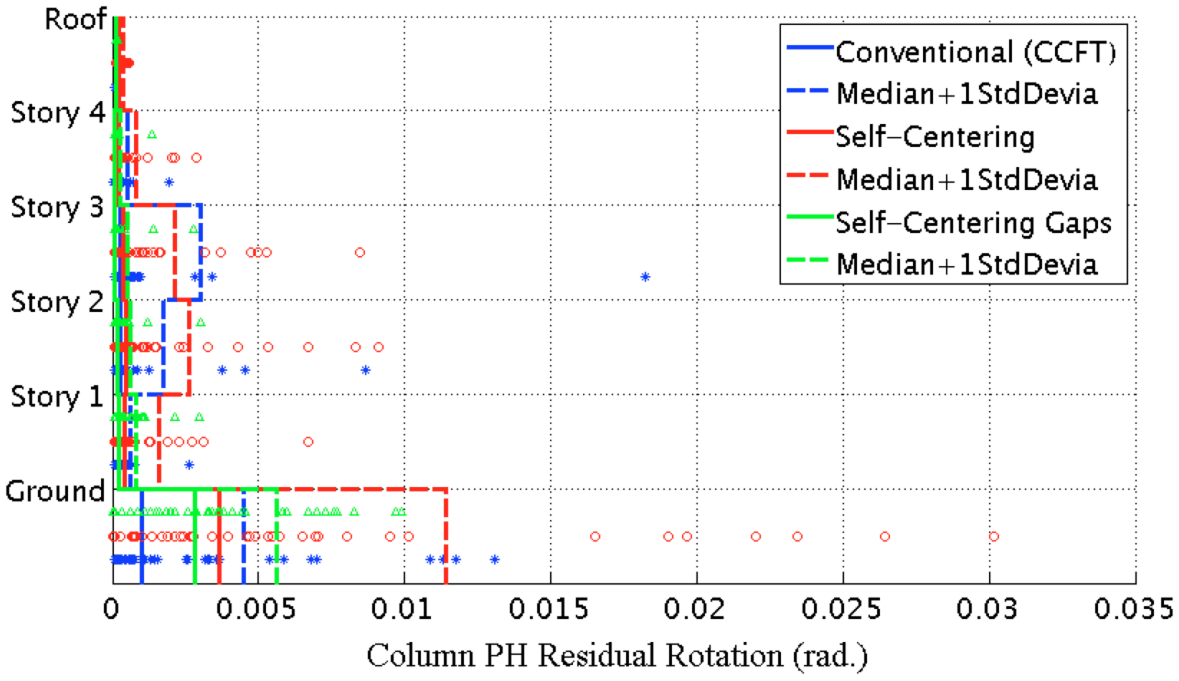

Appendix Figure L-50: Median of the maximum residual rotation of column plastic hinges under 44 MCE level ground motions with a GSR = 1.1 & damping = 5%

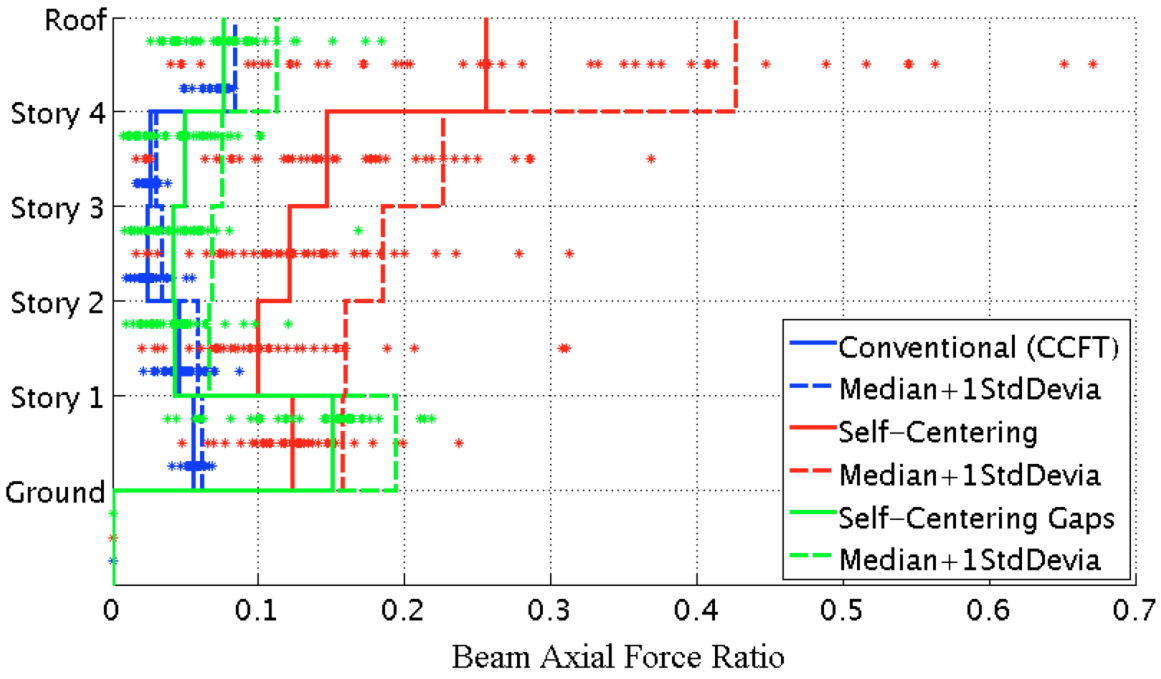

Appendix Figure L-51: Median of the peak axial force in beams under 44 DBE level ground motions with a GSR = 1.1 & damping = 5%

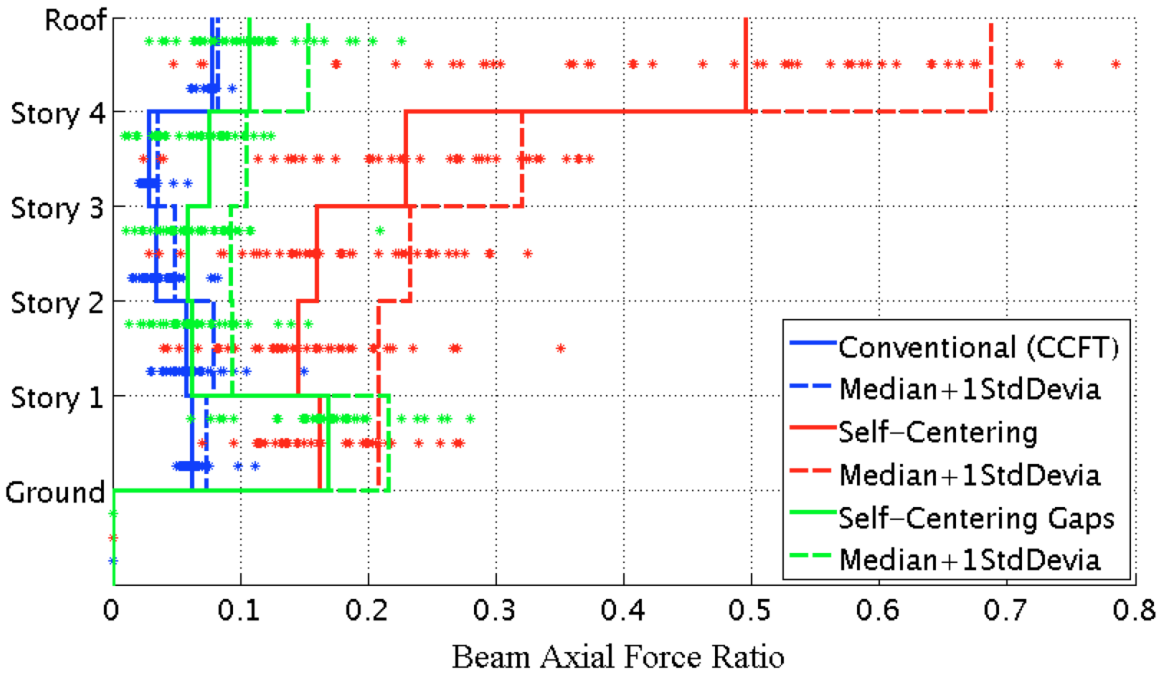

Appendix Figure L-52: Median of the peak axial force in beams under 44 MCE level ground motions with a GSR = 1.1 & damping = 5%

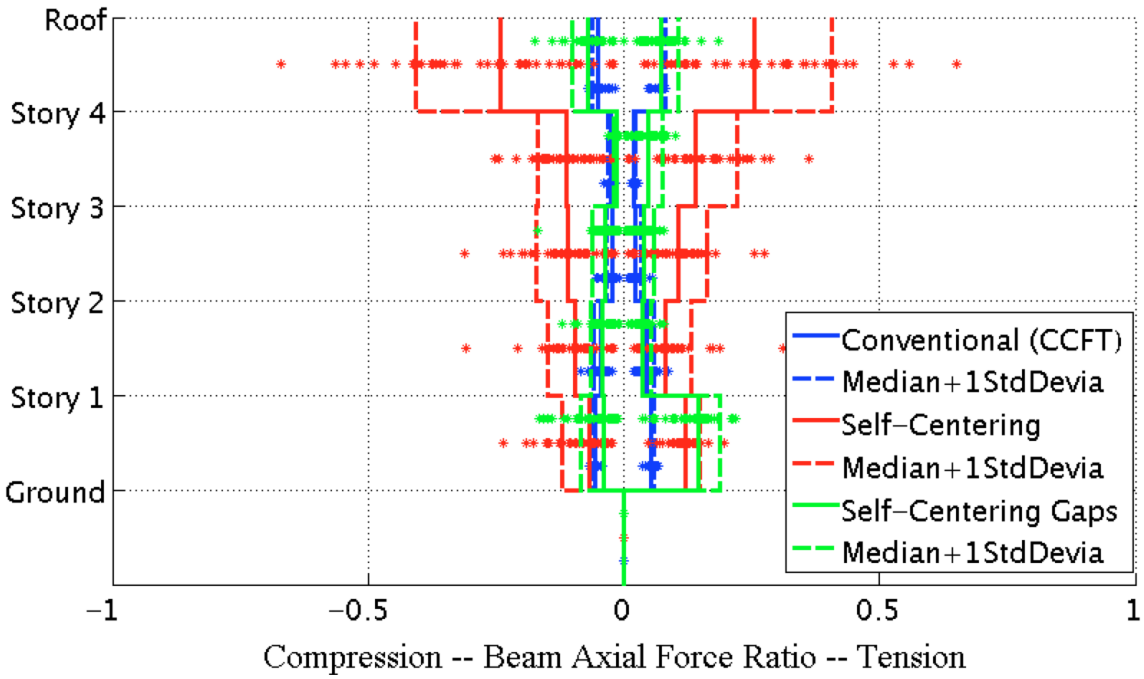

Appendix Figure L-53: Median of the peak tension vs.compression in beams under 44 DBE level ground motions with a GSR = 1.1 & damping = 5%

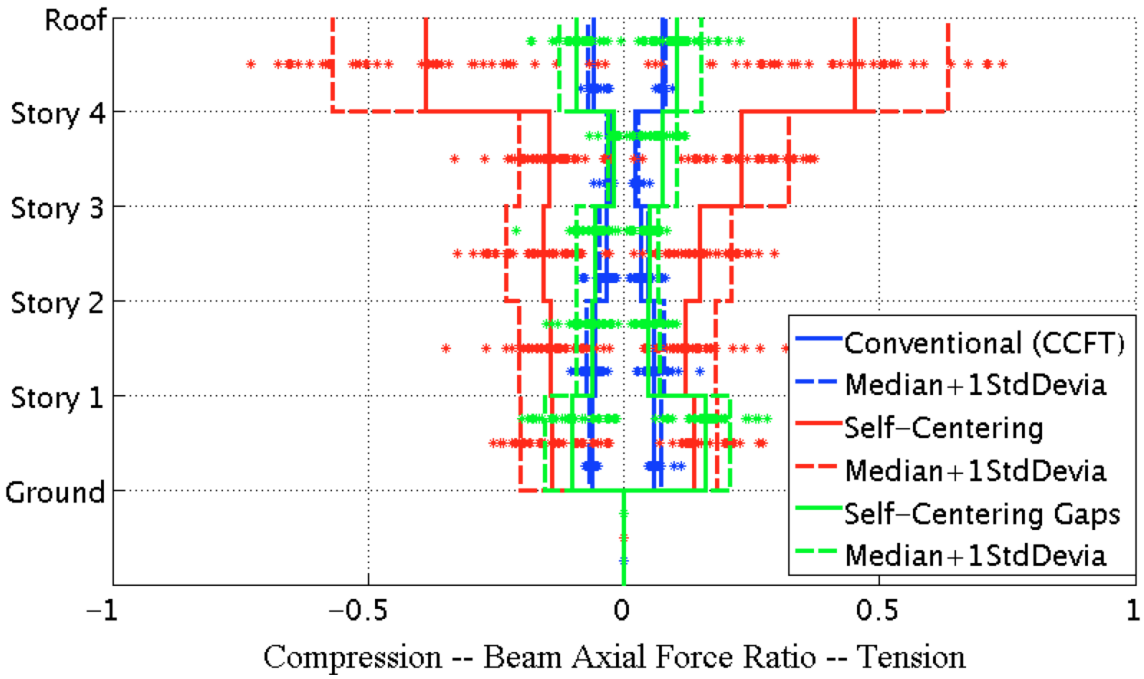

Appendix Figure L-54: Median of the peak tension vs.compression in beams under 44 MCE level ground motions with a GSR = 1.1 & damping = 5%

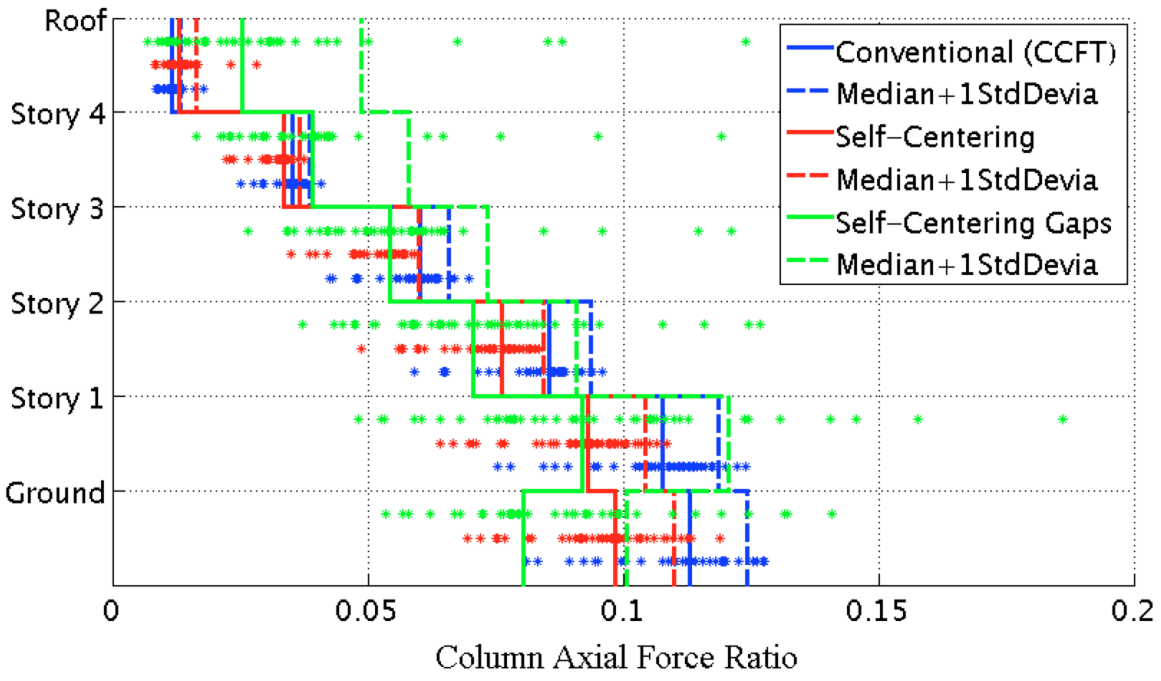

Appendix Figure L-55: Median of the peak axial force in columns under 44 DBE level ground motions with a GSR = 1.1 & damping = 5%

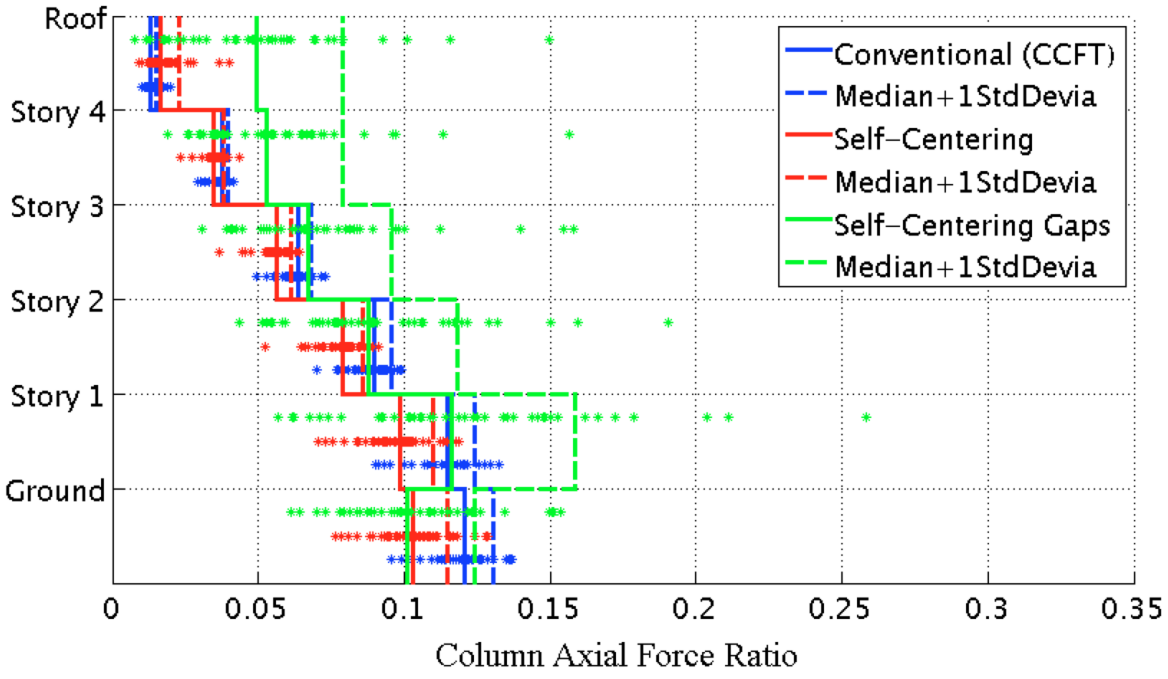

Appendix Figure L-56: Median of the peak axial force in columns under 44 MCE level ground motions with a GSR = 1.1 & damping = 5%

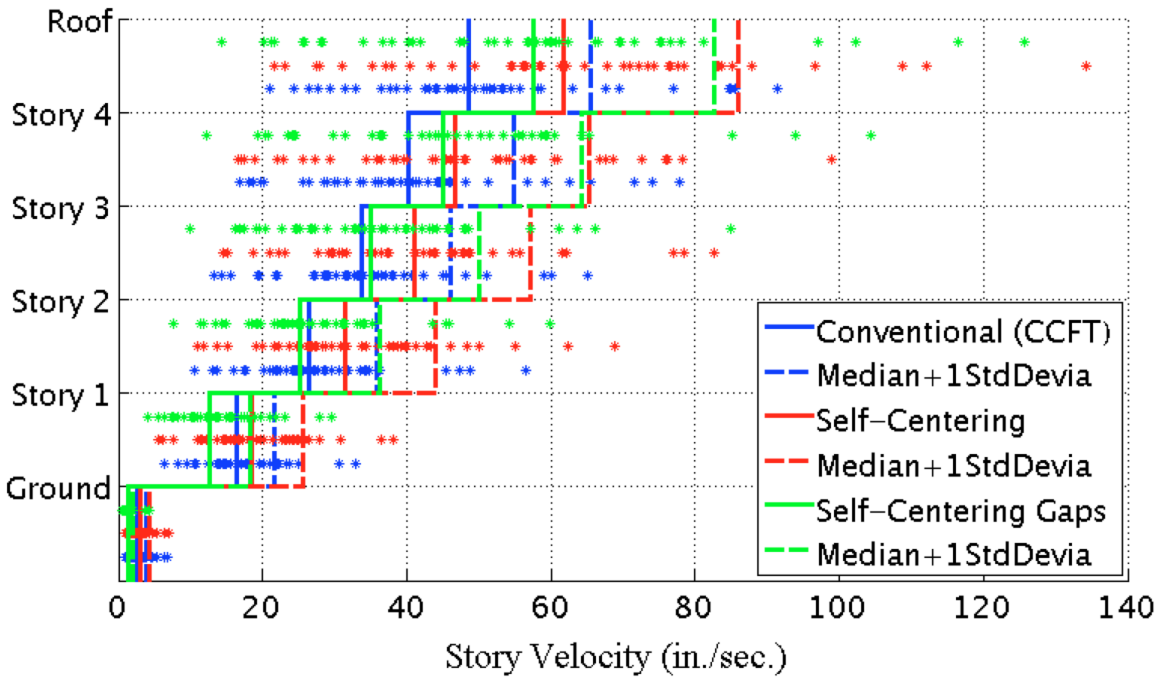

Appendix Figure L-57: Median of the peak story velocity under 44 DBE level ground motions with a GSR = 1.1 & damping = 5%

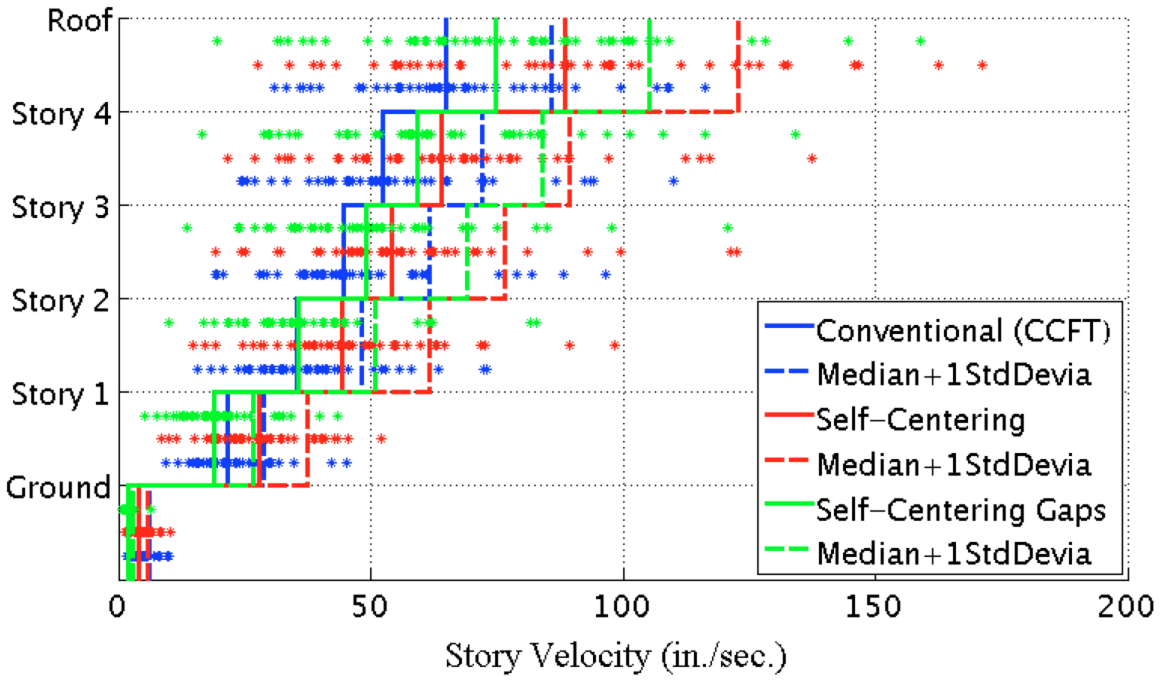

Appendix Figure L-58: Median of the peak story velocity under 44 MCE level ground motions with a GSR = 1.1 & damping = 5%

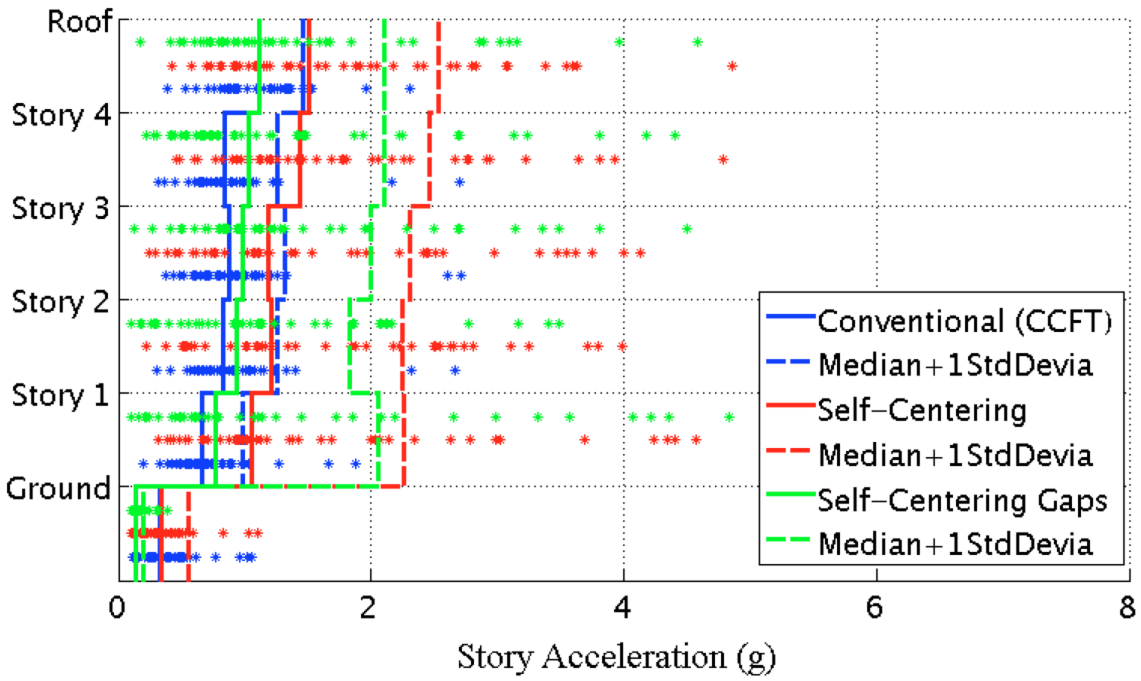

Appendix Figure L-59: Median of the peak story acceleration under 44 DBE level ground motions with a GSR = 1.1 & damping = 5%

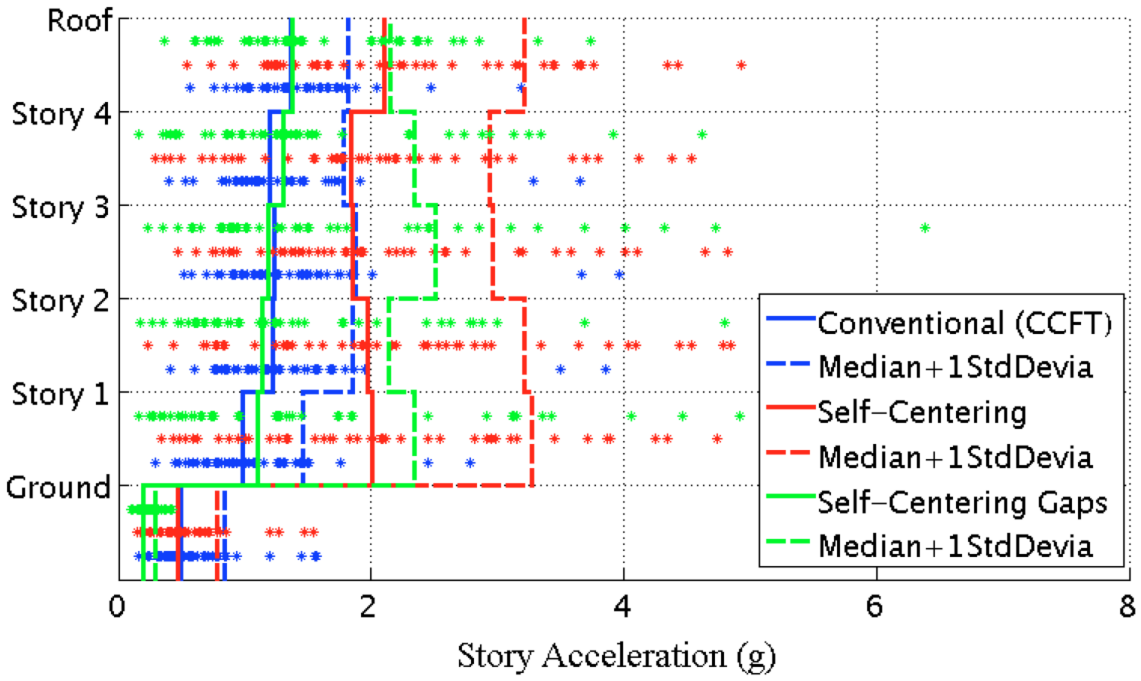

Appendix Figure L-60: Median of the peak story acceleration under 44 MCE level ground motions with a GSR = 1.1 & damping = 5%

L.3 Systems with a GSR = 1.0 & Damping = 10%

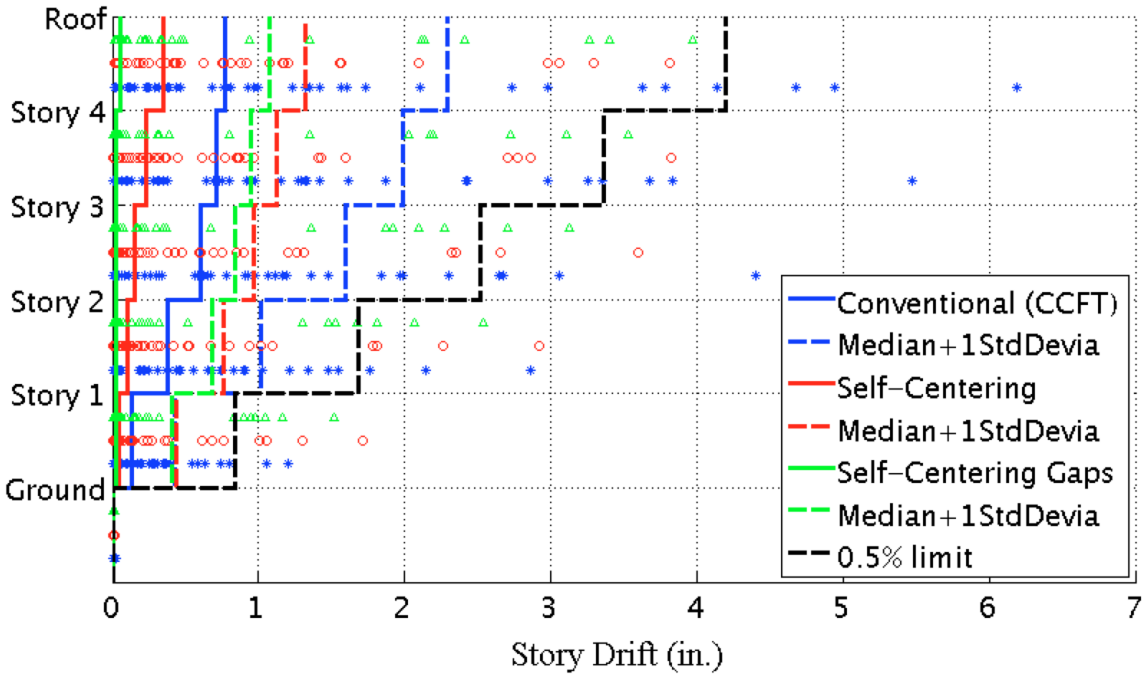

Appendix Figure L-61: Median of the maximum story residual drift under 44 DBE level ground motions with a GSR = 1.0 & damping = 10%

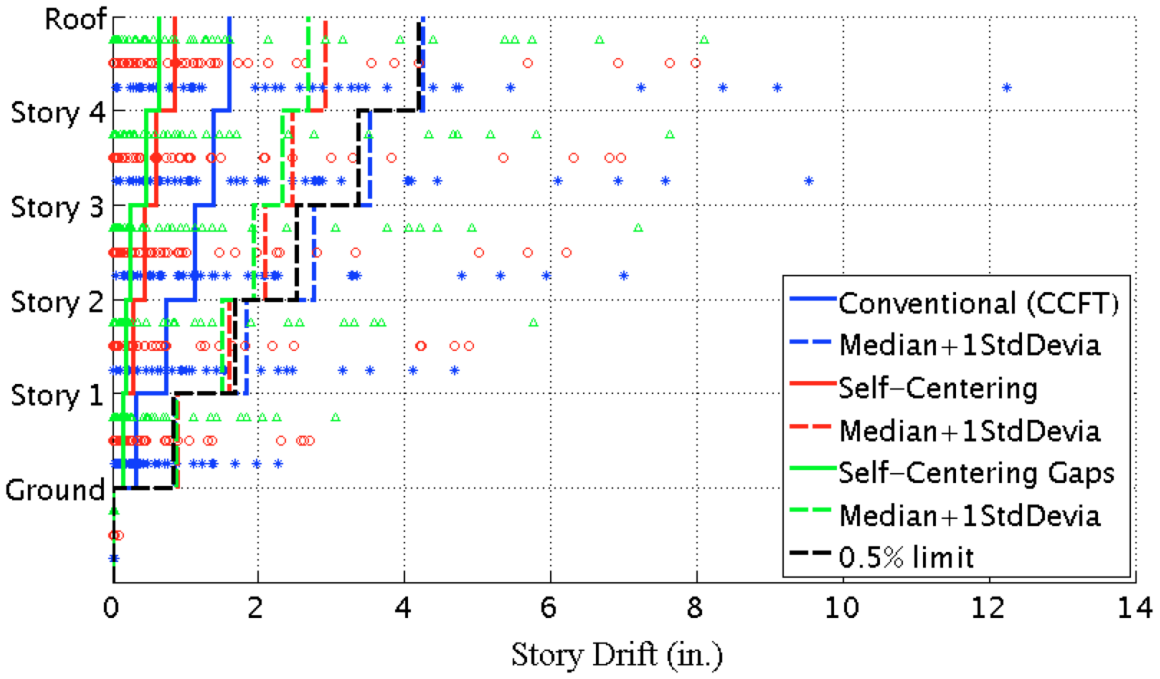

Appendix Figure L-62: Median of the maximum story residual drift under 44 MCE level ground motions with a GSR = 1.0 & damping = 10%

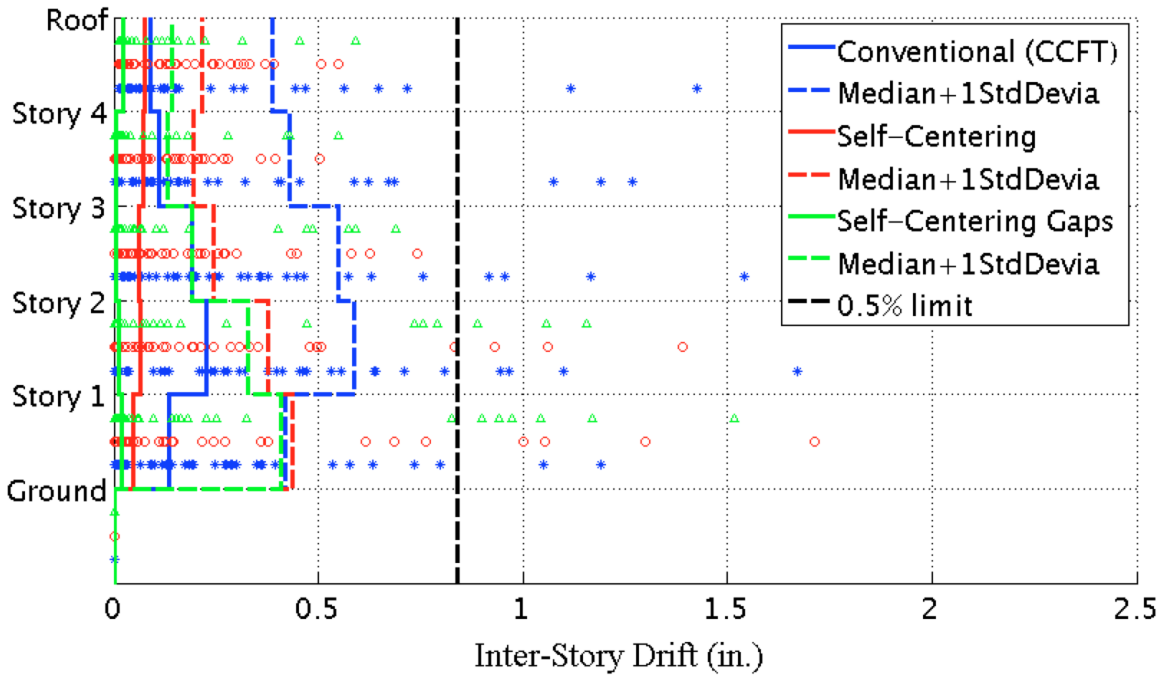

Appendix Figure L-63: Median of the maximum inter-story residual drift under 44 DBE level ground motions with a GSR = 1.0 & damping = 10%

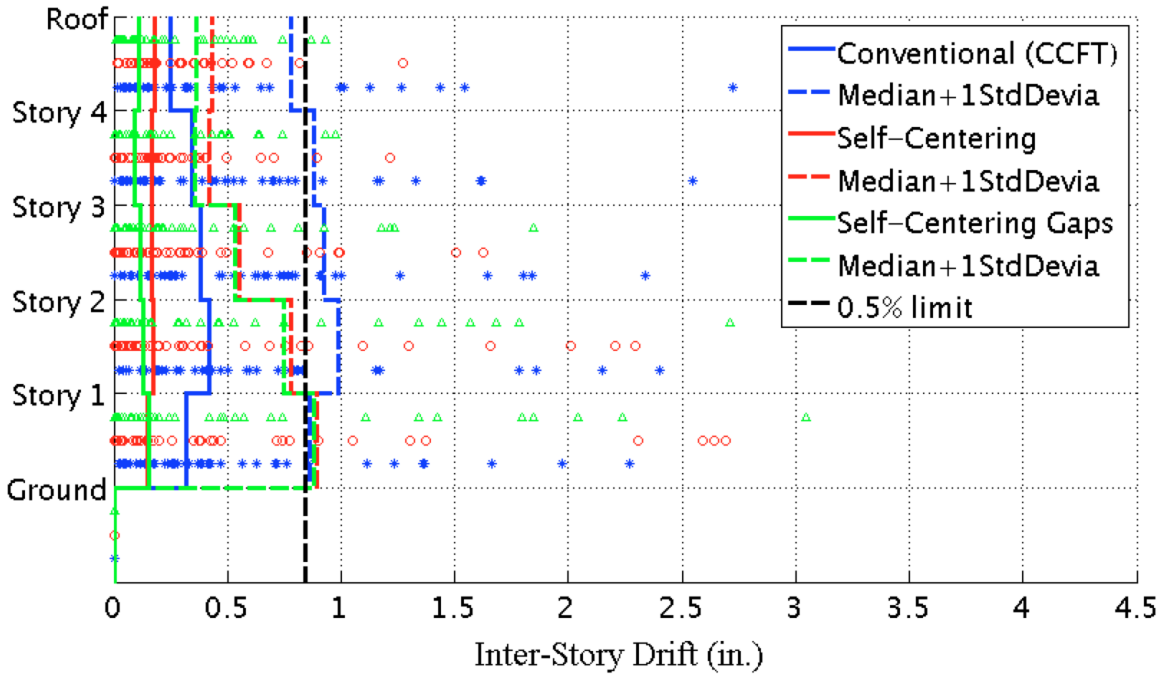

Appendix Figure L-64: Median of the maximum inter-story residual drift under 44 MCE level ground motions with a GSR = 1.0 & damping = 10%

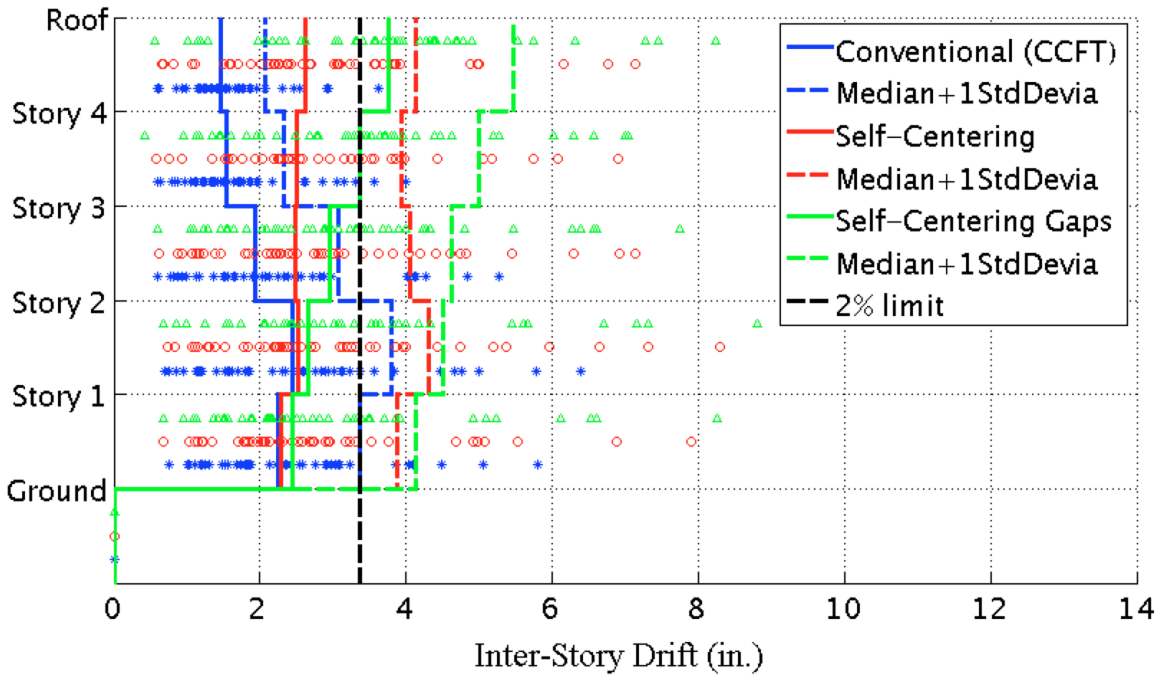

Appendix Figure L-65: Median of the peak inter-story drift under 44 DBE level ground motions with a GSR = 1.0 & damping = 10%

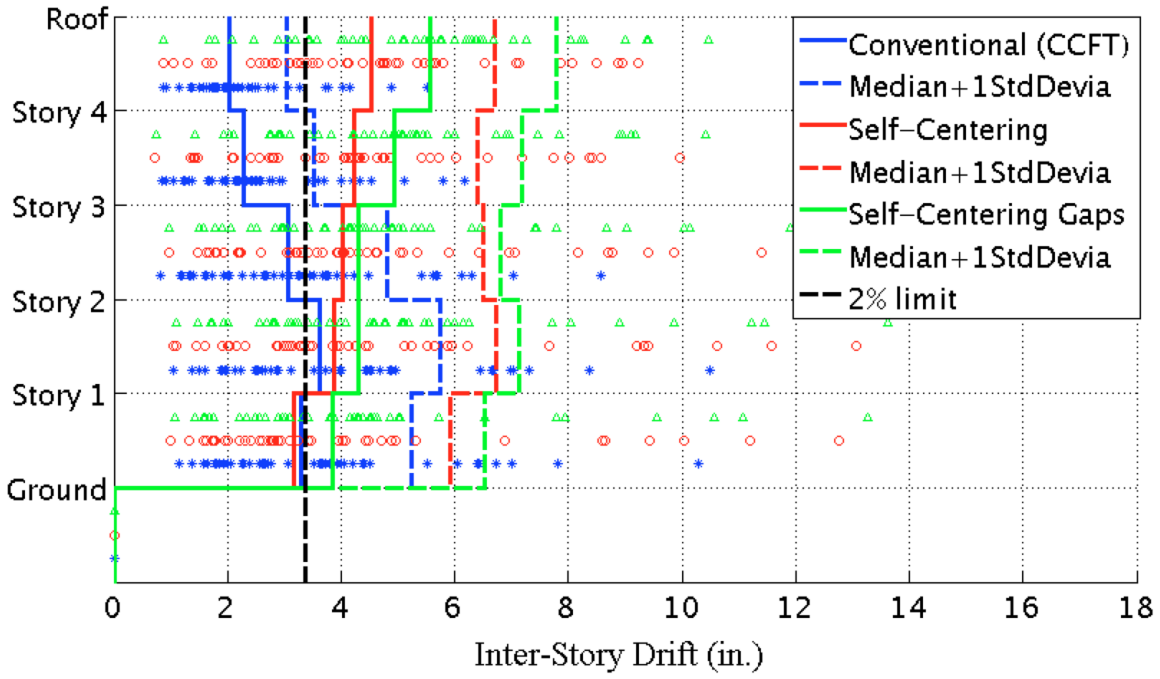

Appendix Figure L-66: Median of the peak inter-story drift under 44 MCE level ground motions with a GSR = 1.0 & damping = 10%

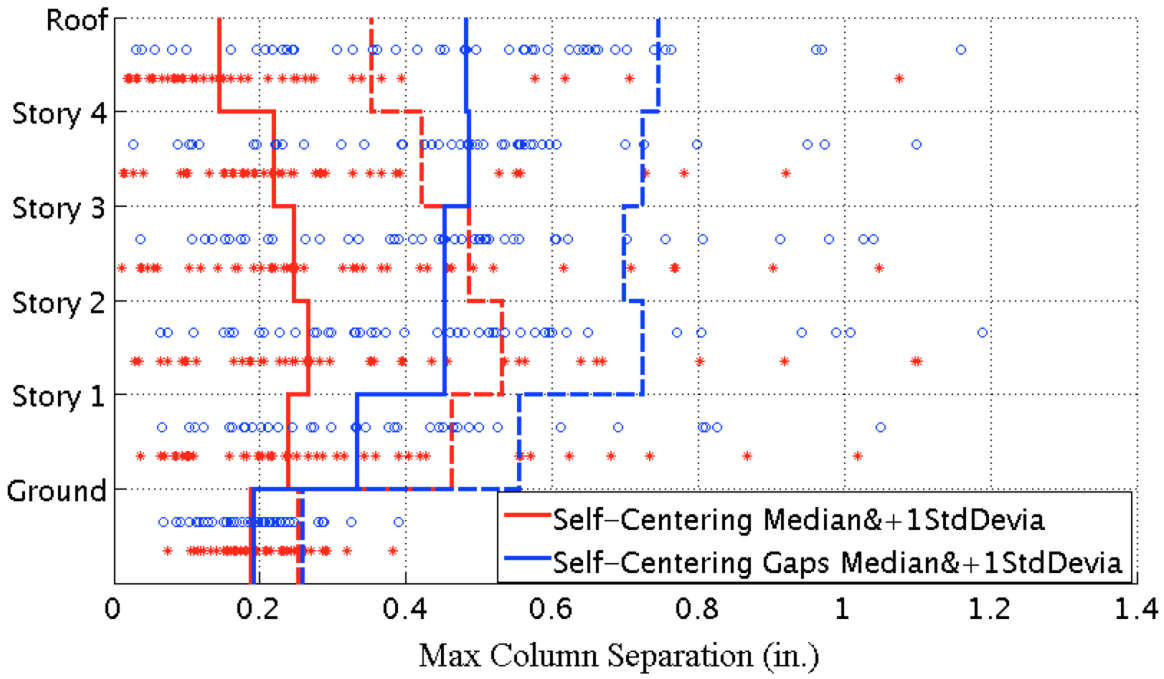

Appendix Figure L-67: Median of the maximum column separation under 44 DBE level ground motions with a GSR = 1.0 & damping = 10%

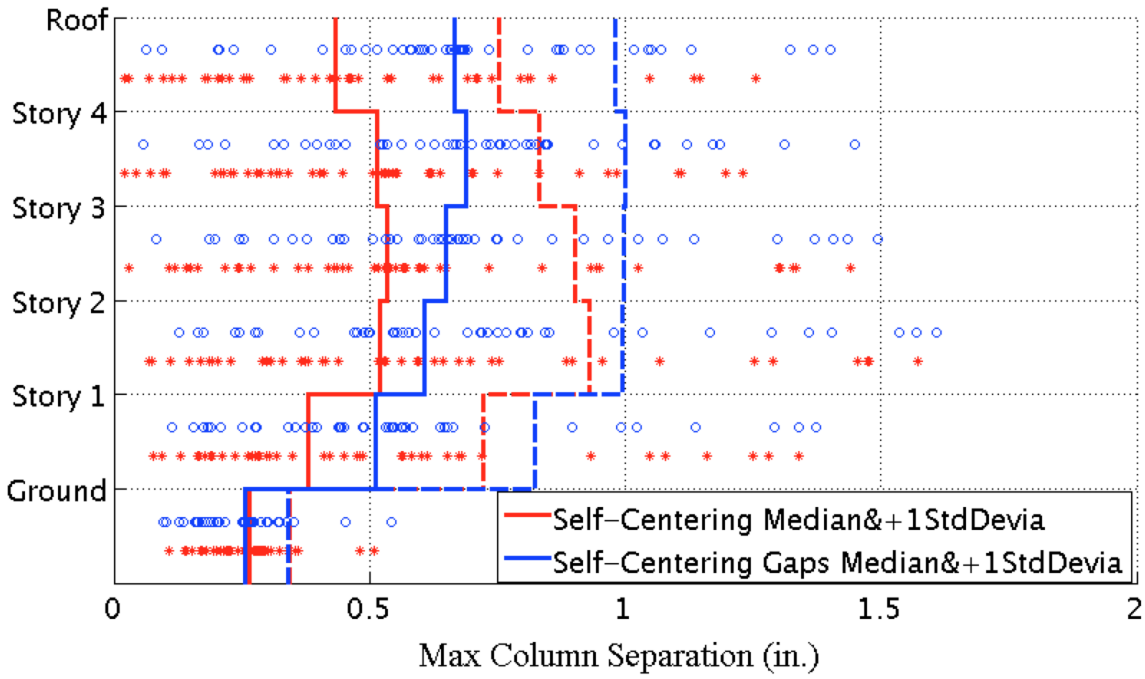

Appendix Figure L-68: Median of the maximum column separation under 44 MCE level ground motions with a GSR = 1.0 & damping = 10%

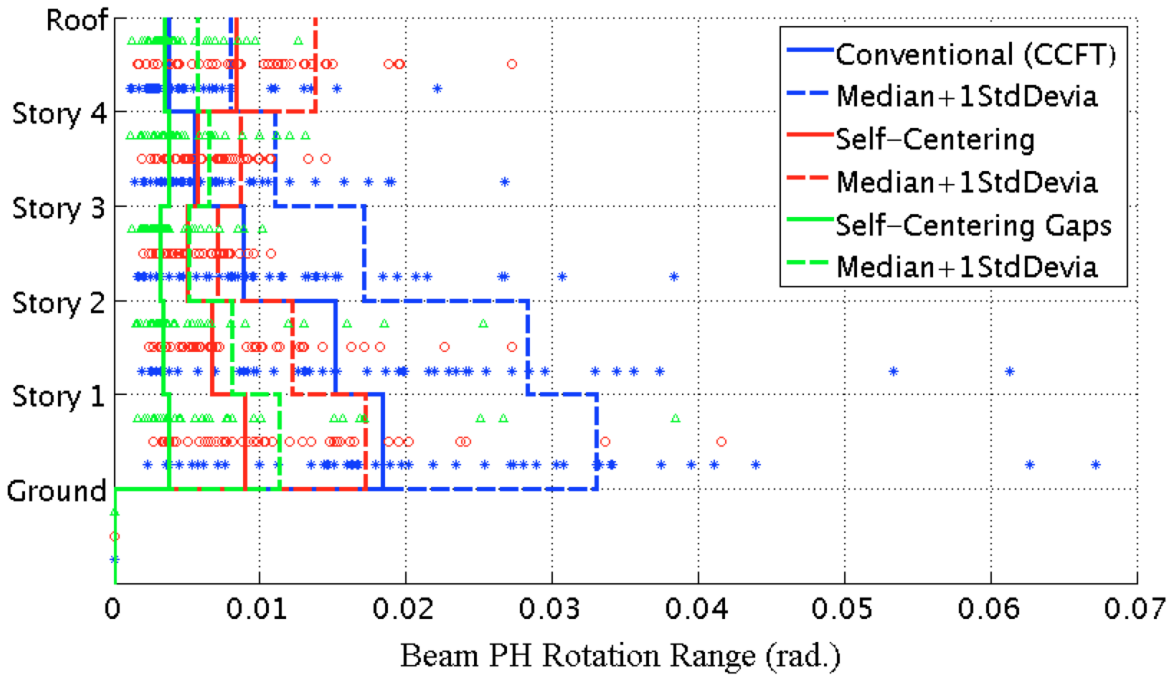

Appendix Figure L-69: Median of the beam PH rotation range under 44 DBE level ground motions with a GSR = 1.0 & damping = 10%

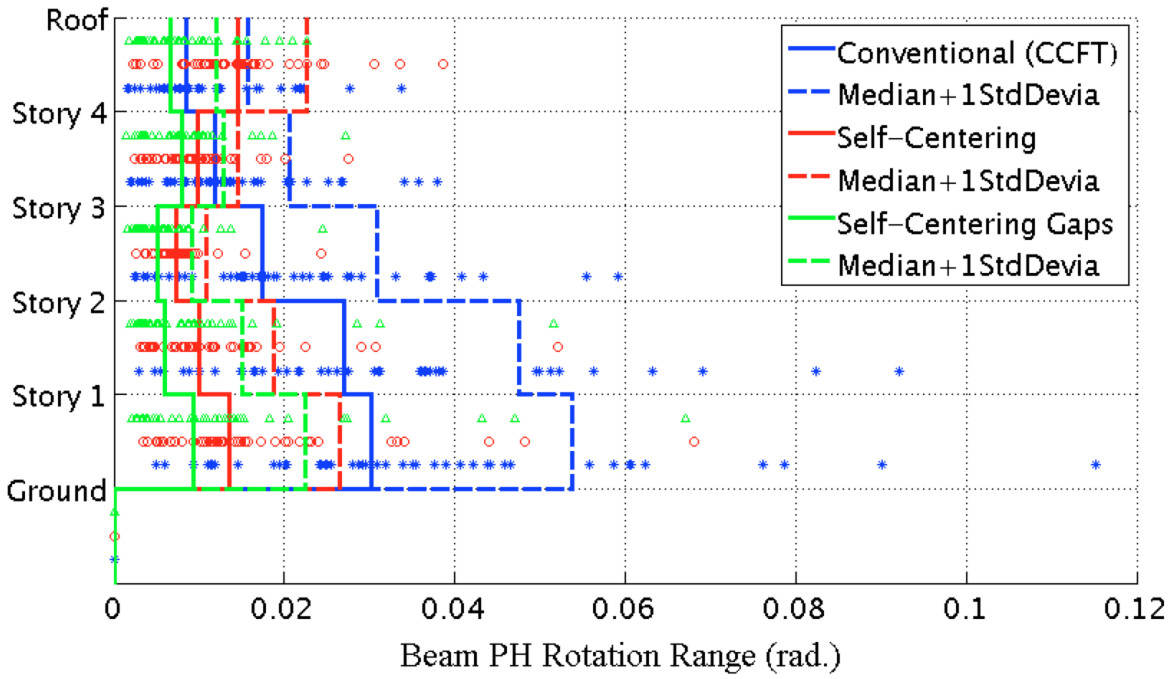

Appendix Figure L-70: Median of the beam PH rotation range under 44 MCE level ground motions with a GSR = 1.0 & damping = 10%

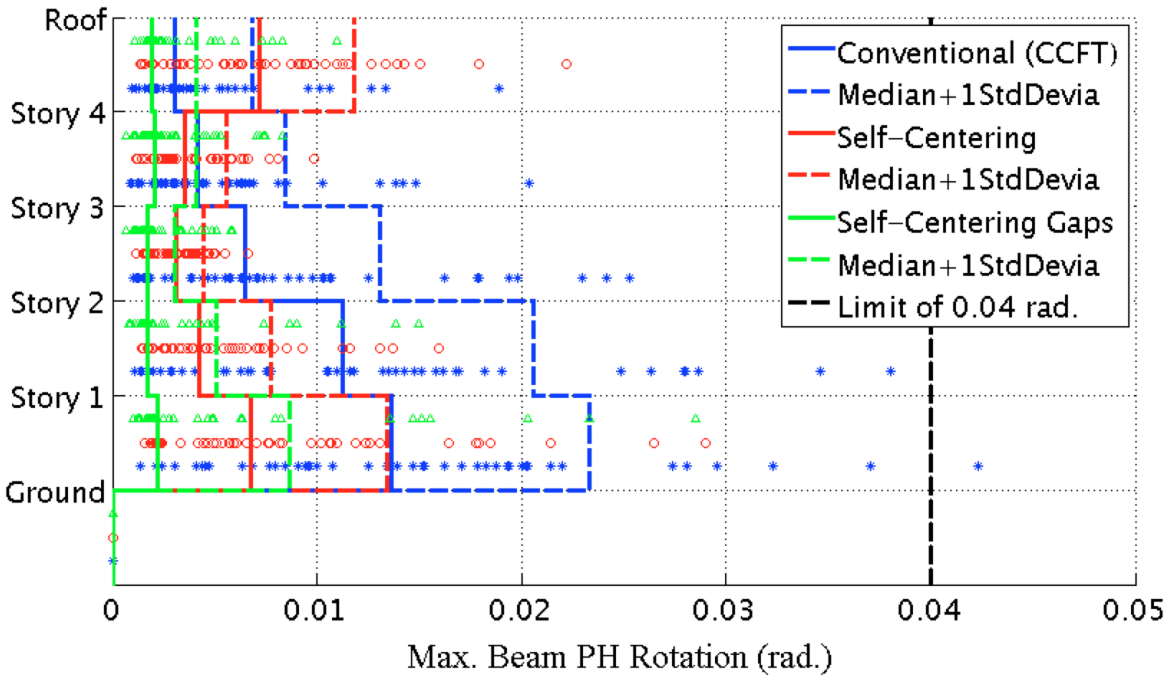

Appendix Figure L-71: Median of the maximum beam PH rotation under 44 DBE level ground motions with a GSR = 1.0 & damping = 10%

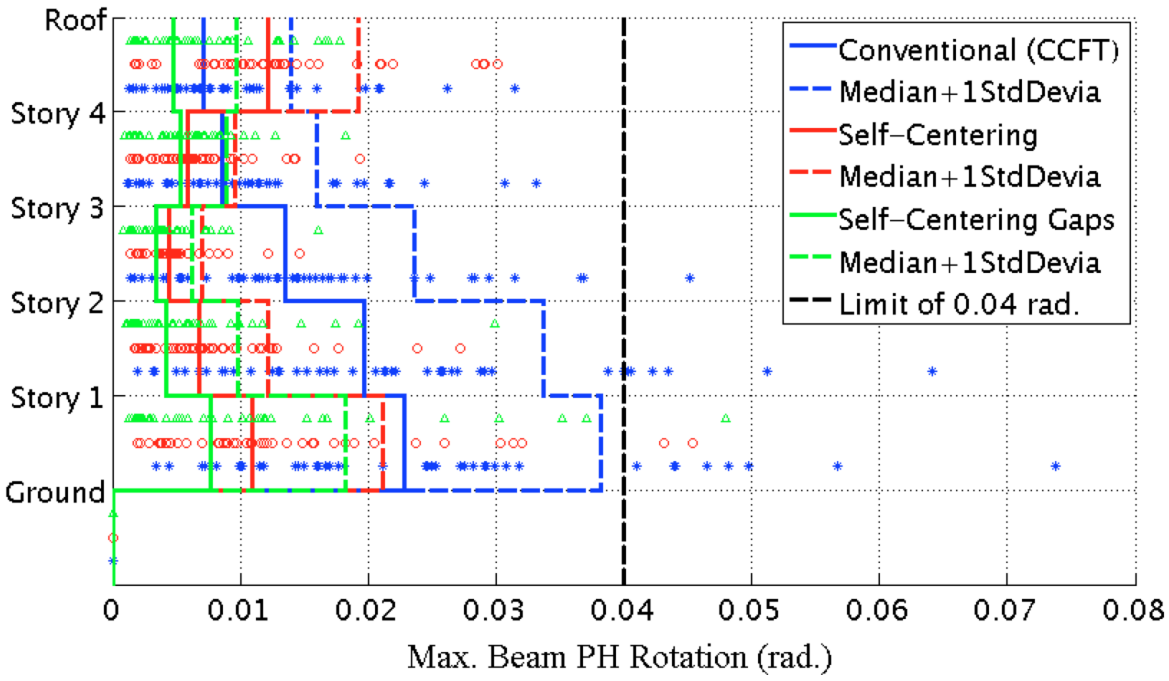

Appendix Figure L-72: Median of the maximum beam PH rotation under 44 MCE level ground motions with a GSR = 1.0 & damping = 10%

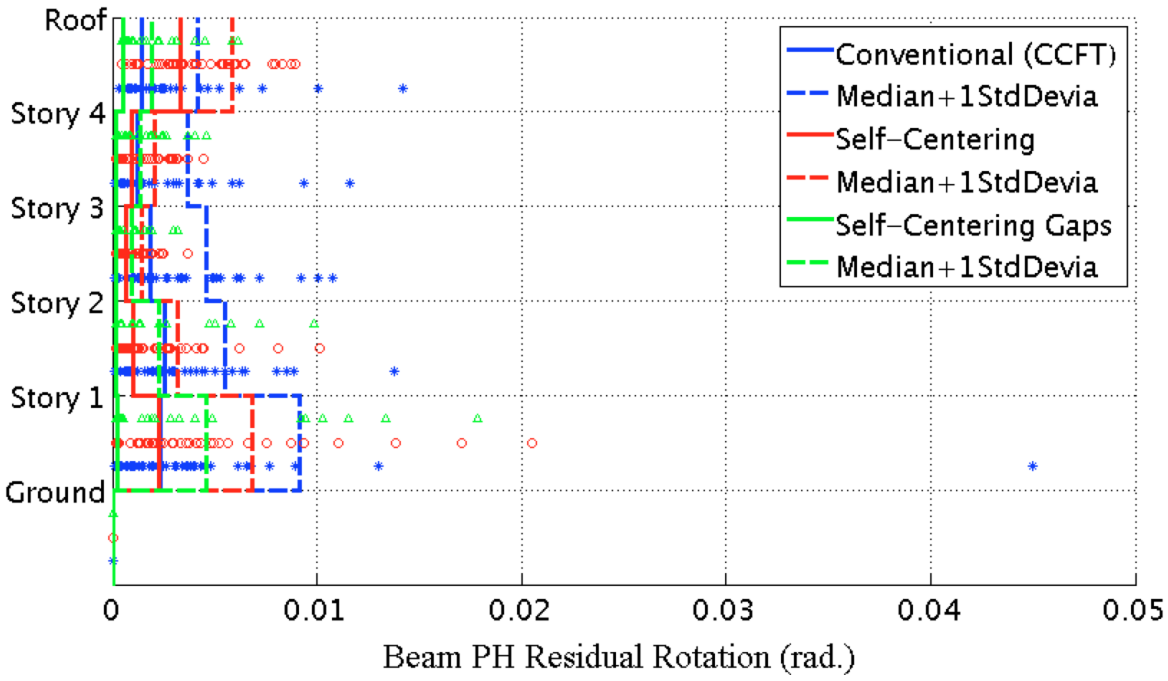

Appendix Figure L-73: Median of the maximum residual rotation of beam plastic hinges under 44 DBE level ground motions with a GSR = 1.0 & damping = 10%

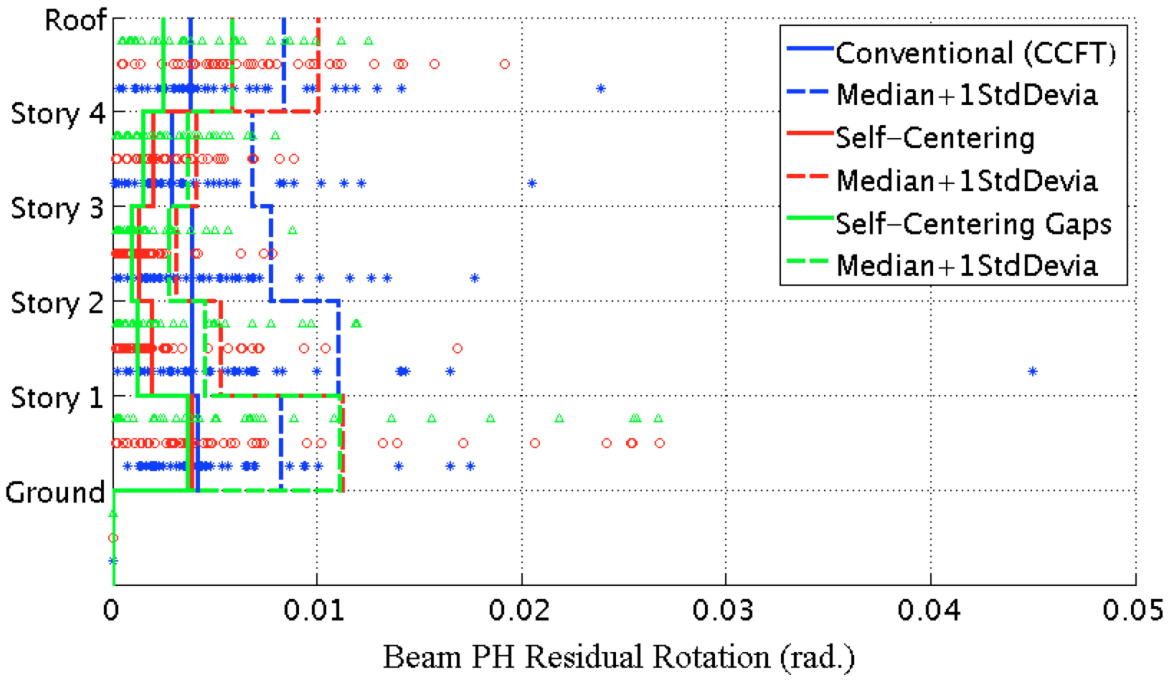

Appendix Figure L-74: Median of the maximum residual rotation of beam plastic hinges under 44 MCE level ground motions with a GSR = 1.0 & damping = 10%

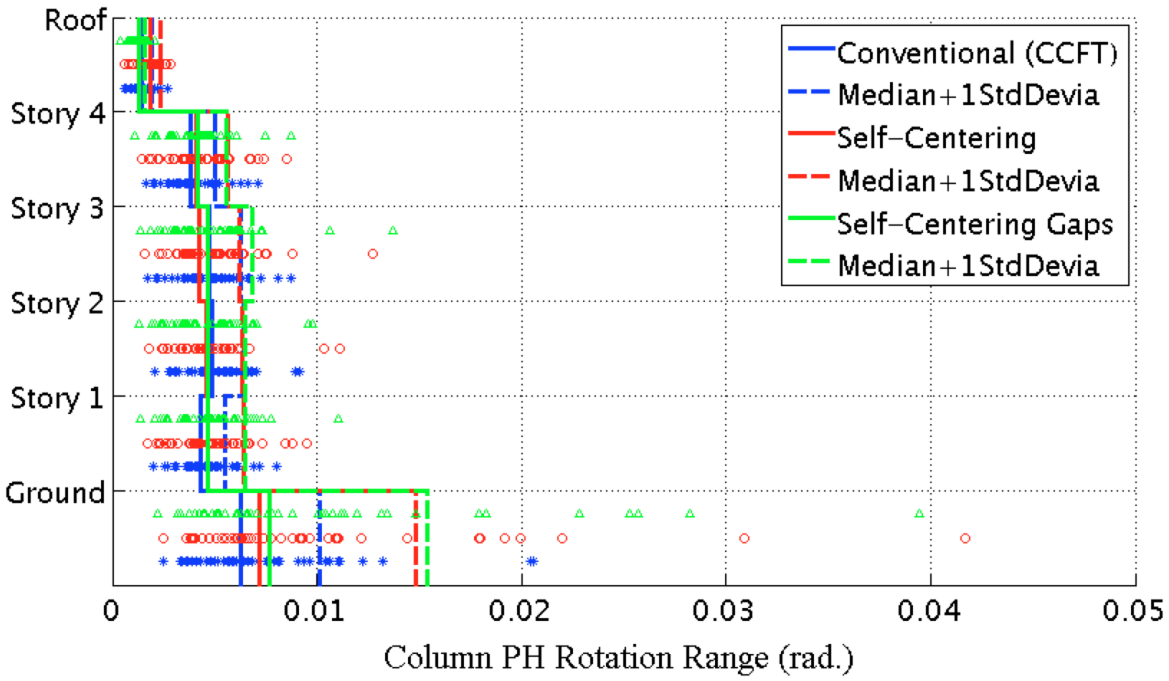

Appendix Figure L-75: Median of the column PH rotation range under 44 DBE level ground motions with a GSR = 1.0 & damping = 10%

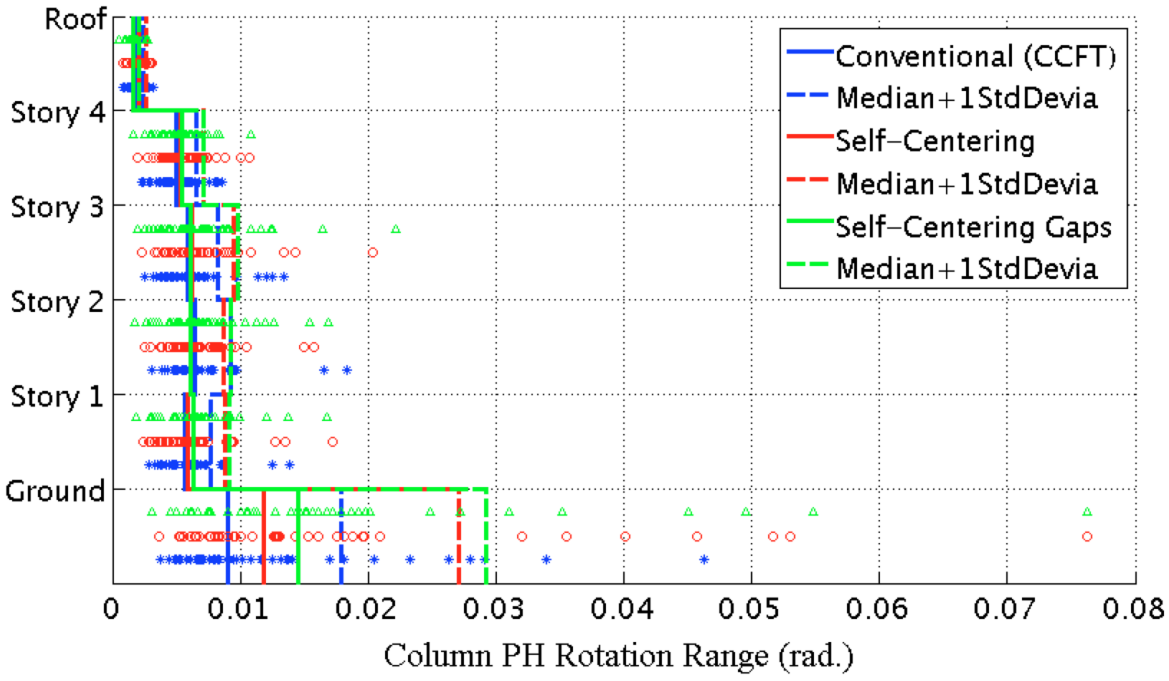

Appendix Figure L-76: Median of the column PH rotation range under 44 MCE level ground motions with a GSR = 1.0 & damping = 10%

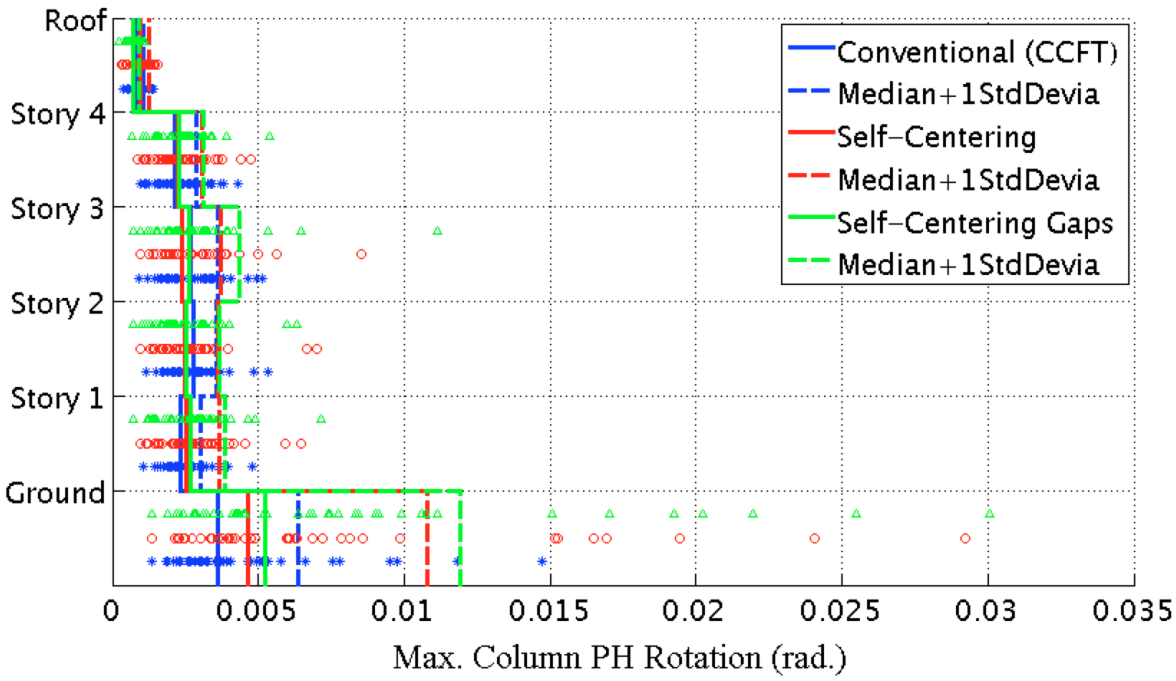

Appendix Figure L-77: Median of the maximum column PH rotation under 44 DBE level ground motions with a GSR = 1.0 & damping = 10%

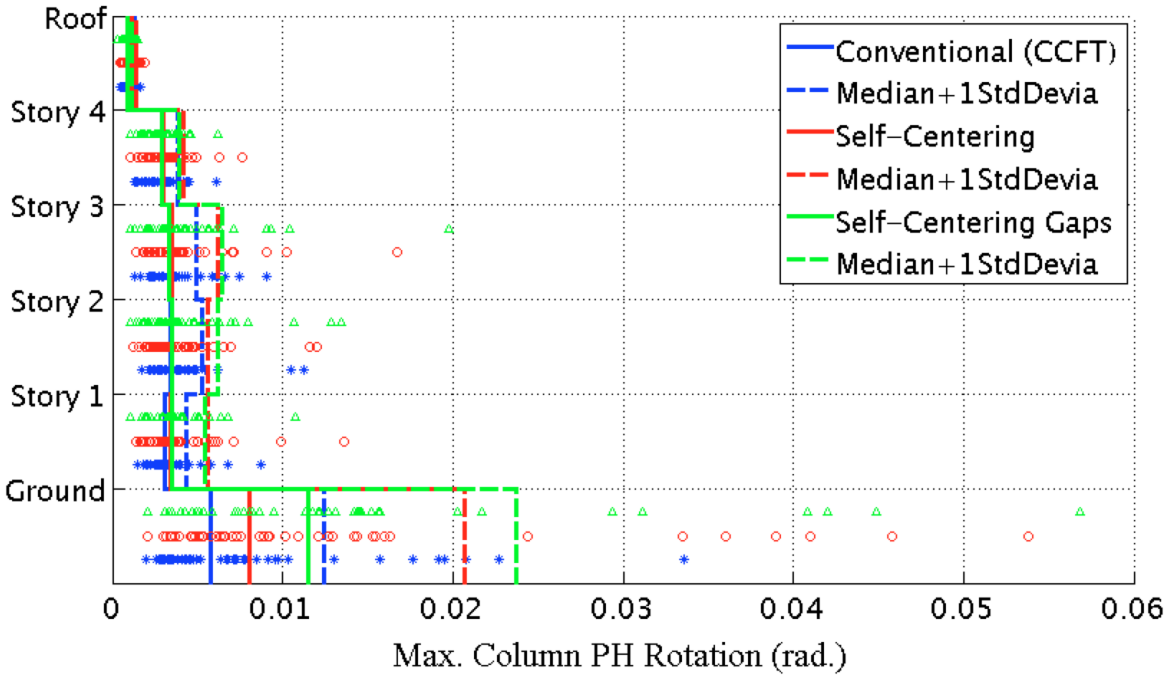

Appendix Figure L-78: Median of the maximum column PH rotation under 44 MCE level ground motions with a GSR = 1.0 & damping = 10%

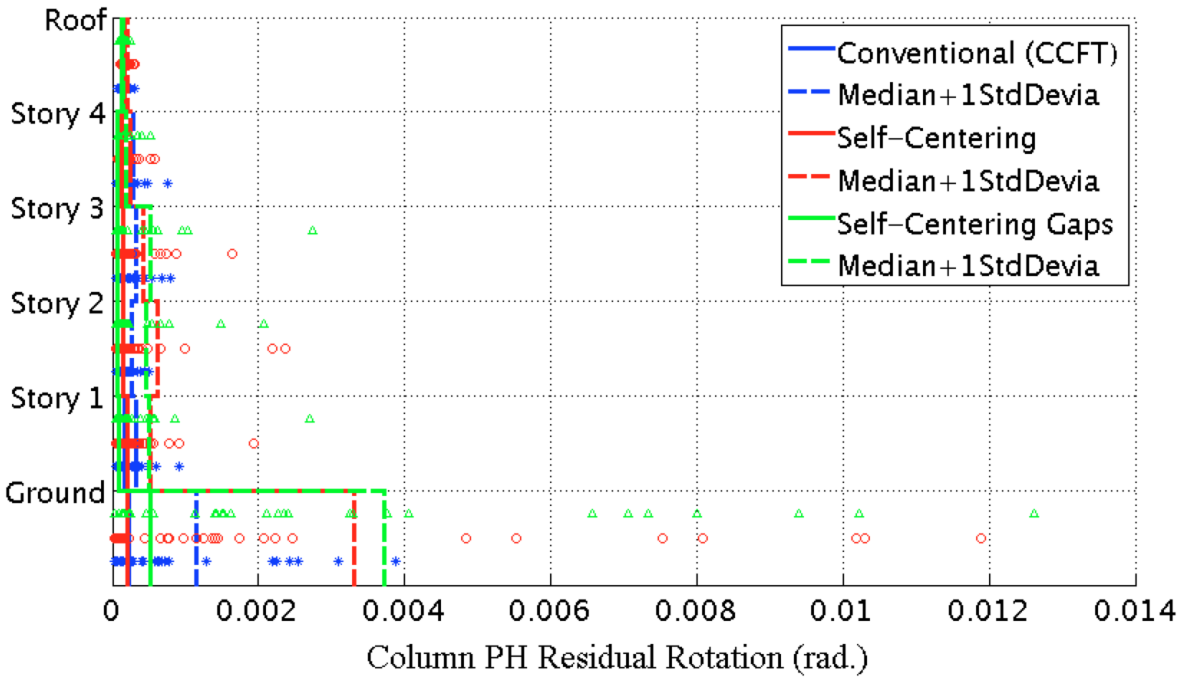

Appendix Figure L-79: Median of the maximum residual rotation of column plastic hinges under 44 DBE level ground motions with a GSR = 1.0 & damping = 10%

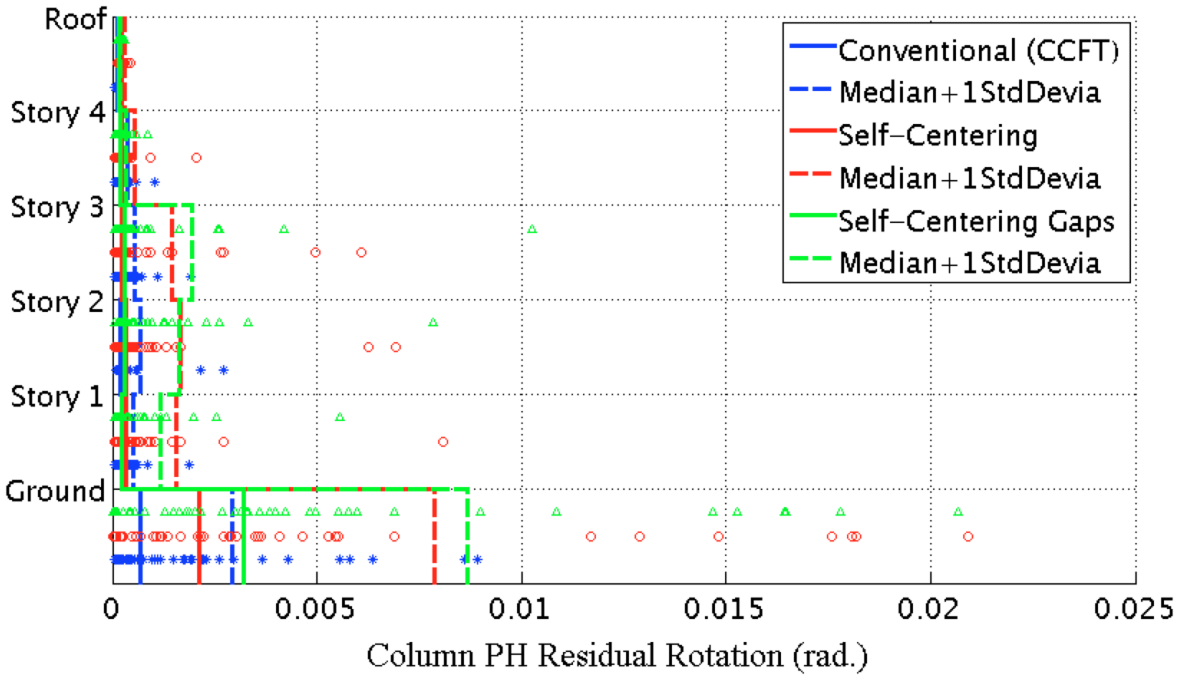

Appendix Figure L-80: Median of the maximum residual rotation of column plastic hinges under 44 MCE level ground motions with a GSR = 1.0 & damping = 10%

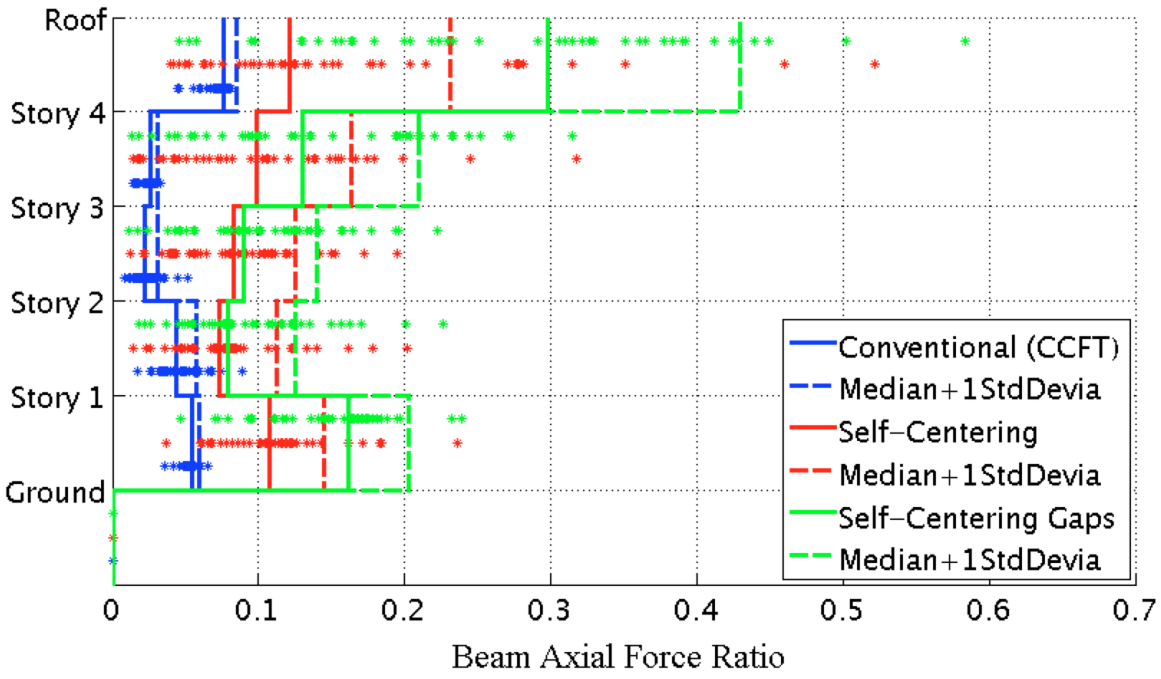

Appendix Figure L-81: Median of the peak axial force in beams under 44 DBE level ground motions with a GSR = 1.0 & damping = 10%

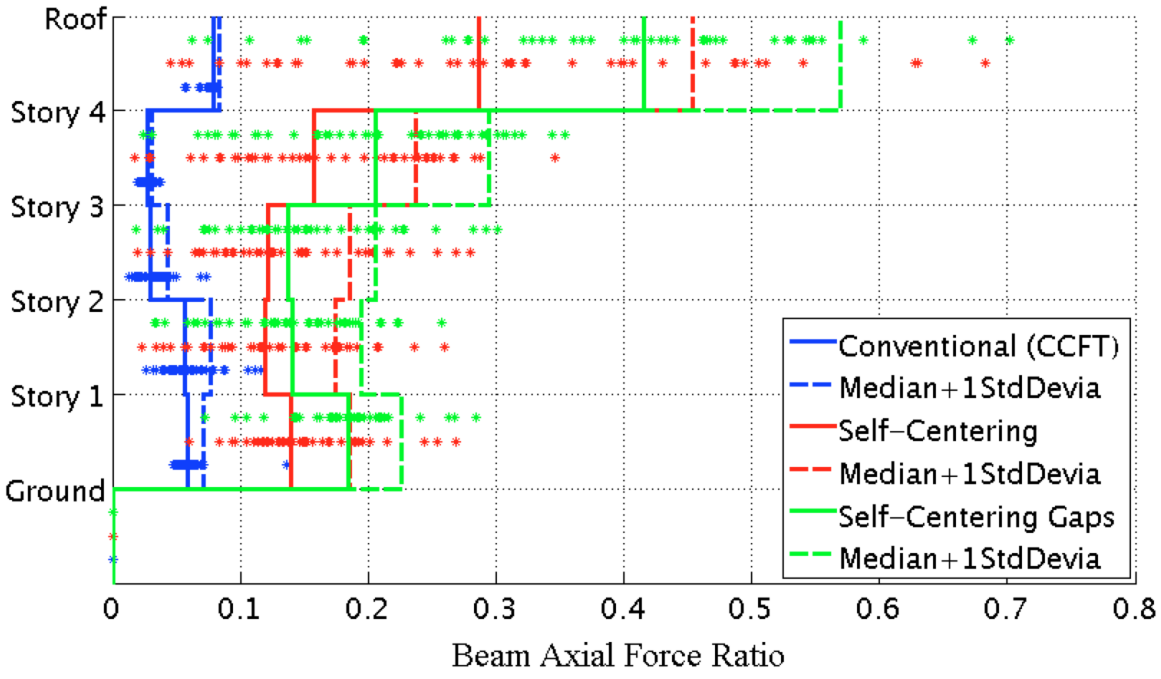

Appendix Figure L-82: Median of the peak axial force in beams under 44 MCE level ground motions with a GSR = 1.0 & damping = 10%

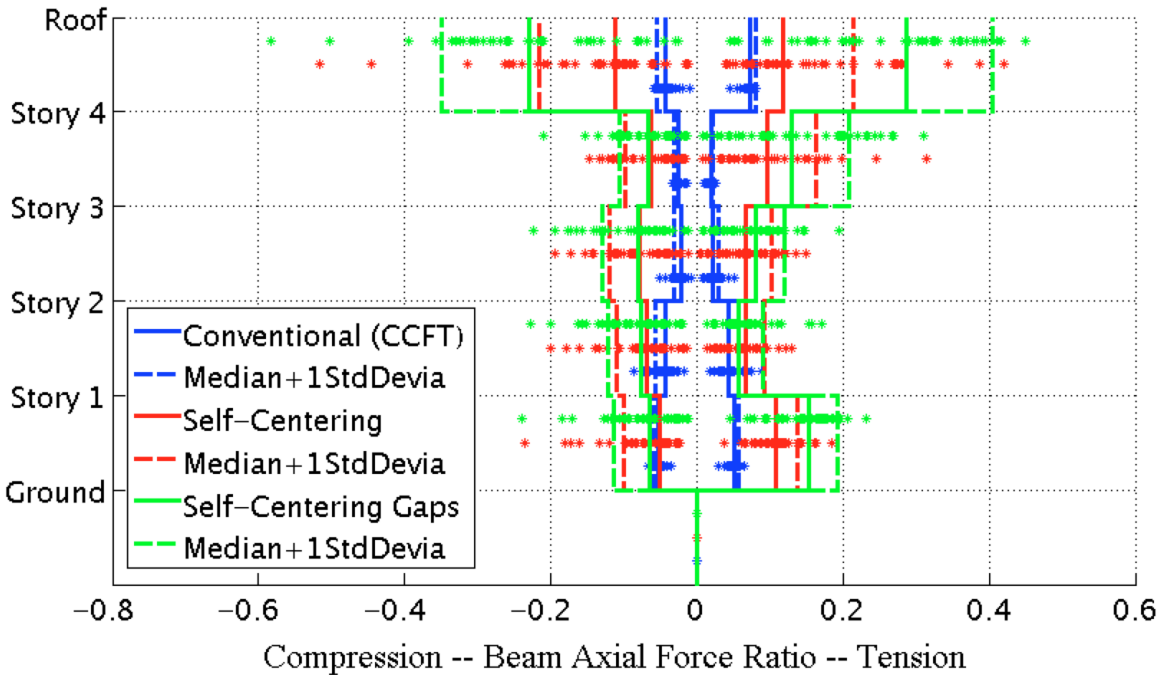

Appendix Figure L-83: Median of the peak tension vs.compression in beams under 44 DBE level ground motions with a GSR = 1.0 & damping = 10%

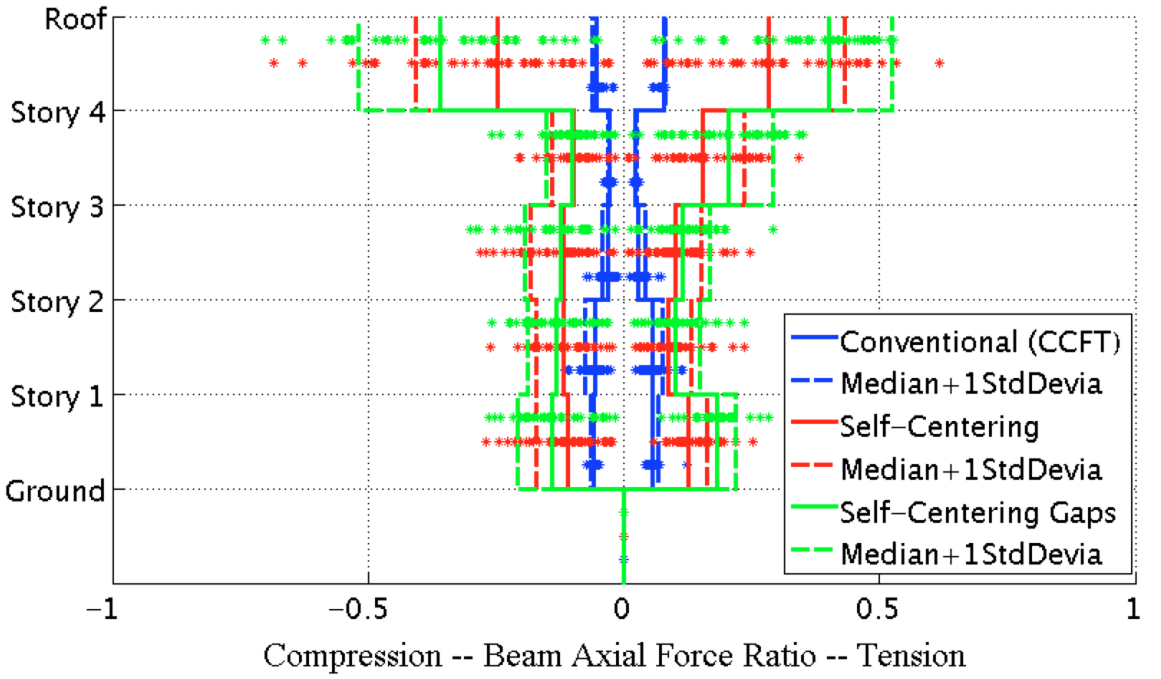

Appendix Figure L-84: Median of the peak tension vs.compression in beams under 44 MCE level ground motions with a GSR = 1.0 & damping = 10%

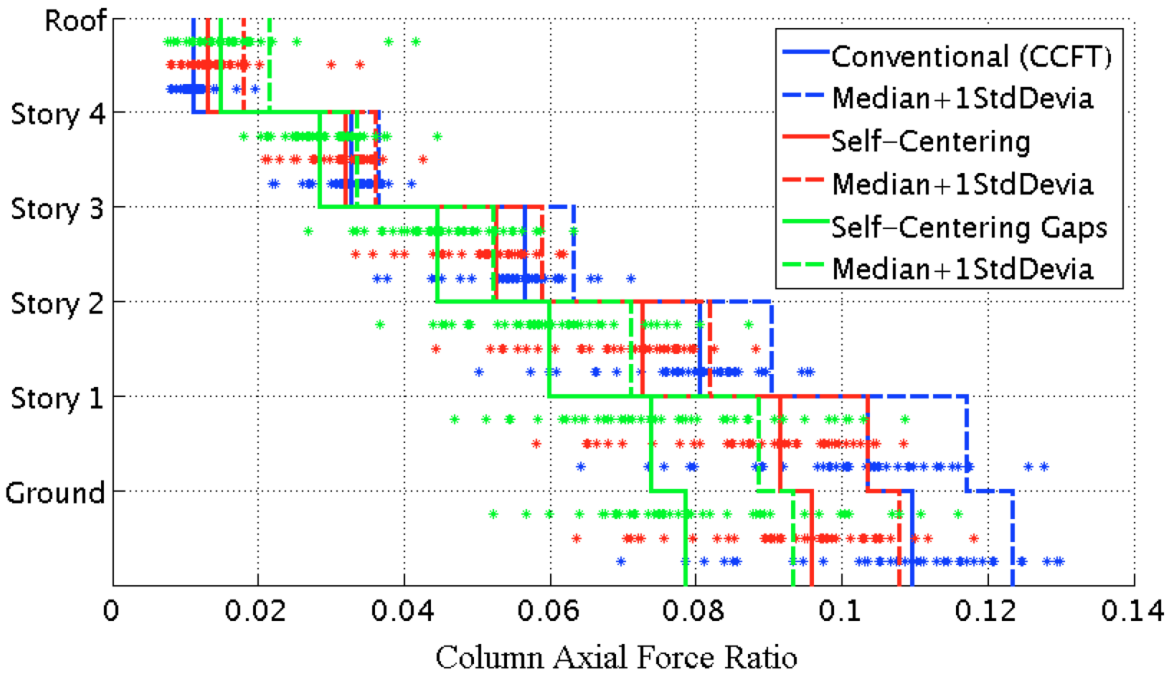

Appendix Figure L-85: Median of the peak axial force in columns under 44 DBE level ground motions with a GSR = 1.0 & damping = 10%

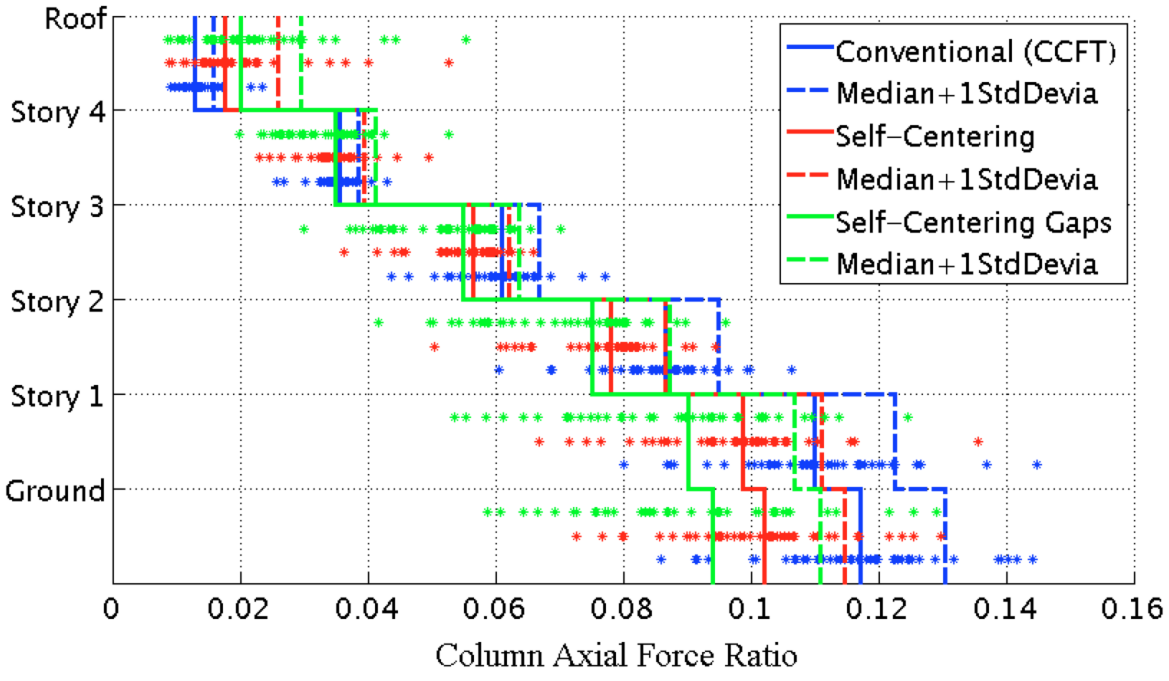

Appendix Figure L-86: Median of the peak axial force in columns under 44 MCE level ground motions with a GSR = 1.0 & damping = 10%

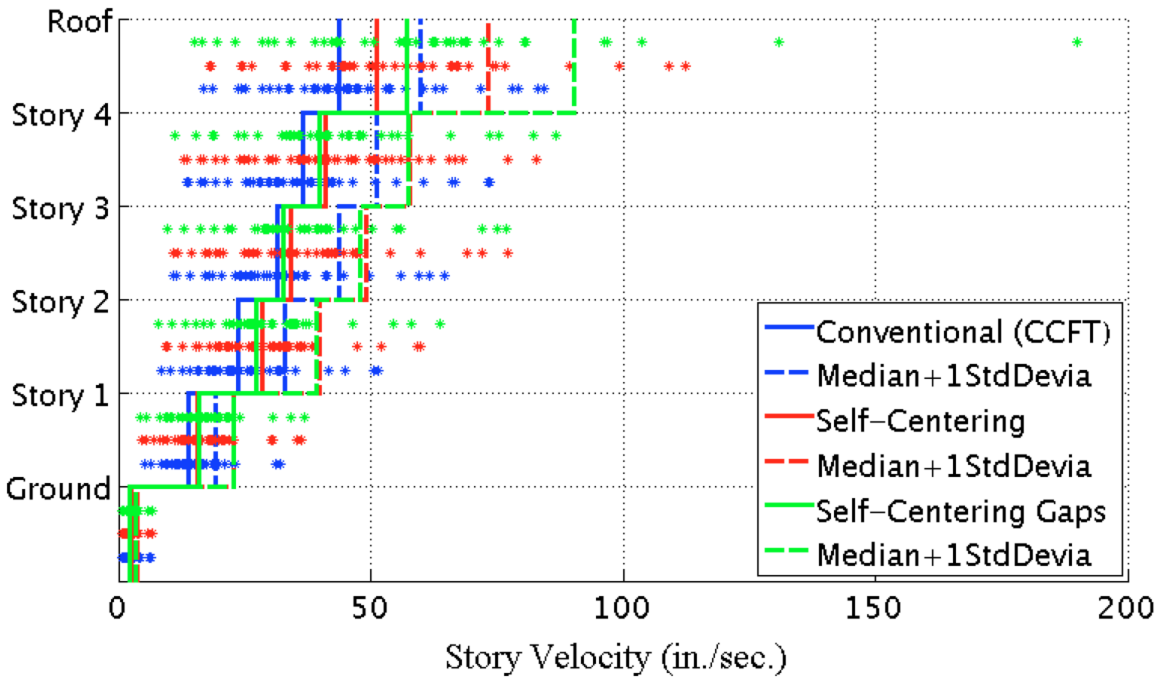

Appendix Figure L-87: Median of the peak story velocity under 44 DBE level ground motions with a GSR = 1.0 & damping = 10%

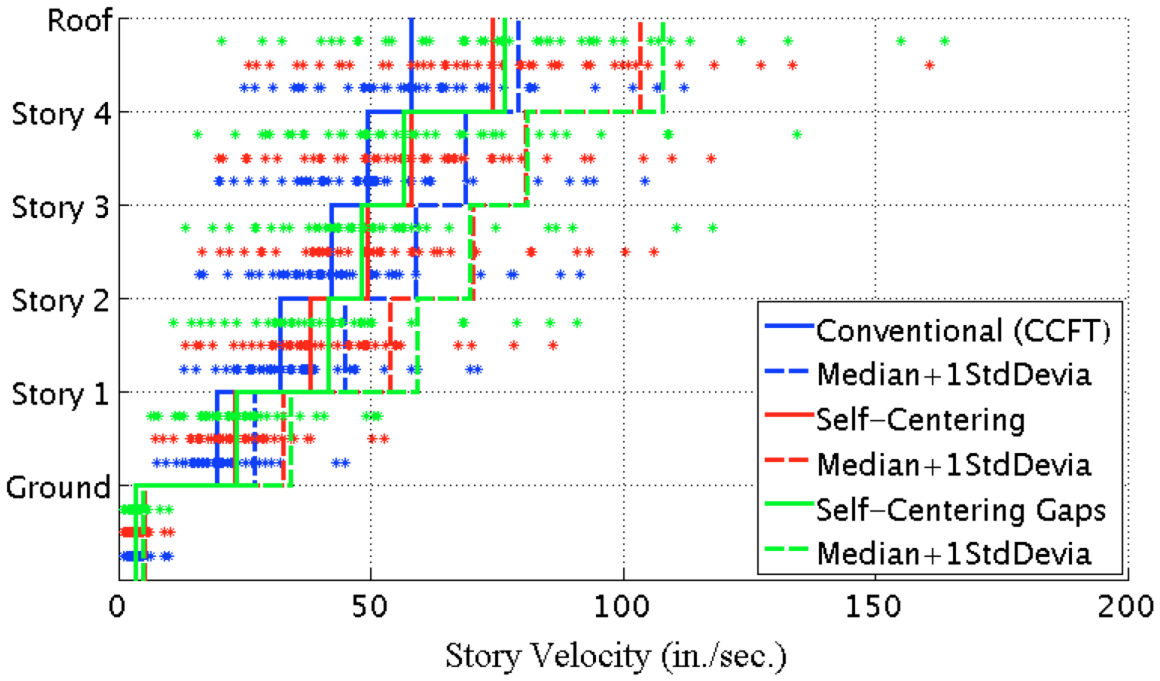

Appendix Figure L-88: Median of the peak story velocity under 44 MCE level ground motions with a GSR = 1.0 & damping = 10%

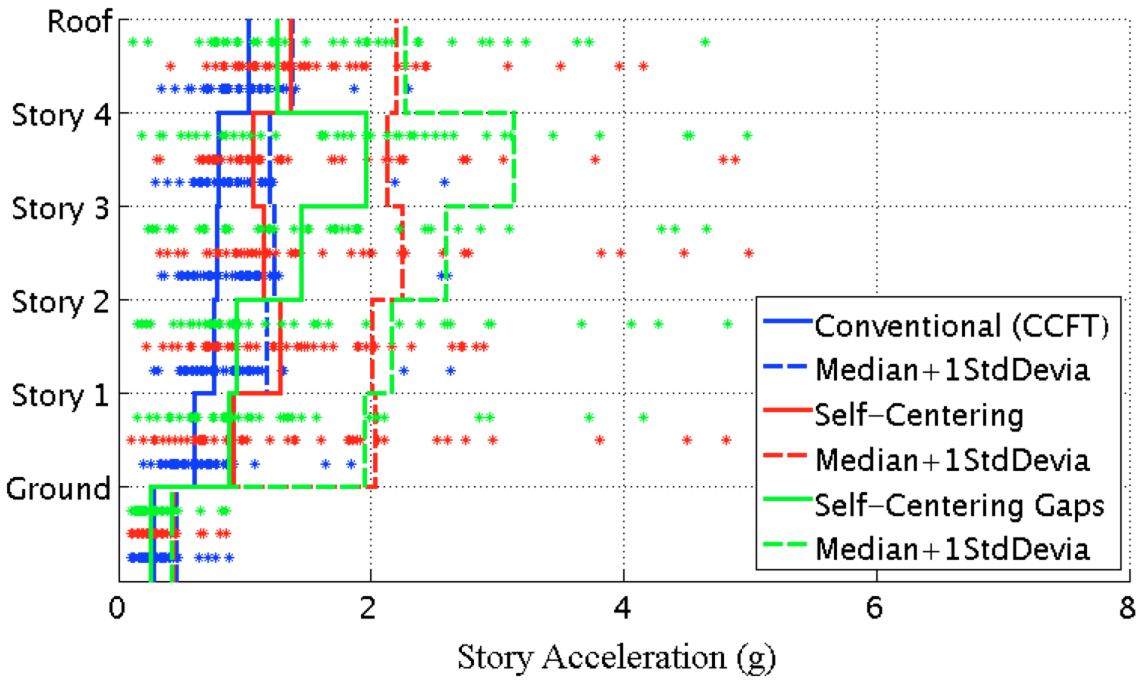

Appendix Figure L-89: Median of the peak story acceleration under 44 DBE level ground motions with a GSR = 1.0 & damping = 10%

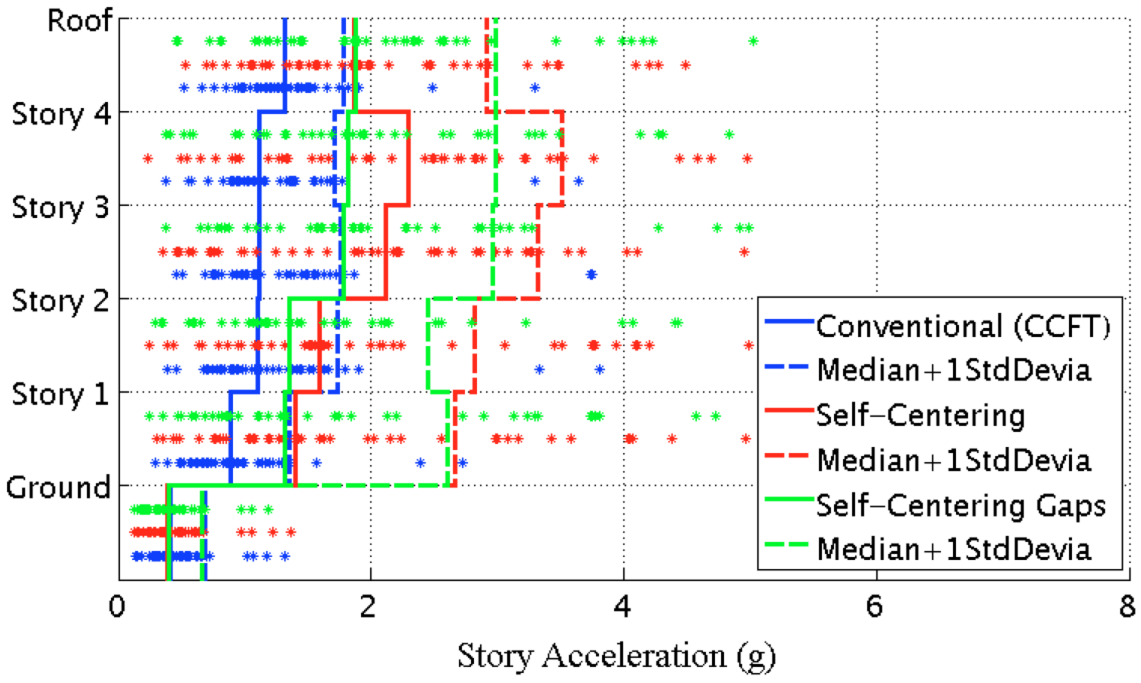

Appendix Figure L-90: Median of the peak story acceleration under 44 MCE level ground motions with a GSR = 1.0 & damping = 10%

L.4 Systems with a GSR = 1.0 & Damping = 2%

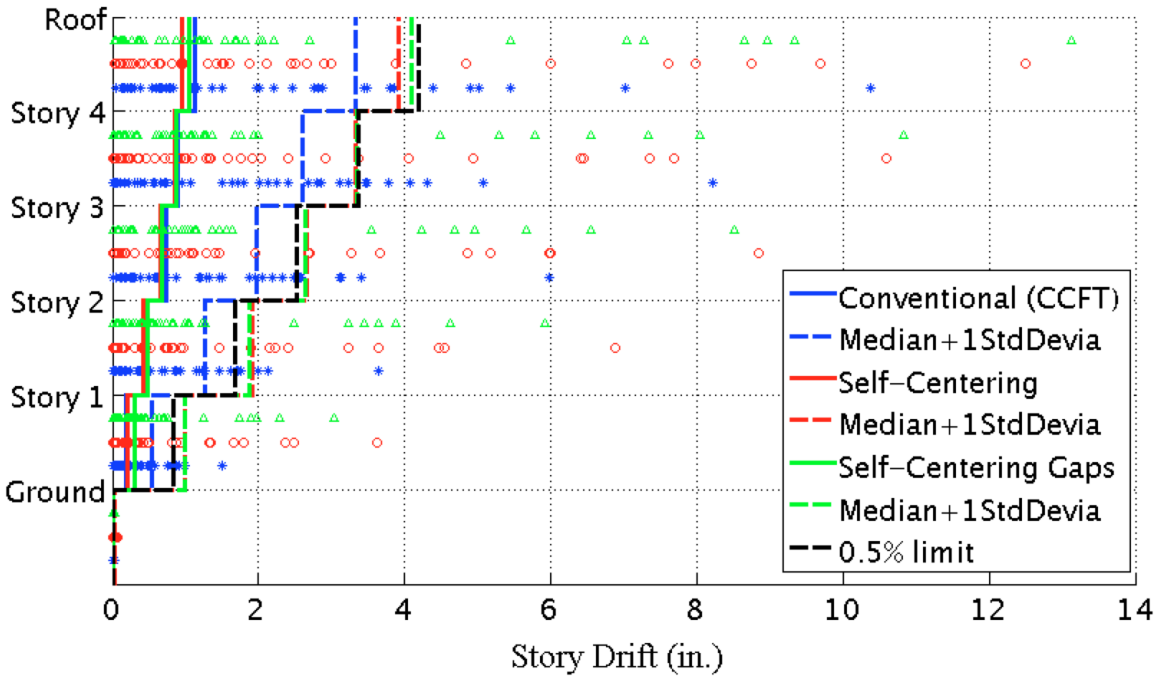

Appendix Figure L-91: Median of the maximum story residual drift under 44 DBE level ground motions with a GSR = 1.0 & damping = 2%

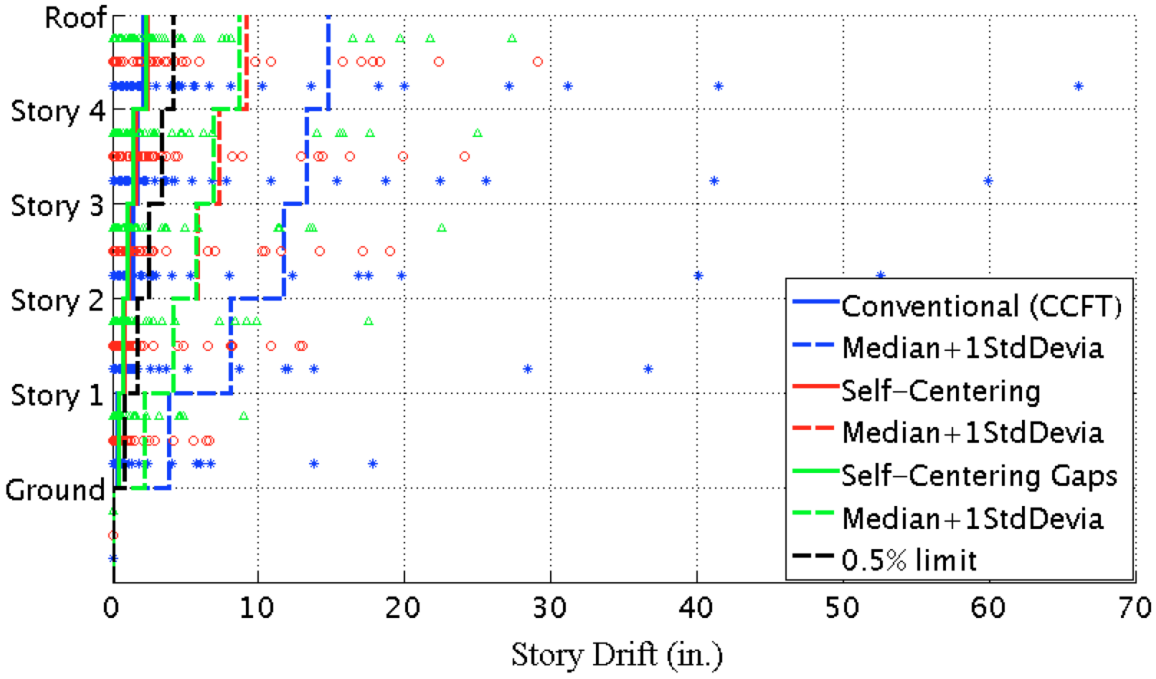

Appendix Figure L-92: Median of the maximum story residual drift under 44 MCE level ground motions with a GSR = 1.0 & damping = 2%

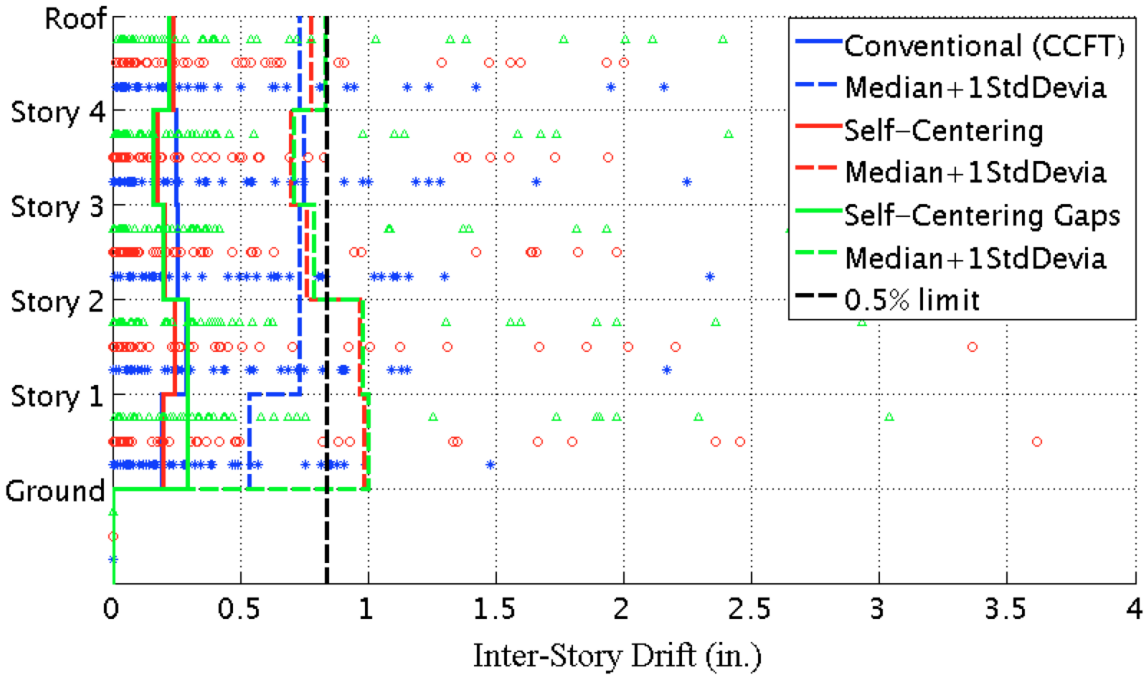

Appendix Figure L-93: Median of the maximum inter-story residual drift under 44 DBE level ground motions with a GSR = 1.0 & damping = 2%

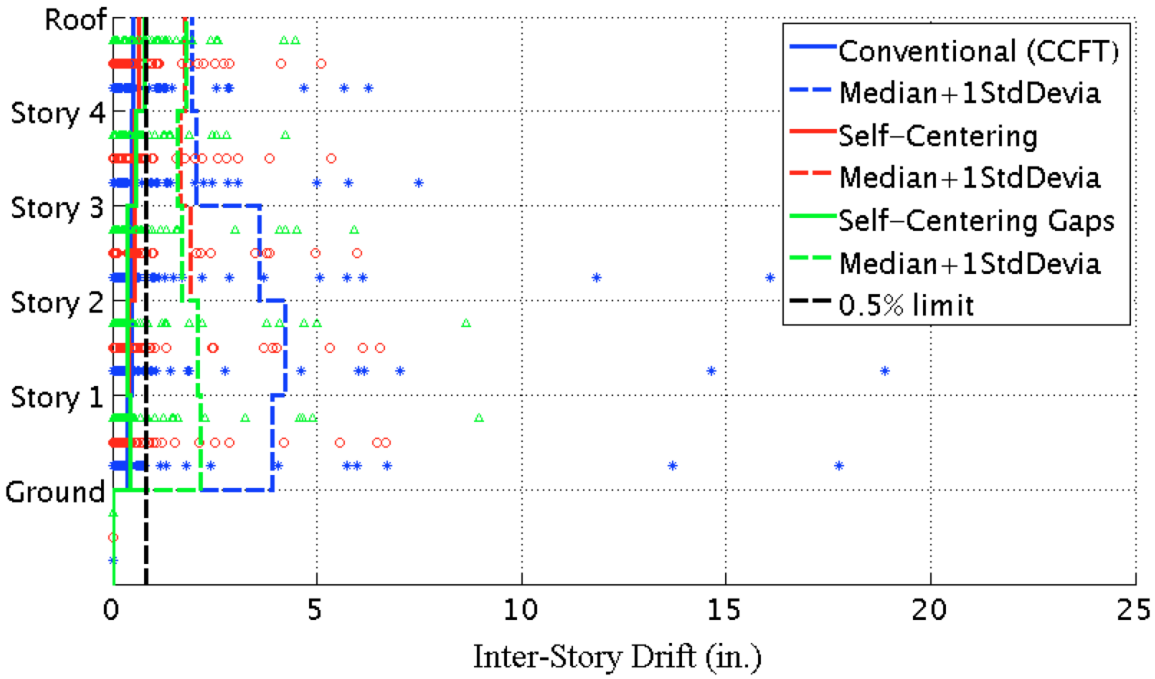

Appendix Figure L-94: Median of the maximum inter-story residual drift under 44 MCE level ground motions with a GSR = 1.0 & damping = 2%

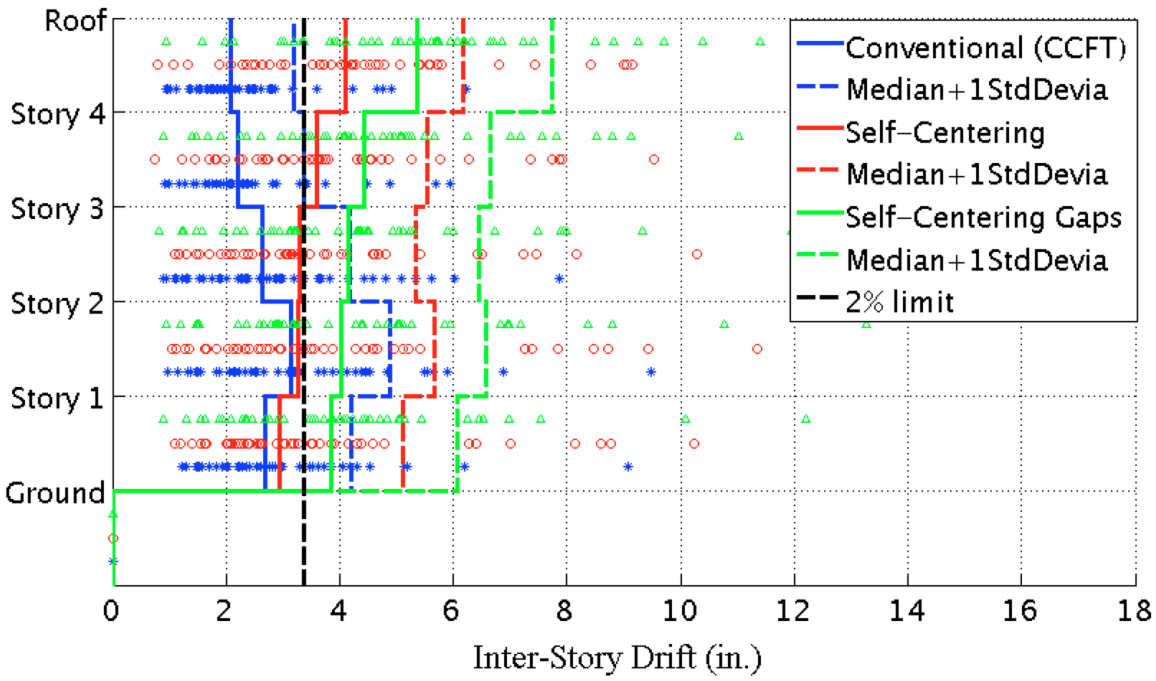

Appendix Figure L-95: Median of the peak inter-story drift under 44 DBE level ground motions with a GSR = 1.0 & damping = 2%

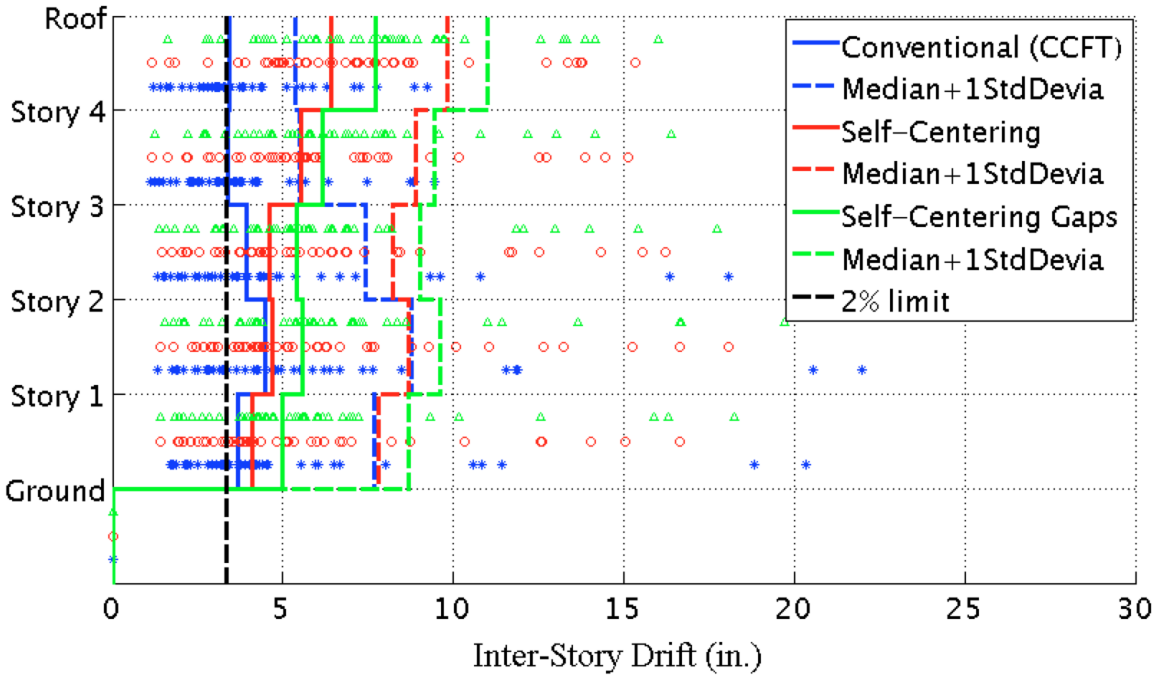

Appendix Figure L-96: Median of the peak inter-story drift under 44 MCE level ground motions with a GSR = 1.0 & damping = 2%

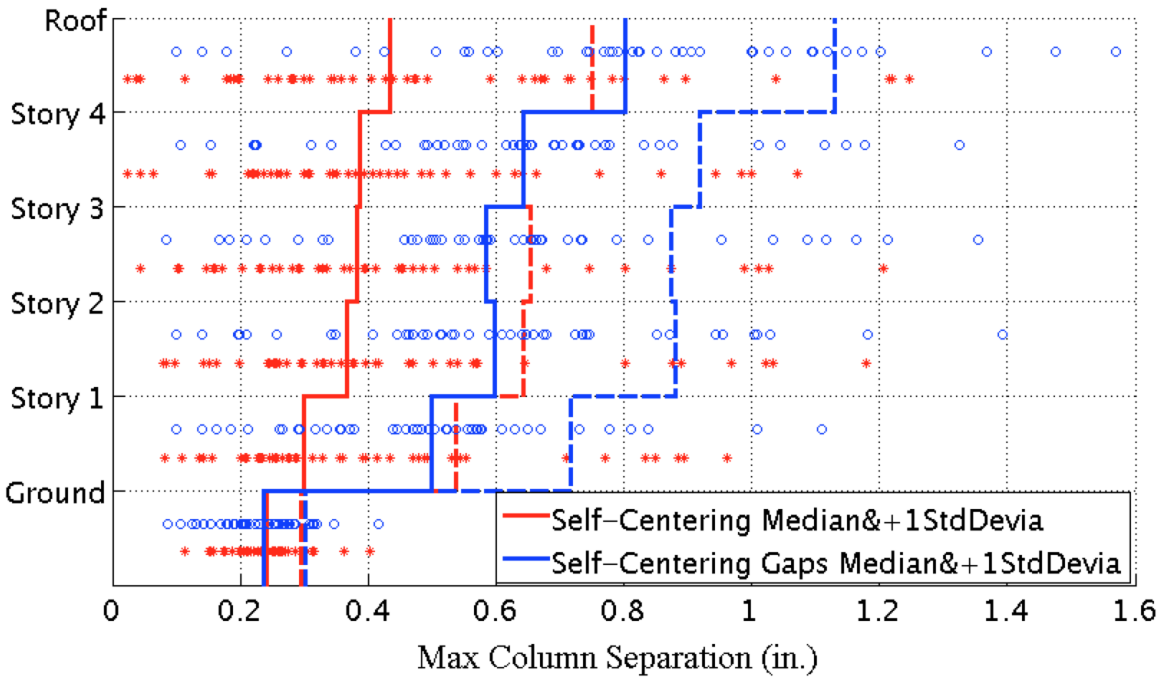

Appendix Figure L-97: Median of the maximum column separation under 44 DBE level ground motions with a GSR = 1.0 & damping = 2%

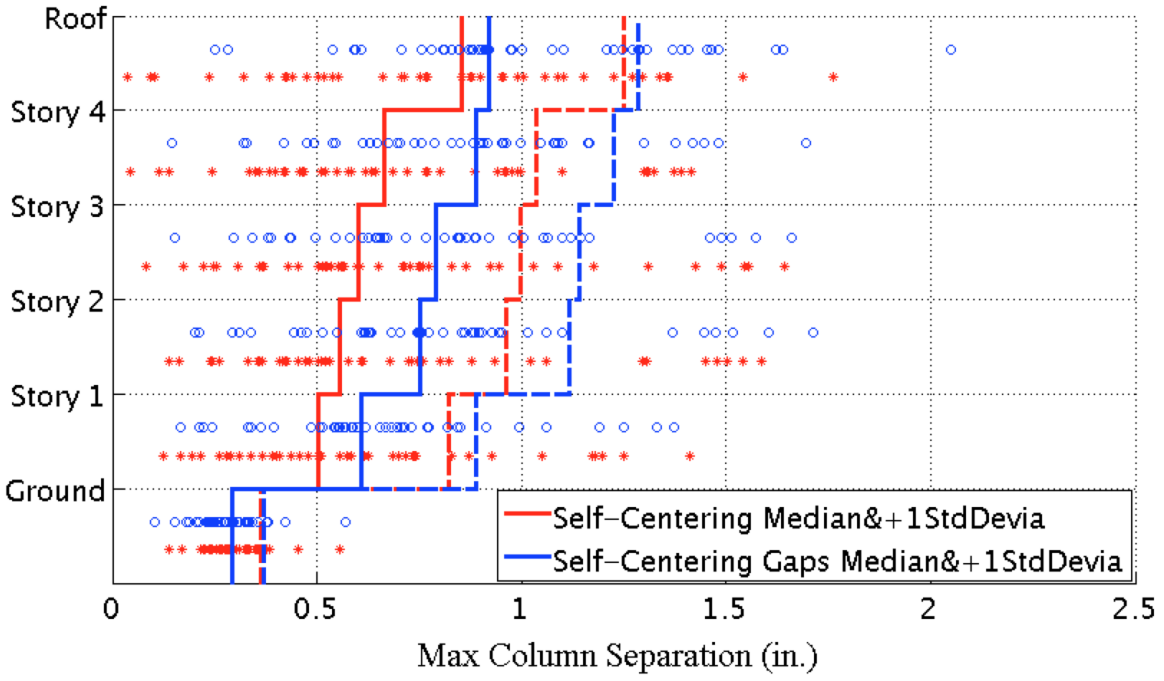

Appendix Figure L-98: Median of the maximum column separation under 44 MCE level ground motions with a GSR = 1.0 & damping = 2%

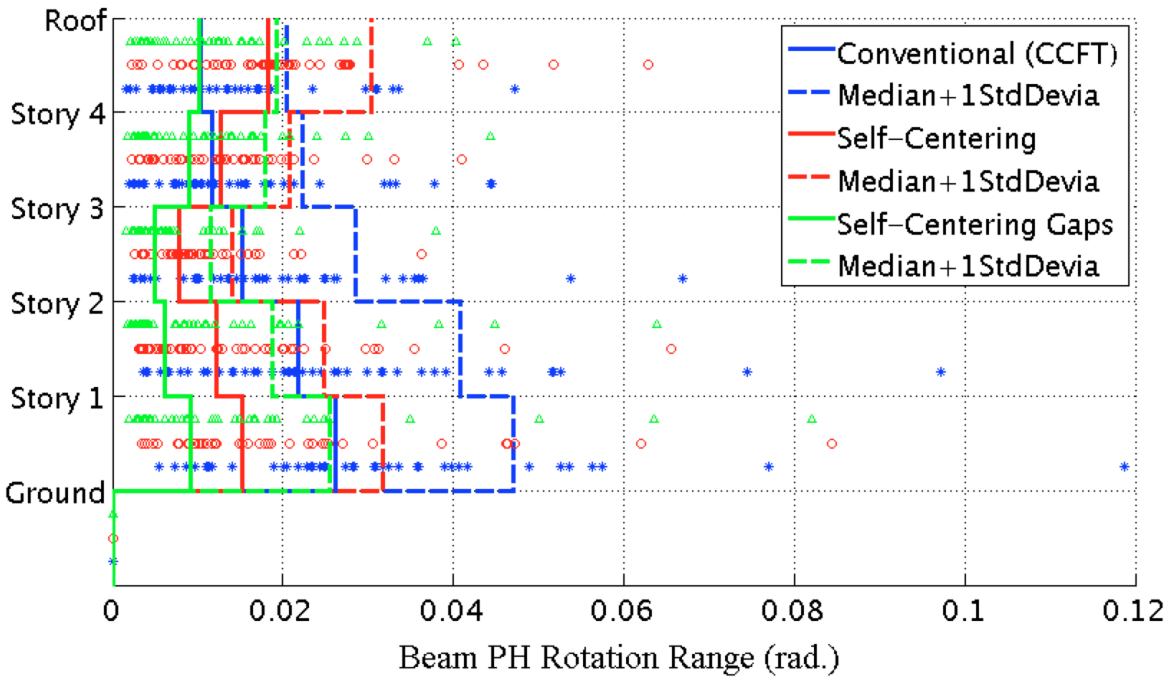

Appendix Figure L-99: Median of the beam PH rotation range under 44 DBE level ground motions with a GSR = 1.0 & damping = 2%

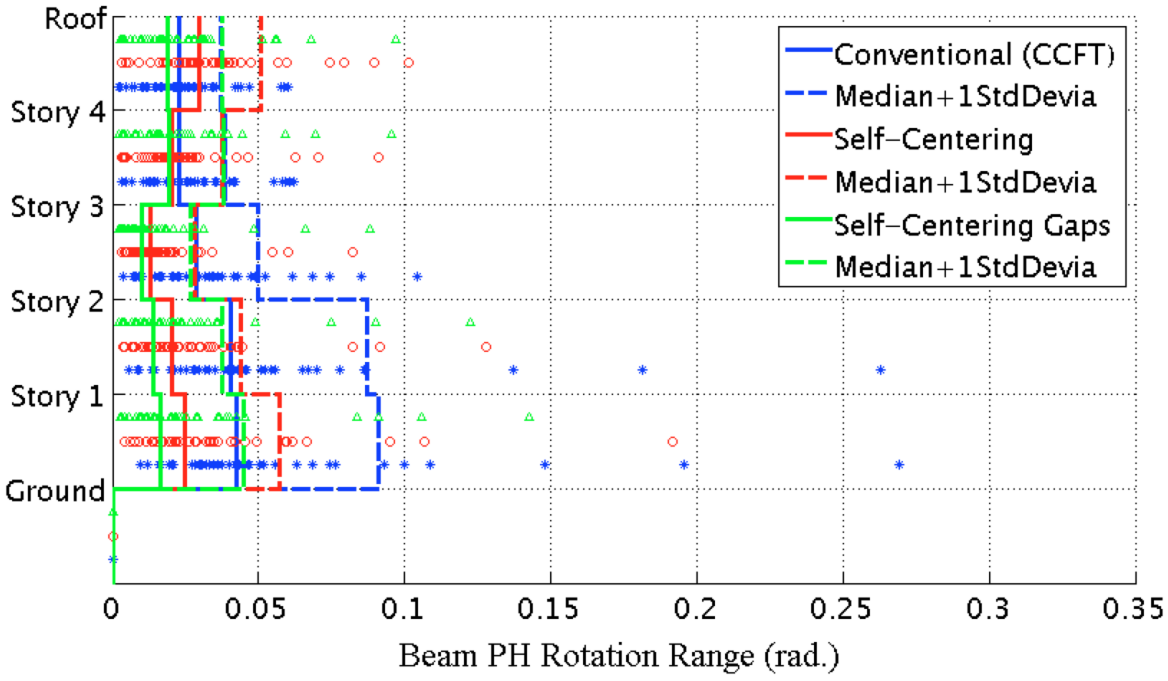

Appendix Figure L-100: Median of the beam PH rotation range under 44 MCE level ground motions with a GSR = 1.0 & damping = 2%

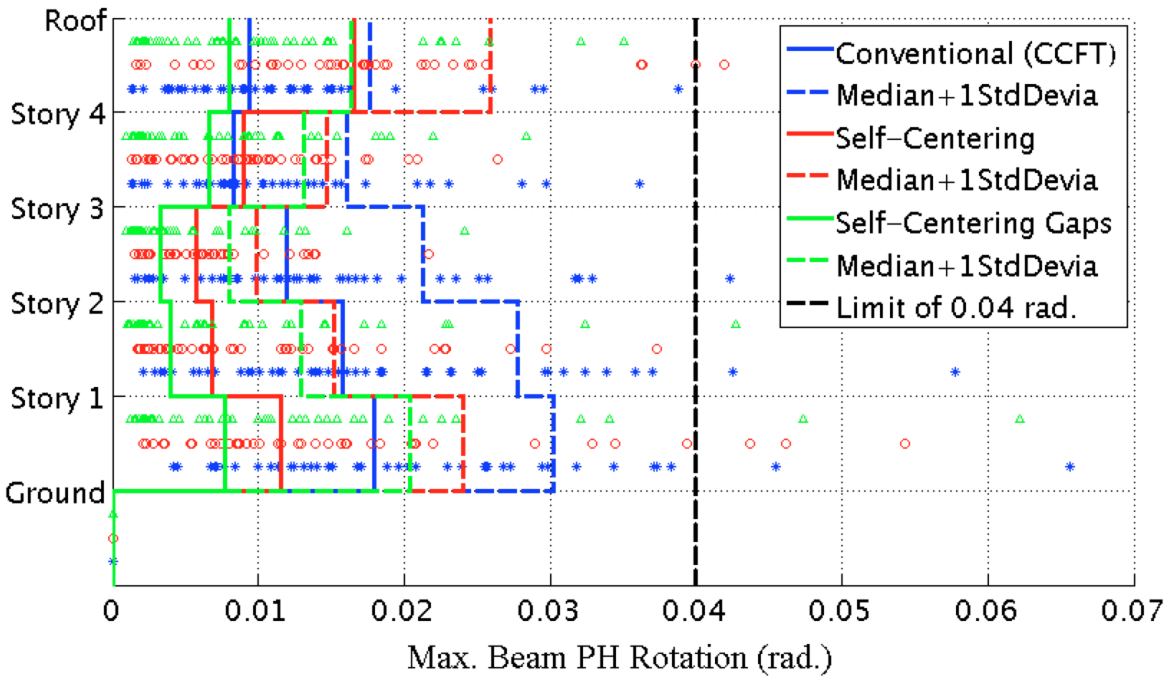

Appendix Figure L-101: Median of the maximum beam PH rotation under 44 DBE level ground motions with a GSR = 1.0 & damping = 2%

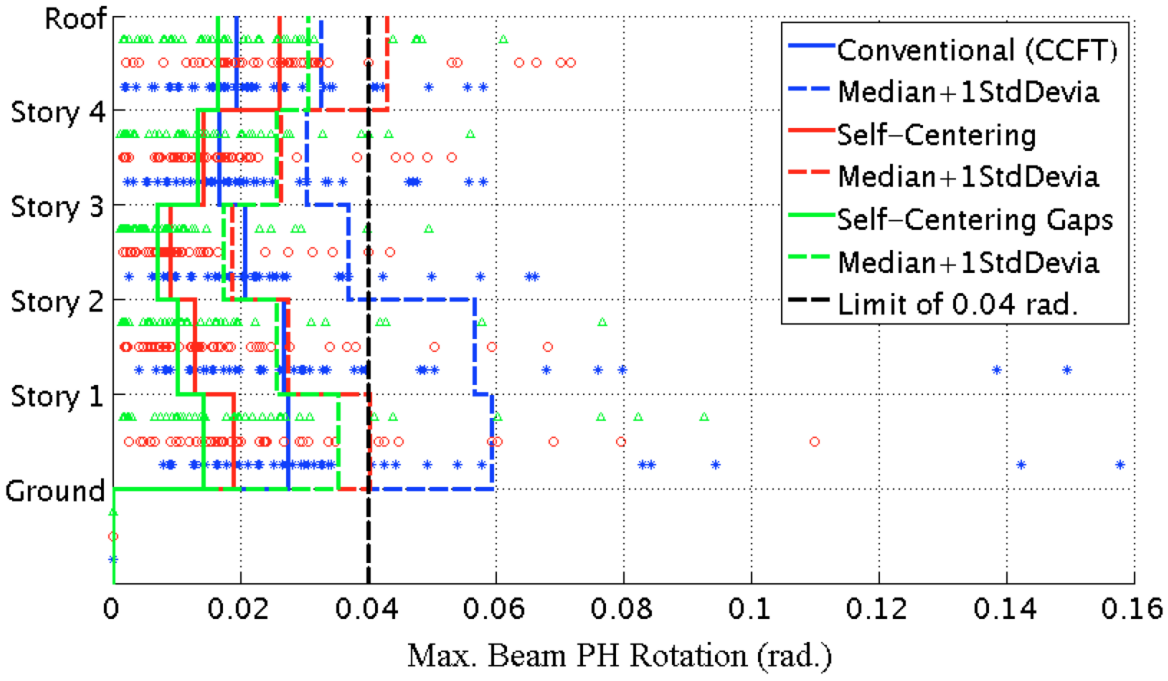

Appendix Figure L-102: Median of the maximum beam PH rotation under 44 MCE level ground motions with a GSR = 1.0 & damping = 2%

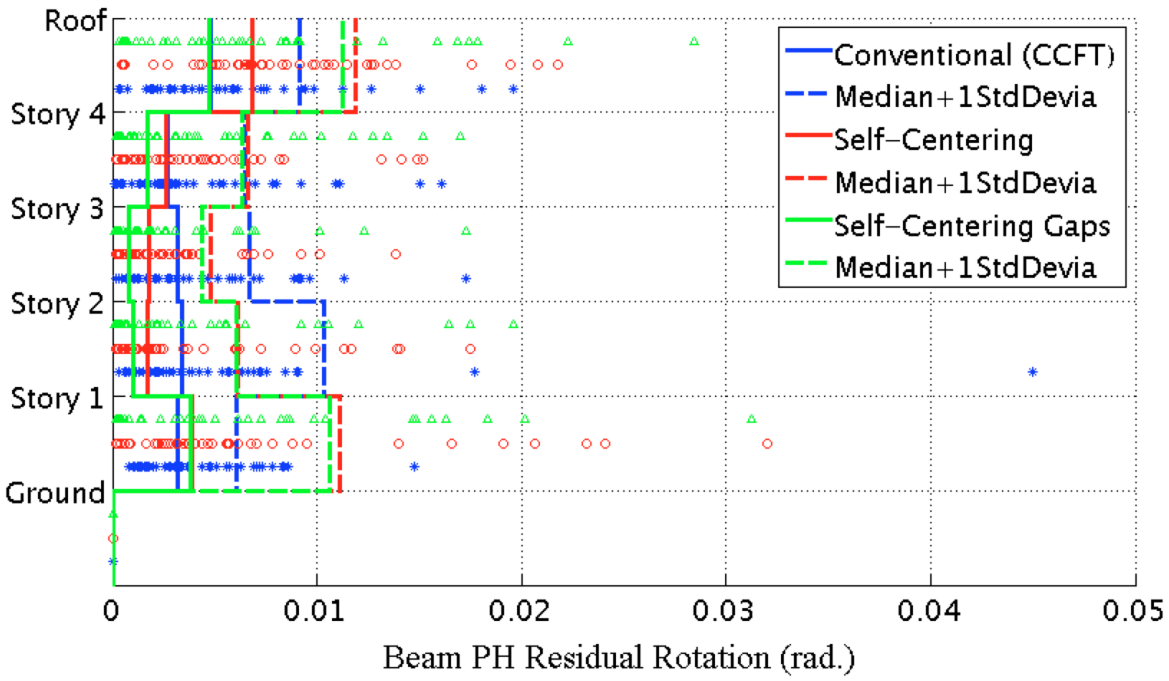

Appendix Figure L-103: Median of the maximum residual rotation of beam plastic hinges under 44 DBE level ground motions with a GSR = 1.0 & damping = 2%

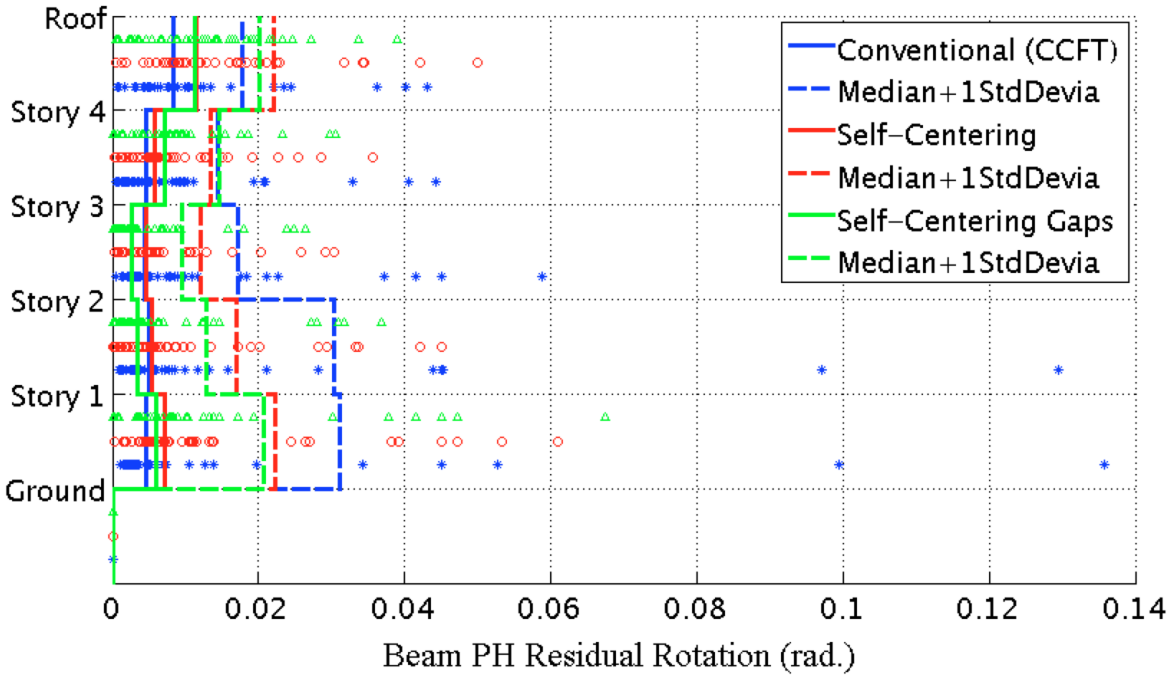

Appendix Figure L-104: Median of the maximum residual rotation of beam plastic hinges under 44 MCE level ground motions with a GSR = 1.0 & damping = 2%

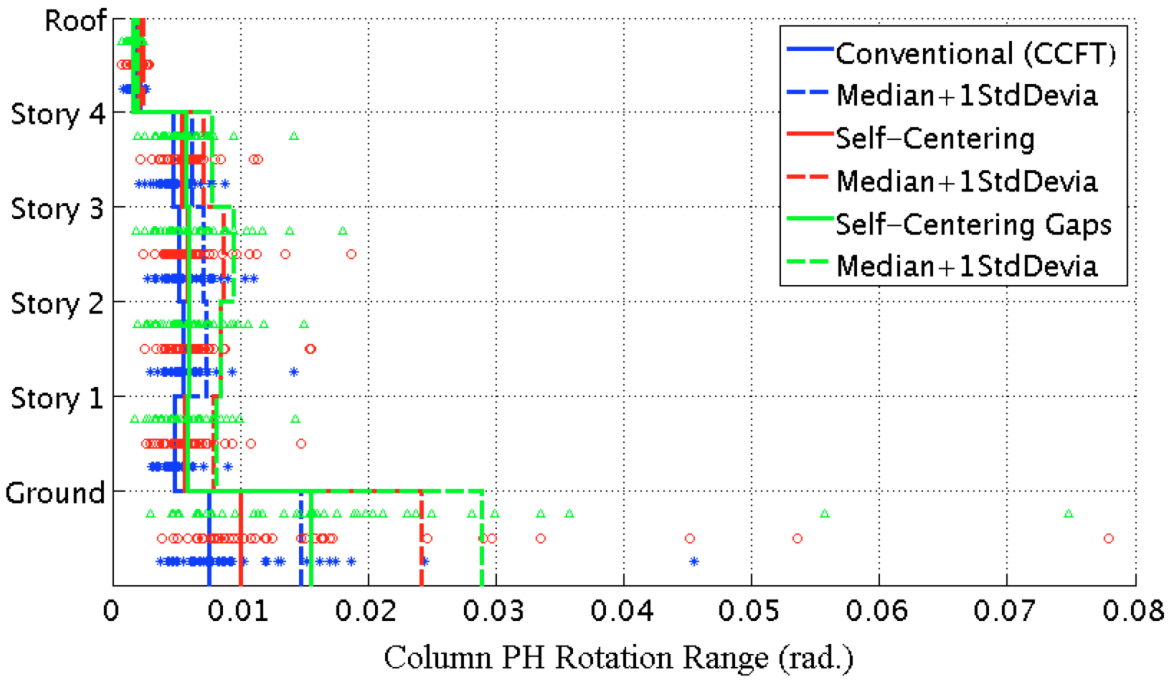

Appendix Figure L-105: Median of the column PH rotation range under 44 DBE level ground motions with a GSR = 1.0 & damping = 2%

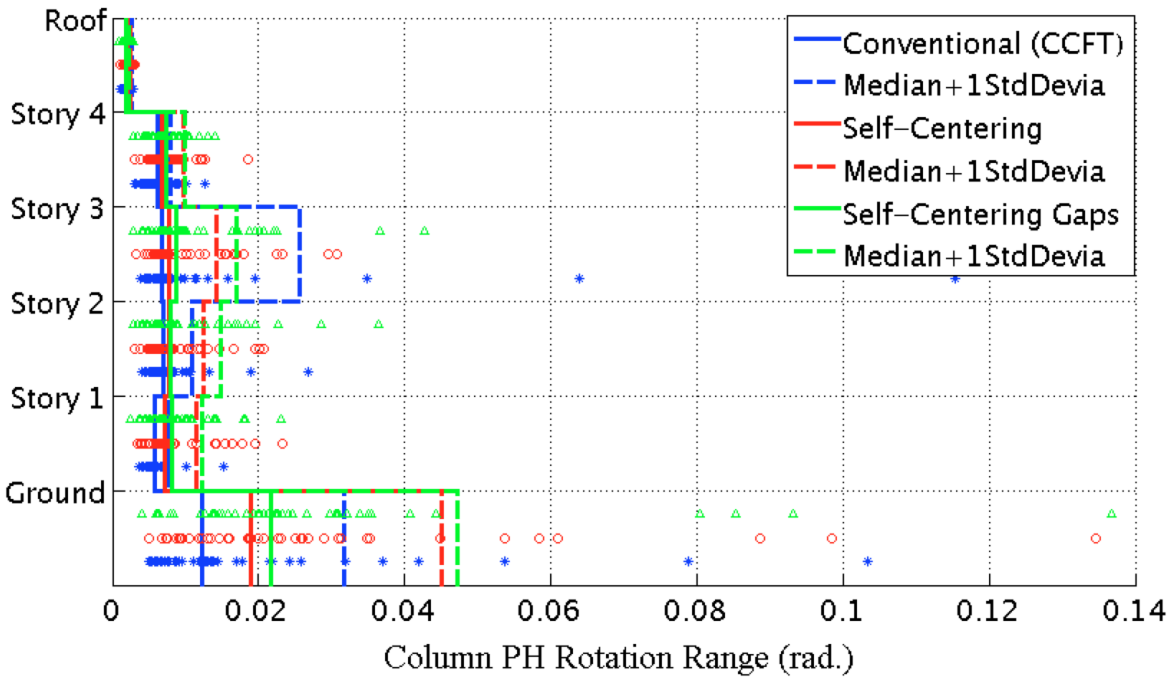

Appendix Figure L-106: Median of the column PH rotation range under 44 MCE level ground motions with a GSR = 1.0 & damping = 2%

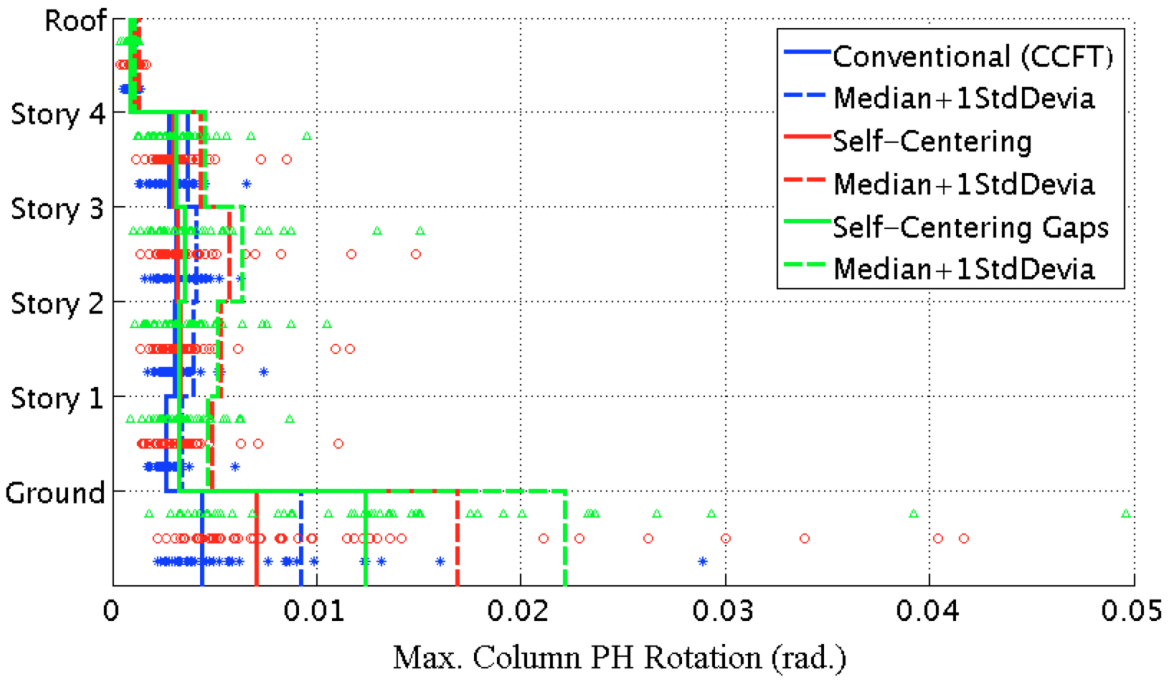

Appendix Figure L-107: Median of the maximum column PH rotation under 44 DBE level ground motions with a GSR = 1.0 & damping = 2%

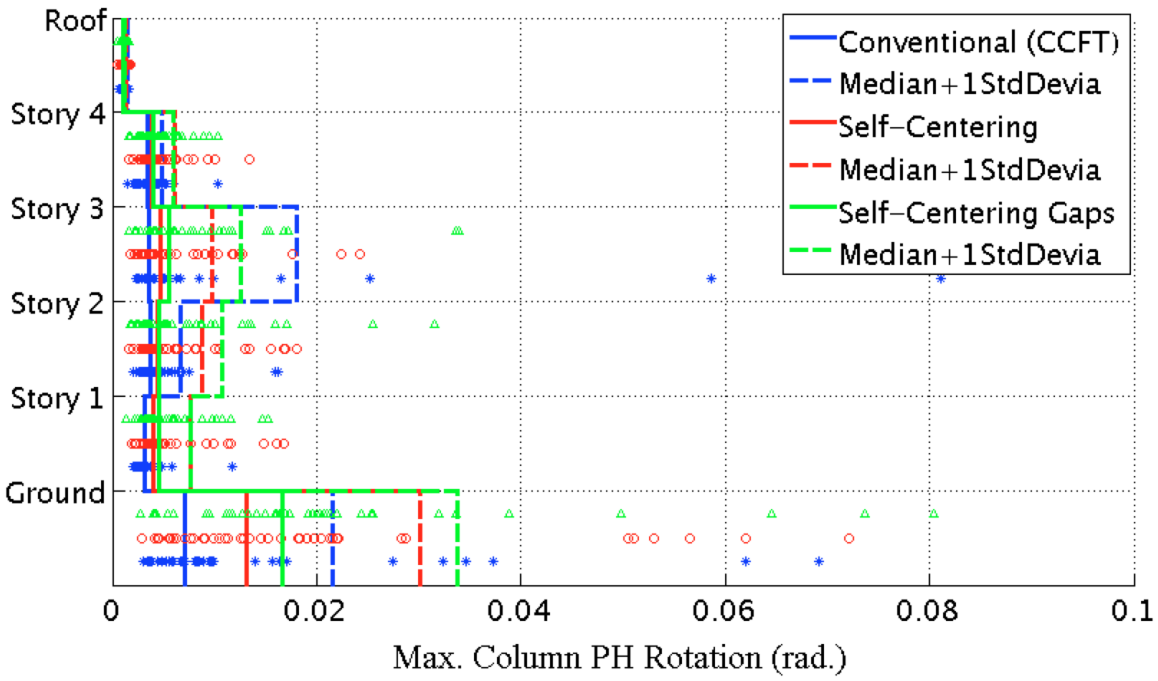

Appendix Figure L-108: Median of the maximum column PH rotation under 44 MCE level ground motions with a GSR = 1.0 & damping = 2%

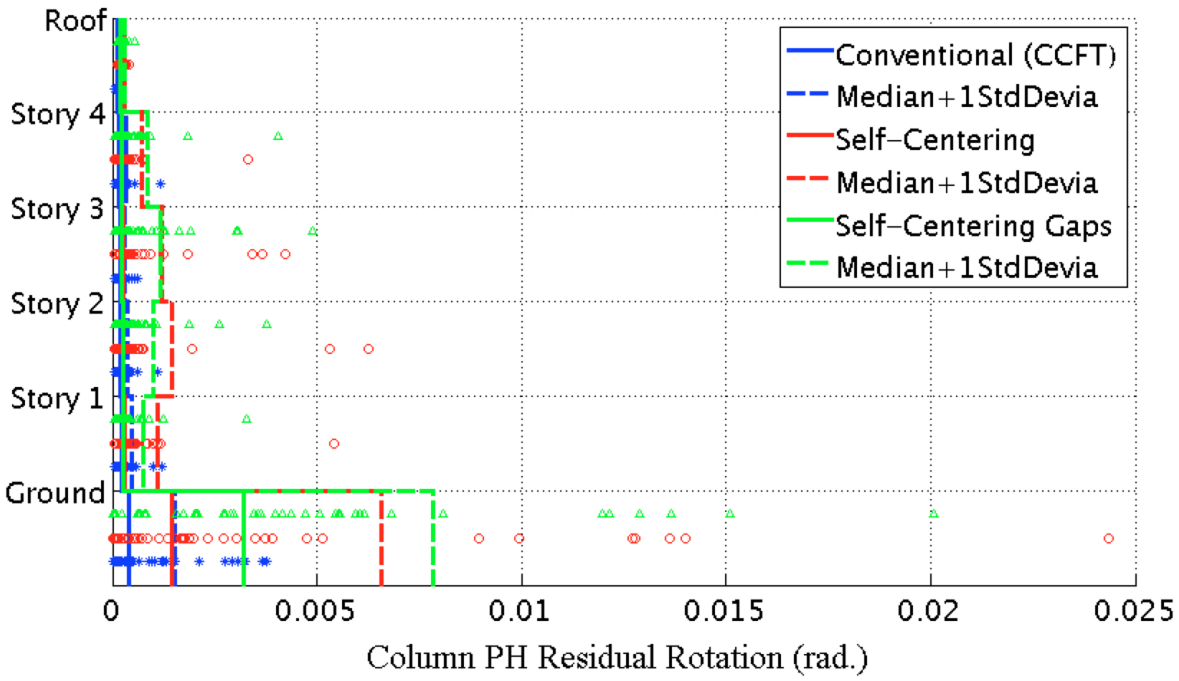

Appendix Figure L-109: Median of the maximum residual rotation of column plastic hinges under 44 DBE level ground motions with a GSR = 1.0 & damping = 2%

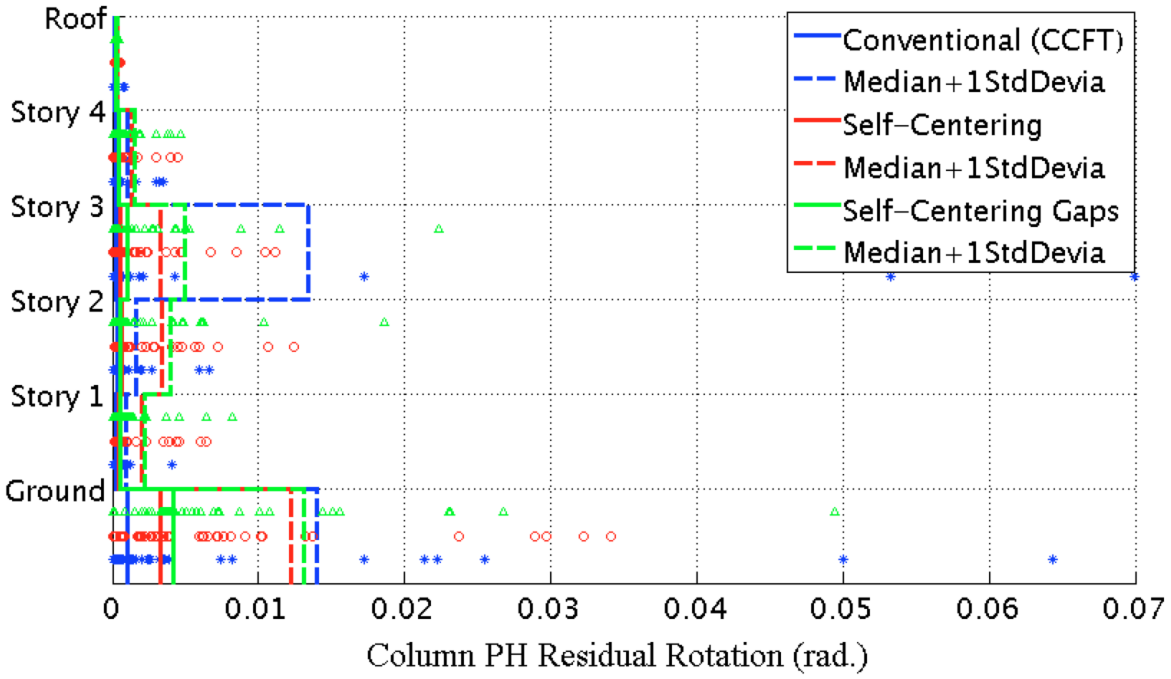

Appendix Figure L-110: Median of the maximum residual rotation of column plastic hinges under 44 MCE level ground motions with a GSR = 1.0 & damping = 2%

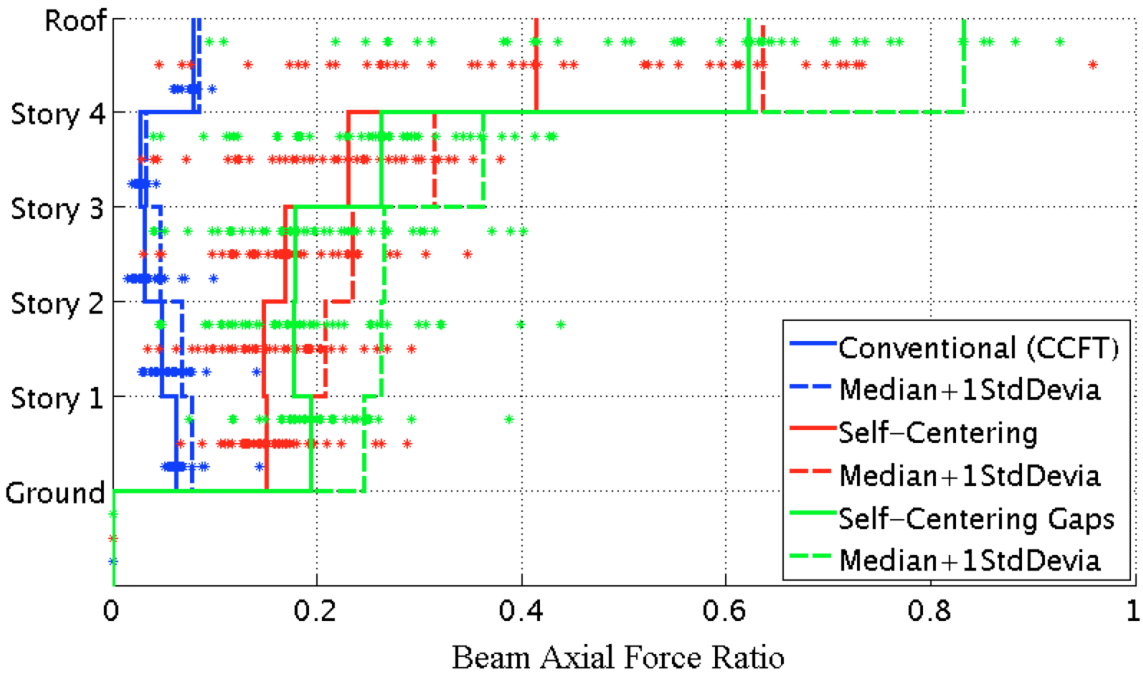

Appendix Figure L-111: Median of the peak axial force in beams under 44 DBE level ground motions with a GSR = 1.0 & damping = 2%

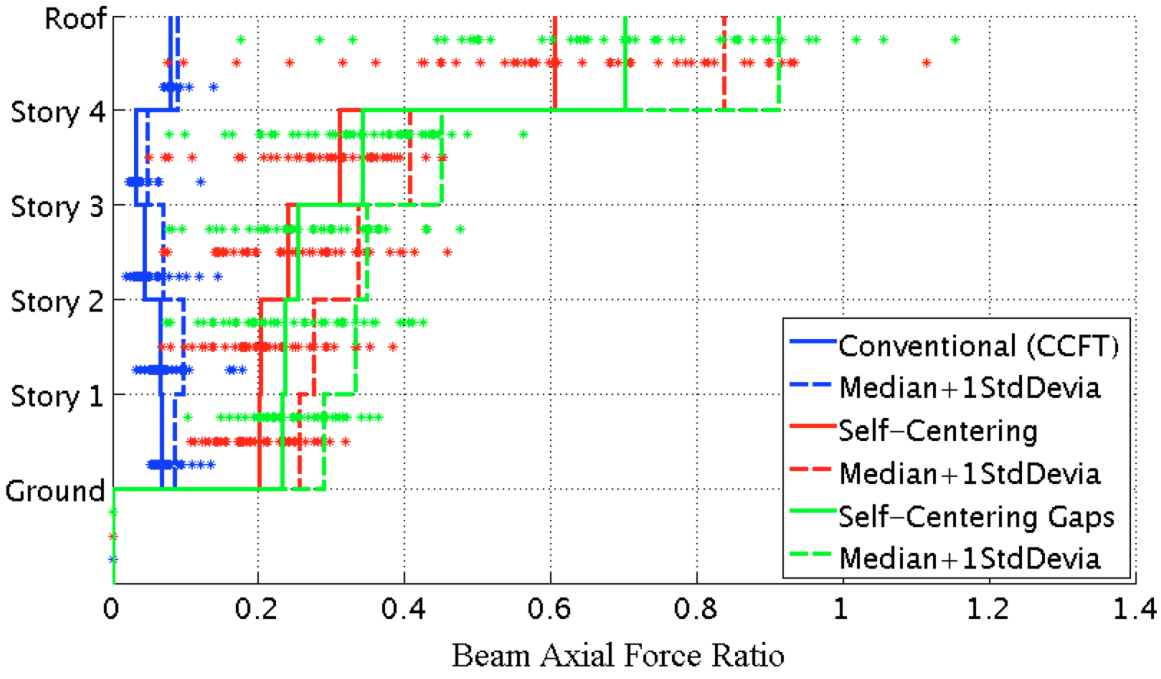

Appendix Figure L-112: Median of the peak axial force in beams under 44 MCE level ground motions with a GSR = 1.0 & damping = 2%

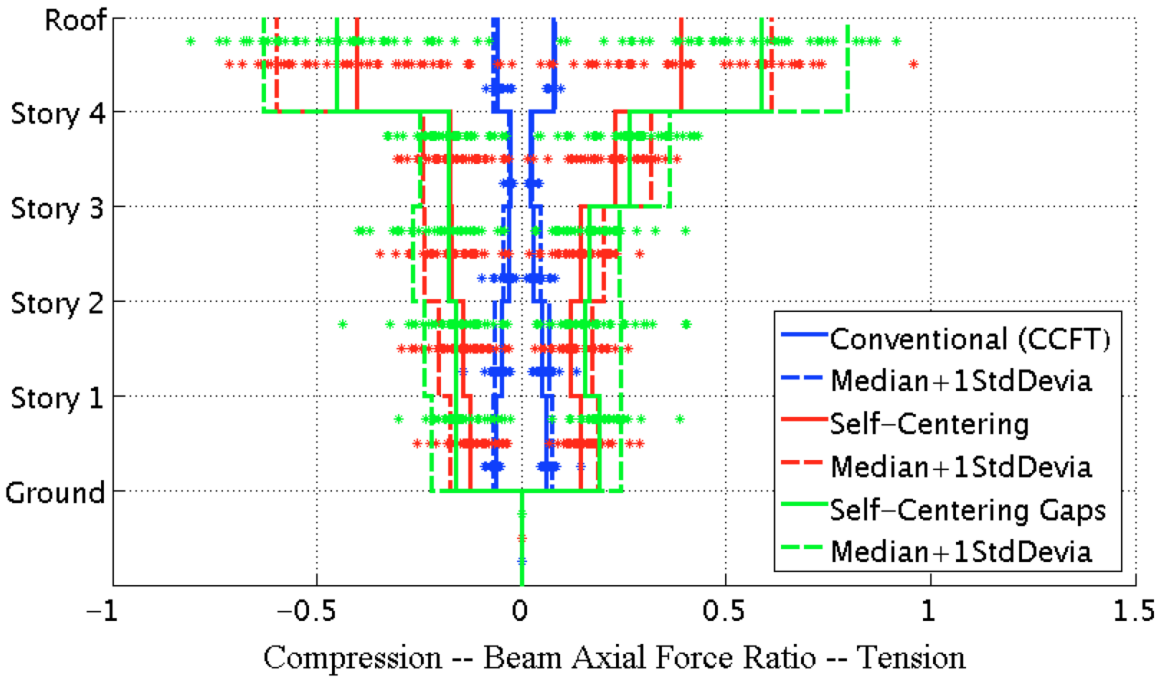

Appendix Figure L-113: Median of the peak tension vs.compression in beams under 44 DBE level ground motions with a GSR = 1.0 & damping = 2%

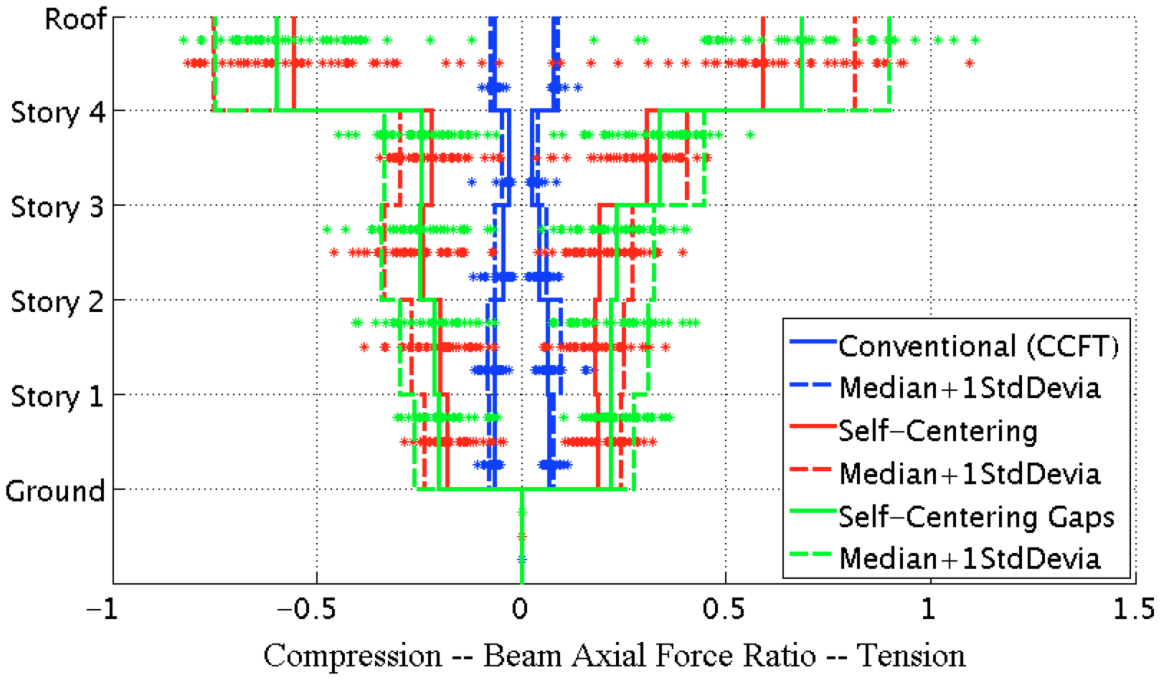

Appendix Figure L-114: Median of the peak tension vs.compression in beams under 44 MCE level ground motions with a GSR = 1.0 & damping = 2%

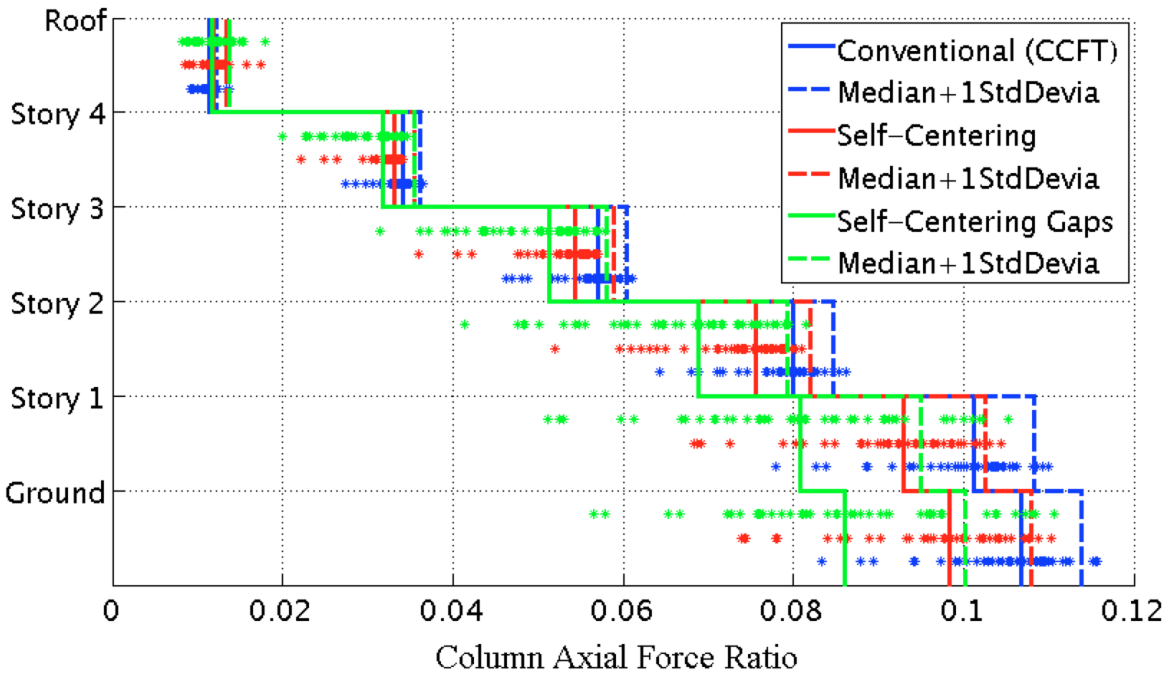

Appendix Figure L-115: Median of the peak axial force in columns under 44 DBE level ground motions with a GSR = 1.0 & damping = 2%

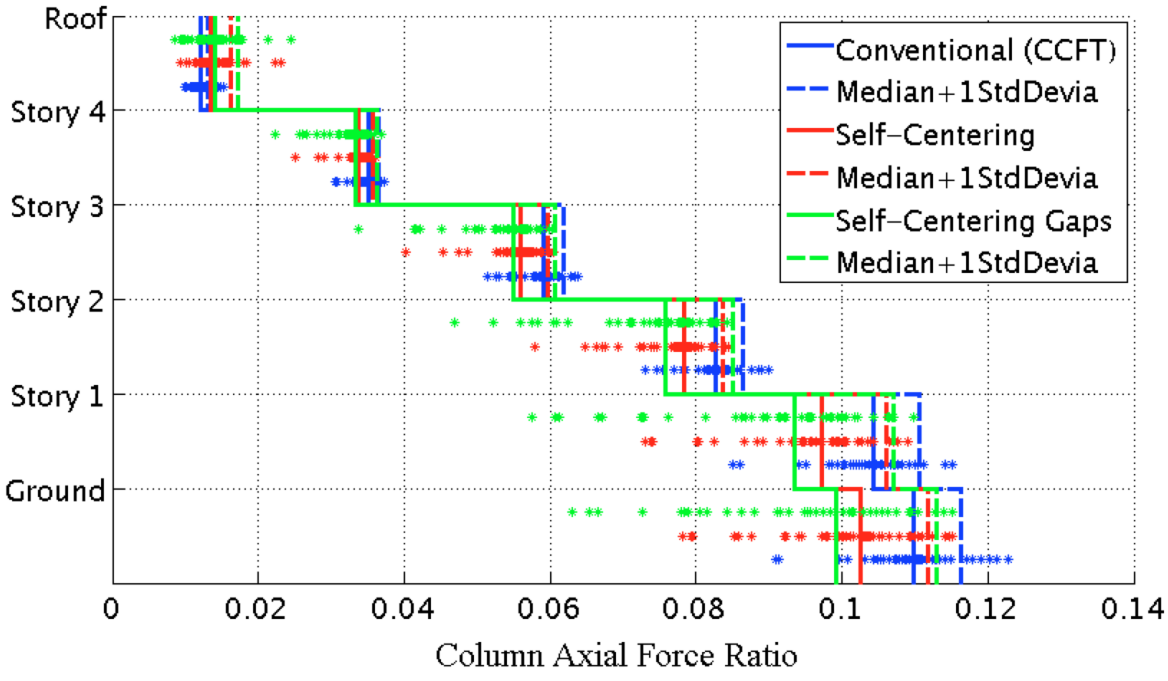

Appendix Figure L-116: Median of the peak axial force in columns under 44 MCE level ground motions with a GSR = 1.0 & damping = 2%

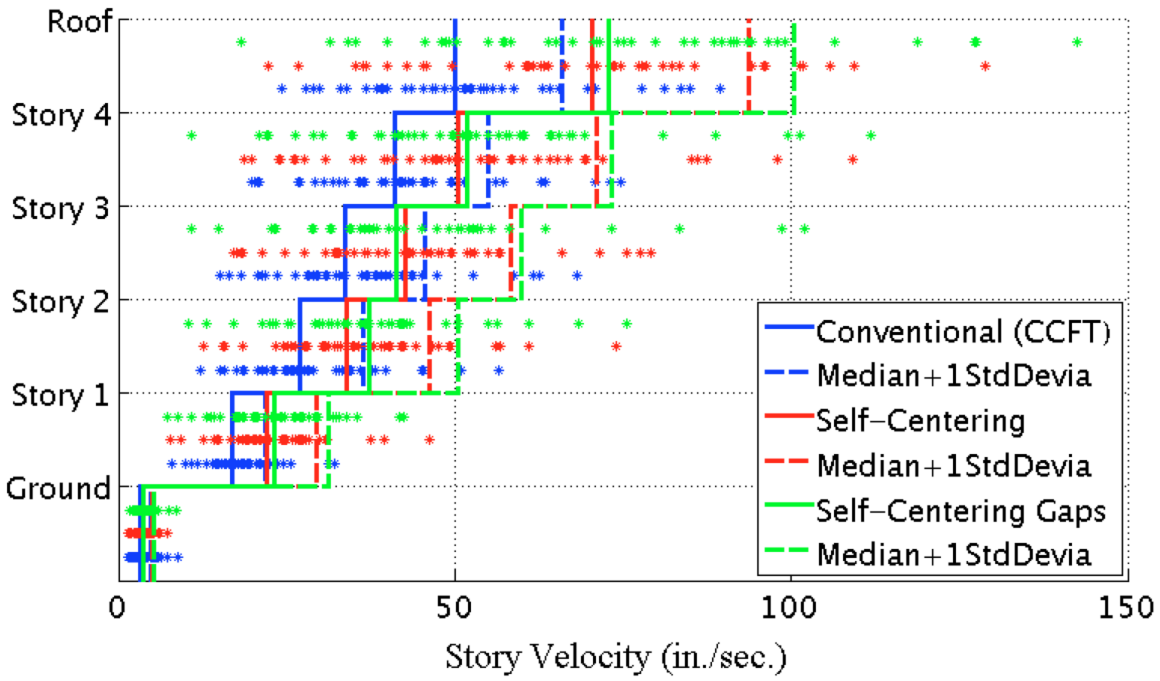

Appendix Figure L-117: Median of the peak story velocity under 44 DBE level ground motions with a GSR = 1.0 & damping = 2%

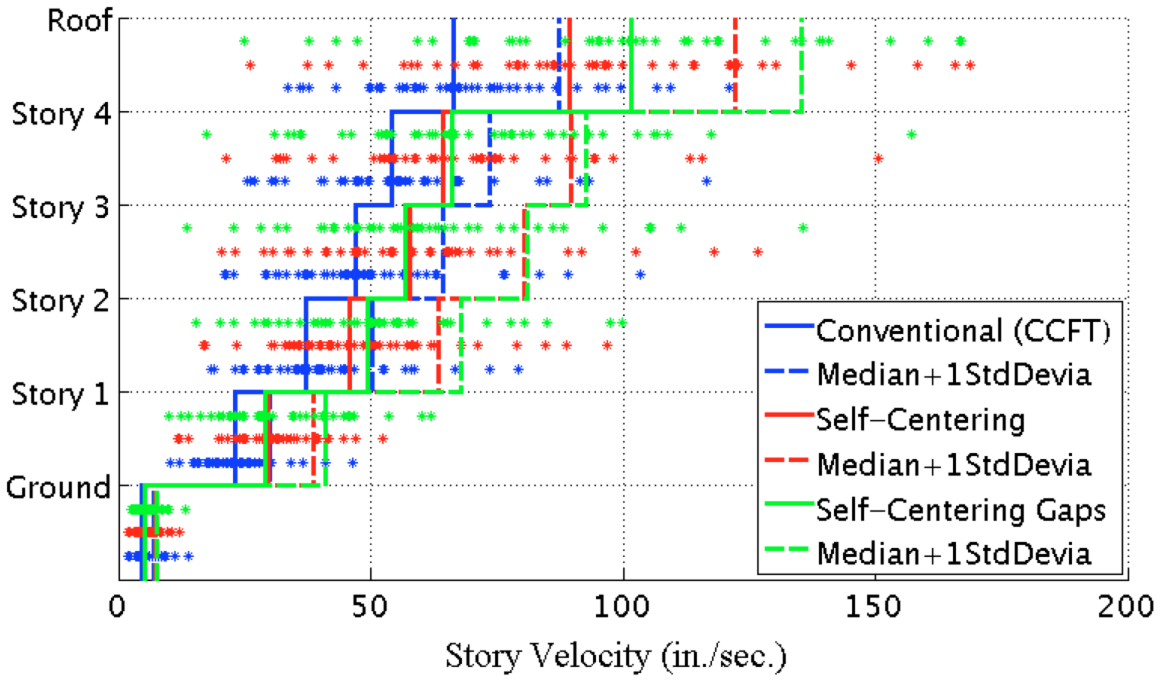

Appendix Figure L-118: Median of the peak story velocity under 44 MCE level ground motions with a GSR = 1.0 & damping = 2%

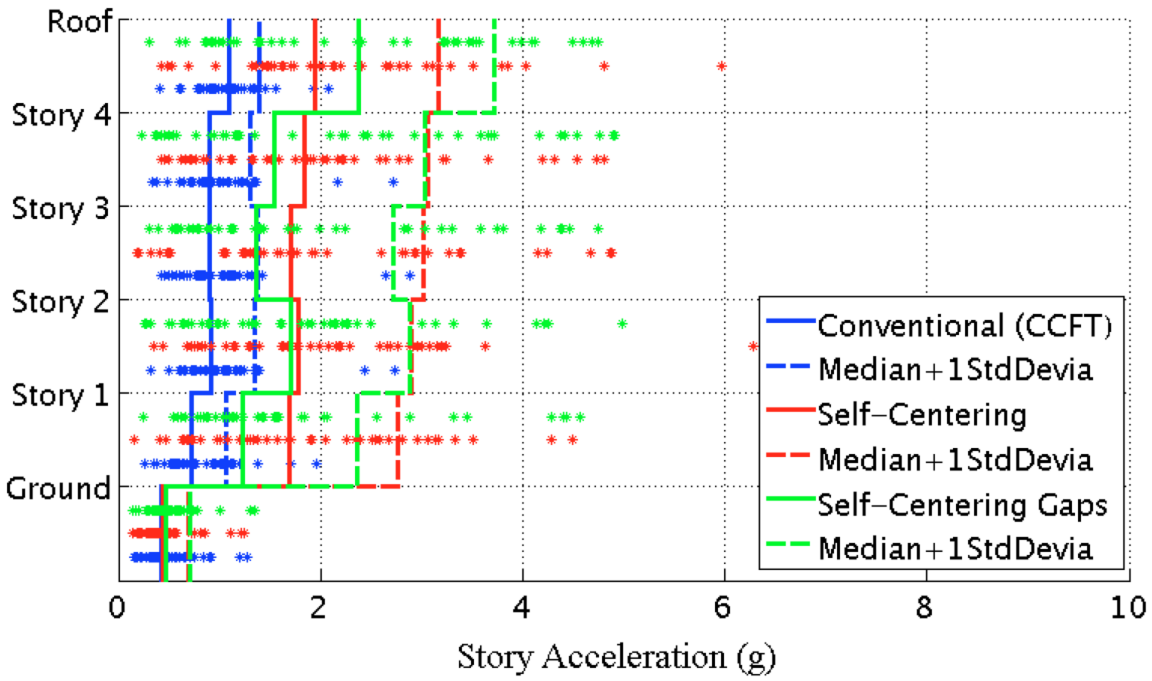

Appendix Figure L-119: Median of the peak story acceleration under 44 DBE level ground motions with a GSR = 1.0 & damping = 2%

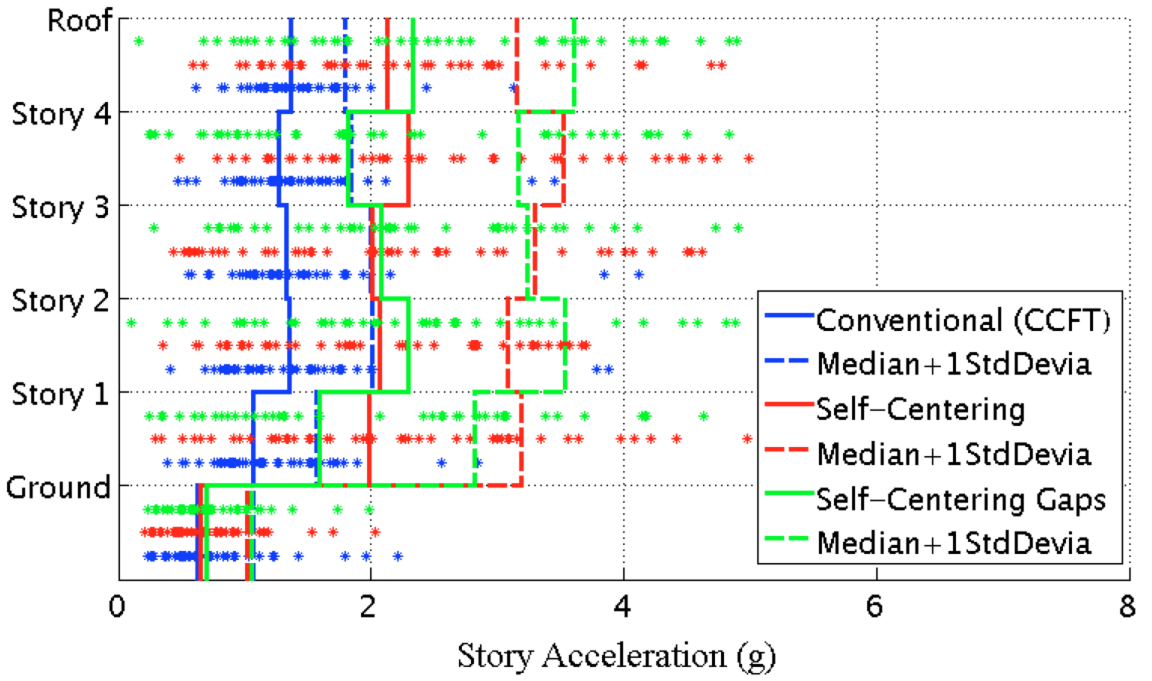

Appendix Figure L-120: Median of the peak story acceleration under 44 MCE level ground motions with a GSR = 1.0 & damping = 2%

L.5 Steel SMF with W Section Columns (Damping = 5%)

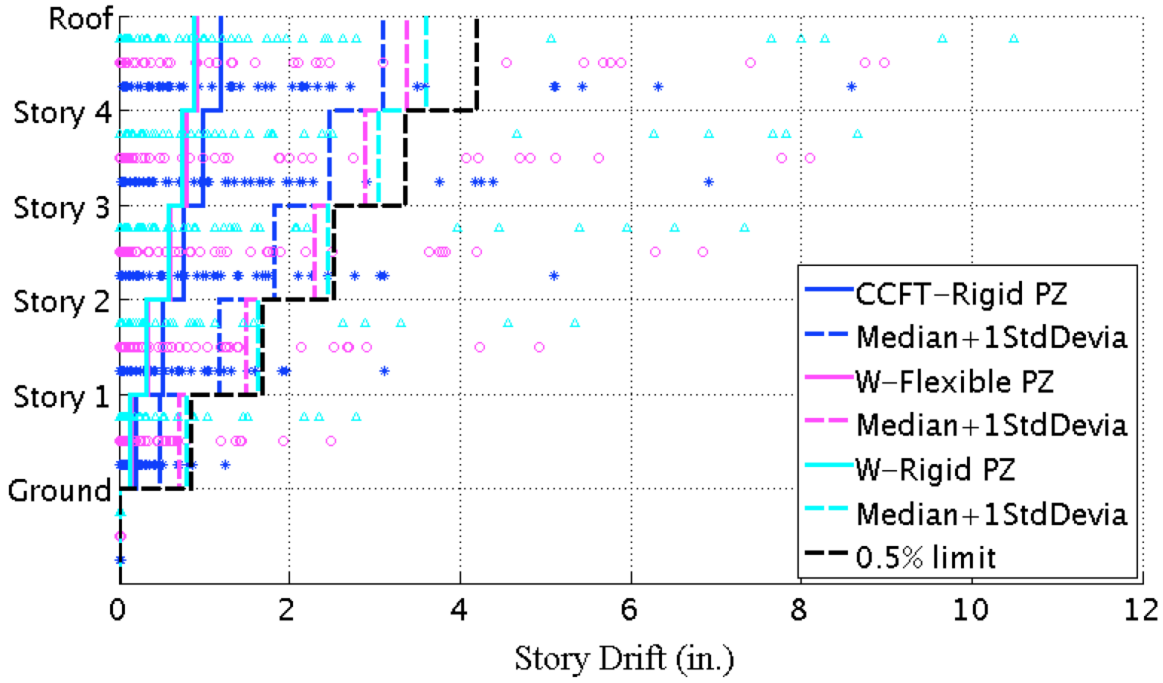

Appendix Figure L-121: Median of the maximum story residual drift under 44 DBE level ground motions with damping = 5% for steel SMFs and CSMF with a GSR = 0.9

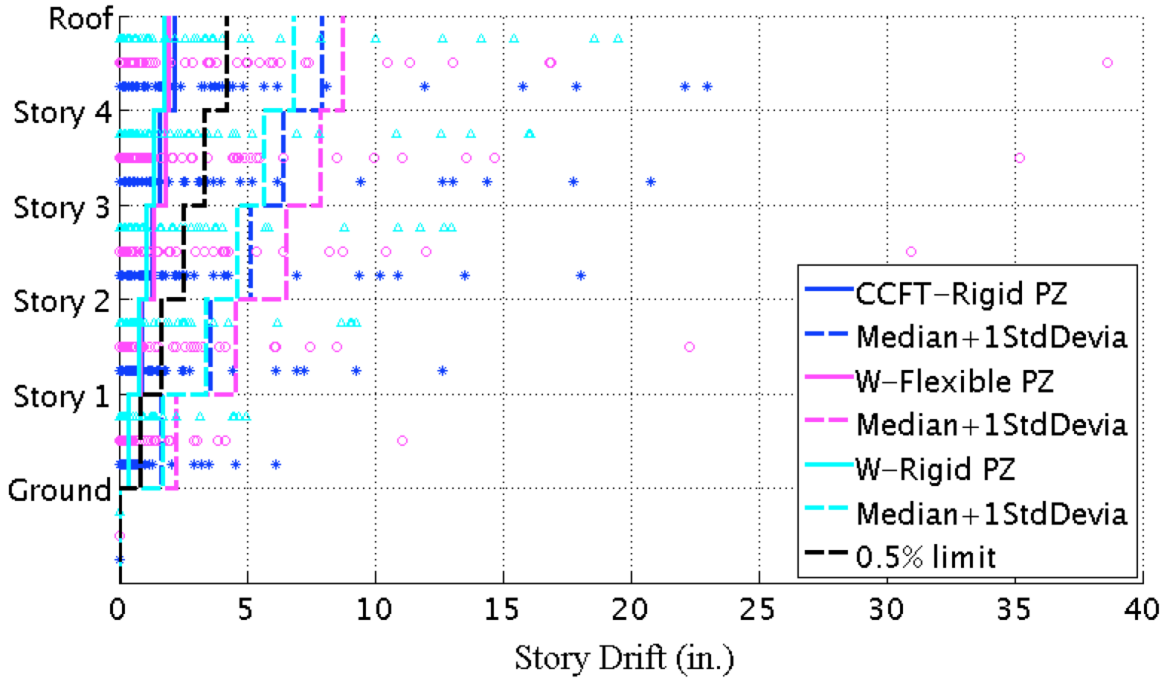

Appendix Figure L-122: Median of the maximum story residual drift under 44 MCE level ground motions with damping = 5% for steel SMFs and CSMF with a GSR = 0.9

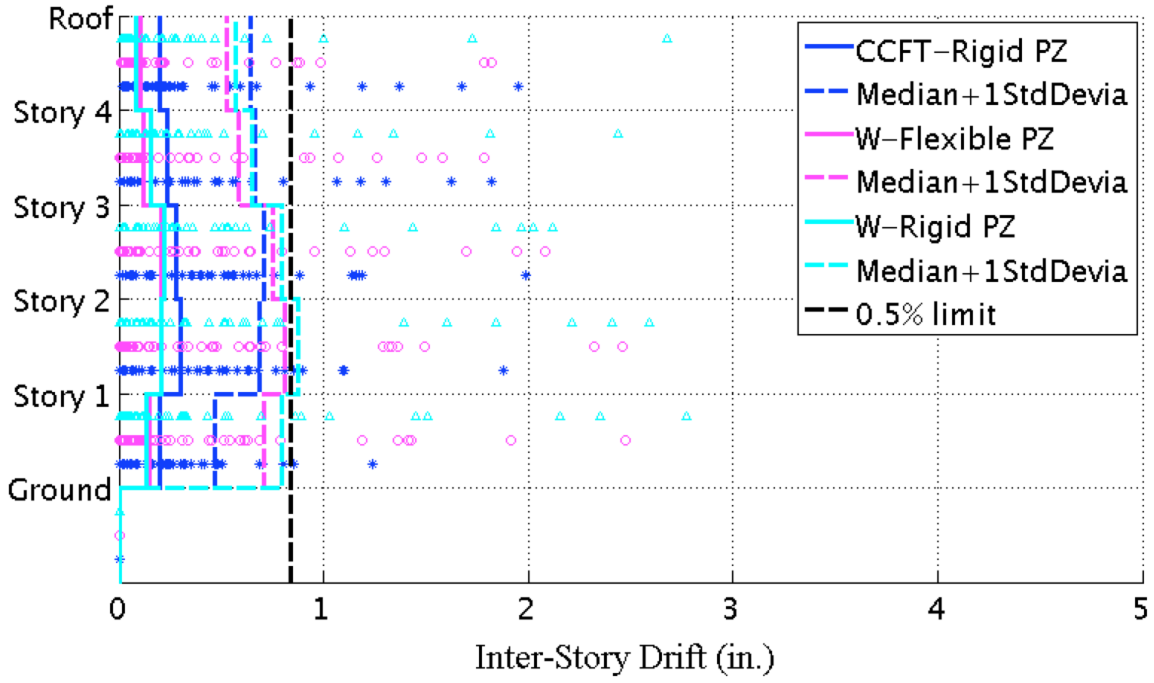

Appendix Figure L-123: Median of the maximum inter-story residual drift under 44 DBE level ground motions with damping = 5% for steel SMFs and CSMF with a GSR = 0.9

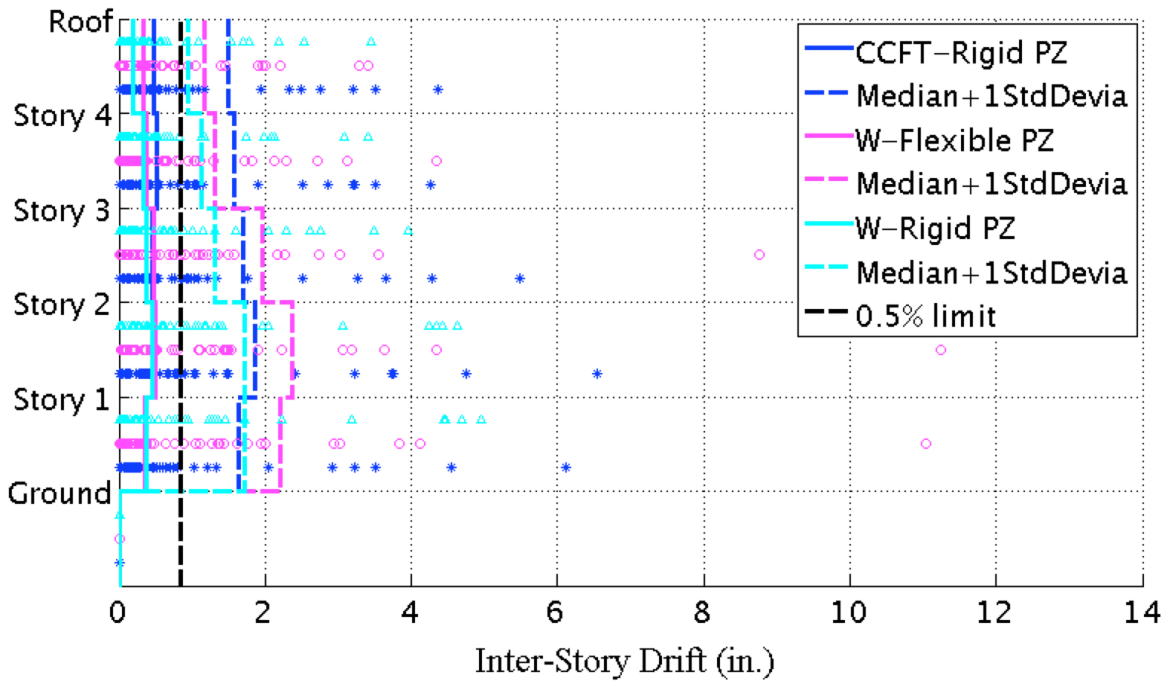

Appendix Figure L-124: Median of the maximum inter-story residual drift under 44 MCE level ground motions with damping = 5% for steel SMFs and CSMF with a GSR =

0.9

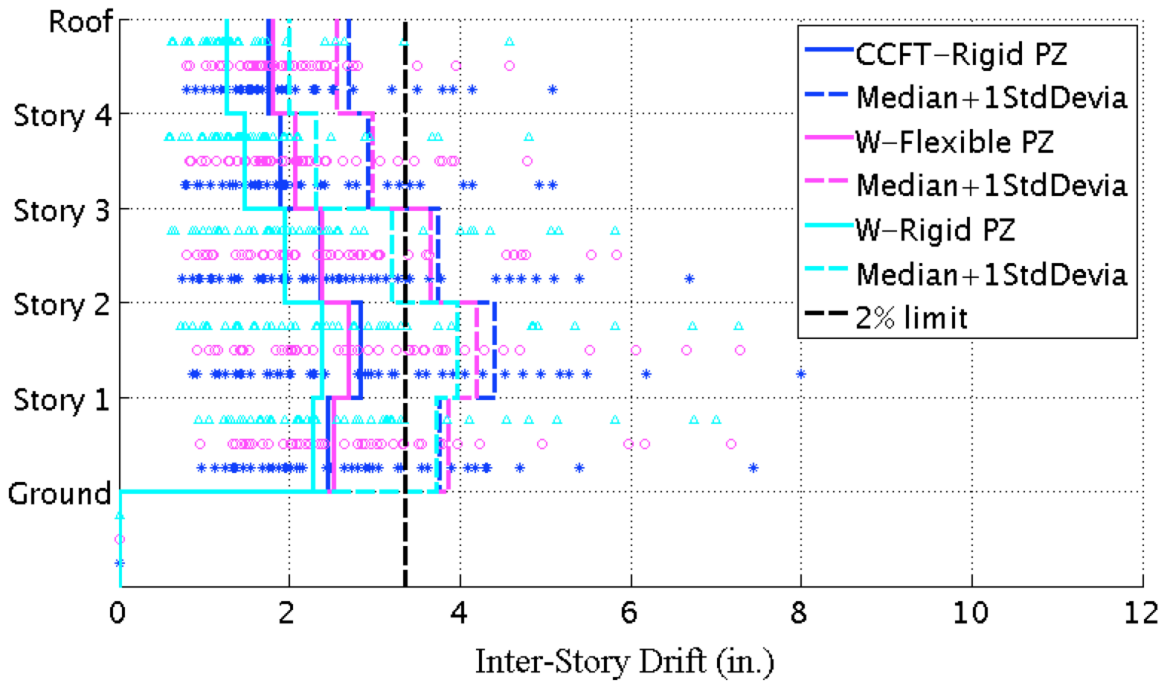

Appendix Figure L-125: Median of the peak inter-story drift under 44 DBE level ground motions with damping = 5% for steel SMFs and CSMF with a GSR = 0.9

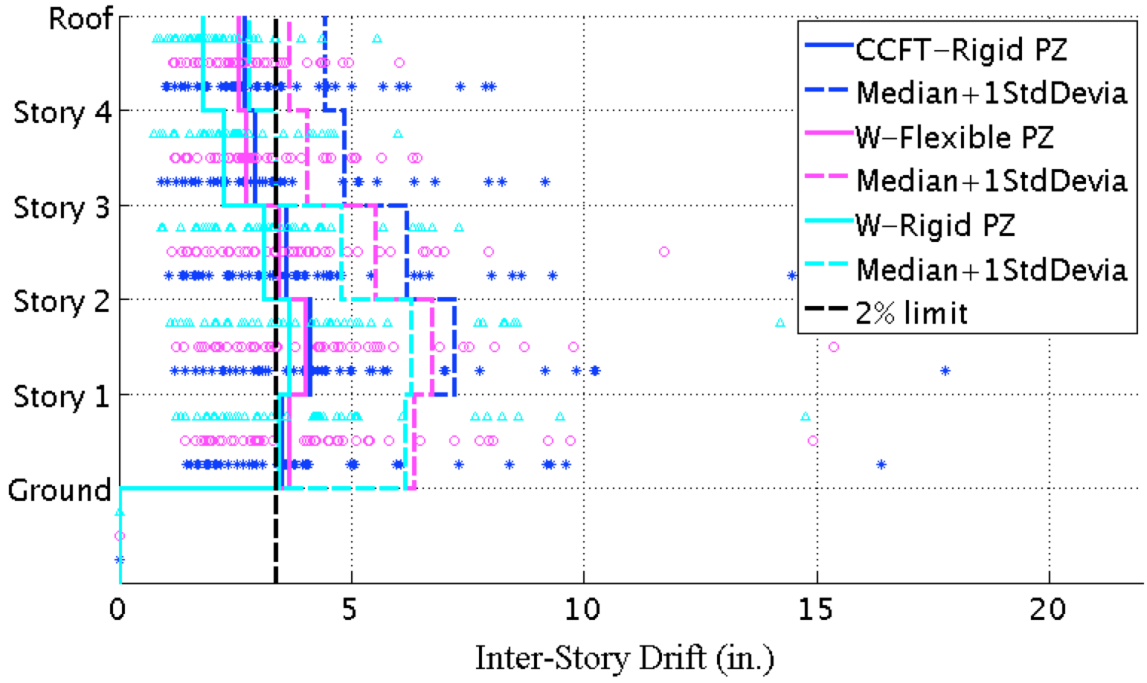

Appendix Figure L-126: Median of the peak inter-story drift under 44 MCE level ground

motions with damping = 5% for steel SMFs and CSMF with a GSR = 0.9

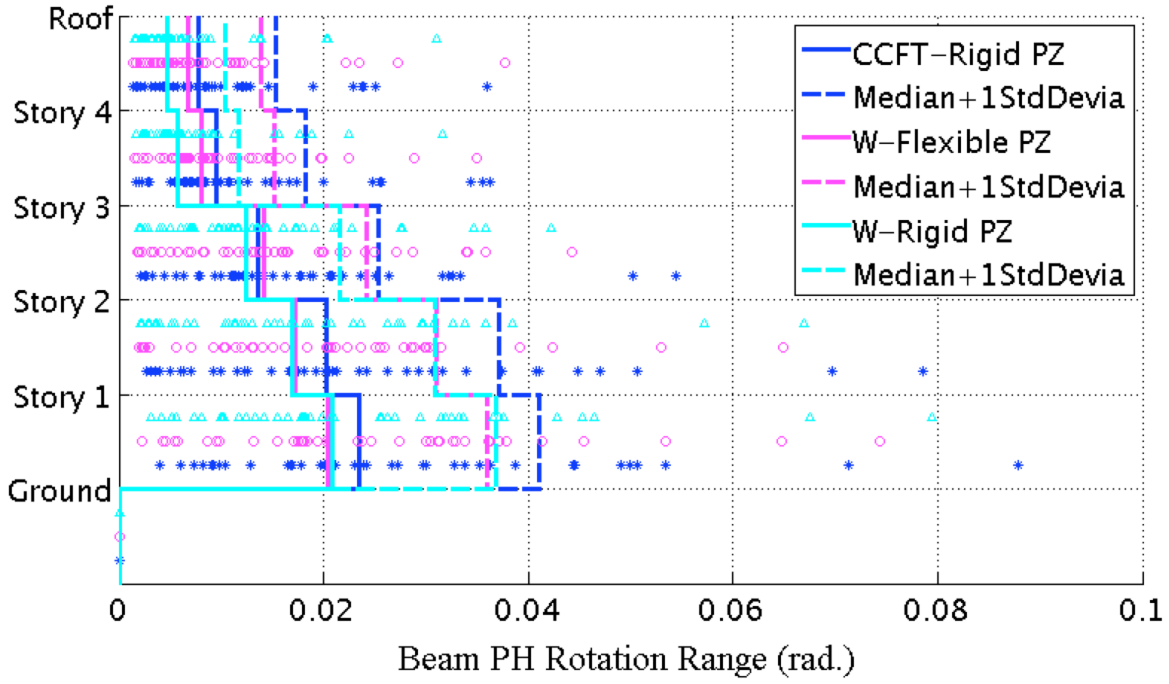

Appendix Figure L-127: Median of the beam PH rotation range under 44 DBE level ground motions with damping = 5% for steel SMFs and CSMF with a GSR = 0.9

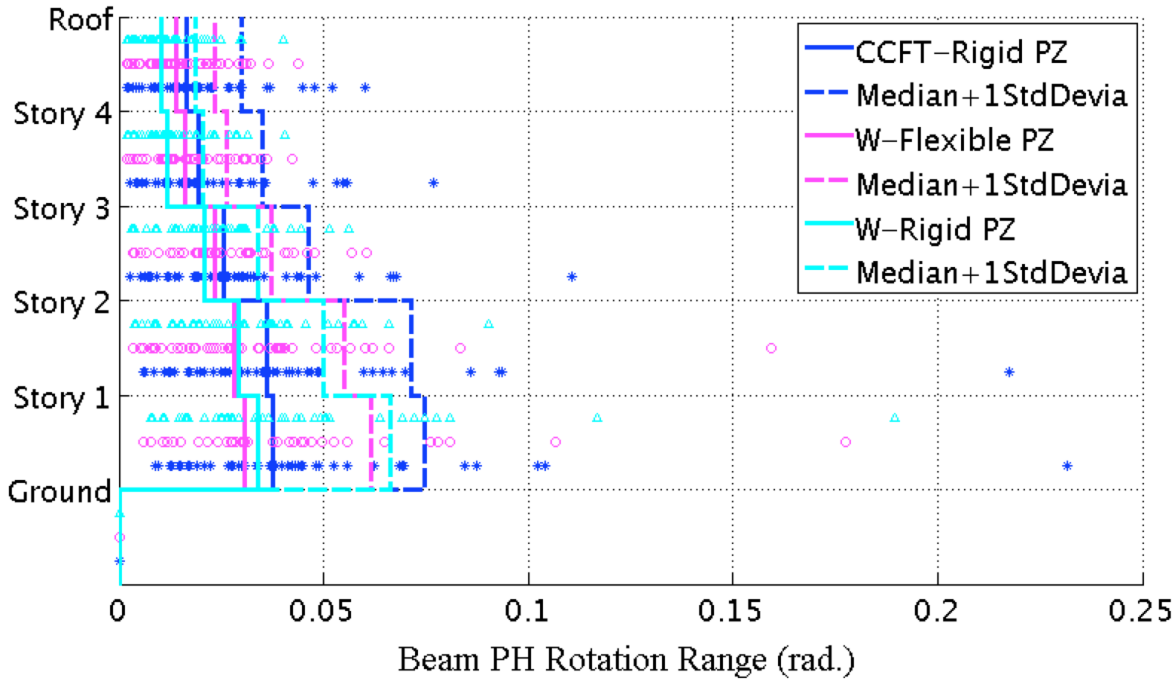

Appendix Figure L-128: Median of the beam PH rotation range under 44 MCE level

ground motions with damping = 5% for steel SMFs and CSMF with a GSR = 0.9

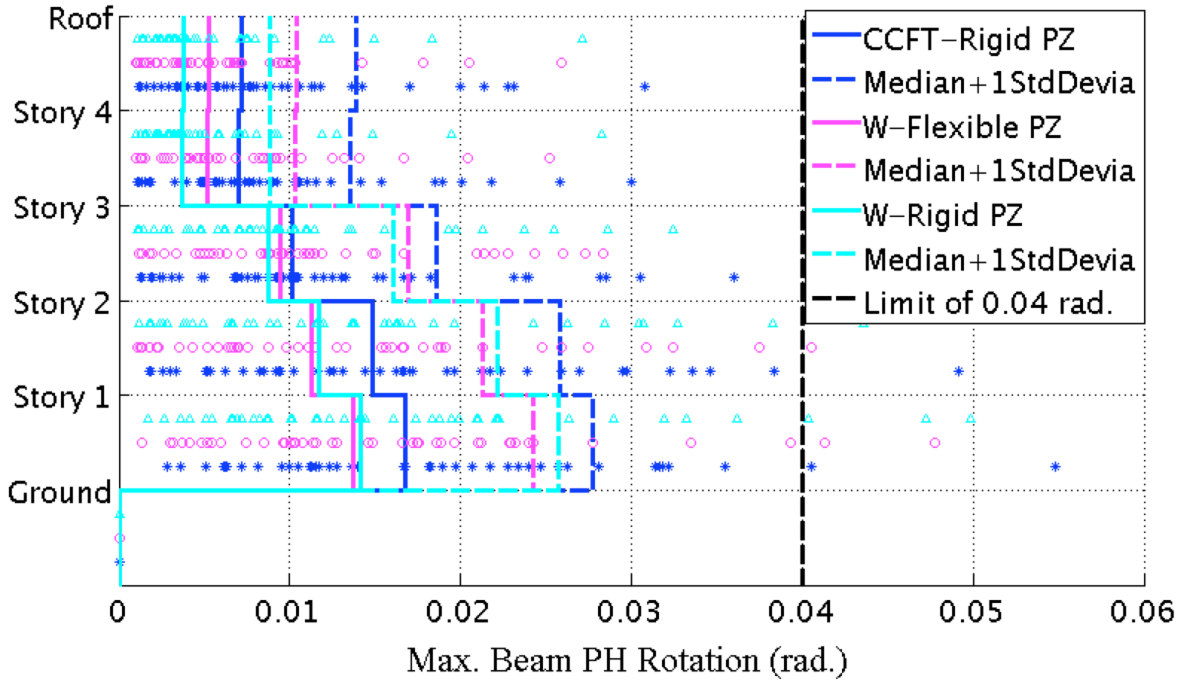

Appendix Figure L-129: Median of the maximum beam PH rotation under 44 DBE level ground motions with damping = 5% for steel SMFs and CSMF with a GSR = 0.9

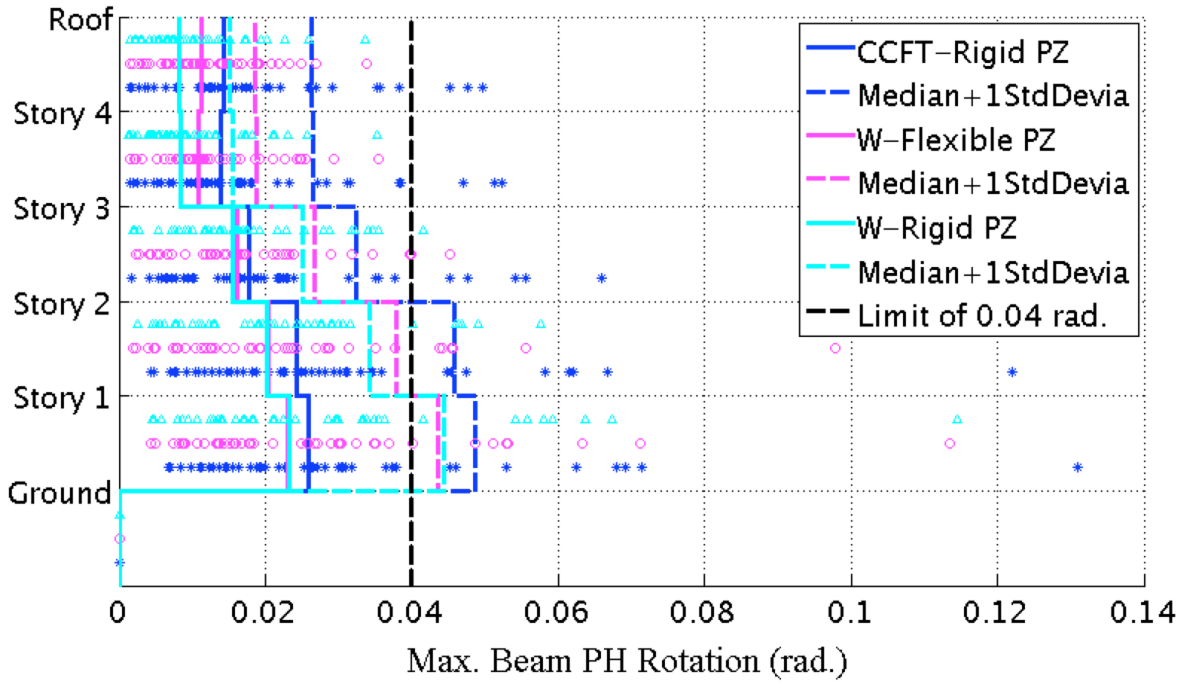

Appendix Figure L-130: Median of the maximum beam PH rotation under 44 MCE level

ground motions with damping = 5% for steel SMFs and CSMF with a GSR = 0.9

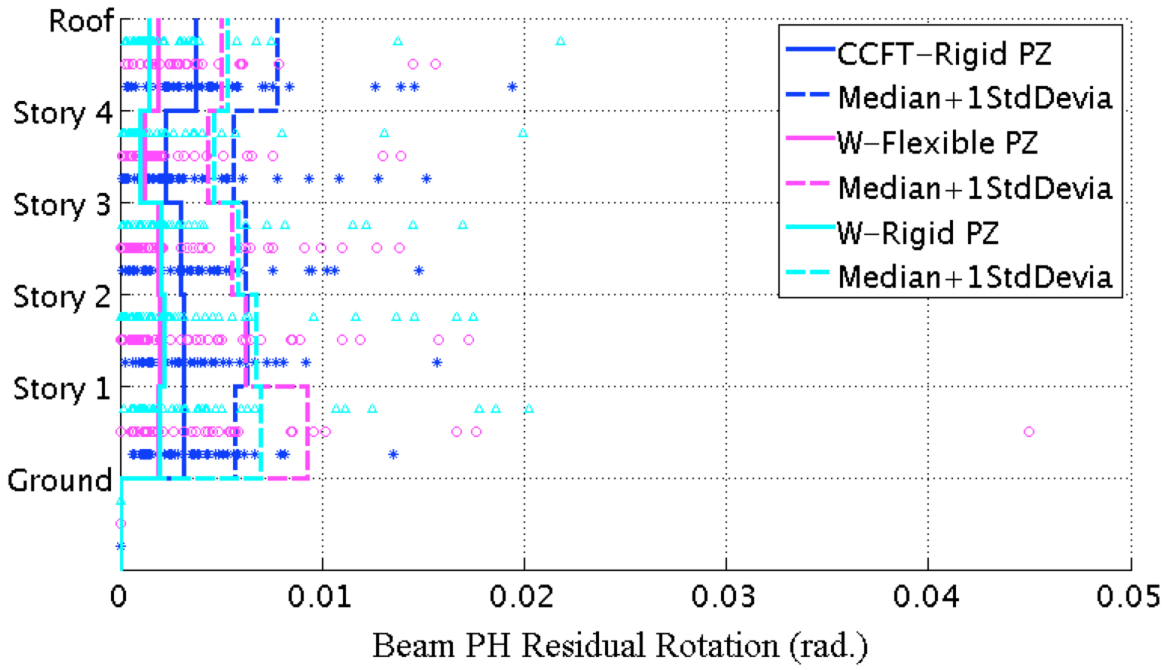

Appendix Figure L-131: Median of the maximum residual rotation of beam plastic hinges under 44 DBE level ground motions with damping = 5% for steel SMFs and CSMF with a GSR = 0.9

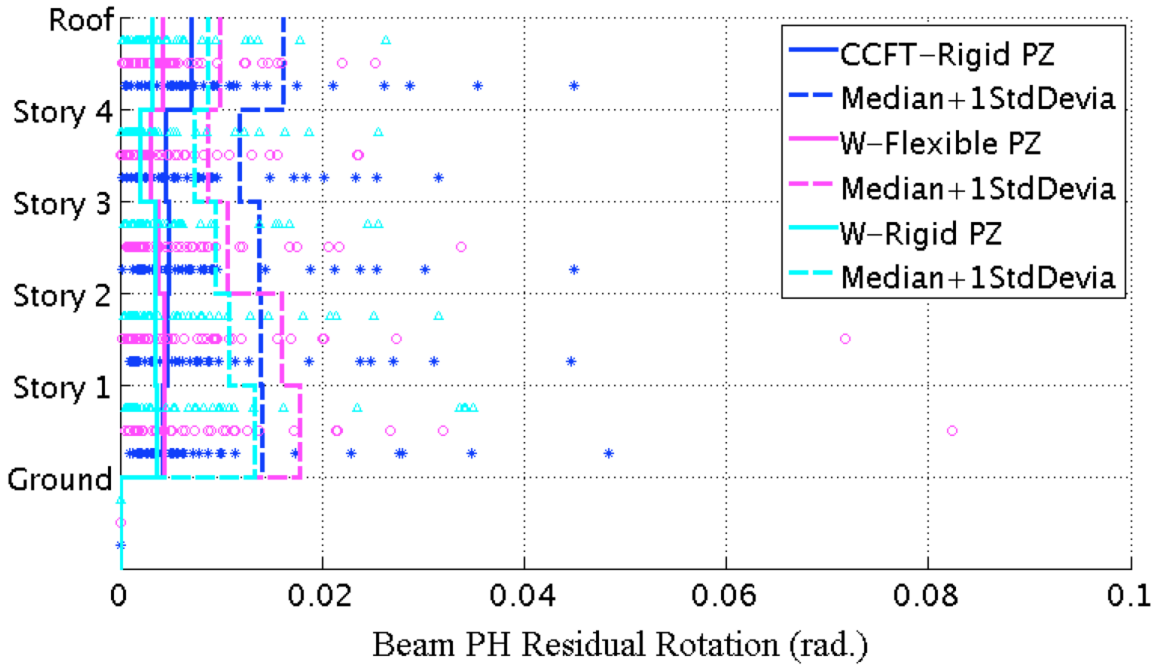

Appendix Figure L-132: Median of the maximum residual rotation of beam plastic hinges under 44 MCE level ground motions with damping = 5% for steel SMFs and CSMF with a GSR = 0.9

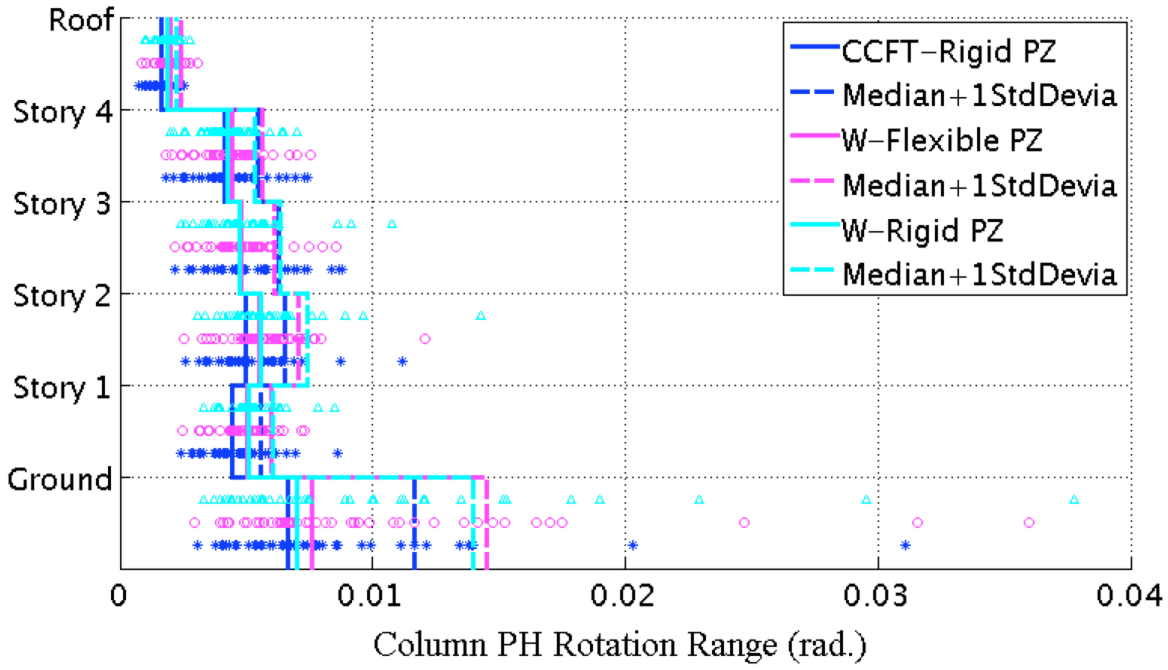

Appendix Figure L-133: Median of the column PH rotation range under 44 DBE level ground motions with damping = 5% for steel SMFs and CSMF with a GSR = 0.9

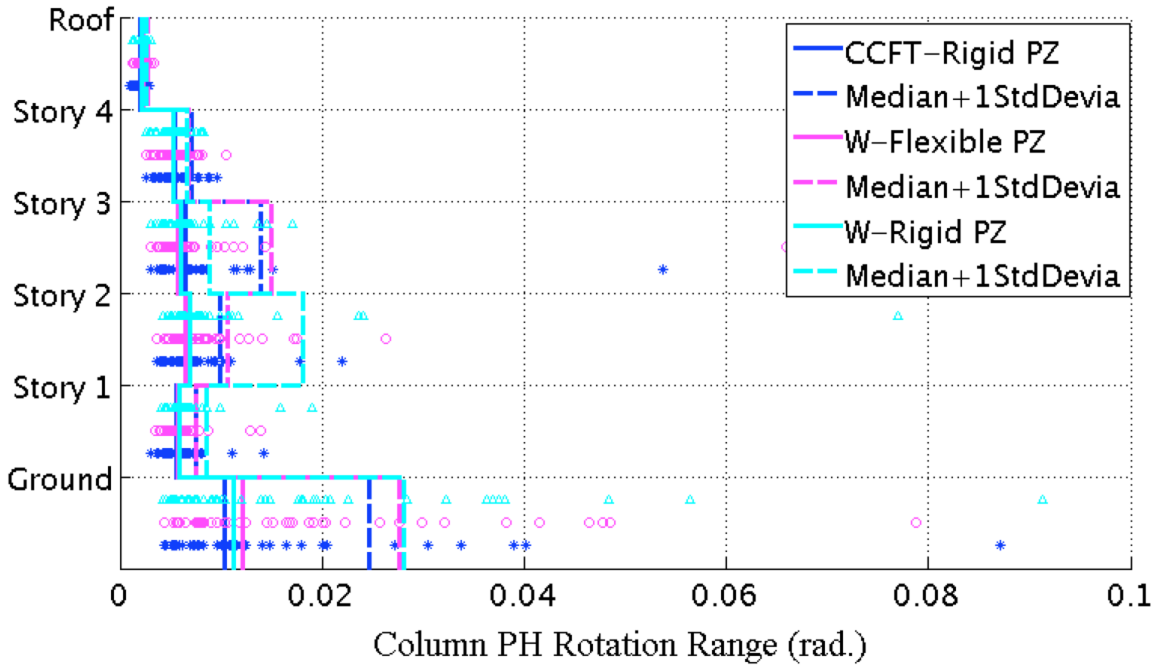

Appendix Figure L-134: Median of the column PH rotation range under 44 MCE level ground motions with damping = 5% for steel SMFs and CSMF with a GSR = 0.9

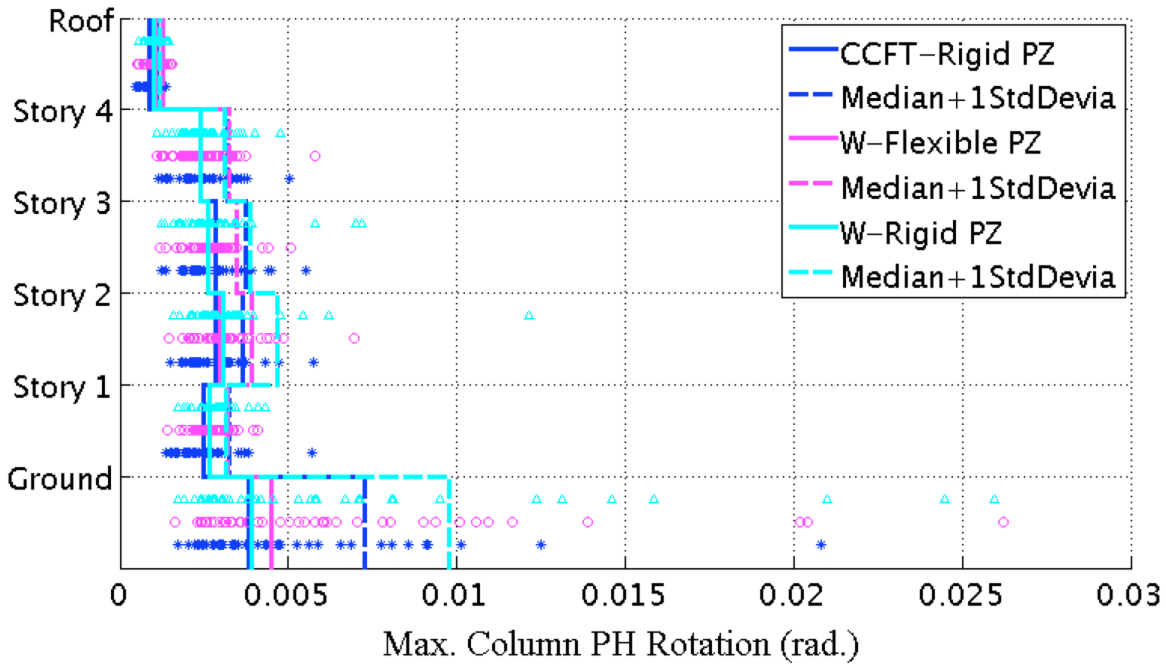

Appendix Figure L-135: Median of the maximum column PH rotation under 44 DBE level ground motions with damping = 5% for steel SMFs and CSMF with a GSR = 0.9

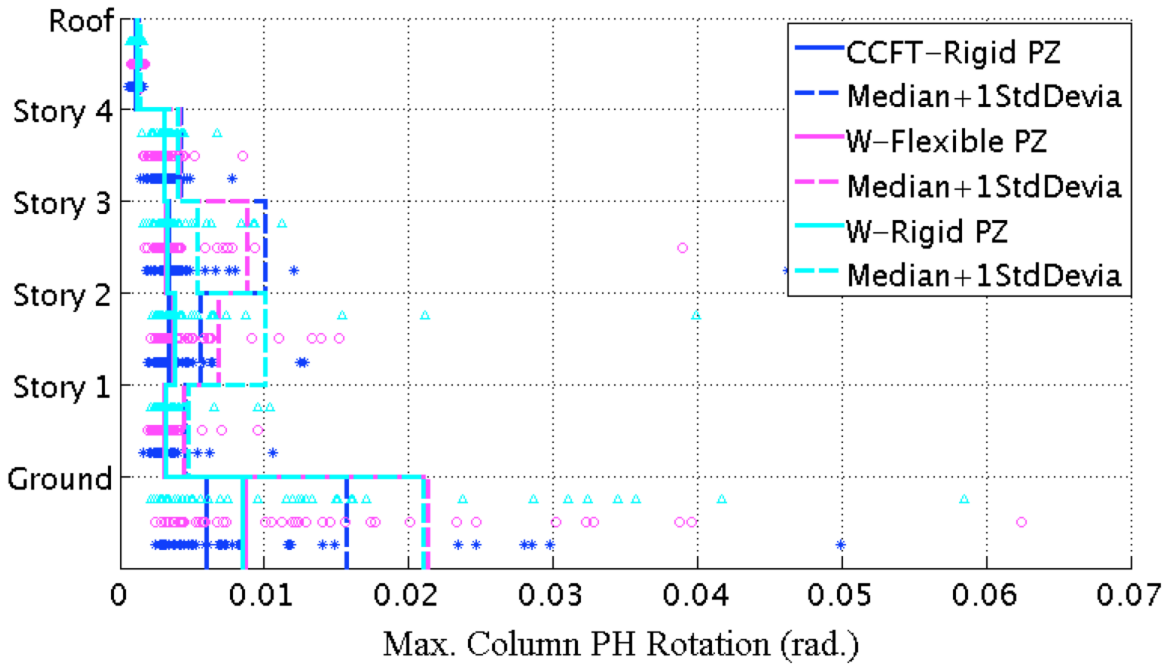

Appendix Figure L-136: Median of the maximum column PH rotation under 44 MCE

level ground motions with damping = 5% for steel SMFs and CSMF with a GSR = 0.9

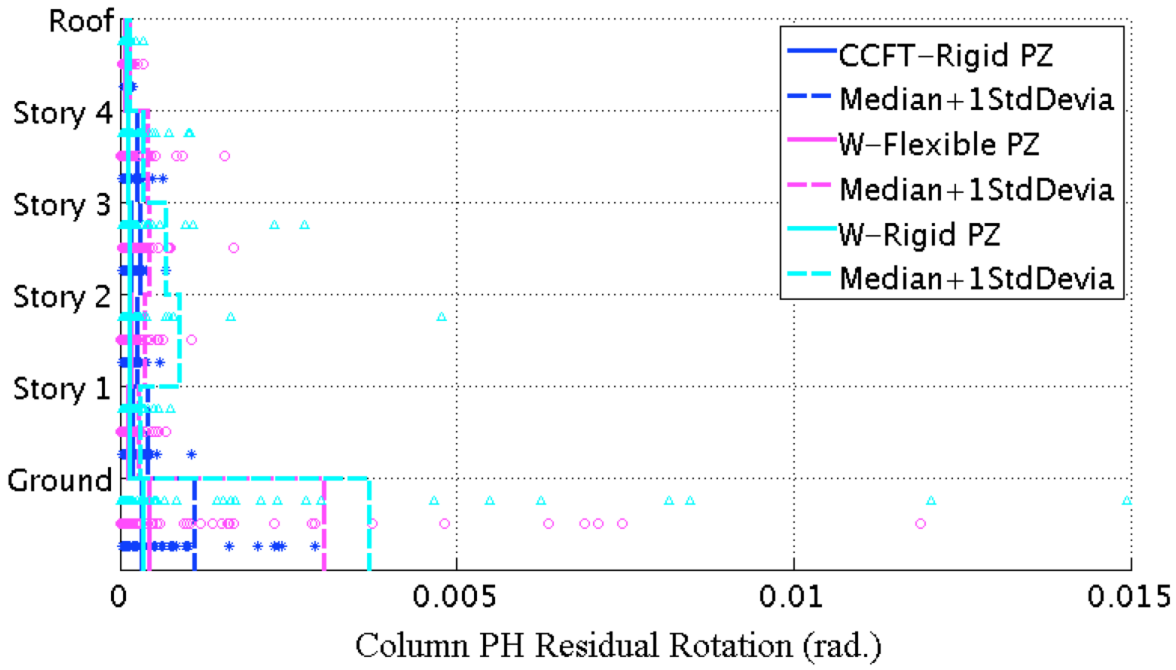

Appendix Figure L-137: Median of the maximum residual rotation of column plastic hinges under 44 DBE level ground motions with damping = 5% for steel SMFs and CSMF with a GSR = 0.9

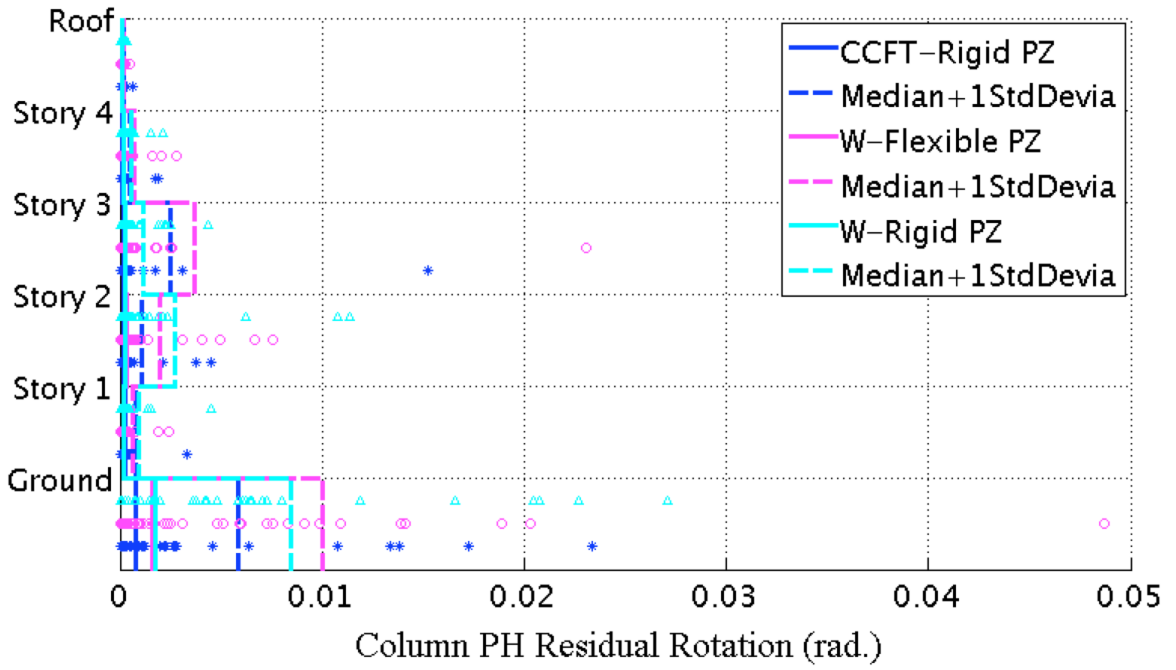

Appendix Figure L-138: Median of the maximum residual rotation of column plastic

hinges under 44 MCE level ground motions with damping = 5% for steel SMFs and CSMF with a GSR = 0.9

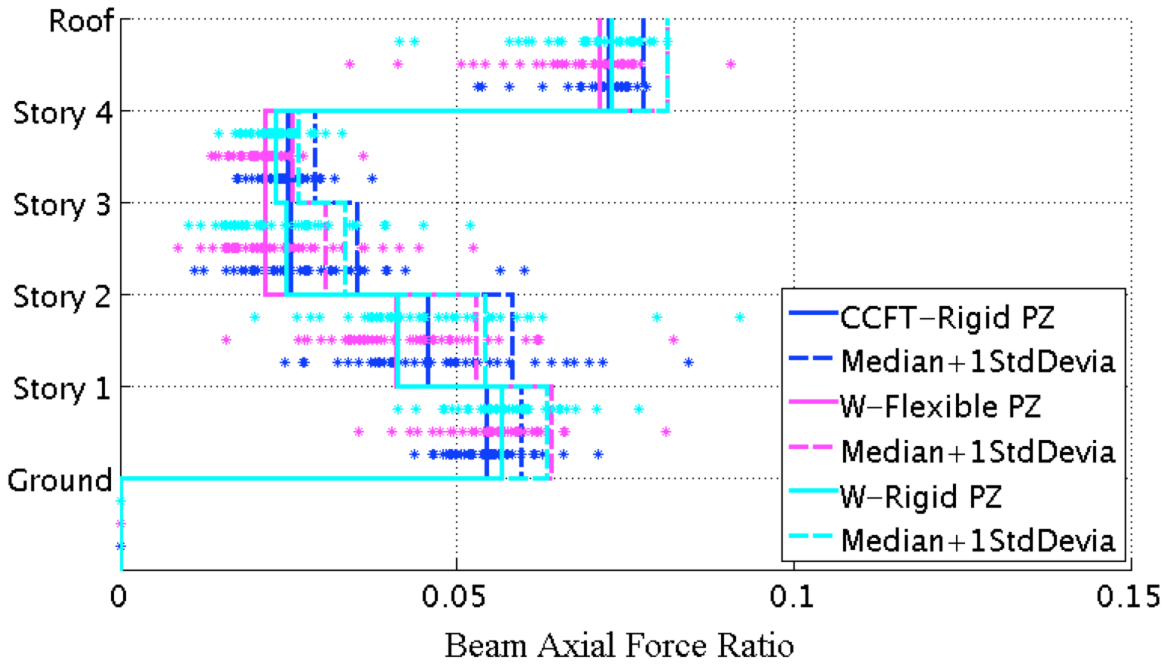

Appendix Figure L-139: Median of the peak axial force in beams under 44 DBE level ground motions with damping = 5% for steel SMFs and CSMF with a GSR = 0.9

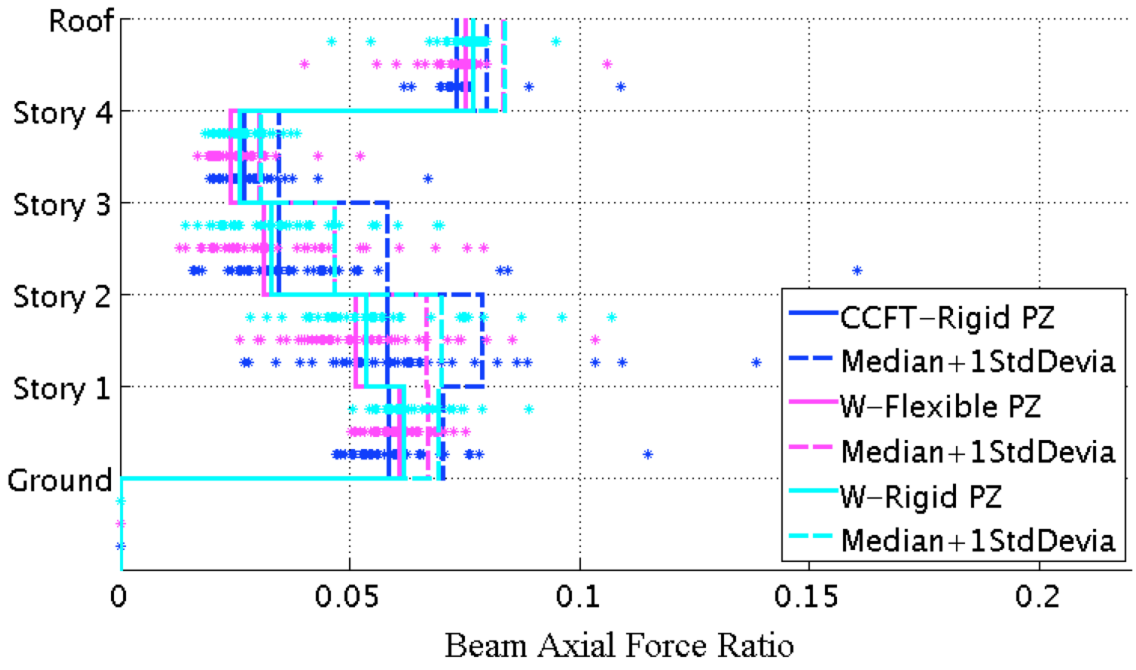

Appendix Figure L-140: Median of the peak axial force in beams under 44 MCE level

ground motions with damping = 5% for steel SMFs and CSMF with a GSR = 0.9

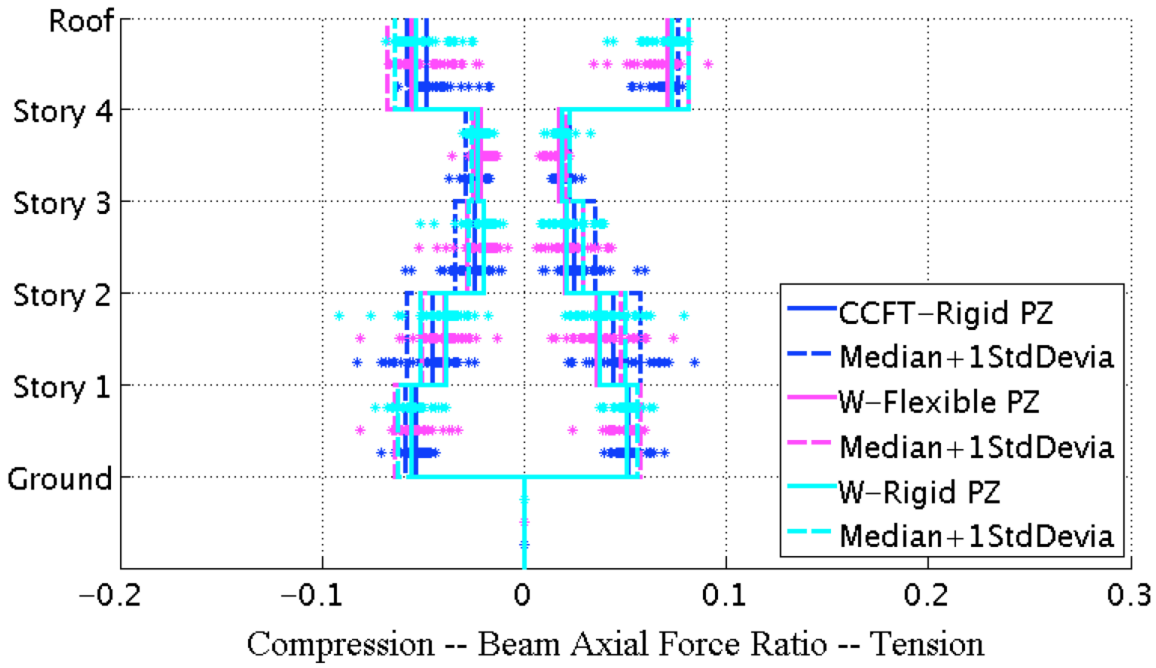

Appendix Figure L-141: Median of the peak tension vs.compression in beams under 44 DBE level ground motions with damping = 5% for steel SMFs and CSMF with a GSR = 0.9

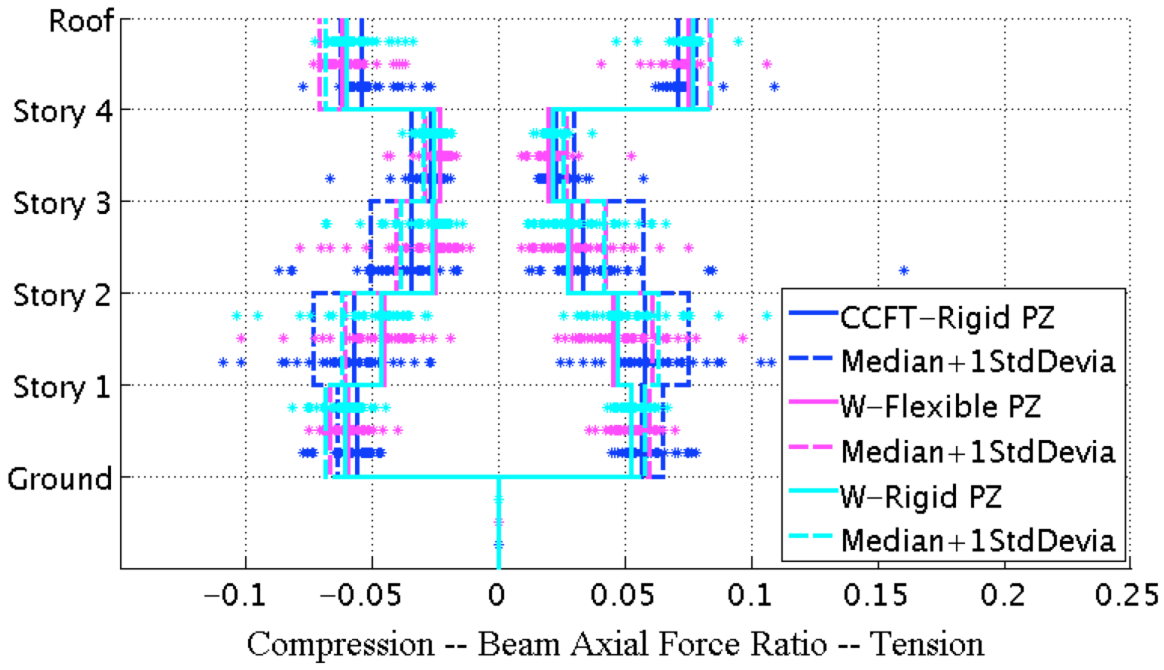

Appendix Figure L-142: Median of the peak tension vs.compression in beams under 44

MCE level ground motions with damping = 5% for steel SMFs and CSMF with a GSR = 0.9

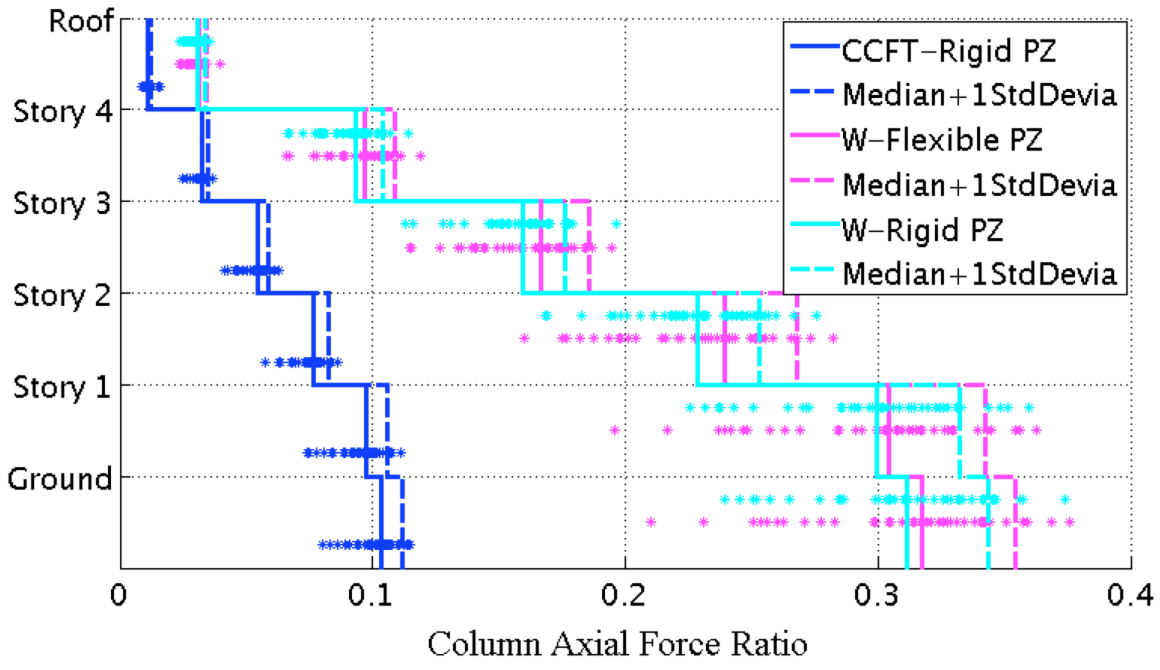

Appendix Figure L-143: Median of the peak axial force in columns under 44 DBE level ground motions with damping = 5% for steel SMFs and CSMF with a GSR = 0.9

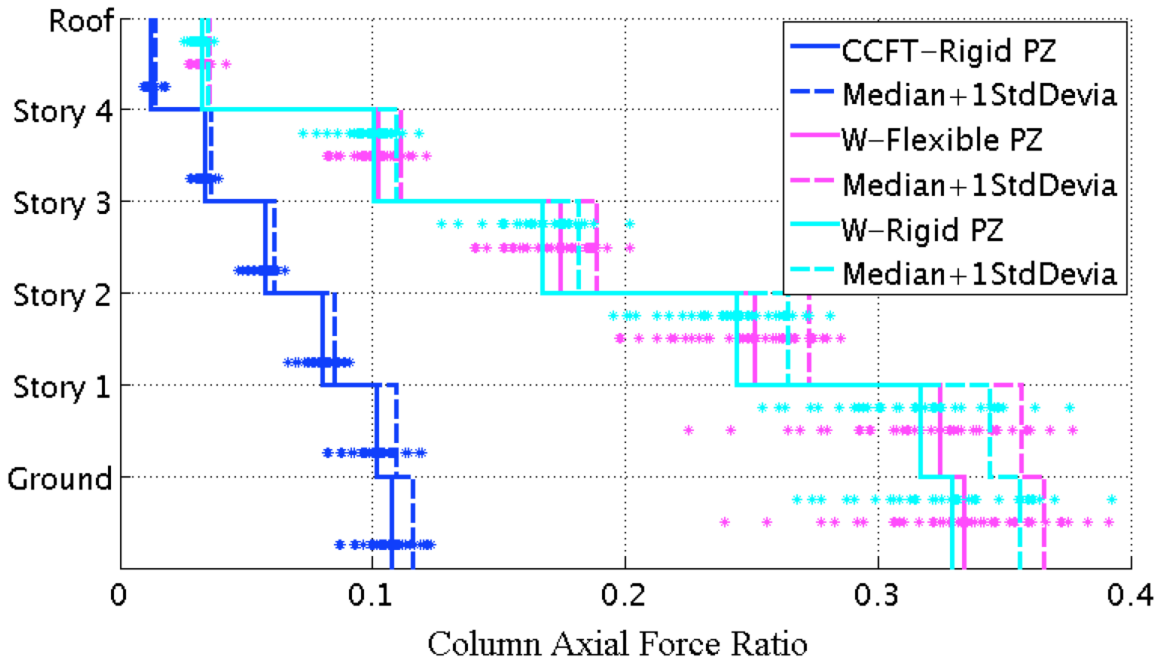

Appendix Figure L-144: Median of the peak axial force in columns under 44 MCE level

ground motions with damping = 5% for steel SMFs and CSMF with a GSR = 0.9

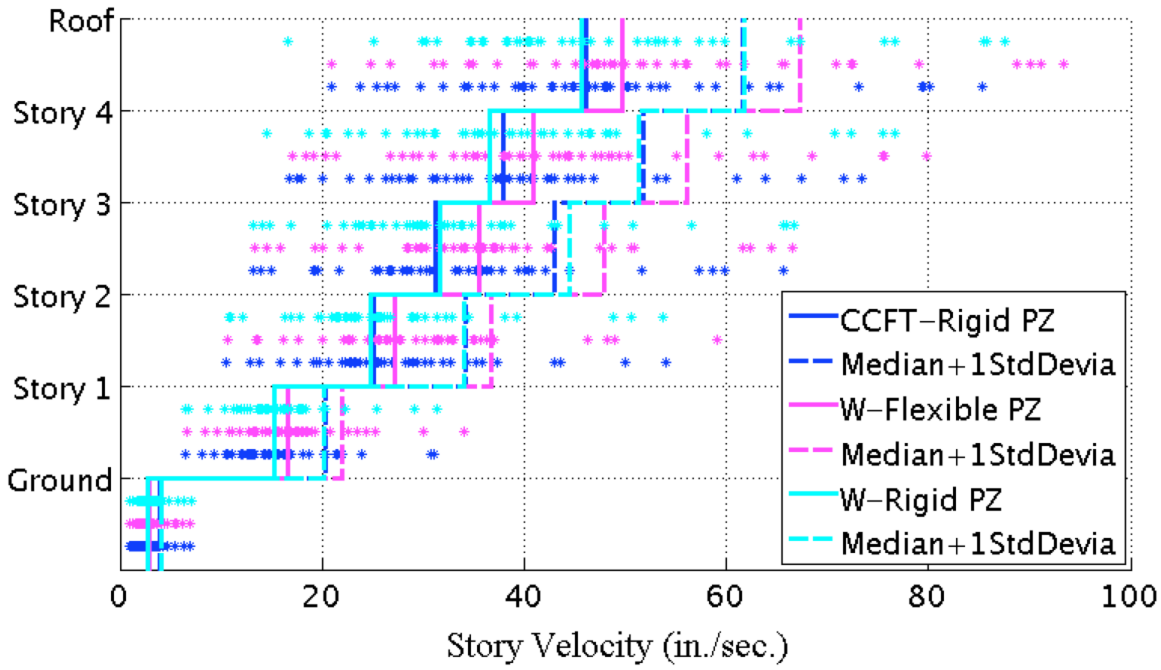

Appendix Figure L-145: Median of the peak story velocity under 44 DBE level ground motions with damping = 5% for steel SMFs and CSMF with a GSR = 0.9

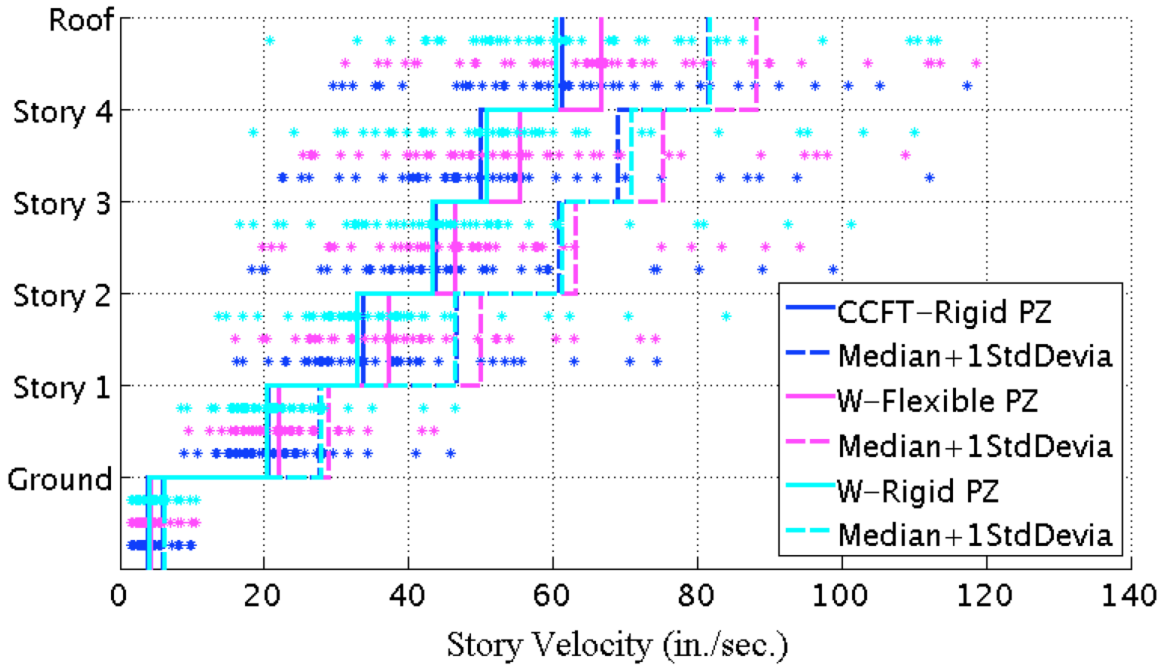

Appendix Figure L-146: Median of the peak story velocity under 44 MCE level ground

motions with damping = 5% for steel SMFs and CSMF with a GSR = 0.9

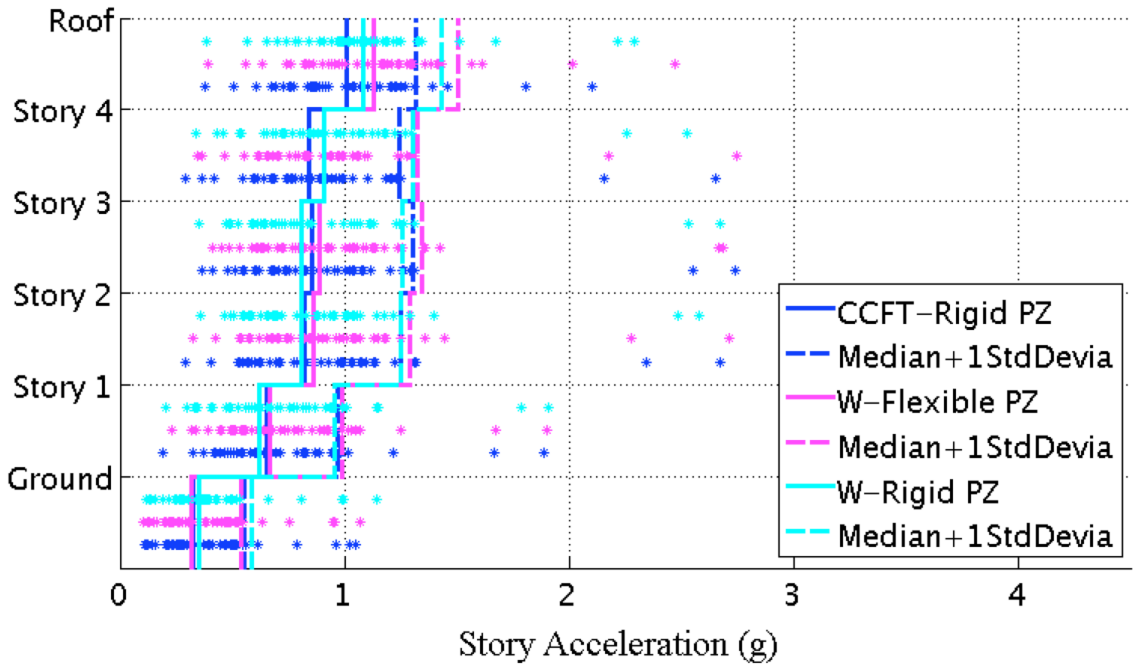

Appendix Figure L-147: Median of the peak story acceleration under 44 DBE level ground motions with damping = 5% for steel SMFs and CSMF with a GSR = 0.9

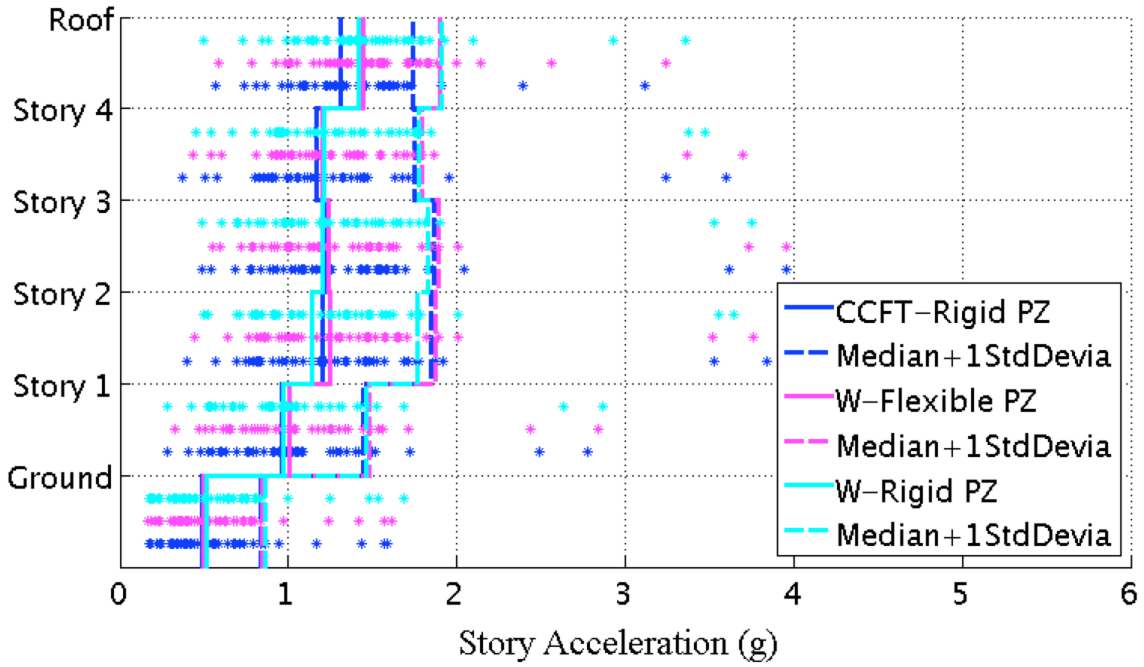

Appendix Figure L-148: Median of the peak story acceleration under 44 MCE level

ground motions with damping = 5% for steel SMFs and CSMF with a GSR = 0.9

L.6 Steel SMF with W Section Columns (Damping = 2%)

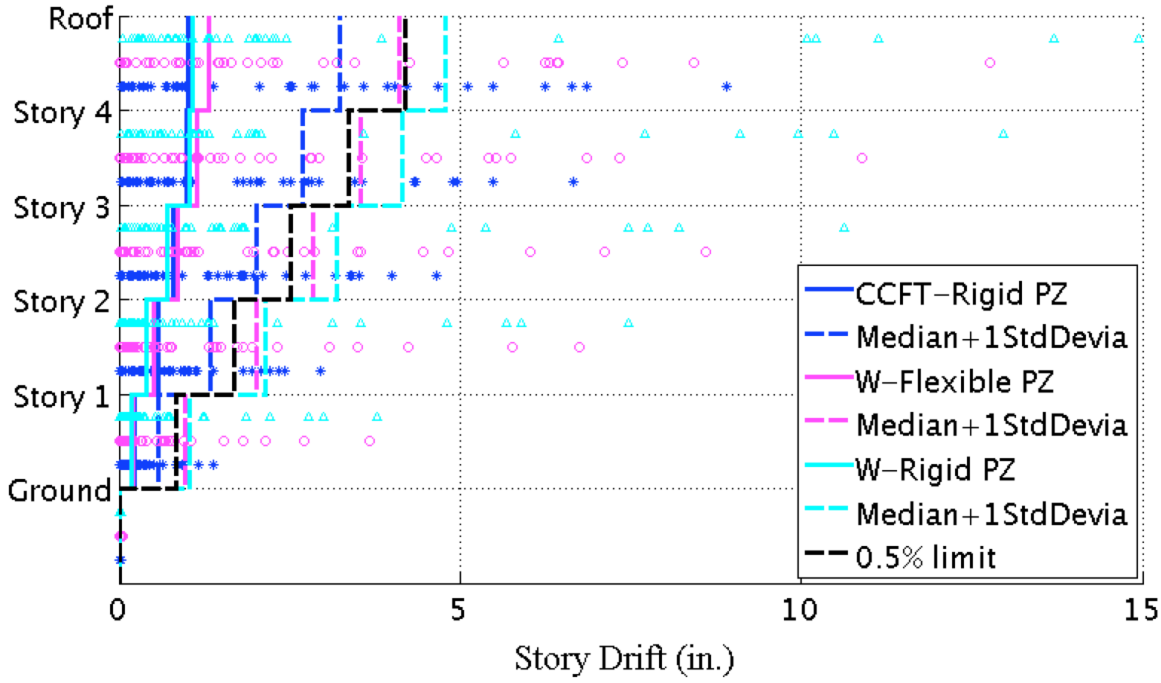

Appendix Figure L-149: Median of the maximum story residual drift under 44 DBE level ground motions with damping = 2% for steel SMFs and CSMF with a GSR = 0.9

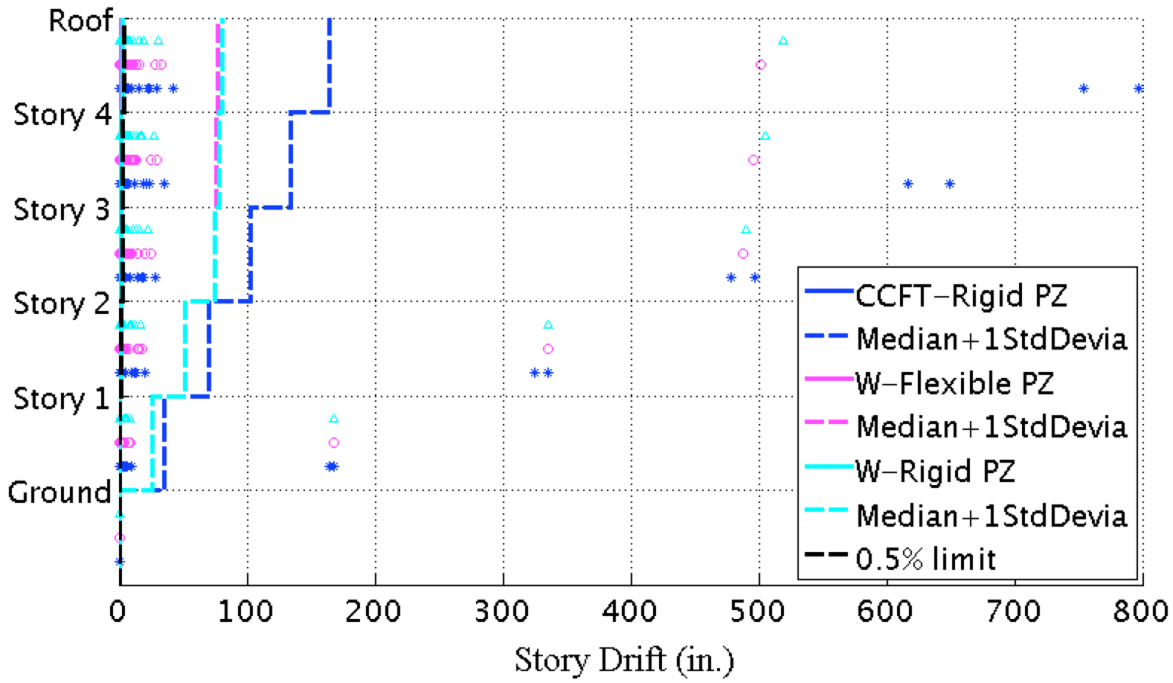

Appendix Figure L-150: Median of the maximum story residual drift under 44 MCE level ground motions with damping = 2% for steel SMFs and CSMF with a GSR = 0.9

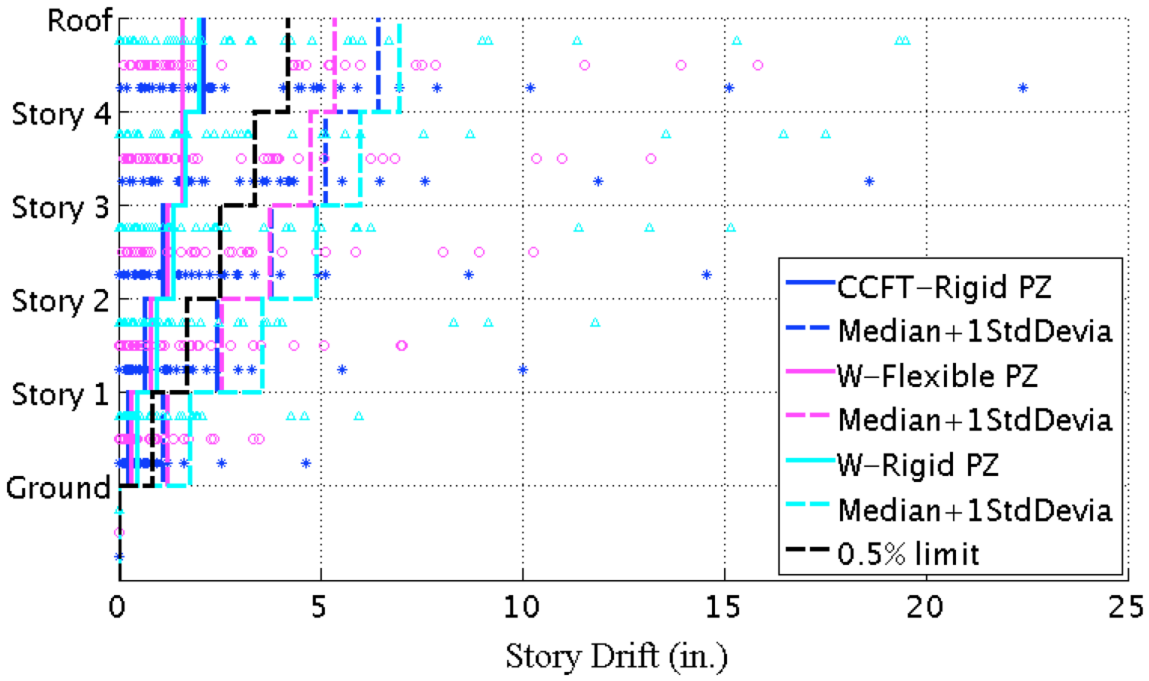

Appendix Figure L-151: Replot of Appendix Figure L-150 under the 'Filtered 44' ground motions

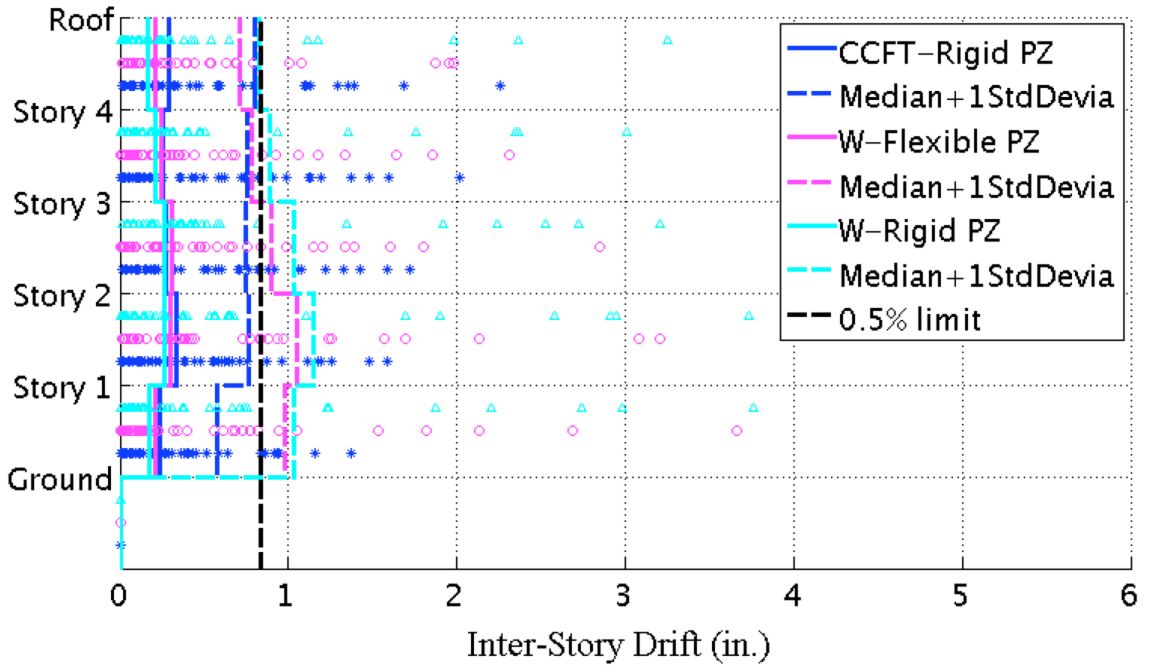

Appendix Figure L-152: Median of the maximum inter-story residual drift under 44 DBE level ground motions with damping = 2% for steel SMFs and CSMF with a GSR = 0.9

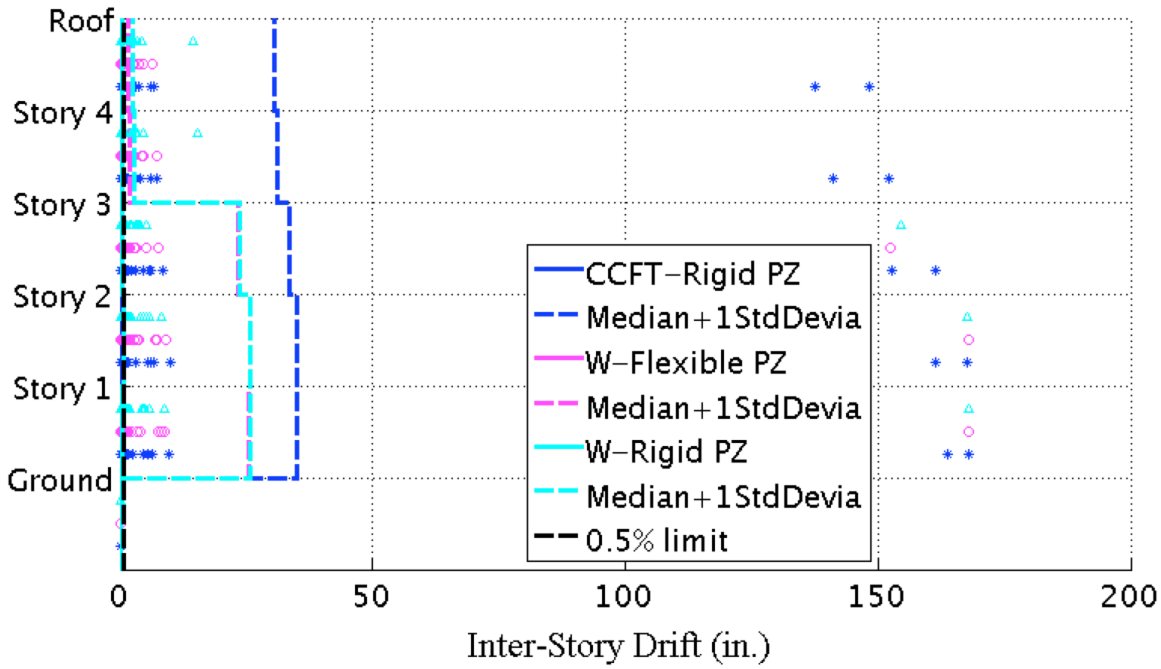

Appendix Figure L-153: Median of the maximum inter-story residual drift under 44 MCE level ground motions with damping = 2% for steel SMFs and CSMF with a GSR = 0.9

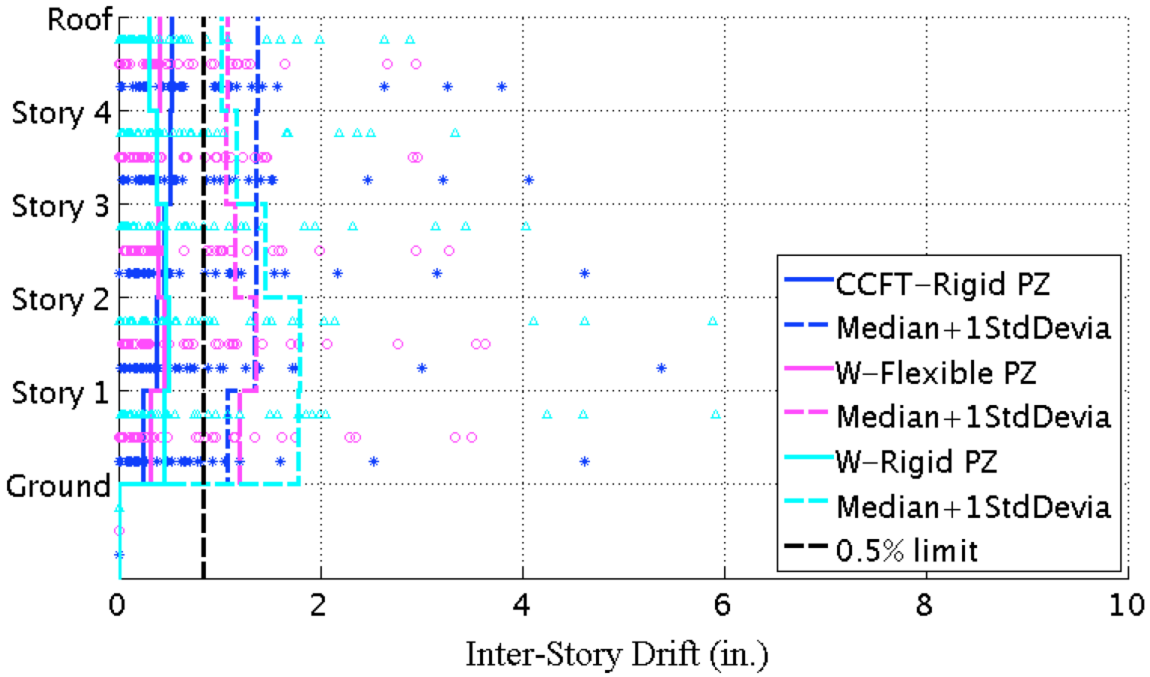

Appendix Figure L-154: Replot of Appendix Figure L-153 under the 'Filtered 44' ground motions

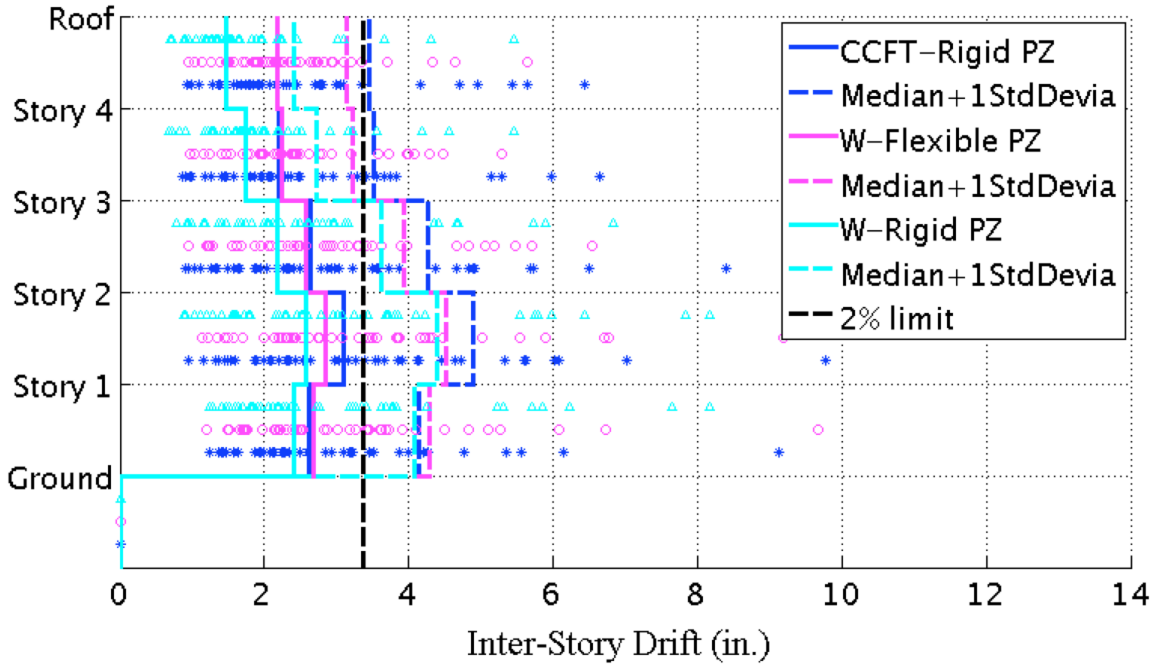

Appendix Figure L-155: Median of the peak inter-story drift under 44 DBE level ground motions with damping = 2% for steel SMFs and CSMF with a GSR = 0.9

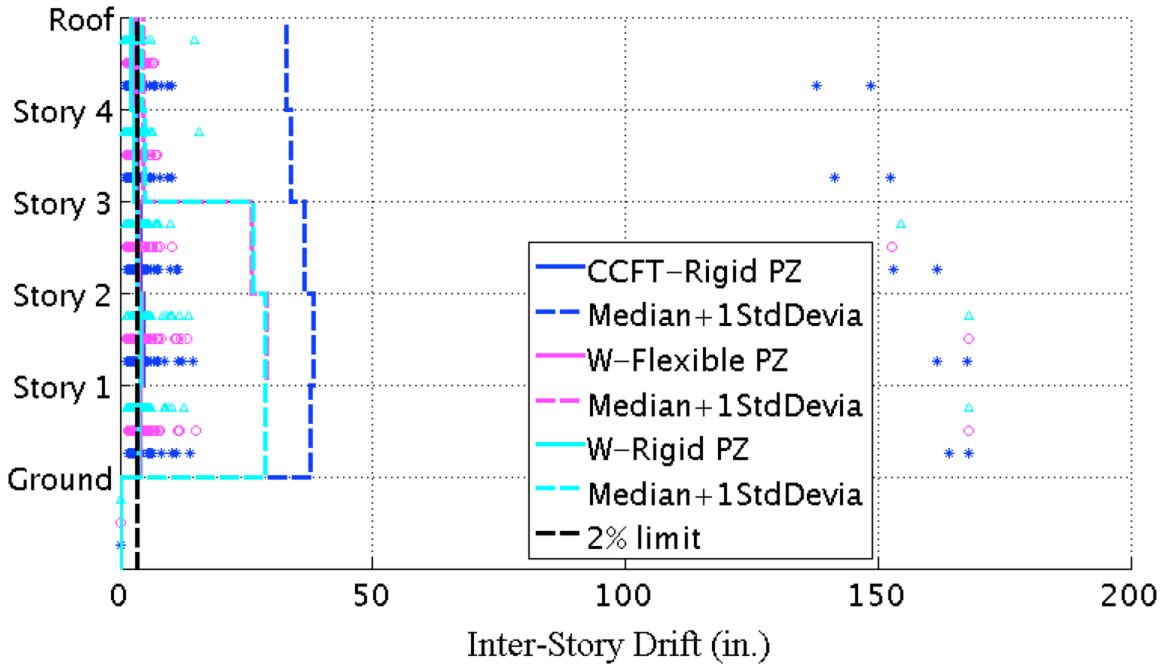

Appendix Figure L-156: Median of the peak inter-story drift under 44 MCE level ground motions with damping = 2% for steel SMFs and CSMF with a GSR = 0.9

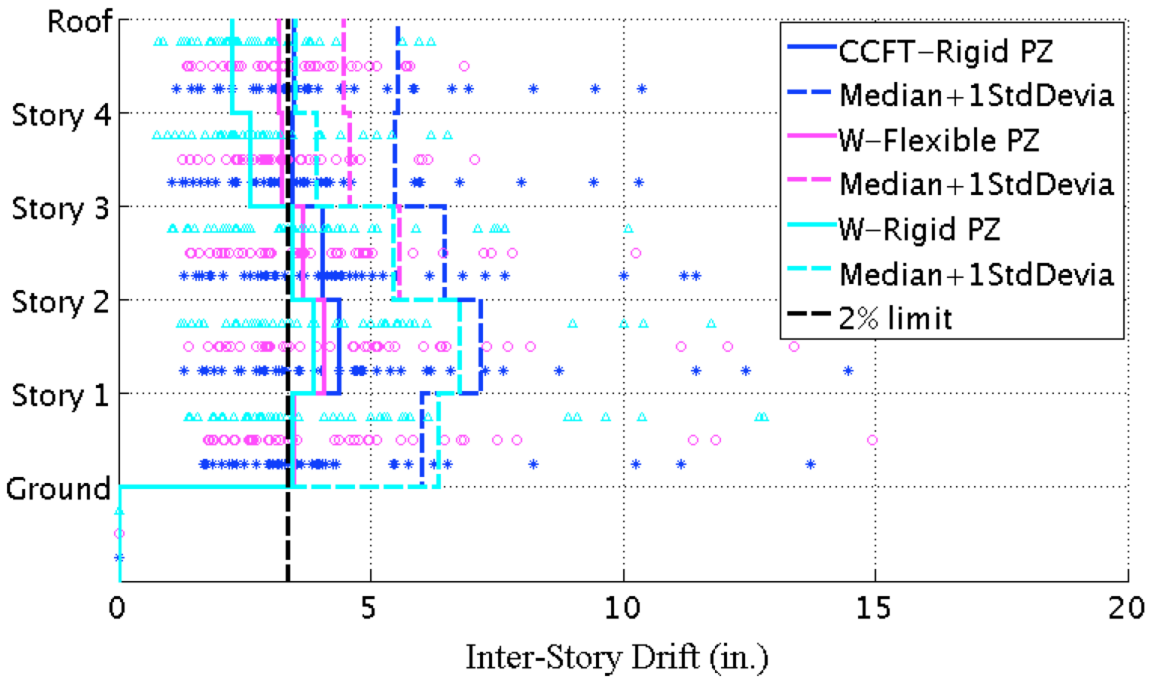

Appendix Figure L-157: Replot of Appendix Figure L-156 under the 'Filtered 44' ground motions

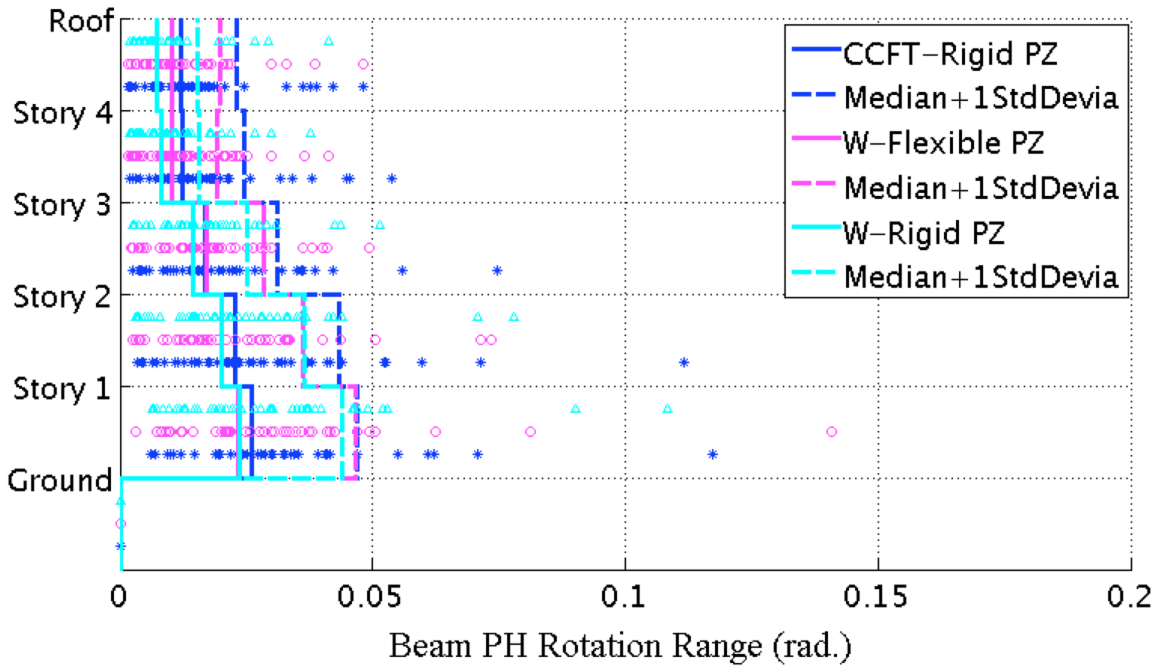

Appendix Figure L-158: Median of the beam PH rotation range under 44 DBE level ground motions with damping = 2% for steel SMFs and CSMF with a GSR = 0.9

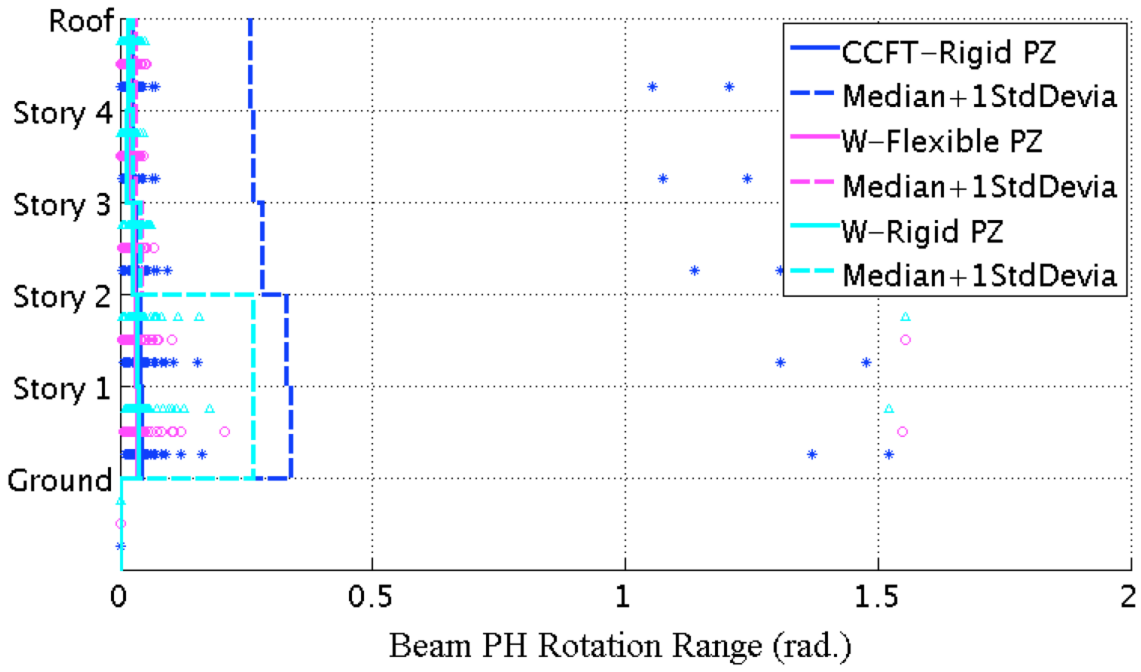

Appendix Figure L-159: Median of the beam PH rotation range under 44 MCE level ground motions with damping = 2% for steel SMFs and CSMF with a GSR = 0.9

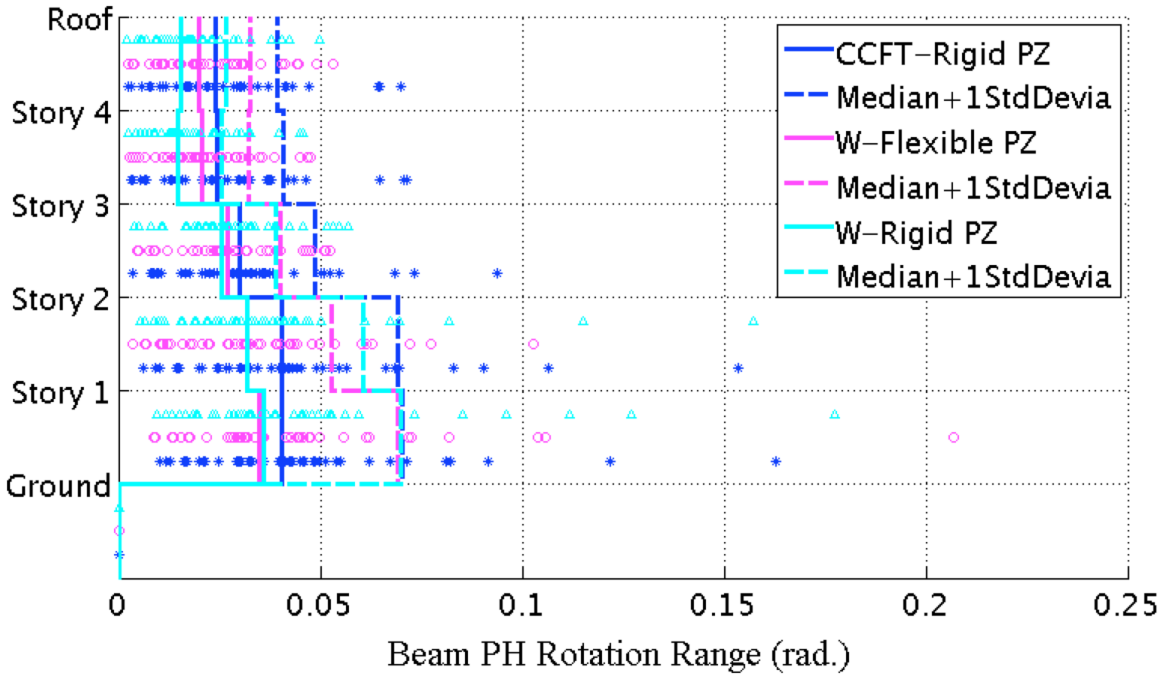

Appendix Figure L-160: Replot of Appendix Figure L-159 under the 'Filtered 44' ground motions

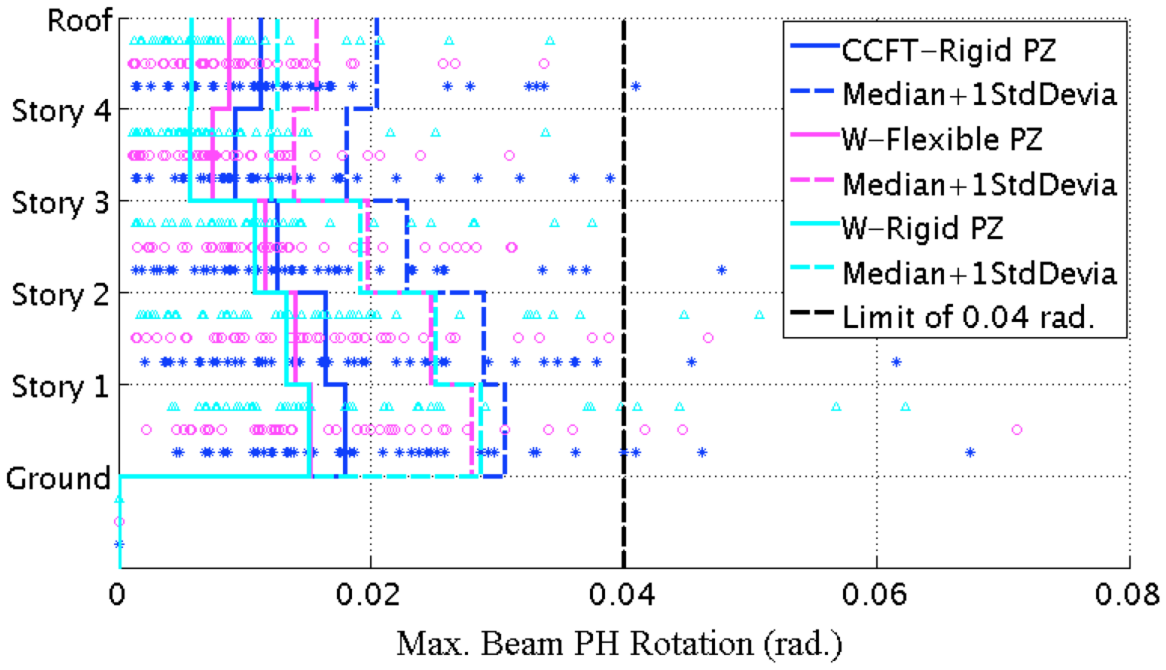

Appendix Figure L-161: Median of the maximum beam PH rotation under 44 DBE level ground motions with damping = 2% for steel SMFs and CSMF with a GSR = 0.9

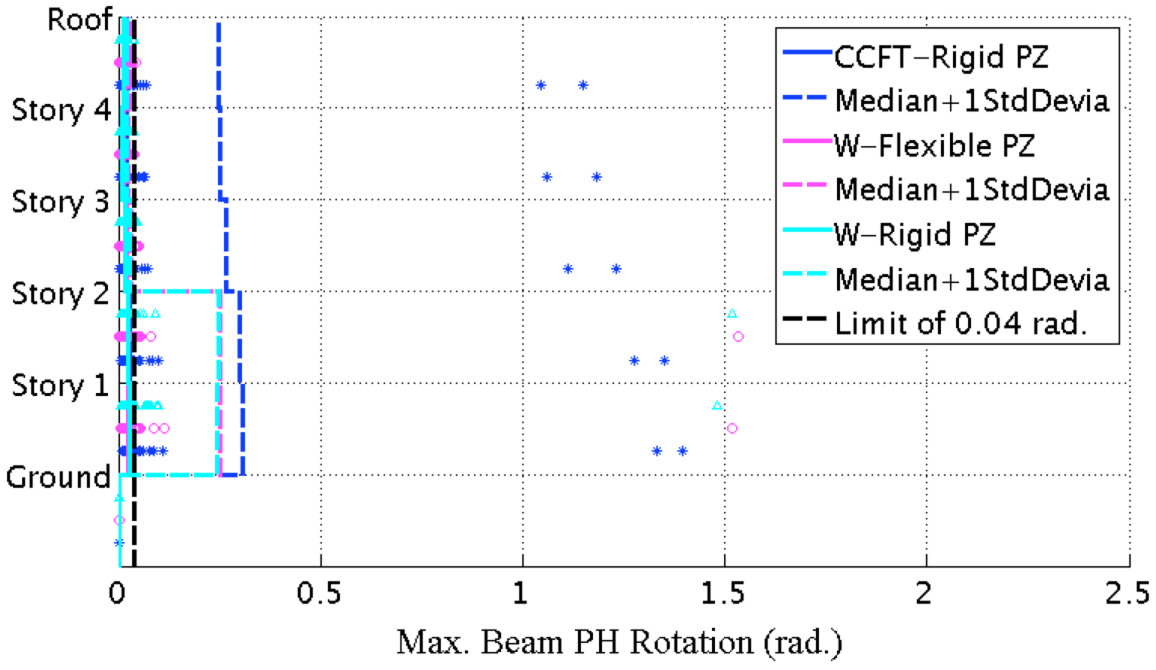

Appendix Figure L-162: Median of the maximum beam PH rotation under 44 MCE level ground motions with damping = 2% for steel SMFs and CSMF with a GSR = 0.9

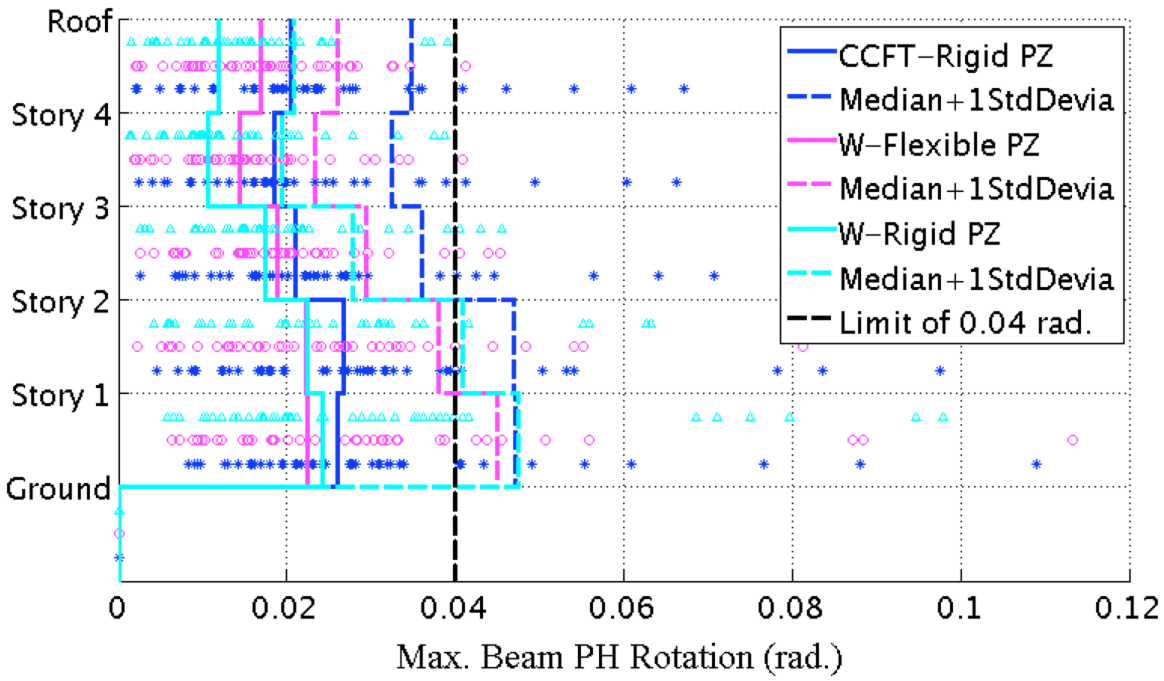

Appendix Figure L-163: Replot of Appendix Figure L-162 under the 'Filtered 44' ground motions

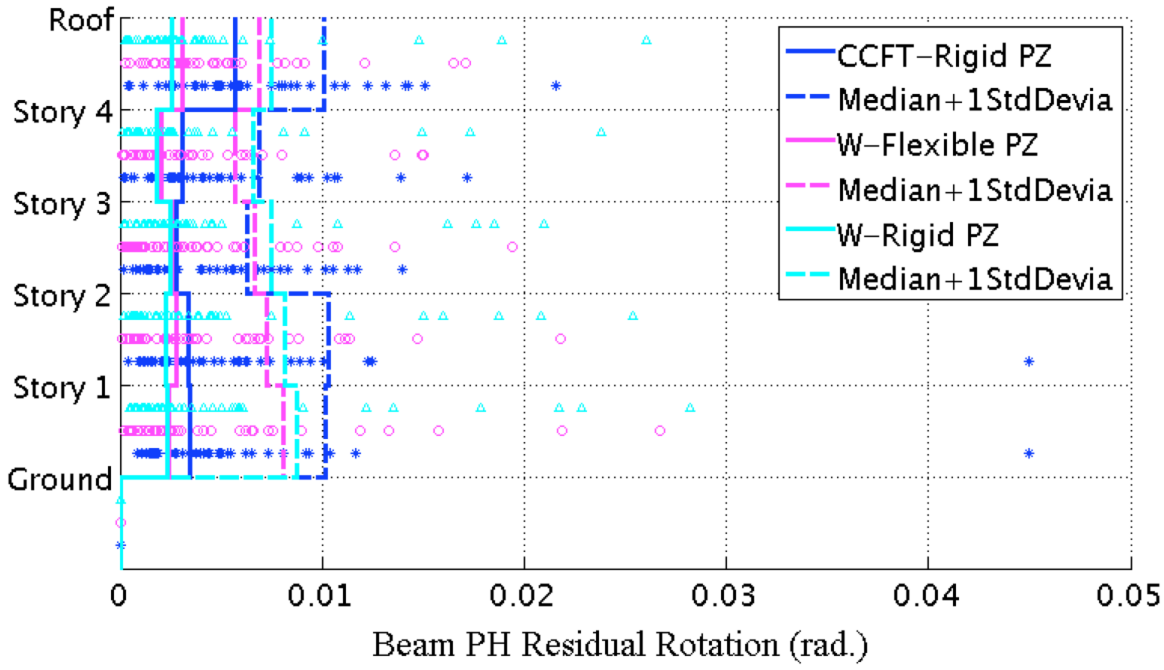

Appendix Figure L-164: Median of the maximum residual rotation of beam plastic hinges under 44 DBE level ground motions with damping = 2% for steel SMFs and CSMF with a GSR = 0.9

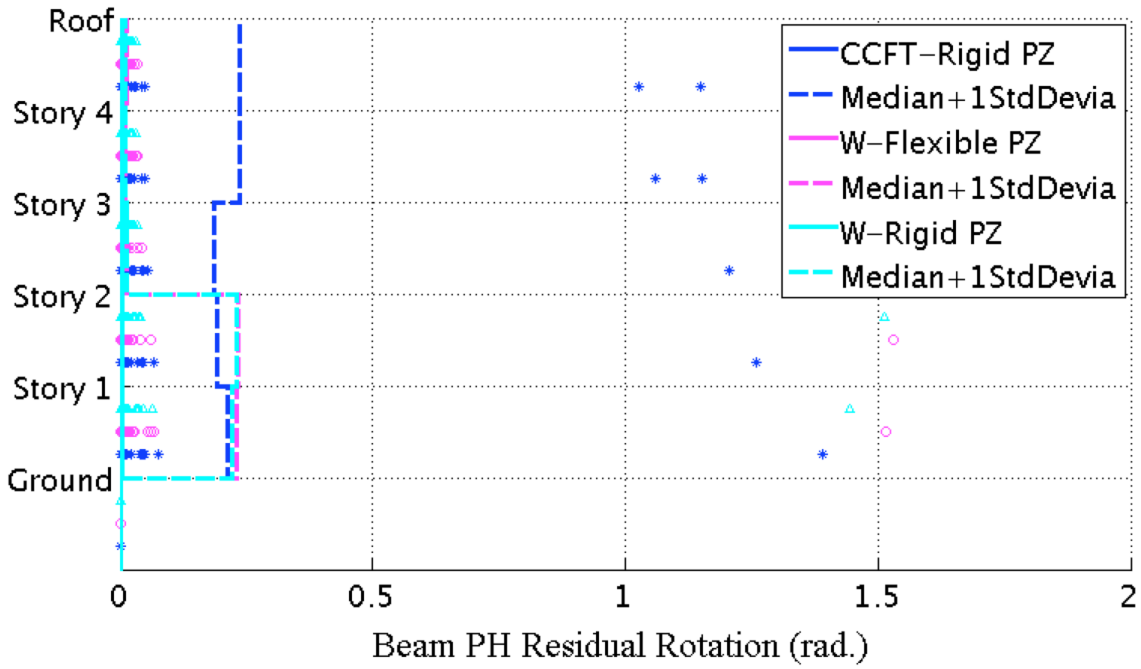

Appendix Figure L-165: Median of the maximum residual rotation of beam plastic hinges under 44 MCE level ground motions with damping = 2% for steel SMFs and CSMF with a GSR = 0.9

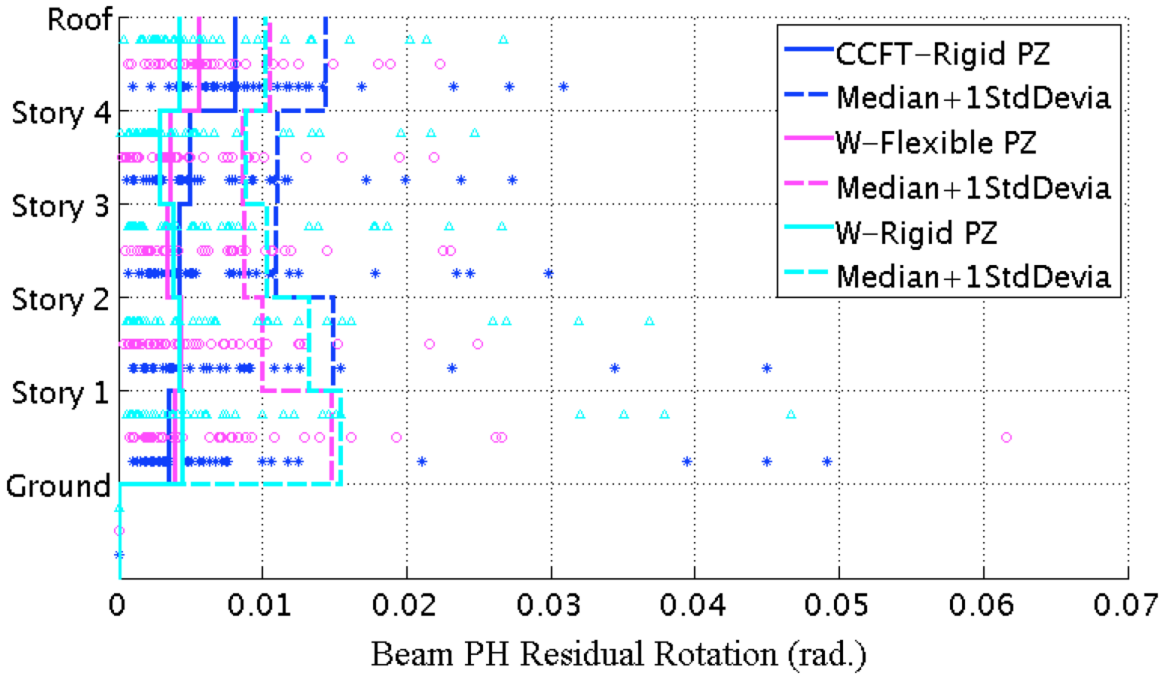

Appendix Figure L-166: Replot of Appendix Figure L-165 under the 'Filtered 44' ground motions

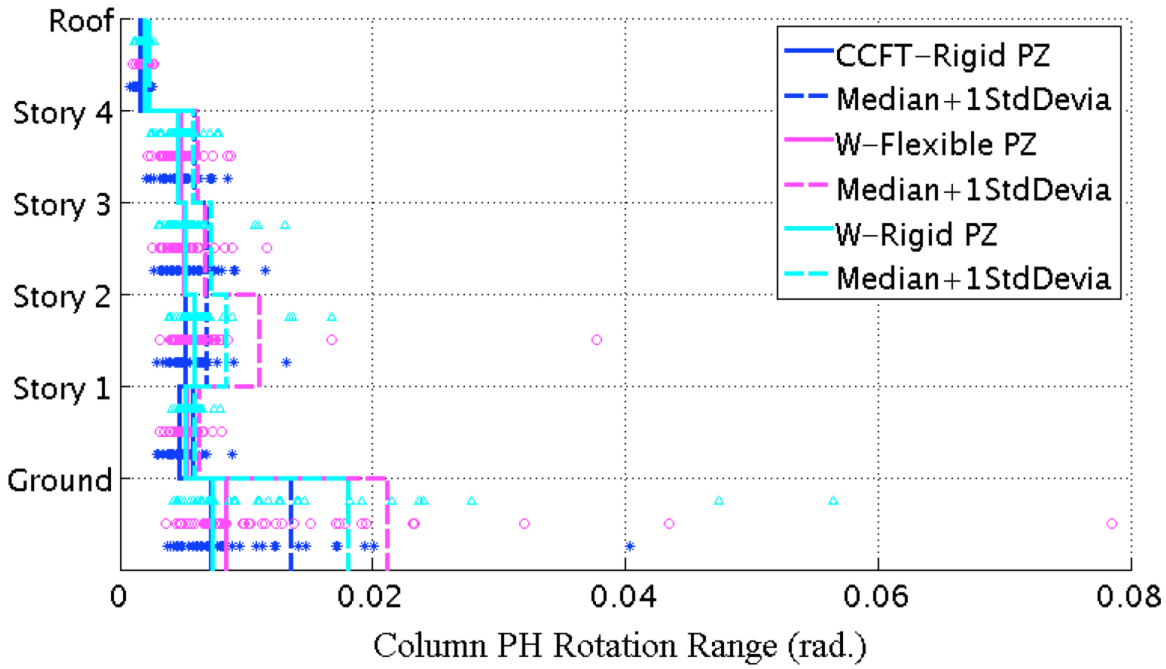

Appendix Figure L-167: Median of the column PH rotation range under 44 DBE level ground motions with damping = 2% for steel SMFs and CSMF with a GSR = 0.9

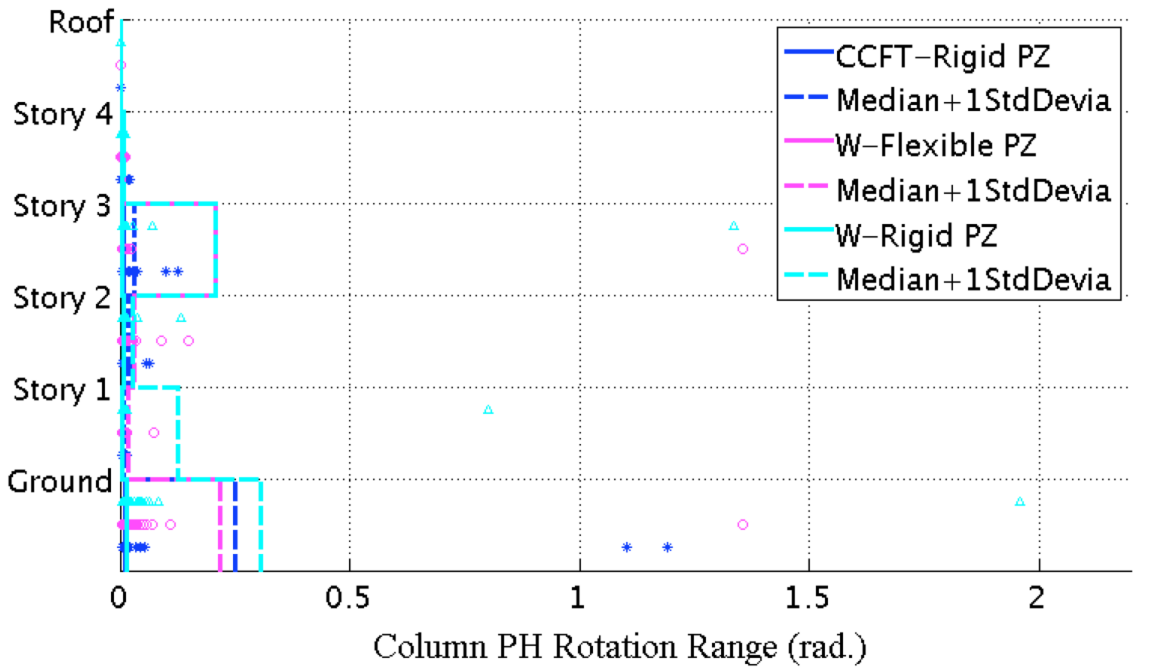

Appendix Figure L-168: Median of the column PH rotation range under 44 MCE level ground motions with damping = 2% for steel SMFs and CSMF with a GSR = 0.9

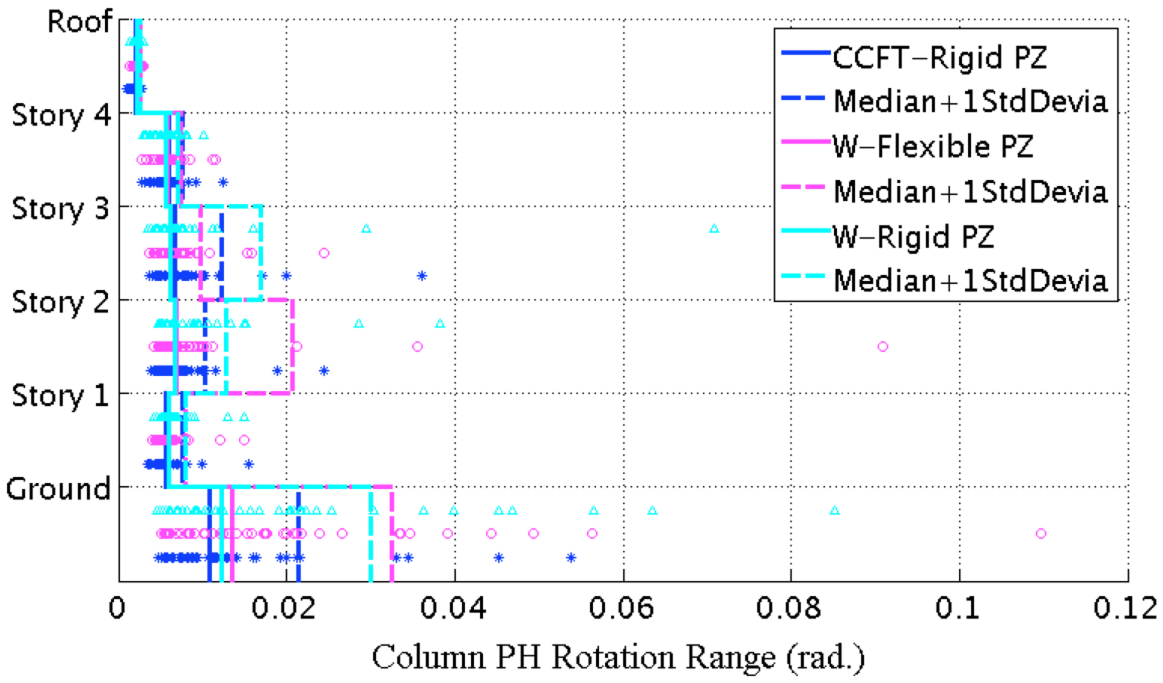

Appendix Figure L-169: Replot of Appendix Figure L-168 under the 'Filtered 44' ground motions

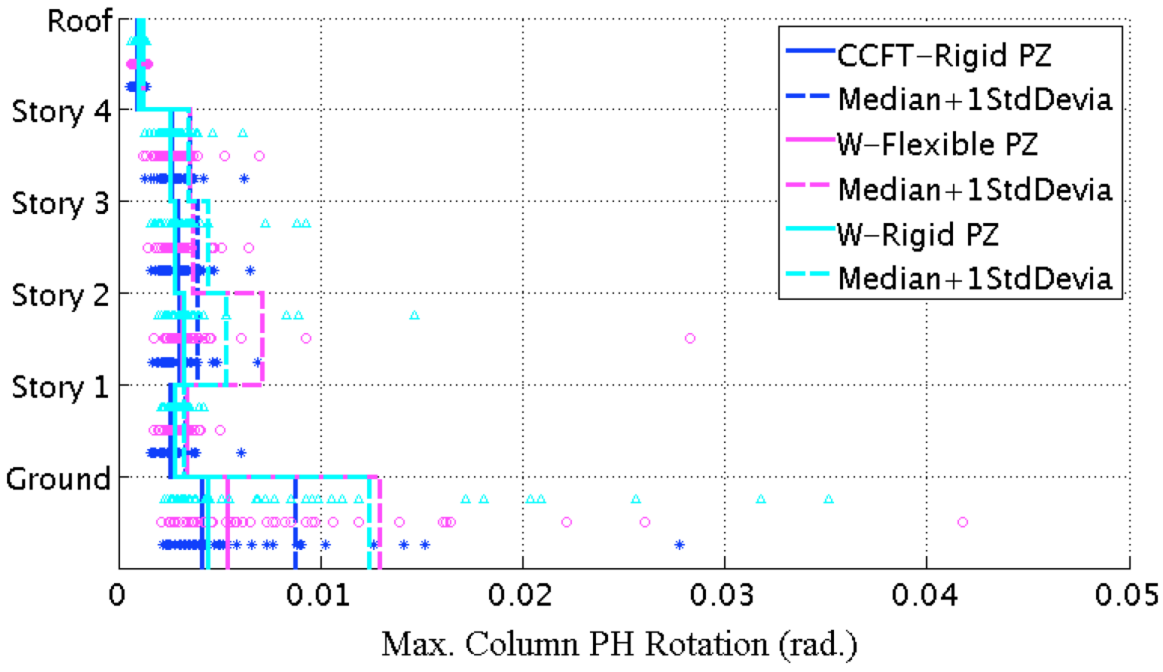

Appendix Figure L-170: Median of the maximum column PH rotation under 44 DBE level ground motions with damping = 2% for steel SMFs and CSMF with a GSR = 0.9

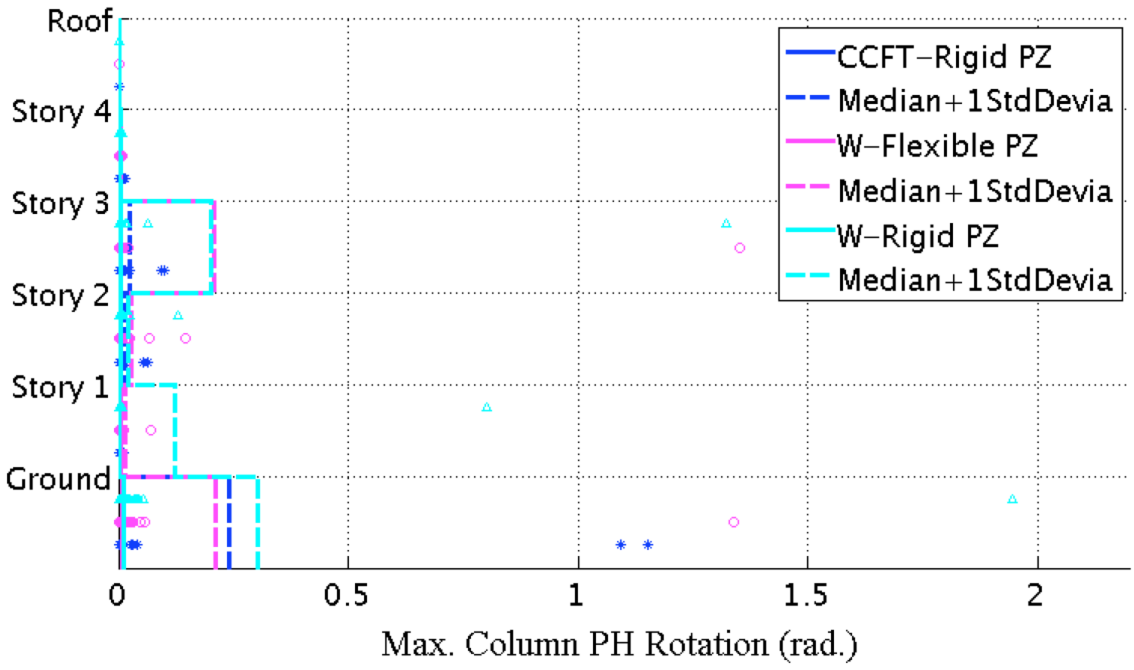

Appendix Figure L-171: Median of the maximum column PH rotation under 44 MCE level ground motions with damping = 2% for steel SMFs and CSMF with a GSR = 0.9

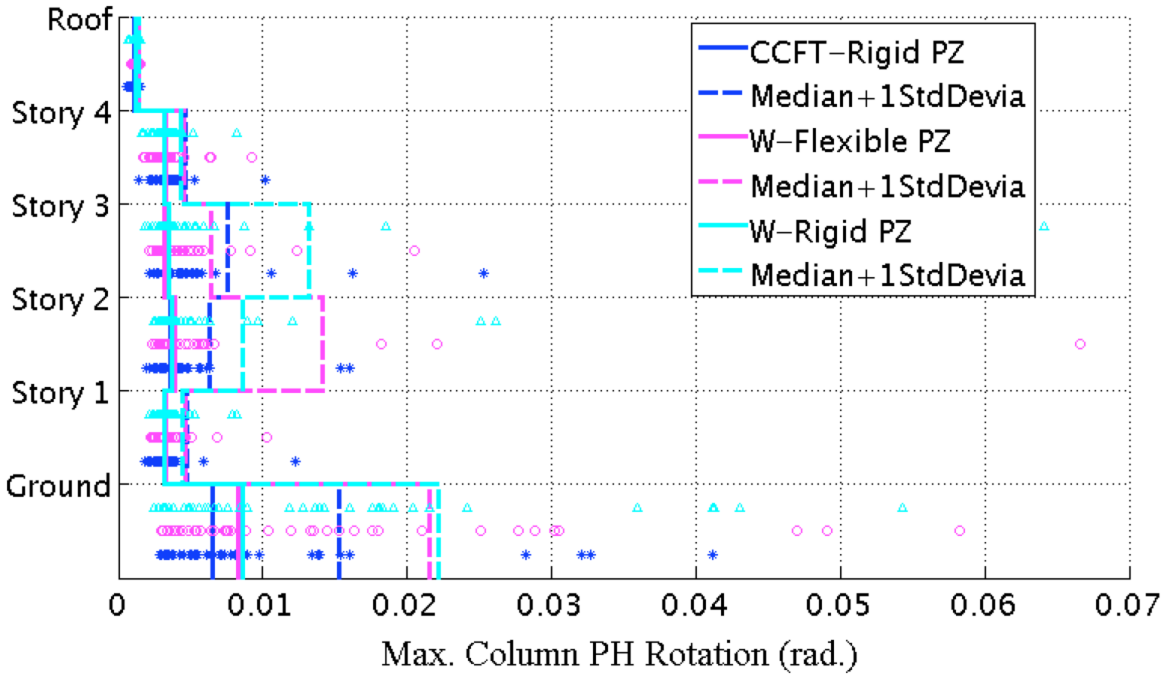

Appendix Figure L-172: Replot of Appendix Figure L-171 under the 'Filtered 44' ground motions

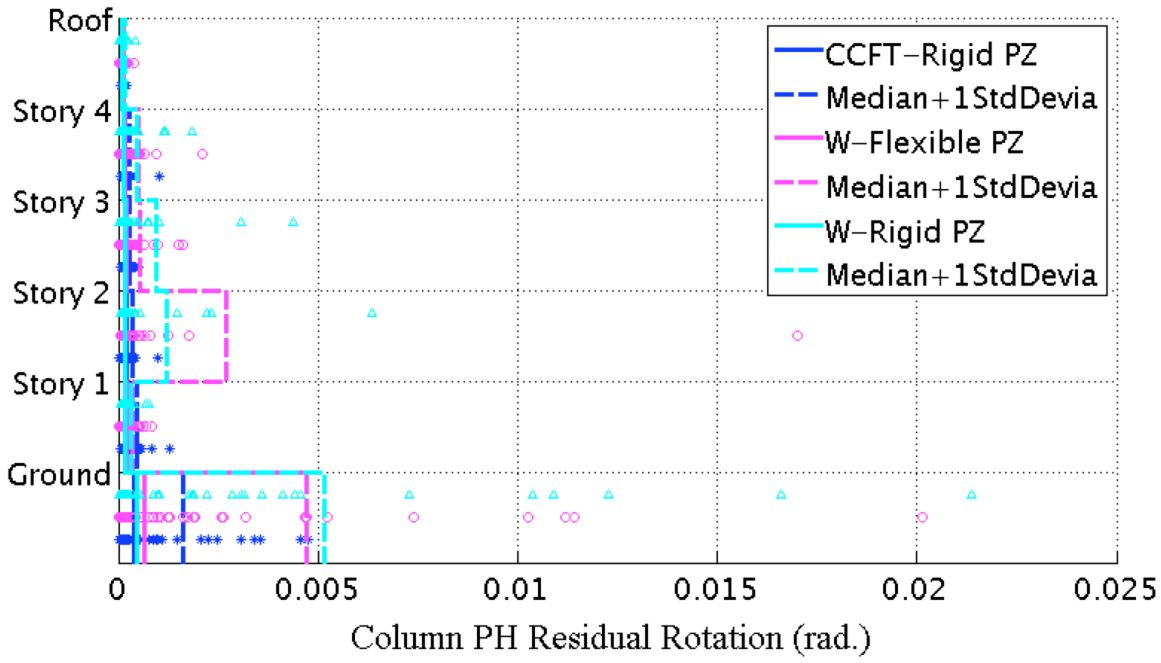

Appendix Figure L-173: Median of the maximum residual rotation of column plastic hinges under 44 DBE level ground motions with damping = 2% for steel SMFs and CSMF with a GSR = 0.9

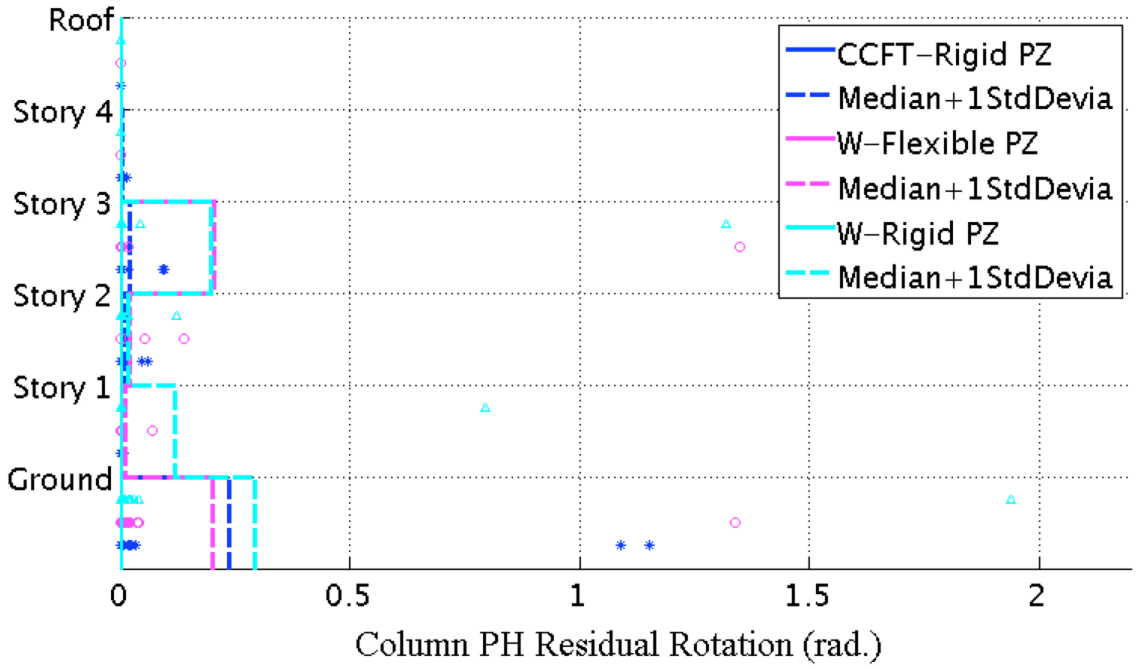

Appendix Figure L-174: Median of the maximum residual rotation of column plastic hinges under 44 MCE level ground motions with damping = 2% for steel SMFs and CSMF with a GSR = 0.9

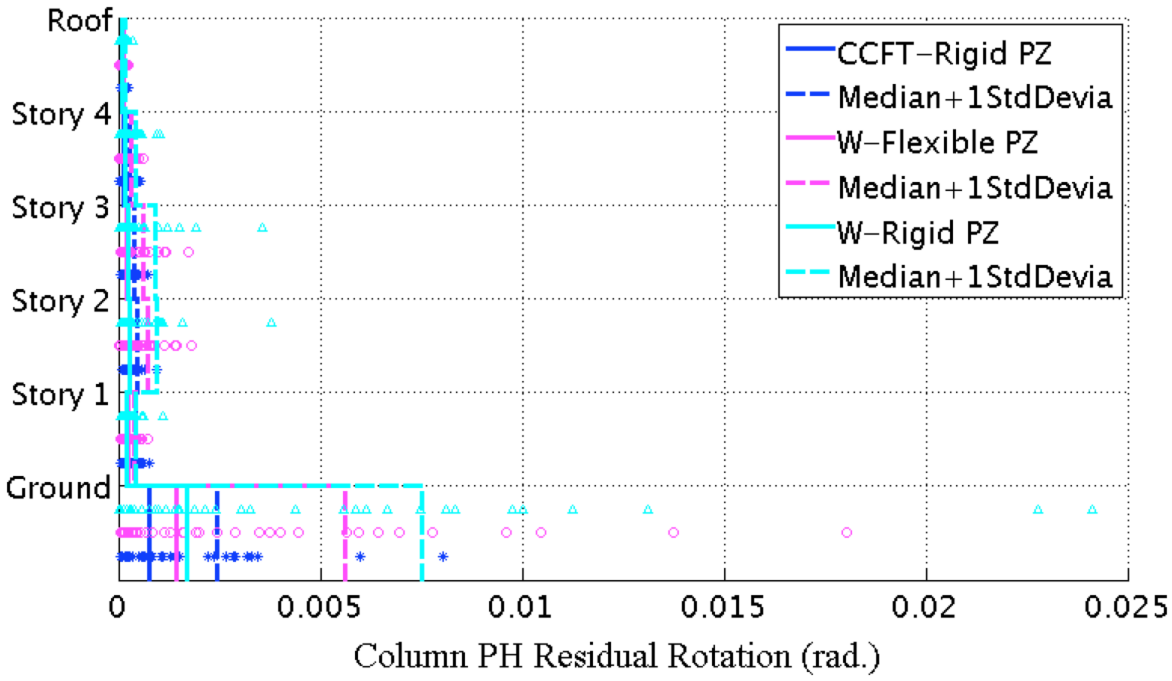

Appendix Figure L-175: Replot of Appendix Figure L-174 under the 'Filtered 44' ground motions

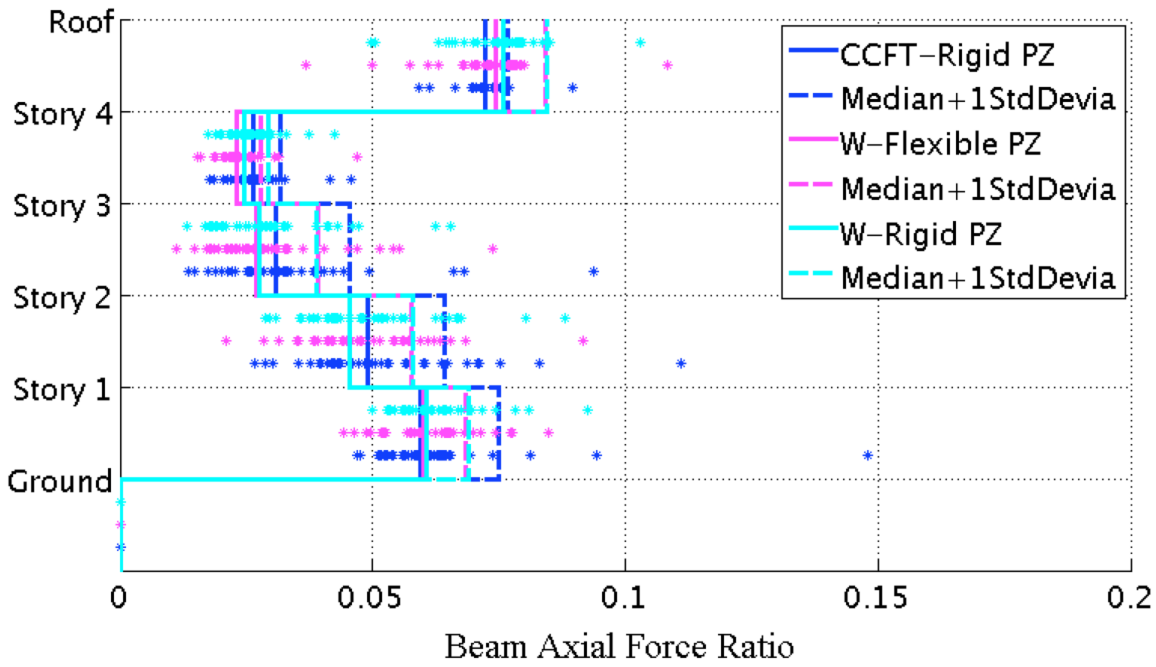

Appendix Figure L-176: Median of the peak axial force in beams under 44 DBE level ground motions with damping = 2% for steel SMFs and CSMF with a GSR = 0.9

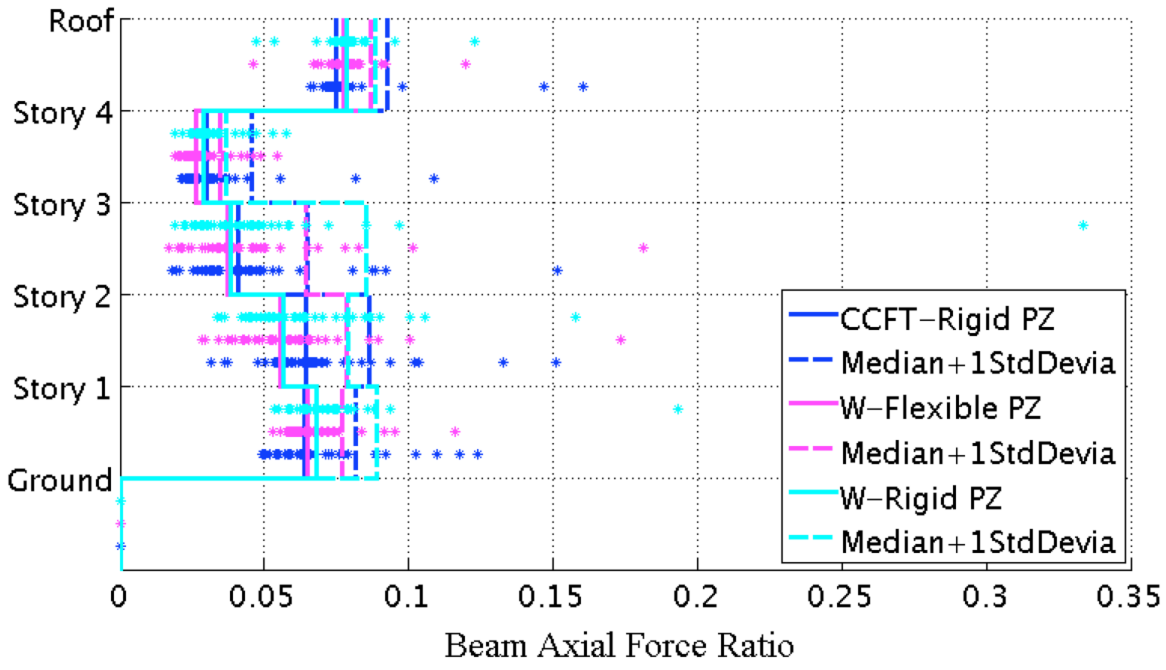

Appendix Figure L-177: Median of the peak axial force in beams under 44 MCE level ground motions with damping = 2% for steel SMFs and CSMF with a GSR = 0.9

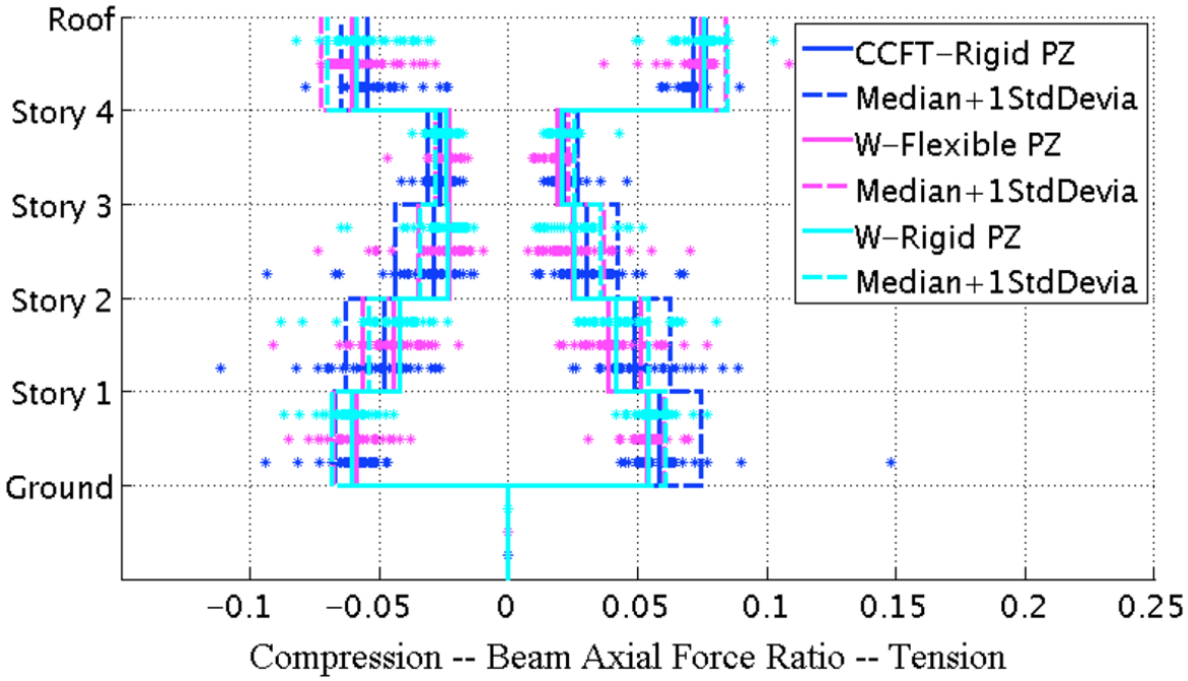

Appendix Figure L-178: Median of the peak tension vs.compression in beams under 44 DBE level ground motions with damping = 2% for steel SMFs and CSMF with a GSR = 0.9

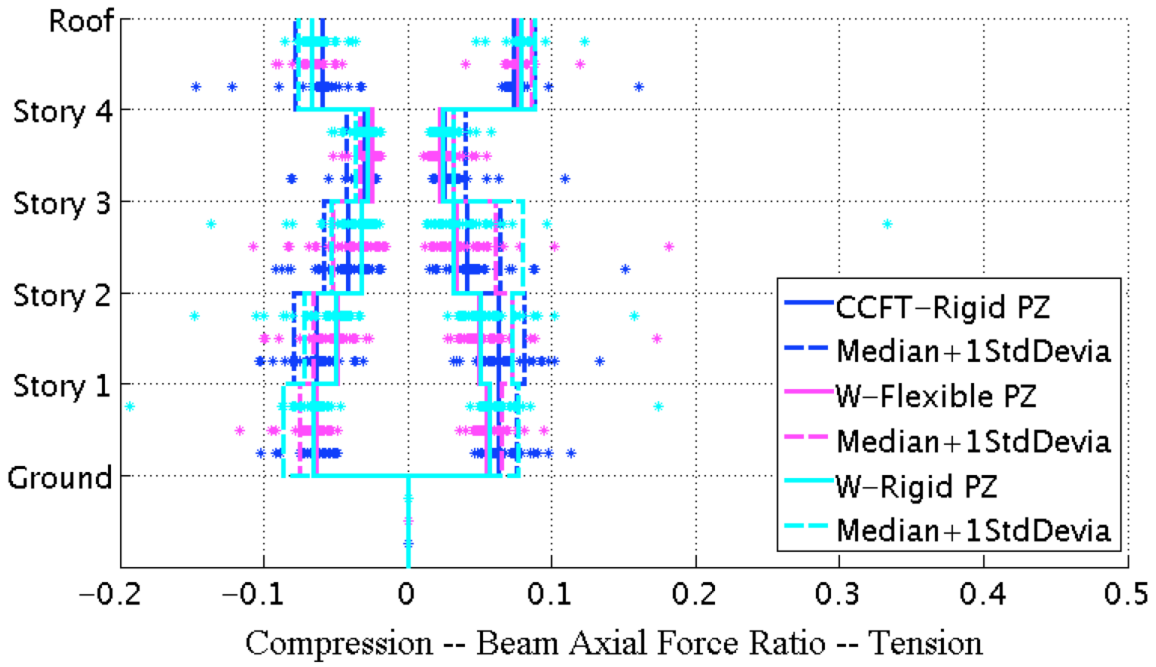

Appendix Figure L-179: Median of the peak tension vs.compression in beams under 44 MCE level ground motions with damping = 2% for steel SMFs and CSMF with a GSR = 0.9

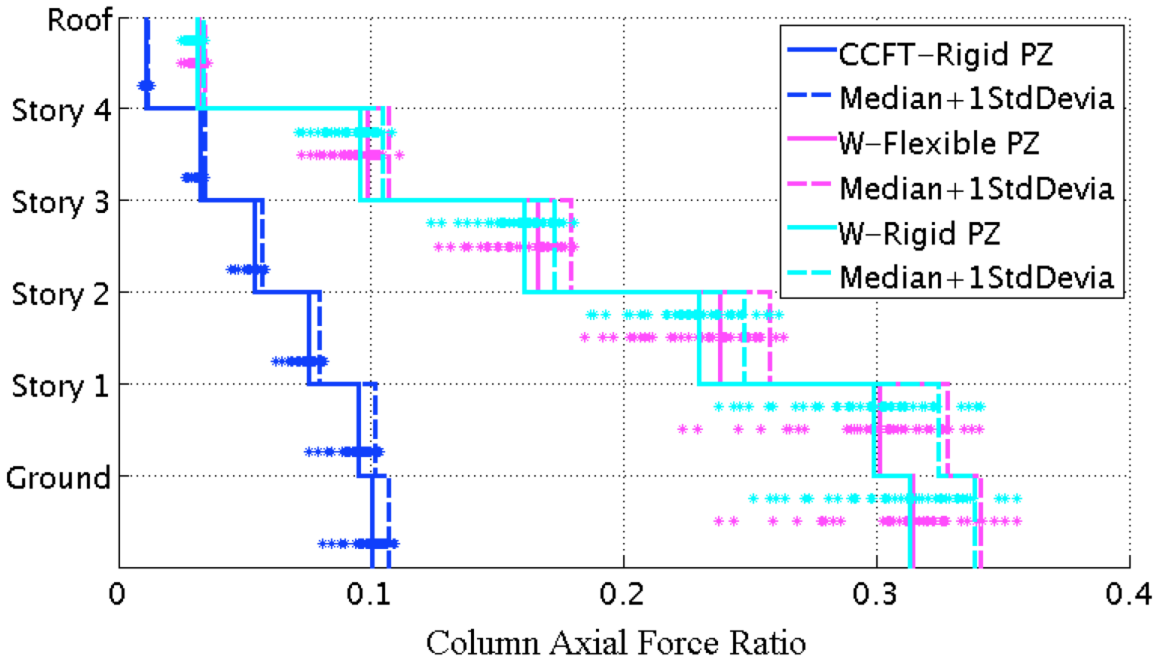

Appendix Figure L-180: Median of the peak axial force in columns under 44 DBE level ground motions with damping = 2% for steel SMFs and CSMF with a GSR = 0.9

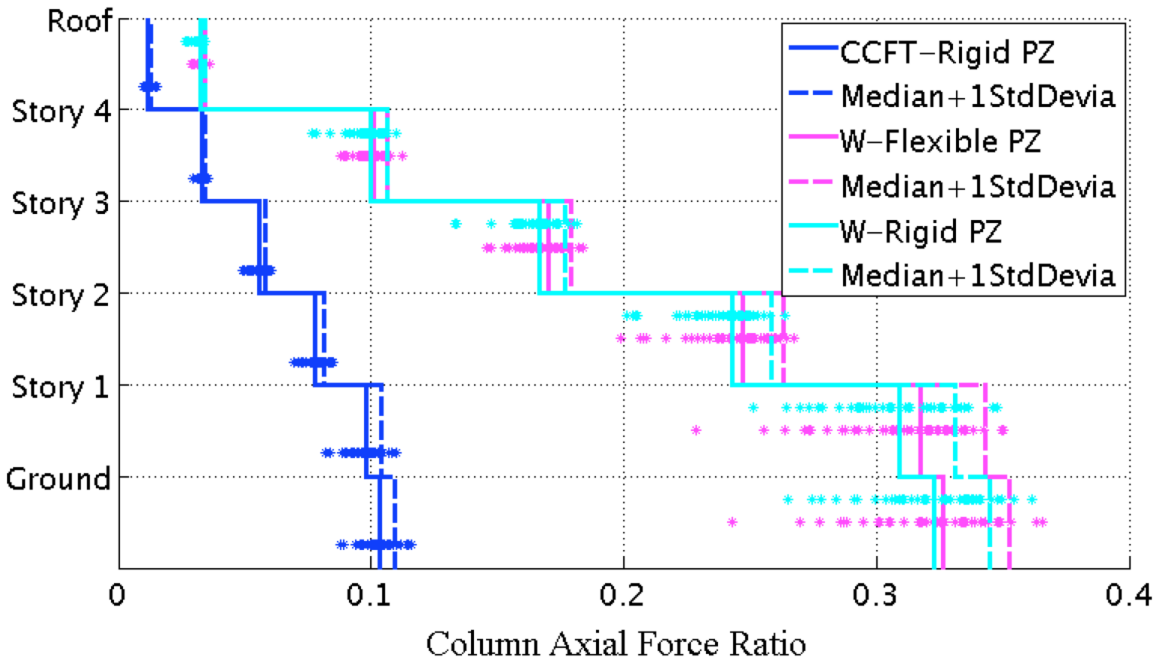

Appendix Figure L-181: Median of the peak axial force in columns under 44 MCE level ground motions with damping = 2% for steel SMFs and CSMF with a GSR = 0.9

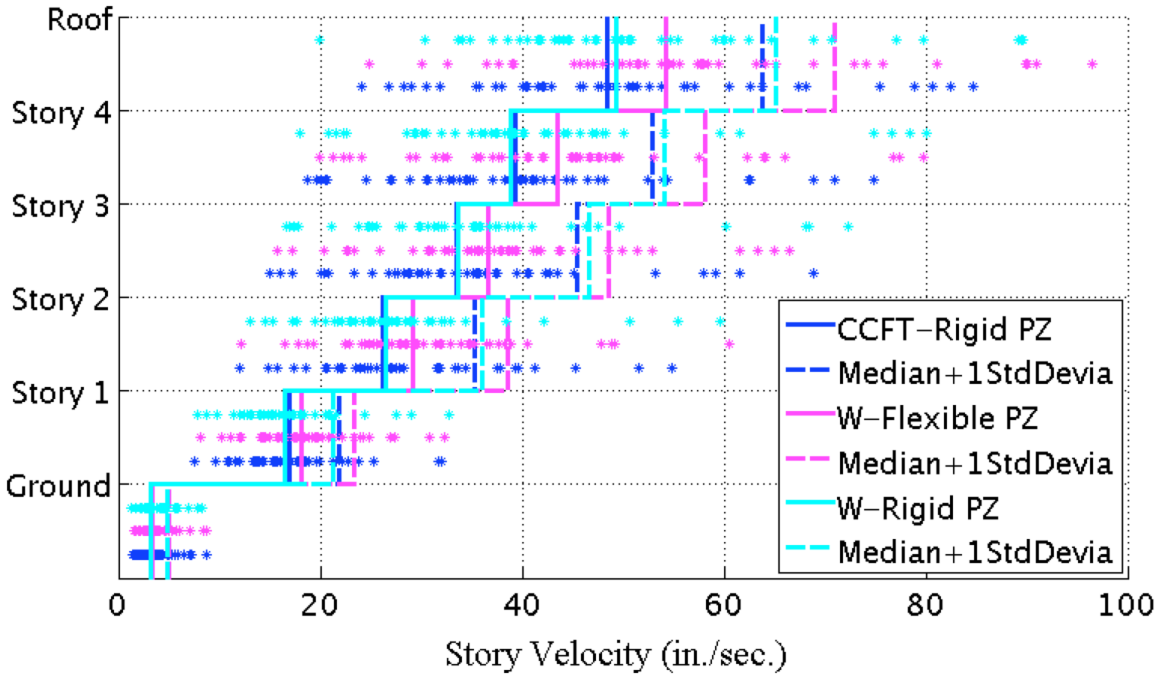

Appendix Figure L-182: Median of the peak story velocity under 44 DBE level ground motions with damping = 2% for steel SMFs and CSMF with a GSR = 0.9

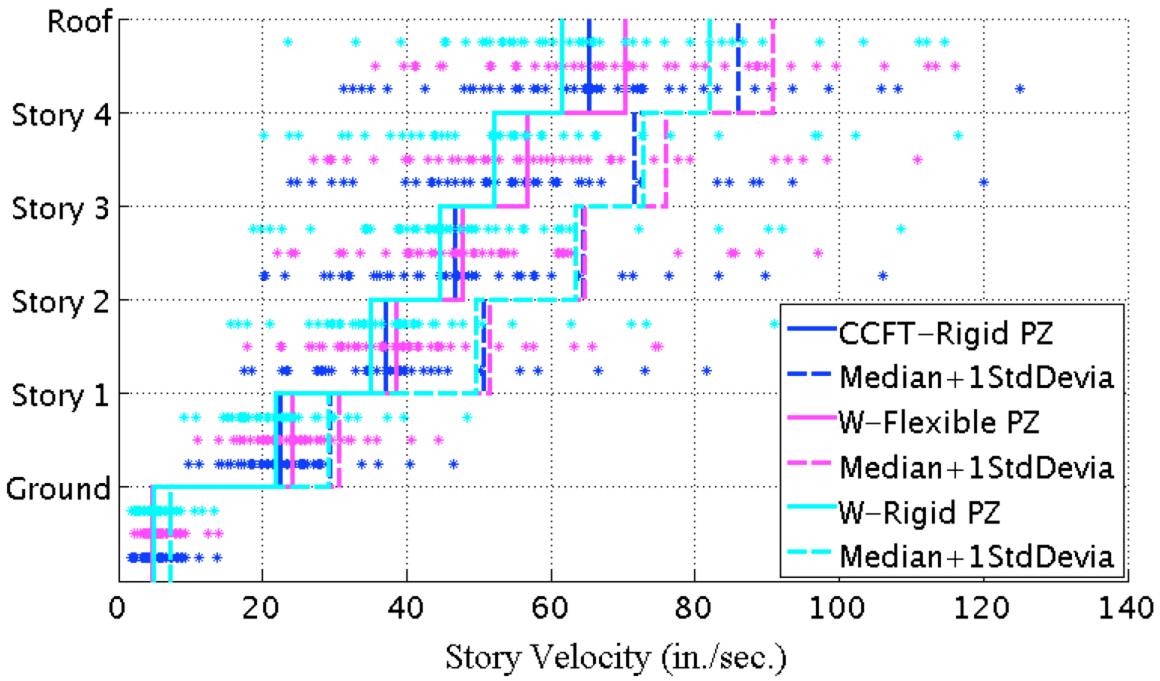

Appendix Figure L-183: Median of the peak story velocity under 44 MCE level ground motions with damping = 2% for steel SMFs and CSMF with a GSR = 0.9

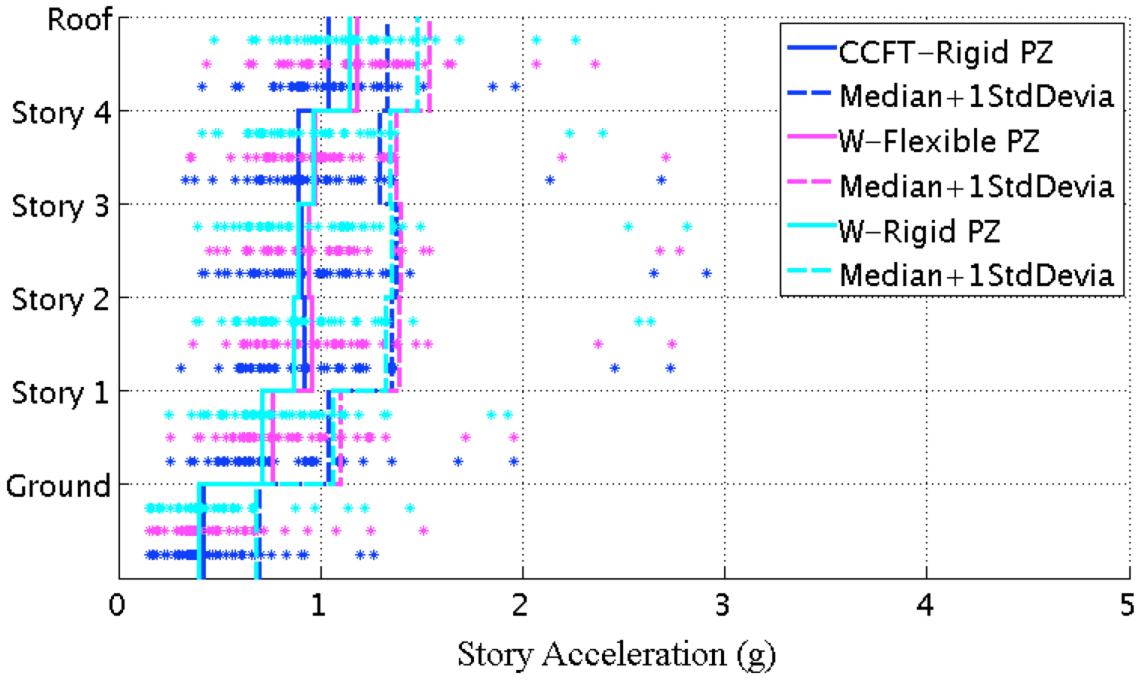

Appendix Figure L-184: Median of the peak story acceleration under 44 DBE level ground motions with damping = 2% for steel SMFs and CSMF with a GSR = 0.9

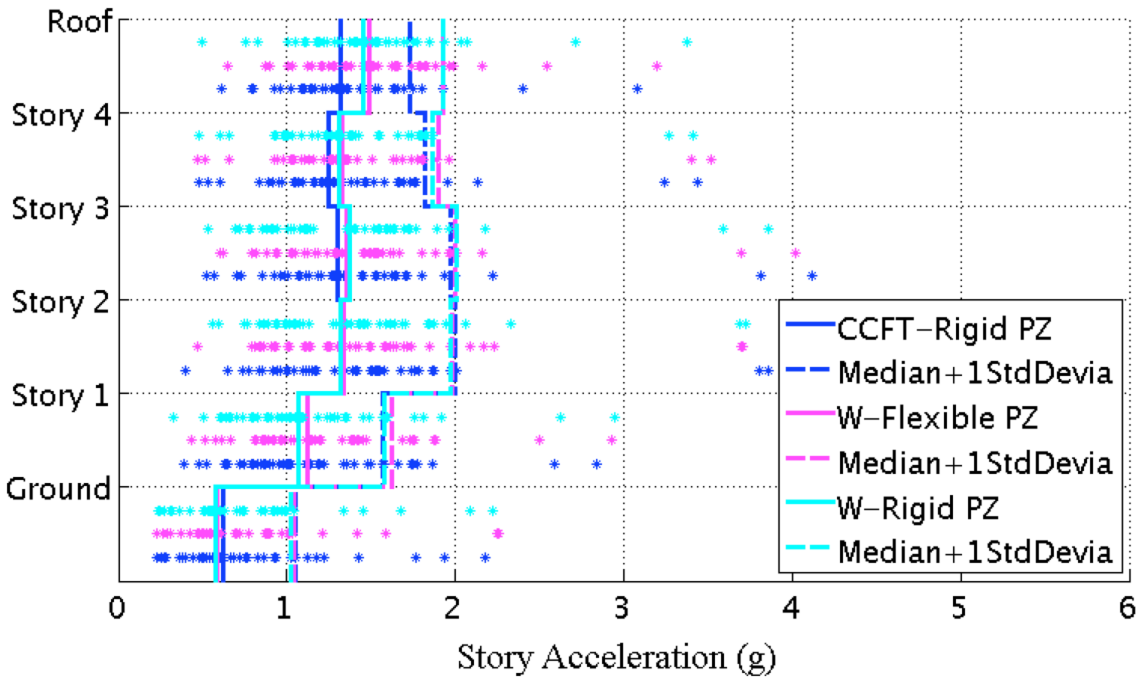

Appendix Figure L-185: Median of the peak story acceleration under 44 MCE level ground motions with damping = 2% for steel SMFs and CSMF with a GSR = 0.9

L.7 Another Methodology to Scale 44 GMs to MCE Level (GSR = 1.0 & Damping = 5%)

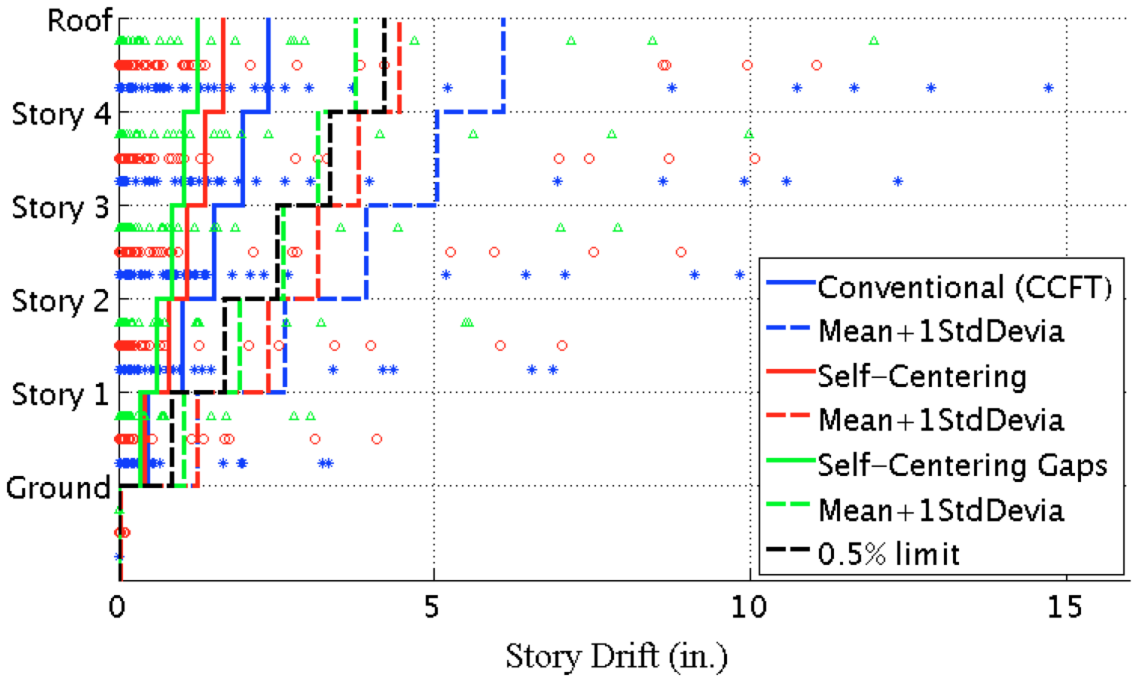

Appendix Figure L-186: Mean of the maximum story residual drift under the 'Filtered 44' DBE level ground motions with a GSR = 1.0 & damping = 5%

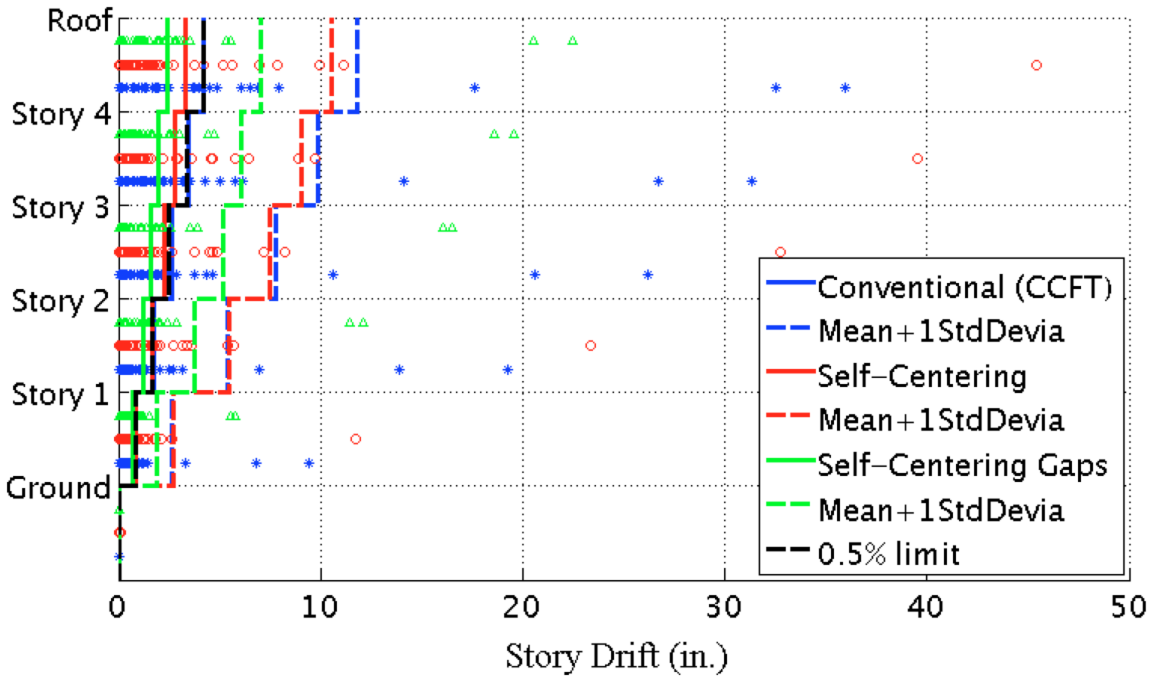

Appendix Figure L-187: Mean of the maximum story residual drift under the 'Filtered 44' MCE level ground motions with a GSR = 1.0 & damping = 5%

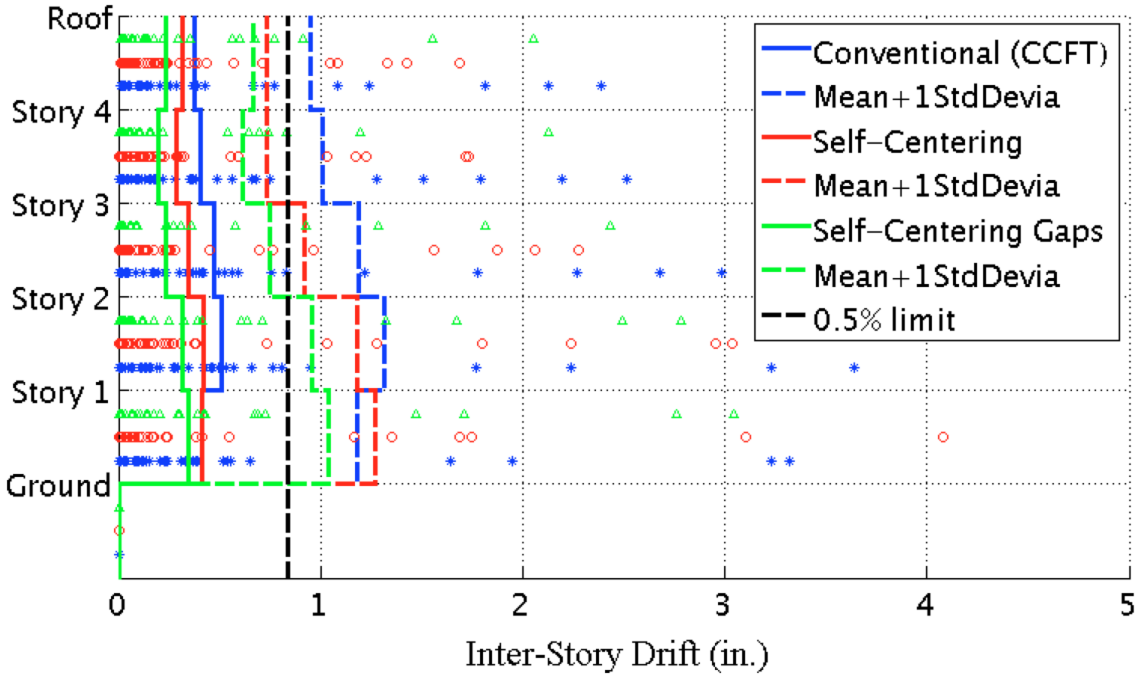

Appendix Figure L-188: Mean of the maximum inter-story residual drift under the 'Filtered 44' DBE level ground motions with a GSR = 1.0 & damping = 5%

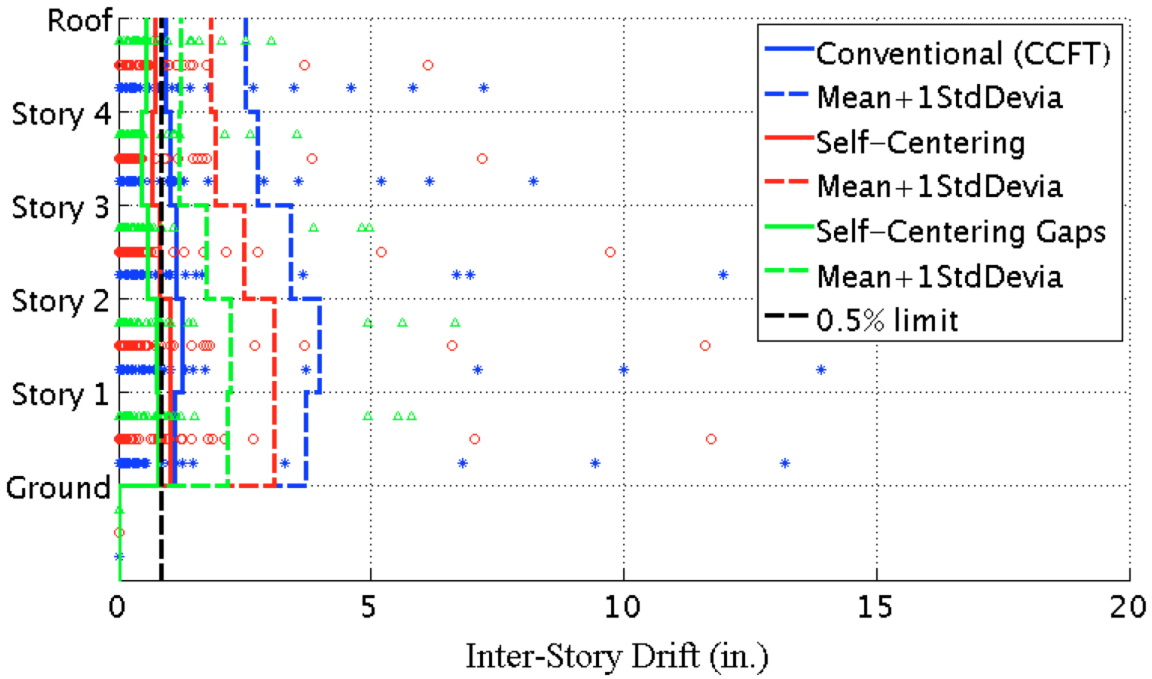

Appendix Figure L-189: Mean of the maximum inter-story residual drift under the 'Filtered 44' MCE level ground motions with a GSR = 1.0 & damping = 5%

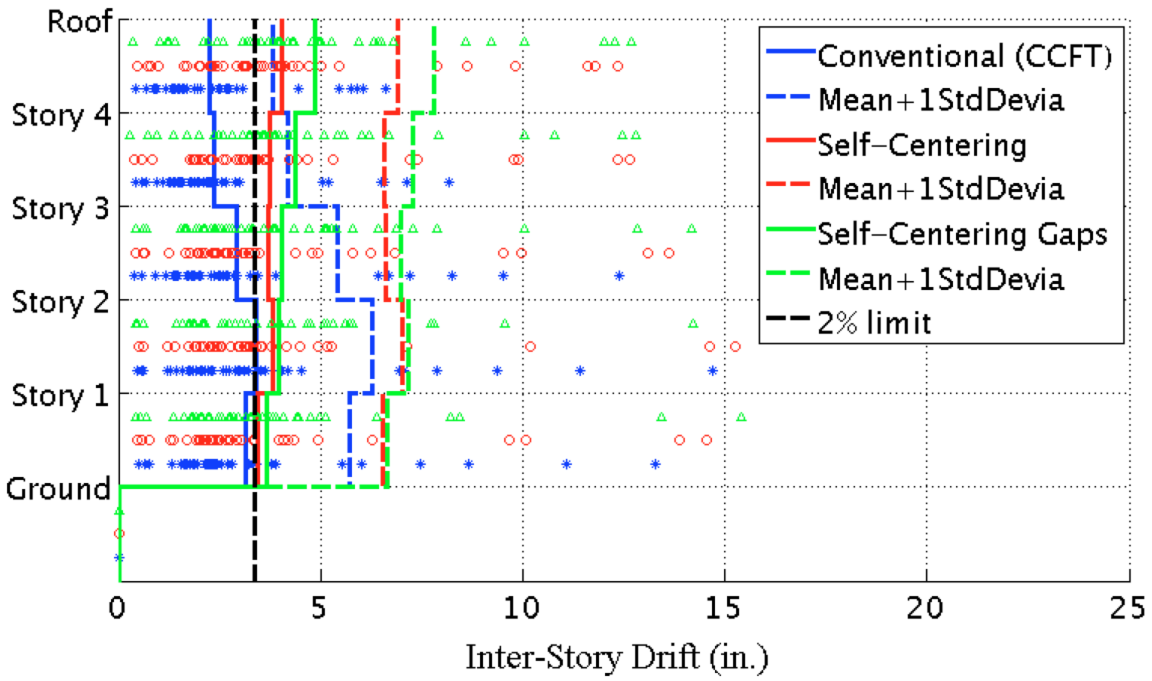

Appendix Figure L-190: Mean of the peak inter-story drift under the 'Filtered 44' DBE level ground motions with a GSR = 1.0 & damping = 5%

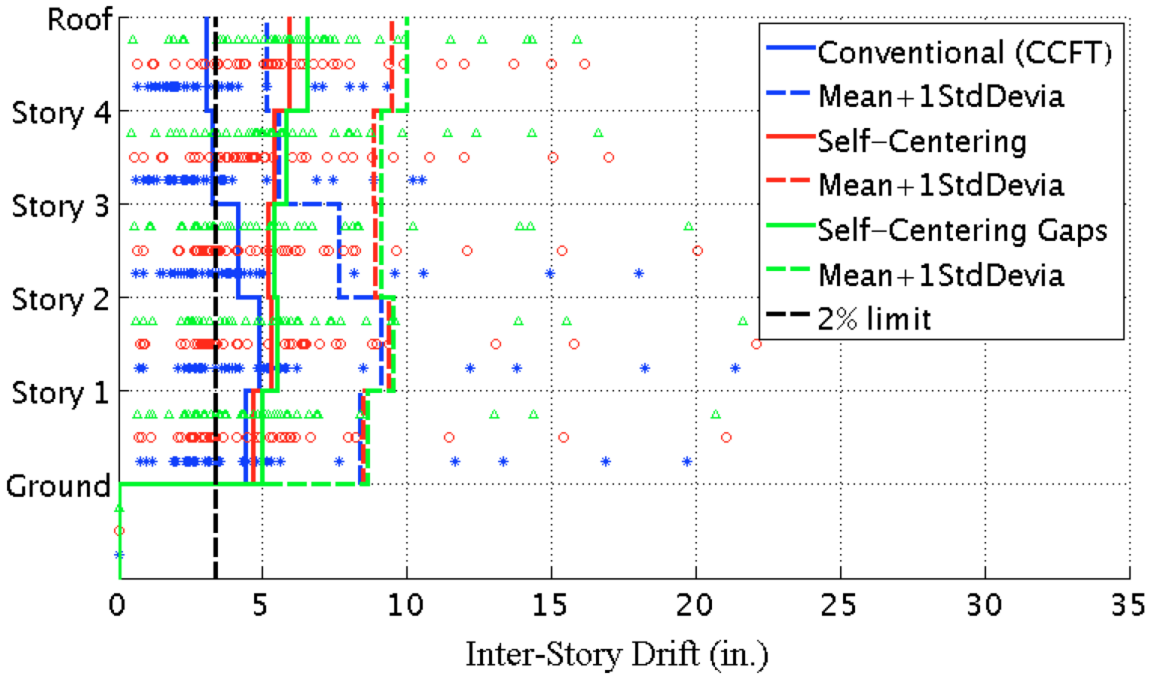

Appendix Figure L-191: Mean of the peak inter-story drift under the 'Filtered 44' MCE level ground motions with a GSR = 1.0 & damping = 5%

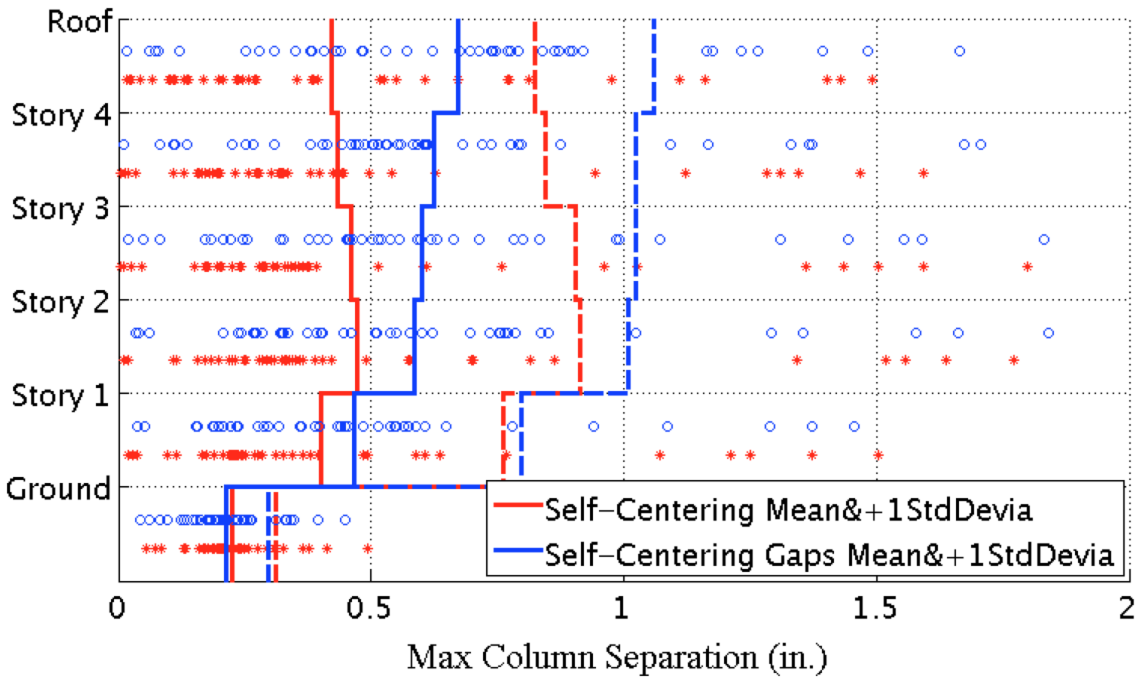

Appendix Figure L-192: Mean of the maximum column separation under the 'Filtered 44' DBE level ground motions with a GSR = 1.0 & damping = 5%

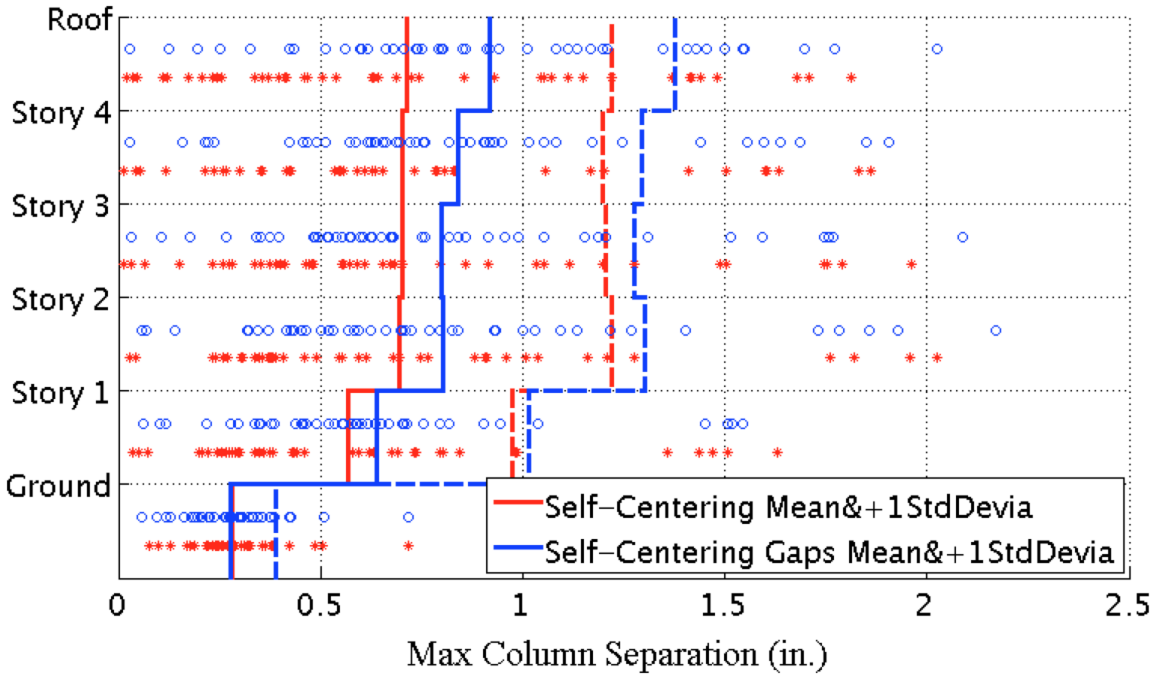

Appendix Figure L-193: Mean of the maximum column separation under the 'Filtered 44' MCE level ground motions with a GSR = 1.0 & damping = 5%

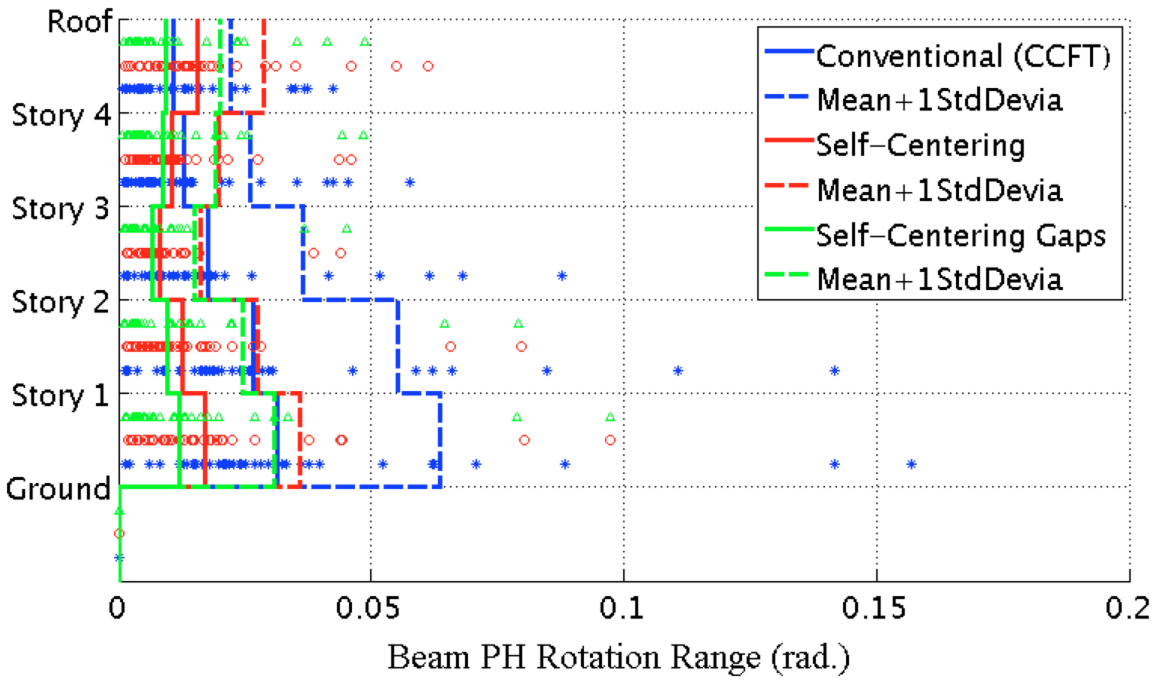

Appendix Figure L-194: Mean of the beam PH rotation range under the 'Filtered 44' DBE level ground motions with a GSR = 1.0 & damping = 5%

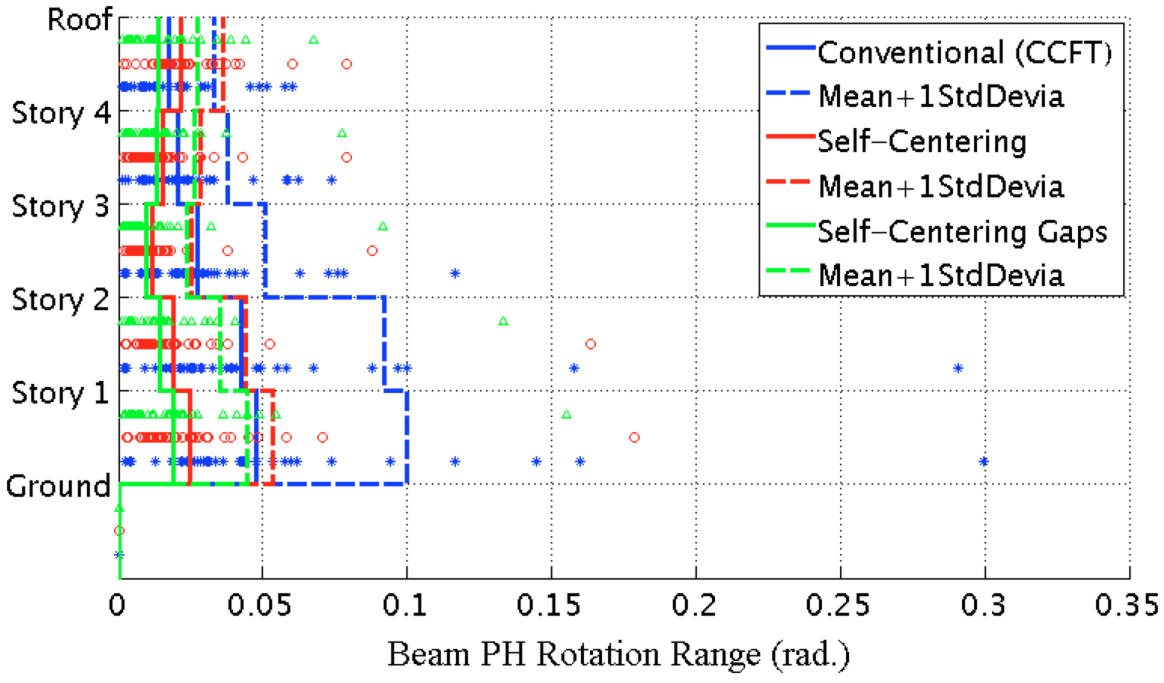

Appendix Figure L-195: Mean of the beam PH rotation range under the 'Filtered 44' MCE level ground motions with a GSR = 1.0 & damping = 5%

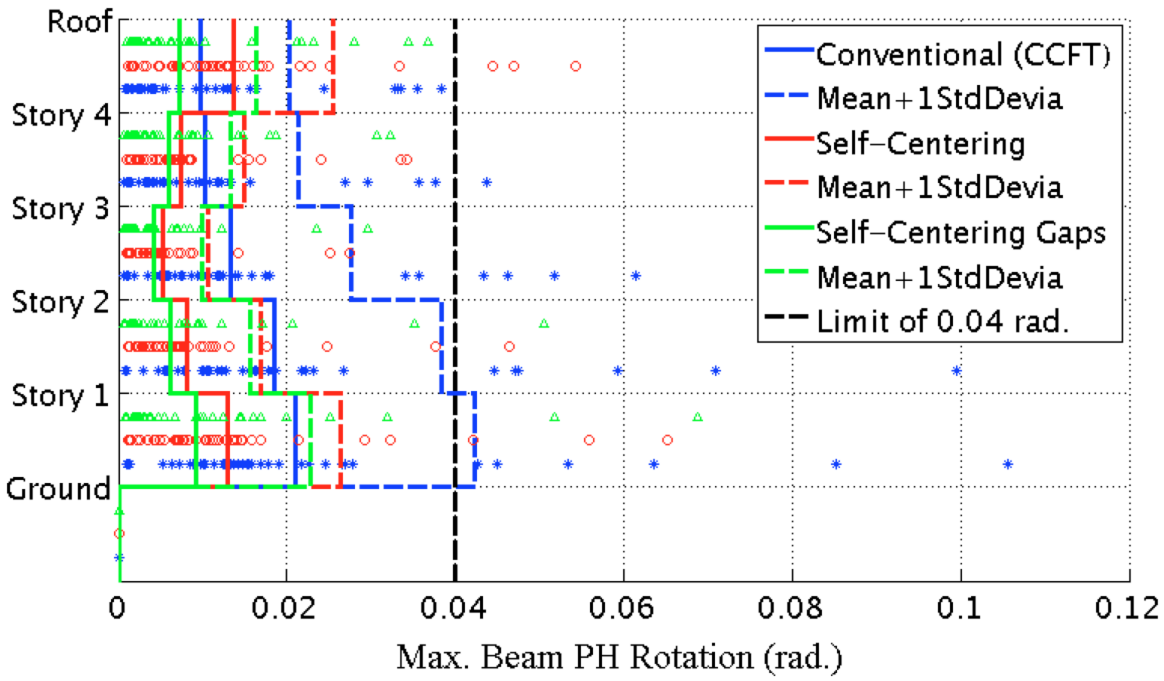

Appendix Figure L-196: Mean of the maximum beam PH rotation under the 'Filtered 44' DBE level ground motions with a GSR = 1.0 & damping = 5%

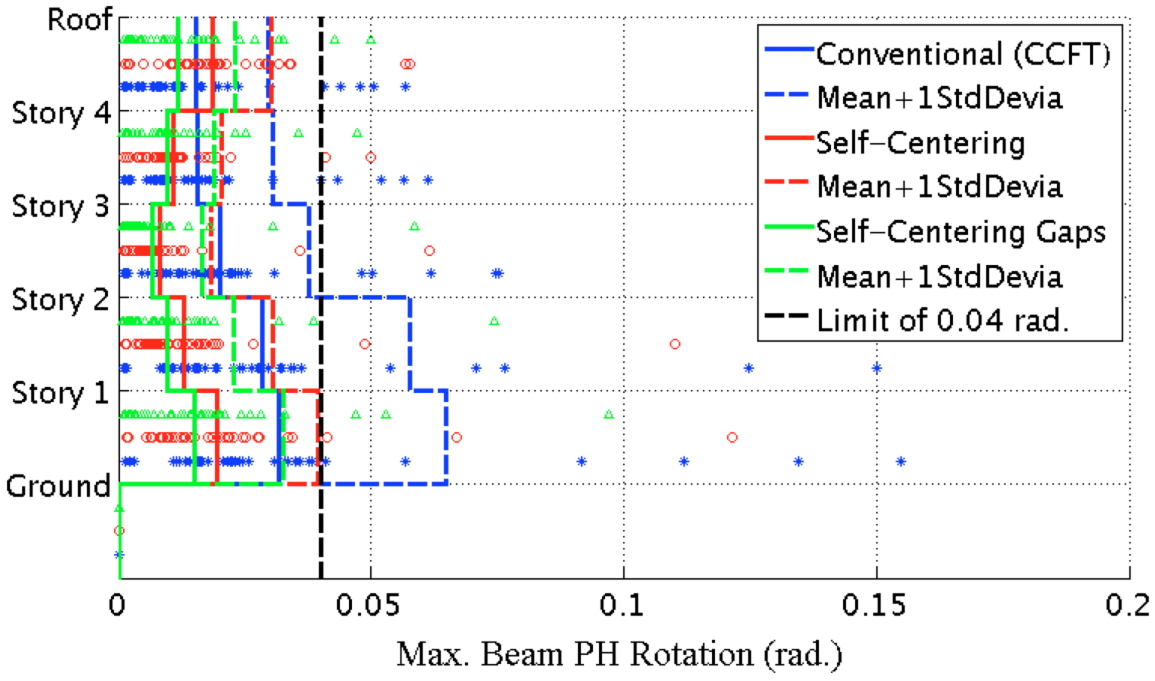

Appendix Figure L-197: Mean of the maximum beam PH rotation under the 'Filtered 44' MCE level ground motions with a GSR = 1.0 & damping = 5%

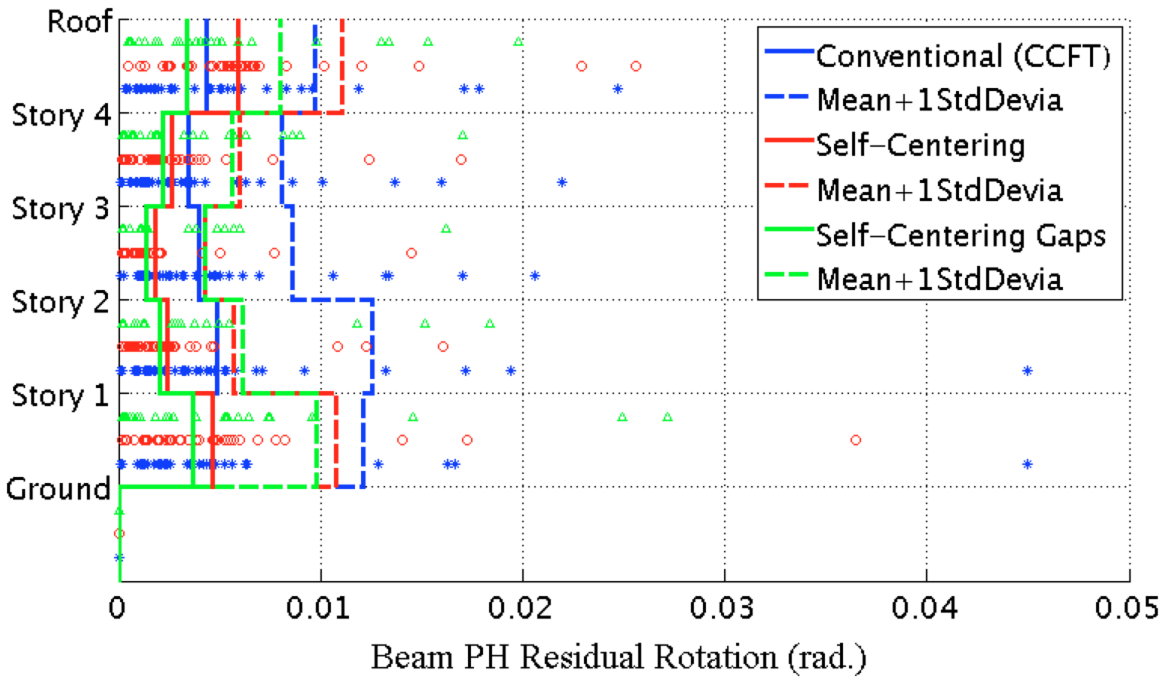

Appendix Figure L-198: Mean of the maximum residual rotation of beam plastic hinges under the 'Filtered 44' DBE level ground motions with a GSR = 1.0 & damping = 5%

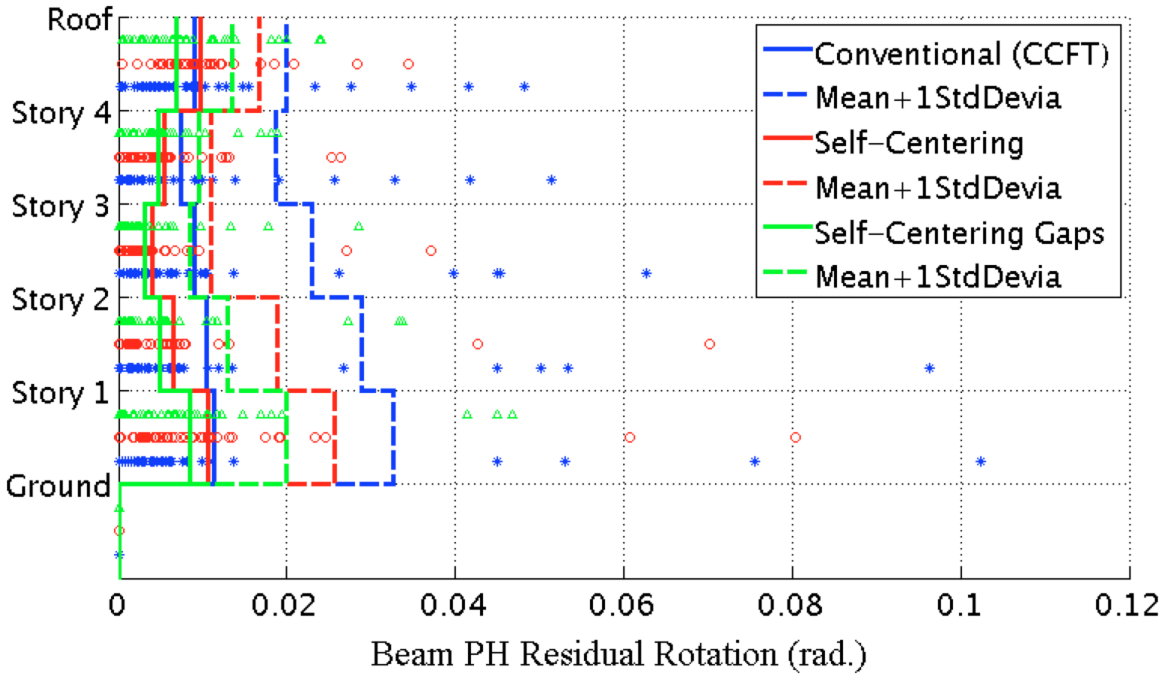

Appendix Figure L-199: Mean of the maximum residual rotation of beam plastic hinges under the 'Filtered 44' MCE level ground motions with a GSR = 1.0 & damping = 5%

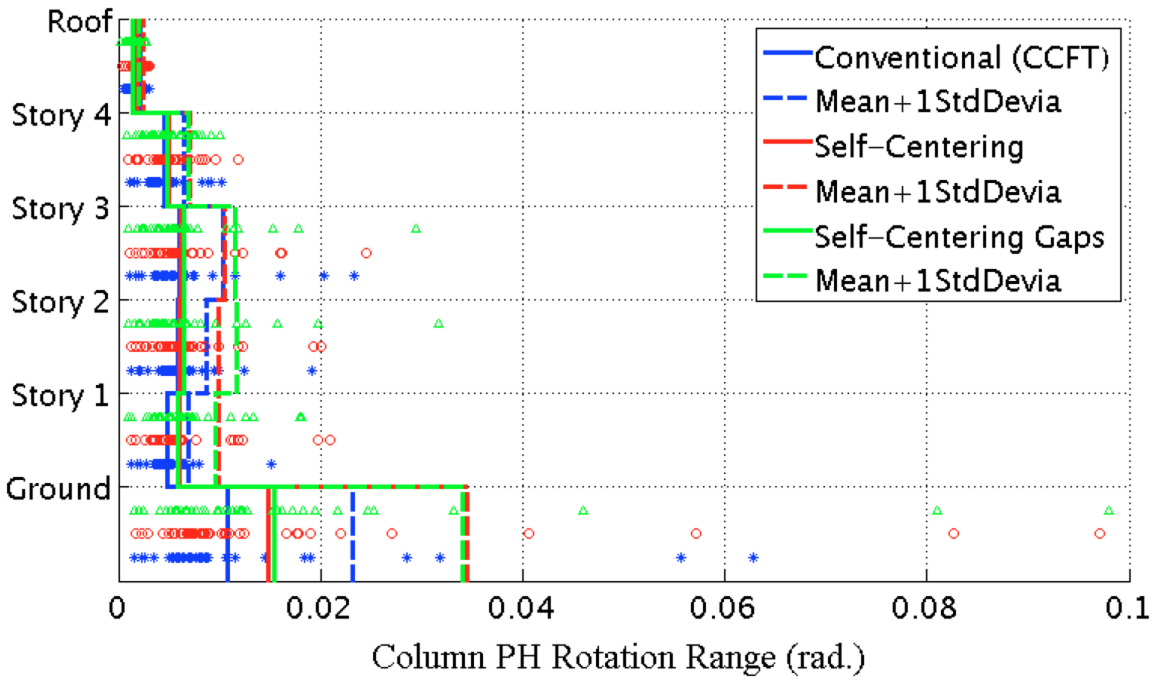

Appendix Figure L-200: Mean of the column PH rotation range under the 'Filtered 44' DBE level ground motions with a GSR = 1.0 & damping = 5%

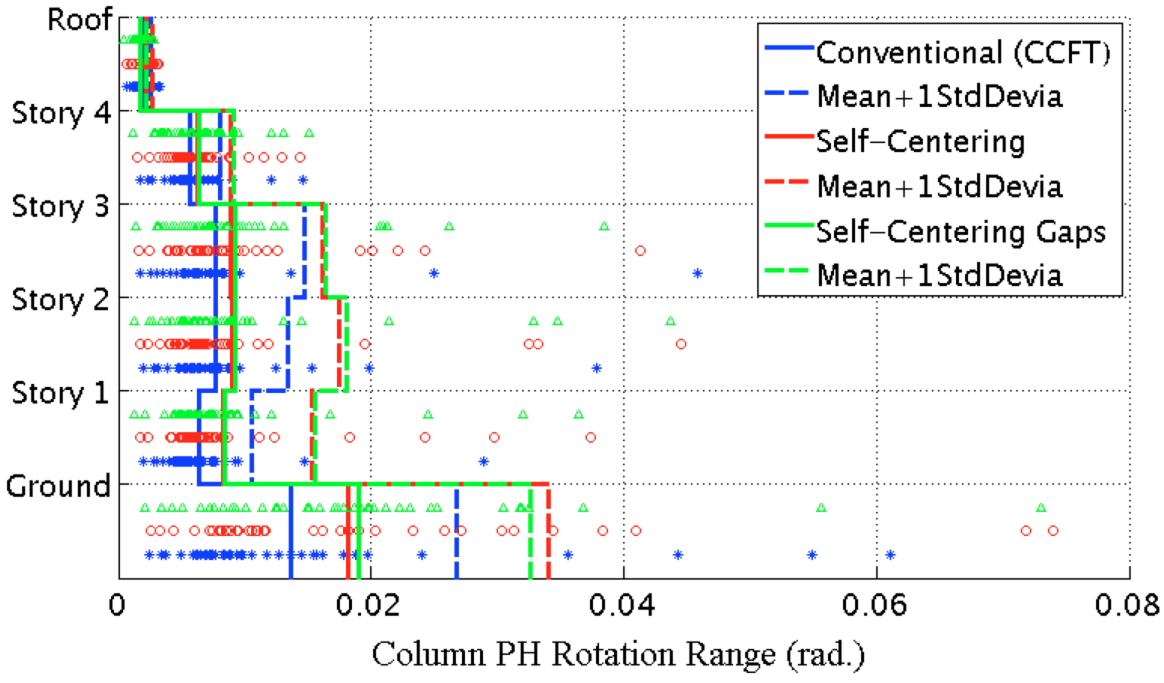

Appendix Figure L-201: Mean of the column PH rotation range under the 'Filtered 44' MCE level ground motions with a GSR = 1.0 & damping = 5%

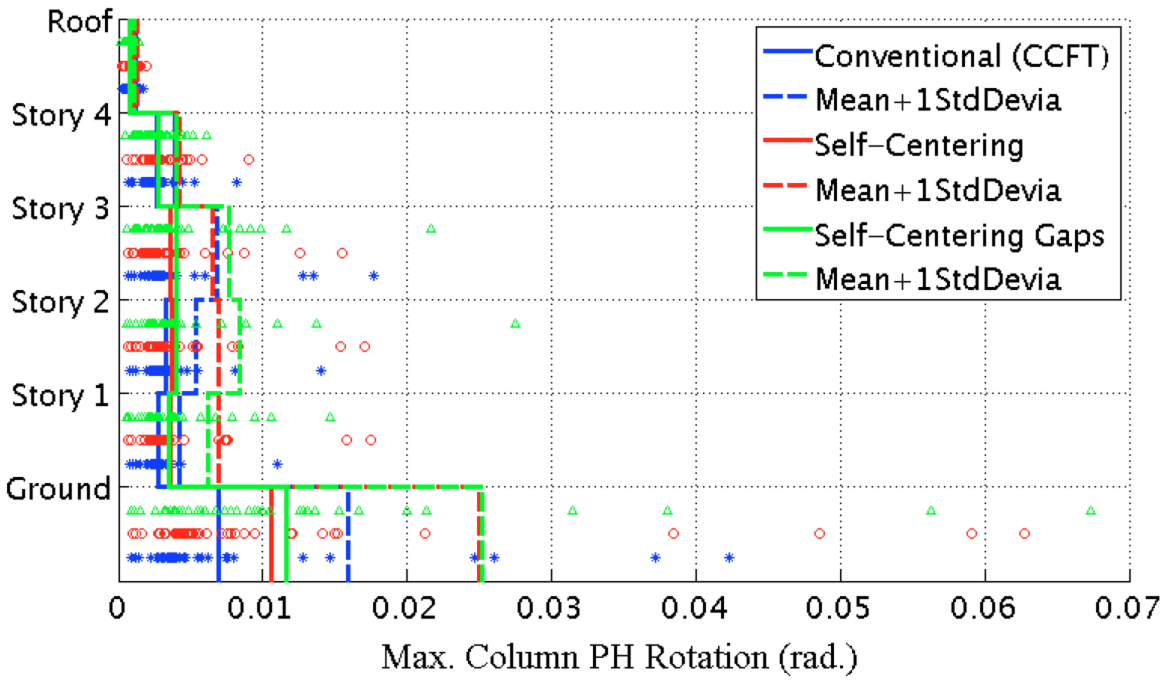

Appendix Figure L-202: Mean of the maximum column PH rotation under the 'Filtered 44' DBE level ground motions with a GSR = 1.0 & damping = 5%

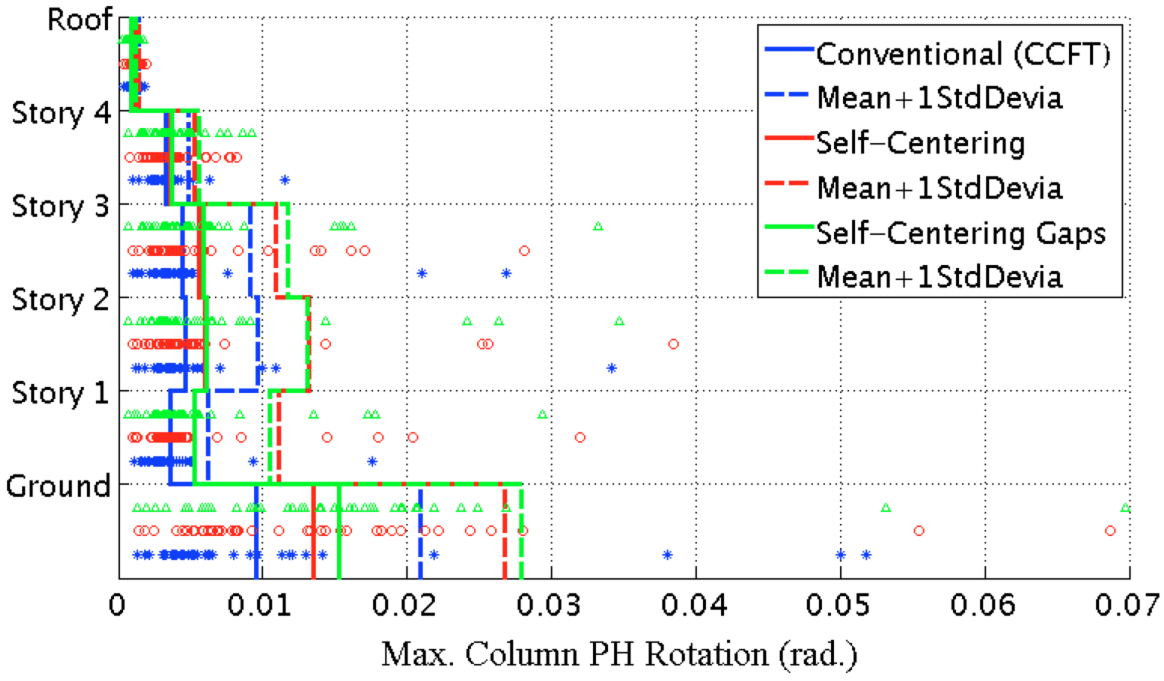

Appendix Figure L-203: Mean of the maximum column PH rotation under the 'Filtered 44' MCE level ground motions with a GSR = 1.0 & damping = 5%

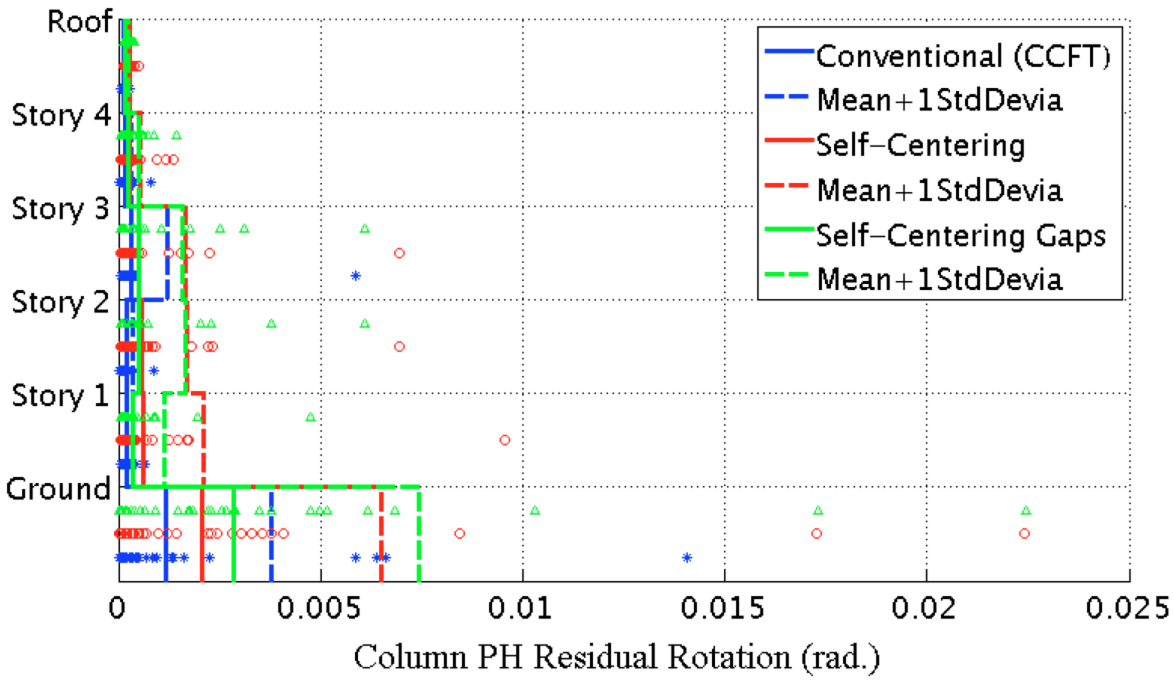

Appendix Figure L-204: Mean of the maximum residual rotation of column plastic hinges under the 'Filtered 44' DBE level ground motions with a GSR = 1.0 & damping = 5%

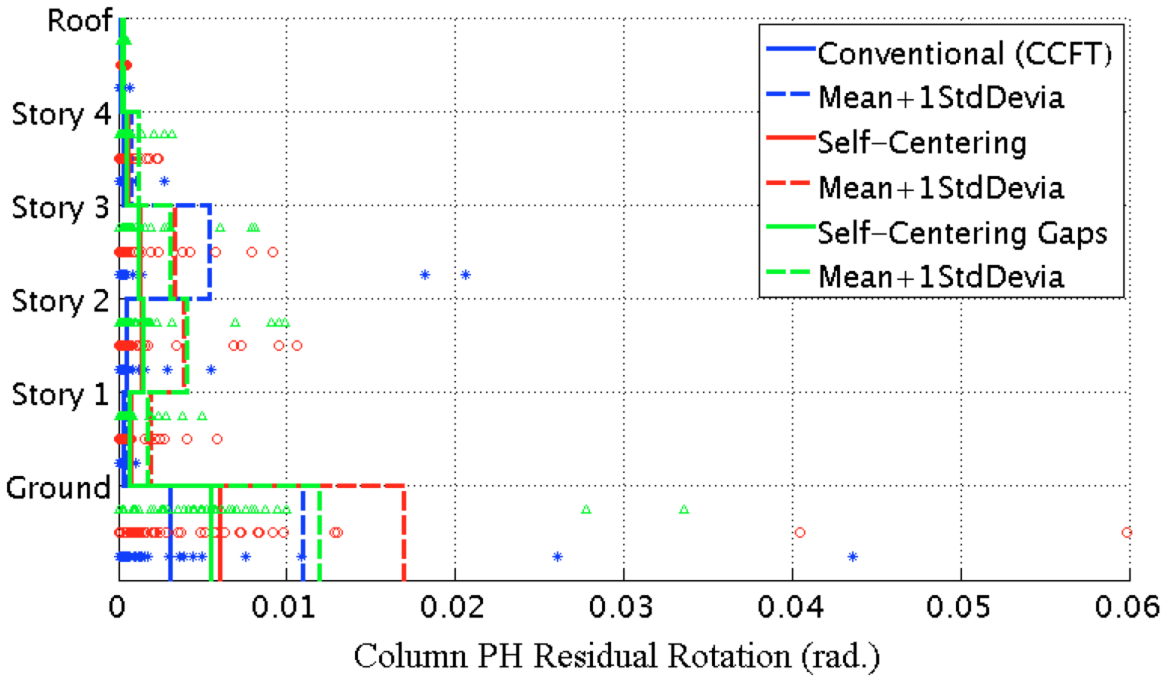

Appendix Figure L-205: Mean of the maximum residual rotation of column plastic hinges under the 'Filtered 44' MCE level ground motions with a GSR = 1.0 & damping = 5%

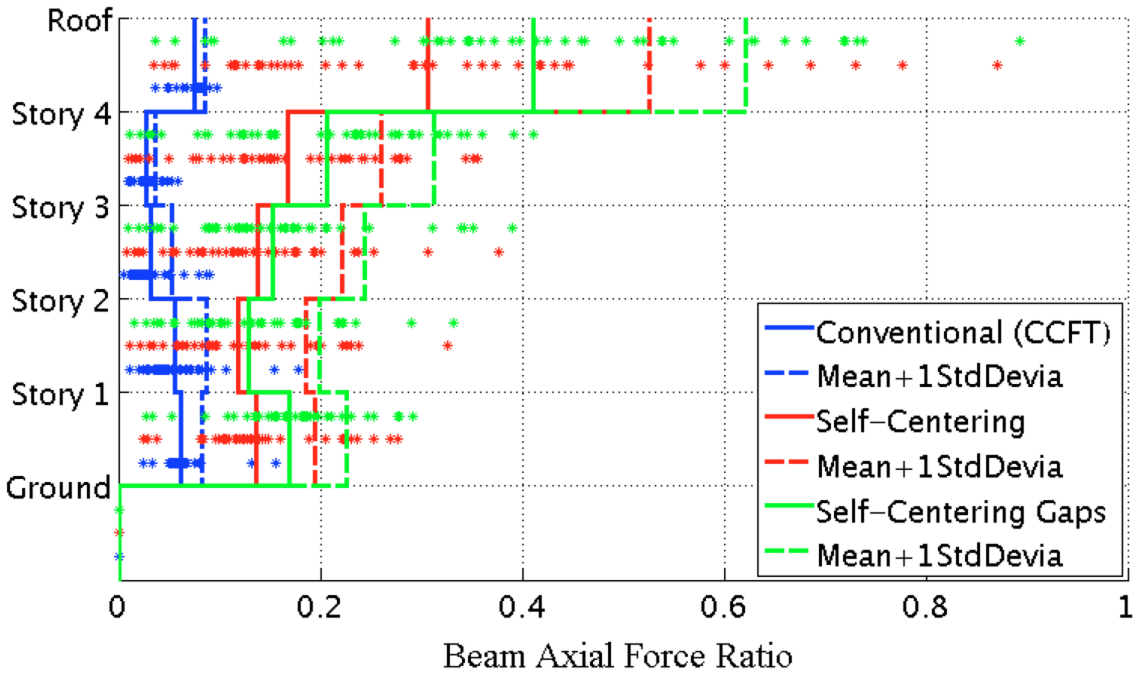

Appendix Figure L-206: Mean of the peak axial force in beams under the 'Filtered 44' DBE level ground motions with a GSR = 1.0 & damping = 5%

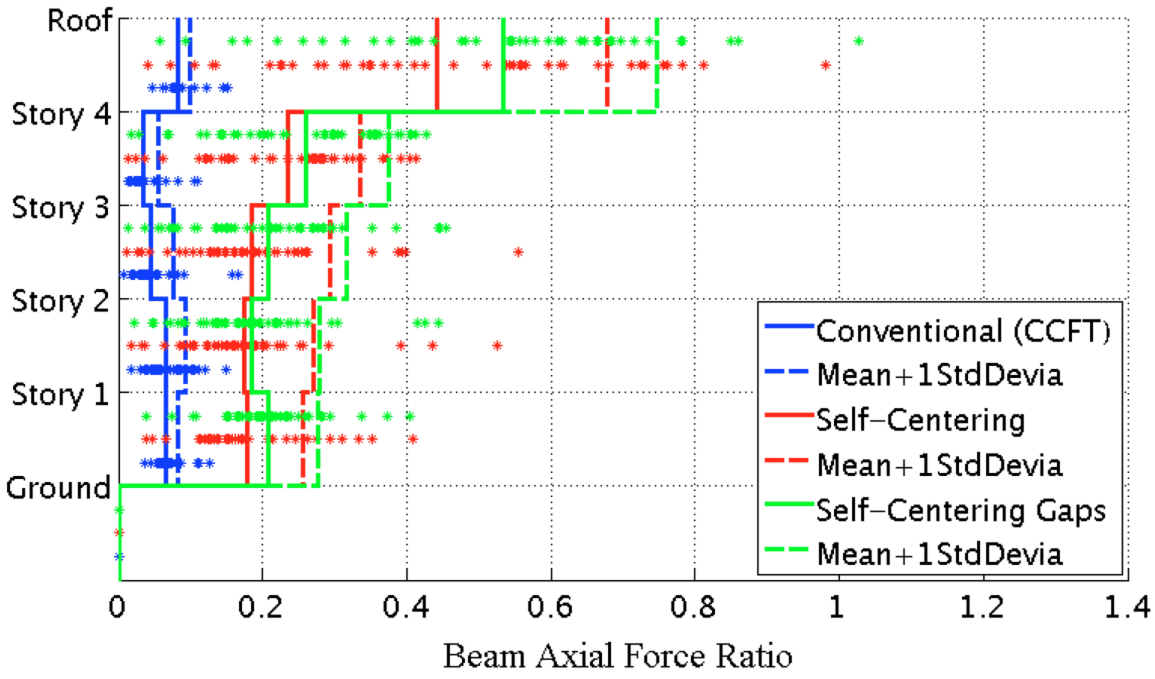

Appendix Figure L-207: Mean of the peak axial force in beams under the 'Filtered 44' MCE level ground motions with a GSR = 1.0 & damping = 5%

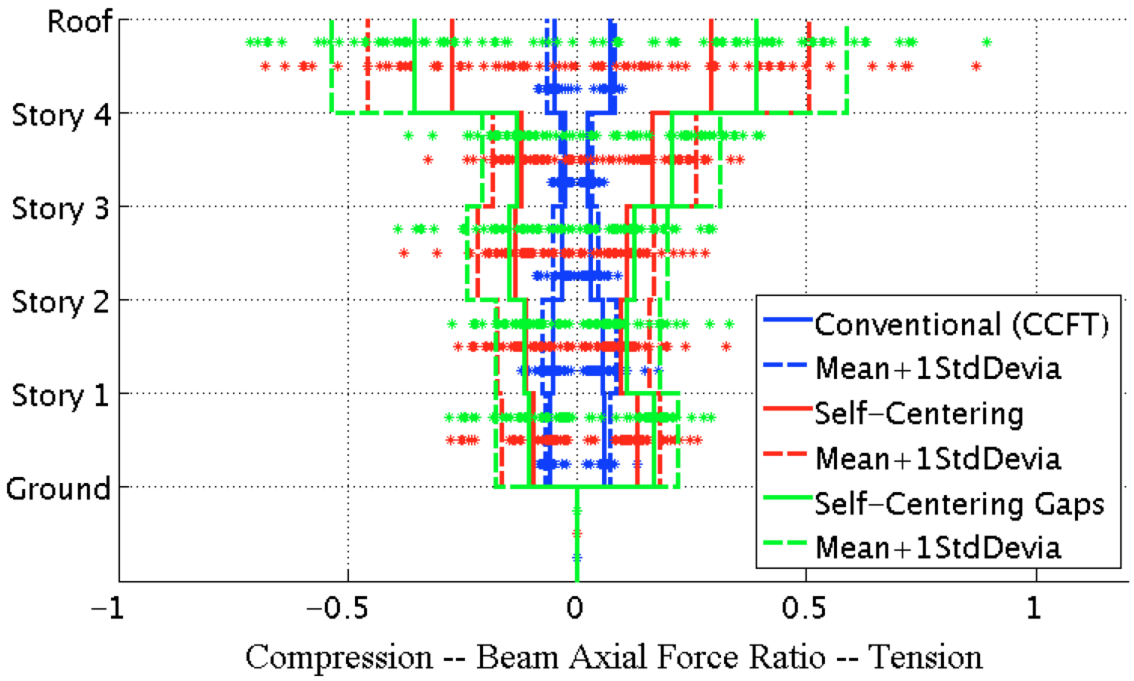

Appendix Figure L-208: Mean of the peak tension vs.compression in beams under the 'Filtered 44' DBE level ground motions with a GSR = 1.0 & damping = 5%

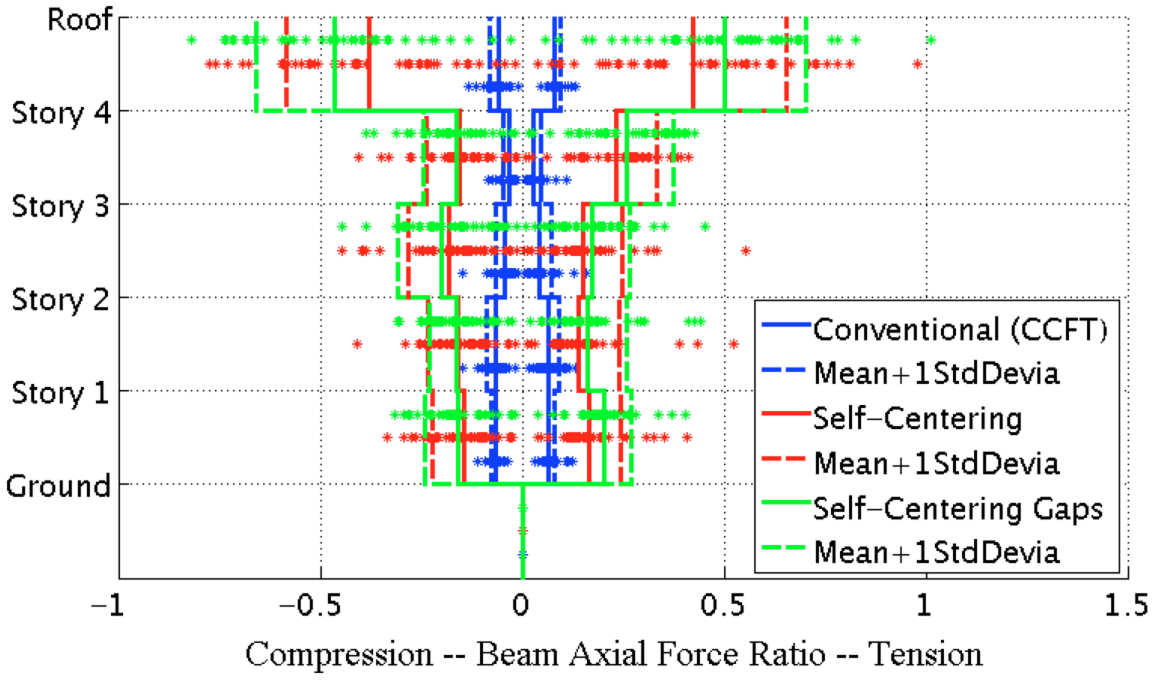

Appendix Figure L-209: Mean of the peak tension vs.compression in beams under the 'Filtered 44' MCE level ground motions with a GSR = 1.0 & damping = 5%

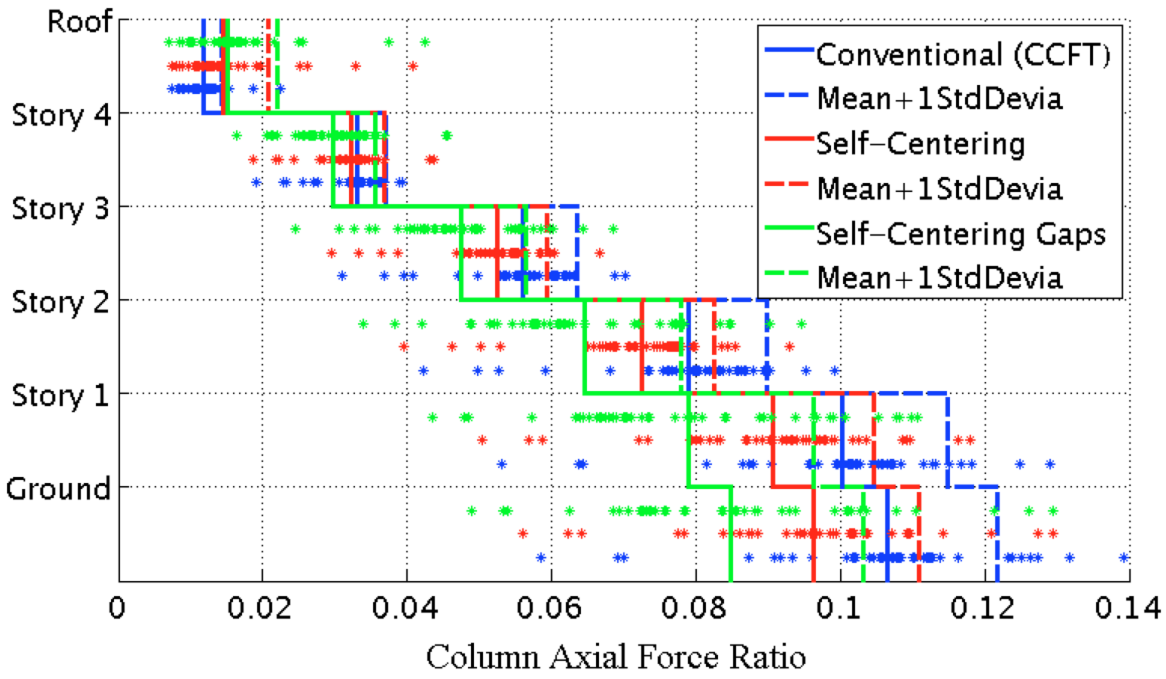

Appendix Figure L-210: Mean of the peak axial force in columns under the 'Filtered 44' DBE level ground motions with a GSR = 1.0 & damping = 5%

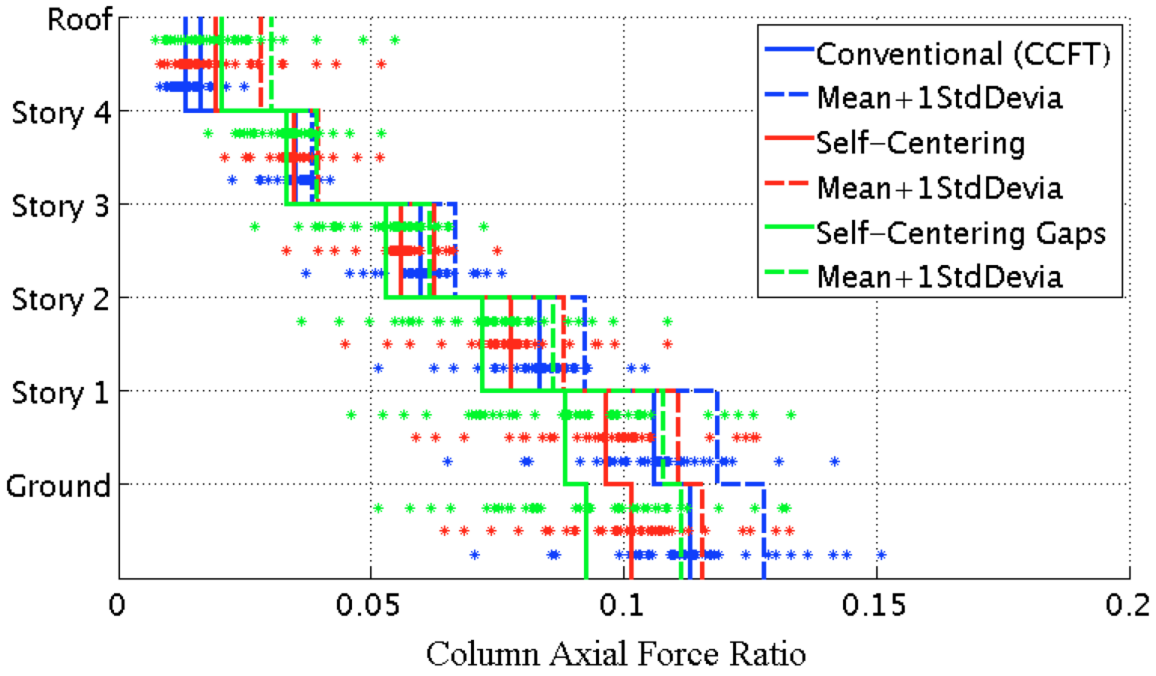

Appendix Figure L-211: Mean of the peak axial force in columns under the 'Filtered 44' MCE level ground motions with a GSR = 1.0 & damping = 5%

Appendix M

Component Behavior for Systems with a GSR = 1.1 & Damping = 5%

M.1 Beam Plastic Hinges

BeamPH_Left_12: 'Left' beam plastic hinge in 'Span 1' and on 'Story 2'.

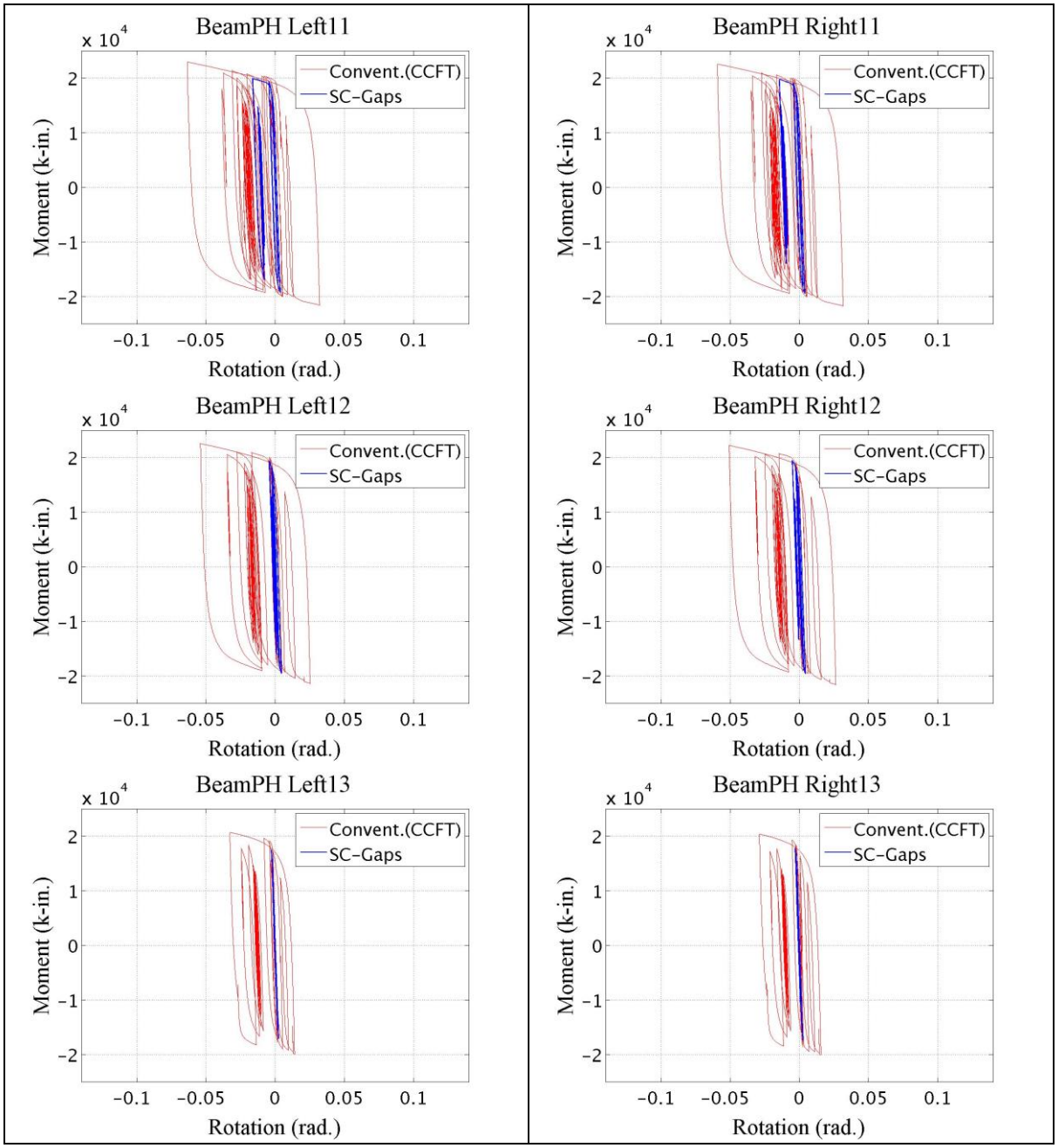

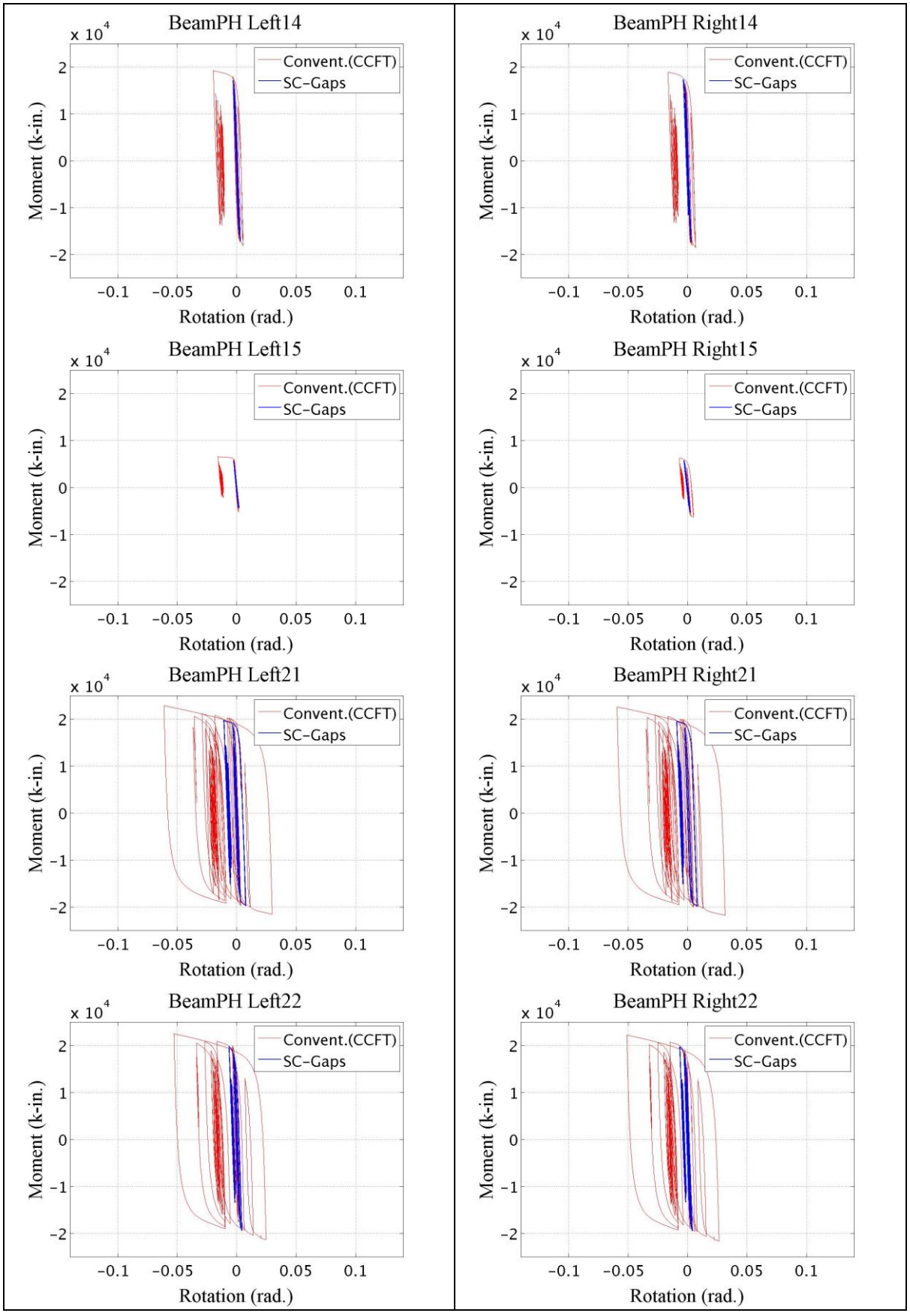
BeamPH Left14
BeamPH Right14
BeamPH Left15
BeamPH Right15
BeamPH Left21
BeamPH Right21
BeamPH Left22
BeamPH Right22
x 10^4
Moment (k-in.)
Rotation (rad.)
Convent.(CCFT)
SC-Gaps

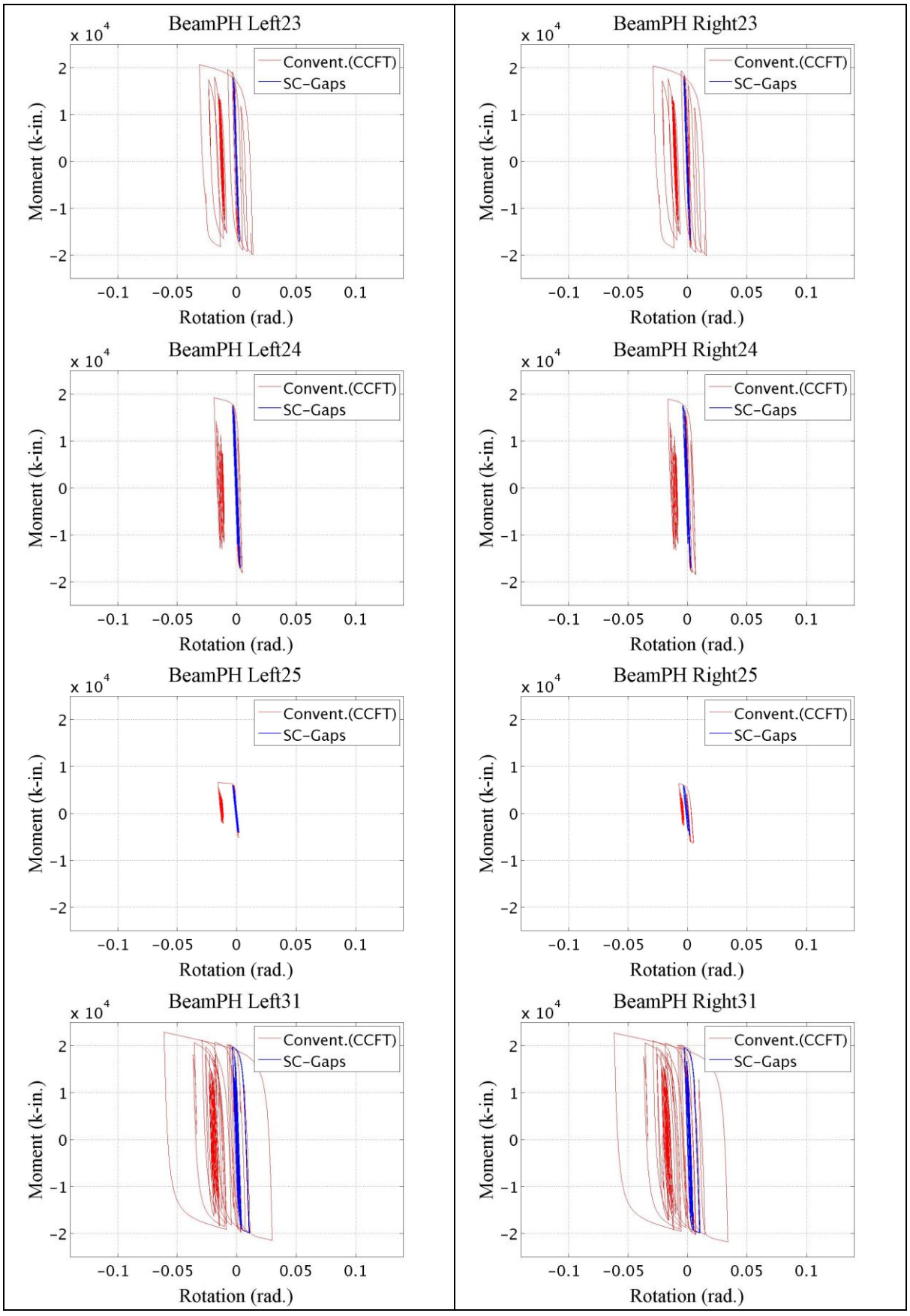
BeamPH Left23
BeamPH Right23
BeamPH Left24
BeamPH Right24
BeamPH Left25
BeamPH Right25
BeamPH Left31
BeamPH Right31
x 10^4
Moment (k-in.)
Rotation (rad.)
Convent.(CCFT)
SC-Gaps

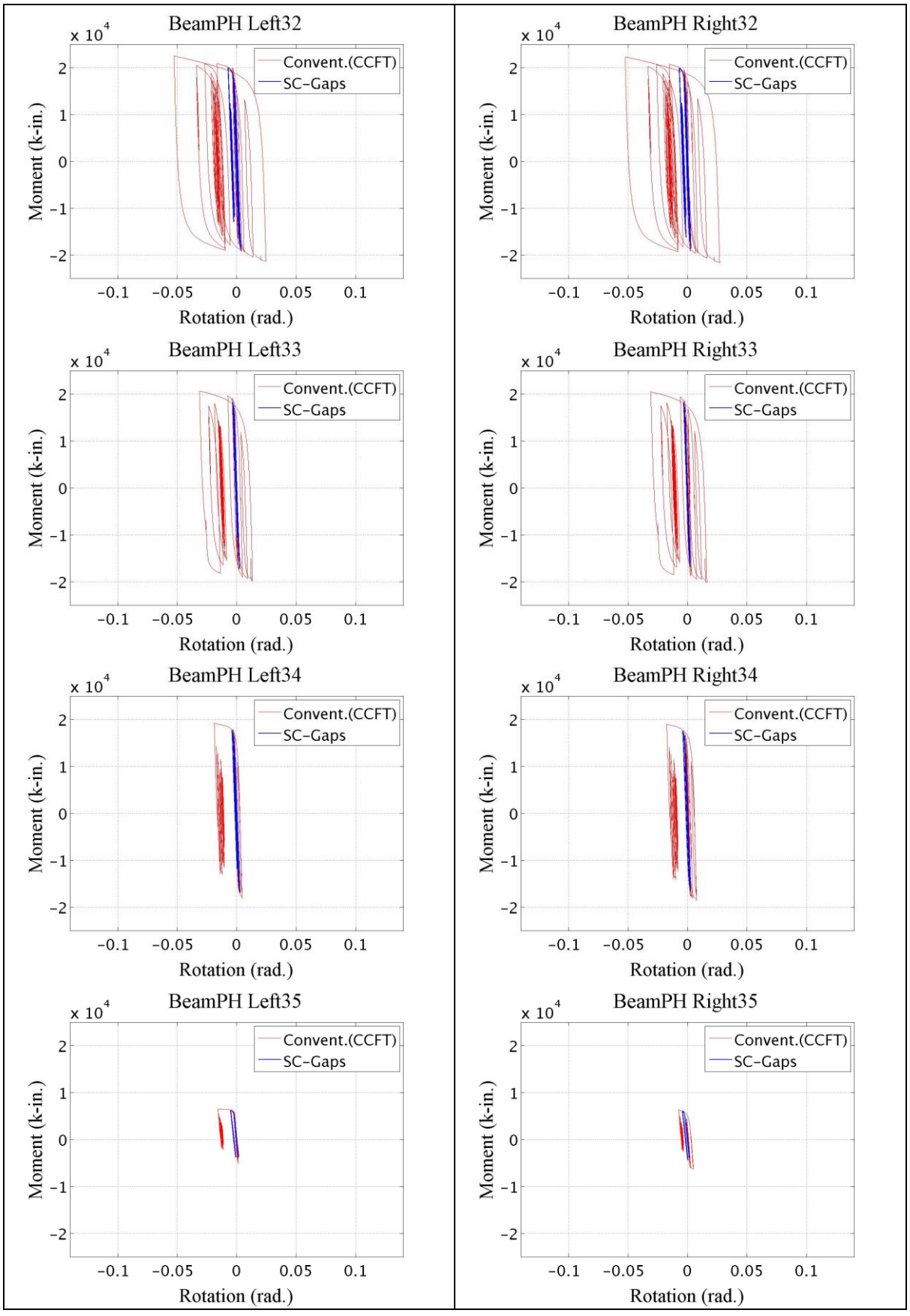

Appendix Figure M-1: Beam plastic hinges

M.2 Column Plastic Hinges

ColPH_Top_10: 'Top' column plastic hinge in 'Column Line 1' and on 'Story 0 (Basement)'.

ColPH_Bottom_11: 'Bottom' column plastic hinge in 'Column Line 1' and on 'Story 1'.

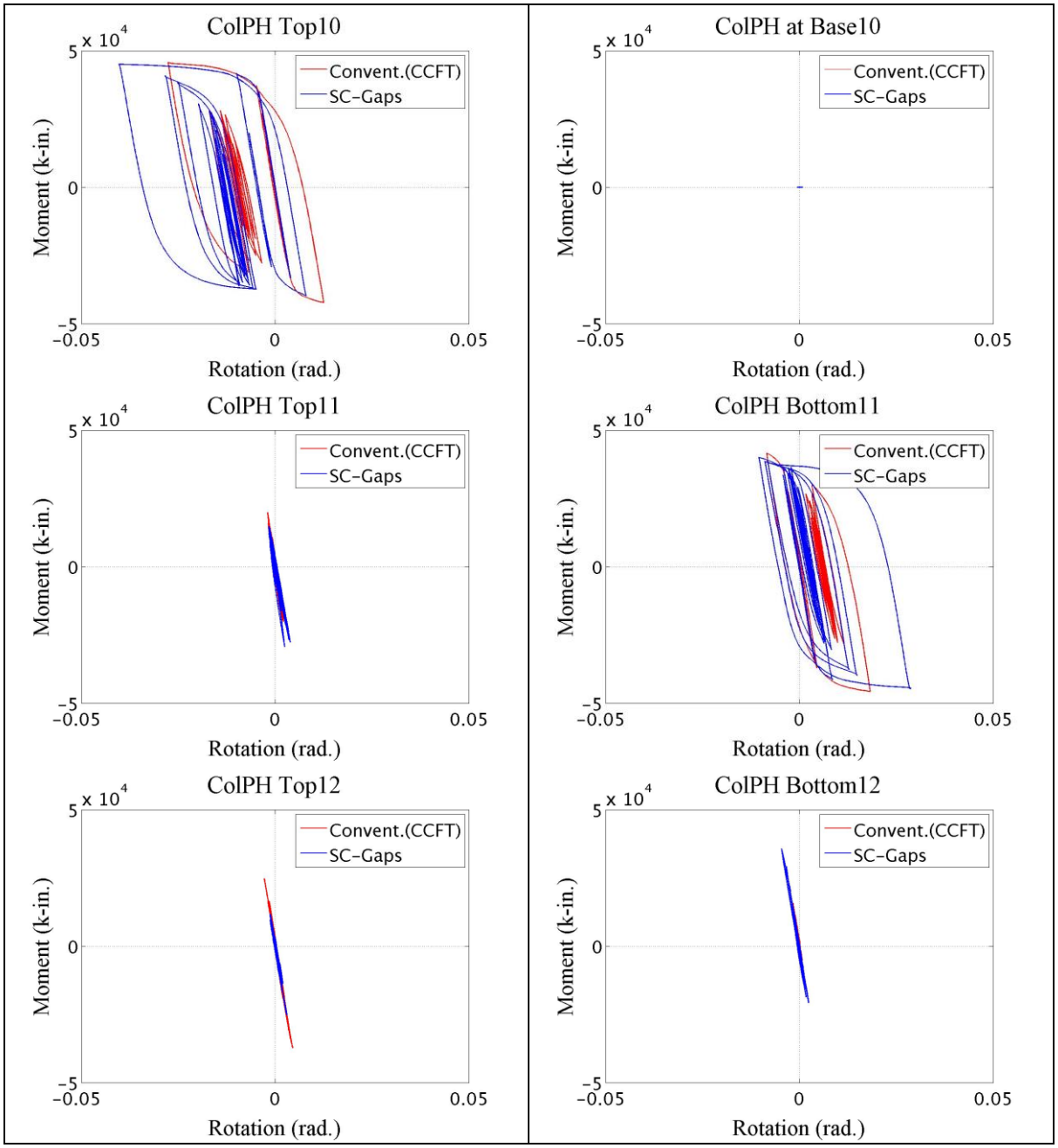

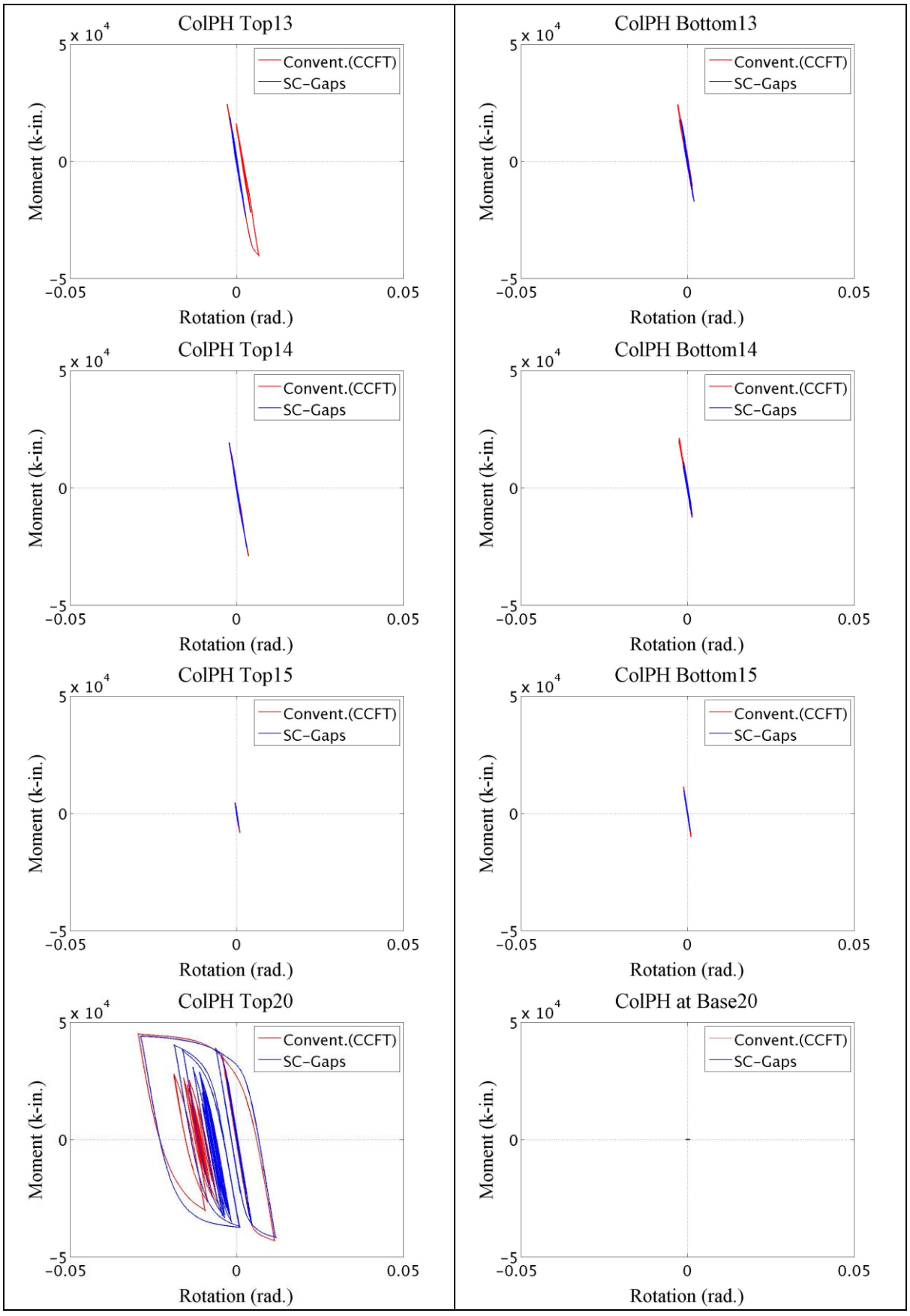
ColPH Top13
ColPH Bottom13
ColPH Top14
ColPH Bottom14
ColPH Top15
ColPH Bottom15
ColPH Top20
ColPH at Base20
x 10^4
5
0
−5
Moment (k-in.)
−0.05
0
0.05
Rotation (rad.)
Convent.(CCFT)
SC-Gaps

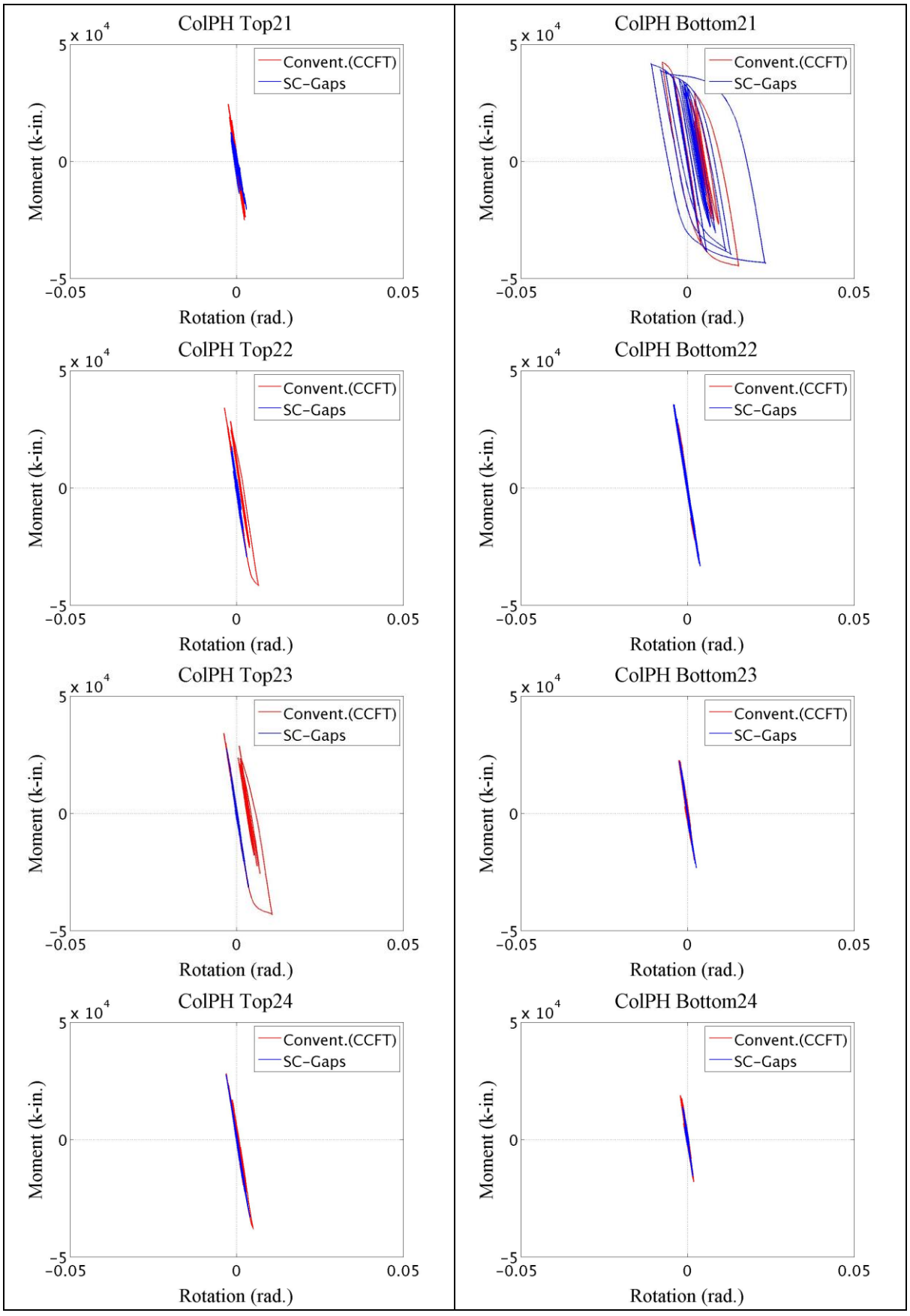
ColPH Top21
ColPH Bottom21
ColPH Top22
ColPH Bottom22
ColPH Top23
ColPH Bottom23
ColPH Top24
ColPH Bottom24
x 10^4
5
0
−5
Moment (k-in.)
−0.05
0
0.05
Rotation (rad.)
Convent.(CCFT)
SC-Gaps

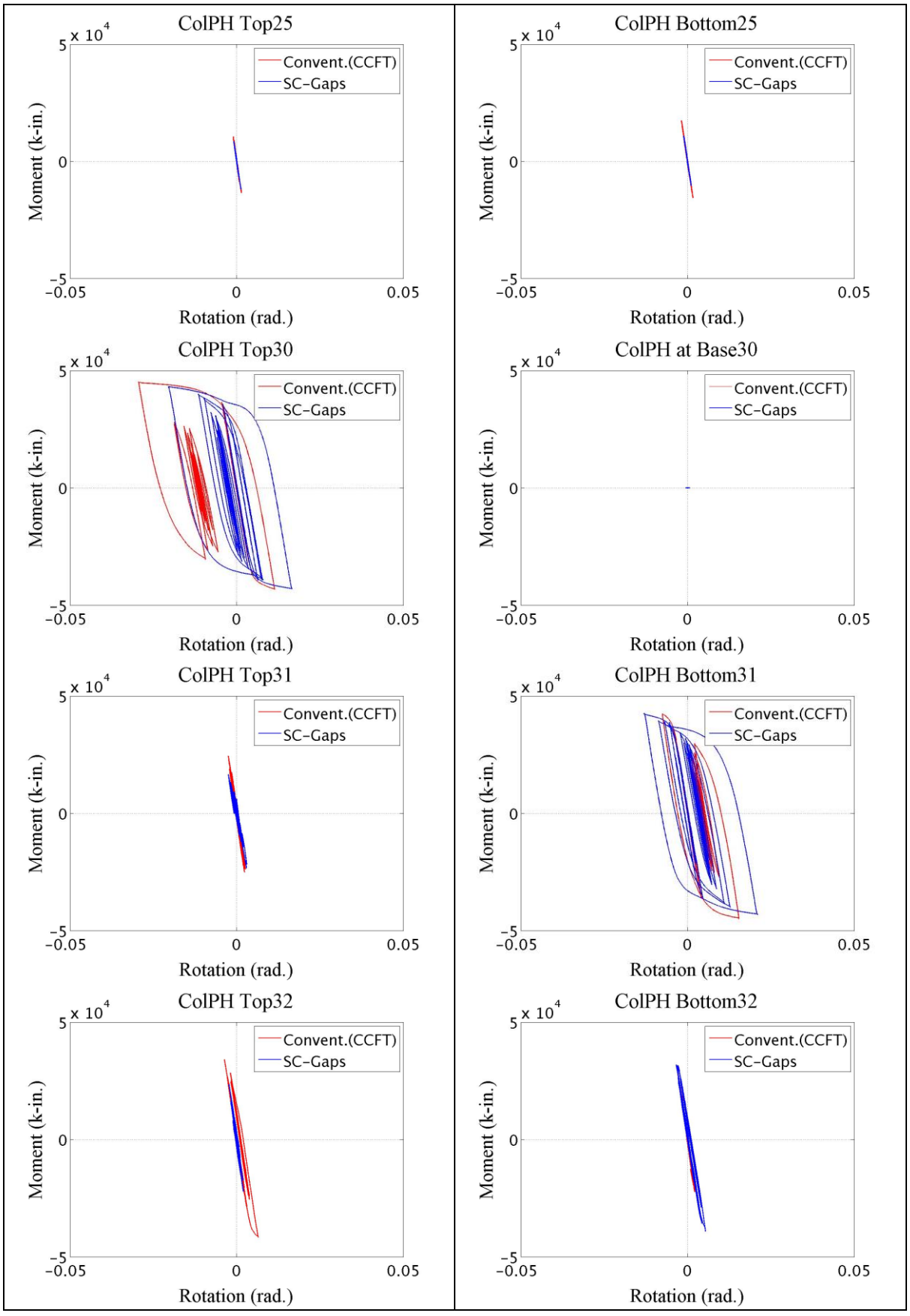
ColPH Top25
ColPH Bottom25
ColPH Top30
ColPH at Base30
ColPH Top31
ColPH Bottom31
ColPH Top32
ColPH Bottom32
x 10^4
5
0
−5
Moment (k-in.)
−0.05
0
0.05
Rotation (rad.)
Convent.(CCFT)
SC-Gaps

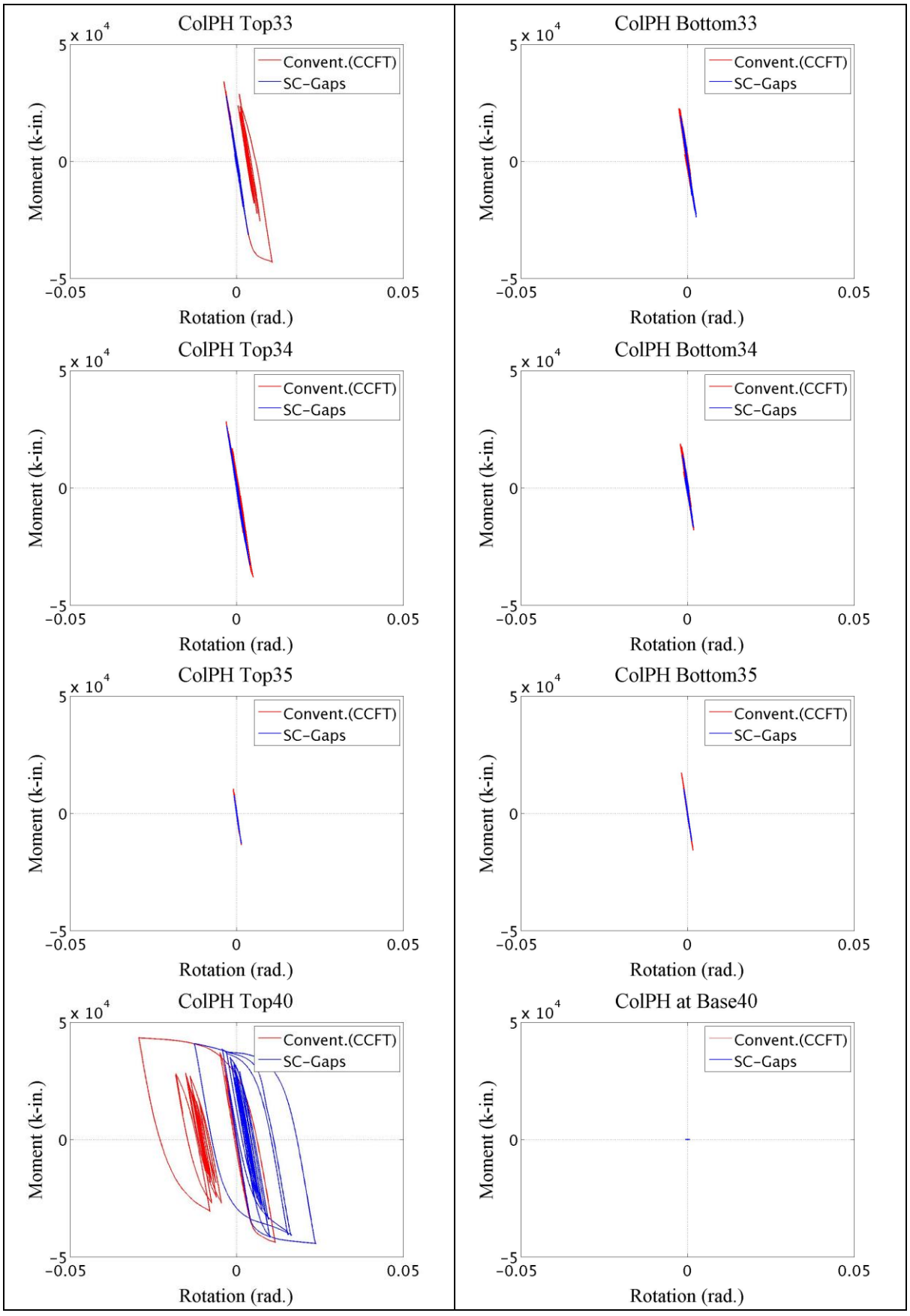
ColPH Top33
ColPH Bottom33
ColPH Top34
ColPH Bottom34
ColPH Top35
ColPH Bottom35
ColPH Top40
ColPH at Base40
x 10^4
5
0
−5
Moment (k-in.)
−0.05
0
0.05
Rotation (rad.)
Convent.(CCFT)
SC-Gaps

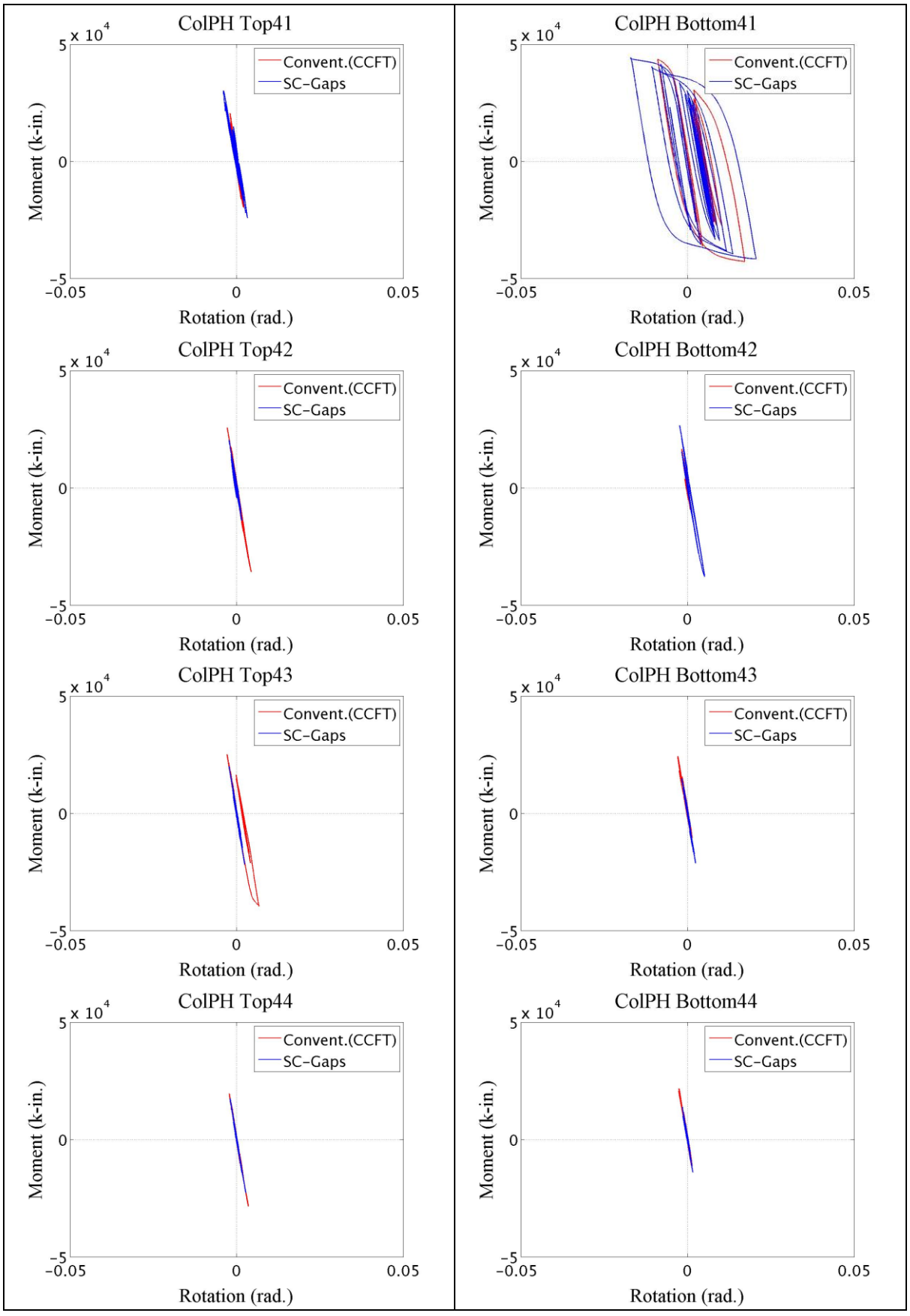
ColPH Top41
ColPH Bottom41
ColPH Top42
ColPH Bottom42
ColPH Top43
ColPH Bottom43
ColPH Top44
ColPH Bottom44
x 10^4
5
0
−5
Moment (k-in.)
−0.05
0
0.05
Rotation (rad.)
Convent.(CCFT)
SC-Gaps

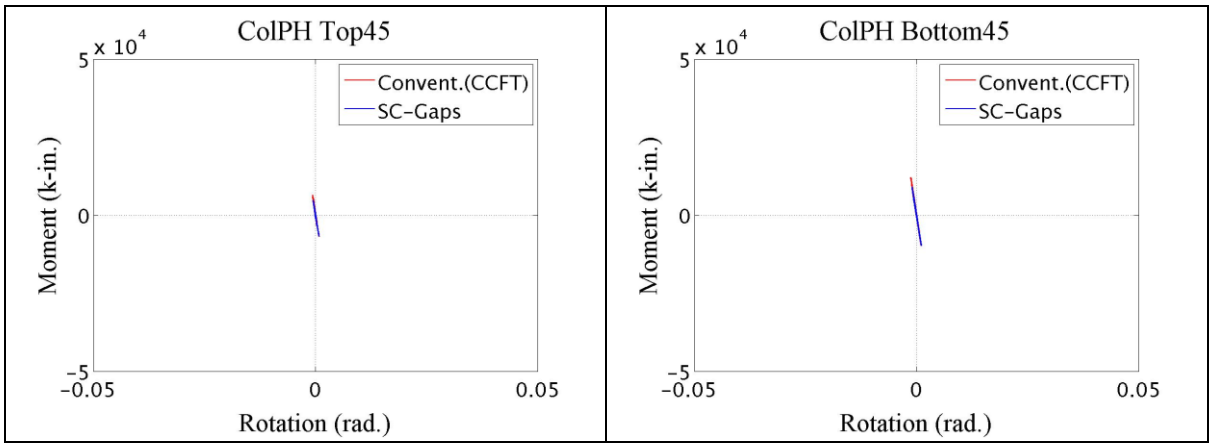

Appendix Figure M-2: Column plastic hinges

M.3 Connection Drift

Drift of Connection 10: Connection in ‘Column Line 1’ and on ‘Story 0 (Basement)’.

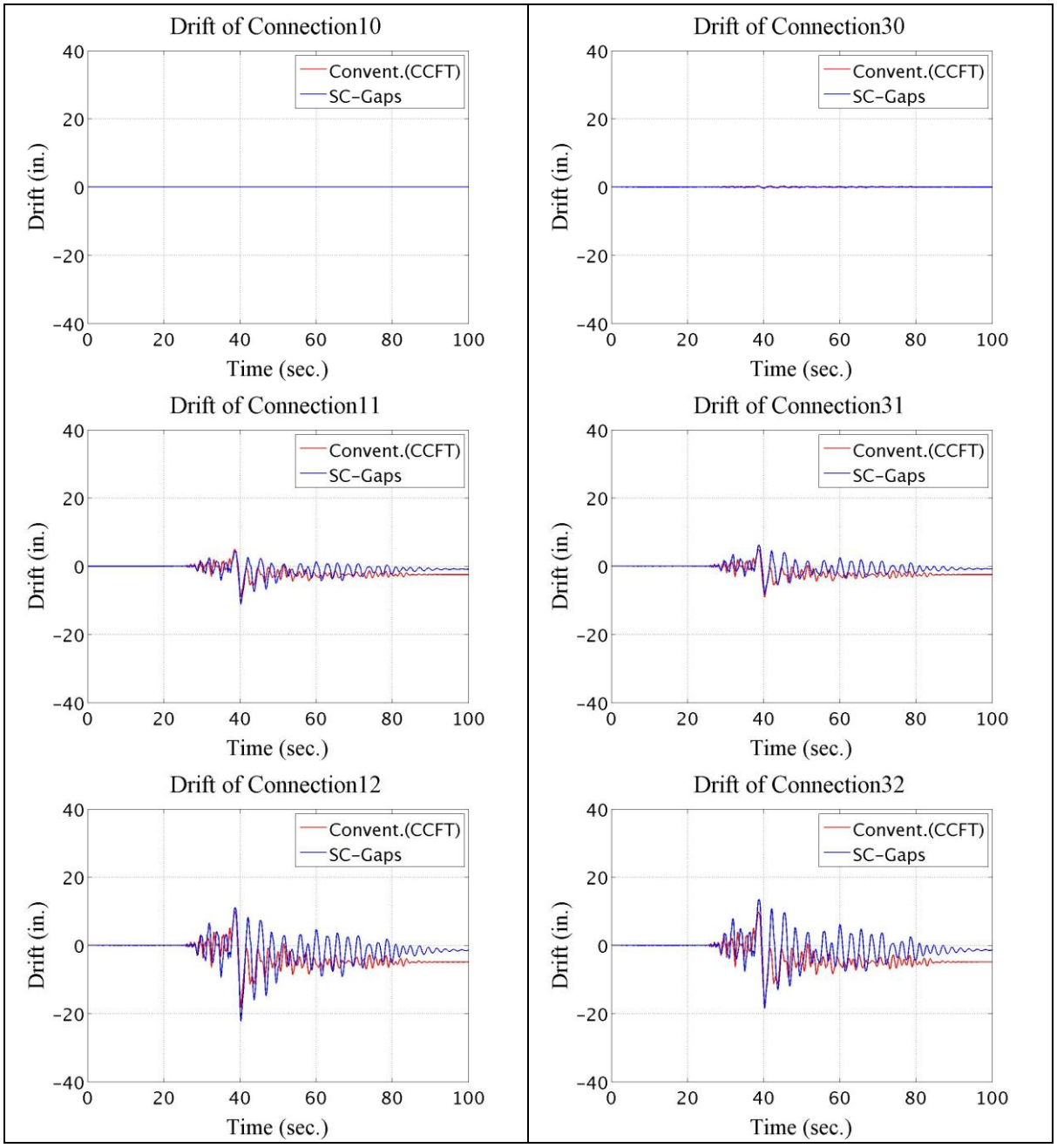

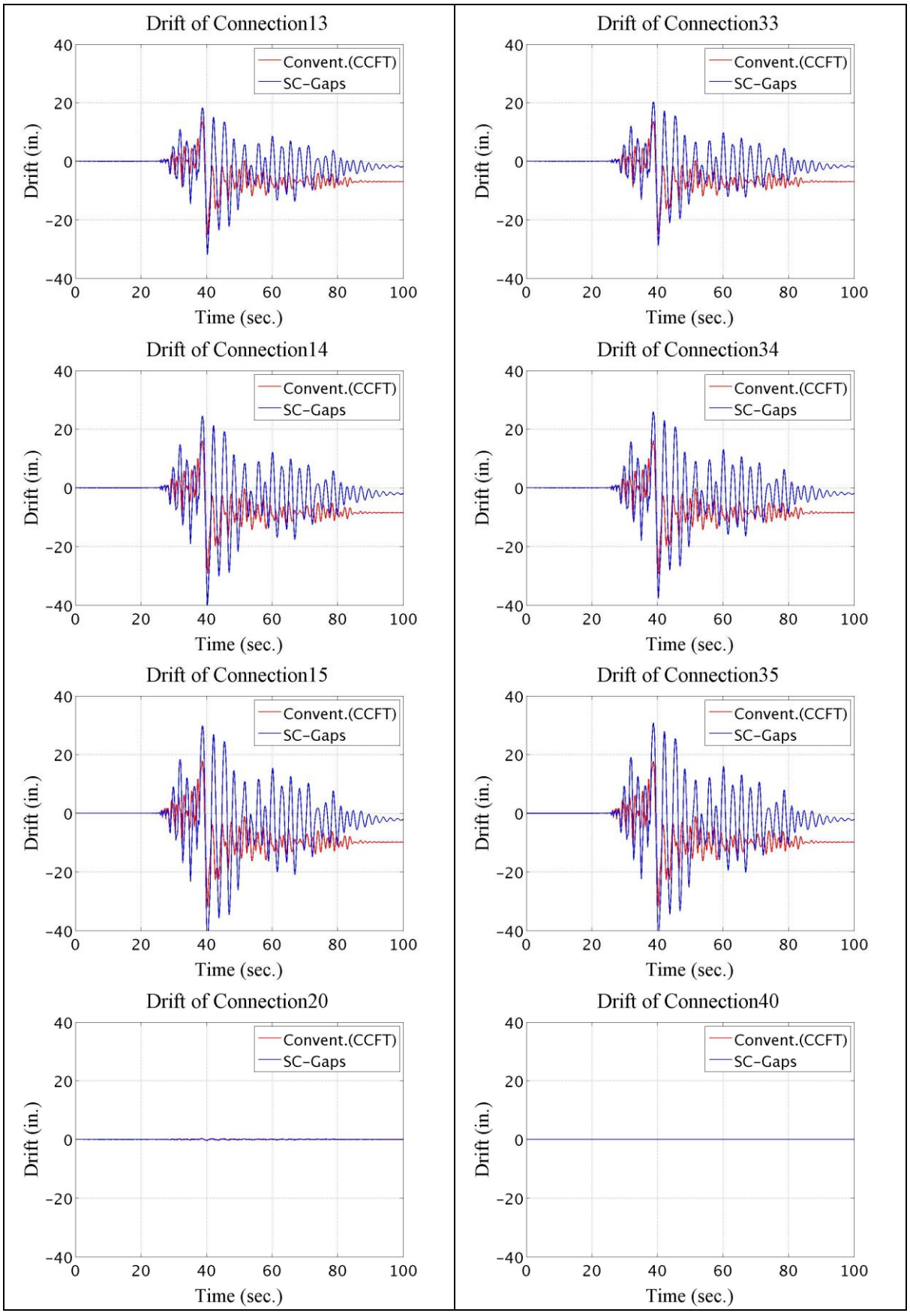
Drift of Connection13
Drift of Connection33
Drift of Connection14
Drift of Connection34
Drift of Connection15
Drift of Connection35
Drift of Connection20
Drift of Connection40
Convent.(CCFT)
SC-Gaps
Drift (in.)
Time (sec.)
40
20
0
-20
-40
0
20
40
60
80
100

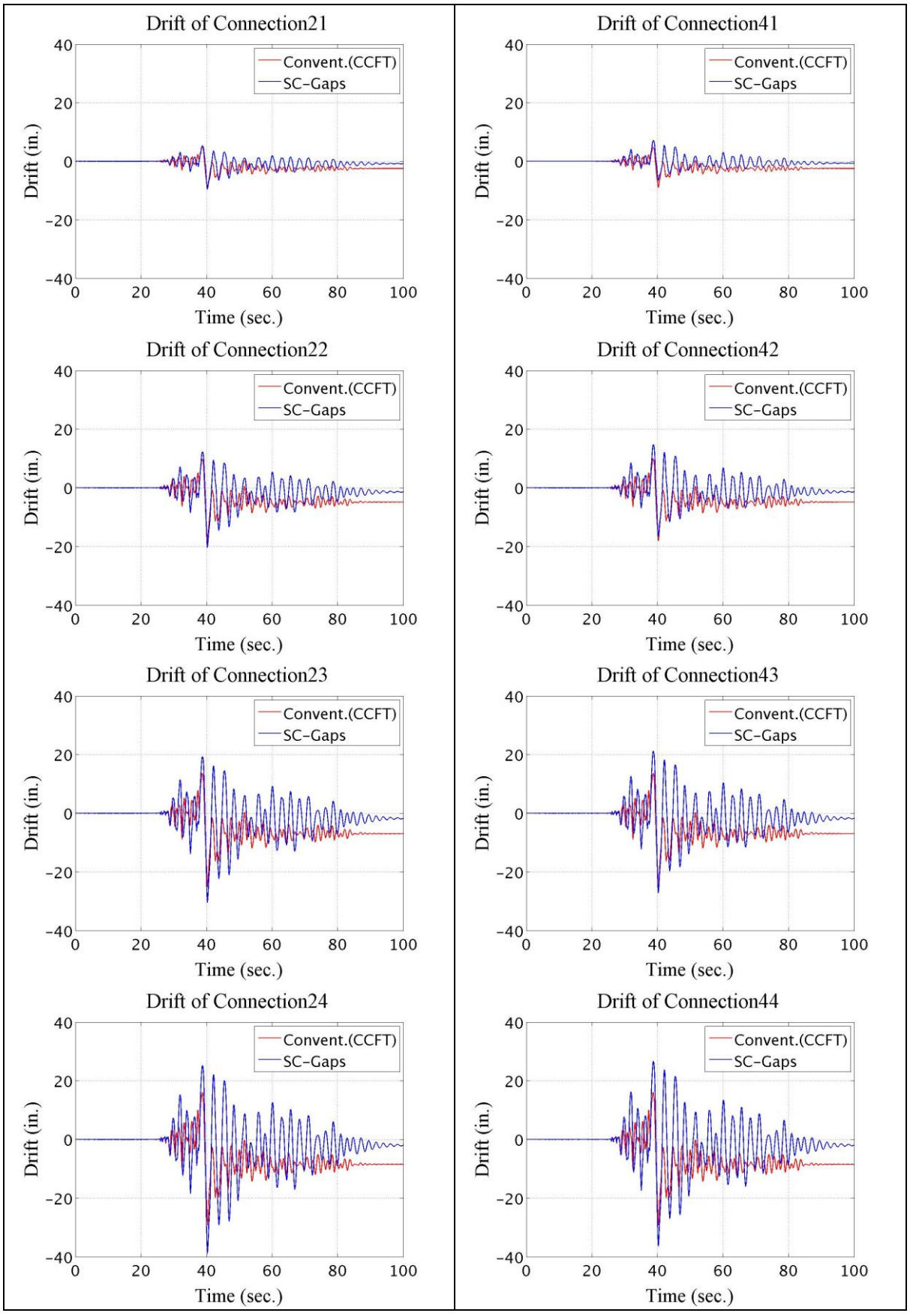
Drift of Connection21
Drift of Connection41
Drift of Connection22
Drift of Connection42
Drift of Connection23
Drift of Connection43
Drift of Connection24
Drift of Connection44
Convent.(CCFT)
SC-Gaps
Drift (in.)
Time (sec.)
40
20
0
-20
-40
0
20
40
60
80
100

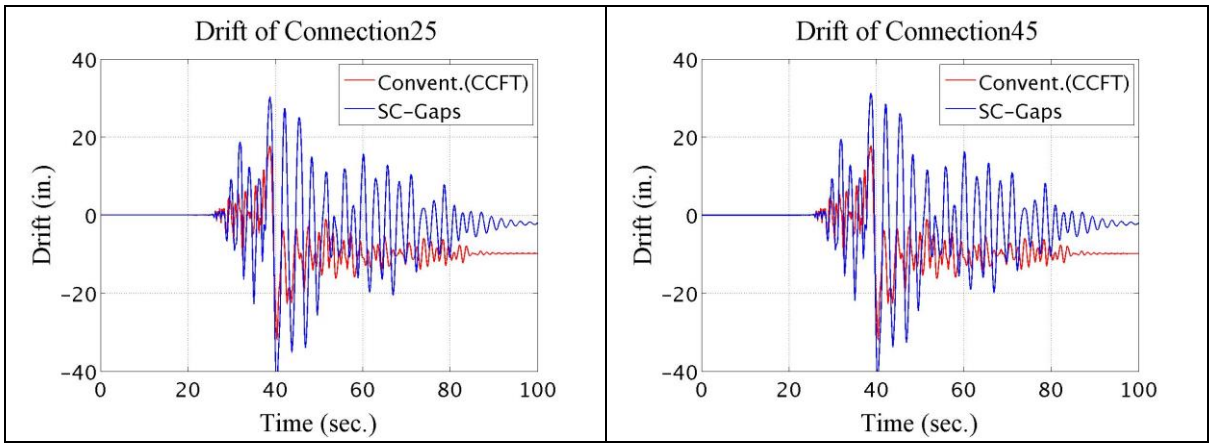

Appendix Figure M-3: Connection drift

M.4 Connection Rotation

Rotation of Connection 10: Connection in ‘Column Line 1’ and on ‘Story 0 (Basement)’.

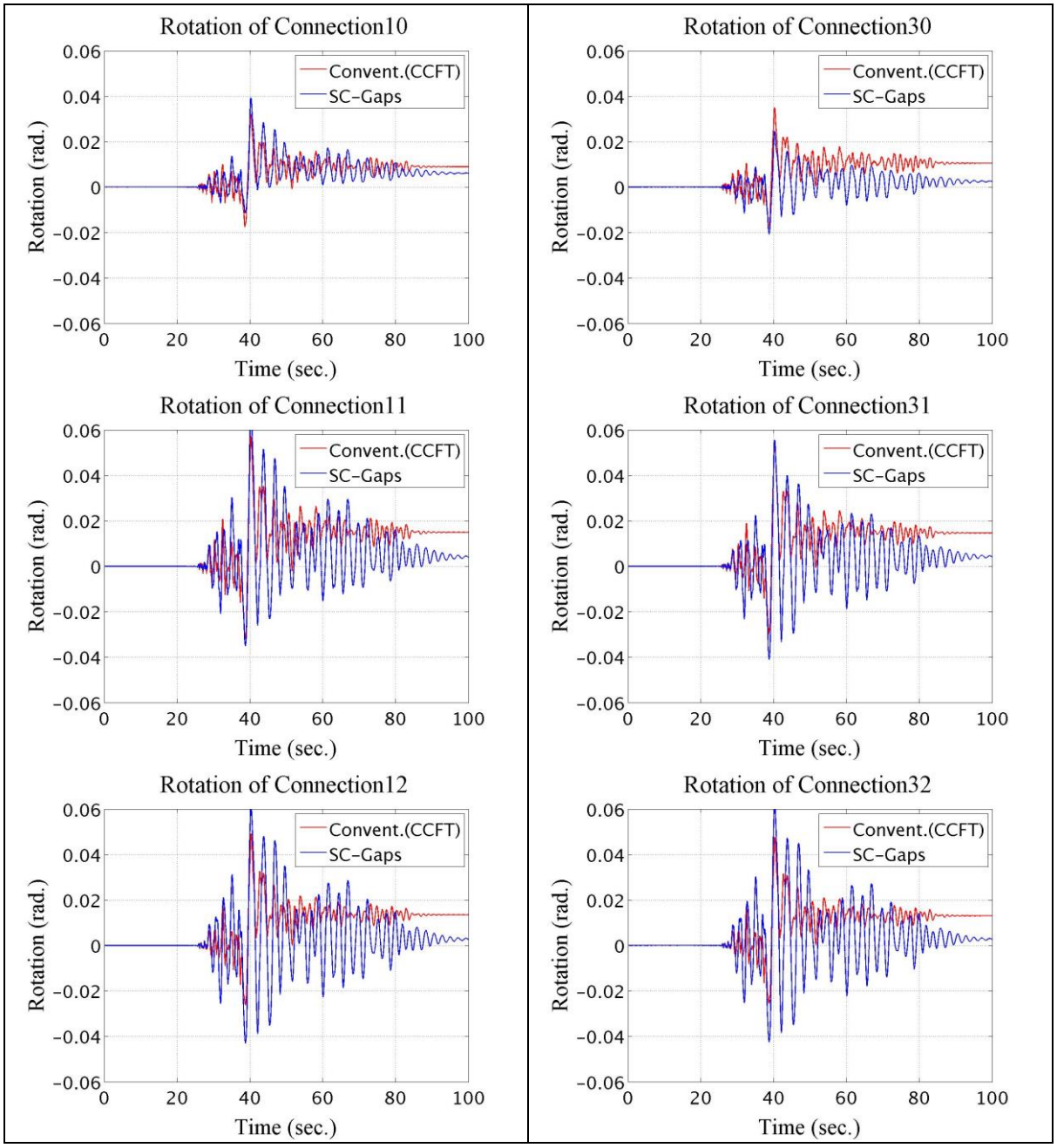

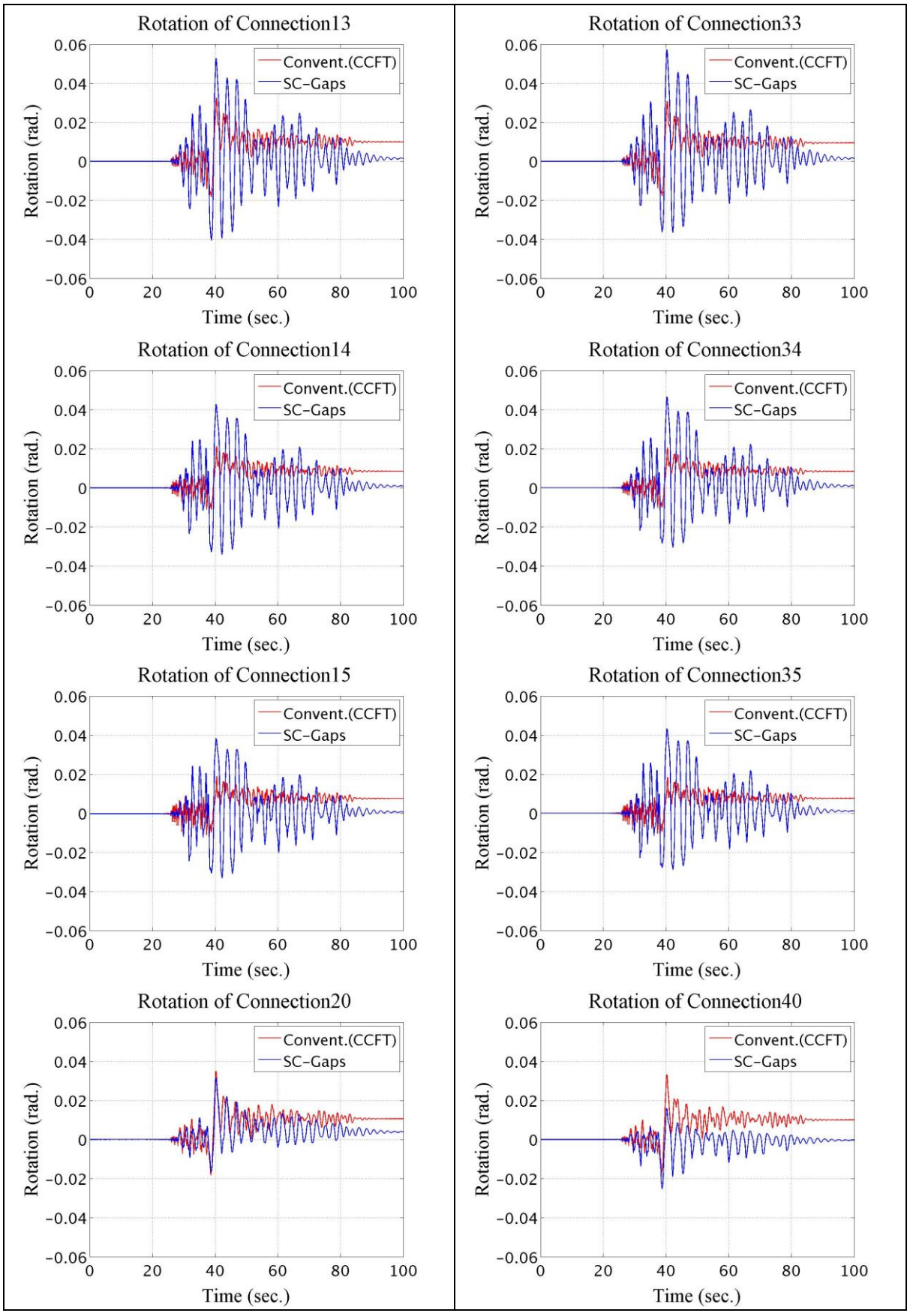
Rotation of Connection13
Rotation of Connection33
Rotation of Connection14
Rotation of Connection34
Rotation of Connection15
Rotation of Connection35
Rotation of Connection20
Rotation of Connection40
Convent.(CCFT)
SC-Gaps
Rotation (rad.)
Time (sec.)
0.06
0.04
0.02
0
-0.02
-0.04
-0.06
0
20
40
60
80
100

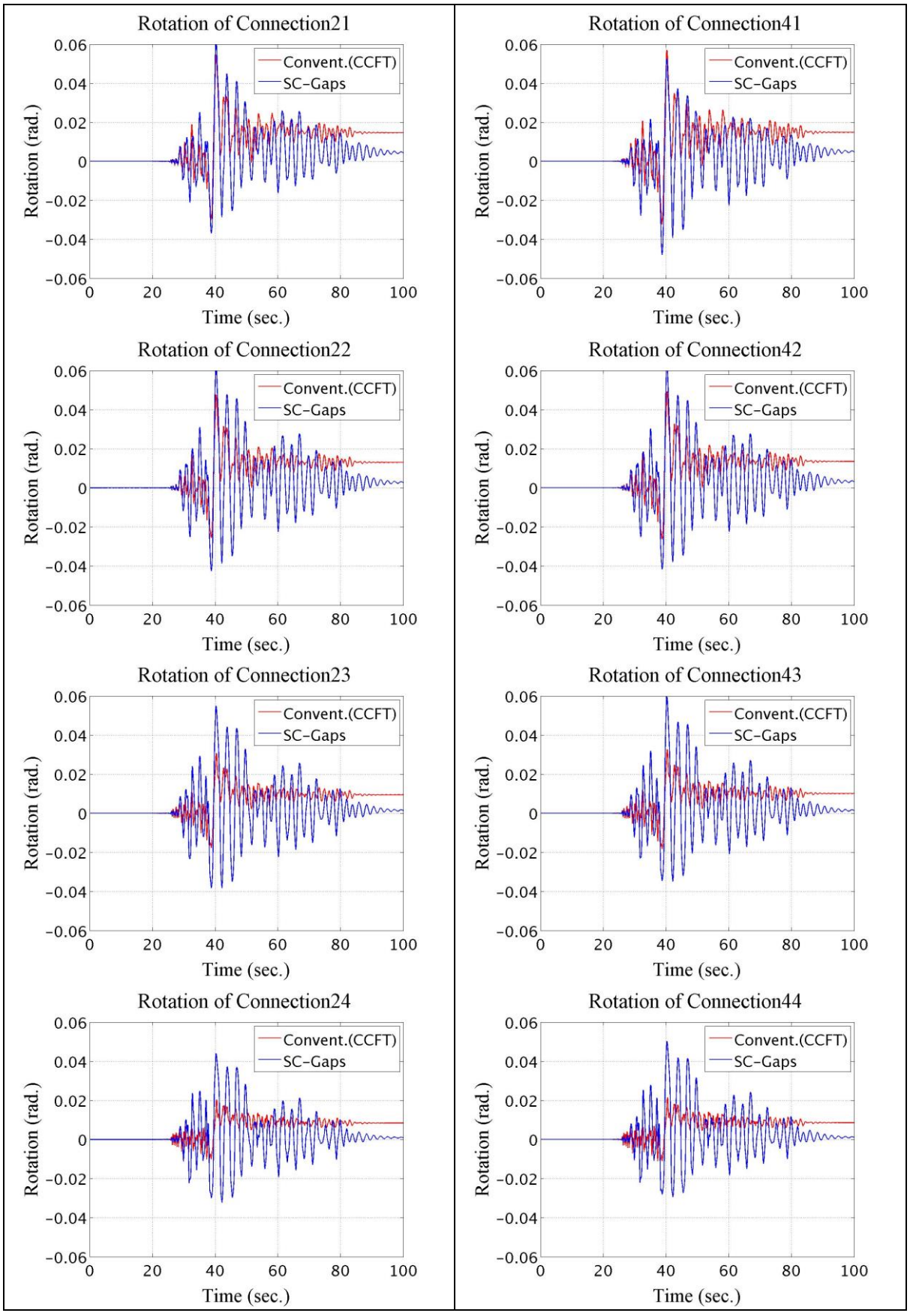
Rotation of Connection21
Rotation of Connection41
Rotation of Connection22
Rotation of Connection42
Rotation of Connection23
Rotation of Connection43
Rotation of Connection24
Rotation of Connection44
Convent.(CCFT)
SC-Gaps
Rotation (rad.)
Time (sec.)
0.06
0.04
0.02
0
-0.02
-0.04
-0.06
0
20
40
60
80
100

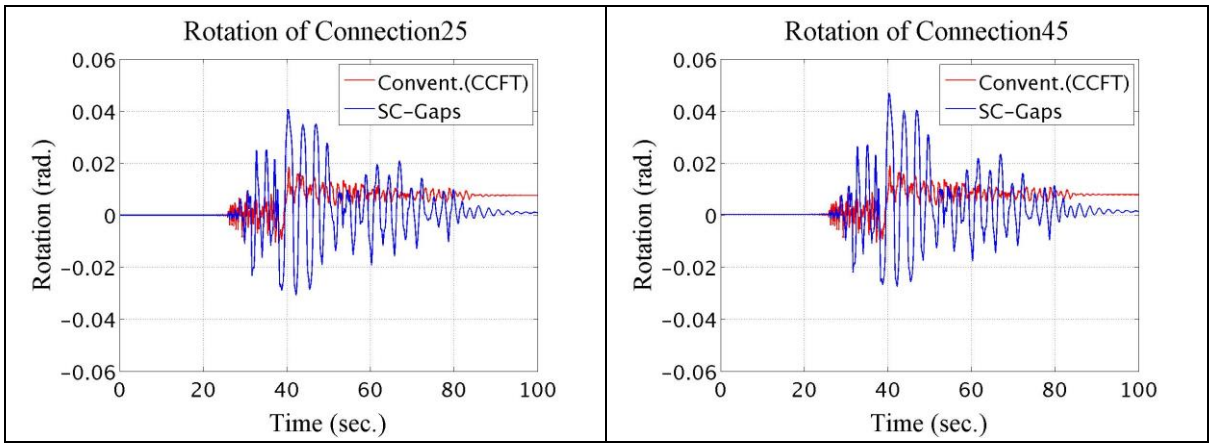

Appendix Figure M-4: Connection rotation

M.5 Story Shear

Story Shear at Level 1: Total Story Shear at 'Story 1'.

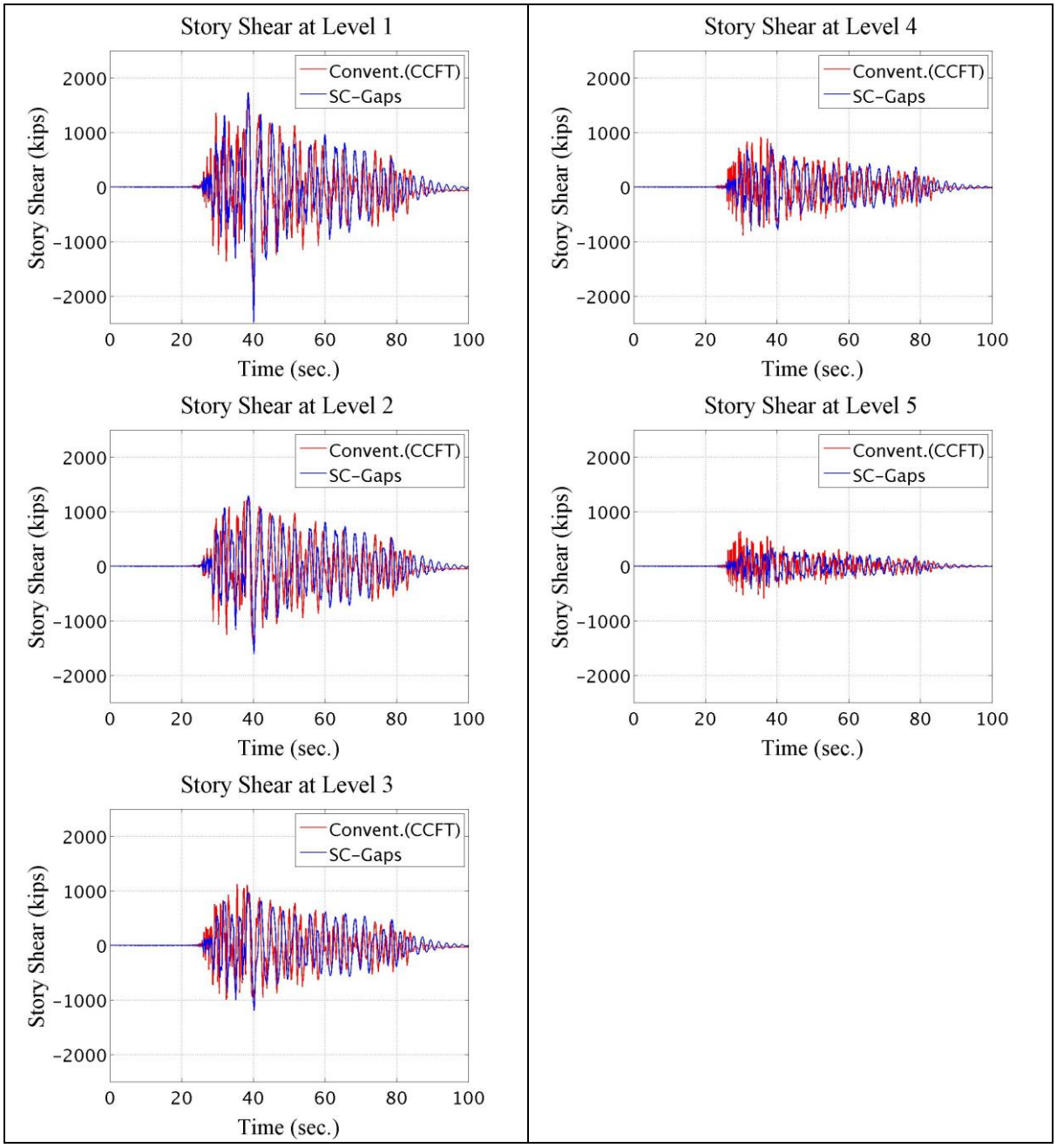

Appendix Figure M-5: Story shear

M.6 SMA Stress-Strain Curve

Stress-Strain Curve of SMA Rod 123: Stress-Strain Curve of SMA rod on 'Rod Level 3' of the 'Connection 12', which is located in 'Column Line 1' on 'Story 2'. (Rod Pattern in Figure 3-8)

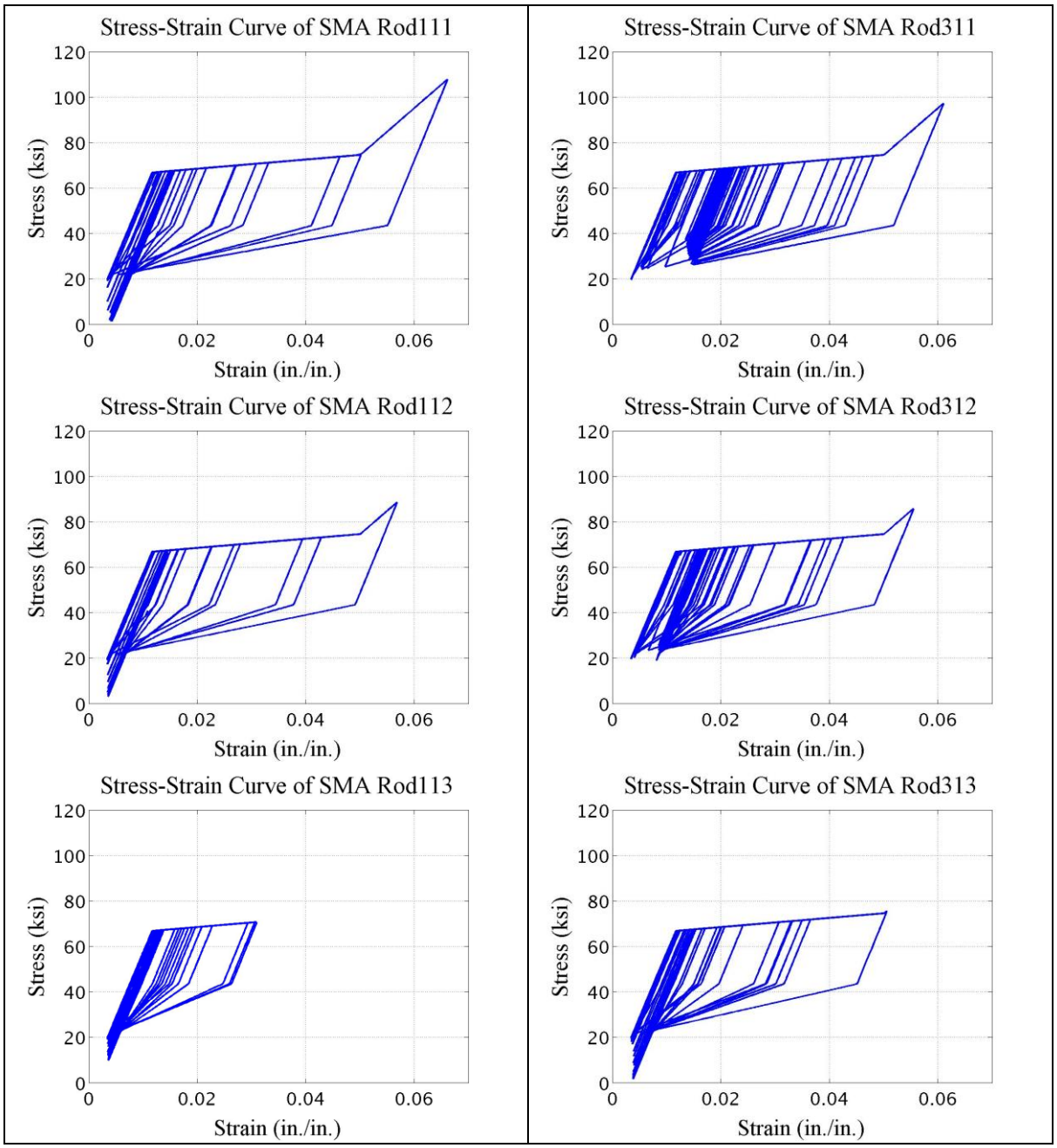

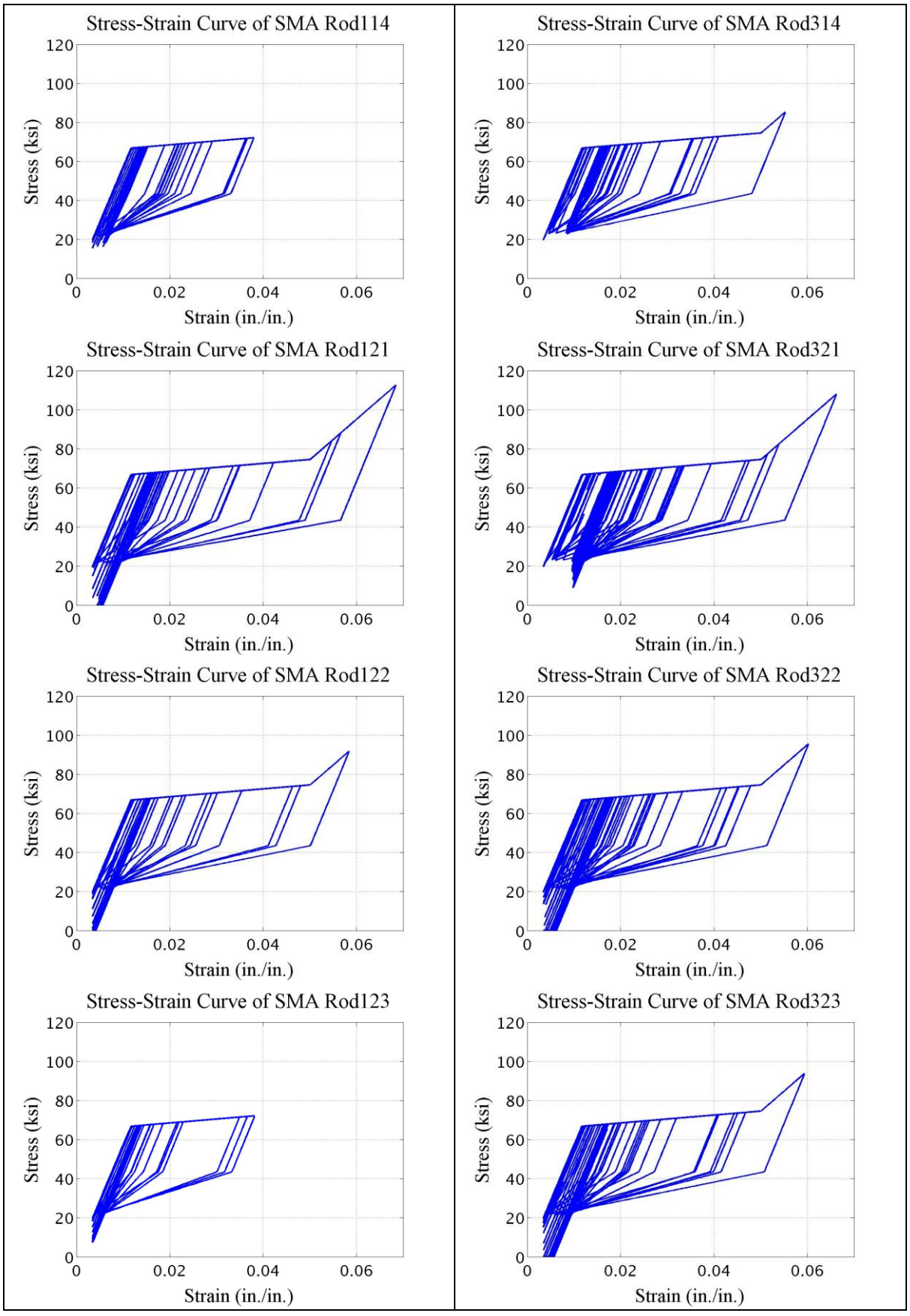
Stress-Strain Curve of SMA Rod114
Stress (ksi)
Strain (in./in.)
Stress-Strain Curve of SMA Rod314
Stress (ksi)
Strain (in./in.)
Stress-Strain Curve of SMA Rod121
Stress (ksi)
Strain (in./in.)
Stress-Strain Curve of SMA Rod321
Stress (ksi)
Strain (in./in.)
Stress-Strain Curve of SMA Rod122
Stress (ksi)
Strain (in./in.)
Stress-Strain Curve of SMA Rod322
Stress (ksi)
Strain (in./in.)
Stress-Strain Curve of SMA Rod123
Stress (ksi)
Strain (in./in.)
Stress-Strain Curve of SMA Rod323
Stress (ksi)
Strain (in./in.)

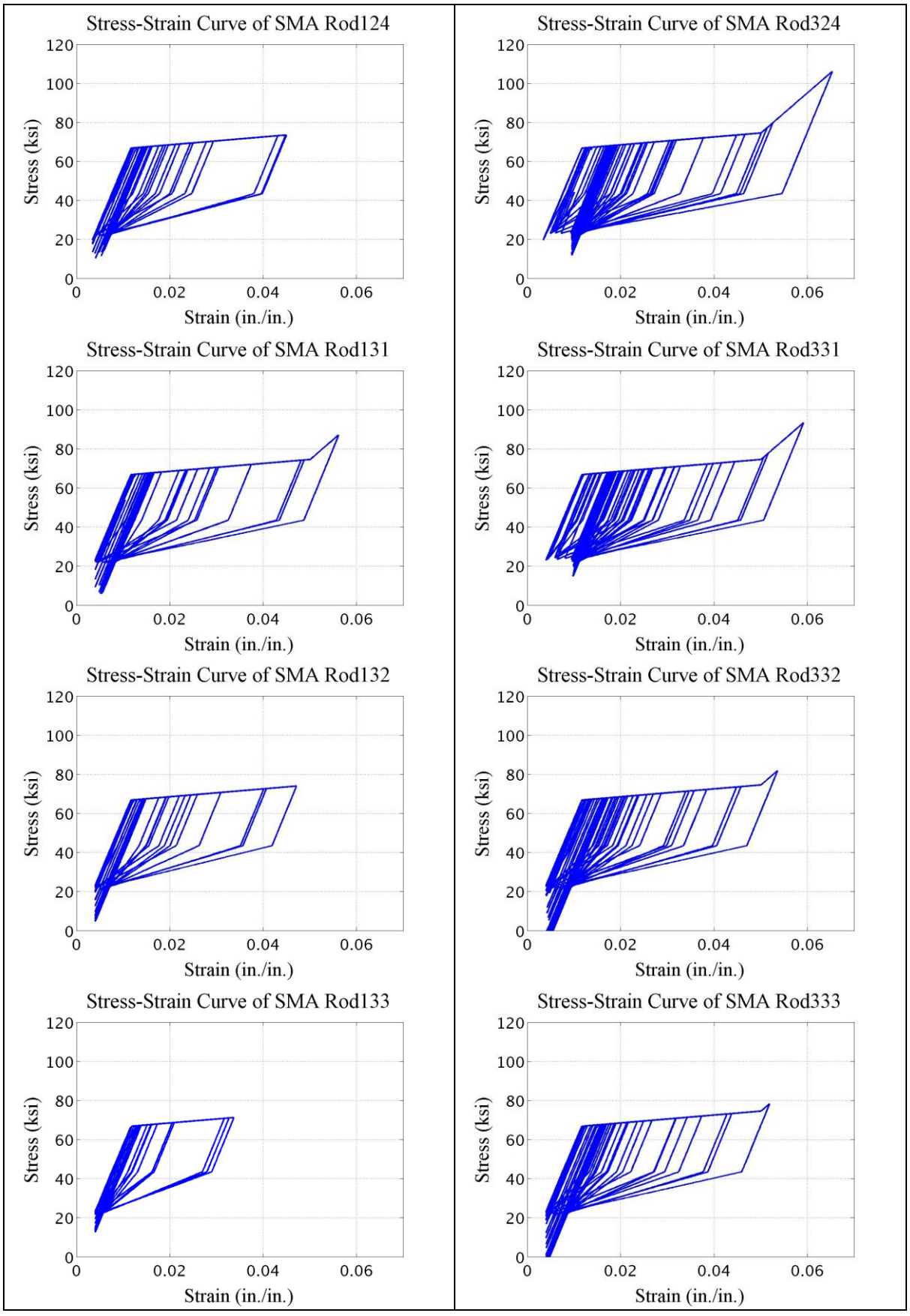
Stress-Strain Curve of SMA Rod124
Stress-Strain Curve of SMA Rod324
Stress-Strain Curve of SMA Rod131
Stress-Strain Curve of SMA Rod331
Stress-Strain Curve of SMA Rod132
Stress-Strain Curve of SMA Rod332
Stress-Strain Curve of SMA Rod133
Stress-Strain Curve of SMA Rod333
Stress (ksi)
Strain (in./in.)
0
20
40
60
80
100
120
0.02
0.04
0.06

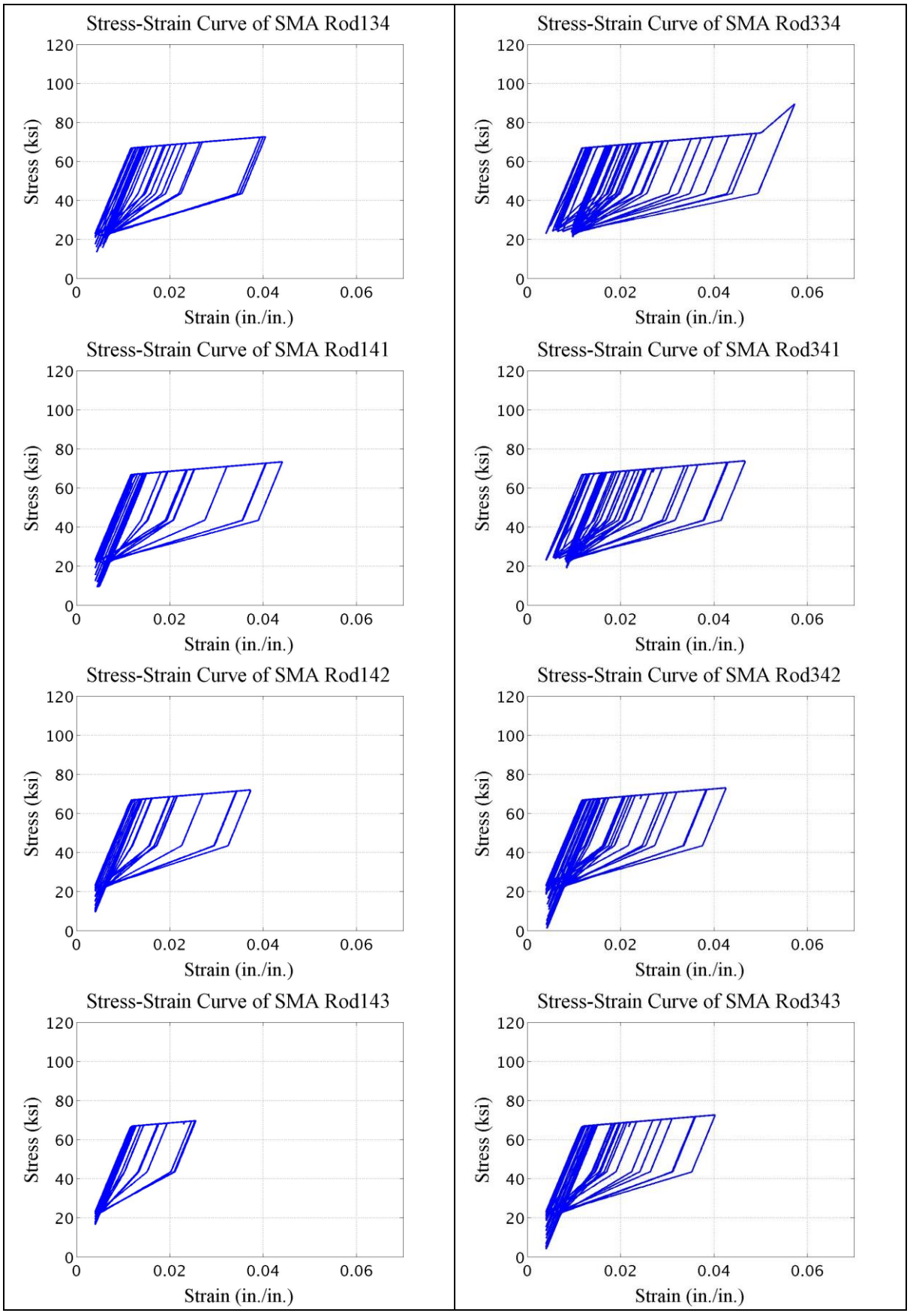
Stress-Strain Curve of SMA Rod134
Stress-Strain Curve of SMA Rod334
Stress-Strain Curve of SMA Rod141
Stress-Strain Curve of SMA Rod341
Stress-Strain Curve of SMA Rod142
Stress-Strain Curve of SMA Rod342
Stress-Strain Curve of SMA Rod143
Stress-Strain Curve of SMA Rod343
Stress (ksi)
Strain (in./in.)
0
20
40
60
80
100
120
0.02
0.04
0.06

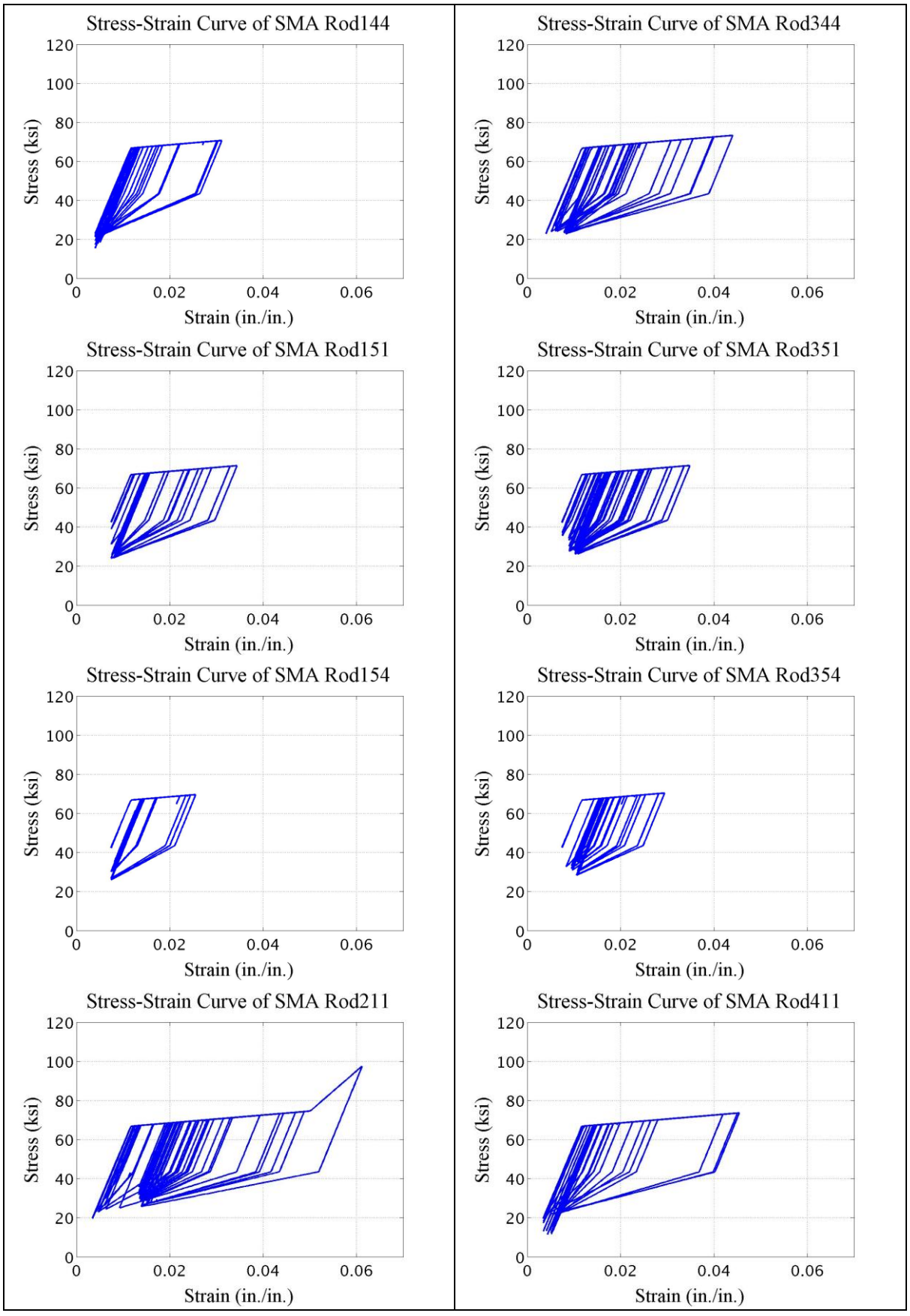
Stress-Strain Curve of SMA Rod144
Stress-Strain Curve of SMA Rod344
Stress-Strain Curve of SMA Rod151
Stress-Strain Curve of SMA Rod351
Stress-Strain Curve of SMA Rod154
Stress-Strain Curve of SMA Rod354
Stress-Strain Curve of SMA Rod211
Stress-Strain Curve of SMA Rod411
Stress (ksi)
Strain (in./in.)
0
20
40
60
80
100
120
0.02
0.04
0.06

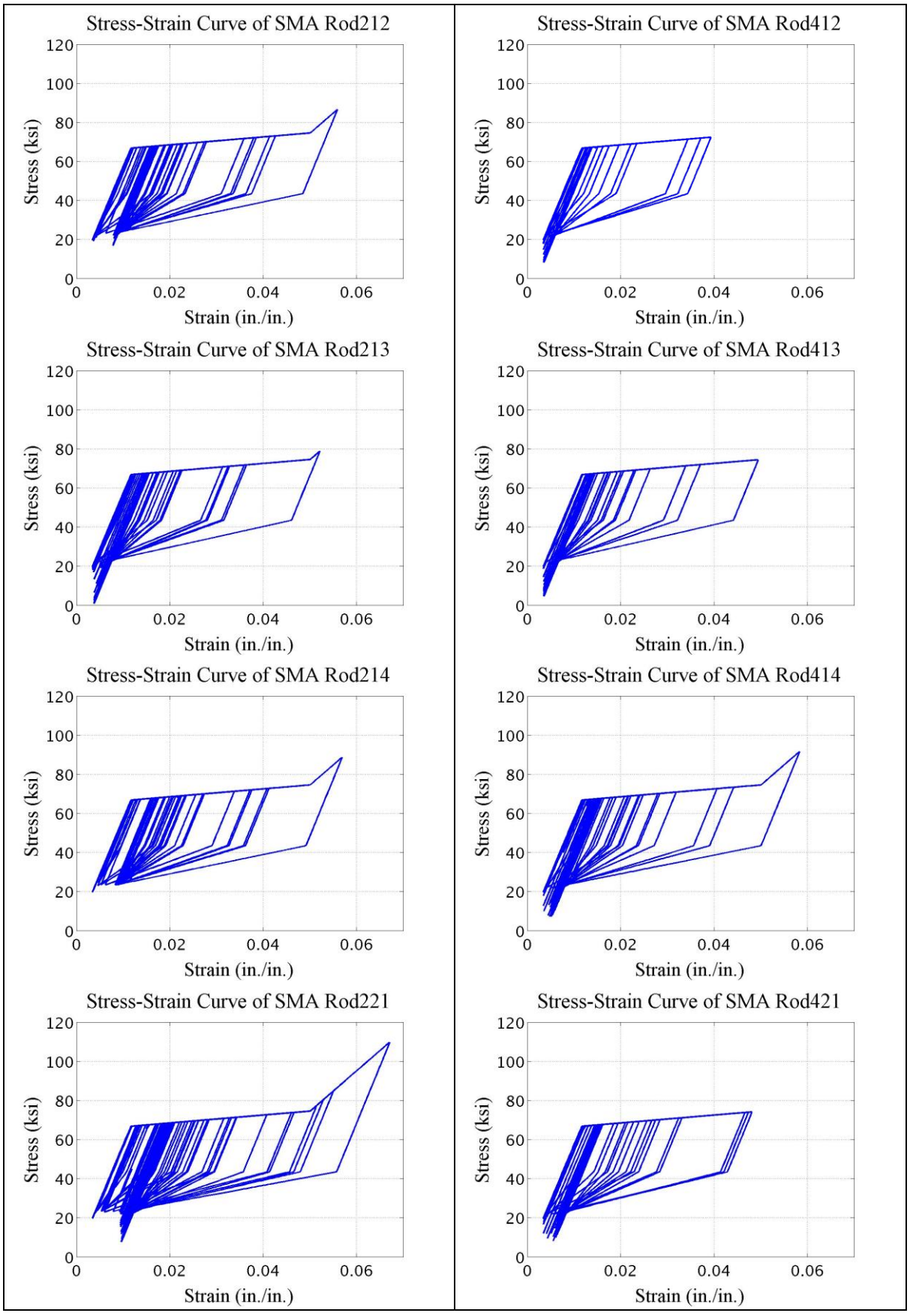
Stress-Strain Curve of SMA Rod212
Stress-Strain Curve of SMA Rod412
Stress-Strain Curve of SMA Rod213
Stress-Strain Curve of SMA Rod413
Stress-Strain Curve of SMA Rod214
Stress-Strain Curve of SMA Rod414
Stress-Strain Curve of SMA Rod221
Stress-Strain Curve of SMA Rod421
Stress (ksi)
Strain (in./in.)
0
20
40
60
80
100
120
0.02
0.04
0.06

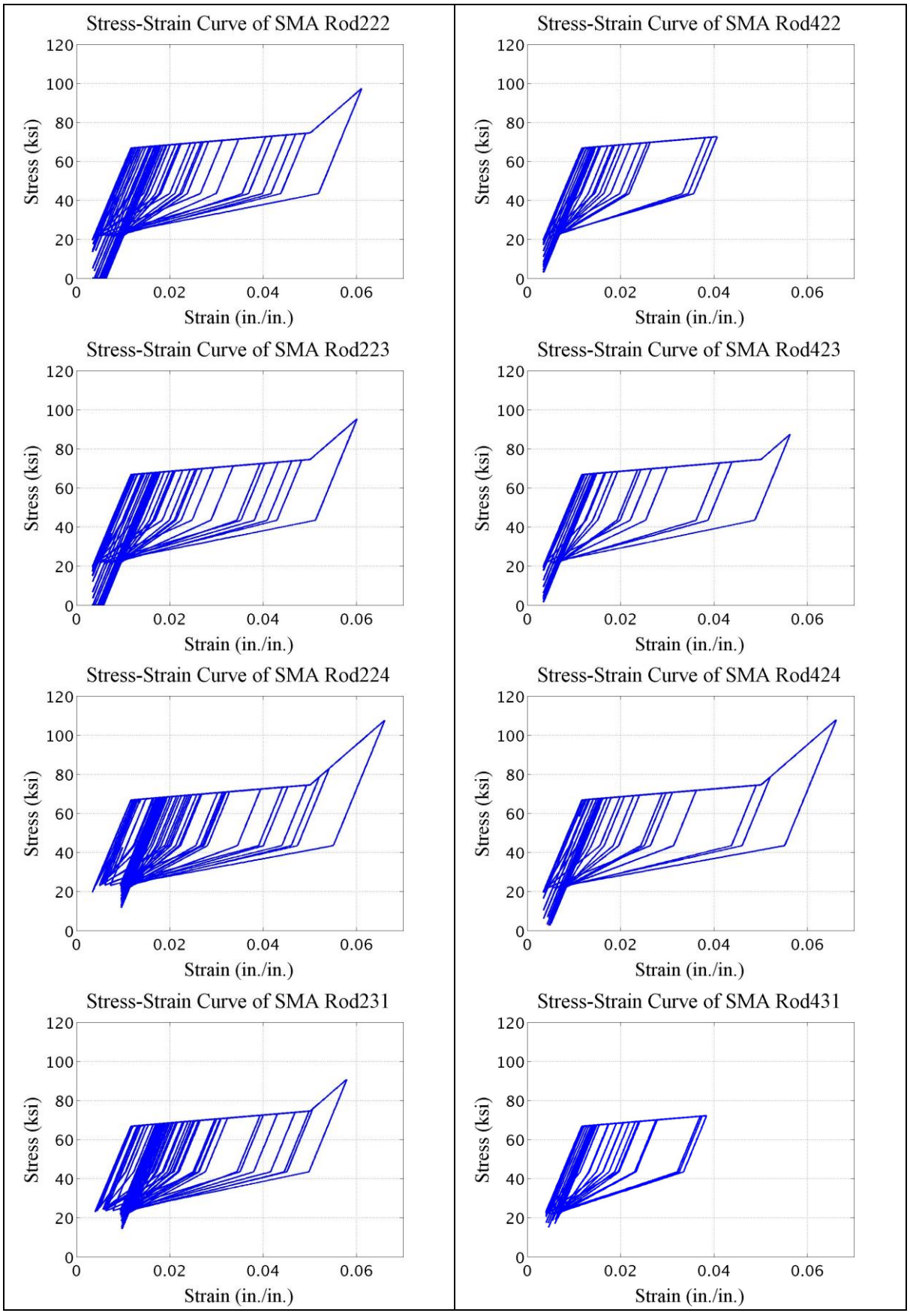
Stress-Strain Curve of SMA Rod222
Stress-Strain Curve of SMA Rod422
Stress-Strain Curve of SMA Rod223
Stress-Strain Curve of SMA Rod423
Stress-Strain Curve of SMA Rod224
Stress-Strain Curve of SMA Rod424
Stress-Strain Curve of SMA Rod231
Stress-Strain Curve of SMA Rod431
Stress (ksi)
Strain (in./in.)
0
20
40
60
80
100
120
0.02
0.04
0.06

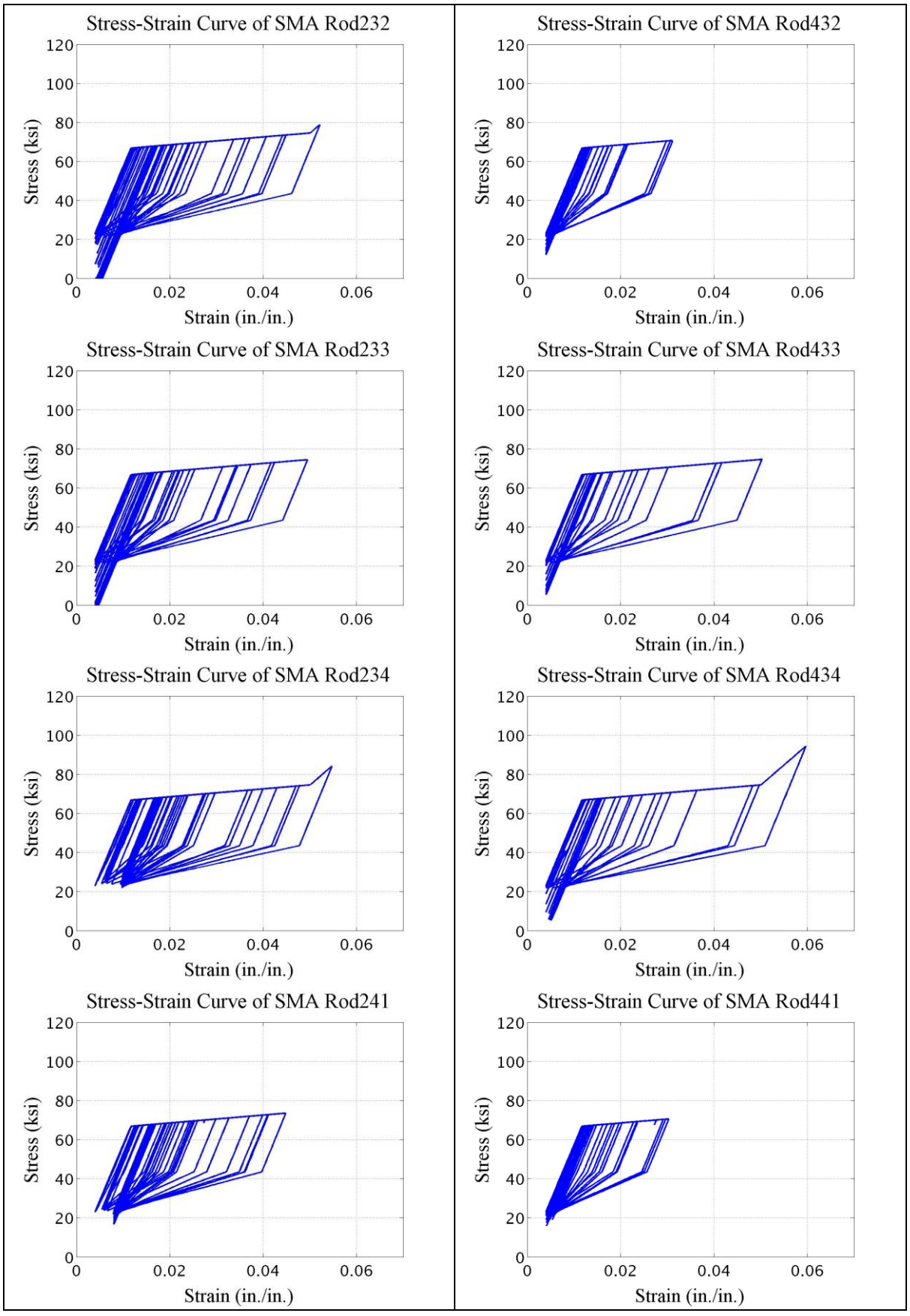
Stress-Strain Curve of SMA Rod232
Stress-Strain Curve of SMA Rod432
Stress-Strain Curve of SMA Rod233
Stress-Strain Curve of SMA Rod433
Stress-Strain Curve of SMA Rod234
Stress-Strain Curve of SMA Rod434
Stress-Strain Curve of SMA Rod241
Stress-Strain Curve of SMA Rod441
Stress (ksi)
Strain (in./in.)
0
20
40
60
80
100
120
0.02
0.04
0.06

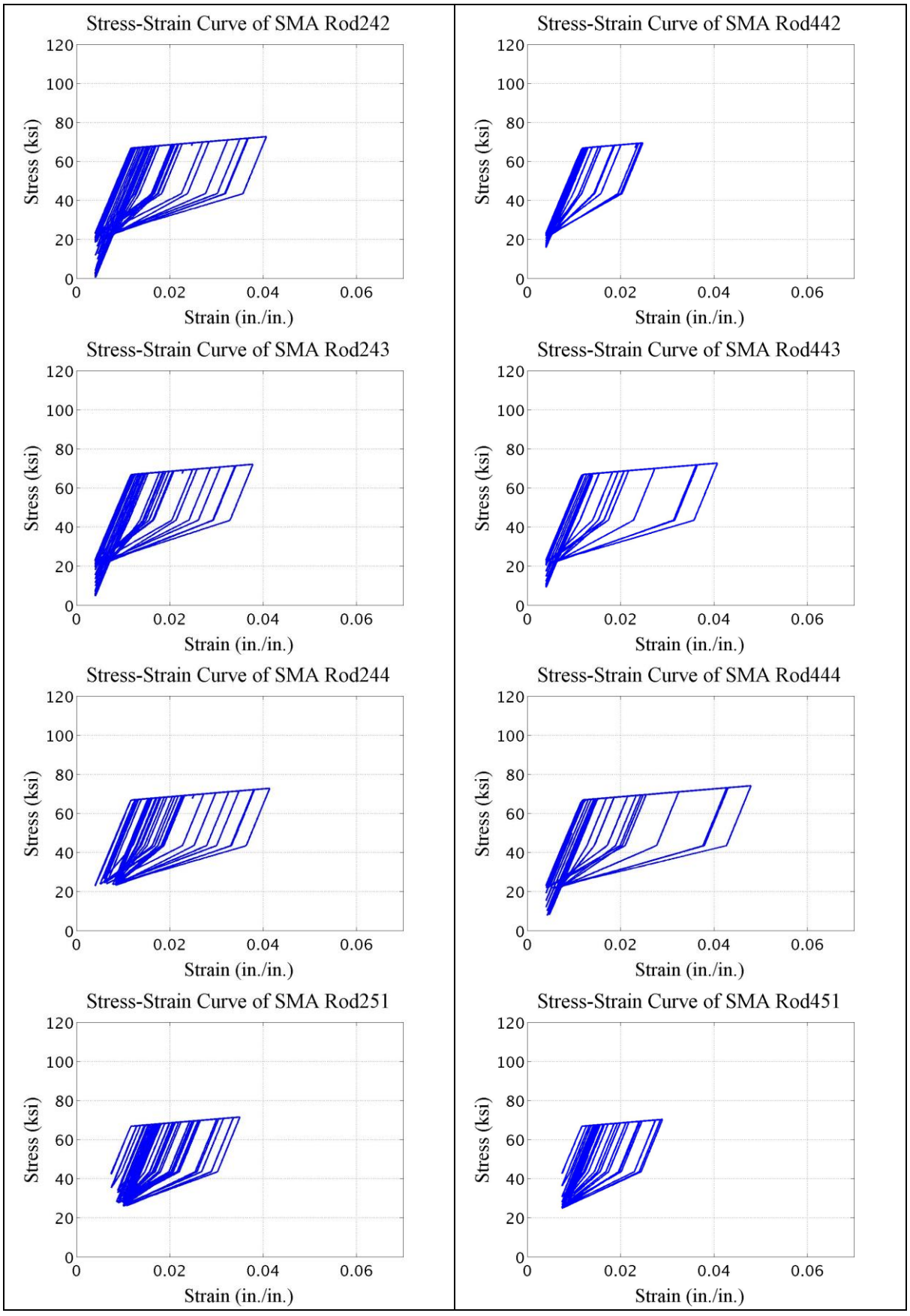
Stress-Strain Curve of SMA Rod242
Stress (ksi)
Strain (in./in.)
Stress-Strain Curve of SMA Rod442
Stress (ksi)
Strain (in./in.)
Stress-Strain Curve of SMA Rod243
Stress (ksi)
Strain (in./in.)
Stress-Strain Curve of SMA Rod443
Stress (ksi)
Strain (in./in.)
Stress-Strain Curve of SMA Rod244
Stress (ksi)
Strain (in./in.)
Stress-Strain Curve of SMA Rod444
Stress (ksi)
Strain (in./in.)
Stress-Strain Curve of SMA Rod251
Stress (ksi)
Strain (in./in.)
Stress-Strain Curve of SMA Rod451
Stress (ksi)
Strain (in./in.)

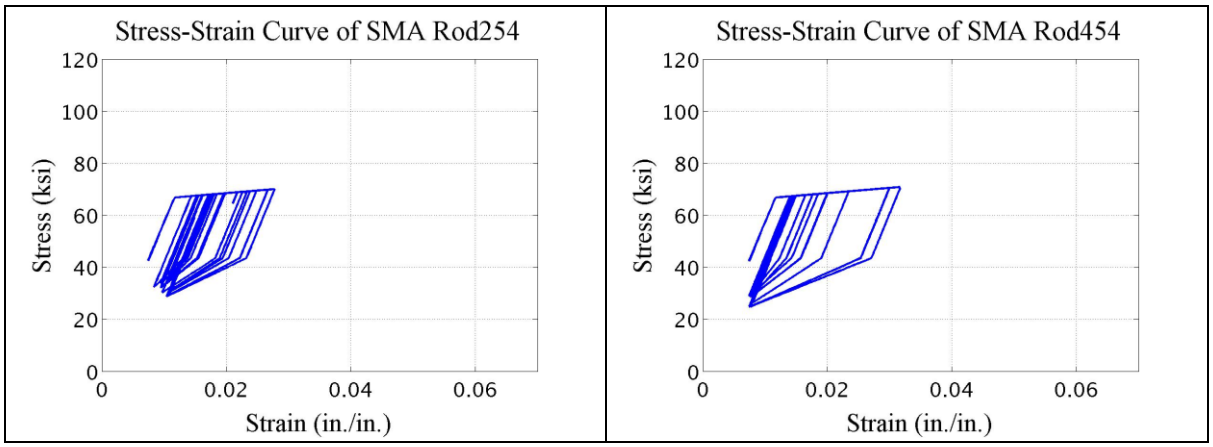

Appendix Figure M-6: SMA stress-strain curve

M.7 SMA Rod Force

Axial Force of SMA Rod 123: Axial force of SMA rod on 'Rod Level 3' of the 'Connection 12', which is located in 'Column Line 1' on 'Story 2'. (See Rod Pattern in Figure 3-8)

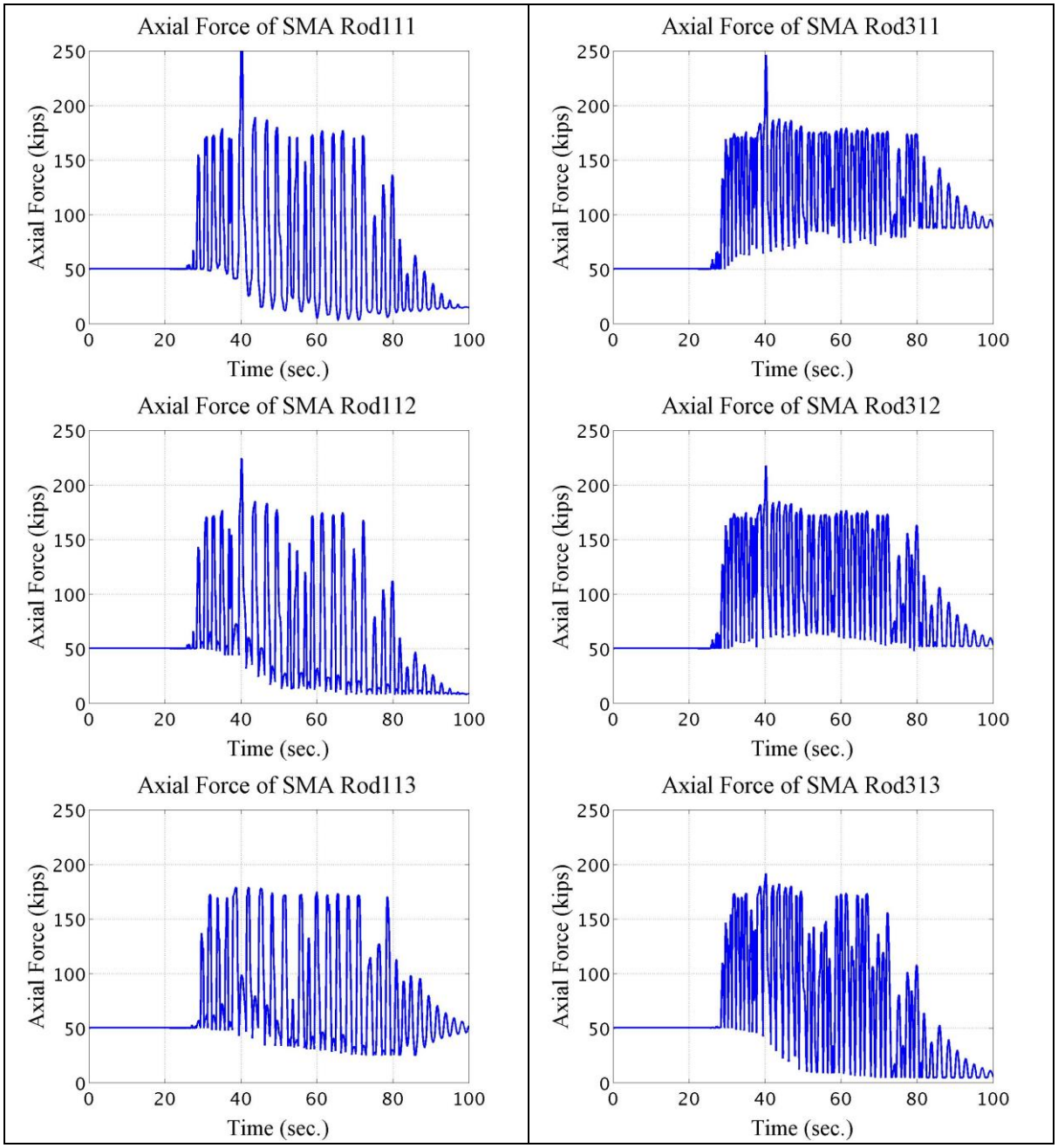

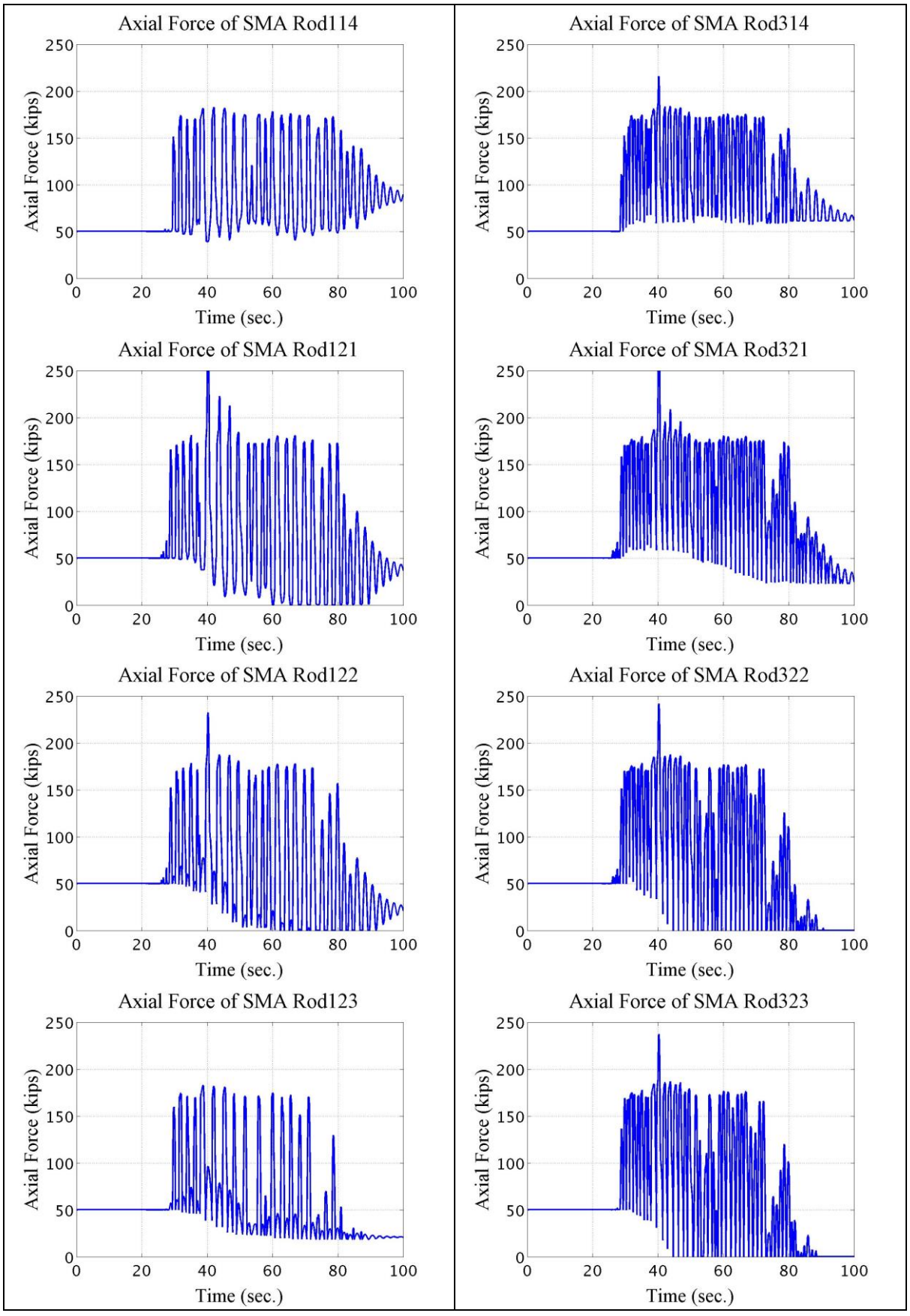
Axial Force of SMA Rod114
Axial Force of SMA Rod314
Axial Force of SMA Rod121
Axial Force of SMA Rod321
Axial Force of SMA Rod122
Axial Force of SMA Rod322
Axial Force of SMA Rod123
Axial Force of SMA Rod323
Axial Force (kips)
Time (sec.)
0
50
100
150
200
250
0
20
40
60
80
100

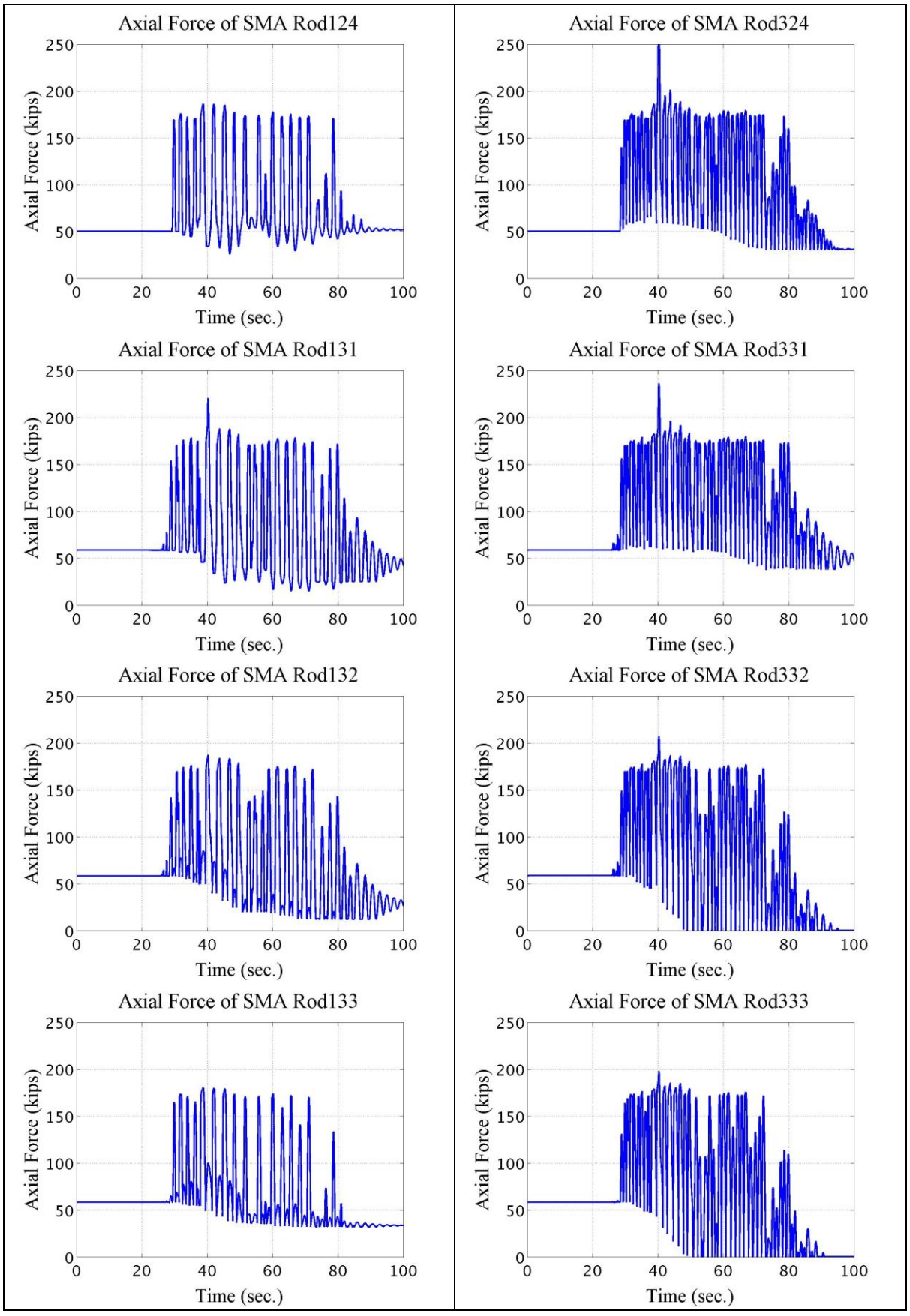
Axial Force of SMA Rod124
Axial Force of SMA Rod324
Axial Force of SMA Rod131
Axial Force of SMA Rod331
Axial Force of SMA Rod132
Axial Force of SMA Rod332
Axial Force of SMA Rod133
Axial Force of SMA Rod333
Axial Force (kips)
Time (sec.)
0
50
100
150
200
250
0
20
40
60
80
100

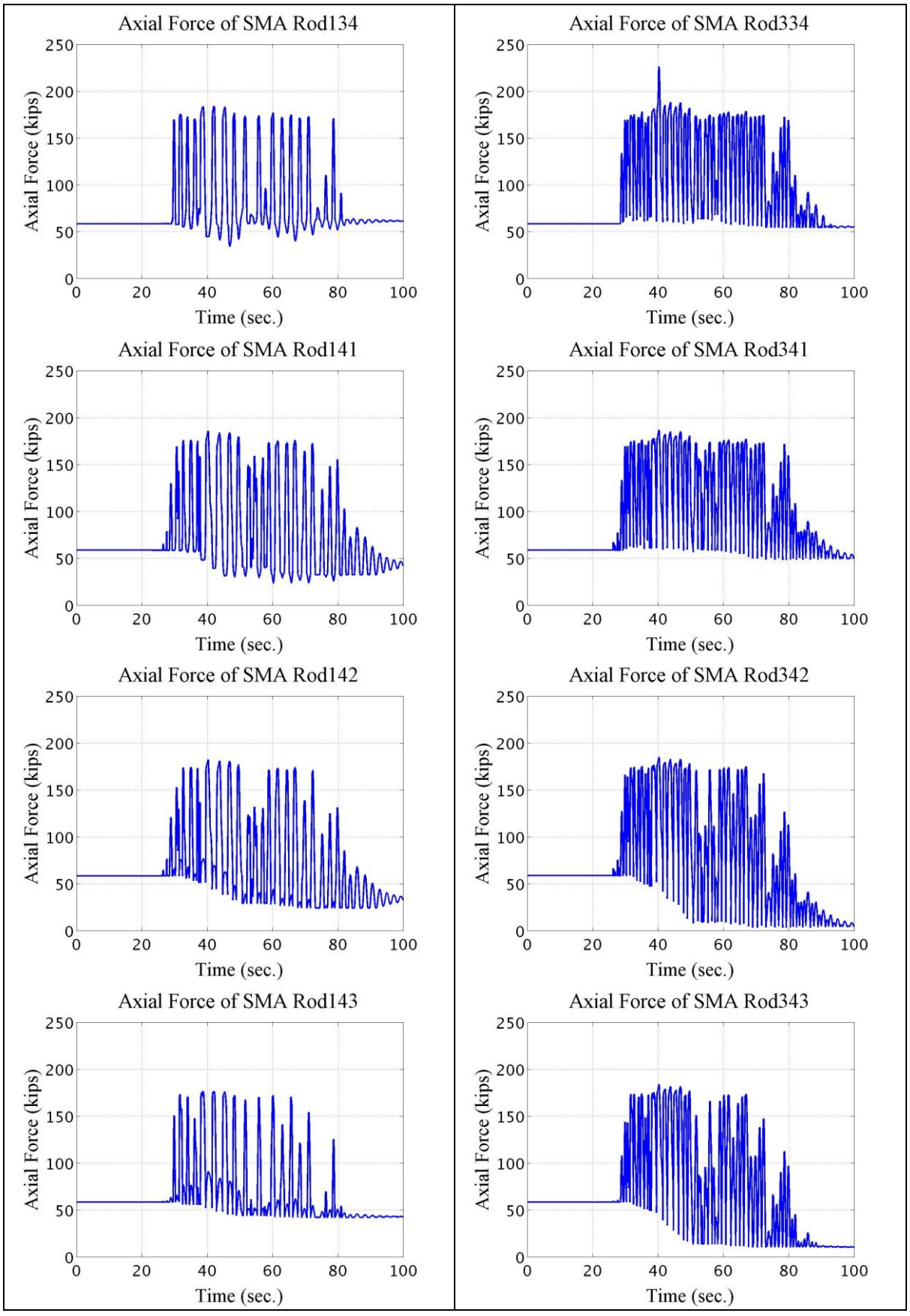
Axial Force of SMA Rod134
Axial Force of SMA Rod334
Axial Force of SMA Rod141
Axial Force of SMA Rod341
Axial Force of SMA Rod142
Axial Force of SMA Rod342
Axial Force of SMA Rod143
Axial Force of SMA Rod343
Axial Force (kips)
Time (sec.)
0
50
100
150
200
250
0
20
40
60
80
100

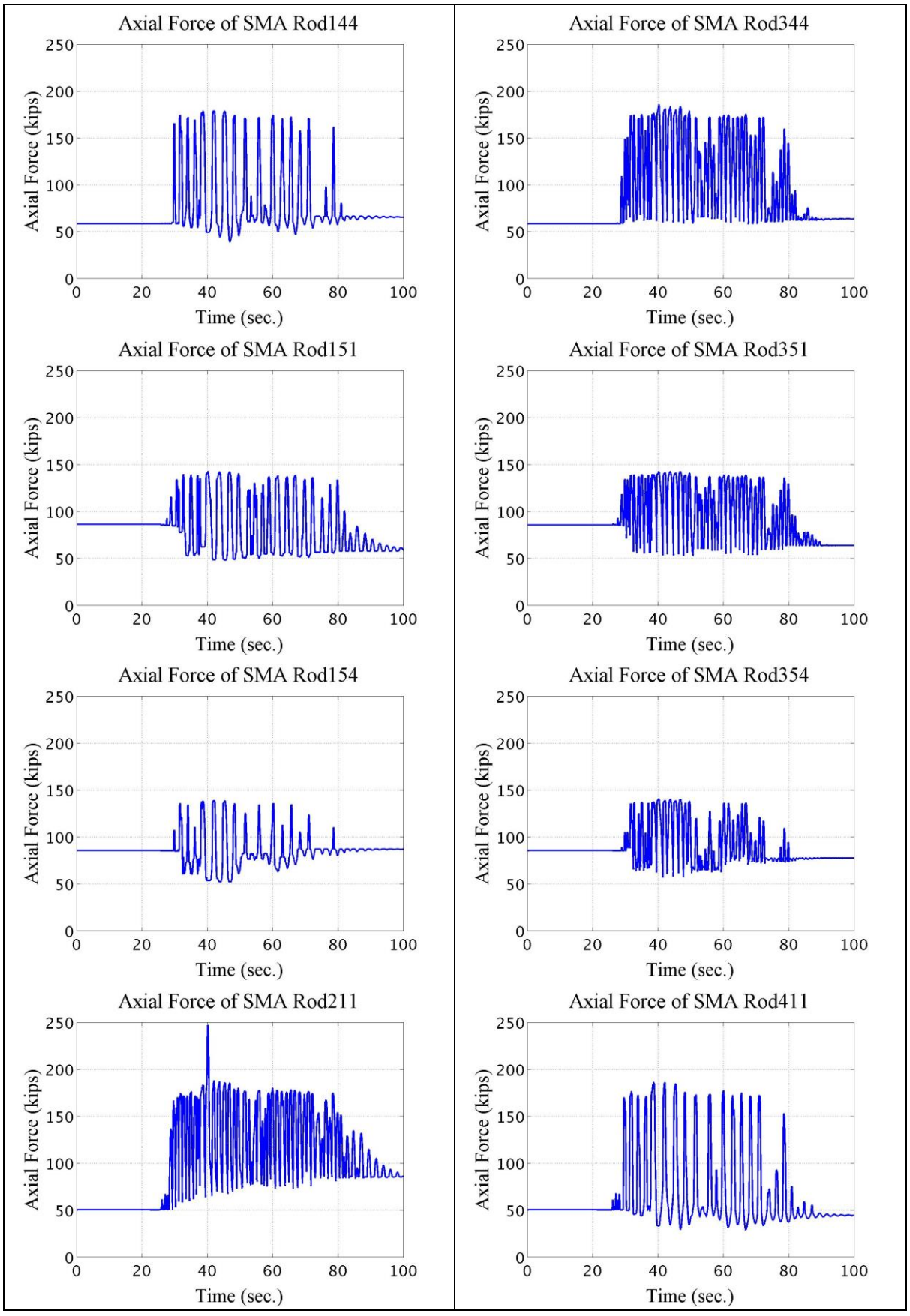
Axial Force of SMA Rod144
Axial Force of SMA Rod344
Axial Force of SMA Rod151
Axial Force of SMA Rod351
Axial Force of SMA Rod154
Axial Force of SMA Rod354
Axial Force of SMA Rod211
Axial Force of SMA Rod411
Axial Force (kips)
Time (sec.)
0
50
100
150
200
250
0
20
40
60
80
100

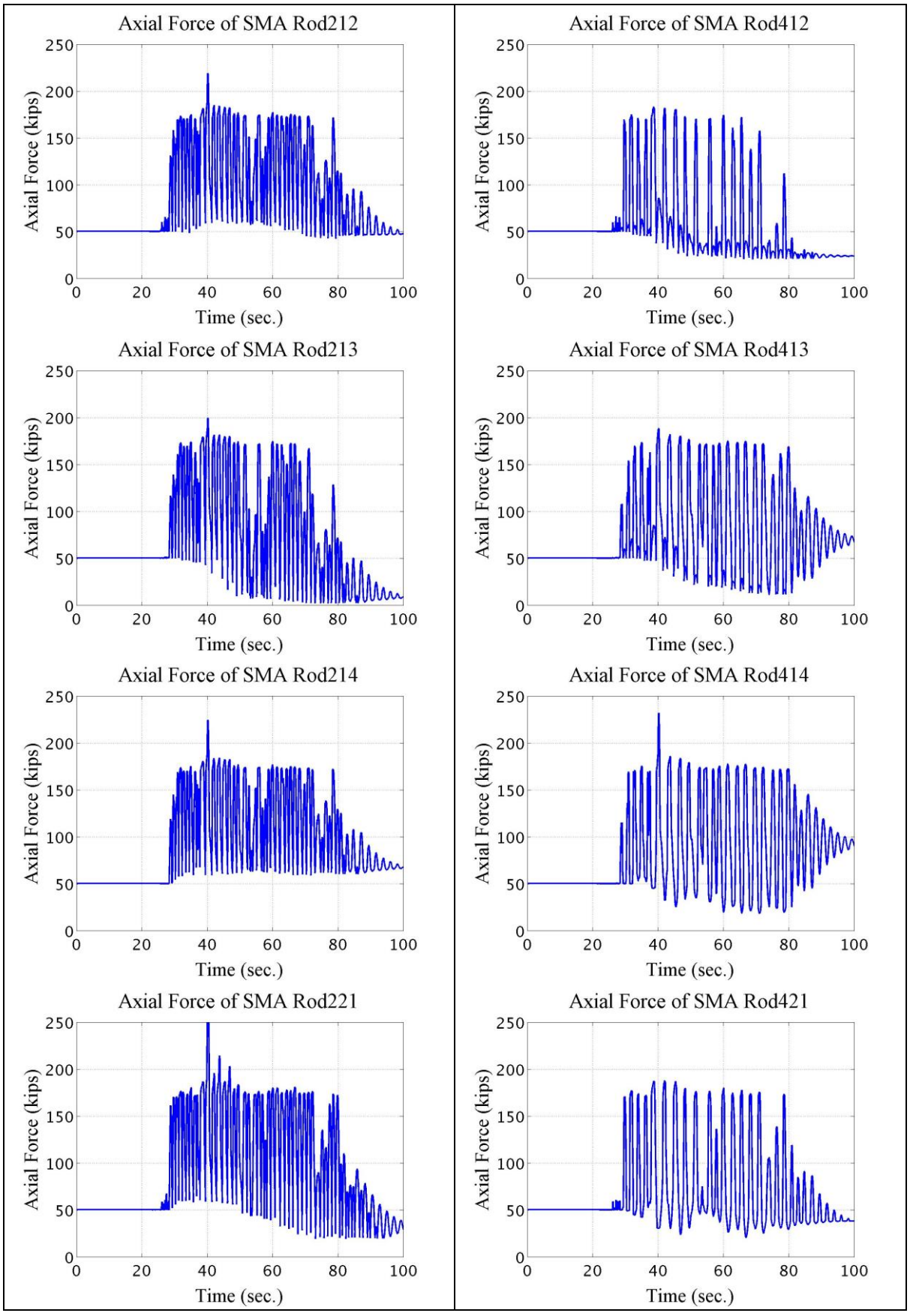
Axial Force of SMA Rod212
Axial Force of SMA Rod412
Axial Force of SMA Rod213
Axial Force of SMA Rod413
Axial Force of SMA Rod214
Axial Force of SMA Rod414
Axial Force of SMA Rod221
Axial Force of SMA Rod421
Axial Force (kips)
Time (sec.)
0
50
100
150
200
250
0
20
40
60
80
100

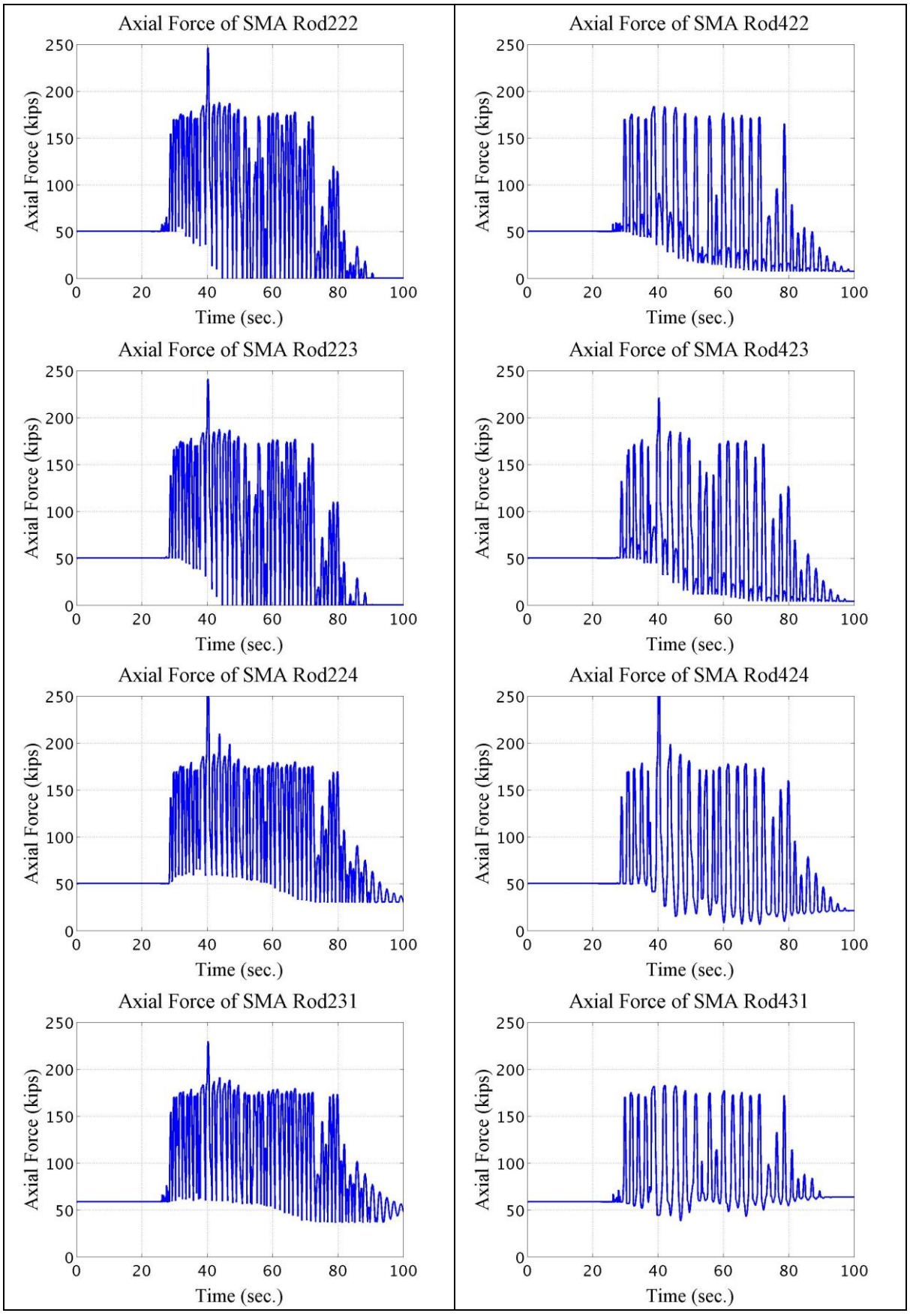
Axial Force of SMA Rod222
Axial Force of SMA Rod422
Axial Force of SMA Rod223
Axial Force of SMA Rod423
Axial Force of SMA Rod224
Axial Force of SMA Rod424
Axial Force of SMA Rod231
Axial Force of SMA Rod431
Axial Force (kips)
Time (sec.)
0
50
100
150
200
250
0
20
40
60
80
100

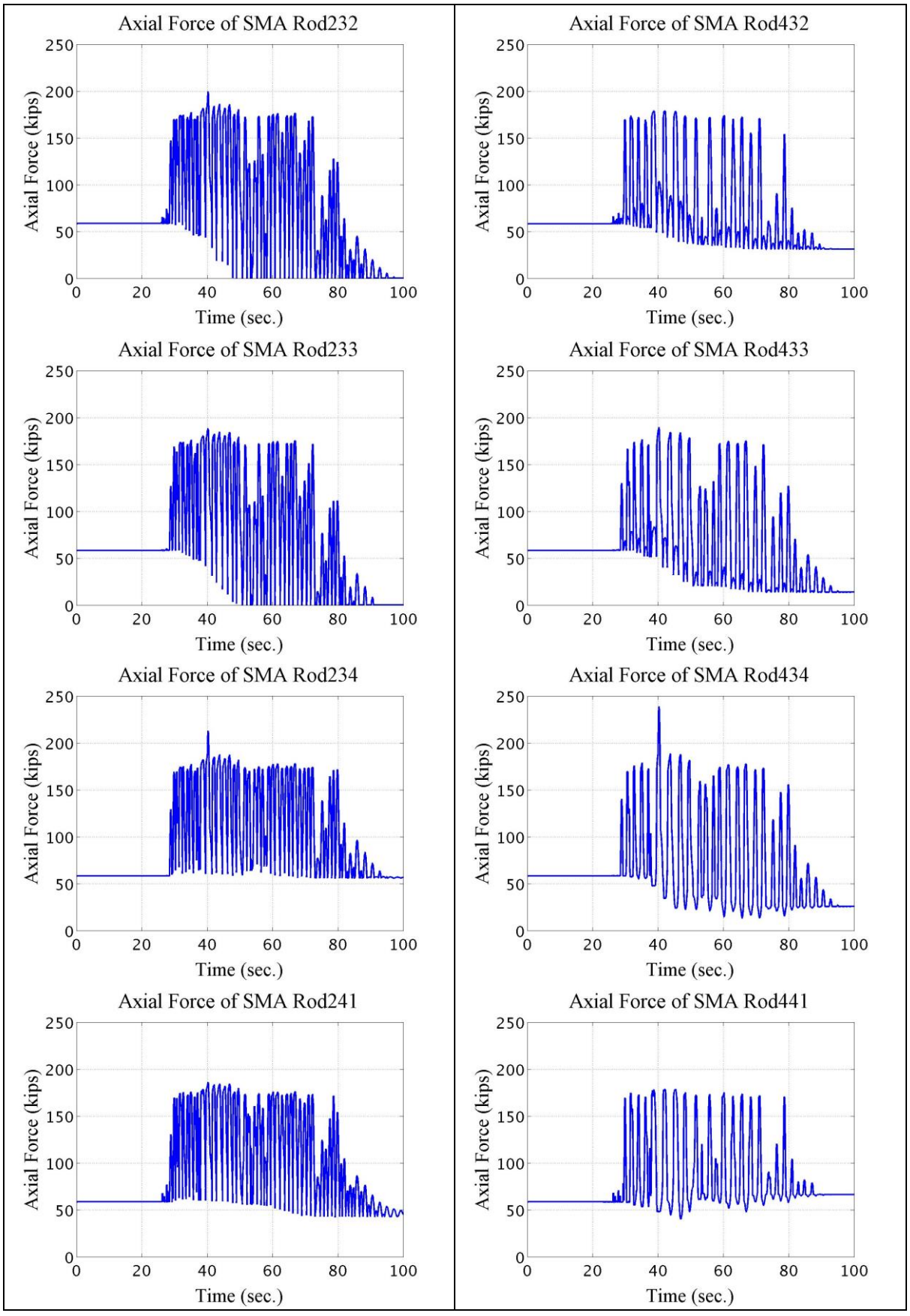
Axial Force of SMA Rod232
Axial Force of SMA Rod432
Axial Force of SMA Rod233
Axial Force of SMA Rod433
Axial Force of SMA Rod234
Axial Force of SMA Rod434
Axial Force of SMA Rod241
Axial Force of SMA Rod441
Axial Force (kips)
Time (sec.)
0
50
100
150
200
250
0
20
40
60
80
100

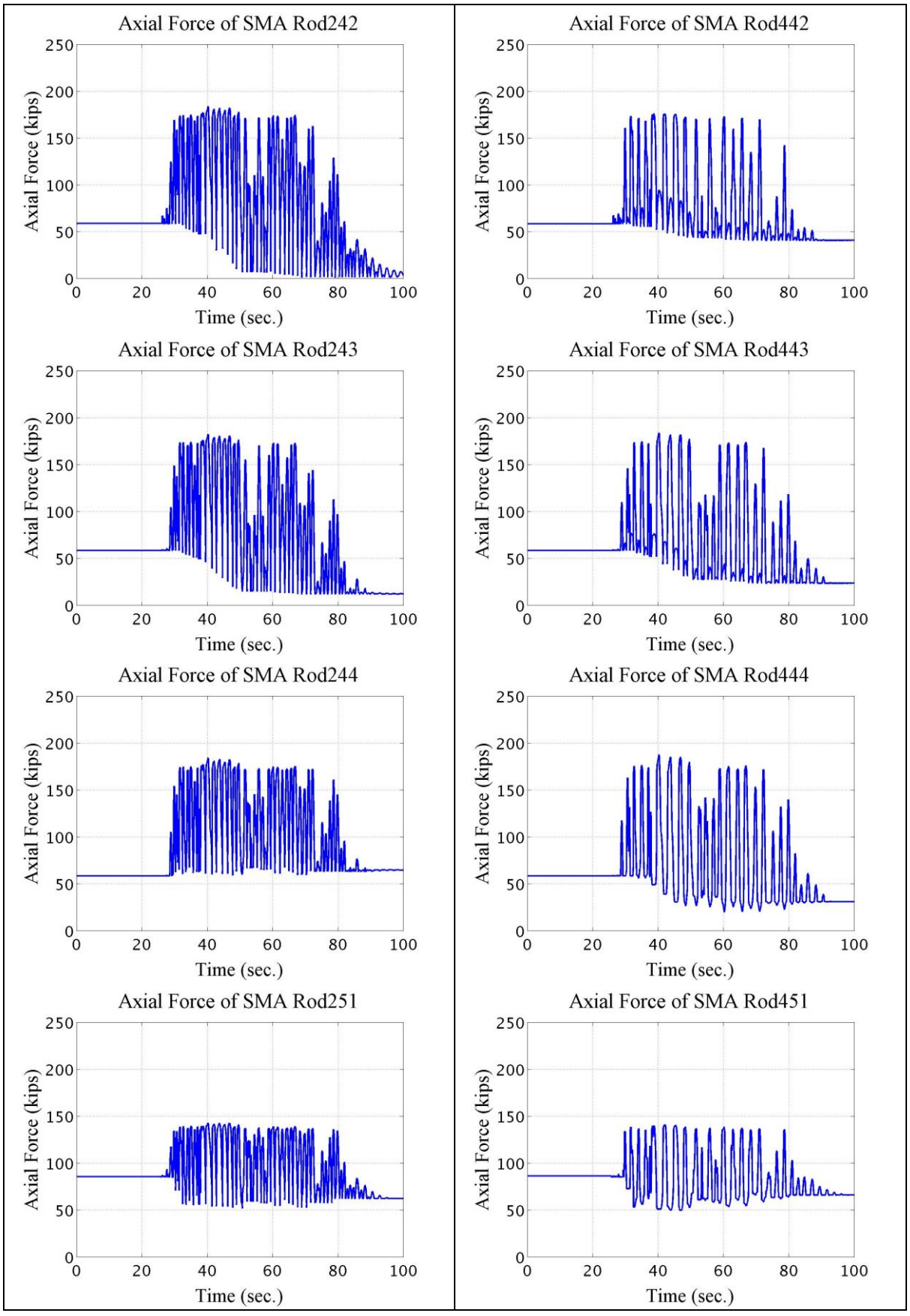
Axial Force of SMA Rod242
Axial Force of SMA Rod442
Axial Force of SMA Rod243
Axial Force of SMA Rod443
Axial Force of SMA Rod244
Axial Force of SMA Rod444
Axial Force of SMA Rod251
Axial Force of SMA Rod451
Axial Force (kips)
Time (sec.)
0
50
100
150
200
250
0
20
40
60
80
100

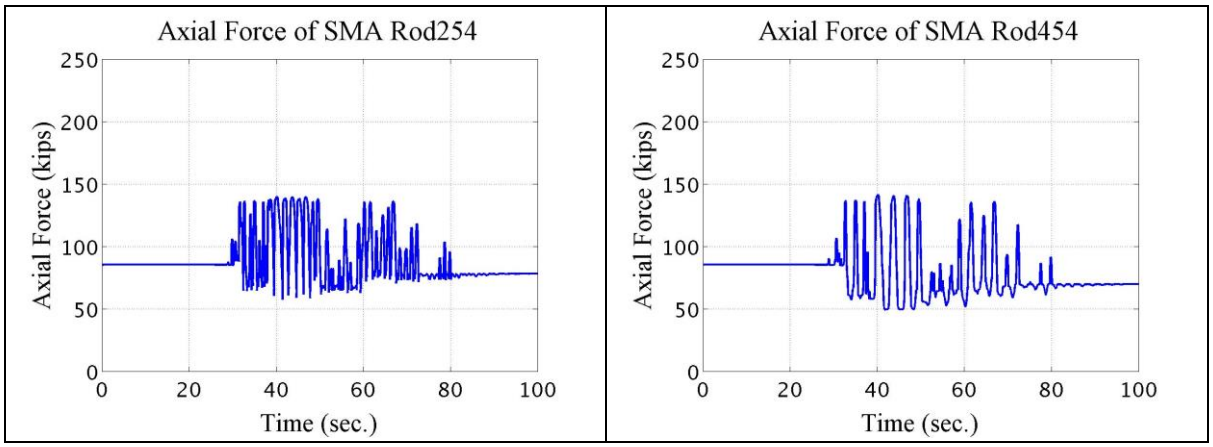

Appendix Figure M-7: SMA rod force

M.8 Total Force of SMA Rods at Each Connection

Total Axial Force of SMA Rods at Conn. 12: Total axial force of all SMA rods of the 'Connection 12', which is located in 'Column Line 1' on 'Story 2'.

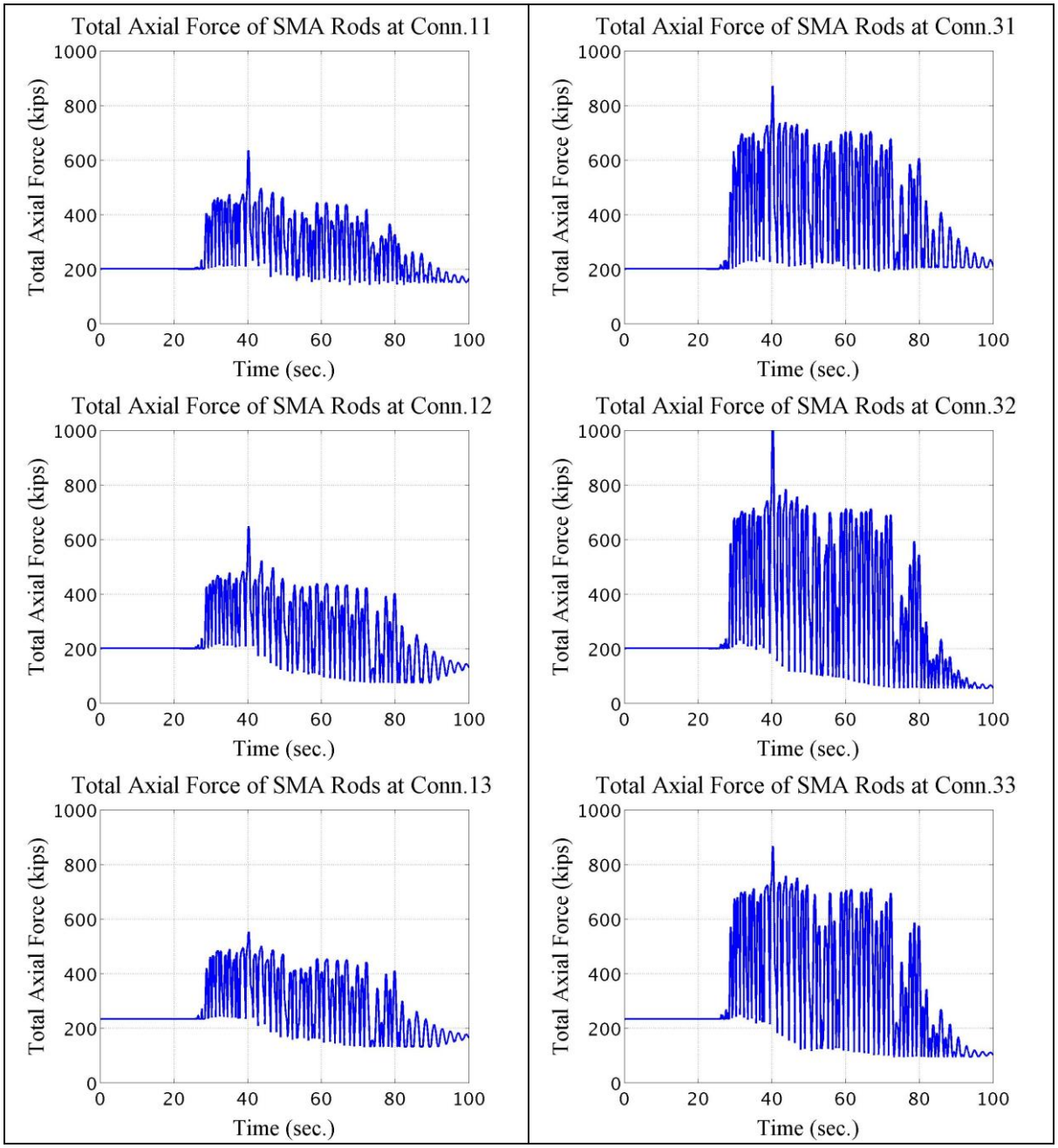

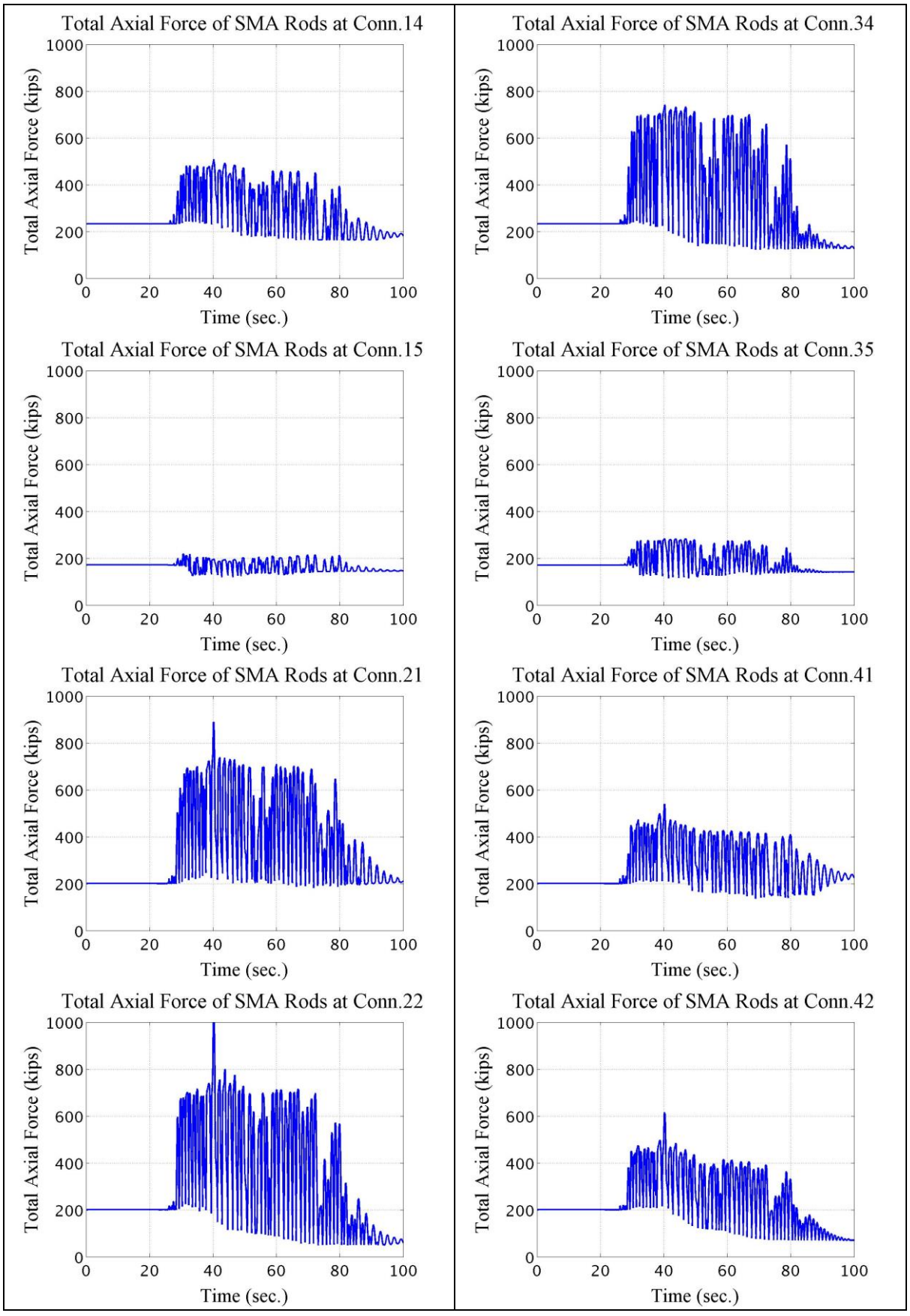
Total Axial Force of SMA Rods at Conn.14
Total Axial Force of SMA Rods at Conn.34
Total Axial Force of SMA Rods at Conn.15
Total Axial Force of SMA Rods at Conn.35
Total Axial Force of SMA Rods at Conn.21
Total Axial Force of SMA Rods at Conn.41
Total Axial Force of SMA Rods at Conn.22
Total Axial Force of SMA Rods at Conn.42
Total Axial Force (kips)
Time (sec.)
0
200
400
600
800
1000
0
20
40
60
80
100

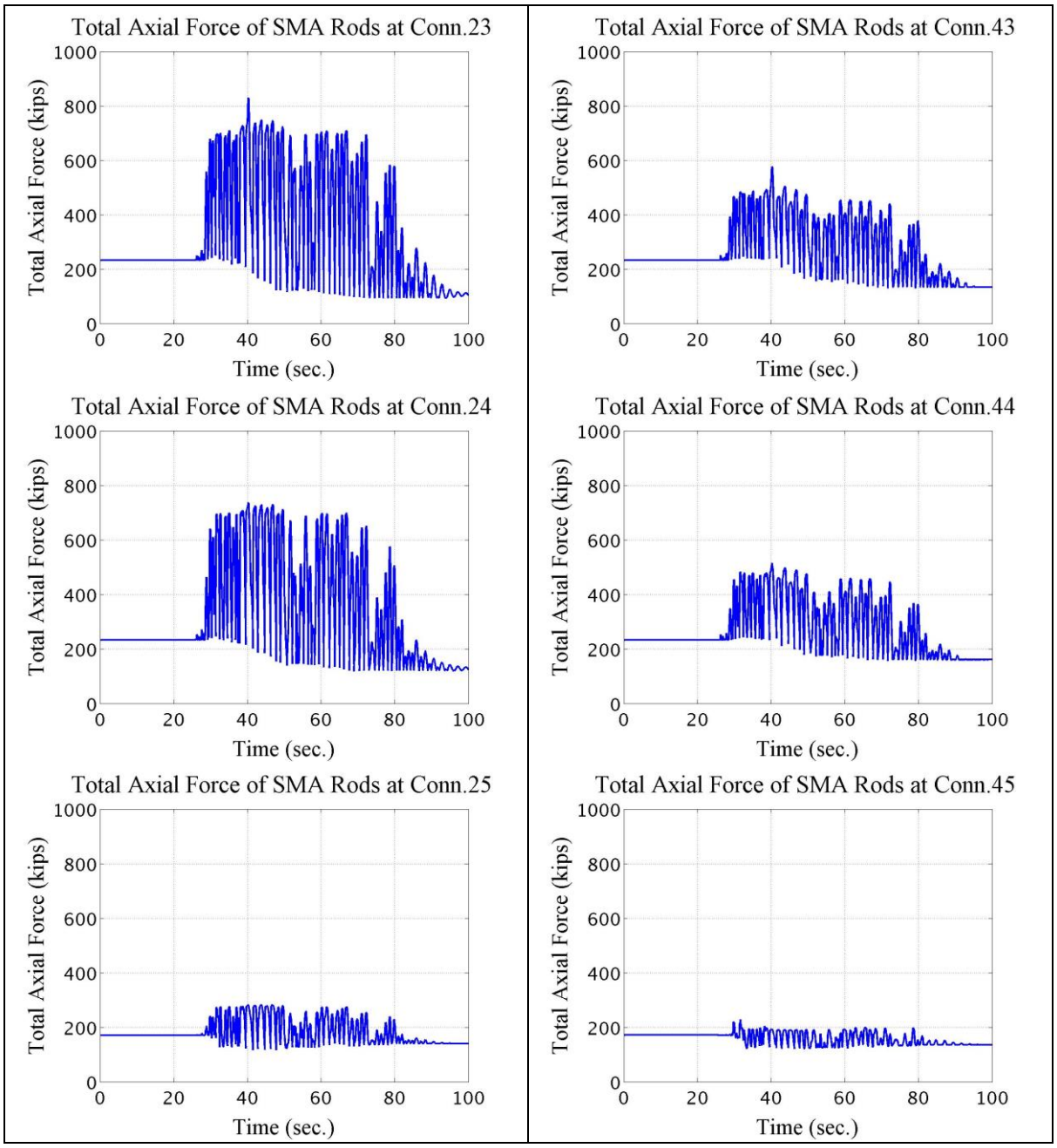

Appendix Figure M-8: Total force of SMA rods at each connection

M.9 Steel Stress-Strain Curve

Stress-Strain Curve of Steel Rod 123: Stress-Strain Curve of Steel rod on 'Rod Level 3' of the 'Connection 12', which is located in 'Column Line 1' on 'Story 2'. (Rod Pattern in Figure 3-8)

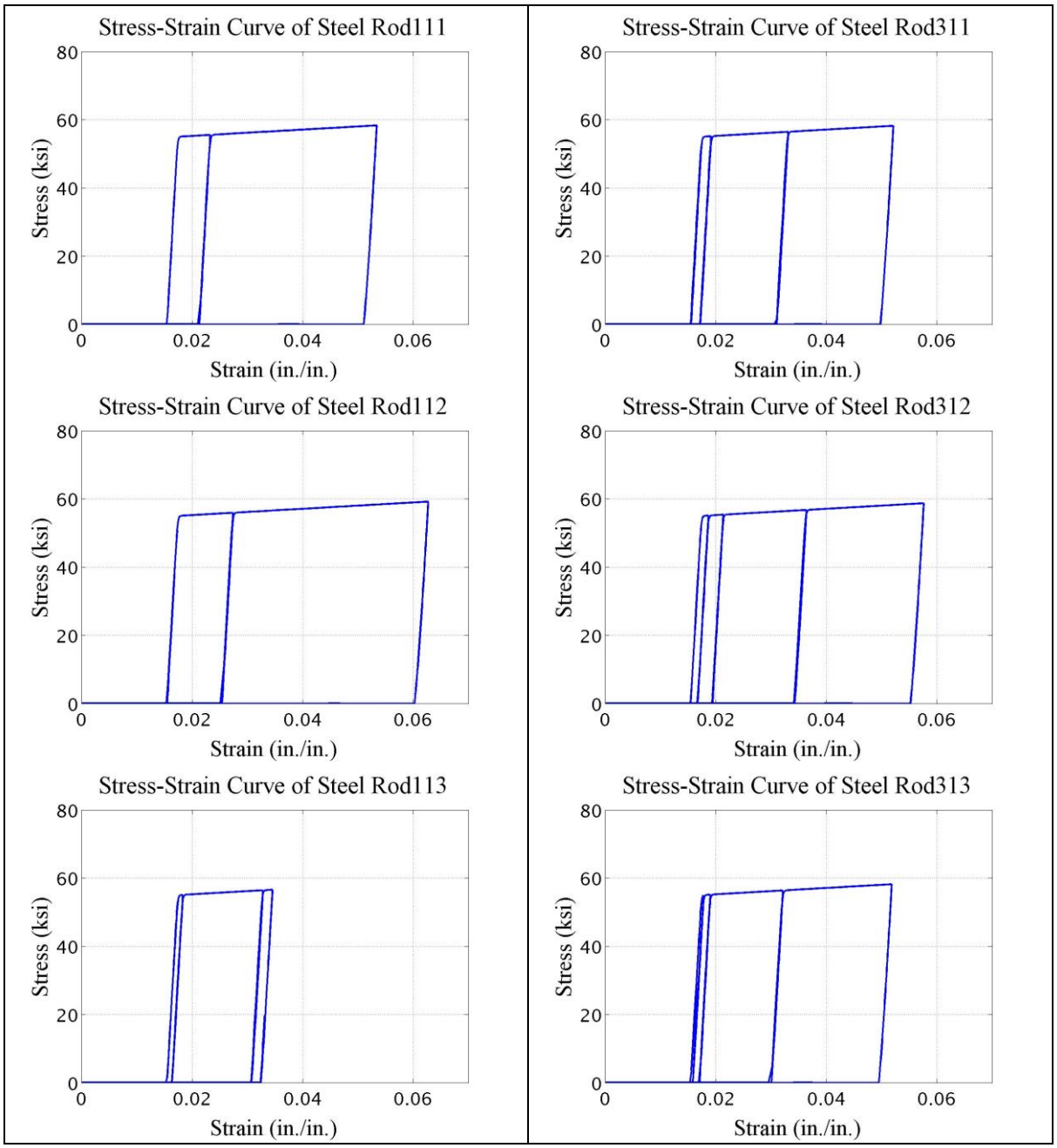

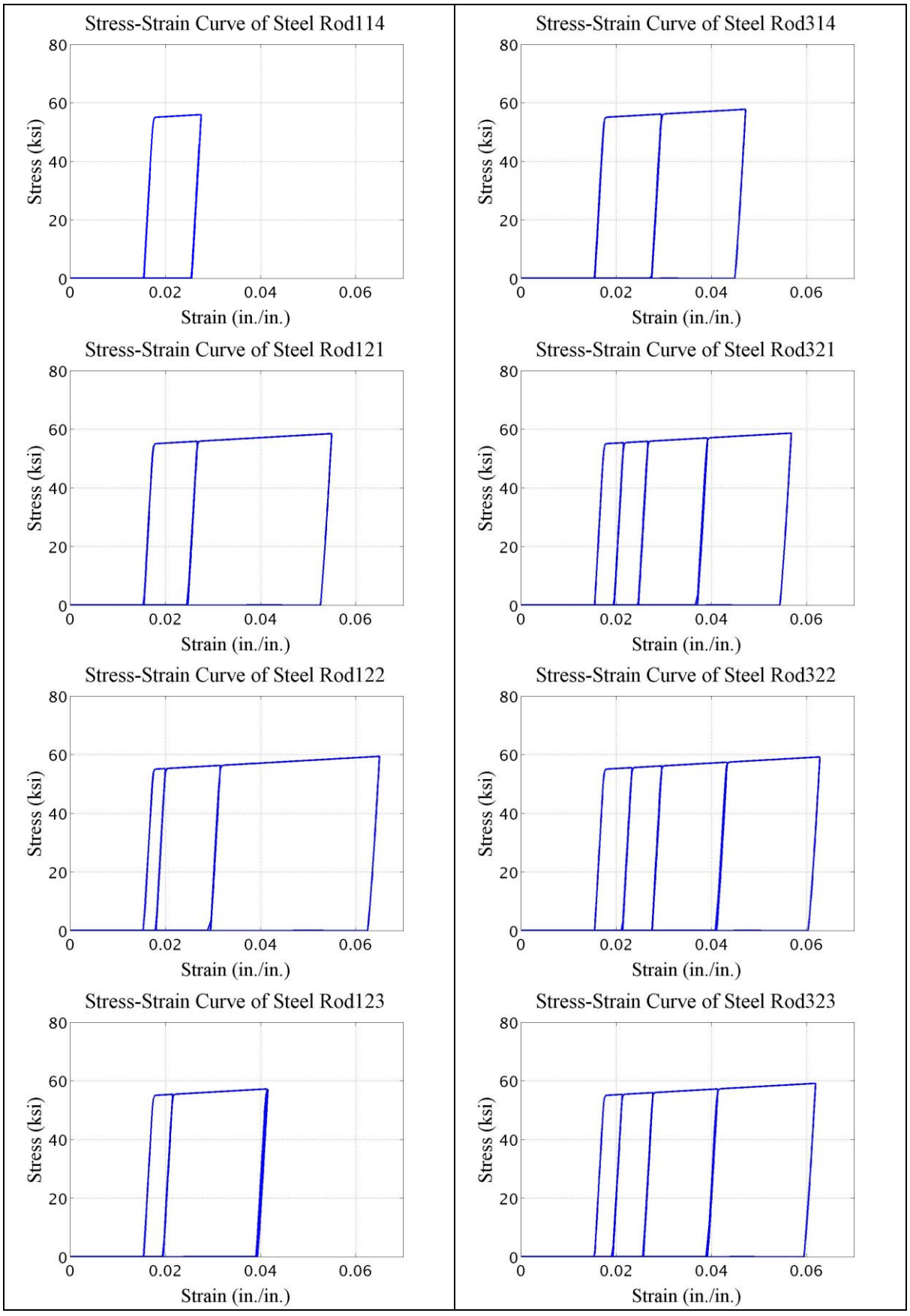
Stress-Strain Curve of Steel Rod114
Stress-Strain Curve of Steel Rod314
Stress-Strain Curve of Steel Rod121
Stress-Strain Curve of Steel Rod321
Stress-Strain Curve of Steel Rod122
Stress-Strain Curve of Steel Rod322
Stress-Strain Curve of Steel Rod123
Stress-Strain Curve of Steel Rod323
Stress (ksi)
Strain (in./in.)
0
20
40
60
80
0.02
0.04
0.06

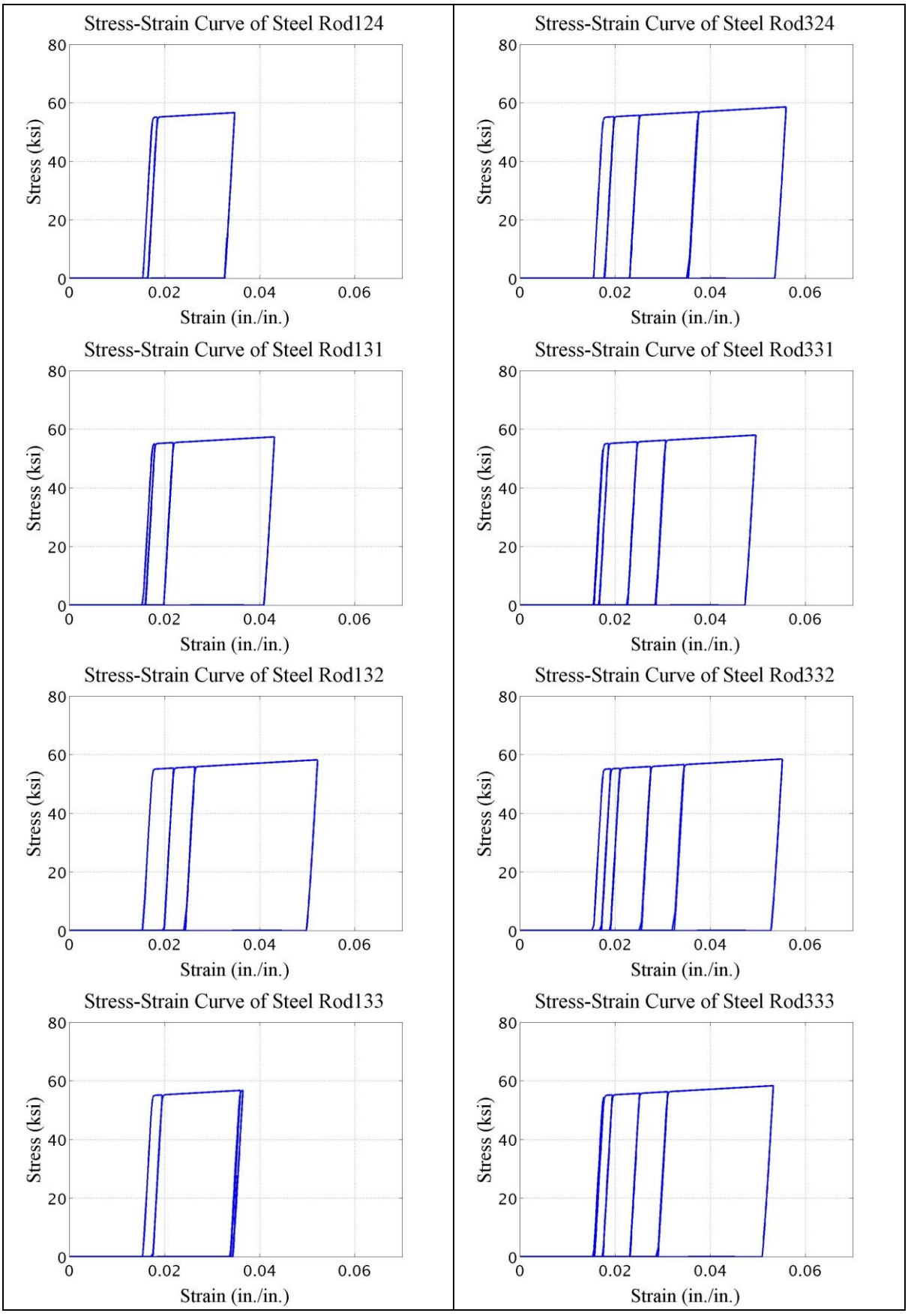
Stress-Strain Curve of Steel Rod124
Stress-Strain Curve of Steel Rod324
Stress-Strain Curve of Steel Rod131
Stress-Strain Curve of Steel Rod331
Stress-Strain Curve of Steel Rod132
Stress-Strain Curve of Steel Rod332
Stress-Strain Curve of Steel Rod133
Stress-Strain Curve of Steel Rod333
Stress (ksi)
Strain (in./in.)
0
20
40
60
80
0.02
0.04
0.06

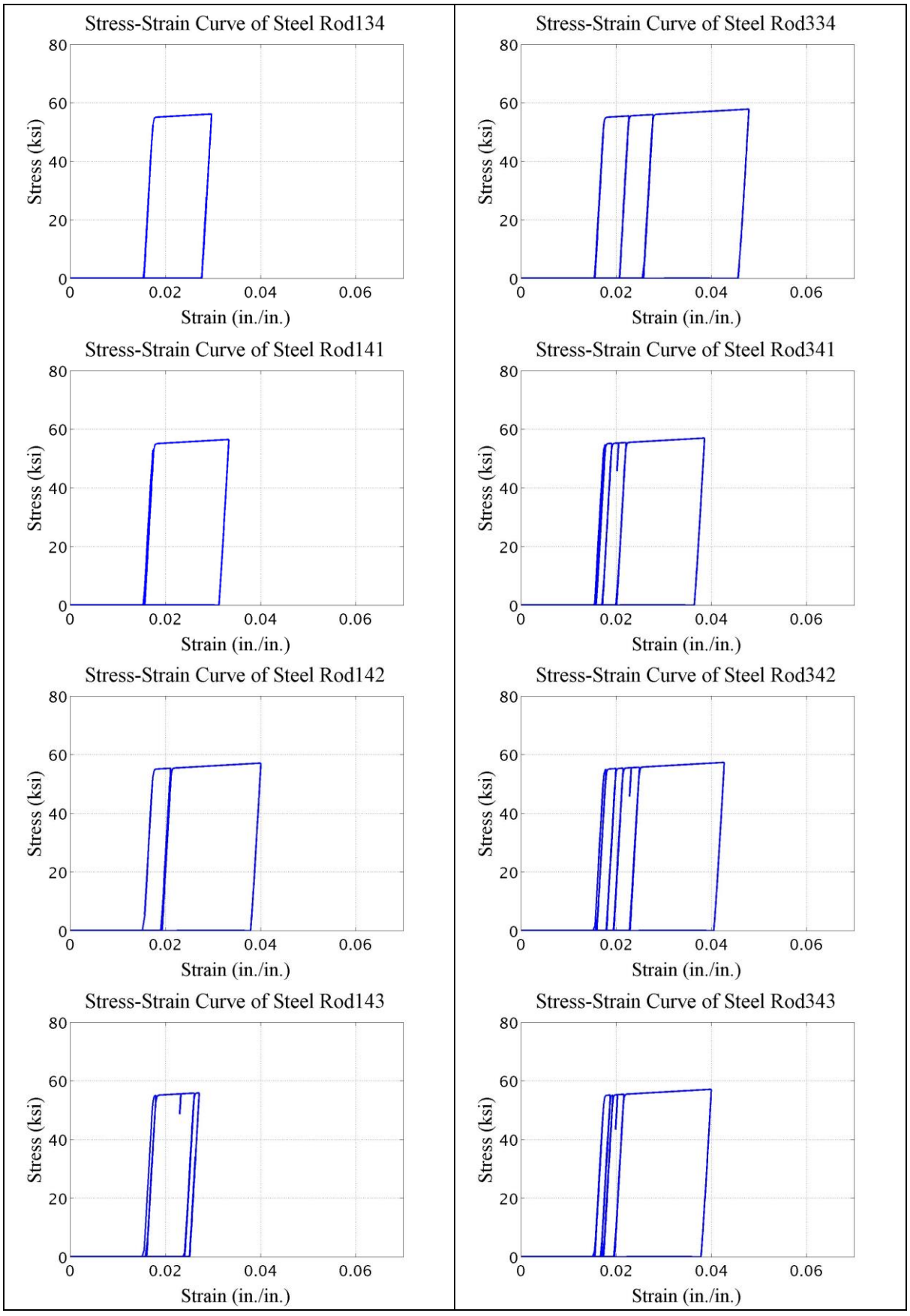
Stress-Strain Curve of Steel Rod134
Stress-Strain Curve of Steel Rod334
Stress-Strain Curve of Steel Rod141
Stress-Strain Curve of Steel Rod341
Stress-Strain Curve of Steel Rod142
Stress-Strain Curve of Steel Rod342
Stress-Strain Curve of Steel Rod143
Stress-Strain Curve of Steel Rod343
Stress (ksi)
Strain (in./in.)
0
20
40
60
80
0.02
0.04
0.06

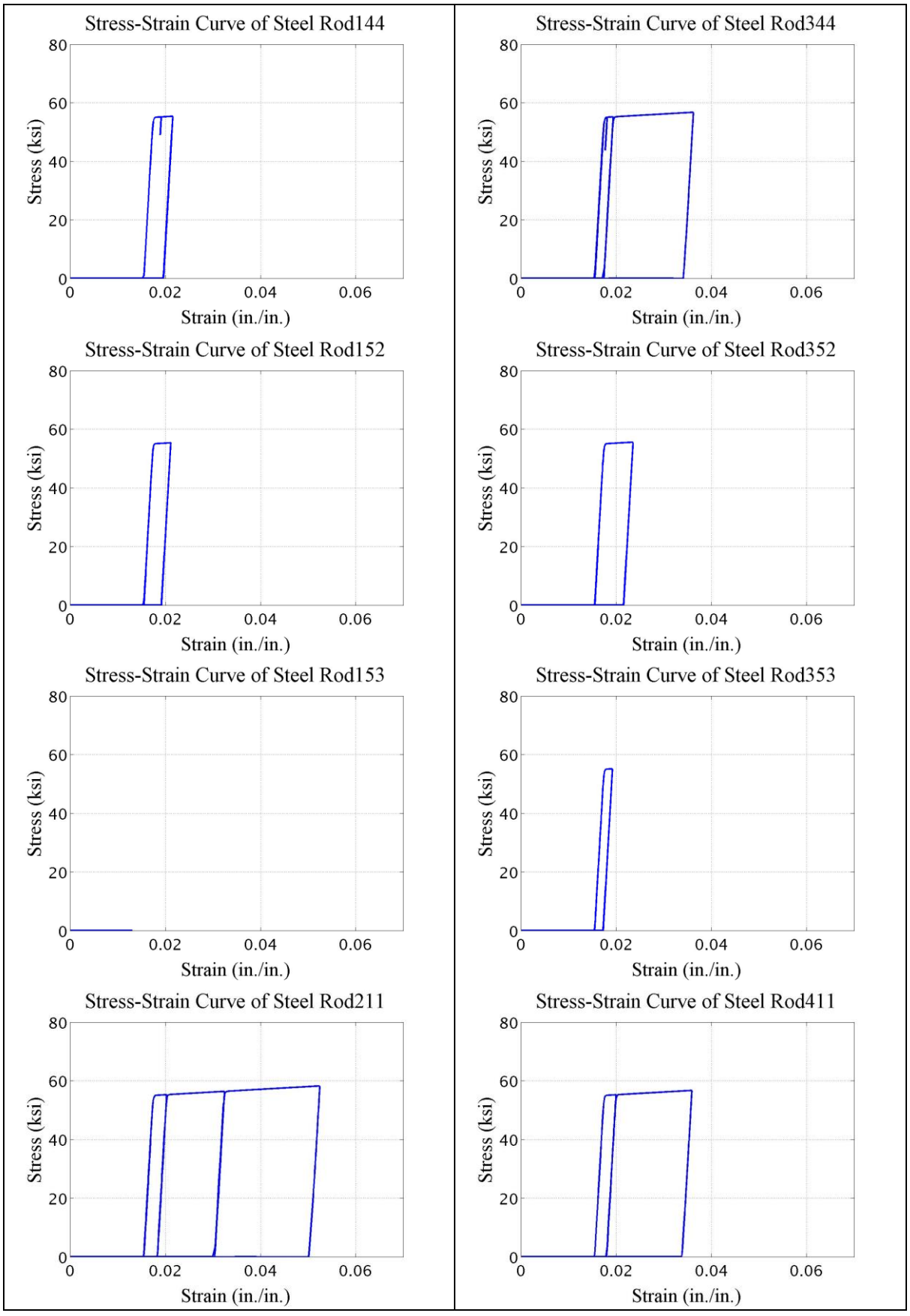
Stress-Strain Curve of Steel Rod144
Stress (ksi)
Strain (in./in.)
Stress-Strain Curve of Steel Rod344
Stress (ksi)
Strain (in./in.)
Stress-Strain Curve of Steel Rod152
Stress (ksi)
Strain (in./in.)
Stress-Strain Curve of Steel Rod352
Stress (ksi)
Strain (in./in.)
Stress-Strain Curve of Steel Rod153
Stress (ksi)
Strain (in./in.)
Stress-Strain Curve of Steel Rod353
Stress (ksi)
Strain (in./in.)
Stress-Strain Curve of Steel Rod211
Stress (ksi)
Strain (in./in.)
Stress-Strain Curve of Steel Rod411
Stress (ksi)
Strain (in./in.)

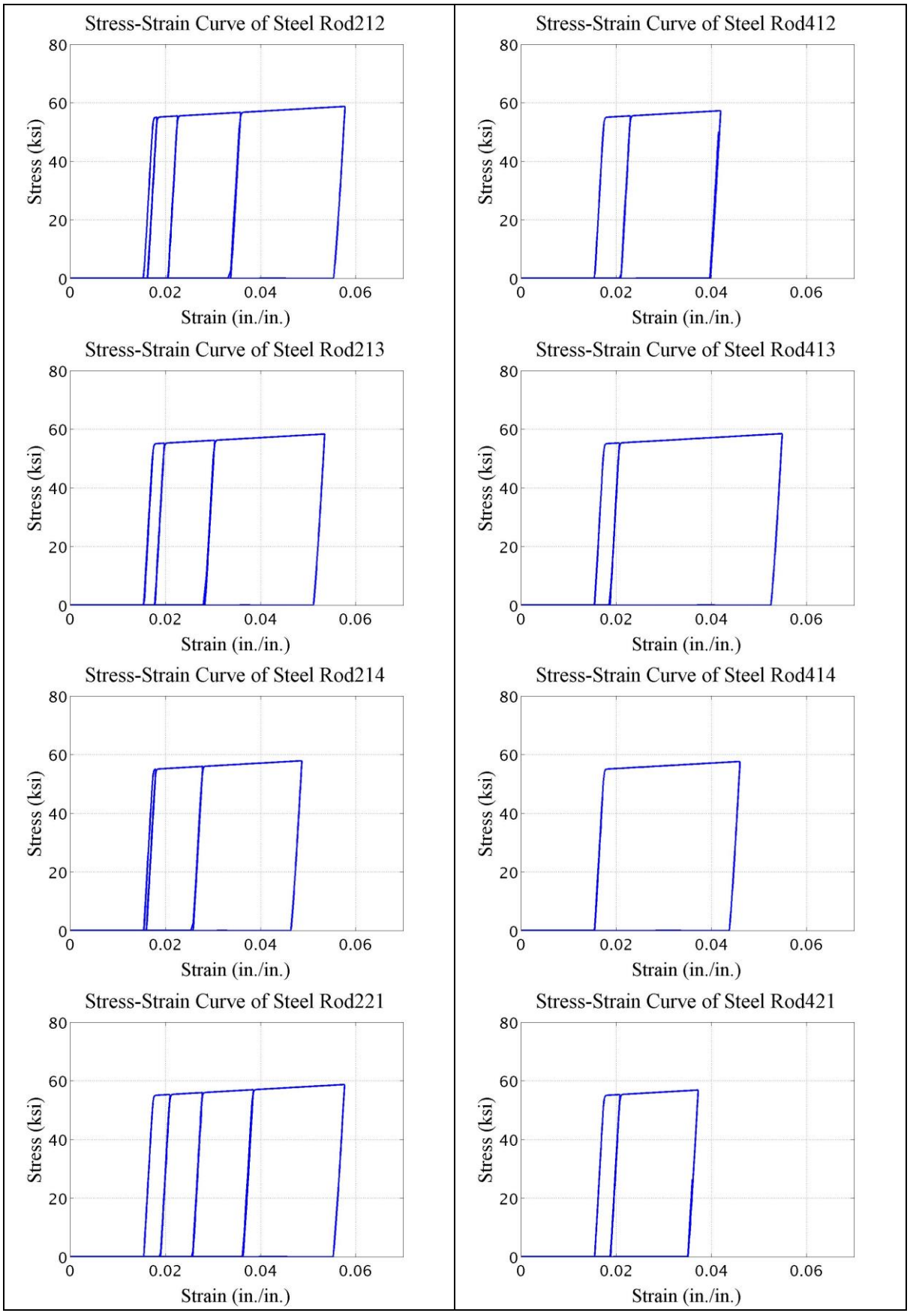
Stress-Strain Curve of Steel Rod212
Stress (ksi)
Strain (in./in.)
Stress-Strain Curve of Steel Rod412
Stress (ksi)
Strain (in./in.)
Stress-Strain Curve of Steel Rod213
Stress (ksi)
Strain (in./in.)
Stress-Strain Curve of Steel Rod413
Stress (ksi)
Strain (in./in.)
Stress-Strain Curve of Steel Rod214
Stress (ksi)
Strain (in./in.)
Stress-Strain Curve of Steel Rod414
Stress (ksi)
Strain (in./in.)
Stress-Strain Curve of Steel Rod221
Stress (ksi)
Strain (in./in.)
Stress-Strain Curve of Steel Rod421
Stress (ksi)
Strain (in./in.)

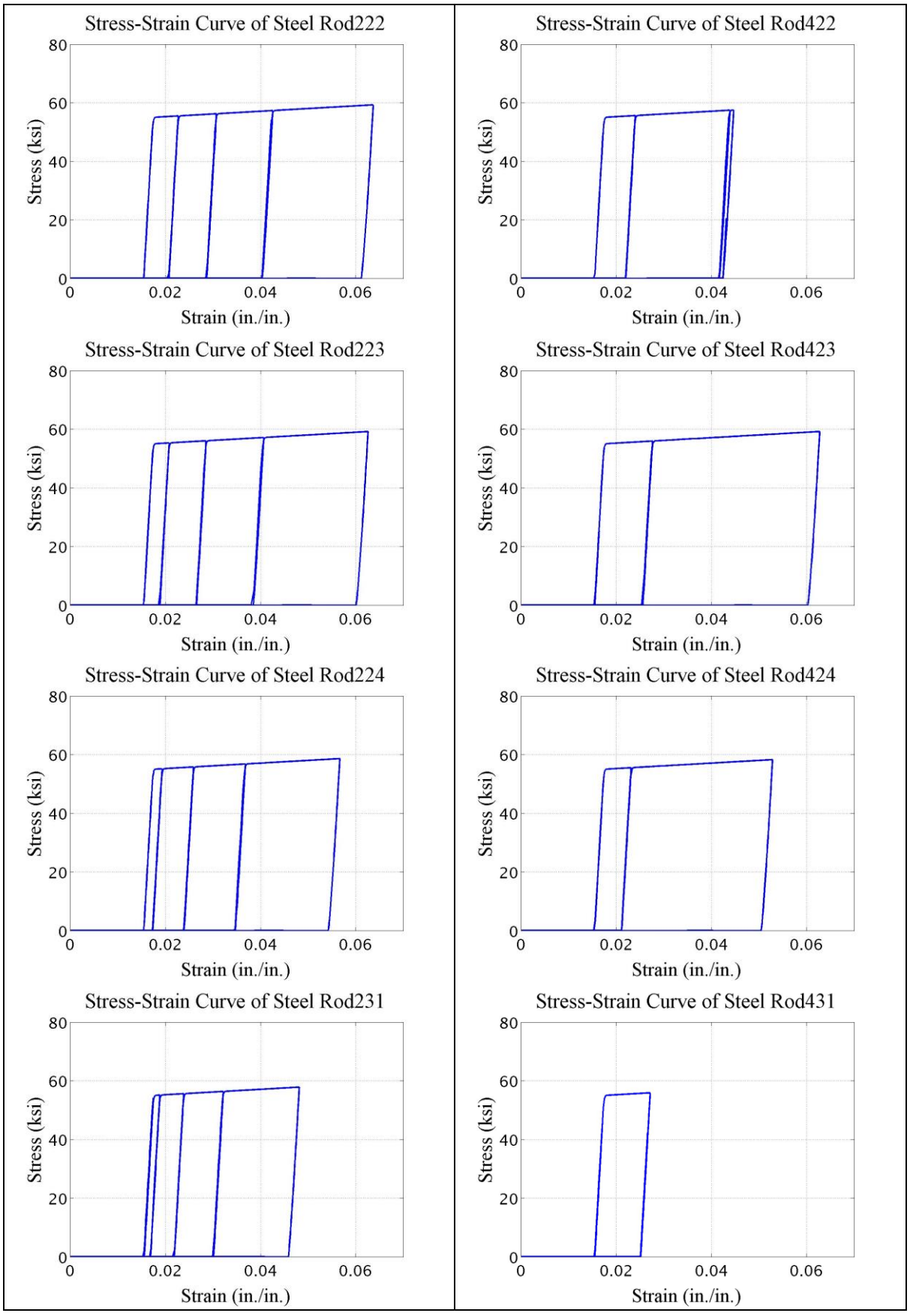
Stress-Strain Curve of Steel Rod222
Stress (ksi)
Strain (in./in.)
Stress-Strain Curve of Steel Rod422
Stress (ksi)
Strain (in./in.)
Stress-Strain Curve of Steel Rod223
Stress (ksi)
Strain (in./in.)
Stress-Strain Curve of Steel Rod423
Stress (ksi)
Strain (in./in.)
Stress-Strain Curve of Steel Rod224
Stress (ksi)
Strain (in./in.)
Stress-Strain Curve of Steel Rod424
Stress (ksi)
Strain (in./in.)
Stress-Strain Curve of Steel Rod231
Stress (ksi)
Strain (in./in.)
Stress-Strain Curve of Steel Rod431
Stress (ksi)
Strain (in./in.)

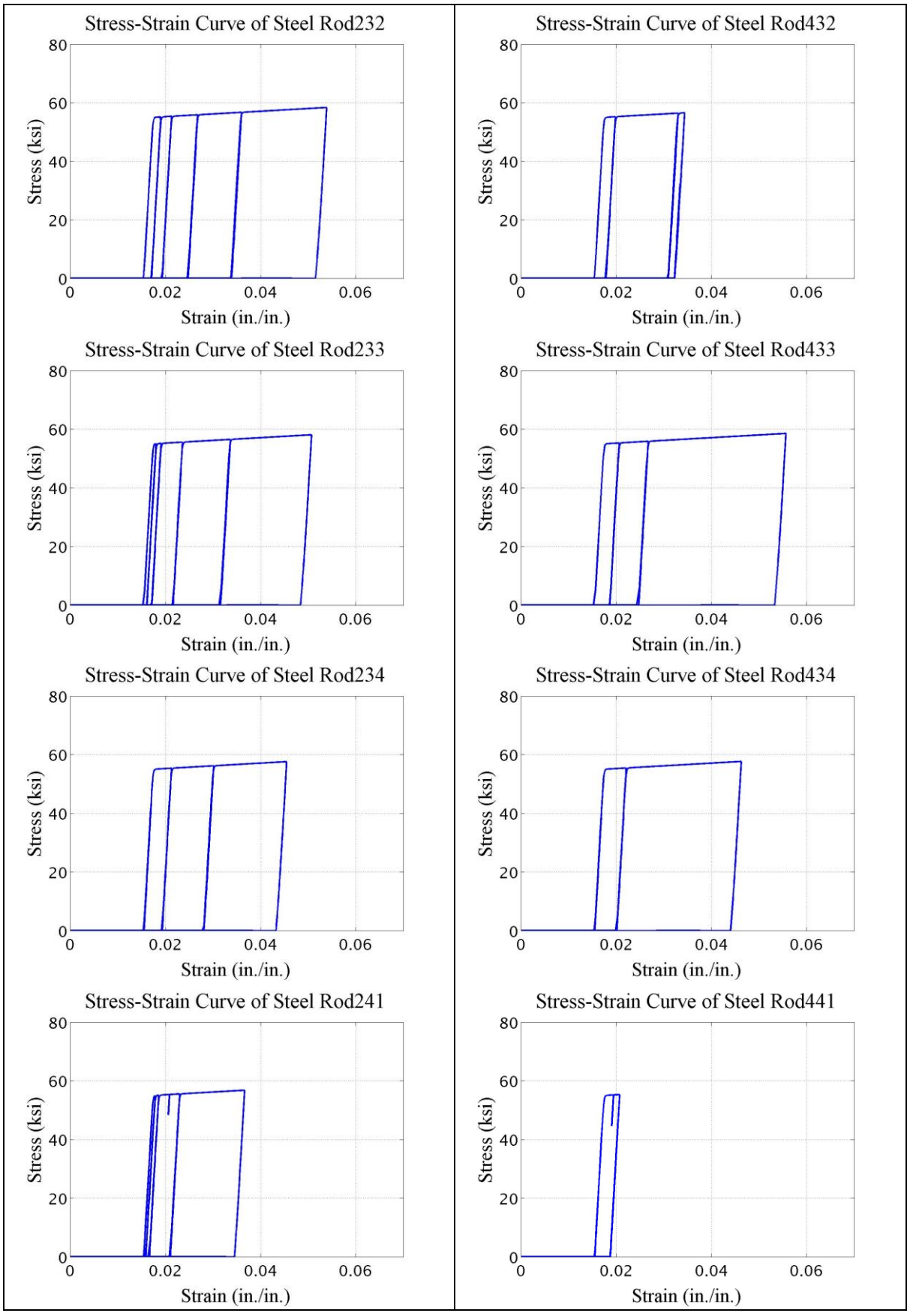
Stress-Strain Curve of Steel Rod232
Stress (ksi)
Strain (in./in.)
Stress-Strain Curve of Steel Rod432
Stress (ksi)
Strain (in./in.)
Stress-Strain Curve of Steel Rod233
Stress (ksi)
Strain (in./in.)
Stress-Strain Curve of Steel Rod433
Stress (ksi)
Strain (in./in.)
Stress-Strain Curve of Steel Rod234
Stress (ksi)
Strain (in./in.)
Stress-Strain Curve of Steel Rod434
Stress (ksi)
Strain (in./in.)
Stress-Strain Curve of Steel Rod241
Stress (ksi)
Strain (in./in.)
Stress-Strain Curve of Steel Rod441
Stress (ksi)
Strain (in./in.)

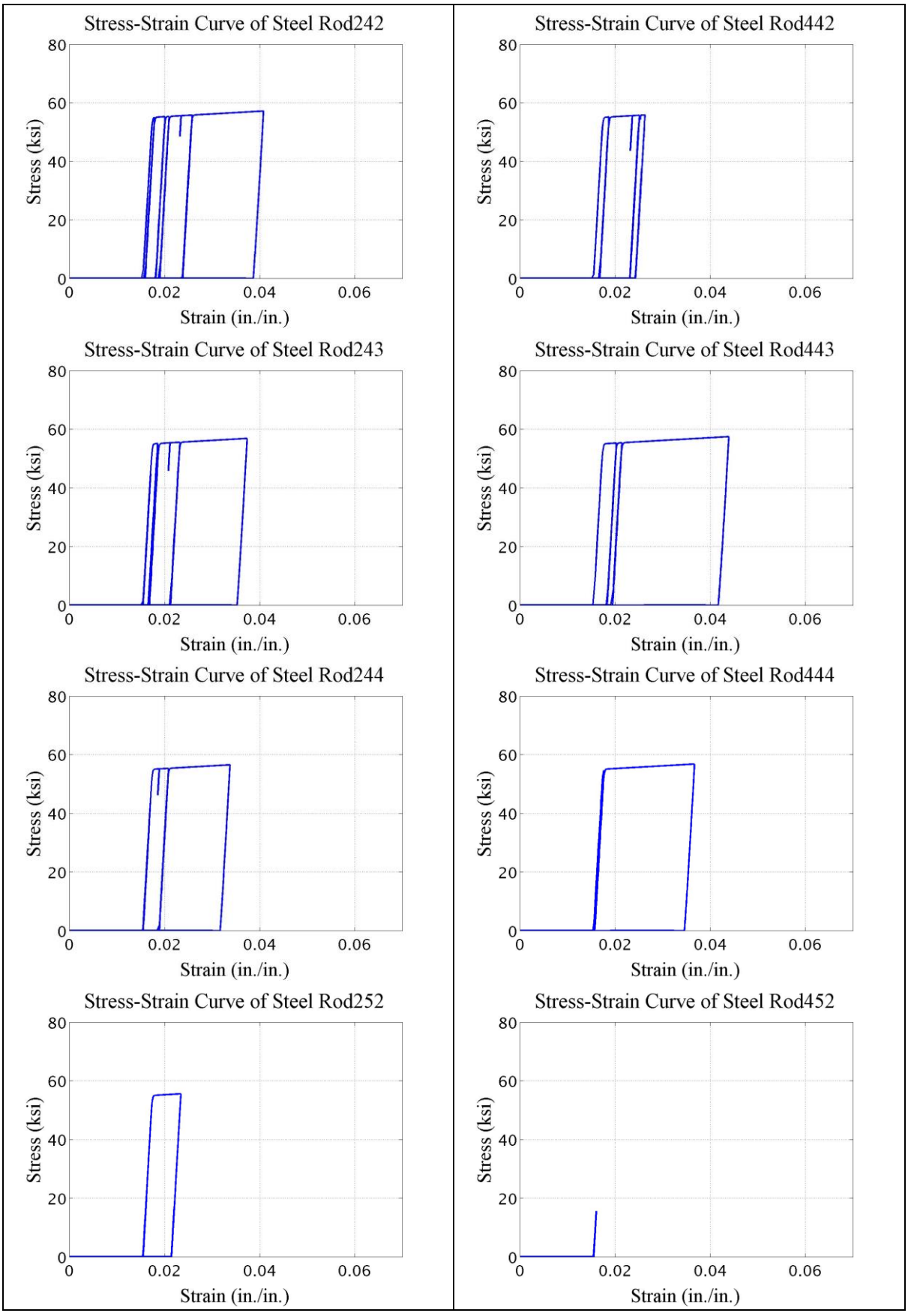
Stress-Strain Curve of Steel Rod242
Stress-Strain Curve of Steel Rod442
Stress-Strain Curve of Steel Rod243
Stress-Strain Curve of Steel Rod443
Stress-Strain Curve of Steel Rod244
Stress-Strain Curve of Steel Rod444
Stress-Strain Curve of Steel Rod252
Stress-Strain Curve of Steel Rod452
Stress (ksi)
Strain (in./in.)
0
20
40
60
80
0.02
0.04
0.06

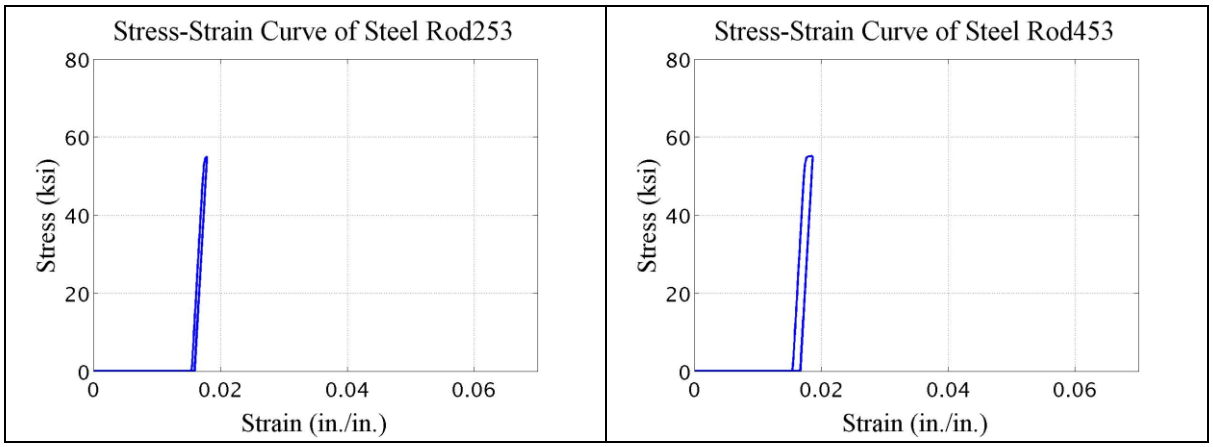

Appendix Figure M-9: Steel stress-strain curve

M.10 Steel Rod Force

Axial Force of Steel Rod 123: Axial force of Steel rod on 'Rod Level 3' of the 'Connection 12', which is located in 'Column Line 1' on 'Story 2'. (See Rod Pattern in Figure 3-8)

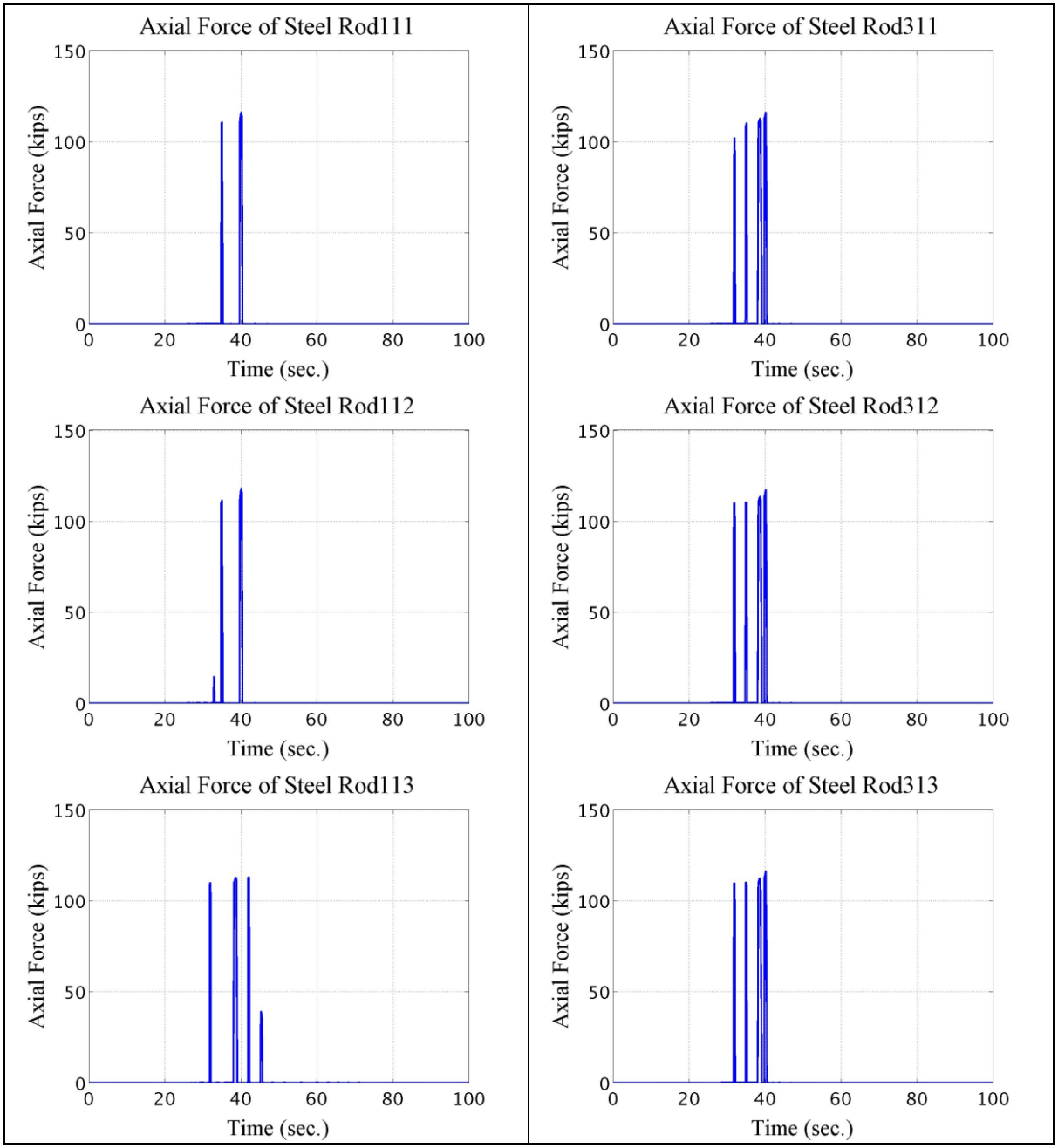

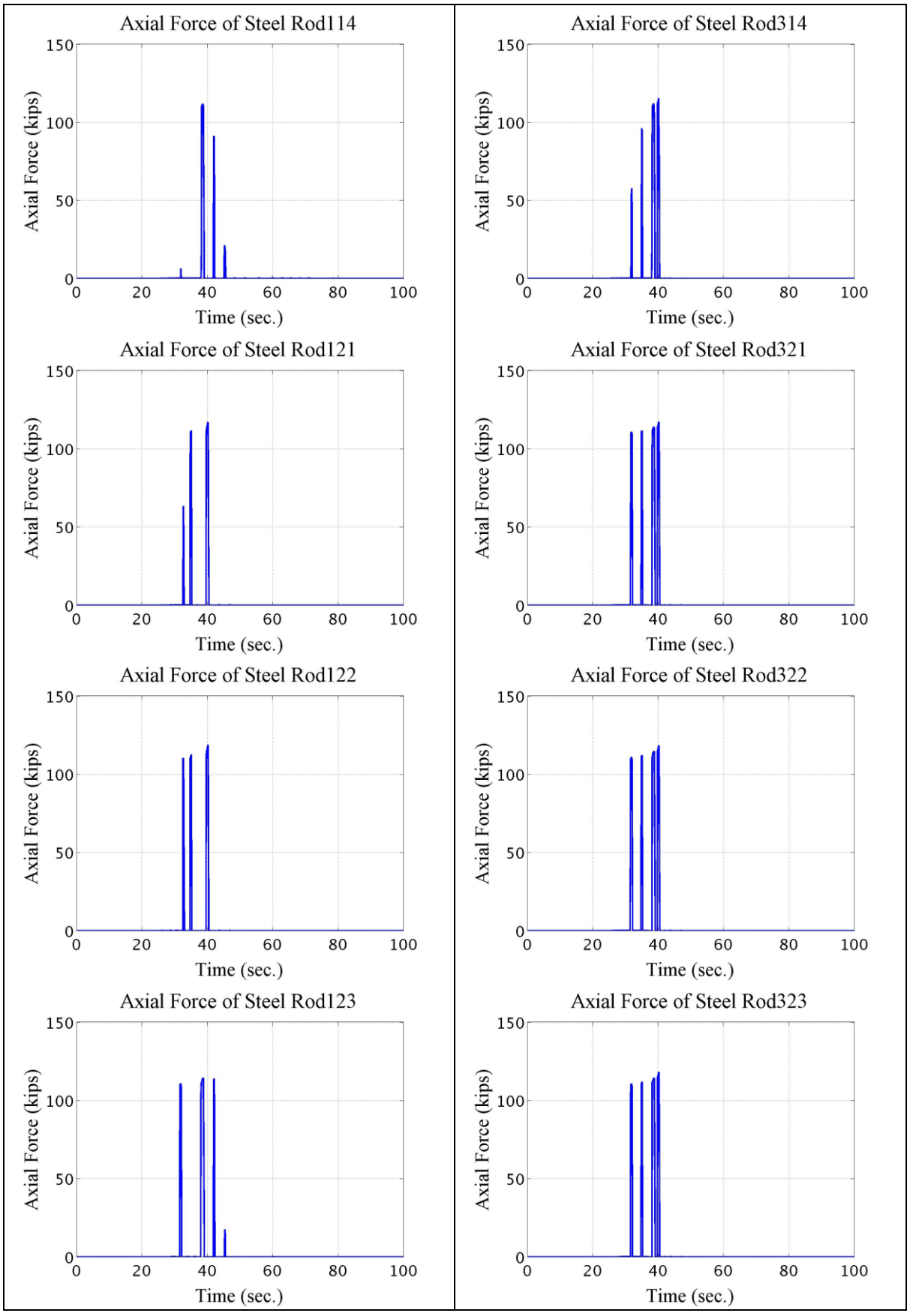
Axial Force of Steel Rod114
Axial Force of Steel Rod314
Axial Force of Steel Rod121
Axial Force of Steel Rod321
Axial Force of Steel Rod122
Axial Force of Steel Rod322
Axial Force of Steel Rod123
Axial Force of Steel Rod323
Axial Force (kips)
Time (sec.)
0
50
100
150
0
20
40
60
80
100

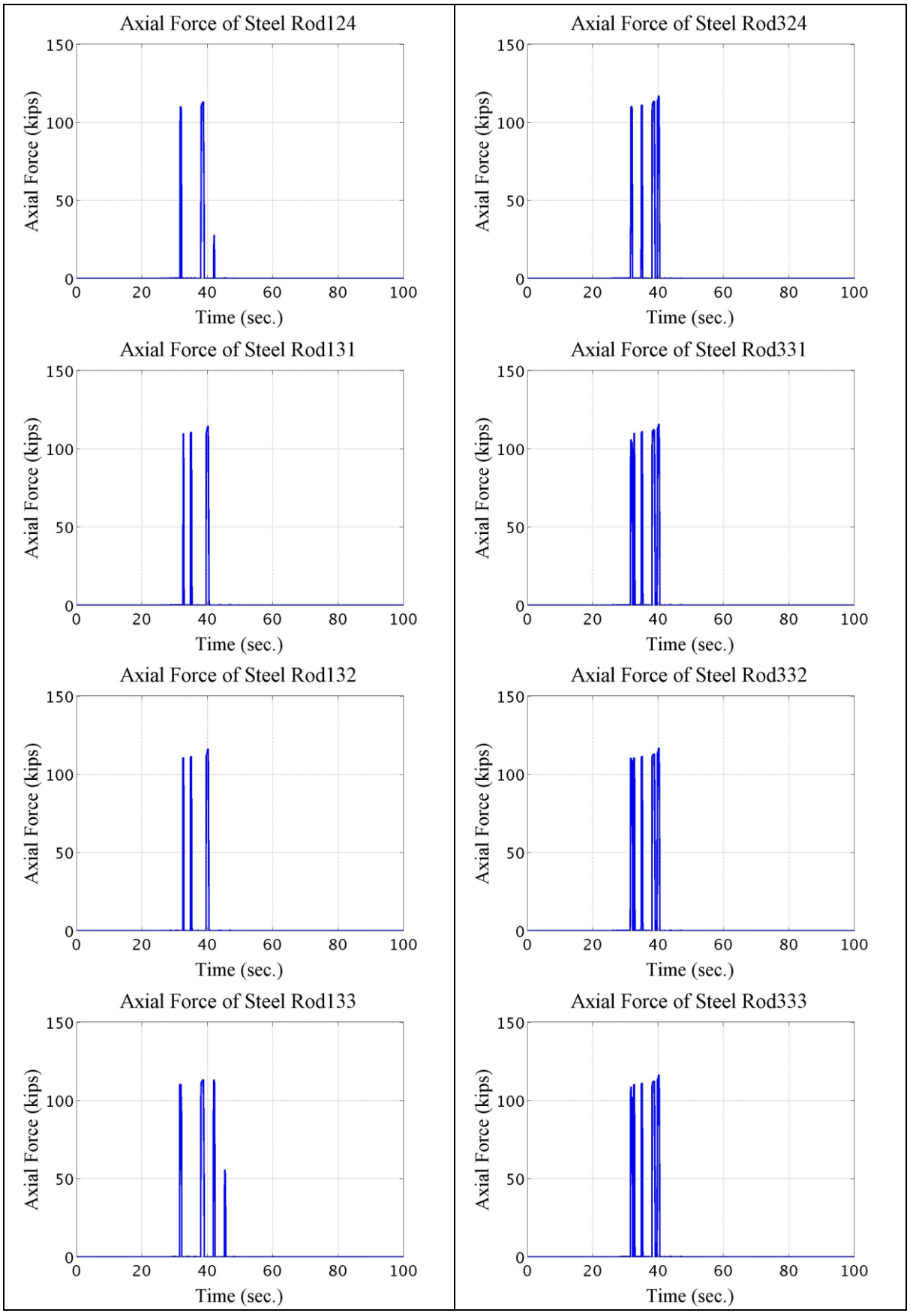
Axial Force of Steel Rod124
Axial Force of Steel Rod324
Axial Force of Steel Rod131
Axial Force of Steel Rod331
Axial Force of Steel Rod132
Axial Force of Steel Rod332
Axial Force of Steel Rod133
Axial Force of Steel Rod333
Axial Force (kips)
Time (sec.)
0
50
100
150
0
20
40
60
80
100

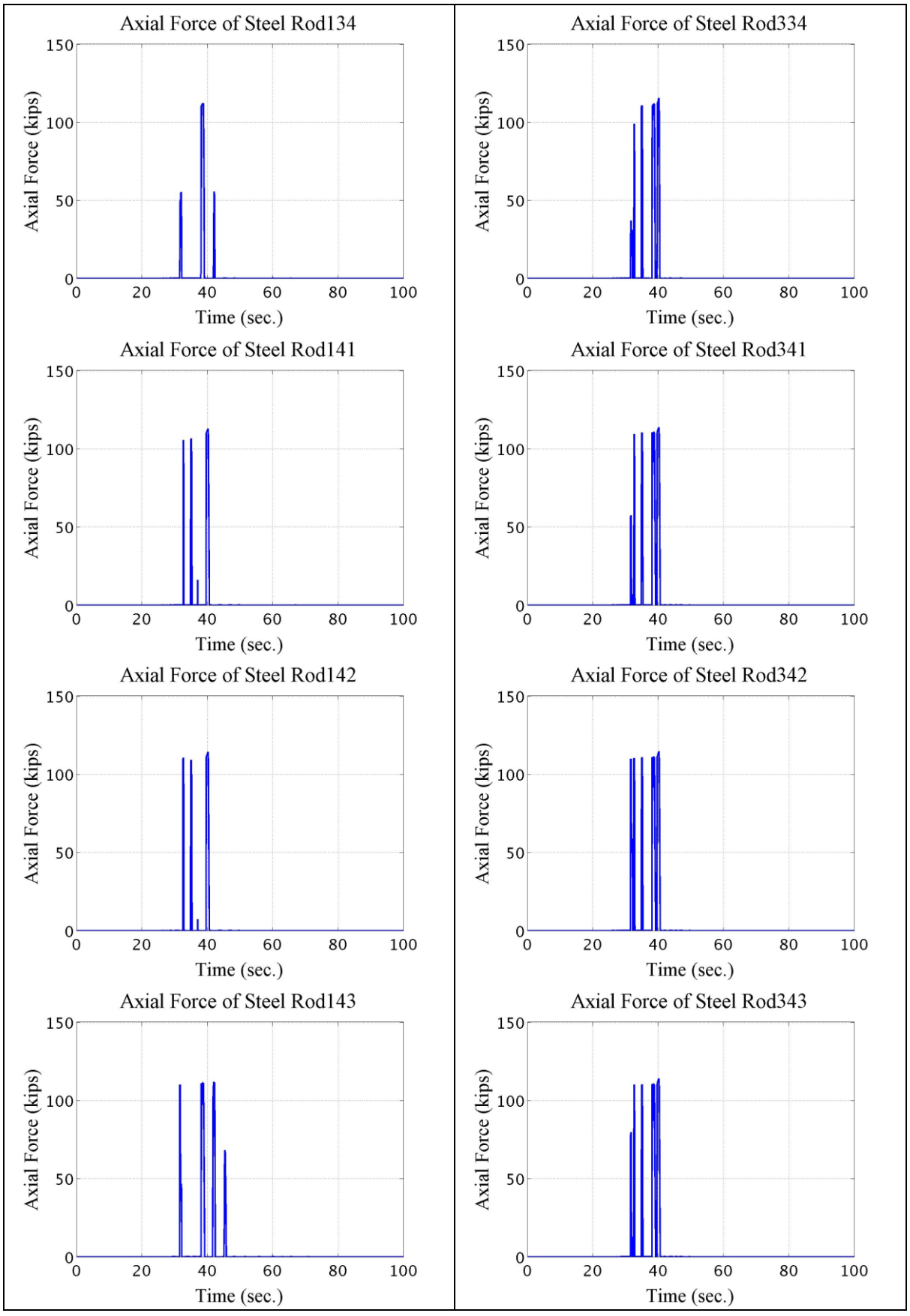
Axial Force of Steel Rod134
Axial Force of Steel Rod334
Axial Force of Steel Rod141
Axial Force of Steel Rod341
Axial Force of Steel Rod142
Axial Force of Steel Rod342
Axial Force of Steel Rod143
Axial Force of Steel Rod343
Axial Force (kips)
Time (sec.)
0
50
100
150
0
20
40
60
80
100

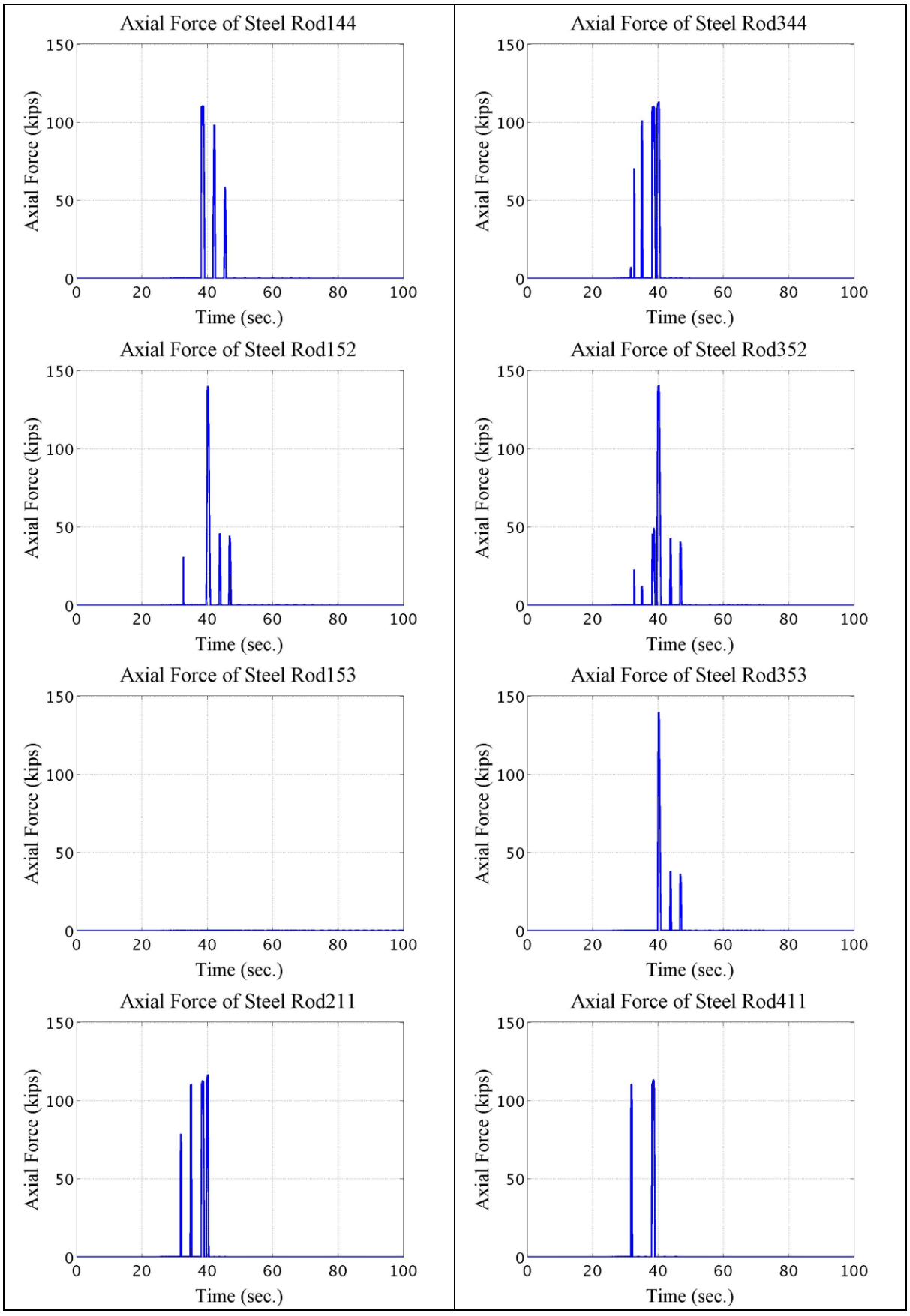
Axial Force of Steel Rod144
Axial Force of Steel Rod344
Axial Force of Steel Rod152
Axial Force of Steel Rod352
Axial Force of Steel Rod153
Axial Force of Steel Rod353
Axial Force of Steel Rod211
Axial Force of Steel Rod411
Axial Force (kips)
Time (sec.)
0
50
100
150
0
20
40
60
80
100

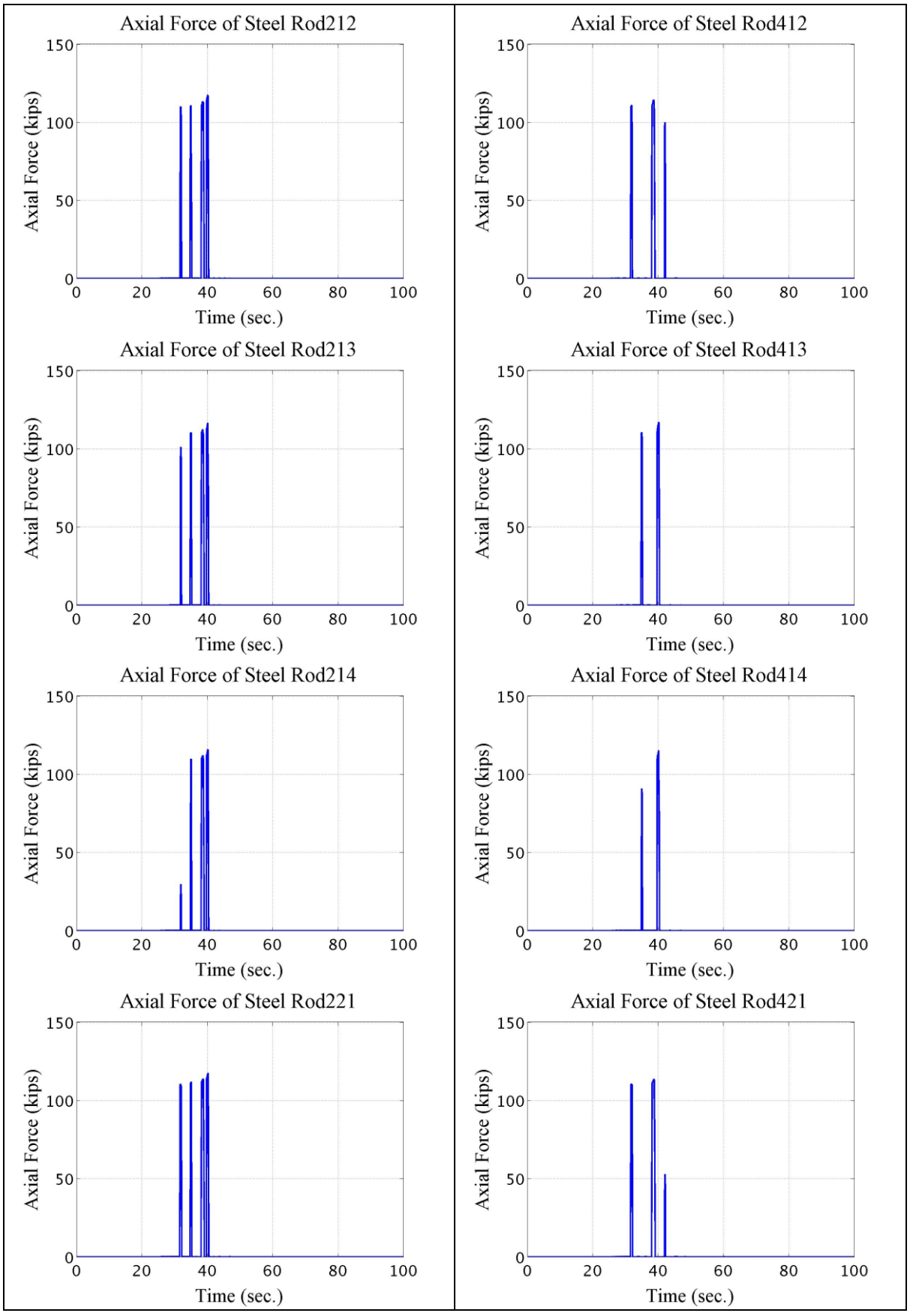
Axial Force of Steel Rod212
Axial Force of Steel Rod412
Axial Force of Steel Rod213
Axial Force of Steel Rod413
Axial Force of Steel Rod214
Axial Force of Steel Rod414
Axial Force of Steel Rod221
Axial Force of Steel Rod421
Axial Force (kips)
Time (sec.)
0
50
100
150
0
20
40
60
80
100

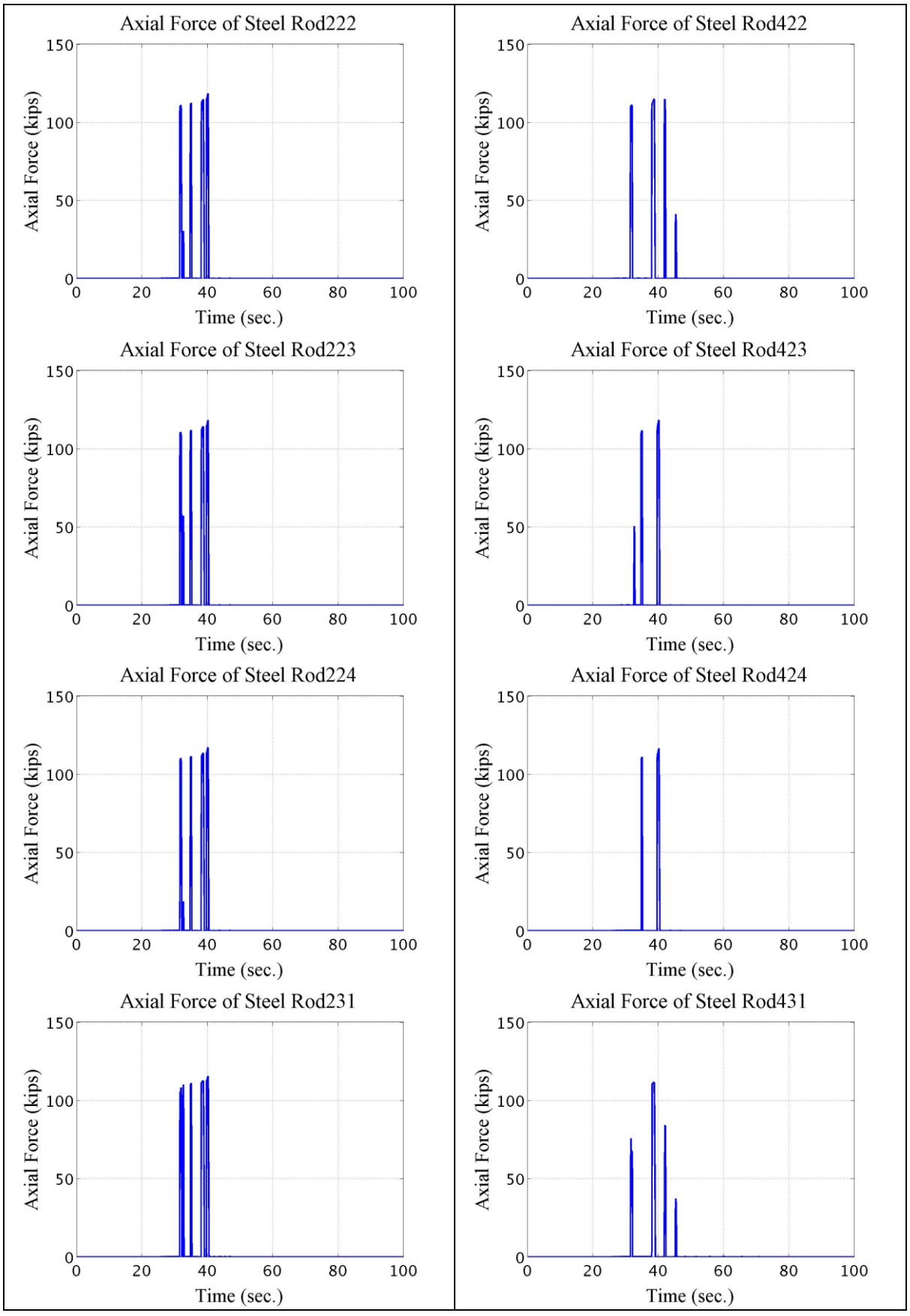
Axial Force of Steel Rod222
Axial Force of Steel Rod422
Axial Force of Steel Rod223
Axial Force of Steel Rod423
Axial Force of Steel Rod224
Axial Force of Steel Rod424
Axial Force of Steel Rod231
Axial Force of Steel Rod431
Axial Force (kips)
Time (sec.)
0
50
100
150
0
20
40
60
80
100

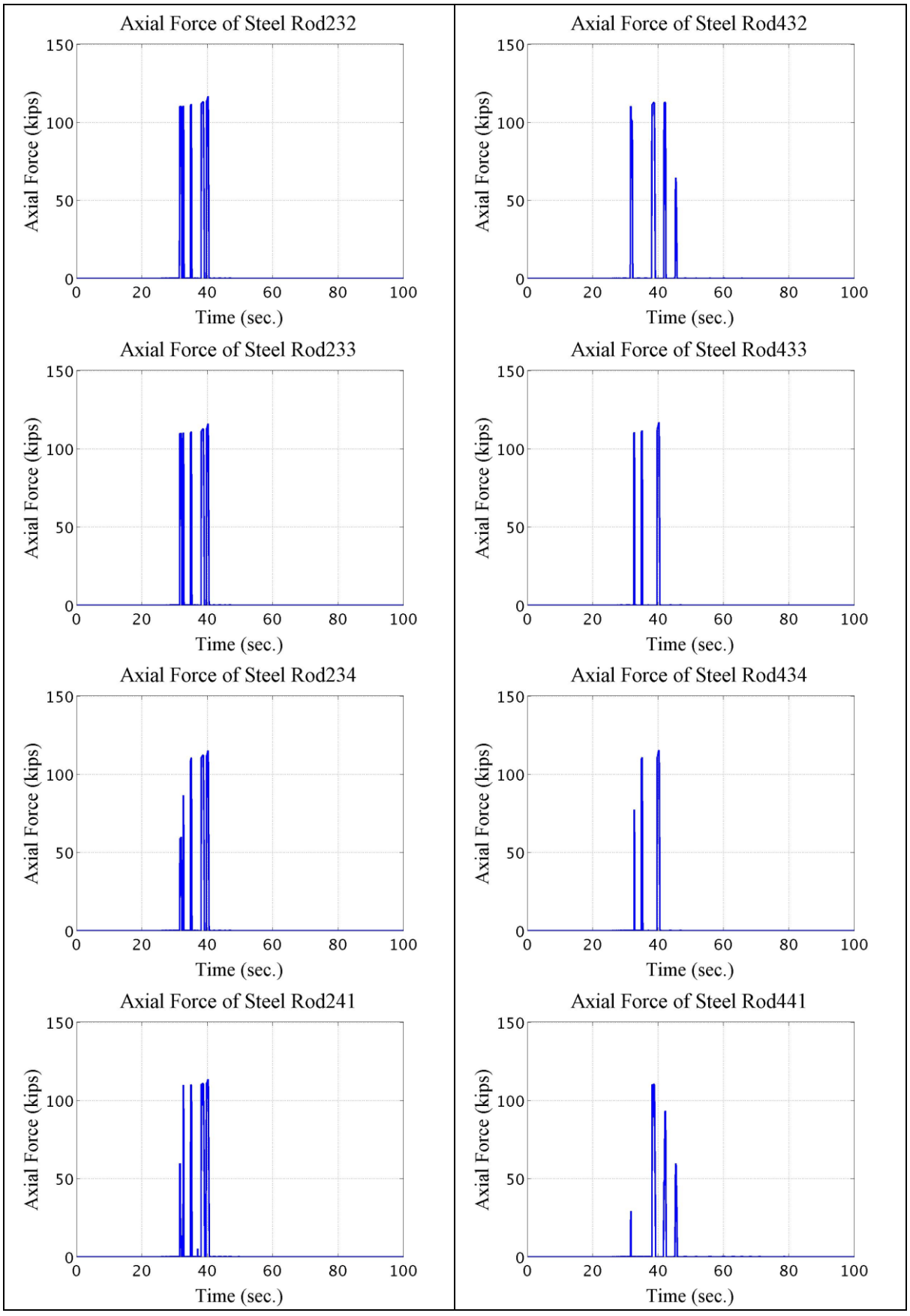
Axial Force of Steel Rod232
Axial Force of Steel Rod432
Axial Force of Steel Rod233
Axial Force of Steel Rod433
Axial Force of Steel Rod234
Axial Force of Steel Rod434
Axial Force of Steel Rod241
Axial Force of Steel Rod441
Axial Force (kips)
Time (sec.)
0
50
100
150
0
20
40
60
80
100

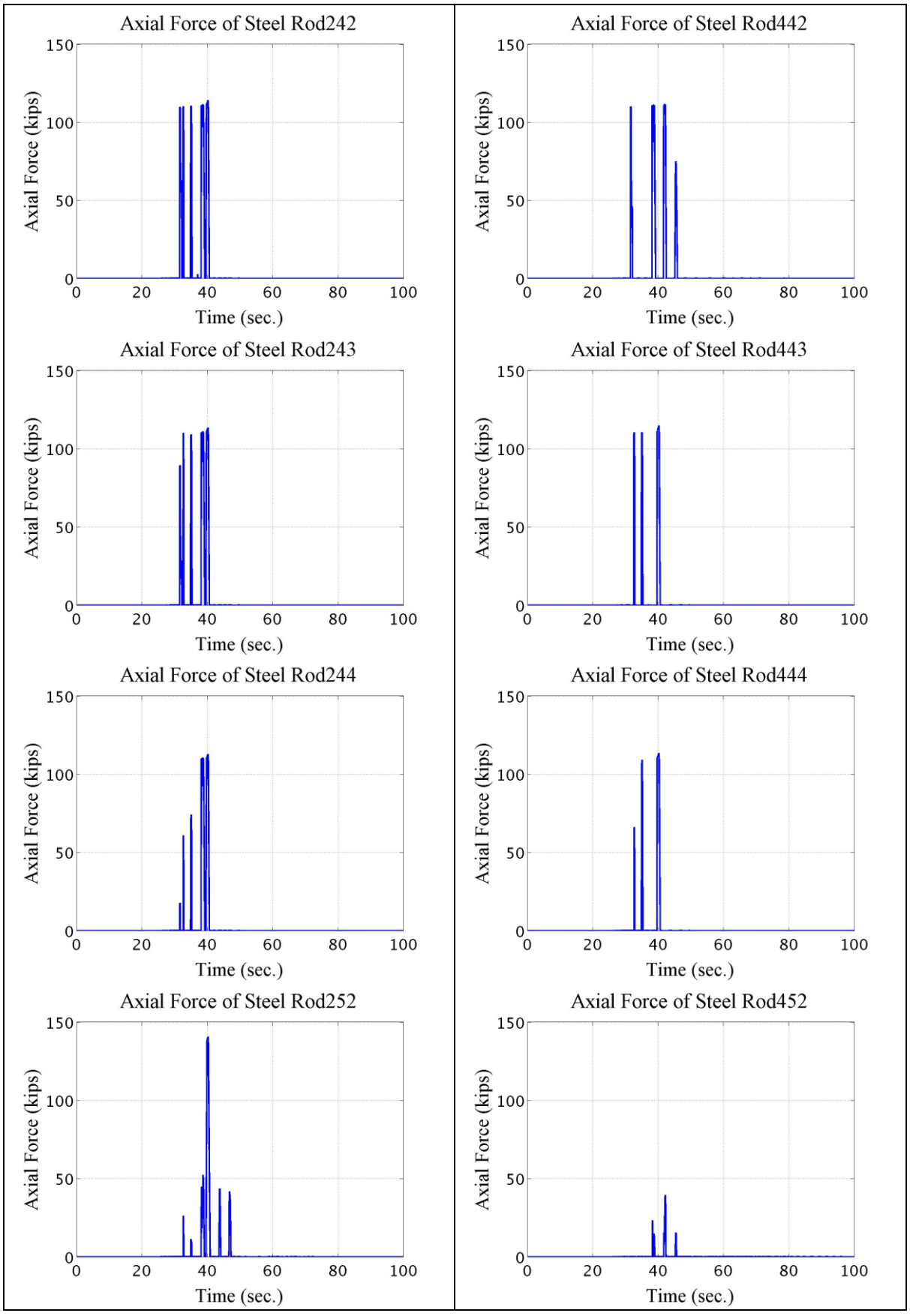
Axial Force of Steel Rod242
Axial Force of Steel Rod442
Axial Force of Steel Rod243
Axial Force of Steel Rod443
Axial Force of Steel Rod244
Axial Force of Steel Rod444
Axial Force of Steel Rod252
Axial Force of Steel Rod452
Axial Force (kips)
Time (sec.)
0
50
100
150
0
20
40
60
80
100

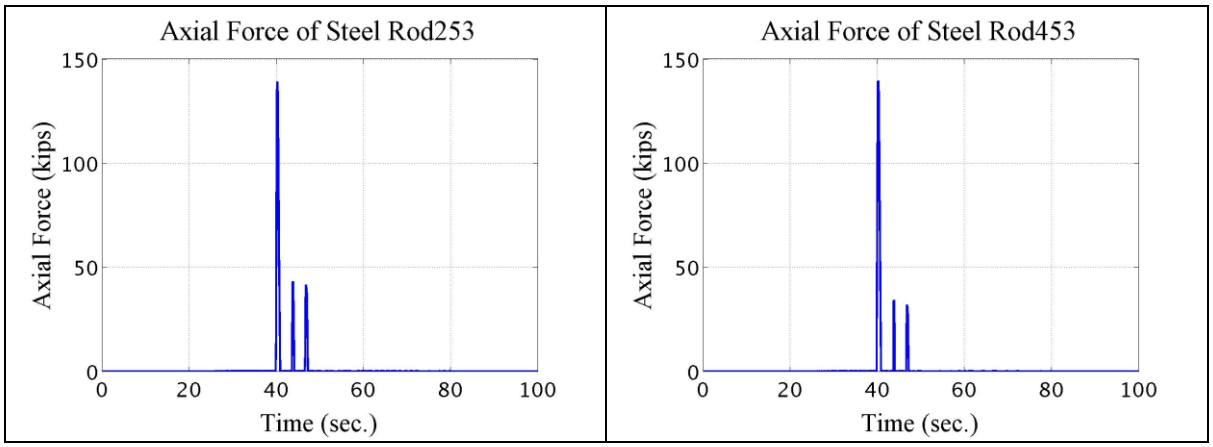

Appendix Figure M-10: Steel rod force

M.11 Total Force of Steel Rods at Each Connection

Total Axial Force of Steel Rods at Conn. 12: Total axial force of all Steel rods of the 'Connection 12', which is located in 'Column Line 1' on 'Story 2'.

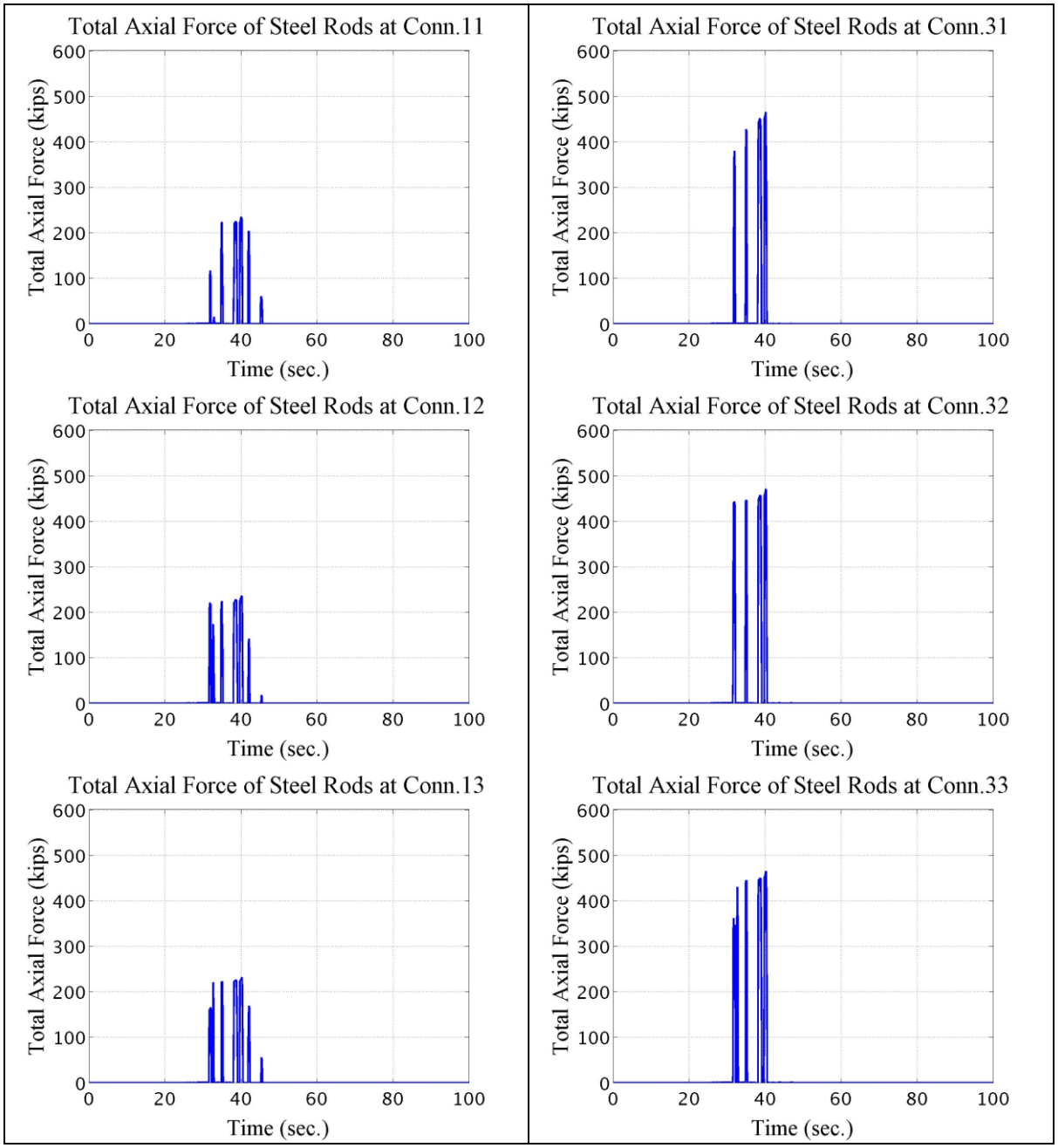

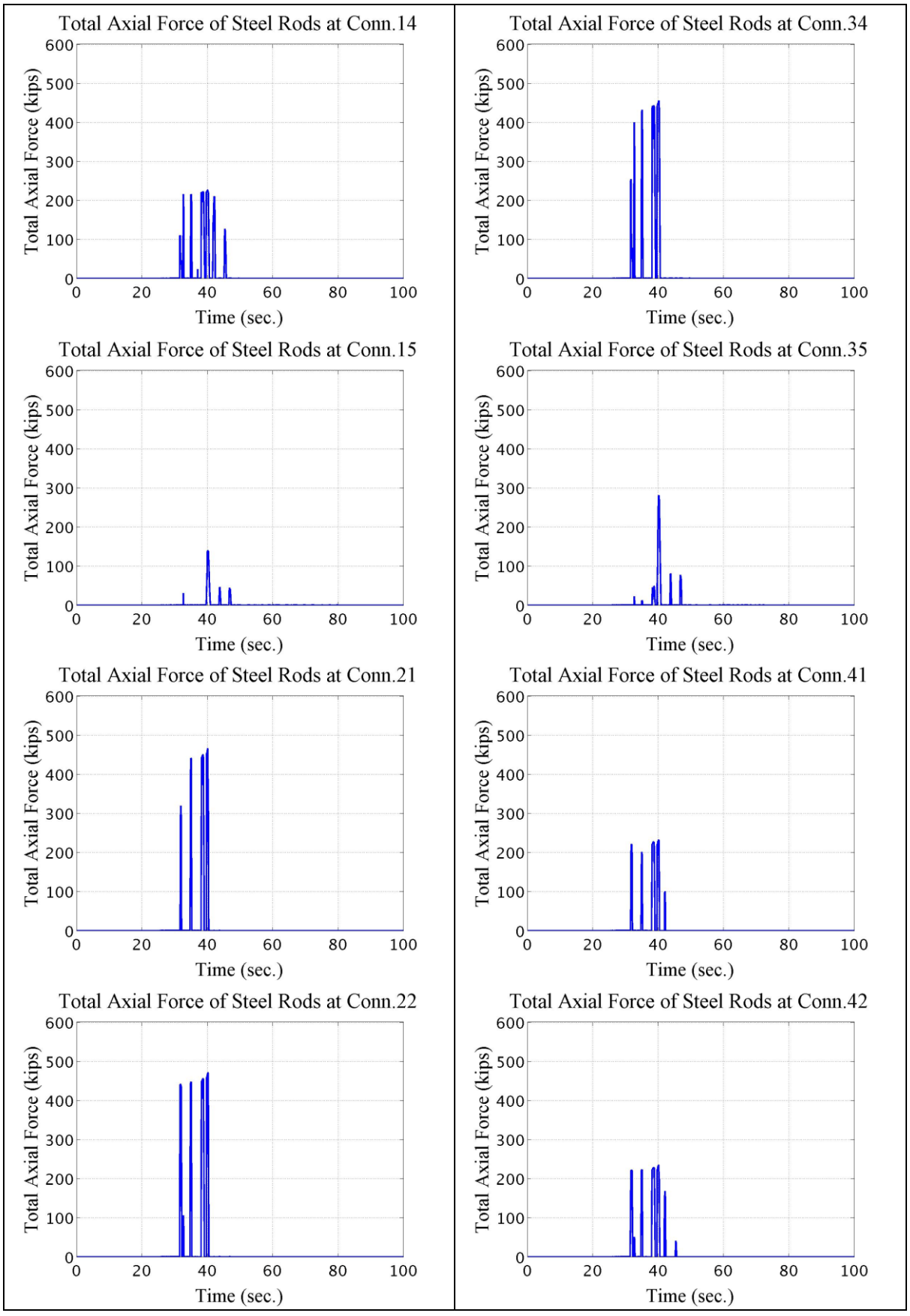
Total Axial Force of Steel Rods at Conn.14
Total Axial Force of Steel Rods at Conn.34
Total Axial Force of Steel Rods at Conn.15
Total Axial Force of Steel Rods at Conn.35
Total Axial Force of Steel Rods at Conn.21
Total Axial Force of Steel Rods at Conn.41
Total Axial Force of Steel Rods at Conn.22
Total Axial Force of Steel Rods at Conn.42
Total Axial Force (kips)
Time (sec.)
0
100
200
300
400
500
600
0
20
40
60
80
100

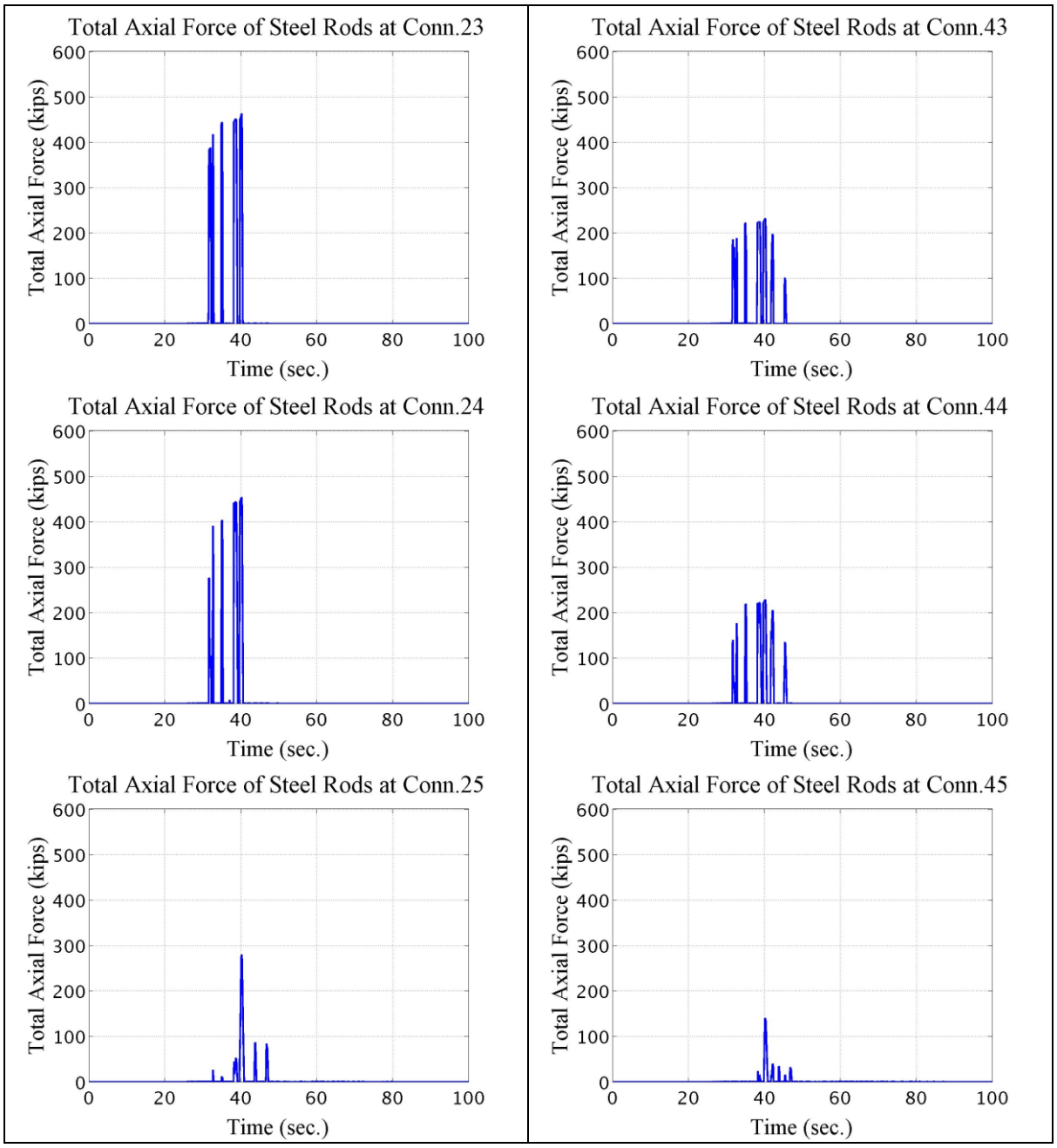

Appendix Figure M-11: Total force of steel rods at each connection